Special Issue Reprint

Testing of Materials and Elements in Civil Engineering (2nd Edition) Volume II

Edited by
Krzysztof Schabowicz

www.mdpi.com/journal/materials

MDPI

Testing of Materials and Elements in Civil Engineering (2nd Edition) —Volume II

Testing of Materials and Elements in Civil Engineering (2nd Edition) —Volume II

Editor

Krzysztof Schabowicz

Editor
Krzysztof Schabowicz
Wroclaw University of
Science and Technology
Poland

This is a reprint of articles from the Special Issue published online in the open access journal *Materials* (ISSN 1996-1944) (available at: https://www.mdpi.com/journal/materials/special_issues/testing_civil_engineering_2nd).

For citation purposes, cite each article independently as indicated on the article page online and as indicated below:

LastName, A.A.; LastName, B.B.; LastName, C.C. Article Title. *Journal Name* **Year**, *Volume Number*, Page Range.

Contents

About the Editor

Krzysztof Schabowicz

Krzysztof Schabowicz is author and co-author of 7 books, over 300 publications and 10 patents and has more than 1000 citations in the Web of Science. He serves as an Editor of *Materials* (MDPI) and Editorial Board member of *Civil Engineering and Architecture* (HRPUB) and *Nondestructive Testing and Diagnostics* (SIMP). He has developed more than 300 reviews of journal and conference articles. He is co-author of 10 patents and 1 patent application and is a member of the Polish Association of Civil Engineers and Technicians (PZITB) and of the Polish Association of Building Mycology (PSMB). His research interests include concrete, fiber-cement, ultrasonic tomography, impact-echo, impulse-response, GPR and other non-destructive tests, and artificial intelligence, among others.

Preface to "Testing of Materials and Elements in Civil Engineering (2nd Edition) —Volume II"

Last year, we ran a successful Special Issue on "Testing of Materials and Elements in Civil Engineering", with over 50 papers published. The field of materials testing in civil engineering is very wide and interesting from an engineering and scientific point of view. Therefore, we have decided make a second edition dedicated to this topic.

This new Issue is proposed and organized as a means to present recent developments in the field of materials testing in civil engineering. The articles highlighted in this Issue should relate to different aspects of the testing of different materials in civil engineering, from building materials and elements to building structures. The current trend in the development of materials testing in civil engineering is mainly concerned with the detection of flaws and defects in elements and structures using destructive, semidestructive, and nondestructive testing.

The topics of interest include but are not limited to:

- Testing of materials and elements in civil engineering;

- Testing of structures made of novel materials;

- Condition assessment of civil materials and elements;

- Detecting defects that are invisible on the surface;

- Damage detection and damage imaging;

- Diagnostics of cultural heritage monuments;

- Structural health monitoring systems;

- Modeling and numerical analyses;

- Nondestructive testing methods;

- Advanced signal processing for nondestructive testing.

Krzysztof Schabowicz
Editor

An Efficient Method for Optimizing HPC-FRP Retrofit Systems of Flexural Strengthened One-Way Continuous Slabs Based on ACI 440.2R

Huy Q. Nguyen [1], Kijae Yang [2] and Jung J. Kim [1,*]

1   Department of Civil Engineering, Kyungnam University, Changwon-si 51767, Republic of Korea
2   Corporate Partnership Center, Korea Authority of Land & Infrastructure Safety, Jinju-si 52856, Republic of Korea
*   Correspondence: jungkim@kyungnam.ac.kr; Tel.: +82-552-496-421; Fax: +82-505-999-2165

Abstract: An innovative retrofit system consisting of fiber-reinforced polymers (FRP) and high-performance concrete (HPC) considering the difficulty of the accessibility and installation of FRP on the underside of reinforced concrete (RC) slabs was found to be efficient in the flexural strengthening of existing RC slabs. It is important to note that continuous slabs using the FRP-HPC retrofit systems are less effective in exploiting FRP tensile strength and can cause sudden failure once excessively enhanced flexural strength exceeds shear strength. A design method to ensure ductile failure mode was also proposed for strengthened continuous RC slabs in the previous literature. Thus, it is necessary to optimize retrofit systems in terms of mechanical performance aspects to improve the efficiency of retrofitted slabs in serviceability. This study proposes a design method for optimizing the strength of materials and inducing ductile failure of continuous slab retrofitting FRP-HPC systems. The proposed approach demonstrated its effectiveness for strengthening a continuous RC slab with various FRP-HPC retrofit systems through a case study. The results show that the design factored load in the serviceability limit state does not change appreciably from a decrease in carbon fiber-reinforced polymers (CFRP) of 38%; the design factored load decreased only by 9% and the ultimate failure load by 13% while reducing CFRP by 20% and HPC by 25%.

Keywords: FRP; continuous RC slab; retrofit; strengthen; optimal design

1. Introduction

Structural strengthening has seen tremendous advancements in materials, methods, and techniques in the last few decades. Enhancing the lifecycle of existing RC structures and reducing environmental impact has become an attractive topic in the structural engineering community [1,2]. The strengthening of existing civil engineering infrastructure with externally bonded FRP has emerged as one of today's state-of-the-art techniques for rehabilitating and improving the load carrying capacity of existing RC structures [3–6]. Of course, concrete substrates of existing RC structures should also possess the required strength to develop the design stresses of the FRP system through the bond regarding flexure or shear strengthening [7]. The acceptance of FRP materials in restoring and strengthening damaged RC structures due to their low weight, high tensile strength, immunity to corrosion, and unlimited sizes is recognized widely in the available literature [8–12]. In addition, novel methods and techniques for strengthened RC structures using FRP composite materials have also been developed in proportion to their growth in the level of popularity [13–17].

Conventionally, methods of strengthening RC slabs by attaching FRP to tensile zones to maximize the high tensile strength of composite materials have gained wide application in practice [18–20]. Unfortunately, it can be impossible to acquire a well-prepared concrete surface in some cases due to the difficulty of the accessibility and installation of FRP on the underside of the RC slabs [21]. Furthermore, the ductility reduction due to the intrinsic bond of the FRP-to-concrete interface leading to brittle failure is one of the notable

drawbacks of strengthening RC structures using FRP [22–24]. The structural ductility factor should be considered the vital requirement for preventing brittle shear failure and warning of forthcoming failure for practical designs [25–27]. With a focus on overcoming the drawbacks of typical strengthening techniques, an innovative hybrid retrofit system using CFRP with HPC overlay on the top surface of the existing RC slab was developed, instead of taking advantage of the high tensile strength of CFRP, as shown in Figure 1. Previous studies have confirmed the efficiency of retrofit systems in improving strength and ductility, along with overcoming logistical challenges without complex engineering requirements [21,28,29].
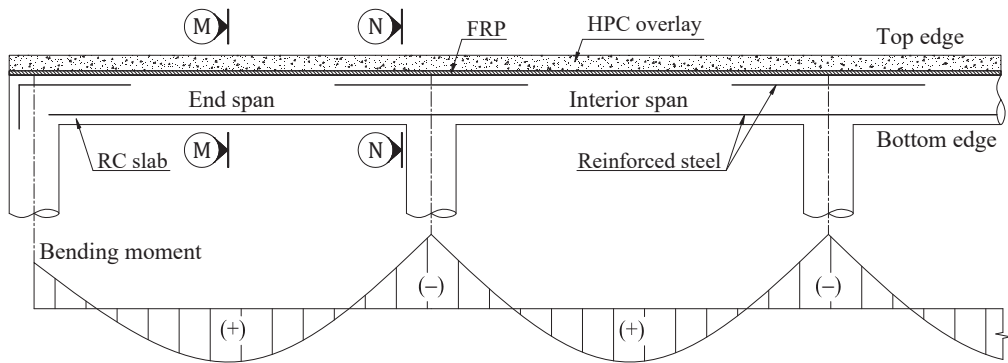
Figure 1. An innovative HPC-FRP hybrid retrofit system for strengthening continuous RC slab.

For post-strengthened slabs, additional strength should be limited to avoid sudden failure, which could result from an excessive enhancement in flexural strength over shear strength. Thus, previous studies have developed novel failure mode classification and failure limits for continuous RC slabs based on their shear- and moment-carrying capacities [30,31]. A calculation method for retrofitted slabs to prevent brittle failure and induce ductile failure was also recommended. Regardless, the design methodology also has restrictions in considering the demand for strengthening each different location appropriately to optimize the strength of the constituent materials consisting of CFRP and HPC.

Although design guidelines for FRP strengthening structures have been reported, optimizing continuous RC slabs using retrofit systems has not been considered comprehensively [32–35]. It is possible, for example, for the mid-span sections to fail before the support sections reach the limit state or vice versa. These guidelines, although applicable, are not appropriate for optimizing the bearing capacity of retrofitted slabs. In addition, these standards were also not developed to ensure ductile failure for strengthened slabs. Optimizing materials' strength and inducing ductile failure of retrofitted slabs should be performed in the design of retrofit systems, resulting in reduced cost and more safety [36–38]. It will also partially overcome the shortcoming of retrofit systems, which cannot take advantage of the high tensile strength of FRP.

In this study, the flexural failure limits for the interior and end spans of continuous RC slabs following their moment and shear capacities are presented. The retrofitting mechanism for negative and positive moment sections of slabs is explained. Optimal criteria and an efficient design procedure for flexural strengthened continuous RC slabs using FRP-HPC retrofit systems are proposed based on ACI 440.2R. Several approaches are considered to develop potential scenarios for strengthening solutions. An innovative method of determining the amount of CFRP and HPC for optimizing the strength of materials and inducing ductile failure of slabs by applying this strengthened technique is illustrated clearly through a case study. The advantages and disadvantages of the proposed method are also discussed based on the obtained results.

2. Theoretical Background

2.1. Failure Limits

According to previous works [30,31], the failure limits of one-way continuous slabs in frames subjected to uniformly distributed loads are defined. The slab's shear and moment carrying capacities are used to predict the failure mode and ultimate failure load. In a frame, the distribution of moments depends on the flexural rigidity of members and supporting columns. The shears at the end of the continuous slab are taken as the simple slab shear, except at the exterior face of the first interior support, where the shear force should be higher because it has greater fixity. The maximum positive and negative moments and shears due to uniformly distributed load are calculated as follows [39]:

$$M_u = C_m \left(w_u l_n^2 \right) \tag{1}$$

$$V_u = C_v \left(\frac{w_u l_n}{2} \right) \tag{2}$$

Considering two adjacent spans of approximately equal length or a longer span not exceeding 1.2 times the shorter, ACI 318M recommends approximate moment and shear coefficients to estimate reasonable moment and shear envelopes for a one-way slab with columns for support [40], as shown in Figure 2.
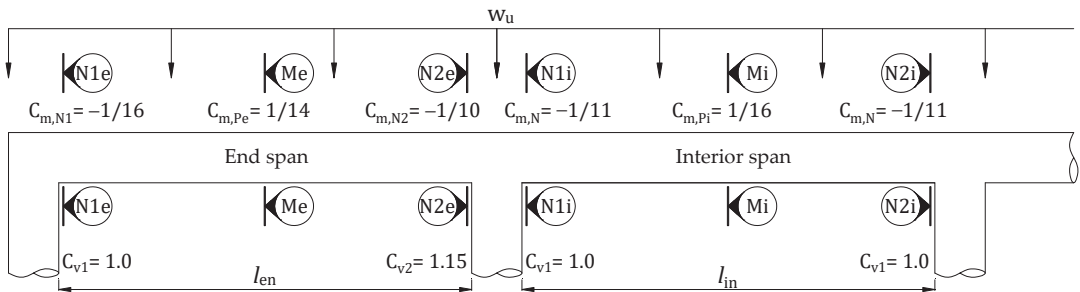
Figure 2. Shear and moment coefficients for continuous RC slabs with column supports, according to ACI 318M.

Previous studies also proposed limit equations to divide distinct regions corresponding to failure modes, described in Appendix A. Based on this, the different failure modes for the end and interior spans of the continuous slab are depicted in Figure 3. Failure modes are also classified based on the order of forming plastic hinges and failure types. The different failure modes for the end and interior span of continuous slabs are summarized in Table 1.

The superposition method considering plastic redistribution of the strengthened slab is applied to calculate the ultimate failure loads. For the end span, the ultimate failure loads for failure modes D-1e, D-2e, and D-3e are calculated from the expressions:

- Failure mode D-1e

$$w_f = \phi_f \frac{8}{l_{en}^2} \left(M_{n,Pe} + M_{n,Ne} \frac{(1/8 - C_{m,Pe})}{C_{m,N2}} \right) \tag{3}$$

- Failure mode D-2e

$$w_f = \phi_f \frac{4}{l_{en}^2} \left(M_{n,Pe} + M_{n,Ne} \frac{(1/4 + C_{m,N2} - C_{m,N1} - C_{m,Pe})}{C_{m,N2}} \right) \tag{4}$$
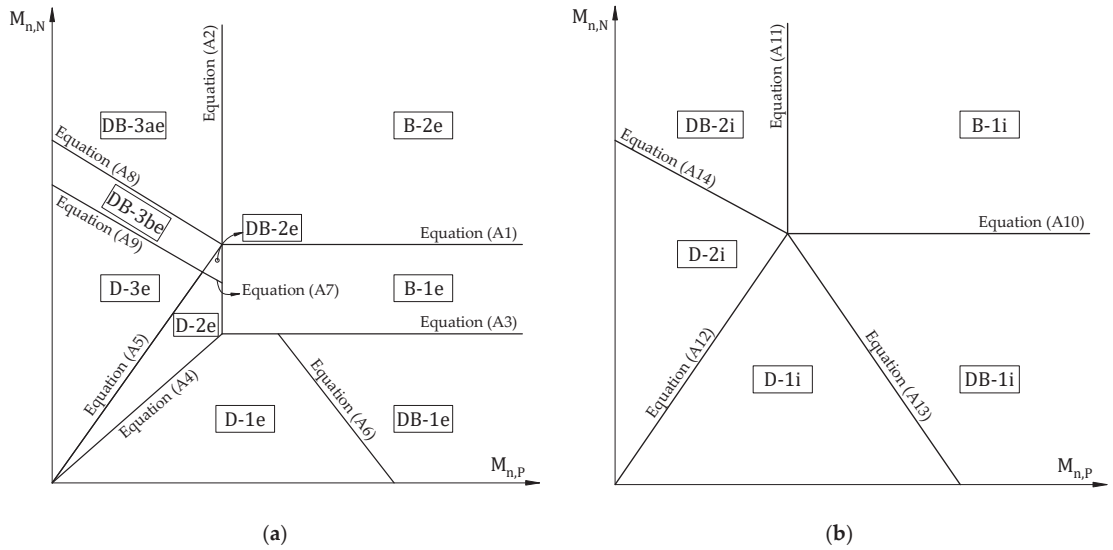
Figure 3. Different failure modes according to moment and shear capacities of continuous RC slabs for (**a**) end span and (**b**) interior span.

Table 1. An overview of the different failure modes of continuous RC slabs.

Location	Failure Modes	First Plastic Hinge	Second Plastic Hinge	Third Plastic Hinge	Shear Failure	Failure Type
End span	D-1e	N2e	N1e	Me	-	Ductile
	D-2e	N2e	Me	N1e	-	Ductile
	D-3e	Me	N2e	N1e	-	Ductile
	DB-1e	N2e	N1e	-	N2e	Brittle
	DB-2e	N2e	Me	-	N2e	Brittle
	DB-3ae	Me	-	-	N2e	Brittle
	DB-3be	Me	N2e	-	N2e	Brittle
	B-1e	N2e	-	-	N2e	Brittle
	B-2e	-	-	-	N2e	Brittle
Interior span	D-1i	N1i, N2i	Mi		-	Ductile
	D-2i	Mi	N1i, N2i		-	Ductile
	DB-1i	N1i, N2i	-		N1i, N2i	Brittle
	DB-2i	Mi	-		N1i, N2i	Brittle
	B-1i	-	-		N1i, N2i	Brittle

- Failure mode D-3e

$$w_f = \phi_f \frac{4}{l_{en}^2} \left(M_{n,Pe} \frac{(1/4 - C_{m,N1})}{C_{m,Pe}} + M_{n,Ne} \right) \quad (5)$$

The ultimate failure loads for failure modes DB-1e, DB-2e, DB-3ae, DB-3be, B-1e, and B-2e are calculated as:

$$w_f = \phi_v \frac{2V_n}{C_{v2} l_{en}} \quad (6)$$

For interior span, it is possible to estimate the ultimate failure loads for failure modes D-1i and D-2i as follows:

- Failure mode D-1i

$$w_f = \phi_f \frac{8}{l_{in}^2} \left(M_{n,Pi} + M_{n,Ni} \frac{(1/8 - C_{m,Pi})}{C_{m,N}} \right) \quad (7)$$

- Failure mode D-2i

$$w_f = \phi_f \frac{8}{l_{in}^2} \left(M_{n,Pi} \frac{(1/8 - C_{m,N})}{C_{m,Pi}} + M_{n,Ni} \right) \tag{8}$$

The ultimate failure loads for failure modes DB-1i, DB-2i, and B-1i can be estimated as follows:

$$w_f = \phi_v \frac{2V_n}{C_{v1}l_{in}} \tag{9}$$

In case the end and interior span have the same length and structure, it is worth noticing that failure types would be determined to follow the limits of the end span, as shown in Figure 4. Otherwise, it is decided through corresponding limit equations, as earlier mentioned.
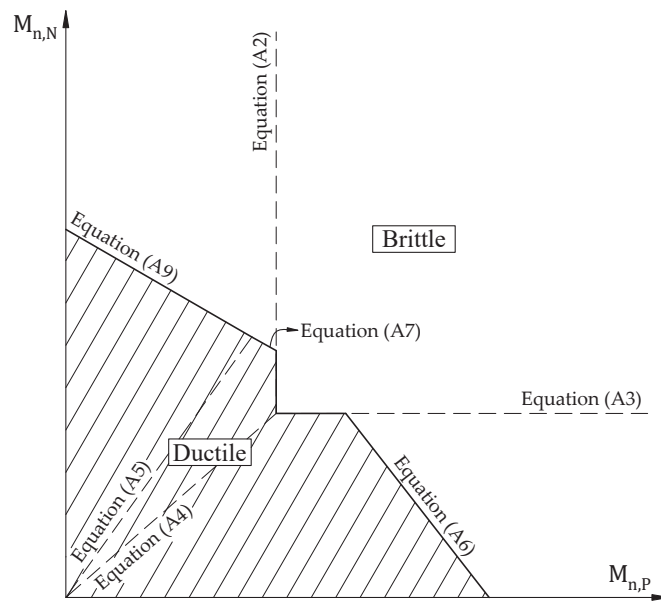
Figure 4. Limit failure regions for a continuous slab with the same clear span.

2.2. Retrofitting System

A hybrid retrofit system of FRP and HPC is installed on top of the existing slab to enhance its strength, as shown in Figure 1. According to ACI 440.2R, the retrofitting mechanism for negative and positive moments of the retrofitted slab was derived based on the sectional compressive force in HPC and the sectional tensile forces in the steel and FRP. For negative moment sections, retrofitting for RC flexural members as section N-N of Figure 1 can be done in a conventional way. The retrofitting mechanism for the FRP-HPC system is estimated based on stress and strain compatibility, as shown in Figure 5. The equilibrium equations must be solved iteratively due to the existence of two sectional forces in steel and FRP, besides the possibility of different failure modes. Assuming concrete with an ultimate strain of 0.003 and steel with yield stress (f_y), the force and moment equilibrium equations based on strain compatibility can be established from the expressions.

$$\alpha_1 f'_c \beta_1 cb = A_s f_y + A_F f_{fe} \tag{10}$$

$$\phi_f M_n = \phi_f \left[A_s f_y \left(d - \frac{\beta_1 c}{2} \right) + \psi_f A_F f_{fe} \left(d_f - \frac{\beta_1 c}{2} \right) \right] \tag{11}$$
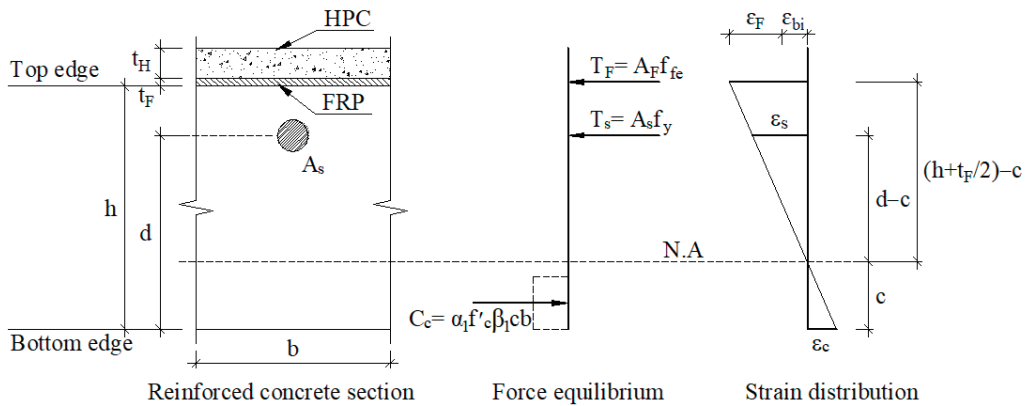
Figure 5. Retrofitting mechanism for negative moment sections (refer to section "N-N" of Figure 1).

For the positive moment sections, the HPC overlay on the top of the slab as section M-M of Figure 1 must have enough thickness and compressive strength to pull the neutral axis towards the overlay zone leading to FRP in tension at failure. The rationale for the retrofitting mechanism is similar to that for negative moment sections, as shown in Figure 6. Based on strain compatibility, the two governing equilibrium equations can be derived as follows:

$$\alpha_1 f'_H \beta_1 cb = A_s f_y + A_F f_{fe} \tag{12}$$

$$\phi_f M_n = \phi_f \left[A_s f_y \left(d + t_H + t_F - \frac{\beta_1 c}{2} \right) + \psi_f A_F f_{fe} \left(t_H + \frac{t_F}{2} - \frac{\beta_1 c}{2} \right) \right] \tag{13}$$
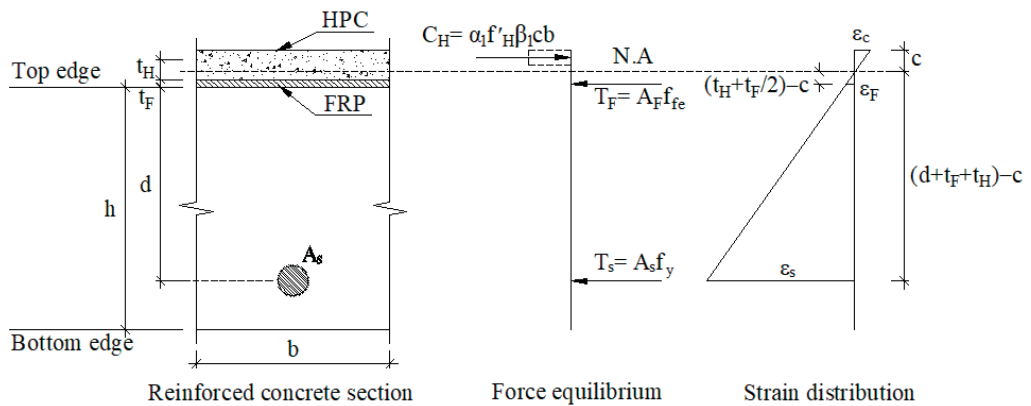
Figure 6. Retrofitting mechanism for positive moment sections (refer to section "M-M" of Figure 1).

3. Optimal Criteria and Design Procedure

3.1. Optimal Design Criteria

The successful design of a composite structure demands efficiency and safety during operation. Thus, optimizing material usability and preventing sudden failure for the retrofitted slabs are considered essential criteria in the optimal design procedure. The enhanced efficiency of the retrofit system would stem from the high compressive strength of the HPC overlay and the high tensile strength of FRP. The HPC overlay significantly enhances flexural strength at the mid-span section and shear strength at the support. On

the other hand, the retrofit system does not focus on exploiting the high tensile strength of FRP at the mid-span section due to its location near the neutral axis. Consequently, FRP contributes a relatively small amount to flexural strength at the mid-span section, whereas it is the main factor in improving flexural strength at support.

For retrofitted slabs, overly thick FRP will result in an excessive enhancement of flexural strength over shear strength at support, resulting in shear failure. A too-thick overlay can excessively improve the mid-span flexural strength over the support and increase the slab's self-weight, which does not take advantage of the structure carrying capacity. Ideally, the moment-carrying-capacity ratio of the mid-span section to the support section should be equivalent to the corresponding proportion of factored moments. For symmetric continuous slabs, the positive to negative moment ratios at the end and interior spans subjected to a uniform distributed load can be computed using ACI 318M as follows:

$$\frac{M_{n,Pe}}{M_{n,N1e}} = \frac{C_{m,Pe}}{C_{m,N1}} = \frac{1/14}{1/16} = 1.14 \tag{14}$$

$$\frac{M_{n,Pe}}{M_{n,N2e}} = \frac{C_{m,Pe}}{C_{m,N2}} = \frac{1/14}{1/10} = 0.71 \tag{15}$$

$$\frac{M_{n,Pi}}{M_{n,N1i}} = \frac{M_{n,Pi}}{M_{n,N2i}} = \frac{C_{m,Pi}}{C_{m,N}} = \frac{1/16}{1/11} = 0.69 \tag{16}$$

The ratios of positive and negative factored moments range from 0.69 to 1.14. Nevertheless, the moment ratio of 1.14 of Equation (14) is not a typical value for a continuous multi-spans RC slab because it is only related to the N1e section of the end span. The average moment ratio of 0.7, derived from Equations (15) and (16), should be used to optimize RC slab performance. The design approach based on failure limit methodology can achieve ductile failure and the desired moment ratio for a strengthened slab with a retrofit system by adjusting the increase of positive and negative moment carrying capacity separately. In addition to meeting the guidelines of ACI committee 440, an optimal retrofit system can be founded once the conditions for ductile failure and optimal moment ratio are satisfied.

3.2. Design Procedure and Flowchart

The thicknesses of FRP and HPC are considered adjustable variables. The long-term effect of service load and different environmental conditions are not evaluated in this case. The design procedure using the proposed optimal criteria and ACI 440.2R, depicted in Figure 7, involves the following steps:

(0) Determine the known design parameters of the existing RC slab and retrofit system (i.e., h, b, A_s, d, f'$_c$, f_y, E_s, f'$_H$, f$^*_{fu}$, E_F, C_E). Then calculate the ultimate strength (f_{fu}) and strain of FRP (ε_{fu}) and the existing state of strain (ε_{bi}) at support from the expressions.

$$f_{fu} = C_E f^*_{fu} \tag{17}$$

$$\varepsilon_{fu} = \frac{f_{fu}}{E_F} \tag{18}$$

$$\varepsilon_{bi} = \frac{M_{D,N2}(h - kd)}{I_{cr} E_c} \tag{19}$$
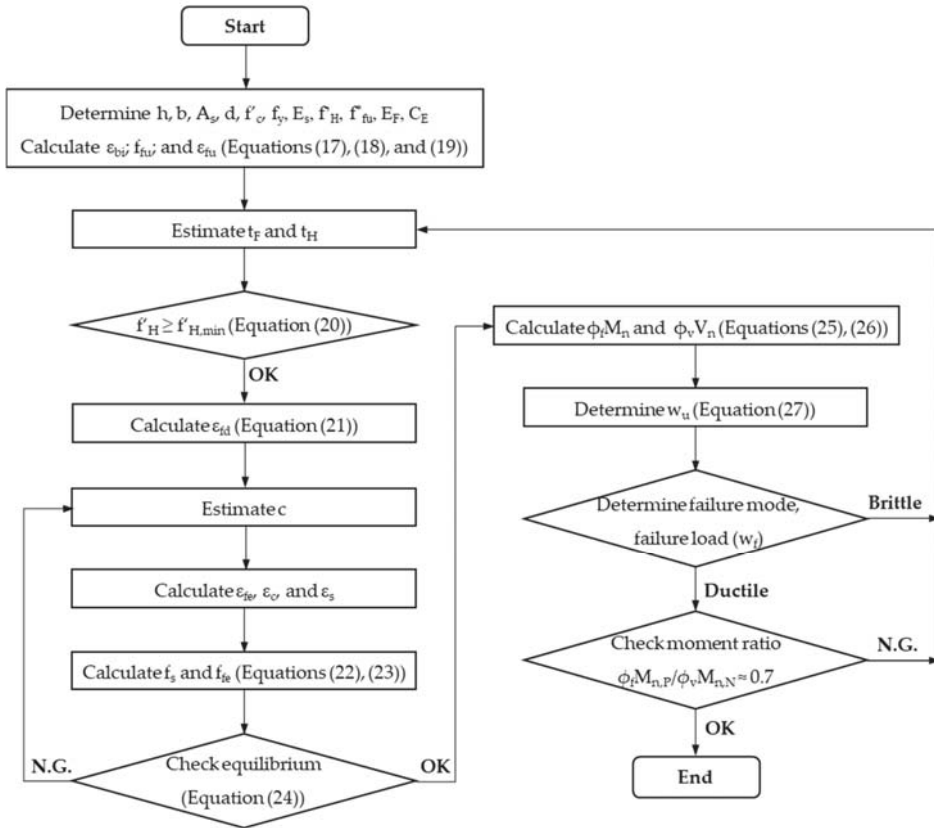
Figure 7. Design procedure flowchart for optimizing retrofit system.

(1) Estimate thicknesses of FRP (t_F) and HPC overlay (t_H)
(2) Check HPC strength to ensure that CFRP holds tension at the failure state at the mid-span section using Equation (20) [21]. If the calculated $f'_{H,min}$ is equal to or less than f'_H, go to the next step; otherwise, return to step 1.

$$f'_{H,min} = max\left[\frac{\varepsilon_{cu}E_F}{1.445}\left(\frac{t_F}{t_H}\right)^2 + \frac{f_y(A_s/b)}{0.7225t_H}; 0.15\,f'_c + \frac{\varepsilon_{cu}E_F}{1.7}\left(\frac{t_F}{t_H}\right)^2 + \frac{f_y(A_s/b)}{0.85t_H}\right] \le f'_H \qquad (20)$$

(3) Calculate the design strain of FRP (ε_{fd}) at the support section as follows:

$$\varepsilon_{fd} = 0.41\sqrt{\frac{f'_c}{nE_Ft_F}} \le 0.9\varepsilon_{fu} \qquad (21)$$

(4) Estimate the neutral axis depth with a reasonable initial value of 0.2d.
(5) Calculate the strains of FRP (ε_{fe}), concrete (ε_c), and tension reinforcing steel (ε_s) using similar triangles based on strain compatibility mentioned in Figures 5 and 6.
(6) Calculate the stresses in tension in reinforcing steel (f_s) and FRP (f_{fe}) as:

$$f_s = \varepsilon_s E_s \le f_y \qquad (22)$$

$$f_{fe} = \varepsilon_{fe}E_F \le f_{fu} \qquad (23)$$

(7) Check the neutral axis depth for force equilibrium using c determined in Equation (24) compared with the assumed value in step 5. If the force equilibrium condition is satisfied, go to the next step; otherwise, return to step 4.

$$c = \frac{A_s f_s + A_F f_{fe}}{\alpha_1 f'_c \beta_1 b} \qquad (24)$$

In the case of concrete strain (ε_c) reaching the ultimate value (ε_{cu}), α_1 and β_1 can be calculated using ACI 318M. By contrast, these values should be calculated based on the Whitney stress block, as recommended by ACI 440.2R.

(8) Calculate design flexural and shear strengths from Equations (25) and (26):

$$\phi_f M_n = \phi_f (M_{ns} + \psi_f M_{nf}) \qquad (25)$$

$$\phi_v V_n = \phi_v \left(d\sqrt{f'_c} + t_H \sqrt{f'_H} \right) \frac{b}{6} \qquad (26)$$

(9) Determine the design factored load using Equations (27)–(29), derived from Equations (1) and (2):

$$w_u = \min(w_{u,M}, w_{u,V}) \qquad (27)$$

$$w_{u,M} = \frac{\phi_f M_n}{C_m l_n^2} \qquad (28)$$

$$w_{u,V} = \frac{\phi_v V_n}{C_v l_n} \qquad (29)$$

(10) Determine the failure mode corresponding to the ultimate failure load based on the proposed failure limit. If the retrofitted slab fails in ductile, go to the next step; otherwise, return to step 1.

(11) If the desirable moment ratio ($\phi_f M_{n,P} / \phi_v M_{n,N}$) is approximately 0.7, the optimal design solution for the retrofit system is achieved; otherwise, re-estimate t_F and t_H.

4. Case Study

The rectangular RC continuous slab with the same clear span of 2.75 m subjected to uniformly distributed load is considered for a case study. As mentioned above, the failure mode of the end span governs corresponding to the moments and shears coefficients as shown in Figure 2, where $C_{m,N1e} = 1/16$, $C_{m,N2e} = 1/10$, $C_{m,Pe} = 1/14$, $C_{v1} = 1$, and $C_{v2} = 1.15$. The environment reduction factor for a retrofit system with CFRP overlaid by HPC (C_E) is equal to 0.95. The strength reduction factors ϕ_f, ϕ_v, and ψ_f are 0.9, 0.75, and 0.85, respectively [7]. The CFRP and overlay thickness of the retrofit system are assumed as design variables, which can be adjusted to induce ductile failure and optimize the performance of a retrofitted slab based on the proposed procedure. Dimensions and material properties of the existing RC slab are provided in Table 2. The mechanical properties of the retrofit system are presented in Table 3. The design procedure considers the reliability factor for debonding CFRP, as recommended by ACI 440.2R. Besides that, a retrofit system should also include shear anchors to maintain integrity until reaching the ultimate carrying capacity. The effectiveness of shear anchors in the retrofit system was confirmed in the previous literature [28]. The preliminary calculation for the control slab and retrofit system is shown in Table 4.

Table 2. Dimensions and material properties of the existing RC slab.

h (mm)	b (mm)	A_s (mm^2)	d (mm)	f'_c (MPa)	γ_c (kg/m^3)	f_y (MPa)	E_s (GPa)
150	900	426	120	30	2400	400	200

Table 3. Mechanical properties of the retrofit system.

HPC			CFRP	
t_H (mm)	f'_H (mm)	t_F (mm)	f^*_{fu}	E_F (GPa)
30	80	1	600	40

Table 4. The preliminary calculation for the control slab and retrofit system.

Analysis	Control Slab
Design section capacity	$\phi_f M_{n,N} = 17.83$ kNm; $\phi_f M_{n,P} = 17.83$ kNm; $\phi_v V_n = 73.9$ kN
Design factored load, using Equation (27) $w_u = \min(w_{uM}, w_{uV}) w_{u,M} = \min\left(\frac{\phi_f M_{n,P}}{C_{m,Pe}l_n^2}, \frac{\phi_f M_{n,N}}{C_{m,N1}l_n^2}, \frac{\phi_f M_{n,N}}{C_{m,N2}l_n^2}\right)$ $w_{u,V} = \min\left(\frac{\phi_v V_n}{C_{v1}l_n}, \frac{\phi_v V_n}{C_{v2}l_n}\right)$	$w_u = \min(23.58; 46.76) = 23.6$ kN/m $w_{u,M} = \min\left(\frac{17.83}{(1/14)2.75^2}; \frac{17.83}{(1/16)2.75^2}; \frac{17.83}{(1/10)2.75^2}\right) = 23.6$ kN/m $w_{u,V} = \min\left(\frac{2(73.9)}{1(2.75)}; \frac{2(73.9)}{1.15(2.75)}\right) = 46.8$ kN/m
Failure mode	D-2e, as shown in Figure 8
Ultimate failure load, using Equation (4) for D-2e	$w_f = \frac{4}{2.75^2}\left(17.83 + 17.83\frac{(1/4+1/10-1/16-1/14)}{1/10}\right) = 29.8$ kN/m
Self-weight $w_c = \gamma_c bh$	$w_c = (2400 \times 10^{-2})(0.9)(0.15) = 3.24$ kN/m
The moment at the N2e section due to dead load $M_{D,N2e} = C_{m,N2} w_c l_n^2$	$M_{D,N2e} = \frac{1}{10}(3.24)(2.75^2) = 2.45 \times 10^6$ Nmm
$E_c = 4700\sqrt{f'_c}$	$E_c = 4700\sqrt{30} = 25,700$ MPa
Crack moment at the N2e section, $I_{cr,N}$	$I_{cr,N} = 3.45 \times 10^7$ mm^4
At the N2e section, kd	kd $= 26.26$ mm
Ultimate strength and strain of CFRP, using Equations (17) and (18)	$f_{fu} = 0.95(600) = 570$ MPa; $\varepsilon_{fu} = \frac{570}{40,000} = 0.0143$
The existing state of strain at the N2e section using Equation (19)	$\varepsilon_{bi} = \frac{(2.45\times10^6)(150-26.26)}{(3.45\times10^7)(25,700)} = 0.00034$
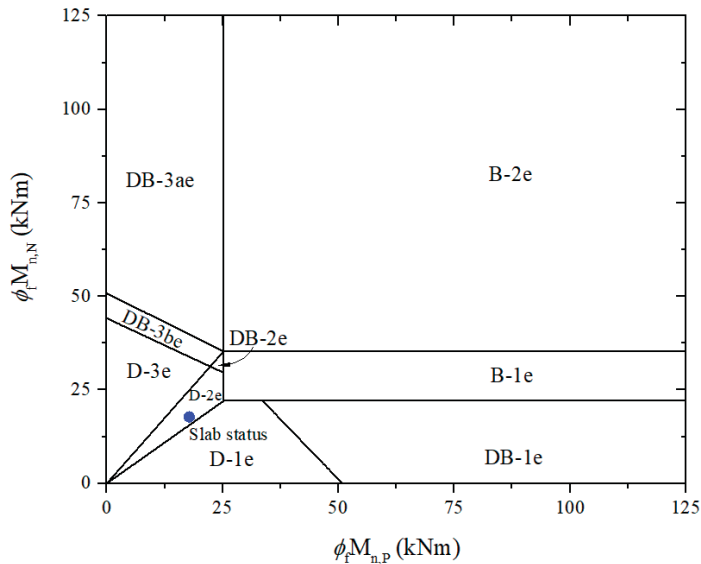
Figure 8. Establish failure limits and predict slab status based on moment carrying capacities for the control slab.

5. Results and Discussions

According to Table 4, the design factored load of the control slab is estimated as 23.6 kN/m, while the ultimate failure load is also expected at 29.8 kN/m with failure mode D-2e, as shown in Figure 8. Besides defining CFRP's ultimate strength and debonding failure strain, the initial calculation related to the existing strain is considered only for the

N-2 section, where the highest internal force is confirmed. For analysis of the retrofitted slab, the thicknesses of FRP and HPC are initially assumed to be 1 mm and 30 mm, respectively, as shown in Table 5. The design flexural and shear strengths are determined after force equilibrium is satisfied via iterative calculation. The failure mode of the retrofitted slab is named DB-3ae according to the proposed failure limit, as shown in Figure 9. The first plastic hinge will be formed at mid-span with the design factored load of 50.1 kN/m before failure in shear at the N-2 section with the ultimate failure load of 65.9 kN/m. Brittle failure is not the desired effect, even though the design factored load and ultimate failure load are higher than the control slab by 2.12 and 2.21 times, respectively.

Table 5. The initial calculation for the retrofitted slab.

Procedure	Retrofitted Slab
1. Estimate thicknesses of: -CFRP -HPC	$t_F = 1$ mm $t_H = 30$ mm
2. Check HPC strength using Equation (20)	$f'_H \geq f'_{H,min} = \max(8.83; 12) = 12$ MPa(OK)
3. Calculate the design strain of CFRP at the N2e section, using Equation (21)	$\varepsilon_{fd} = 0.0112 \leq 0.9\varepsilon_{fu} = 0.0128$
4. Estimate the neutral axis depth (Revise of c until equilibrium achieved)	the N2e section: $c_N = 28.58$ mm mid-span section: $c_P = 9.84$ mm
5. Calculate the strains of CFRP (ε_{fe}), concrete (ε_c), and tension steel (ε_s) at the N2e section $\varepsilon_{fe,N} = \varepsilon_{cu}\left(\frac{h-c_N}{c_N}\right) - \varepsilon_{bi} \leq \varepsilon_{fd}$ $\varepsilon_{c,N} = (\varepsilon_{fe,N} + \varepsilon_{bi})\left(\frac{c_N}{h-c_N}\right)$ $\varepsilon_{s,N} = (\varepsilon_{fe,N} + \varepsilon_{bi})\left(\frac{d-c_N}{h-c_N}\right)$ and mid-span section $\varepsilon_{fe,P} = \varepsilon_{cu}\left(\frac{t_H-c_P}{c_P}\right) \leq \varepsilon_{fd}$ $\varepsilon_{c,P} = \varepsilon_{fe,P}\left(\frac{c_P}{t_H-c_P}\right)$ $\varepsilon_{s,P} = \varepsilon_{c,P}\left(\frac{d+t_H+t_F-c_P}{c_P}\right)$	the N2e section $\varepsilon_{fe,N} = 0.003\left(\frac{150-28.58}{28.58}\right) - 0.00034 = 0.0124 > \varepsilon_{fd} = 0.0112$ $\rightarrow \varepsilon_{fe,N} = \varepsilon_{fd} = 0.0112$ $\varepsilon_{c,N} = (0.0112 + 0.00034)\left(\frac{28.58}{150-28.58}\right) = 0.0027 < \varepsilon_{cu} = 0.003$ $\varepsilon_{s,N} = (0.0112 + 0.00034)\left(\frac{120-28.58}{150-28.58}\right) = 0.0087$ mid-span section $\varepsilon_{fe,P} = 0.003\left(\frac{30-9.84}{9.84}\right) = 0.0061 < \varepsilon_{fd} = 0.0112$ $\varepsilon_{c,P} = 0.0061\left(\frac{9.84}{30-9.84}\right) = 0.003 = \varepsilon_{cu}$ $\varepsilon_{s,P} = 0.003\left(\frac{120+30+1-9.84}{9.84}\right) = 0.043$
6. Calculate the stress in tension steel and CFRP at the N2e section using Equations (22) and (23)	the N2e section $f_{s,N} = 0.0087(200,000) = 1740$ MPa $> f_y = 400$ MPa $\rightarrow f_{s,N} = f_y = 400$ MPa $f_{fe,N} = 0.0112(40,000) = 448$ MPa mid-span section $f_{s,P} = 0.043(200,000) = 8607$ MPa $> f_y = 400$ MPa $\rightarrow f_{s,P} = f_y = 400$ MPa $f_{fe,P} = 0.0061(40,000) = 245.85$ MPa
7. Check the neutral axis depth for force equilibrium $\varepsilon'_c = \frac{1.7f'_c}{E_c}$; $\beta_1 = \frac{4\varepsilon'_c - \varepsilon_c}{6\varepsilon'_c - 2\varepsilon_c}$ $\alpha_1 = \frac{3\varepsilon'_c\varepsilon_c - \varepsilon_c^2}{3\beta_1\varepsilon'^2_c}$ $c = \frac{A_s f_s + A_F f_{fe}}{\alpha_1 f'_c \beta_1 b}$	the N2e section, because $\varepsilon_{c,N} < \varepsilon_{cu}$ $\varepsilon'_{c,N} = \frac{1.7(30)}{25,700} = 0.002$; $\beta_{1,N} = \frac{4(0.002)-0.0027}{6(0.002)-2(0.0027)} = 0.808$ $\alpha_{1,N} = \frac{3(0.002)(0.0027)-(0.0027)^2}{3(0.808)(0.002)^2} = 0.922$ $c_N = \frac{426(400)+900(448)}{0.922(30)(0.808)(900)} = 28.58$ mm(OK) mid-span section, because $\varepsilon_{c,P} = \varepsilon_{cu}$ $\beta_{1,P} = \beta_1 = 0.65$; $\alpha_{1,P} = \alpha_1 = 0.85$ $c_P = \frac{426(400)+900(245.9)}{0.85(80)(0.65)(900)} = 9.85$ mm(OK)

Table 5. *Cont.*

Procedure	Retrofitted Slab
8. Calculate design flexural and shear strengths 8.1 Calculate flexural strength at the N2e section contributed by steel $M_{ns,N} = A_s f_{s,N}\left(d - \frac{\beta_{1,N} c_N}{2}\right)$ and CFRP $M_{nf,N} = A_F f_{fe,N}\left(h - \frac{\beta_{1,N} c_N}{2}\right)$	$M_{ns,N} = \frac{426(400)}{10^6}\left(120 - \frac{0.808(28.58)}{2}\right) = 18.5 \text{ kNm}$ $M_{nf,N} = \frac{(900\times 1)(448)}{10^6}\left(150 - \frac{0.808(28.58)}{2}\right) = 56 \text{ kNm}$
8.2 Calculate flexural strength at the mid-span section contributed by steel $M_{ns,P} = A_s f_{s,P}\left(d + t_H + t_F - \frac{\beta_{1,P} c_P}{2}\right)$ and CFRP $M_{nf,P} = A_F f_{fe,P}\left(t_H - \frac{\beta_{1,P} c_P}{2}\right)$	$M_{ns,P} = \frac{426(400)}{10^6}\left(120 + 30 + 1 - \frac{0.65(9.85)}{2}\right) = 25.2 \text{ kNm}$ $M_{nf,P} = \frac{(900\times 1)(245.9)}{10^6}\left(30 - \frac{0.65(9.85)}{2}\right) = 5.9 \text{ kNm}$
8.3 Calculate the design flexural strength using Equation (25)	the N2e section $\phi_f M_{n,N} = 0.9[18.5 + 0.85(56)] = 59.5 \text{ kNm}$ mid-span section $\phi_f M_{n,P} = 0.9[25.2 + 0.85(5.9)] = 27.1 \text{ kNm}$
8.4 Calculate the design shear strength using Equation (26)	$\phi_v V_n = \frac{0.75}{10^3}\left(120\sqrt{30} + 30\sqrt{80}\right)\frac{900}{6} = 104.1 \text{ kN}$
9. Determine design factored load using Equations (27)–(29)	$w_u = \min(50.1; 65.9) = 50.1 \text{ kN/m}$ $w_{u,M} = \min\left(\frac{27.1}{(1/14)2.75^2}; \frac{59.4}{(1/16)2.75^2}; \frac{59.4}{(1/10)2.75^2}\right) = 50.1 \text{ kN/m}$ $w_{u,V} = \min\left(\frac{2(104.1)}{1(2.75)}; \frac{2(104.1)}{1.15(2.75)}\right) = 65.9 \text{ kN/m}$
10. Determine failure mode and failure load	DB-3ae, as shown in Figure 9 Equation (6), $w_f = \frac{2(104.1)}{1.15(2.75)} = 65.9 \text{ kN/m}$
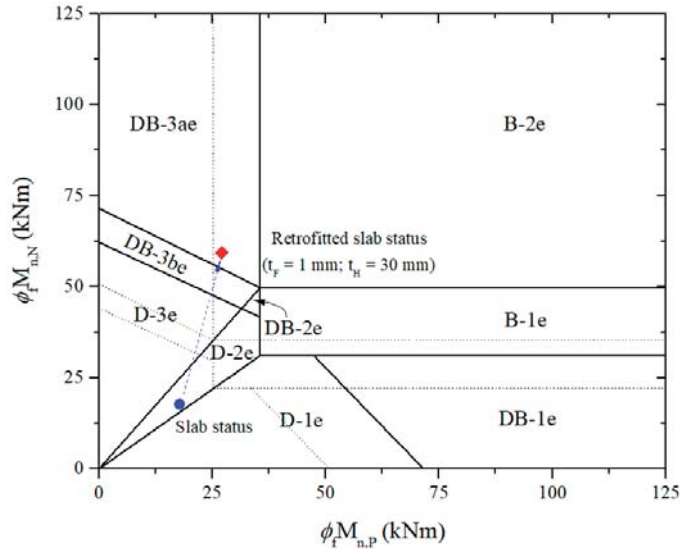
Figure 9. Establish failure limits and predict slab status based on moment carrying capacities for the retrofitted slab.

The retrofit system is optimized by varying the thicknesses of CFRP or HPC to obtain ductile failure mode and desirable moment ratio. A similar calculation process, the R-1 system with only adjustable CFRP thickness, is considered a solution, as shown in Table 6. Figure 10 reveals that the strengthened slab can be failed in ductile failure mode D-3e with the ultimate failure load of 60.9 kN/m by using 0.6 mm-thick CFRP laminate, increased 2.04 times compared to the failure load of the control RC slab. Nonetheless, the positive-to-negative moment ratio of 0.55 may cause the mid-span section to fail before the support

section. CFRP thickness should be iterated until the moment ratio is approximately 0.7, which can be met at 0.37 mm thick, resulting in failure mode D-3e with the design factored load of 46.7 kN/m and the ultimate failure load of 54 kN/m. Compared to the optimized and unoptimized retrofit systems, the former decreases CFRP by 38%, only resulting in a reduced 3% of the design factored load and 11% of the ultimate failure load. For this case, the moment carrying capacity at mid-span controlling the possibility of failure is almost unchanged by a 3% decrease, whereas it fell remarkably by 23% at the support sections. As a result, the optimal retrofit system can be determined with the mid-span and support section simultaneous failures, along with considerable savings in CFRP, while the bearing capacity almost remains unchanged.

Table 6. Analysis to optimize the retrofit system.

Procedure		R-1 System	R-2 System
1. Estimate thicknesses of:	-CFRP -HPC	t_F =0.6 mm t_H =30 mm (keep constant)	t_F =1 mm t_H =75 mm
2. Check HPC strength		It is not required to repeat step 2 once t_F decreases or t_H increases.	
3. Calculate the design strain of CFRP		ε_{fd} =0.0128	ε_{fd} =0.0112
4. Estimate the neutral axis depth		c_N =23 mm c_P =8.44 mm	c_N =28.58 mm c_P =13.8 mm
5. Calculate the strains of CFRP (ε_{fe}), concrete (ε_c), and tension steel (ε_s)		$\varepsilon_{fe,N}$=0.0128, $\varepsilon_{c,N}$ =0.0024, $\varepsilon_{s,N}$ =0.0101 $\varepsilon_{fe,P}$=0.0077, $\varepsilon_{c,P}$ =0.003 $\varepsilon_{s,P}$ =0.0505	$\varepsilon_{fe,N}$ =0.0112, $\varepsilon_{c,N}$ =0.0027, $\varepsilon_{s,N}$ =0.0087 $\varepsilon_{fe,P}$ =0.0112, $\varepsilon_{c,P}$ =0.0025 $\varepsilon_{s,P}$ =0.0334
6. Calculate the stress in tension steel and CFRP		$f_{s,N}$ =400 MPa, $f_{fe,N}$ =513 MPa $f_{s,P}$ =400 MPa, $f_{fe,P}$ =306.5MPa	$f_{s,N}$ =400 MPa, $f_{fe,N}$ =449.1 MPa $f_{s,P}$ =400 MPa, $f_{fe,P}$ =449.1 MPa
7. Check the neutral axis depth for force equilibrium		c_N =22.99 mm (OK) c_P =8.44 mm (OK)	c_N =28.58 mm (OK) c_P =13.8 mm (OK)
8. Calculate design flexural and shear strengths		$\phi_f M_{n,N}$ =46.9 kNm $\phi_f M_{n,P}$ =26.1 kNm $\phi_v V_n$ =104.1 kN	$\phi_f M_{n,N}$ =59.4 kNm $\phi_f M_{n,P}$ =50.9 kNm $\phi_v V_n$ =149.4 kN
9. Determine design factored load		w_u =48.2 kN/m	w_u =78.6 kN/m
10. Determine failure mode and failure load		D-3e, as shown in Figure 10	D-2e, as shown in Figure 11a
11. Check the moments ratio		Equation (5), w_f =60.9 kN/m ($\phi_f M_{n,P}/\phi_f M_{n,N}$)= 0.55 (Not good)	Equation (4), w_f =94.9 kN/m ($\phi_f M_{n,P}/\phi_f M_{n,N}$)= 0.86 (Not good)
Adjust iteratively thicknesses of CFRP and HPC to achieve ductile failure mode and desirable moment ratio		It can be achieved with t_F =0.37 mm and t_H =30 mm; w_u =46.7 kN/m; Failure mode D-3e, as shown in Figure 10; w_f =54 kN/m; ($\phi_f M_{n,P}/\phi_f M_{n,N}$) =25.2/36 = 0.7 (OK)	Not available if t_F is kept constant in this case. It can be achieved with t_F =0.8 mm and t_H =56 mm; w_u =71.7 kN/m; Failure mode D-3e, as shown in Figure 11b; w_f =83 kN/m; ($\phi_f M_{n,P}/\phi_f M_{n,N}$) =38.7/55.3 = 0.7 (OK)

It is noticeable that Table 6 also shows a second alternative approach called the R-2 system with additionally adjusted HPC thickness. According to Figure 11a, ductile failure mode D-2e with the ultimate failure load of 94.9 kN/m can be obtained with thicknesses HPC of 75 mm and CFRP of 1 mm, leading to an increase of 3.18 times over the existing slab's failure load. Nevertheless, the positive-to-negative moment ratio of 0.86 can lead to the support section failing before the mid-span section reaches its critical point. Once the moment ratio exceeds 0.7, along with CFRP being kept constant, the higher the HPC thickness, the higher the moment ratio, leading to the inability to optimize the moment ratio. Consequently, CFRP and HPC thicknesses should be adjusted simultaneously to obtain the moment ratio of 0.7. It is possible to optimize the retrofit system with 0.8 mm and 56 mm CFRP and HPC thicknesses, respectively. The failure mode is D-3e, with the ultimate failure load of 83 kN/m, as shown in Figure 11b. Compared to the unoptimized retrofit system, the optimized retrofit system decreased CFRP by 20% and HPC by 25%. Nonetheless, w_u and w_f were only reduced by 9% and 13%, respectively. In this case, the moment carrying capacity at the supports that govern probable failures did not change substantially,

with a decrease of 7%, whereas in the mid-span section, it dropped significantly, by 24%. Accordingly, a retrofit system is optimized with significant CFRP and HPC savings without a noticeable change in load carrying capacities.
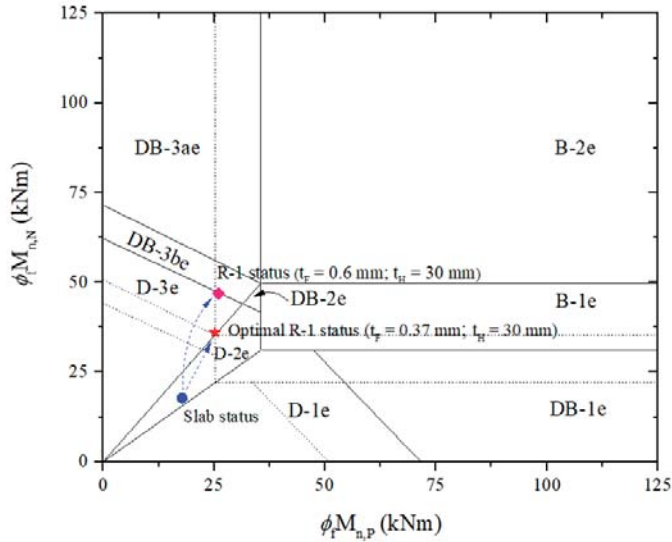
Figure 10. Establish failure limits and predict retrofitted slab status based on moment carrying capacities using the R-1 system.

(a)

(b)
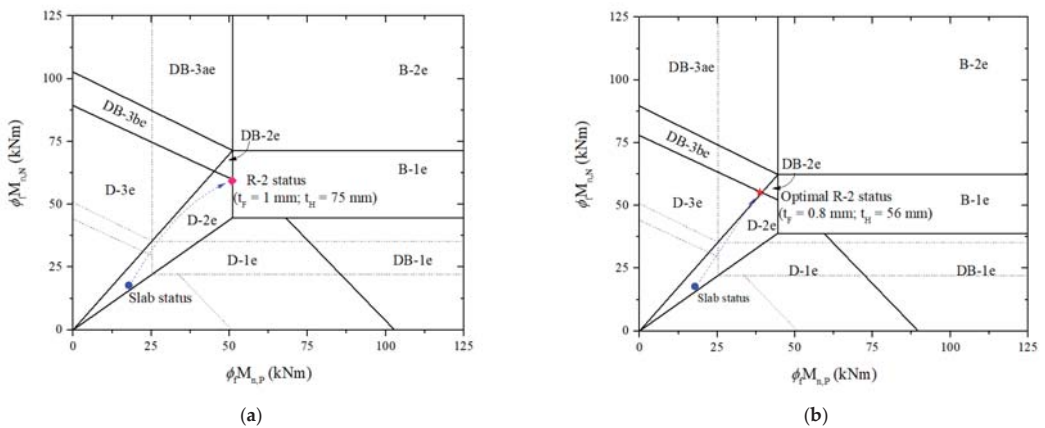
Figure 11. Establish failure limits and predict retrofitted slab status based on moment carrying capacities using the R-2 system, considering (**a**) ductile failure; (**b**) ductile failure and optimal moment ratio.

In this study, the prediction of flexural and shear carrying capacities of strengthening slabs with retrofit systems is shown to be in good agreement with the previous literature [28–31]. Additionally, civil engineers, especially the authors mentioned in this topic, have also long been interested in optimizing the strength of materials for more efficient workability of structures, resulting in cutting construction costs. As a result, evaluating the performance of optimized versus non-optimized retrofit systems is of particular interest in

the present work. Optimized retrofit systems require far fewer resources but still provide significant efficiency in strengthening RC slabs. The strengthened slab capacities using different retrofit systems are summarized in Table 7. In addition, concrete overlays are not required to be high strength to generate tension in CFRP based on the analysis in step 2, as clarified by Mosallam et al. [21]. However, HPC is still recommended to increase flexural strength and avoid potential shear failures.

Table 7. Summary results of the strengthened slab using optimized versus non-optimized retrofit systems.

Slabs	Failure Mode	w_u (kN/m)		w_f (kN/m)		$\phi_f M_{n,P}$ (kNm)		$\phi_f M_{n,N}$ (kNm)		t_F (mm)		t_H (mm)	
Existing slab	D-2e	23.6		29.8		17.8		17.8					
Retrofit with R-1	D-3e	48.2	[100%]	60.9	[100%]	26.1	[100%]	46.9	[100%]	0.60	[100%]	30	[100%]
Retrofit with optimized R-1	D-3e	46.7	[97%]	54.0	[89%]	25.2	[97%]	36.0	[77%]	0.37	[62%]	30	[100%]
Retrofit with R-2	D-2e	78.6	[100%]	94.9	[100%]	50.9	[100%]	59.4	[100%]	1.00	[100%]	75	[100%]
Retrofit with optimized R-2	D-3e	71.7	[91%]	83.0	[87%]	38.7	[76%]	55.3	[93%]	0.80	[80%]	56	[75%]

6. Conclusions

This paper presents the efficient design procedure for strengthening continuous RC slabs using innovative FRP- HPC hybrid retrofit systems based on ACI 440.2R. The different retrofit systems are evaluated for their pros and cons in developing possible strategies for strengthening RC slabs. The efficiency of the proposed approach involving determining the amount of CFRP and HPC to optimize the strength of materials and ensure the ductile failure of slabs using retrofit systems is demonstrated through the case study. Based on the obtained results, the following conclusion can be drawn:

The additional flexure and shear of strengthened slabs using retrofit systems are greatly influenced by the thicknesses of CFRP and overlay.

Quantitative CFRP can be adjusted separately or in parallel with HPC to optimize the retrofit system depending on the demand to improve flexural moment and shear strengths. At mid-span, the additional flexural and shear strength are notably affected by the HPC overlay, whereas at the support, they are individually governed by CFRP and overlay HPC, respectively. In case the appropriate thickness of CFRP laminate is not available, discrete CFRP strips can also be recommended.

The outcomes of the study indicated that a 38% reduction in CFRP does not significantly impact the design factored load in the serviceability limit state, or another solution with a simultaneous reduction in CFRP of 20% and HPC of 25% only lost design factored load and ultimate failure load by 9% and 13%, respectively.

The proposed method has advantages regarding economy and safety due to the ability to optimize the strength of materials and prevent sudden failures for retrofitted slabs. In particular, their carrying capacities are also enhanced considerably.

This study will contribute to simplifying the optimization of strengthened structures using FRP-HPC hybrid retrofit systems and promote the applicability of this technique in practice. Nevertheless, further experimental studies concerning differences in the mechanical properties of retrofit systems, concrete substrates, and environmental conditions are recommended to develop the methodology.

Appendix A

Limit equations to divide specific regions corresponding to failure modes for continuous RC slabs were derived according to the recommendations of the ACI committee [7,40]. The basis for establishing these equations is based on appropriate mechanistic analyses detailed in the available literature [30,31] and validated by experimental works [21,28,29]. For the end span, limit equations in each region are determined from the expressions.

$$M_{n,Ne} = \frac{2C_{m,N2}}{C_{v2}} V_n l_{en} \tag{A1}$$

$$M_{n,Pe} = \frac{2C_{m,Pe}}{C_{v2}} V_n l_{en} \tag{A2}$$

$$M_{N1e} = \frac{2C_{m,N1}}{C_{v2}} V_n l_{en} \tag{A3}$$

$$\frac{M_{n,Ne}}{M_{n,Pe}} = \frac{C_{m,N1}}{C_{m,Pe}} \tag{A4}$$

$$\frac{M_{n,Ne}}{M_{n,Pe}} = \frac{C_{m,N2}}{C_{m,Pe}} \tag{A5}$$

$$M_{n,Pe} + M_{n,Ne}\left(\frac{C_{v2}/8 + C_{m,N1} - C_{m,Pe} - C_{v2}C_{m,N1}}{C_{m,N2}} + C_{v2} - 1\right) = \frac{1}{4} V_n l_{en} \tag{A6}$$

$$M_{n,Pe}(2C_{v2} - 1) + M_{n,Ne}\left(\frac{C_{v2}/4 + C_{m,Pe} - C_{m,N1} - 2C_{v2}C_{m,Pe}}{C_{m,N2}} + 1\right) = \frac{1}{2} V_n l_{en} \tag{A7}$$

$$M_{n,Pe}\left(\frac{C_{v2}/8 - C_{m,N2}}{C_{m,Pe}}\right) + M_{n,Ne} = \frac{1}{4} V_n l_{en} \tag{A8}$$

$$M_{n,Pe}\left(\frac{C_{v2}/4 + C_{m,N2} - C_{m,N1} - 2C_{v2}C_{m,N2}}{C_{m,Pe}}\right) + 2C_{v2}M_{n,Ne} = \frac{1}{2} V_n l_{en} \tag{A9}$$

For interior span, the limit equations for each region are derived from the formulas as follows:

$$M_{n,Ni} = \frac{2C_{m,N}}{C_{v1}} V_n l_{in} \tag{A10}$$

$$M_{n,Pi} = \frac{2C_{m,Pi}}{C_{v1}} V_n l_{in} \tag{A11}$$

$$\frac{M_{n,Ni}}{M_{n,Pi}} = \frac{C_{m,N}}{C_{m,Pi}} \tag{A12}$$

$$M_{n,Ni}\left(\frac{C_{v1}/8 - C_{m,Pi}}{C_{m,Ni}}\right) + M_{n,Pi} = \frac{1}{4} V_n l_{in} \tag{A13}$$

$$M_{n,Ni} + M_{n,Pi}\left(\frac{C_{v1}/8 - C_{m,N}}{C_{m,Pi}}\right) = \frac{1}{4}V_n l_{in} \tag{A14}$$

Nomenclature

A_s	Tensile steel area
A_F	Tensile FRP area
b	Width of RC slab
c	Distance from extreme compression fiber to the neutral axis
C_E	Environmental reduction factor
C_m, C_v	Moment and shear coefficients
d	Distance from the extreme fiber of the compression zone to the center of the steel
d_f	Distance from the extreme fiber of the compression zone to FRP
E_c	Elastic modulus of concrete
E_F	Elastic modulus of CFRP
E_s	Elastic modulus of steel
f'_c	Compressive strength of concrete
f'_H	Compressive strength of the concrete overlay
f_{fe}	Effective stress in FRP
f_{fu}	Design ultimate strength of FRP
f^*_{fu}	Ultimate tensile strength of FRP material, reported by the manufacture
f_s	Stress in tension steel
f_y	Yield stress of steel
h	Height of RC slab
I_{cr}	Cracked moment of a section
k	The ratio of the depth of the neutral axis to reinforcement depth measured from extreme compression fiber
l_{en}	Clear span length of the end span
l_{in}	Clear span length of the interior span
n	Number of CFRP layer
M_n	Moment carrying capacity
$M_{n,Ne}$, $M_{n,Pe}$	Moment carrying capacities of the support and mid-span sections on the end-span
$M_{n,Ni}$, $M_{n,Pi}$	Moment carrying capacities of the support and mid-span sections on the interior span
M_{ns}	Flexural strength contributed by tensile steel
M_{nf}	Flexural strength contributed by CFRP
$M_{D,N2e}$	The moment carrying of the N-2e section
M_u	The factored moment at a section
t_F	The thickness of CFRP laminate
t_H	The thickness of the concrete overlay
V_n	The shear carrying capacity
V_u	Factored shear at a section
w_f	The ultimate failure load
w_u	The design factored load
w_{uM}, w_{uV}	Design factored load governed by moment and shear carrying capacities
ϕ_f, ϕ_v	Strength reduction factors for the flexural and shear strength
ψ_f	Strength reduction factors of FRP
α_1, β_1	Stress block factors
γ_c	Unit weight of concrete
ε_{bi}	The existing state strain of FRP installation
ε_{cu}	The ultimate strain of concrete
ε_{fd}	Debonding strain of FRP
ε_{fe}	Strain of FRP
ε_{fu}	The ultimate strain of FRP
ε_s	The strain of tensile steel

References

1. Maxineasa, S.G.; Taranu, N. 24—Life cycle analysis of strengthening concrete beams with FRP. In *Eco-Efficient Repair and Rehabilitation of Concrete Infrastructures*; Pacheco-Torgal, F., Melchers, R.E., Shi, X., Belie, N.D., Tittelboom, K.V., Sáez, A., Eds.; Woodhead Publishing: Sawston, UK, 2018; pp. 673–721.
2. Ma, Z.; Shen, J.; Wang, C.; Wu, H. Characterization of sustainable mortar containing high-quality recycled manufactured sand crushed from recycled coarse aggregate. *Cem. Concr. Compos.* **2022**, *132*, 104629. [CrossRef]
3. Zamani Beydokhti, E.; Shariatmadar, H. Strengthening and rehabilitation of exterior RC beam–column joints using carbon-FRP jacketing. *Mater. Struct.* **2016**, *49*, 5067–5083. [CrossRef]
4. Martínez, S.; de Diego, A.; Castro, V.J.; Echevarría, L.; Barroso, F.J.; Rentero, G.; Soldado, R.P.; Gutiérrez, J.P. Strengthening of Low-Strength Concrete Columns with Fibre Reinforced Polymers. Full-Scale Tests. *Infrastructures* **2020**, *5*, 91. [CrossRef]
5. Hariri-Ardebili, M.A.; Sanchez, L.; Rezakhani, R. Aging of Concrete Structures and Infrastructures: Causes, Consequences, and Cures. *Adv. Mater. Sci. Eng.* **2020**, *2020*, 9370591. [CrossRef]
6. Nguyen, X.T.; Park, J.S. Flexural Behavior of Steel Beams Strengthened with CFRP Under Fire. *Int. J. Steel Struct.* **2022**, 1–17. [CrossRef]
7. Committee, A.C.I. 440.2R-17: Guide for the Design and Construction of Externally Bonded FRP Systems for Strengthening Concrete Structures. *Tech. Doc.* **2017**. Available online: https://www.concrete.org/publications/internationalconcreteabstractsportal.aspx?m=details&id=51700867 (accessed on 13 November 2022).
8. Haji, M.; Naderpour, H.; Kheyroddin, A. Experimental study on influence of proposed FRP-strengthening techniques on RC circular short columns considering different types of damage index. *Compos. Struct.* **2019**, *209*, 112–128. [CrossRef]
9. Barris, C.; Sala, P.; Gómez, J.; Torres, L. Flexural behaviour of FRP reinforced concrete beams strengthened with NSM CFRP strips. *Compos. Struct.* **2020**, *241*, 112059. [CrossRef]
10. Basaran, B.; Kalkan, I. Development length and bond strength equations for FRP bars embedded in concrete. *Compos. Struct.* **2020**, *251*, 112662. [CrossRef]
11. Mukhtar, F.M.; Arowojolu, O. Recent developments in experimental and computational studies of hygrothermal effects on the bond between FRP and concrete. *J. Reinf. Plast. Compos.* **2020**, *39*, 422–442. [CrossRef]
12. Wang, X.; Yang, Y.; Yang, R.; Liu, P. Experimental Analysis of Bearing Capacity of Basalt Fiber Reinforced Concrete Short Columns under Axial Compression. *Coatings* **2022**, *12*, 654. [CrossRef]
13. Chalioris, C.E.; Kosmidou, P.-M.K.; Papadopoulos, N.A. Investigation of a New Strengthening Technique for RC Deep Beams Using Carbon FRP Ropes as Transverse Reinforcements. *Fibers* **2018**, *6*, 52. [CrossRef]
14. Hosen, M.A.; Jumaat, M.Z.; Alengaram, U.J.; Sulong, N.H.R.; Islam, A.B.M.S. Structural performance of lightweight concrete beams strengthened with side-externally bonded reinforcement (S-EBR) technique using CFRP fabrics. *Compos. Part B Eng.* **2019**, *176*, 107323. [CrossRef]
15. Moshiri, N.; Czaderski, C.; Mostofinejad, D.; Hosseini, A.; Sanginabadi, K.; Breveglieri, M.; Motavalli, M. Flexural strengthening of RC slabs with nonprestressed and prestressed CFRP strips using EBROG method. *Compos. Part B Eng.* **2020**, *201*, 108359. [CrossRef]
16. Golias, E.; Zapris, A.G.; Kytinou, V.K.; Kalogeropoulos, G.I.; Chalioris, C.E.; Karayannis, C.G. Effectiveness of the Novel Rehabilitation Method of Seismically Damaged RC Joints Using C-FRP Ropes and Comparison with Widely Applied Method Using C-FRP Sheets—Experimental Investigation. *Sustainability* **2021**, *13*, 6454. [CrossRef]
17. Esmaeili, J.; Aghdam, O.R.; Andalibi, K.; Kasaei, J.; Gencel, O. Experimental and numerical investigations on a novel plate anchorage system to solve FRP debonding problem in the strengthened RC beams. *J. Build. Eng.* **2022**, *45*, 103413. [CrossRef]
18. Triantafillou, T. Strengthening of existing concrete structures: Concepts and structural behavior. In *Textile Fibre Composites in Civil Engineering*; Elsevier: Amsterdam, The Netherlands, 2016; pp. 303–322.
19. Salman, W.D.; Mansor, A.A.; Mahmood, M. Behavior of Reinforced Concrete One-Way Slabs Strengthened by CFRP sheets in Flexural Zone. *Int. J. Civ. Eng. Technol.* **2018**, *9*, 10.
20. Torabian, A.; Isufi, B.; Mostofinejad, D.; Pinho Ramos, A. Flexural strengthening of flat slabs with FRP composites using EBR and EBROG methods. *Eng. Struct.* **2020**, *211*, 110483. [CrossRef]
21. Mosallam, A.; Taha, M.M.R.; Kim, J.J.; Nasr, A. Strength and ductility of RC slabs strengthened with hybrid high-performance composite retrofit system. *Eng. Struct.* **2012**, *36*, 70–80. [CrossRef]
22. Rabinovitch, O.; Frostig, Y. Experiments and analytical comparison of RC beams strengthened with CFRP composites. *Compos. Part B Eng.* **2003**, *34*, 663–677. [CrossRef]
23. Hawileh, R.A.; Rasheed, H.A.; Abdalla, J.A.; Al-Tamimi, A.K. Behavior of reinforced concrete beams strengthened with externallybonded hybrid fiber reinforced polymer systems. *Mater. Des.* **2014**, *53*, 972–982. [CrossRef]
24. Vu, H.D.; Phan, D.N. A framework for predicting the debonding failure modes of RC beams strengthened flexurally with FRP sheets. *Innov. Infrastruct. Solut.* **2022**, *7*, 292. [CrossRef]
25. Sherwood, E.; Bentz, E. Where is shear reinforcement required? Review of research results and design procedures. *Aci Struct. J.* **2008**, *108*, 590–600.
26. Al-Rousan, R.; Issa, H.S.M. Performance of reinforced concrete slabs strengthened with different types and configurations of CFRP. *Compos. Part B Eng.* **2012**, *43*, 510–521. [CrossRef]

27. Phan Duy, N.; Dang, V. Limiting Reinforcement Ratios for Hybrid GFRP/Steel Reinforced Concrete Beams. *Int. J. Eng. Technol. Innov.* **2021**, *11*, 1. [CrossRef]
28. Moon, J.; Taha, M.M.R.; Kim, J.J. Flexural Strengthening of RC Slabs Using a Hybrid FRP-UHPC System Including Shear Connector. *Adv. Mater. Sci. Eng.* **2017**, *2017*, 4387545. [CrossRef]
29. Nguyen, H.Q.; Nguyen, T.N.M.; Lee, D.H.; Kim, J.J. The Effects of Bond–Slip Laws on the Debonding Failure and Behavior of Flexural Strengthened RC Slabs in Hybrid FRP Retrofit Systems. *Materials* **2022**, *15*, 7453. [PubMed]
30. Kim, J.J.; Noh, H.-C.; Taha, M.M.R.; Mosallam, A. Design limits for RC slabs strengthened with hybrid FRP–HPC retrofit system. *Compos. Part B* **2013**, *51*, 19–27. [CrossRef]
31. Nguyen, H.Q.; Nguyen, T.N.M.; Lee, D.H.; Kim, J.J. A Design Method to Induce Ductile Failure of Flexural Strengthened One-Way RC Slabs. *Materials* **2021**, *14*, 7647. [CrossRef]
32. Triantafillou, T.; Matthys, S.; Audenaert, K.; Balázs, G.; Blaschko, M.; Blontrock, H.; Czaderski, C.; David, E.; di To-masso, A.; Duckett, W.; et al. *Externally Bonded FRP Reinforcement for RC Structures*; FIB: Lausanne, Switzerland, 2001; p. 138.
33. Neale, K.W.; Canada, I. *Strengthening Reinforced Concrete Structures with Externally-Bonded Fibre Reinforced Polymers*; ISIS Canada Research Network: Winnipeg, MB, USA, 2001.
34. Mugahed Amran, Y.H.; Alyousef, R.; Rashid, R.S.M.; Alabduljabbar, H.; Hung, C.-C. Properties and applications of FRP in strengthening RC structures: A review. *Structures* **2018**, *16*, 208–238. [CrossRef]
35. Siddika, A.; Mamun, M.A.A.; Ferdous, W.; Alyousef, R. Performances, challenges and opportunities in strengthening reinforced concrete structures by using FRPs—A state-of-the-art review. *Eng. Fail. Anal.* **2020**, *111*, 104480. [CrossRef]
36. Li, X.; Gao, Z.; Zhou, Y.; Sui, L.; Chen, C. Optimizing natural fiber reinforced polymer strengthening of RC beams. *Mater. Struct.* **2021**, *54*, 66. [CrossRef]
37. Sojobi, A.O.; Liew, K.M. Flexural behaviour and efficiency of CFRP-laminate reinforced recycled concrete beams: Optimization using linear weighted sum method. *Compos. Struct.* **2021**, *260*, 113259. [CrossRef]
38. Ho, H.V.; Choi, E.; Park, S.J. Investigating stress distribution of crimped SMA fibers during pullout behavior using experimental testing and a finite element model. *Compos. Struct.* **2021**, *272*, 114254. [CrossRef]
39. Wight, J.K.; MacGregor, J.G. *Reinforced Concrete: Mechanics and Design*; Pearson Education: London, UK, 2011.
40. Committee, A.C.I. 318M-19: Building Code Requirements for Structural Concrete and Commentary, Metric. *Tech. Doc.* **2019**. Available online: https://www.concrete.org/publications/internationalconcreteabstractsportal.aspx?m=details&id=51722448 (accessed on 13 November 2022).

Article

Non-Destructive Possibilities of Thermal Performance Evaluation of the External Walls

Henryk Nowak and Łukasz Nowak *

Faculty of Civil Engineering, Wroclaw University of Science and Technology, Wybrzeże Wyspiańskiego 27, 50-370 Wrocław, Poland; henryk.nowak@pwr.edu.pl
* Correspondence: lukasz.nowak@pwr.edu.pl

Abstract: Identification of the actual thermal properties of the partitions of building enclosures has a significant meaning in determining the actual energy consumption in buildings and in their thermal comfort parameters. In this context, the total thermal resistance of the exterior walls (and therefore their thermal transmittance) in the building is a major factor which influences its heat losses. There are many methods to determine the total thermal resistance of existing walls, including the quantitative thermography method (also used in this study). This paper presents a comparison of the calculated total thermal resistance values and the measured ones for three kinds of masonry walls without thermal insulation and the same walls insulated with expanded polystyrene boards. The measurements were carried out in quasi-stationary conditions in climate chambers. The following three test methods were used: the temperature-based method (TBM), the heat flow meter method (HFM) and the infrared thermography method (ITM). The measurement results have been found to be in good agreement with the theoretically calculated values: 61% of the measured values were within 10% difference from the mean value of total thermal resistance for a given external wall and 79% of the results were within 20% difference. All of the used measuring methods (TBM, HFM and ITM) have proven to be similarly approximate in obtained total thermal resistances, on average between 6% and 11% difference from the mean values. It has also been noted that, while performing measurements, close attention should be paid to certain aspects, because they can have a major influence on the quality of the result.

Keywords: external walls; thermal measurements; R-value; thermal resistance; temperature-based method; heat flow meter method; infrared thermography method

1. Introduction

Buildings play an important role in achieving sustainable development goals, among others aimed at reducing greenhouse gas emissions, by using renewable energy sources and reducing annual energy consumption. To achieve this goal, one should use known ways of solar energy (passive and active) utilization, low-temperature geothermal energy, highly efficient heating, ventilation and air conditioning (HVAC) equipment and domestic hot water production equipment. However, the key is to achieve the optimal energy performance of the building by significantly limiting heat losses through its thermal envelope, mainly through its exterior walls.

Apart from the behavior of the users, the specific energy consumption in a building strongly depends on the thermophysical properties of its partitions (building envelope elements) [1,2]. The thermal envelope of the building, especially its exterior walls, is an important factor in shaping its annual heat balance and thermal comfort parameters. The basic quantities that characterize the thermal properties of walls are thermal resistance (R), total thermal resistance (R_{tot}) and the thermal transmittance (U). The accuracy with which these quantities are determined can significantly affect the accuracy of the actual and forecasted energy consumption of buildings [3,4]. In situ measurements of the

U-value have been performed since the early 1980s [5–7]. The measurements were found to be very useful for determining the actual thermal performance of the exterior walls in existing buildings, especially since the values determined on-site in buildings in the actual conditions would often significantly differ from the calculated ones. In the subsequent years, several experimental and computational studies aimed at determining the total thermal resistance of walls, using the approach for heat flow steady state, including reviews of the measurement methods [8,9], methodology [10–13], the use of in situ methods [2,14–17] and unsteady state conditions [18–21], were carried out.

There are many different theoretical and practical methods of determining the total thermal resistance of the exterior walls. On the one hand, the simplest way to determine the total thermal resistance of building enclosures consists of performing calculations consistent with ISO 6946 [22], where formulas can be found for the calculations depending on the structural system of the building enclosure. On the other hand, in practice, there often occur discrepancies between the tabular and actual thermal properties of the individual layers of a building partition. This applies mainly to the thermal conductivity coefficient of the particular layers and their density (and therefore their heat capacity) [12,23,24]. As a result, it often becomes necessary to carry out additional measurements, e.g., of the thickness of the individual layers or the density of the materials (destructive methods). Calculations in accordance with ISO 6946 are mainly performed when designing exterior building enclosures for new buildings. Whereas when it is necessary to determine the total thermal resistance through in situ measurements in existing buildings, the international ISO 9869-1 standard [25], recommending the use of the heat flow meter method (HFM), is applied. Although this standard has several advantages, two major problems which can be encountered when using it, i.e., the long duration of the measurements due to unstable boundary conditions and the questionable accuracy of the measurements, were indicated in [26,27]. Standard ISO 9869-1 recommends a minimum measurement duration of 72 h (a multiple of the full 24 h) and that the total thermal resistance values from the two last measurement days should not differ by more than 5%. Moreover, using this standard, one can analyze measurement data by the average method and the dynamic method (the latter yields more accurate measurement results). A new addition to the documents related to in-situ measurement of thermal resistance of building partitions is the ISO 9869-2 standard, which introduces the infrared camera method [28]. In issues related to heat transfer through building partitions and the determination of their thermal resistance, a very important issue is to take into account the variability of material moisture and its transfer [29,30]. However, this research problem was not within the scope of this article.

Another method of determining the total thermal resistance of a building enclosure, and thus determining the latter's U-value, is the generally known and well-established infrared thermography method (ITM). For many years, infrared thermographic surveys of buildings have been a precise and quick quality evaluation method [31–33], mainly used to locate defects in the thermal envelope of buildings [34–36] with presentations of basic and research issues and their applications [37,38]. Using this method, thermal bridges can be identified as caused by discontinuities or absence of thermal insulation [39–42], damp patches in building fabric elements [43–45] and places of air infiltration through the envelope [46–48]. Infrared thermography offers great possibilities to qualitatively assess the heat losses of different types of buildings and to analyze them to fully solve the problem of the energy performance of buildings [49]. This method is most often used as passive thermography, that is, as a method to investigate the building fabric as-is, without controlled outside interference and thermal stimulation of its thermodynamic state [35,38,50,51]. It can also be used as active thermography, i.e., with controlled outside temperature interference in the thermal state of the investigated building fabric [52–55] and inverse contrast in NDT materials' research [56,57]. Furthermore, through thermographic measurements, one can also determine the physical quantities characterizing the investigated building enclosure. Taking this into account, thermal imaging studies have been used to quantify external walls, including the U-value of walls [58,59], heat flux density [60–63] and to compare various

measurement and calculation methods [64,65]. As part of the present study, quantitative thermographic measurements were carried out in climatic test chambers using passive ITM to determine the total thermal resistance of the investigated building enclosure elements, and therefore their thermal transmittance.

For many years, building fabric elements also have been investigated in climate chambers, most often in quasi-stationary conditions. Such investigations deal with many problems related to building physics, energy performance of buildings, including all kinds of building fabric and thermal insulation [66–69], and the effect of ventilation on thermal comfort and indoor air quality (IAQ), particularly in office buildings [70]. The advantage of tests conducted in climate chambers over in situ tests in buildings is that they are independent of the weather conditions and therefore can be conducted practically all year round, whereby they are not limited to only the heating season and can be carried out for a set difference in air temperature between the two sides of a building enclosure. Practically, this means that tests conducted in climate chambers are more productive as regards the number of building fabric elements tested per year.

Taking into account the above, the main aim of the present research was to compare the effectiveness of the various methods of testing masonry walls by comparing the total thermal resistance values calculated and measured under quasi-stationary conditions in climate chambers for three types of masonry walls without thermal insulation and for the same walls insulated with expanded polystyrene. The same difference in air temperature between the walls' two sides was maintained for each of the tested walls. Three testing methods were used and evaluated with respect to the accuracy of the measurement results they produced. The methods were as follows: the temperature-based method (TBM), the heat flow meter method (HFM) and the infrared thermography method (ITM), which is also referred to in the literature as the infrared thermography technique (ITT). The purpose of the investigations was also to evaluate the effectiveness of the methods and to highlight the key factors that influence the accuracy and correctness of the measurement.

2. Thermal Resistance Assessment for Building Enclosure Parts

2.1. Calculation Method

In the design stage, an assessment of the thermal properties of a building enclosure is usually based on calculations of the unidirectional heat transmission process described in ISO 6946 [22]. Heat transmission through a building enclosure consists of the absorption of heat from the environment with a higher temperature (usually a heated room) by the building enclosure's surface, the flow of the heat through the building enclosure and the transfer of the heat from the building enclosure's other surface to the air with a lower temperature, and is defined by the partition's total thermal resistance—R_{tot} ((m^{2}K)/W), determined from the relation:

$$R_{tot} = R_{si} + R + R_{se} \qquad (1)$$

where:

R_{si}, R_{se}—surface thermal resistances, on the internal and external side respectively, assumed or calculated according to Section 2.3.1 ((m^{2}K)/W),

R—the design thermal resistances of the partition layers ((m^{2}K)/W), determined from the relation:

$$R = \sum_{i=1}^{n} \frac{d_i}{\lambda_i} \qquad (2)$$

where:

d_i—the thickness of a given material layer (m),

λ_i—the thermal conductivity coefficient of the given material layer (W/(mK)).

The above method is commonly used in newly designed buildings to evaluate their energy performance and also to confirm that they meet the energy conservation requirements specified by the binding regulations. However, sometimes, there can arise the need to evaluate the thermal performance of building fabric through measurements, i.e.,

- In the case of a new building, when there is a suspicion as to the thermal performance of the materials used when confronted with the design specifications.
- In the case of an existing building, to assess its technical condition or when there is no relevant information in its design documents.

2.2. In Situ Measuring Methods

The thermal properties of building fabric elements are usually measured when a quantitative or qualitative evaluation of their thermal performance is needed. Although thermographic surveys are mainly used for quality assessments of building enclosures, they can also be the basis for a quantitative evaluation of their thermal properties, even without simultaneously carrying out additional measurements of other quantities. Even though qualitative thermographic tests are sufficient for the purpose of assessing the condition of the thermal insulation in building enclosures, for many years in the literature on the subject, attempts have been made to quantitatively evaluate building enclosures through thermographic tests. The following three main methods for solving this problem can be distinguished:

- Method 1—the temperature-based method (TBM), consisting of measuring air temperatures and the building enclosure's surface temperatures on both sides.
- Method 2—the heat flow meter method (HFM), consisting of measuring heat flux densities and the surface temperatures of the building enclosure on both sides.
- Method 3—the infrared thermography method (ITM), consisting of measuring air temperatures and the building enclosure's surface temperatures on both sides (similarly as in Method 1) and performing radiometric measurements on both sides of the building enclosure: this method is precise, but labor-intensive.

2.2.1. Method 1—The Temperature-Based Method (TBM)

The U-value of a building partition can be determined by measuring the appropriate temperatures and calculating its total thermal resistance, expressed by the relation:

$$R_{tot} = \frac{R_{si}(T_i - T_e)}{(T_i - T_{si})} \tag{3}$$

or the relation:

$$R_{tot} = \frac{R_{se}(T_i - T_e)}{(T_{se} - T_e)} \tag{4}$$

where:

R_{si}, R_{se}—internal surface thermal resistance and external surface thermal resistance $((m^2K)/W)$,

T_i, T_e—air temperature on respectively the internal and external side of the tested building partition (K),

T_{si}, T_{se}—the temperature of respectively the internal and external surface of the tested building partition (K).

Temperature sensors should be attached to a building enclosure in a way that ensures proper contact with the latter using, e.g., thermal paste or adhesive tape. Furthermore, they should be so located that air temperature measurements are not exposed to disturbing factors (far from heat sources, windows and air diffusers). Temperature measurements should be conducted for such a period of time that a time window of about 72 h with visible building enclosure surface and air temperature stabilization on both sides of the tested building enclosure could be selected from this period.

2.2.2. Method 2—Heat Flow Meter Method (HFM)

By measuring heat flux density, one can obtain a more accurate result as large fluctuations in air temperature readings can be partially eliminated in this way. In this case, the thermal resistance can be determined from the formula:

$$R = \frac{(T_{si} - T_{se})}{q} \tag{5}$$

and then, total thermal resistance can be calculated from the formula:

$$R_{tot} = R_{si} + R + R_{se} \tag{6}$$

where:

T_{si}, T_{se}—the temperature of respectively the internal and external surface of the tested building enclosure (K),

q—the measured heat flux flowing through the building enclosure (W/m^2),

R_{si}, R_{se}—the calculated surface thermal resistances on respectively the internal and external side of the building partition ((m^{2}K)/W).

2.2.3. Method 3—Infrared Thermography Method (ITM)

In the case of this method, the determination of thermal resistance performed as in Method 1 should be supplemented with radiometric measurements of the mean radiation temperature in the external environment and the mean radiation temperature in the room. This is because the formulas describing the unidirectional steady heat flow through building enclosures were derived assuming that the external air temperature and the mean external environment radiation temperature (representing the influence of the thermal radiation from the nearest surroundings of buildings) are equal. This assumption is a considerable simplification as a complex heat exchange occurs on the boundary surfaces of a building enclosure so that the heat flux density on a given surface of the building enclosure is equal to the sum of the densities of the heat fluxes transferred through convection and radiation. This means that the resultant heat flux proceeds from the building enclosure's external surface via radiation towards ambient radiation temperature, T_r, and via convection towards air temperature, T. The temperature, being a total thermal rating index of a physical environment, taking into account the radiation temperature of the surroundings and the air temperature, is known as operative temperature, T_{op}, in environmental physics and is expressed by the formula:

$$T_{op,i} = \frac{h_{ci}T_i + h_{ri}T_{ri}}{h_{ci} + h_{ri}} \tag{7}$$

or the relation:

$$T_{op,e} = \frac{h_{ce}T_e + h_{re}T_{re}}{h_{ce} + h_{re}} \tag{8}$$

where:

T_i, T_e—air temperature on respectively the internal and external side of the building partition (K),

T_{ri}, T_{re}—mean radiation temperature on respectively the internal and external side of the partition (K),

h_{ci}, h_{ce}—the convection heat transfer coefficient on respectively the internal and external side of the partition (W/(m^{2}K)),

h_{ri}, h_{re}—the radiative heat transfer coefficient on respectively the internal and external side of the partition (W/(m^{2}K)).

Hence, the total thermal resistance of a building partition can be calculated from the relation:

$$R_{tot} = \frac{\left(T_{op,i} - T_{op,e}\right)}{q} \tag{9}$$

where:

q—the heat flux flowing through the building enclosure (W/m^2).

2.3. Surface Thermal Resistances

2.3.1. Simplified Method

The assumption of the correct value of surface thermal resistances (R_{si} and R_{se}) on both sides of the tested building enclosure has a noticeable effect on the calculated values of its total thermal resistance (R_{tot}) and thermal transmittance (U). The European standard ISO 6946 [22] in its Table 7 suggests that $R_{si} = 0.13$ m^{2}K/W and $R_{se} = 0.04$ m^{2}K/W for an external partition and for horizontal heat flow.

2.3.2. Calculation—Surface Temperatures and Air Movement Velocities Are Known

In real situations, depending on weather conditions, surface resistances R_{si} and R_{se} can diverge from the above values. In such cases, a more accurate method can be the one described in Appendix A of the ISO 6946 standard [22], according to which one can use the actual wind speed to obtain the value of the convective heat transfer coefficient, h_c. In the research, it was assumed that the air movement caused by the fans of heating/cooling units in the climate chambers was an equivalent of wind, and because of that, coefficients h_{ci} and h_{ce} for both sides of the tested walls will be calculated in that way. The air movement was measured on, respectively, the internal side and the external side at the tested building enclosure by means of anemometers. Then, surface thermal resistance R_{si} and R_{se} should be determined for both sides for the horizontal heat flux flow, using the formulas:

$$R_{si} = \frac{1}{h_i} = \frac{1}{h_{ci} + h_{ri}} \tag{10}$$

$$R_{se} = \frac{1}{h_e} = \frac{1}{h_{ce} + h_{re}} \tag{11}$$

where:

h_{ci}, h_{ce}—the convective heat transfer coefficient on respectively the internal side and the external side, calculated from the formulas:

$$h_{ci} = 4 + 4v_i \tag{12}$$

$$h_{ce} = 4 + 4v_e \tag{13}$$

where:

v_i, v_e—wind speed adjacent to the surface of respectively the internal and the external side (m/s),

h_{ri}, h_{re}—the radiative heat transfer coefficient on respectively the internal side and the external side, calculated from the formulas:

$$h_{ri} = \varepsilon h_{ri,0} = \varepsilon 4\sigma T_{mi}^3 \tag{14}$$

$$h_{re} = \varepsilon h_{re,0} = \varepsilon 4\sigma T_{me}^3 \tag{15}$$

where:

ε—surface emissivity into a half-space, assumed as equal to 0.9 (–),

$h_{ri,0}$, $h_{re,0}$—a black body radiation heat transfer coefficient (W/m^{2}K),

σ—the Stefan–Boltzmann constant equal to 5.67×10^{-8} (W/(m^{2}K^4)),

T_{mi}, T_{me}—mean thermodynamic temperatures of the surfaces (K).

2.3.3. Calculation—Air Temperatures, Surface Temperatures and Heat Flux Density Are Known

In the case when it is possible to carry out additional surface temperature measurements on both sides of the tested building enclosure and to determine the heat flux, the

surface thermal resistances can be experimentally determined in accordance with the formulas:

$$R_{si} = \frac{(T_i - T_{si})}{q} \tag{16}$$

$$R_{se} = \frac{(T_{se} - T_e)}{q} \tag{17}$$

where:

T_{si}, T_{se}—the temperature of respectively the internal and external surface of the analyzed element (K),

T_i, T_e—the air temperature on respectively the internal side and the external side (K),

q—the heat flux flowing through the building enclosure (W/m^2).

The above methods were used in the analyses carried out by the authors, but this does not exhaust the subject. There are many methods of estimating radiative heat transfer coefficients, h_r, and convective heat transfer coefficients, h_c. A comprehensive analysis of this subject can be found in [63].

3. Materials and Methods

3.1. Tested Elements

The research was carried out for a part of the building enclosure, namely the external walls. Three different materials were tested: aerated concrete blocks, ceramic bricks and concrete blocks, as these are some of the most commonly used materials in residential buildings in Poland. The homogeneous tested walls were divided into two groups: uninsulated and insulated. Wall A was made of 240 mm × 240 mm × 590 mm class 600 H + H aerated concrete blocks laid in Baumit ThermoMörtel 50 insulating mortar. In the case of the insulated version of wall A, 10 cm thick EPS (expanded polystyrene) boards were glued to it on the cooler side and then covered with fiberglass-reinforced mineral render. Wall B was made of 60 mm × 120 mm × 250 mm solid ceramic bricks laid in cement-lime mortar. In the case of the insulated version of wall B, 10 cm thick EPS boards with the same properties as before were glued to it on the cooler side and then covered with fiberglass-reinforced mineral render. Wall C was made of 120 mm × 250 mm × 380 mm solid concrete blocks laid in cement-lime mortar. In the case of the insulated version of wall C, 10 cm thick EPS boards were also used. After building each wall, a time of 4–6 weeks was used to season the construction and to get rid of construction moisture. During that time, the doors of the climate chambers were left open. The basic material specifications of the walls are presented in Table 1. The given thermal conductivity coefficients are declared values and were taken from producer technical specifications, provided by the construction material warehouse or from tabular data from Polish technical standards [71–73]. These values were not experimentally verified (measured) by the authors.

3.2. Test Setup

Measurements of the thermal resistance of selected external walls were conducted in a sleeve between two connected climate chambers, as shown in Figure 1. The major specifications of the set are as follows:

- The warm chamber (on the left side, blue one): capacity 30 m^3, internal dimensions 3.0 m × 4.0 m × 2.5 m, temperature range −30–+80 °C and relative humidity range 10–95%.
- The cold chamber (on the right side, grey one): capacity 30 m^3, internal dimensions 3.0 m × 4.0 m × 2.5 m, temperature range −40–+85 °C and relative humidity range 10–95%.

Table 1. Basic specifications of partitions tested in climate chambers.

Test Object	Material, Thickness (Innermost Layer First)	Declared Thermal Conductivity	Calculated R-Value
		W/mK	m²K/W
Wall A	Aerated concrete blocks, 24 cm	0.210 *	1.313
Wall A (insulated)	Aerated concrete blocks, 24 cm EPS boards, 10 cm Fiberglass mesh-reinforced mineral render, 0.5 cm	0.210 * 0.040 ** 1.000 ***	3.818
Wall B	Solid ceramic brick, 25 cm	0.770 ***	0.495
Wall B (insulated)	Solid ceramic brick, 25 cm EPS boards, 10 cm Fiberglass mesh-reinforced mineral render, 0.5 cm	0.770 *** 0.040 ** 1.000 ***	2.999
Wall C	Concrete blocks, 25 cm	1.000 ***	0.420
Wall C (insulated)	Concrete blocks, 25 cm EPS boards, 10 cm Fiberglass mesh-reinforced mineral render, 0.5 cm	1.000 *** 0.040 ** 1.000 ***	2.925

* Taken from the technical data sheet for the material, ** provided by construction material warehouse, *** taken from tabular data from Polish technical standards.
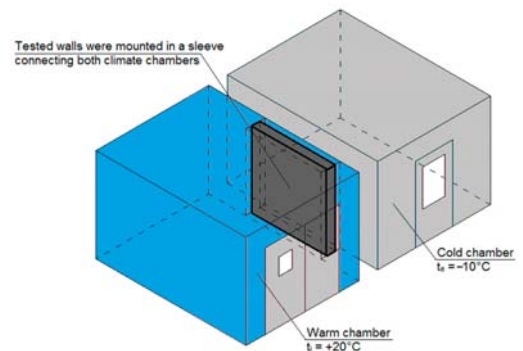
Figure 1. Test setup: (**a**) view of two climate chambers connected together, (**b**) locations of tested walls in sleeve connecting two climate chambers.

The tested wall would be placed in a sleeve connecting the two climate chambers, in which conditions simulating the behavior of building enclosures in the heating season were maintained, that is:

- The warm chamber with activated controlled air temperature θ_i = +20 °C and relative humidity φ_i = 50%.
- The cold chamber with activated controlled air temperature θ_e = −10 °C and uncontrolled relative humidity φ_e in the area of 30%.

All homogenous building enclosures were tested from the instant the temperature settings in the chambers were activated (at the instant of activation the air temperature in the chambers was equal to the temperature in the laboratory room, approximately 20–25 °C) until the temperatures in the chambers and the heat fluxes stabilized. Then, the measurements were conducted for at least 7 days. All the enclosures were positioned along the axis of the sleeve connecting the two climate chambers. The erected wall was left for the mortar to set. A schematic diagram of the sensor connection on both sides of the tested

building enclosures is shown in Figure 2. Then, sensors were placed on both sides, and as part of the measurements, the following were registered:

- Air temperatures in the chambers by means of Ahlborn FHA646-E1 and FHA646-E1C T/RH (temperature and relative humidity) sensors with an accuracy of ± 0.2 °C, in the range of 5–60 °C.
- Air temperature on the warm chamber side with the FLIR P65 thermal imaging camera with an accuracy of ± 2 °C or $\pm 2\%$ of the measured value.
- Air movement velocities in the chambers with the help of the Ahlborn FVA935-TH4K2 TA5O anemometer with an accuracy of ± 0.04 m/s + 1% of the measured value, in the range of 0.08–2 m/s, and the FVA605-TA5O anemometer with an accuracy of $\pm 1.5\%$ of the measured value, in the range of 0.15–5 m/s.
- Wall surface temperatures by means of class 2 NiCrNi thermocouples with an accuracy of ± 2.5 °C or ± 0.0075 multiplied by the measured value, in the range of -45–$+200$ °C, and a FLIR P65 thermal imaging camera on the warm chamber side.
- The density of the heat flux penetrating through the building enclosure with Ahlborn FQA 150–2 m with an accuracy of 5% at 25 °C.
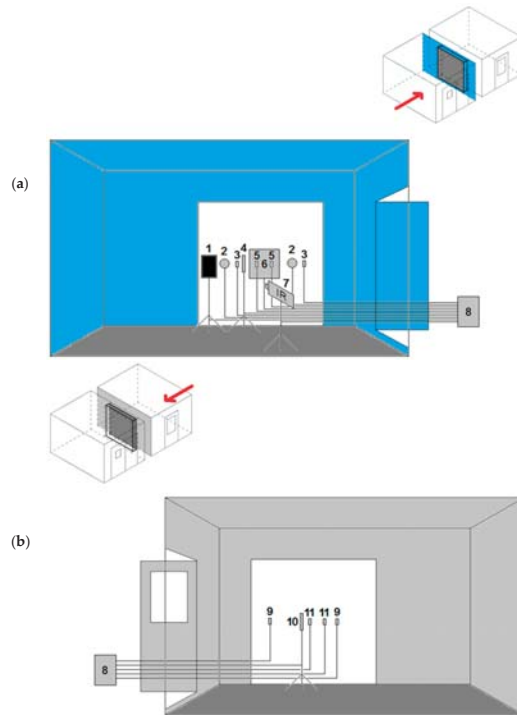
Figure 2. Schematic showing arrangement of sensors and measuring instrumentation on analyzed wall's warm side (**a**) and on its cold side (**b**). Description of visible elements: 1—black sheet of paper (ambient temperature measurement by IR camera), 2—Hukseflux TRSYS01 system heat flux density sensors, 3—Hukseflux TRSYS01 system sensors measuring building enclosure internal surface temperature, 4—Ahlborn thermal anemometer (measuring internal air temperature and humidity), 5—Ahlborn sensors (thermocouples) measuring building enclosure surface temperature, 6—Ahlborn sensor (0.5 m × 0.5 m) measuring heat flux density, 7—FLIR P65 thermal imaging camera, 8—data loggers, 9—Hukseflux TRSYS01 system sensors for measuring building enclosure external surface temperature, 10—Ahlborn thermal anemometer (measuring external air temperature and humidity), 11—Ahlborn sensors (thermocouples) measuring building enclosure surface temperature.

All the Ahlborn sensors were connected to Ahlborn Almemo data loggers (2690-8, 2890-9 or 5690-2M09). In addition to this, a Hukseflux TRSYS01 system, dedicated to measuring the thermal resistance of building enclosures, with an accuracy of ±3% and the operating range of −30–+70 °C, which doubled the surface temperature measurements on both sides of the building enclosure and the density of the heat flux penetrating through the latter, was connected. A photo of one of the measurements carried out is shown in Figure 3.

| (**a**) | (**b**) |

Figure 3. Photo of tested building enclosure (in this case, insulated wall A) with visible arrangement of sensors: (**a**) on warm chamber side, (**b**) on cold chamber side.

3.3. Analyzed Methods of Determining Thermal Resistance for Selected Walls

As part of the investigations, the following methods:

- A computational method (Method 0a),
- A computational-measurement method (Method 0b),
- Measurement methods (Methods 1, 2a, 2b, 3a and 3b),

were compared in determining the thermal resistance of 6 different building enclosures (walls A, B and C in their insulated and uninsulated versions). The methods differed from each other in (among other things):

- The source of the building partition parameters used in calculations—Method 0a is based solely on theoretical calculations using tabular material and surface resistance (R_{si} and R_{se}) values, Method 0b supplements such data with calculated surface resistances and the other methods (1–3b) use measured surface resistances.
- The parameters which need to be measured in order to obtain the total thermal resistance value—in Methods 1, 3a and 3b, the result is determined on the basis of only air and wall surface temperature measurements, whereas in Methods 2a and 2b, it is determined using the measured wall surface temperatures and heat flux densities.
- The way the required parameters are measured—in Methods 2a and 2b, thermocouples are used to measure wall surface temperatures and T/RH sensors are used to measure air temperatures, whereas in Methods 3a and 3b, both air and wall surface temperatures on the warm chamber side are measured by a thermal imaging camera.
- The kind of measuring equipment—in Method 2a, universal temperature sensors and heat flux density measuring sensors are used, whereas in Method 2b, a system dedicated to measuring the thermal resistance of building enclosures is used.
- The way of averaging the measured wall surface temperatures—in Method 3a, the surface temperatures measured by a thermal imaging camera are averaged on the basis of three random thermograms obtained from two spot measurements taken on the wall (six measurements in total), whereas in Method 3b, surface temperatures are averaged on the basis of three random thermograms based on the average for a 25 cm × 40 cm area.

All the above methods are compared in Table 2, which also includes information on how the components of total thermal resistance (R_{tot}), i.e., surface thermal resistances (R_{si} and R_{se}) and thermal resistance (R) of the wall layers, were determined. Since the values of the thermal conductivity coefficients for the materials used (aerated concrete, solid ceramic bricks, concrete blocks, masonry mortar, expanded polystyrene and render) were taken from the specification tables and not verified by the authors, Methods 0a and 0b were not treated as references for the other methods, but on equal terms with the latter.

Table 2. Analyzed methods to determine the thermal resistance of building partitions.

Method of Determining Thermal Resistance of Building Enclosure			R_{si}	R	R_{se}	R_{tot}
Name	**Type**	**Description**	m^{2}K/W	m^{2}K/W	m^{2}K/W	m^{2}K/W
0a	computational	Calculation using material data according to ISO 6946	ISO 6946, Table 7 (Section 2.3.1)	$R = \sum_{i=1}^{n} \frac{d_i}{\lambda_i}$ (Section 2.1)	ISO 6946, Table 7 (Section 2.3.1)	$R_{tot} = R_{si} + R + R_{se}$
0b	computational + measurement	Calculation using material data according to ISO 6946 + measurement of air movement velocity	ISO 6946, Appendix A (Section 2.3.2)	$R = \sum_{i=1}^{n} \frac{d_i}{\lambda_i}$ (Section 2.1)	ISO 6946, Appendix A (Section 2.3.2)	$R_{tot} = R_{si} + R + R_{se}$
1	measurement	Measurement of air and wall surface temperatures and air movement velocity by thermocouples	ISO 6946, Appendix A (Section 2.3.2)	-	ISO 6946, Appendix A Section 2.3.2)	$R_{tot} = \frac{R_{tot,i} + R_{tot,e}}{2}$ where: $R_{tot,i} = \frac{R_{si}(T_i - T_e)}{(T_i - T_{si})}$ (Section 2.2.1) $R_{tot,e} = \frac{R_{se}(T_i - T_e)}{(T_{se} - T_e)}$ (Section 2.2.1)
2a	measurement	Measurement of air and wall surface temperatures by thermocouples and heat flux density (Ahlborn sensors)	$R_{si} = \frac{(T_i - T_{si})}{q}$ (Section 2.3.3)	$R = \frac{(T_{si} - T_{se})}{q}$ (Section 2.2.2)	$R_{se} = \frac{(T_{se} - T_e)}{q}$ (Section 2.3.3)	$R_{tot} = R_{si} + R + R_{se}$
2b	measurement	Measurement of air temperatures by thermocouples and wall surface temperatures and heat flux density by dedicated device (Hukseflux TRSYS01)	ISO 6946, Appendix A (Section 2.3.2)	$R = \frac{R_1 + R_2}{2}$ where: R_1 and R_2 are results of measurement by dedicated device	ISO 6946, Appendix A (Section 2.3.2)	$R_{tot} = R_{si} + R + R_{se}$
3a	measurement	Spot measurement of air and surface temperatures on warm side by IR camera, on cold side by thermocouples	ISO 6946, Appendix A (Section 2.3.2)	-	ISO 6946, Appendix A (Section 2.3.2)	$R_{tot} = \frac{R_{si}(T_i - T_e)}{(T_i - T_{si})}$ (Section 2.2.1)
3b	measurement	Area measurement of air and surface temperatures on warm side by IR camera, on cold side by thermocouples	ISO 6946, Appendix A (Section 2.3.2)	-	ISO 6946, Appendix A (Section 2.3.2)	$R_{tot} = \frac{R_{si}(T_i - T_e)}{(T_i - T_{si})}$ (Section 2.2.1)

3.4. Air and Surface Temperatures from Thermal Imaging Camera (Methods 3a and 3b)

In this case, the temperatures were calculated as the average of readings from three randomly chosen thermograms recorded in the already stabilized heat flow period, selected from the same 72 h window as the measurements taken by the other sensors (i.e., heat

flux density and surface temperature). In both methods, the air temperature was assumed as equal to the temperature of an object with a slight heat capacity and a high surface emissivity, placed at a certain distance from the tested wall. Therefore, the temperature of a spot on a black sheet of paper, denoted as SP01 on the thermogram, was read.

In Method 3a, the wall surface temperature as an average of six values was calculated. That means two spot readings from three random thermograms (two measurements on three thermograms). The spots were randomly selected avoiding wall corners, joints, sensor cables and other places with disturbed temperature fields. The surface temperature reading spots are marked as SP02 and SP03 on the thermograms.

In Method 3b, the wall surface temperature value used in thermal resistance calculations was obtained as the mean surface temperature of a certain area of the wall (1 measurement on 3 thermograms). The areas were randomly selected, but as before, places with temperature field disturbances were avoided. This area covered several masonry elements and the joints between them. On average, it was a 25 cm × 40 cm area. The surface temperature areas are marked as AR01 on the thermograms.

4. Results

4.1. Surface Thermal Resistances on Both Sides of Tested Walls

In the case of the computational method, the surface thermal resistances R_{si} and R_{se} for the tested building enclosure should be assumed in accordance with Table 1. While the value of 0.13 m²K/W assumed as surface resistance, R_{si}, on the warm chamber side did not raise any doubts, the authors had doubts regarding the value of R_{se} to be assumed on the cold chamber side. By assumption, this chamber mimics the external environment, but it was found that the air movement velocity measured there was several times lower (see the next paragraph) than the one assumed in ISO 6946 (v_e = 4 m/s) for the given R_{se} values. Therefore, for further analyses on the cold chamber side, R_{si} = 0.13 m²K/W was assumed as for a horizontal heat flow, but for a space within the building envelope (e.g., for an unheated space).

During one of the measurement sessions in the climate chambers, in which air temperatures $θ_i$ = +20 °C and $θ_e$ = −10 °C were maintained in respectively the warm chamber and the cold chamber, the air movement velocities measured by the anemometers on average amounted to:

- In the warm chamber v_i = 0.56 m/s,
- In the cold chamber v_e = 0.13 m/s.

Assuming that no surface temperature could be measured in this case (no surface temperature sensor is available), the mean thermodynamic temperatures of the two surfaces in Formulas (14) and (15) were set as the air temperatures in climate chambers, so T_{mi} = 293.15 K and T_{me} = 263.15 K. After that, the above air velocities were introduced into Formulas (12) and (13) and the surface thermal resistances were calculated from Formulas (10) and (11). Then, during measurements of the heat flux density and the air and surface temperatures for each tested wall, the actual surface resistances on both sides of the enclosure were determined from Formulas (16) and (17). All of the R_{si} and R_{se} values are presented in Table 3. The clear differences between the calculated surface resistances and the measured ones are due to the measurement conditions that differed from the real building enclosure service conditions. Additionally, the specific way in which air with set temperature is blown into climate chambers (different chamber designs), how closely the temperature sensors adhere to the analyzed wall surface and the heat flux density contribute to the differences.

Table 3. Surface thermal resistances of tested partitions depending on method of determining them.

Method of Determining Surface Thermal Resistances	R_{si}	R_{se}
	m^{2}K/W	m^{2}K/W
Computational—ISO 6946, Table 7 (Section 2.3.1)	0.130	0.130
Computational + measurement—ISO 6946, Appendix A	0.088	0.121
Measurement—Wall A	0.101	0.099
Measurement—Wall B	0.159	0.100
Measurement—Wall C	0.169	0.136
Measurement—Wall A (insulated)	0.083	0.153
Measurement—Wall B (insulated)	0.214	0.134
Measurement—Wall C (insulated)	0.132	0.139
Measurement—mean value	0.143	0.127

4.2. Air Temperatures in Chambers and Wall Surface Temperatures

4.2.1. Measurements with Thermocouples

Diagrams of the internal (warm) surface temperature and external (cold) surface temperature of the walls measured with thermocouples and air temperatures in the warm chamber and in the cold chamber during the measurements are shown in Figure 4 for the walls without insulation and in Figure 5 for the insulated walls.

From the start of the test (switching on the chambers), the temperature values began to approach the target temperature settings, i.e., θ_i = +20 °C and θ_e = −10 °C. The temperature values given below are the average of the temperatures in the 72 h time window (marked with a double-headed arrow in the diagrams) selected from the period of stabilized temperatures. In the case of wall A (Figure 4a), one can notice that the time in which the planned temperature settings were reached amounted to about 24 h, whereby the surface temperatures also stabilized. The latter on average was θ_{si} = +17.8 °C and θ_{se} = −6.8 °C. In the case of wall B (Figure 4b), the time in which the planned temperature settings were reached was similar (about 36 h), but the surface temperatures stabilized after about 96 h from the start, ranging on average to θ_{si} = +10.7 °C and θ_{se} = −0.6 °C. In the case of wall C (Figure 4c), the time in which the planned settings were reached amounted to about 36 h and the surface temperatures stabilized after 90 h, on average amounting to θ_{si} = +9.7 °C and θ_{se} = +0.4 °C. Then, the walls above were insulated with expanded polystyrene and tested again in the climate chambers. The temperature diagrams for insulated wall A are shown in Figure 5a. In this case, the time in which the planned temperature settings were reached was much shorter, slightly more than 6 h. The surface temperatures stabilized after less than 24 h, but probably due to the fact that the door to the warm chamber had been accidentally left open there are visible fluctuations in air temperature in the third 24 h of measurements. Therefore, it was decided to average the temperatures measured from the 72nd hour onwards, whereby θ_{si} = +19.5 °C and θ_{se} = −7.8 °C were obtained. The temperature diagrams for insulated wall B are shown in Figure 5b. In this case, the time to reach the planned temperature settings was disturbed by the abnormal operation of the cold chamber, in which the temperature stabilized as late as after 48 h. The surface temperatures averaged from the 84th hour onwards amounted to θ_{si} = +18.3 °C and θ_{se} = −8.1 °C. In the case of insulated wall C (Figure 5c), the time in which the planned temperature settings were reached was slightly longer, amounting to about 12 h. The surface temperatures stabilized relatively quickly (after less than 24 h), but for averaging purposes, the measurements from the 84th hour onwards were taken, whereby θ_{si} = +18.8 °C and θ_{se} = −7.5 °C were obtained.
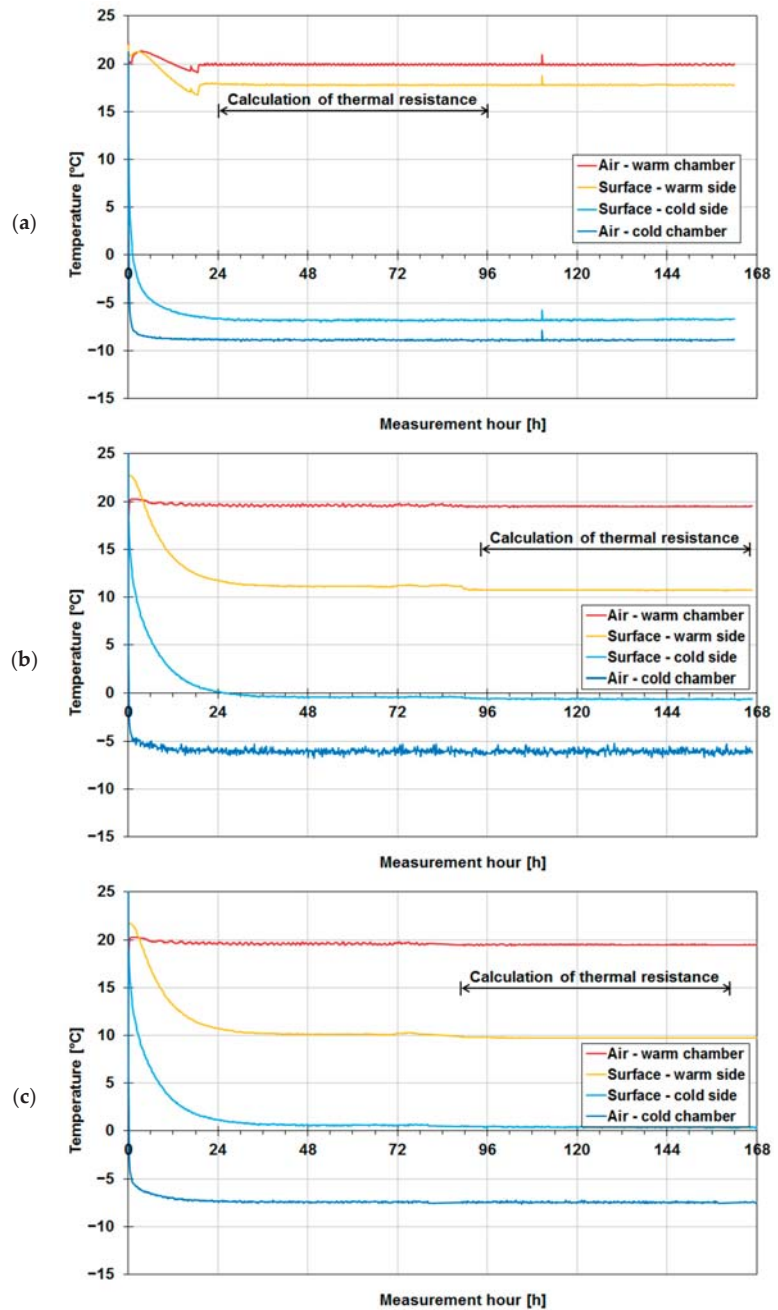
Figure 4. Air temperatures and temperatures of two surfaces of tested walls in their uninsulated version: (**a**) wall A made of aerated concrete, (**b**) wall B made of solid ceramic bricks, (**c**) wall C made of concrete blocks.

Figure 5. Air temperatures and temperatures of two surfaces of tested building partitions in their insulated version: (**a**) wall A made of aerated concrete, (**b**) wall B made of solid ceramic bricks, (**c**) wall C made of concrete blocks.

4.2.2. Thermograms of Tested Walls

While the walls were tested in the climate chambers, they were also observed by means of an infrared camera, which recorded data at certain intervals (usually at every

10 min) during the measurement period. The selected thermograms in Figure 6 show temperature field distributions in the period of stabilized temperatures (72 h period shown in Figures 4 and 5) for the analyzed walls in their uninsulated version (Figure 6a,c,e) and insulated version (Figure 6b,d,f). Table 4 contains measured values for points SP01, SP02 and SP03, and area AR01 for all three randomly chosen thermograms.
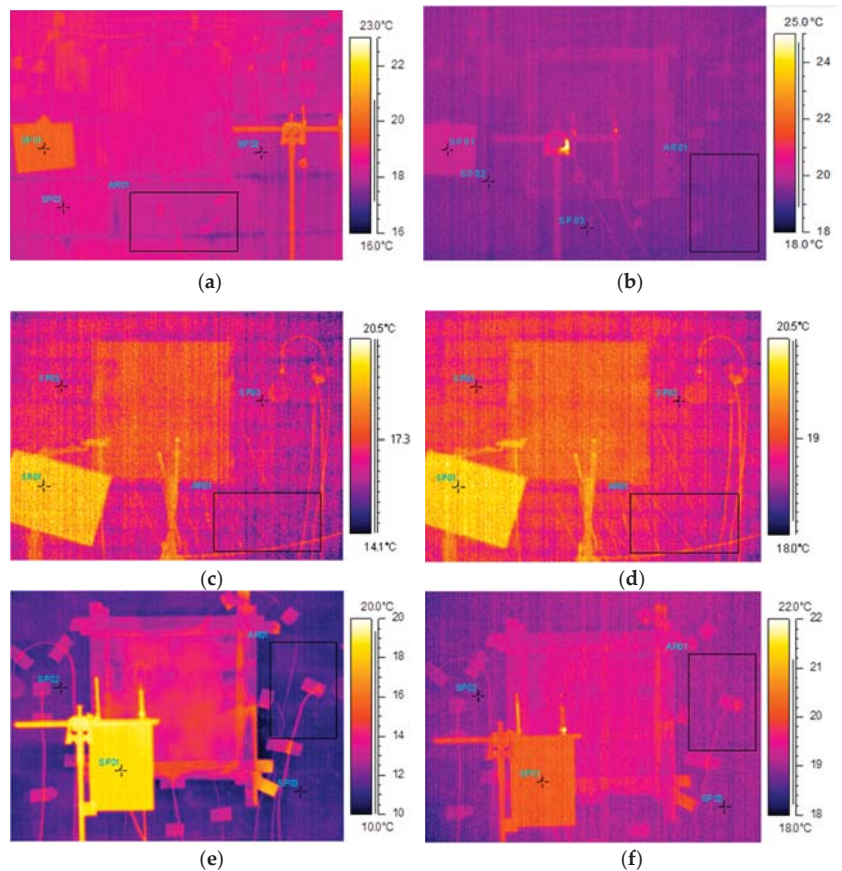
Figure 6. Comparison of thermograms for wall A in uninsulated version (**a**) and insulated version (**b**), wall B in uninsulated version (**c**) and insulated version (**d**) and wall C in uninsulated version (**e**) and insulated version (**f**).

On the thermograms basis it can be, in addition, concluded that:

- Distinct drops in temperature were visible in the joints between the aerated concrete blocks in uninsulated wall A (Figure 6a).
- The joints between the blocks and bricks were practically invisible for insulated wall A (Figure 6b) and for uninsulated and insulated wall B (Figure 6c,d).
- No joints were visible due to the similar thermal conductivity of the mortar and the concrete blocks for uninsulated and insulated wall C (Figure 6e,f).

Table 4. Air and surface temperatures for tested walls by means of infrared camera measurements for all three randomly selected thermograms.

Test Object	Temperature Measurements by Infrared Camera								
	Air (SP01)			Surface (SP02, SP03)			Surface (AR01)		
	Min °C	Max °C	Mean °C	Min °C	Max °C	Mean °C	Min °C	Max °C	Mean °C
Wall A	+19.8	+20.2	+20.0	+17.9	+18.6	+18.3	+18.2	+18.2	+18.2
Wall B	+19.9	+20.3	+20.1	+15.5	+16.0	+15.7	+15.3	+15.5	+15.4
Wall C	+18.4	+20.3	+19.1	+11.0	+12.5	+11.6	+11.5	+11.6	+11.5
Wall A (insulated)	+19.6	+20.2	+20.0	+19.2	+19.7	+19.4	+19.2	+19.4	+19.3
Wall B (insulated)	+20.3	+20.5	+20.4	+19.4	+19.7	+19.5	+19.1	+19.3	+19.2
Wall C (insulated)	+19.9	+20.3	+20.2	+18.9	+19.2	+19.0	+19.1	+19.2	+19.2

4.3. Heat Flux Density

Diagrams of the heat flux density measured by a 0.5 m × 0.5 m Ahlborn plate sensor for all the tested walls are shown in Figures 7 and 8. The density of the heat flux flowing through uninsulated wall A (aerated concrete) is shown in Figure 7a. The heat flux increased to stabilize after about 24 h, ranging instantaneously from 17.0 to 24.8 W/m^2. The average heat flux value in the thermal resistance calculation period amounted to about 21.0 W/m^2. The diagram in Figure 7b is for uninsulated wall B. In this case, the heat flux increased noticeably longer and stabilized only after about 96 h at the mean value of 55.1 W/m^2, ranging instantaneously from 50.9 to 59.2 W/m^2. Figure 7c shows the heat flux for wall C. The heat flux increased to stabilize after about 48 h. However, because of the two visible interruptions in data logging (approximately the 80th and 160th measurement hour), the period from the 90th hour to the 156th hour was selected to determine thermal resistance. The heat flux density on average amounted to 57.7 W/m^2, instantaneously ranging from 51.9 to 66.2 W/m^2.

After the tested walls had been insulated, heat flux density noticeable decreased, as shown in Figure 8. For insulated wall A (Figure 8a), heat flux density stabilized after 72 h, ranging instantaneously from 4.5 to 9.9 W/m^2 and on average amounting to about 7.1 W/m^2. Additionally, an interruption in data logging between the 48th hour and the 66th hour of measurement is visible in the graph. The results for insulated wall B are presented in Figure 8b. In this case, the measurements were undisturbed, and the heat flux stabilized after about 84 h, ranging instantaneously from 6.6 to 9.6 W/m^2, on average amounting to 7.7 W/m^2. In the measurement of heat flux density (Figure 8c) for wall C, one can see distinct vertical heat flux fluctuations, probably due to the "rippling" of the plate sensor caused by heating, resulting in alternately better and worse adhesion of the sensor to the tested wall. The sensor was fixed to the wall with strong duct tape, but it is possible that the tape became unstuck, or due to the deformation of the sensor's material (PTFE), it did not adhere the sensor properly to the surface of the wall. In the case of this building enclosure, the heat flux was averaged from the 84th hour to the 156th hour. In this period, heat flux density ranged instantaneously from 6.7 to 12.4 W/m^2, on average amounting to 9.1 W/m^2.
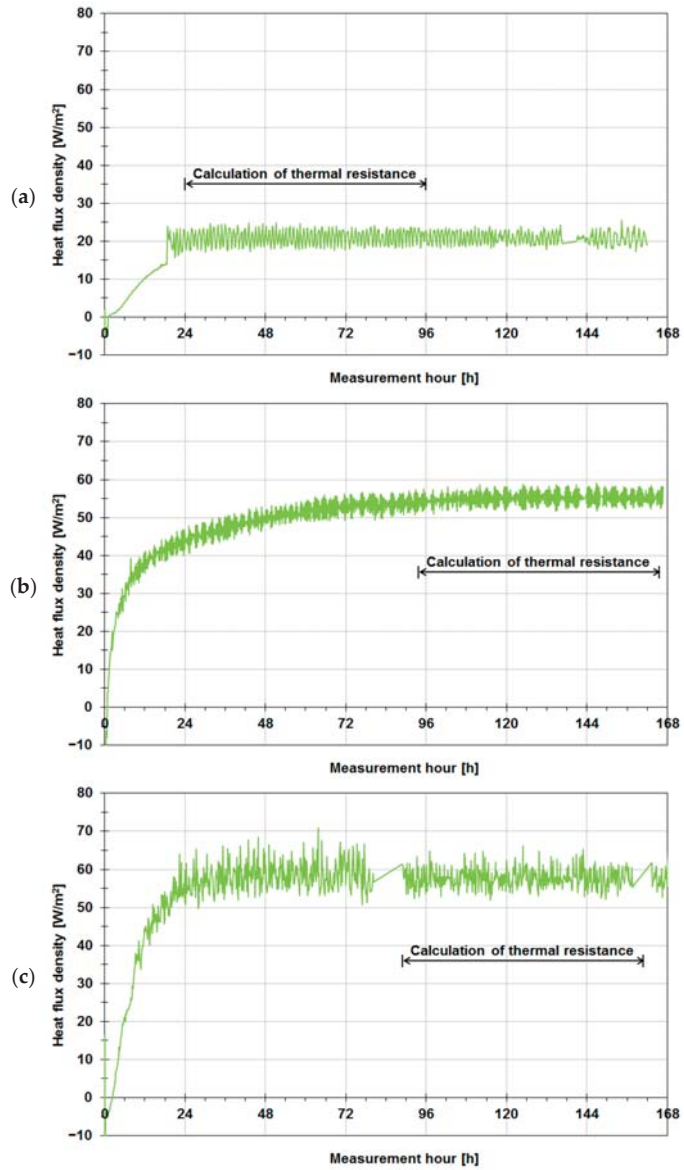
Figure 7. Density of heat flux flowing through tested building enclosures in their uninsulated version: (**a**) wall A made of aerated concrete, (**b**) wall B made of solid ceramic bricks, (**c**) wall C made of concrete blocks.
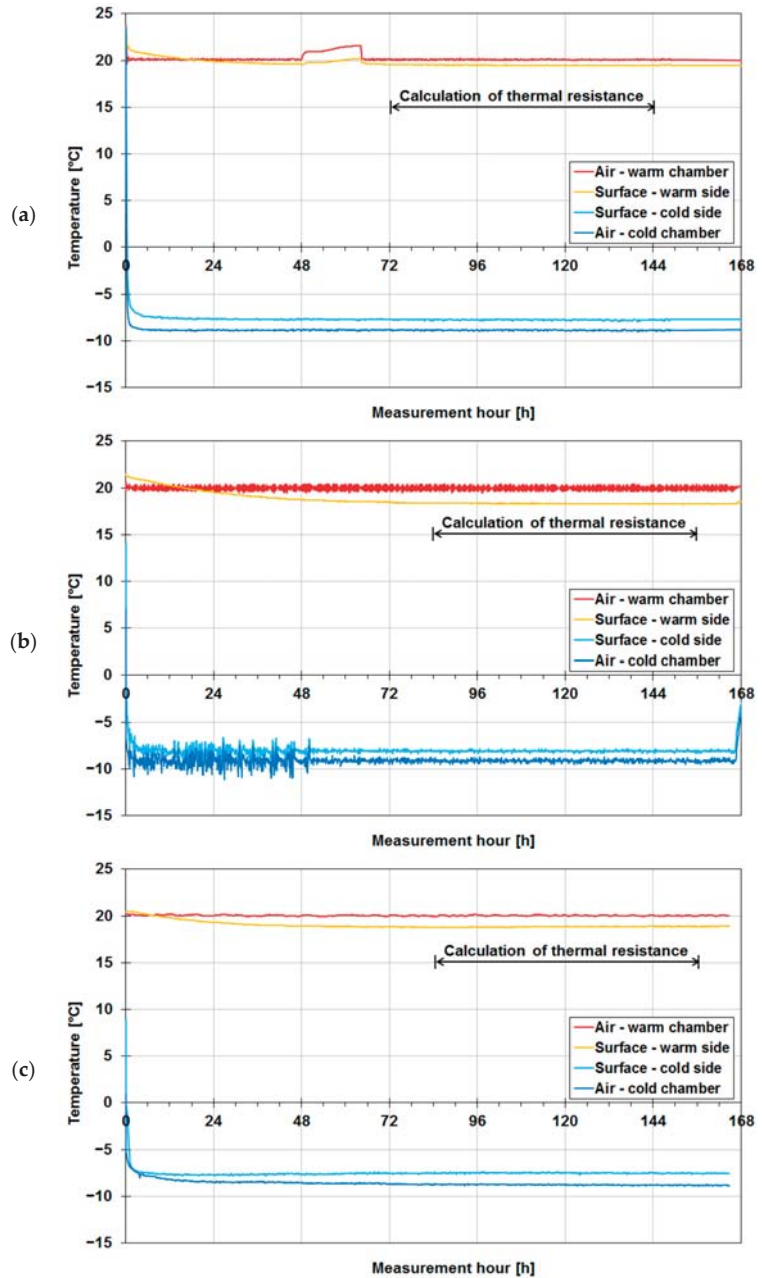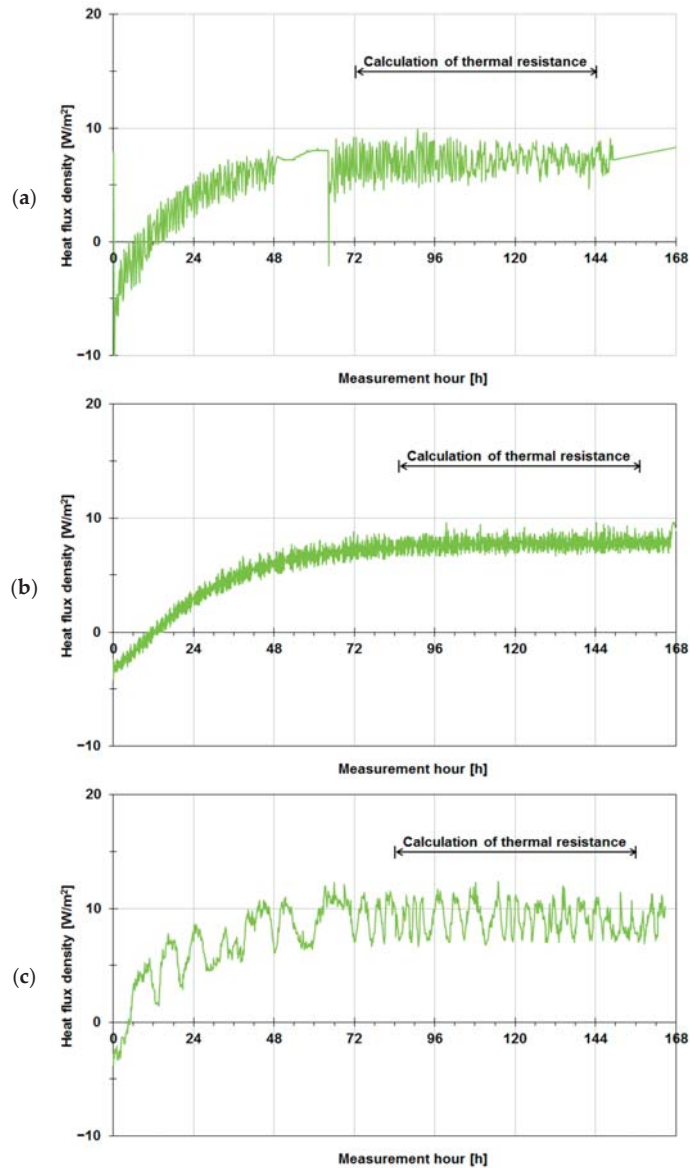
Figure 8. Density of heat flux flowing through tested building enclosures in their insulated version: (**a**) wall A made of aerated concrete, (**b**) wall B made of solid ceramic bricks, (**c**) wall C made of concrete blocks.

4.4. Thermal Resistance of Building Enclosures—Comparison of Methods

The thermal resistance of the tested walls was calculated on the basis of the values, measured within the 72 h interval marked in the diagrams on Figures 7 and 8, and as a result, the total thermal resistance values are presented as bar charts in Figure 9 and in Table 5. The quantitative and percentage differences between the total thermal resistance results are clearly visible in the table.
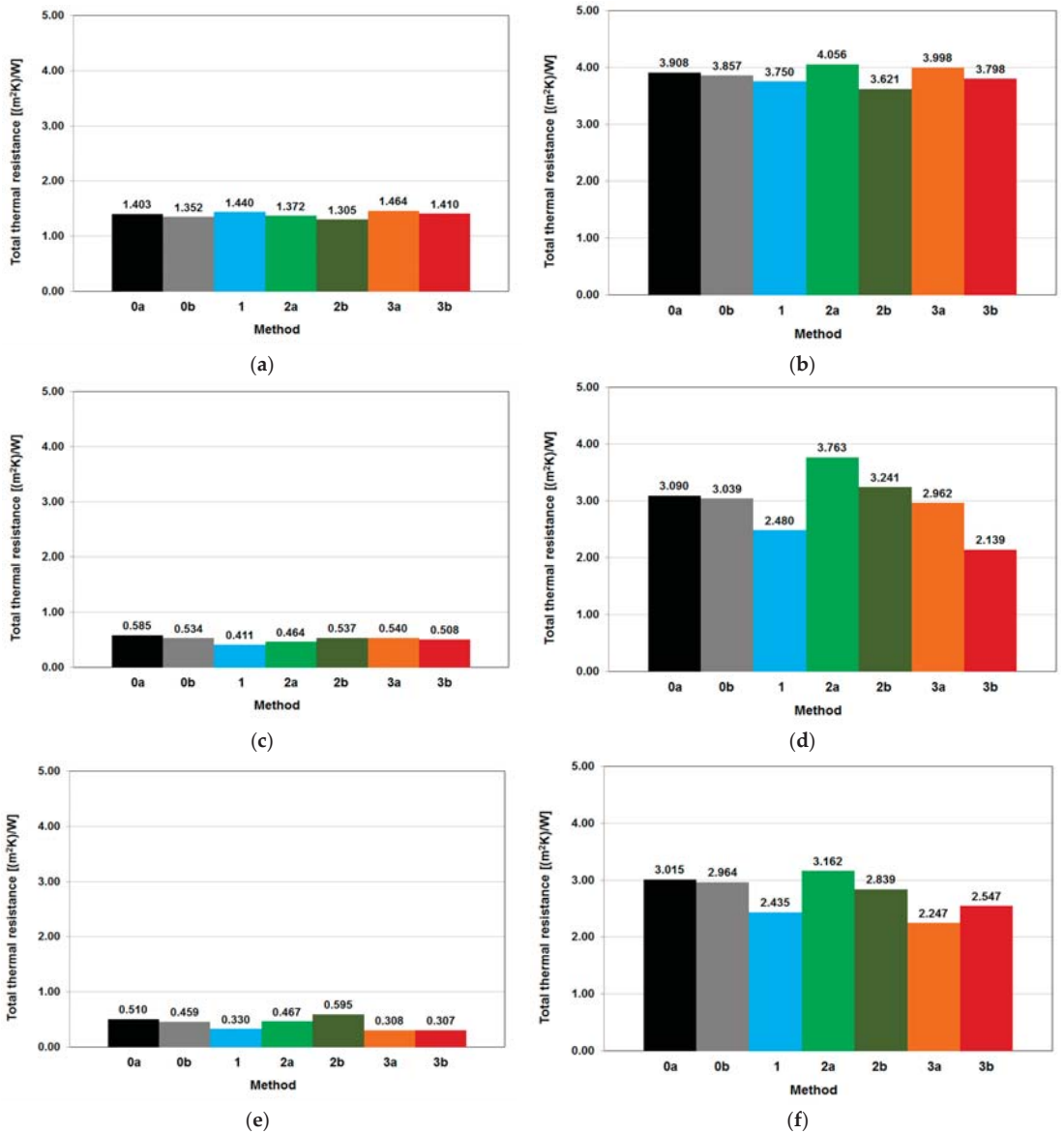
Figure 9. Comparison of thermal resistances measured using different methods for wall A in uninsulated version (**a**) and insulated version (**b**), wall B in uninsulated version (**c**) and insulated version (**d**) and wall C in uninsulated version (**e**) and insulated version (**f**).

Table 5. Comparison of determined total thermal resistances.

Method of Determining Total Thermal Resistance	Total Thermal Resistance, R_{tot} m²K/W					
	Wall A	Wall B	Wall C	Wall A (Insulated)	Wall B (Insulated)	Wall C (Insulated)
0a	1.403	0.585	0.510	3.908	3.090	3.015
0b	1.352	0.534	0.459	3.857	3.039	2.964
1	1.440	0.411	0.330	3.750	2.480	2.435
2a	1.372	0.464	0.467	4.056	3.763	3.162
2b	1.305	0.537	0.595	3.621	3.241	2.839
3a	1.464	0.540	0.308	3.998	2.962	2.247
3b	1.410	0.508	0.307	3.798	2.139	2.547
Average	1.392	0.511	0.425	3.855	2.959	2.744
Standard deviation	0.050	0.053	0.104	0.138	0.486	0.313
Max–Min	0.159	0.173	0.288	0.435	1.624	0.915
Relative range (from average)	−6.2% to +5.2%	−19.5% to +14.3%	−27.8% to +40.0%	−6.1% to +5.2%	−27.7% to +27.2%	−18.1% to +15.2%

It can be seen that, for some of the walls analyzed and the methods used, the results were different by more than 20% from the average value of total thermal resistance—such as wall C, Method 1, 2b, 3a and 3b, or wall B insulated, Method 2a and 3b. The probable reason behind that is presented in the Discussion Section. As it appears from Figure 9, quantitative differences in the results are more noticeable in the thermal resistances calculated for the insulated versions of tested walls, which may suggest that a thermal error or an inaccuracy in the execution of temperature and heat flux density measurements has greater consequences in this case.

The mean difference between the total thermal resistance results obtained for a given method and the average from all methods is shown in the last column in Table 6. When calculating the mean difference, one result most divergent from the other results yielded by a given method was neglected, as it was assumed to be due to an incorrectly performed measurement. The methods ordered from the one yielding results most consistent with the mean value obtained from all the methods are as follows: Method 0b—the R_{tot} results differed on average by 3.6% from the mean value from all the methods, Methods 0a and 2b—by 6.1%, Method 3a—by 6.5%, Method 3b—by 7.7%, Method 2a—by 8.2% and Method 1—by 10.6%.

Table 6. Difference between determined thermal resistances and mean value (colors explained in the text below).

Method of Determining Thermal Resistance	Difference between Given Method and Mean Value ($R_{tot,k} - R_{tot,mean}$) m²K/W (+ Above Mean, − Below Mean) % (Absolute Value)						
	Wall A	Wall B	Wall C	Wall A (Insulated)	Wall B (Insulated)	Wall C (Insulated)	Average (Without One Worst Result)
0a	+0.011 0.8	+0.073 14.3	+0.085 19.9	+0.052 1.4	+0.130 4.4	+0.271 9.9	- 6.1
0b	−0.040 2.9	+0.023 4.4	+0.034 8.0	+0.002 0.0	+0.080 2.7	+0.220 8.0	- 3.6
1	+0.048 3.4	−0.100 19.5	−0.096 22.5	−0.106 2.7	−0.479 16.2	−0.309 11.3	- 10.6
2a	−0.021 1.5	−0.047 9.2	+0.042 9.9	+0.201 5.2	+0.804 27.2	+0.418 15.2	- 8.2
2b	−0.087 6.2	+0.026 5.0	+0.170 40.0	−0.234 6.1	+0.282 9.5	+0.095 3.4	- 6.1
3a	+0.072 5.2	+0.029 5.6	−0.117 27.5	+0.142 3.7	+0.003 0.1	−0.497 18.1	- 6.5
3b	+0.018 1.3	−0.004 0.7	−0.118 27.8	−0.057 1.5	−0.820 27.7	−0.198 7.2	- 7.7

Then, in Table 6, for each of the methods of determining the total thermal resistance of the tested walls, the three results closest to the mean value from the measurements were marked with a green background and those farthest from the mean value were marked with a red background. If one regards closeness of the result to the mean value as indicative of the effectiveness of the method of determining the total thermal resistance, the methods should be ordered as follows:

- Method 0b—5 × the closest results, no farthest results,
- Method 0a—4 × the closest results, 1 × the farthest results,
- Method 3b—4 × the closest results, 2 × the farthest results,
- Method 2b—2 × the closest results, 3 × the farthest results.
- Method 2a—2 × the closest results, 4 × the farthest results.
- Method 3a—1 × the closest results, 4 × the farthest results.
- Method 1—no closest results, 4 × the farthest results.

5. Discussion

The measurement results and the total thermal resistances calculated from them showed, in the majority of cases, good agreement with the theoretically determined values. For the thirty measurements carried out using the five different methods, i.e., 1, 2a, 2b, 3a and 3b, 19 results differed by up to 10% from the average for a given building enclosure, 5 results differed by up to 20%, 5 results differed by up to 30% and only 1 differed by nearly 40% from the mean value. Several practical conclusions concerning the methods used to emerge from the extensive tests are given below:

- Method 0a—theoretical calculations and resistances according to Table 7, ISO 6946, is quite sufficient, in the authors' opinion, to evaluate the thermal performance of the building enclosures being designed, since in this case, it is not possible to assess the actual surface thermal resistances (R_{si} and R_{se}) at the building enclosure surface.
- Method 0b—theoretical calculations supplemented with real measurements of air movement velocity at the building enclosure, used to calculate surface thermal resistances, yields total thermal resistances closest to the mean values.
- Method 1—Temperature-based method (TBM), in theory easy and relatively cheap to implement (only temperature sensors and data acquisition devices are needed), in practice turned out to be least accurate; nevertheless, it can still be regarded as acceptable—the mean error amounting to 10.6% and the maximum measurement deviation from mean value R_T reaching no more than 23%. The accuracy of this method is most affected by the location of the sensor measuring temperature only in a particular spot, and so there is no certainty that this place of measurement is representative enough for the whole building partition.
- Method 2a—Heat flow meter method (HFM), based on measurements by a large (0.50 m × 0.50 m) heat flux density sensor, requires very good contact with the substrate, which is not always easy to achieve. In the above tests, contact of the sensor with the wall surface was ensured by circumferentially sticking it to the latter with strong tape. However, during several measurements, it was noticed that the sensor would undergo slight deformations under the influence of changes in the air and wall surface temperatures (it would bulge out and deflect from the surface). The conclusion is that a large amount of thermal paste should be used, but this would result in irreversible staining of the building enclosure surface.
- Method 2b—heat flow meter method (HFM), i.e., the use of a dedicated system of two small sets of heat flux density sensors and thermocouples in order to double the measurement of the parameters needed to determine thermal resistance, as the results show, is a slightly better solution—it is much easier to ensure proper constant contact of small (8 cm in diameter) heat flux density sensors with the substrate, using much less thermal paste, but it is still an invasive method.
- Methods 3a and 3b—Infrared thermography method (ITM) yielded qualitatively similar results as the ones yielded by the HFM methods, though Method 3a, based on

averages from spot temperature measurements, was slightly more accurate. The great common advantage of the methods is their complete non-invasiveness towards the surface of the tested building enclosure.

When measuring the thermal resistance of building enclosures, the selection of surface thermal resistances, R_s, strongly affects the quality of the results obtained, and in the authors' opinion, resistances, R_s, should also be determined using measurement methods. For this purpose, the air movement velocity at both building enclosure surfaces must be measured and the thermodynamic temperatures of the latter must be known.

Due to the wide range of tests, the following factors have been revealed that can randomly significantly affect the accuracy of the obtained results:

- Adhesion of sensors to the building enclosure surface: Even though small heat flux density sensors provide averages from a smaller area, it is definitely easier to attach them stably than in the case of large sensors. They should be attached using, e.g., thermal paste, but in a possibly small amount so that the thermal paste layer does not affect the measurement.
- Thermocouples are precise temperature sensors, but it is important that the cable connecting them with a data logger has damage-resistant insulation. The authors found silicone insulation to be the best as the fiberglass insulation did not perform well in the difficult measurement conditions (the cables would abrade, whereby the measurements would yield incorrect values).
- Air temperature: one can use a thin black sheet of paper to easily measure this temperature by means of an infrared camera, while taking a thermogram of the building enclosure surface.
- Thermographic measurement: if the building enclosures are relatively homogeneous (as in the analyzed cases), both the spot and area measurements of building enclosure surface temperature can be sufficiently accurate for the purpose of determining the thermal resistance of the building enclosure, but if the latter's material is highly heterogeneous, the area temperature measurement is recommended.

6. Conclusions

The results of determining total thermal resistance in seven different ways based on four different methods (the theoretical method, TBM, HFM and ITM) for six different building enclosures with different thermal insulation properties, with or without a thermal insulation layer, made of different building materials, were presented above. The tests were carried out in climate chambers.

Considering that the values of the thermal conductivity coefficients of the materials used (aerated concrete, solid ceramic bricks, concrete blocks, masonry mortar, expanded polystyrene and render) were not verified by measurements by the authors, the theoretical methods (0a and 0b) were not treated as the references for the other methods, but on equal terms with them. For this reason, the results yielded by a particular method were compared with the average thermal resistances from all the methods.

The measurement results obtained for the purpose of calculating the thermal resistance of the building enclosures showed good agreement with the average thermal resistance, and in most cases, the differences did not exceed 10%, while 97% of determined resistances, R_T (29 per 30 measurements), were within 30% of the difference.

The accuracy of the total thermal resistance measurement results obtained by the infrared thermography methods (for which the mean difference amounted respectively to 6.5% and 7.7%) is comparable with that of the results yielded by the heat flow meter methods (the mean difference amounted to 6.1% and 8.2%). The unquestionable advantage of the ITMs is their complete non-invasiveness, which means no problems with proper adhesion of sensors to the surface of building enclosures. Still, both the infrared thermography methods and the heat flow meter methods require the precise preparation of the test setup as errors affecting the accuracy of the methods can be easily committed. On average, the temperature-based method was characterized by worse accuracy than the

other methods (the mean difference amounted to 10.6%), but unlike the other methods, the thermal resistance values yielded by it did not exceed 23% for any of the walls. When determining the total thermal resistance of a building enclosure, it is worth taking into account all the actual thermal transfer resistance values which may noticeably diverge from the ones assumed in ISO 6946 [22] for the internal and external surfaces of a building enclosure.

In the authors' opinion, this research should continue, but the tests should be supplemented with measurements of the thermal conductivity coefficient of the tested materials by means of a dedicated device of the heat flow meter type (e.g., Fox 314 or Fox 600, etc.), which would provide a proper reference for the measurement methods. Moreover, the authors are inclined to attempt to determine the total thermal resistance by the dynamic method in accordance with ISO 9869-1 [27] and to consider the way in which heat transfer coefficients h_r and h_c are taken into account in the thermal resistance calculations according to the approaches available in the literature, extensively presented in [63].

Author Contributions: Conceptualization, H.N. and Ł.N.; methodology, H.N.; software, Ł.N.; validation, H.N. and Ł.N.; formal analysis, Ł.N.; investigation, Ł.N.; resources, H.N. and Ł.N.; writing—original draft preparation, H.N. and Ł.N.; writing—review and editing, H.N. and Ł.N.; visualization, Ł.N.; supervision, H.N.; project administration, H.N.; funding acquisition, H.N. All authors have read and agreed to the published version of the manuscript.

Institutional Review Board Statement: Not applicable.

Informed Consent Statement: Not applicable.

Data Availability Statement: Not applicable.

Conflicts of Interest: The authors declare no conflict of interest.

References

1. Van den Brom, P.; Meijer, A.; Visscher, H. Performance gaps in energy consumption: Household groups and building characteristics. *Build. Res. Inf.* **2018**, *46*, 54–70. [CrossRef]
2. Desogus, G.; Mura, S.; Ricciu, R. Comparing different approaches to in situ measurement of building components thermal resistance. *Energy Build.* **2011**, *43*, 2613–2620. [CrossRef]
3. Ioannou, A.; Itard, L. Energy performance and comfort in residential buildings: Sensitivity for building parameters and occupancy. *Energy Build.* **2015**, *92*, 216–233. [CrossRef]
4. Majcen, D.; Itard, L.; Visscher, H. Actual and theoretical gas consumption in Dutch dwellings: What causes the differences? *Energy Policy* **2013**, *61*, 460–471. [CrossRef]
5. Siviour, J.B.; McIntyre, D.A. U-value meters in theory and practice. *Build. Serv. Eng. Res. Technol.* **1982**, *3*, 61–69. [CrossRef]
6. McIntyre, D.A. In situ measurement of U-values. *Build. Serv. Eng. Res. Technol.* **1985**, *6*, 1–6. [CrossRef]
7. Modera, M.P.; Sherman, M.H.; Sonderegger, R.C. Determining the U-value of a wall from field measurements of heat flux and surface temperatures. In *Building Applications of Heat Flux Transducers*; ASTP STP 885; American Society for Testing and Materials: Philadelphia, PA, USA, 1985; pp. 203–220.
8. Teni, M.; Krstic, H.; Kosinski, P. Review and comparison of current experimental approaches for in-situ measurements of building walls thermal transmittance. *Energy Build.* **2019**, *203*, 109417. [CrossRef]
9. Soares, N.; Martins, C.; Gonçalves, M.; Santos, P.; da Silva, L.S.; Costa, J.J. Laboratory and in-situ non-destructive methods to evaluate the thermal transmittance and behavior of walls, windows, and construction elements with innovative materials: A review. *Energy Build.* **2019**, *182*, 88–110. [CrossRef]
10. Jiménez, M.J.; Madsen, H.; Andersen, K.K. Identification of the main thermal characteristics of building components using MATLAB. *Build. Environ.* **2008**, *43*, 170–180. [CrossRef]
11. Gutschker, O. Parameter identification with the software package LORD. *Build. Environ.* **2008**, *43*, 163–169. [CrossRef]
12. Biddulph, P.; Gori, V.; Elwell, C.A.; Scott, C.; Rye, C.; Lowe, R.; Oreszczyn, T. Inferring the thermal resistance and effective thermal mass of a wall using frequent temperature and heat flux measurements. *Energy Build.* **2014**, *78*, 10–16. [CrossRef]

13. Piotrowski, J.Z.; Orman, Ł.; Lucas, X.; Zender-Świercz, E.; Telejko, M.; Koruba, D. Tests of thermal resistance of simulated walls with the reflective insulation. In *EPJ Web of Conferences*; EDP Sciences: Les Ulis, France, 2014; Volume 67.

14. Byrne, A.; Byrne, G.; Robinson, A. Compact facility for testing steady and transient thermal performance of building walls. *Energy Build.* **2017**, *152*, 602–614. [CrossRef]

15. Choi, D.S.; Ko, M.J. Comparison of various analysis methods based on heat flowmeters and infrared thermography measurements for the evaluation of the in situ thermal transmittance of opaque exterior walls. *Energies* **2017**, *10*, 1019. [CrossRef]

16. Gaspar, K.; Casals, M.; Gangolells, M. In situ measurement of facades with a low U-value: Avoiding deviations. *Energy Build.* **2018**, *170*, 61–73. [CrossRef]

17. Jin, X.; Zhang, X.; Cao, Y.; Wang, G. Thermal performance evaluation of the wall using heat flux time lag and decrement factor. *Energy Build.* **2012**, *47*, 369–374. [CrossRef]

18. Byrne, A.; Byrne, G.; Davies, A.; Robinson, A.J. Transient and quasi-steady thermal behaviour of a building envelope due to retrofitted cavity wall and ceiling insulation. *Energy Build.* **2013**, *61*, 356–365. [CrossRef]

19. Cesaratto, P.G.; De Carli, M. A measuring campaign of thermal conductance in situ and possible impacts on net energy demand in buildings. *Energy Build.* **2013**, *59*, 29–36. [CrossRef]

20. Li, F.G.N.; Smith, A.; Biddulph, P.; Hamilton, I.G.; Lowe, R.; Mavrogianni, A.; Oikonomou, E.; Raslan, R.; Stamp, S.; Stone, A.; et al. Solid-wall u-values: Heat flux measurements compared with standard assumptions. *Build. Res. Inf.* **2014**, *43*, 238–252. [CrossRef]

21. Naveros, I.; Ghiaus, C.; Ruíz, D.P. Frequency response limitation of heat flux meters. *Build. Environ.* **2017**, *114*, 233–245. [CrossRef]

22. ISO. *ISO 6946: 2017 Building Components and Building Elements—Thermal Resistance and Thermal Transmittance—Calculation Methods*; ISO: Geneva, Switzerland, 2017.

23. Peng, C.; Wu, Z. In situ measuring and evaluating the thermal resistance of building construction. *Energy Build.* **2008**, *40*, 2076–2082. [CrossRef]

24. Baker, P. *Technical Paper 2: In Situ U-Value Measurements in Traditional Buildings—Preliminary Results*; Historic Scotland: Edinburgh, UK, 2008.

25. ISO. *ISO 9869-1:2014, Thermal Insulation—Building Elements—In-Situ Measurement of Thermal Resistance and Thermal Transmittance— Part 1: Heat Flow Meter Method*; ISO: Geneva, Switzerland, 2014.

26. Gaspar, K.; Casals, M.; Gangolells, M. A comparison of standardized calculation methods for in situ measurements of façades U-value. *Energy Build.* **2016**, *130*, 592–599. [CrossRef]

27. Rasooli, A.; Itard, L. In-situ characterization of walls' thermal resistance: An extension to the ISO 9869 standard method. *Energy Build.* **2018**, *179*, 374–383. [CrossRef]

28. ISO. *ISO 9869-2:2018—Thermal Insulation—Building Elements—In-Situ Measurement of Thermal Resistance and Thermal Transmittance— Part 2: Infrared Method for Frame Structure Dwelling*; ISO: Geneva, Switzerland, 2018.

29. Szagri, D.; Nagy, B. Experimental and numerical hygrothermal analysis of a refurbished double-skin flat roof. *Case Stud. Therm. Eng.* **2021**, *25*, 100941. [CrossRef]

30. Orosz, M.; Nagy, B.; Tóth, E. Hygrothermal simulations and In-situ measurements of ultra-lightweight concrete panels. *Pollack Period.* **2017**, *12*, 69–83. [CrossRef]

31. Paljak, I.; Pettersson, B. *Thermography of Buildings. The National Swedish Institute for Building Research*; Report No. T-12/1972; Swedish Council for Building Research: Stockholm, Sweden, 1972.

32. Pettersson, B.; Axen, B. *Thermography Testing of the Thermal Insulation and Airtightness of Buildings*; Swedish Council for Building Research: Stockholm, Sweden, 1980.

33. Grot, R.A.; Silberstein, S. *Measurement Method for Evaluation of Thermal Integrity of Building Envelopes*; Report NBSIR 82-2605; National Bureau of Standards: Washington, DC, USA, 1982; p. 127.

34. Grinzato, E.; Vavilov, V.; Kauppinen, T. Quantitative infrared thermography in buildings. *Energy Build.* **1998**, *29*, 1–9. [CrossRef]

35. Maldague, X. *Theory and Practice of Infrared Technology of Non-Destructive Testing*; JohnWiley & Sons: New York, NY, USA, 2001; ISBN 978-0-471-18190-3.

36. Balaras, C.A.; Argiriou, A.A. Infrared Thermography for building diagnostic. *Energy Build.* **2002**, *34*, 171–183. [CrossRef]

37. Vollmer, M.; Mollmann, K.P. *Infrared Thermal Imaging. Fundamentals, Research and Applications*; Ailey-VCH, GmbH & KgaA: Weinheim, Germany, 2010.

38. Nowak, H. *Application of Infrared Thermography in Building*; Wrocław University of Science and Technology Publishing House: Wrocław, Poland, 2012; ISBN 978-83-7493-676-7. (In Polish)

39. Ascione, F.; Bianco, N.; De Masi, R.F.; Mauro, G.M.; Musto, M.; Vanoli, G.P. Experimental validation of a numerical code by thin film heat flux sensors for the resolution of thermal bridges in dynamic conditions. *Appl. Energy* **2014**, *124*, 213–222. [CrossRef]

40. Atsonios, I.A.; Mandilaras, I.D.; Kontogeorgos, D.A.; Founti, M.A. A comparative assessment of the standardized methods for the in–situ measurement of the thermal resistance of building walls. *Energy Build.* **2017**, *154*, 198–206. [CrossRef]

41. Bianchi, F.; Pisello, A.L.; Baldinelli, G.; Asdrubali, F. Infrared thermography assessment of thermal bridges in building envelope: Experimental validation in a test room setup. *Sustainability* **2014**, *6*, 7107–7120. [CrossRef]

42. O'Grady, M.; Lechowska, A.A.; Harte, A.M. Infrared thermography technique as an in-situ method of assessing heat loss through thermal bridging. *Energy Build.* **2017**, *135*, 20–32. [CrossRef]

43. Sandrolini, F.; Franzoni, F. An operative protocol for reliable measurements of moisture in porous materials of ancient buildings. *Build. Environ.* **2006**, *41*, 1372–1380. [CrossRef]

44. Barreira, E.; Vasco, P. Evaluation of building materials using infrared thermography. *Constr. Build. Mater.* **2007**, *21*, 218–224. [CrossRef]

45. Kandemir-Yucel, A.; Tavukcuoglu, A.; Caner-Saltik, E.N. In situ assessment of structural timber elements of a historic building by infrared thermography and ultrasonic velocity. *Infrared Phys. Technol.* **2007**, *49*, 243–248. [CrossRef]

46. Kalamees, T. Air tightness and air leakages of new lightweight single-family detached houses in Estonia. *Build. Environ.* **2007**, *42*, 2369–2377. [CrossRef]

47. Taylor, T.; Counsell, J.; Gill, S. Energy efficiency is more than skin deep: Improving construction quality control in new-build housing using thermography. *Energy Build.* **2013**, *66*, 222–231. [CrossRef]

48. Lerma, C.; Barreira, E.; Almeida, R.M.S.F. A discussion concerning active infrared thermography in the evaluation of buildings air infiltration. *Energy Build.* **2018**, *168*, 56–66. [CrossRef]

49. Heinrich, H.; Dahlem, K.H. Thermography of low energy buildings. In Proceedings of the QIRT Conference 2000, Reims, France, 18–21 July 2000.

50. Lourenço, T.; Matias, L.; Faria, P. Anomalies detection in adhesive wall tiling systems by infrared Thermography. *Constr. Build. Mater.* **2017**, *148*, 419–428. [CrossRef]

51. Maldague, X. *Nondestructive Evaluation of Materials by Infrared Thermography*; Springer: London, UK, 1993.

52. Vavilov, V.P.; Kauppinen, T.; Grinzato, E. Thermal characterization of defects in buildings envelopes using long square pulse and slow thermal wave techniques. *Res. Nondestr. Eval.* **1997**, *9*, 181–200. [CrossRef]

53. Avdelidis, N.P.; Almond, D.P. Transient thermography as a through skin imaging technique for aircraft assembly: Modelling & experimental results. *J. Infrared Phys. Technol.* **2004**, *45*, 103–114.

54. Omar, M.; Hassan, M.I.; Saito, K.; Alloo, R. IR self-referencing thermography for detection of in-depth defects. *Infrared Phys. Technol.* **2005**, *46*, 283–289. [CrossRef]

55. Arndt, R.W. Square pulse thermography in frequency domain as adaptation of pulsed phase thermography for qualitative and quantitative applications in cultural heritage and civil engineering. *Infrared Phys. Technol.* **2010**, *53*, 246–253. [CrossRef]

56. Vavilov, V.P.; Burleigh, D.D. Review of pulsed thermal NDT: Physical principles, theory and data processing. *NDT E Int.* **2015**, *73*, 28–52. [CrossRef]

57. Noszczyk, P.; Nowak, H. Inverse contrast in non-destructive materials research by using active thermography. *Materials* **2019**, *12*, 835. [CrossRef]

58. Fokaides, P.A.; Kalogirou, S.A. Application of infrared thermography for the determination of the overall heat transfer coefficient (U-Value) in building envelopes. *Appl. Energy* **2011**, *88*, 4358–4365. [CrossRef]

59. Lee, S.; Kato, S. Feasibility study of in situ measurement method using infrared camera to measure U-Value of walls. *J. Environ. Eng.* **2011**, *76*, 289–295. [CrossRef]

60. Ohlsson, K.E.A.; Olafsson, T. Quantitative infrared thermography imaging of the density of heat flow rate through a building element surface. *Appl. Energy* **2014**, *134*, 499–505. [CrossRef]

61. Nardi, I.; Sfarra, S.; Ambrosini, D. Quantitative thermography for the estimation of the U-value: State of the art and a case study. *J. Phys. Conf. Ser.* **2014**, *547*, 1–8. [CrossRef]

62. Albatici, R.; Tonelli, A.; Michela, C. A comprehensive experimental approach for the validation of quantitative infrared thermography in the evaluation of building thermal transmittance. *Appl. Energy* **2015**, *141*, 218–228. [CrossRef]

63. Gasi, M.; Milovanovic, B.; Gumbarevic, S. Comparison of Infrared Thermography and Heat Flux Method for Dynamic Thermal Transmittance Determination. *Buildings* **2019**, *9*, 132. [CrossRef]

64. Nardi, I.; Paoletti, D.; Ambrosini, D.; Rubeis, T.; Sfarra, S. U-value assessment by infrared thermography: A comparison of different calculation methods in a Guarded Hot Box. *Energy Build.* **2016**, *122*, 211–221. [CrossRef]

65. Lu, S. *Infrared (IR) Thermography Measurement of U-Value*; The Department of Ecotechnology and Sustainable Building Engineering, Mid Sweden University: Sundsvall, Sweden, 2015.

66. Piaa, G.; Casnedia, L.; Ricciub, R.; Besalduchb, L.A.; Coccoa, O.; Murrua, A.; Melonia, P. Thermal properties of porous stones in cultural heritage: Experimental findings and predictions using an intermingled fractal units model. *Energy Build.* **2016**, *118*, 232–239. [CrossRef]

67. Bruno, R.; Bevilacqua, P.; Ferraro, V.; Arcuri, N. Reflective thermal insulation in non-ventilated air-gaps: Experimental and theoretical evaluations on the global heat transfer coefficient. *Energy Build.* **2021**, *236*, 110769. [CrossRef]

68. Ricciu, R.; Ragnedda, F.; Galatioto, A.; Gana, S.; Besalduch, L.A.; Frattolillo, A. Thermal properties of building walls: Indirect estimation using the inverse method with a harmonic approach. *Energy Build.* **2019**, *187*, 257–268. [CrossRef]

69. Malz, S.; Steininger, P.; Dawoud, B.; Krenkel, W.; Steffens, O. On the development of a building insulation using air layers with highly reflective interfaces. *Energy Build.* **2021**, *236*, 110779. [CrossRef]

70. Staveckis, A.; Borodinecs, A. Impact of impinging jet ventilation on thermal comfort and indoor air quality in office buildings. *Energy Build.* **2021**, *235*, 110738. [CrossRef]

71. ISO. *PN-EN ISO 6946: 1999—Building Components and Building Elements—Thermal Resistance and Thermal Transmittance—Calculation Methods*; ISO: Geneva, Switzerland, 1999. (In Polish)

72. ISO. *PN-EN 12524: 2003—Building Materials and Products—Hygrothermal Properties—Tabulated Design Values*; ISO: Geneva, Switzerland, 2003. (In Polish)

73. ISO. *PN-EN ISO 10456: 2007—Building Materials and Products—Hygrothermal Properties—Tabulated Design Values and Procedures for Determining Declared and Design Thermal Values*; ISO: Geneva, Switzerland, 2007. (In Polish)

Article

Research and TLS (LiDAR) Construction Diagnostics of Clay Brick Masonry Arched Stairs

Rafał Nowak [1,*]**, Tomasz Kania** [2]**, Radosław Rutkowski** [3] **and Ewa Ekiert** [4]

1   Department of General Civil Engineering, Faculty of Civil and Environmental Engineering, West Pomeranian University of Technology in Szczecin, Piastów Ave. 50a, 70-311 Szczecin, Poland
2   Department of General Civil Engineering, Faculty of Civil Engineering, Wrocław University of Science and Technology, Wybrzeże Wyspiańskiego 27, 50-370 Wrocław, Poland; tomasz.kania@pwr.edu.pl
3   Department of Technological Processes, Faculty of Economics and Transport Engineering, Maritime University of Szczecin, Wały Chrobrego 1-2, 70-500 Szczecin, Poland; szczecin.ar@gmail.com
4   Department of Chemical Inorganic Technology and Environment Engineering, Faculty of Chemical Technology and Engineering, West Pomeranian University of Technology in Szczecin, Piastów Ave. 42, 71-065 Szczecin, Poland; ewa.dabrowa@zut.edu.pl
*   Correspondence: rnowak@zut.edu.pl

Abstract: The study presents the terrestrial laser scanning (TLS) diagnostic of the clay brick masonry arched staircase in a historic building. Based on the measurements of the existing arched stair flights, 1:1 scale experimental models with and without stair treads were made. Strength tests of the models were carried out for different concentrated force locations in relation to the supporting structure. Force, deflections and reaction in the upper support of the run were measured during the tests. The influence of the masonry steps on the curved vault on the load capacity and stiffness of the run structure was analyzed. The conducted experimental investigations showed that the key element responsible for the actual load-bearing capacity and stiffness of this type of stair flights were the treads above the masonry arch.

1. Introduction

In the authors' countries, in historical buildings from the 19th century, masonry arch stairs were commonly used to connect floors [1]. The arches were shaped between steel beams as a load-bearing span for the staircase landings and flights. At that time, the technology of reinforced concrete was not yet known, so steel and masonry construction was the most popular, especially in residential buildings. The construction of staircases was mostly in the form of segmental or cross vaults. The structure of the flights was made as a stair arch with the thickness of half a brick (12 cm) and elevation $f = 1/12–1/14\ L$ [1] (Figures 1 and 2).

A flight of arch stairs is characterized by a slender, long structure with a slope of approximately 35°–40°. One of the main permanent loads on the flight of stairs are the bricks along the entire flight. The steps have the least bricks in the middle of the stairs' arch and the most at the ends. The steps are not connected with a typical masonry bond. The bricks must be cut to fit the actual geometry of the arches.

The flights and landings were supported by steel beams. The construction of flights had a good fire resistance (except for the steel beams), stiffness and durability. The constructions of brick stairs are still in use despite many years of service. Additionally, they are a testament of old times and often protected by the conservator as a part of cultural heritage. Their condition often raises concern because of the damages, mainly cracks or erosion of joints. The typical damages of brick staircase construction are: degradation of mortar and

bricks, flattening of vaults and cracking. The damages arise as a result of overloading, wrongly executed repair works and dynamic loads. Sometimes, one can find constructional errors such as improper fixing of gear plates on I-beam flanges.
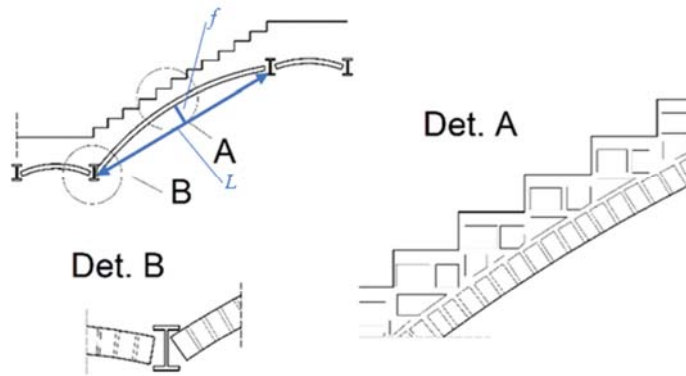
Figure 1. Masonry stairs with segmental vault and arched staircase slab, based on [1].

(**a**)   (**b**)
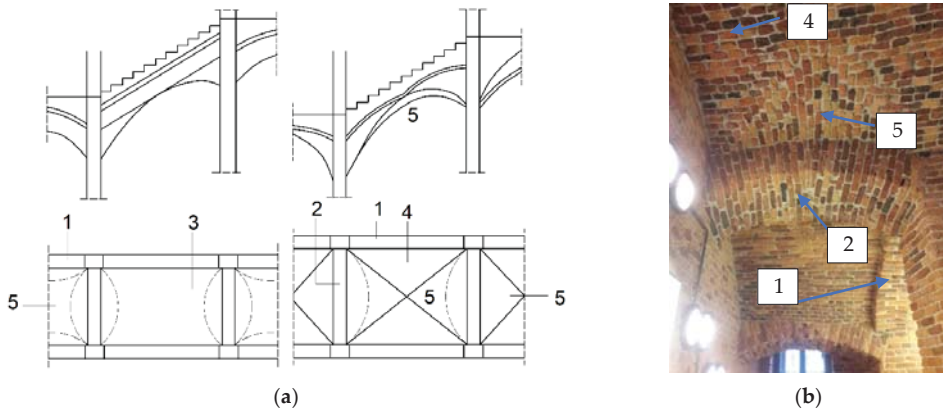
Figure 2. Brick stairs with column supports based on [1]. Scheme (**a**) and partial photo (**b**): 1—arched masonry stair sides; 2—arched masonry bolt; 3—barrel staircase with support on sides; 4—groin vault in stair flight; 5—groin or barrel vaults in stair landing.

Information on calculation methods or principles of construction is often difficult to find. This type of construction was created mainly on the basis of experience with brick vaults. The steel beams supporting the vaults were calculated by the methods available at that time [1]. The operation of landing vaults is similar to balcony or roof vaults. On the other hand, staircase slabs are at an angle depending on their length and height. The distribution of stresses and internal forces is different from other staircase structures. A calculation scheme of an example of an arched masonry stairs with vaulted landings supported on steel beams is shown in Figure 3.
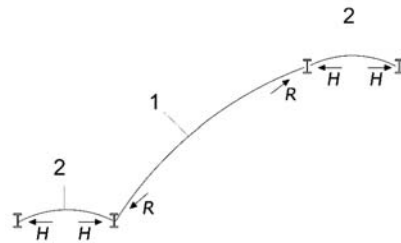
Figure 3. Calculation scheme of masonry stairs with segmental vault and arched staircase slab: 1—arched staircase slab; 2—landings.

One of the most prevalent issues in this type of stairs is the necessity of diagnostics of their technical condition in order to confirm their durability and functional use. The chosen methods used in the diagnostics of masonry structures in the authors' countries are shown in Figure 4.
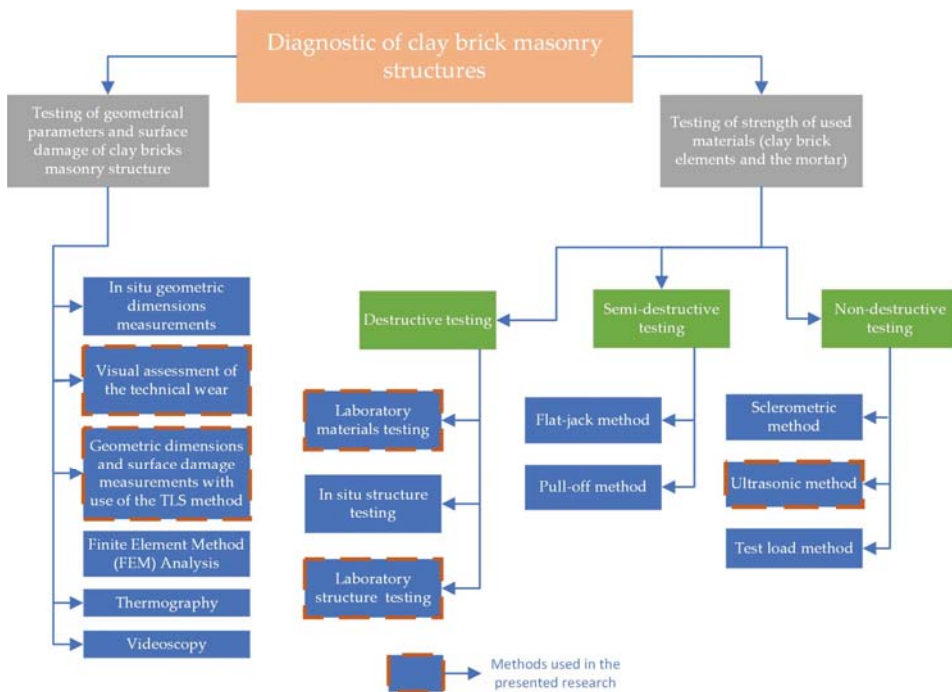
Figure 4. Flowchart for clay brick masonry structure diagnostics.

The diagnosis of masonry structures primarily focuses on a visual assessment in order to detect cracks and damages [2–5]. The early diagnostics usually uses non-destructive measuring equipment, which allows the preliminary characteristics of existing materials or the degree of their degradation to be evaluated [6–10]. Those methods most often include sclerometric measurements (Schmidt hammer) or ultrasonic measurements. At that stage of diagnosis, infrared thermography is a novel and useful method for historic plaster and painted vaults. The management of the data derived from the application of infrared thermography, integrated with the information from visual inspections, the architectural

survey and the historic analysis, allows a complete characterization of the historic plasters and painted masonry vaults to be obtained [11].

A more accurate determination of material properties in masonry structures involves sampling. In the case of brick alone, this process is feasible; however, sampling of mortar is significantly more difficult. Therefore, in many diagnostic operations, core samples are taken, also containing a fragment of mortar and masonry elements adjacent on both sides. The core samples, after certain correlations, are used to determine the load-bearing capacity of the whole masonry structure [12–17]. Even more accurate results may be obtained by test-loading a masonry section with actuators [18]. However, this method requires making cuts in the masonry in order to locate the beams to place the actuators. The method is mostly used as a validation is structural elements that are to undergo alteration, repair, or reconstruction.

A similar effect can be obtained if a section of the masonry is cut out and transported to the laboratory for experimental testing [14,18]. A less destructive solution is the flat-jack method [18,19]. It requires appropriate calibration procedures and precise preparation of the measurement base. Additionally, it may be imprecise in low buildings and lead to permanent damage when testing masonry with weak lime mortar [18]. The best measurement method is to perform a loading test with appropriate measurement [20–24], which does not lead to the destruction of the structure but allows the correlation between stresses and strains to be obtained, in order to assess the actual load-bearing capacity and stiffness. Final results on the load-bearing capacity of the structure can only be obtained from experimental destructive testing.

The finite element method (FEM) is a fundamental analysis for the assessment of masonry in seismic zones [25–28]. Nonlinear static calculation methods are commonly adopted for the evaluation of seismic performance [26–32]. Laurenco et al. [28] presented a research study on that subject with a yield criterion that included different strengths along each material axis. Baraldi et al. [31] presented the rigid beam model for studying the dynamic behavior of cantilever unreinforced masonry walls, considered along their thickness and subjected to out-of-plane loading. Celano et al. [32] presented research on the in-plane resistance of masonry walls with the use of two modeling approaches, a finite element model and a discrete macro-element model, with the use of non-linear analyses.

The TLS (terrestrial laser scanning) measurements using 3D scanners are starting to be used for structural diagnosis. Three-dimensional LiDAR (light detection and ranging) scanners have revolutionized the capability and accuracy of geometry measurements in construction, shipbuilding and other areas of science and technology [33–49]. TLS can be used to measure damage to the surface layers of materials, including bricks and mortar, as well as to track moisture in structures [33,41–49]. TLS in structural analysis is primarily used to measure strain and deflections, as well as deformations, of structural elements [25,42–50]. This technique can also be used for control measurements at the stage of constructing [51]. Some researchers use TLS technology to monitor the condition of construction to prevent possible damage [52,53]. Additionally, detailed geometry studies using TLS are useful in post-disaster analyses of structures, including earthquakes [53].

The assessment of the technical condition of brick stairs is not an easy task. The first step usually consists of initial observations of the geometry and of looking for visible signs of damage. Usually, the construction is protected by plaster, so some defects may be hidden. Modern TLS measuring methods can also be helpful in preliminary surveys. Only by uncovering, it is possible to fully assess the quality of brick and mortar and their degree of degradation. The evaluation of the material properties of the structure is possible by taking representative samples and performing laboratory tests [2,10,54–59]. A deeper analysis of the performance of the structure and the causes of its damage is possible using FEM-based 3D models [57–64]. On this basis, it is possible to precisely select the reinforcement methods. The analysis in the elastic range is rather easy to perform, but the analysis in the plastic range, after cracking has occurred, requires time-consuming and expensive studies [60].

Studies of masonry arches and vaults can be found in the works [61–105]. In these studies, masonry vaults are characterized by significant arch rise and placement of the masonry stairs. A small number of researchers has taken up the problem of load-bearing capacity of masonry stairs. Research has mostly focused on establishing the principles and methods for structural calculations [92–99]. There is a visible lack of research on masonry staircases. The design of staircases is similar to masonry arch work; however, the arrangement of loads is different. In addition, the influence of the steps above the vault on the operation of the system is also significant.

The article presents a novel approach, in which experimental tests for staircases were made in a 1:1 scale resembling a real-life construction. Together with laboratory tests, the TLS diagnosis of an arched staircase in a real-life historic building is presented. The history of the TLS LiDAR measurement method dates back only 20 years [41,42,106]. The authors' research study indicates that it can be used in the diagnosis of some types of building structures [41,42]. It is important to assess the applicability of the TLS method in the diagnosis of masonry stair structures, including arched staircases. The possibilities of its use in this area are presented in this article.

2. Real-Life Structure

2.1. Case Study Description

The building had four residential floors and an attic. The ceilings on the upper floors were made of wooden beams, while, on the first floor, they were made as arched segmental vaults on steel beams. The floors were 3.2 m high. The staircase was 2.5 m wide and 5.3 m long. The length of the landings was 1.6–1.7 m and the length of the flights was 2.6 m, with a width of 1.2 m. The analyzed stair flights were at an angle of 38°. The stairs were made of steel and masonry, with arched spans between the landings. The rise of the stair arch had a value of $f = 1/19\,L$. Figure 5 shows the general view of the arched stair structure under consideration.

Figure 5. View of the researched masonry staircase.

The measured dimensions of the bricks were $25 \times 12 \times 6.5$ cm^3. The brick and mortar compressive strength was estimated with use of the non-destructive, ultrasonic measurements according to the dependencies described in [107]. The dependency of bricks is shown in Equation (1).

$$f_{c,brick} = 1.4949 \cdot e^{0.002 \cdot UPV} \ \text{(MPa),} \tag{1}$$

where $f_{c,brick}$ (MPa) is the compressive strength of the brick element and UPV (m/s) is the measured ultrasonic pulse velocity. The dependency of lime–cement mortar is presented in Equation (2).

$$f_{c,mortar} = -5.5 + 0.007671 \cdot UPV \ (\text{MPa}), \qquad (2)$$

where $f_{c,mortar}$ (MPa) is the compressive strength of lime–cement mortar. The results of the tests are presented in Table 1.

Table 1. Ultrasonic pulse velocity and calculated compressive strength of tested bricks and mortar.

Ordinal No	Bricks		Mortar	
	Ultrasonic Pulse Velocity (m/s)	Compressive Strength (MPa)	Ultrasonic Pulse Velocity (m/s)	Compressive Strength (MPa)
1	1130	14.3	1192	3.6
2	971	10.4	1227	3.9
3	1472	28.4	1317	4.6
4	1172	15.6	1414	5.3
5	1071	12.7	1276	4.3
6	1327	21.2	994	2.1
7	1191	16.2	1321	4.6
8	1432	26.2	1417	5.4
9	1101	13.5	1276	4.3
Mean value	1207.4	17.6	1270.4	4.2

The compressive strength of the bricks varied in a wide range, from 10.4 to 28.4 MPa with a mean value of 17.6 MPa. The compressive strength of lime–cement mortar varied from 2.1 to 5.4 MPa with a mean value of 4.1 MPa. Due to the large discrepancy found between the strength values of the masonry units and mortar, it was decided to carry out laboratory tests using materials with standard properties. In this respect, a brick class of 25 MPa and a mortar class of 5 MPa were assumed.

2.2. TLS Diagnostic on a Real-Life Structure

Stair geometry measurements and diagnostics were performed using TLS technology, using a stationary scanner Focus M70 (Faro, Lake Mary, FL, USA) with a single measurement accuracy of 0.2 mm. From the measurements, a point cloud in Autodesk Recap (RCP) format was obtained, which was then verified in CAD software (Version2021, San Rafael, Autodesk, CA, USA). RCP format files store spatially indexed point cloud data that can be processed in applications to view, edit and analyze object geometry. The purpose of the measurements was to analyze the geometry of the masonry arch. The aim of the study was to indicate the geometric irregularities, whose technical condition was visually inspected. After removing the plaster in the selected irregularity areas, the condition of masonry and mortar was evaluated.

The TLS measurements allowed us to determine the exact geometry of the stair flight. Figure 6 shows a general view of the obtained TLS measurement map along with a picture of the geometry of the curved staircase of the building.

(**b**)
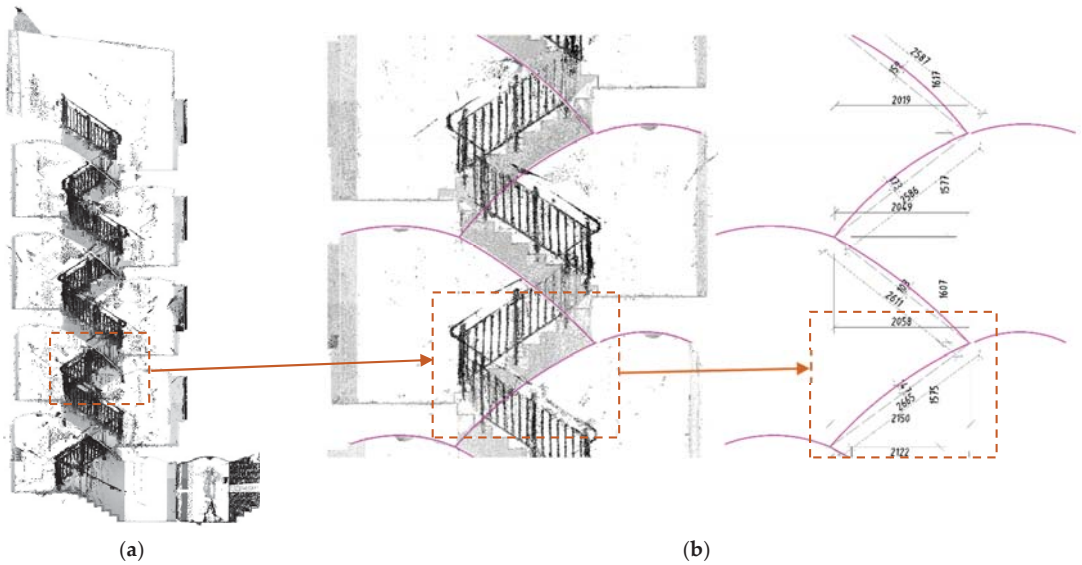
Figure 6. TLS data acquired from existing building: section view of building (**a**) and geometry measurements for analysis (**b**). The dashed line marks the stair flight which was subjected to further laboratory testing.

Alongside TLS measurements, a visual evaluation of the mortar joints in the stair flights as well as of the treads was performed. Numerous damages and cracks were found. The most important was a crack in the joint on the masonry arch presented in Figure 7.

Figure 7. Section of the staircase with visible crack of the arch caused by improper renovation and deterioration of masonry joints.

Incorrectly made support changed the distribution of internal forces in the masonry arch, which was the reason for the whole structural diagnosis. Support should have been put in place for the entire surface of the arch in the form of a centering with an appropriate shape to match the actual geometry of each stair flight arch. Figure 8 shows the output of TLS diagnostics for the run fault of the stair flight.

Figure 8. TLS data output for the point damage of the stair flight: section view of the stair flight (**a**) and point of damage (**b**).

The weakest points of the analyzed masonry arch structure were the joints between bricks and mortar. On the basis of the research work carried out, it was decided to reinforce the whole structure of flights and landings with a steel structure fixed from the bottom.

3. Laboratory Tests

3.1. Materials

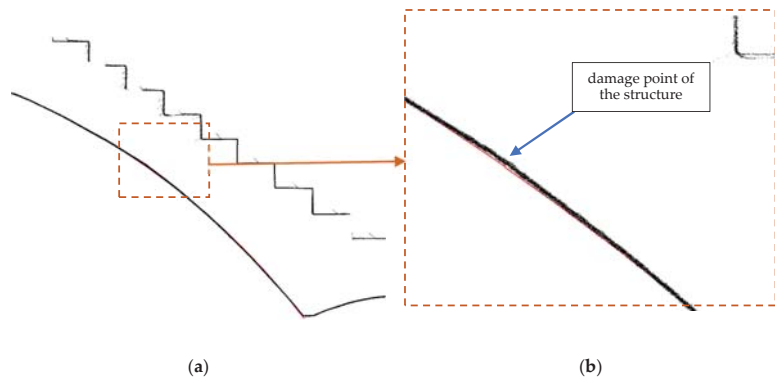The tested samples and elements presented in this research study were built using clay brick, class 25. The dimensions of the bricks were $25 \times 12 \times 6.5$ cm^3 (the same as in the real-life stair flight construction). For the preparation of joints, lime–cement mortar, class M5, was used. For the preparation of masonry mortar, a factory-made, dry, lime–cement mortar class M5 mixture was used (Quick-mix TWM-M5; Sievert, Strzelin, Poland). The mixture consisted of a cement binder, slaked lime, quartz fillers and refining additives. The thickness of the joint was about 1 cm. To determine the properties of the materials used, initial tests in accordance with current standards [108–111] were conducted. The results of the tests are presented in Table 2.

3.2. Laboratory Models of Stair Flights

Laboratory tests were conducted on two models of the stair flights—without stair treads (M1) and with stair treads (M2). The models were made in a 1:1 scale based on the measurements of the analyzed construction, with a width of a single 25 cm brick (Figure 9).

(**a**)   (**b**)
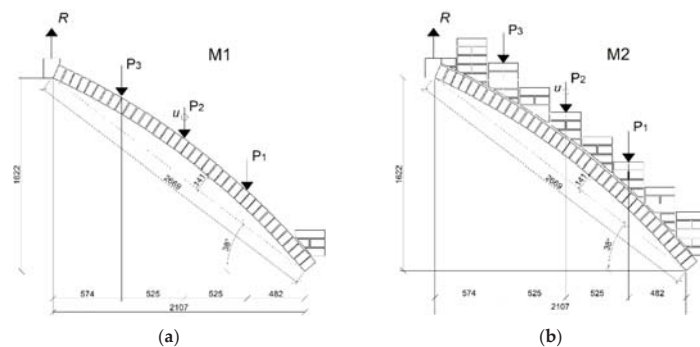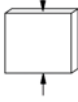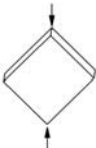
Figure 9. Laboratory models of stair flights (dimensions in mm): model M1—without treads (**a**); model M2—with treads (**b**). P_1–P_3—force application points; R—force from the arch registered with a force gauge; u—vertical displacement in the middle of the arch span.

Table 2. Properties of used materials.

Load Diagram	Test	Material	No. of Samples	Result	Coefficient of Variation
	Compressive strength [108]	Brick	6	f_b = 26.6 MPa	9%
	Tensile strength	Brick	6	f_{tb} = 2.3 MPa	18%
	Flexural strength [109]	Mortar	9	f = 2.7 MPa	17%
	Compressive strength [109]	Mortar	12	f_m = 8.0 MPa	23%
	Tensile strength	Mortar	6	f_{tm} = 1.0 MPa	13%
	Compressive strength [110] Young's modulus [110] Poisson's coefficient [110]	Masonry	6	f_m = 10.8 MPa E = 6.6 GPa ν = 0.14	7% 7% 17%
	Tensile splitting strength [111]	Masonry	6	f_{t45} = 0.52 MPa	11%
	Tensile strength	Masonry	7	f_{t90} = 0.11 MPa	1%

The dimensions of the flight were taken from the real-life structure and were noted as follows:

- Height 162 cm;
- Length 210 cm;
- Slope 38°;
- Arch rise f = 14 cm.

The stair flight construction was supported on a self-made test bench frame. During the masonry works, a wooden structure with expanded polystyrene was used as a centering for the arch. The support was removed while the arch structure was drying, so that the structure could be pressed down naturally. Due to indoor conditions, the bricks were soaked in water before construction, then wetted with water daily during the mortar curing processes. In order to take measurements, a force gauge was placed in the upper corner of the flight to transfer the vertical force.

Measurements were conducted with inductive sensors (for vertical displacements) and two force gauges connected to an MGC Plus HBM Hottinger Bridge. In addition,

the bridge was connected to the ARAMIS optical three-dimensional displacement and strain measurement system. The model was painted on the back side with a white–black pattern to enable image correlation. First, the model was tested in the elastic range with a concentrated force applied at three different locations, P_1, P_2 and P_3. At the force application locations, horizontal surfaces were prepared with quick-setting mortar with a strength, after 24 h, of at least 25 MPa. The assumed limit loads at points P_1 and P_3 were up to 1.5 kN, while the limit for point P_2 was noted when the first crack was registered, after which the test was stopped. The loads at P_1, P_2 and P_3 were applied separately to the tested specimen. Then, on the basis of the M1 model, the M2 model was created by adding treads over the staircase (Figure 3). In order to create the geometry of the steps, it was necessary to precisely cut the bricks at the angles correlating with the arch.

The model with treads (M2) was tested similarly to the model without treads (M1). Points P_1, P_2 and P_3 were determined at the same locations as in the case of the M1 model. Assumed force limits for points P_1 and P_3 were up to 6 kN. At the middle point, P_2, the structure was loaded up to failure. The loads were applied separately to the specimen.

3.3. Results of Laboratory Tests

The model without treads (M1) was loaded with concentrated forces $P_1 = P_3 = 1.5$ kN. The value of the force at point P_2 was increased until the first crack occurred at the load value of 4.5 kN. This moment was considered to be the end of elastic work of the structure. Failure was caused by the opening of the crack within the joint located under the concentrated force at point P_2.

The model with masonry treads (M2) was loaded at the same locations as model M1 by applying concentrated forces on the masonry treads. At points P_1 and P_3, a structural load of $P_1 = P_3 = 6$ kN was applied. At the middle point, P_2, the value of the load was increased until failure due to cracking, which occurred at a force of P = 59.8 kN. The results of the measurements of the displacement and support reactions of the researched models are presented in Figure 10.

By including the treads in the stair flight curve analysis, the load capacity was considerably higher than previously assumed. The load-bearing capacity for the model with treads was 13.3 times higher than in the model without treads. The deflection for the same load level P = 4 kN at point P_2 for model M1 was u = 1.9 mm and, for model M2, u = 0.2 mm. The deflection value of model M2 was 9.5 times smaller than the deflection of model M1. The steps masoned above the staircase significantly increased the load-bearing capacity of the structure, as well as its stiffness. Figure 11 shows the failure mode of the tested models of stair arches and the results of the measurement of the deformations for M2 made with the ARAMIS system at the moment of destruction.

The model of structural failure changed, which, in the case of model M2, occurred as a result of cracking along the arch, at the interface of the arch with the brick treads. First of all, the masonry above the arch detached from the rest of the structure (masoned brick treads). This proved the significant importance of the stair treads above the arch in its load-bearing capacity. Once the crack formed between the arch and the treads, the rest of the structure exhibited rapid failure.

For model M1 (without treads), the deflection measured vertically in the load range up to 0.9 kN developed similarly for points P_1 and P_2. The deflection curve for P_3 was significantly different from that for P_1 and P_2. Comparing the curves for a load level P = 1 kN, it was found that the smallest deflection of the structure was recorded for the load at point P_1 (48.2 cm from the lower support), for which a vertical deflection of the structure u = 0.3 mm was measured. At point P_2 (100.7 cm from the lower support), the vertical deflection u = 0.4 mm was obtained. At point P_3 (153.2 cm from the lower support and 57.4 cm from the upper support), the highest vertical deflection of the structure u = 0.8 mm was achieved. At point P_2, the deflection was 1.3 times higher in relation to point P_1, while, at point P_3, it was 2.7 times higher than at P_1. That is, the lower the location of force along the staircase was, the lower the influence on the deformation of the structure.
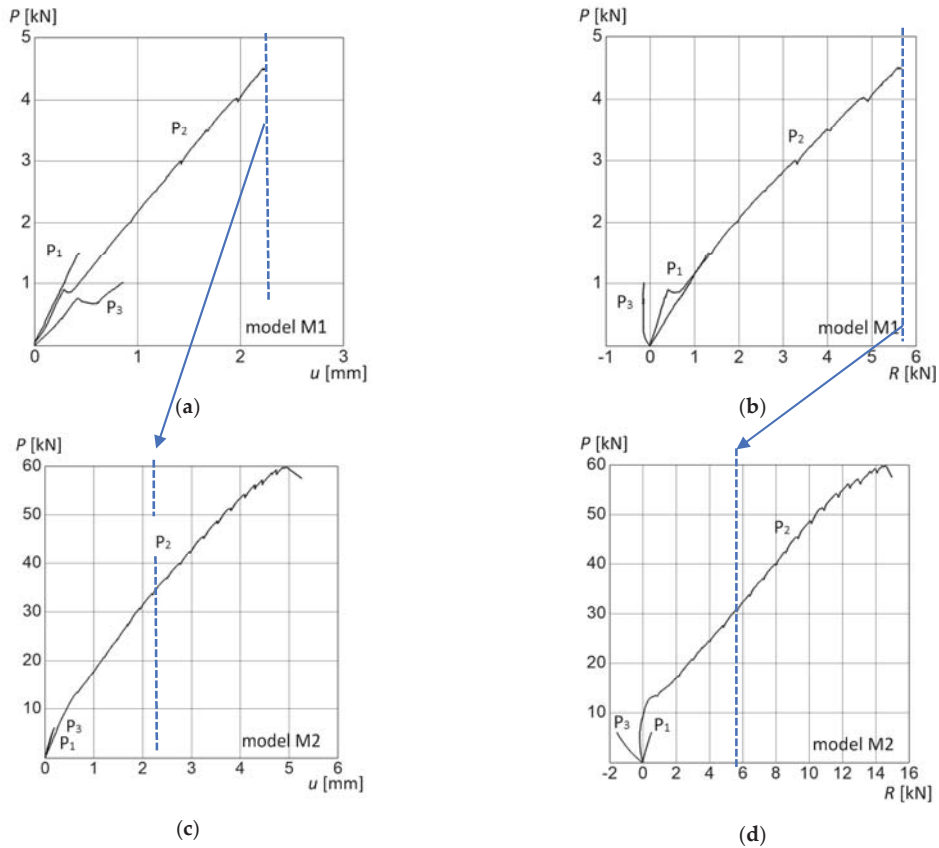
Figure 10. Experimental results of masonry staircases: relation P–u (vertical displacement in the middle of an arch in point P₂) for model M1 (**a**); force P–reaction R for model M1 (**b**); force P–displacement u (vertical displacement in the middle of an arch in point P₂) for model M2 (**c**); force P–reaction R for model M2 (**d**).

Changing the location of the force had also a significant effect on the recorded reaction R in the upper part of the staircase. For model M1, in the case of force applied to the middle and lower parts of the staircase (P_1 and P_2), the reaction was positive, which means that it was directed vertically downwards and balanced the horizontal forces in the arch. However, for the force at point P_3, the situation was completely different. Due to the different geometry of the arch compared to typical vaults, the reaction had the opposite direction. The arch in this place did not generate compressive force on the upper support, but, rather, a tension. Comparing the values of the reaction R between different force points at the force level $P = 1$ kN, it should be noted that the reaction for points P_1 and P_2 was similar and was about $R = 0.8$ kN. For point P_3, the reaction was $R = -0.1$ kN, which was eight times lower. The reactions for points P_1 and P_2 had different values until the inflection point on the P_2 curve, at force $P = 0.9$ kN.
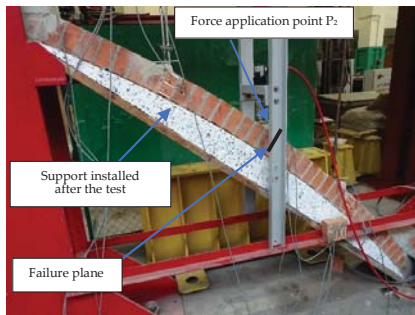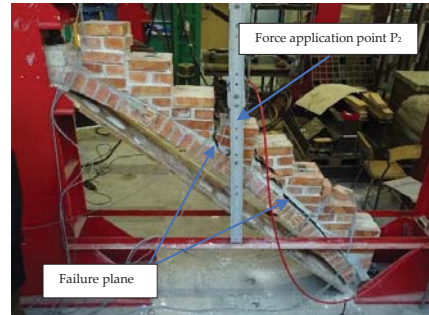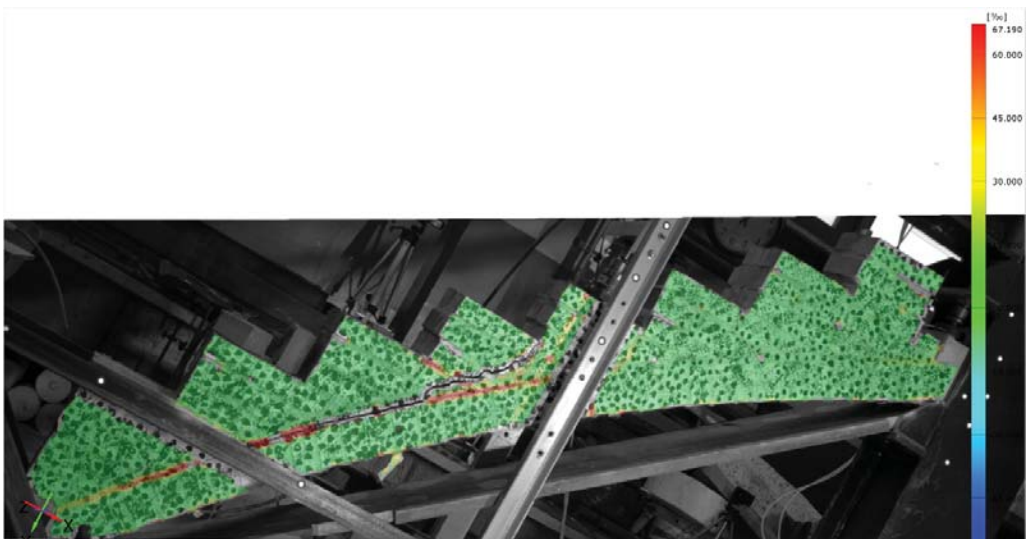
Figure 11. Registered failure mode of tested models of stair arches: model M1 (**a**), model M2 (**b**) and measurements from ARAMIS of deformation during failure of model M2 (**c**).

Different results were obtained for model M2 (with treads). The differences in deflection u were less visible between P_1 and P_3. For the load level P = 5 kN at points P_1 and P_3, the deflection had a value of u = 0.2 mm. In the investigated load range, the addition of stair treads increased the stiffness of the structure regardless of force location.

For model M2, the reaction forces in the support differed from each other. Negative values for the support were registered again for point P_3 but also partially for point P_2. The reaction in the case of the force at the center (P_2) operated in a tension range, up to P = 9 kN, after which it started to work in compression. At the force level P = 5 kN, the reaction at point P_1 was R = 0.4 kN; at point P_2, it was R = −0.2 kN; and, at point P_3, it was R = −1.4 kN. The spreading force for the force P = 5 kN was recorded only for the force at point P_1. In the case of force at points P_2 and P_3, tension was observed. The value of the reaction for P_3 was seven times higher than for P_2.

The results measured using the ARAMIS system allowed us to analyze the displacement with higher precision. For the reference load level P = 6 kN, there were visible differences in the operation of the structure depending on the load application point. Analyzing the displacement maps (Figure 12), it is visible that there were local deformations.

Those were caused by the movement of the bricks toward each other due to the changes in the joints.

For model M2, regardless of the load application point, the values of arch displacement were of the same sign. This is different from a typical operation of a masonry arch. The biggest displacement of the staircase was achieved when the force was applied at point P_2. The results for points P_1 (value for E4, virtual point, in the middle, d = 0.186 mm) and P_3 (also value for E4, virtual point, in the middle, d = 0.189 mm) were similar. The values of deflections at the points directly under the applied forces differed for P_1 (virtual point E2, d = 0.217 mm) and P_3 (virtual point E6, d = 0.144 mm), even though the total deflection at point E2 was similar. For the load level P = 6 kN, the highest resultant deflection for point P_2 was d = 0.274 mm. This is a value that can be hardly seen with a naked eye. The failure of the structure was also at a small resultant displacement of d = 6.714 mm. These results confirm a significant influence of masonry treads on the rigidity of the whole structure. The treads are responsible for increased stiffness of a lean masonry arch. Due to the low values of the displacement of treads, the diagnostic of the structure should be performed with precise measurement equipment, such as 3D scanners (TLS).
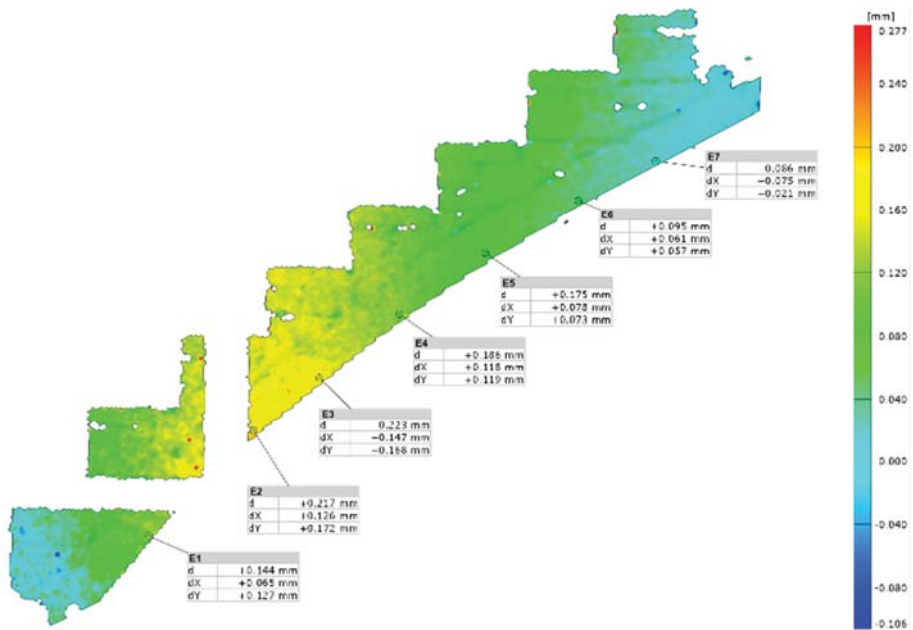
(**a**)

Figure 12. *Cont.*

(**b**)

(**c**)

Figure 12. *Cont.*

(**d**)
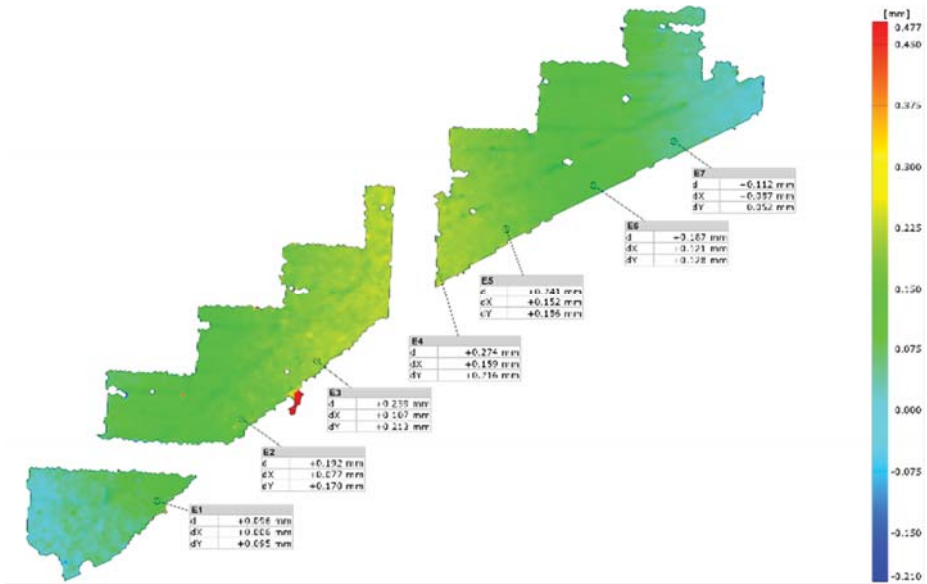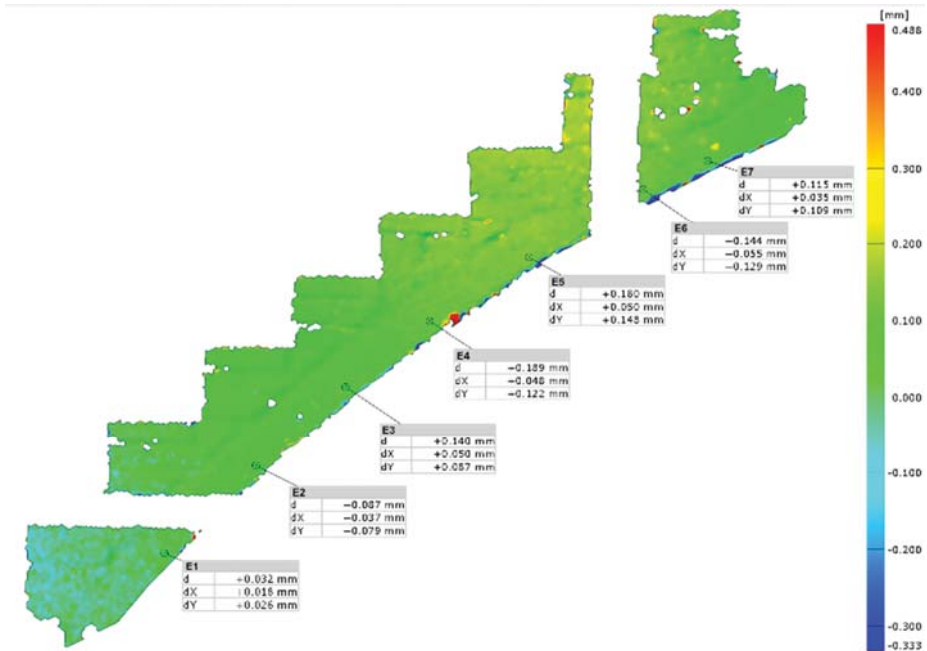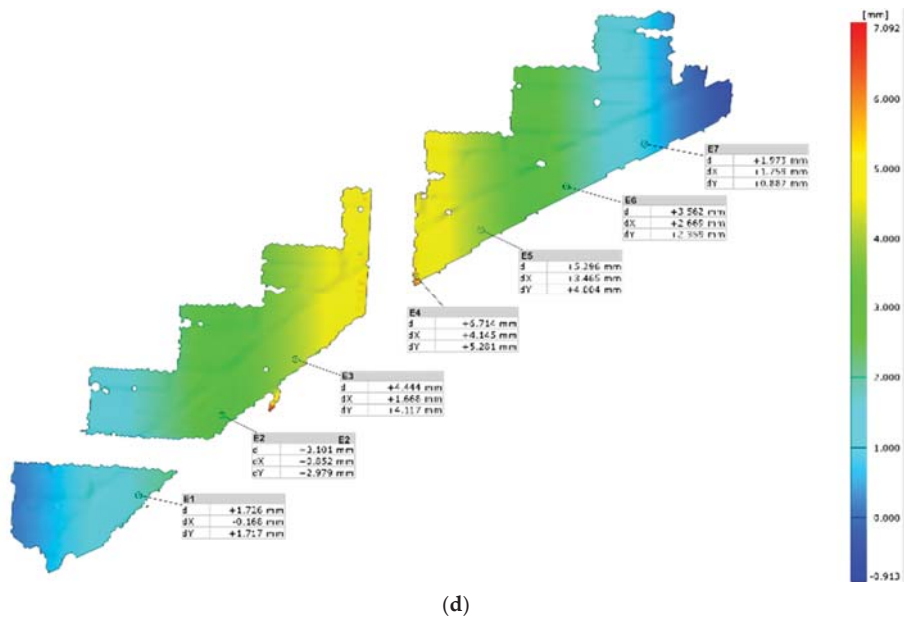
Figure 12. Results of experimental test of masonry staircases—displacement measured by ARAMIS: load P = 6 kN at point P_1 (bottom) (**a**), load P = 6 kN at point P_2 (middle) (**b**), load P = 6 kN at point P_3 (top) (**c**) and load at failure P = 59.8 kN in point P_2 (**d**). d—resultant displacement; dX—horizontal displacement; dY—vertical displacement.

4. Conclusions

Based on the research study presented, the following conclusions were drawn:

- The TLS method allowed us to perform the geometric analysis and dimensioning of the existing arched stair structure.
- The TLS measurements allowed us to detect geometric irregularities, which, complemented by visual diagnostic tests, allowed us to detect damage to their structure.
- The damage to the flight was caused by improperly performed repair works—improper temporary support of the flight.
- The conducted experimental investigations showed that the key element responsible for the actual load-bearing capacity and stiffness of the stair flight were the treads above the masonry arch.
- The load-bearing capacity of the model with treads was 13.3 times higher than that of the model without treads.
- The deflection value of model M2 was 9.5 times smaller than the deflection of model M1.
- A different working mechanism was found for the stair arch model with brick threads (M2) compared to the arch without threads (M1).
- The failure of model M1 was caused by the opening of the crack within the joint located under the concentrated force at point P_2.
- In the case of model M2, failure occurred as a result of cracking along the arch, at the interface of the arch with the brick treads.
- In the case of arched stair renovation, it is crucial to properly connect the arches of the stair flights with the treads above. If there is no proper connection between the vaults and the treads, the increase in the load-bearing capacity shown in the research study should be excluded from the calculations.

References

1. Ahnert, R.; Krause, K.H. *Typische Baukonstruktionen von 1860 bis 1960-Band 3*; Beuth Verlag GmbH: Berlin, Germany, 2014.
2. Małyszko, L.; Orłowicz, R. *Konstrukcje Murowe. Zarysowania i Naprawy. (Structural Masonry. Cracks and Repairs)*; Wydawnictwo Uniwersytetu Warmińsko–Mazurskiego: Olsztyn, Poland, 2000.
3. Nowak, R. Analiza Nośności i Mechanizmów Uszkodzeń Odcinkowych Ceglanych Nadproży Łukowych. Ph.D. Thesis, West Pomeranian University of Technology, Szczecin, Poland, 2014. (In Polish).
4. Pawłowski, W.; Nowak, R. Architektura a statyka ceglanych nadproży łukowych. *Przestrzeń Forma* **2009**, *12*, 115–122.
5. Stawiski, B.; Kania, T. Building diagnostics versus effectiveness of repairs. *MATEC Web Conf.* **2018**, *174*, 03005. [CrossRef]
6. Drobiec, Ł.; Jasiński, R.; Mazur, W. Accuracy of Eddy-Current and Radar Methods Used in Reinforcement Detection. *Materials* **2019**, *12*, 1168. [CrossRef]
7. Jasiński, R.; Drobiec, Ł.; Mazur, W. Validation of Selected Non-Destructive Methods for Determining the Compressive Strength of Masonry Units Made of Autoclaved Aerated Concrete. *Materials* **2019**, *12*, 389. [CrossRef]
8. Hoła, A.; Matkowski, Z.; Hoła, J. Analysis of the Moisture Content of Masonry Walls in Historical Buildings Using the Basement of a Medieval Town Hall as an Example. *Procedia Eng.* **2017**, *172*, 363–368. [CrossRef]
9. Lachowicz, J.; Rucka, M. Diagnostics of pillars in St. Mary's Church (Gdańsk, Poland) using the GPR method. *Int. J. Archit. Herit.* **2018**, *13*, 1223–1233. [CrossRef]
10. Schabowicz, K. Non-Destructive Testing of Materials in Civil Engineering. *Materials* **2019**, *12*, 3237. [CrossRef]
11. Maione, A.; Argiento, L.U.; Cassapulla, C. Management of multi-source information to identify the typology of the horizontal structures in historical masonry buildings: The case study of the Museum of Capodimonte in Naples (Italy). *Frattura Integrità Strutturale* **2018**, *46*, 240–251. [CrossRef]
12. Łątka, D.; Matysek, P. Badania konstrukcji murowych in-situ. *Inżynieria Budownictwo* **2017**, *7*, 360–363.
13. Łątka, D.; Sęręga, S.; Matysek, P. Estimation of Mortar Compressive Strength Based on Specimens Extracted from Masonry Bed Joints. In Proceedings of the Structural Analysis of Historical Constructions, Cusco, Peru, 11–13 September 2018; pp. 577–586.
14. Tkacz, P. Ocena Wytrzymałości na Ściskanie Konstrukcji Murowych z Uwzględnieniem Badań In Situ. Ph.D. Thesis, West Pomeranian University of Technology, Szczecin, Poland, 2015. (In Polish).
15. Matysek, P.; Witkowski, M. A Comparative Study on the Compressive Strength of Bricks from Different Historical Periods. *Int. J. Archit. Herit.* **2015**, *10*, 396–405. [CrossRef]
16. Ramesh, M.; Azenha, M.; Lourenco, P. Mechanical properties of lime–cement masonry mortars in their early ages. *Mater. Struct.* **2019**, *52*, 13. [CrossRef]
17. Ramesh, M.; Azenha, M.; Lourenco, P. Mechanical characterization of lime cement mortars: E-modulus and fracture energy. In Proceedings of the RILEM Spring Convention and Sustainable Materials, Systems and Structures Conference (SMSS 2019), Rovinj, Croatia, 18–22 March 2019.
18. Matysek, P. *Identyfikacja Wytrzymałości na Ściskanie i Odkształcalności Murów Ceglanych w Obiektach Istniejących*; Cracow University o Technology: Cracow, Poland, 2014. (In Polish).
19. Łątka, D.; Matysek, P. The Estimation of Compressive Stress Level in Brick Masonry Using the Flat-jack Method. *Procedia Eng.* **2017**, *193*, 266–272. [CrossRef]
20. Runkiewicz, L.; Rodzik, W. Badania nieniszczące wytrzymałości murowanych obiektów zabytkowych. *Inżynieria Budownictwo* **1990**, *2*, 50–52.
21. Runkiewicz, L.; Sieczkowski, J. Stosowanie obciążeń próbnych do oceny stanu technicznego budynków. *Przegląd Budowlany* **2015**, *86*, 7–8.
22. Runkiewicz, L.; Biegus, A.; Brol, J.; Buczkowski, W.; Drobiec, Ł.; Gajownik, R.; Godlewski, T.; Hoła, J.; Hulimka, J.; Jakimowicz, M.; et al. *Diagnostyka Obiektów Budowlanych. Zasady Wykonywania Ekspertyz*; PWN: Warsaw, Poland, 2020.
23. Kania, T.; Derkach, V.; Nowak, R. Testing Crack Resistance of Non-Load-Bearing Ceramic Walls with Door Openings. *Materials* **2021**, *14*, 1379. [CrossRef]
24. Kregar, K.; Ambrožič, T.; Kogoj, D.; Vezočnik, R.; Marjetič, A. Determining the inclination of tall chimneys using the TPS and TLS approach. *Measurement* **2015**, *75*, 354–363. [CrossRef]
25. Drygala, I.; Dulinska, J.; Bednarz, L.; Jasienko, J. Numerical evaluation of seismic-induced damages in masonry elements of historical arch viaduct. *IOP Conf. Ser. Mater. Sci. Eng.* **2018**, *364*, 012006. [CrossRef]

26. Croce, P.; Beconcini, M.L.; Formichi, P.; Landi, F.; Puccini, B.; Zotti, V. Bayesian Methodology for Probabilistic Description of Mechanical Parameters of Masonry Walls. *ASCE-ASME J. Risk Uncertain. Eng. Syst. Part A Civ. Eng.* **2021**, *7*, 04021008. [CrossRef]
27. Malomo, D.; DeJong, M.J. A Macro-Distinct Element Model (M-DEM) for out-of-plane analysis of unreinforced masonry structures. *Eng. Struct.* **2021**, *244*, 112754. [CrossRef]
28. Lourenco, P.B. Computations on historic masonry structures. *Prog. Struct. Eng. Mater.* **2002**, *4*, 301–319. [CrossRef]
29. Beconcini, M.L.; Croce, P.; Formichi, P.; Landi, F.; Puccini, B. Experimental Evaluation of Shear Behavior of Stone Masonry Wall. *Materials* **2021**, *14*, 2313. [CrossRef]
30. Lourenço, P.B.; Rots, J.G.; Blaauwendraad, J. Continuum model for masonry: Parameter estimation and validation. *J. Struct. Eng.* **1998**, *124*, 642–652. [CrossRef]
31. Baraldi., D.; Milani, G.; Sarhosis, V. A Rigid-Beam-Model for studying the dynamic behaviour of cantilever masonry walls. *Structures* **2021**, *33*, 2950–2963. [CrossRef]
32. Celano, T.; Argiento, L.U.; Ceroni, F.; Casapulla, C. In-Plane Behaviour of Masonry Walls: Numerical Analysis and Design Formulations. *Materials* **2021**, *14*, 5780. [CrossRef]
33. Suchocki, C.; Katzer, J.; Rapinski, J. Terrestrial Laser Scanner as a Tool for Assessment of Saturation and Moisture Movement in Building Materials. *Period. Polytech. Civ. Eng.* **2018**, *62*, 694–699. [CrossRef]
34. Suchocki, C.; Jagoda, M.; Obuchovski, R.; Šlikas, D.; Sužiedelytė-Visockienė, J. The properties of terrestrial laser system intensity in measurements of technical conditions of architectural structures. *Metrol. Meas. Syst.* **2018**, *25*, 779–792. [CrossRef]
35. Suchocki, C.; Katzer, J. TLS Technology in Brick Walls Inspection. In Proceedings of the Conference: 2018 Baltic Geodetic Congress (BGC Geomatics), Olsztyn, Poland, 21–23 June 2018; pp. 359–363.
36. Suchocki, C.; Katzer, J.; Serrat, C.; Jagoda, M. Application of TLS Intensity Data for Detection of Brick Walls Defects. *IOP Conf. Ser. Mater. Sci. Eng.* **2019**, *603*, 022100. [CrossRef]
37. Błaszczak-Bąk, W.; Suchocki, C.; Janicka, J.; Dumalski, A.; Duchnowski, R. Defect detection of historic structures in dark places based on the point cloud analysis by modified OptD Method. *GeoInformation Disaster Manag.* **2019**, *XLII-3/W8*, 71–77. [CrossRef]
38. Suchocki, C.; Błaszczak-Bąk, W.; Damięcka-Suchocka, M.; Jagoda, M.; Masiero, A. On the Use of the OptD Method for Building Diagnostics. *Remote Sens.* **2020**, *12*, 1806. [CrossRef]
39. Suchocki, C.; Błaszczak-Bąk, W.; Janicka, J.; Dumalski, A. Detection of defects in building walls using modified OptD method for down-sampling of point clouds. *Build. Res. Inf.* **2020**, *49*, 197–215. [CrossRef]
40. Błaszczak-Bąk, W.; Suchocki, C.; Janicka, J.; Dumalski, A.; Duchnowski, R.; Sobieraj-Żłobińska, A. Automatic Threat Detection for Historic Buildings in Dark Places Based on the Modified OptD Method. *Int. J. Geo-Inf.* **2020**, *9*, 123. [CrossRef]
41. Suchocki, C. Comparison of Time-of-Flight and Phase-Shift TLS Intensity Data for the Diagnostics Measurements of Buildings. *Materials* **2020**, *13*, 353. [CrossRef]
42. Nowak, R.; Orłowicz, R.; Rutkowski, R. Use of TLS (LiDAR) for Building Diagnostics with the Example of a Historic Building in Karlino. *Buildings* **2020**, *10*, 24. [CrossRef]
43. Wierzbicki, K.; Szewczyk, P.; Paczkowski, W.; Wroblewski, T.; Skibicki, S. Torsional Stability Assessment of Columns Using Photometry and FEM. *Buildings* **2020**, *10*, 162. [CrossRef]
44. Suchocki, C.; Błaszczak-Bąk, W.; Damięcka-Suchocka, M.; Jagoda, M.; Masiero, A. An example of using the OptD method to optimization of point clouds in the buildings diagnostics. In Proceedings of the 4th Joint International Symposium on Deformation Monitoring (JISDM), Athens, Greece, 15–17 May 2018.
45. Suchocki, C.; Błaszczak-Bąk, W. Down-Sampling of Point Clouds for the Technical Diagnostics of Buildings and Structures. *Geosciences* **2019**, *9*, 70. [CrossRef]
46. Dias, I.S.; Flores-Colen, I.; Silva, A. Critical Analysis about Emerging Technologies for Building's Façade Inspection. *Buildings* **2021**, *11*, 53. [CrossRef]
47. Mosalam, K.; Takhirov, S.; Park, S. Applications of laser scanning to structures in laboratory tests and field surveys. *Struct. Control Health Monit.* **2014**, *21*, 115–134. [CrossRef]
48. Liu, J.; Zhang, Q.; Wu, J.; Zhao, Y. Dimensional accuracy and structural performance assessment of spatial structure components using 3D laser scanning. *Autom. Constr.* **2018**, *96*, 324–336. [CrossRef]
49. Leonov, A.V.; Anikushkin, M.N.; Ivanov, A.V.; Ovcharov, S.V.; Bobkov, A.E.; Baturin, Y.M. Laser scanning and 3D modeling of the Shukhov hyperboloid tower in Moscow. *J. Cult. Herit.* **2015**, *16*, 551–559. [CrossRef]
50. Feng, P.; Zou, Y.; Hu, L.; Liu, T. Use of 3D laser scanning on evaluating reduction of initial geometric imperfection of steel column with pre-stressed CFRP. *Eng. Struct.* **2019**, *198*, 109527. [CrossRef]
51. Mora, R.; Martín-Jiménez, J.A.; Lagüela, S.; González-Aguilera, D. Automatic Point-Cloud Registration for Quality Control in Building Works. *Appl. Sci.* **2021**, *11*, 1465. [CrossRef]
52. Erdélyi, J.; Kopáčik, A.; Kyrinovič, P. Spatial Data Analysis for Deformation Monitoring of Bridge Structures. *Appl. Sci.* **2020**, *10*, 8731. [CrossRef]
53. Singhroy, V.; Fobert, M.-A.; Li, J.; Blais-Stevens, A.; Charbonneau, F.; Das, M. *Advanced Radar Images for Monitoring Transportation, Energy, Mining and Coastal Infrastructure*; Singhroy, V., Ed.; Springer: Cham, Switzerland, 2021; pp. 3–40. [CrossRef]
54. Drobiec, Ł.; Piekarczyk, A.; Kubica, J. AAC bocks masonry compressed perpendicular and parallel to the bed joints. In Proceedings of the 12th International Brick/Block Masonry Conference, Madrid, Spain, 25–28 June 2000.
55. Hulimka, J.; Kałuża, M.; Kubica, J. Failure and overhaul of a historic brick tower. *Eng. Fail. Anal.* **2019**, *102*, 46–59. [CrossRef]

56. Hoła, J.; Schabowicz, K. Diagnostyka obiektów budownictwa ogólnego. In Proceedings of the XXX Jubileuszowe Ogólnopolskie Warsztaty Pracy Projektanta Konstrukcji, Szczyrk, Poland, 25–28 March 2015.
57. Drobiec, Ł.; Grzyb, K.; Zając, J. Analysis of Reasons for the Structural Collapse of Historic Buildings. *Sustainability* **2021**, *13*, 10058. [CrossRef]
58. Schabowicz, K. Testing of Materials and Elements in Civil Engineering. *Materials* **2021**, *14*, 3412. [CrossRef]
59. Szabó, S.; Kövesdi, A.; Vasáros, Z.; Csicsely, Á.; Hegyi, D. The Cause of Damage and Failure of the Mud-brick Vault of the Khan in New-Gourna. *Eng. Fail. Anal.* **2021**, *128*, 105567. [CrossRef]
60. Bednarz, Ł.; Drygała, I.; Dulińska, J.; Jasieńko, J. Study of Materials Behavior in a Monumental Vault Strengthened by a Carbon Net in a Mineral Matrix Subjected to Seismic Influence. *Appl. Sci.* **2021**, *11*, 1015. [CrossRef]
61. Uranjek, M.; Lorenci, T.; Skrinar, M. Analysis of Cylindrical Masonry Shell in St. Jacob's Church in Dolenja Trebuša, Slovenia—Case Study. *Buildings* **2019**, *9*, 127. [CrossRef]
62. Bovo, M.; Mazzotti, C.; Savoia, M. Analysis of structural behaviuor of historical stone arches and vaults: Experimental tests and numerical analyses. In Proceedings of the International Conference on Structural Analysis of Historical Constructions (SAHC 2012), Wrocław, Poland, 15–17 October 2012; pp. 635–643.
63. Jasieńko, J.; Bednarz, Ł.; Nowak, T. The effectiveness of strengthening historic brick vaults by contemporary methods. In Proceedings of the Protection of Historical Buildings, PROHITECH 09, Rome, Italy, 21–27 June 2009; Taylor & Francis Group: London, UK, 2009.
64. Jasieńko, J.; Di Tommaso, A.; Bednarz, Ł. Experimental Investigations into Collapse of Masonry Arches Reinforced Using Different Compatible Technologies. In Proceedings of the Mechanics of Masonry Structures Strengthened with Composite Materials, MuRiCo., Venice, Italy, 22–24 April 2009.
65. Boothby, T.E. Analysis of masonry arches and vaults. *Prog. Struct. Eng. Mater.* **2001**, *3*, 246–256. [CrossRef]
66. Foraboschi, P. Strengthening of Masonry Arches with Fiber-Reinforced Polymer Strips. *J. Compos. Constr.* **2004**, *8*, 191–202. [CrossRef]
67. Castori, G.; Borri, A.; Ebaugh, S.; Casadei, P. Strengthening masonry arches with composites. In Proceedings of the Third International Conference on FRP Composites in Civil Engineering (CICE 2006), Miami, FL, USA, 13–15 December 2006.
68. Oliveira, D.; Basílio, I.; Lourenco, P. FRP strengthening of masonry arches towards an enhanced behaviour. In Proceedings of the Third International Conference on Bridge Maintenance, Safety and Management, Porto, Portugal, 16–19 July 2006.
69. Borri, A.; Casadei, P.; Castori, G.; Ebaugh, S. Research on composite strengthening of masonry arches. In Proceedings of the 8th International Symposium on Fiber Reinforced Polymer Reinforcement for Concrete Structures (FRPRCS-8), Patras, Greece, 16 July 2007.
70. Nowak, R.; Orłowicz, R. Mechanisms of brick arched lintels damage. *Conserv. News* **2009**, *26*, 253–259.
71. Borri, A.; Casadei, P.; Castori, G.; Hammond, J. Strengthening of Brick Masonry Arches with Externally Bonded Steel Reinforced Composites. *J. Compos. Constr.* **2009**, *13*, 468–475. [CrossRef]
72. Bati, S.B.; Rovero, S.; Tonietti, U. Experimental analysis on scale models of CFRP reinforced arches. In Proceedings of the Mechanics of Masonry Structures Strengthened with Composite Materials, MuRiCo., Venice, Italy, 22–24 April 2009.
73. Bajno, D.; Bednarz, L.; Matkowski, Z.; Raszczuk, K. Monitoring of Thermal and Moisture Processes in Various Types of External Historical Walls. *Materials* **2020**, *13*, 505. [CrossRef]
74. Bosnjak-Klecina, M.; Lozancic, S. Stability analysis for masonry-arch structures and vaulted structures. *Gradevinar* **2010**, *62*, 409–421.
75. Gago, A.S.; Alfaiate, J.; Lamas, A. The effect of the infill in arched structures: Analytical and numerical modelling. *Eng. Struct.* **2011**, *33*, 1450–1458. [CrossRef]
76. Cecchi, A. The curve of pressure in vertically loaded arches. *Wiad. Konserw.* **2013**, *34*, 18–22.
77. Egidio, R.; Giada, C.; Annalisa, F.; Giuseppe, C. On the mixed collapse mechanism of semi-circular masonry arches. In Proceedings of the Structural Analysis of Historical Constructions–SAHC 2012, Wrocław, Poland, 15–17 October 2012; pp. 541–549.
78. Albuerne, A.; Williams, M.; Lawson, V. Prediction of the Failure Mechanism of Arches under Base Motion Using DEM Based on the NSCD Method. In Proceedings of the Structural Analysis of Historical Constructions–SAHC 2012, Wrocław, Poland, 15–17 October 2012; pp. 41–47.
79. Marfia, S.; Ricamato, M.; Sacco, E. Stress Analysis of Reinforced Masonry Arches. *Int. J. Comput. Methods Eng. Sci. Mech.* **2008**, *9*, 77–90. [CrossRef]
80. Holzer, S.M. Numerical arch and vault analysis. *J. Herit. Conserv.* **2013**, *34*, 7–17.
81. Hojdys, Ł.; Krajewski, P. Behavior of masonry arches strengthened with TRM. In Proceedings of the International Conference on Arch Bridges, Split, Croatia, 2–4 October 2013; pp. 739–746.
82. Chen, J.F. Load-Bearing Capacity of Masonry Arch Bridges Strengthened with Fibre Reinforced Polymer Composites. *Adv. Struct. Eng.* **2016**, *5*, 37–44. [CrossRef]
83. Reccia, E.; Cecchi, A.; Milani, G. FEM/DEM Approach for the Analysis of Masonry Arch Bridges. In *Advances in Civil and Industrial Engineering*; IGI Global: Hershey, PA, USA, 2016. [CrossRef]
84. Ricci, E.; Sacco, E.; Piccioni, M. A method for the analysis of masonry arches. In Proceedings of the 10th International Conference on Structural Analysis of Historical Constructions, SAHC 2016, Leuven, Belgium, 13–15 September 2016; pp. 1067–1068.

85. Pulatsu, B.; Erdogmus, E.; Lourenco, P. Discrete-continuum approach to assess 3D failure modes of masonry arch bridges. In Proceedings of the IABSE Symposium 2019 Guimarães: Towards a Resilient Built Environment-Risk and Asset Management, Guimarães, Portugal, 27–29 March 2019; pp. 570–577.
86. Aucillo, N.M. On the analysis of masonry arches. *Int. J. Mason. Res. Innov.* **2019**, *4*, 50. [CrossRef]
87. Alecci, V.; De Stefano, M.; Focacci, F.; Luciano, R.; Rovero, L.; Stipo, G. Strengthening Masonry Arches with Lime-Based Mortar Composite. *Buildings* **2017**, *7*, 49. [CrossRef]
88. Corradi, M.; Borri, A.; Castori, G.; Coventry, K. Experimental Analysis of Dynamic Effects of FRP Reinforced Masonry Vaults. *Materials* **2015**, *8*, 8059–8071. [CrossRef] [PubMed]
89. Ferretti, E.; Pascale, G. Some of the Latest Active Strengthening Techniques for Masonry Buildings: A Critical Analysis. *Materials* **2019**, *12*, 1151. [CrossRef]
90. Yang, F.; Wen, X.; Wang, X.; Li, X.; Li, Z. A Model Study of Building Seismic Damage Information Extraction and Analysis on Ground-Based LiDAR Data. *Adv. Civ. Eng.* **2021**, *2021*, 5542012. [CrossRef]
91. Filgueira, A.; González-Jorge, H.; Lagüela, S.; Díaz-Vilariño, L.; Arias, P. Quantifying the influence of rain in LiDAR performance. *Measurement* **2017**, *95*, 143–148. [CrossRef]
92. Abdou, O.A.; Burdette, J.Q. Masonry stairs–design and material performance. *Mason. Soc. Boulder* **1993**, *1*, 739–754.
93. Heyman, J. *The Mechanics of Masonry Stairs*; Computational Mechanics Publications Ltd.: Southampton, UK, 1995; pp. 259–265.
94. Baratta, A.; Corbi, I. Statics and equilibrium paths of masonry stairs. *Open Constr. Build. Technol. J.* **2012**, *6*, 368–372. [CrossRef]
95. Angelillo, M. Static analysis of a Guastavino helical stair as a layered masonry shell. *Compos. Struct.* **2015**, *119*, 298–304. [CrossRef]
96. Gesualdo, A.; Cennamo, C.; Fortunato, A.; Frunzio, G.; Monaco, M.; Angelillo, M. Equilibrium formulation of masonry helical stairs. *Meccanica* **2017**, *52*, 1963–1974. [CrossRef]
97. Rigo, B.; Bagi, K. Discrete element analysis of stone cantilever stairs. *Meccanica* **2018**, *53*, 1571–1589. [CrossRef]
98. Briccola, D.; Bruggi, M.; Taliercio, A. Assessment of 3D Linear Elastic Masonry-Like Vaulted Structures. *Key Eng. Mater.* **2019**, *817*, 50–56. [CrossRef]
99. Angelillo, M.; Olivieri, C.; DeJong, M. A new equilibrium solution for masonry spiral stairs. *Eng. Struct.* **2021**, *238*, 112176. [CrossRef]
100. Nowak, R.; Kania, T.; Derkach, V.; Orłowicz, R.; Halaliuk, A.; Ekiert, E.; Jaworski, R. Strength Parameters of Clay Brick Walls with Various Directions of Force. *Materials* **2021**, *14*, 6461. [CrossRef] [PubMed]
101. Nowak, R.; Orłowicz, R. Testing of Chosen Masonry Arched Lintels. *Int. J. Archit. Herit.* **2020**, *15*, 1895–1909. [CrossRef]
102. Nowak, R.; Orłowicz, R. Selected problems of failures and repairs of historic masonry vaults. *MATEC Web Conf.* **2019**, *284*, 05008. [CrossRef]
103. Nowak, R.; Orłowicz, R. Wpływ stanu technicznego muru na nośność zabytkowego łuku w Sankt Petersburgu. *Mater. Bud.* **2019**, *5*, 36–37. [CrossRef]
104. De Santis, S.; Felice, G.; Roscini, F. Retrofitting of Masonry Vaults by Basalt Textile-Reinforced Mortar Overlays. *Int. J. Archit. Herit.* **2019**, *13*, 1061–1077. [CrossRef]
105. Bespalov, V.; Orlovich, R.; Zimin, S. Stress-Strain State of Brick Masonry Vault with an Aperture. *MATEC Web Conf.* **2016**, *53*, 01009. [CrossRef]
106. Pozo-Antonio, J.S.; Puente, I.; Pereira, M.F.C.; Rocha, C.S.A. Quantification and mapping of deterioration patterns on granite surfaces by means of mobile LiDAR data. *Measurement* **2019**, *140*, 227–236. [CrossRef]
107. Stawiska, N.; Stawiski, B. Rewaloryzacja murów w obiektach zabytkowych. *Wiadomości Konserwatorskie* **2005**, *18*, 18–22.
108. En 772-1+a1 Methods of Test for Masonry Units. In *Determination of Compressive Strength*; European Committee for Standardization: Brussels, Belgium, 2015.
109. EN 1015-11 Methods of Test for Mortar for Masonry. In *Determination of Flexural and Compressive Strength of Hardened Mortar*; European Committee for Standardization: Brussels, Belgium, 2020.
110. EN 1052-1 Methods of test for masonry. In *Determination of Compressive Strength*; European Committee for Standardization: Brussels, Belgium, 1998.
111. *ASTM E72 1989*; Standard Tests for Conducting Strength Tests on Panels for Building Construction. American Society for Testing and Materials: West Conshohocken, PA, USA, 1989.

Strength Parameters of Clay Brick Walls with Various Directions of Force

Rafał Nowak [1,*]**, Tomasz Kania** [2]**, Valery Derkach** [3]**, Romuald Orłowicz** [4]**, Anton Halaliuk** [3]**, Ewa Ekiert** [5] **and Rafał Jaworski** [4]

[1] Department of General Civil Engineering, Faculty of Civil and Environmental Engineering, West Pomeranian University of Technology in Szczecin, Piastów Ave. 50a, 70-311 Szczecin, Poland

[2] Department of General Civil Engineering, Faculty of Civil Engineering, Wrocław University of Science and Technology, Wybrzeże Wyspiańskiego 27, 50-370 Wrocław, Poland; Tomasz.Kania@pwr.edu.pl

[3] Branch Office of the "Institute BelNIIS"—Scientific-Technical Center, 224023 Brest, Belarus; v-derkatch@yandex.by (V.D.); institute@belniis.by (A.H.)

[4] West Pomeranian University of Technology in Szczecin, Piastów Ave. 50a, 70-311 Szczecin, Poland; orlowicz@yandex.ru (R.O.); Rafal.Jaworski@op.pl (R.J.)

[5] Department of Chemical Inorganic Technology and Environment Engineering, Faculty of Chemical Technology and Engineering, West Pomeranian University of Technology in Szczecin, Piastów Ave. 42, 71-065 Szczecin, Poland; edabrowa@zut.edu.pl

* Correspondence: rnowak@zut.edu.pl; Tel.: +48-605-642-800

Abstract: The study analyzes the anisotropy effect for ceramic masonry based on experimental tests of samples made of $25 \times 12 \times 6.5$ cm^3 solid brick elements with compressive strength f_b = 44.1 MPa and cement mortar with compressive strength f_m = 10.9 MPa. The samples were loaded in a single plane with a joint angle that varied from the horizontal plane. The load was applied in a vertical direction. The samples were loaded at angles of $90°$, $67.5°$, $45°$, $22.5°$, and $0°$ toward the bed joints. The most unfavourable cases were determined. It was observed that the anisotropy of the masonry significantly influences the load-bearing capacity of the walls depending on the angle of the compressive stresses trajectory. Approximation curves and equations for compressive strength, Young's modulus, and Poisson's coefficient were proposed. It was observed that Young's modulus and Poisson's ratio will also change depending on the trajectory of compressive stresses as a function of the joint angle. Experimental tests allowed to determine the failure mechanism in prepared specimens. The study allowed to estimate the masonry strength with the load acting at different angles toward the bed joints.

Keywords: clay bricks; cement lime mortar; infill masonry wall; destructive force

1. Introduction

Clay (or mud) has been used in the building industry since ancient times [1,2]. Clay-based building materials can be classified in many categories in terms of the preparation process and use, such as mud bricks, clay plasters, cob, and rammed earth [2,3]. Most typical clay brick structures work mainly in compression perpendicular to the bed (horizontal) joints. Therefore, their compressive strength is determined in this particular direction, according to the methodology presented in the standard [4]. It is less common for masonry to work in compression at a different angle from the joints [5–10].

An example of masonry loaded at different angles to the bed joints are walls subjected to seismic actions. The evaluation of the shear behavior of masonry walls is a fundamental step for the assessment of masonry in seismic zones [11,12]. Under lateral forces, the low tensile strength generally leads to local or global failure modes, the latter related to shear or flexural mechanisms [13]. The latest works in the field of research and modeling of masonry structures concern the influence of the value of the modulus of elasticity and Poisson ratio outside the range of 33% of the ultimate stress on the shear behavior of masonry

walls. Nonlinear static analyses are commonly adopted for the evaluation of seismic performance [11–17]. Research on that subject has been presented by Laurenco et al. [14] with a yield criterion that includes different strengths along each material axis. The criterion includes two different fracture energies in tension and two different fracture energies in compression. This model is validated with uniform biaxial loading conditions [11,14]. Celano et al. in [15] presented research on the in-plane resistance of masonry walls by means of two modeling approaches: a finite element model and a discrete macro-element model with the use of non-linear analyses. Beconcini et al. in [12] presented a combined test procedure for the experimental characterization of masonry mechanical parameters and the assessment of the shear behavior of masonry walls.

Another example of masonry with load (P) at an angle to the bed joints is visible in arched lintels (Figure 1a), commonly found in historic buildings. The angle of inclination of the pressure line in the support zones depends on its shape and the span-to-bow ratio. It can range from $\theta = 10°$ to $40°$. As compression is applied to the wall at a lower angle of load capacity, stone blocks were sometimes required to be used as supports [18–20]. (Figure 1b).

(**a**)   (**b**)
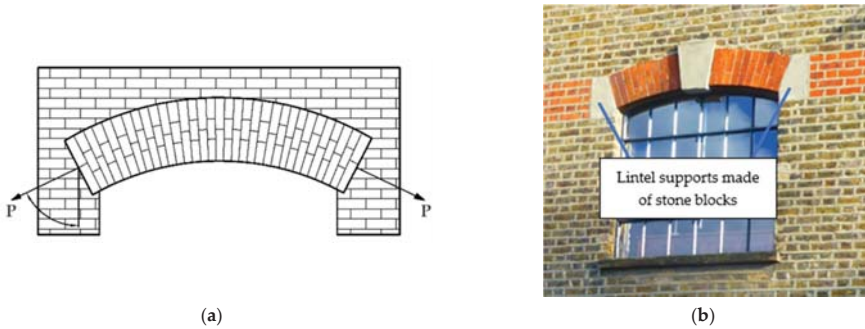
Figure 1. Examples of arched lintels (**a**) diagram with load (P) acting at an angle to the joints; (**b**) image of an arched lintel with stone blocks in support zones.

The supports of masonry vaults also transfer the point load towards the wall at a different angle to the joints. In the case of historical buildings, vault support zones are susceptible to damage and repairs, as they transfer the most stresses (Figure 2).

(**a**)   (**b**)
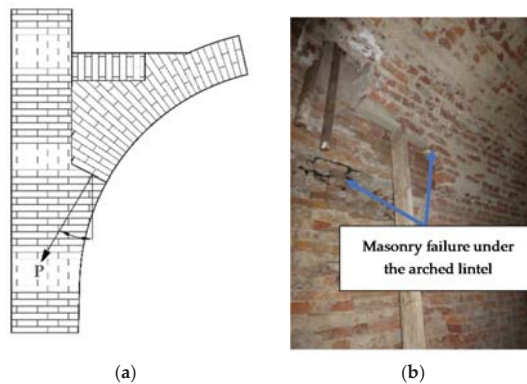
Figure 2. Arched lintels support zones in masonry (**a**) diagram; (**b**) example of failure mechanism.

In most scientific research on design procedures, only the strength perpendicular to the bed joints is usually considered. The anisotropy of the masonry is described as the

ratio of the wall strength at the angle $f_{c,\theta}$ and perpendicular to the bed joints ($f_{c,0}$). The rate depends on the material used, number of hollows, thickness, and type of the joint. The influence of masonry anisotropy is usually neglected and not analyzed. According to [21], with a more precise calibration of the calculation models, a shear test is also performed. Rarely is the strength of the masonry parallel to the bed joints tested, which may be much weaker than perpendicular [22–30]. Tests show that the strength parallel to the bed joints usually differs from the perpendicular strength within the limits $f_{c,90}/f_{c,0}$ = 0.2–1.2. In the study [23] obtained value was $f_{c,90}/f_{c,0}$ = 1.2, however, the models in this direction had a much lower height dimension than in the perpendicular direction—which could have influenced the results.

Even less frequently, the parameters of the wall are tested at different angles. In the studies [31–34], masonry elements were tested on a 1:2 scale for compression and tension at the following angles θ = 0°, 22.5°, 45°, 67.5°, 90° at load in both planes σ_1 and σ_2. For the purpose of that study, the authors used cement and lime mortar with a compressive strength of 5.55 MPa and 15.41 MPa clay bricks. The described research allowed to create calculation criteria for later different FEM (Finite Element Method) models. A different study [19] tested sand plast bricks (calcium silicate form) with a compressive strength of 23.4 MPa and 10.2 MPa cement and lime mortar with joints of approximately 5 mm. The study considered elements of the 1:2 scale in compression and tension at the same angles. The influence of the wall angle on the achieved wall strength, i.e., the degree of anisotropy, was highlighted in that study. In study [35], a failure criterion for biaxially loaded hollow blocks masonry has been researched. 1:1 scale samples of hollow clay blocks were tested, with angles as in previous studies for models with different geometries depending on the size of blocks. Similarly in study [18], but for angles θ = 0°, 15°, 30°, 45°, 60°, 75°, 90°, the tests were carried out on concrete blocks with 20% and 40% hollows, silicate blocks with 20% hollows, and clay blocks with 20% and 40% hollows. This research considered a typical cement–lime mortar. Studies allowed to estimate the degree of anisotropy of masonry for concrete and silicate blocks $f_{c,90}/f_{c,0}$ = 0.71 and for hollow clay blocks $f_{c,90}/f_{c,0}$ = 0.37.

Other structures that work in a state of compressive stress, in a different direction than indicated in the standard [4], are stiffening walls, infilling walls or elements subjected to uneven settlement of the ground. The different direction of the force action results in a complex stress state within the masonry construction, where the main axes are not parallel to the plane of the bed joints. In the case of this type of structure, its damage usually occurs as a result of exceeding its tensile strength. In residential buildings constructed in the last year in Poland, more than 95% of infilling walls were made with masonry technology [36]. Furthermore, 27.5% of the walls were made of clay elements, indicating the essence of the cracking problem that was solved in the presented research.

One of the most common calculation methods for stiffening walls in skeleton buildings is to assume a strut model. In this method, it is assumed that due to the interaction of the reinforced concrete skeleton with the walls, for the purpose of the calculation, compressed equivalent pinned strut masonry elements are being assumed. The elements with width w and length L_d (Figure 3) play the role of stiffeners for the building [37,38]. The width of the element depends on the length of contact between the filling wall and the building skeleton [39–45]. Due to the masonry anisotropy discussed in the article, the actual strength of the wall will change depending on the slope of stress in relation to the plane of the bed joints of the wall. This effect will be particularly visible in walls with a low H/L ratio or in walls made of elements with vertical hollows.

In the analysis of these building elements, it is important to take into account the anisotropy of the strength parameters of the walls in relation to the direction of the compressive forces. As there are not many studies showing the mechanical properties of ceramic walls subjected to angular loads, the authors undertook this task. The novelty state of this study is the determination of the degree of anisotropy, compressive strength, the change of Young's modulus and Poisson's coefficient of 1:1 scale ceramic wall samples made of $25 \times 12 \times 6.5$ cm^3 solid bricks with compressive strength f_b = 44.1 MPa.
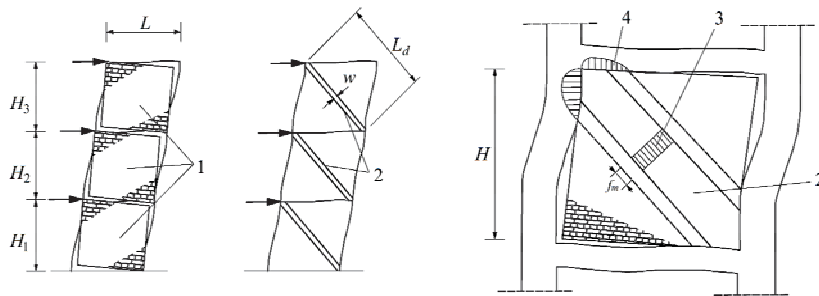
Figure 3. Strut model for the masonry infill wall based on [6] *L, H, H₁, H₂, H₃*—wall geometry, 1—infill wall; 2—equivalent pinned strut; 3—stress distribution in the equivalent pinned strut; 4—contact stresses at corners; *w*—width of the strut; L_d—length of the strut; f_m —compressive strength of the masonry.

2. Materials and Methods

2.1. Materials

The tested samples presented in this research were built using clay brick (FCP, Brest, Republic of Belarus), class 40. These are elements used for bricklaying the stiffening and infilling walls in the authors' countries. The dimensions of the bricks are $25 \times 12 \times 6.5$ cm^3. For the preparation of joints, cement mortar (FCP, Brest, Republic of Belarus) with compressive strength $f_m = 10.9$ MPa has been used. For the preparation of masonry mortars, a factory-made dry mortar mixture was used (FCP, Brest, Republic of Belarus). The thickness of the joint was about 1 cm. To determine the properties of the materials used, initial tests were conducted for bricks and mortar. Tests were performed in accordance with current standards [46–48]. The results are presented in Table 1.

Table 1. Initial material test results.

No.	Load Diagram	Test	Material	Result
A		Compressive strength (EN 772-1 [46])	Brick	$f_b = 44.1$ MPa
B		Young and Poisson	Brick	$E = 11{,}850$ MPa $\nu = 0.11$
C		Flexural strength	Brick	$f = 3.2$ MPa
D		Flexural strength (EN 1015-11 [47])	Mortar	$f = 3.3$ MPa
E		Compressive strength (EN 1015-11 [47])	Mortar	$f_m = 10.9$ MPa
F		Young and Poisson	Mortar	$E = 10{,}580$ MPa $\nu = 0.17$
G		Shear strength (EN 1052-3 [48])	Masonry	$f_{vo} = 0.50$ MPa $tg(\alpha) = 0.5$

2.2. Methods

The main research program was to test 28 wall masonry panels. The specimens were made under laboratory conditions. The preparation of the panels, their curing, testing, and processing of the test results were carried out in accordance with the EN 1052-1 standard [49]. The angle of the bed joint changed: θ = 0°, 22.5°, 45°, 67.5°, 90° (Figures 4 and 5). The samples had standard dimensions of 50 × 50 × 12 cm³, except for those with bed joints parallel to the load direction (θ = 90°) of dimensions 27 × 75 × 12 cm³. The dimensions of the panels were selected in accordance with the RILEM guidelines used in the other discussed works in the field of this research [35,50].
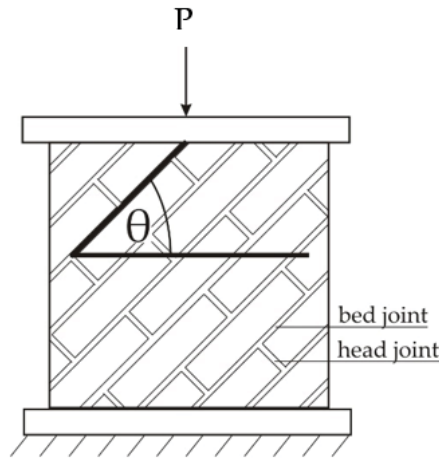
Figure 4. Description of θ angle measurements of tested samples.
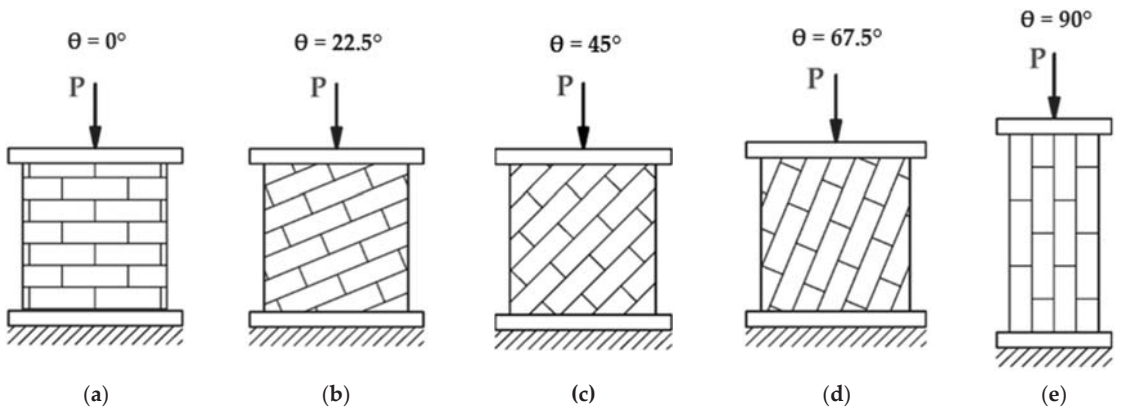
Figure 5. Load application diagram for compressed wall samples at different angles of bed joints (**a**) θ = 0°, (**b**) θ = 22.5°, (**c**) θ = 45°, (**d**) θ = 67.5°, (**e**) θ = 90°.

Five specimens were prepared for each joint angle, except the $\theta = 0°$, where eight specimens were used.

The samples were built on the flat surface of the compressive strength test stand plate on a thin sand bed. Until the test, the elements were stored at a temperature of 20 °C and an air humidity <65%. The tests were carried out 28 days from the date of preparation of the samples.

The models were loaded with a hydraulic actuator (Pneumat P3000, Minsk, Belarus) with a steadily increasing rate on the stand of own production, with the use of a 1250 kN hydraulic press. The samples were loaded with an increase in force equal to 12 kN per minute up to the value at which their collapse occurred. The force was measured with a dynamometer (Pneumat M, Minsk, Belarus). Dial gauges were installed on both surfaces of each sample to measure horizontal and vertical displacements (Figure 6).
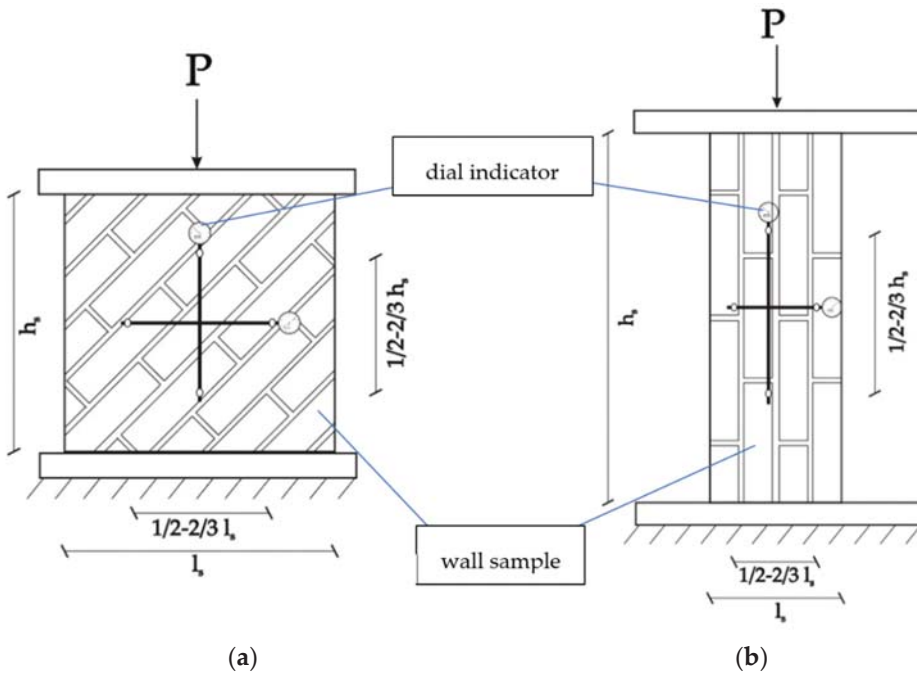
Figure 6. Compressive strength test with dial indicator installation, h_s—height of the sample, l_s—length of the sample (**a**) $\theta = 45°$, (**b**) $\theta = 90°$.

Young's modulus and Poisson's ratio were determined in terms of the elastic work of the samples, in accordance with the requirements of the standard [49].

During the experimental tests, the destruction processes were also recorded with high-resolution cameras.

3. Results and Discussion

3.1. Results of Compressive Strength Tests

The main results obtained during the compressive strength tests are presented in Table 2.

Table 2. Compressive strength testing results of wall samples with different angles of bed joints θ.

Load Angle	Ordinal No	Observed Compressive Strength $f_{c,\,obs}$ (MPa)	Mean Compressive Strength $f_{c,\,mean}$ (MPa)	Coefficient of variation CoV (%)
θ = 0°	A1	16.79	15.1	9.0
	A2	16.94		
	A3	12.16		
	A4	13.98		
	A5	16.14		
	A6	13.18		
	A7	16.39		
	A8	15.08		
θ = 22.5°	B1	6.69	8.0	11.5
	B2	7.78		
	B3	9.27		
	B4	8.12		
	B5	7.99		
θ = 45°	C1	5.72	4.9	13.0
	C2	3.95		
	C3	4.96		
	C4	5.16		
	C5	4.83		
θ = 67.5°	D1	3.78	3.6	18.1
	D2	2.58		
	D3	3.42		
	D4	4.08		
	D5	4.22		
θ = 90°	E1	12.44	11.4	7.4
	E2	10.89		
	E3	10.31		
	E4	11.96		
	E5	11.40		

There are visible changes in the average strength of the masonry with a change in the load angle in relation to the bed joints. The highest compressive strength of 15.1 MPa was obtained for samples loaded in the direction perpendicular to the bed joints ($\theta = 0°$). The lowest results (3.6 MPa) were obtained for the angle $\theta = 67.5°$. The strength of the element was 4.2 times lower than the strength of the model with force acting in the direction perpendicular to the bed joints. Figure 7 presents the changes in the wall strength in relation to the reference model ($\theta = 0°$).
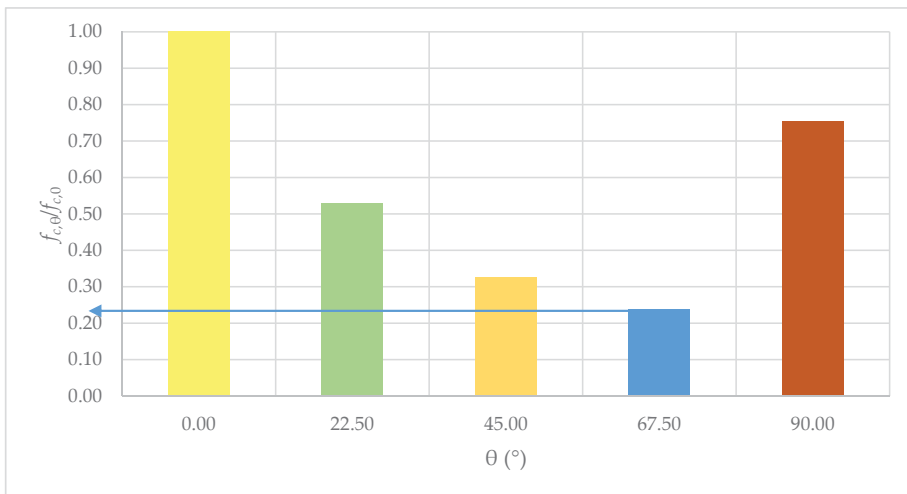
Figure 7. Changes in the compressive strength coefficient $f_{c,\theta}/f_{c,0}$ in relation to the angle of the bed joints angle θ.

As the results obtained show, minimal compressive strength should be expected for the load acting on the samples with the angle of the bed joints $\theta = 57.5°$. Its value is limited to 21% of the compressive strength for the load acting parallel to the bed joints ($\theta = 0°$). For the samples with angle $\theta = 90°$, the compressive strength was limited to 75% of the strength of samples with $\theta = 0°$.

3.2. Results of Deformation, Young's Modulus, and Poisson's Coefficient Tests

3.2.1. Stress–Strain Dependencies

The results of measurements of the dependence of the deformation of the tested samples in the longitudinal and transverse directions to the applied load are shown in Figure 8.

In each of the analyzed cases, the range of compressive strains of the tested samples exceeds the tensile strain values. With the increase in the value of the angle θ of the tested samples, the value of tensile strain (in the direction transverse to the direction of the force) increases. The range of compressive stresses in the area of elastic work of the wall also changes due to the different strength of the tested samples, loaded at different angles θ.
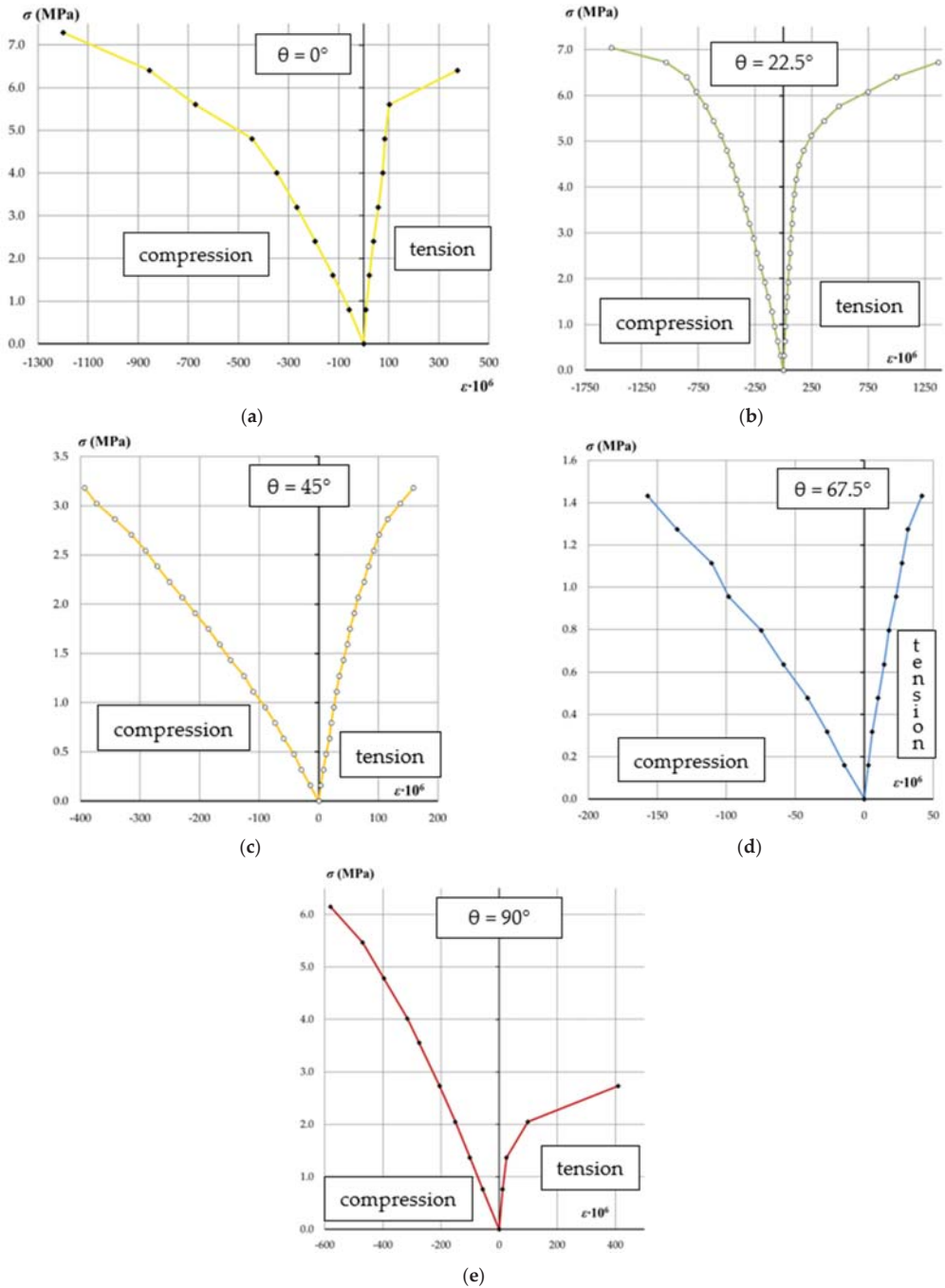
Figure 8. Stress–strain diagrams for compressed wall samples at different joint angles (**a**) θ = 0°, (**b**) θ = 22.5°, (**c**) θ = 45°, (**d**) θ = 67.5°, (**e**) θ = 90°.

3.2.2. Young Modulus Measurements

The results obtained during the Young's modulus measurements are presented in Table 3.

Table 3. Young's modulus test results of wall samples with different angle of bed joints θ.

Load Angle	Ordinal No.	Observed Young's Modulus in Compression	Mean Value of The Young's Modulus	
		$E_{y,obs}$ (MPa)	$E_{y,mean}$ (MPa)	CoV (%)
θ = 0°	A1	9058	11,146	17.81
	A2	8800		
	A3	8750		
	A4	12,605		
	A5	13,330		
	A6	12,719		
	A7	12,759		
	A8	11,144		
θ = 22.5°	B1	8327	9127	15.16
	B2	7982		
	B3	10,954		
	B4	10,272		
	B5	8099		
θ = 45°	C1	7393	8696	11.16
	C2	9240		
	C3	9454		
	C4	7921		
	C5	9470		
θ = 67.5°	D1	10,222	8563	15.77
	D2	9247		
	D3	6685		
	D4	8782		
	D5	7863		
θ = 90°	E1	10,100	9827	2.89
	E2	10,000		
	E3	9380		
	E4	9932		
	E5	9747		

The highest value of the modulus of elasticity (*E* = 11.146 GPa) was obtained for samples loaded perpendicularly to horizontal joints (θ = 0°). The lowest value of *E* = 8.563 GPa was obtained for the samples with angle θ = 67.5°. Figure 9 presents the changes in the Young's modulus of the wall in relation to the reference model (samples θ = 0°) in dependence of the bed joints angle θ.

The lowest value of the coefficient E_θ / E_0 has been obtained for samples with joints rotated at an angle θ = 67.5°.
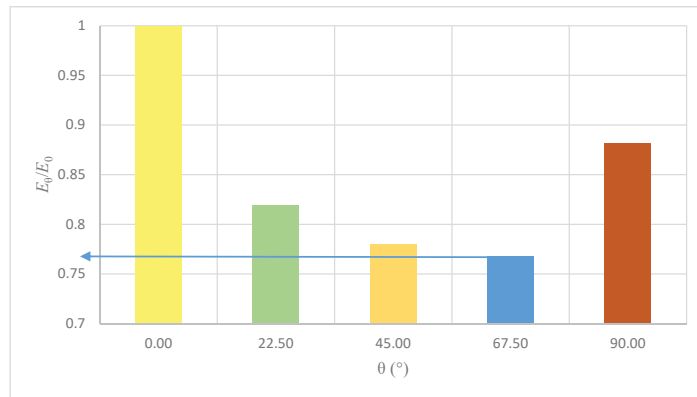
Figure 9. Changes in Young's modulus coefficient E_θ/E_0 in regard to the angle of the head joints angle θ.

3.2.3. Measurements of the Poisson's ratio

The results of the Poisson's coefficient measurements are presented in Table 4.

Table 4. Poisson's ratio testing results of wall samples with different angles of bed joints θ.

Load Angle	Ordinal No.	Observed Poisson's Ratio	Mean Poisson's Ratio	
		$v_{xy,\text{obs}}$	$v_{xy,\text{mean}}$	CoV (%)
θ = 0°	A1	0.16		
	A2	0.17		
	A3	0.14	0.156	7.40
	A4	0.16		
	A5	0.15		
θ = 22.5°	B1	0.16		
	B2	0.15		
	B3	0.25	0.182	23.76
	B4	0.15		
	B5	0.2		
θ = 45°	C1	0.26		
	C2	0.27		
	C3	0.19	0.246	14.82
	C4	0.23		
	C5	0.28		
θ = 67.5°	D1	0.24		
	D2	0.30		
	D3	0.27	0.290	12.19
	D4	0.31		
	D5	0.33		
θ = 90°	E1	0.24		
	E2	0.19		
	E3	0.23	0.220	10.66
	E4	0.24		
	E5	0.20		

The lowest value of the Poisson coefficient $\nu_{xy} = 0.156$ was obtained for samples with a load acting perpendicularly to the bed joints. The highest value $\nu_{xy} = 0.290$ was acquired with the samples rotated with angle $\theta = 22.5°$. Figure 10 presents the graph with an approximate dependence between coefficient ν_θ / ν_0 and the load acting on samples with bed joints rotated with angle θ.
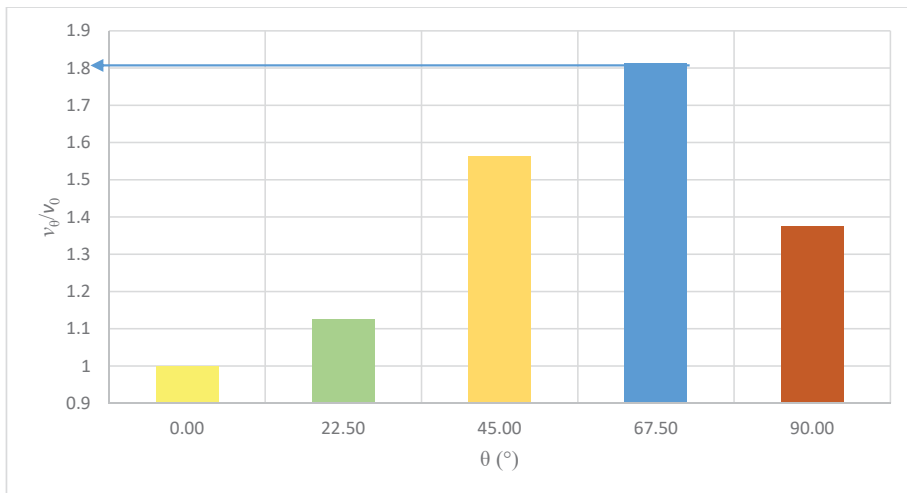
Figure 10. Changes in Poisson's ratio ν_θ / ν_0 in regard to the angle of the bed joints θ.

The maximum value has been obtained with angle $\theta = 67.5°$, with coefficient $\nu_\theta / \nu_0 = 1.81$. Figure 11 presents the representative Poisson's ratio–stress curves of tested wall panels at different angles θ.

The difference in the course of the curves is visible both in the value of the Poisson number after their stabilization from the initial stresses and in the range of their subsequent increases.

For the angle $\theta = 0°$, the course of the curve (after stabilization in the range of the initial stress increase) is characterized by a slight upward trend from $\nu_{xy} = 0.10$ to 0.15 at the end of the measuring range reaching 40–50% of the limit stress. Samples with bed joints turned by the angle $\theta = 22.5°$ are characterized by a parallel course of the dependence ν_{xy}-σ in the range up to 40–60% of the maximum stresses. Then the value of the Poisson number increases with the increase in deformation of the samples in the horizontal direction and the formation of vertical cracks. Along with increasing the value of the angle θ to a value of $67.5°$, the value of the Poisson's ratio increases. For the angle of $\theta = 45°$, it reaches the value of 0.2 with a load equal to 15% of the limit value and 0.25 with 30% of the maximum stress. This increase is related to the formation of the first cracks. As stress increases further, the Poisson ratio also increases. Strain values in the horizontal direction become equal to the vertical direction at stresses equal to half of the limit values. In the case of the tested panels $\theta = 67.5°$, the initial value of the Poisson's ratio is characterized by the highest value among all the tested wall models ($\nu_{xy} = 0.29$) up to the value of 30% of the ultimate stresses. Above 30% of stresses, the value of ν_{xy} increases. In the tested range of deformations, the Poisson's number reaches a value of 0.8 at stresses equal to 40% of the limit value. For $\theta = 90°$, in the range from 5 to 30% of the ultimate stress, the value of ν_{xy} was within the range of 0.22 to 0.25. Above the value of 25–30% of the limit stress, the Poisson number increases, reaching a value of 0.37 at 40% of the limit stress.
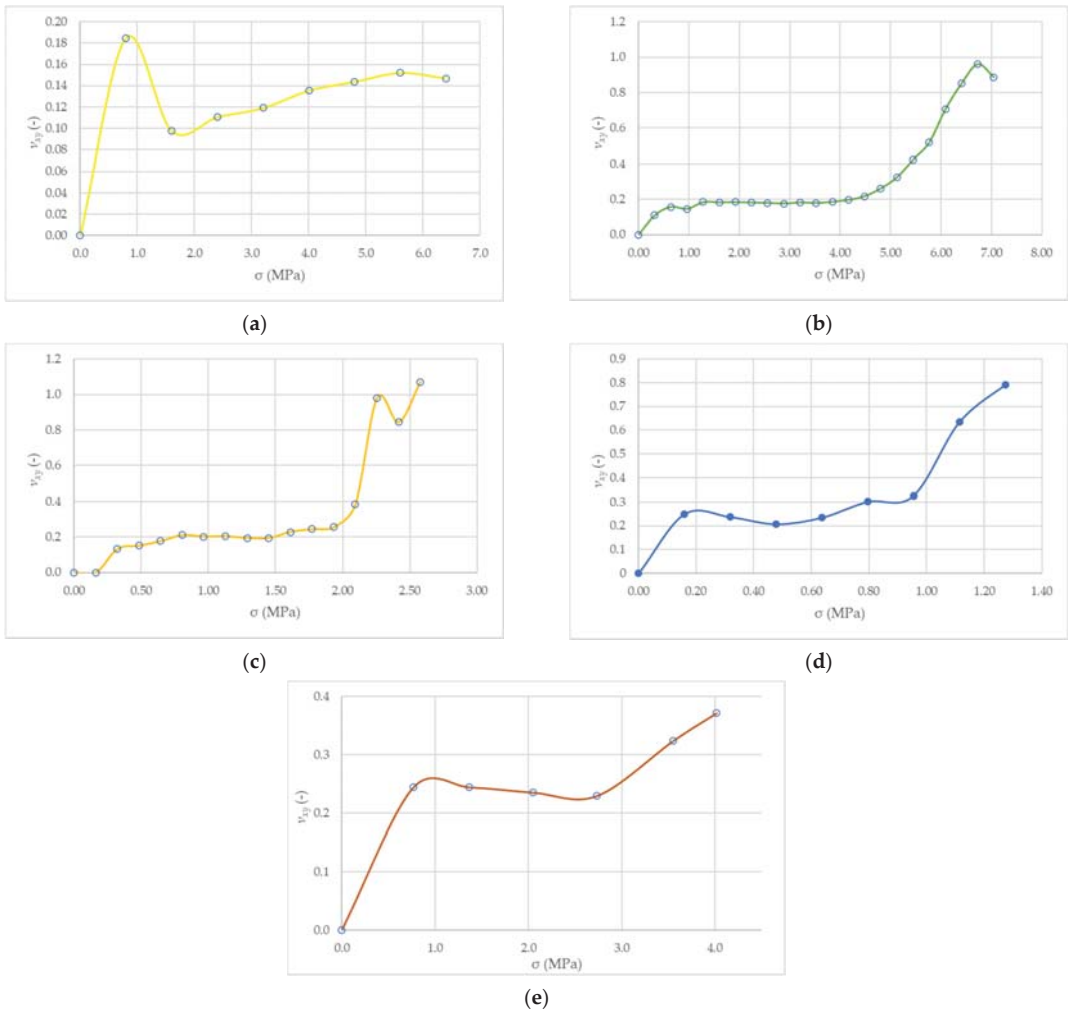
Figure 11. Representative Poisson's ratio–stress curves of tested wall panels at different joint angles (**a**) θ = 0°, (**b**) θ = 22.5°, (**c**) θ = 45°, (**d**) θ = 67.5°, (**e**) θ = 90°.

3.3. Failure Mechanism

The failure mechanism of the specimens depended on the angle of the bed joints θ. In the case of samples with a load acting in the perpendicular direction to the bed joints (θ = 0°), the failure was caused by vertical cracks. The first cracks appeared in the first and last rows of clay elements. At a load varying from 0.7 to 0.8 of the observed strength of the specimens, cracks appeared throughout the height of the specimens. After reaching the maximum stress, the width of the crack increased and local crush zones formed in the lower part of the samples (Figure 12a).
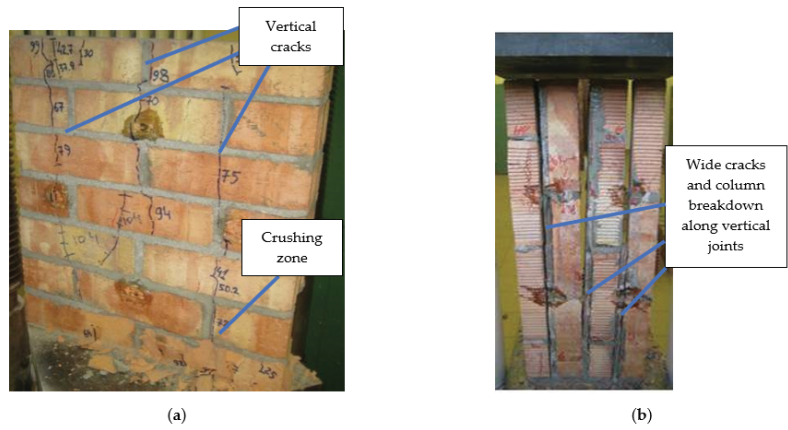
Figure 12. Failure mechanism of wall specimens θ = 0° (**a**) and θ = 90° (**b**).

For the angle θ = 90° (Figure 12b), the adhesion of the mortar and the brick was decisive. The failure occurred by breaking the contact zone between the brick and the mortar, which caused a loss of stability of the element. The first cracks were formed with a load of 10 to 20% of the wall strength. The initial crack length was 100–150 mm and its opening was 0.1 to 0.15 mm. With a load value of 40 to 60% of the breaking limit, the cracks passed through the entire height of the samples, dividing their surface into four columns. After reaching maximum load, there was a sharp increase in the width of all previously formed cracks. The collapse was caused by the loss of stability of the individual columns.

The failure mechanism of the samples loaded at an angle of θ = 22.5° (Figure 13a) was mixed. The main failure is caused by vertical cracks that pass through the bricks and the joins. The first cracks formed at stresses of 40 to 60% of the maximum stress values. After reaching the maximum stresses, the cracks passed through the contact zone of the clay elements and the mortar, and through the brick section. The collapse was accompanied by an increase in the width of the cracks and by crushing fragments of the samples.
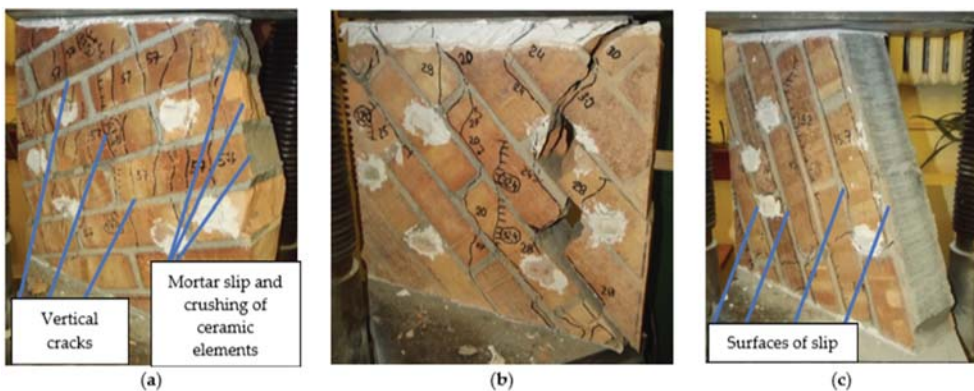
Figure 13. Mechanism of failure of wall specimens θ = 22.5° (**a**), θ = 45° (**b**), and θ = 67.5° (**c**).

For angle θ = 45° (Figure 13b), mortar slip becomes a decisive cause of damage. The first cracks were formed under a load value from 25 to 35% of the observed strength of the wall samples. The initial length of the cracks did not exceed half of the height of the specimen. The width of the crack was 0.15 to 0.20 mm. With the increase in force to

80% of the tested strength, new cracks occurred, passing through the joints and the clay elements of the samples. After reaching maximum stress, the specimens collapsed as a result of cracks that ran through the entire height of the elements and chipping of the wall fragments.

The failure mechanism of the samples loaded at an angle $\theta = 67.5°$ (Figure 13c) mainly on the slip of the mortar in the adhesion plane with the clay elements. The first cracks appeared at loads ranging from 0.3 to 0.5 of the ultimate force. The length of the cracks ranged from 70 to 90% of the height of the specimen, and their width ranged from 0.15 to 0.20 mm. The cracks ran through both the supporting joints and the head joints. After reaching the maximum stress, all samples were damaged due to the sliding of the elements at the point of contact between the mortar and bricks, as shown in Figure 13c.

3.4. General Discussion of the Results

The results obtained were compared with the earlier studies on brick walls quoted in the review of the literature. The studies presented in the articles [18,31–34] do not provide results of load capacity that could be used as a comparison. Previous research of different types of clay bricks, hollowed, biaxially loaded walls [35] has shown different dependencies of strength anisotropy. This comparison is presented in Figure 14.
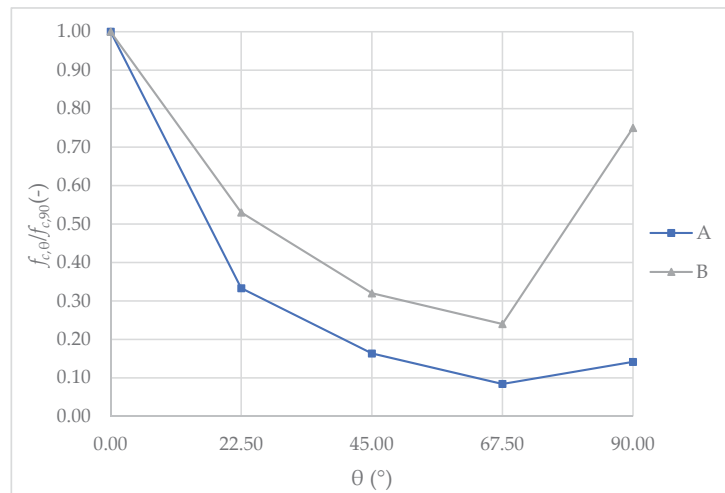
Figure 14. Changes in relative compressive strength $f_{c,\theta}/f_{c,0}$ in regard to angle θ of A— hollow clay blocks in biaxial compression based on [35], B—walls of tested clay bricks.

In the range of $\theta = 0°$ to $67.5°$, the course of the dependency curve for both types of ceramic walls shows some similarities. Coefficient $f_{c,67.5}/f_{c,0}$ (for $\theta = 67.5°$) reached a value of 8% for the biaxially compressed, hollowed blocks walls, and 24% for those tested in this research, uniaxially compressed brick walls. The load-bearing capacity for $\theta = 90°$ of the walls of clay blocks with hollows, in biaxial compression state of compression ($f_{c,90}/f_{c,0} = 14\%$) [35] is much lower than the research for uniaxially loaded brick walls ($f_{c,90}/f_{c,0} = 75\%$).

A comparison made between this study and studies [19,35] indicated that the most unfavorable loading angle is between $\theta = 45°–67.5°$. The decrease in stiffness is also the highest in this direction, based on the research presented in this study.

The designed load-bearing capacity of masonry walls loaded at an angle to the bed joints should be significantly reduced. For estimating the strength of brick walls with differentiated load orientation, presented test results can be used. In the tests presented

in this article, the reduction in strength in extreme cases of rotation was up to 24% of the initial value.

FEM structure modeling is often used for structural analysis of historic masonry buildings. The detailed micro-modeling or simplified micro-modeling is time consuming and requires a lot of calibration data from the existing structure. Very often, such detailed data are difficult or impossible to collect. To simplify these problems, masonry can be calculated as a homogenous composite with macro-modeling technics [11]. Experimental data provided by us could help to implement the change of stiffness of the model and the change of load-bearing capacity in the case of stresses trajectory direction towards the bed joints.

Future research should focus on the analysis of the degree of anisotropy of the masonry of the different types of wall elements. It is important to continue these types of analyses for a wider group of materials. Analyses that allow for the approximation of mechanical properties of the walls loaded in different directions in their surface plane allow, for example, for the proper calculation of the strength of the infilling walls interacting with building structures.

4. Conclusions

The study determined the degree of anisotropy for masonry samples made of solid bricks and cement mortar. The models were made on a 1:1 scale. Based on the research presented, the following conclusions were drawn.

- The mechanical properties of the clay brick walls significantly depend on the angle of the compressive force.
- On the basis of the performed tests, the dependencies allowed for the calculation of the mechanical properties for the designed brick walls operating in a uniaxial state of compressive loads were determined.
- The results obtained, together with the results of other studies, allowed a better understand of the problem regarding the degree of anisotropy in the masonry. The results allowed assessing the significance of strength loss for cases with the load applied at an angle to the bed joints.
- A minimal compressive strength has been obtained for the load acting at an angle $\theta = 67.5°$. Its value is limited to 24% of the compressive strength for the load acting parallel to the bed joints ($\theta = 0°$).
- The lowest modulus of elasticity was researched on the walls with the bed joint angle of $\theta = 67.5°$. Its value was evaluated as 77% of the initial value (measured for samples $\theta = 0°$).
- The maximum of the Poisson's ratio was obtained with angle $\theta = 67.5°$, with coefficient $\nu_\theta / \nu_0 = 181\%$.
- The conducted tests allowed identifying and describing the failure mechanism of the tested wall panels.

References

1. Bajno, D.; Bednarz, L.; Matkowski, Z.; Raszczuk, K. Monitoring of Thermal and Moisture Processes in Various Types of External Historical Walls. *Materials* **2020**, *13*, 505. [CrossRef] [PubMed]
2. Liritzis, I.; Al-Otaibi, F.; Kilikoglou, V.; Perdikatsis, V.; Polychroniadou, E.; Drivaliari, A. Mortar analysis of wall painting at Amfissa Cathedral for conservation-restoration purposes. *Mediterr. Archaeol. Archaeom.* **2015**, *3*, 301–311. [CrossRef]
3. Michalopoulou, A.; Maravelaki, N.P.; Stefanis, N.A.; Theoulakis, P.; Andreou, S.; Kilikoglou, V.; Karatasios, I. Evaluation of nanolime dispersions for the protection of archeological clay-based building materials. *Mediterr. Archaeol. Archaeom.* **2020**, *3*, 221–242. [CrossRef]
4. *PN-EN 1996-1-1+A1 Eurocode 6—Design of Masonry Structures—Part 1-1: General Rules for Reinforced and Unreinforced Masonry Structures*; European Committee for Standardization: Brussels, Belgium, 2013.
5. Małyszko, L.; Jemioło, S.; Bilko, P.; Gajewski, M. *FEM and Constitutive Modelling in Failure Analysis of Masonry Structures. Implementation and Examples*; University of Warmia and Mazury: Olsztyn, Poland, 2015.
6. Małyszko, L.; Orłowicz, R. *Konstrukcje Murowe. Zarysowania i Naprawy. (Structural Masonry. Cracks and Repairs)*; University of Warmia and Mazury: Olsztyn, Poland, 2000.
7. Jemioło, S.; Małyszko, L. *MES i Modelowanie Konstytutywne w Analizie Zniszczenia Konstrukcji Murowych. Tom 1. Podstawy Teoretyczne*; University of Warmia and Mazury: Olsztyn, Poland, 2013.
8. Abdelmoneim Elamin Mohamad, A.-B.; Chen, Z. Experimental and Numerical Analysis of the Compressive and Shear Behavior for a New Type of Self-Insulating Concrete Masonry System. *Appl. Sci.* **2016**, *6*, 245. [CrossRef]
9. Lin, K.; Totoev, Y.Z.; Liu, H.; Wei, C. Experimental Characteristics of Dry Stack Masonry under Compression and Shear Loading. *Materials* **2015**, *8*, 8731–8744. [CrossRef]
10. Jasiński, R.; Drobiec, Ł.; Mazur, W. Validation of Selected Non-Destructive Methods for Determining the Compressive Strength of Masonry Units Made of Autoclaved Aerated Concrete. *Materials* **2019**, *12*, 389. [CrossRef] [PubMed]
11. Lourenco, P.B. Computations on historic masonry structures. *Prog. Struct. Eng. Mater.* **2002**, *4*, 301–319. [CrossRef]
12. Beconcini, M.L.; Croce, P.; Formichi, P.; Landi, F.; Puccini, B. Experimental Evaluation of Shear Behavior of Stone Masonry Wall. *Materials* **2021**, *14*, 2313. [CrossRef] [PubMed]
13. Malomo, D.; DeJong, M.J. A Macro-Distinct Element Model (M-DEM) for out-of-plane analysis of unreinforced masonry structures. *Eng. Struct. June* **2021**, *244*, 112754. [CrossRef]
14. Lourenço, P.B.; Rots, J.G.; Blaauwendraad, J. Continuum model for masonry: Parameter estimation and validation. *J. Struct. Eng.* **1998**, *124*, 642–652. [CrossRef]
15. Celano, T.; Argiento, L.U.; Ceroni, F.; Casapulla, C. In-Plane Behaviour of Masonry Walls: Numerical Analysis and Design Formulations. *Materials* **2021**, *14*, 5780. [CrossRef]
16. Croce, P.; Beconcini, M.L.; Formichi, P.; Landi, F.; Puccini, B.; Zotti, V. Bayesian Methodology for Probabilistic Description of Mechanical Parameters of Masonry Walls. *ASCE-ASME J. Risk Uncertain. Eng. Syst. Part A Civ. Eng.* **2021**, *7*, 04021008. [CrossRef]
17. Zhang, S.; Mohadeseh, S.; Mousavi, T.; Richart, N.; Molinari, J.F.; Beyer, K. Micro-mechanical finite element modeling of diagonal compression test for historical stone masonry structure. *Int. J. Solids Struct.* **2017**, *112*, 122–132. [CrossRef]
18. Mojsilović, N. A Discussion of Masonry Characteristics Derived from Compression Tests. In Proceedings of the 10TH Canadian Masonry Symposium, Banff, AB, Canada, 8–12 June 2005.
19. Senthivel, R.; Sinha, S.N.; Madan, A. Influence of bed joint orientation on the stress-strain characteristics of sand plast brick masonry under uniaxial compression and tension. In Proceedings of the 12TH International Brick/Block Masonry Conference, New Delhi, India, 25–28 June 2000.
20. Jasiński, R. Research on the Influence of Bed Joint Reinforcement on Strength and Deformability of Masonry Shear Walls. *Materials* **2019**, *12*, 2543. [CrossRef]
21. *ASTM E72 1989 Standard Tests for Conducting Strength Tests on Panels for Building Construction*; American Society for Testing and Materials: West Conshohocken, PA, USA, 1989.
22. Małyszko, L. *Modelowanie Zniszczenia w Konstrukcjach Murowych z Uwzględnieniem Anizotropii*; Uniwersytet Warmińsko-Mazurski: Olsztyn, Poland, 2005; p. 157.
23. Jasiński, R. *Nośność I Odkształcalność Zbrojonych Ścian Murowych Ścinanych Poziomo (Strenght and Deformability of Reinforced Clay Brick Masonry Horyzonatally Sheared)*; Silesian University of Technology: Gliwice, Poland, 2005.
24. Drobiec, Ł.; Kubica, J.; Piekarczyk, A. Some Remarks on Poisson's Ratio of Unreinforced Clay Brick Masonry. In *Proceedings of the 77th International Scientific Conference*; BMO: Brno, The Czech Republic, 1999; Volume 7.2, pp. 113–116.
25. Capozucca, R. Masonry Panels with Different Mortar Joints under Compression. In Proceedings of the 13th International Brick and Block Masonry Conference, Amsterdam, The Netherlands, 4–7 July 2004.
26. Hoffmann, G.; Schubert, P. Compresslve strength of masonry parallel to the bed joints. In Proceedings of the 10th IB2MaC, Calgary, AB, Canada, 5–7 July 1994.
27. Sentler, L. Tests of Swedish Masonry. *Mason. Int.* **1996**, *10*, 49–54.

28. Drobiec, Ł.; Piekarczyk, A.; Kubica, J. AAC Bocks Masonry Compressed Perpendicular and Parallel to the Bed Joints. In Proceedings of the 12th International Brick/Block Masonry Conference, New Delhi, India, 25–28 June 2000.
29. Bednarz, Ł.; Drygała, I.; Dulińska, J.; Jasieńko, J. Study of Materials Behavior in a Monumental Vault Strengthened by a Carbon Net in a Mineral Matrix Subjected to Seismic Influence. *Appl. Sci.* **2021**, *11*, 1015. [CrossRef]
30. Jasienko, J.; Raszczuk, K.; Frąckiewicz, P.; Kleszcz, K.; Bednarz, Ł. Strengthening of masonry rings with composite materials. *Herit. Sci.* **2021**, *9*, 11. [CrossRef]
31. Page, A. The biaxial compressive strength of brick masonry. *ICE Proc.* **1981**, *71*, 893–906. [CrossRef]
32. Dhanasekar, M.; Kleeman, P.; Page, A. Biaxial Stress-strain Relations for Brick Masonry. *J. Struct. Eng. ASCE J. Struct. Eng. ASCE* **1985**, *111*, 1085–1100. [CrossRef]
33. Dhanasekar, M.; Kleeman, P.W.; Page, A.W. The failure of brick masonry under biaxial stresses. *ICE Proc.* **1985**, *79*, 295–313. [CrossRef]
34. Page, A. The strength of brick masonry under biaxial compression-tension. *Int. J. Mason. Constr.* **1983**, *3*, 26–31.
35. Guggisberg, R.; Thürlimann, B. *Versuche zur Festlegung der Rechenwerte von Mauerwerksfestigkeiten*; Birkhäuser: Basel, Switzerland, 1988. [CrossRef]
36. Kania, T.; Derkach, V.; Nowak, R. Testing Crack Resistance of Non-Load-Bearing Ceramic Walls with Door Openings. *Materials* **2021**, *14*, 1379. [CrossRef] [PubMed]
37. Drysdale, R.; Hamid, A.; Baker, L. *Masonry Structures: Behavior and Design*; The Masonry Society; Prentice Hall: Englewood Cliffs, NJ, USA, 1999.
38. Radosław, J. *Badania i Modelowanie Murowych Ścian Usztywniających. Research and Modeling of Masonry Shear Walls*; Silesian University of Technology: Gliwice, Poland, 2017.
39. Hendry, A.W.; Sinha, B.P.; Davies, S.R. *Design of Masonry Structures*; E & FN Spon: London, UK, 2004.
40. Ng'Andu, B.M. *Bracing Steel Frames with Calcium Silicate Element Walls*; Technische Universiteit Eindhoven: Eindhoven, The Netherlands, 2006.
41. *ASTM E519/E519M-21, Standard Test Method for Diagonal Tension (Shear) in Masonry Assemblages*; ASTM International: West Conshohocken, PA, USA, 2021.
42. Ali, A.A.A.; Jony, H.H. Shear Wall Analysis Using Framework Method: Comparison with Shell Element Method and Column Analogy. *Eng. Technol. J.* **2013**, *31*, 1949–1961.
43. Roca, P. Assessment of masonry shear-walls by simple equilibrium models. *Constr. Build. Mater.* **2006**, *20*, 229–238. [CrossRef]
44. Roca, P.; Viviescas, Á.; Lobato, M.; Gomez, C.; Serra, I. Capacity of Shear Walls by Simple Equilibrium Models. *Int. J. Archit. Herit.* **2011**, *5*, 412–435. [CrossRef]
45. Kok Choon, V. *Bracing Capacity of Partially Grounted Concrete Masonry Walls with Openings*; Department of Civil and Enviromental Engineering, The University of Auckland: Auckland, New Zeland, 2006.
46. *En 772-1+a1 Methods of Test for Masonry Units. Determination of Compressive Strength*; European Committee for Standardization: Brussels, Belgium, 2015.
47. *EN 1015-11 Methods of Test for Mortar for Masonry. Determination of Flexural and Compressive Strength of Hardened Mortar*; European Committee for Standardization: Brussels, Belgium, 2020.
48. *EN 1052-3 Methods of Test for Masonry. Determination of Initial Shear Strength*; European Committee for Standardization: Brussels, Belgium, 2002.
49. *EN 1052-1 Methods of Test for Masonry. Determination of Compressive Strength*; European Committee for Standardization: Brussels, Belgium, 1998.
50. RILEM TC 76-LUM General recommendations for methods of testing load-bearing masonry. *RILEM Publ. SARL* **1988**, *21*, 123.

Article

Estimating Mechanical Properties of Wood in Existing Structures—Selected Aspects

Tomasz Nowak *, Filip Patalas and Anna Karolak

Faculty of Civil Engineering, Wroclaw University of Science and Technology, Wybrzeze Wyspianskiego 27, 50-370 Wroclaw, Poland; filippatalas@wp.pl (F.P.); anna.karolak@pwr.edu.pl (A.K.)
* Correspondence: tomasz.nowak@pwr.edu.pl; Tel.: +48-71-320-22-63

Abstract: The paper presents and discusses selected methods of wood classification and the evaluation of its mechanical properties. Attention was mainly paid to methods that may be particularly useful for examining existing elements and structures. The possibility of estimating the modulus of rupture—MOR and modulus of elasticity—MOE based on the non- destructive (NDT), semi-destructive (SDT), and destructive tests (DT) were considered. Known international, European, and American standards and research approaches were indicated. The selected testing methods and their interpretation were presented. These were, among others, the method of visual assessment, the resistance drilling method, methods of determining the dynamic modulus of elasticity, and procedures for testing small clear specimens. Moreover, some of our own research results from the conducted experimental tests were presented and discussed. In the destructive tests, both large elements and small clear specimens were examined. The results obtained from individual methods were compared and some conclusions were presented. The summary discusses the fundamental difficulties and limitations in applying the presented procedures and interpretations.

Keywords: timber structures; estimating mechanical parameters; small clear specimens; non-destructive tests; semi-destructive tests; resistance drilling; ultrasonic wave; stress wave; visual grading

1. Introduction

Wood is one of the oldest building materials in the world. Its widespread availability and good mechanical parameters have contributed to its wide application in civil engineering. The continued popularity of timber structures is also due to the growing interest in the use of organic materials in architecture [1].

Wood is a natural, nonhomogeneous, and anisotropic material of complex structure. Formulating a constitutive model of wood is very difficult [2]. Its mechanical parameters are influenced by many factors, among others, wood species and latewood to earlywood ratio. Moreover, in structural elements made of construction timber, the strength of the material is limited by many additional factors, such as knots (size and position), slope of grain, cracks, element size, and moisture content [3–5]. The precise determination of mechanical material parameters, especially in existing constructions, is a significant issue from the point of view of structural analysis. However, it is not always easy and leaves a wide freedom of interpretation. Moreover, in the case of existing structures in use, it is usually not possible to obtain much material for testing. When rebuilding, strengthening, and repairing existing structures, designers very often have the problem of assuming the proper properties and appropriate class of wood. Opposite to concrete and steel structures, where the methods of material testing are well recognized, in timber structures this problem is not clearly explained.

Researchers often use non-destructive testing (NDT) (i.e., [2,6–10]) or semi-destructive testing (SDT) (i.e., [11–14]). These methods do not affect the properties of the tested samples. They allow for the estimation of wood parameters without reducing the value of the tested element. In addition, a great advantage is the mobility of the used research equipment,

allowing for in-situ tests when it is not possible to collect a material sample for research in a laboratory, which may be a common problem when existing and historic objects are considered [14]. Non-destructive methods also enable the detection of internal damage or material defects that may be difficult to detect with, for example, visual assessment [15]. To obtain detailed data on the physical and mechanical parameters of wood, the best method would be the use of non-destructive and destructive testing [2]. Combining the results from both methods can provide a comprehensive range of data useful for the further analysis of structural elements or entire building structures.

The aim of this article is to present selected methods of wood strength classification, which are particularly suitable for the evaluation of material in existing and historic structures.

2. Selected Methods for Estimation Wood Structural Properties

2.1. Selected Standard Procedures and Tests

There are many standards describing the procedures for in situ testing of existing and historic timber structures, including international ISO 13822 [16], European PN-EN 17121 [17], Italian UNI 11119 [18], UNI 11138 [19], and Swiss SIA 269/5 [20]. Publications of the International Council on Monuments and Sites (ICOMOS) are also widely recognized. Usually, the above standards describe the use of, non-destructive and semi-destructive methods to assess wood [14,21]. The most commonly used testing methods of NDT and SDT are presented in the diagram in Figure 1.

NON-DESTRUCTIVE METHODS

SEMI-DESTRUCTIVE METHODS
resistance drilling
core-drilling
screw withdrawal
hardness tests
needle penetration
pin pushing

ORGANOLEPTIC METHODS
visual evaluation
acoustic evaluation
fragrance evaluation

ACOUSTIC METHODS
stress waves
ultrasonic technique
acoustic emission

RADIOGRAHPIC METHODS
X-rays
gamma rays
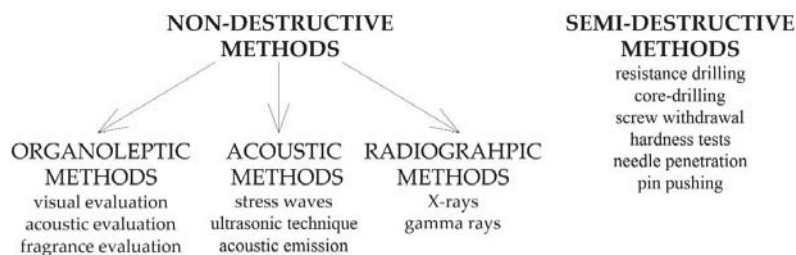
Figure 1. Non-destructive and semi-destructive testing methods.

The aim of the research on existing structures is to obtain the most extensive and comprehensive understanding of the material structure. The applied methods give selective results and a reliable inference about the mechanical properties of the tested wood, which is possible only when many methods are combined. The literature [9–11,22] presents numerous examples of wood testing using the NDT and SDT methods. In addition to commonly known methods, new ones, such as air-coupled ultrasound, are also being developed [23]. The authors most often search for the correlation of NDT test results with the results of destructive tests for strength parameters. Unfortunately, publications do not always provide clear results. In the research based on acoustic methods, the correlation between MOE_{dyn} and the physical and mechanical properties of wood is sought. The analyzes (i.e., in [24,25]) most often present a strong correlation ($R^2 \approx 0.9$) between the dynamic modulus of elasticity (MOE_{dyn}) obtained from acoustic methods (NDT) and the static modulus of elasticity (MOE_{stat}) from destructive tests (DT). Some examples of resistance drilling tests are presented in [26]. Among the cited studies, a correlation was found between the resistance measure (RM) obtained from the resistance drilling device and density, the modulus of elasticity parallel and perpendicular to the grain, and compressive strength. The coefficients of determination R^2 were within the range: RM-density $R^2 = 0.004$–0.88, RM-MOE parallel to grain $R^2 = 0.14$–0.60, RM-MOE perpendicular to grain $R^2 = 0.01$–0.61, RM-compressive strength parallel to grain $R^2 = 0.52$–0.64, RM-compressive strength perpendicular to grain $R^2 = 0.05$–0.78. It is usually possible to collect a small amount of material from the existing structures, which can be sufficient to perform the test

on small specimens as well [27]. Apart from the currently recommended tests performed on full-size elements in accordance with the applicable European standards [28,29], the literature presents numerous MOR and MOE determinations conducted on small clear specimens in accordance with the national and international standards [30–36]. Attempts to determine the dependence of the influence of the size of the specimens used in the research on the obtained parameter values are also made (i.e., [37–43]). The analyses concern the wood of trees of various exotic species (e.g., [42,43]), but also species commonly used in construction objects on the European continent, such as spruce (*Picea* sp.), pine (*Pinus* sp.) and fir (*Abies* sp.) [39]. However, the difference between the tests conducted on small specimens and the tests on structural timber should be emphasized. In the first case, the parameters of the idealized material, and in the second case, the actual building material in elements on a technical scale, are determined. Among the numerous factors affecting the mechanical parameters of wood, such factors as: different species, age of the tree from which the wood was obtained, tree growth rate, density, and local imperfections or singularities, such as cracks, knots, slope of grain, fiber deviations, depth, length etc. can be listed. The indicated material imperfections must be considered when determining the mechanical properties of wood on a technical scale on the basis of small clear specimens.

In the further part of this paper, the authors present methods of estimating the strength properties of wood based on selected methods of NDT, SDT, DT, and the method of testing small clear specimens and establishing structural properties in accordance with the American standard ASTM D245 [44].

2.2. Mechanical Properties Assessment Based on Visual Grading

According to the standard PN-EN 17121 [17] it is recommended that the visual assessment of wood should be based on the identification of factors that reduce its strength indicated in the standard EN-14081-1 Annex A [45]. The characteristics indicated in the standard [17], that reduce strength and can be examined in detail on site, in a non-destructive way, are knots, fiber deviation, and shrinkage gaps. It is recommended that the influence of gaps and knots be carefully assessed considering the type of structural element. Due to the great variety of rules of visual grading used in different countries, the standard [45] does not indicate a clear set of acceptable rules, only the basic criteria. Detailed descriptions of the measurement methods, classification criteria, and strength classes used should be defined at the national level. Wood can be assigned to a specific class only when all growth characteristics and properties that reduce strength are within the limits required by the class. The visual grading should be performed by qualified and experienced specialists in the field of timber structures. The rules of the visual assessment procedure may be adjusted by a specialist, provided that they are indicated in the report. According to the standard [17], the classification of existing structural elements into strength classes based on EN 338 [46] probably results in a conservative assessment. The standard [17] provides general principles for assessing existing elements. The quality class of visually graded timber is determined based on the grain, density, and species, dimensions and degree of severity of wood defects that can be seen with the unaided eye. These factors determine the strength properties of structural timber. The quality of the piece of structural timber is determined at the point of the maximum intensity of the wood defects. Depending on the quality of the wood and the quality of wood processing, according to the standard PN-D-94021 [47] the structural timber in Poland is divided into the following quality classes: KW–choice class, KS–medium quality class, KG–lower quality class. The classification is presented in Table 1.

Table 1. The criteria for the visual grading of wood according to the PN-D-94021 [47,48].

The Classification Basis		KW (Choice Class)	KS (Middle Quality Class)		KG (Lower Quality Class)	
			Variant 1	Variant 2	Variant 1	Variant 2
Knots, regardless of quality, expressed as a knotting index USM		$\leq 1/4$	$\leq 1/4$	$\leq 1/2$	$\leq 1/2$	$> 1/2$
Over the entire cross-section of timber USC		$\leq 1/4$	$\leq 1/3$	$\leq 1/4$	$\leq 1/2$	$\leq 1/3$
Slope of grain (diagonal grain path)		$\leq 7\%$ (1:14)	$\leq 10\%$ (1:10)		$\leq 16\%$ (1:6)	
Cracks, resin pockets, bark pockets and catfaces	Deep, not crossing to the face, sides and opposite plane (not including defects less than 300 mm in length)	Permissible, length up to $\frac{1}{4}$ of the piece length and not longer than 600 mm	Permissible, length up to $\frac{1}{4}$ of the piece length and not longer than 600 mm		Permissible, length up to $\frac{1}{4}$ of the piece length and not longer than 900 mm	
	Frontal non-crossing, crossing and circular	Depth up to 1/3 of the piece thickness	Depth up to 1/2 of the piece thickness		Depth up to 2/3 of the piece thickness	
Decay		Impermissible	Impermissible		Impermissible	
Insect damage		Impermissible	Impermissible		Impermissible	
Sapstain		Permissible	Permissible		Permissible	
Reaction wood (compression wood)		Permissible up to 1/5 of the girth	Permissible up to 2/5 of the girth		Permissible up to 3/5 of the girth	
Growth ring index		≤ 4 mm	≤ 6 mm		≤ 10 mm	
Minimum density of timber at a moisture content of 20%		≥ 450 kg/m^3	≥ 420 kg/m^3		≥ 400 kg/m^3	
Wane is permitted along the entire length of two edges of one plane or on side, occupying a total of		Up to $\frac{1}{4}$ thickness and $\frac{1}{4}$ width of timber piece	Up to $\frac{1}{4}$ thickness and $\frac{1}{4}$ width of timber piece		(a) at a distance of up to 300 mm from faces up to 1/3 of the thickness and 1/3 of the piece width (b) at a distance of more than 300 mm from faces up to 1/2 of the thickness and 1/3 of the piece width	
Bow-longitudinal curvature of planes		≤ 10 mm	≤ 10 mm		≤ 20 mm	
Spring-longitudinal curvature of the sides		≤ 8 mm	≤ 8 mm		≤ 12 mm	
Twist in relation up to width		≤ 1 mm/25 mm	≤ 1 mm/25 mm		≤ 2 mm/25 mm	
Cup-cross curvature to width		≤ 1 mm/25 mm	≤ 1 mm/25 mm		≤ 2 mm/25 mm	
Cracks, kerf waviness		Permissible within the thickness and width deviations specified for basic dimensions				
Parallelism of planes and sides		Planes should be parallel to each other; sides of edged timber should be perpendicular to planes; deviations from parallelism should be within the limits of acceptable thickness and width deviations specified for the basic dimensions				
Non-perpendicularity of faces		Faces should be perpendicular to planes and sides; deviations from perpendicularity should be within the permissible deviations in timber length				

The classification of wood strength class can be done on the basis of PN EN 1995-1-1-NA.8.5 (Polish National Annex) [49] (Table 2). The strength class is determined directly by the relationship between the sorting class defined according to PN-D-94021 [47] and the strength class according to PN-EN 338 [46].

Table 2. The relationship between grading classes (PN-D-94021) [47] of domestic structural timber and grading strength classes C (PN-EN 338) [46].

Tree Species	Thickness	KW (Choice Class)	KS (Middle Quality Class)	KG (Lower Quality Class)
Scots pine (*Pinus sylvestris*)	≥ 22 mm	C35	C24	C20
European spruce (*Picea abies*)		C30	C24	C18
European silver fir (*Abies alba*)		C22	C18	C14
European larch (*Larix decidua*)		C35	C30	C24

An alternative methodology for visual assessment is presented in the American standard ASTM D245 [44]. This standard refers directly to the results of testing small clear specimens. The influence of individual factors reducing the mechanical properties is clearly included as reducing coefficients. The standard [44] is discussed in more detail in Section 2.5, where the procedure for testing small clear specimens was presented.

2.3. Mechanical Properties Assessment Based on the Determination of the Dynamic Modulus of Elasticity

The dynamic modulus of elasticity of wood can be determined by various methods. Two of them are used most often: the beam vibration measurement method—the mechanical method used in strength sorting machines and the acoustic method—the stress wave or the ultrasonic wave velocity measurement.

The basic parameter required to determine the velocity of the wave propagation (v) is defined as follows:

$$v = L/T \tag{1}$$

Or

$$v = \lambda \cdot f \tag{2}$$

where L is the distance (between two measuring points) covered by the wave; T is the time needed to cover this distance; λ is the length of the wave; and f is the frequency of the wave.

Knowing the wave propagation velocity (v) and the density of the wood (ρ), it is possible to determine the dynamic modulus of elasticity (MOE_{dyn}), that can be related to the static modulus of elasticity (MOE_{stat}) [50]. The dynamic modulus of elasticity can be calculated using the following formula:

$$MOE_{dyn} = v^2 \cdot \rho \tag{3}$$

where v is the velocity of the acoustic wave and ρ is the density of the wood.

In the case of the beam vibration measurement method, the density of the tested structural timber is determined and then, by hitting the beam front, it is brought into free vibration. Measuring instruments record vibrations by determining their frequency. On the basis of the determined first harmonic information about the length of the element and the density of the wood, the dynamic modulus of elasticity (average for the element) is determined. The selected machines operating in accordance with this method are: Grade Master, Dynagrade, Mobile Timber Grader, and Visca [50].

In the case of the acoustic methods (stress wave or ultrasonic wave), devices such as the Fakopp Microsecond Timer (Fakopp Enterprise Bt., Agfalva, Hungary) or the Sylvatest (Swiss company CBS-CBT, Saint-Sulpice, Switzerland) are used. Testing with the Fakopp MS device (Fakopp Enterprise Bt., Agfalva, Hungary) (Figure 2b,c) requires the initiation of the wave with a single hit to the head with a hammer intended for this purpose. The device transmitting probes are placed in the sample, without the need to drill holes. The device measures the time of wave propagation between two transmitters. There is also a second way to measure the speed of the wave–with one transmitting probe (echo). The reflected signal is then recorded. This method significantly increases the scope of application of this method—also to elements where the access is only from one side.
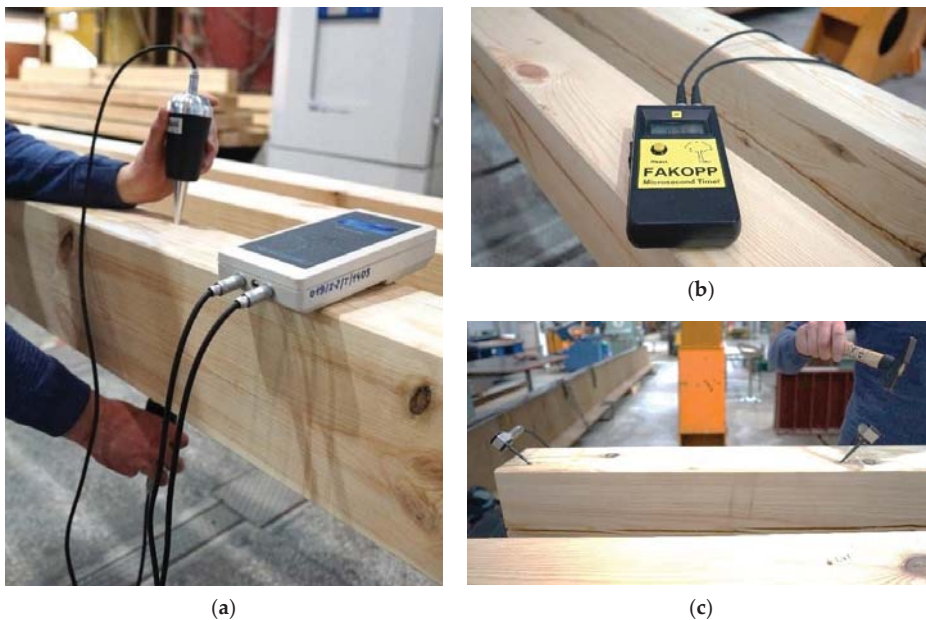
Figure 2. Determination of the dynamic modulus of elasticity using the acoustic method: (**a**) testing with the Sylvatest Trio device, (**b**,**c**) testing with the Fakopp MS device

When conducting the test with the Sylvatest Trio device (Figure 2a), the time of propagation of the ultrasonic wave between the transmitting and receiving probes, as well as the energy of this wave, are measured. This test requires drilling holes with a diameter of 5 mm and a depth of 10 mm in which the transmitting probes are placed. Due to the high sensitivity of the device, the measurement results may be influenced by other mechanical waves occurring near the test site, material moisture and internal stresses.

It is worth mentioning that acoustic methods require a large number of tests to eliminate measurement errors.

The velocity of the sound wave in a material is directly related to its internal structure. In the case of wood, it depends, inter alia, on the direction of the grain. Its value is several times higher parallel to the grain than perpendicular to it [50,51]. This phenomenon is due to the fact that the wave that propagates across the grain encounters more obstacles in the form of cell walls and it takes additional time to transit through them. Moreover, the examination of wood with the use of ultrasonic waves allows not only to determine MOE_{dyn}, but also enables the detection of discontinuities in the material structure and assessment of its degradation. According to [51], for wood without significant structure defects, the speed of propagation of the sound wave parallel to the grain is 3500–5000 m/s, and perpendicular to the grain—1000–1500 m/s. Other values may indicate internal discontinuities in the material structure.

There are numerous attempts to correlate MOE_{dyn} with the physical and mechanical properties of wood presented in the literature. The correlation between MOE_{dyn} and MOE_{stat} obtained by destructive tests is particularly interesting. Based on the analyses presented in the literature, it can be concluded that there is a strong correlation between MOE_{dyn} and MOE_{stat} and the value of the dynamic modulus is usually about 5–15% higher than the value of the static modulus [52]. The formulas for converting the value of MOE_{dyn} to MOE_{stat} were proposed by Íñiguez-González [53] (Table 3).

Table 3. Formulas for converting MOE$_{dyn}$ [MPa] to MOE$_{stat}$ [MPa] [53].

Wood Species	Vibration Method	Acoustic Method
Scots pine (Pinus sylvestris)	MOE$_{stat}$ = 0.9599 × MOE$_{dyn}$ + 407.2	MOE$_{stat}$ = 0.7548 × MOE$_{dyn}$ + 579.5
Radiata Pine (Pinus radiata)	MOE$_{stat}$ = 0.9599 × MOE$_{dyn}$ + 253.26	MOE$_{stat}$ = 0.7548 × MOE$_{dyn}$ − 86.15

2.4. Mechanical Properties Assessment Based on the Resistance Drilling Method

The drilling resistance test is a semi-destructive method that consists in drilling with a small diameter steel drill (1.5–3.0 mm) into a timber element and measuring the encountered resistance as a function of penetration depth. The drill bit advances and rotates at a constant speed. The drilling resistance corresponds to the torque required to maintain a constant drilling speed. Less torque is required in less dense areas. These are internal zones, such as the locations of corrosion, voids, gaps, and cracks. The results are presented in diagrams, examples of which are shown in Figure 3. The shape of the graph of the resistance drilling of a healthy material depends on the differences in the density of earlywood and latewood zones, the annual growth rings and the drilling angle. The most precise results are obtained by inserting the drill at an angle of 90 degrees to the annual rings and drilling in the radial direction [9,54]. The peaks in the graph indicate high drilling resistance and high density, while the dips correspond to low resistance and low density. Wood that has completely decayed or decomposed shows no resistance to drilling.
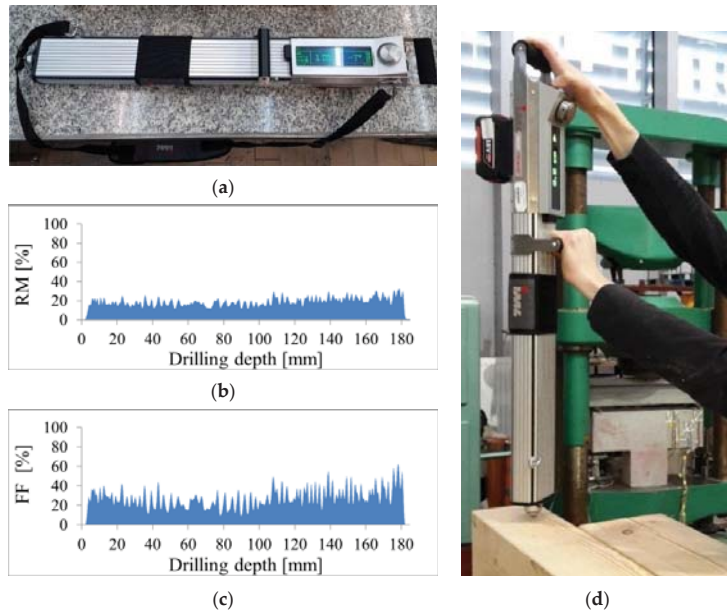
Figure 3. Drilling resistance test (**a**) device IML RESI PD-400S used in tests (**b**,**c**) charts obtained from test (**d**) test procedure.

The drilling resistance method used in in situ tests enables the location of defects and internal discontinuities in timber elements without interfering with their properties. It also allows to assess the extent of wood destruction in the tested elements, to inspect the condition of wood covered with other materials (such as plaster, gypsum coatings, walls, formwork, decking, etc.), without the need to disassemble them. The weak areas

and areas exposed to degradation are particularly important for testing, e.g., places where the wood contacts the ground or other materials, zones with visible moisture or biological degradation, as well as areas near door and window openings [55]. The drilling resistance method is also used in the analysis of the condition of wood in carpentry joints [56] and in elements made of glue laminated timber. However, attention should be paid to the differences in the resistographic diagrams for individual lamellas [9].

It is worth noticing that resistance drilling has a negligible effect on the mechanical and aesthetic properties of the tested element, because the diameter of the holes made during the test does not exceed 3 mm, which corresponds to the exit hole of the common wood pest in Europe-*Anobium punctatum*.

Numerous attempts are made to correlate the results of tests conducted with a resistance drilling device with the results of strength tests. Most often, based on the results of the relationship between relative resistance (RA) and drilling depth (H), the average value of the Resistance Measure (RM) parameter is determined and its relationship with the density, strength and modulus of elasticity is sought [57]. The value of RM can be calculated from the following formula:

$$RM = \frac{\int_0^H RA \times dh}{H} \tag{4}$$

where: $\int_0^H RA \cdot dh$ is the area under the drilling resistance graph and H is the drilling depth.

2.5. Mechanical Properties Assessment Based on Small Clear Wood Specimens Tests

The determination of the structural timber's characteristic values of mechanical properties and density by destructive testing may be performed in accordance with the applicable European standard PN-EN 384 + A1 [28]. According to the standard [28], structural full-size elements with defects that are representative for the population, should be tested. The standard PN-EN 384 [58] of 2011 allowed for the testing of MOR and MOE on small specimens in the case of hardwood species. The 2018 update of the standard [28] has narrowed the testing possibility to hardwood exotic species only. Moreover, it is recommended to use a minimum subsample of 40 pieces for testing.

In the case of testing single elements, particularly in existing or historic structures, examining options are very limited. In this paper, we consider testing small clear specimens (without defects) and adjusting their mechanical parameters based on ASTM D245 [44].

The calculation of the minimum quantity of samples to be tested can be performed using ISO 3129 [59] based on the determination of the testing objective, e.g., testing of a single piece of wood, the sampling method to be used and the assumed test accuracy index. According to the standard, the accuracy of 5% with a confidence level of 0.95 when determining basic physical and mechanical properties is recommended. The minimum number of samples n_{min} is calculated indicatively according to the formula:

$$n_{min} = \frac{V^2 t^2}{p^2} \tag{5}$$

where V is the percentage coefficient of variation for the property to be determined; t is the index of result authenticity (a half-length of the confidence interval in fractions of the standard deviation); p is the percentage index of test precision (the relation between the standard deviation of the arithmetic mean and the arithmetic mean). The average values of the coefficients of variation for basic wood properties that can be used in calculating the approximate minimum number of specimens to be taken for testing are presented in Table 4. The authors of this paper suggest taking the value of the coefficient from the column associated with ISO 3129 [59].

Table 4. Mean coefficient of variation [%] values for main wood properties.

Wood Property	Coefficient of Variation V [%]		
	ISO 3129 [59]	Krzysik [60]	Wood Handb. [61]
Number of growth rings in 1 cm	37	-	-
Percentage of late wood	28	28	-
Density	10	10	10
Equilibrium moisture content	5	-	-
Coefficient of shrinkage: linear	28	28	-
Coefficient of shrinkage: volumetric	16	16	-
Ultimate compressive strength parallel to grain	13	13	18
Ultimate strength in static bending	15	15	16
Ultimate shearing strength parallel to grain	20	19	14
Modulus of elasticity in static bending	20	20	22
Proportional limit (conventional ultimate strength) in compression perpendicular to grain	20	30	28
Ultimate tensile strength parallel to grain	20	20	25
Ultimate tensile strength perpendicular to grain	20	-	-
Impact strength in bending	32	32	25
Hardness	17	17	20

The procedure for testing samples should be conducted in accordance with relevant standards–for MOR, for example: ISO 13061-3, PN-77/D-04103 (ISO 3133), BS 373, ASTM D143 [30,32,33,35,36], for MOE–ISO 13061-4, PN-63/D-04117, BS 373, ASTM D143 [31,33–35]. According to Krzysik [60], testing specimens with cross-sections ranging from 20 mm × 20 mm to 60 mm × 60 mm yields nearly equal MOR results. The author also notes that specifying the cross-sectional dimension within these limits seems to be arbitrary. Furthermore, with the increase of the support spacing, the bending strength increases within certain limits. The ratio of length to section height (l/h) is particularly important here. The ratio l/h of 10 to 15 is most commonly used for small specimens. The results increase slightly above the value l = 12 h and remain basically unchanged above l = 20 h. However, specimens with spacing less than l = 12 h are not recommended due to the effects of shear and distortion of the specimens at the locations of support and loading application. The static bending modulus according to the current testing standards for small specimens can be determined at the time of bending strength determination. There are different recommendations of the test method selection presented in the literature. According to Krzysik [60], a higher accuracy of measurement is possible to obtain in the 3-point bending test due to the larger deflections and therefore a smaller measurement error. According to BS 373 [35], the determination of MOE in cases requiring particular accuracy should be conducted in 4-point bending test, because the bending moment is constant along the section between the points of load application and, unlike in the case of 3-point bending test, there is no shear along this section, therefore there is no need to include it in the MOE calculations.

The adjustment of the strength properties of clear wood (without defects) to structural timber (with defects) can be performed according to the standard ASTM D245 [44]. The values obtained for small specimens without defects are modified by applicable factors depending on, among other things, moisture content or wood defects. General formulas for calculating mechanical properties are given below [52]:

$$F = l_5 \times k_t \times k_s \times k_p \times k_d \times k_g \times k_m \tag{6}$$

$$E = \overline{E} \times k_t \times k_p \times k_d \times k_g \times k_m \tag{7}$$

where F is the allowable stress; E is the modulus of elasticity; l_5 is the lower 5% exclusion limit for strength; $\overline{E}$ is the mean modulus of elasticity; k_t is the load duration factor, k_s is the coefficient adjusting the characteristic values to the allowable values, k_p is the special factor, k_d is the strength ratio, dependent on wood defects, k_g is the special grading, k_m is the moisture-dependent coefficient.

A detailed discussion of the reducing factors and an example of their application can be found in the standard [44].

3. Materials and Methods

In the experimental part of the research, three technical scaled elements of Scots pine (*Pinus sylvestris*) with dimensions of 120 mm × 180 mm × 3600 mm were tested. The beams were initially evaluated in vibration testing and classified according to the requirements of the standard [46] into class C24.

Destructive tests were performed in a four-point bending test according to the standard PN EN 408 [29] (Figure 4a). The spacing between the supports was 3240 mm. The experimental testing was conducted in the Laboratory of Civil Engineering Structures at the Faculty of Civil Engineering of the Wroclaw University of Science and Technology. An electronically controlled linear hydraulic jack, the Instron 500 (Instron®, Norwood, MA, USA), was used. The results were registered using the MGC plus measurement system made by Hottinger Baldwin Messtechnik. The measurement equipment used in the experimental testing was calibrated to at least class 1 accuracy.

(**a**)   (**b**)

Figure 4. View of experimental stands for testing: (**a**) technical scale beam, (**b**) small clear specimen (Group 2).

From the A-beams it was possible to collect 60 small specimens of clear wood without defects, which were divided into two groups. The first group (Group 1) of specimens with dimensions of 20 mm × 20 mm × 300 mm was the reference group. Specimens were tested in 3-point bending test according to the standards PN-77/D-04103, ISO 3133, ISO 13061-3, and PN-63/D-04117 [30,32,34,36]. The second group (Group 2) was the comparison group and contained specimens with dimensions of 20 mm × 20 mm × 400 mm, which were tested in a 4-point bending test. The scheme of the test stand corresponds to the testing conditions of full-size elements with defects according to the European standard PN-EN 408 [29], that finds its primary application in the testing of technical scale beams. Test schemes are shown in Figures 4 and 5. The estimation of the test accuracy index values for MOR and MOE according to ISO 3129 [59] for 30 specimens is presented in Table 5.
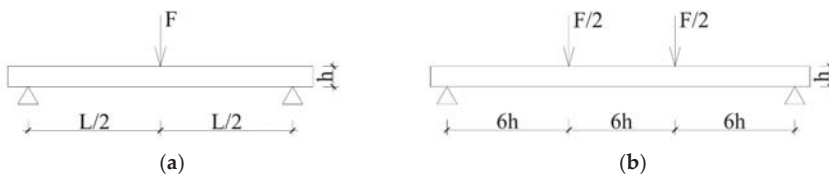

(**a**)   (**b**)

Figure 5. Scheme of testing: (**a**) small specimens Group 1, (**b**) small specimens Group 2 and technical scale beams, where F—load, L—span in bending, h—height of the beam.

Table 5. Estimation of the test accuracy rates.

	MOR	MOE
Number of samples	30	30
Coefficient of variation according to ISO 3129	15%	20%
Confidence level	0.95	0.95
Estimated test accuracy rate	5.37%	7.16%

The beams were tested by acoustic method (NDT) with the use of Fakopp Microsecond Timer and Sylvatest Trio. The reference test was performed with the Fakopp MS, taking 61 parallel and 8 perpendicular to the grain measurements for each tested beam. Additionally, for control purposes, for each beam, 5 measurements parallel and 8 perpendicular to the grain were made using the Sylvatest Trio device.

SDT tests were also conducted using the drilling resistance method. The studies were performed with the IML RESI PD-400S (IML, Wiesloch, Germany). For this, 40 drillings perpendicular to the grain were made for each beam. The drilling points were distributed evenly at both endings of the beams—every 150 mm along the lengthwise, every 40 mm width wise and 45 mm height wise, in such a way that the drilling paths did not intersect each other and not to weaken the central part of the beam. The grid of measurement points is presented in Figure 6. During the measurements, the values of Resistance Measure (RM) and Feed Force (FF) were determined.
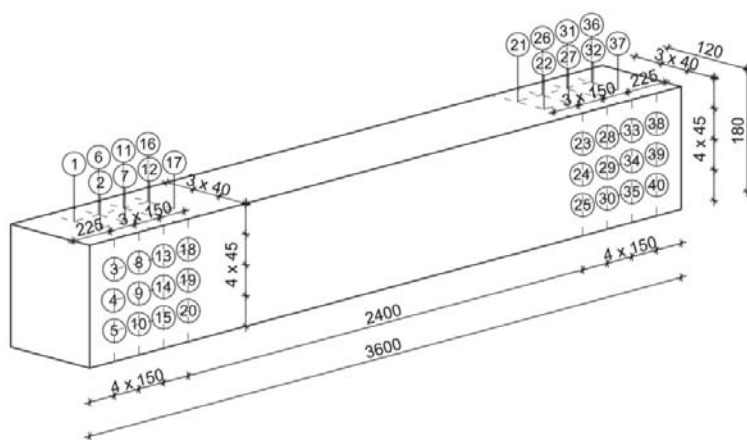
Figure 6. Diagram of the location of drilling points, unit: [mm].

The analyses were carried out with a reference moisture content equal to 12%. It is important to consider the significant influence of moisture content on wooden elements [14,62]. When testing wood with moisture contents differing from the reference moisture content (usually 12%)—these differences should be taken into account using the correction formulas indicated in the relevant standards.

Statistical analyses of the results were carried out using the Real Statistics Resource Pack software (Release 7.6.1). Copyright (2013–2021) Charles Zaiontz. www.real-statistics.com (accessed on 10 April 2021).

4. Results

4.1. Results of Destructive Testing of Technical Scale Beams and Density Determination

In the study of beams on a technical scale, carried out in accordance with PN-EN 408 [29], the values of MOR, MOE and density were determined and are presented in Table 6. The MOR values obtained for the beams differed significantly from each other

(MOR^{A01} = 37.46 MPa, MOR^{A02} = 31.27 MPa, MOR^{A03} = 46.45 MPa). The MOE values obtained for the beams were similar (MOE^{A01} = 11.62 MPa, MOE^{A02} = 10.85 MPa, MOE^{A03} = 11.63 MPa). The MOE values determined in the destructive test and calculated on the basis of the standard PN-EN 408 [29] (Table 6) do not take into account the shear deformation. The procedure for assigning strength classes in PN-EN 384 [28] includes formulas to take into account the effect of shear deformation. The E_0 modules determined in accordance with the standard [28], based on MOE, taking into account the influence of shear deformation, were E_0^{A01} = 12.42 GPa, E_0^{A02} = 11.42 GPa, E_0^{A03} = 12.43 GPa. Based on the determined values of MOR and E_0, it can be concluded that the beams A01, A02, A03 met the criteria of the classes C30, C24, C30 respectively [46].

Table 6. The results of bending technical scale beams and values of their density.

Beam	MOR				MOE				Density [kg/m^3]
	Value [MPa]	Mean [MPa]	Standard Deviation [MPa]	Variation Coefficient ν [%]	Value [GPa]	Mean [GPa]	Standard Deviation [GPa]	Variation Coefficient ν [%]	
A01	37.46				11.62				497
A02	31.27	38.39	6.23	16.23	10.85	11.36	0.37	3.23	484
A03	46.45				11.63				496

The variety of mechanical properties allows for the assessment of the sensitivity of the methods used in terms of capturing these differences.

4.2. Results of Tests with Acoustic Method

The aim of the acoustic analysis was to determine the velocity of the wave emitted by the devices and then calculate the MOE_{dyn}. The calculated values of MOE_{dyn} were used to estimate the MOE_{stat} according to Table 3. The results are shown in Table 7 and in Figures 7 and 8. The velocities obtained for both devices were similar but slightly lower for the Sylvatest Trio. The MOE_{stat} values of the reference measure (Fakopp MS) parallel to the grain for beams A01, A02, A03 were 11.11 GPa, 10.70 GPa, and 10.29 GPa respectively, and differed from the results of destructive testing of technical scale beams by 4.4%, 1.4%, 11.6%. The MOE_{stat} values do not take into account the influence of shear deformation. The E_0 modules determined in accordance with the standard [28], based on MOE_{stat} of the Fakopp MS test parallel to the grain, taking into account the influence of shear deformation, were E_0^{A01} = 11.75 MPa, E_0^{A02} = 11.22 MPa, E_0^{A03} = 10.69 MPa. Based on the determined values of E_0, it can be concluded that the beams A01, A02, and A03 met the criteria of the classes C27, C24, and C22, respectively [46].

Table 7. The results of the acoustic tests with Fakopp MS and Sylvatest Trio- mean values.

Beam	Direction Relative to Grain	Velocity [m/s]		MOE_{dyn} [GPa]		MOE_{stat} [1] [GPa]	
		Fakkop MS	Sylvatest Trio	Fakkop MS	Sylvatest Trio	Fakkop MS	Sylvatest Trio
A01	parallel	5292	5134	13.95 [2]Δ = 20.1%	13.10 Δ = 12.7%	11.11 Δ = 4.4%	10.47 Δ = 9.9%
	perpendicular	1689	1617	1.42	1.31	1.65	1.57
A02	parallel	5262	5155	13.41 Δ = 23.6%	12.87 Δ = 18.6%	10.70 Δ = 1.4%	10.29 Δ = 5.1%
	perpendicular	1742	1559	1.47	1.18	1.69	1.47
A03	parallel	5090	5038	12.86 Δ = 10.6%	12.59 Δ = 8.3%	10.29 Δ = 11.6%	10.08 Δ = 13.3%
	perpendicular	1668	1573	1.38	1.23	1.62	1.51

[1] MOE_{stat} was determined by the formula in Table 3. [2]Δ are the percentages of the difference of MOE determined from acoustic methods with MOE values obtained by destructive testing of technical scale beams (Table 6).
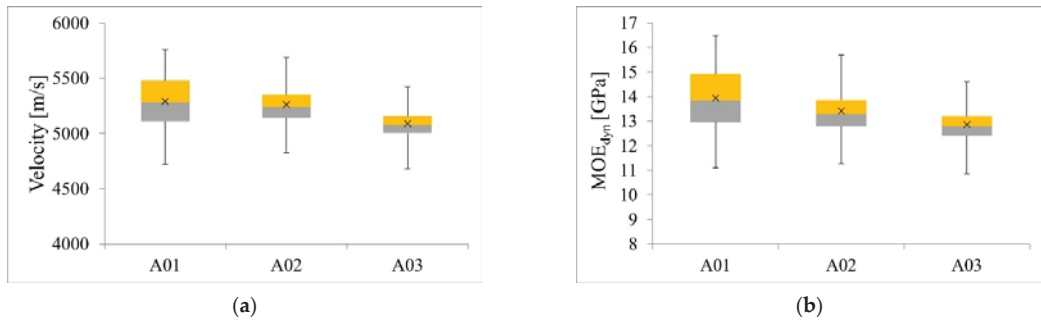
Figure 7. Box plots for Fakopp MS measurement parallel to the grain: (**a**) velocity, (**b**) MOE$_{dyn}$.
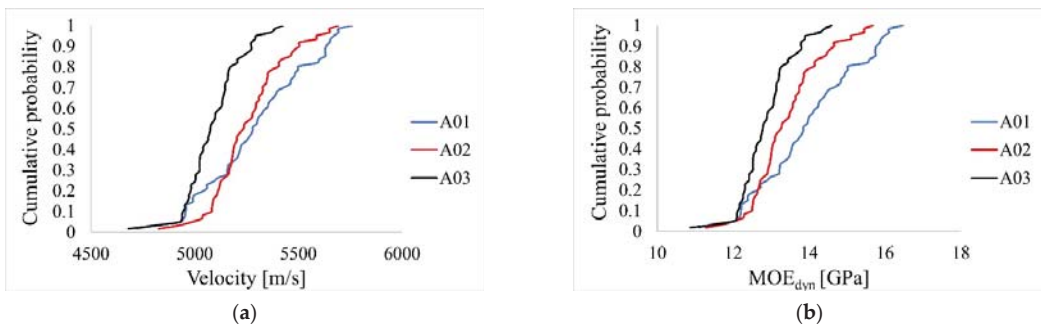

Figure 8. Empirical cumulative distribution function for Fakopp MS measurement parallel to the grain: (**a**) velocity, (**b**) MOE$_{dyn}$.

The aim of the first statistical analysis was to check whether the differences in the mean values of velocity obtained from the basic measurement (Fakopp MS parallel to the grain) for individual beams were statistically significant. Based on the Shapiro–Wilk test, the normality assumption for all beams A01, A02, A03 was met ($p = .242$, $p = .324$, $p = .244$). There was heterogeneity of variances for all beams, as assessed by Levene's test for equality of variances ($p < .001$). Due to the normality of the distribution of measurements and the heterogeneity of variance, we decided to perform Welch's one-way analysis of variance (Welch's ANOVA) with the Games–Howell post-hoc test. The conducted analysis showed a statistically significant difference in the mean velocity values measured for individual beams ($p < .001$). The post-hoc test showed a statistically significant difference in the mean values between groups A01-A03, A02-A03.

In the second statistical analysis, it was checked whether the differences in the mean values of MOE$_{dyn}$ obtained for the basic measurement (Fakopp MS parallel to the grain) for individual beams were statistically significant. Based on the Shapiro–Wilk test, the normality assumption for all beams was met ($p = .221$, $p = .195$, $p = .229$). There was heterogeneity of variances for all beams, as assessed by Levene's test for equality of variances ($p < .001$). Due to the normality of the distribution of measurements and the heterogeneity of variance, we decided to perform Welch's one-way analysis of variance (Welch's ANOVA) with the Games–Howell post-hoc test. The conducted analysis showed a statistically significant difference in the mean MOE$_{dyn}$ values measured for individual beams ($p < .001$). The post-hoc test showed a statistically significant difference in the mean values between all beams.

4.3. Results of Test with Drilling Resistance Method

The purpose of testing the beams by measuring the drilling resistance was first to determine FF and RM values. The results are presented in Tables 8 and 9 and in Figures 9–11.

Based on the FF and RM values determined, statistical analyses were carried out to find the relationship between these values and the MOR, MOE, and density of elements on the technical scale.

The aim of the first statistical analysis was to check whether the differences in the median values of RM obtained in the measurement for individual beams were statistically significant. Based on the Shapiro–Wilk test, it was determined that not all distributions were normal for beams A01, A02, A03 (p = .250, p = .110, p = .017). There was heterogeneity of variance for all beams, as assessed by Levene's test for equality of variance (p < .001). Due to the fact that not all distributions were normal, and variances were heterogeneous, we decided to perform Kruskal–Wallis test with the Games–Howell post-hoc test. The conducted analysis showed a statistically significant difference in the mean RM values measured for individual beams (p < .001). The post-hoc test showed a statistically significant difference in the median values between groups A01-A02, A02-A03.

Table 8. Mean drilling resistance test results.

| Beam | Number of Measurements | Resistance Measure RM [%] | | | |
		Mean	Range	Standard Deviation	Coefficient of Variation
A01	40	21.86	17.34–24.93	1.96	8.99
A02	40	18.84	17.33–20.67	0.95	5.04
A03	40	22.66	22.66–21.40	0.99	4.38
Summary	120	21.12	17.33–24.93	2.15	10.17

Table 9. Mean feed force test results.

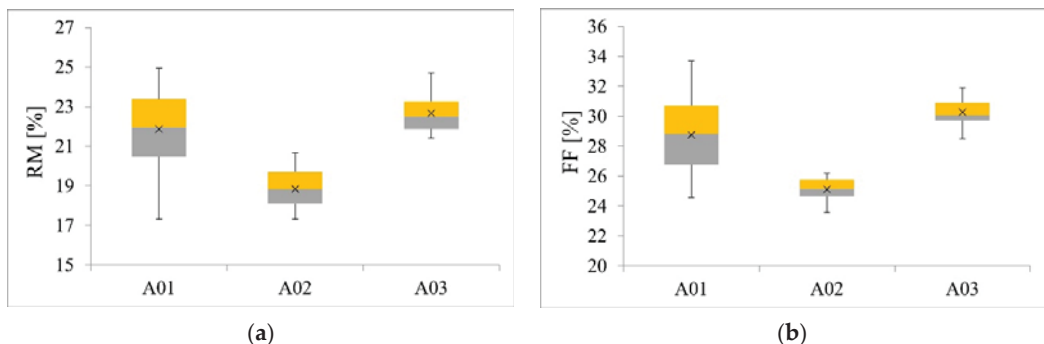| Beam | Number of Measurements | Feed Force FF [%] | | | |
		Mean	Range	Standard Deviation	Coefficient of Variation
A01	40	28.76	24.56–33.68	2.41	8.39
A02	40	25.11	23.57–26.22	0.76	3.02
A03	40	30.28	28.49–31.90	0.75	2.48
Summary	120	28.05	23.57–33.68	2.65	9.44

Figure 9. Box plots: (**a**) Resistance Measure–RM, (**b**) Feed Force–FF.
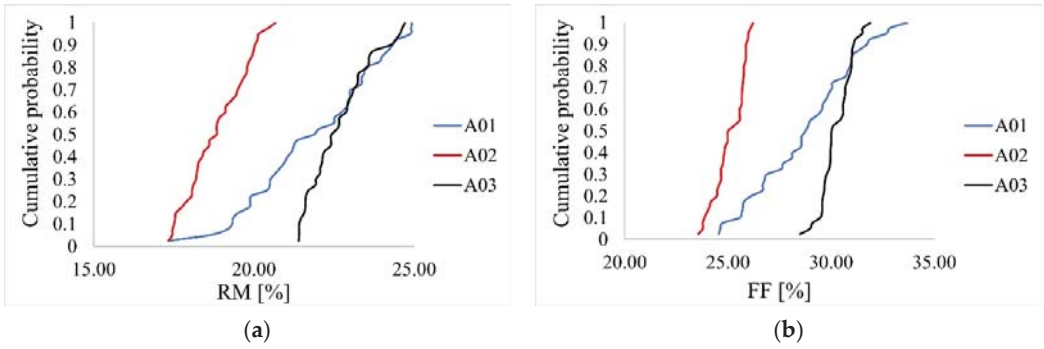
Figure 10. Empirical cumulative distribution function: (**a**) Resistance Measure–RM, (**b**) FF–Feed Force.
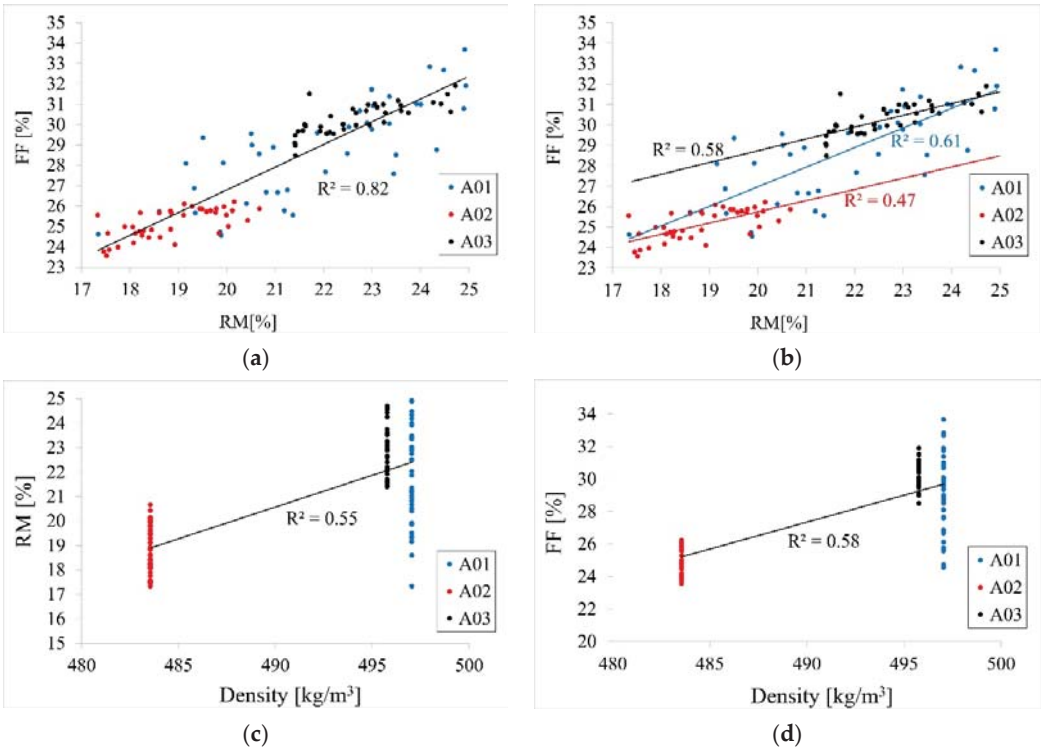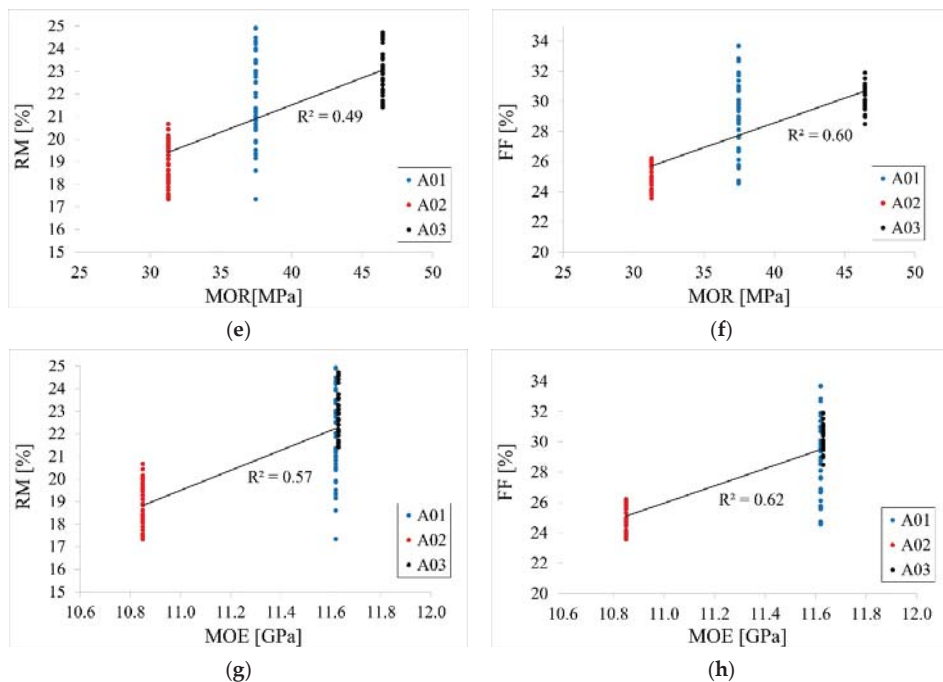

Figure 11. *Cont.*

Figure 11. Correlation plots of Resistance Measure and Feed Force results (**a**) correlation between RM and FF, (**b**) correlation between RM and FF for beams separately, (**c**) correlation between RM and density, (**d**) correlation between FF and density, (**e**) correlation between RM and MOR obtained from structural size beam bending test, (**f**) correlation between FF and MOR obtained from structural size beam bending test, (**g**) correlation between RM and MOE obtained from structural size beam bending test, (**h**) correlation between FF and MOE obtained from structural size beam bending test.

In the second statistical analysis it was checked whether the differences in the median values of FF obtained in the basic measurement for individual beams were statistically significant. Based on the Shapiro–Wilk test, it was determined that not all distributions were normal for the beams ($p = .22$, $p = .20$, $p = .23$). There was heterogeneity of variance for all beams, as assessed by Levene's test for equality of variance ($p < .001$). Due to the fact that not all distributions were normal, and variances were heterogeneous, we decided to perform Kruskal- Wallis test with the Games–Howell post-hoc test. The conducted analysis showed a statistically significant difference in the mean FF values measured for individual beams ($p < .001$). The post-hoc test showed a statistically significant difference in the median values between all beams.

Pearson correlation coefficients between FF and RM for the three different beams were equal 0.78, 0.68, and 0.76 for beams A01, A02, and A03, respectively. Figure 11b shows parallel trends for beams A02 and A03, indicating the same effects of RM on FF for those two beams. A higher trend effect was observed for beam A01. Linear regression models were fitted first for FF response and RM as the predictor separately for all three beams. The estimates from these models are presented in Table 10. The regression coefficients are significantly different from 0 for all three beams, indicating a significant correlation between FF and RM. For beam A01, with 1 unit increase of RM, FF increases by 0.96 units. For beam A02 with one unit increase of RM, FF increases by 0.55 and for beam A03 by 0.58. To investigate the differences in these trend effects between the beams, one regression model was fitted with FF as the response, RM and beam as the predictors, as well as the RM*beam interaction term. The results for this model are presented in Table 11. As can be observed, there is a significant value of beam A03 versus A01 as well as significant

interaction terms confirming differences between the trend effect of RM on FF between beam A01 and the other two beams. The equality of effects for beams A02 and A03 were not tested in this model since beam A01 was the reference beam. However, in the model with changed reference beam group, the equality of these two effects were confirmed (results omitted).

Table 10. Estimates for regression models of FF vs. RM for different beams.

Beam	Variable	Estimate	Standard Error	*p*-Value
A01	Intercept	7.79	2.73	.007
	RM	0.96	0.12	<.001
A02	Intercept	14.78	1.78	<.001
	RM	0.55	0.09	<.001
A03	Intercept	17.19	1.80	<.001
	RM	0.58	0.08	<.001

Table 11. Estimates for regression models of FF with RM beam as the predictor and RM*Beam interaction term.

Variable	Estimate	Standard Error	*p*-Value
Intercept	7.79	1.76	<.001
RM	0.96	0.08	<.001
Beam A02 vs. A01	6.99	3.58	.053
Beam A03 vs. A01	9.40	4.00	.021
RM: beam A02 vs. A01	−0.41	0.18	.027
RM: beam A03 vs. A01	−0.38	0.18	.034

Therefore, it can be concluded that the effect of RM on FF is the same for beams A02 and A03 and higher for beam A01.

To investigate the effect of density on FF and RM, the regression model was fitted with only density as the continuous predictor and FF or RM as the response. The results are presented in Table 12. Pearson correlation coefficient between density and RM was equal 0.74, between density and FF 0.76. The fitted linear trends are presented in Figure 11c,d. As can be seen, the effect of density is significant both for FF and RM. With 1 unit increase in density, both FF and RM increase by around 0.36 and 0.28 units, respectively. Similar models were fitted for FF and RM and MOR or MOE as predictors (Tables 13 and 14). Pearson correlation coefficient between MOR and RM was equal 0.70, between MOR and FF 0.77. The fitted linear trends are presented in Figure 11e,f. Pearson correlation coefficient between MOE and RM was equal 0.76, between MOE and FF 0.79. The fitted linear trends are presented in Figure 11g,h. With 1 unit increase in MOR, both FF and RM increase by around 0.33 and 0.24 for FF and RM %, respectively (Table 13). On the other hand, with 1 unit increase in MOE, both FF and RM increase by around 5.7 and 4.4 for FF and RM %, respectively (Table 14).

Table 12. Estimates for regression models of FF and RM with density as the predictor.

Feed Force/Resistance Measure	Variable	Estimate	Standard Error	*p*-Value
FF	Intercept	−148.28	13.79	<.001
	Density	0.36	0.03	<.001
RM	Intercept	−117.11	11.68	<.001
	Density	0.28	0.02	<.001

Table 13. Estimates for regression models of FF and RM with MOR as the predictor.

Feed Force/Resistance Measure	Variable	Estimate	Standard Error	*p*-Value
FF	Intercept	15.47	0.96	<.001
	MOR	0.33	0.02	<.001
RM	Intercept	11.90	0.88	<.001
	MOR	0.24	0.02	<.001

Table 14. Estimates for regression models of FF and RM with MOE as the predictor.

Feed Force/Resistance Measure	Variable	Estimate	Standard Error	*p*-Value
FF	Intercept	−36.78	4.64	<.001
	MOE	5.70	0.41	<.001
RM	Intercept	−29.19	4.01	<.001
	MOE	4.43	0.35	<.001

4.4. Results of Tests of Small Clear Specimens and Their Adjustment to Structural Size Beams

The purpose of the small specimen test was to determine MOR and MOE values. The following Table 15 and Figures 12–14 show the results of the conducted tests. The estimation of the 5% exclusion limit values can be done by several approaches, for example, according to ISO 12491:1997 [63] using classical statistics (EN 14358:2016 [64]) or Bayesian approach (PN-EN 1990 [65]). The 5% exclusion limit values indicated in Table 15 were determined according to PN-EN 1990 [65].

Table 15. Results of small clear specimen bending tests.

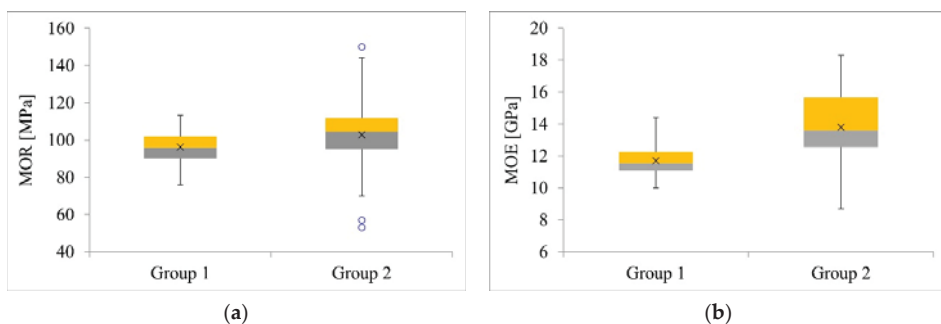|	Group 1		Group 2	
	MOR	MOE	MOR	MOE
Number of specimens	30 pieces		30 pieces	
Mean value	96 MPa	11.7 GPa	103 MPa	13.8 GPa
Standard deviation	9.3 MPa	1.11 GPa	21.2 MPa	2.57 GPa
Coefficient of variation	9.6%	9.5%	20.2%	18.3%
Confidence interval for the mean (0.95)	92.7–99.3 MPa	11.43–12.23 GPa	95.1–110.3 MPa	12.88–14.72 GPa
5% exclusion limit	80 MPa	9.8 GPa	66 MPa	9.4 GPa

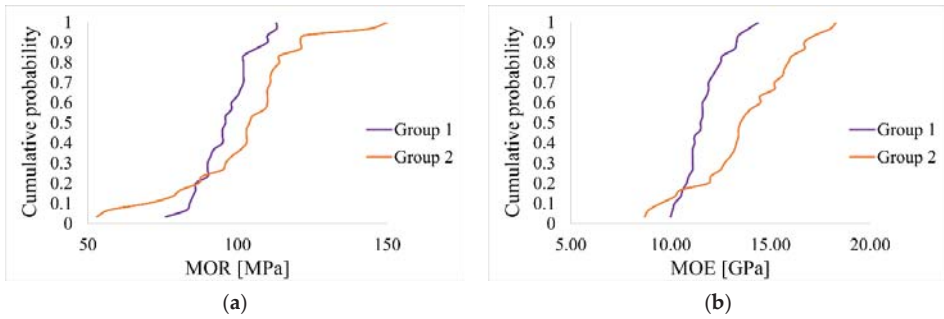

Figure 12. Box plots: (**a**) MOR, (**b**) MOE.

Figure 13. Empirical cumulative distribution function: (**a**) MOR, (**b**) MOE.
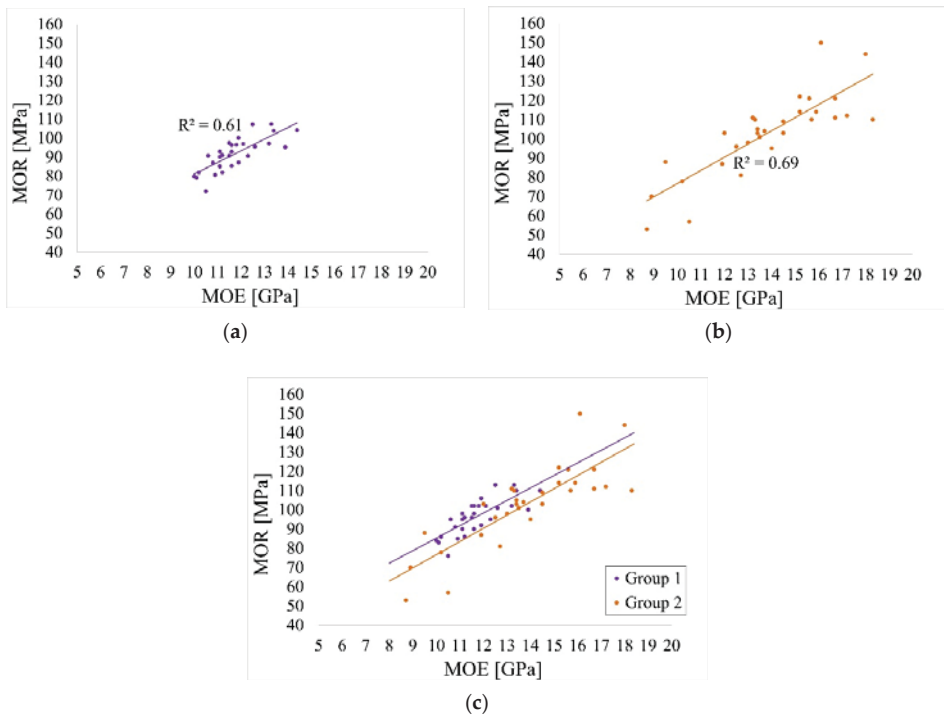

Figure 14. Correlation between MOE and MOR: (**a**) Group 1, (**b**) Group 2, (**c**) both Groups.

Statistical analyses were performed to determine whether there were significant differences between Group 1 and Group 2.

The aim of the first statistical analysis was to check whether the differences in the mean values of MOR between Group 1 and Group 2 were statistically significant. Based on the Shapiro–Wilk test, it was determined that both distributions were normal ($p = .738$, $p = .134$). There was heterogeneity of variance, as assessed by Levene's test for equality of variance ($p = .010$). Due to the fact that both distributions were normal, and variances were heterogeneous, we decided to perform Welch's t-test. The analysis showed no significant differences between the mean MOR values ($p = .137$).

In the second statistical analysis, we checked whether the differences in the mean values of MOE were statistically significant. Based on the Shapiro–Wilk test, it was determined that both distributions were normal ($p = .166$, $p = .565$). There was heterogeneity of

variance, as assessed by Levene's test for equality of variance ($p < .001$). Due to the fact that both distributions were normal, and variances were heterogeneous, we decided to perform a Welch's *t*-test. The analysis showed statistically significant differences between the mean MOE values ($p < .001$).

Pearson correlation coefficients between MOE and MOR in both groups were equal 0.78 and 0.83 for Group 1 and Group 2, respectively. Linear regression models were fitted for MOR response and MOR as the predictor separately for both groups and the fitted linear trends are presented in Figure 14.

The estimates from these models are presented in Table 16. As can be seen, the regression coefficients are significantly different from zero for both groups, indicating a significant correlation between MOE and MOR. For Group 1 with 1 unit increase of MOE, MOR increases by 6.52 units and for Group 2 with one unit increase of MOE, MOR increases by 6.86. To investigate the differences in these trend effects between the groups, a regression model was fitted with MOR as the response, MOE and Group as the predictors, as well as the MOE * Group interaction term. The results for this model are presented in Table 17. As can be observed, there is no significance of Group, neither the significant interaction term. Therefore, there are no significant differences between the trend effect of MOE on MOR between Group 1 and Group 2.

Table 16. Estimates for regression models of MOR vs. MOE for Groups 1 and 2.

Group	Variable	Estimate	Standard Error	*p*-Value
Group 1	Intercept	19.99	11.52	0.094
	MOE	6.52	0.98	<0.001
Group 2	Intercept	8.08	12.07	0.509
	MOE	6.86	0.86	<0.001

Table 17. Estimates for regression models of MOR with MOE, Group as the predictor and MOE * Group interaction term.

Variable	Estimate	Standard Error	*p*-Value
Intercept	19.99	18.44	0.283
MOE	6.52	2.07	<0.001
Group 2 vs. 1	−11.91	20.75	0.568
MOE * Group	0.33	1.71	0.846

This is depicted in Figure 14. The fitted trend lines are almost parallel.

The wood defects that occurred on individual beams and potentially determined their load-carrying capacity according to ASTM D245 [44] are presented in Figure 15.

The results of the MOR and MOE values adjustment determined on small clear specimens of technical scale beams using the factors indicated in ASTM D245 [44] are presented in Table 18.

Standard ASTM D245 [44] aims to define an allowable property based on formulas (6) and (7). In laboratory testing of single elements, it seems appropriate to compare the MOR and MOE of technical scale beams with the "Characteristic" and "Mean" values of the MOR and "Mean" value of MOE estimated from small clear specimens (Table 18). The MOR "Characteristic" values of the beams were very similar in both groups. The MOE values estimated in Group 1 for beams A01, A02, A03 were 11.7 GPa, 10.5 GPa, 11.7 GPa respectively, and differed from the values obtained in the destructive test of technical scale beams by 0.7%, 3.2%, 0.7%. The MOE values estimated in Group 2 for beams A01, A02, A03 were 13.8 GPa, 12.4 GPa, 13.8 GPa respectively, and differed significantly from the values obtained in the destructive test of technical - the differences were 18.8%, 14.3%, 18.8% respectively. The MOE values do not consider the shear deformation. The procedure for assigning strength classes in PN-EN 384 [28] includes formulas to take into account the effect of shear deformation. The E_0 modules determined in accordance with

the standard [28], based on MOE, taking into account the influence of shear deformation, were for Group 1: E_0^{A01} = 12.52 GPa, E_0^{A02} = 11.00 GPa, E_0^{A03} = 12.52 GPa, for Group 2: E_0^{A01} = 15.25 GPa, E_0^{A02} = 13.46 GPa, E_0^{A03} = 15.25 GPa. Based on the determined values of MOR ("CHARACTERISTIC") and E_0, it can be concluded that the beams A01, A02, A03 for Group 1 met the criteria of the classes C30, C24, C30 respectively, and for Group 2: C30, C27, C35 [46].

(**a**)

(**b**)

(**c**)

Figure 15. Defects indicated according to ASTM D245 [44] and potentially determining the load-bearing capacity of the beams: (**a**) beam A01-damage initiation caused by crushing of compressed fibers in the corner knot area (compression near knot [52]), (**b**) beam A02-damage initiation caused by rupture of tensioned fibers near the corner knot and slope of grain (cross grain tension/diagonal tension [33,52]) (**c**) beam A03-damage initiation caused by crushing of compressed fibers in corner knot area (cross grain tension/diagonal tension caused by compression near knot [33,52]).

Table 18. Estimation of MOR and MOE of technical scale beams from small clear specimens according to the standard ASTM [44].

	Beam A01				Beam A02				Beam A03			
	Group 1		Group 2		Group 1		Group 2		Group 1		Group 2	
	MOR	MOE	MOR	MOE	MOR	MOE	MOR	MOE	MOR	MOE	MOR	MOE
Mean [MPa]	96	11,700	103	13,800	96	11,700	103	13,800	96	11,700	103	13,800
5% exclusion value (MPa)	80	9800	66	9400	80	9800	66	9400	80	9800	66	9400
Special factor k_p [1] [-]	0.68	-	0.78	-	0.68	-	0.78	-	0.68	-	0.78	-
Factor k_d [2] [-]	0.60	1.0	0.60	1.0	0.53	0.90	0.53	0.90	0.75	1.00	0.75	1.00
5% exclusion value $\times k_p \times k_d$ [MPa] "Characteristic"	33	-	31	-	29	-	27	-	41	-	39	-
Mean $\times k_p \times k_d$ [MPa] "Mean"	39	11,700	48	13,800	35	10500	43	12,400	49	11,700	60	13,800

[1] k_p—special factor for 4-point bending was determined based on the formula proposed in [61]. [2] k_d—strength ratio dependent on wood defects [44].

5. Discussion

The main objective of this paper was to attempt to indicate the practical aspect of testing timber elements in existing structures, especially historic ones, and to interpret the results. A strict analysis of three elements with similar MOE but significantly different MOR values is presented. The focus was on the interpretation of the results oriented towards single elements, which also refers to the study of historic structures, where sometimes even a single element subjected to multiple tests may be of interest. The authors were mainly interested in practical conclusions, while statistical analyses were carried out to complete the research overview. The authors were concerned to indicate that NDT and SDT methods should not be used selectively (alone) in timber assessment.

Those testing methods were chosen which were considered to be the most applicable, fast, useful in-situ, and uncomplicated in terms of conducting the tests and processing the results. The acoustic method and resistance drilling are well known in the literature. Especially the reliability and effectiveness of the former has been proven [24,25]. Most often, the literature looks for correlations between the results obtained and the mechanical properties, while the practical aspect of interpreting the results is neglected. In addition, the standards for testing existing structures are not unambiguous and the interpretation of the research results is largely unsystematic.

Studies reported in the literature indicate strong correlations between MOE_{dyn} values obtained from the acoustic method and actual MOE_{stat} values from DT testing. Based on the study, MOE_{stat} values differing from the actual values within 5% were obtained for beams A01 and A02, but for beam A03 the difference was more than 11%. Such a difference in MOE_{stat} values can result in incorrect timber assignment, even by several classes.

The resistance drilling method study indicated the presence of statistically significant correlations between FF and RM values and density, MOE and MOR, but they are so weak that it seems inappropriate to infer strength properties on their basis. Nevertheless, the drilling resistance method has excellent applications in qualitative wood assessment—e.g., determining the degree of biological degradation and finding hidden defects within the element.

In addition, small samples without defects were tested and the results were interpreted in accordance with ASTM D245. The use of ASTM D245 in combination with EN and ISO standards, especially for testing historic elements, seems unique but possible. By using simple statistical methods and the methodology of reducing the strength properties of clear wood without defects based on ASTM D245, good results and an accurate classification in the reference group (Group 1) were obtained. However, it should be noted that it is not always possible to extract enough material from an existing structure for testing and accurate visual assessment is not always possible.

6. Conclusions

The primary goal of this paper was to consider possible methods useful in determining MOR and MOE in existing structures where testing capabilities are limited. Attention is drawn to the problem of obtaining a sufficient amount of material for testing and comprehensive assessment of wood. On the basis of the conducted non-destructive, semi-destructive and destructive tests, it was possible to determine the following conclusions:

- In the conducted research, very good correlations were obtained between MOE_{stat} from the acoustic method and MOE from beams on the technical scale. Nevertheless, the difference in the value of the modulus determined by the acoustic method may be high enough to result in an incorrect assignment of wood class.
- In the drilling resistance test, statistically significant correlations were observed between the density, MOR and MOE as predictors and FF or RM as the response (R^2 = 0.49–0.62). However, it is considered that resistance drilling should be used for qualitative rather than quantitative evaluation of timber.
- In the conducted study, the MOE values determined in accordance with the ASTM standard, based on the results for small clear specimens, correspond very well with the actual values from the technical scale element tests.
- The failure of the technical scale beams in the bending tests was observed in the areas of occurrence of defects considered by ASTM D245 [44] to be critical for load-bearing capacity.
- It is recommended to use different methods in parallel, as no single method is sufficiently reliable.

It should be noted that the research was conducted on elements made of pine (*Pinus sylvestris*), which, due to its good availability, low price, and good strength properties, is the most popular structural wood in Poland [66]. The results of wood testing should be considered in the context of a specific species.

Numerous ISO, EN and ASTM standards were used in the analyses. Special care should be taken when combining the standards. The material properties to be compared should be determined from the analogous, well-known formulas and the relationships from materials mechanics.

The laboratory tests and analyses presented in this paper are part of an ongoing research project. Due to limited data, the conclusions and observations presented should be considered possible but not certain.

References

1. Šubic, B.; Fajdiga, G.; Lopatič, J. Bending stiffness, load-bearing capacity and flexural rigidity of slender hybrid wood-based beams. *Forests* **2018**, *9*, 703. [CrossRef]
2. Nowak, T.; Karolak, A.; Sobótka, M.; Wyjadłowski, M. Assessment of the condition of wharf timber sheet wall material by means of selected non-destructive methods. *Materials* **2019**, *12*, 1532. [CrossRef] [PubMed]

3. Baño, V.; Arriaga, F.; Guaita, M. Determination of the influence of size and position of knots on load capacity and stress distribution in timber beams of Pinus sylvestris using finite element model. *Biosyst. Eng.* **2013**, *114*, 214–222. [CrossRef]
4. Vavrusova, K.; Lokaj, A.; Mikolasek, D.; Sucharda, O. Analysis of longitudinal timber beam joints loaded with simple bending. *Sustainability* **2020**, *12*, 9288. [CrossRef]
5. Oliveira, J.; Xavier, J.; Pereira, F.; Morais, J.; de Moura, M. Direct evaluation of mixed mode I+II cohesive laws of wood by coupling MMB test with DIC. *Materials* **2021**, *14*, 374. [CrossRef] [PubMed]
6. Piazza, M.; Riggio, M. Visual strength-grading and NDT of timber in traditional structures. *J. Build. Apprais.* **2008**, *3*, 267–296. [CrossRef]
7. Ilharco, T.; Lechner, T.; Nowak, T. Assessment of timber floors by means of non-destructive testing methods. *Constr. Build. Mater.* **2015**, *101*, 1206–1214. [CrossRef]
8. Lechner, T.; Nowak, T.; Kliger, R. In situ assessment of the timber floor structure of the Skansen Lejonet fortification, Sweden. *Constr. Build. Mater.* **2014**, *58*, 85–93. [CrossRef]
9. Riggio, M.; Anthony, R.; Augelli, F.; Kasal, B.; Lechner, T.; Muller, W.; Tannert, T. In situ assessment of structural timber using non-destructive techniques. *Mater. Struct.* **2014**, *47*, 749–766. [CrossRef]
10. Dackermann, U.; Crews, K.; Kasal, B.; Li, J.; Riggio, M.; Rinn, F.; Tannert, T. In situ assessment of structural timber using stress-wave measurements. *Mater. Struct.* **2014**, *47*, 787–803. [CrossRef]
11. Tannert, T.; Anthony, R.; Kasal, B.; Kloiber, M.; Piazza, M.; Riggio, M.; Rinn, F.; Widmann, R.; Yamaguchi, N. In situ assessment of structural timber using semi-destructive techniques. *Mater. Struct.* **2014**, *47*, 767–785. [CrossRef]
12. Kloiber, M.; Tippner, J.; Hrivnák, J. Mechanical properties of wood examined by semi-destructive devices. *Mater. Struct.* **2014**, *47*, 199–212. [CrossRef]
13. Kasal, B. Semi-destructive method for in-situ evaluation of compressive strength of wood structural members. *For. Prod. J.* **2003**, *53*, 55–58.
14. Jaskowska-Lemanska, J.; Przesmycka, E. Semi-destructive and non-destructive tests of timber structure of various moisture contents. *Materials* **2021**, *14*, 96. [CrossRef]
15. Dolwin, J.A.; Lonsdale, D.; Barnett, J. Detection of decay in trees. *Arboric. J.* **1999**, *23*, 139–149. [CrossRef]
16. *ISO 13822:2010—Bases for Design of Structures—Assessment of Existing Structures*; International Organization for Standardization: Geneva, Switzerland, 2010.
17. *PN-EN 17121:2020-01—Conservation of Cultural Heritage. Historic Timber Structures. Guidelines for the On-Site Assessment of Load-Bearing Timber Structures*; Polish Committee for Standardization: Warsaw, Poland, 2020.
18. *UNI 11119:2004—Cultural Heritage—Wooden Artefacts—Load-Bearing Structures—On Site Inspections for the Diagnosis of Timber Members*; Ente Nazionale Italiano di Unificazione (UNI): Milano, Italy, 2004.
19. *UNI 11138:2004—Cultural Heritage—Wooden Artefacts—Building Load Bearing Structures—Criteria for the Preliminary Evaluation, the Design and the Execution of Works*; Ente Nazionale Italiano di Unificazione (UNI): Milano, Italy, 2004.
20. *SIA 269/5:2011—Existing Structures—Timber Structures*; Swiss Society of Engineers and Architects (SIA): Zurich, Switzerland, 2011.
21. Perria, E.; Sieder, M. Six-steps process of structural assessment of heritage timber structures: Definition based on the state of the art. *Buildings* **2020**, *10*, 109. [CrossRef]
22. Jasieńko, J.; Nowak, T.; Hamrol, K. Selected methods of diagnosis of historic timber structures—Principles and possibilities of assessment. *Adv. Mater. Res.* **2013**, *778*, 225–232. [CrossRef]
23. Sanabria, S.; Furrer, R.; Neuenschwander, J.; Niemz, P.; Sennhauser, U. Air-coupled ultrasound inspection of glued laminated timber. *Holzforschung* **2011**, *65*, 377–387. [CrossRef]
24. As, N.; Senalik, C.A.; Ross, R.J.; Wang, X.; Farber, B. *Nondestructive Evaluation of the Tensile Properties of Structural Lumber from the Spruce-Pine-Fir Species Grouping: Relationship between Modulus of Elasticity and Ultimate Tension Stress*; Research Note FPL-RN-0383; Department of Agriculture, Forest Service, Forest Products Laboratory: Madison, WI, USA, 2020; p. 12.
25. Divos, F.; Tanaka, T. Relation between static and dynamic modulus of elasticity of wood. *Acta Silv. Lign. Hung.* **2005**, *1*, 105–110.
26. Nowak, T.; Jasieńko, J.; Hamrol-Bielecka, K. In situ assessment of structural timber using the resistance drilling method—Evaluation of usefulness. *Constr. Build. Mater.* **2016**, *102*, 403–415. [CrossRef]
27. Jasieńko, J.; Nowak, T.; Bednarz, Ł. Wrocław University's Leopoldinum Auditorium—Tests of its ceiling and a conservation and strengthening concept. *Adv. Mater. Res.* **2010**, *133*, 265–270. [CrossRef]
28. *PN-EN 384+A1:2018—Structural Timber. Determination of Characteristic Values of Mechanical Properties and Density*; Polish Committee for Standardization: Warsaw, Poland, 2018.
29. *PN-EN 408+A1: 2012—Structural Timber and Glued Laminated Timber. Determination of Some Physical and Mechanical Properties*; Polish Committee for Standardization: Warsaw, Poland, 2012.
30. *ISO 13061-3—Physical and Mechanical Properties of Wood—Test Methods for Small Clear Wood Specimens—Part 3: Determination of Ultimate Strength in Static Bending*; International Organization for Standardization: Geneva, Switzerland, 2014.
31. *ISO 13061-4—Physical and Mechanical Properties of Wood—Test Methods for Small Clear Wood Specimens—Part 4: Determination of Modulus of Elasticity in Static Bending*; International Organization for Standardization: Geneva, Switzerland, 2014.
32. *PN-77/D-04103—Wood. Determination of Static Bending Strength*; Polish Committee for Standardization: Warsaw, Poland, 1977.
33. *ASTM D143-14—Standard Test Method for Small Clear Specimen of Timber*; American Society for Testing Material Standard: West Conshohocken, PA, USA, 2014.

34. *PN-63/D-04117—Physical and Mechanical Properties of Wood. Determination of the Elasticity Coefficient for Static Bending*; Polish Committee for Standardization: Warsaw, Poland, 1963.
35. *BS 373:1957—Methods of Testing Small Clear Specimens of Timber*; British Standards Institution: London, UK, 1957.
36. *ISO 3133:1975—Wood—Determination of Ultimate Strength in Static Bending*; International Organization for Standardization: Geneva, Switzerland, 1975.
37. Hu, W.; Wan, H.; Guan, H. Size effect on the elastic mechanical properties of beech and its application in finite element analysis of wood structures. *Forests* **2019**, *10*, 783. [CrossRef]
38. Straže, A.; Gorišek, Z. Analysis of size effect on determination of mechanical properties of Norway spruce wood. In Proceedings of the 22nd International Scientific Conference on Wood is Good-EU Pre Accession Challenges of the Sector, Zagreb, Croatia, 21 October 2011; pp. 183–190.
39. Madsen, B.; Tomoi, M. Size effects occurring in defect-free spruce-pine-fir bending specimens. *Can. J. Civ. Eng.* **1991**, *18*, 637–643. [CrossRef]
40. Madsen, B.; Nielsen, P.C. *In-Grade Testing: Size Investigation on Lumber Subjected to Bending*; Structural Research Series; Report No. 15; Department of Civil Engineering, University of British Columbia: Vancouver, BC, Canada, 1976; p. 10.
41. Fotsing, J.A.; Foudjet, A. Size effect of two Cameroonian hardwoods in compression and bending parallel to the Grain. *Holzforschung* **1995**, *49*, 376–378. [CrossRef]
42. Zhou, H.B.; Ren, H.Q.; Lu, J.X. Size effect of length on flexural strength of Chinese fir dimension lumber used in wood structure. *J. Build. Mater.* **2009**, *12*, 501–504. (In Chinese)
43. Zhou, H.B.; Han, L.Y.; Ren, H.Q.; Lu, J.X. Size effect on strength properties of Chinese larch dimension lumber. *BioResources* **2015**, *10*, 3790–3797. [CrossRef]
44. *ASTM D245-06(2019)—Standard Practice for Establishing Structural Grades and Related Allowable Properties for Visually Graded Lumber*; ASTM International: West Conshohocken, PA, USA, 2019.
45. *PN-EN 14081-1:2016—Timber Structures. Strength Graded Structural Timber with Rectangular Cross Section. Part 1: General Requirements*; Polish Committee for Standardization: Warsaw, Poland, 2016.
46. *PN-EN 338: 2016—Structural Timber. Strength Classes*; Polish Committee for Standardization: Warsaw, Poland, 2016.
47. *PN-D-94021:2013—Strength Graded Structural Timber*; Polish Committee for Standardization: Warsaw, Poland, 2013.
48. Wdowiak, A.; Brol, J. Methods of strength grading of structural timber—Comparative analysis of visual and machine grading on the example of scots pine timber from four natural forest regions of Poland. *Struct. Environ.* **2019**, *11*, 210–224. [CrossRef]
49. *PN-EN 1995-1-1:2010—Eurocode 5: Design of Timber Structures—Part 1: General-Common Rules and Rules for Buildings*; Polish Committee for Standardization: Warsaw, Poland, 2010.
50. Kasal, B.; Lear, G.; Tannert, T. Stress waves. In *In Situ Assessment of Structural Timber. RILEM State-of-the-Art Reports*; Kasal, B., Tannert, T., Eds.; Springer: Dordrecht, The Netherlands, 2010; Volume 7, pp. 5–24. ISBN 978-94-007-0559-3.
51. Wang, X.; Divos, F.; Pilon, C.; Brashaw, B.K.; Ross, R.J.; Pellerin, R.F. *Assessment of Decay in Standing Timber Using Stress Wave Timing Nondestructive Evaluation Tools: A Guide for Use and Interpretation*; Gen. Tech. Rep. FPL-GTR-147; US Department of Agriculture, Forest Service, Forest Products Laboratory: Madison, WI, USA, 2004.
52. Bodig, J.; Jayne, B.A. *Mechanics of Wood and Wood Composites*; Van Nostrand Reinhold: New York, NY, USA, 1982.
53. Íñiguez- González, G. Clasificación Mediante Técnicas no Destructivas y Evaluación de las Propiedades Mecánicas de la Madera Aserrada de Coníferas de Gran Escuadría Para uso Structural. Ph.D. Thesis, Universidad Politécnica de Madrid, ETS de Ingenieros de Montes, Madrid, Spain, 2007. (In Spanish)
54. Rinn, F. Basics of micro-resistance drilling for timber inspection. *Holztechnologie* **2012**, *53*, 24–29.
55. Anthony, R.W. Nondestructive evaluation: Wood. *APT Bull.* **2010**, *41*, 1–6.
56. Feio, A.O.; Lourenço, P.B.; Machado, J.S. Testing and modeling of a traditional timber mortise and tenon joint. *Mater. Struct.* **2014**, *47*, 213–225. [CrossRef]
57. Feio, A.O.; Machado, J.S.; Lourenço, P.B. Compressive behavior and NDT correlations for chestnut wood (*Castanea sativa* Mill.). In Proceedings of the 4th International Seminar on Structural Analysis of Historical Constructions, Padova, Italy, 10–13 November 2004; pp. 369–375.
58. *PN-EN 384:2011—Structural Timber. Determination of Characteristic Values of Mechanical Properties and Density*; Polish Committee for Standardization: Warsaw, Poland, 2011.
59. *ISO 3129:2019—Wood—Sampling Methods and General Requirements for Physical and Mechanical Testing of Small Clear Wood Specimens*; International Organization for Standardization: Geneva, Switzerland, 2019.
60. Krzysik, F. *Nauka o Drewnie (Wood Science)*; PWN: Warsaw, Poland, 1978. (In Polish)
61. Ross, R.J. *Wood Handbook: Wood as an Engineering Material, Centennial Edition*; U.S. Dept. of Agriculture, Forest Service, Forest Products Laboratory: Madison, WI, USA, 2010.
62. Lokaj, A.; Dobes, P.; Sucharda, O. Effects of loaded end distance and moisture content on the behavior of bolted connections in squared and round timber subjected to tension parallel to the grain. *Materials* **2020**, *13*, 5525. [CrossRef] [PubMed]
63. *ISO 12491:1997—Statistical Methods for Quality Control of Building Materials and Components*; International Organization for Standardization: Geneva, Switzerland, 2010.
64. *PN-EN 14358:2016-08—Timber Structures. Calculation and Verification of Characteristic Values*; Polish Committee for Standardization: Warsaw, Poland, 2016.

65. *PN-EN 1990:2004—Basis of Structural Design*; Polish Committee for Standardization: Warsaw, Poland, 2004.
66. Mirski, R.; Dziurka, D.; Chuda-Kowalska, M.; Wieruszewski, M.; Kawalerczyk, J.; Trociński, A. The usefulness of pine timber (Pinus sylvestris L.) for the production of structural elements. Part I: Evaluation of the quality of the pine timber in the bending test. *Materials* **2020**, *13*, 3957. [CrossRef] [PubMed]

Article

Effective Length Prediction and Pullout Design of Geosynthetic Strips Based on Pullout Resistance

Jeongjun Park [1] and Gigwon Hong [2],*

[1] Incheon Disaster Prevention Research Center, Incheon National University, Incheon 22012, Korea; smearjun@hanmail.net
[2] Department of Civil and Disaster Prevention Engineering, Halla University, Wonju-si 26404, Korea
* Correspondence: g.hong@halla.ac.kr

Abstract: In this study, pullout tests were conducted on geosynthetic strips which can be applied to a block-type front wall. Based on the test results, the effective length is predicted, and the pullout design results are presented. In other words, the pullout displacement–pullout load relationship of all geosynthetic strips was analyzed using the pullout test results, and their effective lengths were predicted. It was found that the reinforcement width affected the pullout force for the geosynthetic strips at the same tensile strength. The pullout behavior was evidenced within a range of approximately 0.45 L of the total length of the reinforcement (L) and hardly occurred beyond a certain distance from the geosynthetic strips front regardless of the normal stress. Based on these pullout behavioral characteristics, a method is proposed for the prediction of the effective length (L_E) and maximum effective length ($L_{E(max)}$) of a geosynthetic strip. The pullout strength was compared using the total area and effective area methods in accordance with the proposed method. In the case of the total area method, GS50W (width: 50 mm) and GS70W (width: 70 mm) exhibited similar pullout strengths. The pullout strength by the effective area method, however, was found to be affected by the soil-reinforcement interface adhesion. The proposed method used for the prediction of the effective length of a geosynthetic strip was evaluated using a design case. It was confirmed that the method achieved an economical design in instances in which the pullout resistance by the effective length (L_E) was applied compared with the existing method.

Keywords: geosynthetic; design; pullout resistance; effective length; reinforced earth

1. Introduction

Reinforced earth achieves reinforcement with high-tensile strength, and it has been used as a method to improve the stability of various geotechnical structures by decreasing the earth pressure and by increasing the shear strength [1–13]. Among the various structures, mechanically stabilized earth (MSE) walls are mainly divided in panel and block types, depending on the type of the facing wall. Because the inhibition of horizontal deformation in the facing wall is required for vertical MSE walls using reinforced earth, various reinforcements have been developed. Reinforcements that are applied to MSE walls are classified as inextensible and extensible reinforcements, depending on the material, and extensible reinforcements, such as geogrids and geosynthetic strips, have been mainly used in the late stages. In South Korea, in particular, block-type MSE walls with geogrids have been mainly applied owing to their economic feasibility and appearance, and geosynthetic strips that are applicable to block-type facing walls have been developed.

The design of the MSE walls was based on internal and external stability. To achieve internal stability, fracture and failure are determined by the tensile strength of the reinforcement. The pullout failure of the resistance area is based on the soil-reinforcement interaction, which is very important for the behavior of MSE walls. The mechanism associated with this failure is very complex because it depends on the characteristics of the

soil-reinforcement interaction [14]. In particular, because embedded extensible reinforcement may exhibit tensile deformation owing to load transfer during the pullout process, load transfer must be considered in pullout resistance evaluation. Therefore, it is necessary to analyze the pullout behavior of the reinforcement to secure the stability of the MSE walls and to calculate reasonable design parameters. Many studies have been conducted on the reinforcement interaction. Experimental studies have been conducted on the pullout behavior of grid-type inextensible and extensible reinforcements applied in sand and cohesive soil [15–22]. In addition, studies on methods for evaluating the pullout resistance of reinforcement have been conducted based on experimental research [23–25], and a number of studies on the theoretical and numerical analysis of the soil-reinforcement interaction have also been conducted [26–29]. Studies have been conducted on the influence of soil conditions on the pullout resistance of reinforcement [30–32]. Additional studies have been conducted on the shear resistance of reinforced soil and on interactions using mixed soil [33–35]. Grid-type reinforcement has been used in many studies, but studies on the pullout behavior of geosynthetic strips have been conducted to extend the applicability of geosynthetic strips [27,28,36,37].

In this study, pullout tests on geosynthetic strips were conducted to ensure the design applicability of these strips to block-type facing walls. Based on the test results, the pullout displacement–pullout load relationship was analyzed to evaluate the pullout behavior of the geosynthetic strips. In addition, the effective length that induced the pullout resistance of a geosynthetic strip in the soil was predicted. The pullout parameters were derived using the predicted effective length, and they were applied to a design case to evaluate the effective length prediction method.

2. Theoretical Background of Reinforcement Pullout

2.1. Soil-Reinforcement Interaction under Pullout Condition

The interaction between the soil and embedded reinforcement consists of two mechanisms: the shear resistance (friction resistance) on the top and bottom surfaces of the reinforcement, and the bearing resistance of the supporting member. The pullout resistance that uses these mechanisms is expressed by Equation (1) by FHWA [38].

$$P_r = 2 \, L_e \, \sigma'_v \, \alpha \, F^*, \tag{1}$$

where L_e is the embedded length in the resistant zone; σ'_v is effective vertical stress at soil-reinforcement interfaces, α is the scale effect correction factor, $F^*(= f_b \cdot tan\varnothing = tan\delta)$ is the pullout resistance factor, f_b is the soil-reinforcement bond coefficient, $\varnothing$ is the internal friction angle of soil, and δ is the soil-reinforcement interface friction angle.

The pullout resistance factor includes both friction and bearing resistance elements. Because geosynthetic strips develop pullout resistance owing to friction, the pullout resistance factor is identical to the friction angle of the soil-reinforcement interface. The pullout resistance factor is determined by the bond coefficient (f_b, soil-reinforcement bond coefficient) caused by the soil-reinforcement interaction. The bond coefficient is defined as the ratio of the shear strength on the soil-reinforcement interface to the shear strength of the soil, as shown by Equation (2) [33].

$$f_b = \frac{\tau_p}{\tau} = \frac{c_p + \sigma'_v \, tan\delta}{c + \sigma'_v \, tan\varnothing}, \tag{2}$$

where τ_p is the shear strength at the soil-reinforcement interface, τ is the shear strength of the soil, c_p is the soil-reinforcement interface adhesion, and c is the cohesion in the soil.

In this instance, the shear strength at the soil-reinforcement interface can be calculated using the surface area of the reinforcement and the pullout force from the pullout test results. The mechanism of soil-reinforcement interaction can be confirmed in detail through schematic diagrams in previous studies [33,38].

2.2. Evaluation Method on Pullout Resistance of Geosynthetic Strip

For inextensible reinforcement, the pullout resistance design parameters can be easily calculated using the shear strength on the soil-inextensible reinforcement interface because there is little change in the contact area between the reinforcement and soil attributed to tensile deformation during the pullout process. However, extensible reinforcement exhibits tensile deformation in normal stress conditions in soil. In other words, the pullout displacement of the reinforcement decreased as the distance from the front increased during the pullout process. Therefore, the effective area (contact area between the reinforcement and soil) is a very important factor for the calculation of the pullout resistance design parameters of extensible reinforcement.

Ochiai et al. [23] proposed a soil-reinforcement shear strength evaluation method using pullout test results to evaluate the pullout resistance of the extensible reinforcement. This evaluation method comprises a mobilizing process method and an average resistance method. The mobilizing process method evaluates the pullout resistance using the difference in tensile forces between two nodes in arbitrary pullout force conditions and is applicable only to grid-type reinforcement. The average resistance method evaluates the pullout resistance by considering the pullout force distribution along the reinforcement length subject to the maximum pullout force condition and based on the use of the average pullout force. The average resistance method is subclassified in the total area, effective area, and maximum slope methods, depending on the average value calculation method. Their evaluation methods were as follows.

First, the total area method assumes that the pullout resistance applies to the entire area of the reinforcement and is expressed in the form of Equation (3).

$$\tau_{av} = \frac{F_{T_{max}}}{2BL}, \tag{3}$$

where B and L are the width and length of the reinforcement, respectively, and $F_{T_{max}}$ is the maximum pullout force.

The effective area method assumes that the pullout resistance applies only to the area wherein the tensile deformation of the reinforcement occurs and is expressed in the form of Equation (4).

$$\tau_{av} = \frac{F_{T_{max}} - F_r}{2BL_T}, \tag{4}$$

where L_T is the effective length of the reinforcement, and $F_{T_{max}} - F_r$ is the effective tensile force corresponding to L_T.

Finally, the maximum slope method assumes the pullout resistance when the slope of the tangent in the reinforcement-length–tensile-force distribution curve has a maximum value and is expressed according to Equation (5).

$$\tau_{av} = \left(\frac{dF}{dL}\right)_{max} \tag{5}$$

The mechanism of each evaluation method can be confirmed in detail through the figures in the previous study [23].

3. Pullout Tests

Large-scale pullout tests were conducted to evaluate the pullout behavior of the geosynthetic strips.

3.1. Apparatus of Large-Scale Pullout Test

The apparatus for the large-scale pullout test was composed of a rigid (soil) box, a load (normal and pullout) device, and a control box as shown in Figure 1. The rigid box (length: 1600 mm, width: 760 mm, and height: 550 mm) was larger than the minimum recommendations (610 mm length, 460 mm width, and 305 mm height) specified in ASTM

D6706-01 [39]. For normal stress, uniformly distributed loading was enabled using an air bag in consideration of the field loading conditions, and up to 500 kN/m^2 could be applied. For pullout loads, up to 200 kN could be applied using the displacement control method (0.5 to 30 mm/min).
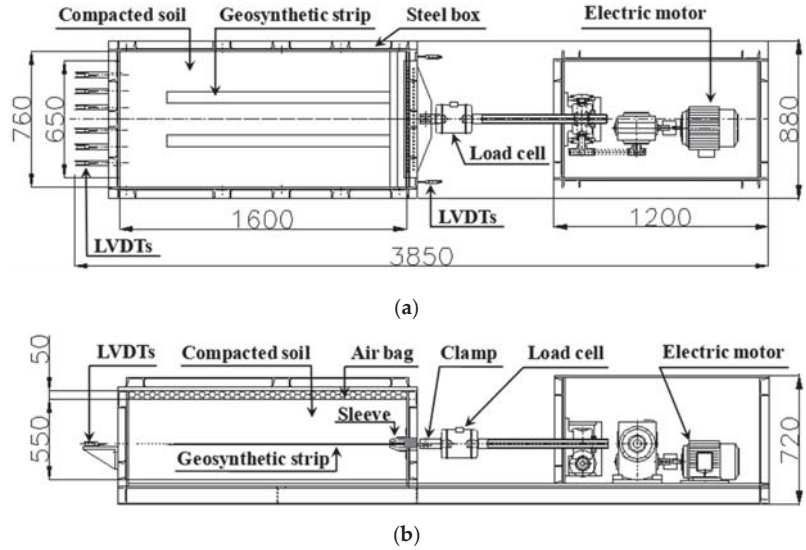

(**a**)

(**b**)

Figure 1. Schematic of large-scale pullout test apparatus: (**a**) plan view; (**b**) cross-sectional views (dimensions in millimeters).

3.2. Materials

3.2.1. Soil

The soil samples used in this study were weathered granite soil samples. It is the most extensively distributed soil type in Korea [40] and is a typical nonplastic cohesive soil that contains fine-grained soil. The soil sample was classified as SW based on the USCS. The particle size distribution and engineering properties of the soil are shown in Figure 2 and Table 1, respectively. The model soil for the pullout tests was compacted with an optimum water content of 14.1%, and a maximum dry unit weight of 18.8 kN/m^2 was achieved. The shear strength of the soil by direct shear tests was 8.7 kPa, and the internal friction angle was 35.6°.
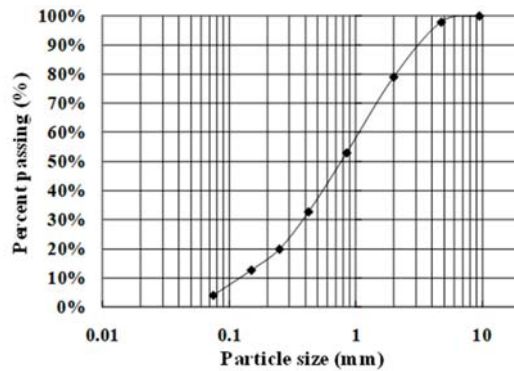

Figure 2. Particle size distribution of soil.

Table 1. Engineering properties of weathered granite soil.

Specific Gravity (G_S)	Plastic Limit (w_P, %)	Maximum Dry Unit Weight ($\gamma_{d,max}$, kN/m³)	Optimum Water Content (w_{op}, %)	Friction Angle (Φ, °)	Cohesion (c, kPa)	USCS
2.67	NP (Nonplastic)	18.8	14.1	35.5	8.7	SW (Well-graded sand)

3.2.2. Geosynthetic Strip

As shown in Figure 3, the geosynthetic strips used in the pullout tests consisted of high-strength polyester and polyethylene. The widths of the geosynthetic strips were 50 and 70 mm, respectively, and both had a manufacturing strength of 25 kN. Geosynthetic strips with widths of 50 and 70 mm were used to investigate the pullout resistance characteristics according to the effective area for the same tensile strength condition.
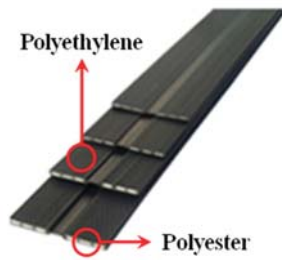

Figure 3. Composition of geosynthetic strip.

The wide-width tensile test on the geosynthetic strips with different widths was conducted five times, and the averaged results are shown in Figure 4.
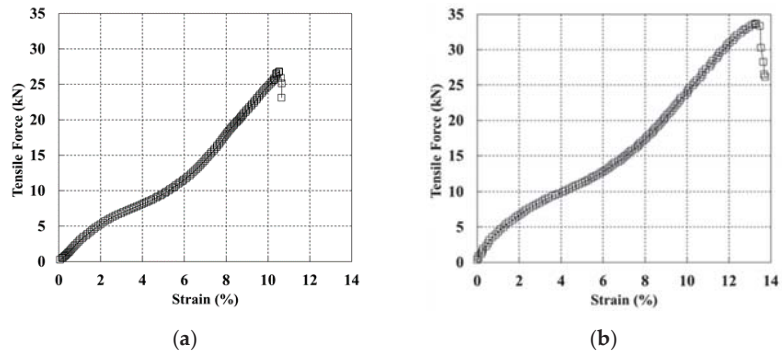

Figure 4. Relationship between tensile force and strain on the reinforcement with widths equal to: (**a**) width 50 mm; (**b**) width 70 mm.

For the geosynthetic strip with a width of 50 mm, the maximum tensile strength was found to be 26.8 kN, and the tensile strain was 10.5%. For the geosynthetic strip with a width of 70 mm, the maximum tensile strength and tensile strain were found to be 33.6 kN and 13.3%, respectively. The tensile strength and tensile strain increased as the width increased, and the two geosynthetic strips exhibited similar tensile deformation behaviors. As the tensile strengths obtained from the wide-width tensile test were higher than the manufacturing strength, there was no problem in applying the geosynthetic strips to pullout tests.

3.3. Testing Program

Large-scale pullout tests were conducted in accordance with the ASTM D 6706-01 test method [39].

As shown in Figure 5, the model soil was divided into upper and lower parts with respect to the reinforcement and each part was compacted in three layers with the use of a rammer (impact number per min: 640–680) with an impact force of 14 kN. The compaction rate of each layer was higher than 95%. Figure 5 shows the reinforcement installed in the soil and the deformation measurement positions. The deformation measurement positions were selected to evaluate the effective length through the tensile strain and pullout force distribution in the reinforcement based on previous studies [23,28,30]. In all cases, the pullout deformation was controlled with a strain rate of 1 mm/min, and a backfill height of approximately 8.0 m was applied for the maximum normal stress. In addition, lubrication was performed using wrap and oil to minimize the influence of the wall friction of the soil box.
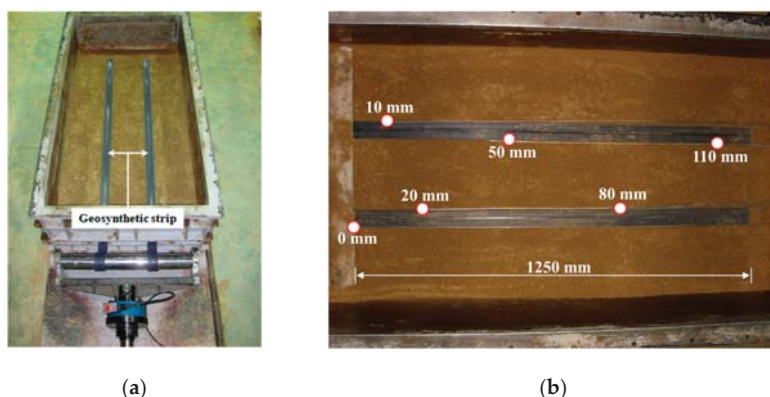

(a)   (b)

Figure 5. View of the installed geosynthetic strip: (**a**) setup view; (**b**) measurement locations.

In the testing program, different horizontal spacings (260 and 210 mm) were applied for the installation of the two types (50 and 70 mm widths) of the geosynthetic strips based on considerations of the applied block-type facing wall, as shown in Table 2. In this instance, when the horizontal spacing was 210 mm, pullout tests were conducted only in the normal stress condition (100 kPa). This corresponded to a backfill height of approximately 5 m in consideration of the most extensively applied MSE wall height in Korea for examination of the influence of the horizontal spacing.

Table 2. Testing program of geosynthetic strip pullout.

Reinforcement Width (mm)	Horizontal Spacing of Reinforcement (mm)	Normal Stress (σ_v, kPa)	Test Classification
50	260	50, 100, 150	GS50W
	210	100	GS50N
70	260	50, 100, 150	GS70W
	210	100	GS70N

4. Test Results and Analysis

4.1. Test Results

Based on the pullout force–pullout displacement relationship from the pullout test results, the pullout strength characteristics of the reinforcement can be evaluated using the maximum pullout force at each normal stress condition. In this study, the maximum

pullout force for pullout strength evaluation was selected by referring to the displacement criteria suggested in the FHWA design criteria [38]. In other words, when the end displacement of the reinforcement installed in soil was less than 15 mm, it was necessary to determine the development of the maximum pullout force. This means that the pullout force corresponding to an end displacement of 15 mm must be applied as the maximum pullout force if the end displacement of the replacement exceeds 15 mm in the case in which the maximum pullout force was developed. Therefore, as shown in Figure 5b, the measurement position of 110 m from the front sides of the linear variable differential transformers installed in the reinforcement was applied as the end displacement.

In the cases of normal stress conditions of 50, 100, and 150 kPa, the maximum pullout forces were found to be 14.6, 20.4, and 26.8 kN for GS50W, and 19.3, 28.2, and 34.3 kN for GS70W, respectively.

Considering the FHWA design criteria [38], the relationships between the pullout force and front/end displacement according to the width of the geosynthetic strip and the horizontal spacing of reinforcement are shown in Figures 6 and 7. In all experimental cases, the maximum pullout force was observed when the front displacement ranged between 25 and 35 mm (Figure 6). Specifically, the maximum pullout force was approximately 5 to 8 kN higher when the width was 70 mm compared with a width of 50 mm. This is similar to the results of the wide-width tensile test. The maximum pullout force generated at the end displacement also satisfied the FHWA design criteria [38] (Figure 7).
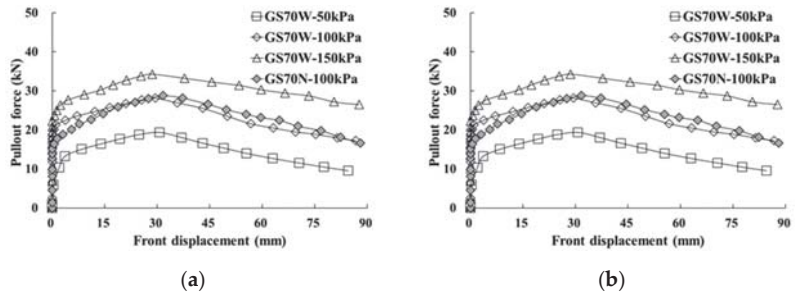

Figure 6. Relationship between pullout force and front displacement for widths equal to: (**a**) 50 mm; (**b**) 70 mm.
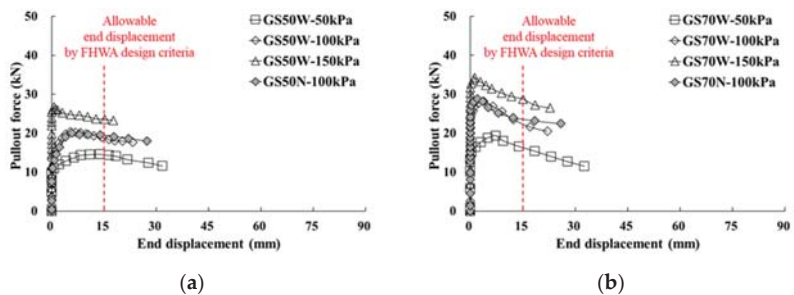

Figure 7. Relationship between pullout force and end displacement for widths equal to: (**a**) 50 mm; (**b**) 70 mm.

From the pullout force–pullout displacement relationship at a normal stress of 100 kPa, the pullout force–front displacement relationship and the pullout force–end displacement relationship exhibited similar behaviors regardless of the horizontal spacing of the reinforcement. In other words, it was confirmed that friction-resistance reinforcement with the

same tensile strength exhibited the same pullout resistance and similar pullout behavior if the installation areas per unit width were identical. Therefore, the analysis used for the prediction of the pullout behavior and effective length of the reinforcement was conducted using only the test results with a larger horizontal spacing (260 mm, GS50W, and GS70W).

4.2. Pullout Behavior of Geosynthetic Strip

Figure 8a–c or Figure 9a–c show the pullout displacements as a function of the distance from the reinforcement front. The front pullout displacement was applied to a maximum of 60 mm after the maximum pullout force was developed. As the front pullout displacement increased, the displacement at each position showed a tendency to increase regardless of the reinforcement width. The displacement difference increased as the distance from the reinforcement front approached zero. This tendency was more obvious when the reinforcement width was wider (GS70W) and during exposure to higher normal stress conditions. Therefore, it was found that the pullout force transmitted to the reinforcement in soil during the pullout process was maximized at the front and decreased as the distance from the front increased. It was also found that the pullout force induced by the increase in normal stress was concentrated at the front.
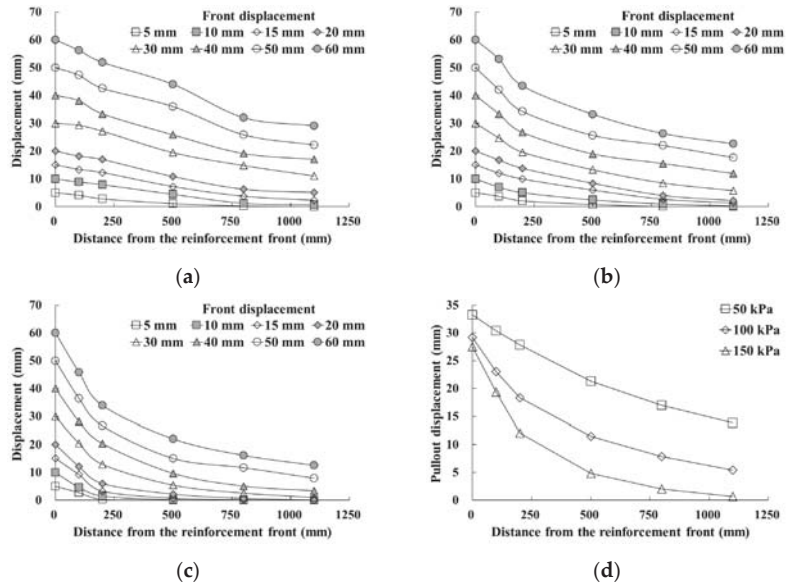

Figure 8. Displacement as a function of distance from the geosynthetic strip front: (**a**) GS50W-50 kPa; (**b**) GS50W-100 kPa; (**c**) GS50W-150 kPa; (**d**) pullout displacement of reinforcement in maximum pullout force.

Figure 8d or Figure 9d show the pullout displacement according to the distance from the reinforcement front under the maximum pullout force condition. As shown in the figures, the pullout displacement decreased as the normal stress increased. At positions near the front, the reduction rate of the displacement increased at normal stress conditions. However, when the distance from the front exceeded approximately 45% to 50% of the entire reinforcement length, the reduction rates were found to be similar.

Figure 10 shows the results of analyzing the pullout force induced in the geosynthetic strips at the maximum pullout condition using the pullout displacement evaluation results according to the distance from the reinforcement front. The distance from the front was

applied as the ratio of the displacement measurement position length (L_i) to the total length of the reinforcement (L).
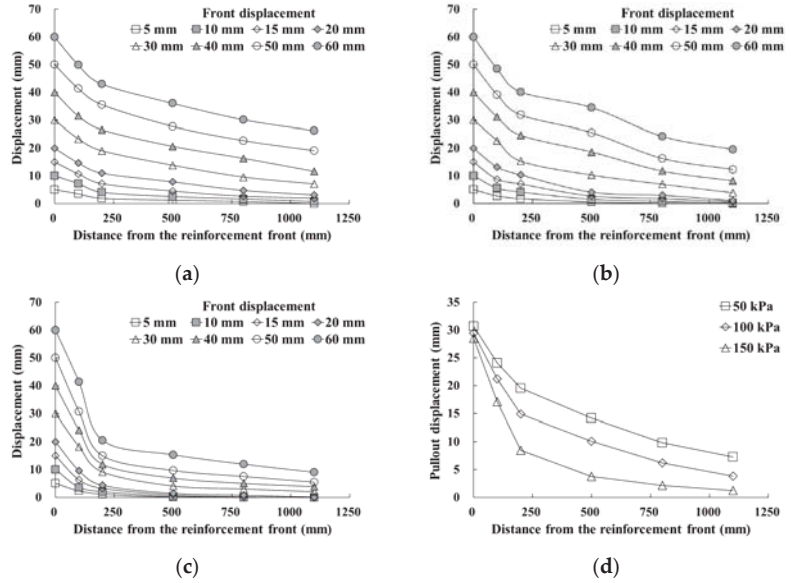

Figure 9. Displacement as a function of distance from the geosynthetic strip front: (**a**) GS70W-50 kPa; (**b**) GS70W-100 kPa; (**c**) GS70W-150 kPa; (**d**) pullout displacement of reinforcement in maximum pullout.
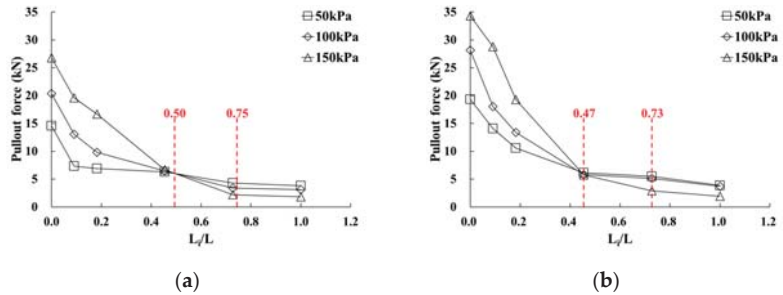

Figure 10. Relationship between pullout force and L_i/L according to reinforcement width: (**a**) GS50W; (**b**) GS70W.

It was found that the pullout force induced in the geosynthetic strips occurred for a length ratio (L_i/L) of approximately 0.45. In addition, it was found that 57–75% of the pullout force was induced at the front in the case of GS50W, and 68–83% in the case of GS70W, depending on normal stress conditions. For cases GS50W and GS70W, similar pullout forces were induced subject to the length ratio conditions of 0.5 L and 0.47 L, respectively. Furthermore, there was little change in the induced pullout force after 0.75 L and 0.73 L, at which the tensile strain values of GS50W and GS70W (calculated based on Figures 8 and 9) were approximately 1%.

4.3. Prediction of Effective Length Considering Pullout Force

The pullout force distribution in the geosynthetic strip occurred within a limited reinforcement length range. Therefore, it will be possible to achieve a more economical design if the effective length at which the pullout resistance is induced by the pullout force is calculated. The relationship between the pullout force and L_i/L (as shown in Figure 10) can be simplified as shown in Figure 11, and it is possible to be used to reflect the experimental results. As mentioned previously, in the cases of GS50W and GS70W, the pullout forces of the reinforcement at normal stress conditions became almost similar at a length ratio (L_i/L) of approximately 0.5 L. Subsequently, the induced pullout force decreased and then hardly changed after 0.75 L, at which the strain became approximately 1%. Therefore, the effective length of the geosynthetic strips used in this study was determined as follows: the effective length ($L_E = 0.5$ L) was defined as the length at which the pullout force became almost similar, regardless of the normal stress, and the maximum effective length ($L_{E(max)} = 0.75$ L) as the distance at which the pullout force hardly changed.
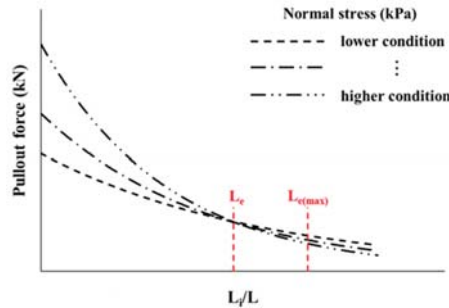

Figure 11. Prediction of effective length using the pullout force generated in reinforcement cases.

4.4. Evaluation of Pullout Resistance Considering the Prediction of Effective Length

To evaluate the effective length prediction method presented in Section 4.3, the pullout strength was evaluated according to the effective length (L_E) and maximum effective length ($L_{E(max)}$), respectively, based on the use of the average resistance method proposed by [23]. The pullout strength was evaluated using the total and effective area methods based on consideration of the extensibility of the geosynthetic strips, and the results are shown in Figure 12 and Table 3.
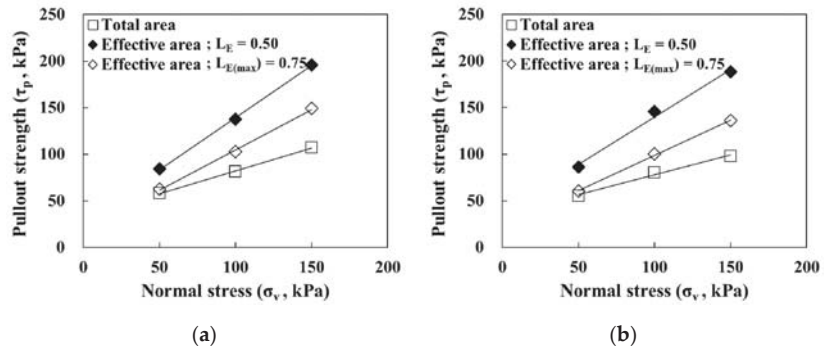

Figure 12. Relationship between normal stress and pullout strength: (**a**) GS50W; (**b**) GS70W.

Regarding the pullout strength of GS50W based on considerations of the maximum effective length ($L_{E(max)}$), the results of the effective area method and total area method

were similar at low normal stress conditions because the pullout force was transmitted to the maximum effective length ($L_{E(max)}$). However, as the normal stress increased, the pullout strength gradually increased because the pullout force transmitted to the maximum effective length ($L_{E(max)}$) decreased. For GS50W, the effective area method that considered the effective length (L_E) yielded a higher pullout strength in normal stress conditions compared with the total and the effective area methods that considered the maximum effective length ($L_{E(max)}$) because the distance from the front decreased. The same tendency was observed for GS70W.

Table 3. Summary of pullout parameters.

Classification Tests	Pullout Resistance Evaluation Methods	Pullout Parameter	
		Soil-Reinforcement Interface Friction Angle (c_p, °)	Soil-Reinforcement Interface Friction Angle (δ, °)
50	Total area	33.6	26.0
	Effective area (L_E)	27.4	48.2
	Effective area ($L_{E(max)}$)	18.6	40.8
70	Total area	35.1	23.1
	Effective area (L_E)	38.1	45.6
	Effective area ($L_{E(max)}$)	23.2	37.1

The pullout strengths of GS50W and GS70W with respect to the reinforcement width were compared. GS50W and GS70W exhibited similar pullout strengths based on the total area method. The pullout strength obtained by the effective area method, however, showed that the reinforcement width had an influence on the soil-reinforcement interface adhesion. This was more obvious when the effective length (L_E) was applied.

Figure 13 shows the calculation results of the bond coefficient of the geosynthetic strips using the shear strength of the soil and the pullout strength ratio of the soil-reinforcement interface. For all evaluation methods, the bond coefficient slowly decreased and then exhibited a tendency to converge as the normal stress increased. Tatlisoz et al. [33] reported that the soil-reinforcement interface adhesion was sufficient when the bond coefficient was 1.0, and the adhesion was low when the bond coefficient was 0.5 or less. For GS50W and GS70W, the bond coefficient was the lowest when the normal stress was 150 kPa; the respective values were 0.88 and 0.80 in the case of the total area method, respectively. These values are higher than the friction coefficient of soil (0.71) and are, thus, considered stable. Therefore, for a more efficient design of geosynthetic strips, the effective length (L_E) and maximum effective length ($L_{E(max)}$) can be considered. However, it is reasonable to apply the effective length (L_E) because there is no significant difference in the pullout force between the effective length (L_E) and maximum effective length ($L_{E(max)}$).
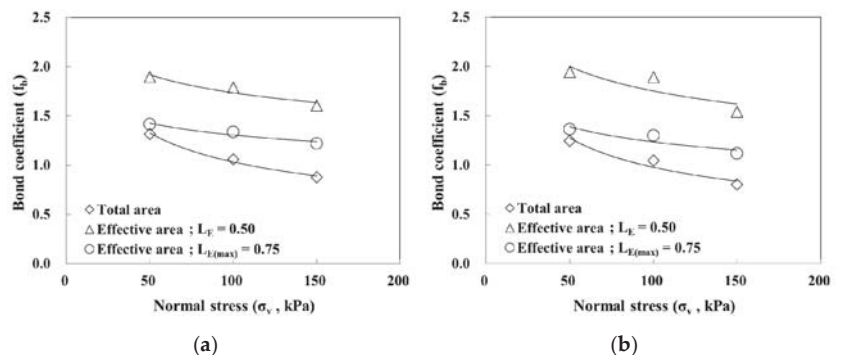

Figure 13. Relationship between normal stress and bond coefficient: (**a**) GS50W; (**b**) GS70W.

4.5. Design Case on Pullout Resistance Based on Considerations of the Effective Length

The effective length prediction method and bond coefficient were used and applied to the design case. The height of the block-type MSE wall applied to the design case was set to 7.8 m, which is close to the standard section of the block-type MSE wall in Korea. In this instance, the bond coefficient was set to the minimum value, which corresponded to the normal stress condition at 150 kPa to secure the stability of the structure, and the reinforcement installation length was set to 5.46 m (Figure 14). The FHWA design criteria [38] were applied to the design method.
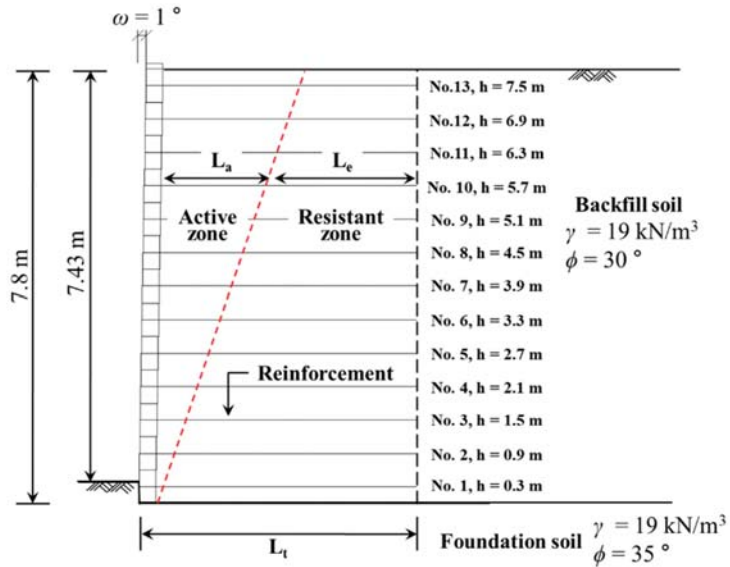

Figure 14. Cross-sectional view of design case.

Based on the proposed pullout resistance design method, the effective length of the reinforcement that satisfied the minimum stability for the internal and external stability of the MSE wall was calculated, and the results are listed in Table 4. Because all conditions were identical except for the bond coefficient, the reinforcement length (L_a) in the active zone was identical. However, when the effective length prediction method was applied to the pullout resistance evaluation method, the effective length and total length of the reinforcement in the resistant zone were calculated differently. In other words, the total area method exhibited the largest effective lengths for GS50W and GS70W, which satisfied the external and internal stability of the MSE wall, followed by $L_{E(max)}$ and L_E. This means that the design pattern that applied the total area method to the design of the pullout resistance of extensible reinforcement underestimated the stability of the structure. Therefore, the application of the effective area method that considered the effective length can lead to economical designs.

The effective length of GS70W was shorter than that of GS50W in the resistant zone because it had a higher area ratio owing to the reinforcement width. Therefore, it is possible to secure stability even if the total length of the reinforcement was reduced by 0.5 to 1 m based on the effective area evaluation method.

L_E can be applied to the design of the pullout resistance by considering the effective length of the geosynthetic strip. This method can satisfy both economic feasibility and stability. In the case of the application of weathered granite soil, which is generally used as backfill soil, it was confirmed that L_E and $L_{E(max)}$ took values that ranged from approximately 0.5 L to 0.75 L. Given that the pullout force generated between 0.5 L and

0.75 L had no significant influence on the stability of the MSE wall, the pullout resistance design method that used L_E based on the proposed method was sufficiently applicable.

Table 4. Design results according to pullout resistance methods (dimensions in m).

Reinforcement No.	Embbeded Height (m)	L_a, Active Zone (m)	L_e, Resistant Zone (m)						Stability on Pullout Resistance
			GS50W			**GS70W**			
			Total Area Method	Effective Area Method		Total Area Method	Effective Area Method		
				$L_E = 0.5$	$L_{E(max)} = 0.75$		$L_E = 0.5$	$L_{E(max)} = 0.75$	
1	0.3	0.168	6.332	5.332	5.732	5.832	5.292	5.332	
2	0.9	0.504	5.996	4.996	5.396	5.496	4.956	4.996	
3	1.5	0.840	5.660	4.660	5.060	5.160	4.620	4.660	
4	2.1	1.176	5.324	4.324	4.724	4.824	4.284	4.324	
5	2.7	1.512	4.988	3.988	4.388	4.488	3.948	3.988	Safety factor
6	3.3	1.848	4.652	3.652	4.052	4.152	3.612	3.652	(FS_{po}) on L_e
7	3.9	2.184	4.316	3.316	3.716	3.816	3.276	3.316	of geosynthetic
8	4.5	2.520	3.980	2.980	3.380	3.480	2.940	2.980	strip ≥ 1.5
9	5.1	2.855	3.645	2.645	3.045	3.145	2.605	2.645	
10	5.7	3.191	3.309	2.309	2.709	2.809	2.269	2.309	
11	6.3	3.527	2.973	1.973	2.373	2.473	1.933	1.973	
12	6.9	3.863	2.637	1.637	2.037	2.137	1.597	1.637	
13	7.5	4.199	2.301	1.301	1.701	1.801	1.261	1.301	

5. Conclusions

In this study, the effective length of reinforcement was predicted by considering the pullout force distribution using the indoor pullout test results for the geosynthetic strips. In addition, the applicability of the predicted effective length was evaluated using a design case. The analyzed results were as follows:

(1) The geosynthetic strips with the same tensile strength exhibited similar pullout behaviors regardless of the horizontal spacing of reinforcement, but the reinforcement width had a more significant influence on the tensile strength and pullout force than the horizontal reinforcement spacing.

(2) The pullout behavior of the geosynthetic strips was concentrated at the front, and this was more obvious as the normal stress increased. Beyond a certain distance from the front, however, the pullout behavior of the reinforcement hardly occurred regardless of the normal stress. Based on this, it was possible to propose a method to predict the effective length (L_E) and maximum effective length ($L_{E(max)}$).

(3) The pullout resistance estimated based on the predicted effective length showed results that could secure stability. In addition, it was found that the effective area method—that considered the prediction of the effective length based on the use of the pullout test geosynthetic strip results—was applicable as an efficient pullout resistance design method. In other words, the proposed method was found to be more suitable for economical designs than the existing method based on the results of the design case that used the effective length for the pullout resistance of the geosynthetic strips.

In this study, soils which has a specific particle size distribution and optimum water content were applied to the pullout test. The water content and particle size distribution of soils may affect pullout resistance, effective length prediction, and pullout design because the soil conditions applied in this study are limited. Therefore, it is necessary to study the pullout resistance applied to various soil conditions.

Institutional Review Board Statement: Not applicable.

Informed Consent Statement: Not applicable.

Data Availability Statement: Data presented in this study are available on request from the corresponding author. The data are not publicly available due to data that are also part of an ongoing study.

Conflicts of Interest: The authors declare no conflict of interest.

References

1. Giresini, L.; Puppio, M.L.; Taddei, F. Experimental pull-out tests and design indications for strength anchors installed in masonry walls. *Mater. Struct.* **2020**, *53*, 103. [CrossRef]
2. Girard, H.; Berroir, G.; Gourc, J.P.; Matheu, G. Frictional behaviour of geosynthetic and slope stability of lining systems. In Proceedings of the 5th International Conference on Geotextiles Geomembranes and Related Products, Singapore, 5–9 September 1994; pp. 339–342.
3. Yoo, C.; Jung, H.Y. Case History of Geosynthetic Reinforced Segmental Retaining Wall Failure. *J. Geotech. Geoenvironmental Eng.* **2006**, *132*, 1538–1548. [CrossRef]
4. Chen, H.T.; Hung, W.Y.; Chang, C.C.; Chen, Y.J.; Lee, C.J. Centrifuge modeling test of a geotextile reinforced wall with a very wet clayey backfill. *Geotext. Geomembr.* **2007**, *25*, 346–359. [CrossRef]
5. Won, M.S.; Kim, Y.S. Internal deformation behavior of geosynthetic-reinforced soil walls. *Geotext. Geomembr.* **2007**, *25*, 10–22. [CrossRef]
6. Bergado, D.T.; Teerawattanasuk, C. 2D and 3D numerical simulations of reinforced embankments on soft ground. *Geotext. Geomembr.* **2008**, *26*, 39–55. [CrossRef]
7. Briancon, L.; Villard, P. Design of geosynthetic-reinforced platforms spanning localized sinkholes. *Geotext. Geomembr.* **2008**, *26*, 416–428. [CrossRef]
8. Chen, Y.M.; Cao, W.P.; Chen, R.P. An experimental investigation of soil arching within basal reinforced and unreinforced piled embankments. *Geotext. Geomembr.* **2008**, *26*, 164–174.
9. Chen, R.H.; Chiu, Y.M. Model tests of geocell retaining structures. *Geotext. Geomembr.* **2008**, *26*, 56–57. [CrossRef]
10. Li, A.L.; Rowe, R.K. Effects of viscous behaviour of geosynthetic reinforcement and foundation soils on embankment performance. *Geotext. Geomembr.* **2008**, *26*, 317–334.
11. Rowe, R.K.; Taechakumthorn, C. Combined effect of PVDs and reinforcement on embankments over rate-sensitive soils. *Geotext. Geomembr.* **2008**, *26*, 239–249. [CrossRef]
12. Yoo, C.; Kim, S.B. Performance of a two-tier geosynthetic reinforced segmental retaining wall under a surcharge load: Full-scale load test and 3D finite element analysis. *Geotext. Geomembr.* **2008**, *26*, 460–472. [CrossRef]
13. Tatsuoka, F.; Hirakawa, D.; Nojiri, M.; Aizawa, H.; Nishikiori, H.; Soma, R.; Tateyama, M.; Watanabe, K. A new type of integral bridge comprising geosynthetic-reinforced soil walls. *Geosynth. Int.* **2009**, *16*, 301–326. [CrossRef]
14. Palmeira, E.M. Soil-geosynthetic interation: Modelling and analysis. *Geotext. Geomembr.* **2009**, *27*, 368–390. [CrossRef]
15. Ingold, T.S. Laboratory pull-out testing of grid reinforcements in sand. *Geotech. Test. J.* **1983**, *6*, 101–111.
16. Jewell, R.A.; Milligan, G.W.E.; Sarsby, R.W.; Dubois, D. Interaction between soil and geogrids. In *Symposium on Polymer Grid Reinforcement in Civil Engineering*; Thomas Telford Publishing: London, UK, 1984; pp. 18–30.
17. Juran, I.; Chen, C.L. Soil-geotextile pullout interaction properties: Testing and interpretation. *Transp. Res. Rec.* **1988**, *1188*, 37–47.
18. Palmeira, E.M.; Milligan, G.W.E. Scale and other factors affecting the results of pullout tests of grids buried in sand. *Géotechnique* **1989**, *39*, 511–524. [CrossRef]
19. Bergado, D.T.; Chai, J.C.; Abiera, H.O.; Alfaro, M.C.; Balasubramaniam, A.S. Interaction between cohesive-frictional soil and various grid reinforcements. *Geotext. Geomembr.* **1993**, *12*, 327–349. [CrossRef]
20. Bergado, D.T.; Macatol, K.C.; Amin, N.U.; Chai, J.C.; Alfaro, M.C.; Anderson, L.R. Interaction of lateritic soil and steel grid reinforcement. *Can. Geotech. J.* **1993**, *30*, 376–384. [CrossRef]
21. Wilson-Fahmy, R.F.; Koerner, R.M.; Sansone, L.J. Experimental behaviour of polymeric geogrids in pullout. *J. Geotech. Eng.* **1994**, *120*, 661–677. [CrossRef]
22. Lopes, M.L.; Ladeira, M. Influence of confinement, soil density and displacement ratio on soil–geogrid interaction. *Geotext. Geomembr.* **1996**, *14*, 543–554. [CrossRef]
23. Ochiai, H.; Otani, J.; Hayashic, S.; Hirai, T. The Pull-Out Resistance of Geogrids in Reinforced Soil. *Geotext. Geomembr.* **1996**, *14*, 19–42. [CrossRef]
24. Moraci, N.; Gioffrè, D. A simple method to evaluate the pullout resistance of extruded geogrids embedded in a compacted granular soil. *Geotext. Geomembr.* **2006**, *24*, 116–128. [CrossRef]
25. Teixeira, S.H.C.; Bueno, B.S.; Zornberg, J.G. Pullout resistance of individual longitudinal and transverse geogrid ribs. *J. Geotech. Geoenvironmental Eng.* **2007**, *133*, 37–50. [CrossRef]
26. Wilson-Fahmy, R.F.; Koerner, R.M. Finite element modelling of soil–geogrid interaction with application to the behavior of geogrids in a pullout loading condition. *Geotext. Geomembr.* **1993**, *12*, 479–501. [CrossRef]
27. Abdelouhab, A.; Dias, D.; Freitag, N. Physical and analytical modelling of geosynthetic strip pull-out behavior. *Geotext. Geomembr.* **2010**, *28*, 44–53. [CrossRef]

28. Abdelouhab, A.; Dias, D.; Freitag, N. Numerical analysis of the behaviour of mechanically stabilized earth walls reinforced with different types of strips. *Geotext. Geomembr.* **2011**, *29*, 116–129. [CrossRef]
29. Dong, Y.L.; Han, J.; Bai, X.H. Numerical analysis of tensile behavior of geogrids with rectangular and triangular apertures. *Geotext. Geomembr.* **2011**, *29*, 83–91. [CrossRef]
30. Ghionna, V.N.; Moraci, N.; Rimoldi, P. Experimental evaluation of the factors affecting pull-out test results on geogrids. In Proceedings of the International Symposium: Landmarks in Earth Reinforcement, Fukuoka, Kyushu, Japan, 14–16 November 2001; pp. 31–36.
31. Sugimoto, M.; Alagiyawanna, A.N.M.; Kadoguchi, K. Influence of rigid and flexible face on geogrid pullout tests. *Geotext. Geomembr.* **2001**, *19*, 257–277. [CrossRef]
32. Moraci, N.; Recalcati, P. Factors affecting the pullout behaviour of extruded geogrids embedded in a compacted granular soil. *Geotext. Geomembr.* **2006**, *24*, 220–242. [CrossRef]
33. Tatlisoz, N.; Edil, T.B.; Benson, C.H. Interaction between Reinforcing Geosynthetics and Soil-Tire Chip Mixtures. *J. Geotech. Geoenvironmental Eng.* **1998**, *124*, 1109–1119. [CrossRef]
34. Tanchaisawat, T.; Bergado, D.T.; Voottipruex, P.; Shehzad, K. Interaction between geogrid reinforcement and tire chip–sand lightweight backfill. *Geotext. Geomembr.* **2010**, *28*, 119–127. [CrossRef]
35. Kim, D.; Ha, S. Effects of Particle Size on the Shear Behavior of Coarse Grained Soils Reinforced with Geogrid. *Materials* **2014**, *7*, 963–979. [CrossRef]
36. Racana, N.; Grédiac, M.; Gourvès, R. Pull-out response of corrugated geotextile strips. *Geotext. Geomembr.* **2003**, *21*, 265–288. [CrossRef]
37. Li, L.H.; Chen, Y.J.; Ferreira, P.M.V.; Liu, Y.; Xiao, H.L. Experimental Investigations on the Pull-Out Behavior of Tire Strips Reinforced Sands. *Materials* **2017**, *10*, 707. [CrossRef] [PubMed]
38. Elias, V.; Christopher, B.R.; Berg, R.R. *Mechanically Stabilized Earth Walls and Reinforced Soil Slopes Design and Construction Guidelines*; Publication No. FHWA-NHI-00-043; Federal Highway Administration: Washington, DC, USA, 2001.
39. ASTM. *Standard Test Method for Measuring Geosynthetic Pullout Resistance in Soil*; ASTM D 6706-01, ASTM Book of Standards; ASTM International: Philadelphia, PA, USA, 2003; Volume 4, p. 13.
40. Kim, Y.S. Development of the Method to Determine the Weathering Degree of Decomposed Granite Soil for the Evaluation of the Engineering Properties. Ph.D. Thesis, Chung-Ang University, Seoul, Korea, 2002.

Review

A Literature Review of Concrete Ability to Sustain Strength after Fire Exposure Based on the Heat Accumulation Factor

Michał Pasztetnik and Roman Wróblewski *

Faculty of Civil Engineering, Wroclaw University of Science and Technology, 50-370 Wrocław, Poland; michal.pasztetnik@pwr.edu.pl
* Correspondence: roman.wroblewski@pwr.edu.pl

Abstract: Concrete is susceptible to damage during and after high-temperature exposure (most frequently in fire). The concrete partial strength re-gain after a high-temperature exposure obtained by the rehydration process is undoubtedly an advantage of this construction material. However, to use fire-damaged concrete, one has to know why the strength deteriorates and what makes the partial re-gain. Within this framework, the paper aims to find what factors influence the strength re-gain. Moreover, an attempt is made to introduce a measure collecting various influences such as the modified heat accumulation factor—accounting only for that which is important for the process, the temperature decomposing cement paste (i.e., above 400 °C). Several factors, i.e., peak temperature, heating time and rate, cooling regime, post-fire re-curing, concrete composition, age of concrete at exposure, porosity, load level at exposure, and heat accumulation are presented by their influence on the relative residual compressive strength, i.e., a portion of initial strength that is obtained after temperature exposure and strength re-gain. Since the relative strength unifies various concretes, a more general assessment and discussion are presented based on the experimental results and correlation factors. As fundamental influences determining the residual strength, the heating time, peak temperature, cooling, or post-heating re-curing regimes are found with the load level at exposure being inadequately examined. This paper also shows the superiority of the modified heat accumulation factor, but the results obtained are not satisfactory, and additional experimental data are necessary to develop a theoretical model of the residual strength.

Keywords: concrete; compressive strength; high temperature; fire temperature; residual strength; heat accumulation factor

1. Introduction

Concrete provides the best fire resistance out of typically used construction materials. Compared to timber or steel, concrete has low thermal conductivity, high heat capacity, and its strength degrades slower with increasing temperature. As a result, it is a material that performs well not only as a separator between fire-affected spaces but also as a material for elements that need to perform under extreme thermal conditions. The vast majority of concrete structures can withstand fire conditions for the designed duration. This is due to the fact that concrete properties at high temperatures are well known and examined [1].

Standards provide safe approaches and mathematical models [2–4] that help design concrete structures for fire safety. Stress–strain curves for concrete exposed to high temperatures are also provided [5–7], and the behavior of concrete structures, elements, and sections are widely investigated, e.g., [8–10]. The research and design effort result in structures that handle fires so well that the question arises: Can this structure be used as it was before the fire?

Destructive and non-destructive assessment of strength is possible [11–14], but providing enough information for structural calculations is a crucial issue. The temperature field inside the concrete element depends on many uncertain parameters, and this results

in residual properties that are difficult to estimate. Therefore, to answer any question about residual properties, theoretical models would be helpful.

From both research and practical perspectives, the residual strength of concrete is a complex matter [15], because many factors must be considered, e.g., peak temperature, heating time, rate of increase in temperature, concrete composition, and others).

Since concrete is a composite material (composed of aggregate, cement, water, and additives), its final properties vary depending on the ratio and type of components used, but subjected to fire, other variables influence the properties. When a cement paste is exposed to high temperatures, the following physicochemical reactions are observed [16]:

- At 100 °C, bound water is being evaporated;
- At 180 °C, hydrate calcium silicate is beginning to dehydrate;
- At 500 °C, the decomposition of calcium hydroxide is observed;
- At 700 °C, the decomposition of calcium silicate hydrate occurs.

These phenomena cause a degradation of the mechanical properties of the cement paste [17]. In addition, the thermal expansion of the aggregate leads to an increase in internal stresses and can result in microcracks of the concrete body. The deterioration of mechanical properties can be represented by the relative residual strength. Compressive and tensile strength degrade rapidly as they halve at 400 °C and 300 °C, respectively [18]. The decline is not only a function of the peak temperature but also of the heating time and rate. It was proven that a higher heating rate results in lower relative strength at the same peak temperature [19]. Heating time is also crucial, as maintaining a low temperature for a long time can cause more damage to the concrete than a higher peak temperature for a short time. What should be remembered is the fact that concrete becomes less brittle after exposure to a high temperature (intrinsic length increases) [20]. The size effect can influence the tensile strength. Although it has a marginal effect on compression [21], it makes the tensile test results sample size dependent. It was found that the strain rate does not influence compressive behavior [22].

After the concrete is cooled down to ambient temperature, it retains residual strength that is affected not only by the mentioned factors but also by the cooling regime, post-fire re-curing regime, and time. There exists a correlation between strength at high temperature and residual strength, but they cannot be treated in the same way.

This review paper summarizes up-to-date progress in experimental research on the residual strength of concrete after high-temperature exposure. The results of the tests on the most important factors that influence concrete residual strength are presented and discussed in the following sections of the article. Each section is dedicated to a separate factor. Although there are consistent results for obvious factors, such as peak temperature and heating time, the influence of less pronounced factors, such as the w/c ratio and cement type, still requires further research. Furthermore, current research lacks a general approach to the influences that will lead to a function or algorithm capable of assessing the residual strength of concrete.

2. Peak Temperature

According to [2], the strength of the concrete at high temperature is a function of only the temperature that the concrete reaches. With residual strength, more factors need to be considered, but peak temperature is crucial amongst them. Extensive research was done to connect the peak temperature and residual strength of the concrete (Table 1). Comparison between the results is very limited, as factors besides peak temperature are often disparate for different authors.

Table 1. Summary of research on the peak temperature.

Author	Citation	Sample Type	Sample Size	Concrete Strength	Temp. Range	Heating Time	Heating Rate	Age of Concrete at Exposure
Toumi	24	Cubic	100 mm	NSC, HSC	300–700 °C	3–9 h	10 °C/min	28 days
Yang	25	Cylindrical	D 100 mm H 200 mm	NSC	400–600 °C	0–2 h	2.5 °C/min	90 days
Phan	26	Cylindrical	D 100 mm H 200 mm	NSC, HSC	100–450 °C	5 h 30 min	5 °C/min	200 + days
Netinger	27	Beam	40 mm × 40 mm × 160 mm	NSC	200–1000 °C	1 h 30 min	-	28 days
Hager	28	Cubic Cylindrical	Cubic: 150 mm Cyl.: D 100 mm H 200 mm	HSC	200–1000 °C	3 h	0.5 °C/min	90 days
Krzemień	29	Cubic	150 mm	NSC	200–1000 °C	3 h	0.5 °C/min	120 days
Xiao	30	Cubic	100 mm	HSC	100–900 °C	3 h	ISO-834	NA
Chan	31	Cubic	100 mm	NSC, HSC	400–1200 °C	1 h	BS476:Part20:1987	90 days
Tolentino	32	Cylindrical	D 100 mm H 200 mm	NSC, HSC	600 °C	2 h	0.5 °C/min	NA
Xiao	34	Cubic	100 mm	HSC	200–800 °C	2–3 h	25 °C/min	150 days

In [23–25], cylindrical concrete samples were heated to temperatures ranging from 100 to 450 °C; then, after reaching steady state, they were cooled to room temperature inside the furnace, and the compressive strength was tested (Figure 1). In [26], research was performed for a very broad range of temperatures (200, 400, 600, 800, and 1000 °C). Concrete samples of size 40 mm × 40 mm × 160 mm at the age of 28 days were placed in the furnace and kept at the target temperature for 1.5 h; then, they were taken out and left to cool in an ambient environment. Compressive tests were performed on prism halves resulting from flexural tests.
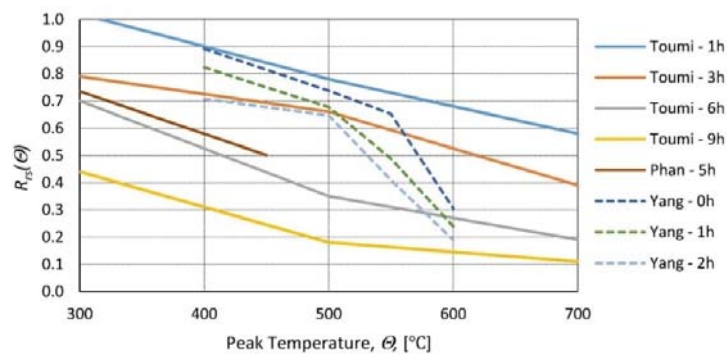

Figure 1. Relative residual strength of concrete as a function of peak temperature for the different times maintained at peak temperature of 1, 3, 5, 6, and 9 h according to [23]—Toumi, [25]—Phan, and 0, 1, and 2 h according to [24]—Yang.

The HSC (high-strength concrete) samples [27] and the NSC (normal-strength concrete) samples [28] were heated in a furnace test (to temperatures: 200, 400, 600, 800, and 1000 °C). A low heating rate of 0.5 °C/min was applied, and the peak temperature was maintained for 3 h. Subsequently, the samples were cooled inside the furnace, taken out, and tested

(Figure 2). In [29], the samples were tested at 10 set temperature values (20, 100, . . . , 900 °C). The temperature was increased according to the standard fire curve (Figure 3), and the peak temperature was maintained for 3 h. Then, the furnace door was opened, and the samples were cooled inside before compressive tests (Figure 2). In [30], HSC and NSC samples were heated to temperatures ranging from 400 to 1200 °C. After the specimens were allowed to cool naturally to room temperature, compressive tests were performed (Figure 2). In [31], the residual strength of NSC and HSC after exposure to elevated temperatures (from 200 to 600 °C) was compared.
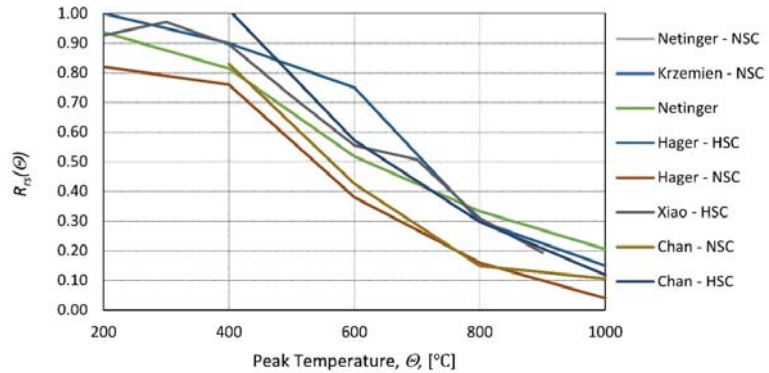

Figure 2. Relative residual strength of different types of concrete (NSC and HSC) as a function of the peak temperature according to [26]—Netinger, [27]—Hager, [28]—Krzemien, [29]—Xiao, and [30]—Chan.

Moreover, the results demonstrate that the relative loss of strength is higher for HSC than for NSC. A similar conclusion was reached in [32,33]. Correlation factors were calculated for all the data collected, with respect to the heating time at peak temperature (Table 2). The Pearson and Spearman factors signify a strong negative linear relationship between relative residual strength and peak temperature. The Kendal coefficient supports this observation, as it indicates a monotonic relationship. The graphic representation of the collected results is presented in Figure 4. Residual strength behaves in a way similar to changes in concrete strength at high temperature according to, e.g., [2]. Varying the test conditions and concrete composition in the research considered in Figure 4 can make a substantial difference in residual strength for peak temperatures ranging from 300 to 750 °C. For peak temperatures lower than 300 °C, almost no loss is observed, and for peak temperatures higher than 750 °C, residual strength is almost equal to strength at high temperatures, meaning that concrete damaged to a very high degree exhibits a smaller ability to regain strength. Taking into account all this, the residual strength function for temperatures up to 300 °C and more than 750 °C can be derived based on the peak temperature only, but for the remaining range, a more accurate function would require considering other factors, which were mentioned further in this paper. In [34], a function was proposed to relate the residual strength with the maximum temperature, but it is considered as a rough approximation.

Table 2. Correlation factors between peak temperature and relative residual strength for two different heating times at peak temperature as presented by various authors.

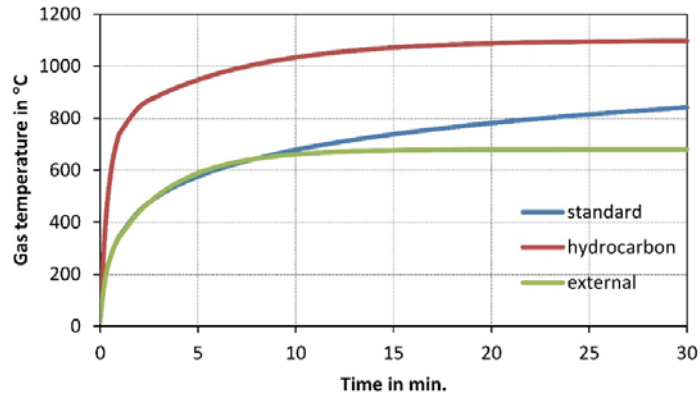| Heating Time	1 h	3 h
Pearson	−0.90	−0.95
Spearman	−0.94	−0.96
Kendall	−0.82	−0.87

Figure 3. Development of gas temperature in hydrocarbon, external, and standard fires according to [35].
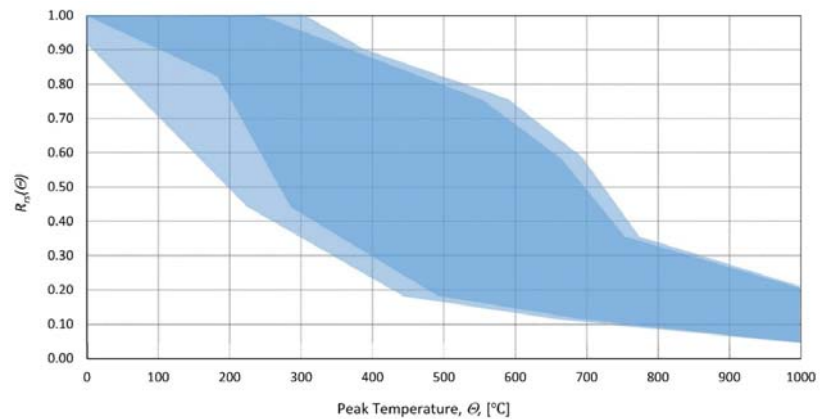

Figure 4. Range of the relative residual strength of concrete as a function of peak temperature. Collection of data from different heating rates, types of concrete, sample sizes, etc. presented by various authors.

3. Heating Time

The heating time, that is, how long the peak temperature is kept, is crucial in assessing the residual strength of concrete, which is demonstrated in the research presented (Table 3). In [23], this relationship is presented based on concrete made of crushed limestone and CEM I 42.5 in two variants (Figure 5):

- Normal-strength concrete (NSC) with a w/c ratio of 0.5;
- High-strength concrete (HSC) with a w/c ratio of 0.37.

At 28 days, samples were heated at a rate of 10 °C/min to target temperatures 300, 500, and 700 °C and kept for 1, 3, 6, and 9 h. The samples were tested after 24 h of cooling at room temperature (Figure 5). In [36], concrete samples of compressive strength of 20, 30, and 35 MPa were investigated 28 days after casting; cubic (150 mm) samples were heated to 400 and 600 °C for a duration of 3, 6, or 9 h and tested after cooling to room temperature (Figure 6).

Table 3. Summary of the research for heating time.

| Author	Citation	Sample Type	Sample Size	Concrete Strength	Temp. Range	Heating Time	Heating Rate	Age of Concrete at Exposure
Toumi	24	Cubic	100 mm	NSC, HSC	300–700 °C	3–9 h	10 °C/min	28 days
Yang	25	Cylindrical	D 100 mm H 200 mm	NSC	400–600 °C	0–2 h	2.5 °C/min	90 days
Pertiwi	38	Cubic	150 mm	NSC	400–600 °C	3–9 h	NA	28 days
Wu	39	Cylindrical	D 100 mm H 200 mm	NSC	100–600 °C	1–6 h	5 °C/min	28 days
Mohamedbhai	40	Cubic	100 mm	NSC	200–800 °C	1–4 h	-	84 days
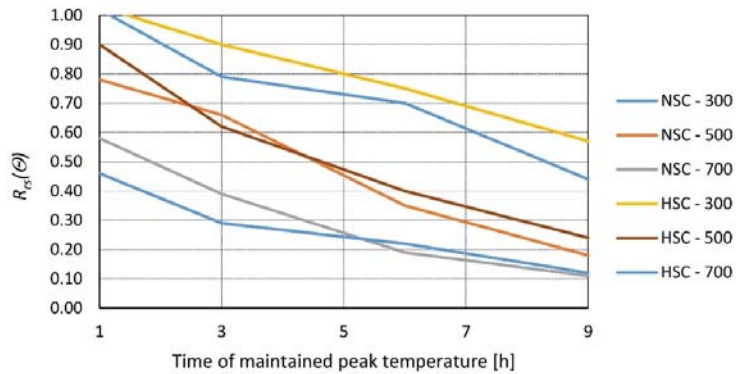
Figure 5. Relative residual strength of NSC and HSC as a function of time maintained at the peak temperature of θ = 300, 500, and 700 °C according to [23].
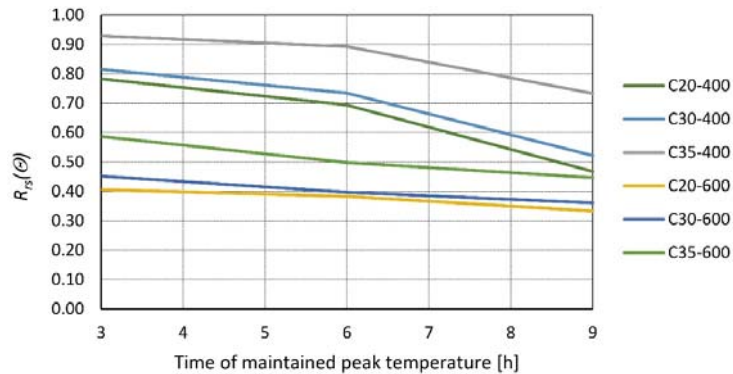

Figure 6. Relative residual strength of the concrete class C20/25, C30/37, and C35/45 as a function of time maintained at the peak temperature of θ = 400 and 600 °C according to [36].

Cylindrical samples (100 mm in diameter and 200 mm high) were tested in [24] at the age of 90 days. Two water–cement (w/c) ratios were used: 0.58 and 0.68. The heating rate was set at 2.5 °C/min to achieve peak temperatures of 400, 500, 550, and 600 °C. Temperatures were maintained for 0, 1, and 2 h, and then strength tests were performed after 7 days of cooling (Figure 7).
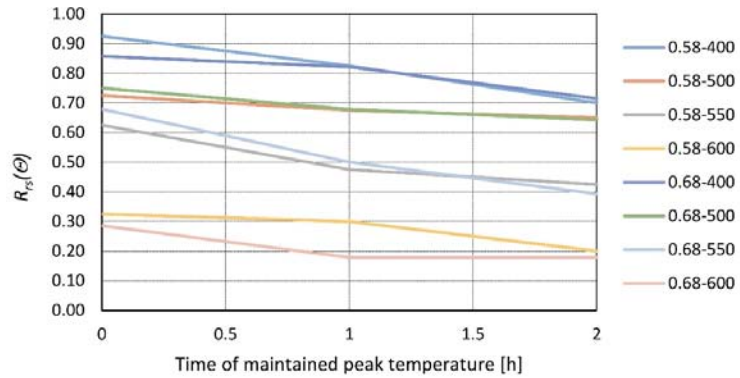
Figure 7. Relative residual strength of concrete with different water to cement ratios (0.58 and 0.68) as a function of time maintained at peak temperature of θ = 400, 500, 550, and 600 °C according to [24].

Cylindrical specimens were also tested in [37] by exposing them to temperatures ranging from 200 to 600 °C. The heating rate was set at 5 °C/min, and the exposure time varied from 1 to 6 h. Compressive tests were performed directly after cooling down. Another test is reported in [38]. Cubic samples (100 mm) were heated to temperatures from 200 to 800 °C with various heating rates and exposure times. The tests were performed after 14 days of re-curing. It was found that the main strength loss occurs within the first two hours of high-temperature exposure, and later, the impact is minimal. Comparing all of the data, it is clear and confirmed that a longer heating time deteriorates the residual strength of concrete, where most of the loss occurs in the first two hours. The correlation between residual strength and time maintained at peak temperature was calculated for 500 °C (as it provides the broadest range of results), and the factors are presented in Table 4. A strong, negative, monotonic, and linear relationship is evident.

Table 4. Correlation factors between the time maintained at the peak temperature and the relative residual strength for a peak temperature of 500 °C, presented by various authors.

Correlation Coefficient	Coefficient Value
Pearson	−0.98
Spearman	−0.86
Kendall	−0.75

Data reported by different authors result in the strength dispersion presented in Figure 8. Peak temperature and other variables impact the residual strength, so the data range is very wide. The bottom line represents the loss of residual strength for higher temperature ranges (700 °C) and the top line represents the loss of residual strength for lower peak temperatures (300 °C). This suggests that it is impossible to develop a proper function based only on time maintained in peak temperature. However, the derivative of this function is constant in segments and does not depend on the peak temperature value. The first segment is from 0 to 2 h (rapid loss of strength) and from 2 h onward (minimal loss of strength). This derivative gives a chance to isolate the influence of heating time on residual strength in the form of a coefficient implemented on an already known strength value with longer (or shorter) heating time.
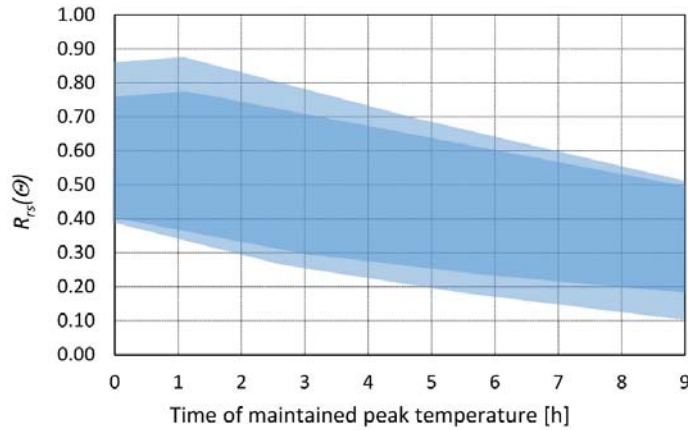
Figure 8. Range of the relative residual strength of the concrete as a function of time maintained at peak temperature. Collection of data from different heating rates, types of concrete, sample sizes, etc. presented by various authors.

4. Heating Rate

Although the gas temperature in a fire can rise extremely fast, as presented in Figure 3 [35], the temperature inside an element does not follow the same rate. The size of the concrete element, the high specific heat, and the thermal conductivity of around 1 W/mK result in very slow heat transfer throughout the element [2]. Additionally, the specific heat doubles at around 100 °C because the water changes state and the thermal conductivity decreases with rising temperature. Thus, only the external part of the cross-section is exposed to very high temperature, while internal parts record noticeably lower ones.

Although there are very different heating rates (3.5 and 10 °C/min) in [39], the test results obtained suggest a minimal influence of the heating rate. In [38], the influence of the heating rate was confirmed. However, no clear trend could be drawn in peak temperatures up to 600 °C. Beyond that level of peak temperature, no substantial influence was observed for different heating rates. The 2.5 °C/min rate applied in [24] results in a sharper decline in strength than with the 10 °C/min proposed in [23]. This leads to the conclusion that the damage caused by the high heating rate makes concrete less prone to further deterioration, while the low rate results in concrete that is susceptible to the effects of prolonged high temperature exposure. However, an immediate relationship has not been proven. Correlation factors between the heating rate and residual strength were calculated for the collected data, and the factors are presented in Table 5. Low positive values suggest a minimal influence in favor of the higher heating rate.

Table 5. Correlation factors between the heating rate and the relative residual strength for the peak temperature of 500 °C, presented by various authors.

Correlation Coefficient	Coefficient Value
Pearson	0.21
Spearman	0.21
Kendall	0.17

5. Cooling Regime

After heating or a fire, an element subjected to high temperature cools down, and how it happens is called the cooling regime. There exist three basic types of the regime used in tests:

- High-temperature environment cooling—concrete and environment maintain a high temperature for a long time, and slow temperature lowering from peak value to ambient is performed. This type of cooling corresponds to what happens in the inner parts of the fire-affected elements. The relatively high thermal capacity of concrete and low thermal conductivity cause temperature changes inside elements to be slow, both during heating up and cooling down.
- Cooling at the ambient temperature environment—hot concrete is kept at room temperature for cooling. This can be equated to the occurrence in the outer parts of fire-affected elements.
- Water cooling—hot concrete is treated with cold water and cooled down. This type can be compared with the outer parts of fire-affected elements covered by water used to extinguish the fire.

According to the available research (Table 6), the degradation of the mechanical properties depends on the type of cooling. Ambient temperature and water cooling were used in [40] but with cylindrical samples (diameter/height = 100/200 mm) heated to 330, 450, and 550 °C and removed from the furnace. Then, five types of cooling were performed: ambient temperature air cooling, water cooling by immersing samples in 15 °C water for 5, 10, 15, and 20 min and then air-cooled to room temperature. The next day, strength tests were performed. When air-cooled samples were compared with top-water-cooled samples, it appeared that peak temperature was not important for the decline rate of relative residual strength. Strength loss depends mainly on the duration of immersion in water (Figure 9).

Table 6. Summary of research on the cooling regime.

| Author	Citation	Sample Type	Sample Size	Concrete Strength	Temp. Range	Heating Time	Cooling Regime	Age of Concrete at Exposure
Kowalski	42	Cylindrical	D 100 mm, H 200 mm	NSC	330–550 °C	3–5 h	Air cooling Water cooling	130 days
Peng	43	Cubic	100 mm	HSC	200–800 °C	1 h	Air cooling Water cooling	56 days
Yang	44	Cubic	100 mm	NSC	200–800 °C	3 h	Air cooling Water cooling	90 days 120 days
Husem	45	Beam	40 mm × 40 mm × 160 mm	NSC, HSC	200–1000 °C	1 h	Air cooling Water cooling	28 days
Mendes	46	Cylindrical	D 100 mm, H 200 mm	NSC	400–800 °C	1 h	Air cooling Water cooling	90 days
Bingol	47	Cylindrical	D 100 mm, H 200 mm	NSC	100–700 °C	3 h	Air cooling Water cooling	28 days
Li	48	Cubic	100 mm	HSC	100–800 °C	0	Air cooling	90 days
Luo	49	Cubic	100 mm	NSC, HSC	800–1100 °C	1 h	Air cooling Water cooling	90 days
Shaikh	50	Cylindrical	D 100 mm, H 200 mm	NSC	200–800 °C	2 h	Air cooling Water cooling	56 days
Wang	51	Cubic	100 mm	NSC	200–800 °C	3 h	Air cooling Water cooling	130–142 days
Li	52	Cylindrical	D 100 mm, H 200 mm	NSC	150–750 °C	2 h 30 min	Air cooling Water cooling	90 days
Karakoç	53	Cylindrical	D 100 mm, H 200 mm	NSC	700 °C	1 h	Air cooling Water cooling	1 year
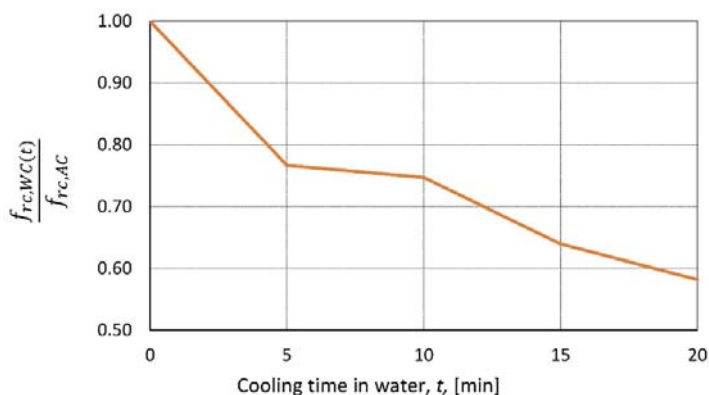
Figure 9. $\frac{f_{rc,WC}(t)}{f_{rc,AC}}$ as a function of the cooling time in water according to [40].

Similar tests are presented in [41–43], and the conclusions reached are the same. In [44], the impact of rapid water cooling on concrete made with the addition of slag was tested. Specimens were exposed to elevated temperatures of 400 and 800 °C and cooled in air or 20 °C water. For 400 °C, the strength loss of all water-cooled samples reaches an additional 20% compared to air cooling. It is interesting to note that for 800 °C samples made with OPC (ordinary Portland cement), the loss of an additional 14% points is observed when water-cooled samples made with a partial replacement of OPC by slag lose only 4–5% points. This phenomenon can be explained by the rehydration of CaO in Ca(OH)$_2$ accompanied by the expansion and thus further deterioration of concrete.

In [45], cubic samples (100 mm) were tested by exposing them to elevated temperatures (from 50 to 700 °C) and then cooling in two ways: by leaving them to cool in the furnace and by immersing them in water. The conclusion was drawn that air cooling results in higher residual strength, especially in the 400–500 °C peak temperature range.

Cubic specimens (100 mm) specimens were tested 90 days after casting in [46]. Temperature exposure was carried out in an electric furnace with the heating rate set at 10 °C/min for the first 100 °C and 20 °C/min from 100 to 800 °C. After reachifng peak temperature, samples were divided. One part was taken out of the furnace and cooled at room temperature; the second part was left in the turned-off furnace (door closed). Then, the tests were performed in two groups: directly after and 30 days after cooling. The results provide interesting facts: high-temperature cooling causes an additional dehydration of hardened cement and further deterioration of the strength (Table 7). Air cooling stopped the dehydration process but caused more internal cracks due to the temperature gradient. When comparing results obtained directly after cooling, dehydration had a greater impact than internal cracks but is also more reversible. After 30 days of re-curing, cement rehydrates and concrete regains most of its initial strength, while internal cracks caused by temperature gradient are unable to close.

Table 7. Comparison of the relative residual strength for different cooling methods according to [46].

Cooling Method	Re-Curing Time	0 Days	30 Days
$\frac{f_{rc,AC}}{f_{c,20}}$		0.77	0.82
$\frac{f_{rc,FC}}{f_{c,20}}$		0.65	0.87

In [47], water and furnace (air) cooling is compared by heating the NSC and HSC samples to 800 °C at a rate of 5–7 °C/min and cooling them in either a turned-off furnace or in a water tank. The difference between the cooling methods was visible for the residual

strength tested directly after cooling. The NSC strength was reduced to 0.32 for water and 0.45 for air cooling. The impact of the cooling regime on the residual strength of HSC was less pronounced, as the strength was reduced to 0.21 for water and 0.26 for air cooling.

A difference in the cooling regime for various peak temperatures is presented in [48]. Temperatures ranged from 200 to 800 °C. The residual strength resulting from slow air cooling was higher compared to water cooling for all temperature cases by 4–7% points. The difference was not substantial but noticeable. In [49], the influence of water cooling on the residual strength of concrete was tested. The samples were cooled in two ways: air-cooled in a furnace and water-cooled by sprinkling water for 30 min directly after temperature exposure. Compressive tests were performed one month after high-temperature exposure. The influence of the cooling regime was found for exposure temperature from 200 to 600 °C; water cooling resulted in lower residual strength by 5–7%. Only for 800 °C was there a difference of 1.5% (air cooling resulted in lower residual strength). The same cooling regime was used in [50]; later samples were tested after different re-curing times (0, 30, 60, and 90 days). The results proved that water cooling lowers the residual strength tested directly after cooling (especially after exposure to temperatures higher than 600 °C), but after re-curing for a longer period, the difference caused by the cooling method was minimal (Table 8).

Table 8. Difference between the relative residual strength for air and water cooling according to [49,50].

		$\frac{(f_{rc,AC}-f_{rc,WC})}{f_{c,20}}\cdot 100\%$							
	Temp. **Re-Curing**	**150 °C**	**200 °C**	**300 °C**	**400 °C**	**450 °C**	**600 °C**	**750 °C**	**800 °C**
[50]	0 days	1.5%	-	2.5%	-	5.8%	14.0%	13.6%	-
	30 days	0.0%	-	−0.2%	-	2.9%	4.5%	1.5%	-
	60 days	0.1%	-	2.9%	-	3.7%	−6.3%	−3.0%	-
	90 days	−1.1%	-	0.5%	-	1.7%	−6.5%	−2.5%	-
[49]	30 days	-	5.5%	-	6.7%	-	-	-	−1.5%

Three cooling methods were examined in [51]: that is, furnace air cooling, room temperature air cooling, and full immersion water cooling after exposure to 700 °C. Compressive tests were performed after the samples reached ambient temperatures. In contrast to the other experiments, samples cooled in water demonstrated the highest residual strength, whereas furnace and room temperature cooling showed very similar, but lower, results.

The cooling regime is an important factor in the evaluation of the residual strength of the concrete. According to [52], rapid cooling produces more internal damage due to the temperature gradient [53,54], but it stops dehydration processes. The slower cooling process results in longer exposure to high temperatures and longer dehydration. It is worth mentioning that water cooling results in lower weight loss [55].

The available data indicate that water cooling results in lower residual strength directly after cooling. Nevertheless, after post-fire re-curing, the difference between residual strengths for different cooling types becomes small and can be neglected.

6. Post-Fire Re-Curing Effect on Residual Strength

The recovery of the strength of concrete due to post-fire re-curing is important when assessing the residual strength of concrete, and it was proven in many articles (Table 9). This restoration can be attributed to the rehydration of cement that was dehydrated at high temperatures [56]. An essential factor in this phenomenon is moisture, which is similar to the initial curing of concrete. While full recovery is impossible (only the pore structure can return to pre-fire state), mechanical properties can return to surprisingly high levels. Some of the concrete phases form active products at elevated temperatures, such as limes

and calcium silicates; the effect of water and carbon dioxide on these can contribute to increased residual properties [57]. Post-fire re-curing methods can be classified into three basic categories: water post-fire re-curing, air–water post-fire re-curing, and air post-fire re-curing. [58].

Table 9. Summary of research on the post-fire re-curing.

Author	Cit.	Sample Type	Sample Size	Concrete Strength	Temp. Range	Heating Time	Cooling Regime	Re-Curing Regime	Re-Curing Time	Age of Concrete at Exposure
Li	52	Cylindrical	D 100 mm, H 200 mm	NSC	150–750 °C	2 h 30 min	Air cooling Water cooling	Air re-curing	30–90 days	90 days
Papayianni	61	Cylindrical	D 150 mm, H 300 mm	NSC	200–800 °C	3 h	Air cooling	NA	1–90 days	180 days
Poon	62	Cubic	100 mm	NSC, HSC	600–800 °C	1 h	Air cooling	Air re-curing Water re-curing	7–56 days	60 days
Souza	63	Cylindrical	D 100 mm, H 200 mm	NSC	300–600 °C	2 h 2 h 40 min	Air cooling	Air re-curing Water re-curing	28–112 days	100 days
Lin	64	NA	NA	NSC	400–1000 °C	2 h	NA	Air re-curing Water re-curing	7–180 days	90 days
Mirmomeni	65	Cylindrical	D 40 mm, H 40 mm	NSC	300–600 °C	15 min 2 h	Air cooling Water cooling	Water re-curing	2–28 days	28 days
Horiguchi	66	NA	NA	HSC	200–400 °C	2 h	NA	Air re-curing Water re-curing	90–180 days	NA
Park	67	Cylindrical	D 100 mm, H 25 mm	NSC	300–700 °C	1 h	Water cooling	Air re-curing Water re-curing	7–30 days	28 days

The difference between them is defined by the supply of water, from full immersion for a whole amount of time to no water at all. In [59], concrete samples were exposed to various temperatures ranging from 200 to 800 °C and then re-cured in air. Compressive tests were performed after 1, 7, 30, and 90 days after cooling. The results presented for 200 and 400 °C show that there is a rapid decrease in residual strength for the first week and then a slow increase. At 90 days, re-cured residual strength is higher than the initial residual strength.

In [60], various concrete mixes were tested by heating samples to temperatures of 600 and 800 °C with a heating rate of 2.5 °C/min and a time maintained at the peak temperature of 1 h. After exposure, the specimens were tested at four different times: directly after cooling, 7, 28, and 56 days of re-curing. Moreover, two re-curing regimes were used; the first was water re-curing, where samples were cooled down to room temperature naturally and then placed in water, while the second consisted of cooling down to room temperature, soaking in water for 2 h, and air curing for the remaining time. Results show that post-fire re-curing can produce tremendous effect (Figure 10). Samples that were heated to 800 °C and water re-cured increased their compressive strength three times. The regaining of mechanical properties is rapid in the first 7 days when the average gain is 75% (compared to the test directly after cooling); later, growth is linear. At 28 days, the average increase is 100%, and at 56 days, it is 115%.

The re-curing method shows differences in the first 7 days, water re-curing rates at 100% of increase, while air curing rates at 50%, but later, the growth becomes linear and very similar for both methods. In [61], concrete samples were heated up to 300 or 600 °C (heating rate 1 °C/min) and then re-cured for 28, 56, or 112 days at three different re-curing regimes. First, samples were covered in plastic film (PF) to prevent any moisture from reaching the re-curing concrete. The second was standard air curing (AC), and the third was water re-curing (WC). Then, the results were compared with the strength before heating. It was found that residual strength growth is more pronounced at the beginning

stage of re-curing, and it slows over time (Figure 11). The rate at which strength is regained varies, depending on the re-curing method, with the rule that more moisture gives better results. In [62], similar research was performed, and the statement that water re-curing gives better results than air re-curing was confirmed.

In [50], the residual compressive strength was tested as a function of re-curing time and the cooling regime, samples were re-cured after fire for 0, 30, 60, and 90 days depending on peak temperature with two different cooling regimes: air cooling and water cooling. The difference between air and water cooling is most visible for the test directly after cooling: the higher the temperature, the larger the initial difference. Then, with re-curing time increasing, the method of cooling is of small relevance (Figure 11).

Self-compacting concrete samples were examined in [63] by heating to 300, 450, and 600 °C and then tested after 0, 2, 7, and 28 days after cooling. The results prove the great potential of concrete to regain strength, in some instances even exceeding strength before high-temperature exposure (Figure 10). In [64], the recovery behavior of hybrid fiber HSC after fire exposure was tested. The samples were exposed to 200 and 400 °C. After exposure, strength tests were performed directly after, 90 days after, and 180 days after in two different re-curing conditions. Air re-curing resulted in a slight regain of compressive strength, while water re-curing essentially reinstated concrete to the initial strength. It is worth noticing that the regain occurred in the first 90 days; after that time, only a small increase was recorded.
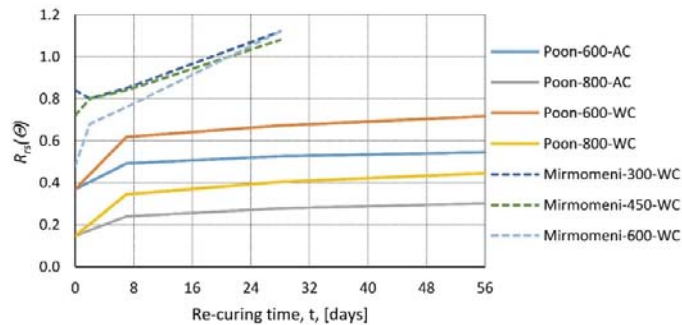
Figure 10. Relative residual strength of concrete [60] and self-compacting concrete [64] as a function of re-curing time (t) for different re-curing methods (AC—air re-curing, WC—water re-curing) and different peak temperatures $\theta = 300, 450, 600,$ and 800 °C according to [60]—Poon and [63]—Mirmomeni.
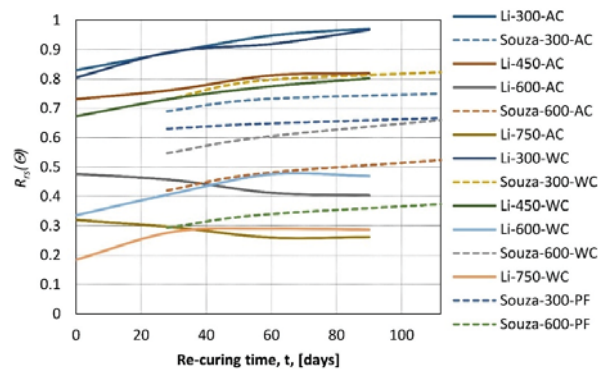

Figure 11. Relative residual strength of concrete as a function of re-curing time (t) for different peak temperatures $\theta = 300, 450, 600,$ and 750 °C, and different re-curing methods (AC—air re-curing, WC—water re-curing, PF—re-curing in a plastic film) according to [61]—Souza and [50]—Li.

Initially, the insufficient concrete strength over time can become high enough to carry the necessary stresses. Correlation calculated for re-curing time and residual strength displays a positive relation (factors presented in Table 10). The values of the factors suggest that a monotonic relationship exists but does not have to be a linear one. This fact shows that post-fire re-curing is significant and must be taken into account. It is proven that the most rapid growth of mechanical properties takes place in the first 7 days; later, it slows down similar to the logarithmic function (Figure 12). Concrete recovery coincides with the rehydration of cement, and moisture is critical. Curing methods involving water provide better results while completely sealing the moisture flow results in a much slower regain of mechanical properties [65]. Although it should be noted that in concrete heated to less than 300 °C, ongoing deterioration of concrete can be observed due to sulfate-induced expansion [66]. This phenomenon can mitigate some residual strength gain and should be taken into account.

Table 10. Correlation factors between re-curing time and the relative residual strength for the peak temperature of 500 °C, presented by [61,63].

Correlation Coefficient	Coefficient Value
Pearson	0.617
Spearman	0.777
Kendall	0.661
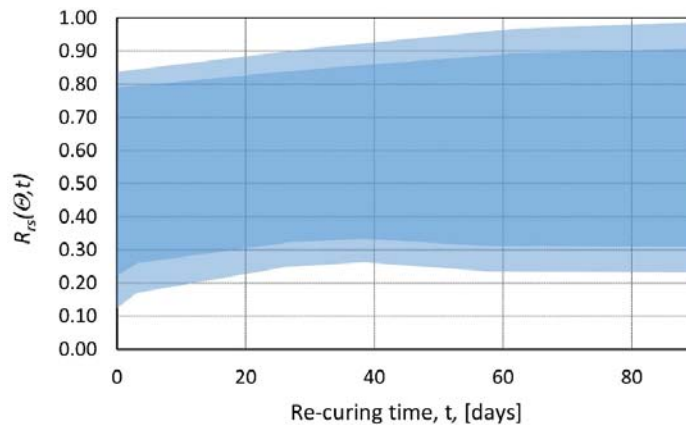
Figure 12. Range of the relative residual strength of concrete as a function of re-curing time. Collection of data from different heating rates, types of concrete, sample sizes, etc. presented by various authors.

7. Concrete Composition

The composition of the concrete mix determines its initial mechanical properties. The question about its influence on the residual strength was studied multiple times, as it is naturally supposed. Concrete is formed by mixing aggregates, cement, water, and additives. Furthermore, research on recycled materials was implemented, creating possibilities for future usage [67]. The influence of each component is analyzed and discussed in the following sections. As the amount of data on concrete composition is vast, a summary of the examined components in all papers analyzed in this paragraph can be found in the supplementary file attached to the paper.

7.1. Type of Aggregate

The aggregate contributes to the largest part of the concrete mix (approximately 70% in terms of volume) and is expected to have an essential influence on the behavior of

concrete. A comprehensive study on aggregate behavior at elevated temperatures in [68] provides information on the phenomena that occur in concrete. An important conclusion was made that the siliceous/calcareous categorization used by [35] is not enough, as the aggregate within one of the 'groups' can vary significantly in terms of mechanical response to elevated temperature. The type of aggregate influence was studied in [27]: four types of HSCs were purchased and differed solely by aggregate type (Figure 13). Then, after exposure to high temperature, tests were performed to identify differences in residual strength directly after cooling. The results show that the relative residual compressive strength is very similar for all types of aggregates at a peak temperature above 600 °C; at lower temperatures, there are slight differences favoring granite [69]. Samples with granite, heated to 300 °C, show a higher residual strength than limestone. For 600 °C, this difference diminishes. Considering the gain in granite strength in the lower temperature range, the conclusion that all aggregate behaves similarly can be drawn. Furthermore, the type of aggregate does not influence the relative residual strength. These results show a very similar behavior compared to [27] for a lower temperature register (up to 300 °C). In [26], seven types of aggregate were tested, samples were heated to target temperatures and, after 1.5 h of heating, left to cool at room temperature. After the samples cooled, compressive tests were performed. Figure 13 presents a decrease in relative residual strength with respect to peak temperature following a similar trend for all aggregate types. A conclusion could be made that the aggregate type does not influence the deterioration of mechanical properties; all tested types show similar degradation over time.
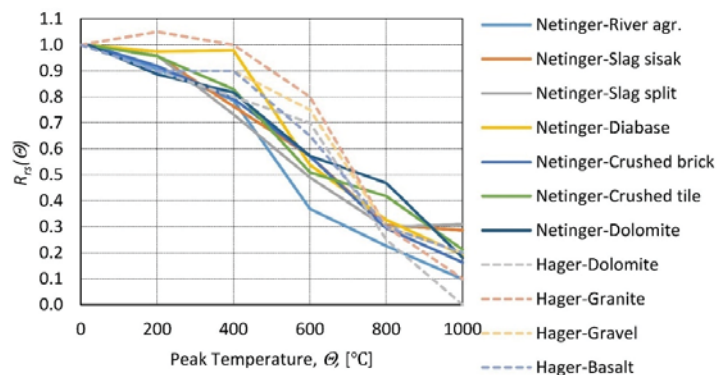

Figure 13. Relative residual strength of concrete as a function of peak temperature for different types of aggregate according to [27]—Hager and [26]—Netinger.

In [61], residual strength research was performed by testing concrete with three different types of aggregate: expanded clay, basalt, and limestone. Specimens were heated to 300 and 600 °C and, after cooling to room temperature, tested. The results bring the same conclusion that the type of aggregate plays a minimal role in the relative residual strength of concrete. All three types of samples had very comparable relative strengths, and regrowth follows an analogous rate (Figure 14).

In [70], a comparison was made between crushed and river aggregates. Both had similar mineralogical compositions (river with negligible higher SiO_2 content) after exposure to elevated temperatures (from 200 to 1000 °C). The results showed that the crushed aggregate regained a higher residual strength value. In [71], research on the thermomechanical behavior of baritic concrete exposed to high temperature was conducted, and the results showed that it behaves very similar to regular concrete. In contrast to the negligible influence of the type of aggregate in normal-weight concrete, the authors of [72] researched the influence of high temperature on heavy-weight concrete properties. As a result, ilmenite concrete was found to have much higher residual strength than regular gravel concrete.
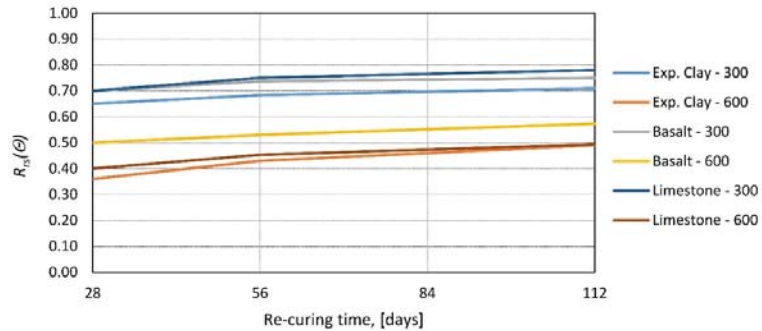
Figure 14. Relative residual strength of concrete as a function of re-curing time for different types of aggregate and different peak temperatures θ = 300 and 600 °C according to [61].

In [49], the recycled concrete aggregate was exposed to temperatures of 200 to 800 °C, and the residual strength was tested after 30 days of re-cure. Specimens differed only in aggregate type, and three types were considered: coarse, fine, and 50/50 fine and coarse. Results proved that the aggregate size did not influence the residual strength. In [73], samples made with three different aggregate types: river gravel, crushed limestone, and RCA (recycled concrete aggregate) were tested by exposing them to elevated temperatures (250, 500, 750 °C) and then, after natural cooling, their residual prosperities were tested. The results suggest that the concrete made with crushed limestone and RCA had higher relative residual strength than the river gravel. At [42], coarse RCA was also tested using different ratios (from 0 to 100%) of coarse aggregate, and the conclusion was drawn that its content is not significant for residual strength (peak temperatures of 200 to 800 °C). Similar results were reached in [74–77], although two subsequent articles pointed out that there is a small residual strength difference in favor of regular concrete. A similar experiment was carried out in [78], except for fine aggregate, which was also made from recycled concrete. The conclusion that RCA concrete has higher residual strength than normal concrete (especially for 50, 70, and 100% replacement ratios) was reached and later confirmed with a very similar test in [79]. However, in [80], contrary results were reached: for every 1% of RCA replacement, the residual strength was reduced by 0.2%. This discrepancy can be accounted for by different RCA origins, and it is of importance in residual behavior.

In [81], tests were performed on concrete made with coarse aggregate made from recycled ceramic exposed to elevated temperatures (200, 400, 600 °C), and the researchers concluded that specimens with replacement with RCCA (coarse aggregate made from recycled ceramic) had improved relative residual strength. Crushed brick aggregate was tested in [82] by replacing 30% of standard aggregate in concrete mix and exposing it to elevated temperatures. The result proved that concrete made in this way behaves very similarly to the control mix. The possibilities of replacing fine aggregate with non-ground granulated blast-furnace slag and coal bottom ash were checked [83]. Samples were made with different replacement ratios (ranging from 10 to 50%) and exposed to a temperature of 800 °C. The results showed that there are no significant differences in residual strength for different types and ratios of aggregate replacement. In [84], siliceous and calcareous aggregates were used to study the influence on the residual strength of concrete. A suggestion was made that the type of aggregate was an important factor of residual strength and that siliceous/calcareous division was not sufficient to receive precisely characterized concrete behavior.

Research carried out on the influence of aggregate type on relative residual strength proves that the limited influence exists and the change is especially noticeable for heavy-weight concrete [72]. In the temperature range tested, the fundamental factor governing the residual strength of concrete is the dehydration and rehydration of cement. Changes that

occur in aggregates [85], in addition to obvious thermal expansion, minimally influence the above-mentioned strength. In assessing the deterioration of the concrete strength after a fire, an aggregate type is not a deciding factor. However, it should be noted that the aggregate type influences the spalling. The incompatibility of strains between hardened cement paste and aggregates that cause thermal instability depends on the type of aggregate [86]. The initial moisture state is crucial for flint aggregates due to their low porosity, and the build-up of vapor pressure causes explosive spalling in the temperature range of 150 to 450 °C [87].

7.2. Cement Dosage and Type

Concrete strength is among other functions a function of the water to cement ratio, so naturally, it influences residual strength. Very few papers tackle cement dosage, and even fewer address cement types. In [46], concrete samples with three different cement dosages and the same w/c ratio were tested. Normal Portland cement with the addition of fly ash was used; it can be classified as CEM II/B-V. Two different cooling regimes were used: inside the furnace and at room temperature. Tests were performed directly after cooling and after 30 days of re-curing. Analyzing the test results, one can conclude that the cement dosage is not influencing the residual strength, as all mixtures behave in a very similar way. In [24], the influence of the w/c ratio on the residual strength was tested. Two types of specimens with different w/c ratios were used (both using CEM I). The tests were performed after 7 days of re-curing. The results show that although the difference between the w/c ratios is substantial (17%), the influence on relative residual strength is negligible. In [50], three different w/c ratios: 0.35, 0.5, and 0.55 were tested. Specimens were heated to 600 °C, cooled down, and tested after various re-curing times. Results for w/c of 0.5 and 0.55 are almost identical, and for 0.35, the initial residual strength is much lower but the increment is similar for all w/c ratios.

Other w/c ratios (0.31 and 0.45) were examined in [42]. For all peak temperatures ranging from 200 to 800 °C, the w/c ratio has been shown to be insignificant when considering its influence on relative residual strength (Table 11). In [88], concrete with a w/c ratio of 0.22, 0.33, and 0.57 at temperatures up to 450 °C was tested. The results showed that the loss of initial strength was lowest for 0.22 (approximately 20%) and higher for 0.33 and 0.57 (approximately 30%). In [82], research on the w/c ratio was performed by exposing three different concrete mixes, with w/c ratios of 0.6, 0.42, and 0.27, to temperatures ranging from 150 to 900 °C. The heating rate was set at 3 °C/min, and the exposure time at the peak temperature was 1 h. The results show that the smaller w/c ratios perform slightly better and maintain more strength. A similar test was performed in [70]; concretes with w/c ratios of 0.5 and 0.7 were exposed to elevated temperatures (ranging from 200 to 1000 °C), and after 28 days of re-curing, residual strength was tested. The results showed that w/c influences residual properties in higher temperature registers, i.e., 600 °C and above. Higher w/c ratios resulted in lower residual strength. Both [89,90] present the influence of the w/c ratio on the residual strength of the concrete after exposure to 500 °C for 1 h and 4 h, respectively. Concrete mixes were prepared with normal and recycled aggregates. The results showed that a lower w/c is beneficial for residual strength, especially for recycled aggregate concrete.

In [59], concretes with different pozzolanic materials used as a partial replacement for Portland cement were tested. These were natural pozzolana and lignite fly ash. The conclusion was made that samples with pozzolanic additives are more sensitive to high temperatures, especially in the temperature magnitude of 200 to 400 °C. For 200 °C, OPC concrete registered a 25% reduction in strength, while in concretes with pozzolanic materials, this reduction ranged from 38 to 50%. Taking into account 400 °C, the disproportion was smaller: 50 to 65%. This behavior can be explained by the higher amount of calcium aluminates hydrate (loses part of its combined water at 105 °C), calcium aluminate sulfate hydrate (dehydrates at 150 °C), and amorphous tobermorite gel (dehydrates at 120 °C) in OPC–pozzolana and OPC–fly ash paste mixtures. The amount of strength gained in the

re-curing period is dependent on additives, where OPC concrete regains strength faster than concrete with pozzolanic additives.

Table 11. Relative residual compressive strength for different w/c ratios (0.58 and 0.68) and the difference between relative residual strengths of different w/c ratios according to [42].

	w/c = 0.58		Peak temperature		
	Time * [h]	400 °C	500 °C	550 °C	600 °C
	0	0.93	0.73	0.63	0.33
	1	0.83	0.68	0.48	0.30
$R_{rs}(\theta)$	2	0.70	0.65	0.43	0.20
	w/c = 0.68		Peak temperature		
	Time * [h]	400 °C	500 °C	550 °C	600 °C
	0	0.86	0.75	0.68	0.29
	1	0.82	0.68	0.50	0.18
	2	0.71	0.64	0.39	0.18
	Difference		Peak temperature		
	Time * [h]	400 °C	500 °C	550 °C	600 °C
$f_{rc,20}\left(\frac{w}{c}=0.58\right)-f_{rc,20}\left(\frac{w}{c}=0.68\right)$	0	6.79%	−2.50%	−5.36%	3.93%
	1	0.36%	−0.36%	−2.50%	12.14%
	2	−1.43%	0.71%	3.21%	2.14%

* Time maintained at peak temperature.

Four types of concrete with fly ash replacement for Portland cement were tested in [48]. The influence of the amount of fly ash directly after cooling was tested. Replacement ratios ranged from 10 to 40%. The results showed that there is no correlation between the residual strength directly after cooling and the quantity of fly ash. In [91], the influence of fly ash and metakaolin on the residual strength of HSC was tested. The results reveal that there is no large difference in residual strength directly after cooling for all mixes.

The role of peak temperature and fly ash dosage on the residual strength of lightweight concrete was examined in [92]. The level of importance determined by the Anova method was extremely favorable to the peak temperature, showing that the fly ash quantity impact was minimal. In [93], fly ash dosage did not influence the self-compacting concrete residual strength for peak temperatures up to 300 °C. In [94], research on the influence of finely ground pumice and silica fume on the residual properties of concrete was carried out. Specimens with different dosages of FGP (finely ground pumice) and SF (silica fume) were exposed to high temperatures ranging from 400 to 800 °C and then tested. The results indicate (Figure 15) that FGP additions are beneficial for residual strength, while SF slightly reduces residual strength. A similar conclusion was reached regarding SF in [95].
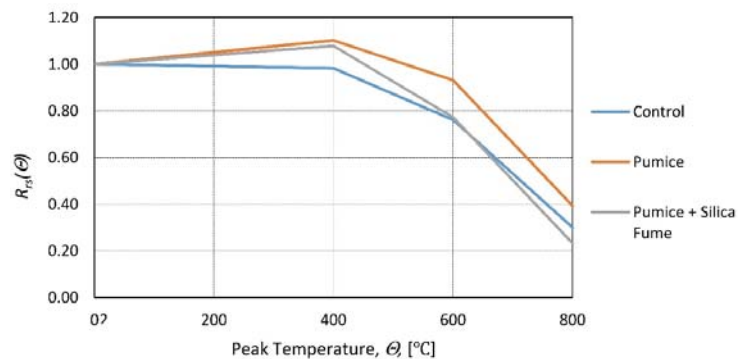

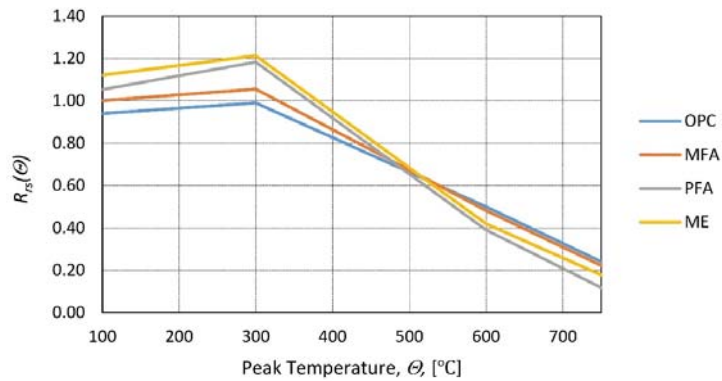**Figure 15.** Relative residual compressive strength as a function of the peak temperature for different cement replacements according to [94].

In [69], the residual strength of the samples with pozzolanic cement replacement was tested. Three types of binder were chosen: the replacement of ME (natural pozzolan), PFA (high calcium fly ash), and MFA (low calcium fly ash), and ordinary Portland cement (OPC) was proposed to be 10 and 30% high. The difference in residual strength induced by the replacement ratio of Portland cement was minimal, so only types of replacement binder were considered. The samples were heated to temperatures of 100 to 750 °C, and the heating rate was set at 2.5 °C/min. After exposure to a peak temperature of 2 h, the samples were naturally cooled inside of the furnace. The residual compressive strength was investigated, and the conclusion was reached that the type of pozzolanic replacement is important only in the lower temperature range (100–400 °C) (Figure 16).

Figure 16. Relative residual compressive strength as a function of the peak temperature for different cement replacements (ME—natural pozzolan, PFA—high calcium fly ash, MFA—low calcium fly ash, OPC—ordinary Portland cement) according to [69].

Another cement replacement, ground granulated blast furnace slag (GGBFS), was investigated in [96]. Mixes were made with the replacement ratios of 10, 30, and 50%. After exposure to elevated temperature (ranging from 150 to 700 °C) and natural cooling in the furnace, compressive tests were performed. The results presented in Figure 17 demonstrate that for low peak temperatures (below 400 °C), replacement of residual strength is insignificant. For higher temperature registers, mixes with the GGBSF replacement resulted in a lower residual strength. The higher replacement ratio resulted in lower mechanical properties.
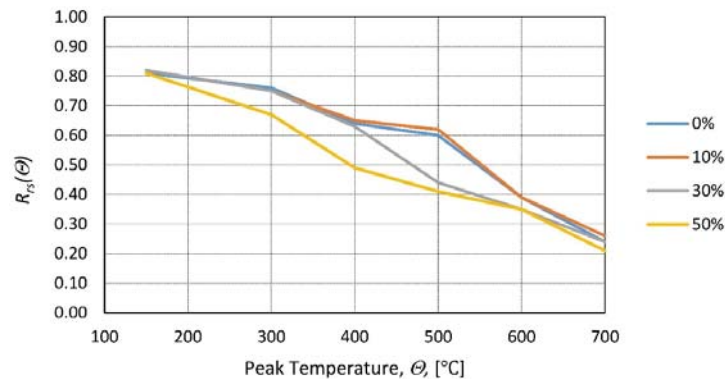
Figure 17. Relative residual compressive strength as a function of the peak temperature for different GGBFS replacement ratios (0, 10%, 30%, and 50%) according to [96].

The available test data prove that the w/c ratio does not have a big influence on the residual strength; only in cases of drastically different ratios, the initial strength differs by a noticeable margin. The rate at which the concrete regains strength is similar for all tested w/c ratios. The cement type (binder additives) is crucial; pozzolans or slag [97] plays an important role in the strength of the cement paste after a fire. More research is needed to fully explain the influence it has on residual strength.

7.3. Additives and Fibers

Many additives can improve concrete properties. Macro-additives, such as polypropylene or steel fibers [98] and micro-additives, such as reactive powder [99] or palm oil fuel ash [55], are only a few examples. In [100], the influence of superplasticizer, hardening accelerator, setting retarders, and air entertainers was found to be minimal (only air entertainers showed a noticeable decrease in residual properties). A similar conclusion can be reached by analyzing the paper [101]. Polypropylene (PP) fibers are said to explicitly improve concrete strength at elevated temperatures. PP (polypropylene) fibers melt and create channels that help release the internal water pressure that was built due to the increase in temperature [102]. Without a doubt, it increases the strength of hot concrete, but its influence on residual strength is less pronounced [103,104]. In [23,29], the residual strength of HSC was tested with and without PP fibers. The tests were performed after cooling, and the same conclusion was reached: PP fibers increase residual strength by a small margin (Figures 18 and 19). In [105,106], the influence of different dosages of PP fibers on the residual strength of HSC was tested. The results showed that the differences between various dosages are limited (Figures 18 and 19). The marginal influence of PP and steel fibers on the residual strength of NSC was also reached in [107].
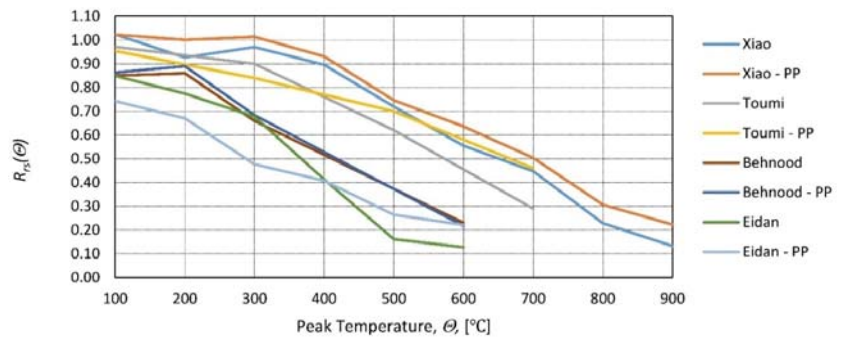
Figure 18. Relative residual compressive strength as a function of peak temperature—with and without PP fibers by [29]—Xiao, [23]—Toumi, [105]—Behnood, and [106]—Eidan.

PP fibers improve residual compressive strength directly after cooling but to a very limited degree. It should not be taken into account when assessing the residual strength of concrete. More tests need to be performed on the influence of PP fibers on the re-curing rate. Channels made by melted PP fibers are impossible to repair, as they do not regenerate. The pore structure of concrete without PP can be restored to a value similar to the initial one, while concrete with PP cannot regain its previous state. In [108], it was suggested that microchannels created in place of melted PP fibers have a positive effect on water re-curing of concrete, as they accelerate the water diffusion rate but negatively impact the residual strength of air re-cured concrete. The influence of steel and PP fibers on NSC and residual properties of HSC was studied in [109], and it was found that steel fibers have a minimal effect on NSC and change the spalling temperature to a higher level. The use of PP fibers increased the spalling resistance for all samples, but a negative effect on residual mechanical properties was noticed. In [110] the influence of steel fibers on residual strength at very high temperatures (900–1200 °C) was analyzed, and a minimal influence

was observed. Concrete with glass and steel fibers tests were performed in [111]. Up to 30%, higher compressive strength was noted for steel fiber concrete (for glass fiber, up to 20%). This increase was especially visible for the 300–500 °C temperature range. In [112], PP fibers in concrete mixes were tested, and the results showed that thermal behavior and stability are not influenced by type and dosage. Similar research should be conducted on residual mechanical properties.
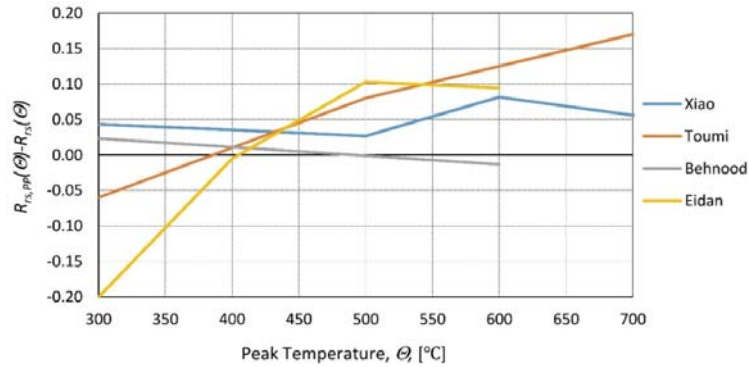

Figure 19. The difference in relative residual compressive strength with and without PP fibers by [29]—Xiao, Toumi [23], Behnood [105], and Eidan [106].

8. Porosity

Porosity, pore size, and pore distribution are the primary factors influencing the strength, durability, and permeability of concrete. Research already done in this area is collected in Table 12. High-temperature exposure increases the porosity and coarsening of the pore structure of concrete [58]. The dehydration process that occurs in the C-S-H (calcium–silicate–hydrate) gel decreases its volume and subsequently increases its porosity. Although up to 200 °C, a slight expansion of the cement paste is observed, above this temperature, rapid shrinkage occurs. This phenomenon greatly influences the evolution of porosity. In [60], porosity was measured using the mercury intrusion porosimeter (MIP). Compared to the preheating values, porosity directly after cooling was two times higher for 600 °C and three times higher for 800 °C. However, post-fire re-curing significantly reduced the porosity by the rehydration of particles that filled capillaries. Lower porosity results in a dense microstructure and better mechanical properties. When comparing the results presented in [60] (Figure 20), lower initial porosity leads to slightly higher relative residual strength. If two concretes with different initial porosities are compared with relation not to initial but after cooling strength and porosity, then re-curing gains are very similar (Table 13).

Table 12. Summary of the research on porosity.

Author	Citation	Sample Type	Sample Size	Concrete Strength	Temp. Range	Heating Time	Porosity	Age of Concrete at Exposure
Hager	28	Cubic Cylindrical	Cubic: 150 mm Cyl.: D 100 mm, H 200 mm	HSC	200–1000 °C	3 h	1.4–2%	90 days
Poon	62	Cubic	100 mm	NSC, HSC	600–800 °C	1 h	6.69–9.52%	60 days
Chromá	115	Beam	40 mm × 40 mm × 160 mm	NSC	200–1200 °C	2 h	15%	28 days
Chan	116	Cubic	NA	NSC, HSC	800–1100 °C	1 h	NA	90 days

Table 13. Porosity and relative porosity as a function of re-curing time for different concrete mixes (CC—control sample, FA30—30% of cement replaced by fly ash) according to [49].

	Directly after Cooling—t = 0 Days				Re-Curing—Air—t = 28 Days				Re-Curing—Water—t = 56 Days			
Peak Temp. [°C] Initial Porosity [%]	$\theta = 600$ $p_{rc}(\theta,0)$	$\theta = 600$ $R_{rs}(\theta,t)$	$\theta = 800$ $p_{rc}(\theta,0)$	$\theta = 800$ $R_{rs}(\theta,t)$	$\theta = 600$ $p_{rc}(\theta,t)$	$\theta = 600$ $R_{rs}(\theta,t)$	$\theta = 800$ $p_{rc}(\theta,t)$	$\theta = 800$ $R_{rs}(\theta,t)$	$\theta = 600$ $p_{rc}(\theta,t)$	$\theta = 600$ $R_{rs}(\theta,t)$	$\theta = 800$ $p_{rc}(\theta,t)$	$\theta = 800$ $R_{rs}(\theta,t)$
HS-CC 9.52	18.3	0.58	17.71	0.24	16.56	0.67	26.66	0.37	16.96	0.69	23.04	0.52
HS-FA30 6.69	11.3	0.67	10.44	0.32	10.1	0.77	19.6	0.47	7.96	0.93	11.91	0.79
HS-CC $\frac{p_{rc}(\theta,t)}{p_{rc}(\theta,0)}$ / $\frac{R_{rs}(\theta,t)}{R_{rs}(\theta,0)}$	1.00	1.00	1.00	1.00	0.90	1.16	1.51	1.54	0.93	1.19	1.30	2.17
HS-FA30	1.00	1.00	1.00	1.00	0.90	1.15	1.88	1.47	0.71	1.39	1.14	2.47
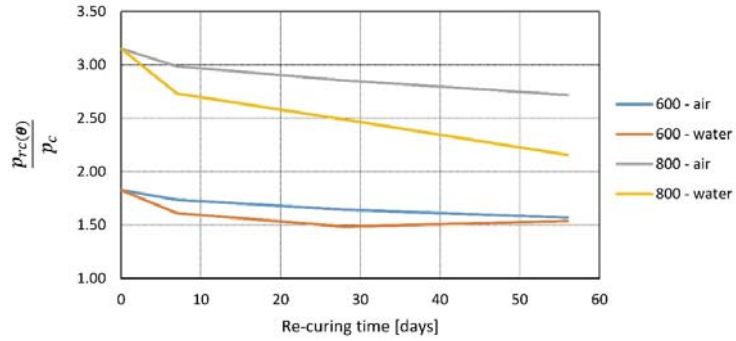
Figure 20. Relative porosity as a function of re-curing time with different re-curing methods (air re-curing and water re-curing) and different peak temperatures θ = 600 and 800 °C according to [60].

In [27], an MIT (mercury intrusion porosimetry test) test was used to measure changes in connected porosity (open pore network). Tests were performed after cooling. The results compared to previous research are consistent as presented in Table 14. The relative porosity increases at a rate similar to that observed in [60], and the relative residual strength at the corresponding temperature is similar.

Table 14. Relative residual compressive strength and relative porosity as a function of the peak temperature according to [27].

	Temperature [°C]				
	20	**200**	**400**	**600**	**800**
$\dfrac{p_{rc}(\theta)}{p_c}$	1.00	1.65	1.85	2.46	2.74
$R_{rs}(\theta)$	1.00	1.00	0.90	0.70	0.25

An interesting relation was observed in [113], comparing porosity at relative peak temperature, between tests performed directly after cooling (a) and 2 months of water curing (b). Porosity in the temperature range of up to 400 °C is constant. In the range from 400 to 800 °C, porosity is increasing for the sample that was tested directly after cooling, but the porosity level of the water-cured sample is still constant. From 800 to 1000 °C, (a) is slowly increasing, while (b) noted rapid growth, and at temperatures above 1000 °C, the type of curing is irrelevant (Figure 21).
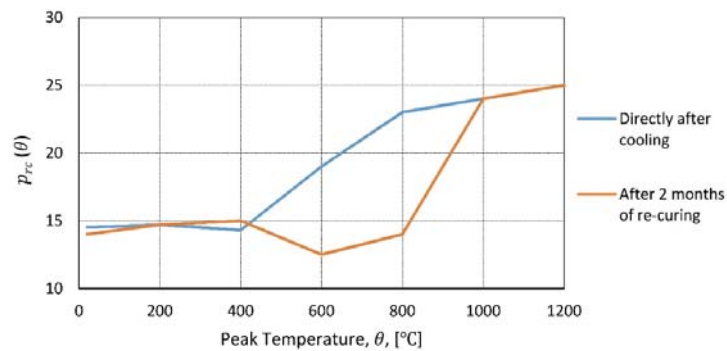
Figure 21. Total porosity as a function of the peak temperature and curing according to [113].

Porosity is rapidly growing, with temperature increasing above 400 °C and having a great impact on the strength of concrete. The calculated correlation factors between porosity after exposure and residual strength shows a significant negative porosity influence (Table 15). This relationship can be nonlinear, as the Pearson and Spearman coefficients are not very high. It was noted that the porosity growth is higher for HSC [114]. Nevertheless, damages caused by dehydration can be repaired by rehydration of the concrete. With an appropriate curing method applied to concrete exposed to peak temperatures not exceeding 800 °C, porosity can be regenerated to levels before heating. Taking these facts into account, the initial porosity of concrete plays a marginal role in the relative residual strength. The relative growth of residual strength (with relation to strength directly after cooling) of concretes with different initial porosities is very similar.

Table 15. Correlation factors between porosity after exposure and relative residual strength, based on data presented by various authors.

Correlation Coefficient	Coefficient Value
Pearson	−0.697
Spearman	−0.755
Kendall	−0.593

9. Age of Concrete at Exposure

Fire can happen in a building regardless of its age. Both very old buildings and new buildings (or even still under construction) can experience exposure to fire situations. The behavior of concrete at high temperatures will be different in the mentioned cases. Moisture and the amount of concrete that was already hydrated influence both hot and residual strength but also the re-curing rate. In [115,116], concrete that was exposed to an elevated temperature at an early age (from 1 to 28 days after casting) was tested. Residual strength tests showed that young concrete had a better recovery rate (with the exception of 1-day-old concrete, as it did not have enough strength to withstand high temperature, and damage during the heating period was considerable. In [117], the strain-hardening cementitious composite was tested, and a similar conclusion was reached.

10. Load Level at Exposure

The level of load at exposure is an important issue that needs to be addressed, as every building is constantly subjected to loads. Strength at high temperature is positively affected by load level, as it reduces the speed of decrease of strength [118–120]. In [121], the influence of preload on residual strength was analyzed. There were three preload levels (0, 20, and 40% of the ultimate load at room temperature), and after exposure to high temperature and cooling, compressive tests were performed. The results showed that preload results in a higher residual strength (for 20% of preload increase, it is approximately 15%). This can be attributed to the restriction of thermal expansion by acting on the load, thus minimizing concrete damage. In [122], free expansion deformation of unstressed specimens exposed to high temperature at different heating rates was investigated. The linear expansion rate (LER) measured at high temperature was a linear function of temperature and did not depend on the heating rate. Restraining expansion and thus minimalizing internal cracking can greatly benefit residual strength. Thus, compressive stress plays a positive role.

11. Heat Accumulation Factor

The hot and residual strengths of concrete depend on the dehydration of the cement gel. Dehydration is mainly related to high exposure to heat, both the peak temperature and the exposure time. The factor that evaluates high-temperature exposure is the heat accumulation factor. It is defined as the area under the temperature–time curve. This idea was proposed in [46], and various studies [60,123–125] show that cement paste decomposition begins when the temperature exceeds 400 °C. Thus, the heat accumulation factor influencing the strength of the concrete should take into account only temperatures above

400 °C. Exposure to 200 °C will damage the concrete to an incomparably smaller degree than short exposure to 400 °C.

The heat accumulation factor can be calculated in two ways (Figure 22), as originally proposed in [46] by the use of Equation (1) $\left(H^{400}\right)$ and by the method proposed by the authors $\left(H^{400r}\right)$:

$$H^{400} = \int_{tr}^{ts} T(t)dt \tag{1}$$

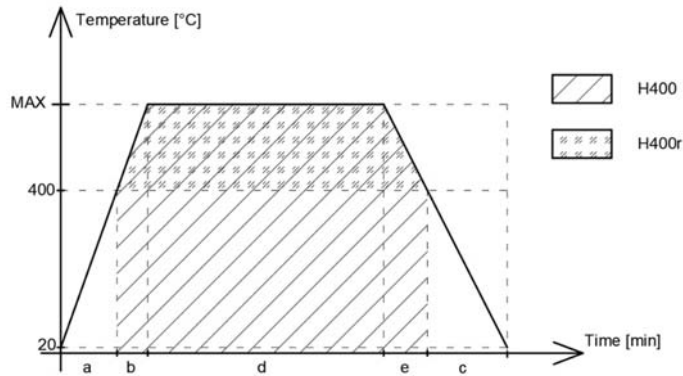$$H^{400r} = \int_{tr}^{ts} \left(T(t) - 400\right) dt. \tag{2}$$

Figure 22. Diagram of the calculation of the heat accumulation factor, H^{400} and H^{400r}.

A summary of the existing data is presented in Figures 23–30. Heating and cooling rates were treated as constant to simplify the calculation. It is visible that H^{400} follows a certain decreasing line (Figures 23 and 25), which was easy to predict, but the scatter is big, and there is no easy way to generalize the results. *The H^{400r} is* less scattered, but it is still hard to derive a solid function (Figures 24 and 26). A comparison between H^{400} and H^{400r} is presented in Figures 27 and 28 for NSC and Figures 29 and 30 for HSC. The three correlation factors presented in Table 16 demonstrate the superiority of the modified heat accumulation factor (Equation (2)). The values of the factors suggest a nonlinear relationship.

Table 16. Correlation factors between heat accumulation factors and relative residual strength based on data presented by various authors.

Coefficient	NSC		HSC	
	H^{400}	H^{400r}	H^{400}	H^{400r}
Pearson	−0.455	−0.543	−0.434	−0.498
Spearman	−0.494	−0.615	−0.500	−0.675
Kendall	−0.335	−0.435	−0.363	−0.490

Thus, nonlinear exponential fitting was made. The R^2 factor (not deciding for nonlinear regression) was again higher in the H^{400r} variation. However, the data of NSC and HSC behave similarly. With this in mind, for future reference, NSC and HSC can be treated identically, and separation is unnecessary.
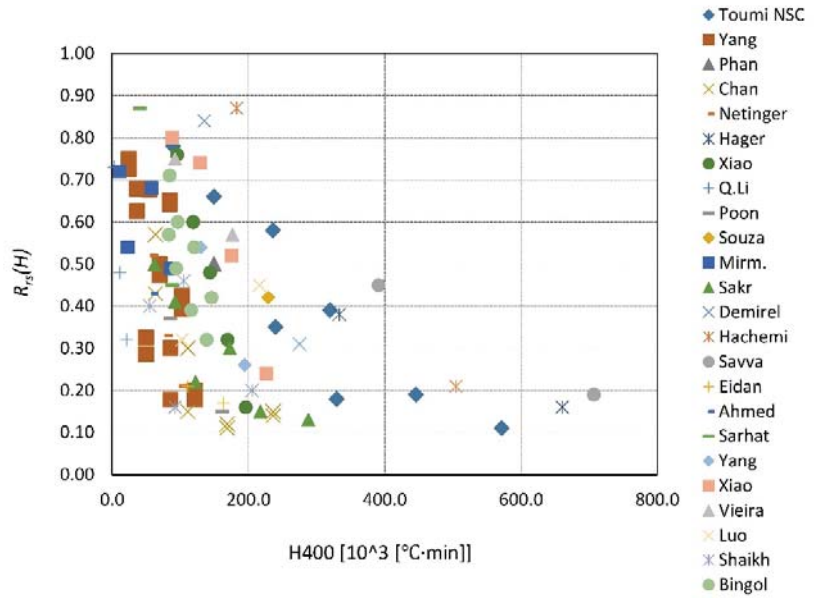
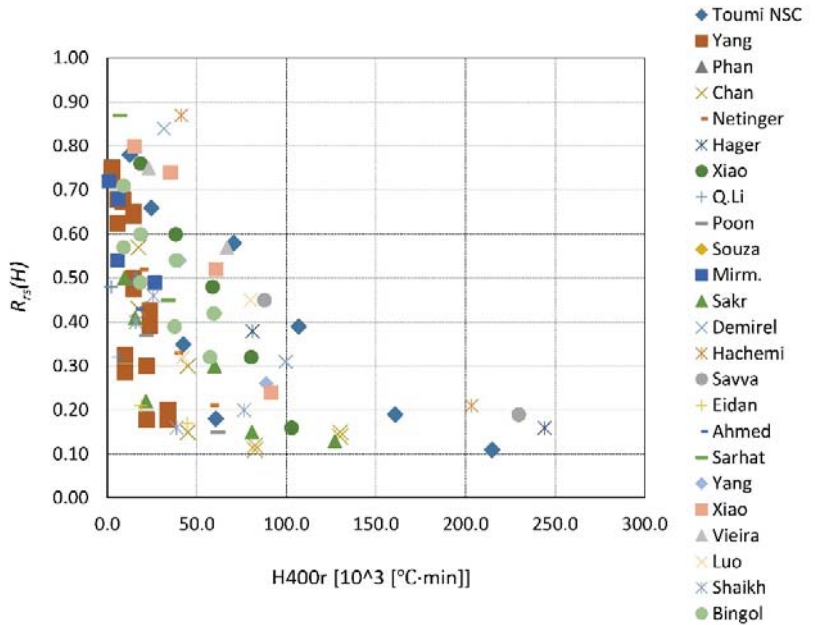**Figure 23.** H^{400} coefficient for NSC by different authors.

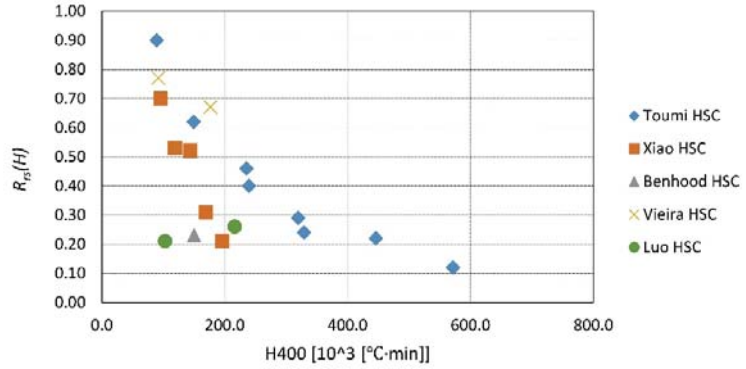**Figure 24.** H^{400r} coefficient for NSC by different authors.

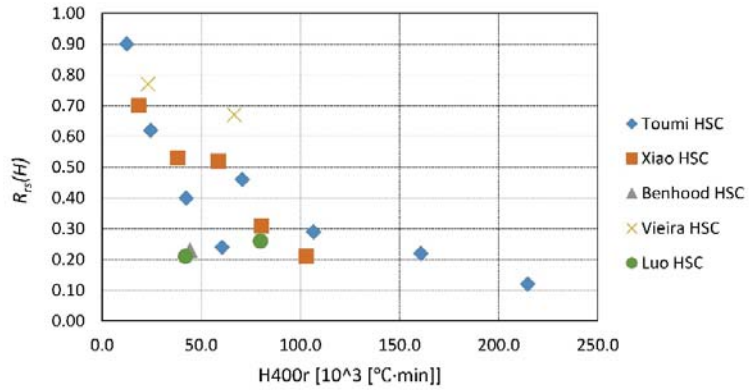**Figure 25.** H^{400} coefficient for HSC by different authors.

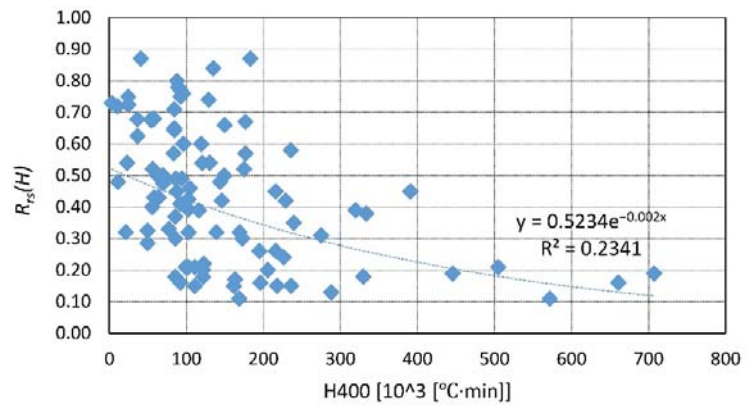**Figure 26.** H^{400r} coefficient for HSC by different authors.

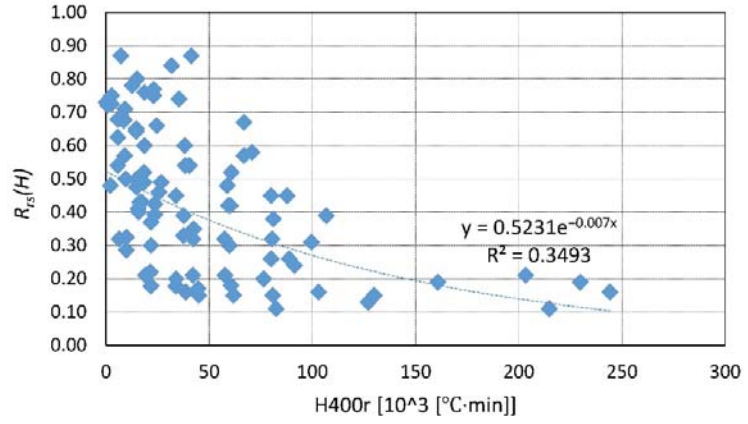**Figure 27.** H^{400} coefficient for NSC—summary and fitting.

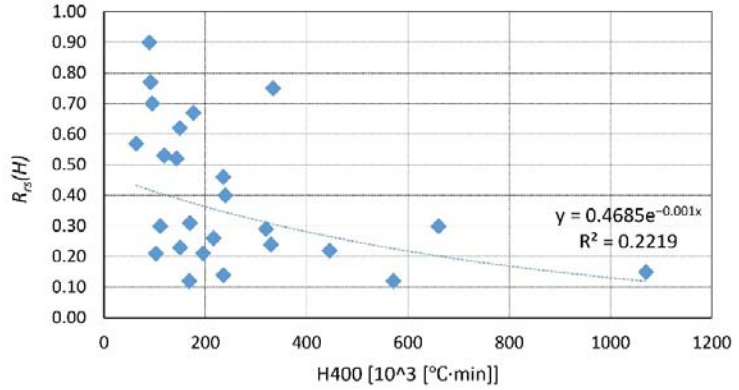**Figure 28.** H^{400r} coefficient for NSC—summary and fitting.
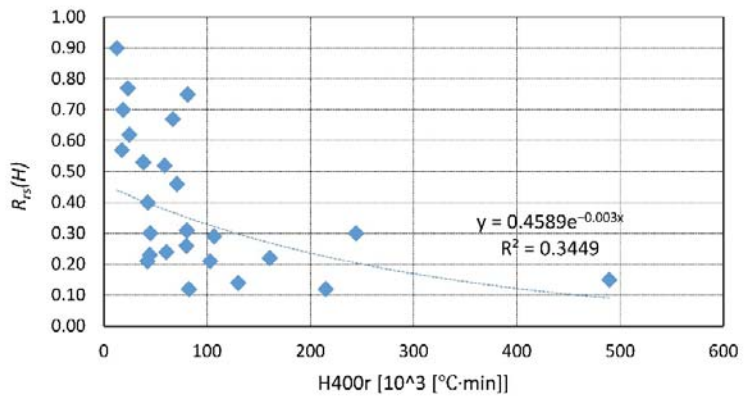

Figure 29. H^{400} coefficient for HSC—summary and fitting.

Figure 30. H^{400r} coefficient for HSC—summary and fitting.

12. Discussion

Although experimental research on the residual strength of concrete is extensive, the results appear to be incomplete. The main factors influencing residual strength (peak temperature, heating time, cooling regime, post-heating re-curing, load level at exposure) are already identified. Other factors, but with less pronounced effects (heating rate, type of aggregate, cement type, and dosage) have also been examined. However, some factors do not contribute to the strength, such as common additives, or the influence is not straightforward, such as porosity. However, with this in mind, experimental research can be limited to the temperature range 300–700 °C because the residual strength for temperatures up to 300 °C and more than 750 °C can be obtained only on the basis of the peak temperature. Moreover, the limit of two hours of high-temperature exposure can be used, as the main strength loss occurs within this period, and later, the impact is minimal.

Both essential factors influencing the residual strength (i.e., peak temperature and heating time) exhibit a negative linear influence on the residual strength, while for the other factors, the influence is not so straightforward, as the correlation factors are smaller. Thus, nonlinear functions would properly govern these relationships. Furthermore, the influence of the peak temperature on the residual strength is not as direct as on the hot concrete strength. Only the strength directly after cooling is highly dependent on the peak temperature reached. A similar conclusion is drawn for the cooling regime; e.g., for water cooling, its negative impact is apparent in the early stage of recurring but for the longer re-curing time, the impact diminishes. The influence of rapid cooling is also limited to the external layers, and it is not deciding for whole structure load capacity.

What should be stressed is the ability of concrete to regain its strength due to the rehydration of cement paste. Therefore, re-curing time and type are crucial for assessing the residual strength of concrete. From this perspective, it is not surprising that the influence of the w/c ratio can be omitted. However, there are reports where a lower w/c ratio results in a higher residual strength. This problem may be posed by cement type, as there is not enough comparative research focusing on the type of cement and its influence on residual strength. There exists also an indirect relationship between rehydration and porosity that requires further research. Porosity is notably higher after high-temperature exposure, and reversal is possible if the temperature was not greater than 800 °C. Moreover, lower porosity results in higher residual strength directly after cooling, but after re-curing, this difference is equalized.

The time after cooling and its type also regulate the residual strength. Directly after water cooling, a lower residual strength is obtained. Nevertheless, the re-curing significantly reduces the influence of cooling type. However, additional consideration of these phenomena is necessary for the external part of an element that is severely damaged. The internal part, which is crucial from a residual strength point of view, is immune to damages caused by different types of cooling. The interaction between layers of heated and cooled concrete should also be studied. The transient temperature field and associated strain and stress can contribute to material damage and strength reduction. Moreover, the possible volume changes due to chemical reactions and thermal expansion would also be considered.

There is also a need for more research on the influence of PP fibers on regaining residual strength. Changes in concrete structure left by PP fibers are evident, and their impact needs to be assessed. More research is also needed to determine the relation between preload level and residual strength, as it can be important in practice.

Since the ability of concrete to regain its strength due to rehydration determines the residual strength, only temperatures above 400 °C should be taken into account, because the decomposition of cement paste starts at this temperature. The modified heat accumulation factor H^{400r} gives more coherent results than the unmodified H^{400} as demonstrated by correlation factors, and therefore, it can be used to assess the residual strength of concrete.

13. Conclusions

The research presented in the paper signifies the determination of the peak temperature and the heating time of the residual strength. The other factors do not directly influence the residual strength. However, as concrete regains its strength due to the rehydration of cement paste, the re-curing time and type are also crucial factors.

The proposed modified heat accumulation factor can be considered as a measure that collects all influences. However, more research needs to be done to increase accuracy and prove that the modified accumulation factor is universal, i.e., if in changing experimental conditions, the same values of the factor are associated with the same values of the residual strength. If not, other measures of damage should be considered.

If the other measures of damage are proposed, they should take into account that the derivative of residual strength regarding heating time is constant, and the residual strength can be described as a logarithmical function of re-curing time and type. Thus, to create a function that will precisely assess the residual strength of concrete, one needs to solve an equation system that takes all influential variables into account. Considering only part of the variables will result in an approximate solution. A comprehensive function of residual strength can be found only after the above-mentioned factors, extended by necessary research, are rationalized by mathematical function, compressed to the equation system, and then solved.

Abbreviation

Upper case letters

C-S-H gel	calcium-silicate-hydrate gel
FGP	finely ground pumice
GGBFS	ground granulated blast furnace slag
HSC	high strength concrete
ME	natural pozzolana of volcanic origin, Milos Earth
MFA	Megalopolis fly ash
MIT	mercury intrusion porosimetry test
NSC	normal strength concrete
OPC	ordinary Portland cement
PFA	Ptolemaida fly ash
PP fibers	polypropylene fibers
RCA	recycled concrete aggregate
RCCA	recycled ceramic coarse aggregate
SF	silica fume

Lower case letters

$f_{rc,T_t}(\theta)$	residual strength of concrete after exposure to elevated temperature (θ) then cooled down and tested in temperature (T_t)
f_{c,T_t}	strength of unexposed concrete tested in temperature (T_t)
$f_{rc,AC}$	residual strength of concrete after exposure to elevated temperature then cooled down to ambient temperature in air and tested
$f_{rc,WC}$	residual strength of concrete after exposure to elevated temperature then cooled down in the water to ambient temperature and tested
$f_{rc,WC}(t)$	residual strength of concrete after exposure to elevated temperature then cooled down in the water for time (t), then cooled down to ambient temperature in air and tested
$f_{rc,FC}$	residual strength of concrete after exposure to elevated temperature then cooled down in closed furnace to ambient temperature and tested
p_c	porosity of unexposed concrete
$p_{rc}(\theta,\,t)$	porosity of concrete after exposure to elevated temperature (θ) then cooled down and tested at a temperature of 20 °C after (t) days of re-curing
$\dfrac{p_{rc}(\theta)}{p_c}$	relative porosity of concrete tested in 20 °C
w/c	water to cement ratio

Subscripts

AC	value pertaining to air re-curing
c	value pertaining to unexposed concrete
FC	value pertaining to cooling in closed furnance
rc	residual value
T_t	temperature of sample in test
WC	value pertaining to water re-curing

References

1. Kim, G.Y.; Kim, Y.S.; Lee, T.G. Mechanical properties of high-strength concrete subjected to high temperature by stressed test. *Trans. Nonferrous Met. Soc. China* **2009**, *19*, s128–s133. [CrossRef]
2. *EN 1992-1-2 Eurocode 2: Design of Concrete Structures–Part. 1–2: General Rules–Structural Fire Design*; Comité Européen de Normalisation. Rules-Structural Fire Design de Normalisation: Brussels, Belgium, 2004.
3. RILEM Technical Committee 200-HTC. Recommendation of RILEM TC 200-HTC: Mechanical concrete properties at high temperatures—modelling and applications. *Mater. Struct.* **2007**, *40*, 855–864. [CrossRef]
4. *ASTM Standard E119-20 Standard Test. Methods for Fire Tests of Building Construction and Materials*; ASTM International: West Conshohocken, PA, USA, 2020.
5. Chang, Y.F.; Chen, Y.H.; Sheu, M.S.; Yao, G.C. Residual stress-strain relationship for concrete after exposure to high temperatures. *Cem. Concr. Res.* **2006**, *36*, 1999–2005. [CrossRef]
6. Nassif, A. Postfire Full Stress–Strain Response of Fire-Damaged Concrete. *Fire Mater.* **2006**, *30*, 323–332. [CrossRef]
7. Hager, I.; Krzemień, K. An Overview of Concrete Modulus of Elasticity Evolution with Temperature and Comments to European Code Provisions. In Proceedings of the IFireSS—International Fire Safety Symposium, Coimbra, Portugal, 20–23 April 2015.
8. Felicetti, R.; Gambarova, P.G.; Meda, A. Residual behavior of steel rebars and R/C sections after a fire. *Constr. Build. Mater.* **2009**, *23*, 3546–3555. [CrossRef]
9. Kodur, V.K.R.; Raut, N.K.; Mao, X.Y.; Khaliq, W. Simplified approach for evaluating residual strength of fire-exposed reinforced concrete columns. *Mater. Struct. Constr.* **2013**, *46*, 2059–2075. [CrossRef]
10. Wróblewski, R.; Gierczak, J.; Smardz, P.; Kmita, A. Fire and collapse modelling of a precast concrete hall. *Struct. Infrastruct. Eng.* **2016**, *12*, 714–729. [CrossRef]
11. Mróz, K.; Hager, I. Non-Destructive Assessment of Residual Strength of Thermally Damaged Concrete Made with Different Aggregate Types. *IOP Conf. Ser. Mater. Sci. Eng.* **2017**, *245*, 32034. [CrossRef]
12. Hager, I.; Carré, H.; Krzemie, K. Damage Assessment of Concrete Subjected To High Temperature By Means of the Ultrasonic Pulse Velocity–Upv Method. *Stud. Res.* **2013**, *32*, 197–211.
13. Hager, I. Methods for assessing the state of concrete in fire damaged structures | Metody oceny stanu betonu w konstrukcji po pożarze. *Cem. Wapno Bet.* **2009**, *29*, 167–178.
14. Wróblewski, R.; Stawiski, B. Ultrasonic Assessment of the Concrete Residual Strength after a Real Fire Exposure. *Buildings* **2020**, *10*, 154. [CrossRef]
15. Ma, Q.; Guo, R.; Zhao, Z.; Lin, Z.; He, K. Mechanical properties of concrete at high temperature—A review. *Constr. Build. Mater.* **2015**, *93*, 371–383. [CrossRef]
16. Luccioni, B.M.; Figueroa, M.I.; Danesi, R.F. Thermo-mechanic model for concrete exposed to elevated temperatures. *Eng. Struct.* **2003**, *25*, 729–742. [CrossRef]

17. Türkmen, İ.; Fındık, S.B. Several properties of mineral admixtured lightweight mortars at elevated temperatures. *Fire Mater.* **2013**, *37*, 337–349. [CrossRef]

18. Kodur, V. Properties of concrete at elevated temperatures. *ISRN Civ. Eng.* **2014**, *2014*, 468510. [CrossRef]

19. Sarshar, R. Effect of Elevated Temperatures on the Strength of Different Cement Pastes and Concretes. Ph.D. Thesis, University of London, London, UK, 1989.

20. Biolzi, L.; Cattaneo, S.; Rosati, G. Evaluating residual properties of thermally damaged concrete. *Cem. Concr. Compos.* **2008**, *30*, 907–916. [CrossRef]

21. Arioz, O. Retained properties of concrete exposed to high temperatures: Size effect. *Fire Mater.* **2009**, *33*, 211–222. [CrossRef]

22. Xiao, J.; Li, Z.; Xie, Q.; Shen, L. Effect of strain rate on compressive behaviour of high-strength concrete after exposure to elevated temperatures. *Fire Saf. J.* **2016**, *83*, 25–37. [CrossRef]

23. Toumi, B.; Resheidat, M.; Guemmadi, Z.; Chabil, H. Coupled effect of high temperature and heating time on the residual strength of normal and high-strength concretes. *Jordan J. Civ. Eng.* **2009**, *3*, 322–330.

24. Yang, H.; Lin, Y.; Hsiao, C.; Liu, J.Y. Evaluating residual compressive strength of concrete at elevated temperatures using ultrasonic pulse velocity. *Fire Saf. J.* **2009**, *44*, 121–130. [CrossRef]

25. Phan, L.T.; Lawson, J.R.; Davis, F.L. Effects of elevated temperature exposure on heating characteristics, spalling, and residual properties of high performance concrete. *Mater. Struct. Constr.* **2001**, *34*, 83–91. [CrossRef]

26. Netinger, I.; Kesegic, I.; Guljas, I. The effect of high temperatures on the mechanical properties of concrete made with different types of aggregates. *Fire Saf. J.* **2011**, *46*, 425–430. [CrossRef]

27. Hager, I.; Tracz, T.; Śliwiński, J.; Krzemień, K. The influence of aggregate type on the physical and mechanical properties of high-performance concrete subjected to high temperature. *Fire Mater.* **2016**, *40*, 668–682. [CrossRef]

28. Krzemień, K.; Hager, I. Post-fire assessment of mechanical properties of concrete with the use of the impact-echo method. *Constr. Build. Mater.* **2015**, *96*, 155–163. [CrossRef]

29. Xiao, J.; Falkner, H. On residual strength of high-performance concrete with and without polypropylene fibres at elevated temperatures. *Fire Saf. J.* **2006**, *41*, 115–121. [CrossRef]

30. Chan, Y.N.; Peng, G.F.; Anson, M. Residual strength and pore structure of high-strength concrete and normal strength concrete after exposure to high temperatures. *Cem. Concr. Compos.* **1999**, *21*, 23–27. [CrossRef]

31. Tolentino, E.; Lameiras, F.S.; Gomes, A.M.; da Silva, C.A.R.; Vasconcelos, W.L. Effects of High Temperature on the Residual Performance of Portland Cement Concretes. *Mater. Res.* **2002**, *5*, 301–307. [CrossRef]

32. Ashkezari, G.D.; Razmara, M. Thermal and mechanical evaluation of ultra-high performance fiber-reinforced concrete and conventional concrete subjected to high temperatures. *J. Build. Eng.* **2020**, *32*, 101621. [CrossRef]

33. Xiao, J.; Xie, M.; Zhang, C. Residual compressive behaviour of pre-heated high-performance concrete with blast-furnace-slag. *Fire Saf. J.* **2006**, *41*, 91–98. [CrossRef]

34. Zhai, Y.; Deng, Z.; Li, N.; Xu, R. Study on compressive mechanical capabilities of concrete after high temperature exposure and thermo-damage constitutive model. *Constr. Build. Mater.* **2014**, *68*, 777–782. [CrossRef]

35. Comité Européen de Normalisation. *EN 1991-1-2 Eurocode 1. Actions on Structures. General Actions. Actions on Structures Exposed to Fire*; Comité Européen de Normalisation: Brussels, Belgium, 2002.

36. Pertiwi, N.; Ahmad, I.A.; Taufieq, N.A.S. Analysis-Residual Strength of Post Fire Concrete. *Asian J. Appl. Sci.* **2017**, *5*, 602–607.

37. Wu, Y.; Wu, B. Residual compressive strength and freeze-thaw resistance of ordinary concrete after high temperature. *Constr. Build. Mater.* **2014**, *54*, 596–604. [CrossRef]

38. Mohamedbhai, G.T.G. Effect of exposure time and rates of heating and cooling on residual strength of heated concrete. *Mag. Concr. Res.* **1986**, *38*, 151–158. [CrossRef]

39. Annerel, E.; Taerwe, L.R. Approaches for the assessment of the residual strength of concrete exposed to fire. In *Concrete Repair, Rehabilitation and Retrofitting II*; CRC Press: Boca Raton, FL, USA, 2007; p. 12.

40. Kowalski, R. The effects of the cooling rate on the residual properties of heated-up concrete. *Struct. Concr.* **2007**, *8*, 11–15. [CrossRef]

41. Peng, G.F.; Bian, S.H.; Guo, Z.Q.; Zhao, J.; Peng, X.L.; Jiang, Y.C. Effect of thermal shock due to rapid cooling on residual mechanical properties of fiber concrete exposed to high temperatures. *Constr. Build. Mater.* **2008**, *22*, 948–955. [CrossRef]

42. Yang, H.; Zhao, H.; Liu, F. Residual cube strength of coarse RCA concrete after exposure to elevated temperatures. *Fire Mater.* **2018**, *42*, 424–435. [CrossRef]

43. Husem, M. The effects of high temperature on compressive and flexural strengths of ordinary and high-performance concrete. *Fire Saf. J.* **2006**, *41*, 155–163. [CrossRef]

44. Mendes, A.; Sanjayan, J.G.; Collins, F. Effects of slag and cooling method on the progressive deterioration of concrete after exposure to elevated temperatures as in a fire event. *Mater. Struct. Constr.* **2011**, *44*, 709–718. [CrossRef]

45. Bingöl, A.F.; Gül, R. Effect of elevated temperatures and cooling regimes on normal strength concrete. *Fire Mater.* **2009**, *33*, 79–88. [CrossRef]

46. Li, L.; Jia, P.; Dong, J.; Shi, L.; Zhang, G.; Wang, Q. Effects of cement dosage and cooling regimes on the compressive strength of concrete after post-fire-curing from 800 °C. *Constr. Build. Mater.* **2017**, *142*, 208–220. [CrossRef]

47. Luo, X.; Sun, W.; Chan, S.Y.N. Effect of heating and cooling regimes on residual strength and microstructure of normal strength and high-performance concrete. *Cem. Concr. Res.* **2000**, *30*, 379–383. [CrossRef]

48. Shaikh, F.U.A.; Vimonsatit, V. Effect of cooling methods on residual compressive strength and cracking behavior of fly ash concretes exposed at elevated temperatures. *Fire Mater.* **2016**, *40*, 335–350. [CrossRef]
49. Wang, Y.; Liu, F.; Xu, L.; Zhao, H. Effect of elevated temperatures and cooling methods on strength of concrete made with coarse and fine recycled concrete aggregates. *Constr. Build. Mater.* **2019**, *210*, 540–547. [CrossRef]
50. Li, Q.; Yuan, G.; Shu, Q. Effects of heating/cooling on recovery of strength and carbonation resistance of fire-damaged concrete. *Mag. Concr. Res.* **2014**, *66*, 925–936. [CrossRef]
51. Karakoç, M.B. Effect of cooling regimes on compressive strength of concrete with lightweight aggregate exposed to high temperature. *Constr. Build. Mater.* **2013**, *41*, 21–25. [CrossRef]
52. Yu, J.; Weng, W.; Yu, K. Effect of different cooling regimes on the mechanical properties of cementitious composites subjected to high temperatures. *Sci. World J.* **2014**, *2014*, 1–7. [CrossRef]
53. Tanaçan, L.; Ersoy, H.Y.; Arpacıoğlu, Ü. Effect of high temperature and cooling conditions on aerated concrete properties. *Constr. Build. Mater.* **2009**, *23*, 1240–1248. [CrossRef]
54. Zhai, Y.; Li, Y.; Li, Y.; Wang, S.; Liu, Y.; Song, K.I. Impact of high-temperature-water cooling damage on the mechanical properties of concrete. *Constr. Build. Mater.* **2019**, *215*, 233–243. [CrossRef]
55. Awal, A.S.M.A.; Shehu, I.A.; Ismail, M. Effect of cooling regime on the residual performance of high-volume palm oil fuel ash concrete exposed to high temperatures. *Constr. Build. Mater.* **2015**, *98*, 875–883. [CrossRef]
56. Xuan, D.X.; Shui, Z.H. Rehydration activity of hydrated cement paste exposed to high temperature. *Fire Mater.* **2011**, *35*, 481–490. [CrossRef]
57. Akca, A.H.; Özyurt, N. Effects of re-curing on microstructure of concrete after high temperature exposure. *Constr. Build. Mater.* **2018**, *168*, 431–441. [CrossRef]
58. Li, L.; Shi, L.; Wang, Q.; Liu, Y.; Dong, J.; Zhang, H.; Zhang, G. A review on the recovery of fire-damaged concrete with post-fire-curing. *Constr. Build. Mater.* **2020**, *237*, 117564. [CrossRef]
59. Papayianni, J.; Valiasis, T. Residual mechanical properties of heated concrete incorporating different pozzolanic materials. *Mater. Struct.* **1991**, *24*, 115–121. [CrossRef]
60. Poon, C.S.; Azhar, S.; Anson, M.; Wong, Y.L. Strength and durability recovery of fire-damaged concrete after post-fire-curing. *Cem. Concr. Res.* **2001**, *31*, 1307–1318. [CrossRef]
61. de Souza, A.A.A.; Moreno, A.L., Jr. Assessment of the influence of the type of aggregates and rehydration on concrete submitted to high temperatures. *Rev. IBRACON Estrut. Mater.* **2010**, *3*, 477–493. [CrossRef]
62. Lin, Y.; Hsiao, C.; Yang, H.; Lin, Y.F. The effect of post-fire-curing on strengthvelocity relationship for nondestructive assessment of fire-damaged concrete strength. *Fire Saf. J.* **2011**, *46*, 178–185. [CrossRef]
63. Mirmomeni, M.; Heidarpour, A.; Schlangen, E.; Smith, S. Effect of Post-Fire Curing on the Residual Mechanical Properties of Fire-Damaged Self-Compacting Concrete. In Proceedings of the 9th International Conference on Fracture Mechanics of Concrete and Concrete Structures, Berkeley, CA, USA, 29 May–1 June 2016. [CrossRef]
64. Horiguchi, T.; Suhaendi, S.L. Recovery behavior of hybrid fiber reinforced high strength concrete after fire exposure. *J. Struct. Fire Eng.* **2010**, *1*, 219–229. [CrossRef]
65. Park, S.J.; Yim, H.J.; Kwak, H.G. Effects of post-fire curing conditions on the restoration of material properties of fire-damaged concrete. *Constr. Build. Mater.* **2015**, *99*, 90–98. [CrossRef]
66. Eden, M.A. Fire damaged concrete—The potential for on-going deterioration post-fire in concrete heated to temperatures of less than 300 °C. In *Concrete Solutions 2011*, 1st ed.; Grantham, M., Mechtcherine, V., Schneck, U., Eds.; CRC Press: Boca Raton, FL, USA, 2012. [CrossRef]
67. Cree, D.; Green, M.; Noumowé, A. Residual strength of concrete containing recycled materials after exposure to fire: A review. *Constr. Build. Mater.* **2013**, *45*, 208–223. [CrossRef]
68. Razafinjato, R.N.; Beaucour, A.-L.; Hebert, R.L.; Ledesert, B.; Bodet, R.; Noumowe, A. High temperature behaviour of a wide petrographic range of siliceous and calcareous aggregates for concretes. *Constr. Build. Mater.* **2016**, *123*, 261–273. [CrossRef]
69. Savva, A.; Manita, P.; Sideris, K.K. Influence of elevated temperatures on the mechanical properties of blended cement concretes prepared with limestone and siliceous aggregates. *Cem. Concr. Compos.* **2005**, *27*, 239–248. [CrossRef]
70. Al-Jabri, K.S.; Waris, M.B.; Al-Saidy, A.H. Effect of aggregate and water to cement ratio on concrete properties at elevated temperature. *Fire Mater.* **2016**, *40*, 913–925. [CrossRef]
71. Monte, F.L.; Gambarova, P.G. Thermo-mechanical behavior of baritic concrete exposed to high temperature. *Cem. Concr. Compos.* **2014**, *53*, 305–315. [CrossRef]
72. Sakr, K.; El-Hakim, E. Effect of high temperature or fire on heavy weight concrete properties. *Cem. Concr. Res.* **2005**, *35*, 590–596. [CrossRef]
73. Sarhat, S.R.; Sherwood, E.G. Residual mechanical response of recycled aggregate concrete after exposure to elevated temperatures. *J. Mater. Civ. Eng.* **2013**, *25*, 1721–1730. [CrossRef]
74. Vieira, J.P.B.; Correia, J.R.; De Brito, J. Post-fire residual mechanical properties of concrete made with recycled concrete coarse aggregates. *Cem. Concr. Res.* **2011**, *41*, 533–541. [CrossRef]
75. Zhao, H.; Liu, F.; Yang, H. Residual compressive response of concrete produced with both coarse and fine recycled concrete aggregates after thermal exposure. *Constr. Build. Mater.* **2020**, *244*, 118397. [CrossRef]

76. Laneyrie, C.; Beaucour, A.L.; Green, M.F.; Hebert, R.L.; Ledesert, B.; Noumowe, A. Influence of recycled coarse aggregates on normal and high performance concrete subjected to elevated temperatures. *Constr. Build. Mater.* **2016**, *111*, 368–378. [CrossRef]

77. Khan, A.U.R.; Aziz, T.; Fareed, S.; Xiao, J. Behaviour and Residual Strength Prediction of Recycled Aggregates Concrete Exposed to Elevated Temperatures. *Arab. J. Sci. Eng.* **2020**, *45*, 8241–8253. [CrossRef]

78. Xiao, J.; Fan, Y.; Tawana, M.M. Residual compressive and flexural strength of a recycled aggregate concrete following elevated temperatures. *Struct. Concr.* **2013**, *14*, 168–175. [CrossRef]

79. Kou, S.C.; Poon, C.S.; Etxeberria, M. Residue strength, water absorption and pore size distributions of recycled aggregate concrete after exposure to elevated temperatures. *Cem. Concr. Compos.* **2014**, *53*, 73–82. [CrossRef]

80. Gales, J.; Parker, T.; Cree, D.; Green, M. Fire Performance of Sustainable Recycled Concrete Aggregates: Mechanical Properties at Elevated Temperatures and Current Research Needs. *Fire Technol.* **2016**, *52*, 817–845. [CrossRef]

81. Martins, D.J.; Correia, J.R.; de Brito, J. The effect of high temperature on the residual mechanical performance of concrete made with recycled ceramic coarse aggregates. *Fire Mater.* **2016**, *40*, 289–304. [CrossRef]

82. Hachemi, S.; Ounis, A. Performance of concrete containing crushed brick aggregate exposed to different fire temperatures. *Eur. J. Environ. Civ. Eng.* **2015**, *19*, 805–824. [CrossRef]

83. Yüksel, S.; Siddique, R.; Özkan, Ö. Influence of high temperature on the properties of concretes made with industrial by-products as fine aggregate replacement. *Constr. Build. Mater.* **2011**, *25*, 967–972. [CrossRef]

84. Xing, Z.; Hébert, R.; Beaucour, A.L.; Ledésert, B.; Noumowé, A. Influence of chemical and mineralogical composition of concrete aggregates on their behaviour at elevated temperature. *Mater. Struct. Constr.* **2014**, *47*, 1921–1940. [CrossRef]

85. Biró, A.; Lublóy, É. Classification of aggregates for fire. *Constr. Build. Mater.* **2020**, *266*, 121024. [CrossRef]

86. Mindeguia, J.C.; Pimienta, P.; Carré, H.; La Borderie, C. On the influence of aggregate nature on concrete behaviour at high temperature. *Eur. J. Environ. Civ. Eng.* **2012**, *16*, 236–253. [CrossRef]

87. Xing, Z.; Beaucour, A.L.; Hebert, R.; Noumowe, A.; Ledesert, B. Influence of the nature of aggregates on the behaviour of concrete subjected to elevated temperature. *Cem. Concr. Res.* **2011**, *41*, 392–402. [CrossRef]

88. Phan, L.T.; Carino, N.J. Effects of test conditions and mixture proportions on behavior of high-strength concrete exposed to high temperatures. *ACI Mater. J.* **2002**, *99*, 54–66. [CrossRef]

89. Zega, C.J.; Di Maio, A.A. Recycled concrete made with different natural coarse aggregates exposed to high temperature. *Constr. Build. Mater.* **2009**, *23*, 2047–2052. [CrossRef]

90. Zega, C.J.; Di Maio, A.A. Recycled concrete exposed to high temperatures. *Mag. Concr. Res.* **2006**, *58*, 675–682. [CrossRef]

91. Nadeem, A.; Memon, S.A.; Lo, T.Y. The performance of Fly ash and Metakaolin concrete at elevated temperatures. *Constr. Build. Mater.* **2014**, *62*, 67–76. [CrossRef]

92. Tanyildizi, H.; Coskun, A. The effect of high temperature on compressive strength and splitting tensile strength of structural lightweight concrete containing fly ash. *Constr. Build. Mater.* **2008**, *22*, 2269–2275. [CrossRef]

93. Pathak, N.; Siddique, R. Properties of self-compacting-concrete containing fly ash subjected to elevated temperatures. *Constr. Build. Mater.* **2012**, *30*, 274–280. [CrossRef]

94. Demirel, B.; Keleştemur, O. Effect of elevated temperature on the mechanical properties of concrete produced with finely ground pumice and silica fume. *Fire Saf. J.* **2010**, *45*, 385–391. [CrossRef]

95. Behnood, A.; Ziari, H. Effects of silica fume addition and water to cement ratio on the properties of high-strength concrete after exposure to high temperatures. *Cem. Concr. Compos.* **2008**, *30*, 106–112. [CrossRef]

96. Li, Q.; Li, Z.; Yuan, G. Effects of elevated temperatures on properties of concrete containing ground granulated blast furnace slag as cementitious material. *Constr. Build. Mater.* **2012**, *35*, 687–692. [CrossRef]

97. Mendes, A.; Sanjayan, J.G.; Collins, F. Long-term progressive deterioration following fire exposure of OPC versus slag blended cement pastes. *Mater. Struct. Constr.* **2009**, *42*, 95–101. [CrossRef]

98. Sadrmomtazi, A.; Gashti, S.H.; Tahmouresi, B. Residual strength and microstructure of fiber reinforced self-compacting concrete exposed to high temperatures. *Constr. Build. Mater.* **2020**, *230*, 116969. [CrossRef]

99. Abid, M.; Hou, X.; Zheng, W.; Hussain, R.R. High temperature and residual properties of reactive powder concrete—A review. *Constr. Build. Mater.* **2017**, *147*, 339–351. [CrossRef]

100. Maanser, A.; Benouis, A.; Ferhoune, N. Effect of high temperature on strength and mass loss of admixtured concretes. *Constr. Build. Mater.* **2018**, *166*, 916–921. [CrossRef]

101. Ahmad, A.H.; Abdulkareem, O.M. Effect of High Temperature on Mechanical Properties of Concrete Containing Admixtures. *AL-Rafdain Eng. J.* **2010**, *18*, 43–54. [CrossRef]

102. Zeiml, M.; Leithner, D.; Lackner, R.; Mang, H.A. How do polypropylene fibers improve the spalling behavior of in-situ concrete? *Cem. Concr. Res.* **2006**, *36*, 929–942. [CrossRef]

103. Yermak, N.; Pliya, P.; Beaucour, A.L.; Simon, A.; Noumowé, A. Influence of steel and/or polypropylene fibres on the behaviour of concrete at high temperature: Spalling, transfer and mechanical properties. *Constr. Build. Mater.* **2017**, *132*, 240–250. [CrossRef]

104. Poon, C.S.; Shui, Z.H.; Lam, L. Compressive behavior of fiber reinforced high-performance concrete subjected to elevated temperatures. *Cem. Concr. Res.* **2004**, *34*, 2215–2222. [CrossRef]

105. Behnood, A.; Ghandehari, M. Comparison of compressive and splitting tensile strength of high-strength concrete with and without polypropylene fibers heated to high temperatures. *Fire Saf. J.* **2009**, *44*, 1015–1022. [CrossRef]

106. Eidan, J.; Rasoolan, I.; Rezaeian, A.; Poorveis, D. Residual mechanical properties of polypropylene fiber-reinforced concrete after heating. *Constr. Build. Mater.* **2019**, *198*, 195–206. [CrossRef]
107. Serrano, R.; Cobo, A.; Prieto, M.I.; de las Nieves González, M. Analysis of fire resistance of concrete with polypropylene or steel fibers. *Constr. Build. Mater.* **2016**, *122*, 302–309. [CrossRef]
108. Akca, A.H.; Özyurt, N. Deterioration and recovery of FRC after high temperature exposure. *Cem. Concr. Compos.* **2018**, *93*, 260–273. [CrossRef]
109. Sideris, K.K.; Manita, P.; Chaniotakis, E. Performance of thermally damaged fibre reinforced concretes. *Constr. Build. Mater.* **2009**, *23*, 1232–1239. [CrossRef]
110. Düʒenci, O.; Haktanir, T.; Altun, F. Experimental research for the effect of high temperature on the mechanical properties of steel fiber-reinforced concrete. *Constr. Build. Mater.* **2015**, *75*, 82–88. [CrossRef]
111. Moghadam, M.A.; Izadifard, R.A. Effects of steel and glass fibers on mechanical and durability properties of concrete exposed to high temperatures. *Fire Saf. J.* **2020**, *113*, 102978. [CrossRef]
112. Rudnik, E.; Drzymała, T. Thermal behavior of polypropylene fiber-reinforced concrete at elevated temperatures. *J. Therm. Anal. Calorim.* **2018**, *131*, 1005–1015. [CrossRef]
113. Chromá, M.; Vo, D.; Bayer, P. Concrete Rehydration after Heating to Temperatures of up to 1200 °C. In Proceedings of the International Conference on Durability of Building Materials and Components, Porto, Portugal, 12–15 April 2011.
114. Chan, S.Y.N.; Luo, X.; Sun, W. Effect of high temperature and cooling regimes on the compressive strength and pore properties of high performance concrete. *Constr. Build. Mater.* **2000**, *14*, 261–266. [CrossRef]
115. Chen, B.; Li, C.; Chen, L. Experimental study of mechanical properties of normal-strength concrete exposed to high temperatures at an early age. *Fire Saf. J.* **2009**, *44*, 997–1002. [CrossRef]
116. Endait, M.; Wagh, S. Effect of elevated temperature on mechanical properties of early-age concrete. *Innov. Infrastruct. Solut.* **2020**, *5*, 4. [CrossRef]
117. Yu, K.Q.; Lu, Z.D.; Yu, J. Residual compressive properties of strain-hardening cementitious composite with different curing ages exposed to high temperature. *Constr. Build. Mater.* **2015**, *98*, 146–155. [CrossRef]
118. Kowalski, R. Mechanical properties of concrete subjected to high temperature. *Archit. Civ. Eng. Environ.* **2010**, *3*, 61–70.
119. Castillo, C. Effect of Transient High Temperature on High Strength Concrete. Master's Thesis, Rice University, Houston, TX, USA, 1987.
120. Yoon, M.; Kim, G.; Choe, G.C.; Lee, Y.; Lee, T. Effect of coarse aggregate type and loading level on the high temperature properties of concrete. *Constr. Build. Mater.* **2015**, *78*, 26–33. [CrossRef]
121. Kim, Y.S.; Lee, T.G.; Kim, G.Y. An experimental study on the residual mechanical properties of fiber reinforced concrete with high temperature and load. *Mater. Struct. Constr.* **2013**, *46*, 607–620. [CrossRef]
122. Li, Q.; Wang, M.; Sun, H.; Yu, G. Effect of heating rate on the free expansion deformation of concrete during the heating process. *J. Build. Eng.* **2020**, *34*, 101896. [CrossRef]
123. Shui, Z.; Xuan, D.; Chen, W.; Yu, R.; Zhang, R. Cementitious characteristics of hydrated cement paste subjected to various dehydration temperatures. *Constr. Build. Mater.* **2009**, *23*, 531–537. [CrossRef]
124. Vyšvařil, M.; Bayer, P.; Chromá, M.; Rovnaníková, P. Physico-mechanical and microstructural properties of rehydrated blended cement pastes. *Constr. Build. Mater.* **2014**, *54*, 413–420. [CrossRef]
125. Wang, G.; Zhang, C.; Zhang, B.; Li, Q.; Shui, Z. Study on the high-temperature behavior and rehydration characteristics of hardened cement paste. *Fire Mater.* **2015**, *39*, 741–750. [CrossRef]

Article

Numerical Analysis of Steel Geodesic Dome under Seismic Excitations

Dominika Pilarska and Tomasz Maleska *

Faculty of Civil Engineering and Architecture, Opole University of Technology, 45-758 Opole, Poland;
d.pilarska@po.edu.pl
* Correspondence: t.maleska@po.edu.pl; Tel.: +48-77-449-8568

Abstract: The paper presents the response of two geodesic domes under seismic excitations. The structures subjected to seismic analysis were created by two different methods of subdividing spherical triangles (the original octahedron face), as proposed by Fuliński. These structures are characterised by the similar number of elements. The structures are made of steel, which is a material that undoubtedly gives lightness to structures and allows large spans. Designing steel domes is currently a challenge for constructors, as well as architects, who take into account their aesthetic considerations. The analysis was carried out using the finite element method of the numerical program. The two designed domes were analysed using four different seismic excitations. The analysis shows what influence particular earthquakes have on the geodesic dome structures by two different methods. The study analysed the maximum displacements, axial forces, velocities, and accelerations of the designed domes. In addition, the Time History method was used for the analysis, which enabled the analysis of the structure in the time domain. The study will be helpful in designing new structures in seismic areas and in assessing the strength of various geodesic dome structures under seismic excitation.

Keywords: geodesic dome; seismic response; dynamic analysis; seismic analysis

1. Introduction

Strut domes are an effective two-curved cover, which is approximated by a mesh of struts. The use of less material and lower costs, combined with the possibility of covering very large areas, is a definite advantage of this type of structure. The stiffness of these three-dimensional systems justifies their ability to cover large spans with a small amount of construction material. Architects and engineers all over the world use a wide range of possibilities of connecting strut elements, constituting a mesh of dome covers. The aesthetic potential of this engineering system means that the structure has a valuable architectural aspect [1]. This aspect was important not only in steel geodesic domes but also in other spatial structures (e.g., made of concrete) [2].

From dome ceilings and full buildings to Arctic homes and artificial biomes, geodesic domes around the world continue to inspire and amaze both architecture enthusiasts and curious travellers. The elegant and aerodynamic form of geodesic domes creates expansive yet economical spaces that are ideal for greenhouses, arenas, sports facilities, entertainment halls, swimming pools, and other uses. For centuries, dome structures were used due to their thermal advantages, structural benefits, and availability of construction materials [1].

After Fuller [1] patented methods of dividing a sphere into spherical triangles in 1954 (based on an icosahedron as the initial solid), steel mesh domes of the geodetic type have almost completely replaced the use of other types of domes. In 1967, his design was shown to the world as a 'Biosphere', with a diameter of 76 m, constructed for Expo '67 in Montreal (Figure 1).

Fuller [1] believed that the geodesic dome was nature's perfect structure, enclosing the greatest space with the least amount of material. While remaining in tune with the

environment, the dome supports itself without the need for any internal columns or walls. The largest geodesic dome projects include the Fukuoka Dome (built in Fukuoka, Japan in 1993, 216 m), Nagoya Dome (Nagoya, Japan in 1997, 187 m), Louvre (Abu Dhabi, United Arab Emirates, 180 m), Tacoma Dome (Tacoma, WA, USA, 161 m), and the Superior Dome (Northern Michigan University, Marquette, MI, USA, 160 m).

Figure 1. Biosphere, Montreal from 1967 (Fulller [1]).

The advantage of Fuller's geodesic strut domes is the small number of struts required at different lengths. According to his patent, the domes were formed on the basis of the icosahedron, which requires the smallest number of groups of struts of equal lengths. There were many papers related to such geodesic domes. Significant and excellent achievements in lightweight, durable, and self-supporting structures have been attained by Makowski [3,4], Clinton [5,6], Tarnai [7–9], Huybers [10–15], Lalvani [16–19], Pavlov [20,21], Ramaswamy [22], Obrębski [23], Szmit [24,25], and Rębielak [26].

Although dome structures are economical in terms of consumption of construction materials compared to the conventional forms of structures [27], a more lightweight design can be obtained using optimisation methods. The optimum solution of the geometry design was obtained by Saka [28], Kaveh and Talatahari [29], Carvalho et al. [30], Saka and Carbas [31], Gholizadeh and Barati [32], Kaveh and Rezaei [33,34], Kaveh et al. [35], and Ye and Lu [36]. Other structures were analysed from the economical aspect, e.g., bridge [37,38], but in these cases, the methods and reasons of optimisation were totally different.

An analysis of the behaviour of shallow geodesic lattice domes was presented by Guan et al. [39]. Barbieri et al. [40] analysed the dynamic behaviour of a geodesic dome in aluminium alloy through numerical models obtained using the finite element method. Szaniec and Zielinska [41] presented the results of a dynamic analysis of an existing reticulated dome under wind loads. The calculation model of the structure was constructed using the finite element method. The dome was subjected to the standard wind pressure, assuming that it operates harmonically. Satria et al. [42] considered the dynamic behaviour

of a new type of two-way single layer lattice dome with nodal eccentricity. Fu [43] presented a static analysis and design of tensegrity domes. New forms of the tensegrity domes were proposed.

Studies of geodesic domes under seismic loads have rarely been investigated. A few papers on this subject can be found. In the paper of Cai et al. [44], the dynamic characteristics of a space beam string structure was determined. The aim of the paper was to determine the structure's response to seismic excitation using the Time History method and the modal method. These methods were used to determine the structure's response to the given seismic excitation. In the paper by Takeuchi et al. [45], the response evaluation method of domes and cylindrical shell roofs with substructures was shown. In addition, the response amplification factors approach was proposed. Furthermore, Nakazawa et al. [46] focused on methods for evaluating responses under seismic loads to metal roof spatial structures. In addition, papers by Kato and Nakazawa [47], Li et al. [48], and Qin et al. [49] focused on the assessment of lightweight structure responses exposed to earthquakes. In addition, the dynamic stability and failure probability analysis of dome structures under stochastic seismic excitation was presented by Li and Xu [50].

It should be added that the most of the analysis on geodesic domes relate to space frames, the basis of which is the icosahedron, which is the development of Fuller's patent. Davis [51] showed that the octahedron might seem to be a better option for geodesic domes than the icosahedron. However, the problems arise because more subdivisions were required, and thus, more different lengths were required.

The paper presents the numerical analysis of the geodesic domes under seismic excitations. The developed structures were created on the basis of the regular octahedron, which was a polyhedron that has not been considered in great detail so far [52–54]. Two different methods for the subdivision of the spherical triangle proposed by Fuliński [1,55] were used to design the two geodesic domes under seismic analysis. The numerical analyses were carried out for four different seismic excitations. Different times and intensities of the seismic records were presented. The results obtained from numerical analysis were compared with two structures differing in subdivision methods and under four different excitations. The presented analysis was the first step for further consideration of the optimisation of the geodesic dome. It is very important to take into account the wider possibilities of using this type of structure to cover large areas. It should be added that the geodesic domes around the world continue to inspire and amaze both architectural enthusiasts and curious travellers.

2. Description of Numerical Modelling

2.1. Subdivision Methods for Spherical Dome (Strut) Structures Based on the Regular Octahedron

The two developed geodesic domes under the seismic excitations were shaped in accordance with two methods proposed by Fuliński [55]. The structures were designed on the basis of being regular octahedra, subdividing their equilateral faces into smaller sub-faces and taking the resulting face vertices to define the nodes of the structural grid, while the edges of the sub-faces define the axes of the structural members. Both of the methods used lead to the division of the initial triangle of the octahedron into smaller triangles by frequency (V), i.e., the number of subdivisions. The subdivision process naturally leads to the generation of a three-way grid on every face of the basis octahedron. The central projection of this grid's vertices on the octahedron's circumscribed sphere leads to a polyhedron approximating the sphere in which only the grid's nodes lie on the sphere's surface. More parts give smoother spheres. The mentioned methods were developed in detail in the paper by Pilarska [54]. Figure 2 shows the difference in the shaping of geodesic domes using the first and second subdivision methods.

2.2. Tested Models

Two geodesic strut domes were subjected to numerical analysis, taking into account the seismic excitations. These structures were designed according to the two different

methods of creating geodesic domes proposed by Fuliński [55], which are presented in Section 2.1 and described in detail in the papers by Pilarska [52–54]. The basis for generating the meshes of both structures was a regular octahedron. It was an initial triangle and was divided into as many parts to finally obtain domes characterised by a similar number of struts. Including the first method, after dividing the initial triangle of the regular octahedron into 19 parts, 2888 hedra were obtained, i.e., a structure consisting of 761 nodes and of 2204 struts (Figure 3a). The analysed dome was 49.97 m wide and 25.0 m high. Using the second method, after dividing the initial triangle of the regular octahedron into 22 parts, 2904 hedra were modelled. This dome consists of 749 nodes and 2156 struts (Figure 3b), with a width of 50.0 m and a height of 25.0 m.
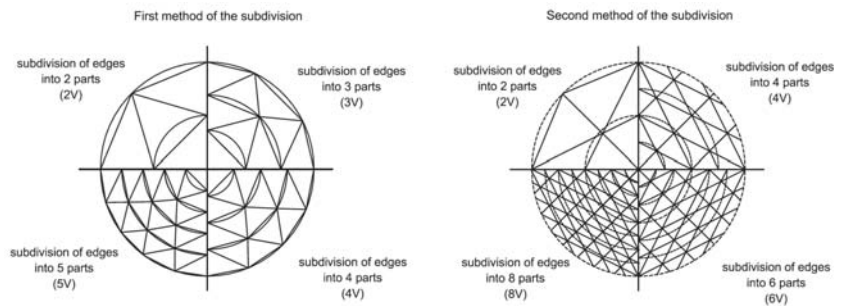
Figure 2. Methods of subdividing the initial triangle edge, according to Fuliński.
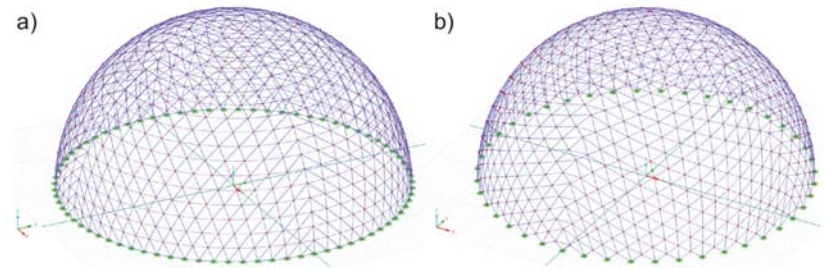
Figure 3. View of numerical model: (**a**) method 1 and (**b**) method 2.

2.3. Material of Numerical Models

The analysed geodesic domes were made of steel struts (round pipes) of S235 standard steel. The properties of this steel grade were: (i) Young modulus (E) 210 GPa, (ii) Kirchhoff module (G) 80.76 GPa, (iii) Poisson ratio (ν) 0.3, (iv) volumetric weight (γ) 7850 kg/m^3, (v) thermal expansion coefficient (α) 1.2×10^{-5}, and (vi) partial safety factor (γ_M) 1.0. The steel elements were modelled as a linearly elastic isotropic material (according to Eurocode 3 [56]). All of the struts in both analysed domes were grouped into four groups, taking into account a different cross-section (commonly used cross-section) of the elements, as shown in Table 1.

Table 1. Division of the analysed geodesic domes into four groups of struts.

Groups of Struts	
2888-Hedron (Method 1)	**2904-Hedron (Method 2)**
RO 70.0 × 8.0	RO 70.0 × 7.1
RO 63.5 × 8.8	RO 63.5 × 8.0
RO 44.5 × 5.6	RO 57.0 × 5.6
RO 44.5 × 3.6	RO 51.0 × 3.2

2.4. Description of Numerical Analysis

The DLUBAL RFEM 5.21.01 (2020, Dlubal Software GmbH from Tiefenbach, Germany) numerical program was used to analyse the effect of seismic excitations of the geodesic domes. This program is based on the finite element method. This method enables the determination of the maximum value (e.g., displacement or acceleration) in a given node of a finite element. The mentioned numerical program (RFEM) is widely used by engineers all over the world. It gained its popularity thanks to extensive specialised modules. In this paper, the RF-DYNAM PRO 5.21.01 (2020, Dlubal Software GmbH from Tiefenbach, Germany) module was used for dynamic analysis of the structure response. In the analysed numerical models, the size of the finite elements did not exceed of 0.2 m. The supports of dome were modelled as rigid. The purpose of such modelling of the supports was to obtain the maximum response of the dome structure to the given excitation. This proposition of support was commonly used in engineering practice, e.g., by Chmielewski et al. [57], Tabatabaiefar and Massumi [58]. In a geodesic dome, the Soil–Structure Interaction (SSI) effect can be omitted, because in these structures, there is no effect of: (i) second order, (ii) massive, (iii) slender tall structure, (iv) or soft soil from Eurocode 8 [59].

2.5. Seismic Excitation

In order to assess the effect of seismic response on geodesic domes, four different seismic records were used, i.e., (i) Ancona, (ii) Denizli, (iii) Friuli, and (iv) Kilini. The Ancona record (Italy) comes from the Genio-Civile station on June 14, 1972. It was characterised by ground acceleration equal to -3.740 m/s^2 (Figure 4a) and duration of 7.76 s. The second record Denizli (Turkey) was recorded at the station Denizli-Bayindirlik ve Iskan Mudurlugu and dates from August 19, 1976. For this recording, the ground acceleration value was -3.387 m/s^2 (Figure 4b); this recording lasted 17.31 s. Another record came from Italy (Friuli), exactly from the Somplago-Uscita Galleria station on September 16, 1977. The maximum value of ground acceleration during this earthquake was -1.870 m/s^2 (Figure 4c) and lasted 16.30 s. The last weakest record came from Kilini (Greece) at Vartholomio Residence station on October of 31, 1998, and its maximum ground acceleration was 0.714m/s^2 (Figure 4d) in 16.18 s.
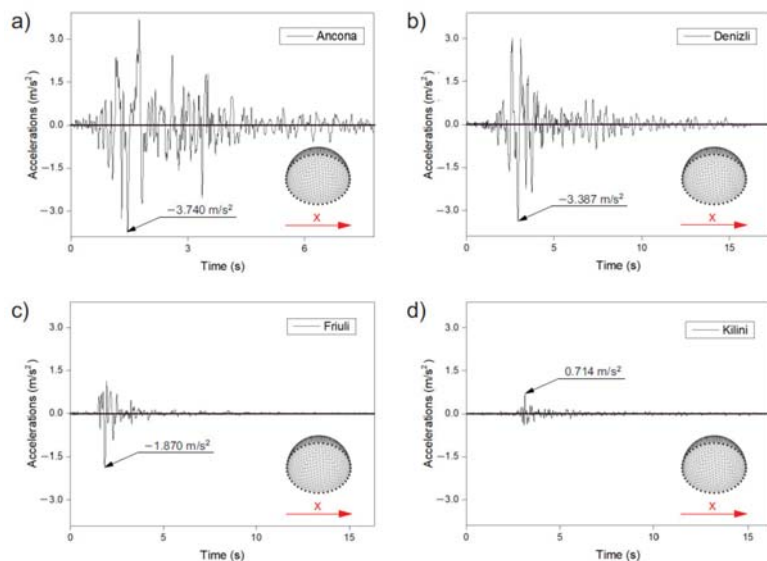

Figure 4. The most intensive component of seismic excitations (x-direction): (**a**) Ancona (Italia), (**b**) Denizli (Turkey), (**c**) Friuli (Italia), (**d**) Kilini (Greece).

3. Result of Numerical Analysis

3.1. Method of Numerical Analysis

The study assesses the effect of seismic excitations on the geodesic domes, which were designed in accordance with two different methods for creating these types of structures. As mentioned earlier, these methods have been described in detail in the papers [52–54]. The numerical program RFEM and the Time History method were used for the analysis. This method allows for the analysis of the structure in given time steps. The time step of numerical analysis was equal to 0.02 s. The load was applied in accordance with the standard rules [59], i.e., in two horizontal directions (X and Y) and in the vertical direction (Z). In addition, the seismic excitations were applied simultaneously in all direction (direction of X, Y and Z) to the rigid supports.

Table 1 shows the results for the analysed domes under seismic excitations. The analysed records had different durations and intensities. The dynamic (seismic) analysis was carried out on the basis of the numerical models presented in [52–54]. The above-mentioned publications applied the rule that the most stressed strut in a given group was at a level of 90%. For the purposes of analysing the obtained results, eight numerical models were created, by different structural methods (method 1 or method 2). In addition, the seismic excitations (Ancona, Denizil, Friuli, and Kilini) were used. As a result, eight models were obtained, i.e., model I (method 1, Ancona), model II (method 2, Ancona), model III (method 1, Denizil), model IV (method 2, Denizil), model V (method 1, Friuli), model VI (method 2, Friuli), model VII (method 1, Kilini), and model VIII (method 2, Kilini).

3.2. Displacements

Based on the analysis, it can be seen that the maximum displacement values were recorded for the horizontal directions X and Y (for the Ancona and Denzil records in the Y direction, for the Friuli and Kilini records in the X direction). In the vertical direction, the displacements were much smaller (Table 2). For all four of the seismic records analysed, higher values were obtained for the dome designed according to method 1 than for the dome generated according to method 2.

Table 2. Results from numerical analysis.

	Seismic Records							
	Ancona (Italia)		Denizil (Turkey)		Friuli (Italia)		Kilini (Greece)	
	Method							
Direction	1	2	1	2	1	2	1	2
	Model I	Model II	Model III	Model IV	Model V	Model VI	Model VII	Model VIII
	Displacement (mm)							
x	17.4	6.8	8.3	6.6	3.9	2.3	−1.9	1.1
y	23.4	−7.6	13.3	−6.9	3.6	2.1	1.1	0.9
z	10.2	4.5	6.7	5.6	1.7	0.9	1.0	0.6
	Axial forces (kN)							
	−69.54	47.01	40.54	37.63	12.82	13.31	5.56	−6.76
	Velocity (m/s)							
x	0.99	0.42	0.50	0.44	0.18	0.09	0.12	0.07
y	1.34	0.45	0.79	0.42	0.23	0.10	0.07	0.05
z	0.62	0.32	0.44	0.36	0.10	0.07	0.06	0.05
	Acceleration (m/s^2)							
x	64.14	29.34	33.77	26.48	10.67	5.88	8.90	4.78
y	81.71	30.19	55.78	27.44	13.50	6.66	4.89	3.49
z	39.21	32.42	28.06	−34.35	6.26	6.01	4.51	3.79

In the case of structures shaped on the basis of method 1, the highest displacement values were obtained with the Ancona record (model I, 23.4 mm; Figure 5a). In the case of other records, the displacement values were smaller. In relation to Ancona, they accounted for 56% for Denizli (model III, 13.3 mm; Figure 5b), 17% for Friuli (model V, 3.9 mm; Figure 5c), and 8% for Kilini (model VII, −1.9 mm; Figure 5d). A similar tendency was noticeable with the domes created according to method 2. The Ancona forcing caused the highest displacement values (model II, −7.6 mm; Figure 5a), while for the remaining records, the maximum displacement values were 90% (model IV, Denizli, −6.9 mm; Figure 5b), 30% (model VI, Friuli, 2.3 mm; Figure 5c) and 14% (model VIII, Kilini, 1.1 mm; Figure 5d) of the values from the Ancon record, respectively.
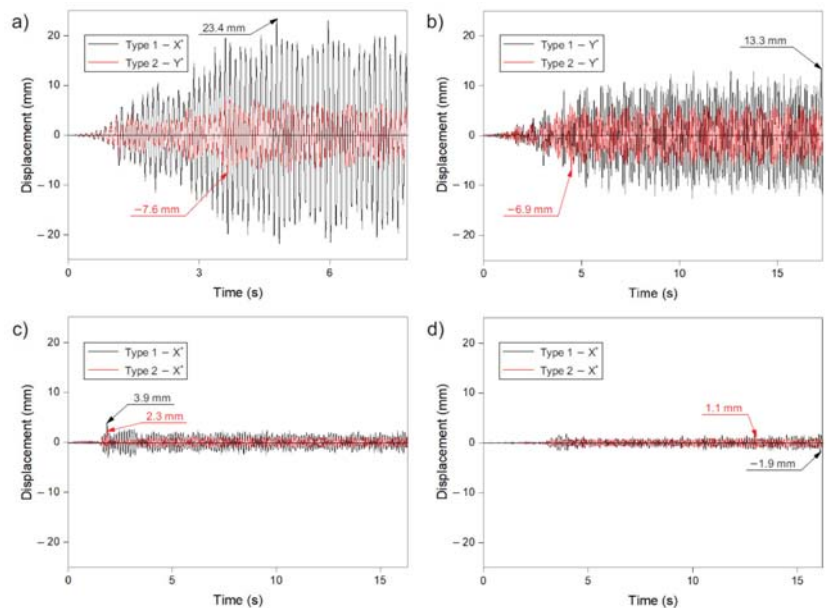
Figure 5. Maximum displacements in numerical model records: (**a**) Ancona—models I and II, (**b**) Denizli—models III and IV, (**c**) Friuli—models V and VI, (**d**) Kilini—models VII and VIII.

There was also a noticeable difference in the size of the maximum displacements between the structures shaped according to methods 1 and 2. The greatest differences were obtained for the Ancona record, in which the dome shaped according to method 1 showed about three times greater maximum displacements (model I, 23.4 mm; Figure 5a) than the dome designed according to method 2 (model II, 7.6 mm; Figure 5b). In the case of the records of Denizli, Friuli, and Kilini, the differences were about two times greater for method 1 compared to method 2.

It should be added that the value of displacements for the analysed numerical models decreases with a decrease in the value of ground acceleration, which was recorded for individual earthquake records. The highest values were obtained for the Ancona record, i.e., the record with the greatest ground acceleration (3.740 m/s^2).

It can also be seen that the domes were excited for approximately 1.5 to 4.0 s of the recording duration as a result of the imposed excitation. In the first stages of the excitation, the displacements had a negligible value, which was undoubtedly influenced by the characteristics of the given excitation (in the first seconds of recording, the acceleration values were low). However, after the occurrence of the maximum acceleration in a given record (Ancona, Denizli, Friuli, Kilini), the recorded displacements had a similar value to the maximum ones. This tendency was noticeable for all analysed records, regardless

of the direction of the excitation. Even the decrease in acceleration did not cause any significant reduction in the displacements of the analysed domes. For both of the domes created according to methods 1 and 2, it can be seen that the moments of occurrence of the maximum values of displacement in the domes were similar to each other. They occurred at very similar time intervals. Only when recording Denizli (model III and model IV) did the maximum displacements appear at significant time intervals: for method 1 (model III) around 17 s and, for method 2 (model IV), approximately 5 s.

3.3. Axial Forces

Based on the numerical analysis, it can be concluded that the maximum axial forces occurring in the struts in both of the analysed methods of shaping geodetic strut domes (methods 1 and 2) were similar for each given excitation. Thus, there was no clear trend as in the case of displacements where, for the analysed models built according to method 1, the maximum values of displacement were always higher than for the models shaped according to method 2. It was noticed that for high-intensity records (Ancona and Denizli excitations—Figure 4a,b), higher values of axial forces were obtained for models I and III, where method 1 was used to generate the structure. However, in the case of records of lower intensity (Friuli and Kilini—Figure 4c,d), higher values were recorded for the dome designed according to method 2 (models VI and VIII). The difference in the maximum values of the axial forces of the domes generated according to methods 1 and 2, for the four records analysed, was from 4% to 32% and was largest (32%) was for the Ancona record.

The greatest forces were recorded with the Ancon excitation in model I (-69.54 kN— Figure 6a), which was designed according to method 1. In the other models, the values were lower and amounted to: (i) 47.01 kN (method 2, model II, Ancona—Figure 6a), (ii) 40.54 kN (method 1, model III, Denizli—Figure 6b), (iii) 37.63 kN (method 2, model IV, Denizli— Figure 6b), (iv) 13.31 kN (method 2, model VI, Friuli—Figure 6c), (v) 12.82 kN (method 1, model V, Friuli—Figure 6c), (vi) -6.76 kN (method 2, model VIII, Kilini—Figure 6d), and (vii) 5.56 kN (method 1, model VII, Kilini—Figure 6d). On the basis of the obtained results presented in Figure 6, it can be seen that the tensile and compression forces in the struts were of a similar value. In some models, almost identical values for the compressive and tensile forces were obtained.

It can also be seen that the axial forces for all analysed models (I–VIII) were recorded after the appearance of the maximum acceleration in the record. From that moment, they remained at relatively equal levels, similar to the displacements. Concentrating on Figure 6, it can also be seen that the maximum forces (for method 1 and 2 of strut dome design) appeared at a similar time. Thus, it can be concluded that the method of shaping the dome structure does not have a significant impact on the moment of the maximum axial forces in the structure appearance. Moreover, no clear tendency can be drawn as to how the length of the records and their intensity impacts the appearance of maximum values over time. As can be seen in Figure 6, the location of the maximum axial forces occurrence in time was very varied.

3.4. Velocity

Analysing the maximum velocities, the impact of two different methods of creating strut dome structures can be observed. Based on the obtained results, it can be seen that using method 1 for the construction of a dome, the vibration of velocities as a result of the seismic excitation was much higher than for the structures formed according to method 2 (Figure 7). This tendency was noted in both the records with high ground acceleration (Ancona, Denizli) and records with low ground acceleration (Friuli, Kilini).

In the analysed numerical models (models I–VIII), the highest values for velocity were obtained in model I, i.e., in the dome created according to method 1, with the Ancona record. This value was 1.34 m/s (Figure 7a). In the other models, lower values, ranging from 41% to 95%, (compared to model I) were obtained.
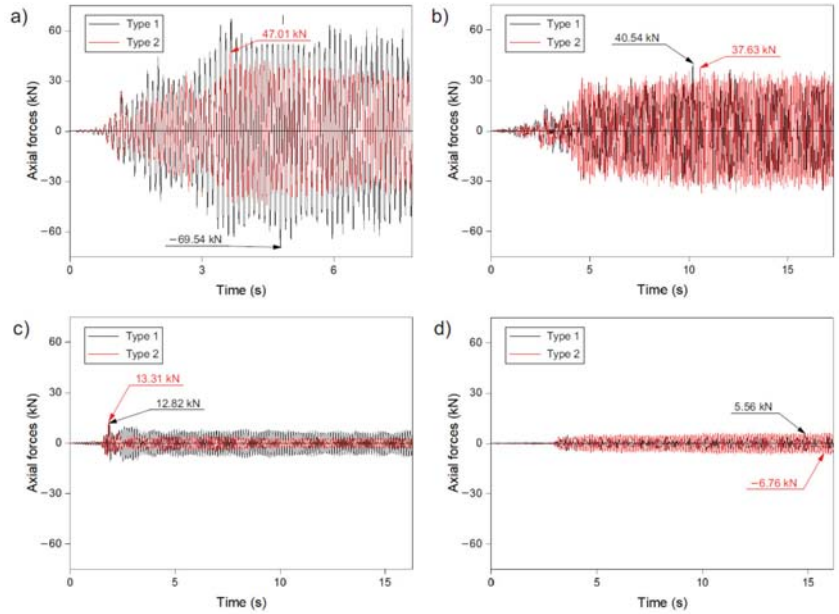
Figure 6. Maximum axial forces in numerical model records of: (**a**) Ancona—models I and II, (**b**) Denizli—models III and IV, (**c**) Friuli—models V and VI, (**d**) Kilini—models VII and VIII.
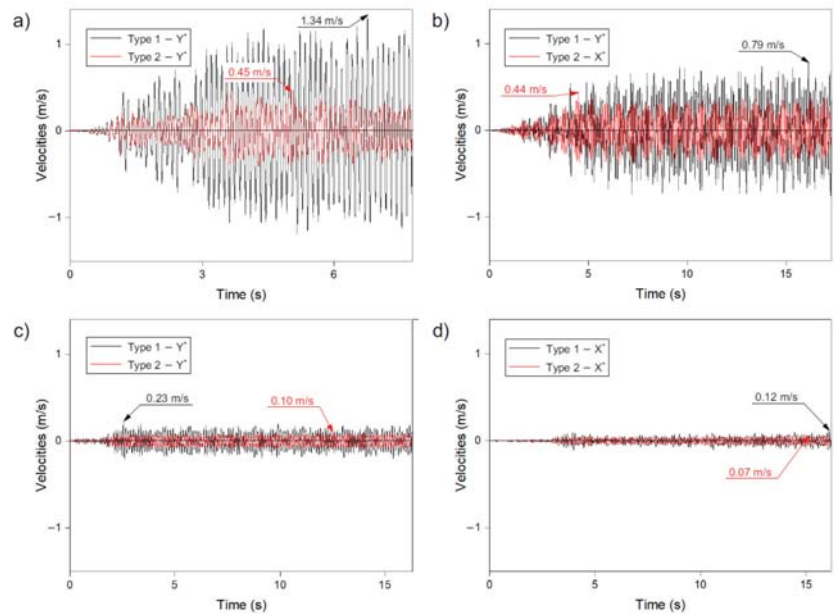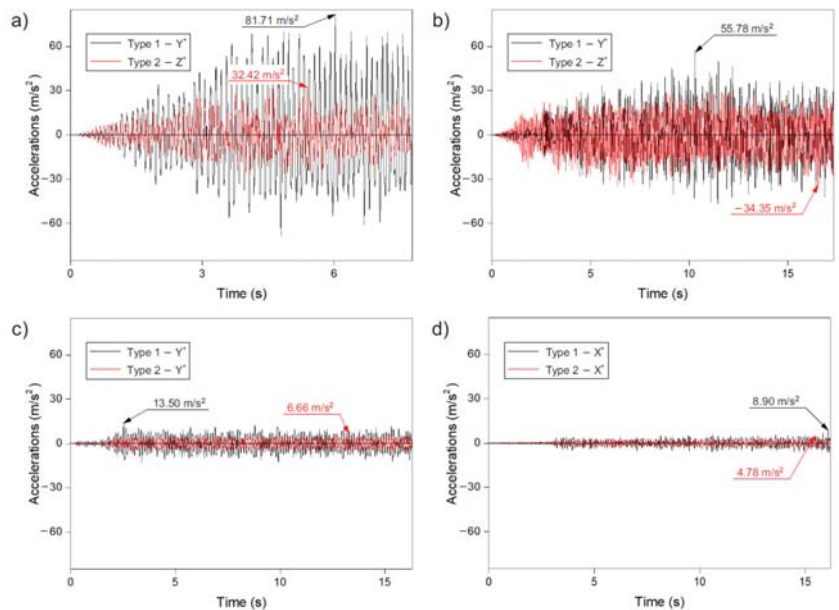

Figure 7. Maximum velocities in numerical model record of: (**a**) Ancona—models I and II, (**b**) Denizli—models III and IV, (**c**) Friuli—models V and VI, (**d**) Kilini—models VII and VIII.

It should also be mentioned that there was a slight difference between the velocities from models II and IV (method 2), which was only 2%. This was not much, considering the

fact that for the same excitations in the case of method 1, the difference between models I and III was 41%.

On the basis of Figure 7, it can be seen that the places of the occurrence of the maximum velocities in time for individual records and methods of shaping the dome structure were different. Therefore, it was not possible to clearly define the influence of the acceleration value of the analysed recording as well as the method of shaping the dome (methods 1 or 2). On the other hand, it can be seen (especially in the case of domes designed according to method 1) that as the record intensity decreases, the velocity values decrease. For method 2, it was less noticeable because the obtained results were lower in the range of 42% to 66% (compared to method 1).

However, it can be seen that the strut domes were excited as a result of the seismic excitation application. Figure 7 shows that after the maximum ground acceleration occurs in the record (Figure 4), the vibration velocities remain at relatively the same level for a particular record for the rest of its duration. The method of shaping (method 1 or 2) of the strut domes does not matter.

3.5. Acceleration

In the case of maximum accelerations, a similar tendency can be observed for displacements, axial forces, and velocities. The method of generating the strut dome structure clearly matters. For method 1, higher values were obtained than for method 2. This trend was repeated for all analysed records, i.e., Ancona, Denizli, Friuli, and Kilini (Figure 8).

Figure 8. Maximum accelerations in numerical model record of: (**a**) Ancona—models I and II, (**b**) Denizli—models III and IV, (**c**) Friuli—models V and VI, (**d**) Kilini—models VII and VIII.

It was noticed that with a decrease in the intensity of the excitation, the maximum accelerations of the dome structure were reduced. Thus, it can be concluded that for the accelerations of the domes, the ground acceleration value has greater significance than the duration of the earthquake.

The highest accelerations were observed in model I (method 1, Ancona), where the obtained value was 81.71 m/s^2 (Figure 8a). In the other analysed models, the acceleration values in the dome were lower compared to model I and amounted to (i) 55.78 m/s^2 (method 1,

model III, Denizil—Figure 8b), (ii) -34.35 m/s^2 (method 2, model IV, Denizil—Figure 8b), (iii) 32.42 m/s^2 (method 2, model II, Ancona—Figure 8a), (iv) 13.50 m/s^2 (method 1, model V, Friuli—Figure 8c), (v) 8.90 m/s^2 (method 1, model VII, Kilini—Figure 8d), (vi) 6.66 m/s^2 (method 2, model VI, Friuli—Figure 8c) and (vii) 4.78 m/s^2 (method 2, model VIII, Kilini—Figure 8d). Analysing the results of the obtained values, it should be also noted that in the case of domes created according to method 2, higher values were obtained in model IV (Denizil) than in model II (Ancona), although the value of ground acceleration for the given excitation in model II was higher by 10%.

Taking into account the time of the appearance of the maximum accelerations in the dome, it can be seen that it was not identical for the analysed methods of creating the dome (methods 1 and 2). In models I and II, as well as VII and VIII, the time when the maximum values appeared was similar. On the other hand, in models III, IV, V, and VI, big differences were noted between the time when the maximum acceleration values appeared in the dome. The difference was 10 s (V and VI models), which was a very significant value with the recording duration of about 17 s.

As in the case of the previously analysed quantities (displacements, axial forces, and velocities), it was noticed that after the occurrence of the maximum input in the record, the structure was excited. From that moment, the acceleration values were relatively close to the maximum values.

4. Conclusions

After the numerical analysis, it can be concluded that the method of shaping the steel structure of domes (methods 1 and 2) has a significant impact on the obtained values of displacements, axial forces, velocities, and accelerations. In addition, the following were noted:

- Displacements in strut domes, constructed according to method 1, were much greater than for domes constructed according to method 2. This tendency was repeatable for high and low intensity records;
- The length of the earthquake record was not significant. The value of the ground acceleration recorded during the earthquake seems more important;
- After the occurrence of the maximum ground acceleration in the analysed record, the steel structure of the cover was excited (regardless of the method of shaping the dome). After excitation of the structure, for the rest of the record, the values remain near the maximum values recorded in the given record,
- The maximum values were mainly obtained in the horizontal directions (X and Y). Only the maximum accelerations for models II and IV, generated according to method 2, were obtained in the vertical direction Z. This shows a close relationship between the shape of the dome structure and their seismic response.

Undoubtedly, the numerical analysis that was performed allowed the determination of how seismic excitation affects the dome shaping method. However, the obtained results were carried out only on relatively small domes. They were new structures, without damage, which was also important. In future, additional analyses are planned for domes of different sizes, as well as damaged domes. In addition, it is planned to optimise the dome structure under seismic excitation.

The obtained results may be helpful in designing this type of structure in seismic areas and may also be a source of information for architects when designing geodesic domes. Additionally, this paper can be helpful in assessing the effects of earthquakes on lightweight structures.

References

1. Fuller, B.R. Geodesic Dome. U.S. Patent 2,682,235, 29 June 1954.
2. Barazzetta, G.; Mossa, E.; Poggi, C.; Simoncelli, M. The Airplane hangars of pier Luigi Nervi: Digital and scaled models. *J. Int. Assoc. Shell Spat. Struct.* **2020**, *61*, 187–200. [CrossRef]
3. Makowski, Z.S. *Raümliche Tragwerke Aus Stahl*; Verlag Stahleisen G.m.b.H.: Düsseldorf, Germany, 1963.
4. Makowski, Z.S. *Space Structures—A Review of the Developments within the Last Decade. Space Structures 4*; Thomas Telford: London, UK, 1993.
5. Clinton, J.D. *Advanced Structural Geometry Studies. Part I, Polyhedral Subdivision Concept for Structural Application*; NASA Contractor Report, NASA CR-1734; NASA: Washington, DC, USA, 1971.
6. Clinton, J.D. Lowest common frequency: b2 + bc + c2. *Int. J. Space Struct.* **1990**, *7*, 213–222. [CrossRef]
7. Tarnai, T. *Spherical Grid Structures: Geometric Essays on Geodesic Domes*; Hungarian Institute for Building Science: Budapest, Hungary, 1987.
8. Tarnai, T. Geodesic domes: Natural and man-made. *Int. J. Space Struct.* **1996**, *11*, 13–25. [CrossRef]
9. Tarnai, T.; Lengyel, A.; Gaspar, Z. The Roundest Polyhedra with Symmetry Constraints. *Symmetry* **2017**, *9*, 41.
10. Huybers, P. The use of polyhedral for building structures. *Struct. Topol.* **1982**, *6*, 33–42.
11. Huybers, P. *The Polyhedral World. Beyond the Cube. The Architecture of Space Frames and Polyhedra*; Gabriel, J.F., Ed.; John Wiley & Sons, Inc.: Chichester, UK, 1997; pp. 243–279.
12. Huybers, P. Dome-type space structures of ellipsoidal form. *Int. J. Space Struct.* **1990**, *7*, 299–310. [CrossRef]
13. Huybers, P. The chiral polyhedra. *J. Int. Assoc. Shell Spat. Struct.* **1999**, *40*, 133–143.
14. Huybers, P.; van der Ende, G. Polyhedral patterns. In Proceedings of the International Symposium on Theory, Design and Realization of Shell and Spatial Structures, Nagoya, Japan, 9–13 October 2001; Kunieda, H., Ed.; IASS & Architectural Institute of Japan: Nagoya, Japan, 2001.
15. Huybers, P. The Morphology of Building Structures. In *ICCS'02: Proceedings of the International Conference on Computational Science—Part III, Amsterdam, The Netherlands,21–24 April 2002*; Springer: Berlin/Heidelberg, Germany, 2002.
16. Lalvani, H. Structures on hyper-structures. *Struct. Topol.* **1982**, *6*, 13–16.
17. Lalvani, H. Continuous transformations of subdivided periodic surfaces. *Int. J. Space Struct.* **1990**, *5*, 255–279. [CrossRef]
18. Lalvani, H.; Katz, N. Computer-generated transformations of geodesic spheres. In *Space Structures 4*; Thomas Telford: London, UK, 1993.
19. Lalvani, H. Higher dimension periodic table of regular and semi-regular polytopes. *Int. J. Space Struct.* **1996**, *11*, 27–57. [CrossRef]
20. Pavlov, G.N. Determination of parameters of crystal latticed surfaces composed of hexagonal plane faces. *Int. J. Space Struct.* **1990**, *7*, 169–187. [CrossRef]
21. Pavlov, G.N. Calculation of geometrical parameters and projection of geodesic domes and shells based on the network subdivision of the system D. In *Space Structures 4*; Thomas Telford Ltd.: London, UK, 1993.
22. Ramaswamy, S.G.; Eukhout, M.; Suresh, R.G. *Analysis, Design and Construction of Steel Space Frames*; Thomas Telford Ltd.: London, UK, 2002.
23. Obrębski, J.B. Unidom-space bar system. In Proceedings of the Local Seminar of IASS Polish Charter, XII LSCE 2006, Warsaw, Poland, 1 December 2006.
24. Szmit, R. Analysis and design of geodesic domes. *Inżynieruia i Budownictwo.* **2016**, *72*, 310–312.
25. Szmit, R. Geometry Design and Structural Analysis of Steel Single-Layer Geodesic Domes. In Proceedings of the Baltic Geodetic Congress (BGC Geomatics), Gdańsk, Poland, 22–25 June 2017. [CrossRef]
26. Rębielak, J. *Shaping of Space Structures. Examples of Applications of Formian in the Design of Tension-Strut Systems*; Oficyna Wydawnicza Politechniki Wrocławskiej: Wroclaw, Poland, 2005.
27. Makowski, Z.S. A history of the development of domes and a review of recent achievements world-wide. In *Analysis, Design and Construction of Braced Domes*; Granada Technical Books: London, UK, 1984; pp. 1–85.
28. Saka, M.P. Optimum topological design of geometrically nonlinear single layer latticed domes using coupled genetic algorithm. *Comput. Struct.* **2007**, *85*, 1635–1646. [CrossRef]
29. Kaveh, A.; Talatahari, S. Geometry and topology optimization of geodesic domes using charged system search. *Struct. Multidiscip. Optim.* **2011**, *43*, 215–229. [CrossRef]
30. Carvalho, J.P.G.; Lemonge, A.C.C.; Hallak, P.H.; Vargas, D.E.C. Simultaneous sizing, shape, and layout optimization and automatic member grouping of dome structures. *Structures* **2020**, *28*, 2188–2202. [CrossRef]

31. Carbas, S.; Saka, M.P. Optimum topology design of various geometrically nonlinear latticed domes using improved harmony search method. *Struct. Multidiscip. Optim.* **2012**, *45*, 377–399. [CrossRef]
32. Gholizadeh, S.; Barati, H. Topology Optimization of nonlinear single layer domes by a new metaheuristic. *Steel Compos. Struct.* **2014**, *16*, 681–701. [CrossRef]
33. Kaveh, A.; Rezaei, M. Optimum topology design of geometrically nonlinear suspended domes using ECBO. *Struct. Eng. Mech.* **2015**, *65*, 667–694. [CrossRef]
34. Kaveh, A.; Rezaei, M. Topology and geometry optimization of single-layer domes utilizing CBO and ECBO. *Sci. Iran.* **2016**, *23*, 535–547. [CrossRef]
35. Kaveh, A.; Rezaei, M.; Shiravand, M.R. Optimal design of nonlinear large-scale suspendome using cascade optimization. *Int. J. Space Struct.* **2018**, *33*, 3–18. [CrossRef]
36. Ye, J.; Lu, M. Optimizations of domes against instability. *Steel Compos. Struct.* **2018**, *28*, 427–438. [CrossRef]
37. Drygala, I.J.; Dulinska, J.M.; Ciura, R.; Lachawiec, K. Vibration Serviceability of Footbridges: Classical vs. Innovative Material Solutions for Deck Slabs. *Materials* **2020**, *13*, 3009. [CrossRef]
38. Eom, G.H.; Kim, S.J.; Lee, T.H.; Kim, J.H.J. Design Optimization and Structural Performance Evaluation of Plate Girder Bridge Constructed Using a Turn-Over Process. *Materials* **2017**, *10*, 283. [CrossRef]
39. Guan, Y.; Virgin, L.N.; Helm, D. Structural behavior of shallow geodesic lattice domes. *Int. J. Solids Struct.* **2018**, *15515*, 225–239. [CrossRef]
40. Barbieri, N.; Machado, R.D.; Barbieri, L.S.V.; Lima, K.F.; Rossot, D. Dynamic Behavior of the Geodesic Dome Joints. *Int. J. Comput. Appl.* **2016**, *40*, 40–44. [CrossRef]
41. Szaniec, W.; Zielinska, K. Harmonic analysis of the windloaded bar dome at the Satellite Services Centre in Psary. *Arch. Civ. Eng.* **2016**, *62*, 37–50. [CrossRef]
42. Satria, E.; Kato, S.; Nakazawa, S.; Kakuda, D. Study on dynamic behavior of a new type of two-way single layer lattice dome with nodal eccentricity. *Steel Compos. Struct.* **2008**, *8*, 511–530. [CrossRef]
43. Fu, F. Non-linear static analysis and design of Tensegrity domes. *Steel Compos. Struct.* **2006**, *6*, 417–433. [CrossRef]
44. Cai, J.G.; Feng, J.; Chen, Y.; Huang, L.F. Study on the seismic performance of space beam string structure. In Proceedings of the 14th World Conference on Earthquake Engineering, Beijing, China, 12–17 October 2008.
45. Takeuchi, T.; Ogawa, T.; Kumagai, T. Seismic response evaluation of lattice shell roofs using amplification factors. *J. Int. Assoc. Shell Spat. Struct.* **2007**, *48*, 197–210.
46. Nakazawa, S.; Kato, S.; Takeuchi, T.; Xue, S.D.; Lazaro, D. State of the art of seismic response evaluation methods for metal roof spatial structures. *J. Int. Assoc. Shell Spat. Struct.* **2012**, *53*, 117–130.
47. Kato, S.; Nakazawa, S. Seismic risk analysis of large lattice dome supported by buckling restrained braces. In Proceedings of the 6th International Conference on Computation of Shell and Spatial Structures IASS-IACM 2008, New York, NY, USA, 28–31 May 2008; Abel, J.F., Cooke, J.R., Eds.; Cornell University: Ithaca, NY, USA, 2008.
48. Li., H.; Li., J.; Zhi, F.; Ma, F.; Qin, D. A parameter study on dynamic buckling of spatial arch trusses under seismic action. In Proceedings of the 6th International Conference on Computation of Shell and Spatial Structures IASS-IACM 2008, New York, NY, USA, 28–31 May 2008; Abel, J.F., Cooke, J.R., Eds.; Cornell University: Ithaca, NY, USA, 2008.
49. Qin, J.; Shen, B.; Li, G. Dynamic field test on elliptical suspen-dome. In Proceedings of the 6th International Conference on Computation of Shell and Spatial Structures IASS-IACM 2008, New York, NY, USA, 28–31 May 2008; Abel, J.F., Cooke, J.R., Eds.; Cornell University: Ithaca, NY, USA, 2008.
50. Li, J.; Xu, J. Dynamic Stability and Failure Probability Analysis of Dome Structures Under Stochastic Seismic Excitation. *Int. J. Struct. Stab. Dyn.* **2014**, 1–14. [CrossRef]
51. Davis, T. Geodesic Domes. 2011. Available online: http://www.geometer.org/mathcircles (accessed on 18 February 2011).
52. Pilarska, D. Octahedron—Based spatial bar structures–the form of large areas covers. In Proceedings of the Third Scientific Conference Environmental Challenges in Civil Engineering, Opole, Poland, 23–25 April 2018.
53. Pilarska, D. Comparative analysis of various design solutions of octahedron—Based spatial bar structures. In Proceedings of the XXIV Conference of Lightweight Structures in Civil Engineering, Lodz, Poland, 7 December 2018.
54. Pilarska, D. Two subdivision methods based on the regular octahedron for single-and double-layer spherical geodesic domes. *Int. J. Space Struct.* **2020**. [CrossRef]
55. Fuliński, J. *Geometria Kratownic Powierzchniowych*; The Work of Wrocław Scientific Society; Państwowe Wydawnictwo Naukowe: Wroclaw, Poland, 1973.
56. EN. *EN 1993: Eurocode 3: Design of Steel Structures*; European Committee for Standardization: Brussels, Belgium, 2005.
57. Chmielewski, T.; Górski, P.; Beirow, B.; Kretzschma, J. Theoretical and experimental free vibrations of tall industrial chimney with flexibility of soil. *Eng. Struct.* **2005**, *27*, 25–34. [CrossRef]
58. Tabatabaiefar, H.R.; Massumi, A. A simplified method to determine seismic responses of reinforced concrete moment resisting building frames under influence of soil–structure interaction. *Soil Dyn. Earthq. Eng.* **2010**, *30*, 1259–1267. [CrossRef]
59. EN. *EN 1998: Eurocode 8: Design of Structures for Earthquake Resistance*; European Committee for Standardization: Brussels, Belgium, 2004.

Concrete Containing Waste Glass as an Environmentally Friendly Aggregate: A Review on Fresh and Mechanical Characteristics

Shaker Qaidi [1,*]**, Hadee Mohammed Najm** [2,*]**, Suhad M. Abed** [3]**, Yasin Onuralp Özkılıç** [4]**, Husam Al Dughaishi** [5]**, Moad Alosta** [5]**, Mohanad Muayad Sabri Sabri** [6]**, Fadi Alkhatib** [7] **and Abdalrhman Milad** [5,*]

1   Department of Civil Engineering, College of Engineering, University of Duhok, Duhok 42001, Iraq
2   Department of Civil Engineering, Zakir Husain Engineering College, Aligarh Muslim University, Aligarh 202002, India
3   Department of Highways & Airports Engineering, College of Engineering, University of Diyala, Baqubah 32001, Iraq
4   Department of Civil Engineering, Faculty of Engineering, Necmettin Erbakan University, Konya 42000, Turkey
5   Department of Civil and Environmental Engineering, College of Engineering, University of Nizwa, P.O. Box 33, Nizwa 616, Oman
6   Peter the Great St. Petersburg Polytechnic University, 195251 St. Petersburg, Russia
7   Department of Structural Engineering, Faculty of Civil Engineering and Built Environment, Universiti Tun Hussein Onn Malaysia (UTHM), Parit Raja 86400, Malaysia
*   Correspondence: shaker.abdal@uod.ac (S.Q.); gk4071@myamu.ac.in (H.M.N.); a.milad@unizwa.edu.om (A.M.)

Abstract: The safe disposal of an enormous amount of waste glass (WG) in several countries has become a severe environmental issue. In contrast, concrete production consumes a large amount of natural resources and contributes to environmental greenhouse gas emissions. It is widely known that many kinds of waste may be utilized rather than raw materials in the field of construction materials. However, for the wide use of waste in building construction, it is necessary to ensure that the characteristics of the resulting building materials are appropriate. Recycled glass waste is one of the most attractive waste materials that can be used to create sustainable concrete compounds. Therefore, researchers focus on the production of concrete and cement mortar by utilizing waste glass as an aggregate or as a pozzolanic material. In this article, the literature discussing the use of recycled glass waste in concrete as a partial or complete replacement for aggregates has been reviewed by focusing on the effect of recycled glass waste on the fresh and mechanical properties of concrete.

Keywords: waste glass; recycling; construction materials; sustainable concrete; mechanical properties

1. Introduction

Glass is one of the world's most diverse substances because of its substantial properties, such as chemical inertness, optical clarity, low permeability, and high authentic strength [1–3]. The usage of glass items has greatly increased, leading to enormous quantities of WG. Globally, it is estimated that 209 million tons of glass are produced annually [4–6]. In the U.S., according to the Environmental Protection Agency (EPA) [7–9], 12.27 million tons of glass were created in 2018 in municipal solid waste (MSW), as shown in Figure 1, most of which were containers for drinking and food. Furthermore, in 2018, the EU generated 14.5 million tons of glass package wastes [10–12]. The quantity of generated WG will increase due to the increasing demand for glass components [13–16].

Recycling and reducing waste are key parts of a waste-management system since they contribute to conserving natural resources, reducing requests for waste landfill space, and reducing pollution of water and air [17,18]. According to Meyer [19], by 2030, the EU zero-waste initiative estimates that improvements in resource efficiency throughout the

chain could decrease material input requirements by 17% to 24%, satisfying the demand for raw materials between 10% to 40%, and could contribute to reducing emissions by 40% [20–22].
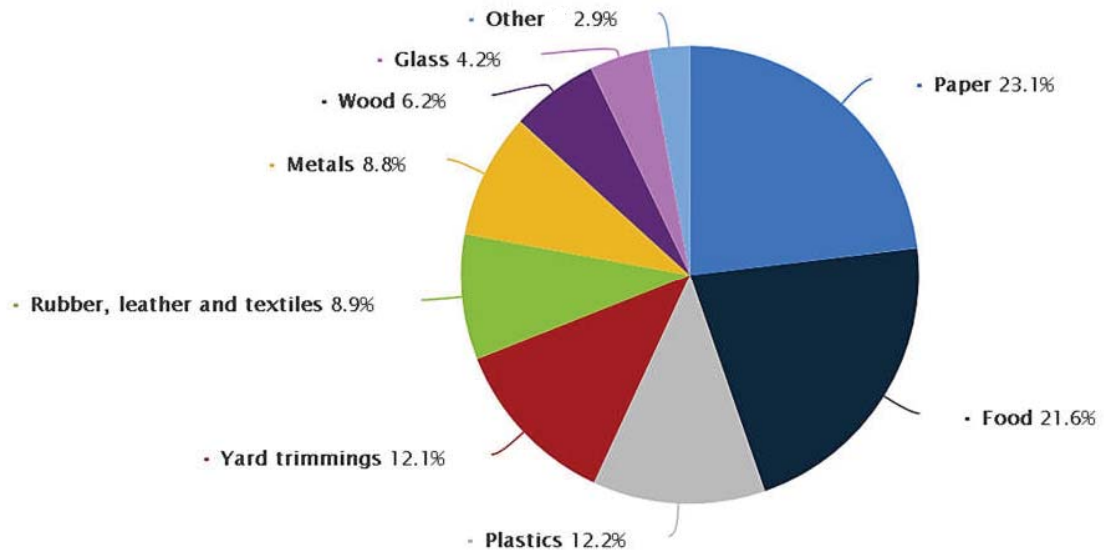

Figure 1. Distribution of MSW stream produced in the U.S in 2018. Adapted from [7].

In fact, innovative options for recycling WG must be developed. One significant option is to use WG for construction materials [23]. The recycling of WG not only decreases the demand for landfill sites in the building sector but also significantly helps in decreasing the carbon footprint and saving resources [24–26]. In 1963, Schmidt and Saia [27] performed the first research on the use of WG for building materials. The authors recycled WG into useful glass particles for wall-panel production. Subsequently, a significant study was conducted in order to use recycled glass for fine or coarse aggregate in mortar and concrete, because of the good hardness of the glass [14,28,29]. This study aims at reviewing the possibilities of utilizing WG in concrete as a partial or full replacement for fine or coarse aggregates in order to give practical and brief guidance on recycling and using WG [30–33].

2. Research Significance

Besides the above-mentioned dangers of WG and the need to recycle it economically and environmentally, this research explores the source of WG as well as its physical and chemical characteristics. In addition, this study aims to review the literature that discusses the use of recycled WG in concrete as a partial or complete alternative to aggregates by focusing on the effect of this waste on the fresh and mechanical properties of concrete in order to demonstrate the possibilities of using recycled WG in concrete and to provide practical and brief guidance. Furthermore, we are establishing a foundation for future study on this material and describing research insights, existing gaps, and future research goals.

3. Properties of Glass

3.1. Chemical Properties of Glass

Glass exists in various colors and types, with various chemical components. Tables 1 and 2 show the chemical compositions of different colors and types of typical glass, respectively.

Table 1. Chemical components of glass for various colors.

Color	Chemical Compositions											Refs.
	SiO_2	CaO	Na_2O	Al_2O_3	MgO	Fe_2O_3	K_2O	SO_3	TiO_2	Cr_2O_3	Others	
White	70.39	6.43	16.66	2.41	2.59	0.32	0.23	0.19	0.08	-	0.04 (MnO), 0.02 (Cl)	[34]
Clear	72.42	11.50	13.64	1.44	0.32	0.07	0.35	0.21	0.035	0.002	-	[35]
Flint	70.65	10.70	13.25	1.75	2.45	0.45	0.55	0.45	-	-	-	[36]
Amber	70.01	10.00	15.35	3.20	1.46	-	0.82	0.06	0.11	-	0.04 (MnO)	[34]
Brown	71.19	10.38	13.16	2.38	1.70	0.29	0.70	0.04	0.15	-	-	[37]
Green	72.05	10.26	14.31	2.81	0.90	-	0.52	0.07	0.11	-	0.04 (MnO)	[34]

Table 2. Chemical components of glass for various types. Adapted from [38,39].

Type	Uses	Chemical Compositions									
		SiO_2	K_2O	Na_2O	Al_2O_3	MgO	PbO	BaO	CaO	B_2O_3	Others
Barium glasses	Optical-dense barium crown	36			4		41			10	9% ZnO
	Color TV panel	65	9	7	2	2	2	2	2		10% SrO
Soda-Lime Glasses	Containers	66–75	0.1–3	12–16	0.7–7	0.1–5			6–12		
	Light bulbs	71–73									
	Float sheet	73–74									
	Tempered ovenware	0.5–1.5								13.5–15	
Lead glasses	Color TV funnel	54	9	4	2		23				
	Electronic parts	56	9	4	2		29				
	Neon tubing	63	6	8	1		22				
	Optical dense flint	32	2	1			65				
Aluminosilicate glasses	Combustion tubes	62		1	17	7			8	5	
	Resistor substrates	57			16	7		6	10	4	
	Fiberglass	64.5		0.5	24.5	10.5					
Borosilicate	Chemical apparatus	81		4	2					13	
	Tungsten sealing	74		4	1					15	
	Pharmaceutical	72	1	7	6					11	

3.2. Physical and Mechanical Properties of Glass

The physical and mechanical properties of crushed WG are listed in Tables 3 and 4, respectively.

Table 3. Physical properties of crushed WG.

Property		Refs.
Specific gravity	2.4–2.8 2.51 (Green), 2.52 (Brown)	[40]
Fineness Modulus	4.25 0.44–3.29	[41,42]
Bulk Density	1360 kg/m^3	[43,44]
Shape Index (%)	30.5	
Flakiness Index	84.3–94.7	[45]

Table 4. Mechanical properties of crushed WG.

Property		Refs.
CBR (California bearing ratio) (%)	Approx. 50–75.	[46]
	38.4	[43,45]
Los Angeles Value (%)	24.8–27.8	[44]
	27.7	[47]
Friction Angle	critical = 38 (Loose recycled glass) critical = 51–61 (Dense recycled glass)	[46]

4. Fresh Concrete Properties

4.1. Workability

There are two parallel points of view on the workability of WG-containing concrete. A review of past studies on the impact of WG aggregates on the mixes of workability

is summarized in Table 5. It can be noticed that various research investigations have shown that the mixing of WG increases workability. They connected this beneficial impact of WG on the workability to the weaker cohesive between the cement mortar and the smooth surfaces of waste glass [48–52]. The smooth surface and low absorption capacity of WG are also important factors in increasing workability [53,54]. For example, Ali and Al-Tersawy [55] substitute fine aggregate in self-compacting concrete (SCC) mixes with recycled WG at levels of 10% to 50% by volume. Constant content of water–cement ratio and various superplasticizer doses have been used. They stated that slump flow increased by 2%, 5%, 8%, 11%, and 85%, with the incorporating of 10%, 20%, 30%, 40% and 50% of WG, respectively. In addition, Liu, Wei, Zou, Zhou and Jian [56] substitute fine aggregate in ultra-high-performance concrete (UHPC) mixes with recycled liquid crystal display (CRT) glass at levels of 25% to 100% by volume. Constant content of water–cement ratio and various superplasticizer (SP) doses have been used. Moreover, they stated that flowability increased by 11, 14, 16, and 12 mm, compared to the control sample, incorporating 25%, 50%, 75%, and 100% WG, respectively. Enhancing the workability by including WG is a benefit of utilizing this recycled material [57–60]. There is potential to utilize glass to create HPC in which high workability is necessary. In addition, WG can be used to boost workability rather than employing admixtures such as HRWR or superplasticizers [61–64].

Contrastingly, some studies have stated that including waste glass into the mixes lowered workability. Nevertheless, such a decrease has been associated with sharp edges, higher glass particle aspect ratio, and angular form, with obstruction of the movement of particles and cement mortar [65–71]. For example, Wang [72] substitutes fine aggregate in liquid crystal display glass concrete (LCDGC) mixes with recycled LCD at levels of 20% to 80% by volume. Various contents of w/c ratio (0.38–0.55) and various superplasticizer doses have been used. The author stated that slump flow decreased by 4%, 7%, 19%, and 26%, incorporating 20%, 40%, 60%, and 80% of WG, respectively, for w/c of 0.44. In addition, Arabi, Meftah, Amara, Kebaïli and Berredjem [73] substitute coarse aggregate in SCC mixes with recycled windshield glass at levels of 25% to 10% by volume. Various contents of w/c ratio (0.60–0.69) and various superplasticizer doses have been used. They stated that slump flow decreased by 3%, 8%, 9%, and 11%, incorporating 20%, 40%, 60%, and 80% of WG, respectively. According to Rashad [61], the optimal content of glass waste to achieve good workability is 20%.

Table 5. Summary of the results of past studies on the workability of waste-glass concrete.

Refs.	Type of Composite	Source	Type of Sub.	WG Sub. Ratio%	WG Size (mm)	w/c or w/b	Addit. or Admix.	Outcomes
[74]	SCGC	LCD	F.A	10, 20, & 30 (vol.%)	11.8	0.28	SP	Slump flow increased by 11%, 17%, and 21%, respectively.
[75]	HPGC	LCD	F.A	10, 20, & 30 (vol.%)	0.149–4.75	0.25, 0.32, & 0.34	SP	Slump flow increased, ranged between 7–9%.
[76]	Steel slag concrete	WG	C.A	16.5 & 17.5 (vol.%)	4.9–10 & 4.9–16	0.4 & 0.55	WR	Slump increased by 167%, for substitution 16.5% (w/c of 0.55, and size of 4.9–10 mm). Slump increased by 8%, for substitution 17.5% (w/c of 0.40, and size of 4.9–16 mm).
[77]	Cement concrete	WG & PVC	F.A	5, 10, 15, 20, 25, & 30 (wt.%)	0.15–0.6	0.44, 0.5, & 0.55	-	Slump value changed by −7%, +33%, +47%, +31, +36, and +40%, respectively, for w/c of 0.5.
[78]	Waste glass concrete	WG	F.A	18, 19, 20, 21, 22, 23, & 24 (vol.%)	0.15–0.6	0.4	SP	Workability decreased by increasing the WG ratio.
[79]	Waste glass concrete	CRT	F.A	50 & 100 (vol.%)	≤5	0.35, 0.45, & 0.55	WR & AE	Slump increased by 55%, and 115%, respectively, for w/c of 0.45.
[80]	Waste glass concrete	WG	C.A	10, 20, & 30 (wt.%)	≤20	0.55	-	Slump decreased by 3%, 5%, and 9%, respectively.
[73]	SCC	Windshield	C.A	25, 50, 75, & 100 (vol.%)	9.5 & 12.7 (mixed)	0.6–0.69	Marble filler & SP	Slump flow decreased by 3%, 8%, 9%, and 11%, respectively.
[81]	UHPC	WG	F.A	25, 50, 75, & 100 (vol.%)	≤0.6	0.19	Steel fiber & HRWRA	Slump increased by 25%, 111%, 321%, and 532%, respectively.
[56]	UHPC	CRT	F.A	25, 50, 75, & 100 (vol.%)	0.6–1.18	0.19	Steel fiber, SF, & SP	Flowability increased by 11, 14, 16, and 12 mm, respectively, compared to control (200 mm).

Table 5. *Cont.*

Refs.	Type of Composite	Source	Type of Sub.	WG Sub. Ratio%	WG Size (mm)	w/c or w/b	Addit. or Admix.	Outcomes
[82]	Waste glass concrete	WG	F.A	15 & 30 (vol.%)	≤4.75	0.5	-	Slump decreased by 9%, and 39%, respectively.
[83]	Waste-based concrete	WG	F.A	100 (vol.%)	≤1.9	0.47	SP & GBFS	Glass sand showed lower workability compared to Lead smelter slag (LSS).
[84]	Waste glass concrete	WG	F.A	5, 15, & 20 (vol.%)	0.15–4.75	0.55	-	Slump decreased by 19%, 29%, and 35%, respectively.
[55]	SCC	WG	F.A	10, 20, 30, 40, & 50 (vol.%)	0.075–5	0.4	SF & SP	Slump flow increased by 2%, 5%, 8%, 11%, and 85%, respectively.
[85]	Cement concrete	WG	F.A	5, 10, 15, & 20 (vol.%)	0.15–9.5	0.56	-	Slump decreased by 1%, 3%, 4%, and 5%, respectively.
[86]	Waste glass concrete	Waste E-glass	F.A	10, 20, 30, 40, & 50 (wt.%)	≤4.75	0.68	SF & F.A.	Slump decreased by 2%, 1%, 50%, 55, and 54%, respectively.
[87]	Waste glass concrete	WG	F.A	10, 15, & 20 (vol.%)	0.15–4.75	0.52	-	Slump decreased by 24%, 23%, and 33%, respectively.
[88]	Waste glass concrete	WG	F.A	15, 20, 30, & 50 (wt.%)	≤5	0.52, 0.57, & 0.67	-	Slump decreased by 0%, 0%, 13%, and 13%, respectively, for w/c of 0.57.
[89]	Waste glass concrete	Green waste glass	F.A	30, 50, & 70 (wt.%)	≤5	0.5	AE	Workability decreased, ranged between 19–44%.
[65]	Waste glass concrete	Soda-lime glass	F.A	50 & 100 (vol.%)	≤5	0.38	MK	Slump decreased by 0%, and 38%, respectively.
[48]	Waste glass concrete	WG	F.A & C.A	10, 25, 50, & 100 (vol.%)	N.M	0.48	-	Slump value changed by −6%, +6%, +18%, and +6%, respectively.
[72]	LCDGC	LCD	F.A	20, 40, 60, & 80 (vol.%)	≤4.75	0.38, 0.44, & 0.55	-	Slump flow decreased by 4%, 7%, 19%, and 26%, respectively.
[90]	Cement concrete	LCD	F.A	20, 40, 60, & 80 (vol.%)	≤4.75	0.48	-	Slump value changed by 0%, −5%, −5%, and +20%, respectively.
[91]	Alkali-activated mortar	Cullet	F.A	25, 50, 75, & 100 (vol.%)	≤2.36	0.6	F.A., GBFS, SH, & SS	Flowability increased, ranged between 4–15%.
[92]	Waste glass concrete	WG	F.A	25, 50, 75, & 100 (wt.%)	≤5	0.5	-	Slump decreased by 9%, 7%, 15%, and 27%, respectively.

Where: SCGC is self-compacting glass concrete; SCC is self-compacting concrete; HPGC is high performance recycled liquid crystal glasses concrete; UHPC is ultra-high performance concrete; LCDGC is liquid crystal display glass concrete; LCD is liquid crystal display; CRT is cathode ray tube; WG is waste glass; PVC is polyvinyl chloride; SP is superplasticizer; HRWRA is a high-range water-reducing agent; WR is water-reducing; AE is air-entraining; SF is silica fume; F.A. is fly ash; GBFS is granulated blast furnace slag; MK is metakaolin; SH is sodium hydroxide solution; SS is sodium silicate solution; F.A is fine aggregate; C.A is coarse aggregate; vol. is replacing by volume; wt. is replacing by weight.

4.2. Bulk Density

Past studies on the impact of WG aggregates on the bulk density, which are summarized in Figure 2, revealed that the majority of studies showed that incorporating glass waste into mixtures reduces density. This decrease can be ascribed to the lesser density of WG compared to natural aggregate [42,65,93,94], as well as the lower specific gravity [43,66,87,93,95]. For example, Taha and Nounu [65] substitute fine aggregate in waste-glass concrete (WGC) mixes with recycled soda-lime glass at levels of 50% to 100% by volume. They stated that the fresh density of WG concrete mixes reduced by 1% and 2% incorporating 50% and 100% of WG, respectively. This density drop might be realized as one benefit of using this material in concrete for engineering purposes [96–99].

On the other hand, Liu, Wei, Zou, Zhou and Jian [56] stated that concrete of 10 to 50% WG had a fresh density greater than reference. The authors substitute F.A in UHPC mixes with recycling CRT glass at levels of 25% to 100% by volume. They stated that the fresh density of waste-glass concrete mixtures increased by 1% 2.5%, 3.5%, and 6%, incorporating 25%, 50%, 75%, and 100% of WG, respectively. The authors attributed the reason to the fact that the density of CRT glass (2916 kg/m^3) was larger than that of fine aggregate (2574 kg/m^3) [100–104].
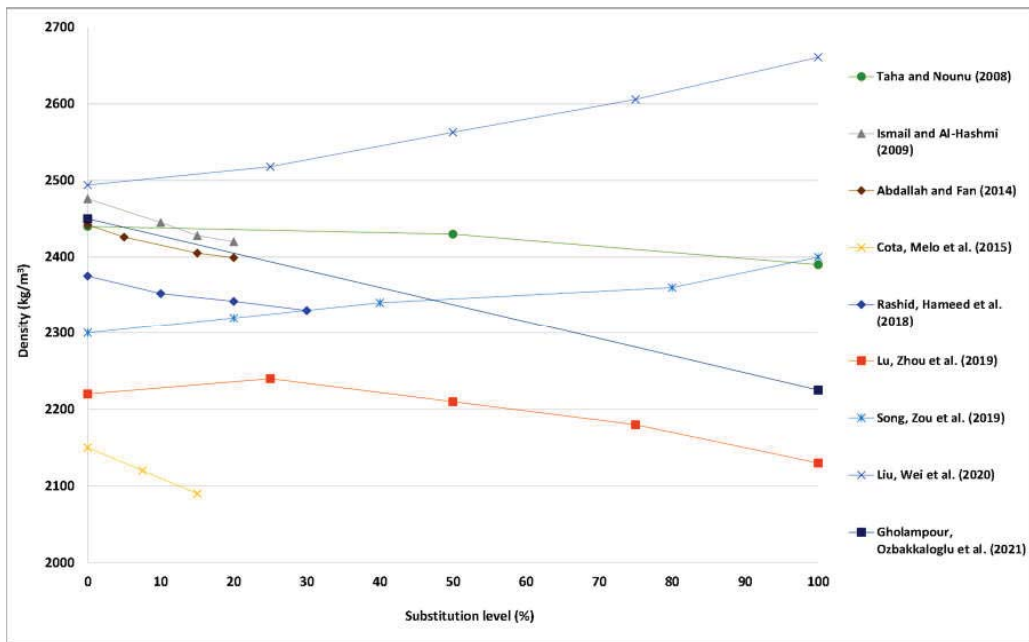
Figure 2. Bulk density of concrete with various content of WG. Adapted from references [56,65,80,83,84,87,105–107].

5. Mechanical Properties

5.1. Compressive Strength

By reviewing past studies on the impact of WG aggregates on the compressive strength of waste-glass concrete, summarized in Table 6, it can be noticed that most studies shown that incorporating glass waste into concrete reduces compressive strength. The researchers ascribed this behavior to (i) the sharp edges and smooth particle surfaces, leading to a poorer bond between cement mortar and glass particles at the interfacial transition zone (ITZ) [14,40,42,43,55,66,87,90,108,109]; (ii) increased water content of the glass aggregate mixes due to the weak ability of WG to absorb water [43,110]; and (iii) the cracks caused by expanding stress formed by the alkali-silica reaction produced from the silica in WG [40]. For example, Park, Lee and Kim [89] substitute fine aggregate in WGC with recycled green WG at levels of 30% to 70% by weight. They stated that the compressive strength of concrete decreased by 3%, 13%, and 18%, incorporating 30%, 50%, and 70% of WG, respectively. In addition, Terro [48] noted that concrete, which contains up to 25% of WG, showed compressive strength values greater than the reference, whereas concrete with a substitution level of over 25% declined in compressive strength.

In order to better understand the impact of glass waste on the properties of the waste-glass concrete [111–114]. Omoding, Cunningham and Lane-Serff [115] investigated the concrete microstructure via SEM by replacing between 12.5–100% of the coarse aggregate with green waste glass with a size of 10–20 mm. The authors stated (i) that there is a weak connection between the waste glass and the cement matrix. This is because of a reduction in bonding strength between the waste glass and the cement paste because of the high smoothness of waste glass, consequently resulting in cracks and poor adherence between waste glass and cement paste; and (ii) as the content of waste glass increases, the proportion of cracks and voids increases in the concrete's matrix.

However, some studies have stated that waste glass increases mechanical strength. This increase is primarily realized because of the surface texture and strength of the waste

glass particles compared to natural sand [116–118] and the pozzolanic reaction of waste glass aggregate [119–121]. For example, Jiao, Zhang, Guo, Zhang, Ning and Liu [81] substitute fine aggregate in UHPC with recovered WG at levels of 25% to 100% by weight. They stated that the compressive strength of concrete increased by 2%, 17%, 34%, and 20%, incorporating 25%, 50%, 75%, and 100% WG, respectively.

Regarding the influence of WG color on properties, some studies have stated that the color of WG did not produce any noticeable variation in strength [89,122]. On the contrary, Tan and Du [66] claimed that clear waste glass showed less strength.

Table 6. Summary of the results of past studies on the compressive strength of waste-glass concrete.

Refs.	Type of Composite	Source	Type of Subs.	WG Subs. Ratio	WG Size (mm)	w/c or w/b	Addit. or Admix.	Com. Str. of Control (MPa)	Outcomes
[74]	SCGC	LCD	F.A	10, 20, & 30 (vol.%)	11.8	0.28	SP	65	Decreased by 2%, 5%, and 3%, respectively.
[75]	HPGC	LCD	F.A	10, 20, & 30 (vol.%)	0.149–4.75	0.25, 0.32, & 0.34	SP	56	Decreased by 25%, 32%, and 29%, respectively, for w/c of 0.32.
[123]	Autoclaved aerated concrete	CRT	F.A	5 & 10 (vol.%)	2.16–3.3	N.M	-	29	Decreased by 2%, and 0%, respectively.
[77]	Cement concrete	WG & PVC	F.A	5, 10, 15, 20, 25, & 30 (wt.%)	0.15–0.6	0.44, 0.5, & 0.55	-	34	Decreased by 1%, 4%, 4%, 6%, 7%, and 9%, respectively, for w/c of 0.50.
[78]	Waste glass concrete	WG	F.A	18, 19, 20, 21, 22, 23, & 24 (vol.%)	0.15–0.6	0.4	SP	33	Changed by +6%, +9%, +12%, +9%, +3%, −6% and −9%, respectively.
[79]	Waste glass concrete	CRT	F.A	50 & 100 (vol.%)	≤5	0.35, 0.45, & 0.55	WR & AE	28	Decreased by 21%, and 32%, respectively, for w/c of 0.45.
[80]	Waste glass concrete	WG	C.A	10, 20, & 30 (wt.%)	≤20	0.55	-	24	Decreased by 13%, 15%, and 23%, respectively.
[105]	Waste glass concrete	WG	F.A	25, 75, & 100 (wt.%)	0.15–5	0.48–0.66	-	38	Changed by +5%, +8%, +3%, and −8%, respectively.
[124]	Waste glass concrete	Cullet	C.A	25, 50, & 75 (wt.%)	2.36–5	0.29	SF	32	Decreased by 6%, 3%, 22%, and 25%, respectively.
[73]	SCC	Windshield	C.A	25, 50, 75, & 100 (vol.%)	9.5 & 12.7	0.6–0.69	Marble filler & SP	33	Decreased by 15%, 24%, 24%, and 30%, respectively.
[125]	HSPC	WG	C.A	25, 50, 75, & 100 (vol.%)	2.36–5	0.14	SF & SP	50	Decreased by 4%, 20%, 30%, and 36%, respectively.
[81]	UHPC	WG	F.A	25, 50, 75, & 100 (wt.%)	≤0.6	0.19	Steel fiber & HRWRA	108	Increased by 2%, 17%, 34%, and 20%, respectively.
[56]	UHPC	CRT	F.A	25, 50, 75, & 100 (vol.%)	0.6–1.18	0.19	Steel fiber, SF, & SP	180	Decreased by 7%, 11%, 16%, and 18%, respectively.
[115]	Glass aggregate concretes	WG	C.A	12.5, 25, 50, & 100 (vol.%)	10–20	0.52	SP	45	Decreased by 4%, 16%, 20%, and 27%, respectively.
[82]	Waste glass concrete	WG	F.A	15 & 30 (vol.%)	≤4.75	0.5	-	48	Decreased by 6%, and 0%, respectively.
[84]	Waste glass concrete	WG	F.A	5, 15, & 20 (vol.%)	0.15–4.75	0.55	-	33	Decreased by 6%, 3%, and 0%, respectively.
[55]	SCC	WG	F.A	10, 20, 30, 40, & 50 (vol.%)	0.075–5	0.4	SF & SP	62	Decreased by 5%, 15%, 18%, 23%, and 24%, respectively.
[85]	Cement concrete	WG	F.A	5, 10, 15, & 20 (vol.%)	0.15–9.5	0.56	-	32	Increased by 9%, 44%, 25%, and 38%, respectively.
[87]	Waste glass concrete	WG	F.A	10, 15, & 20 (vol.%)	0.15–4.75	0.52	-	44	Changed by −9%, −9%, and +5%, respectively.
[88]	Waste glass concrete	WG	F.A	15, 20, 30, & 50 (wt.%)	≤5	0.52, 0.57, & 0.67	-	48	Decreased by 2%, 4%, 13%, and 19%, respectively, for w/c of 0.57.
[89]	Waste glass concrete	Green waste glass	F.A	30, 50, & 70 (wt.%)	≤5	0.5	AE	38	Decreased by 3%, 13%, and 18%, respectively.
[48]	Waste glass concrete	WG	F.A & C.A	10, 25, 50, & 100 (vol.%)	N.M	0.48	-	40	Changed by +38%, +3%, −5%, and −50%, respectively.
[72]	LCDGC	LCD	F.A	20, 40, 60, & 80 (vol.%)	≤4.75	0.38, 0.44, & 0.55	-	39	Decreased by 3%, 10%, 13%, and 15%, respectively, for w/c of 0.44.
[90]	Cement concrete	LCD	F.A	20, 40, 60, & 80 (vol.%)	≤4.75	0.48	-	36	Decreased by 6%, 11%, 22%, and 25%, respectively.
[107]	Waste glass concrete	CRT	F.A	20, 40, 60, 80, & 100 (vol.%)	4.75	0.45	F.A.	38	Decreased by 5%, 8%, 8%, 11%, and 13%, respectively.
[126]	Resin concretes	WG	F.A	0–100 (wt.%)	≤2	N.M	Epoxy resin	95	Decreased by 33%, for substitution of 100%.
[127]	Concrete blocks	WG	F.A	100 (vol.%)	4.75, 2.36, 1.18, & 0.6	0.23	-	34	Decreased by 18%.

Table 6. *Cont.*

Refs.	Type of Composite	Source	Type of Subs.	WG Subs. Ratio	WG Size (mm)	w/c or w/b	Addit. or Admix.	Com. Str. of Control (MPa)	Outcomes
[91]	Alkali-activated mortar	Cullet	F.A	25, 50, 75, & 100 (vol.%)	≤2.36	0.6	F.A., GBFS, SH, & SS	70	Decreased by 3%, 6%, 7%, and 10%, respectively.
[128]	Waste glass concrete	WG	F.A	25, 50., 75, & 100 (wt.%)	≤5	0.5	-	20	Changed by +20%, +15%, −10%, and −35%, respectively.

Where: SCGC is self-compacting glass concrete; SCC is self-compacting concrete; HPGC is high performance recycled liquid crystal glasses concrete; HSPC is high-strength pervious concrete; UHPC is ultra-high performance concrete; LCDGC is liquid crystal display glass concrete; LCD is liquid crystal display; CRT is cathode ray tube; WG is waste glass; PVC is polyvinyl chloride; SP is superplasticizer; HRWRA is a high-range water-reducing agent; WR is water-reducing; AE is air-entraining; SF is silica fume; F.A. is fly ash; GBFS is granulated blast furnace slag; MK is metakaolin; SH is sodium hydroxide solution; SS is sodium silicate solution; F.A is fine aggregate; C.A is coarse aggregate; vol. is replacing by volume; wt. is replacing by weight.

5.2. Splitting Tensile Strength

Past studies on the impact of WG aggregates on the splitting tensile strength of waste-glass concrete, which are summarized in Table 7, revealed that incorporating glass waste into concrete reduces tensile strength. Similarly, as in compressive strength, studies have attributed the main reason for this behavior to the poor bond between cement paste and glass particles at the ITZ. For example, Wang [72] substitutes fine aggregate in liquid crystal display glass concrete (LCDGC) with recycled LCD glass at levels of 20% to 80% by volume. The author stated that splitting tensile strength of concrete decreased by 1%, 7%, 8%, and 9%, incorporating 20%, 40%, 60%, and 80% of WG, respectively, for w/c of 0.44. Moreover, Ali and Al-Tersawy [55] substitute fine aggregate in self-compacting concrete (SCC) with recycled WG at levels of 10% to 50% by volume. They stated that tensile strength of waste-glass concrete decreased by 9%, 15%, 16%, 24%, and 28% incorporating 10%, 20%, 30%, 40%, and 50% of WG, respectively [129–132].

In contrast, Jiao, Zhang, Guo, Zhang, Ning and Liu [81] indicated that concrete of 25% to 100% WG had a tensile strength greater than reference. The authors substitute fine aggregate in ultra-high-performance concrete (UHPC) with recycled WG at levels of 25% to 100% by weight. They stated that the splitting tensile strength of concrete increased by 1%, 3%, 11%, and 7%, incorporating 25%, 50%, 75%, and 100% of WG, respectively. The author attributed the reason to the effect of using steel fibers.

Table 7. Summary of the results of past studies on the splitting tensile strength of waste-glass concrete.

Refs.	Type of Composite	Source	Type of Sub.	WG Sub. Ratio%	WG Size (mm)	w/c or w/b	Addit. or Admix.	Split ten. str. of Control (MPa)	Outcomes
[81]	UHPC	WG	F.A	25, 50, 75, & 100 (wt.%)	≤0.6	0.19	Steel fiber & HRWRA	11.7	Increased by 1%, 3%, 11%, and 7%, respectively.
[82]	Waste glass concrete	WG	F.A	15 & 30 (vol.%)	≤4.75	0.5	-	4.5	Changed by +4%, and −1%, respectively.
[84]	Waste glass concrete	WG	F.A	5, 15, & 20 (vol.%)	0.15–4.75	0.55	-	2.5	Increased by 4%, 12%, and 24%, respectively.
[55]	SCC	WG	F.A	10, 20, 30, 40, & 50 (vol.%)	0.075–5	0.4	SF & SP	6.8	Decreased by 9%, 15%, 16%, 24%, and 28%, respectively.
[85]	Cement concrete	WG	F.A	5, 10, 15, & 20 (vol.%)	0.15–9.5	0.56	-	3.9	Decreased by 0%, 8%, 15%, and 23%, respectively.
[133]	Waste glass concrete	WG	F.A	10, 20, 30, & 40 (wt.%)	≤4.75	0.45	-	2.5	Decreased by 2%, 8%, 10%, and 12%, respectively.
[72]	LCDGC	LCD	F.A	20, 40, 60, & 80 (vol.%)	≤4.75	0.38, 0.44, & 0.55	-	2.38	Decreased by 1%, 7%, 8%, and 9%, respectively, for w/c of 0.44.

Table 7. *Cont.*

Refs.	Type of Composite	Source	Type of Sub.	WG Sub. Ratio%	WG Size (mm)	w/c or w/b	Addit. or Admix.	Split ten. str. of Control (MPa)	Outcomes
[107]	Waste glass concrete	CRT	F.A	20, 40, 60, 80, & 100 (vol.%)	4.75	0.45	F.A.	4.48	Decreased by 6%, 6%, 13%, 15%, and 19%, respectively.
[128]	Waste glass concrete	WG	F.A	25, 50., 75, & 100 (wt.%)	≤5	0.5	-	3.6	Decreased by 22%, 39%, 39%, and 44%, respectively.

Where: UHPC is ultra-high-performance concrete; LCDGC is liquid crystal display glass concrete; LCD is liquid crystal display; CRT is cathode ray tube; WG is waste glass; SP is superplasticizer; HRWRA is a high-range water-reducing agent; SF is silica fume; F.A. is fly ash; F.A is fine aggregate; C.A is coarse aggregate; vol. is replacing by volume; wt. is replacing by weight.

5.3. Flexural Strength

The flexural strength of waste-glass concrete shows comparable tendencies to its compressive strength and tensile strength. Most of the research revealed that introducing WG aggregates reduced flexural strength. However, other research showed that flexural strength increased when WG was included [134–136]. For instance, Kim, Choi and Yang [79] substitute fine aggregate in WGC with recycled CRT glass at levels of 50% to 100% by volume. They stated that flexural strength of concrete decreased by 9% and 14%, incorporating 50% and 100% of WG, respectively, for w/c of 0.45. On the contrary, Jiao, Zhang, Guo, Zhang, Ning and Liu [81] substitute fine aggregate in UHPC with recovered WG at levels of 25% to 100% by weight. They stated that flexural strength of concrete increased by 2%, 1%, 5%, and 1%, incorporating 25%, 50%, 75%, and 100% of WG, respectively.

Moreover, it can be concluded that the discrepancy between studies may be related to the type, size, and source of WG used in the mixtures. The mineral composition varies as the type of glass changes. Therefore, changing the mechanisms of interaction with binders in concrete, in turn, affects the properties. Table 8 presents the outcomes of various studies on the flexural strength of waste-glass concrete.

Table 8. Summary of the results of past studies on the flexural strength of waste-glass concrete.

Refs.	Type of Composite	Source	Type of Sub.	WG Sub. Ratio%	WG Size (mm)	w/c or w/b	Addit. or Admix.	Flex. str. of Control (MPa)	Outcomes
[74]	SCGC	LCD	F.A	10, 20, & 30 (vol.%)	11.8	0.28	SP	5.1	Changed by +16%, −12%, and −2%, respectively.
[78]	Waste glass concrete	WG	F.A	18, 19, 20, 21, 22, 23, & 24 (vol.%)	0.15–0.6	0.4	SP	4.84	Changed by +5%, +6%, +8%, +7%, +1%, −5% and −6%, respectively.
[79]	Waste glass concrete	CRT	F.A	50 & 100 (vol.%)	≤5	0.35, 0.45, & 0.55	WR & AE	4.4	Decreased by 9%, and 14%, respectively, for w/c of 0.45.
[81]	UHPC	WG	F.A	25, 50, 75, & 100 (wt.%)	≤0.6	0.19	Steel fiber & HRWRA	21	Increased by 2%, 1%, 5%, and 1%, respectively.
[56]	UHPC	CRT	F.A	25, 50, 75, & 100 (vol.%)	0.6–1.18	0.19	Steel fiber, SF, & SP	39	Decreased by 5%, 8%, 18%, and 21%, respectively.
[84]	Waste glass concrete	WG	F.A	5, 15, & 20 (vol.%)	0.15–4.75	0.55	-	4.7	Increased by 6%, 11%, and 15%, respectively.
[55]	SCC	WG	F.A	10, 20, 30, 40, & 50 (vol.%)	0.075–5	0.4	SF & SP	7.4	Decreased by 3%, 11%, 12%, 23%, and 24%, respectively.
[87]	Waste glass concrete	WG	F.A	10, 15, & 20 (vol.%)	0.15–4.75	0.52	-	5.89	Increased by 4%, 7%, and +11%, respectively.

Table 8. *Cont.*

Refs.	Type of Composite	Source	Type of Sub.	WG Sub. Ratio%	WG Size (mm)	w/c or w/b	Addit. or Admix.	Flex. str. of Control (MPa)	Outcomes
[88]	Waste glass concrete	WG	F.A	15, 20, 30, & 50 (wt.%)	≤5	0.52, 0.57, & 0.67	-	4.5	Decreased by 11%, 22%, 33%, and 44%, respectively, for w/c of 0.57.
[72]	LCDGC	LCD	F.A	20, 40, 60, & 80 (vol.%)	≤4.75	0.38, 0.44, & 0.55	-	3.5	Decreased by 6%, 9%, 10%, and 11%, respectively, for w/c of 0.44.
[126]	Resin concretes	WG	F.A	0–100 (wt.%)	≤2	N.M	Epoxy resin	24.3	Decreased by 1%, for substitution of 100%.

Where: SCGC is self-compacting glass concrete; SCC is self-compacting concrete; UHPC is ultra-high-performance concrete; LCDGC is liquid crystal display glass concrete; LCD is liquid crystal display; CRT is cathode ray tube; WG is waste glass; SP is superplasticizer; HRWRA is a high-range water-reducing agent; WR is water-reducing; AE is air-entraining; SF is silica fume; F.A is fine aggregate; C.A is coarse aggregate; vol. is replacing by volume; wt. is replacing by weight.

5.4. Modulus of Elasticity (MOE)

The modulus of elasticity of concrete (MOE) depends on the normal and lightweight aggregates elasticity modulus, cement matrix, and their relative ratios in the mixes [39]. In general, the incorporation of WG aggregates into concrete increases the modulus of elasticity [72,84]. For instance, Steyn, Babafemi, Fataar and Combrinck [82] substitute fine aggregate in WGC with recovered WG at levels of 15% to 30% by volume. They stated that MOE of concrete increased by 1%, and 7%, incorporating 15% and 30% of WG, respectively. In addition, Omoding, Cunningham and Lane-Serff [115] substitute coarse aggregate in glass aggregate concretes with recycled WG at levels of 12.5% to 100% by volume. They stated that MOE of concrete increased by 2% to 4% for a replacement rate of 12.5% to 50%, then decreased by 3% to 9% for replacement ratios above 50% [137,138].

However, some studies have stated that including WG decreases the MOE of concrete. For instance, Ali and Al-Tersawy [55] substitute fine aggregate in SCC with recovered WG at levels of 10% to 50% by volume. They stated that MOE of concrete decreases by 2%, 8%, 9%, 12%, and 13%, incorporating 10%, 20%, 30%, 40% and 50% of WG, respectively. Figure 3 presents the outcomes of various studies on the MOE of WG concrete.
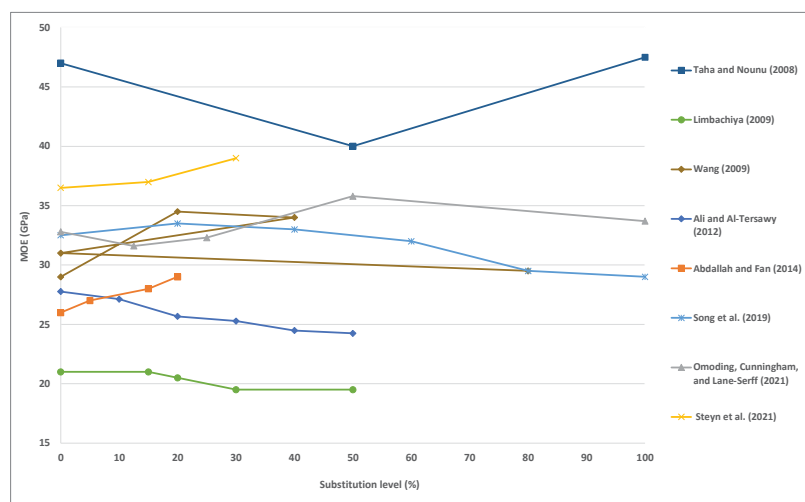
Figure 3. Modulus of elasticity of concrete with various contents of the waste glass. Adapted from references [55,65,72,82,84,88,107,115].

6. Conclusions

The utilization of WG in concrete affects the fresh and mechanical properties of waste-glass concrete, which must be taken into consideration before being used in structures. The overall conclusions of this review are:

1. The workability of waste-glass-containing concrete mixtures for fine or coarse aggregates was less than for natural aggregate-containing mixtures. Nevertheless, despite the poorer workability, some studies found that the mixtures were still workable.
2. Most studies indicated that with the introduction of WG, the density of concrete decreased due to the decreased density and specific gravity of waste glass aggregates.
3. The findings of the literature have been somewhat indecisive regarding the properties of concrete, such as compressive strength, splitting tensile strength, flexural strength, and modulus of elasticity.
4. The findings revealed that the compressive strength, splitting tensile strength, and flexural strength of concrete deteriorated by integrating WG. Nevertheless, the findings concerning the elastic modulus of concrete were conflicting. This decrease was essential because of the sharp edges and smooth surface of the waste glass that caused the poorer bond between cement mortar and waste glass particles at the ITZ.
5. Studies also showed that the optimal aggregate substitution level was about 20%. In addition, the glass color does not have a substantial influence on the strength. Although the results are indecisive, WG has the possibility to be an acceptable substitute for fine or coarse concrete aggregates in concrete.
6. Adding waste glass to the concrete mixture may improve certain mechanical characteristics of concrete, reduce concrete dead load, and provide an ecological substitute for normal aggregates.

7. Recommendations

This paper makes the following broad recommendations for future investigations:

1. More investigation is required into the mechanical characteristics of high-performance and high-strength waste-glass concrete.
2. The effects of different glass kinds and colors on concrete mixes should be thoroughly investigated in the future.
3. Test fewer common types of glass as aggregates in concrete because the vast majority of research only covers soda-lime glass.
4. Conduct a comprehensive evaluation of the real environmental effects through life-cycle assessment to evaluate the feasibility of using this waste.

Conflicts of Interest: The authors declare no conflict of interest.

References

1. Lu, J.-X.; Zhan, B.-J.; Duan, Z.-H.; Poon, C.S. Using glass powder to improve the durability of architectural mortar prepared with glass aggregates. *Mater. Des.* **2017**, *135*, 102–111. [CrossRef]
2. Ahmad, J.; Aslam, F.; Martinez-Garcia, R.; de-Prado-Gil, J.; Qaidi, S.M.A.; Brahmia, A. Effects of waste glass and waste marble on mechanical and durability performance of concrete. *Sci. Rep.* **2021**, *11*, 21525. [CrossRef]
3. Ahmed, H.U.; Mohammed, A.S.; Qaidi, S.M.A.; Faraj, R.H.; Sor, N.H.; Mohammed, A.A. Compressive strength of geopolymer concrete composites: A systematic comprehensive review, analysis and modeling. *Eur. J. Environ. Civ. Eng.* **2022**, 1–46. [CrossRef]
4. ICG. *An Economic Argument for an IYOG 2022*; The International Commission on Glass (ICG): Venice, Italy, 2020.
5. Aslam, F.; Zaid, O.; Althoey, F.; Alyami, S.H.; Qaidi, S.M.A.; de Prado Gil, J.; Martínez-García, R. Evaluating the influence of fly ash and waste glass on the characteristics of coconut fibers reinforced concrete. *Struct. Concr.* **2022**. [CrossRef]
6. Martínez-García, R.; Jagadesh, P.; Zaid, O.; Șerbănoiu, A.A.; Fraile-Fernández, F.J.; de Prado-Gil, J.; Qaidi, S.M.A.; Grădinaru, C.M. The Present State of the Use of Waste Wood Ash as an Eco-Efficient Construction Material: A Review. *Materials* **2022**, *15*, 5349. [CrossRef]
7. EPA. Advancing Sustainable Materials Management: 2018 Tables and Figures. *Environ. Prot. Agency* **2021**, 1–80.
8. Maglad, A.M.; Zaid, O.; Arbili, M.M.; Ascensão, G.; Șerbănoiu, A.A.; Grădinaru, C.M.; García, R.M.; Qaidi, S.M.A.; Althoey, F.; de Prado-Gil, J. A Study on the Properties of Geopolymer Concrete Modified with Nano Graphene Oxide. *Buildings* **2022**, *12*, 1066. [CrossRef]
9. Ahmed, H.U.; Mohammed, A.A.; Rafiq, S.; Mohammed, A.S.; Mosavi, A.; Sor, N.H.; Qaidi, S.M.A. Compressive Strength of Sustainable Geopolymer Concrete Composites: A State-of-the-Art Review. *Sustainability* **2021**, *13*, 13502. [CrossRef]
10. Eurostat. *Packaging Waste Statistics*; Eurostat: Luxemburg, 2020.
11. Ahmad, J.; Majdi, A.; Elhag, A.B.; Deifalla, A.F.; Soomro, M.; Isleem, H.F.; Qaidi, S. A Step towards Sustainable Concrete with Substitution of Plastic Waste in Concrete: Overview on Mechanical, Durability and Microstructure Analysis. *Crystals* **2022**, *12*, 944. [CrossRef]
12. Ahmad, J.; Kontoleon, K.J.; Majdi, A.; Naqash, M.T.; Deifalla, A.F.; Kahla, N.B.; Isleem, H.F.; Qaidi, S.M.A. A Comprehensive Review on the Ground Granulated Blast Furnace Slag (GGBS) in Concrete Production. *Sustainability* **2022**, *14*, 8783. [CrossRef]
13. Rahim, N.L.; Amat, R.C.; Ibrahim, N.M.; Salehuddin, S.; Mohammed, S.A.; Rahim, M.A. Utilization of Recycled Glass Waste as Partial Replacement of Fine Aggregate in Concrete Production. *Mater. Sci. Forum* **2015**, *803*, 16–20. [CrossRef]
14. Topçu, İ.B.; Canbaz, M. Properties of concrete containing waste glass. *Cem. Concr. Res.* **2004**, *34*, 267–274. [CrossRef]
15. Zheng, K. 11-Recycled glass concrete. In *Eco-Efficient Concrete*; Pacheco-Torgal, F., Jalali, S., Labrincha, J., John, V.M., Eds.; Woodhead Publishing: Cambridge, UK, 2013; pp. 241–270.
16. Tayeh, B.A.; Al Saffar, D.M.; Aadi, A.S.; Almeshal, I. Sulphate resistance of cement mortar contains glass powder. *J. King Saud Univ. -Eng. Sci.* **2020**, *32*, 495–500. [CrossRef]
17. Ling, T.-C.; Poon, C.-S.; Wong, H.-W. Management and recycling of waste glass in concrete products: Current situations in Hong Kong. Resources. *Conserv. Recycl.* **2013**, *70*, 25–31. [CrossRef]
18. Contrafatto, L.; Gazzo, S.; Purrazzo, A.; Gagliano, A. Thermo-mechanical Characterization of Insulating Bio-plasters Containing Recycled Volcanic Pyroclasts. *Open Civ. Eng. J.* **2020**, *14*, 66–77. [CrossRef]
19. Meyer, B. Macroeconomic modelling of sustainable development and the links between the economy and the environment. In *Final Report of the MacMod project (ENV. F. 1/ETU/2010/0033) to the European Commission*; Institute of Economic Structures Research: Osnabrück, Germany, 2011.
20. Khan, M.; Cao, M.; Ali, M. Experimental and Empirical Study of Basalt Fibber Reinforced Concrete. In Proceedings of the Building Tomorrow's Society, Fredericton, NB, Canada, 13–16 June 2018. Paper ID–MA39_0610035833.
21. Khan, M.; Lao, J.; Dai, J.-G. Comparative study of advanced computational techniques for estimating the compressive strength of UHPC. *J. Asian Concr. Fed.* **2022**, *8*, 51–68. [CrossRef]
22. Parvez, I.; Shen, J.; Khan, M.; Cheng, C. Modeling and solution techniques used for hydro generation scheduling. *Water* **2019**, *11*, 1392. [CrossRef]
23. Afshinnia, K.; Rangaraju, P.R. Influence of fineness of ground recycled glass on mitigation of alkali–silica reaction in mortars. *Constr. Build. Mater.* **2015**, *81*, 257–267. [CrossRef]
24. Jiang, Y.; Ling, T.-C.; Mo, K.H.; Shi, C. A critical review of waste glass powder–Multiple roles of utilization in cement-based materials and construction products. *J. Environ. Manag.* **2019**, *242*, 440–449. [CrossRef]
25. Qaidi, S.M.A.; Tayeh, B.A.; Ahmed, H.U.; Emad, W. A review of the sustainable utilisation of red mud and fly ash for the production of geopolymer composites. *Constr. Build. Mater.* **2022**, *350*, 128892. [CrossRef]

26. Qaidi, S.M.A.; Atrushi, D.S.; Mohammed, A.S.; Ahmed, H.U.; Faraj, R.H.; Emad, W.; Tayeh, B.A.; Najm, H.M. Ultra-high-performance geopolymer concrete: A review. *Constr. Build. Mater.* **2022**, *346*, 128495. [CrossRef]

27. Schmidt, A.; Saia, W. Alkali-aggregate reaction tests on glass used for exposed aggregate wall panel work. *ACI Mater. J.* **1963**, *60*, 1235–1236.

28. Kozlova, S.; Millrath, K.; Meyer, C.; Shimanovich, S. A suggested screening test for ASR in cement-bound composites containing glass aggregate based on autoclaving. *Cem. Concr. Compos.* **2004**, *26*, 827–835. [CrossRef]

29. Oliveira, R.; de Brito, J.; Veiga, R. Incorporation of fine glass aggregates in renderings. *Constr. Build. Mater.* **2013**, *44*, 329–341. [CrossRef]

30. Khan, M.; Cao, M.; Chu, S.; Ali, M. Properties of hybrid steel-basalt fiber reinforced concrete exposed to different surrounding conditions. *Constr. Build. Mater.* **2022**, *322*, 126340. [CrossRef]

31. Khan, U.A.; Jahanzaib, H.M.; Khan, M.; Ali, M. Improving the tensile energy absorption of high strength natural fiber reinforced concrete with fly-ash for bridge girders. In *Key Engineering Materials*; Trans Tech Publ.: Cham, Switzerland, 2018; pp. 335–342.

32. Arshad, S.; Sharif, M.B.; Irfan-ul-Hassan, M.; Khan, M.; Zhang, J.-L. Efficiency of supplementary cementitious materials and natural fiber on mechanical performance of concrete. *Arab. J. Sci. Eng.* **2020**, *45*, 8577–8589. [CrossRef]

33. Khan, M.; Cao, M.; Xie, C.; Ali, M. Hybrid fiber concrete with different basalt fiber length and content. *Struct. Concr.* **2022**, *23*, 346–364. [CrossRef]

34. Dyer, T.D.; Dhir, R.K. Chemical Reactions of Glass Cullet Used as Cement Component. *J. Mater. Civ. Eng.* **2001**, *13*, 412–417. [CrossRef]

35. Shayan, A.; Xu, A. Value-added utilisation of waste glass in concrete. *Cem. Concr. Res.* **2004**, *34*, 81–89. [CrossRef]

36. Karamberi, A.; Moutsatsou, A. Participation of coloured glass cullet in cementitious materials. *Cem. Concr. Compos.* **2005**, *27*, 319–327. [CrossRef]

37. Sobolev, K.; Türker, P.; Soboleva, S.; Iscioglu, G. Utilization of waste glass in ECO-cement: Strength properties and microstructural observations. *Waste Manag.* **2007**, *27*, 971–976. [CrossRef]

38. Shand, E.B. *Glass Engineering Handbook*; Amazon: Seattle, WA, USA, 1958.

39. Mohajerani, A.; Vajna, J.; Cheung, T.H.H.; Kurmus, H.; Arulrajah, A.; Horpibulsuk, S. Practical recycling applications of crushed waste glass in construction materials: A review. *Constr. Build. Mater.* **2017**, *156*, 443–467. [CrossRef]

40. Park, S.-B.; Lee, B.-C. Studies on expansion properties in mortar containing waste glass and fibers. *Cem. Concr. Res.* **2004**, *34*, 1145–1152. [CrossRef]

41. Lam, C.S.; Poon, C.S.; Chan, D. Enhancing the performance of pre-cast concrete blocks by incorporating waste glass–ASR consideration. *Cem. Concr. Compos.* **2007**, *29*, 616–625. [CrossRef]

42. Lee, G.; Poon, C.S.; Wong, Y.L.; Ling, T.C. Effects of recycled fine glass aggregates on the properties of dry–mixed concrete blocks. *Constr. Build. Mater.* **2013**, *38*, 638–643. [CrossRef]

43. de Castro, S.; de Brito, J. Evaluation of the durability of concrete made with crushed glass aggregates. *J. Clean. Prod.* **2013**, *41*, 7–14. [CrossRef]

44. Serpa, J.d.B.D.; Jorge, P. Concrete Made with Recycled Glass Aggregates: Mechanical Performance. *ACI Mater. J.* **2015**, *112*, 29–38. [CrossRef]

45. Disfani, M.M.; Arulrajah, A.; Bo, M.W.; Hankour, R. Recycled crushed glass in road work applications. *Waste Manag.* **2011**, *31*, 2341–2351. [CrossRef] [PubMed]

46. Ooi, P.S.K.; Li, M.M.W.; Sagario, M.L.Q.; Song, Y. Shear Strength Characteristics of Recycled Glass. *Transp. Res. Rec.* **2008**, *2059*, 52–62. [CrossRef]

47. Ali, M.M.Y.; Arulrajah, A. *Potential Use of Recycled Crushed Concrete-Recycled Crushed Glass Blends in Pavement Subbase Applications*; GeoCongress: Los Angeles, CA, USA, 2012; pp. 3662–3671.

48. Terro, M.J. Properties of concrete made with recycled crushed glass at elevated temperatures. *Build. Environ.* **2006**, *41*, 633–639. [CrossRef]

49. Ling, T.-C.; Poon, C.-S. A comparative study on the feasible use of recycled beverage and CRT funnel glass as fine aggregate in cement mortar. *J. Clean. Prod.* **2012**, *29–30*, 46–52. [CrossRef]

50. Qaidi, S.M.A.; Mohammed, A.S.; Ahmed, H.U.; Faraj, R.H.; Emad, W.; Tayeh, B.A.; Althoey, F.; Zaid, O.; Sor, N.H. Rubberized geopolymer composites: A comprehensive review. *Ceram. Int.* **2022**, *48*, 24234–24259. [CrossRef]

51. He, X.; Yuhua, Z.; Qaidi, S.; Isleem, H.F.; Zaid, O.; Althoey, F.; Ahmad, J. Mine tailings-based geopolymers: A comprehensive review. *Ceram. Int.* **2022**, *48*, 24192–24212. [CrossRef]

52. Faraj, R.H.; Ahmed, H.U.; Rafiq, S.; Sor, N.H.; Ibrahim, D.F.; Qaidi, S.M.A. Performance of Self-Compacting mortars modified with Nanoparticles: A systematic review and modeling. *Clean. Mater.* **2022**, *4*, 100086. [CrossRef]

53. Ling, T.-C.; Poon, C.-S.; Kou, S.-C. Feasibility of using recycled glass in architectural cement mortars. *Cem. Concr. Compos.* **2011**, *33*, 848–854. [CrossRef]

54. Ling, T.-C.; Poon, C.-S. Effects of particle size of treated CRT funnel glass on properties of cement mortar. *Mater. Struct.* **2013**, *46*, 25–34. [CrossRef]

55. Ali, E.E.; Al-Tersawy, S.H. Recycled glass as a partial replacement for fine aggregate in self compacting concrete. *Constr. Build. Mater.* **2012**, *35*, 785–791. [CrossRef]

56. Liu, T.; Wei, H.; Zou, D.; Zhou, A.; Jian, H. Utilization of waste cathode ray tube funnel glass for ultra-high performance concrete. *J. Clean. Prod.* **2020**, *249*, 119333. [CrossRef]
57. Khan, M.; Ali, M. Earthquake-Resistant Brick Masonry Housing for Developing Countries: An Easy Approach. Available online: https://www.nzsee.org.nz/db/2017/P2.43_Ali.pdf (accessed on 30 July 2022).
58. Khan, M.; Cao, M.; Hussain, A.; Chu, S.H. Effect of silica-fume content on performance of CaCO3 whisker and basalt fiber at matrix interface in cement-based composites. *Constr. Build. Mater.* **2021**, *300*, 124046. [CrossRef]
59. Zhang, N.; Yan, C.; Li, L.; Khan, M. Assessment of fiber factor for the fracture toughness of polyethylene fiber reinforced geopolymer. *Constr. Build. Mater.* **2022**, *319*, 126130. [CrossRef]
60. Khan, M.; Rehman, A.; Ali, M. Efficiency of silica-fume content in plain and natural fiber reinforced concrete for concrete road. *Constr. Build. Mater.* **2020**, *244*, 118382. [CrossRef]
61. Rashad, A.M. Recycled waste glass as fine aggregate replacement in cementitious materials based on Portland cement. *Constr. Build. Mater.* **2014**, *72*, 340–357. [CrossRef]
62. Emad, W.; Mohammed, A.S.; Bras, A.; Asteris, P.G.; Kurda, R.; Muhammed, Z.; Hassan, A.M.T.; Qaidi, S.M.A.; Sihag, P. Metamodel techniques to estimate the compressive strength of UHPFRC using various mix proportions and a high range of curing temperatures. *Constr. Build. Mater.* **2022**, *349*, 128737. [CrossRef]
63. Almeshal, I.; Al-Tayeb, M.M.; Qaidi, S.M.A.; Bakar, B.H.A.; Tayeh, B.A. Mechanical properties of eco-friendly cements-based glass powder in aggressive medium. *Mater. Today Proc.* **2022**, *58*, 1582–1587. [CrossRef]
64. Al-Tayeb, M.M.; Aisheh, Y.I.A.; Qaidi, S.M.A.; Tayeh, B.A. Experimental and simulation study on the impact resistance of concrete to replace high amounts of fine aggregate with plastic waste. *Case Stud. Constr. Mater.* **2022**, *17*, e01324. [CrossRef]
65. Taha, B.; Nounu, G. Properties of concrete contains mixed colour waste recycled glass as sand and cement replacement. *Constr. Build. Mater.* **2008**, *22*, 713–720. [CrossRef]
66. Tan, K.H.; Du, H. Use of waste glass as sand in mortar: Part I–Fresh, mechanical and durability properties. *Cem. Concr. Compos.* **2013**, *35*, 109–117. [CrossRef]
67. Yildizel, S.A.; Tayeh, B.A.; Calis, G. Experimental and modelling study of mixture design optimisation of glass fibre-reinforced concrete with combined utilisation of Taguchi and Extreme Vertices Design Techniques. *J. Mater. Res. Technol.* **2020**, *9*, 2093–2106. [CrossRef]
68. Al Saffar, D.M.; Tawfik, T.A.; Tayeh, B.A. Stability of glassy concrete under elevated temperatures. *Eur. J. Environ. Civ. Eng.* **2020**, *26*, 1–12. [CrossRef]
69. Akeed, M.H.; Qaidi, S.; Ahmed, H.U.; Faraj, R.H.; Mohammed, A.S.; Emad, W.; Tayeh, B.A.; Azevedo, A.R.G. Ultra-high-performance fiber-reinforced concrete. Part IV: Durability properties, cost assessment, applications, and challenges. *Case Stud. Constr. Mater.* **2022**, *17*, e01271. [CrossRef]
70. Akeed, M.H.; Qaidi, S.; Ahmed, H.U.; Faraj, R.H.; Mohammed, A.S.; Emad, W.; Tayeh, B.A.; Azevedo, A.R.G. Ultra-high-performance fiber-reinforced concrete. Part I: Developments, principles, raw materials. *Case Stud. Constr. Mater.* **2022**, *17*, e01290. [CrossRef]
71. Akeed, M.H.; Qaidi, S.; Ahmed, H.U.; Faraj, R.H.; Mohammed, A.S.; Emad, W.; Tayeh, B.A.; Azevedo, A.R.G. Ultra-high-performance fiber-reinforced concrete. Part II: Hydration and microstructure. *Case Stud. Constr. Mater.* **2022**, *17*, e01289. [CrossRef]
72. Wang, H.-Y. A study of the effects of LCD glass sand on the properties of concrete. *Waste Manag.* **2009**, *29*, 335–341. [CrossRef]
73. Arabi, N.; Meftah, H.; Amara, H.; Kebaïli, O.; Berredjem, L. Valorization of recycled materials in development of self-compacting concrete: Mixing recycled concrete aggregates–Windshield waste glass aggregates. *Constr. Build. Mater.* **2019**, *209*, 364–376. [CrossRef]
74. Wang, H.-Y.; Huang, W.-L. Durability of self-consolidating concrete using waste LCD glass. *Constr. Build. Mater.* **2010**, *24*, 1008–1013. [CrossRef]
75. Chen, S.-H.; Chang, C.-S.; Wang, H.-Y.; Huang, W.-L. Mixture design of high performance recycled liquid crystal glasses concrete (HPGC). *Constr. Build. Mater.* **2011**, *25*, 3886–3892. [CrossRef]
76. Yu, X.; Tao, Z.; Song, T.-Y.; Pan, Z. Performance of concrete made with steel slag and waste glass. *Constr. Build. Mater.* **2016**, *114*, 737–746. [CrossRef]
77. Patel, H.G.; Dalal, S.P. An Experimental Investigation on Physical and Mechanical Properties of Concrete with the Replacement of Fine Aggregate by Poly Vinyl Chloride and Glass Waste. *Procedia Eng.* **2017**, *173*, 1666–1671. [CrossRef]
78. Bisht, K.; Ramana, P.V. Sustainable production of concrete containing discarded beverage glass as fine aggregate. *Constr. Build. Mater.* **2018**, *177*, 116–124. [CrossRef]
79. Kim, I.S.; Choi, S.Y.; Yang, E.I. Evaluation of durability of concrete substituted heavyweight waste glass as fine aggregate. *Constr. Build. Mater.* **2018**, *184*, 269–277. [CrossRef]
80. Rashid, K.; Hameed, R.; Ahmad, H.A.; Razzaq, A.; Ahmad, M.; Mahmood, A. Analytical framework for value added utilization of glass waste in concrete: Mechanical and environmental performance. *Waste Manag.* **2018**, *79*, 312–323. [CrossRef]
81. Jiao, Y.; Zhang, Y.; Guo, M.; Zhang, L.; Ning, H.; Liu, S. Mechanical and fracture properties of ultra-high-performance concrete (UHPC) containing waste glass sand as partial replacement material. *J. Clean. Prod.* **2020**, *277*, 123501. [CrossRef]
82. Steyn, Z.C.; Babafemi, A.J.; Fataar, H.; Combrinck, R. Concrete containing waste recycled glass, plastic and rubber as sand replacement. *Constr. Build. Mater.* **2021**, *269*, 121242. [CrossRef]

83. Gholampour, A.; Ozbakkaloglu, T.; Gencel, O.; Ngo, T.D. Concretes containing waste-based materials under active confinement. *Constr. Build. Mater.* **2021**, *270*, 121465. [CrossRef]
84. Abdallah, S.; Fan, M. Characteristics of concrete with waste glass as fine aggregate replacement. *Int. J. Eng. Tech. Res.* **2014**, *2*, 11–17.
85. Batayneh, M.; Marie, I.; Asi, I. Use of selected waste materials in concrete mixes. *Waste Manag.* **2007**, *27*, 1870–1876. [CrossRef] [PubMed]
86. Chen, C.H.; Huang, R.; Wu, J.K.; Yang, C.C. Waste E-glass particles used in cementitious mixtures. *Cem. Concr. Res.* **2006**, *36*, 449–456. [CrossRef]
87. Ismail, Z.Z.; Al-Hashmi, E.A. Recycling of waste glass as a partial replacement for fine aggregate in concrete. *Waste Manag.* **2009**, *29*, 655–659. [CrossRef]
88. Limbachiya, M.C. Bulk engineering and durability properties of washed glass sand concrete. *Constr. Build. Mater.* **2009**, *23*, 1078–1083. [CrossRef]
89. Park, S.B.; Lee, B.C.; Kim, J.H. Studies on mechanical properties of concrete containing waste glass aggregate. *Cem. Concr. Res.* **2004**, *34*, 2181–2189. [CrossRef]
90. Wang, H.-Y.; Zeng, H.-h.; Wu, J.-Y. A study on the macro and micro properties of concrete with LCD glass. *Constr. Build. Mater.* **2014**, *50*, 664–670. [CrossRef]
91. Khan, M.N.N.; Sarker, P.K. Effect of waste glass fine aggregate on the strength, durability and high temperature resistance of alkali-activated fly ash and GGBFS blended mortar. *Constr. Build. Mater.* **2020**, *263*, 120177. [CrossRef]
92. Naeini, M.; Mohammadinia, A.; Arulrajah, A.; Horpibulsuk, S. Recycled Glass Blends with Recycled Concrete Aggregates in Sustainable Railway Geotechnics. *Sustainability* **2021**, *13*, 2463. [CrossRef]
93. Taha, B.; Nounu, G. Utilizing Waste Recycled Glass as Sand/Cement Replacement in Concrete. *J. Mater. Civ. Eng.* **2009**, *21*, 709–721. [CrossRef]
94. Tayeh, B.A. Effects of marble, timber, and glass powder as partial replacements for cement. *J. Civ. Eng. Constr.* **2018**, *7*, 63–71. [CrossRef]
95. Borhan, T.M. Properties of glass concrete reinforced with short basalt fibre. *Mater. Des.* **2012**, *42*, 265–271. [CrossRef]
96. Akeed, M.H.; Qaidi, S.; Ahmed, H.U.; Faraj, R.H.; Majeed, S.S.; Mohammed, A.S.; Emad, W.; Tayeh, B.A.; Azevedo, A.R.G. Ultra-high-performance fiber-reinforced concrete. Part V: Mixture design, preparation, mixing, casting, and curing. *Case Stud. Constr. Mater.* **2022**, *17*, e01363. [CrossRef]
97. Akeed, M.H.; Qaidi, S.; Ahmed, H.U.; Emad, W.; Faraj, R.H.; Mohammed, A.S.; Tayeh, B.A.; Azevedo, A.R.G. Ultra-high-performance fiber-reinforced concrete. Part III: Fresh and hardened properties. *Case Stud. Constr. Mater.* **2022**, *17*, e01265. [CrossRef]
98. Aisheh, Y.I.A.; Atrushi, D.S.; Akeed, M.H.; Qaidi, S.; Tayeh, B.A. Influence of polypropylene and steel fibers on the mechanical properties of ultra-high-performance fiber-reinforced geopolymer concrete. *Case Stud. Constr. Mater.* **2022**, *17*, e01234. [CrossRef]
99. Aisheh, Y.I.A.; Atrushi, D.S.; Akeed, M.H.; Qaidi, S.; Tayeh, B.A. Influence of steel fibers and microsilica on the mechanical properties of ultra-high-performance geopolymer concrete (UHP-GPC). *Case Stud. Constr. Mater.* **2022**, *17*, e01245. [CrossRef]
100. Ahmed, S.N.; Sor, N.H.; Ahmed, M.A.; Qaidi, S.M.A. Thermal conductivity and hardened behavior of eco-friendly concrete incorporating waste polypropylene as fine aggregate. *Mater. Today: Proc.* **2022**, *57*, 818–823. [CrossRef]
101. Ahmed, H.U.; Mohammed, A.S.; Faraj, R.H.; Qaidi, S.M.A.; Mohammed, A.A. Compressive strength of geopolymer concrete modified with nano-silica: Experimental and modeling investigations. *Case Stud. Constr. Mater.* **2022**, *16*, e01036. [CrossRef]
102. Qaidi, S. Ultra-High-Performance Fiber-Reinforced Concrete: Fresh Properties. *Preprints* **2022**. [CrossRef]
103. Qaidi, S. Ultra-High-Performance Fiber-Reinforced Concrete: Applications. *Preprints* **2022**. [CrossRef]
104. Qaidi, S. Ultra-high-performance fiber-reinforced concrete (UHPFRC): A mini-review of the challenges. *Sci. Prepr.* **2022**. [CrossRef]
105. Lu, J.-X.; Zhou, Y.; He, P.; Wang, S.; Shen, P.; Poon, C.S. Sustainable reuse of waste glass and incinerated sewage sludge ash in insulating building products: Functional and durability assessment. *J. Clean. Prod.* **2019**, *236*, 117635. [CrossRef]
106. Cota, F.P.; Melo, C.C.D.; Panzera, T.H.; Araújo, A.G.; Borges, P.H.R.; Scarpa, F. Mechanical properties and ASR evaluation of concrete tiles with waste glass aggregate. *Sustain. Cities Soc.* **2015**, *16*, 49–56. [CrossRef]
107. Song, W.; Zou, D.; Liu, T.; Teng, J.; Li, L. Effects of recycled CRT glass fine aggregate size and content on mechanical and damping properties of concrete. *Constr. Build. Mater.* **2019**, *202*, 332–340. [CrossRef]
108. Ling, T.-C.; Poon, C.-S. Properties of architectural mortar prepared with recycled glass with different particle sizes. *Mater. Des.* **2011**, *32*, 2675–2684. [CrossRef]
109. Ali, M.H.; Dinkha, Y.Z.; Haido, J.H. Mechanical properties and spalling at elevated temperature of high-performance concrete made with reactive and waste inert powders. *Eng. Sci. Technol. Int. J.* **2017**, *20*, 536–541. [CrossRef]
110. Polley, C.; Cramer, S.M.; de la Cruz, R.V. Potential for Using Waste Glass in Portland Cement Concrete. *J. Mater. Civ. Eng.* **1998**, *10*, 210–219. [CrossRef]
111. Khan, M.; Ali, M. Improvement in concrete behavior with fly ash, silica-fume and coconut fibres. *Constr. Build. Mater.* **2019**, *203*, 174–187. [CrossRef]
112. Khan, M.; Ali, M. Optimization of concrete stiffeners for confined brick masonry structures. *J. Build. Eng.* **2020**, *32*, 101689. [CrossRef]

113. Cao, M.; Khan, M. Effectiveness of multiscale hybrid fiber reinforced cementitious composites under single degree of freedom hydraulic shaking table. *Struct. Concr.* **2021**, *22*, 535–549. [CrossRef]

114. Xie, C.; Cao, M.; Guan, J.; Liu, Z.; Khan, M. Improvement of boundary effect model in multi-scale hybrid fibers reinforced cementitious composite and prediction of its structural failure behavior. *Compos. Part B Eng.* **2021**, *224*, 109219. [CrossRef]

115. Omoding, N.; Cunningham, L.S.; Lane-Serff, G.F. Effect of using recycled waste glass coarse aggregates on the hydrodynamic abrasion resistance of concrete. *Constr. Build. Mater.* **2021**, *268*, 121177. [CrossRef]

116. Najm, H.M.; Ahmad, S. The Use of Waste Ceramic Optimal Concrete for A Cleaner and Sustainable Environment - A Case Study of Mechanical Properties. *Civ. Environ. Eng. Rep.* **2022**, *32*, 85–102.

117. Qaidi, S. *Behaviour of Concrete Made of Recycled Waste PET and Confined with CFRP Fabrics*; University of Duhok: Duhok, Iraq, 2021.

118. Qaidi, S.M.A. *Ultra-High-Performance Fiber-Reinforced Concrete: Fresh Properties*; University of Duhok: Duhok, Iraq, 2022.

119. Shao, Y.; Lefort, T.; Moras, S.; Rodriguez, D. Studies on concrete containing ground waste glass. *Cem. Concr. Res.* **2000**, *30*, 91–100. [CrossRef]

120. Qaidi, S.M.A. *Ultra-High-Performance Fiber-Reinforced Concrete: Hydration and Microstructure*; University of Duhok: Duhok, Iraq, 2022.

121. Qaidi, S.M.A. *PET-Concrete*; University of Duhok: Duhok, Iraq, 2021.

122. Degirmencia, N.; Yilmazb, A.; Cakirc, O.A. Utilization of waste glass as sand replacement in cement mortar. *Indian J. Eng. Mater. Sci.* **2011**, *18*, 303–308.

123. Walczak, P.; Małolepszy, J.; Reben, M.; Szymański, P.; Rzepa, K. Utilization of Waste Glass in Autoclaved Aerated Concrete. *Procedia Eng.* **2015**, *122*, 302–309. [CrossRef]

124. Lu, J.-X.; Yan, X.; He, P.; Poon, C.S. Sustainable design of pervious concrete using waste glass and recycled concrete aggregate. *J. Clean. Prod.* **2019**, *234*, 1102–1112. [CrossRef]

125. Shen, P.; Zheng, H.; Liu, S.; Lu, J.-X.; Poon, C.S. Development of high-strength pervious concrete incorporated with high percentages of waste glass. *Cem. Concr. Compos.* **2020**, *114*, 103790. [CrossRef]

126. Dębska, B.; Lichołai, L.; Silva, G.J.B. Effects of waste glass as aggregate on the properties of resin composites. *Constr. Build. Mater.* **2020**, *258*, 119632. [CrossRef]

127. Yang, S.; Ling, T.-C.; Cui, H.; Poon, C.S. Influence of particle size of glass aggregates on the high temperature properties of dry-mix concrete blocks. *Constr. Build. Mater.* **2019**, *209*, 522–531. [CrossRef]

128. Olofinnade, O.M.; Ede, A.N.; Ndambuki, J.M.; Ngene, B.U.; Akinwumi, I.I.; Ofuyatan, O. Strength and microstructure of eco-concrete produced using waste glass as partial and complete replacement for sand. *Cogent Eng.* **2018**, *5*, 1483860. [CrossRef]

129. Qaidi, S.M.A. *PET-Concrete Confinement with CFRP*; University of Duhok: Duhok, Iraq, 2021.

130. Qaidi, S.M.A. *Ultra-High-Performance Fiber-Reinforced Concrete: Principles and Raw Materials*; University of Duhok: Duhok, Iraq, 2022.

131. Qaidi, S.M.A. *Ultra-High-Performance Fiber-Reinforced Concrete: Applications*; University of Duhok: Duhok, Iraq, 2022.

132. Qaidi, S.M.A. *Ultra-High-Performance Fiber-Reinforced Concrete: Challenges*; University of Duhok: Duhok, Iraq, 2022.

133. Malik, M.I.; Bashir, M.; Ahmad, S.; Tariq, T.; Chowdhary, U. Study of concrete involving use of waste glass as partial replacement of fine aggregates. *IOSR J. Eng.* **2013**, *3*, 8–13. [CrossRef]

134. Qaidi, S.M.A. *Ultra-High-Performance Fiber-Reinforced Concrete: Cost Assessment*; University of Duhok: Duhok, Iraq, 2022.

135. Qaidi, S.M.A. *Ultra-High-Performance Fiber-Reinforced Concrete: Durability Properties*; University of Duhok: Duhok, Iraq, 2022.

136. Qaidi, S.M.A. *Ultra-High-Performance Fiber-Reinforced Concrete: Mixture Design*; University of Duhok: Duhok, Iraq, 2022.

137. Qaidi, S.M.A. *Ultra-High-Performance Fiber-Reinforced Concrete: Hardened Properties*; University of Duhok (UoD): Duhok, Iraq, 2022.

138. Mansi, A.; Sor, N.H.; Hilal, N.; Qaidi, S.M. The impact of nano clay on normal and high-performance concrete characteristics: A review. In *IOP Conference Series: Earth and Environmental Science*; IOP Publishing: Bristol, UK, 2022; p. 012085.

Analysis of the Possibility of Plastic Deformation Characterisation in X2CrNi18-9 Steel Using Measurements of Electromagnetic Parameters

Maciej Roskosz [1,*], Krzysztof Fryczowski [2], Lechosław Tuz [3], Jianbo Wu [4], Krzysztof Schabowicz [5] and Dominik Logoń [5]

[1] Faculty of Mechanical Engineering and Robotics, AGH University of Science and Technology, al. Mickiewicza 30, 30-059 Kraków, Poland

[2] Department of Power Engineering and Turbomachinery, Faculty of Energy and Environmental Engineering, Silesian University of Technology, Akademicka 2A, 44-100 Gliwice, Poland; kfryczowski@polsl.pl

[3] Faculty of Metals Engineering and Industrial Computer Science, AGH University of Science and Technology, al. Mickiewicza 30, 30-059 Kraków, Poland; ltuz@agh.edu.pl

[4] Department of Engineering Science and Mechanics, Sichuan University, Chengdu 610065, China; wujianbo@scu.edu.cn

[5] Faculty of Civil Engineering, Wrocław University of Science and Technology, Wybrzeże Wyspiańskiego 27, 50-370 Wrocław, Poland; krzysztof.schabowicz@pwr.edu.pl (K.S.); dominik.logon@pwr.edu.pl (D.L.)

* Correspondence: mroskosz@agh.edu.pl

Abstract: An analysis was conducted on the possibility of making an assessment of the degree of plastic deformation ε in X2CrNi18-9 steel by measuring three electromagnetic diagnostic signals: the Barkhausen noise features, the impedance components in in-series LCR circuits, and the residual magnetic field components. The impact of ε on a series of different extracted features of diagnostic signals was investigated. The occurrence of two regions of sensitivity was found for all the features of the analysed signals. The two regions were separated by the following critical deformation value: $\varepsilon \sim 10\%$ for the components of the residual magnetic field and $\varepsilon \sim 15\%$ for the normalised components of impedance. As for the Barkhausen noise signal, the values were as follows: $\varepsilon \sim 20\%$ for the mean value, $\varepsilon \sim 20\%$ for the peak value of the signal envelope, and $\varepsilon \sim 5\%$ for the total number of the signal events. Metallographic tests were performed, which revealed essential changes in the microstructure of the tested material for the established critical values. The martensite transformation occurring during the plastic deformation process of X2CrNi18-9 austenitic steel process generated a magnetic phase. This magnetic phase was strong enough to relate the strain state to the values of diagnostic signals. The changes in the material electromagnetic properties due to martensitic transformation ($\gamma \rightarrow \alpha'$) began much earlier than indicated by the metallographic testing results.

Keywords: residual magnetic field; Barkhausen noise; LCR circuits; plastic deformation; austenitic steel

1. Introduction

Research is now being conducted in many scientific centres on methods that will enable the determination of the effect of cold plastic strain [1–4], mechanical fatigue [5–7], heat treatment [8], and creep [9] on the state and electromagnetic properties of austenitic steels. The applied diagnostic signals are the quantities describing the magnetic hysteresis loop, the eddy currents, the Barkhausen noise parameters, and the changes in the anisotropy of electromagnetic properties. The variations in these parameters result from the state of the microstructure, the grain size, and the impact of the dislocation density on the material electromagnetic properties.

Austenitic steels are widely used materials, and the strain-induced martensite transformation occurring in them, depending on the chemical composition, the magnitude of the rolling reduction, and the deformation temperature can have both favourable effects

causing the material strengthening (a higher yield point or an increase in tensile strength) and unfavourable consequences causing a decrease in corrosion resistance and the appearance of the ferromagnetic phase [10–15]. Under the influence of cold plastic strain, a change occurs in the dislocation structure. As a result, metastable austenite undergoes a partial transformation into martensite ε and ferromagnetic martensite α' with a body-centred cubic lattice [12,13].

Novotný et al. [1] introduced a novel application of magneto-optical films. At the magnetic field sensitivity of 100 A/m, coercivity can be mapped with a resolution as high as 50 μm. Promising results were obtained for austenitic steel by applying the magneto-optical method to indicate critically degraded (plastically deformed) locations.

O'Sullivan et al. [2] characterised work hardening of an austenitic stainless steel grade (SS404) using non-destructive magnetic measurement techniques, including measurements of the magnetic Barkhausen noise, the ferromagnetic phase, and coercivity. It was found that the material work-hardening was caused by the dislocation density rather than by the α'-martensite phase. The coercivity measurement proved to be a useful non-destructive quantitative method for characterizing work hardening in relation to the degree of plastic deformation.

In [3], the authors investigated selected phase transformations of the AISI 304 austenitic steel. The Barkhausen noise, coercivity, and ferrite content were measured to identify changes in the strain-induced α'-martensite phase due to cold rolling and elongation. The research proved that it was possible to study the mechanism of austenite transformation into the α' phase, and the reverse transformation of the α' phase into austenite.

In [4], the authors presented experimental studies on the amount of transformed martensite by measuring the continuous change in impedance during plastic deformation on specimens made of the 304 steel grade. The specimens were cores of a prototype solenoidal coil, which was subjected to compressive load.

In [5], the authors investigated specimens of the chromium-nickel steel used to make the generator retaining rings and the generator rotor shrouding. The specimens were subjected to fatigue and static loads. The austenite instability became apparent after plastic deformation (increase in the material permeability by about 0.1 μ_r). Magnetic measurements based on austenite instability detection in mechanical and thermal correlations are an alternative to ultrasonic wave attenuation tests. Moreover, they give a more complete picture of the wear degree of the retaining ring (material degradation evaluation).

Vincent et al. [6] investigated the low-cycle fatigue (LCF) of steel 304L and the influence of the strain-induced α'-martensite on the magnetic Barkhausen noise (BN). It was shown that the variations of the martensite content induced by LCF could be related to and characterised by the BN. The number of cycles had an effect on the α'-martensite phase, and the α' peak was clearly visible in the BN signal envelope.

In [7], AISI 31 austenitic stainless steel samples were subjected to fatigue testing. The effect of fatigue on the accumulation of damage and changes in the content of the α'-martensite was investigated. The obtained results showed the possibility of assessing the fatigue state of the AISI 31 steel using acoustic nonlinearity measurements and magnetic coercivity.

In [8], the authors investigated the relationship between the eddy current output signal and the surface hardness of a martensitic AISI 410 stainless steel sample in terms of impedance and inductance. They also examined the effects of different quenching temperatures on the steel surface hardness.

Augustyniak et al. [9] tested samples of 347, 321, and 304 austenitic steels taken from service-aged power plant boiler tubing. The accumulation of damage due to the creep process was proportional to the concentration of the created magnetic oxide layer. Simultaneously, a magnetic ferrite phase also formed in the grains and at grain boundaries under the scale layer. The content of the ferrite-phase layer was proportional to the initial creep-related damage. These changes were related to the eddy current signal.

This paper is focused on the analysis of the possibility of characterizing the plastic—strain ratio in specimens made of X2CrNi18-9 steel by measuring the residual magnetic field, the impedance components in in-series LCR circuits, and the Barkhausen noise. The same measurement quantities were used to characterise the active stress state in [16]. Additionally, metallographic tests were performed to observe the structural changes occurring due to deformation during static tensile testing.

2. Theoretical Basics

The authors of this paper have often used magnetic methods of non-destructive testing to solve various problems related to the broadly understood characterisation of the material state. For this reason, the theoretical foundations have already been presented many times. A synthetic description of the theoretical basis related to this article is included in [16], where an analysis was conducted of the possibility of assessing active stresses in steel elements by measuring electromagnetic diagnostic signals. Many articles were referred to in [17–35], where information can be found on the theoretical basis of the applied electromagnetic methods.

In chromium-nickel alloy steels, e.g., X5CrNi18-10, X2CrNi18-9, or X18CrNiSi18-9, depending on the concentration of Cr and Ni and other alloying elements (e.g., Mo, Mn, N, Si), an austenitic structure occurs in the supersaturated state at room temperature. The austenitic structure gets stabilised with an increase in Ni and other austenitic elements. In addition, the structure may also contain some ferromagnetic ferrite δ arising due to the conditions of steel crystallization. Depending on the amount of alloying elements, the ferrite content may increase up to several percent. To evaluate the structure and compactness of the magnetic phase, equivalents of austenite- and ferrite-forming elements can be used. This indicates that the chemical composition of steel itself has a direct impact on the content of the magnetic phase, which can be changed, usually increased, by heat treatment, strain due to cold or hot working, or by welding processes.

Austenitic Fe-Cr-Ni steels in the post-supersaturation state retain the austenitic structure (γ-phase) with a face-centred cubic (fcc) lattice. Depending on the chemical composition, austenite can be a metastable phase undergoing martensite transformation at cooling below temperature M_s, or due to critical plastic deformation at temperatures higher than M_s. Due to the chemical composition, temperature M_s is lower than room temperature, which ensures high durability of austenite. Austenitic steels are commonly used materials, and the strain-induced martensite transformation occurring in them can have both favourable effects strengthening the material and unfavourable consequences resulting in a decrease in their corrosion resistance and the appearance of the ferromagnetic phase [10–13].

Due to cold plastic strain, austenitic chromium-nickel steels undergo significant strengthening depending on their chemical composition, the magnitude of the rolling reduction, and the deformation temperature. Under the influence of cold plastic strain, a change occurs in the dislocation structure. As a result, metastable austenite undergoes a partial transformation into martensite ε and ferromagnetic martensite α′ with a body-centred cubic lattice [12,13]. A similar transformation for austenitic steels occurs during quenching at low temperatures. It is believed that there are two possible mechanisms corresponding to such transformations [36,37]: one is the γ → ε → α′ transformation, where the ε phase is an intermediate phase with a closely packed hexagonal structure; in the other, a direct γ → α′ transformation is possible. Independently, the γ → ε transformation may also occur.

The factor deciding about the possibility of martensite ε formation is the austenite stacking fault energy (SFE), which depends on the steel chemical composition and the deformation temperature. Martensite ε can be created during cold plastic deformation if the SFE at room temperature is <30 MJm^{-2} [38]. The SFE parameter determines the type of the deformation (slip) system, which enables the formation of the intermediate ε phase or leads to the direct formation of the α′ phase. In steels with a higher SFE value, where the basic system of {111} austenite deformation occurs [39], the formation of the ε phase was

not observed. However, it has been shown that, depending on the deformation conditions, in the same steel the transformation can occur directly or with the participation of the intermediate phase. The element, which strongly inhibits the $\gamma \rightarrow \varepsilon$ transformation, is nickel. In this case, the austenite-to-martensite transformation occurs directly $\gamma \rightarrow \alpha'$ [36], which means that, under small deformation below the critical deformation value, the changes occur only in the region of single grains, while above the critical point they will affect the whole cross-section.

3. Experimental Details

The testing was performed for flat specimens made of X2CrNi18-9 steel (chemical composition—cf. Table 1), whose initial geometry is shown in Figure 1. Figure 2 shows the relationship for the tested steel between the set value of engineering stress in the loading process and the plastic deformation value measured after the unloading of the specimens (between the 60th and the 140th measuring point). The specimens were subjected to static tensile loads to obtain appropriate plastic deformation.

Table 1. Chemical composition of X2CrNi18-9 steel (% by mass).

C	Si	Mn	P	S	N	Cr	Mo	Nb	Ni	Ti
0.02	0.45	1.43	0.031	0.008	-	18	0.3	0.017	7.94	0.01
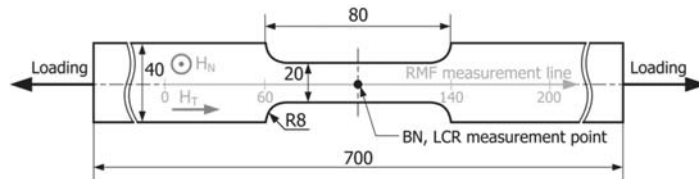
Figure 1. Tested specimen geometry with marked measuring points (RMF—residual magnetic field, H_N—normal component of the RMF, H_T—tangential component of the RMF, LCR—impedance components of the LCR measuring circuit, BN—Barkhausen noise).
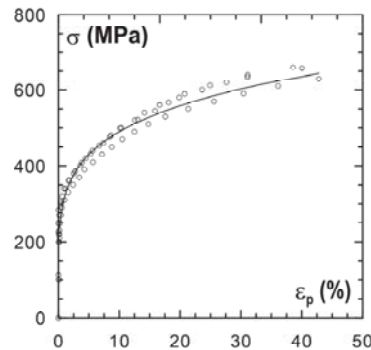
Figure 2. Relationship between engineering stress σ and plastic deformation ε_P.

The specimens were loaded using the Galdabini Sun 10P tensile strength testing machine (Galdabini, Cardano al Campo, Italy). The test conditions were as follows: temperature: $21 \pm 2\,°C$ and the traverse speed: 2 mm/min. After the set value of deformation was achieved, the specimens were unloaded and examined beyond the machine on the test stand, keeping the same orientation of the specimen in relation to the Earth's magnetic field. Relative deformation was defined for an 80 mm long section of the specimen (between the 60th and 140th measuring point—cf. Figure 1). The initial distance between the points

was 1 mm, but it increased with the rise in plastic deformation. The test was carried out for as-received samples with an elongation between 0% to 55% (no fracture). All the specimens, both in the as-received state and after plastic deformation, were tested using the MPD-100A magnetic field detector (R&J Measurement, Borowa, Poland). The results of the measurements of the magnetic phase are presented in Table 2. Of all the deformed specimens, fifty were selected for the testing of magnetic parameters, and the order of the measurements was as follows: residual magnetic field (RMF) components, LCR circuit impedance components, the Barkhausen noise. Metallographic testing was carried out only for selected specimens with 10%, 20%, and 40% elongation.

Table 2. Magnetic phase content.

Strain ε (%)	No. of Samples	Magnetic Phase Content—Min (%)	Magnetic Phase Content—Max (%)
as-received state	90	0.1	0.2
0–8	31	0.1	0.3
8–15	16	1.1	1.8
15–25	12	2.2	3.9
25–35	14	6.0	9.8
35–45	13	11.6	23.9
45–55	4	25.9	29.3

The TSC-1M-4 magnetometer (Energodiagnostika Co. Ltd., Moscow, Russia) was used for RMF measurements. For RMF, two components (H_N—normal component, H_T—tangential component measured in the direction parallel to the applied load) were measured using the TSC-2M (Energodiagnostika Co. Ltd., Moscow, Russia) measuring head. The measuring apparatus was calibrated in the magnetic field of the Earth, with the assumed value of 40 A/m. The measurements on the test stand were always carried out in the same place and with the same position of the specimen. The magnetic field components in the location where the measurements were performed had the following values: $H_T = 8$ A/m, $H_N = 40$ A/m. The magnetic field strength was measured along the measurement line (cf. Figure 1) in 200 points.

The system measuring the LCR components is schematically shown in Figure 3. It consists of a CEM DT-9935 automatic LCR bridge and a Fastron 09P-152J-50 choke coil (winding inductance 1.5 mH ± 5%, ferrite core with a diameter of 8.5 mm at the point of contact with the tested surface, resistance 1 Ω, test line resistance: 26.7 Ω).
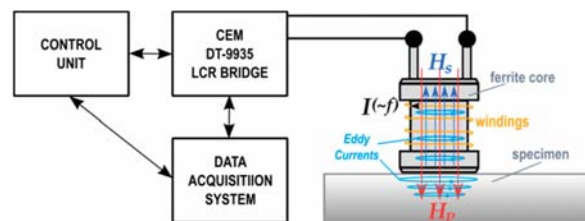
Figure 3. Measuring circuit diagram.

Due to the magnetic coupling and the self-induction phenomenon, the characteristic values of the measuring coil change when it is applied to the specimen surface. The flow of electric current I with frequency f results in an alternating magnetic field H_p. At the same time, eddy currents I_{EC} are induced in the tested material, generating the H_s field. The electromagnetic properties of the material affect the obtained values. The degree of plastic deformation causes a change in permittivity ε, relative magnetic permeability μ_r, and conductivity γ. The changes in these quantities influence the resistance and the inductance value of the measuring coil coupled to the surface.

The Barkhausen noise was measured using the MEB4-C system (Mag-Lab, Gdańsk, Poland). The system diagram is shown in Figure 4. It enables measurements with the use of a surface measurement sub-system (upper part of Figure 4) and a circumferential measurement sub-system (lower part of Figure 4). The former was used during the testing. The measuring head contains a magnetic field excitation system and the Barkhausen noise signal detection system. The system configuration was as follows: sampling frequency—800 kHz, magnetizing current frequency—2.04 Hz, magnetizing current amplitude—200 mA, pre-amplifier gain PR1—× 1, main amplifier gain MA1—35 dB.
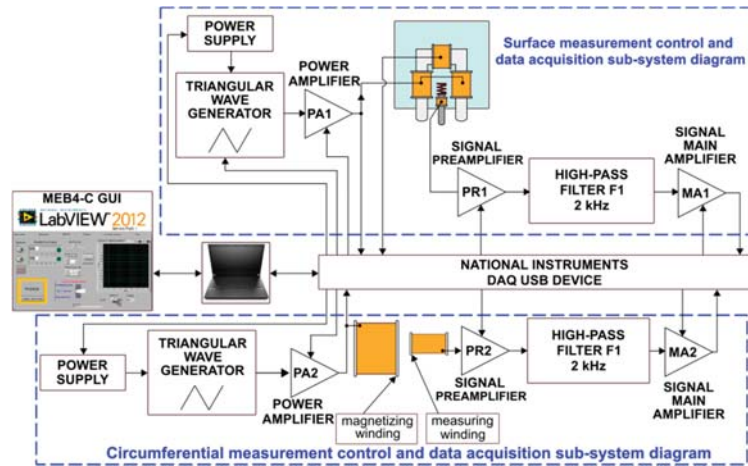
Figure 4. Schematic diagram of the MEB4-C system.

The Barkhausen noise was measured only in two directions: perpendicular ($\perp$) and parallel ($\parallel$) to the load. The choice of such directions of measurements results from the authors' own research related to changes in hardness due to cold working [17] and from the literature on the influence of plastic deformation on the Barkhausen noise [40,41].

The absolute values of the Barkhausen noise parameters are calculated using the following Equation (1):

$$V = \sqrt{V_\perp^2 + V_\parallel^2} \tag{1}$$

where: $V_\perp$ and $V_\parallel$, respectively, are the parameter values for the two directions of the magnetizing field application.

The metallographic examination was conducted to verify the changes in the material indicated in the NDT test. To avoid the influence of the directionality of the ferrite bands, the tested material was sampled transversely to the rolling direction. The deformed part was sectioned using a precise cut-off machine (Struers, Willich, Germany), and intensive cooling was applied.

The metallographic observations were conducted using light microscopy (Leica LM/DM microscope—Leica, Wetzlar, Germany) and scanning electron microscopy (Phenom XL—Thermo Fisher Scientific, Waltham, MA, USA). The specimens were pre-ground using water abrasive paper and then polished and etched electrolytically (time: 10–15 s, current: 20 mA, voltage: 35 V) to avoid the influence of the effect of abrasive papers on the surface of the specimen. A cross-sectional microscopic examination was carried out after polishing and electrolytic etching in a 10% CrO_3 water solution. Due to the applied preparation method, local etch defects, so-called etch pits, were observed on the surface of the metallographic specimens. XRD was performed in a D8 Advance Diffractometer (Bruker, Billerica, MA, USA) using $Cu_{K\alpha}$ radiation; the magnetic phase (the content of the

strain-induced martensite α'-phase) was measured using the MPD-100A magnetic field detector (R&J Measurement, Borowa, Poland).

Hardness measurements were performed using the Vickers method with an intender load of 10 kG (98.07 N), with a Zwick/Roell ZHU 187.5 hardness tester (Zwick Roell Group, Ulm, Germany).

The tested steel was characterised by an austenitic structure, with a small content of ferrite δ arranged in the steel rolling direction. The structure showed only a few twin boundaries (annealing twins)—Figure 5. The testing of the steel magnetic phase content in the as-received state showed a value below 0.2%.
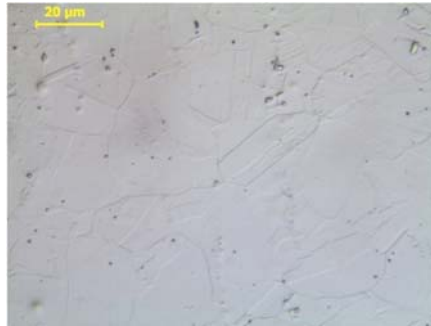
Figure 5. Austenitic structure of X2CrNi18-9 steel in the as-received state.

4. Analysis Results and Discussion

4.1. Residual Magnetic Field

Figure 6a,b shows the example distributions of the RMF components for the initial state (I.S.) and selected values of plastic strain. The plastically deformed region of the specimen with a smaller cross-section, lying between the 60th and the 140th measuring point, stands out in the distributions of both RMF components under analysis. As the plastic deformation degree got higher, the values of tangential component H_T increased, while the curves of normal component H_N in the plastically deformed region made an anticlockwise rotation. In the place of transition from the deformed to the non-deformed region, local extrema occurred of both tangential component H_T (Figure 6a) and normal component H_N (Figure 6b). They definitely took different values and had a different trend of changes compared to the rest of the sample. Due to the high variability of the values of the RMF components in the plastically deformed area, the further analysis of the measurement results aiming to develop a diagnostic relation was focused on the analysis of the gradients of the RMF components. The gradients of the changes in the RMF components (understood as absolute values of function derivatives) were determined by segmental approximation of the measurement results using third-degree spline functions. Example distributions of gradients, corresponding to the distributions of the RMF components, presented in Figure 6a,b, are shown in Figure 7a,b. The gradient distributions were dominated by two maxima in the zones of transition from the deformed to the non-deformed region.

An analysis was performed on the impact of the plastic deformation degree on the maximum values of gradients of the RMF components occurring in the transition zones and on the mean values of gradients of the RMF components determined for an area with a constant cross-section on the segment between the 90th and the 110th point on the specimen measurement line (cf. Figure 1).
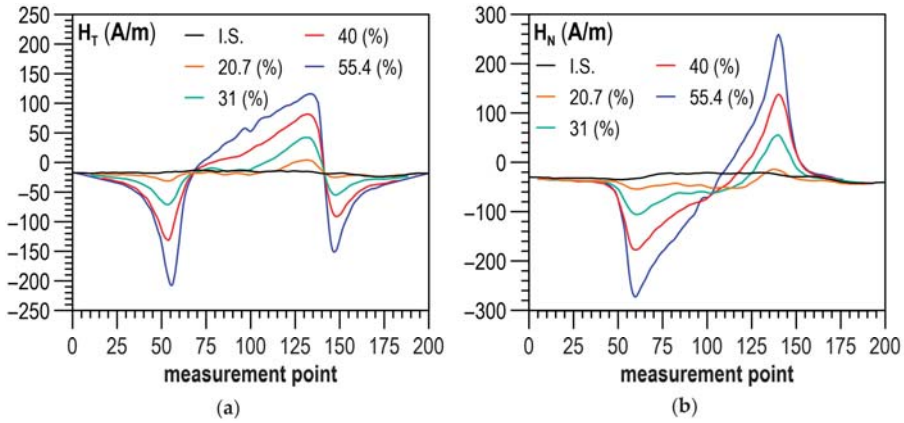
Figure 6. Distribution of the RMF components for different plastic deformation states: (**a**) tangential component H_T; (**b**) normal component H_N.
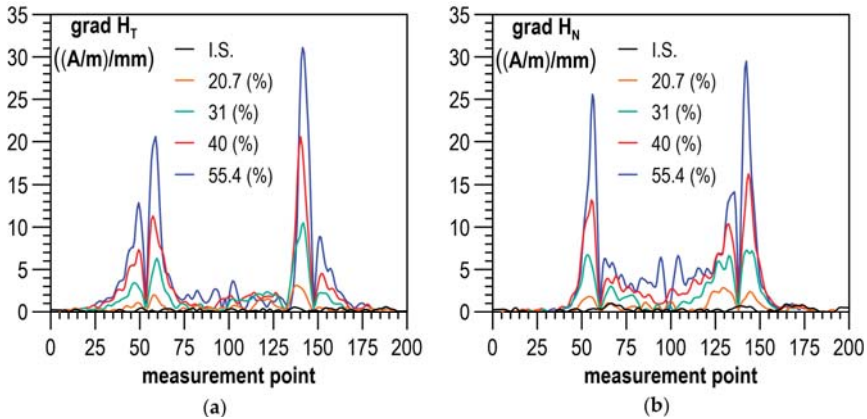
Figure 7. Distribution of the gradient of the RMF components for different plastic deformation states: (**a**) gradient of tangential component grad H_T; (**b**) gradient of normal component grad H_N.

The relations determined for the X2CrNi18-9 steel specimens between the plastic deformation degree and the maximum gradients of the RMF components are shown in Figure 8a,b, whereas Figure 9a,b illustrates the relations between the plastic deformation degree and the mean gradients of the RMF components. As the deformation degree got higher, both maximum and mean values of the gradients of the RMF components increased. Unfortunately, for the tested X2CrNi18-9 steel, it could be seen that relatively unequivocal relations between the degree of plastic deformation and the values of the RMF gradients occurred only after the plastic deformation degree exceeded 10%. For lower plastic deformation values, the gradients of the RMF components did not change noticeably.
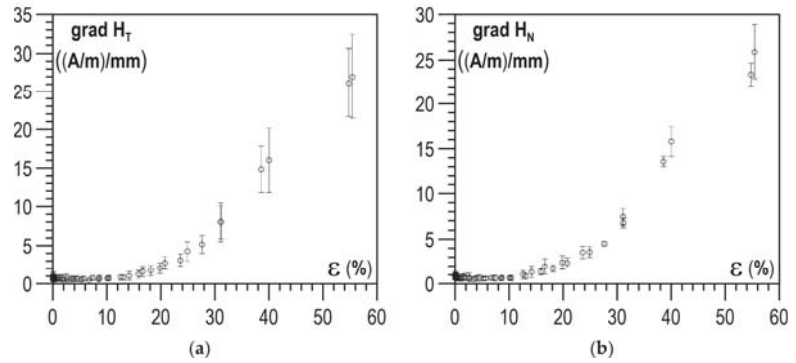
Figure 8. Relation between the maximum gradient value and the plastic deformation degree: (**a**) max gradient of tangential component grad H_T; (**b**) max gradient of normal component grad H_N.
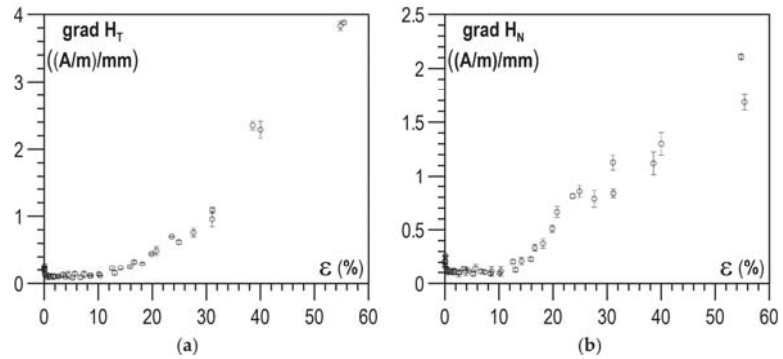
Figure 9. Relation between the mean gradient value and the plastic deformation degree: (**a**) mean gradient of tangential component grad H_T; (**b**) mean gradient of normal component grad H_N.

4.2. Components of Impedance of the In-Series LCR Circuit

For each plastic strain, value curves of normalised impedance components were developed. The curves in Figure 10a illustrate the normalised impedance components and, Figure 10b–f presents the distributions of normalised impedance components.

In Figure 10a–f, it can be seen that the effect of the plastic deformation degree on normalised components of impedance $(R - R_0)/\omega L_0$, $\omega L/\omega L_0$ becomes unequivocally visible only when plastic deformation reaches the level of about 15% and higher. For frequencies in the range from 0.1 kHz to 10 kHz, an increase in the plastic deformation degree was accompanied by a rise in the value of $\omega L/\omega L_0$, while for the frequency of 100 kHz, $\omega L/\omega L_0$ first increased until the plastic deformation degree reached the level of about 15% to show a decreasing trend later on. A constant trend in changes in the $(R - R_0)/\omega L_0$ component occurred only at frequencies f equal to 1 kHz and 10 kHz for plastic deformation degrees higher than 15%.
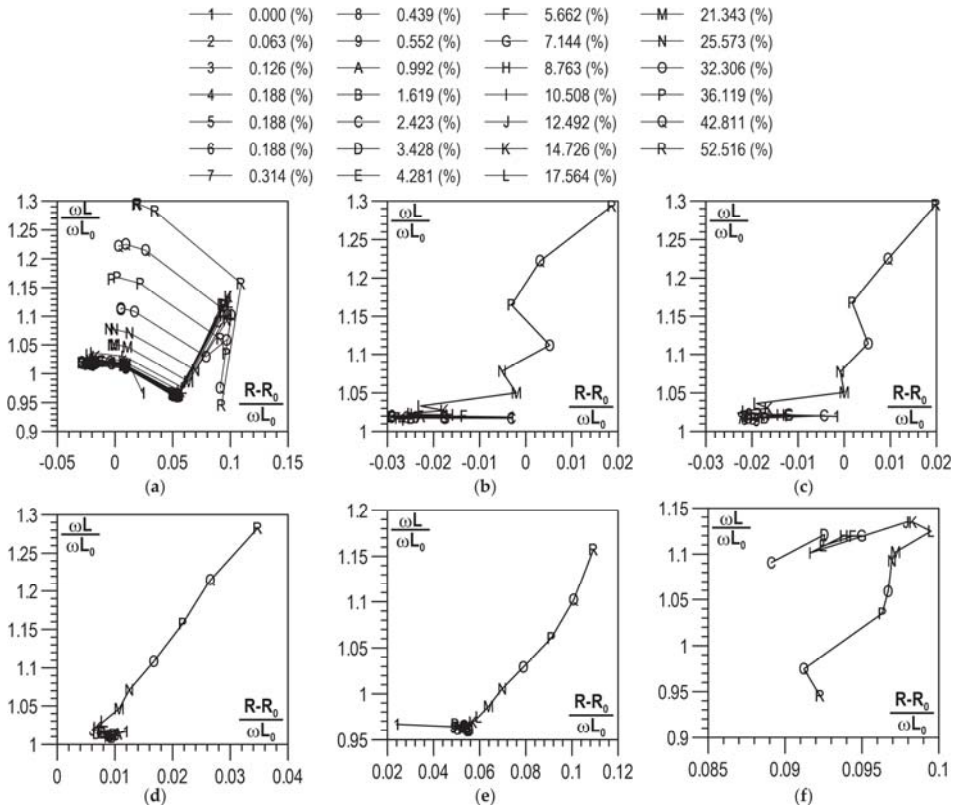
Figure 10. Results obtained from the analysis of the LCR measurements: (**a**) curves of normalised impedance components for different states of plastic deformation; distribution of normalised impedance components for: (**b**) f = 0.1 kHz; (**c**) f = 0.12 kHz; (**d**) f = 1 kHz; (**e**) f = 10 kHz; (**f**) f = 100 kHz.

4.3. Barkhausen Effect

An analysis was performed of the possibilities of developing a correlation between the plastic deformation degree and the Barkhausen noise signal. The Barkhausen noise was measured for 10 magnetisation cycles. Two halves could be distinguished in a single magnetisation cycle (cf. Figure 11)—the first marked as I$\searrow$ (exciting current diminishes) and the second marked as I$\nearrow$ (exciting current rises).
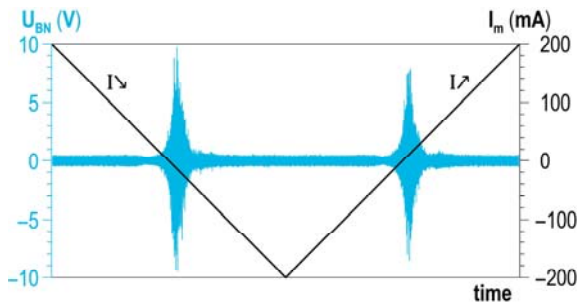
Figure 11. Detailed description of a single cycle of changes in magnetisation.

The following BN quantitative parameters were analysed: the RMS voltage value U_{RMS}, the envelope of the BN signal (peak value), and the distribution of the total number of events NoE_{TOT}. The formula for RMS voltage U_{RMS} was described in [16], and the distribution of the total number of events NoE_{TOT} was characterised in [16,17].

The BN envelope was obtained through the smoothing averaging operation on the absolute values of the U_{BNi} voltage pulses. A multiple smoothing filtering operation using the Savitzky–Golay filter was used for this purpose. The envelope was characterised by local extrema, which could be described using their coordinates defining the magnetisation current $PEAK_{POS}$ and the Barkhausen noise voltage $PEAK_{VAL}$, which are graphically presented in Figure 12.
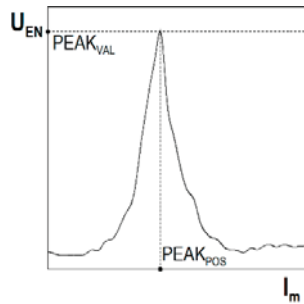
Figure 12. Characteristic quantities of the envelope.

The effect of the plastic deformation degree on the RMS value of voltage (U_{RMS}) is shown in Figure 13a–c. Distinct changes could be observed in the U_{RMS} values from plastic deformation ε of about 20%, both for the parallel and the perpendicular direction (Figure 13a,b, respectively). However, for the latter, the U_{RMS} values were significantly lower compared to the parallel direction. The dependence of voltage U_{RMS} on ε for the module (Figure 13c) resembled both qualitatively and quantitatively the relation for the parallel direction (Figure 13a)—the values were substantially higher for the parallel direction and had a decisive impact on the value of the module.
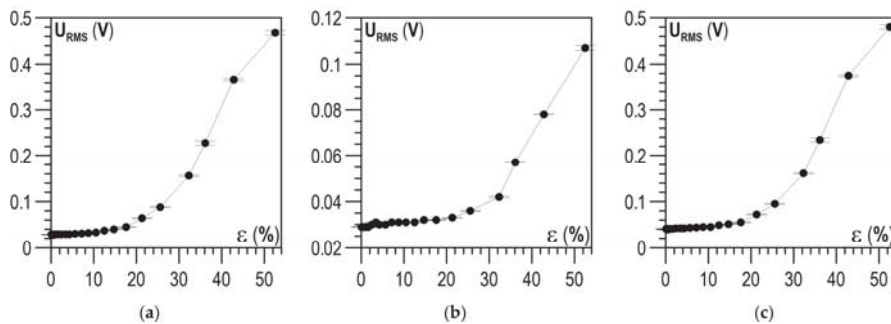
Figure 13. Relation between plastic deformation ε and U_{RMS}: (**a**) parallel direction; (**b**) perpendicular direction; (**c**) module of directions.

An analysis was conducted on the impact of plastic deformation ε on the values of the total number of events NoE_{TOT} for the entire range of discrimination voltage U_g between -10 V and 10 V. It was found that when approaching the value of 0 V on the side of negative voltage, a rise in plastic deformation caused a drop in the number of events. Close to 0 V on the side of positive voltage values, the opposite trend could be observed—as the degree of plastic deformation got higher, the number of events increased. This phenomenon occurred

for both the parallel and the perpendicular direction of magnetisation (cf. Figure 14a,b, respectively). The influence of the magnetisation direction (the magnetic field direction in relation to the direction of the tensile force) was slight.
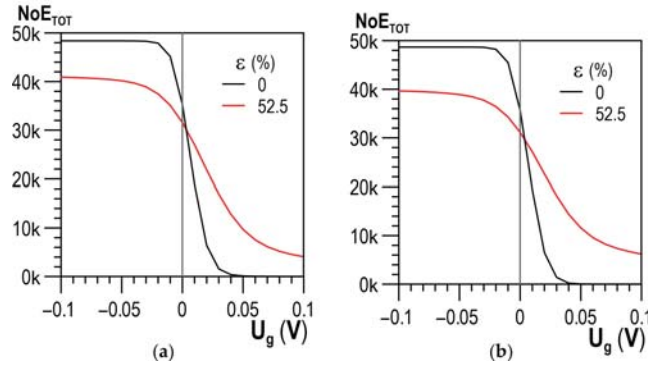
Figure 14. Distribution of the total number of events NoE_{TOT} depending on the threshold voltage for two strain states: (**a**) parallel direction; (**b**) perpendicular direction.

Figure 15a–c present the dependence of the total number of events (NoE_{TOT}) on ε for close-to-zero positive and negative values of voltage U_g. It could be assumed that above $\varepsilon \sim 5\%$, two NoE_{TOT} values corresponded to a given deformation state, identifying this state unequivocally. This made it possible to develop a solution to an inverse problem—the evaluation of the plastic deformation degree based on the number of total events NoE_{TOT}.
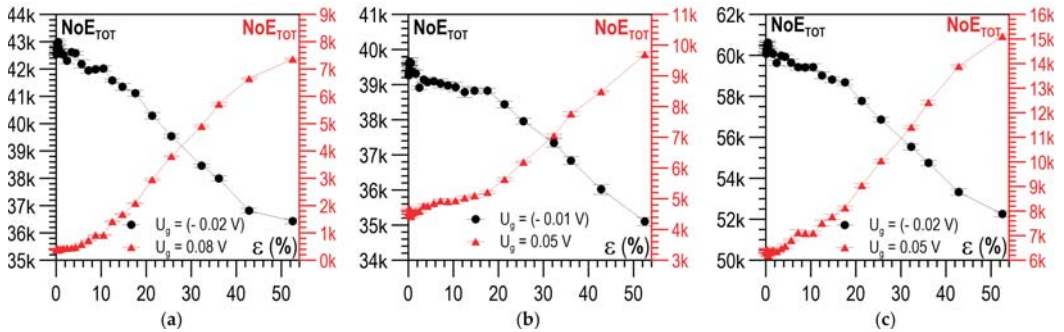
Figure 15. Relation between plastic deformation ε and mean NoE_{TOT} values for different values of threshold voltage U_g: (**a**) parallel direction; (**b**) perpendicular direction; (**c**) module of directions.

The analysis then covered the next parameter of the Barkhausen noise: $PEAK_{VAL}$, the values of which were analysed for the descending and ascending halves of the magnetisation. The relations between ε and $PEAK_{VAL}$ for the descending halves of the magnetisation are shown in Figure 16a–c, whereas Figure 17a–c shows the relations for the ascending halves of the magnetisation. For the parallel direction of both halves of the magnetisation (Figure 16a or Figure 17a) and up to about $\varepsilon = 5\%$, no clear changes in $PEAK_{VAL}$ values were observed; in the range of ε from 5 to 20%, these changes were slight, after $\varepsilon = 20\%$ a significant increase in $PEAK_{VAL}$ values was observed. For the perpendicular direction, clear changes could be seen when the plastic deformation degree exceeded $\varepsilon \sim 30\%$ (Figure 16b or Figure 17b). Like in the case of U_{RMS}, the $PEAK_{VAL}$ module (Figure 16c or Figure 17c) qualitatively and quantitatively resembled the relation for the parallel direction (Figure 16a or Figure 17a).
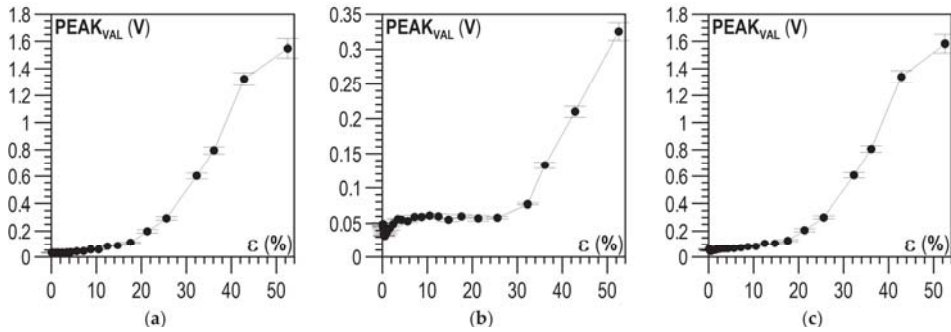
Figure 16. Relation between plastic deformation ε and mean PEAK$_{VAL}$ for descending halves of magnetisation I$\searrow$: (**a**) parallel direction; (**b**) perpendicular direction; (**c**) module of directions.
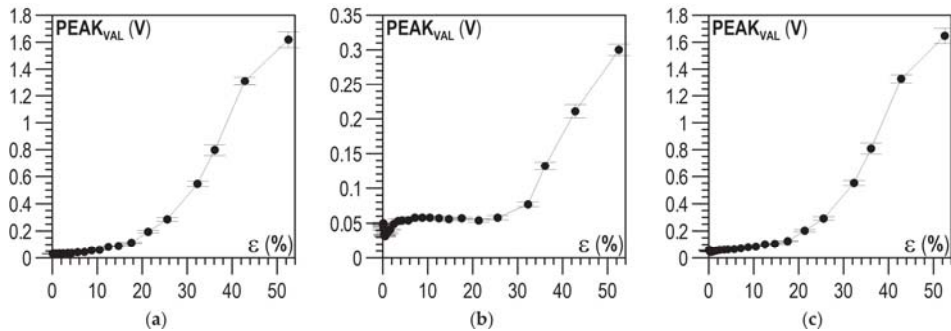
Figure 17. Relation between plastic deformation ε and mean PEAK$_{VAL}$ for ascending halves of magnetisation I$\nearrow$: (**a**) parallel direction; (**b**) perpendicular direction; (**c**) module of directions.

4.4. Metallographic Testing

Metallographic tests were carried out to reveal structural changes occurring during the plastic deformation of steel. The three figures below show the structures observed at different degrees of deformation of 10%, 20%, and 40% (Figures 18–20, respectively). The observations carried out using light and scanning electron microscopy revealed that the number of structural defects rose with an increase in the deformation degree. The initial structure was austenitic with a small number of twin boundaries (annealing twins)—Figure 5.
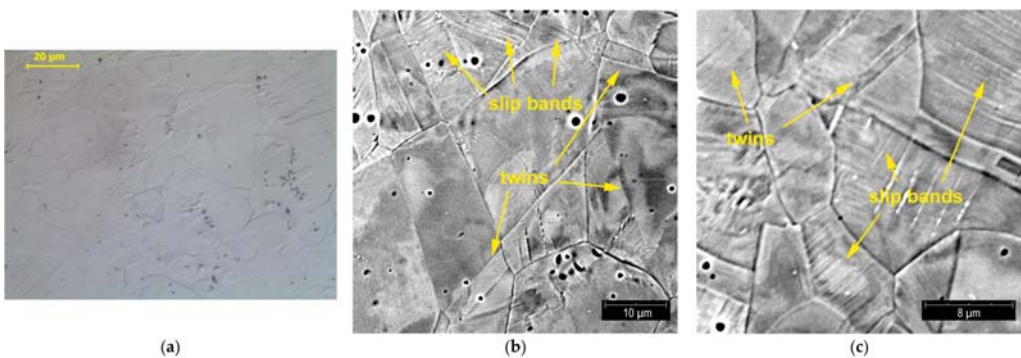
Figure 18. Structure of X2CrNi18-9 steel after 10% plastic deformation; LM (**a**) and SEM (**b**,**c**) observations.
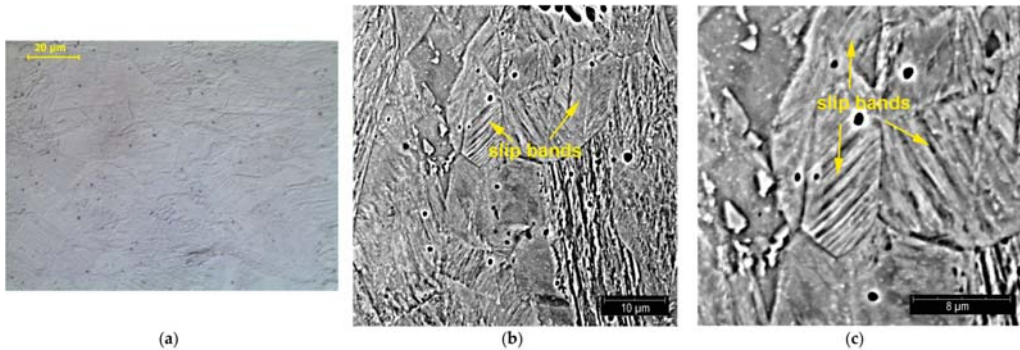
Figure 19. Structure of X2CrNi18-9 steel after 20% plastic deformation; LM (**a**) and SEM (**b**,**c**) observations.
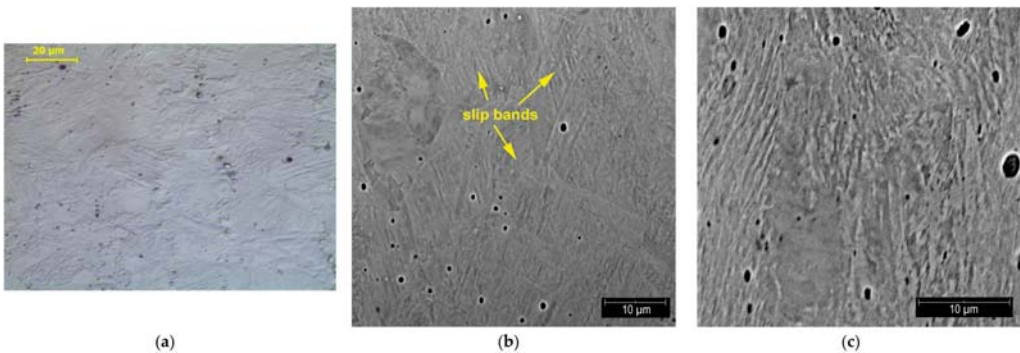
Figure 20. Structure of X2CrNi18-9 steel after 40% plastic deformation; LM (**a**) and SEM (**b**,**c**) observations.

A small deformation caused the appearance of slip bands, the density of which increased with a rise in the deformation degree. The formation of the observed slip bands is related to a system within one grain, and the observed effect is the formation of parallel slip faults. The performed observations revealed that, even at 10% deformation of steel, slip bands were arranged in different directions, which indicated that deformation took place in different slip systems—Figure 18.

The highest density of slip bands was obtained at the deformation degree of 40%—Figure 20. A higher degree of deformation was also accompanied by deformation of the grain: i.e., its elongation in the direction of the tensile force.

The higher number of defects in the structure caused an increase in the steel hardness, from 280 HV10 for the material in the as-received state to almost 400 HV10 at the 40% deformation degree. On the other hand, no significant increase was observed in the magnetic phase determined using a magnetic field detector, where a value of $0.2 \pm 0.1\%$ was recorded for the state at delivery conditions (measurements on specimens after mechanical treatment); after 10% deformation, the magnetic phase increased only up to $1.4 \pm 0.1\%$. An increase in deformation to 20% caused a rise in the magnetic phase content to about $3.0 \pm 0.1\%$, and after 40% deformation to about $14.8 \pm 0.1\%$. The observed increase should be considered to be a value included within the measurement error. The presence of α', as the effect of deformation, is visible in the XRD analysis. The diffraction lines for the material in the delivery condition (DC) revealed only the γ-phase. Changes could be observed in the diffraction diagrams for the steel post-deformation state in comparison to the DC. An increase in the specimen deformation decreased the intensity of austenite lines, and new martensite lines appeared, whose intensity increased with deformation (Figure 21).
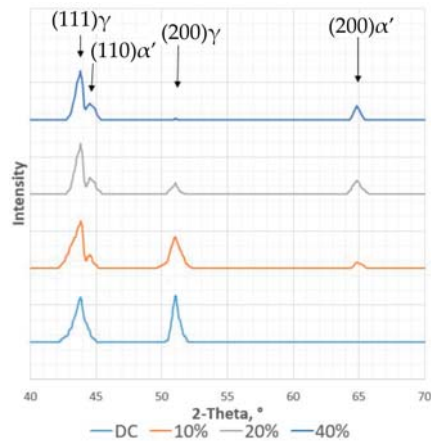
Figure 21. X-ray diffraction patterns of X2CrNi18-9 steel in the initial state (DC) and after selected degrees of deformation (10%, 20%, 40%).

5. Summary and Conclusions

The considered issue of the evaluation of plastic deformation based on changes in electromagnetic quantities is one of the so-called inverse problems of non-destructive testing.

Three case studies were presented, in which the following diagnostic signals were used: the residual magnetic field components, the impedance components of the in-series LCR circuit, and the Barkhausen noise features. The changes in microstructure and the resulting changes in electromagnetic properties generated diagnostic signals with an averaged and repeatable value that could be captured using relatively wide-range measuring transducers [42].

Two ranges of strain variability could be distinguished for the extracted features of the diagnostic signals. The ranges differed significantly in the changes in the signal value due to an increment in deformation. Up to the critical plastic deformation degree, the features of diagnostic signals did not show significant changes in value. They could then be related to the content of ferrite δ (chemical composition of steel). However, in the case of deformation higher than critical, where the martensite transformation began, it was possible to use them to evaluate the state of the material. The critical deformation degree determined, based on the performed analyses of diagnostic signals, was as follows: for the RMF $\varepsilon \sim 10\%$, the LCR $\varepsilon \sim 15\%$, and for the U_{RMS}, $PEAK_{VAL}$, and NoE_{TOT} parameters it was $\varepsilon \sim 20\%$, $\varepsilon \sim 20\%$, and $\varepsilon \sim 5\%$, respectively. The differences in the critical deformation value were due to the specificity of the signal individual features. At the same time, they indicated that the changes in the material physical properties (electromagnetic properties, e.g., NoE_{TOT} $\varepsilon \sim 5\%$) began much earlier compared to what was suggested by the results of magnetic phase measurements (cf. Table 2). Based on the obtained results, it should be concluded that, depending on the degree of material deformation, different signals should be used for the assessment of the material state.

The NDT results were verified by metallographic examination. In the tested X2CrNi18-9 steel, the ferromagnetic phase—ferrite δ—was present in small amounts already in the non-deformed state. As the deformation increased, and then after a certain critical strain was exceeded, a clear increment in the total share of ferromagnetic phases occurred due to the occurrence of martensite transformation and the formation of martensite α′, as revealed by the XRD and hardness testing.

While typical testing methods showed that the content of the magnetic phase was relatively small even at high deformation (40%), the assessment based on the discussed diagnostic signals made it possible to reveal those changes even for the deformation

degree as low as 10–15%. Structural changes (LM and SEM) related to the presence of slip bands were observed already at the deformation degree of 10%, with their density causing significant scattering of diagnostic signals. It was only when the strain exceeded the critical deformation degree of 10% that the martensite transformation ($\gamma \rightarrow \alpha'$) occurred and, thereby, a significant amount of the magnetic phase appeared. In 10% deformation, the content of the magnetic phase increased from 0.2% to 1.4%. This value rose up to 14.8% for 40% deformation. The wide range of results provided by the magnetic field detector led to the conclusion that the content of the magnetic phase strongly depends on the strain rate and the material condition (i.e., chemical composition, heat treatment, residual stress), which indicates that varying conditions of the operating environment can result in different content of the magnetic phase and cause differences in the received diagnostic signals. The presence of the phase, related to the occurrence of the phase transformation, involved the occurrence of signals strong enough to be interpreted and used in diagnostic works aiming to evaluate the state of steel.

The changes in the ferromagnetic phase during plastic deformation of austenitic steels created an opportunity to assess the state of austenitic steel using electromagnetic non-destructive testing methods. The obtained results were unique to the analysed cases. Depending on the properties of the measuring apparatus and its calibration, the initial state of the material, and many other influencing factors [16], the obtained values may differ from those revealed by the tests. The testing results indicated that a further increase in the level of measurement sensitivity in relation to individual diagnostic signals for deformation above the critical deformation degree is of no significance. For deformation lower than critical, further testing and analyses are necessary.

References

1. Novotný, P.; Macháč, P.; Sajdl, P. Diagnostics of Austenitic Steels by Coercivity Mapping. *NDT E Int.* **2008**, *41*, 530–533. [CrossRef]
2. O'Sullivan, D.; Cotterell, M.; Meszaros, I. The Characterisation of Work-Hardened Austenitic Stainless Steel by NDT Micro-Magnetic Techniques. *NDT E Int.* **2004**, *37*, 265–269. [CrossRef]
3. Mészáros, I.; Prohászka, J. Magnetic Investigation of the Effect of A'-Martensite on the Properties of Austenitic Stainless Steel. *J. Mater. Process. Technol.* **2005**, *161*, 162–168. [CrossRef]
4. Inoshita, D.; Yamanaka, S.; Iwamoto, T. An Experimental Evaluation on Change in Impedance of TRIP Steel Subjected to Plastic Deformation at Various Strain Rates. *Key Eng. Mater.* **2013**, *535–536*, 445–448. [CrossRef]
5. Żurek, Z.H.; Sieradzki, S.; Adamek, J. Assessment of Technical Condition of Generator Rotors End Winding Retaining Rings Based on Magnetic Measurements of Instability of G18H18 Steel Austenite. *Weld. Technol. Rev.* **2011**, *83*, 8–12. [CrossRef]
6. Vincent, A.; Pasco, L.; Morin, M.; Kleber, X.; Delnondedieu, M. Magnetic Barkhausen Noise from Strain-Induced Martensite during Low Cycle Fatigue of 304L Austenitic Stainless Steel. *Acta Mater.* **2005**, *53*, 4579–4591. [CrossRef]
7. Kim, C. Nondestructive Evaluation of Strain-Induced Phase Transformation and Damage Accumulation in Austenitic Stainless Steel Subjected to Cyclic Loading. *Metals* **2017**, *8*, 14. [CrossRef]
8. Zhang, H.; Wei, Z.; Xie, F.; Sun, B. Assessment of the Properties of AISI 410 Martensitic Stainless Steel by an Eddy Current Method. *Materials* **2019**, *12*, 1290. [CrossRef]
9. Augustyniak, B.; Chmielewski, M.; Sablik, M.J.; Augustyniak, M.; Walker, S. A New Eddy Current Method for Nondestructive Testing of Creep Damage in Austenitic Boiler Tubing. *Nondestruct. Test. Eval.* **2009**, *24*, 121–141. [CrossRef]
10. Takahashi, S.; Echigoya, J.; Ueda, T.; Li, X.; Hatafuku, H. Martensitic Transformation Due to Plastic Deformation and Magnetic Properties in SUS 304 Stainless Steel. *J. Mater. Process. Technol.* **2001**, *108*, 213–216. [CrossRef]

11. Nagy, E.; Mertinger, V.; Tranta, F.; Sólyom, J. Deformation Induced Martensitic Transformation in Stainless Steels. *Mater. Sci. Eng. A* **2004**, *378*, 308–313. [CrossRef]
12. Shin, H.C.; Ha, T.K.; Chang, Y.W. Kinetics of Deformation Induced Martensitic Transformation in a 304 Stainless Steel. *Scr. Mater.* **2001**, *45*, 823–829. [CrossRef]
13. Milad, M.; Zreiba, N.; Elhalouani, F.; Baradai, C. The Effect of Cold Work on Structure and Properties of AISI 304 Stainless Steel. *J. Mater. Process. Technol.* **2008**, *203*, 80–85. [CrossRef]
14. Wang, Z.; Xu, J.; Yan, Y.; Li, J. The Influence of Microstructure on the Mechanical Properties and Fracture Behavior of Medium Mn Steels at Different Strain Rates. *Materials* **2019**, *12*, 4228. [CrossRef] [PubMed]
15. Kozłowska, A.; Grzegorczyk, B.; Morawiec, M.; Grajcar, A. Explanation of the PLC Effect in Advanced High-Strength Medium-Mn Steels. A Review. *Materials* **2019**, *12*, 4175. [CrossRef]
16. Roskosz, M.; Fryczowski, K. Magnetic Methods of Characterization of Active Stresses in Steel Elements. *J. Magn. Magn. Mater.* **2020**, *499*, 166272. [CrossRef]
17. Roskosz, M.; Fryczowski, K.; Schabowicz, K. Evaluation of Ferromagnetic Steel Hardness Based on an Analysis of the Barkhausen Noise Number of Events. *Materials* **2020**, *13*, 2059. [CrossRef]
18. Morrish, A.H. *The Physical Principles of Magnetism*; John Wiley and Sons: New York, NY, USA, 1965.
19. Augustyniak, B. *Magnetoelastic Phenomena and Their Use in Non-Destructive Testing of Materials*; Wydawnictwo Politechniki Gdańskiej: Gdańsk, Poland, 2003; ISBN 8373480420.
20. Jiles, D.C. Theory of the Magnetomechanical Effect. *J. Phys. D Appl. Phys.* **1995**, *28*, 1537–1546. [CrossRef]
21. Kaminski, D.A.; Jiles, D.C.; Biner, S.B.; Sablik, M.J. Angular Dependence of the Magnetic Properties of Polycrystalline Iron under the Action of Uniaxial Stress. *J. Magn. Magn. Mater.* **1992**, *104–107*, 382–384. [CrossRef]
22. Biełow, K.P. *Phenomena in Magnetic Materials*; PWN: Warszawa, Poland, 1962.
23. Augustyniak, B.; Degauque, J. Magneto-Mechanical Properties Evolution of Fe–C Alloy during Precipitation Process. *Mater. Sci. Eng. A* **2004**, *370*, 376–380. [CrossRef]
24. Bozorth, R.M. *Ferromagnetism*; Wiley-IEEE Press: Hoboken, NJ, USA, 1993; ISBN 978-0780310322.
25. Makar, J.M.; Tanner, B.K. The in Situ Measurement of the Effect of Plastic Deformation on the Magnetic Properties of Steel. *J. Magn. Magn. Mater.* **1998**, *187*, 353–365. [CrossRef]
26. Thompson, S.M.; Tanner, B.K. The Magnetic Properties of Plastically Deformed Steels. *J. Magn. Magn. Mater.* **1990**, *83*, 221–222. [CrossRef]
27. Jiles, D.C.; Atherton, D.L. Theory of Ferromagnetic Hysteresis. *J. Magn. Magn. Mater.* **1986**, *61*, 48–60. [CrossRef]
28. Dutta, S.M.; Ghorbel, F.H.; Stanley, R.K. Dipole Modeling of Magnetic Flux Leakage. *IEEE Trans. Magn.* **2009**, *45*, 1959–1965. [CrossRef]
29. Junker, W.R.; Clark, W.G. Eddy Current Characterization of Applied and Residual Stresses. In *Review of Progress in Quantitative Nondestructive Evaluation*; Springer: Boston, MA, USA, 1983; pp. 1269–1286.
30. Liu, J.-G.; Becker, W.-J. Force and Stress Measurements with Eddy Current Sensors. In Proceedings of the 10. International Sensor fairs and Conference, Nuremberg, Germany, 8–10 May 2001; pp. 23–28.
31. Fryczowski, K.; Roskosz, M.; Żurek, Z.H. Preliminary Studies on Impact of Tensile Loads on the Parameters of the RLC Circuit. *Weld. Technol. Rev.* **2015**, *87*, 45–49. [CrossRef]
32. Barkhausen, H. Zwei Mit Hilfe Der Neuen Verstärker Entdeckte Erscheinungen. *Phys. Z* **1919**, *20*, 401–403.
33. Wolter, B.; Gabi, Y.; Conrad, C. Nondestructive Testing with 3MA—An Overview of Principles and Applications. *Appl. Sci.* **2019**, *9*, 1068. [CrossRef]
34. Maciusowicz, M.; Psuj, G. Use of Time-Frequency Representation of Magnetic Barkhausen Noise for Evaluation of Easy Magnetization Axis of Grain-Oriented Steel. *Materials* **2020**, *13*, 3390. [CrossRef]
35. Ding, S.; Tian, G.Y.; Dobmann, G.; Wang, P. Analysis of Domain Wall Dynamics Based on Skewness of Magnetic Barkhausen Noise for Applied Stress Determination. *J. Magn. Magn. Mater.* **2017**, *421*, 225–229. [CrossRef]
36. Mangonon, P.L.; Thomas, G. The Martensite Phases in 304 Stainless Steel. *Metall. Trans.* **1970**, *1*, 1577–1586. [CrossRef]
37. Kiahosseini, S.R.; Javad, S.; Baygi, M.; Khalaj, G.; Khoshakhlagh, A.; Samadipour, R. A Study on Structural, Corrosion, and Sensitization Behavior of Ultrafine and Coarse Grain 316 Stainless Steel Processed by Multiaxial Forging and Heat Treatment. *J. Mater. Eng. Perform.* **2018**, *27*, 271–281. [CrossRef]
38. Sato, K.; Ichinose, M.; Hirotsu, Y.; Inoue, Y. Effects of Deformation Induced Phase Transformation and Twinning on the Mechanical Properties of Austenitic Fe–Mn–Al Alloys. *ISIJ Int.* **1989**, *29*, 868–877. [CrossRef]
39. Babiński, W.; Griner, S. Testing of Austenitic Chromium-Nickel Steel Wires for Woven Screens. *Inst. Mater. Effic.* **1980**, *1/2*, 25.
40. Haušild, P.; Kolařík, K.; Karlík, M. Characterization of Strain-Induced Martensitic Transformation in A301 Stainless Steel by Barkhausen Noise Measurement. *Mater. Des.* **2013**, *44*, 548–554. [CrossRef]
41. Stefanita, C.-G.; Atherton, D.; Clapham, L. Plastic versus Elastic Deformation Effects on Magnetic Barkhausen Noise in Steel. *Acta Mater.* **2000**, *48*, 3545–3551. [CrossRef]
42. Zeng, K.; Tian, G.; Liu, J.; Gao, B.; Qiu, F. Repeatability and Stability Study of Residual Magnetic Field for Domain Wall Characterization. *J. Magn. Magn. Mater.* **2019**, *485*, 391–400. [CrossRef]

Article

Development of Impact-Echo Multitransducer Device for Automated Concrete Homogeneity Assessment

Bartłomiej Sawicki [1,2], Tomasz Piotrowski [1,*] and Andrzej Garbacz [1]

[1]   Department of Building Materials Engineering, Faculty of Civil Engineering, Warsaw University of Technology, Al. Armii Ludowej 16, 00-637 Warsaw, Poland; bartek.sawicki@epfl.ch (B.S.); a.garbacz@il.pw.edu.pl (A.G.)

[2]   Laboratory for Maintenance and Safety of Structures, Civil Engineering Institute, Swiss Federal Institute of Technology Lausanne (EPFL), EPFL ENAC IIC MCS Station 18, CH-1015 Lausanne, Switzerland

*   Correspondence: t.piotrowski@il.pw.edu.pl; Tel.: +48-22-234-64-80

Abstract: A combination of multiple nondestructive testing (NDT) methods speeds up the assessment of concrete and increases the precision. This is why the UIR-Scanner was developed at Warsaw University of Technology. The scanner uses an Impact-Echo (IE) method with a unique arrangement of multiple transducers. This paper presents the development of the IE module using numerical models validated with experimental testing. It was found that rectangular arrangement of four transducers with the impactor in the middle is optimal for quick scanning of area for faults and discontinuities, changing the method from punctual to volumetric. A numerical study of void detectability depending on its position with respect to the IE module is discussed as well. After confirmation of the findings of models using experimental tests, the module was implemented into the scanner.

Keywords: concrete; NDT; finite element method; experiment; automated inspection; frequency domain; validation

1. Introduction

Nondestructive techniques (NDT) for examination of structures without their degradation are within the essential field of engineering art development [1–3]. Each of them has its own characteristics in terms of accuracy, rapidity and kind of faults they can detect. This is why a combination of multiple techniques is of interest. Usage of different NDTs brings the problem of results' correlation and necessity of execution of multiple measurements. Nevertheless, it speeds up the assessment and this is why merging multiple techniques into one device is currently an emerging trend [1,2,4].

According to this philosophy, a scanner for nondestructive testing of concrete slabs was developed at Warsaw University of Technology [5]. The UIR-Scanner merges complementary NDT methods: **U**ltrasonic pulse velocity (UPV), **I**mpact-echo (IE) and ground penetrating **R**adar (GPR) to deliver reliable results in an automated and user-friendly manner.

This paper presents the conceptual development of an Impact-Echo module for the scanner. Its task is to detect anomalies in the tested region, which may indicate presence of a fault. Once areas with the anomalies are marked, they can be tested in more detailed ways to obtain the precise location of fault. The detectability criterion should be quantitative allowing automated analysis by software.

2. Impact-Echo Method

The Impact-Echo (IE) method is a nondestructive technique invented at the turn of '70 s and '80 s for the testing of solid concrete and multilayer [6–9] elements. This method is based on application of impact of a steel ball at the surface of the structure to evoke an elastic stress wave, which later reflects and is recorded with a piezoelectric transducer. The

received signal in time domain is changed to frequency domain by Fast Fourier Transform (FFT) and then it is analyzed and interpreted to obtain the thickness of the element and, possibly, the depth of reinforcement and flaws (Figure 1).
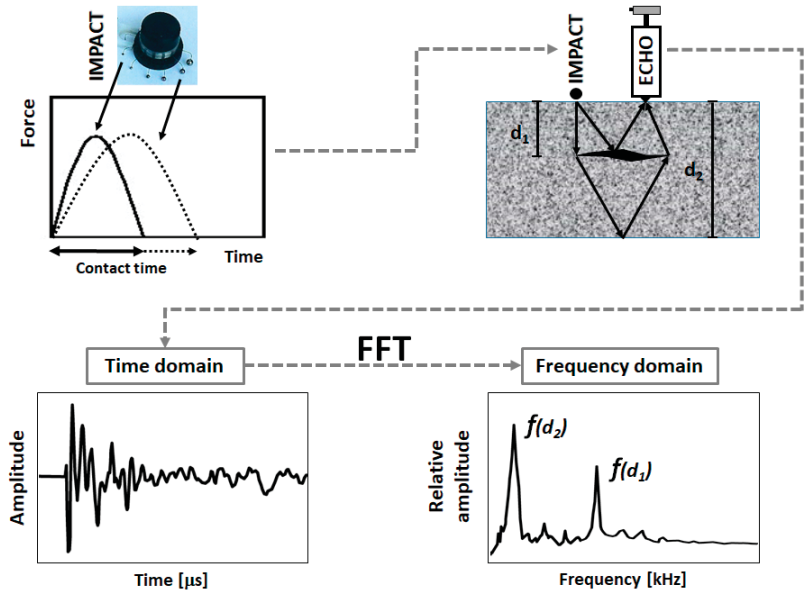
Figure 1. Scheme of impact-echo method with an example of waveform time-domain spectrum and corresponding frequency spectrum when defect in concrete is observed.

A hammer or, most commonly, a steel ball is used as an impactor. The diameter of the ball governs the contact time [7,10], and thus, the frequency content of produced wave. The expected resonance frequency of the tested element should be included in the produced frequency range [11]. Usually, steel balls of diameters 4 mm to 30 mm are used, which allows for the testing of the concrete element of thickness up to 1 m [12]. Another wave source, like an air gun [13], can be used as well.

An elastic stress wave produced with an impactor contains three components: (I) Rayleigh (R) surface wave, (II) Shear (S) wave and (III) Compression (P) wave [9,11]. The P wave travels the medium and reflects from lower and upper faces of the element, as well as from any faults or borders of underlying layers. This phenomenon is caused by a difference in the mechanical impendences of materials in the element, and especially between air and concrete [7,12]. The periodicity of echoes produces resonance frequencies.

These periodic reflections are recorded with a piezoelectric transducer. A device with a large bandwidth between 2 kHz and 50 kHz is used. The abovementioned frequencies correspond to average thickness of concrete element between 5 cm and 1 m [12]. Another technique, e.g., laser interferometry [14] or microphone [15,16], can be used in the air-coupled approach.

For sake of interpretation, the registered signals are usually presented in frequency domain using fast Fourier transform [17]. The use of frequency domain allows for observation of multiple reflections of wave between upper and lower face of the element, making the measurement insensitive to the distance between impactor and receiver [9]. The wavelet analysis can be used in the analysis as well [18].

The thickness of the element can be computed knowing both: (I) the resonance frequency of P wave, and thus the travelling time, and (II) the velocity of P wave. The velocity of the P wave can be either measured [12] or obtained empirically [6]. A similar

procedure is adopted for any layers' interfaces or faults present in the tested element, visible as peaks in the frequency spectrum (Figure 1).

IE is very similar to the ultrasonic method, but two significant differences are present: (I) ultrasonic waves are linear, which enables measurement only in line of excitation, while stress-waves in the IE propagate spherically; and (II) the frequency of waves in the IE method is lower, and therefore, heterogeneity of concrete has neglectable influence on the results. Additionally, the spherical wave propagation allows for separation of the excitor and receiver, making IE more flexible and capable of testing bigger areas and volumes, thus making it faster in use.

Beside measurement of the thickness of element, the Impact-Echo method has been used to detect: flaws [8], cracks [19], voids and debondings [7], honeycombing [20], delaminations and quality of interfaces [21,22] or voids in grouted tendon ducts [23].

The numerical finite element methods are important to ensure the IE development [8]. They have been used extensively to simulate different types of flaws and understand the results obtained with IE testing. From point of view of this paper, the sensitivity of IE to size of faults [23] and fusion of results from multiple sensors [24] are especially important.

Several trials with automated NDT using IE [25,26] and its fusion with other techniques [27] has been undertaken before. The commercial devices were also developed, e.g., Olson Engineering INC-Bridge Deck Scanner (BDS) [28] or BAM NDT Stepper [29].

3. Preparation and Validation of Finite Element Model

To obtain reliable results from the numerical model, verification and validation is needed [30]. The parametrical studies by variating modulus of elasticity, Poisson ratio and density of concrete to change wave velocity, as well as finite element size, were conducted. The results were verified against analytical solution as described below and good agreement was found. For sake of brevity, detailed results are not presented here, and are available in [31].

3.1. Experiment for Validation

To validate the numerical model, an experiment on solid concrete slab was used. The slab of dimensions 50 cm × 50 cm × 7 cm was casted using C20/25 class concrete according to Eurocode and supported on 5 cm by 5 cm washers in four corners. After curing, 30 IE tests using commercial DOCter® Mark IV commercial device [32] were executed. A 2 mm ball was used to evoke the wave in a distance of 5 cm from the receiver. All the measurements show the thickness of 70 mm, so no internal faults were present. The signal was probed approximately every 2×10^{-3} ms, and the total length of the obtained signal was 1.9 ms per measurement. All the results were recorded and saved for further comparison with the numerical model.

3.2. Numerical Model

The abovementioned slab was modeled in a commercial program LS-DYNA® [33] and is presented in Figure 2a. A three-dimensional model was built using 8 nodes hexahedron 7 mm × 7 mm constant stress solid elements of type ELFORM 1. This type of element, with a single integration point, was chosen for better computational efficiency considering the relatively simple stress-state and shape of the modeled structure. Viscous control of hourglass (type 1) was chosen as it is recommended for higher velocity waves and is computationally the cheapest. Considering the relatively low size of mesh, good results were obtained with this simple modeling method and explicit integration.
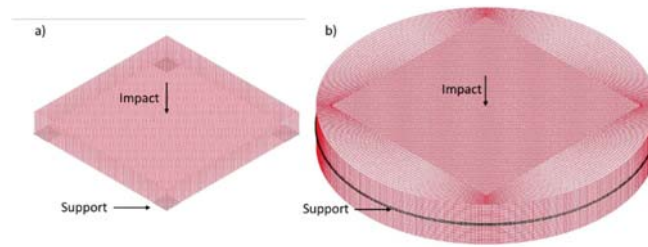
Figure 2. Isometric view of Finite Element Models (**a**) model of 50 cm × 50 cm × 7 cm plate for validation; (**b**) model of infinitely large slab for layout testing.

Vertical displacements were constrained in corners on the lower face of the plate. The material was modeled as perfectly elastic, with modulus of elasticity 38 GPa, density 2400 kg/m^3 and Poisson ratio 0.2, corresponding to C20/25 concrete [10]. The excitement was applied by force with sine function variability of 2 kN. Such variability is commonly used and its magnitude does not influence the results thanks to the elastic material model [6,9]. The excitation impulse lasted for 8.4 × 10^{-6} s, corresponding to a 2 mm ball [6]. Vertical displacement of the node in location of the transducer was registered for 2 ms, with a time step of 1.4 × 10^{-3} ms.

3.3. Signal Processing

To validate the model, two signals collected in different ways needed to be compared. During the experiment, variation of current voltage due to pressure waves acting on piezoelectric in transducer was registered, while the direct displacement of node could be obtained from the model. This is why a proper filtering is important [17].

For validation, the surface (Rayleigh) wave was removed by cutting the first 0.5 ms of signal. Then, the Butterworth filter was applied for frequencies outside $\frac{1}{2}f$–$2f$ window, where f is the frequency expected due to plate thickness. The filtering was needed mostly due to numerical noise and eigenvibrations present in numerical results, as well as high frequency noise due to the concrete inhomogeneity in slabs. Then, the Fast Fourier Transform (FFT) was used to present and compare the frequency spectrum.

3.4. Results

Thickness of the tested plate, and depth of possible fault, can be found on the basis of the passage time of the pressure wave through the material. Since the wave is reflected multiple times from the bottom and top surfaces, frequency of the wave passage is used. The velocity of wave can be obtained from the empirical Equation (1) [6]:

$$C_p = \sqrt{\frac{E(1-v)}{\rho(1+v)(1-2v)}} \tag{1}$$

where E stands for Young's modulus of elasticity of concrete, ρ for density of concrete and v is Poisson's ratio. This velocity is, however, dependent on the element's shape; thus, for plates, an apparent velocity should be used [8,9], leading to the Equation (2):

$$T = \frac{C_{pp}}{2f} \tag{2}$$

where f stands for frequency of signal, T for thickness (depth) of element and $C_{pp} = 0.96C_p$ is the reduced, apparent wave velocity for the concrete plate with $v = 0.2$ due to resonance and the creation of Lamb waves [34,35].

A good correlation between registered signals and their frequency spectra was obtained. The dominating frequency from experiment is 27.40 kHz, while from the model it is

27.19 kHz. With C_{pp} = 3830 m/s, the thickness of 70.0 mm and 70.4 mm can be calculated, respectively.

Thus, the model was validated and good agreement with the experiment was found.

4. Experimental Studies on a Large Span Floor

The bigger the spacing between impactor and transducer, the larger the distance that wave travels in the material. Because of this, the area tested at once can be increased, reducing the time needed for the whole slab or floor, and IE can be used to test a certain volume of concrete at once. This is why balance between the reliability of results and the distance between impactor and receiver needed to be found.

An experiment was prepared to investigate the maximum distance between the impact and read-out points at which results remain clear and reliable. Because the circular wave reflects not only from faces of the element but from other boundaries as well, interference may influence the results. To avoid this, the large span 40 cm thick concrete floor was chosen. The span-to-depth ratio was big enough to considered it as an element of infinite area.

Measurements were taken in the three directions (each 45°) to avoid influence of reinforcement. The distance between points of impact and signal reception varied from 10 cm to 300 cm. A 12 mm impactor was used according to the geometry of slab and detection ability as presented by Carino [9]. Each measurement was repeated three times.

Measurements show that the maximum distance between impactor and receiver giving reliable results is around 90 cm and above this distance, the wave reaching transducer was too weak (Figure 3). It has to be stressed that energy produced by the smaller ball is lower, and thus, this distance would decrease. This result can be influenced by the type of the concrete used and serves merely as estimation of possibility of change Impact-Echo from punctual into volumetric method. Taking into account the expected range of thicknesses of slabs to be tested with the device under design, as well as convenience of its use, a square 60 cm × 60 cm was assumed as a maximal testing area. Furthermore, it was concluded that an automated impact procedure should be implemented to make uniform the subsequent readouts. The exact results and discussion can be found in [31].
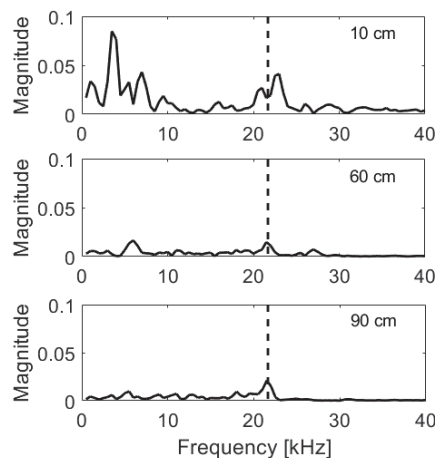
Figure 3. Frequency spectra of measurements taken at a large span floor in distance of 10 cm, 60 cm and 90 cm from impactor; frequency due to thickness marked with dashed line.

5. Finite Element Model of Plate with Voids

Knowing the maximum dimensions of the IE module that could be incorporated into the automated scanner combining different NDT techniques [5], the best layout was pursued. The IE module should allow for testing in an automated way the biggest possible

area at once. At this stage, the presence or lack of fault or void should be determined. The depth and exact location within the tested area can be found using more precise testing later. In this way, the large area of slab can be scanned in a quicker manner, showing the points of possible further interest.

5.1. Numerical Model Modification

It was decided to model the plate for further investigation as an infinitely large slab. The purpose of this was to avoid possible reflections from the boundaries of the element. To do this, a square plate 90 cm × 90 cm × 20 cm was modeled with further extension to obtain a circular external surface (Figure 2b). To this side surface, nonreflective boundary conditions were assigned. The vertical supports were assigned at the mid-span on the whole perimeter.

The void was modeled by removal of elements in the box 20 cm × 20 cm × 2 cm at mid-depth (Figure 4). The expected peaks, calculated with formula (2), are presented in Table 1, respectively, for the top and bottom of the void, and for the thickness of whole element. Since the element's size, material properties and finite elements type remained the same as in validated model, no additional verification or validation was needed.

(a) (b)
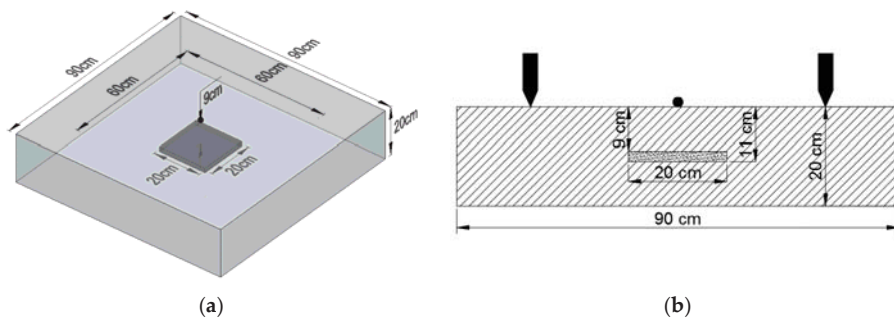
Figure 4. The plate with void: (**a**) view and (**b**) section.

Table 1. Expected peaks for plate with voids (C_{pp} = 3834 m/s).

Depth [cm]	Frequency [kHz]
9	21.3
11	17.4
20	9.6

5.2. Possible Linear Layouts

The standard IE layout consist of one impactor and one receiver. If the void or fault is below one of them or between them, it can be detected.

The first considered layout was one receiver and one impactor spaced by 40 cm, moving along the line perpendicular to them. This way, subsequent cross-sections of slab can be examined. However, to obtain the necessary resolution, many measurements were needed (e.g., every 10 cm), leading to a time-consuming procedure.

To cover a bigger area at once, a set of four impactor–receiver pairs each spaced at 10 cm, covering an area of 30 cm by 40 cm, can be used. All the impactors would be released at same time. However, due to wave interference, the readouts were difficult to analyze, and this approach was given up. Furthermore, the release of impactors at exactly the same time could be problematic.

The third layout would be a modification of the above. Instead of using four impactors, only one could be used. However, the distance between the impactor and each of the receivers would not be equal and analysis of such a signal would be difficult.

On the basis of the numerical models of the three abovementioned arrangements, it was decided that for the proper layout, the distance between each of receivers and impactor should be equal. Furthermore, to avoid interference of waves, only one impactor should be used for the IE module.

5.3. Square Layout

As mentioned above, it was decided that the distance between impactor and all transducers should be equal for sake of simplicity of comparison. Although the maximum distance between points of impact and read-out was found to be 90 cm, the IE module should fit within the UIR integrated scanner. Therefore, the distances were reduced. The transducer layout should allow diagnostics of the largest possible area at once. This is why the square scheme was investigated with piezoelectric receivers in points 1 to 4 (Figure 5). Then, the applicability of this layout with different positioning of void was modeled.
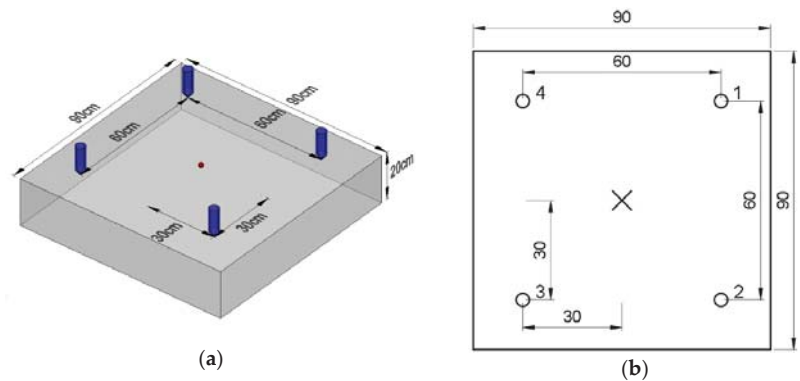
Figure 5. Square measurement system layout: (**a**) isometric and (**b**) top views.

5.4. Signal Processing

The signal was processed in similar way as in the experimental validation (see Section 3.3). Filtering out the frequencies outside of $\frac{1}{2}f$–$4f$ was performed to exclude the eigenvibrations of plate and numerical noise, but to keep the high-frequency waves due to reflections from the void. The Raleigh wave was removed by cutting out first 0.5 ms of signal.

6. Results of Simulations

The results are compared in both qualitative and quantitative ways. The qualitative way is by comparison of frequency spectra and peaks that they reveal. This process can be automatized in the scanner. The quantitative ways used in this paper are: (I) integration of the frequency spectra, and (II) calculation of the root mean square (RMS) of the frequency spectra. The outcome of the comparison should be whether some anomaly in the measurement results can be spotted, and thus, if the void can be detected and indicate that there exists a need for further testing of the area.

6.1. Solid Plate (No Void) vs. Plate with Void

First, the comparison between solid plate and plate with void below the impactor and transducer was done.

In the case of the solid plate, the peak due to thickness (9.95 kHz) was clearly visible for all sensors (Figure 6). The second highest peak (18.0 kHz) lied the around half-depth (10.4 cm) and might be the result of wave interference. The integral and RMS values (Table 2) were slightly different, possibly due to numerical noise. However, the obtained variation remained below 3%. Thus, if the absolute value of variation (Δ) of both integral

and RMS is outside of 10% interval of the Reference Value (RV), the fault is detected. If only one value is outside of the interval, it indicates warning. The RV was taken as the mean value of integrals and RMS from a solid plate.
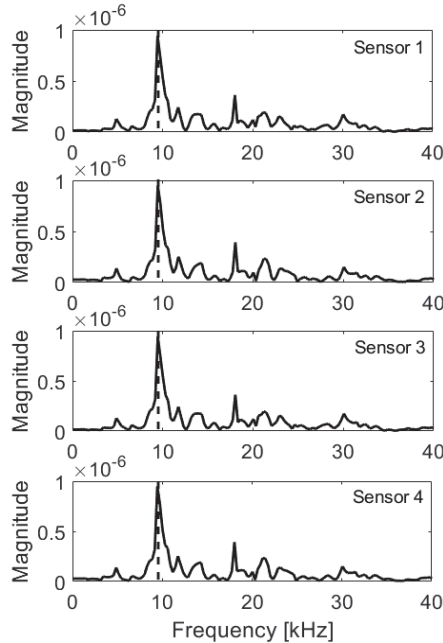
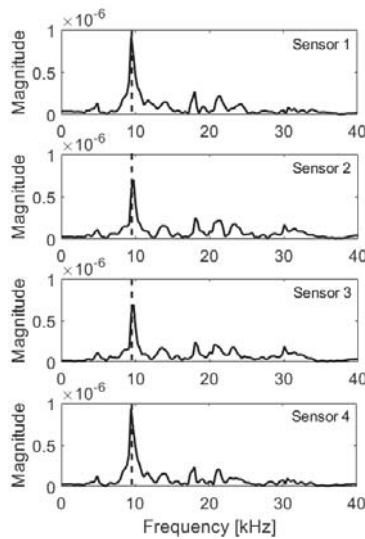**Figure 6.** Frequency spectra, solid plate; expected frequency marked with dashed line.

Table 2. Integral and RMS of frequency spectrum, solid plate.

Sensor N°	Integral (10^{-6})	Δ [%]	RMS (10^{-7})	Δ [%]	Detected?
1	3.616	3	1.537	2	N
2	3.521	0	1.515	0	N
3	3.436	2	1.481	2	N
4	3.521	0	1.515	0	N
Mean (RV [1])	3.523	-	1.512	-	-

[1] Reference Value (RV); Detected Y—Yes, N—No, W—Warning.

When the void was located below impact point (Figure 7, Table 3), a big difference could be noticed from the previous case in the value of the integral and RMS. The values were smaller as the energy was largely dumped by discontinuity. Additional peaks for frequencies about 22.4 kHz were visible in the frequency spectrum, which allowed for detection of the void in the investigated area (Figure 8).

If the void was located only under one transducer (Figure 9), it was highly affected by dumping, as visible in Table 4. However, the sensor No.3 was surprisingly slightly dumped as well, possibly by interference with wave reflected from edge of the fault. In frequency spectra (Figure 10) for test point 1, the decrease in magnitude of peak due to plate thickness (9.95 kHz) was clear, as well as the additional peak due to the void (22 kHz).
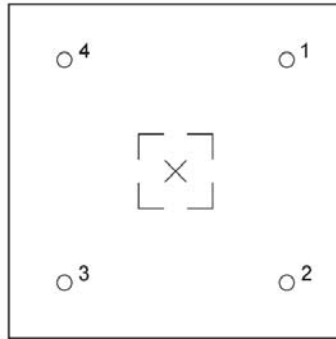
Figure 7. Scheme of void and IE device layout.

Table 3. Integral and RMS of frequency spectrum, void below impactor.

Sensor N°	Integral (10^{-6})	Δ [%]	RMS (10^{-7})	Δ [%]	Detected?
1	2.657	25	0.872	42	Y
2	2.473	30	0.832	45	Y
3	2.331	34	0.791	48	Y
4	2.473	30	0.833	45	Y

Detected Y—Yes, N—No, W—Warning.
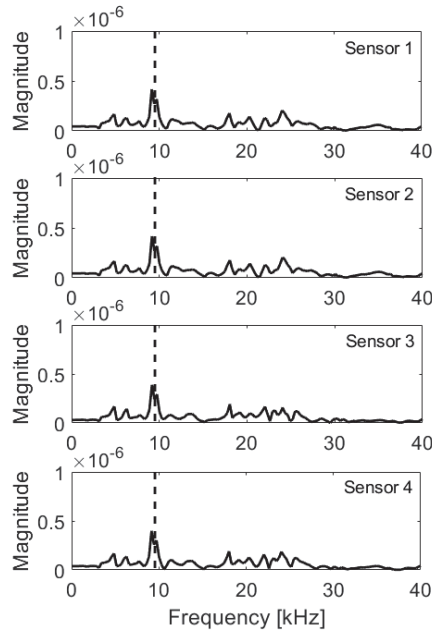
Figure 8. Frequency spectra, void below impactor; expected frequency marked with dashed line.
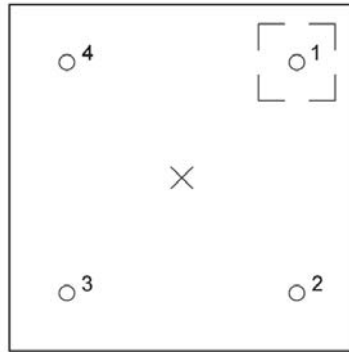
Figure 9. Scheme of void and IE device layout, void below sensor 1.

Table 4. Integral and RMS of frequency spectrum, void below sensor 1.

Sensor N°	Integral (10^{-6})	Δ [%]	RMS (10^{-7})	Δ [%]	Detected?
1	2.686	24	0.891	41	Y
2	3.549	1	1.510	0	N
3	2.838	19	1.300	14	Y
4	3.549	1	1.510	0	N

Detected Y—Yes, N—No, W—Warning.
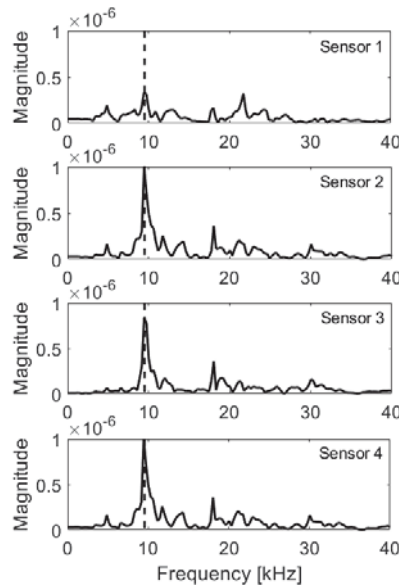
Figure 10. Frequency spectra, void below sensor 1; expected frequency marked with dashed line.

6.2. Edge of Void below Impactor

Another interesting case is the location of edge of the void directly below the impact point (Figure 11). While comparing the integrals and RMS values (Table 5) or frequency spectra obtained here and for the solid plate, a reduction of energy delivered to transducers was visible. It is most evident for sensors close to the void (i.e., 1 and 4, Figure 12). Thus, the void can be detected and its approximated location can be given, but not the depth.
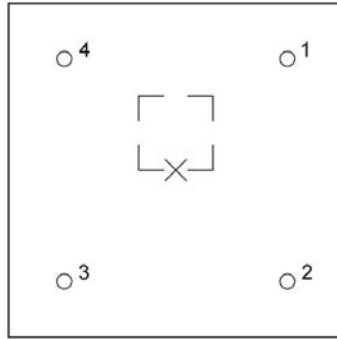
Figure 11. Scheme of void and IE device layout, edge below impactor.

Table 5. Integral and RMS of frequency spectrum, edge below impactor.

Sensor N°	Integral (10^{-6})	Δ [%]	RMS (10^{-7})	Δ [%]	Detected?
1	2.812	20	0.989	34	Y
2	2.632	25	0.874	42	Y
3	2.445	30	0.858	43	Y
4	2.617	26	0.971	36	Y

Detected Y—Yes, N—No, W—Warning.
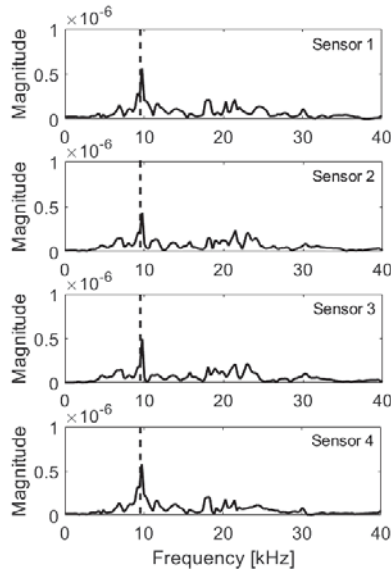
Figure 12. Frequency spectra, edge below impactor; expected frequency marked with dashed line.

6.3. Void Moving Away from Impactor

One more situation is the void moving away from the impact point (or, rather, when the scanner is moving away from the void, (Figures 13 and 14). Although the frequency spectra (Figures 15 and 16) did not precisely reveal the depth of the void, its location could be determined. Not only did the transducer closest to the fault reveal the biggest dumping of energy (Tables 6 and 7) as described previously, but also a linear relation between received energy and void position could be found. In the Figure 17, the variation

of RMS values with respect to reference value of solid slab are presented for three cases, as well as the linear fit quality.
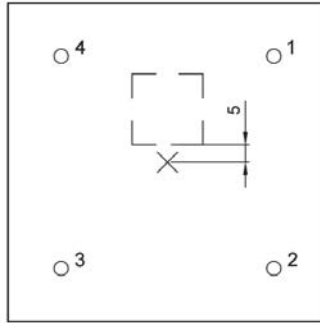
Figure 13. Scheme of void and IE device layout, edge 5 cm from impactor.
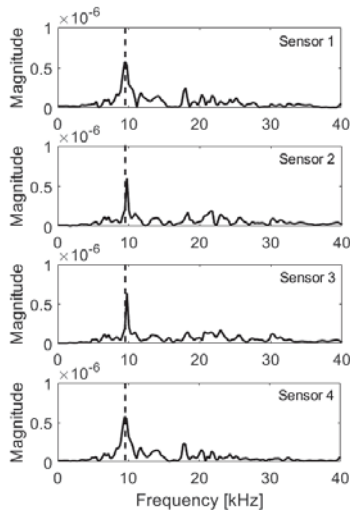
Figure 14. Frequency spectra, edge 5 cm from impactor; expected frequency marked with dashed line.
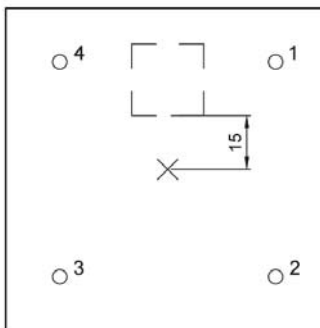
Figure 15. Scheme of void and IE device layout, edge 15 cm from impactor.

Figure 16. Frequency spectra, edge 15 cm from impactor; expected frequency marked with dashed line.

Table 6. Integral and RMS of frequency spectrum, edge below impactor.

Sensor N°	Integral (10^{-6})	Δ [%]	RMS (10^{-7})	Δ [%]	Detected?
1	2.816	20	1.113	26	Y
2	2.490	29	0.886	41	Y
3	2.445	30	0.884	41	Y
4	2.698	23	1.103	27	Y

Detected Y—Yes, N—No, W—Warning.

Table 7. Integral and RMS of frequency spectrum, edge below impactor.

Sensor N°	Integral (10^{-6})	Δ [%]	RMS (10^{-7})	Δ [%]	Detected?
1	3.230	8	1.407	7	N
2	3.206	9	1.219	20	W
3	3.178	10	1.203	20	Y
4	3.179	10	1.404	7	W

Detected Y—Yes, N—No, W—Warning.

6.4. Summary

Simulations presented above clearly show that with a square set of 4 transducers and 1 impact point, the impact-echo method turns into volumetric, and a void can be detected if it lays within the area covered by the device. Its approximated position can be given in any case. However, the depth can be found only if it lays below the impact point or under one of the sensors. However, this precision is sufficient and thus, the proposed scheme can be adopted in UIR-Scanner.

The sensitivity of setup regarding minimum detectable fault was not analyzed. It can be expected that ability of detection is restricted by limits of impact-echo method [21], e.g., ratio of minimal lateral dimension of void to stress wavelength (impactor size) and element's depth. Furthermore, the numerical model presents an idealized medium, which is not the case in real application. Therefore, during the implementation of proposed layout into UIR-Scanner, the limitations and problems that are inherent in the chosen NDT method need to be borne in mind [36], i.e., (1) reflection coefficient R between fault and medium

needs to be large enough; (2) possible multiple reflections, e.g., due to reinforcement, can impair obtained results; (3) source of external vibrations and difference in vibration modes between types of plates can influence results.
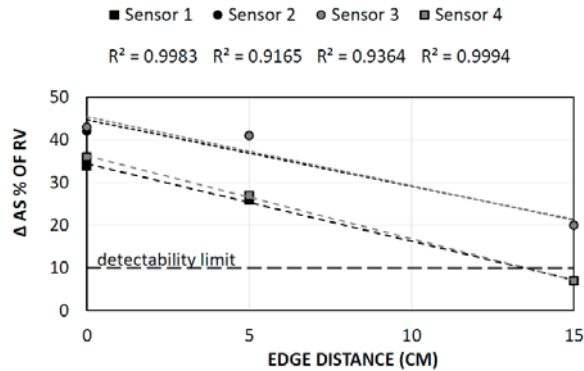
Figure 17. RMS of signal received by each transducer with change of void edge distance from impact point.

7. Experimental Validation of Adopted Layout

Before implementation of an IE module in the UIR-Scanner, the layout was experimentally validated on a concrete slab using DOCter Mark IV transducers. The 50 cm thick slab of C30/37 concrete was used. At a depth of around 5 cm, a void was modeled by foamed polystyrene plate, 5 cm × 5 cm × 2 cm.

Measurements were executed with one transducer and one 2 mm impactor. The transducer was subsequently moved between positions 1 and 4, and the impact was applied in the center of setup (Figure 5). Two cases were considered—with no void, and with void below the impact point. The measurement was repeated 7 times at each measurement location (measurement A to G).

For obtained frequency spectra, Integral and RMS were calculated in range 0 Hz–70 Hz, where 70 Hz corresponds to twice the frequency due to the mid-depth of the void according to formula (2). The results for each measurement are presented in Tables 8–11.

Table 8. Integral of frequency spectrum (10^{-1}), slab with no void.

Sensor N°	Measurement						
	A	B	C	D	E	F	G
1	1.4604	1.7889	1.6837	0.8747	1.4098	1.6977	1.3303
2	1.7374	0.8333	1.6095	1.8303	1.1254	2.3219	0.9677
3	1.0635	1.2686	1.2494	1.1608	1.7251	1.4504	2.2510
4	1.1031	1.9778	1.1016	0.8069	1.1877	1.6299	1.5897

Table 9. RMS of frequency spectrum (10^{-3}), slab with no void.

Sensor N°	Measurement						
	A	B	C	D	E	F	G
1	2.7935	3.4939	3.3806	1.6329	2.7753	3.6157	3.1040
2	3.3197	1.5470	3.0592	3.6199	2.1701	5.0211	1.7858
3	2.6369	3.5801	2.6805	2.4723	3.9014	3.4583	4.8312
4	2.7986	5.0711	2.4122	2.0223	2.7992	3.9092	3.7139

Table 10. Integral of frequency spectrum (10^{-1}), slab with void below impactor.

Sensor N°	Measurement						
	A	B	C	D	E	F	G
1	1.1421	1.0405	0.8709	0.9281	1.5843	0.9358	0.9063
2	1.1993	1.0262	1.5378	1.2899	0.8842	2.0402	1.0260
3	0.8347	1.0381	1.0210	0.9872	0.6384	1.5853	1.1728
4	0.8289	0.8052	0.8035	0.8139	1.2276	0.9977	0.8849

Table 11. RMS of frequency spectrum (10^{-3}), slab with void below impactor.

Sensor N°	Measurement						
	A	B	C	D	E	F	G
1	2.1684	1.8025	1.5266	1.5733	2.8588	1.7611	1.7008
2	2.0785	1.8145	2.7309	2.4415	1.5800	3.7172	1.8479
3	1.5824	2.0308	1.9463	1.7742	1.1389	3.8032	2.4548
4	1.4977	1.4021	1.4673	1.5174	3.0528	2.1219	1.6850

For each measurement, the elastic wave was induced by separate impact and transducer was lifted and pressed again every time. Therefore, the measurements are uncorrelated. To analyze the results, and eliminate isolated events of different impact energy or imperfect contact of transducer with surface, average values from seven measurements (A to G) were calculated and presented in Tables 12 and 13 for slab without and with the void, respectively. The same criteria of detection as for numerical model were used; therefore, Δ above 10% for one of indicators (Integral of RMS) results in warning and for both indicators results in detection.

Table 12. Integral and RMS of frequency spectrum, solid slab.

Sensor N°	Integral (10^{-1})	Δ [%]	RMS (10^{-3})	Δ [%]	Detected?
1	1.464	2	2.971	5	N
2	1.489	4	2.932	6	N
3	1.453	1	3.366	8	N
4	1.342	7	3.247	4	N
Mean (RV [1])	1.437	-	3.129	-	-

[1] Reference Value (RV); Detected Y—Yes, N—No, W—Warning.

Table 13. Integral and RMS of frequency spectrum, slab with void below impactor.

Sensor N°	Integral (10^{-1})	Δ [%]	RMS (10^{-3})	Δ [%]	Detected?
1	1.058	26	1.913	39	Y
2	1.286	10	2.316	26	Y
3	1.040	28	2.104	33	Y
4	0.909	37	1.821	42	Y

Detected Y—Yes, N—No, W—Warning.

Despite relatively large discrepancies between individual measurements due to manual excitation of elastic stress-wave, average values clearly indicate presence of the void. The results confirm the need for automated excitation and simultaneous measurement with all four transducers. This experiment confirmed applicability of IE as a volumetric method. Therefore, the numerical modeling results were validated, and the IE module was implemented into the UIR-scanner (Figures 18 and 19) and issued for further sensitivity studies.
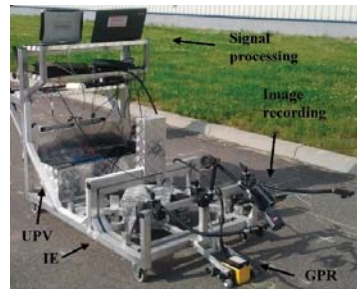
Figure 18. UIR-Scanner (a prototype) for nondestructive testing using complementary NDT methods: GPR (Ground Penetrating Radar), IE (Impact-Echo) and UPV (Ultrasonic Pulse Velocity) equipped with computer systems for signal analysis.
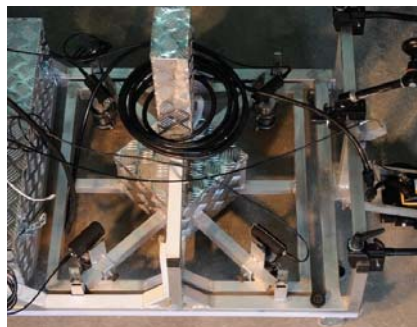
Figure 19. Impact-Echo module integrated into scanner.

8. Conclusions

The aim of research presented in this paper was to find the optimal design of an Impact-Echo module for automated detection of horizontal faults in concrete slabs. The IE module was to be incorporated into integrated UIR-Scanner combining three nondestructive methods. The IE module should determine possible locations of faults in the slab in the rapid, volumetric manner. Then, in indicated locations, further tests can be conducted to confirm the outcome.

The following recommendations were issued: (1) the impact should be automated to allow comparison of magnitude of frequency spectra between the measurements; (2) layout with four transducers at corners of square 60 cm by 60 cm and one impact point in the middle should be adopted as it allows the most efficient testing; (3) clear rules for signal analysis and interpretation, with use of frequency spectra's integral and RMS, are established. They can be further introduced in the software of the scanner to automatize the procedure of detection. This layout was adopted into the UIR-Scanner, validated and issued for further experimental testing.

The current research has clearly presented that relatively simple Impact-Echo method, usually used for punctual measurement of element's thickness or detection of faults, can be modified into volumetric method by use of multiple transducers. Despite loss of precision and ability to localize the fault, this approach allows for much faster scanning of structures and opens new possibilities of application of the IE method for nondestructive testing of concrete.

Author Contributions: Conceptualization, B.S., T.P. and A.G.; methodology, T.P.; software, B.S.; validation, T.P. and B.S.; formal analysis, B.S.; investigation, B.S.; resources, T.P. and A.G.; data

Institutional Review Board Statement: Not applicable.

Informed Consent Statement: Not applicable.

Data Availability Statement: The data presented in this study are available in [31] (numerical modeling and validation of models) or is available on request from the corresponding author (validation of layout).

Conflicts of Interest: The authors declare no conflict of interest.

References

1. Hoła, J.; Schabowicz, K. State-of-the-art non-destructive methods for diagnostic testing of building structures—Anticipated development trends. *Arch. Civ. Mech. Eng.* **2010**, *10*, 5–18. [CrossRef]
2. Hoła, J.; Sadowski, L.; Schabowicz, K. Nondestructive identification of delaminations in concrete floor toppings with acoustic methods. *Automat. Constr.* **2011**, *20*, 799–807. [CrossRef]
3. Sansalone, M.J.; Streett, W.B. Impact-echo. In *Non-Destructive Evaluation of Concrete and Masonry*; Bullbrier Press: Jersey Shore, PA, USA, 1997; ISBN 0961261064.
4. Hoła, J.; Schabowicz, K. New technique of nondestructive assessment of concrete strength using artificial intelligence. *NDT E Int.* **2005**, *38*, 251–259. [CrossRef]
5. Garbacz, A.; Piotrowski, T.; Zalegowski, K.; Adamczewski, G. UIR-Scanner Potential to Defect Detection in Concrete. *Adv. Mater. Res.* **2013**, *687*, 359–365. [CrossRef]
6. Garbacz, A. *Nieniszczące Badania Betonopodobnych Kompozytów Polimerowych za Pomocą fal Sprężystych-Ocena Skuteczności Napraw, Prace Naukowe Politechniki Warszawskiej, Budownictwo (147)*; OWPW: Warszawa, Poland, 2007; pp. 3–208. (In Polish)
7. Sansalone, M.J.; Carino, N.J. Detecting delaminations in concrete slabs with and without overlays using the impact-echo method. *ACI Mater. J.* **1989**, *86*, 175–184.
8. Sansalone, M.J. Impact-echo: The complete story. *ACI Struct. J.* **1997**, *94*, 777–786.
9. Carino, N.J. The impact-echo method: An overview. In Proceedings of the 2001 World Structural Engineering Congress, Washington, DC, USA, 21–23 May 2001.
10. Piotrowski, T. Zastosowanie Analizy Sygnału Impact-Echo Do Oceny Jakości Zespolenia w Układach Naprawczych Betonu. Ph.D. Thesis, Warsaw University of Technology, Warsaw, Poland, 2009. (In Polish).
11. Abraham, O.; Leonard, C.; Cote, P.; Piwakowski, B. Time frequency analysis of impact-echo signals: Numerical modeling and experimental validation. *ACI Mater. J.* **2000**, *97*, 645–657.
12. Abraham, O.; Popovics, J.S. Impact-echo techniques for evaluation of concrete structures. In *Non-Destructive Evaluation of Reinforced Concrete Structures*; Maierhofer, C., Reinhardt, H.-W., Dobmann, G., Eds.; Woodhead Publishing: Cambridge, UK, 2010; Volume 2, pp. 466–489. [CrossRef]
13. Mori, K.; Spagnoli, A.; Murakami, Y.; Kondo, G.; Torigoe, I. A new non-contacting non-destructive testing method for defect detection in concrete. *NDT E Int.* **2002**, *35*, 399–406. [CrossRef]
14. Abraham, O.; Cottineau, L.M.; Valade, M.; Bedaoui, S.; Argoul, P. Laser interferometer robot for the detection of voids in tendon ducts with the impact echo method. In Proceedings of the NDTCE'09, Non-Destructive Testing in Civil Engineering, Nantes, France, 30 June–3 July 2009.
15. Zhu, J.; Popovics, J.S. Imaging Concrete Structures Using Air-Coupled Impact-Echo. *J. Eng. Mech.* **2007**, *133*, 628–640. [CrossRef]
16. Algernon, D.; Ernst, H.; Dressler, K. Assessment of Structural Concrete Components using Air-Coupled Impact-Echo. In Proceedings of the 9th International Conference on NDE in Relation to Structural Integrity for Nuclear and Pressurized Components, Seattle, WA, USA, 22–24 May 2012.
17. Agilent Technologies. *The Fundamentals of Signal Analysis, Application Note 243*; Hewlett Packard Intercontinental: Palo Alto, CA, USA, 2000.
18. Epp, T.; Cha, Y.-J. Air-coupled impact-echo damage detection in reinforced concrete using wavelet transforms. *Smart Mater. Struct.* **2016**, *26*, 025018. [CrossRef]
19. Grosse, C.U.; Reinhardt, H.W.; Krüger, M.; Beutel, R. Application of Impact-Echo techniques for crack detection and crack parameter estimation in concrete. In Proceedings of the 11th International Conference on Fracture (ICF11), Turin, Italy, 20–25 March 2005; pp. 4884–4889.

20. Carino, N.J.; Sansalone, M. Flaw Detection in Concrete Using the Impact-Echo Method. In *Bridge Evaluation, Repair and Rehabilitation*; NATO ASI Series (Series E: Applied Sciences) 187; Nowak, A.S., Ed.; Springer: Dordrecht, The Netherlands, 1990; pp. 101–118. [CrossRef]
21. Garbacz, A.; Piotrowski, T.; Kwasniewski, L.; Courard, L. On the evaluation of interface quality in concrete repair system by means of impact-echo signal analysis. *Constr. Build. Mater.* **2017**, *134*, 311–323. [CrossRef]
22. Schubert, F.; Köhler, B. Ten Lectures on Impact-Echo. *J. Nondestruct. Eval.* **2008**, *27*, 5–21. [CrossRef]
23. Abraham, O.; Cote, P. Impact Echo Thickness Frequency Profiles for detection of voids in tendon ducts. *ACI Struct. J.* **2002**, *3*, 239–248.
24. Zhang, Y.; Wei, X.; Tsai, Y.-T.; Zhu, J.; Fetrat, F.A.; Gucunski, N. Multisensor data fusion for impact-echo testing of concrete structures. *Smart Mater. Struct.* **2012**, *21*, 075021. [CrossRef]
25. Li, B.; Xiao, J.; Xiao, J.; Zhang, X.; Wang, H. Robotic impact-echo Non-Destructive Evaluation based on FFT and SVM. In Proceedings of the 11th World Congress on Intelligent Control and Automation (WCICA), Shenyang, China, 27–30 June 2014; pp. 2854–2859.
26. Guthrie, W.S.; Larsen, J.L.; Baxter, J.S.; Mazzeo, B.A. Automated Air-Coupled Impact-Echo Testing of a Concrete Bridge Deck from a Continuously Moving Platform. *J. Nondestruc. Eval.* **2019**, *38*, 1–8. [CrossRef]
27. Streicher, D.; Niederleithinger, E.; Wöstmann, J.; Algernon, D.; Milmann, B. *Demonstration of Measurements Using Impulse-Radar, Ultrasonic Echo and Impact-Echo on a Pre-Stressed Concrete Railway Bridge in Duisburg, Germany, Sustainable Bridges Background Document SB 3.17*; Diva: London, UK, 2007.
28. Bridge Deck Scanning Using Impact Echo. Available online: https://olsonengineering.com/methods/structural-pavement-tunnel-methods/impact-echo-bridge-deck-scanning// (accessed on 22 April 2021).
29. Wiggenhauser, H. Advanced NDT methods for the assessment of concrete structures. In *Concrete Repair, Rehabilitation and Retrofitting II, Proceedings of the 2nd International Conference on Concrete Repair, Rehabilitation and Retrofitting, ICCRRR-2, Cape Town, South Africa, 24–26 November 2008*; Alexander, M.G., Beushausen, H.-D., Dehn, F., Moyo, P., Eds.; CRC Press: Boca Raton, FL, USA, 2008; pp. 19–30. [CrossRef]
30. Kwasniewski, L.; Bojanowski, C. Principles of verification and validation. *J. Struct. Fire Eng.* **2015**, *6*, 29–40. [CrossRef]
31. Sawicki, B. Numerical Analyses of Stress Wave Propagation for Impact-Echo Testing Procedure. Bachelor's Thesis, Warsaw University of Technology, Warsaw, Poland, 2013. [CrossRef]
32. Germann Instruments A/S. *Viking 6.0 Software Instruction Manual for Docter Impact-Echo Test System*; Germann Instruments A/S: Copenhagen, Denmark, 2005.
33. Hallquist, J.O. (Ed.) *Ls-Dyna Keyword User's Manual*; Livermore Software Technology Corporation: Livermore, CA, USA, 2007.
34. Gibson, A.; Popovics, J.S. Lamb wave basis for impact-echo method analysis. *J. Eng. Mech.* **2005**, *131*, 438–443. [CrossRef]
35. Baggens, O.; Ryden, N. Systematic errors in Impact-Echo thickness estimation due to near field effects. *NDT E Int.* **2015**, *69*, 16–27. [CrossRef]
36. Carino, N.J. Impact Echo: The Fundamentals. In Proceedings of the International Symposium Non-Destructive Testing in Civil Engineering (NDT-CE), Berlin, Germany, 15–17 September 2015.

Article

Assessment of the Destruction of a Fibre Cement Board Subjected to Fire in a Large-Scale Study

Krzysztof Schabowicz [1], Paweł Sulik [2], Tomasz Gorzelańczyk [1] and Łukasz Zawiślak [1,*]

[1] Faculty of Civil Engineering, Wrocław University of Science and Technology, Wybrzeże Wyspiańskiego 27, 50-370 Wrocław, Poland; krzysztof.schabowicz@pwr.edu.pl (K.S.); tomasz.gorzelanczyk@pwr.edu.pl (T.G.)
[2] Instytut Techniki Budowlanej, Filtrowa 1, 00-611 Warszawa, Poland; p.sulik@itb.pl
* Correspondence: lukasz.zawislak@pwr.edu.pl

Abstract: This article presents the results of a study involving the assessment of the structural destruction of fibre cement boards taken from a large-scale model subjected to fire. These were subjected to a three-point bending test using the acoustic emission method. The analysis of the obtained results took into account the course of bending stresses σ_m, the modulus of rupture (MOR), the number of acoustic emission events N_{zd} and the sum of EA events $\sum N_{zd}$. The conducted tests showed that the samples subjected to fire exhibited a clear decrease, up to 72%, in the recorded sum of EA events compared to a reference board (not subjected to fire). The analysis of the obtained modulus of rupture (MOR) values showed a similar trend—the reduction of the modulus of rupture for the degraded samples was in the range of 66–96%. In order to illustrate the changes taking place in the structure of the tested plates more precisely, analyses were carried out using the optical method and a digital microscope. This method may be sufficient for the final evaluation of degraded samples.

Keywords: ventilated facades; large-scale model; fibre cement boards; fire exposure; acoustic emission method

1. Introduction

Fibre cement boards are products used in construction since the early 20th century. In the 1990s, they underwent a transformation, whereby asbestos fibres, which constitute a health hazard, were replaced by other fibres, mainly cellulose fibres. The fibre cement boards manufactured nowadays consist of cement, cellulose fibres, synthetic fibres, and various additives and admixtures, i.e., limestone dust, mica, perlite, kaolin, microsphere [1–4]. Fibre cement boards are classified as composite construction materials and are defined as any multiphase material that exhibits a significant portion of the properties of both constituent phases and has been artificially made. The individual constituent phases must be chemically distinct and separated by a distinct interface [5]. Composite materials consist of two phases: the first is the matrix phase, which is continuous and surrounds the second phase, called the dispersed phase (reinforcing elements).

Composite materials are divided into particle-reinforced, fibre-reinforced and structural composites. Fibre cement boards are classified as fibre-reinforced composites, and the phases are dispersed in each direction. The classification of composites is shown in Figure 1.

The main goal in the design of fibre-reinforced composites is increased strength and/or rigidity without increased weight. Fibre-reinforced composites with exceptionally high strengths often contain low-density fibres. The most important factor that increases their strength is the appropriate fibre length (not too short). The mechanical and strength properties of these composites depend not only on fibre properties, but also on the extent to which load is transferred to the fibres by the matrix. The manner of that transfer is shown in Figure 2.
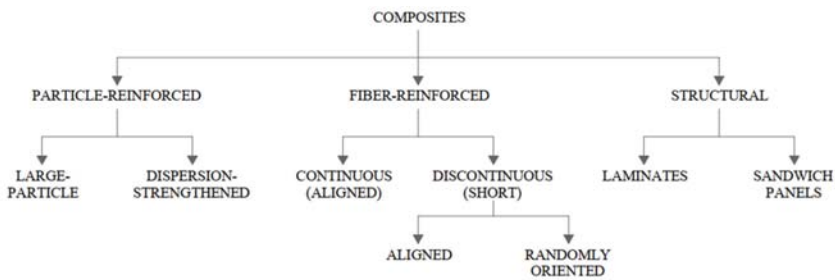
Figure 1. Classification of composite materials.
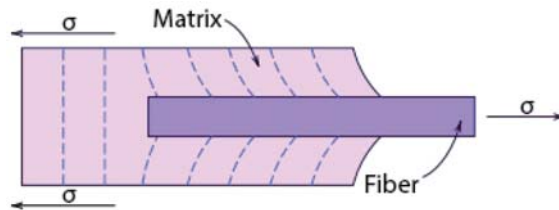
Figure 2. Deformation pattern in the matrix surrounding a fibre that is subjected to tension.

As fibre-reinforced composite materials, fibre cement boards have a matrix phase; in their case, the matrix is based on Portland cement which is responsible for binding the matrix and giving it durability. The second phase is the dispersed phase in the form of fibres. Apart from Portland cement, the matrix contains additional components and fillers, i.e., limestone dust, mica, perlite, kaolin, microspheres. The dispersed phase is characterised by the discontinuous and randomly oriented distribution of fibres. Fibres used in the manufacture of these composites include cellulose fibres, PVA (poly(vinyl alcohol)) synthetic fibres and PP (polypropylene) fibres. Most fibre cement boards make use of all these fibres, with each fibre serving a slightly different role. Cellulose fibres form a spatial mesh that reinforces the entire composite, polyvinyl alcohol (PVA) fibres are added to increase the strength and durability of fibre cement boards, especially those intended for outdoor use.

Fibre cement composites are used both indoors and outdoors. Outdoors, they are used mainly as façade cladding. They are expected to comply with a number of performance requirements referred to in harmonised standards [6]. These boards must also meet a number of resistance and strength requirements under fire conditions. As shown in [7,8], the strength of fibre cement boards after façade fires is significantly reduced, often preventing the ensuing safe use of such a façade. For cladding exposed to fire, it would be necessary to define a zone that requires the complete removal of the façade, including the partial disposal and partial use in other construction elements that do not have to meet such drastic requirements.

2. Literature Review

High temperatures have an extremely degrading effect on most building materials including composites (such as fibre cement boards). Composites characterised by two phases in view of the preliminary analysis and identification of degradation after high-temperature exposure can be analysed as separate, independent phases: the matrix phase and the dispersed phase. After this preliminary identification, the composite should be analysed and tested as an integrated, homogeneous product.

In terms of the cement matrix, the analysis of post-fire degradation can be based on studies of concrete samples that are used in many building structural elements exposed to fires. The strain analyses carried out in works on degraded concrete [9–11] indicate that

temperatures in the range of 300–400 °C are not critically degrading to concrete as opposed to boards, due to the presence in concrete of coarse aggregate fractions, and it is important that the samples are volumetric elements (three of the same order of magnitude). The authors subjected several different cement variants to high-temperature annealing tests in a study [10]. CEM I 42.5 R, a fast-setting and fast-maturing variant of Portland cement, showed poor performance in terms of resistance at high temperatures. The cement matrix in the experimental tests showed residual strength at 500 °C [10]–600 °C [12], while at 800 °C [10], the samples disintegrated spontaneously. Other studies [10,12] demonstrated that any temperature higher than 400 °C [12] has a negative effect on the strength of the matrix. The regression in cement strength starts almost immediately; initially, however, these values are relatively small. Thus, it can be assumed that significant strength regression begins at temperatures above 100 °C [10,13]. It is worth noting that the strength of concrete in a fire situation is also affected by the type of aggregate used.

In the dispersed phase, cellulose fibres, PVA synthetic fibres and PP fibres are used in fibre cement boards. The individual fibres have the following melting points: synthetic fibres PVA (polyvinyl alcohol)—about 200–220 °C [14,15]; PP (polypropylene) fibres—about 175 °C [14,16]; cellulose fibres—260–270 °C [17]. In the case of fibre cement boards, there is a lack of knowledge about the behaviour of this composite and how it degrades at fire temperatures. Most of the scientific literature analysing fibre cement boards focuses on the production process, its possible subsequent optimisation in terms of fibres and the testing of its basic physical properties. One of the few examples is the study presented in [18], where it has been shown that fibres in fibre cement boards degrade at 230 °C only after approx. 3 h of exposure. Damage to such degraded boards, during a three-point bending test, occurs through high-energy brittle fracture. It is noticeable that for fibre-reinforced cement composites, the modulus of rupture rises as the temperature increases up to about 300 °C [19] in a short period of time. It is, therefore, reasonable to believe that such temperatures are safe for these boards over the short term. Destruction of the fibres and cement matrix at a temperature of around 300 °C only occurs after a long period of time. This is influenced by the protection (encapsulation) of the fibres by the matrix phase (cement or concrete). These temperatures correspond approximately to the melting point of cellulose fibres. Szymków carried out tests on fibre cement board samples at 400 °C [18]. The samples showed much less stability at this temperature and degraded at a faster rate. The results exhibited large discrepancies because, depending on the manufacturer, the ingredients and the manufacturing technology, some samples "lasted" a maximum of several minutes while, while others were destroyed during the test.

Based on a study of large-scale models, Schabowicz et al. [7] showed the percentage of loss of strength parameters of fibre cement boards under the influence of fire. These studies demonstrated differences from model studies on small samples, but the temperatures at which degradation started, i.e., around 200 °C, was consistent for both types of study. Large-scale studies, compared to studies on small-scale samples, established different times for the occurrence of significant degradation. This is mainly due to the fact that studies on small-scale samples are mostly characterised by constant and uniform temperature effects. Hence, it follows that the structural expansion of fibre cement boards at high temperatures and the duration of action on such products is critical.

Failure to maintain the production regime (e.g., maintaining the appropriate temperature and humidity) may lead to fluctuations in the strength of concrete during a compression test, even up to 20%, which may cause significant differences in reference samples [20–22]. In concrete, as well as in a cement matrix, the major component is cement. When testing concrete samples, fluctuations in reference samples from other batches may be characterized by significant differences in strength, which may ultimately affect how individual results relate to each other. The authors of the article dealt with the problem of assessing the failure of fibre cement boards by reviewing the scientific literature and drawing conclusions from it and then conducting experimental research. The experimental tests were performed on samples taken from the actual model of the elevation that had been

exposed to fire. Samples were taken from various locations and then analysed and assessed. The assessment was made on the basis of the analysis of AE signals recorded during the course of three-point bending, and the assessment of strength during three-point bending. On the basis of these analyses, the state of destruction was determined, and conclusions were drawn.

3. Research Model and Testing Method

The actual façade model was a ventilated façade attached to a test platform, which was also the substrate on which the fire impact and progression tests were performed. Large-scale models are a very good way to study fire development and evaluate individual façade elements in terms of flammability, the behaviour of individual materials during a fire and the fire safety of the whole system. Large-scale studies may produce different results and present different critical areas with respect to studies on small samples.

The façade cladding analysed in this paper, installed on the real model, was made of 8 mm-thick fibre cement boards of natural colour, i.e., not dyed in the mass. It was mounted with mechanical connections to an aluminium substructure. The substructure consisted of metal vertical profiles mounted mechanically via brackets to the ground. There was a fire coming out of the combustion chamber, which was affecting the façade with high temperatures, realising the scenario of a fire in the room spreading through the window opening to the façade. A ventilation device was placed in the combustion chamber on the rear wall, which allowed the reproduction of a real fire situation. The division of the façade into cladding panels and the location of thermocouples and sampling sites are shown in Figure 3. The dimensions of the actual large-scale façade model were ~3 m × 3.5 m, and it was attached to a wall made of autoclaved aerated concrete, 600 kg/m^3 variety, with dimensions of 3.98 m × 3.98 m.

Subsequently, samples D5, D4 and D3 from the large-scale fire-affected model were taken from the above combustion chambers; they fell off at 13:30 min, 17:15 min and 34:00 min, respectively. The temperature course was recorded by the thermocouples TE3, TE7 and TE9 for the samples D5, D4 and D3, respectively. In the case of sample D5 located in the immediate area of the fire source, the temperature reached over 600 °C. Conversely, for sample D4, the temperatures were between 400 and 500 °C, and for sample D3, between 300 and 400 °C. The dimensions of the samples taken were 20 mm × 100 mm, with a thickness of 8 mm.

In order to identify the effect of high-temperature exposure on the degradation of fibre cement boards, tests were carried out using the acoustic emission method during a three-point bending test. Similar issues on fibre cement boards have also been analysed by other authors [23,24]. The test samples were cut from the façade board subjected to the fire according to their location shown in Figure 4. The cut-out samples were 20 mm × 100 mm in size. They were then placed in a testing machine, and a three-point bending test was carried out. For the three-point bending test, the PASCAL MIKROPRASA P—3 kN was used, with a load range between 0 and 3 kN. A constant crossbeam travel increment of 0.1mm/min was set during the testing of the fibre cement samples. The three-point bending test stand with the acoustic emission measurement setup is shown in Figure 5.

Figure 4 presents the large-scale study model during the course of the study along with the actual sampling location.
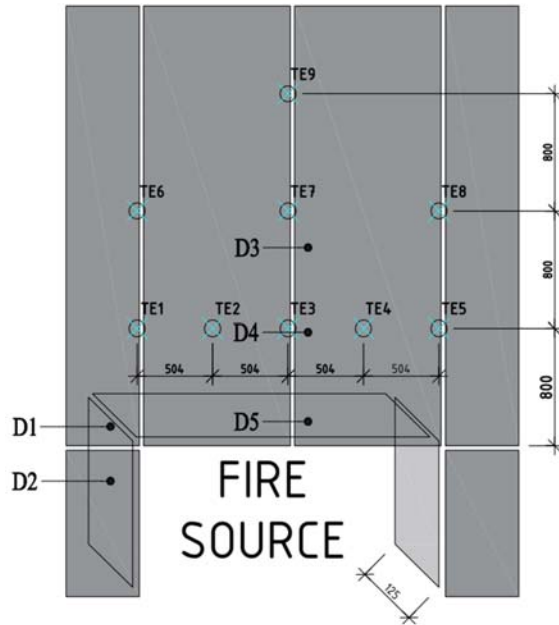
Figure 3. Layout of the exterior cladding panels and thermocouples along with sampling location.
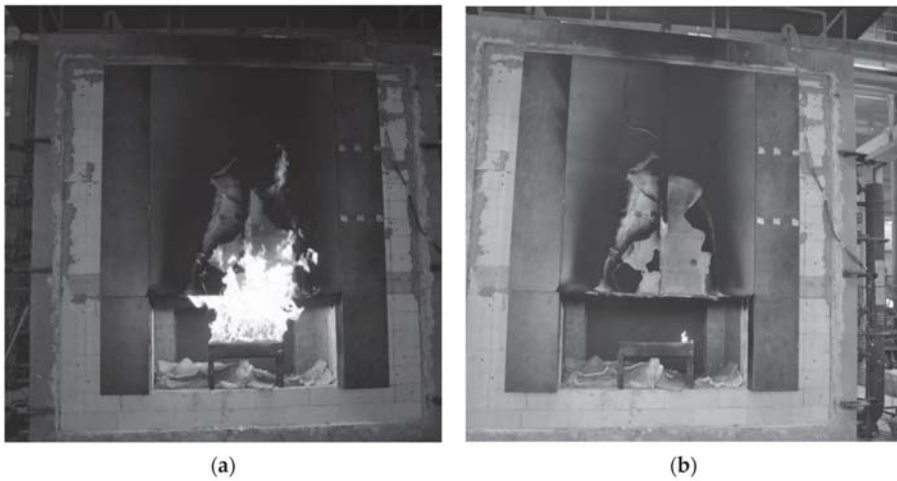
Figure 4. Large-scale model: (**a**) during the study; (**b**) after the study, with the indication of the sampling location.

Figure 5. Test stand for acoustic emission measurements and the fibre cement board used during the test: (**a**) view of the testing machine; (**b**) view of the specimen during its destruction.

The analysis of the obtained results of three-point bending tests took into account the course of bending stresses σ_m, the modulus of rupture (*MOR*), the number of EA events N_{zd} and the sum of EA events $\sum N_{zd}$. The modulus of rupture (*MOR*) was determined from the standard formula [5]:

$$MOR = \frac{3Fl_s}{2b\ e^2} \tag{1}$$

where:

MOR—modulus of rupture [MPa],
F—load (force) [N],
l_s—length of the support span [mm],
b—sample width [mm],
e—sample thickness [mm].

In addition, in order to verify the degraded element samples taken after testing, a structure analysis was performed on a Keyence VHX-7000 series microscope. The digital microscope used to verify the structure of the fibre cement boards and the test stand are shown in Figure 6.

Figure 6. Keyence VH×-7000 series digital microscope.

The device was equipped with a digital microscope unit which, depending on the type of lens, allowed taking pictures within the zoom range of $\times 20$–$\times 4000$ (a wide-angle lens was used in this study, as well as a standard lens with a maximum zoom of $\times 200$).

4. Study Results

The evaluation of the destruction of fibre-cement board structures under the influence of fire was made through the analysis of EA signals recorded during the course of the three-point bending test and was based on EA descriptors such as the number of events N_{zd} and the sum of events $\sum N_{zd}$. Figures 7–10 show a recording of the event rate N_{zd} and bending stress σ_m versus time for selected samples designated D3, D4, D5 and, for comparison, an untreated reference board. Table 1 summarises the resulting modulus of rupture (*MOR*) values and $\sum N_{zd}$ event sum values for the tested samples.

Table 1. Summary of averaged modulus of rupture (*MOR*) and example event sum $\sum N_{zd}$.

Sample Identification	Bending Strength (*MOR*) [MPa]	Sum of Events $\sum N_{zd}$ [–]
Reference	43.45	1715
D3	1.72	228
D4	14.83	475
D5	0.22	198
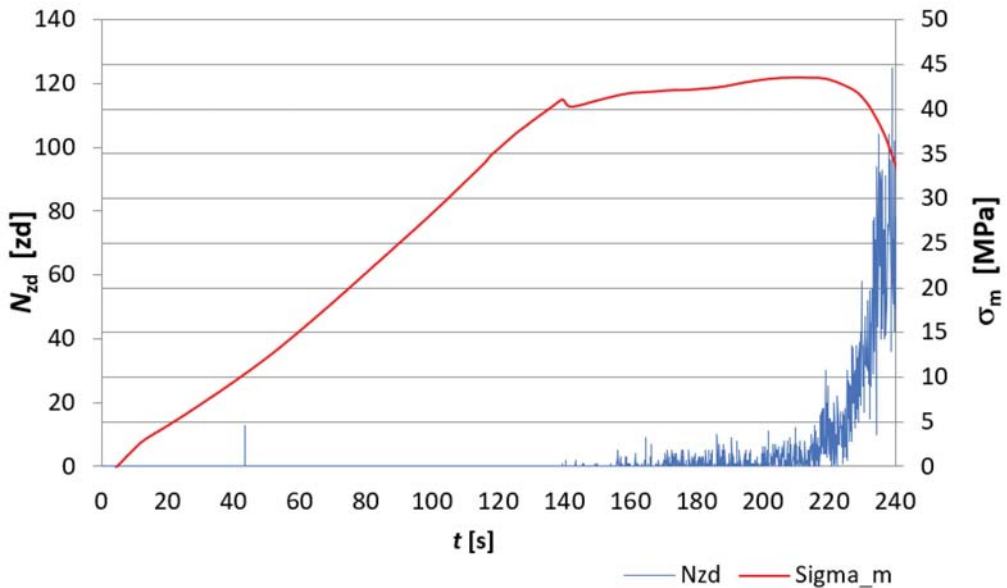
Figure 7. Recording of the event rate N_{zd} and bending stress σ_m versus time for the reference board.
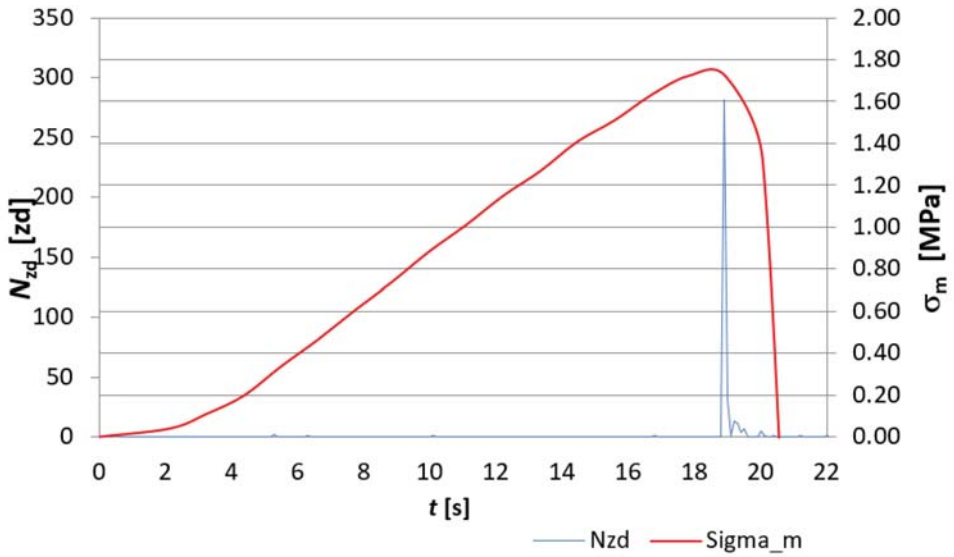
Figure 8. Recording of the event rate N_{zd} and bending stress σ_m versus time for the D3 board.
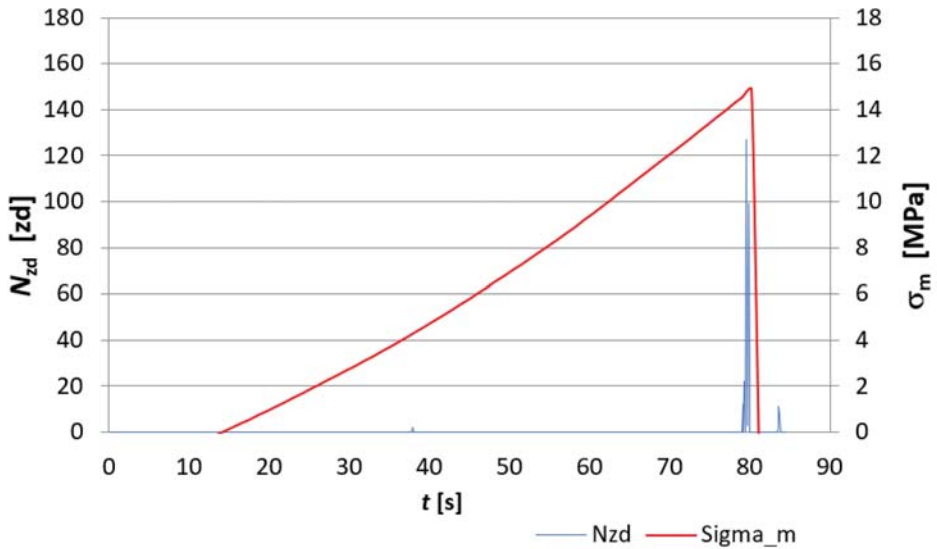
Figure 9. Recording of the event rate N_{zd} and bending stress σ_m versus time for the D4 board.
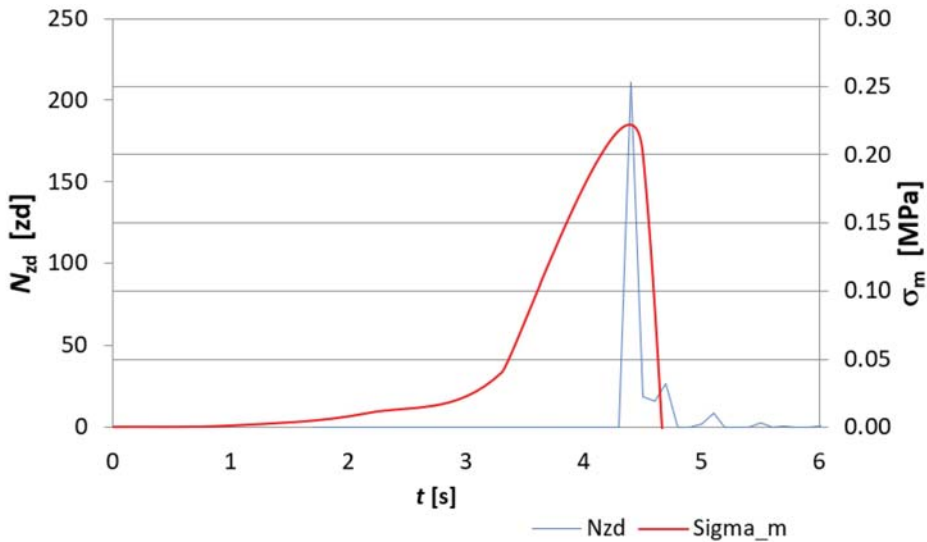
Figure 10. Recording of the event rate N_{zd} and bending stress σ_m versus time for the D5 board.

When analysing Figures 7–10, it is clear that the fire had a clear effect on the values of the EA descriptors recorded in the three-point bending test of the fibre cement boards in question. Thus, the recording of the rate of N_{zd} events as a function of time for the reference board (Figure 7) differed significantly from that obtained for the fire-treated boards. In the case of the reference board, it can be seen that from about the 140th second of the test, the rate of N_{zd} events started to increase steadily until the maximum value of the *MOR* modulus of rupture was reached, at which point there was a clear spike in this descriptor. In the case of the samples labelled D3, D4 and D5 (Figures 8–10, respectively), one can see a completely different course of degradation. Namely, there was a sharp spike (peak) in the recorded EA event rate values around the time the test samples reached the modulus of rupture (*MOR*). Analysing the results presented in Table 1, it can be seen that a significantly higher sum of EA events was recorded for the reference sample. In contrast, for samples D3, D4 and D5, a clear decrease in the recorded sum of EA events can be seen. A trend can be observed: as the temperature to which the tested samples were exposed and the time of exposure increased, the sum of EA events decreased. In analysing the values of the obtained modulus of rupture (*MOR*), a similar trend was noticed. The reference plate had the highest modulus of rupture (*MOR*) (43.45 MPa). With the increase of the temperature to which the boards were subjected during the fire, there was a clear decrease in the modulus of rupture (*MOR*), ranging from a value of 14.83 MPa for board D4 through to 1.72 MPa for board D3, with a value of 0.22 MPa for board D5.

The above results indicate that as the temperature and the time of its action on the subject boards during the fire increased, the nature of the sample degradation course during the three-point bending test changed significantly, as can be seen from the recorded acoustic emission descriptors and the obtained modulus of rupture s (*MOR*). It can be concluded unequivocally that a high temperature has a destructive effect on the structure of fibre cement boards. Thus, analysing the results obtained using the acoustic emission method shown in Figures 7–10, it can be seen that the boards subjected to fire were damaged by brittle fracture when the modulus of rupture (*MOR*) was reached. This was evidenced by the EA event rate recording, which was essentially a single peak compared to what observed for the reference board. On this basis, the authors conclude that a high temperature caused damage to the cellulose fibres (pyrolysis) contained in the board structure. The brittle fracture recorded during the tests may be indicative of the complete pyrolysis of the

cellulose fibres and, therefore, of the resulting structure of the board, consisting only of the cement matrix. This was particularly evident in samples D3 and D5.

In order to verify the destruction of the structure of the boards subjected to fire, the authors additionally performed an analysis of the fracture structure using a digital microscope. Figure 11 shows a view of the fracture of the reference sample after the three-point bending test. It should be noted that the fractured sample showed fibres that were destroyed by pulling or tearing, as well as delamination—the result of manufacturing technology.
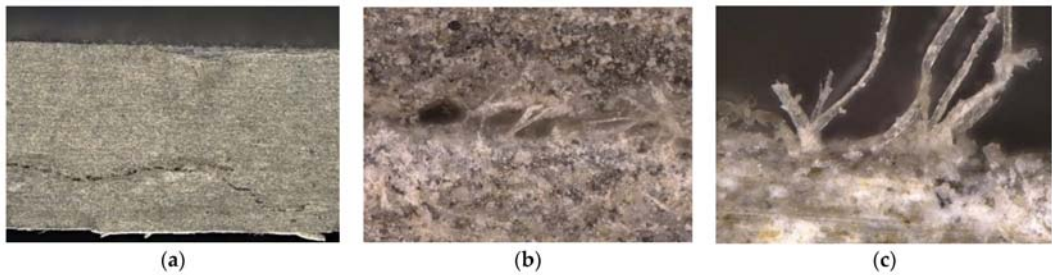
Figure 11. View of the reference sample under a digital microscope: (**a**) magnification ×20, (**b**) magnification ×150, (**c**) magnification ×400.

Figure 12 shows a view of the sample D5 fracture after the three-point bending test. A change in the structure of the board could be seen through the precipitation of individual cement matrix materials (known as crystallisation) and the delamination of the fibre cement board. Delamination was caused by the temperature gradient between the outer surface and the inner surface (mounted from the platform) and the total thermal expansion of the material. In addition, complete pyrolysis of the fibres could be seen—caverns and voids left after the melting of the fibres (Figure 12b). The fracture shape was straight, which indicated that it followed the shortest line. From this figure, it is clear that the sample was completely destroyed.

Figure 12. Example view of the D5 sample under a digital microscope: (**a**) magnification ×150, (**b**) magnification ×20.

5. Discussion

All samples were taken from the actual façade model, from materials that fell off during the test. It should be noted that the samples did not show a trend for the measured values, the lowest modulus of rupture (*MOR*) being that of sample D5, which was located closest to the combustion chamber. The higher modulus of rupture (*MOR*) was found FOR sample D3, which was located 120 cm above the combustion chamber. In contrast, sample D4 located 80 cm above the combustion chamber showed a much higher strength (*MOR*)

than samples D3 and D5. It should be noted that for all locations sampled, the fibre melting point and the temperature at which the cement matrix degraded were exceeded, which, for the area directly above the fire source, amounted to a maximum of 28% of the number of EA events of the reference sample. The loss of the modulus of rupture (*MOR*) is also worth noting. For the degraded sample D4, this was up to 34% (14.83 MPa) of the strength of the reference sample (43.45 MPa).

When we examined sample degradation by the action of fire temperatures, we observed a completely different course of degradation of the tested boards with respect to the reference board. Namely, there was a sharp spike (peak) in the recorded EA event rate values around the time the test samples reached the modulus of rupture (*MOR*). This indicates that destruction occurred by brittle high-energy fracture, with a low number of EA events. This was also found in other studies. Szymków, in his work [18], also showed a similar convergence—i.e., degraded samples were more brittle, were characterized by the lack of the "flow" phase, showed brittle high-energy cracking with a small number of EA events.

The conducted tests showed that a significantly higher sum of EA events was recorded for the reference sample. In contrast, a clear decrease in the recorded sum of EA events was seen for the fire-treated samples. The following trend was observed: as the temperature to which the tested samples were exposed and the time of exposure increased, the sum of EA events decreased.

The analysis of the obtained modulus of rupture (*MOR*) values showed a similar trend. The reference plate had the highest modulus of rupture (*MOR*) (43.45 MPa). With the increase of the temperature to which the boards were subjected during the fire, there was a clear decrease in the modulus of rupture (*MOR*), ranging from a value of 14.83 Mpa for board D4 through to 1.72 Mpa for board D3, with a value of 0.22 Mpa for board D5.

Digital microscope studies of the degraded samples indicated complete pyrolysis of the fibres and crystallisation of the internal composite structure. We also observed significant delamination of the sample due to the temperature gradient acting on it, i.e., the outer and inner layers of the cladding surface, as well as a significant value of the expansion of the sample (caused by high temperatures).

6. Summary

The effects of high temperatures are inherently destructive to most building products. Heat resistance is defined as the period of time during which a product retains the desired properties. It is worth noting that large-scale studies provide very significant opportunities for the analysis of façade cladding exposed to high temperatures caused by fire. Fire temperatures occurring directly above the fire source are critical for this composite and reach values between 500 °C and 700 °C. In order to determine the destructive effect of high temperature on the structure of the fibre cement boards tested, samples were examined in a three-point bending test using the acoustic emission method. In addition, in order to analyse further the effect of fire on the structure of the boards, board samples were observed using a digital microscope. The fibre cement boards tested in this study showed different ranges of resistance to fire. The most important observations and conclusions formulated by the authors on the basis of the obtained results are summarised below.

- In the destruction critical zone, i.e., where the fibre melting point and the temperature at which the cement matrix is destroyed have been exceeded, the samples cannot be used repeatedly.
- Critically degraded samples are destroyed by a sharp spike (peak) in the recorded EA event rates.
- Research using a digital microscope is sufficient to assess the complete degradation of the fibre cement composite materials, in terms of the assessment of fibre pyrolysis and the crystallization of the internal structure of the composite

Summarising the information presented above, the authors would like to point out that the tests carried out in this study are very important from the point of view of construction

practice, particularly due to the fact that little information is available in the literature on the behaviour of ventilated façades and, thus, of the cladding installed on them at high temperatures, i.e., under fire conditions. Furthermore, it should be emphasised that the above tests are only pilot tests. The authors are investigating fire-exposed fibre cement boards through other methods. The results of these studies will be the subject of further scientific work.

Author Contributions: Conceptualization, K.S.; Data curation, P.S.; Investigation, T.G.; Project administration, Ł.Z.; Validation, T.G.; Writing—original draft, Ł.Z. All authors have read and agreed to the published version of the manuscript.

Institutional Review Board Statement: Not applicable.

Informed Consent Statement: Not applicable.

Data Availability Statement: The data presented in this study are available on request from the corresponding author.

Conflicts of Interest: The authors declare no conflict of interest.

References

1. Available online: http://www.equitone.com (accessed on 20 August 2021).
2. Available online: http://www.esal.si (accessed on 20 August 2021).
3. Available online: http://www.cembrit.com (accessed on 20 August 2021).
4. Callister, W.D.; Tethwisch, D.G. *Materials Science and Engineering: An introduction*, 10th ed.; Wiley: Hoboken, NJ, USA, 2009; ISBN 978-1-119-40549-8.
5. Mansouri, I.; Shahheidari, F.S.; Ali Hashemi, S.M.; Farzampour, A. Investigation of steel fiber effects on concrete abrasion resistance. *Adv. Concr. Constr.* **2020**, *9*, 367–374. [CrossRef]
6. *EN 12467*, Fibre-Cement Flat Sheets—Product Specification and Test Methods.
7. Schabowicz, K.; Sulik, K.; Zawiślak, Ł. Reduction of load capacity of fiber cement board facade cladding under the influence of fire. *Materials* **2021**, *14*, 1769. [CrossRef]
8. Schabowicz, K.; Zawiślak, Ł.; Sulik, P. Identification of the destruction model of ventilated facade under the influence of fire. *Materials* **2021**, *13*, 2387. [CrossRef] [PubMed]
9. Bednarek, Z.; Drzymała, T. Fire Temperature Influence on Strength Parameter in Fiber-reinforced Concrete. *Zesz. Nauk. SGSP* **2008**, *36*, 61–84. (In Polish)
10. Lublóy, E.; Kopecskó, K.; Balázs, G.L.; Restas, A.; Szilágyi, I.A. Improved fire resistance by using Portland-pozzolana or Portland-fly ash cement. *J. Therm. Anal. Calorim.* **2017**, *129*, 925–936. [CrossRef]
11. Xu, Y.; Wong, Y.L.; Poon, C.S.; Anson, M. Influence of PFA on cracking of concrete and cement paste after exposure to high temperatures. *Cem. Concr. Res.* **2003**, *33*, 2009–2016. [CrossRef]
12. Heikal, M.; El-Didamony, H.; Sokkary, T.M.; Ahmed, I.A. Behavior of composite cement pastes containing microsilica and fly ash at elevated temperature. *Constr. Build. Mater.* **2003**, *38*, 1180–1190. [CrossRef]
13. Doleželová, M.; Scheinherrová, L.; Krejsová, J.; Vimmrová, A. Effect of high temperatures on gypsum-based composites. *Constr. Build. Mater.* **2018**, *168*, 82–90. [CrossRef]
14. Sanchayan, S.; Foster, S.J. High temperature behaviour of hybrid steel–PVA fibre reinforced reactive powder concrete. *Mater. Struct.* **2016**, *49*, 769–782. [CrossRef]
15. Abdullah Shukry, N.; Ahmad Sekak, K.; Ahmad, M.; Bustami Effendi, T. Characteristics of Electrospun PVA-Aloe vera Nanofibres Produced via Electrospinning. In *Proceedings of the International Colloquium in Textile Engineering, Fashion, Apparel and Design 2014 (ICTEFAD 2014)*; Springer: Singapore, 2014; pp. 7–12. [CrossRef]
16. Kalifaa, P.; Chene, G.; Galle, C. High-temperature behaviour of HPC with polypropylene fibres from spalling to microstructure. *Cem. Concr. Res.* **2001**, *31*, 1487–1499. [CrossRef]
17. Schroeter, J.; Felix, F. Melting cellulose. *Cellulose* **2005**, *12*, 159–165. [CrossRef]
18. Szymków, M. Identification of the Degree of Destruction of Fiber-Cement Boards under the Effects of High Temperature. Raport Serii PRE nr 9/2018. Ph.D. Thesis, Wydział Budownictwa Lądowego i Wodnego, Politechnika Wrocławska, Wrocławska, Poland, 2018. (In Polish).
19. Drzymała, T.; Ogrodnik, P.; Zegardło, B. Effects of high temperature on flexural strength of concrete composites modified by addition of polypropylene fibres. *Tech. Transp. Szyn.* **2016**, *23*, 82–86. (In Polish)
20. Farzampour, A. *Compressive Strength of Concrete, A Compressive Behavior of Concrete under Environmental Effects*; IntechOpen: London, UK, 2019. [CrossRef]
21. Farzampour, A. Temperature and humidity effects on behavior of grouts. *Adv. Concr. Constr.* **2017**, *5*, 659–669.

22. Chalangaran, N.; Farzampour, A.; Paslar, N. Nano Silica and Metakaolin Effects on the Behavior of Concrete Containing Rubber Crumbs. *CivilEng* **2020**, *1*, 264–274. [CrossRef]

23. Adamczak-Bugno, A.; Świt, G.; Krampikowska, A. Fibre-Cement Panel Ventilated Façade Smart Control System. *Materials* **2021**, *14*, 5076. [CrossRef] [PubMed]

24. Schabowicz, K. *Ventilated Façades. Fibre-Cement Board Production Technology and Testing Methods*; Oficyna Wydawnicza Politechniki Wrocławskiej: Wrocław, Poland, 2018. (In Polish)

Article

Effect of Confining Conditions on the Hydraulic Conductivity Behavior of Fiber-Reinforced Lime Blended Semiarid Soil

Abdullah Ali Shaker [1], Mosleh Ali Al-Shamrani [1,*], Arif Ali Baig Moghal [2,*] and Kopparthi Venkata Vydehi [2]

[1] Bugshan Research Chair in Expansive Soils, Department of Civil Engineering, College of Engineering, King Saud University, P.O. Box 800, Riyadh 11421, Saudi Arabia; shaker83@windowslive.com

[2] Department of Civil Engineering, National Institute of Technology, Warangal 506004, India; kvvydehi252@gmail.com

* Correspondence: shamrani@ksu.edu.sa (M.A.A.-S.); baig@nitw.ac.in (A.A.B.M.)

Abstract: The hydraulic properties of expansive soils are affected due to the formation of visible cracks in the dry state. Chemical stabilization coupled with fiber reinforcement is often considered an effective strategy to improve the geotechnical performance of such soils. In this study, hydraulic conductivity tests have been conducted on expansive clay using two different types of fibers (fiber cast (FC) and fiber mesh (FM)) exhibiting different surface morphological properties. The fiber parameters include their dosage (added at 0.2% to 0.6% by dry weight of soil) and length (6 and 12 mm). Commercially available lime is added to ensure proper bonding between clay particles and fiber materials, and its dosage was fixed at 6% (by dry weight of the soil). Saturated hydraulic conductivity tests were conducted relying on a flexible wall permeameter on lime-treated fiber-blended soil specimens cured for 7 and 28 days. The confining pressures were varied from 50 to 400 kPa, and the saturated hydraulic conductivity values (k_{sat}) were determined. For FC fibers, an increase in fiber dosage caused k_{sat} values to increase by 9.5% and 94.3% for the 6 and 12 mm lengths, respectively, at all confining pressures and curing periods. For FM fibers, k_{sat} values for samples mixed with 6 mm fiber increased by 12 and 99.2% for 6 and 12 mm lengths, respectively for all confining pressures at the end of the 28-day curing period. The results obtained from a flexible wall permeameter (FWP) were compared with those of a rigid wall permeameter (RWP) available in the literature, and the fundamental mechanism responsible for such variations is explained.

Keywords: confining pressure; expansive clay; fiber; flexible wall permeameter; hydraulic conductivity; lime; rigid wall permeameter

1. Introduction

Desiccation heave and shrinkage characteristics of expansive soils have limited their application as a subbase for roadway pavements material in arid and semiarid climates. Randomly oriented fibers are often used to reduce the problems associated with clayey soils. The cost-effectiveness and chemical inertness of the fibers makes them useful as a soil additive [1,2]. To develop the bonding between soil grains, researchers used chemical stabilizers such as lime, cement, EICP, MICP, biopolymer, etc., in combination with fiber to improve the geotechnical properties [3–6]. The addition of fiber to the soil increases shear strength [7], reduces swelling [8,9], reduces desiccation cracking [10], and increases hydraulic conductivity (k) values [11,12]. Although fiber inclusion reduces the desiccation cracking, an increase in k values of soil limited its application in the subbase for the construction of pavements. However, the resultant properties of fiber-reinforced soil depend on the fiber type, dosage, and aspect ratio [13]. Experimental investigations on medium plasticity clay with polypropylene fiber (at 2%) inclusion results in an increase in k values by 10^{-3} cm/s compared to untreated clay. The fiber dosage up to 0.5% resulted in acceptable hydraulic conductivity values [12]. On the contrary, k values of lime-amended high-plastic clay reduced by 10^{-2} cm/s with a fiber dosage of 0.2% and length of 6 mm at the end of a

28-day curing period compared to specimens without curing [14]. To meet the requirements of hydraulic conductivity values for lime-stabilized high-plastic clay reinforced with fiber, an optimum length of 10.5 mm with 0.5% dosage for a 15-day curing period is proposed using the response surface method [15]. On the other hand, few researchers have studied the effect of lime on the hydraulic conductivity of soils. The results showed an increase in the hydraulic conductivity with lime [16–18]. In addition, the k value of lime-treated soil increased at initial curing periods and then decreased at higher curing periods [19,20]. Earlier research concentrated on evaluating the hydraulic conductivity of fiber-reinforced soil using a conventional rigid wall permeameter (RWP).

However, for a compacted clay as a subgrade layer, the surcharge load coming on it plays a major role in controlling the hydraulic conductivity values. According to Daniel et al. [21], complete control over imposed stress on the soil is not possible, resulting in the inability of RWP to measure vertical and horizontal deformations. To overcome these limitations, a flexible wall permeameter (FWP) was introduced, in which back pressure saturation and the minimization of sidewall leakages facilitate in determining the accurate value of saturated hydraulic conductivity values (k_{sat}) [22]. Therefore, to simulate the real field conditions, researchers proposed using FWP to evaluate k_{sat} values. Experimental investigations on sand–Alqatif clay mixture revealed that k_{sat} values reduced with an increase in confining pressure [23]. The generalized mechanism proposed for the reduction of k_{sat} values using FWP is that an increase in confining pressure reduces the effective pore spaces, and an increase in unit weight leads to a reduction of effective flow paths.

There are limited studies on the evaluation of k_{sat} values for fiber-reinforced soil using FWP. In lieu of this, the present research evaluates the k_{sat} values of a lime-stabilized Al-Ghat soil with fiber inclusion using FWP. The effect of dosage, length of the fiber, and curing period are considered in evaluating the k_{sat} values. Then, the values obtained from the study are compared with the values in the literature [13] to evaluate the effectiveness of FWP in the accurate measurement of k_{sat} values.

2. Materials

2.1. Soil

Locally available natural soil sourced from Al Ghat (26°1′36″ N, 44°57′39″ E) town, Riyadh Province, Saudi Arabia, was selected for the present study. Disturbed samples were obtained from open test pits excavated to a depth of 1.5–3.0 m below the ground surface. The physical characterization of soil (carried out in accordance with relevant ASTM standards) seen from Table 1 reveals that the selected soil is a high plastic clay (CH) as per the Unified Soil Classification System (USCS), and it is expansive in nature [13].

Table 1. Physical properties of studied soil.

Physical Property	Value
Liquid Limit (%)	66
Plastic Limit (%)	32
Plasticity Index (%)	34
Shrinkage Limit (%)	15
Linear Shrinkage (%)	31
% Finer No.200 sieve	87
Natural Moisture Content (%)	3.2
Maximum Dry Density (kN/m^3)	16.08
Optimum Water Content (%)	25
Specific Gravity	2.85
Specific Surface Area (BET Method) (m^2/g)	27.08
USCS Classification	CH
Color	light brown

2.2. Fiber

Two types of fibers FM 300 and FC 500 supplied by Propex operating company (Chattanooga, TN, USA) were used for the present study. The physicochemical properties of two fibers are provided in Table 2. The length of fiber adopted for the experimental work is 6 mm and 12 mm for both FM and FC (Figure 1); the dosage of each fiber is fixed at 0.2% and 0.6% by weight of dry soil mass.

Table 2. Physicochemical properties of fibers.

Property	Fiber Cast 500 (FC)	Fiber Mesh 300 (FM)
Tensile Strength	440 N/mm^2	330 N/mm^2
Specific Gravity	0.91	0.91
Electrical Conductivity	Low	Low
Acid and Salt Resistance	High	High
Melt Point	324 °F (162 °C)	324 °F (162 °C)
Ignition Point	1100 °F (593 °C)	1100 °F (593 °C)
Thermal Conductivity	Low	Low
Water Absorption	Nil	Nil
Alkali Resistance	Alkali Proof	Alkali Proof
Surface Texture	Relatively Smooth	Rough with Protrusions
Shape	Fibrillated	Monofilament
Aspect Ratio (L/D)	42.8 and 120	193.5 and 387
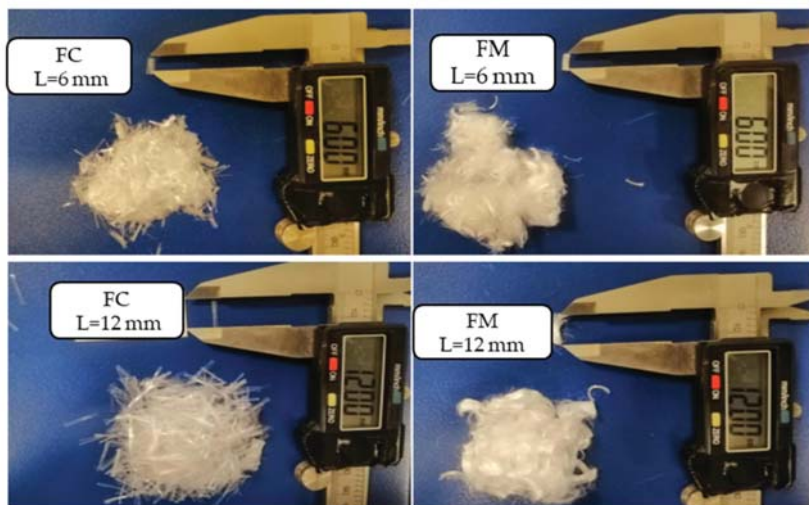
Figure 1. Fibers used in the study.

2.3. Lime

Locally available commercial-grade hydrated lime is used as a soil stabilizer. The percentage of lime was standardized at 6% for all tests by dry weight of the soil. This optimum quantity of lime was fixed relying on the soil–pH response upon the addition of lime [14,24].

3. Experimental Program

3.1. Sample Preparation

The expansive soil obtained from the field was air-dried, pulverized, and sieved using sieve No. 20. The soil fraction is mixed with optimum lime content (i.e., 6% of lime added to the soil by dry weight) and fiber (FC and FM) at selected dosages of 0.2% and 0.6%. The

lengths of fibers were kept at 6 mm and 12 mm, resulting in 17 mix combinations in triplicates (including untreated soil) for the entire experimental work. A total of 51 specimens (including triplicates) were tested in FWP. Previous studies on the compaction properties of fiber-reinforced soil have revealed that the fiber inclusion had little or no effect on variations in maximum dry density (MDD) and optimum moisture content (OMC) of various mix proportions [12,25,26]. Based on this, all the specimens in the present study were molded at fixed MDD (16.08 kN/m^3) and corresponding OMC (25%). Soil, lime, and fibers at various proportions were mixed in dry condition; then, the target moisture content was added and mixed thoroughly to obtain a homogenous mixture. Statically compacted specimens of 70 mm diameter and 35 mm height were kept in a desiccator at a relative humidity > 95% and cured for a period of 7 and 28 days.

3.2. Testing Procedure

The evaluation of saturated hydraulic conductivity (k_{sat}) was performed in accordance with ASTM D5084—Method A [27], using a flexible wall constant head permeameter. A schematic diagram of the test setup used in the present study is shown in Figure 2. At the end of each curing period, the prepared specimens were transferred to the cell. Porous stone and filter paper were kept on the top and bottom end of the specimen. A rubber membrane was used to confine the specimen; two O-rings placed at both ends provide a complete seal against any water leakage. The cell was filled with distilled water, and the drainage line at the bottom and top of the cell was flushed until no more air bubbles were observed inside the cell. The various stages involved in the testing phase are described below.
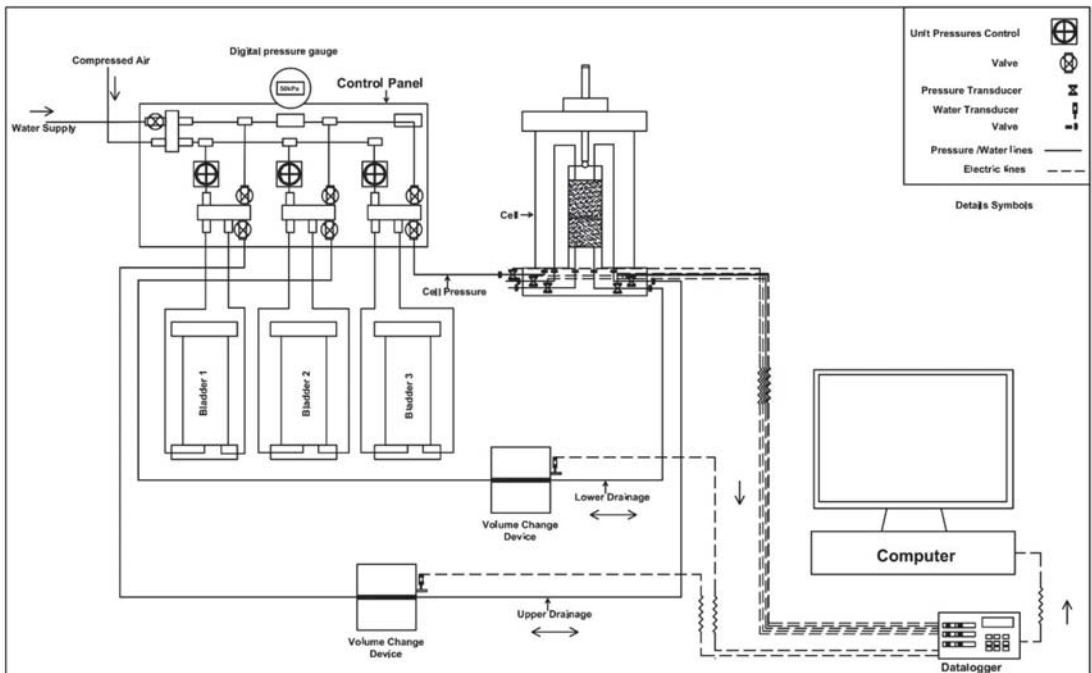
Figure 2. Schematic diagram of a flexible wall constant head permeameter.

I.   Back-Pressure Saturation:

This stage involved a simultaneous increase of both the cell pressure (CP) and the back pressure (BP) to reduce air bubbles or voids within the test sample. In this study, the effective confining pressure (defined as cell pressure minus back pressure, CP-BP) was kept at approximately 10 kPa throughout the saturation process for all specimens. This effective

confining pressure was selected to maintain sample stability without significantly affecting the stress history of the specimen. The (CP-BP) was maintained for one day. Specimen saturation was verified by measuring the B coefficient (defined as the difference in pore-water pressure (Δu), divided by the difference in pressure of the cells (ΔCP) of the porous material). A saturation check involved increasing the pressure of the cell on the specimen and monitoring the pore pressure response using a pore pressure transducer connected at the top and bottom of the specimen. The theoretical B value for a fully saturated specimen reaches 1. However, in fluid flow experiments, specimens were considered saturated with the assurance of B values ≥ 0.95. If the B value is less than 0.95, the above procedure of increasing CP and BP and B value checking was repeated until the B value is >0.95.

II. Consolidation:

The specimens were consolidated under effective confining pressure (CP-BP) of 50, 100, 200, and 400 kPa. Effective confining pressure was applied by increasing the cell pressure to the level necessary to develop the desired effective confining pressure while maintaining a constant back pressure. Drainage was allowed from the base of the specimen. The outflow volumes were recorded to confirm that primary consolidation has been completed before the initiation of the next stage.

III. Permeation:

This stage involved inducing flow-through test specimens by applying a differential pressure between the top and bottom of the specimens. The differential pressure was applied by reducing the top pressure and increasing the bottom pressure such that the difference was equal to the pressure head corresponding to the desired hydraulic gradient. To speed up the test, the hydraulic gradient was fixed at 30 [27]. The water inflow and outflow were continuously monitored until a steady-state condition was established as defined by the inflow rate being equal to the outflow rate.

4. Results and Discussion

4.1. Effect of Confining Pressure

Figures 3–6 show the variation in saturated hydraulic conductivity (k_{sat}) values for lime-treated (at 6%) expansive soil with fiber inclusion (0.2% and 0.6%) at various effective confining pressures at the end of each curing period.

In general, the k_{sat} values reduced with an increase in confining pressure for all the tested specimens irrespective of fiber type, dosage, and curing period. A noticeable reduction in k_{sat} values is observed when the confining pressure is increased from 50 to 200 kPa. The flow of water through the compacted specimen depends on the availability and connectivity of inter and intra-aggregate flow channels, and the k value is directly related with inter-aggregate flow paths [28,29]. Increased confining pressure contributes to a significant reduction in inter-aggregate flow paths compared to intra-aggregate flow paths. Due to this, with the increase in pressure from 50 to 200 kPa, a significant reduction in inter-aggregate flow channels causes a decrease in k_{sat} values. A further increment in confining pressure from 200 to 400 kPa has less effect in reducing these flow paths and leads to a marginal reduction in k_{sat} values for all the tested specimens.

For any type of soil, the higher the confining pressure, the lower the k_{sat} values, irrespective of the permeating liquid [23]. Increased confinement causes a reduction in pore spaces and increases the unit weight, thus reducing the hydraulic conductivity [30]. Similar results were reported by de Brito Galvão et al. [31] and Shaker and Elkady [32].

The boundary condition adopted in the present study is highly correlated with the field conditions for the case of a subbase for pavements material in which the subbase material will be subjected to surcharge load coming on it.
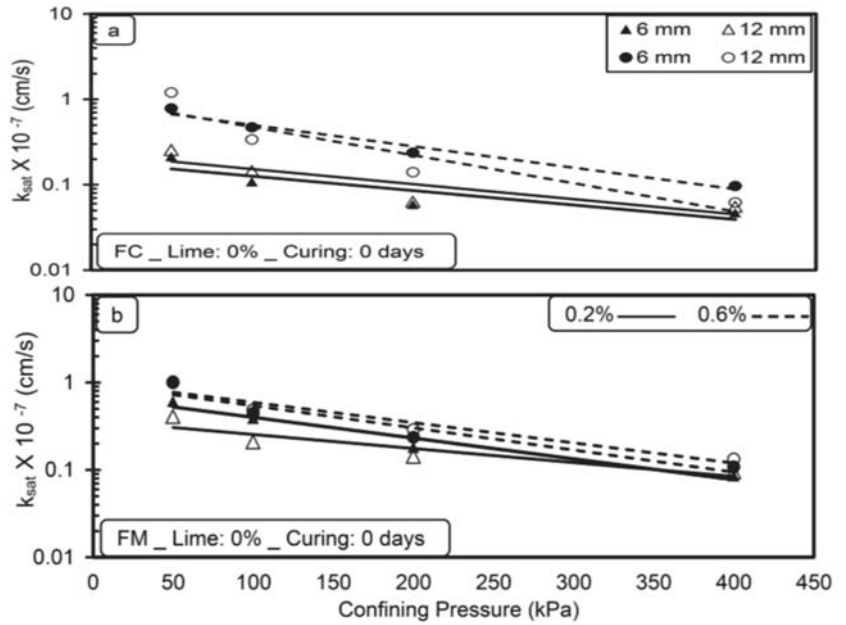
Figure 3. Variations in saturated hydraulic conductivity (k_{sat}) with confining pressure (**a**) FC (**b**) FM without lime treatment (without curing).
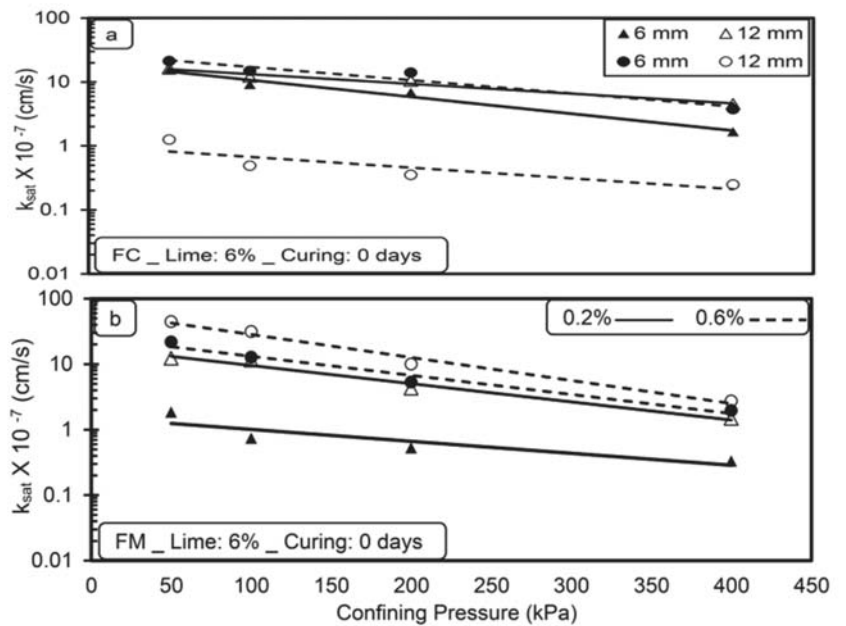
Figure 4. Variations in saturated hydraulic conductivity (k_{sat}) with confining pressure (**a**) FC (**b**) FM with lime treatment (without curing).
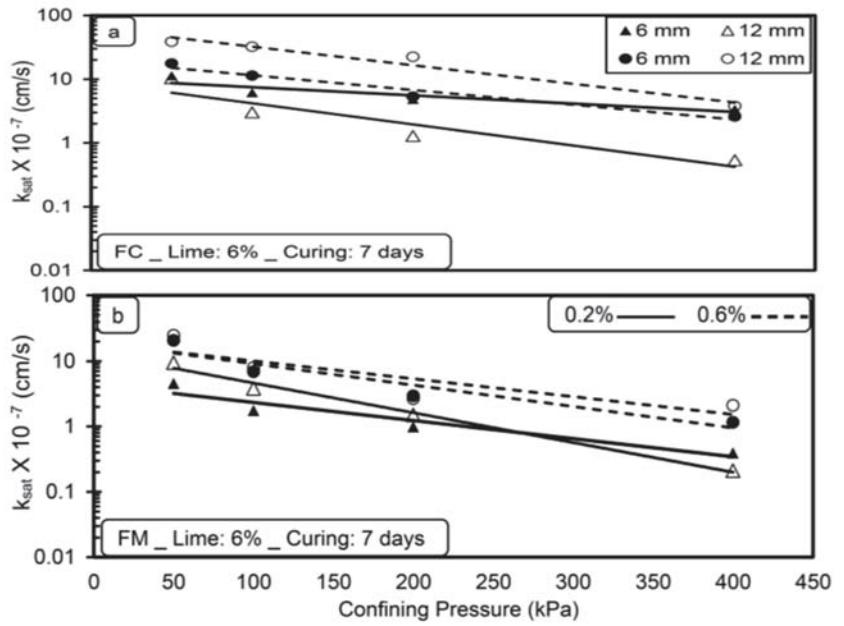
Figure 5. Variations in saturated hydraulic conductivity (k_{sat}) with confining pressure (**a**) FC (**b**) FM with lime treatment (after 7-day curing period).
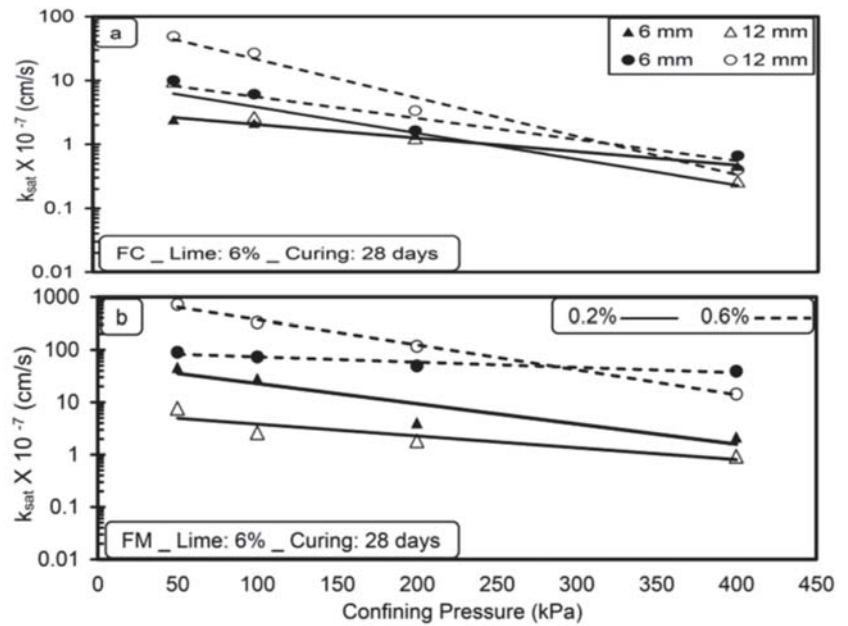
Figure 6. Variation of saturated hydraulic conductivity with confining pressure (**a**) FC (**b**) FM with lime treatment (after 28-day curing period).

4.2. Effect of Lime

Figure 7 shows the variations in (k_{sat}) values with and without lime treatment for fiber-reinforced clay (FC and FM) without any curing. The addition of 6% lime causes an increase in k_{sat} values in the order of 10^{-1} cm/s for fiber-reinforced clay compared to that of an untreated case. The addition of lime leads to the aggregation of soil grains by Ca^{2+} ions, resulting in the formation of a flocculated structure [33,34]. The increased porosity of soil improves the connectivity of inter-aggregate pores and leads to an increase in k_{sat} values [31]. A similar trend is observed for all the tested specimens; however, the rate of increase in k_{sat} values is a function of fiber type, dosage, and length.
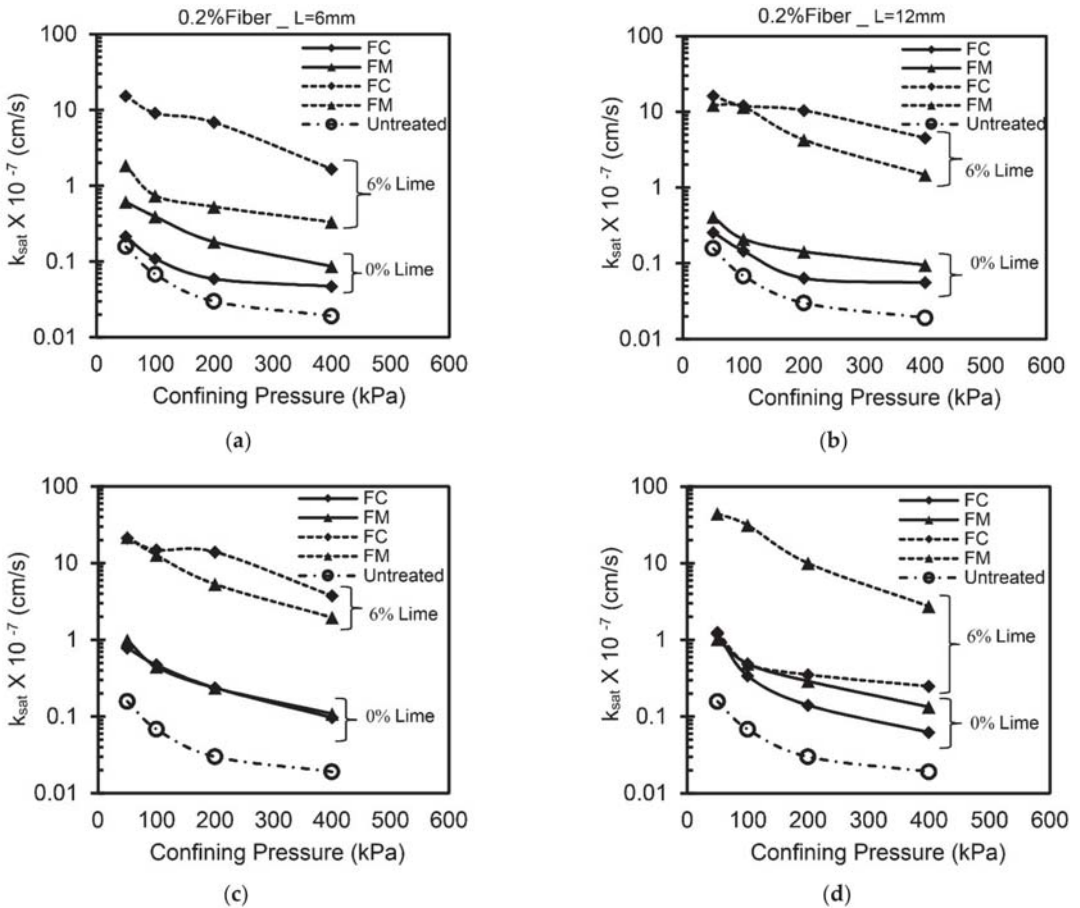
Figure 7. Variation of saturated hydraulic conductivity with lime content and confining pressure (**a**) 0.2%, 6mm; (**b**) 0.2%, 12mm; (**c**) 0.6%, 6mm; (**d**) 0.6%, 12mm.

4.3. Effect of Curing Time

The effect of the curing period on the k_{sat} values of all samples with lime-treated expansive clay under different confining pressures is illustrated in Figure 8. Lime-treated soil reinforced with 0.2% FC (both 6 mm and 12 mm) exhibited a reduction in k_{sat} values with an increase in curing period, as seen from Figure 8a. This is attributed to the fact that the cementitious compounds formed at a higher curing period fill the void spaces within the clay and the soil becomes less conductive [13]. At 0.6% FC, for 6 mm length

of fibers, k_{sat} values reduced marginally at a lower confining pressure (at 50 kPa), and a significant reduction is observed at higher confining pressure (at 400 kPa). Whereas, an increase in fiber length to 12 mm leads to an increase in k_{sat} values up to 7 days of curing and thereafter reduced at the end of a 28-day curing period (Figure 8b). This might be due to an increase in the length of fiber creating more drainage paths during the first 7 days of curing. However, after a 28-day curing period, this effect is dominated by the formation of cementitious compounds, which reduces the k_{sat} values with 12 mm fiber length.
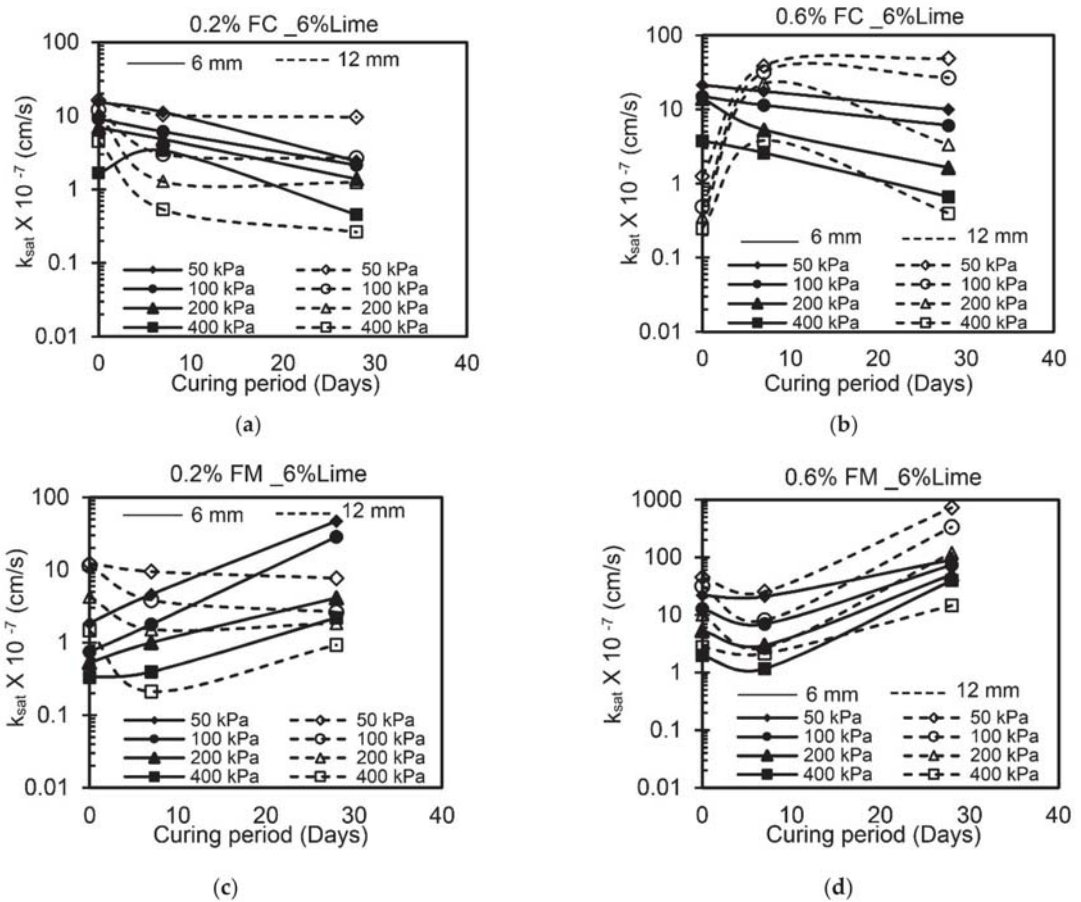
Figure 8. Variation of k_{sat} values with curing period and confining pressure (**a**) FC_0.2% (**b**) FC_0.6% (**c**) FM_0.2% (**d**) FM_0.6%.

Figure 8c,d depict the variations in k_{sat} values with FM addition at various curing periods. The k_{sat} values increased at the end of the 28-day curing period with a marginal reduction at 7 days compared with specimens without curing. Irrespective of the dosage and length of FM, the k_{sat} values increased at all confining pressures.

4.4. Effect of Fiber

The results of permeability tests indicate that the k_{sat} is a function of fiber type, dosage, and length (Figure 8). With an increase in dosage from 0.2 to 0.6%, the k_{sat} values increased irrespective of the type of fiber for all specimens and are attributed to the randomly distributed fibers increasing the flow paths and causing free movement of the permeating liquid. In addition, an increase in fiber length from 6 to 12 mm results in an increase in

k_{sat} values. However, this effect is not significant at higher curing periods. Relatively, the inclusion of FM results in increased k_{sat} values compared to the inclusion of FC, especially at 0.6% dosage. This behavior is attributed to the fact that the FM has a rough surface with protrusions (Table 2) compared to FC, which facilitates in creating more drainage paths and leading to an increase in the resultant k_{sat} values; whereas FC having a relatively smooth texture offers fewer drainage paths and leads to a reduction in k_{sat} values at higher curing periods. Similar observations were reported by Abdi et al. [10] and Maher and Ho [11].

4.5. Comparison between Flexible Wall Permeameter and Rigid Wall Permeameter

A comparison of the k_{sat} values obtained from the present study (using FWP at 50 kPa) and Moghal et al. [13] (using RWP) is presented in Figures 9–11 for the same materials under the same testing conditions. From Figures 9 and 10, the k_{sat} values obtained from FWP are lower than the k_{sat} values obtained from RWP tests for the fiber-reinforced lime-treated soil specimens up to a 7-day curing period irrespective of fiber type. A notable variation in k_{sat} values (in the order of 10^{-1}) is observed for specimens with 0.6% dosage and 12 mm length of fiber (FC and FM) compared to other combinations. Since complete control over the confining pressure and back saturation of a specimen prior to testing is possible in FWP, it leads to an accurate measurement of vertical and horizontal deformations and thus k_{sat} values [21]. From the comparison, it is understood that FWP gives reliable results simulating the prevailing conditions in the field. For specimens cured for 28 days, the values of k_{sat} obtained using FWP are higher than those obtained from RWP (Figure 11). Experimental results on RWP have revealed that at higher curing periods (28 days), the leakage of liquid through the sidewalls of RWP due to loss of soil contact may significantly influence the k_{sat} values.
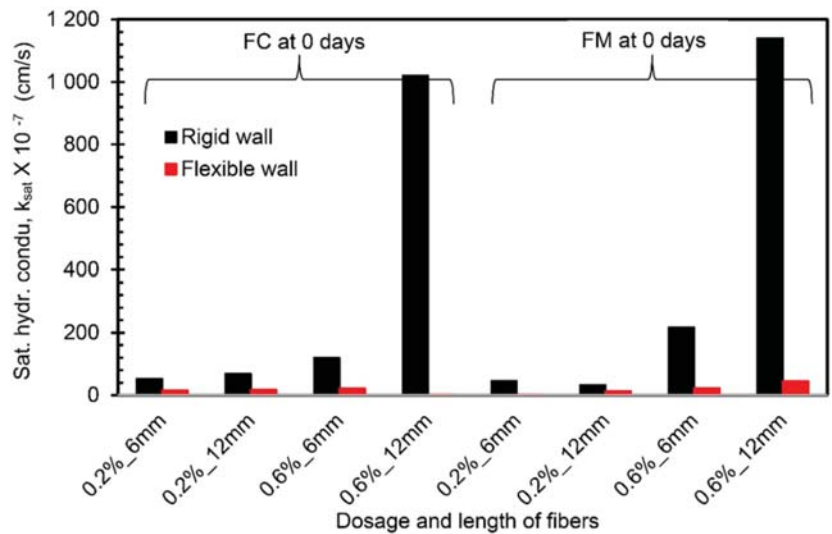
Figure 9. Comparison of hydraulic conductivity values from FWP and RWP (0-day curing period).
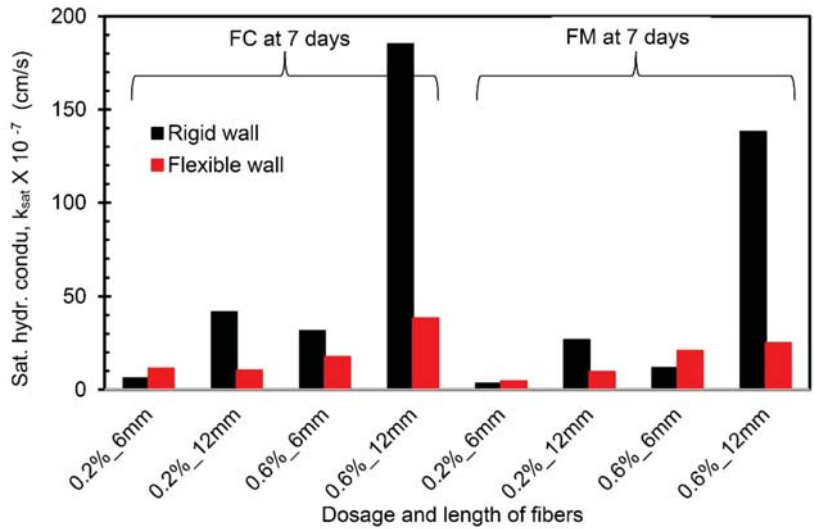
Figure 10. Comparison of hydraulic conductivity values from FWP and RWP (7-day curing period).
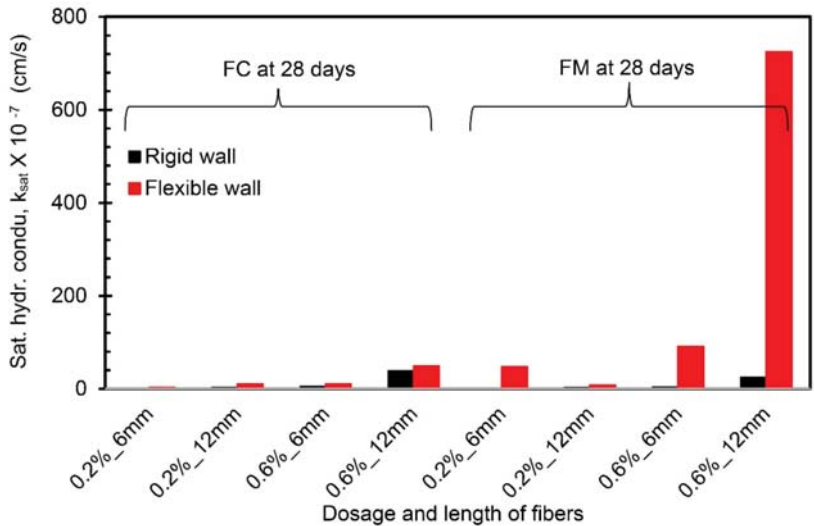
Figure 11. Comparison of hydraulic conductivity values from FWP and RWP (28-day curing period).

5. Conclusions

The present study evaluated the effect of fiber inclusion (FC and FM) on saturated hydraulic conductivity (k_{sat}) of lime-treated expansive clay. The constant head method using FWP at various confining pressures is adopted for experimental work. The k_{sat} values were evaluated at various dosages (0.2% and 0.6%), fiber lengths (6 and 12 mm), and curing periods (7 and 28 days). The following conclusions are drawn:

- The addition of lime significantly increased the k_{sat} values compared to untreated specimens.
- At lower confining pressures (50 to 200 kPa), the reduction in k_{sat} values is attributed to a decrease in inter-aggregate flow paths. This effect is not significant at higher confining pressure (400 kPa).

- An increase in the dosage and lengths of fiber leads to an increase in k_{sat} values irrespective of the fiber type.
- For FC at 0.2%, the k_{sat} values reduced at the end of the 28-day curing period irrespective of the length of fiber used. At 0.6% dosage, the values marginally increased for the 12 mm fiber length due to increased drainage paths.
- For FM, the k_{sat} values increased at the end of 28 days irrespective of dosage and fiber length at all confining pressures.
- k_{sat} values are directly dependent on the nature and type of fiber used, of which FM fibers with extended protrusions enable higher friction levels. For FC fibers, increased fiber dosage from 0.2 to 0.6% has caused an increase in k_{sat} values by 9.5% and 94.3% for the 6 and 12 mm lengths, respectively, at all confining pressures. In contrast, for a similar change in fiber amount for FM fibers, the k_{sat} values for samples mixed with 6 mm fiber increased by 12 and 99.2% for 6 and 12 mm lengths, respectively for all confining pressures.

Abbreviations

The following symbols are used in this paper:

B	Coefficient of Saturation
BP	Back Pressure
CP	Cell Pressure
FC	Fiber Cast
FM	Fiber Mesh
FWP	Flexible Wall Permeameter
k_{sat}	Saturated hydraulic conductivity
RWP	Rigid Wall Permeameter
ΔCP	The difference in cell pressure
Δu	The difference in pore-water pressure

References

1. Puppala, A.J.; Musenda, C. Effects of fiber reinforcement on strength and volume change in expansive soils. *Transp. Res. Rec.* **2000**, *C*, 134–140. [CrossRef]
2. Yetimoglu, T.; Salbas, O. A study on shear strength of sands reinforced with randomly distributed discrete fibers. *Geotext. Geomembr.* **2003**, *21*, 103–110. [CrossRef]
3. Moghal, A.A.B.; Bhaskar, C.S.C.; Basha, B.M. Effect of fibre reinforcement on CBR behaviour of lime-blended expansive soils: Reliability approach. *Road Mater. Pavement Des.* **2017**, *19*, 690–709. [CrossRef]
4. Moghal, A.A.B.; Lateef, M.A.; Mohammed, S.A.S.; Ahmad, M.; Usman, A.R.A.; Almajed, A. Heavy Metal Immobilization Studies and Enhancement in Geotechnical Properties of Cohesive Soils by EICP Technique. *Appl. Sci.* **2020**, *10*, 7568. [CrossRef]

5. Almajed, A.; Lateef, M.A.; Moghal, A.A.B.; Lemboye, K.K. State-of-the-Art Review of the Applicability and Challenges of Microbial-Induced Calcite Precipitation (MICP) and Enzyme-Induced Calcite Precipitation (EICP) Techniques for Geotechnical and Geoenvironmental Applications. *Crystals* **2021**, *11*, 370. [CrossRef]

6. Moghal, A.A.B.; Vydehi, K.V. State-of-the-art review on efficacy of xanthan gum and guar gum inclusion on the engineering behavior of soils. *Innov. Infrastruct. Solut.* **2021**, *6*, 1–14. [CrossRef]

7. Khattak, M.J.; Alrashidi, M. Durability and mechanistic characteristics of fiber reinforced soil-cement mixtures. *Int. J. Pavement Eng.* **2006**, *7*, 53–62. [CrossRef]

8. Viswanadham, B.V.S.; Phanikumar, B.R.; Mukherjee, R.V. Swelling behaviour of a geofiber-reinforced expansive soil. *Geotext. Geomembr.* **2009**, *27*, 73–76. [CrossRef]

9. Moghal, A.A.B.; Bhaskar, C.S.C.; Basha, B.M.; Al-Mahbashi, A.M. Effect of polypropylene fibre reinforcement on the consolidation, swell and shrinkage behaviour of lime-blended expansive soil. *Int. J. Geotech. Eng.* **2018**, *12*, 462–471. [CrossRef]

10. Abdi, M.R.; Parsapajouh, A.; Arjomand, M.A. Effects of Random Fiber Inclusion on Consolidation, Hydraulic Conductivity, Swelling, Shrinkage Limit and Desiccation Cracking of Clays. *Int. J. Civ. Eng.* **2008**, *6*, 284–292.

11. Maher, M.; HO, Y. Mechanical properties of kaolinite/fiber soil composite. *J. Geotech. Eng. ASCE* **1994**, *120*, 1381–1393. [CrossRef]

12. Miller, C.J.; Rifai, S. Fiber Reinforcement for Waste Containment Soil Liners. *J. Environ. Eng.* **2004**, *130*, 891–895. [CrossRef]

13. Moghal, A.A.B.; Basha, B.M.; Ashfaq, M. *Probabilistic Study on the Geotechnical Behavior of Fiber Reinforced Soil*; Springer: Singapore, 2019; ISBN 9789811358715.

14. Moghal, A.A.B.; Basha, B.M.; Chittoori, B.; Al-Shamrani, M.A. Effect of fiber reinforcement on the hydraulic conductivity behavior of lime-treated expansive soil—Reliability-based optimization perspective. *ASCE Geotech Spec. Publ. No* **2016**, *263*, 25–34. [CrossRef]

15. Almajed, A.; Dinesh, S.; Moghal, A.A.B. Response Surface Method Analysis of Chemically Stabilized Fiber-Reinforced Soil. *Materials* **2021**, *14*, 1535. [CrossRef] [PubMed]

16. Shaker, A.A.; Elkady, T.Y. Investigation of the hydraulic efficiency of sand-natural expansive clay mixtures. *Int. J. Geomate* **2016**, *11*, 2410–2415. [CrossRef]

17. Nalbantoglu, Z.; Tuncer, E.R. Compressibility and hydraulic conductivity of a chemically treated expansive clay. *Can. Geotech. J.* **2001**, *38*, 154–160. [CrossRef]

18. Locat, J.; Trembaly, H.; Leroueil, S. Mechanical and hydraulic behaviour of a soft inorganic clay treated with lime. *Can. Geotech. J.* **1996**, *33*, 654–669. [CrossRef]

19. Metelková, Z.; Bohác, J.; Sedlárová, I.; Prikryl, R. Changes of pore size and of hydraulic conductivity by adding lime in compacting clay liners. In *Geotechnical Engineering: New Horizons, Proceedings of the 21st European Young Geotechnical Engineers Conference Rotterdam 2011, Amsterdam, The Netherlands, 4–7 September 2011*; IOS Press: Amsterdam, The Netherlands, 2011; Volume 2011, pp. 93–98. [CrossRef]

20. Tran, T.D.; Cui, Y.J.; Tang, A.M.; Audiguier, M.; Cojean, R. Effects of lime treatment on the microstructure and hydraulic conductivity of Héricourt clay. *J. Rock Mech Geotech.* **2014**, *6*, 399–404. [CrossRef]

21. Daniel, D.E.; Anderson, D.C.; Boynton, S.S. Fixed-wall versus flexible-wall permeameters. In *Hydraulic Barriers in Soil and Rock*; ASTM STP, 874; Johnson, A.I., Frobel, R.K., Cavalli, N.J., Pettersson, C.B., Eds.; ASTM: West Conshohoken, PA, USA, 1985; pp. 107–126. [CrossRef]

22. Kang, J.; Shackelford, C.D. Clay membrane testing using a flexible-wall cell under closed-system boundary conditions. *Appl. Clay Sci.* **2009**, *44*, 43–58. [CrossRef]

23. Dafalla, M.; Shaker, A.A.; Elkady, T.; Al-Shamrani, M.; Dhowian, A. Effects of confining pressure and effective stress on hydraulic conductivity of sand-clay mixtures. *Arab. J. Geosci.* **2015**, *8*, 9993–10001. [CrossRef]

24. Eades, J.L.; Grim, R.E. A Quick Test to Determine Lime Requirements For Lime Stabilization. *Highw. Res. Rec.* **1966**, *5*, 61–72.

25. Nataraj, M.S.; McManis, K.L. Strength and deformation properties of soils reinforced with fibrillated fibers. *Geosynth. Int.* **1997**, *4*, 65–79. [CrossRef]

26. Soganci, A.S. The Effect of Polypropylene Fiber in the Stabilization of Expansive Soils. *Int. J. Environ. Chem. Ecol. Geophys. Eng.* **2015**, *9*, 956–959. [CrossRef]

27. ASTM International. *ASTM D5084-03: Standard Test Methods for Measurement of Hydraulic Conductivity of Saturated Porous Materials Using a Flexible Wall Permeameter*; ASTM International: West Conshohocken, PA, USA, 2003.

28. Olsen, H.W. Hydraulic flow through saturated clays. In Proceedings of the 9th National Conference on Clays and Clay Minerals, Lafayette, IN, USA, 5–8 October 1960; pp. 131–161. [CrossRef]

29. Scholes, O.N.; Clayton, S.A.; Hoadley, A.F.A.; Tiu, C. Permeability anisotropy due to consolidation of compressible porous media. *Transp Porous Media.* **2007**, *68*, 365–387. [CrossRef]

30. Elkady, T.Y.; Shaker, A.; Al-Shamrani, M. Hydraulic Conductivity of Compacted Lime-Treated Expansive Soils. In Proceedings of the Fourth Geo-China International Conference, Geo-China 2016, Shandong, China, 25–27 July 2016; ASCE: Shandong, China, 2016; pp. 52–59. [CrossRef]

31. de Brito Galvão, T.C.; Elsharief, A.; Simões, G.F. Effects of Lime on Permeability and Compressibility of Two Tropical Residual Soils. *J. Environ. Eng.* **2004**, *130*, 881–885. [CrossRef]

32. Shaker, A.A.; Elkady, T.Y. Hydraulic performance of sand–clay mixtures: Soil fabric perspective. *Géotechnique Lett.* **2015**, *5*, 198–204. [CrossRef]
33. Bell, F.G. Lime stabilization of clay minerals and soils. *Eng. Geol.* **1996**, *42*, 223–237. [CrossRef]
34. Moghal, A.A.B.; Rehman, A.U.; Vydehi, K.V.; Umer, U. Sustainable Perspective of Low-Lime Stabilized Fly Ashes for Geotechnical Applications: PROMETHEE-Based Optimization Approach. *Sustainability* **2020**, *12*, 6649. [CrossRef]

The Experimental Investigation on Mechanics and Damage Characteristics of the Aeolian Sand Paste-like Backfill Materials Based on Acoustic Emission

Xiaoping Shao [1,2,*], Chuang Tian [1], Chao Li [3], Zhiyu Fang [1,*], Bingchao Zhao [1,2], Baowa Xu [1], Jianbo Ning [1], Longqing Li [1,2] and Renlong Tang [1,2]

[1] Energy School, Xi'an University of Science and Technology, Xi'an 710054, China
[2] Key Laboratory of Western Mines and Hazards Prevention, Ministry of Education of China, Xi'an 710054, China
[3] Shaanxi Coal and Chemical Technology Institute Co., Ltd., Xi'an 710054, China
*   Correspondence: shaoxp@xust.edu.cn (X.S.); 17203078034@stu.xust.edu.cn (Z.F.)

Abstract: With the wide application of the filling mining method, it is necessary to consider the influence of rock activity on the filling body, reflected in the laboratory, that is, the influence of loading rate. Therefore, to explore the response characteristics of loading rate on the mechanical and damage characteristics of aeolian sand paste filling body, DNS100 electronic universal testing machine and DS5-16B acoustic emission (AE) monitoring system were used to monitor the stress–strain changes and AE characteristic parameters changes of aeolian sand paste filling body during uniaxial compression, and the theoretical model of filling sample damage considering loading rate was established based on AE parameters. The experimental results show that: (1) With the increase in loading rate, the uniaxial compressive strength and elastic modulus of aeolian sand paste-like materials (ASPM) specimens are significantly improved. ASPM specimens have ductile failure characteristics, and the failure mode is unidirectional shear failure → tensile failure → bidirectional shear failure. (2) When the loading rate is low, the AE event points of ASPM specimens are more dispersed, and the large energy points are less. At high loading rates, the AE large energy events are more concentrated in the upper part, and the lower part is more distributed. (3) The proportion of the initial active stage is negatively correlated with the loading rate, and the proportion of the active stage is positively correlated with the loading rate. The total number of AE cumulative ringing decreases with the increase in loading rate. (4) Taking time as an intermediate variable, the coupling relationship between ASPM strain considering loading rate and the AE cumulative ringing count is constructed, and the damage and stress coupling model of ASPM specimen considering loading rate is further deduced. Comparing the theoretical model with the experimental results shows that the model can effectively reflect the damage evolution process of ASPM specimens during loading, especially at high loading rates. The research results have significant reference value for subsequent strength design of filling material, selection of laboratory loading rate and quality monitoring, and early warning of filling body in goaf.

Keywords: backfill mining; loading rate; mechanical properties; acoustic emission; cumulative ringing count; damage constitutive model

1. Introduction

As an environmentally friendly mining method, the filling mining method can improve resource recovery rate, control rock migration and surface subsidence, treat solid waste accumulation, improve stope environment and prolong mine service life so as to reduce the influence and damage of resource mining on natural, social and living environment [1–6]. The technology has been successfully applied in various engineering environments in many countries [7–9]. The Yushenfu mining area in northern Shaanxi is located at western China's

edge of the Maowusu Desert. The surface of the area is covered with a large amount of aeolian sand, and there are many power plants around the mining area. These power plants will produce a large amount of solid waste in the production process, such as fly ash and slag. The accumulation of the solid waste seriously pollutes the ecological environment, and it is necessary to dispose of the solid waste reasonably. Therefore, scholars have proposed a new filling material for the Yushenfu mining area—aeolian sand paste filling material, in which aeolian sand as aggregate, cement and fly ash as cementitious materials [10]. Currently, many coal mines in the mining area are using this filling material to fill the goaf. The filling mainly transports the filling body with bearing characteristics to the goaf after resource mining to support, let the pressure, and prevent rock deformation, to control large area roof and ground pressure activities [11–13]. A filling body is a key to ensuring the stope's safety and stability. Its strength is the core of mechanical problems of filling the body and is also the focus and hotspot of many scholars [14–17].

The material's mechanical properties vary with the loading rate, mainly because the loading rate affects the storage characteristics of the elastic energy of the material itself. Komurlu [18], Fujita [19], Huang [20], Cao [21], Yang [22], and Ma [23] have explored the influence of different loading rates on the mechanical behaviour of rock materials. It is believed that changing the loading rate can influence the stress–strain curve, uniaxial compressive strength, peak strain, and failure mode. Pedersen [24], Vidya [25], Ma [26], Dang [27], Zhang [28], Rezaei [29] et al. conducted tests on concrete materials at different loading rates and clarified that the loading rate also impacted the mechanical properties of concrete materials.

The damage study of cemented backfill is one of the most basic and essential research contents in backfill mechanics. Zhao et al. [30] built uniaxial compression damage constitutive model based on Weibull distribution. Based on the energy dissipation theory and damage mechanics theory, Hou et al. [31] constructed the damage constitutive model of cemented tailings backfill considering the curing age. Tu et al. [32] constructed the damage constitutive model of cemented tailings backfill (CTB) under uniaxial compression based on Weibull distribution, strain equivalent principle, and damage mechanics theory. They verified the model's validity using different solid content and ash-sand ratio. Fu et al. [33,34] established the damage evolution model, damage constitutive model, and strength criterion of layered structure cemented paste backfill based on damage theory and absolute differential rule. The above damage constitutive model does not consider the influence of loading rate on the strength and damage evolution of the filling body.

Currently, the research on the mechanical properties of materials under loading rate mainly focuses on rock and concrete materials. However, there are few studies on the damage characteristics of filling materials with lower strength than rock and concrete and ductile failure characteristics, especially considering the loading rate based on AE parameters. As one of the mainstream dynamic non-destructive testing techniques, AE has attracted wide attention in studying material damage and failure characteristics. The uniaxial compressive strength test can effectively reflect the strength and failure characteristics of the filling body. AE technology can dynamically monitor the damage generation and development of the filling body during loading and provide data for experimental analysis [35–37]. When the filling body is subjected to load, the internal structure will deform or rupture, and accompanied by different sizes of energy, different frequencies of elastic wave release phenomenon is called AE of filling body [38]. To study the influence of loading rate on the characteristics of the aeolian sand paste filling body, this paper studies the influence of different loading rates (0.002 mm/s, 0.005 mm/s, 0.0075 mm/s, and 0.01 mm/s) on the strength, macroscopic failure characteristics, AE characteristic parameters and damage characteristics of aeolian sand paste filling body. The research results can provide experimental and theoretical references for the strength design of the filling body and the damage assessment under mining influence.

2. Experimental Materials and Methods

2.1. Experimental Materials

The selected experimental materials include aggregate (aeolian sand), cementitious materials (fly ash, cement), and water [39]. The aeolian sand is from Yuyang District in northern Shaanxi, the fly ash is from the filling station of Changxing Coal Mine in Yuyang District, the cement is ordinary Portland cement (OPC) 42.5, according to Chinese national standard GB175-2007, and the water is Xi'an ordinary tap water.

2.1.1. Aggregate

As the fourth monsoon product, aeolian sand mainly comprises lithic, feldspar, and quartz. The main chemical composition is shown in Table 1. As shown in Figure 1, the particle size distribution of aeolian sand is 0.412~493.6 μm, where d_{10} = 8.1 μm, d_{50} = 214.5 μm, d_{90} = 357.9 μm, and 100~400 μm accounts for about 80%. Aeolian sand's uniformity coefficient (Cu) is about 30.3, and the optimum value of particle gradation is between 4 and 6, which conforms to the Talbot equation [40]. The particle size distribution curve shows that the coarse particle content is low, and the natural gradation is mostly discontinuous.

Table 1. Main chemical composition of Aeolian sand.

Composition	CaO	Al_2O_3	SiO_2	Fe_2O_3	K_2O	Others
Content, %	5.3	10.3	67.8	5.8	7.5	3.3
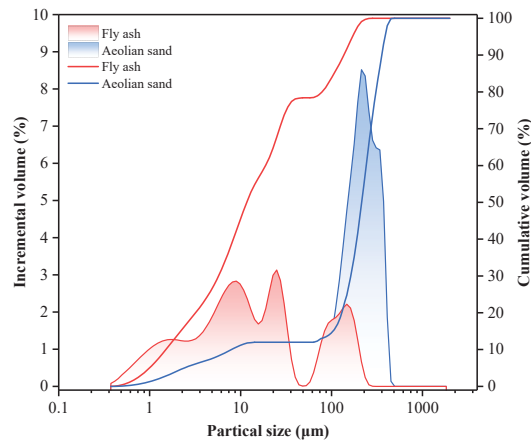
Figure 1. Particle size distribution of raw materials.

2.1.2. Cementitious Materials

Cement is a cementitious material, and its main mineral components are C_2S, C_3S, C_3A, C_4AF, etc. The main chemical composition is shown in Table 2. The main hydration products are calcium hydroxide (CH), calcium silicate hydrate (C-S-H), calcium aluminate hydrate (C-A-H), and calcium alumino-ferrite hydrate (C-A-F-H).

Table 2. Main chemical composition of Cement.

Composition	CaO	Al_2O_3	SiO_2	Fe_2O_3	MgO	Others
Content, %	65.08	5.53	22.36	3.46	1.27	2.30

As a kind of cementitious admixture, fly ash is used in mine filling, which can not only save cement and reduce filling costs but also improve the fluidity of pipeline slurry and the

suspension performance of filling aggregate and effectively improve the late strength of the filling body. As shown in Figure 1, the particle size distribution of fly ash is 0.412~309 μm, of which d_{10} = 1.51 μm, d_{50} = 11.67 μm, d_{90} = 136.02 μm, 1~40 μm accounts for about 74%. The uniformity coefficient (C_u) of fly ash is about 11.9, and the optimal particle gradation is between 4 and 6, which conforms to the Talbot equation [40]. The particle size distribution curve shows that the content of coarse particles is low, showing a discontinuous natural gradation. The main minerals are aluminosilicate, sponge-like vitreous, quartz, iron oxide, carbon particles, and sulfate. The main chemical composition is shown in Table 3.

Table 3. Main chemical composition of Fly ash.

Composition	CaO	Al$_2$O$_3$	SiO$_2$	Fe$_2$O$_3$	K$_2$O	Others
Content, %	10.51	17.82	55.46	5.32	2.81	8.08

2.2. Fabrication of Pecimens

The experimental ratio was fly ash: cement: aeolian sand = 35 wt.%: 12 wt.%: 53 wt.%, in which the solid mass concentration was 78% [41]. The mixing ratio of experimental materials can meet the engineering requirements by industrial field verification. The filling material was poured into the standard cylindrical mould with a diameter of 50 mm and a height of 100 mm after fully stirring according to the experimental ratio. A total of 12 filling specimens were made. After curing for 24 h, the mould was demoulded and put into the HWS constant temperature, and humidity curing box for 28 d, where the temperature was (20 ± 1) °C and the relative humidity was (95 ± 2)% [42].

2.3. Experimental Methods

When the ASPM specimen reaches the specified curing time, the UCS test is carried out according to the standard for test methods of concrete physical and mechanical properties (GB/T 50081-2019) [43]. The experimental device is shown in Figure 2. The uniaxial compression tests of ASPM specimens with different loading rates were carried out by DNS100 electronic universal testing machine (SinoTest, Changchun, China). There is no uniform standard for the selection of loading rate in mechanical test experiments, and the stress recovery stage of rock mass in engineering sites after mining disturbance is mostly considered static loading, so it is feasible to use static loading research in the laboratory. Referring to the strain rate loading range of 10^{-5}–10^{-1} mm/s in rock statics [44], different gradient loading rates were selected as 0.002 mm/s, 0.005 mm/s, 0.0075 mm/s, and 0.01 mm/s. The DS5-16B acoustic emission monitoring equipment of Beijing Softland Company was used to monitor the test process synchronously, and the parameters such as load, deformation, AE ringing count, and event number were recorded in real-time. Three AE sensors were arranged at 15 mm from the upper and lower ends of the specimen side, and vaseline was smeared on the contact part of the specimen and the probe to reduce the influence of AE caused by the friction between the probe and the specimen on the test. To avoid the loss of test data caused by the sensor shedding, 12 mm rubber reinforcement was used to fix the AE sensor on the specimen side. The AE threshold is 40 mV, and the sampling frequency is 3 MHz.
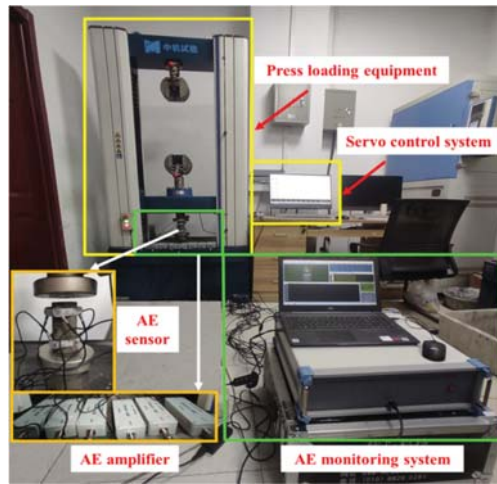
Figure 2. Experiments test system.

3. Results and Discussion

3.1. Mechanical Properties of the ASPM

3.1.1. Results of UCS Analysis

The UCS test results of ASPM specimens under different loading rates are shown in Table 4. It shows that the standard deviation of the UCS of each group of specimens is slight, and the discreteness of the test results is small. When the loading rate increased from 0.002 mm/s to 0.005 mm/s, the average compressive strength of ASPM increased from 4.175 MPa to 4.641 MPa, with an increase of 11.17%. When the loading rate increased from 0.005 mm/s to 0.0075 mm/s, the average compressive strength of ASPM increased from 4.641 MPa to 5.191 MPa, with an increase of 11.85%. When the loading rate increased from 0.0075 mm/s to 0.01 mm/s, the average compressive strength of ASPM increased from 5.191 MPa to 5.408 MPa, with an increase of 4.18%. With the increase in loading rate, the change rate of peak strength of ASPM filling body increased first and then decreased, and the peak strength of ASPM filling body increased as a whole. It shows that the increase in loading rate has a noticeable strengthening effect on the peak strength of the ASPM filling body. This is due to the increase in loading rate, which shortens the failure time of the filling body and thus limits the full development of micro cracks, micropores, and other defects in the filling body. Therefore, the UCS increases macroscopically.

Table 4. UCS of the ASPM specimens with different loading rates.

Specimen Number	Loading Rate mm/s	Compressive Strength/MPa	Average Compressive Strength/MPa	Standard Deviation	Elastic Modulus/GPa
A11		4.151			0.4279
A12	0.0020	4.239	4.175	0.0461	0.4213
A13		4.134			0.4361
A21		4.712			0.5548
A22	0.0050	4.628	4.641	0.0531	0.5437
A23		4.584			0.5472
A31		5.034			0.5698
A32	0.0075	5.348	5.191	0.1282	0.5796
A33		5.192			0.5755
A41		5.377			0.6948
A42	0.0100	5.489	5.408	0.0580	0.7120
A43		5.357			0.7083

The experimental data were fitted, and it was found that the quantitative relationship between the average UCS of the specimen and the loading rate was more suitable for linear fitting, as shown in Figure 3. The fitting form is as follows:

$$y = 3.8867 + 149.4072v \tag{1}$$
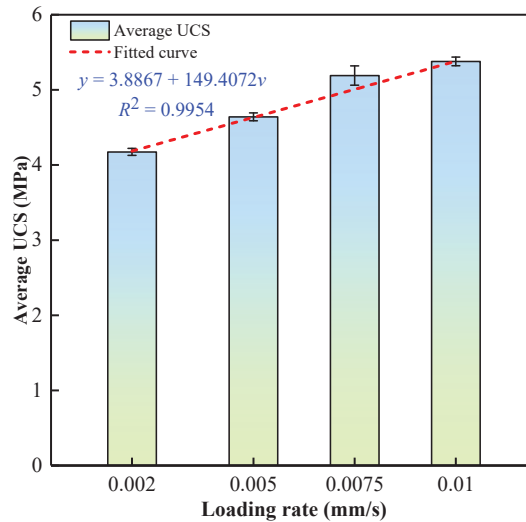
Figure 3. Relationship between average UCS and loading rate.

The typical stress–strain curves of the backfill specimens corresponding to different loading rates during uniaxial compression are shown in Figure 4. It can be seen from Figure that the ASPM specimen can be divided into four stages in the uniaxial compression process [36,45]: initial compaction stage (concave curve), elastic rise stage (oblique line), plastic failure stage (concave curve), and post-peak failure stage (post-peak curve). With the increased loading rate, the specimen experienced a shorter compaction stage and entered the linear elastic stage faster. Because the ASPM specimen is a kind of artificial production material, there are inevitably micropores and micro-cracks in the production process [46,47]. The higher the loading rate, the shorter the time internal defects are compacted, so it enters the linear elastic stage faster. The filling specimens have ductile failure characteristics and have residual strength after the peak [48,49]. In Figure, the stress–strain curve corresponding to 0.0050 mm/s appeared with two small peaks after the peak failure stage, indicating that ASPM specimens still have strong bearing capacity after reaching the peak failure [50].

3.1.2. Results of Elastic Modulus Analysis

The elastic modulus of the filling body characterizes the deformation resistance of the material, and the physical essence is to characterize the binding force between the atoms of the material [51,52]. This paper defines the slope of the stress–strain curve's elastic stage as the elastic modulus. The elastic modulus corresponding to different loading rates is shown in Table 4. Compared with the elastic modulus corresponding to the loading rate of 0.002 mm/s, the elastic modulus of the filling specimen increases by 29.65 % (0.005 mm/s), 35.44 % (0.0075 mm/s) and 65.53 % (0.01 mm/s) with the increase of loading rate, respectively. The elastic modulus of ASPM increases with the increase in loading rate, indicating that the increase in loading rate also has a strengthening effect on the stiffness of the ASPM filling body. Based on the above experimental results, a regression equation was established to characterize the quantitative relationship between elastic modulus and the

loading rate of ASPM. Linear and polynomial methods fitted the relationship between the elastic modulus of ASPM and the loading rate. The fitting results are shown in Figure 5. It can be seen from Figure that the correlation coefficients R^2 corresponding to linear fitting and polynomial fitting are 0.9449 and 0.9954, respectively, showing high fitting characteristics. However, the polynomial fitting degree is the highest, indicating that the polynomial fitting is more suitable to characterize the quantitative relationship between the loading rate and the elastic modulus of ASPM.
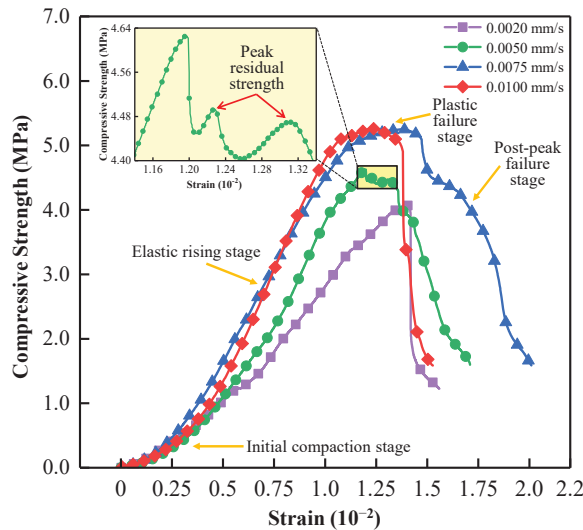
Figure 4. Stress–strain curve of ASPM specimen.
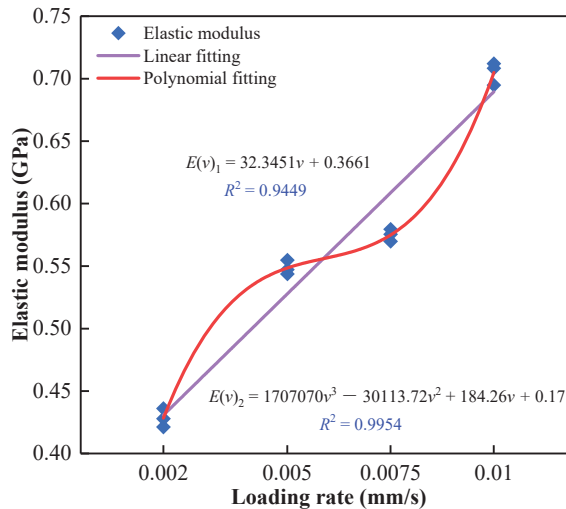
Figure 5. Relationship between elastic modulus and loading rate.

3.1.3. Results of Failure Characteristics Analysis

Figure 6 shows the failure modes of ASPM specimens under different loading rates. When the loading rate is 0.002 mm/s and 0.005 mm/s, the specimen shows unidirectional shear failure, and the internal micro defects of the filling specimen have enough time to

develop, making the internal defects develop fully. The cracks have sufficient time to penetrate each other, and the main cracks mostly accompany the secondary cracks. The specimen exhibits axial tensile failure when the loading rate increases to 0.0075 mm/s. When the loading rate is further increased to 0.01 mm/s, the internal micro pores and micro-cracks cannot be fully developed, and the weak surface in the specimen cannot be penetrated, so it can only develop along the respective dominant cracks. At the same time, under the action of positive pressure, the specimen has not only positive stress but also shear stress on the oblique section. At this time, the specimen will produce bidirectional shear failure. In summary, when the loading rate increases from 0.0020 mm/s to 0.01 mm/s, the failure mode of the ASPM specimen is mainly unidirectional shear failure → tensile failure → bidirectional shear failure. Therefore, the loading rate can have a particular impact on the failure mode of the ASPM filling body.
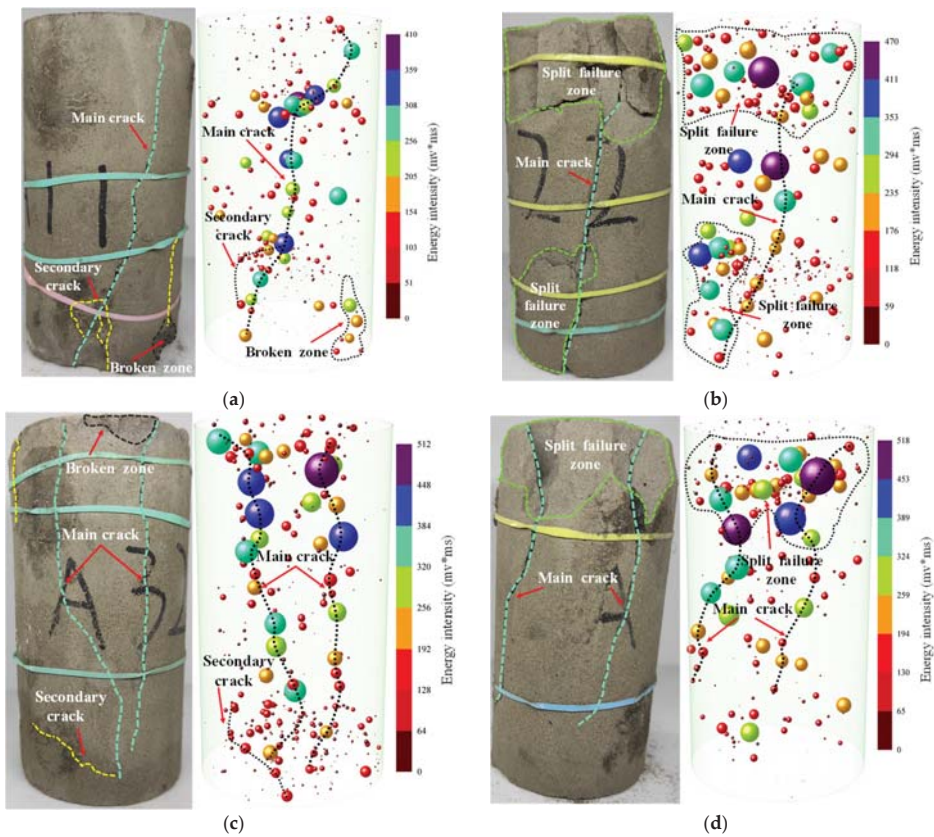
Figure 6. Failure mode and AE event points of ASPM specimens under different loading rates. (**a**) 0.002; (**b**) 0.005; (**c**) 0.0075; (**d**) 0.01.

AE three-dimensional positioning can effectively reflect the formation location and spatial evolution of micro cracks in filling specimens and evaluate the damage and failure of the specimen [53,54]. The ball in the diagram represents the event point, and the ball size represents the energy size. AE has an apparent response to the loading rate. At a low loading rate, the AE events inside the specimen are more dispersed, and the significant energy event points are less. This is because the specimen has more time to make each part uniformly compressed at low-speed loading, so the AE energy is primarily tiny. Under

the high loading rate, the AE events in the specimen are more concentrated, and the large energy points are more. This is because the high loading rate makes the rapid internal response of the filling body, and the AE events begin to occur at the weak surface. The AE events are more concentrated due to the independent development of the weak surface. The energy generated by the increase of the loading rate is also increased accordingly. It can be seen from the graph that under the high loading rate, the large energy events are primarily concentrated in the upper part, and the lower part is more distributed with small energy events. It shows that the internal energy accumulates to a certain extent during the loading process and releases energy first in the upper part to produce cracks. The cracks propagate from top to bottom, and the internal energy releases slowly with the crack propagation. It is found that the AE event points are consistent with the experimental crack development.

3.2. Results of AE Analysis

As the number of oscillations exceeds the AE threshold, the AE ring count can further characterize filling specimens' internal micro-fracture and damage evolution. The AE cumulative ringing count refers to the cumulative value of the ringing count of AE in an AE process. This parameter can describe the total strength of AE and the accumulation of internal damage to materials, which is the external manifestation of the accumulation effect of internal structural changes in materials. Through AE monitoring of ASPM specimens under uniaxial compression test at different loading rates, the internal defects and damage can be reflected, and the failure of the filling body can be predicted [55].

AE Ringing Count Analysis

The AE ringing counts, stress, and time relationships of the filling specimens under uniaxial compression at different loading rates are shown in Figure 7. It can be seen from Figure 7 that the number of AE ringing reaches the maximum when the peak stress approaches. The reason is that the micro-cracks initiate, develop and expand after the micro-pore compaction in the early stage of the specimen. The macroscopic penetrating cracks are formed near the peak stress. The accumulated energy is released rapidly so that the AE ringing count signal value is suddenly increased to the peak value, which can be used as a precursor signal to determine the failure of the filling specimen [50].

According to the change rule of AE ringing count, the whole loading process can be divided into four stages: initial active stage, pre-peak rise stage, active stage, and post-peak stability stage.

(1) The initial active stage T_1 (A11: 0~211 s, A21: 0~81 s, A32: 0~39 s, A43: 0~22 s): This stage corresponds to the initial compaction stage of the stress–strain curve. The internal pore defects of the specimen are compacted, accompanied by friction between the filling materials, resulting in a sporadic sharp increase in the ringing count, but the sudden increase is small. This stage accounts for about 27.1%, 23.6%, 17.5%, and 18.5% of the process, as shown in Figure 8. The proportion of the initial active stage was negatively correlated with the loading rate. The results show that the increase in loading rate makes the filling specimen enter the next stage faster, which is consistent with the findings in 3.1.1.

(2) The pre-peak rise stage T_2 (A11: 211~530 s, A21: 81~209 s, A32: 39~114 s, A43: 22~67 s): This stage corresponds to the elastic stage of the stress–strain curve. With the increase in loading, new cracks begin to initiate and expand and continuously release AE signals. There is no mutation in the ringing count of AE at this stage, and the overall ringing count is stable and high, so the cumulative ringing count curve can be seen that the whole is in a steady growth stage. This stage accounts for about 40.9%, 37.3%, 33.6%, and 38.4% of the process, as shown in Figure 8.

(3) The active stage T_3 (A11: 530~714 s, A21: 209~292 s, A32: 114~177 s, A43: 67~104 s): After the previous energy savings to the stage of AE parameters into the active phase. In the pre-peak stage, the ringing number increased sharply with the increase of axial stress, reaching the maximum near the peak, and then decreased sharply with the

decrease of axial stress after the peak. This stage accounts for about 23.6%, 24.2%, 28.0%, and 32.1% of the process, as shown in Figure 8. The proportion of the active stage is positively correlated with the loading rate, indicating that the increase in the loading rate that makes the internal energy in the compression process cannot be released until close to the peak. The higher the loading rate is, the more energy is released, so it can be seen that the proportion of this stage is gradually increasing.

(4) The post-peak stability stage T_4 (A11: 714~779 s, A21: 292~342 s, A32: 177~223 s, A43: 104~117 s): This stage corresponds to the post-peak failure stage of the stress–strain curve. After the sudden increase and decrease of the ringing count in the previous stage, the ringing count in this stage is at a low level as a whole. Because there is some friction and slipping between the fracture surfaces after the failure of the specimen, there is a small range of growth at some time, but it does not affect the overall development trend. This stage accounts for 8.3%, 14.9%, 20.9%, and 11.0% of the process, as shown in Figure 8.
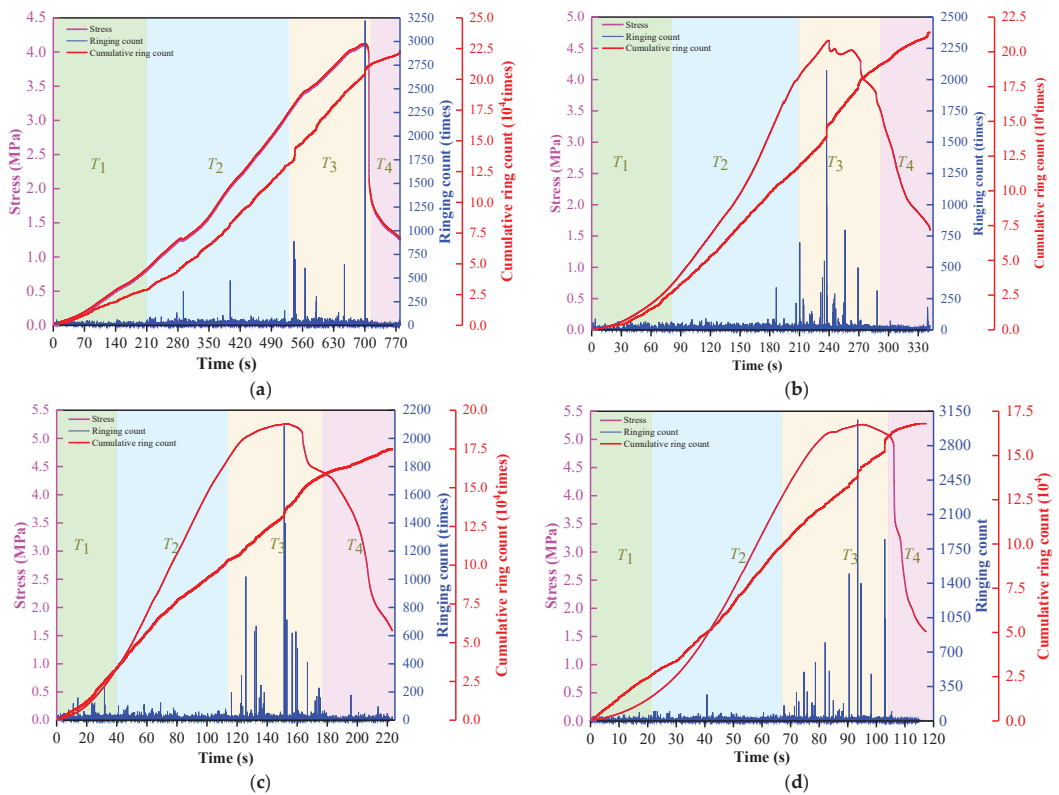
Figure 7. AE ringing counts, stress and time curves of ASPM specimens. (**a**) 0.002; (**b**) 0.005; (**c**) 0.0075; (**d**) 0.01.
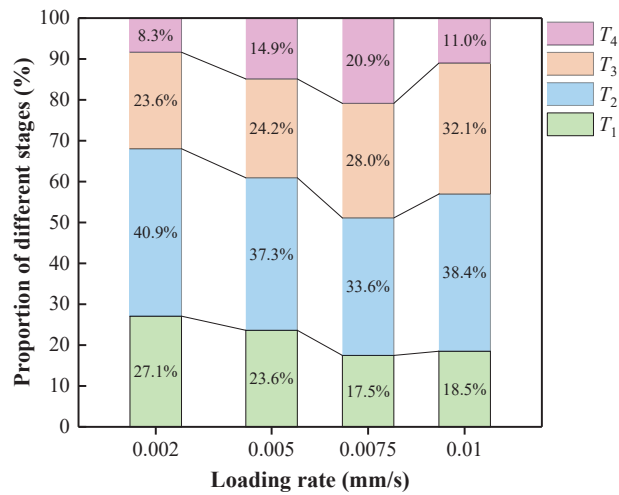
Figure 8. The proportion of each stage.

As shown in Figure 9, it can be seen that with the increase in loading rate, the AE cumulative ringing count negatively correlates with the loading rate. It is concluded that when the loading rate is less than 0.002 mm/s, the total number of AE cumulative ringing will be at a high level. When the loading rate exceeds 0.01 mm/s, the total number of AE cumulative ringing will be further reduced.
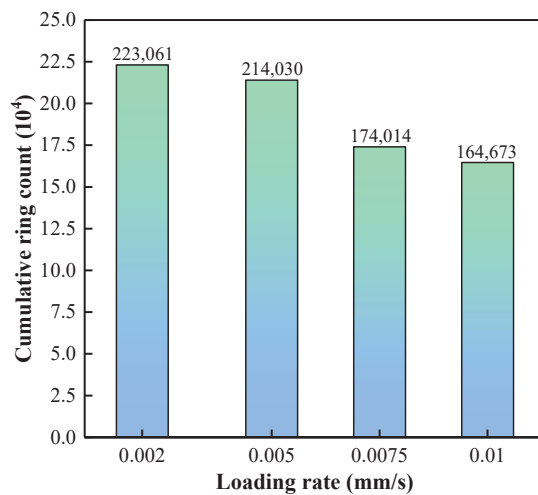
Figure 9. Relationship between cumulative ringing count and loading rate.

4. Establishment of Damage Constitutive Model of the ASPM

4.1. Fitting of AE Cumulative Ringing Count and Strain

The analysis of the above experimental results shows that the AE characteristics are closely related to the development of microcracks in ASPM specimens. Cracks and defects inside the filling specimen are essential factors affecting its mechanical properties. Therefore, there is an inevitable connection between the AE cumulative ringing count and the mechanical properties of the filling specimen.

According to the experimental data, the relationship between strain and time is fitted. That is the following relationship between ε and time:

$$\varepsilon = kt + \varepsilon_0 \tag{2}$$

The formula: ε is the strain of the filling body specimen; k is the strain rate; t is time; ε_0 is the initial strain of the filling body, obtained by linear fitting experimental data.

The Boltzmann function can express the relationship between the measured cumulative ringing count and time [56,57], that is:

$$N = \frac{A - B}{1 + \exp\left(\frac{t - C}{G}\right)} + B \tag{3}$$

The formula: N is the AE cumulative ringing count in the loading stage; t is time; A, B, C, and G are all fitting parameters.

According to the experimental results, the total number of AE cumulative ringing decreases with the increase of loading rate, the loading rate v is introduced, and the fitting relationship is further modified as follows:

$$N = \frac{A - B}{1 + \exp\left[\frac{v(t - C)}{G}\right]} + B \tag{4}$$

The formula: v is the uniaxial loading rate of the filling specimen.

Using the Formula (4) to fit, as shown in Figure 10, the correlation coefficients corresponding to different loading rates are 0.9992 (0.002 mm/s), 0.9988 (0.005 mm/s), 0.9972 (0.0075 mm/s) and 0.9987 (0.01 mm/s). Therefore, the function can represent AE cumulative ringing count and time variation.

Formulas (2) and (4) can be obtained:

$$N = \frac{A - B}{1 + \exp\left[\frac{v(\varepsilon - \varepsilon_0 - kC)}{kG}\right]} + B \tag{5}$$

$$\varepsilon = k\left[\frac{G}{v} \ln\left(\frac{A - N}{N - B} + C\right)\right] + \varepsilon_0 \tag{6}$$

Formulas (5) and (6) establish the coupling relationship between cumulative ringing counts and strain of ASPM specimens under different loading rates.

4.2. Establishment of the ASPM Damage Model

In this paper, AE ringing count and AE cumulative ringing count are selected as characteristic parameters to characterize the damage characteristics of filling specimens during compression.

Kachanov [58] proposed the concept of damage variable D and defined it as:

$$D = \frac{A'}{A} \tag{7}$$

The formula A is the total area of micro defects on the bearing section and A' is the fracture area when there is no initial damage.

Considering that it is difficult to determine the effective bearing area of damaged materials, Lemaitre [59] proposed the strain equivalence hypothesis, that is, to indirectly measure the damage through effective stress:

$$\sigma = \sigma * (1 - D) = E\varepsilon(1 - D) \tag{8}$$
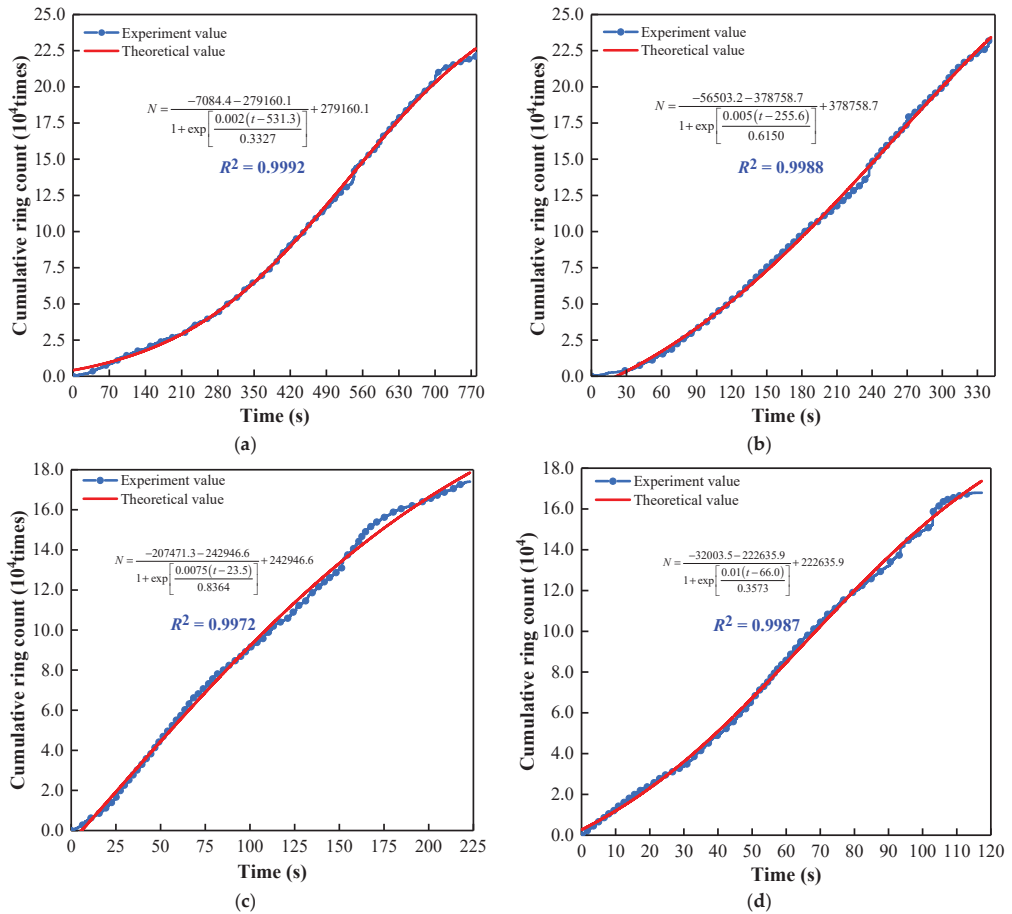
Figure 10. Fitting of the AE cumulative ringing count with time. (**a**) 0.002; (**b**) 0.005; (**c**) 0.0075; (**d**) 0.01.

Formula: σ is nominal stress, σ^* is effective stress, E is the elastic modulus of the filling body, and ε is strain.

Assuming that the AE cumulative ringing count is N_f when the whole section A of the non-destructive material is completely damaged, the AE ringing count N_w when the unit area is damaged is:

$$N_w = \frac{N_f}{A} \qquad (9)$$

When the cross-section damage reaches A', the AE cumulative ringing count is:

$$N_d = N_w A' = \frac{N_f}{A} A' \qquad (10)$$

Formulas (7) and (10) show that the relationship between the damage variable and AE cumulative ringing count is:

$$D = \frac{A'}{A} = \frac{N_d}{N_f} \qquad (11)$$

During the experiment, due to the insufficient stiffness of the testing machine or the different failure conditions set, the testing machine was stopped when the specimen was

not completely damaged (the damage variable D does not reach 1). There is still a specific residual strength of the specimen. Therefore, the modified damage variable is:

$$D = D_u \frac{N_d}{N_f} \tag{12}$$

Formula: D_u is the critical value of the damage.

For the convenience of calculation, the critical damage value D_u is:

$$D_u = 1 - \frac{\sigma_c}{\sigma_{pk}} \tag{13}$$

Formula: σ_{pk} is peak strength, σ_c is residual strength.

The coupling relationship between cumulative ringing count N, damage variable D, and stress σ of ASPM at different loading rates can be obtained by combining Formulas (5), (8), (12), and (13) as follows:

$$D = (1 - \frac{\sigma_c}{\sigma_{pk}})\frac{N_d}{N_f} \tag{14}$$

$$\sigma = E\varepsilon(1 - D) = E\varepsilon\left[1 - (1 - \frac{\sigma_c}{\sigma_{pk}})\frac{N_d}{N_f}\right] \tag{15}$$

Formula: N_f is the cumulative ringing count produced at the end of the experiment,
$N_d = \frac{A-B}{1+\exp\left[\frac{v(\varepsilon-\varepsilon_0-kC)}{kG}\right]} + B.$

4.3. Model Validation and Discussion

To verify the rationality and effectiveness of the model, combined with experimental data, the strain-time curve and the cumulative count-time curve of AE ringing are fitted, respectively. The statistical fitting parameters are shown in Table 5. They are substituting the fitting parameters into formulas (6), (4) and (15), the comparison between AE cumulative ringing count and strain, damage variable and strain, stress–strain fitting based on AE ringing count, and measured stress–strain under ASPM uniaxial compression can be determined.

Table 5. Fitting parameters of different loading rates.

Specimen Number	Loading Rate mm/s	Fitting Parameters							σ_{pk}	σ_c
		A	B	C	G	R^2	k	ε_0		
A11		−7084.4	279,160.1	531.3	0.3327	0.9992	2.0×10^{-5}	1.3×10^{-6}	4.151	1.225
A12	0.0020	−34,910.9	262,770.0	367.7	0.3274	0.9988	2.0×10^{-5}	9.6×10^{-7}	4.239	1.251
A13		−47,599.4	397,075.6	720.4	0.6441	0.9975	2.0×10^{-5}	7.8×10^{-7}	4.134	1.285
A21		−56,503.2	378,758.7	255.6	0.6150	0.9988	5.0×10^{-5}	4.5×10^{-6}	4.712	1.597
A22	0.0050	−29,520.9	219,770.7	146.0	0.3434	0.9989	5.0×10^{-5}	5.3×10^{-6}	4.628	1.364
A23		−45,896.4	268,022.9	163.1	0.4310	0.9994	5.0×10^{-5}	5.6×10^{-6}	4.584	1.362
A31		−34,700.4	198,133.6	79.8	0.3045	0.9981	7.5×10^{-5}	7.5×10^{-5}	5.034	1.489
A32	0.0075	−207,471.3	242,946.6	23.5	0.8364	0.9972	7.5×10^{-5}	1.1×10^{-5}	5.348	1.587
A33		−110,341.6	256,808.5	88.1	0.6429	0.9975	7.5×10^{-5}	8.4×10^{-6}	5.192	1.533
A41		−41,430.5	185,097.7	49.8	0.2979	0.9995	1.0×10^{-4}	1.2×10^{-5}	5.377	1.609
A42	0.0100	−16,918.1	236,993.5	96.2	0.3439	0.9983	1.0×10^{-4}	1.2×10^{-5}	5.489	1.598
A43		−32,003.5	222,635.9	66.0	0.3573	0.9987	1.0×10^{-4}	1.5×10^{-5}	5.357	1.587

As shown in Figure 11, the comparison between the experimental and theoretical results shows that the theoretical and experimental curves of strain and AE cumulative ringing count have a high matching, which indicates that the coupling relationship between AE cumulative ringing count and strain considering loading rate is appropriate. The model can provide a reference for the deformation prediction of the same type of filling materials.
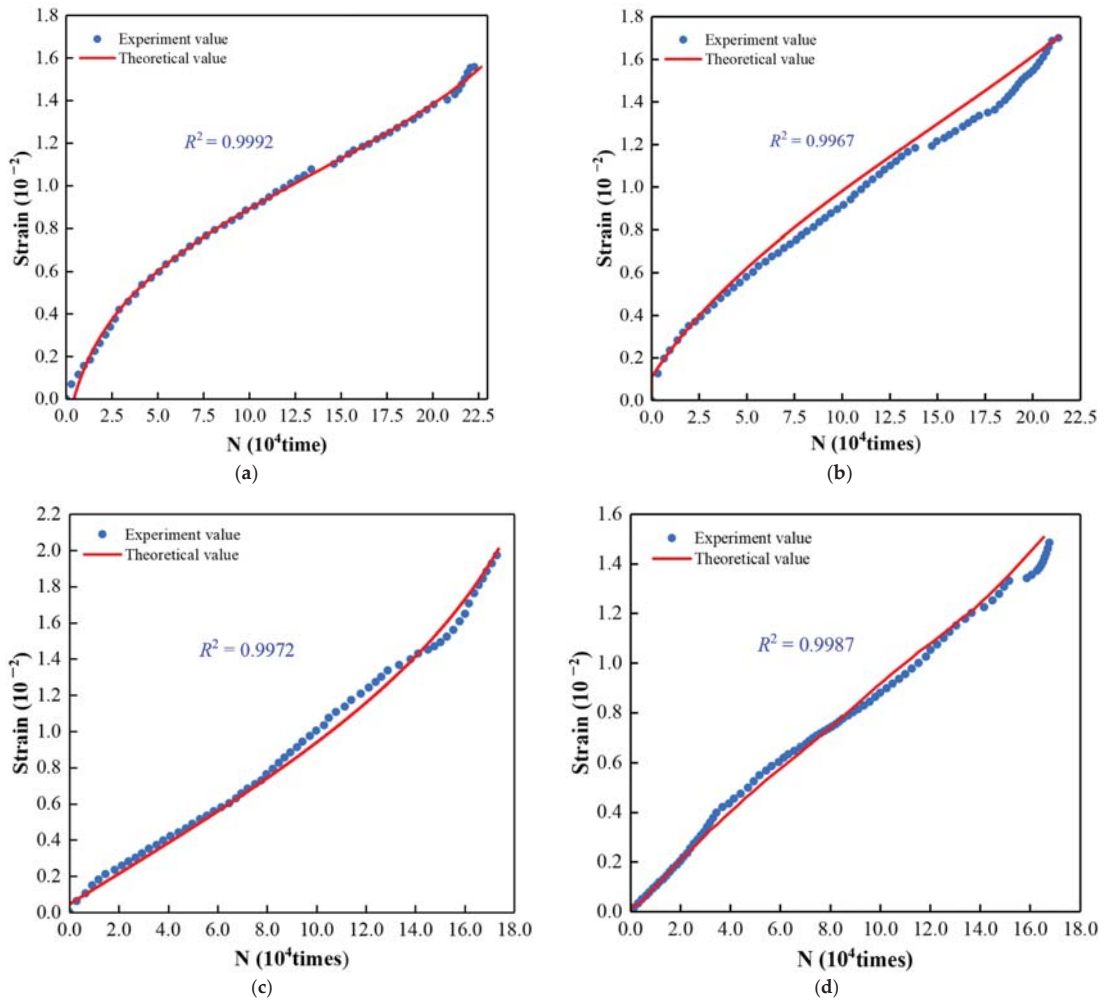
Figure 11. Comparison of Experiment value and Theoretical value of *N* and *ε*. (**a**) 0.002; (**b**) 0.005; (**c**) 0.0075; (**d**) 0.01.

Figure 12 compares the stress–strain curves of ASPM specimens under different loading rates and the experimental results. At a low loading rate, the theoretical stress peak is smaller than the measured stress peak, and the peak strain is ahead of the measured value. With the increased loading rate, the theoretical peak stress and peak strain are close to the experimental results, which can better reflect the failure process of ASPM specimens from linear elastic transition to plastic deformation. Compared with the experimental results, the established model cannot effectively reflect the compaction stage of ASPM specimens under different loading rates, and the theoretical residual strength after the peak is greater than the experimental value.
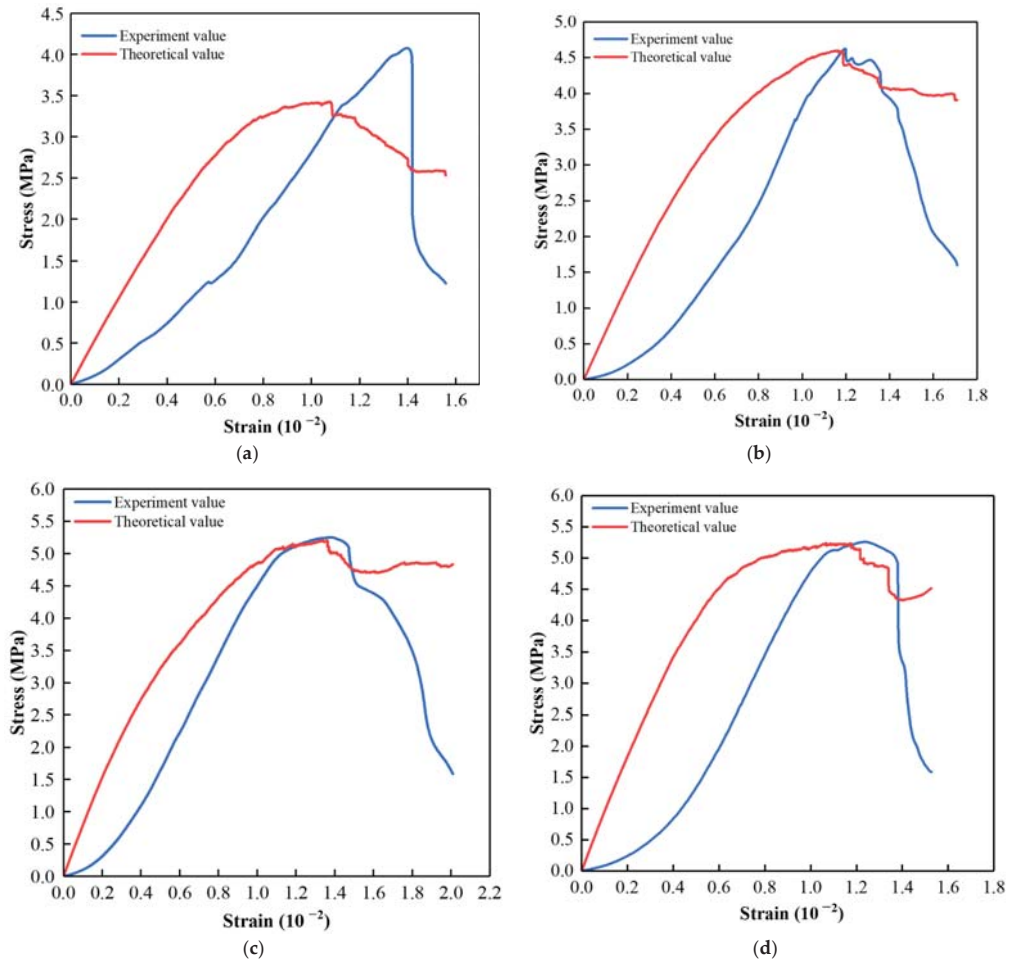
Figure 12. Comparison of Experiment value and Theoretical value of σ and ε. (**a**) 0.002; (**b**) 0.005; (**c**) 0.0075; (**d**) 0.01.

Figure 13 shows the relationship between AE cumulative ringing counts and damage variables at different loading rates. It can be seen that the higher the loading rate is, the smaller the final AE cumulative ringing counts are. The final damage values at different loading rates are about 0.7, which again shows that ASPM specimens still have a specific residual strength at the end of the experiment. In the Figure, the higher the loading rate is, the greater the slope of the curve is, indicating that the higher the loading rate per unit time is, the greater the damage to the ASPM specimen is.

Overall, the strain, stress, and damage variables of ASPM specimens agree with the measured and simulated cumulative counts of AE ringing, which proves the rationality and effectiveness of the coupling model.
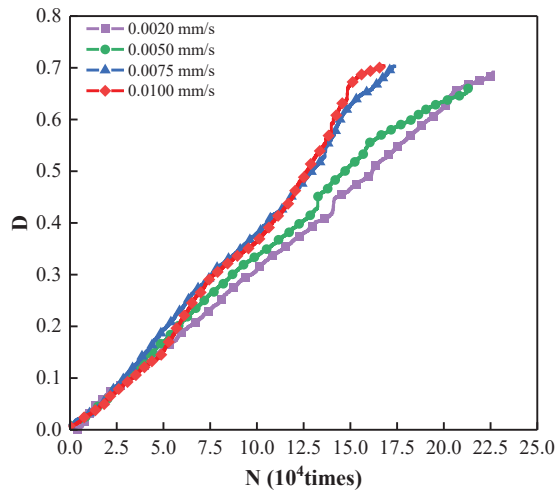
Figure 13. Relationship between *N* and *D*.

5. Conclusions

(1) Based on the AE monitoring technology, this study analysed the comprehensive influence of loading rate on the strength, deformation, AE characteristics and damage characteristics of ASPM, a lower strength filling material. The following conclusions can be drawn: The loading rate strengthens the uniaxial compressive strength and elastic modulus of ASPM specimens. When the loading rate increased from 0.002 mm/s to 0.01 mm/s, the uniaxial compressive strength increased by 29.5% and the elastic modulus increased by 65.53%. The average uniaxial compressive strength and loading rate are linear function distributions, and the elastic modulus and loading rate are polynomial. The failure mode is mainly unidirectional shear failure when there is a low loading rate. When the loading rate is high, it presents tensile failure mode, and the loading rate further increases, showing a bidirectional shear failure mode.

(2) Under a low loading rate, the internal event points of ASPM specimens are more dispersed, and the large energy points are less. Under a high loading rate, the internal event points are more concentrated, and the large energy points are more. The large energy events are primarily concentrated in the upper part, and the lower part is more distributed with small energy events. AE events correspond to experimental crack development and failure.

(3) According to the change in AE ringing count, the loading process is roughly divided into four stages: initial active, pre-peak rise, active, and post-peak stability. The loading rate increased from 0.002 mm/s to 0.01 mm/s, the proportion of the initial active stage decreased from 27.1% to 18.5%, and the active stage increased from 23.6% to 32.1%. The total number of AE cumulative ringing decreases with the increase in loading rate.

(4) By fitting the strain of ASPM specimen, AE cumulative ringing count, and time, the relationship model between AE cumulative ringing count and strain of ASPM specimen considering loading rate is constructed; the damage and stress coupling model of ASPM specimens under different loading rates based on AE cumulative ring count can better reflect the damage evolution process of ASPM under higher loading rates. The construction of the coupling model under a low loading rate remains to be further studied.

References

1. Ng, C.; Alengaram, U.J.; Wong, L.S.; Mo, K.H.; Jumaat, M.Z.; Ramesh, S. A review on microstructural study and compressive strength of geopolymer mortar, paste and concrete. *Constr. Build. Mater.* **2018**, *186*, 550–576. [CrossRef]
2. Li, M.; Zhang, J.; Li, A.; Zhou, N. Reutilisation of coal gangue and fly ash as underground backfill materials for surface subsidence control. *J. Clean. Prod.* **2020**, *254*, 120113. [CrossRef]
3. Zhu, W.; Xu, J.; Xu, J.; Chen, D.; Shi, J. Pier-column backfill mining technology for controlling surface subsidence. *Int. J. Rock Mech. Min. Sci.* **2017**, *96*, 58–65. [CrossRef]
4. Sun, W.; Wang, H.; Hou, K. Control of waste rock-tailings paste backfill for active mining subsidence areas. *J. Clean. Prod.* **2017**, *171*, 567–579. [CrossRef]
5. Wang, M.; Liu, P.; Shang, S.; Chen, Q.; Zhang, B.; Liu, L. Numerical and experimental studies on the cooling performance of backfill containing phase change materials. *Build. Environ.* **2022**, *218*, 109155. [CrossRef]
6. Zhang, X.-Y.; Zhao, M.; Liu, L.; Huan, C.; Song, K.-I.; Xu, M.-Y.; Wen, D. Numerical simulation on thermal accumulation of cemented tailings backfill. *J. Central South Univ.* **2021**, *28*, 2221–2237. [CrossRef]
7. Deng, X.; Yuan, Z.; Li, Y.; Liu, H.; Feng, J.; de Wit, B. Experimental study on the mechanical properties of microbial mixed backfill. *Constr. Build. Mater.* **2020**, *265*, 120643. [CrossRef]
8. Yin, S.; Shao, Y.; Wu, A.; Wang, H.; Liu, X.; Wang, Y. A systematic review of paste technology in metal mines for cleaner production in China. *J. Clean. Prod.* **2019**, *247*, 119590. [CrossRef]
9. Yilmaz, E.; Yilmaz, E. Sustainability and tailings management in the mining industry: Paste technology. *Mugla J. Sci. Technol.* **2018**, *4*, 16–28. [CrossRef]
10. Liu, P.; Zhang, H.; Cui, F.; Sun, K.; Sun, W. Technology and practice of mechanized backfill mining for water protection with aeolian sand paste-like. *J. China Coal Soc.* **2017**, *42*, 118–126.
11. Petlovanyi, M. Physicochemical mechanism of structure formation and strengthening in the backfill massif when filling underground cavities. *Vopr. Khimii i Khimicheskoi Tekhnologii* **2020**, *6*, 142–150. [CrossRef]
12. Zhang, J.; Li, B.; Zhou, N.; Zhang, Q. Application of solid backfilling to reduce hard-roof caving and longwall coal face burst potential. *Int. J. Rock Mech. Min. Sci.* **2016**, *88*, 197–205. [CrossRef]
13. Guo, Y.; Ran, H.; Feng, G.; Du, X.; Zhao, Y.; Xie, W. Deformation and instability properties of cemented gangue backfill column under step-by-step load in constructional backfill mining. *Environ. Sci. Pollut. Res.* **2021**, *29*, 2325–2341. [CrossRef] [PubMed]
14. Basarir, H.; The University of Western Australia; Bin, H.; Fourie, A.; Karrech, A.; Elchalakani, M. University of Science and Technology Beijing An adaptive neuro fuzzy inference system to model the uniaxial compressive strength of cemented hydraulic backfill. *Min. Miner. Deposits* **2018**, *12*, 1–12. [CrossRef]
15. Wang, J.; Fu, J.; Song, W.; Zhang, Y.; Wang, Y. Mechanical behavior, acoustic emission properties and damage evolution of cemented paste backfill considering structural feature. *Constr. Build. Mater.* **2020**, *261*, 119958. [CrossRef]
16. Cao, S.; Song, W.; Yilmaz, E. Influence of structural factors on uniaxial compressive strength of cemented tailings backfill. *Constr. Build. Mater.* **2018**, *174*, 190–201. [CrossRef]
17. Cao, S.; Song, W.-D. Effect of Filling Interval Time on Long-Term Mechanical Strength of Layered Cemented Tailing Backfill. *Adv. Mater. Sci. Eng.* **2016**, *2016*, 1–7. [CrossRef]
18. Komurlu, E. Loading rate conditions and specimen size effect on strength and deformability of rock materials under uniaxial compression. *Int. J. Geo-Engineering* **2018**, *9*, 17. [CrossRef]
19. Fujita, Y.; Fujii, Y.; Ishijima, Y. Influence of Water and Loading Rate on Deformation and Failure Behavior of Shirahama Sandstone. *Shigen Sozai* **2000**, *116*, 565–571. [CrossRef]
20. Huang, B.; Liu, J. The effect of loading rate on the behavior of samples composed of coal and rock. *Int. J. Rock Mech. Min. Sci.* **2013**, *61*, 23–30. [CrossRef]

21. Cao, A.; Jing, G.; Dou, L.; Wang, G.; Liu, S.; Wang, C.; Yao, X. Damage evolution law based on acoustic emission of sandy mudstone under different uniaxial loading rate. *J. Min. Saf. Eng.* **2015**, *32*, 923–928. [CrossRef]
22. Yang, W.; Xie, Q.; Ban, Y.; He, X.; Guanying, P. The Acoustic Emission Characteristics and Damage Constitutive Model of Sandstone under Variable Loading Rates. *Chin. J. Undergr. Space Eng.* **2021**, *17*, 71–79.
23. Ma, Q.; Tan, Y.-L.; Liu, X.-S.; Zhao, Z.-H.; Fan, D.-Y.; Purev, L. Experimental and numerical simulation of loading rate effects on failure and strain energy characteristics of coal-rock composite samples. *J. Central South Univ.* **2021**, *28*, 3207–3222. [CrossRef]
24. Pedersen, R.; Simone, A.; Sluys, L. Mesoscopic Modeling of Concrete under Different Moisture Conditions and Loading Rates. *Underst. Tensile Prop. Concr.* **2013**, *42*, 268–294.
25. Sagar, R.V.; Rao, M. An experimental study on loading rate effect on acoustic emission based b-values related to reinforced concrete fracture. *Constr. Build. Mater.* **2014**, *70*, 460–472. [CrossRef]
26. Ma, M.-H.; Wu, Z.-M.; Zheng, J.-J.; Wang, Y.-J.; Yu, R.C.; Fei, X.-D. Effect of loading rate on mixed mode I-II crack propagation in concrete. *Theor. Appl. Fract. Mech.* **2021**, *112*, 102916. [CrossRef]
27. Dang, V.P.; Le, H.V.; Kim, D.J. Loading rate effects on the properties of fiber-matrix zone surrounding steel fibers and cement based matrix. *Constr. Build. Mater.* **2021**, *283*, 122694. [CrossRef]
28. Zhang, R.; Jin, L.; Liu, M.; Du, X.; Liu, J. Refined modeling of the interfacial behavior between FRP bars and concrete under different loading rates. *Compos. Struct.* **2022**, *291*, 115676. [CrossRef]
29. Rezaei, M.; Issa, M.A. Specimen and aggregate size effect on the dynamic fracture parameters of concrete under high loading rates. *Eng. Fract. Mech.* **2021**, *260*, 108184. [CrossRef]
30. Zhao, S.; Su, D.; Wu, W.; Zhang, Y. Study on damage model of backfill based on Weibull distribution under uniaxial compression. *China Min. Mag.* **2017**, *26*, 106–111.
31. Hou, Y.; Yin, S.; Chen, X.; Zhang, M.; Yang, S. Study on characteristic stress and energy damage evolution mechanism of cemented tailings backfill under uniaxial compression. *Constr. Build. Mater.* **2021**, *301*, 124333. [CrossRef]
32. Tu, B.; Liu, L.; Cheng, K.; Zhang, B.; Zhao, Y.; Yang, Q.; Song, K. A Constitutive Model for Cemented Tailings Backfill Under Uniaxial Compression. *Front. Phys.* **2020**, *8*, 173. [CrossRef]
33. Fu, J.; Wang, J.; Song, W. Damage constitutive model and strength criterion of cemented paste backfill based on layered effect considerations. *J. Mater. Res. Technol.* **2020**, *9*, 6073–6084. [CrossRef]
34. Wang, J.; Zhang, C.; Fu, J.; Song, W.; Zhang, Y. The Energy Dissipation Mechanism and Damage Constitutive Model of Roof–CPB–Floor (RCF) Layered Composite Materials. *Minerals* **2022**, *12*, 419. [CrossRef]
35. Li, J.; Huang, Y.; Zhai, W.; Li, Y.; Ouyang, S.; Gao, H.; Li, W.; Ma, K.; Wu, L. Experimental Study on Acoustic Emission of Confined Compression of Crushed Gangue under Different Loading Rates: Disposal of Gangue Solid Waste. *Sustainability* **2020**, *12*, 3911. [CrossRef]
36. Qiu, H.; Zhang, F.; Liu, L.; Huan, C.; Hou, D.; Kang, W. Experimental study on acoustic emission characteristics of cemented rock-tailings backfill. *Constr. Build. Mater.* **2021**, *315*, 125278. [CrossRef]
37. Wu, J.; Feng, M.; Ni, X.; Mao, X.; Chen, Z.; Han, G. Aggregate gradation effects on dilatancy behavior and acoustic characteristic of cemented rockfill. *Ultrasonics* **2019**, *92*, 79–92. [CrossRef] [PubMed]
38. Wang, L.; Xie, J.; Qiao, D.; Wang, J.; Huang, F. Damage evolution model of cemented tailing backfill based on acoustic emission energy. *IOP Conf. Series: Earth Environ. Sci.* **2021**, *631*, 012071. [CrossRef]
39. Shao, X.; Wang, L.; Li, X.; Fang, Z.; Zhao, B.; Tao, Y.; Liu, L.; Sun, W.; Sun, J. Study on Rheological and Mechanical Properties of Aeolian Sand-Fly Ash-Based Filling Slurry. *Energies* **2020**, *13*, 1266. [CrossRef]
40. Jackson, M.; Talbot, C. External shapes, strain rates, and dynamics of salt structures. *GSA Bull.* **1986**, *97*, 305–323. [CrossRef]
41. Shao, X.; Sun, J.; Xin, J.; Zhao, B.; Sun, W.; Li, L.; Tang, R.; Tian, C.; Xu, B. Experimental study on mechanical properties, hydration kinetics, and hydration product characteristics of aeolian sand paste-like materials. *Constr. Build. Mater.* **2021**, *303*, 124601. [CrossRef]
42. Shao, X.; Sun, W.; Li, X.; Wang, L.; Fang, Z.; Zhao, B.; Sun, J.; Tian, C.; Xu, B. Experimental Study on the Mechanical Properties and Failure Characteristics of Layered Aeolian Sand Paste-like Backfill—A Case Study from Shanghe Coal Mine. *Minerals* **2021**, *11*, 577. [CrossRef]
43. GB/T 50081-2019; Standard for Test Methods of Concrete Physical and Mechanical Properties; Ministry of Housing and Urban-Rural Development of the PRC: Beijing, China, 2019.
44. Liang, C.; Li, X.; Li, S.; He, J.; Ma, C. Study of strain rates threshold value between static loading and quasi-dynamic loading of rock. *Chin. J. Rock Mech. Eng.* **2012**, *31*, 1156–1161.
45. Guo, Y.; Zhao, Y.; Feng, G.; Ran, H.; Zhang, Y. Study on damage size effect of cemented gangue backfill body under uniaxial compression. *Chin. J. Rock Mech. Eng.* **2021**, *40*, 2434–2444. [CrossRef]
46. Liu, L.; Xin, J.; Qi, C.; Jia, H.; Song, K.-I. Experimental investigation of mechanical, hydration, microstructure and electrical properties of cemented paste backfill. *Constr. Build. Mater.* **2020**, *263*, 120137. [CrossRef]
47. Liu, L.; Fang, Z.; Qi, C.; Zhang, B.; Guo, L.; Song, K.-I. Experimental investigation on the relationship between pore characteristics and unconfined compressive strength of cemented paste backfill. *Constr. Build. Mater.* **2018**, *179*, 254–264. [CrossRef]
48. Wu, X.; Liu, J.; Liu, X.; Zhao, K.; Zhang, Y. Study on the coupled relationship between AE accumulative ring-down count and damage constitutive model of rock. *J. Min. Saf. Eng.* **2015**, *32*, 28–34.

49. Kasap, T.; Yilmaz, E.; Guner, N.U.; Sari, M. Recycling Dam Tailings as Cemented Mine Backfill: Mechanical and Geotechnical Properties. *Adv. Mater. Sci. Eng.* **2022**, *2022*, 6993068. [CrossRef]
50. Cheng, A.; Shu, P.; Zhang, Y.; Wang, P.; Wang, M. Acoustic emission characteristics and damage constitution of backfill-surrounding rock combination. *J. Min. Saf. Eng.* **2020**, *37*, 1238–1245.
51. Iordanov, I.; Novikova, Y.; Simonova, Y.; Yefremov, O.; Podkopayev, Y.; Korol, A. Experimental characteristics for deformation properties of backfill mass. *Min. Miner. Depos.* **2020**, *14*, 119–127. [CrossRef]
52. Li, X.; Liu, C. Mechanical Properties and Damage Constitutive Model of High Water Material at Different Loading Rates. *Adv. Eng. Mater.* **2018**, *20*, 1701098. [CrossRef]
53. Li, S.; Cheng, X.; Liu, C.; Cheng, C.; Yang, M. Damage characteristics and space-time evolution law of rock similar material under uniaxial compression. *J. China Coal Soc.* **2017**, *42* (Suppl. S1), 104–111.
54. Cheng, A.; Zhang, Y.; Dai, S.; Dong, F.; Zeng, W.; Li, D. Space-time evolution of acoustic emission parameters of cemented backfill and its fracture prediction under uniaxial compression. *Rock Soil Mech.* **2019**, *40*, 2965–2974.
55. Cao, S.; Yilmaz, E.; Song, W.; Yilmaz, E.; Xue, G. Loading rate effect on uniaxial compressive strength behavior and acoustic emission properties of cemented tailings backfill. *Constr. Build. Mater.* **2019**, *213*, 313–324. [CrossRef]
56. Lai, Y.; Zhao, K.; Yan, Y.; Yang, J.; Wu, J.; Ao, W.; Guo, L. Damage study of fiber-doped superfine tailings cemented backfill based on acoustic emission cumulative ringing count. *J. Mater. Sci.* **2022**, *57*, 11612–11629. [CrossRef]
57. Liu, W.; Guo, Z.; Niu, S.; Hou, J.; Zhang, F.; He, C. Mechanical properties and damage evolution behavior of coal–fired slag concrete under uniaxial compression based on acoustic emission monitoring technology. *J. Mater. Res. Technol.* **2020**, *9*, 9537–9549. [CrossRef]
58. Kachanov, M. On the time to failure under creep conditions. *Izv AN SSSR Otd Tekhn Nauk.* **1958**, *8*, 26–31.
59. Lemaitre, J. A Continuous Damage Mechanics Model for Ductile Fracture. *Trans. Asme J. Eng. Mater. Technol.* **1985**, *107*, 83–89. [CrossRef]

Statistical Quality Inspection Methodology in Production of Precast Concrete Elements

Izabela Skrzypczak

Faculty of Civil and Environmental Engineering and Architecture, Rzeszow University of Technology, Powstancow Warszawy 12, 35-959 Rzeszow, Poland; izas@prz.edu.pl

Abstract: Today, prefabricated concrete elements are used in many construction areas, including in industrial, public, and residential construction; this was confirmed via questionnaire research. In the article, the prospects for precast concrete development are presented, and the factors determining the use of this technology are defined. Based on a review of the literature, it was shown that currently, higher-quality prefabricated elements are primarily created through the implementation of innovative materials and production technologies. For this reason, the lack of research regarding quality control in prefabricated elements based on statistical quality control is particularly noticeable. The quality control process is one of the most important distinguishing features in prefabrication due to the increasingly stringent expectations of customers; it helps to ensure that the desired durability of implemented constructions is achieved. Issues related to assessing the effectiveness of standard procedures presented in this paper were analyzed using statistical methods in the form of OC (operating characteristic) and AOQ (average outgoing quality) curves. Thus, a new approach was proposed because these methods have not been previously used in precast concrete. The shape of the curves obtained confirmed the significant dependence of the value of the acceptance probability on the defectiveness of production. In AQL control systems based on OC and AOQ curves, it is necessary to calculate the current average defectiveness, which should be treated as a basis for the decision to switch from one type of control (normal, tightened, or reduced) to another. In this respect, the standard requirements of quality control have been simplified, and it has not been considered necessary to determine the average defectiveness value in production processes. The examples included in this study, including the analysis of curb production data, clearly show the harmful effects of ignoring the actual process defectiveness. As a result of the calculations, it was found that the average actual defectiveness of the curbs produced could not be equated with batch defectiveness. The analyses carried out in this study prove that equating batch defectiveness with process defectiveness is not an appropriate approach, which was confirmed through the producer's/customer's risk analysis. The approach proposed in this study, the analysis of OC and AOQ curves, is an innovative solution in prefabrication and can be an effective tool for managing the quality of prefabricated products, taking into account economic boundary conditions.

Keywords: precast concrete products; quality control; OC curve; AOQ curve

1. Introduction

The existence of prefabrication plants and numerous successful construction projects realized with precast concrete elements for all or part of a building structure demonstrate that this technology is effective and economical [1]. In [2], the author contended that by employing industrialized and automated building system methods, the amount of manual labor on-site could be reduced, and the construction speed could be increased along with higher construction quality being achieved. The advantages of prefabrication, i.e., ensuring repeatability, increasing efficiency, and achieving lower unit prices compared to traditional technology, mean that recently, prefabricated concrete elements have been increasingly used. These elements are manufactured under controlled conditions and strict supervision,

and their standard—ensuring the requirements for mechanical properties, accuracy, and quality are met—is becoming increasingly higher. Quality control is a key element in management at all levels of production. Quality control makes it possible to verify the characteristics of prefabricated elements and ensures their ability to meet the needs and requirements of the customer [2]. Customer requirements are most often specified in the contract specification.

On the other hand, the level of quality in terms of efficiency, usability, aesthetics, strength characteristics, or geometric features are formulated in the relevant industry standards. The purpose of quality assurance and quality control systems is to maximize the repeatability of the manufactured prefabricated elements, and to ensure that the standard requirements are met [3,4]. In [4], a precast segment (rings for tunnel linings) manufacturing process's quality control processes are presented and discussed. Despite the quality control system, some areas of weakness were identified. These arose primarily due to non-conformance in the casting process and a lack of maintenance. A substantial number of non-conformances were associated with surface defects in the segments. A review of the QA/QC control system showed there were no inadequacies in the system, but certain aspects could have been improved. These include the workflow of remedial works, equipment maintenance, and staff's working attitude. Amongst the factors that affect the maintenance of good quality, workers' cost and skill level were considered. It was shown that higher-quality precast segments are attainable through the careful choice of materials, the use of better production tools in batching and casting processes, and strict quality control. By considering time and cost factors, constraints may have been added to the selection of materials for quality testing. The frequency of selective testing was once every 12 months for raw materials and reinforcement and one monthly cycle for steel molds and reinforcement cages. The authors of [4] suggested that the variation in the test result should be scrutinized according to other standard practices. The variation might have resulted from non-random sampling, probability causes, or other factors that were not readily detectable. A predictable pattern, such as a normal distribution, should become a parameter of the chance of variation. Tightened quality control is necessary to minimize the impact of cost and time constraints in the production of precast products.

The standards provide recommendations, guidelines, and procedures for users, designers, and manufacturers to ensure the desired level of quality is achieved. These include production, aesthetic, technological, and economic considerations. Thus, quality control is an integral aspect of the production of precast concrete elements. Great importance has always been placed on assessing the building elements quality and structures and improving the safety and reliability of implemented facilities [5–11]. As noted in the research conducted to date, an efficient quality control system is the most critical and important process link in the mass production of prefabricated elements [3]. Currently, prefabrication plants evaluate prefabricated manufactured elements in several stages specified in industry standards [12,13] and codes, e.g., [14–22]. In addition to the quality control of each component, the mechanical properties of finished prefabricated elements are assessed.

On the other hand, the key features that ensure the high quality of the final product are, in addition to providing strength and deformation parameters: the geometric dimensions, the location of the reinforcement, and the surface finish. It is also challenging to measure and evaluate quality characteristics in a highly reproducible and efficient manner. Therefore, innovative measurement and quality control methods have been proposed [23–30]. Usually, the first step is to assess the quality indicators on an ongoing basis concerning the properties of both the input materials and the finished prefabricated elements, i.e., strength and deformation parameters, as well as data related to the geometric dimensions, reinforcement positions, and surface quality. The next evaluation stage is the acceptance of the finished products, which includes selective tests to assess the already-finished, full-size prefabricated elements using destructive methods [31–34]. The necessity of moving from selective inspection to full factory inspection has been demonstrated in previous research [30,35]. According to the research described in [25,30], the selective control systems for prefabricated

elements in the standards do not always take into account the variability in the production process and do not always ensure the appropriate quality and reliability of all of the components of the manufactured elements from a given batch of tests. Therefore, in [30], the quality control of finished prefabricated elements based on reliability was proposed. Software systems for quality control based on probabilistic algorithms were also proposed, which allowed the influence of the variability in process factors and controlled parameters on the properties of the output products to be taken into account. Methodology for the automated quality control of reinforced concrete prefabricated elements was proposed based on ensuring the reliability of manufactured concrete elements.

Quality-related aspects are fundamentals in concrete precast plants, as prefabricated elements are the basis of modern construction [1,34]. The production of prefabricated concrete elements requires the essential requirement to be met—quality—while ensuring the statistically needed minimum number of elements are tested with the minimum control costs. The fulfillment of these aspects is possible through the continuous implementation of statistical quality control procedures with the production process itself, as well as the properly designed and implemented selective quality control of ready-made prefabricated elements. It allows achievement by applying standard quality control procedures formulated in codes and by automating production processes. Therefore, to ensure the quality of the manufactured elements, e.g., in [6,24,25,34], it was proposed to automate construction processes that covers the project's entire life cycle. However, decisiveness is required in quality assurance to ensure the correct implementation of the appropriate technology [26]. Many companies and countries have recognized the great potential of automation, resulting in various pilot projects, patent applications, and many automation and robotic solutions being implemented in the construction sector. Qualitative and quantitative studies regarding the limitations and prospects for using robotics in construction are presented in [27]. According to [28], the degree of automation in producing precast concrete products is more advanced than in any other industry. As concrete is the most widely used building material worldwide [35,36], well-developed quality control procedures already exist for this material in terms of design and production. The methods are reflected in the compliance criteria recommended in concrete codes. Currently, in principle, the entire concrete industry has started to implement automated optimization processes for the product and production. In [37], the interdependencies between the material, structure, and production of precast concrete elements were described, and optimizations—including ecological-, economic-, and quality-related optimizations—of the manufactured precast concrete were indicated as overarching strategies for possible enhancement. In addition to optimizing the materials used, the composition of the concrete mix, reinforcement, production, and quality should be considered in relation to costs and the minimum number of elements being tested [38].

As was found, e.g., in [39,40], most published articles regarding concrete prefabrication focus on a specific method of producing prefabricated elements, as well as defining the categorization of significant interdependencies in the production of precast concrete elements [37]. Higher-quality prefabricated elements are primarily created through innovative materials [41–52] and production technologies [53–69]. Reducing carbon dioxide emissions is the future of the construction industry; hence, the work on the development of materials based on waste is an essential aspect in the development of prefabrication [41–45]. In [41], to increase concrete toughness, the crushed rubber with sizes from 1 to 3 mm and 3 to 6 mm was replaced by 5%, 10%, and 15% sand. To compensate the degradation of the strength and improve the workability of the concrete, the combination of two additives of nano silica and metakaolin additives with optimum values was used. Moreover, the compressive strength, tensile behavior, and modulus of elasticity were measured and compared. The results indicate that the optimum use of nano silica and metakaolin additives could compensate for the negative effects of the rubber material implementation in the concrete mixture while improving the overall workability and flowability of the concrete mixture. For this reason, the importance of research regarding the quality control of prefabricated elements based on statistical quality control is particularly noticeable. As seen

from the literature review, the problem of the number of samples used in research in the production of prefabricated elements is also important to the effectiveness and efficiency of quality control and economic procedures, and very few articles have been published on this subject. The quality control process is one of the most important distinguishing features in prefabrication due to the increasingly stringent expectations of customers; its use can also ensure that the desired durability of implemented constructions is achieved. Issues related to assessing the effectiveness of standard procedures presented in the paper were analyzed using statistical methods in the form of OC (operating characteristic) and AOQ (average outgoing quality) curves.

1.1. Advantages of Prefabrication

The use of precast concrete elements has many advantages compared to the production of individual elements on a construction site. According to [1,46], the advantages of the prefabrication process and prefabricated elements which establish the competitiveness of this solution in the construction market include:

- The actual high quality of the product, which is produced in a controlled environment using standardized methods.
- Advanced quality control that goes far beyond fresh concrete control.
- Dimensional accuracy, ensuring the properties of both hardened concrete and the position of the reinforcement can be checked before being embedded in the element structure.
- Factory production is independent of weather conditions and can be carried out independently of on-site construction works.
- Design flexibility: For a designer, a significant advantage of prefabricated elements is their great architectural value. The material offers unlimited possibilities in its formation, and the color, texture, and detail can be modified. The material can be used to implement design ideas in various architectural styles.
- Economy: An important advantage of precast concrete elements is the production process itself; it ensures a low level of material consumption (concrete and steel). The prestressed process saves up to 50% of steel and higher. In addition, the factory production process is highly developed. The techniques used in the prefabrication industry make it possible to provide a high-quality finished product that meets the project requirements in terms of cost and schedule.
- Low negative impact on the environment: Precast concrete is an environmentally friendly material. It is made of natural materials. No toxic substances are produced during its production and use.

Within the advantages of prefabrication, the key advantage is the high real quality of the product, which is guaranteed by standardized production methods and advanced quality control. The process of creating prefabricated elements with appropriate quality takes place through the implementation of basic management functions in production processes, i.e., planning, organizing, and controlling all of the activities in such a way that the result is a product that meets the assumed final needs. Quality is not only created during the final processing stage of the product on the production line but is also "created" in the preproduction, production, and post-production phases, determining the interdependence of a number of activities and leading to the creation of the final product. Repeatability throughout the cycle enables production development, constantly adapting it to customers' needs, and emphasizing the constant interpenetration of production and consumption [47]. Quality planning sets goals and quality requirements as well as requirements for the application of the statistical quality control system. The quality of a final product depends primarily on the method of its design (including the quality of input materials), the quality of the workmanship, or the conditions connected with the production technology, such as temperature, humidity, pollution, or shocks caused by operating devices.

Companies producing prefabricated concrete products on the construction materials market are expected to continuously increase their production capacity, maintain the high-

quality level of the offered products, and conduct a flexible pricing policy. Achieving these goals is possible through quality control at every stage of production, from the selection of input materials to ready-made prefabricated elements. To stay on the market, prefabrication plants must not only guarantee the high quality of the manufactured goods but also sell them at attractive prices for the customer. That dependence leads to the necessity of estimating the costs of controls related to the introduction of a given acceptance plan before its application. Therefore, manufacturing companies must carry out the acceptance control of a batch of products by a plan that guarantees the assumed level of quality with the lowest possible control costs. Then, it is essential to implement statistical control and an appropriate test plan for manufactured prefabricated elements in prefabrication plants. The goal is essential during the implementation of the quality control of prefabricated reinforced concrete elements, which, due to the complexity of climatic conditions, constitute the basis of modern construction in many European countries, including Poland. The production of prefabricated reinforced concrete structures requires the provision of the basic conditions which will ensure their reliability with minimal expenditure. This engineering and economic problem must be solved to improve the control system during the production process and the quality control of the output products to ensure that they meet the consumer requirements [30].

Currently, precast prefabrication plants assess the operational integrity of the output products in several stages specified in the applicable codes. First, the current control of individual quality indicators is carried out (for the properties of strength and deformation materials, data regarding geometric parameters, and reinforcement). The final product acceptance stage includes periodic tests to assess full-size elements. As described in [30], the selective control system is not always economically effective, does not consider the variability in the production process, and does not ensure the quality and reliability of all the elements in the tested batch. The need to move from selective to full factory control has been found in studies, e.g., [48].

The most rational solution is to evaluate the acceptance test plans used in ongoing inspections about specific parameters of the manufactured prefabricated elements. Consequently, the evaluation of the recommended test plans in the codes for precast elements of reinforced concrete structures based on statistical methods is gaining importance in research. The operational characteristic curves proposed in the article and the curves of average defectiveness after inspection, constructed for codes' acceptance plans, allow one to account for the influence of variability in process factors and controlled parameters of prefabricated elements (the number of elements to be tested or the defectiveness of manufactured elements) on the consumer properties of output products. Therefore, this article aimed not only to determine the discriminant power of the recommended attribute test plans in the codes for prefabricated elements but also to determine the effectiveness of the quality control of precast elements at the acceptance testing stage.

1.2. Development Prospects for Prefabrication in Poland

The economic market crisis in 2020 led to implementing methods that will improve the construction process. Above all, this is the result of the work carried out in parallel in many segments of the construction industry, which generates many problems. The most significant factors for construction companies were the limited availability of employees, the duration of construction investments, and the assurance of the appropriate quality of the facilities. They, along with emerging difficulties, solutions, and technologies limiting negative premises, have gained importance. Modern prefabrication is the solution to these challenges. Therefore, it is not surprising that an increasing number of actors in the construction market are looking more and more favorably toward prefabricated elements than in previous years; their increased use not only allows the implementation of works to be significantly accelerated but also allows the appropriate levels of quality and durability of the facilities to be guaranteed. Therefore, in the first stage of the research, to assess the condition and prospects for the development of concrete prefabrication in Poland, a

survey was carried out among investors, architects, and contractors. The research included 15 respondents from each target group. Based on the survey, it was found that prefabricated concrete elements represent a well-known and relatively commonly used solution in the implementation of most types of investments [49–52]. On average, it was shown that three out of four respondents implementing industrial and warehouse construction projects use prefabricated concrete elements. The responses obtained from the respondents also indicate the good popularity of this type of technological solution in particular segments of the construction industry (Figure 1). However, the widespread use of prefabricated concrete elements in a given construction segment does not necessarily translate into a large scale and a large share of this technology in the context of the entire investment (Figure 1).
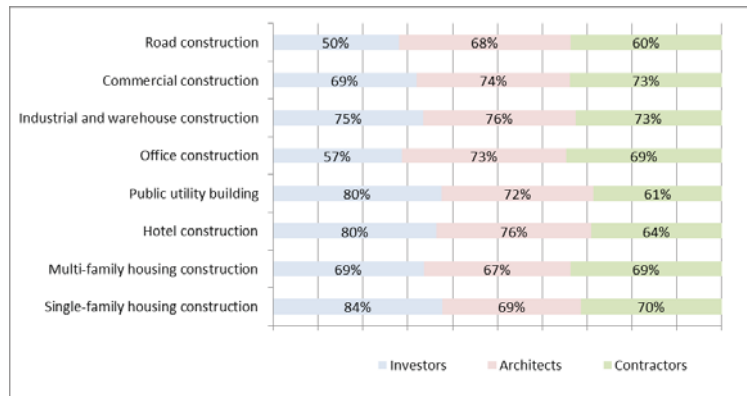
Figure 1. The use of prefabricated concrete elements during the implementation of the investment.

The factors that determine the use of precast concrete elements in a construction site are shown in Figure 2. The distribution of responses differed depending on the group of respondents (Figure 2).
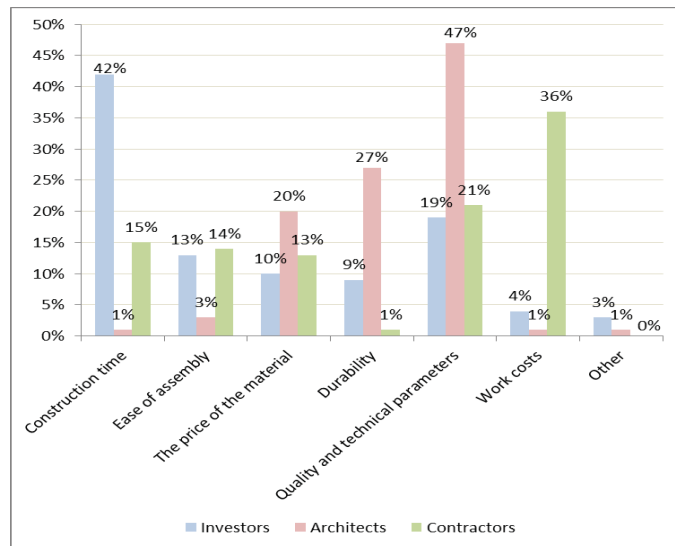
Figure 2. Factors that determine the choice of precast concrete technology.

The factor that determines the use of precast concrete technology is the reduction in construction times. This aspect was shown to be crucial for almost half of the respondents in this group (42%) (Figure 3). It was found that quality is a decisive factor for architects in choosing prefabricated technology. For contractors, work cost is a crucial factor.
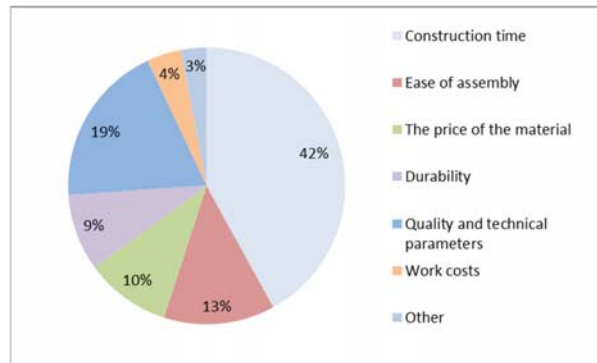
Figure 3. The most important factor when choosing the technology of precast concrete elements in the opinion of investors.

Another important factor when choosing a prefabricated technology for investors is quality and technical parameters. The ease of assembly is another factor that determines the use of this technology. However, for investors, factors such as material costs and durability are practically just as important.

From the perspective of contractors, concrete prefabrication technology was very positively evaluated. As a result of the research, the contractors positively (good and very good) assessed precast concrete elements (Figure 4).
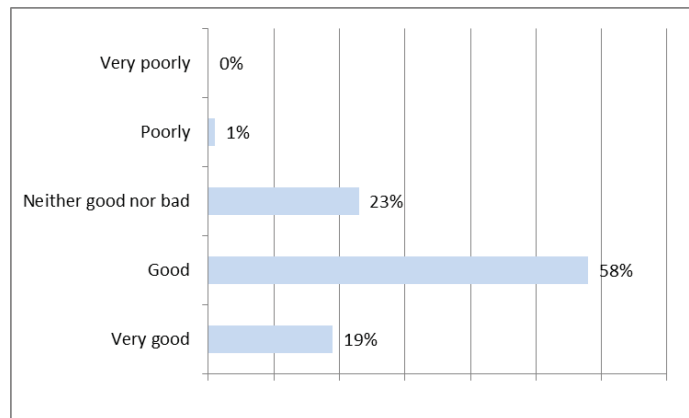
Figure 4. Evaluation of precast concrete elements—contractors.

When asked whether the share of contractors using precast concrete products will increase, up to 27% of contractors responded positively (Figure 5). This relatively high degree of popularization of this type of technology will reduce the potential for a further upward trend in the future.
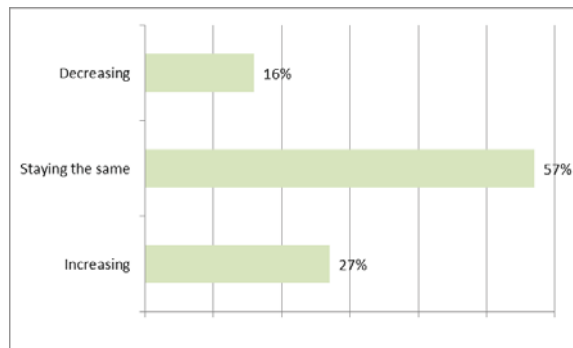
Figure 5. Expected change in the share of contractors using precast concrete.

It was shown that the surveyed contractors have no doubts about the time savings that result from using prefabricated elements (Figure 6). In the opinion of the contractors, none of the elements mentioned in the study (Figure 6) can be realized faster using traditional technology. Only in the case of walls did a noticeable percentage of respondents (31%) believe that both technologies are comparable in terms of time. On the other hand, it was shown that the surveyed contractors have no doubts about the speed with which lintels, balconies, staircases, and stairs can be created. Everyone indicated that the use of prefabricated technology translates into time savings.
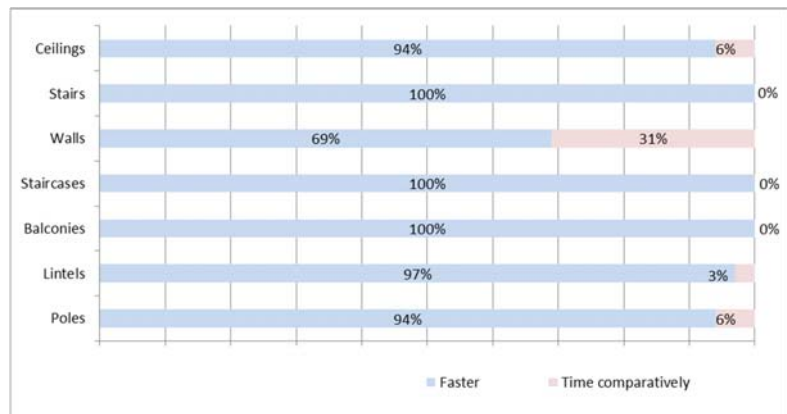
Figure 6. Implementation time—prefabricated technology and traditional technology—contractors.

The issue of the mentality and preferences of market participants remains a significant barrier to the dissemination of this technology in Poland, which results from bad experiences and associations with concrete prefabrication from the 1950s to the 1970s. However, as our research shows, favorable changes have occurred in this regard, largely due to the positive ratings from those who have already used this technology. The promotion of investments made of prefabricated elements is significant to the increase in awareness and the better perception of this technology, which we should expect an increasing level of in the future (especially in terms of housing construction). Research shows that the advantages of prefabrication, especially the shorter construction times and the stable quality of the manufactured prefabricated elements, are reflected in the use of this technology. Prefabricated product manufacturers have been modernizing their technological lines for years, increasing not only the number of products and solutions but mostly improving their quality parameters by implementing the statistical quality control procedures recommended in

the codes. Therefore, the next research stage is the analyses of the procedures' statistical quality control used in the quality assurance of the prefabricated elements produced. The results obtained from the questionnaire are similar to the research results in [52].

Quality assurance is based on the idea of preventing quality defects. It is the next step in developing quality concepts after quality control, which is based on statistical methods and developed research plans.

1.3. Statistical Quality Control

Statistical quality control (SQC) may include statistical acceptance control (SAC) and refer to statistical product acceptance (SPA) or statistical process control (SPC) focused on the production process [53–57], which may be combined with control charts [53], for example, Cusum charts (method C in the control of concrete compressive strength according to EN 206 + A2: 2021-08 [14]) (Figure 7).
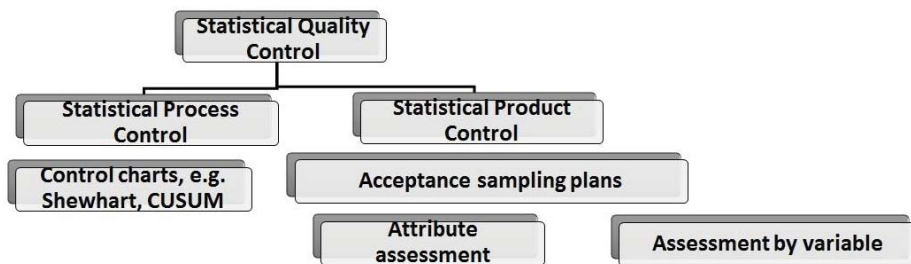
Figure 7. Scheme of quality control.

The aim of SQC, in addition to ensuring the required level of the tested feature of products, is to reduce the cost of control and, in some cases, even to enable control.

SQC mainly deals with issues related to statistical methods of receipt of piece products and current control carried out during production on a random basis, i.e., a representative part of the examined whole.

These methods make it possible to reduce the number of erroneous judgments about the quality of tested batches of products, making the probabilities of rejecting a good batch (meeting the quality requirements) low enough (the first type of error) and accepting poor-quality products low enough (the second type error), as well as protecting against excessive shortages in production.

Acceptance control due to the measured and calculated parameters and the method of evaluation is divided into [48,57]:

- Control based on attribute assessment: Batches of products subjected to checks should be considered compliant if the number of non-compliant items in the tested sample does not exceed the qualifying number.
- Control based on variable inspection: A batch of products subject to control is considered compliant if the number of quality statistics do not exceed the qualifying number k.

The discriminatory power (effectiveness) of different sampling plans can be assessed by comparing how they perform their function at different possible levels of quality. The practical difficulty in finding the perfect random sampling plan is that you cannot change the laws governing random events. Therefore, when choosing collection plans based on batch testing with defective items, a decision should be made regarding what risks may be incurred in each case, and this is most often an economic decision. In the case of batch acceptance, according to an attribute assessment, the value of the risk of acceptance of batches containing a certain percentage of defective elements is given by the operating characteristic curve of a given acceptance plan.

1.4. Statistical Acceptance Control According to the Attribute Assessment

Statistical acceptance control methods define random sampling and provide the rules of a procedure to qualify the quality of finished product batches. On their basis, we can consider a batch good or defective. In the latter case, it is possible to lower the element's class or sort and reject the defective precast elements and in justified cases, destroy and recycle them.

One of the methods used is so-called acceptance plans. The simplest is a single (one-step) attribute assessment plan classifying each item as good or defective. The quality of the batch is then understood as the quotient $j = (n - k)/n$, where n is the number of simples in the batch with k defective items, and the batch defect is called $w = k/n$. A single test plan is a formal record specifying the size of a random sample taken at one time from a lot and the allowable k number of defective items in the sample; exceeding the allowable number leads to the lot being classified as bad. The number k is called the qualifying number, and the plan is denoted by the symbol $k\|n$, where n is the number of test results for precast elements [48,57].

To create such a plan, the acceptable quality level (AQL) that meets the inequality $w \leq AQL$ is determined in each batch. The probability that, in an n-element sample taken from a batch with a defect in w, there will be at most k defective pieces, can be calculated from the Bernoulli formula (RB—Bernoulli distribution) for independent samples (1) [57]:

$$P_a = \sum_{k=1}^{n} \begin{pmatrix} n \\ k \end{pmatrix} w^k (1-w)^{n-k} \tag{1}$$

The acceptance probability (P_a) of a defective lot (w) in the $k\|n$ plan is called the characteristic of a single plan, and the graph of dependence on (w) is called the operating characteristic curve (OC curve). An ideal would be a plan to ensure that all of the lots with defectiveness $w \leq AQL$ are accepted and rejected when $w \geq AQL$. However, this is only possible with faultless 100% control (Figure 8).

(**a**)   (**b**)
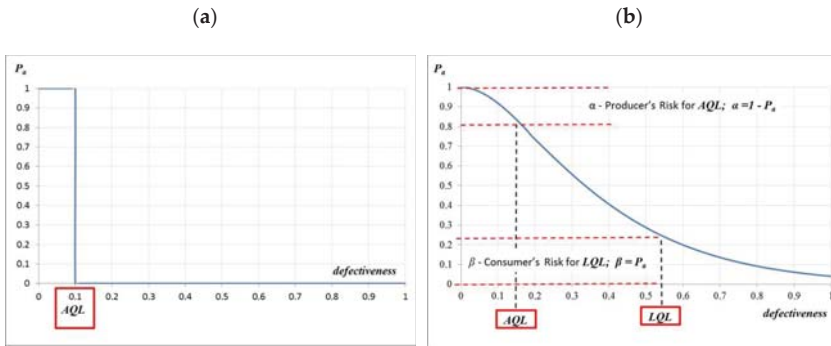
Figure 8. OC curve: (**a**) at 100% control and (**b**) with producer's and customer's risks.

The better—or more selective—the reception plan is, the closer the OC curve plot is to that shown in Figure 8 (steeper).

When constructing the OC curves, it is possible to assume a different distribution of the analyzed features/parameters of the precast elements; therefore, Equation (1) can be approximated by the formulas [57]:

- Poisson distribution—RP (2):

$$P(w) = \sum_{k=0}^{n} \frac{\lambda \exp(-\lambda)}{k!} \tag{2}$$

where $\lambda = nw$.

- Gaussian distribution—RG (3):

$$P(w) \approx \varphi\left(\frac{k - nw + 0.5}{\sqrt{nw(1-w)}}\right) \tag{3}$$

where $\varphi(x) = \frac{1}{\sqrt{2\pi}} \int_{-\infty}^{x} \exp\left(-\frac{t^2}{2}\right) dt$ is a function of the normal distribution N(0,1).

- Normal distribution—RN for a random variable k with n and w parameters (4):

$$N\left(nw, \sqrt{nw(1-nw)}\right) \tag{4}$$

While for a random variable $\frac{k}{n} \rightarrow$ the distribution of RN has the form (5):

$$N\left(w, \sqrt{\frac{w(1-w)}{n}}\right) \tag{5}$$

Formula (5) can be used when the condition is met $nw(1-w) > 4$.

- Pascal distribution (RPa) for a random variable n with parameters k i w (6):

$$P(w) = \binom{n-1}{k-1} w^k (1-w)^{n-k} \tag{6}$$

- Gamma distribution—RGa with the scale parameter $b = 1/w$ and the random variable $n - 1$ (7):

$$P(w) = \frac{n-1^{(\frac{1}{w}-1)}e^{-\frac{(n-1)}{2}}}{2^{\frac{1}{w}}\Gamma\left(\frac{1}{w}\right)} \tag{7}$$

- The χ^2 distribution—RChi^2 with $2k$ degrees of freedom of a random variable $2w(n-1)$ (8):

$$P(w) = \frac{2w(n-1)^{(\frac{n-2}{2})}e^{-\frac{2w(n-1)}{2}}}{2^{\frac{n}{2}}\Gamma(2k)} \tag{8}$$

The main purpose of the random acceptance of products is to determine whether the batch from which the collected element comes meets the previously assumed quality requirements and, thus, whether it can be considered compliant with these requirements. If the tested element does not meet the requirements, the entire batch should be considered non-compliant, and the procedure of dealing with a non-compliant product should be implemented. Due to the evaluation of the examined features, the acceptance inspection can be performed by an attribute or by a variables inspection. Only the measurable features are assessed during the acceptance test, e.g., size, density, and strength, using the variables inspection. A batch of products is considered compliant if the so-called quality statistic does not exceed the qualifying constant k, depending on the specified value of the acceptable quality level (*AQL*) and the number of samples—elements taken for testing [58,59].

According to the recommendations of the code ISO 2859-0: 2002 [18], non-conformities (defectiveness) should be classified in terms of their validity. Typically, a division of non-conformities into more significant—class A—and less significant—class B—is used. More important non-conformities will be controlled more strictly. By definition, the *AQL* is "a quality level that corresponds to the worst tolerated average process level" [18]. The *AQL* is a parameter of the process scheme because the *AQL* value, together with the letter sign of the sample size, allows one to determine the test plan and the control scheme. It is assumed that the average process level should be less than or equal to the *AQL* value in order to not reject too many batches produced.

During production control, a prefabricated element for testing is taken from each manufactured batch. The batch is considered compliant if the number of non-compliant units does not exceed the qualifying number A_c (9) [18,19,57]:

$$k \leq A_c \tag{9}$$

where k—number of non-compliant items per 10 items taken for testing;

A_c—constant qualifying or disqualifying number of non-conforming items.

The control plan and control procedures using variables inspection define, e.g., code ISO 3951:1997 [20,21], complementary to ISO 2859-1:2003 [19]. In order to use variables inspection in the sampling procedure, the following conditions must be met:

- A series of product batches supplied by a specific manufacturer using the same production process repeatedly is systematically checked;
- The analyzed feature of the product is measurable on a continuous scale;
- The production is statistically regulated, and the tested feature of the product has a normal or close to normal distribution.

All of the above-mentioned requirements are met for the production of precast concrete products (e.g., concrete paving stones, concrete paving slabs, and concrete curbs).

To determine the acceptance test plan, the values of the acceptable defectiveness are used, i.e., the AQL limit of acceptable quality, amounting to 0.1 (analogous to ISO 2859-1:2003 [19]). Depending on the severity of the non-conformities, different levels of AQL are used, e.g., significant non-conformities (e.g., the strength of paving slabs and the strength of curbs) are classified as class 1 and assigned higher values than less significant non-conformities (e.g., the dimensions of slabs and the dimensions of curbs).

Acceptance tests are carried out assuming a certain level of control, strictly related to the size of the batch and the number of samples taken. The code ISO 3951:1997 [21] provides three general levels of control: I, II, and III; and four special levels: S-1, S-2, S-3, and S-4. If there are no specific provisions in the relevant standards, level II data are usually used. Where stricter control is required, level III should be used, and when less severe control is needed, level I should be used. Special levels of control are used when a small number of test specimens and a high risk of random control (e.g., in a destructive strength test) are required simultaneously. For example, such situations occur when inspecting precast concrete products. The number of test samples can also be reduced by applying transition conditions between the different control levels.

Concerning the adopted test plans, it is possible to determine the dependence of the average defectiveness after the inspection of the defect and before the inspection, i.e., an actual defect in manufactured prefabricated elements (with a decreasing quality level). This relationship is called the average defectiveness curve after inspection (AOQ curve—average outgoing quality curves [56,58,59]. These curves can present the risk associated with acceptance plans for the quality control of the concrete used for production and the ready-made prefabricated elements.

Average outgoing quality limit (AOQL) can be treated as a criterion for the selection of a research plan, thus verifying the correctness of the adopted acceptance plans. Furthermore, the AOQL contains very important information for the recipient/consumer regarding the maximum defectiveness that can be expected with successive receipts of a number of batches over a long period of time based on the adopted acceptance inspection criteria. The practical significance of AOQL is that its value can be equated with the quantile level for the verified property (feature), and thus reflect the quality of the manufactured precast elements.

In AOQ charts, an extreme expresses the AOQL value. The coordinates of the AOQ plot can be determined based on the operational characteristics curve (OC) according to the formula [56,57]:

$$AOQ = w \cdot P_a \tag{10}$$

where AOQ—the average defectiveness after inspection;

w—the defectiveness before inspection;

P_a—the probability of acceptance of the batch of precast elements with defective *w*.

When verifying the correctness of the compliance criteria and the quality of the batch of precast elements, one can refer to two defectiveness values: 5% (AQL—acceptable quality level) and 10% (LQL—limiting quality level), for which L. Taewre [60] proposed formulas for boundary curves for three areas: controlled, unsafe, and uneconomical. In the case of concrete quality control, the determination of the impact of compliance control on the assumed concrete class requires the determination of the statistical quantile of the concrete compressive strength distribution after the compliance control. The quantile estimation for the compressive strength requires the determination of the concrete's defectiveness after a compliance check. Such inference can be made using AOQ (average outgoing quality) curves (Figure 9).
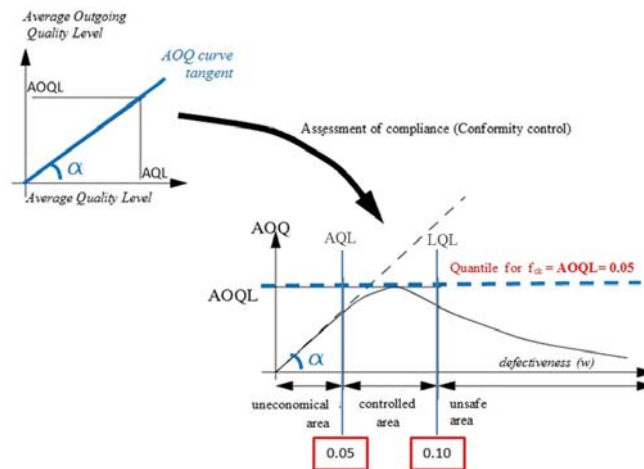
Figure 9. Diagram of the relationship between the defectiveness before and after quality control for compressive strength of concrete.

AOQ curves are also constructed for acceptance plans, i.e., for plans used in the acceptance of precast concrete elements. AOQ curves are curves obtained for the state after inspection; therefore, these curves make it possible to assess the discriminant power of acceptance criteria or compliance criteria in the case of concrete quality. Using AOQL for compliance control, the concrete compressive strength can be identified with the quantile defined for the concrete class, i.e., the quantile of the characteristic strength. According to EN 206 + A2: 2021-08 [14], if the industry standards do not define otherwise, the value of the permissible defectiveness after the inspection performed can be assumed to be at the level of 0.05 (11):

$$AOQL = 0.05 \tag{11}$$

2. Materials and Methods

2.1. Code Quality Control Procedures for Precast Elements

Contemporary codes for precast concrete products recommend acceptance control using statistical methods. In the case of prefabricated concrete products, an additional legal requirement [13] is the obligation to use CE marking for most of these products. This obligation is connected with the necessity of, among others, determining the type of product with the determination of its functional properties and conducting factory production control (FPC). Factory production control means "permanent internal control" carried out by the manufacturer to ensure the required product properties (both identification and use) [12]. FPC covers not only direct product control but also all aspects related to the production and supervision of this production [14,48,57], i.e.,:

-    The preparation stage of production, which includes, among others, the purchase and control of raw materials;
-    The production stage, including its supervision, control, and testing according to a predetermined plan;
-    Procedures for dealing with a non-conforming product;
-    The supervision of machinery and equipment, as well as equipment needed for inspection and testing;
-    The determination of the requirements for the competence of personnel;
-    Marking and securing products during storage and transport;
-    Corrective actions in the event of any non-conformities.

All of these activities should be properly documented. Therefore, the manufacturer should carry out controls and tests in all the stages of product manufacturing in accordance with the established frequency, which results from the technical specifications for a specific product and its production conditions. The frequency and number of samples taken for testing, and thus the control cost, are influenced by the level of control, among other things.

In addition, the subject standards for precast concrete products (e.g., PN-EN 13369:2018-05 [17]) emphasize that if the manufacturer has a quality management system in the company compliant with ISO 9001:2015-10 [22] and takes into account the requirements of the subject codes, it meets the requirements for implementing and conducting factory production control. On the other hand, the ISO 9001:2015-10 code [22], in chapter 9 on the evaluation of the effects of action, recommends the use of statistical methods for the analysis and evaluation of data, including for the conformity assessment of offered products (point 9.1.3 of code ISO 9001:2015-10 [22]). As can clearly be seen, statistical product quality control falls within the scope of obligatory factory production control, but it is only one of the activities leading to the obtainment of a product compliant with standard requirements and a good-quality product that will quickly attract customers.

2.2. Attribute Acceptance Plans for Selected Kinds of Precast Elements

Industry codes recommend using attribute acceptance plans for all precast concrete products [14–22]. In the case of the quality control of prefabricated concrete products, acceptance control always starts with normal control, and then, when the production level is good enough, reduced control can be applied, which involves fewer test samples and a lower qualifying constant k. Regarding prefabricated concrete products, the subject standards recommend that the qualifying constant k remain unchanged, but the number of samples can be reduced. Figure 10 shows the transition conditions between the levels of strength control levels for precast concrete elements according to the recommendations of EN 13369:2018-05 [17].
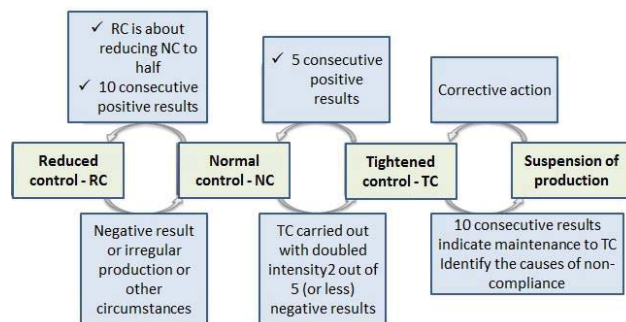
Figure 10. Conditions for the transition between the levels of strength control for precast concrete elements according to EN 13369:2018-05 [17].

Each transition from a more severe to milder-level results in a reduction in the amount of control during the production of precast concrete elements.

Transitions between individual levels of control are formulated in the subject codes dedicated to specific precast products, e.g., in accordance with EN 1339:2005 [15], the control of paving slabs includes: the visual inspection of the product's appearance, the measurement of the shape and dimensions of prefabricated slabs, the examination of wear layer thickness, strength determination to bending and breaking loads, and the determination of resistance to freezing/thawing with the use of de-icing salt (in resistance class 2). For each of these features, the EN 1339:2005 code [15] specifies the frequency and number of samples taken for the above-mentioned tests and the so-called conditions for the transition between the levels of control of the above-mentioned product characteristics. For example, when testing the flexural strength of concrete paving slabs with nominal lengths and widths of less than 300 mm, eight slabs of the strength family should be taken from the production machine on the day of production under normal inspection. During reduced control, this number is reduced to 4, and in additionally reduced control—to 2. In the event of disruption to the production process and the introduction of more restrictive control, the number of slabs is doubled with normal control and amounts to 16 units. Each transition between control levels is associated with a reduction or increase in the costs of conducting this control.

However, in the case of control and acceptance plans for the strength of concrete curbs, the EN 1340:2004 [16] code limits the testing plan of two levels of control (Figure 11).
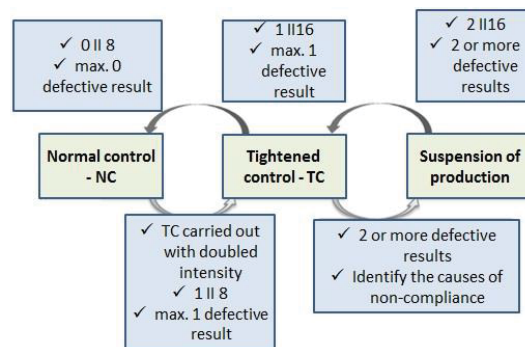
Figure 11. Conditions for the transition between the levels of control for the strength of concrete curbs (EN 1340:2004 [16]).

For features other than strength, quality control covers three levels as standard (Figure 12).
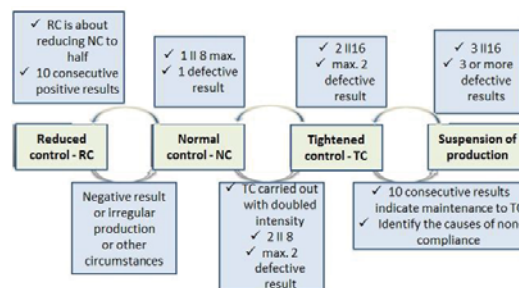
Figure 12. Transition conditions between the levels of control plans for assessing characteristics other than strength for concrete curbs (EN 1340:2004 [16]).

2.3. OC and AOQ Curves Constructed for Acceptance Plans of Selected Precast Elements

In all the AQL-based test plans, normal inspection acceptance criteria are selected to protect the manufacturer from rejecting batches with acceptable quality for the inspected precast elements of the batch. However, in most test methods, the producer's risk that such batches will be rejected varies depending on the plan adopted. Producer's and customer's risk analysis was performed regarding various permissible AQL defects, the sample number of n, the qualifying constant Ac, and various distributions of the analyzed feature. It was found that the customer's risk that a batch with a quality worse than the AQL will be accepted is much greater with a small sample size, which was confirmed using the values of the dependence of the acceptance probability on the defectiveness shown in Figure 13 and the values in Table 1. The analyses were carried out by constructing OC curves for 5 types of distributions: RB—Bernoulli distribution; RP—Poisson distribution; RN—normal distribution; RCh²—χ^2 distribution; and Gamma distribution—RG.

$$1 \| 5$$

(**a**)   (**b**)

$$1 \| 16$$

(**c**)   (**d**)
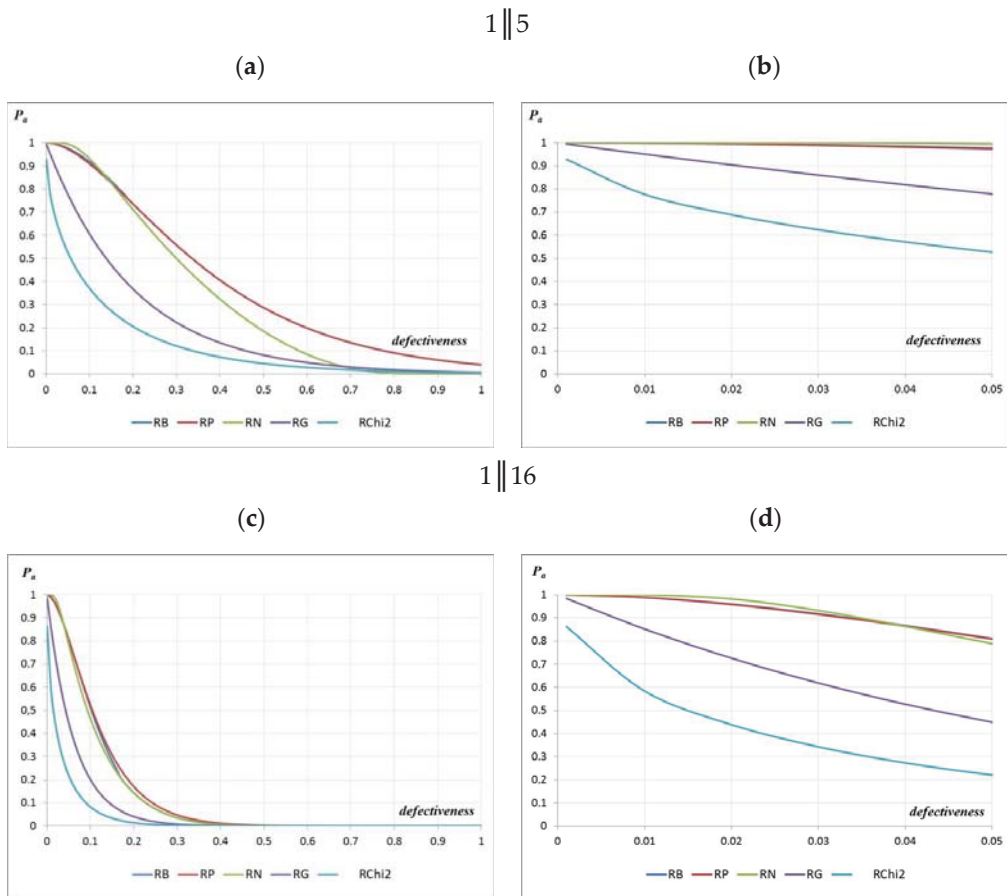
Figure 13. OC curves for testing plans: (**a**) 1‖5 and (**b**) 1‖5; 1‖16 (**c**) 1‖16 and (**d**) 1‖16.

Table 1. The values of the acceptance probability estimated for various acceptance plans related to normal control and the transition from strict to normal control of the considered precast concrete products.

	Probability of Acceptance—$P(w)$ for Different Types of Distribution									
$A_c \| n$	RB	RP	RN	RG	RChi^2	RB	RP	RN	RG	RChi^2
	AQL = 0.05					AQL = 0.10				
0‖5	0.774	0.779	0.696	-	-	0.590	0.607	0.500	-	-
0‖8	0.773	0.670	0564	-	-	0.590	0.449	0.362	-	-
2‖5	0.998	0.997	0.999	0.974	0.819	0.991	0.986	0.998	0.910	0.670
1‖8	0.942	0.939	0.963	0.670	0.403	0.813	0.809	0.795	0.449	0.237
1‖16	0.811	0.808	0.789	0.448	0.221	0.515	0.525	0.466	0.202	0.083
2‖16	0.957	0.952	0.916	0.750	0.472	0.789	0.783	0.630	0.525	0.223

Legend: RB—Bernoulli distribution; RP—Poisson distribution; RN—normal distribution; RCh^2—χ^2 distribution; RG—Gamma distribution.

To assess the defectiveness after the quality control of the manufactured precast elements, AOQ curves were constructed for the acceptance plans 1‖5 and 1‖16. These curves were also constructed for 5 distribution types: RB—Bernoulli distribution; RP—Poisson distribution; RN—normal distribution; RG—Gamma distribution; RChi^2—χ^2 distribution (Figure 14).

1‖5

(**a**) (**b**)

1‖16

(**c**) (**d**)
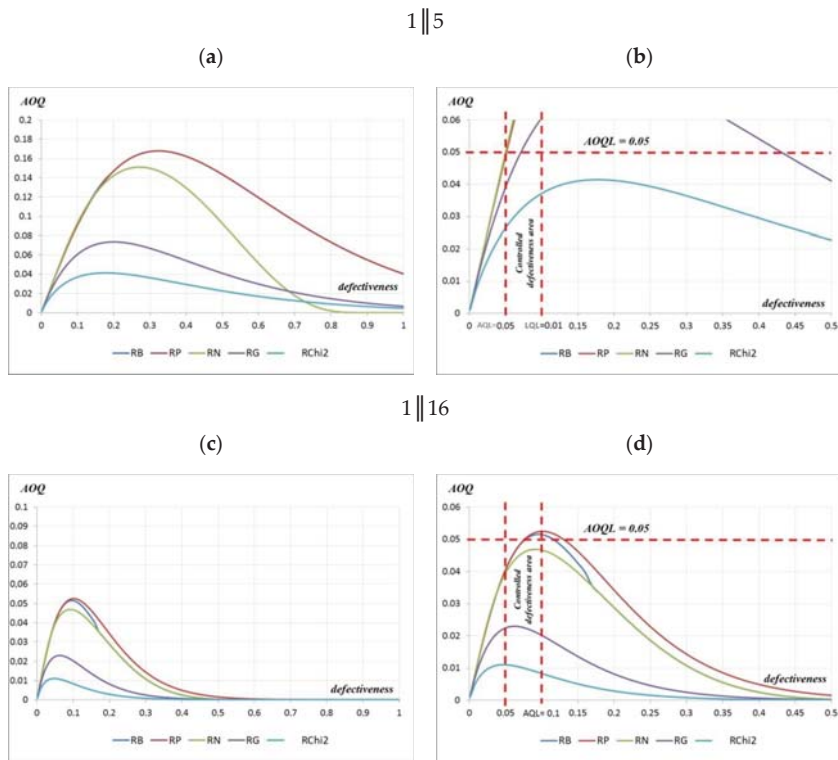
Figure 14. AOQ curves for testing plans: (**a**) 1‖5 and (**b**) 1‖5; 1‖16 (**c**) 1‖16 and (**d**) 1‖16.

2.4. Case Study of Concrete Curb Units

Styrobud of Podkarpacie Province in Poland provided the data for the analysis. Quality analysis was carried out regarding the continuous production of concrete curb units. In accordance with the recommendations of the EN 1340:2004 code [16], the test covered 8 curb units. The curb units had production dimensions of 998mm × 300mm × 198mm. The geometry and bending strength were evaluated. The description of the element's geometry was adopted following the standard (Figure 15).
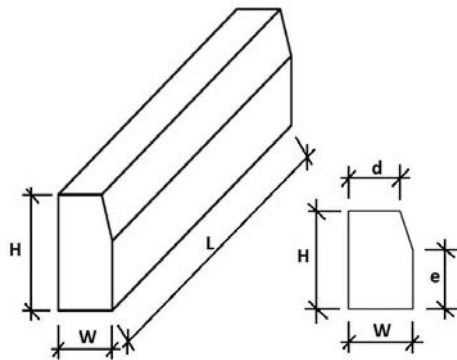
Figure 15. Description of the curbs' geometry according to EN 1340:2004 [16].

The curbs belonged to quality class 2 (marking T), for which the characteristic bending strength is 5.0 MPa, and the minimum bending strength is 4.0 MPa. An alternative method was used to evaluate the geometric dimensions and the bending strength. Each of the requirements specified in the standard regarding geometry and bending strength were met by all the curbs, due to which, both the sample and the production lot from which they were taken were considered compliant with the requirements of the standard (Figures 16 and 17).
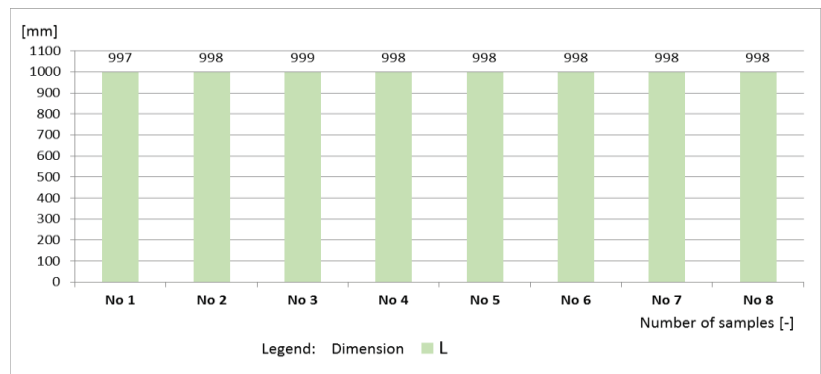
Figure 16. Values of L of the tested curbs.
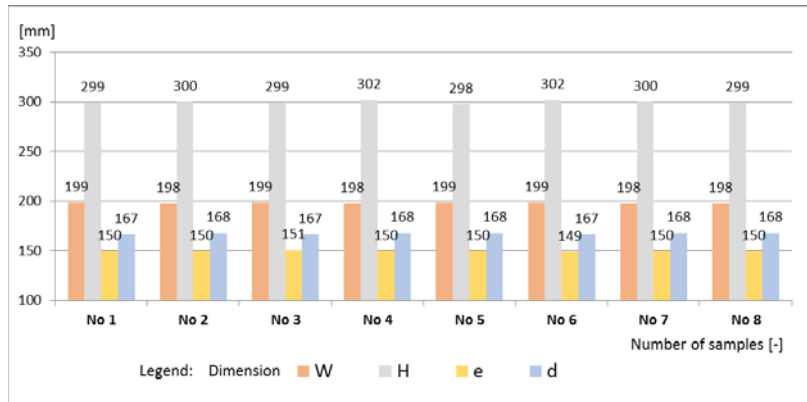
Figure 17. Values geometry of W, H, e, and d of the tested curbs.

No curbs were shown to have a bending strength lower than the characteristic value of the declared class T (Figure 18).
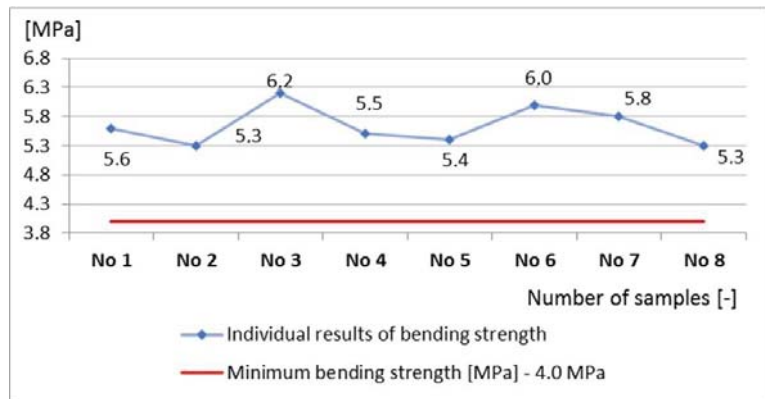
Figure 18. Bending strength values of the tested curbs.

Analyses of the geometry and bending strength were also carried out using 80 results (eight measurement cycles). The defectiveness was calculated in terms of the bending strength of the tested curbs—w = 0.04. Descriptive statistics for bending strength were determined (mean value—5.6 MPa and standard deviation—0.4 MPa), and the characteristic value of the bending strength was determined, which was 5.0 MPa. Based on the determined parameters, the characteristic value of the bending strength was calculated, which was slightly higher than the minimum characteristic value specified in the standard 5.3 MPa > 5.0 MPa. It was found that the requirements for the verified batch of curbs were met. However, the production defectiveness in terms of the height of the curbs, which was estimated based on 80 curb units, did not meet the requirements. The estimated defectiveness, w = 0.12, was greater than the permissible defectiveness of 0.10 (w = 0.12 > 0.10). The obtained values of defectiveness were lower than the limit values of the quantiles given in the EN 1340:2004 code [16] for bending—w = 0.03 < 0.05—and geometric dimensions other than height. The OC and AOQ curves were also constructed for the considered test plan 0‖8, and the acceptance probabilities of the tested curbs were determined for the geometry P_a (0.05) = 0.564 and the bending strength P_a (0.05) = 0.705 (Figure 19).

$$0\,\|\,8$$

| **(a)** | **(b)** |
| OC curve | AOQ curve |
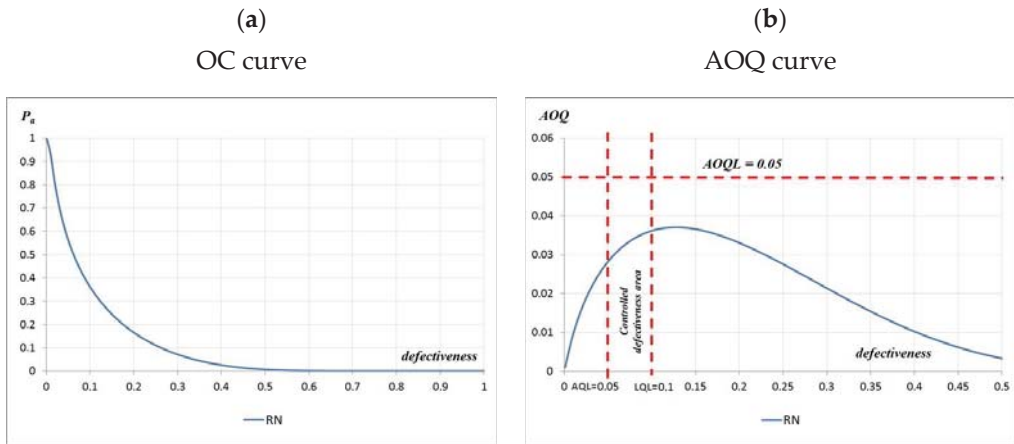
Figure 19. OC and AOQ curves for testing plan: (**a**) 0‖8 and (**b**) 0‖8.

The evaluated batch of curbs, in terms of geometry and bending strength, could therefore be considered as products that meet the requirements of the EN 1340:2004 code [16]. However, doubts were raised in terms of the actual defectiveness of the curbs produced; therefore, the OC and AOQ curves were constructed, and the producer's and the customer's risks were estimated. In the analyzed case, the customer's risk was 0.308, and the producer's risk was 0.436. These values indicate how important the ongoing control of the actual defectiveness is. Thus, it was shown that using single simple plans according to the codes to evaluate small sets of test results (fewer than 15 elements) does not provide the trade-off between customer risk and manufacturer risk that is required in the development of reasonable quality plans. Based on the analyses carried out, it is recommended that, in addition to applying standard procedures to control individual batches, the actual defectiveness of the precast elements should be assessed. In the case of the inspection of a produced batch of precast elements, it is common practice that elements rejected during production are not included in the inspection, because the average process effectiveness is not calculated. In some cases, the number of defective elements identified prior to batch testing may justify the acceptance or rejection of the batch.

3. Results and Discussion

In engineering practice, the recognition of a material's compliance with the specification is decided in the adopted plan for statistical quality control. It is a standard approach based on binary criteria (met/unmet). The action is of particular significance in the case of doubts concerning the quality of precast elements, in which the material quality is closely linked with the structure's safety and reliability. It is essential to adopt an appropriate sample quantity when assessing quality.

The calculation of OC curves is based on the assumption of random sampling; however, obtaining a small number of non-biased samples from a very large batch is difficult. Larger numbers of batches with steeper OC curves allow for a more sensitive distinction between good and bad batches; the larger the batch, the more significant this distinction can be. The shapes of the OC curves in the acceptance plan mainly depend on the number of precast elements in the batch, the acceptance criterion, and the type of the adopted distribution (Figure 13).

The probability of accepting precast concrete products on the basis of an assessment of attributes with the assumed permissible defectiveness (AQL), the determined number of precast elements in the batch (n), and the qualifying number (A_c) is variable and increases

with the increasing number of samples (Table 1). As the number of samples increases, the OC curves become steeper.

It was found that the OC curves constructed for the Bernoulli, normal, and Poisson distribution and for the 1‖16 criterion equally protect the buyer against accepting batches with a defect of 0.05 (Figure 13, Table 1). It was shown that a test plan for normal distribution much more effectively protects the manufacturer against rejecting batches with a defect greater than 0.05. Several rejection values for batches with defect levels of 0.01, 0.05, and 0.10 in Table 2 confirm this fact.

Table 2. Number of rejected lots (1-P (w)) according to Table 1 for 1‖16 plan.

Defectiveness [–]	Probability of Acceptance for the 1‖16 Plan For Different Types of Distribution				
	RB	**RP**	**RN**	**RG**	**RChi^2**
0.01	0.011	0.012	0.001	0.148	0.416
0.05	0.189	0.191	0.211	0.551	0.779
0.10	0.485	0.475	0.534	0.798	0.917

When determining the acceptance probability, it is very important to assume the distribution of the measurable parameters/features and that the test result of the prefabricated element is random. It is, therefore, advisable not to stop at the one-time examination of the distribution form of the feature/parameter one is interested in but to examine as many independent elements as possible to be sure about the type of distribution form of a given feature/parameter so that it is possible to determine the effectiveness of the acceptance plan constructed for the assumed type of distribution.

However, when assessing defectiveness after the tests of the manufactured precast elements based on the constructed AOQ curves for the 1‖5 acceptance plan, it can be seen that only for the Chi^2 distribution for the defect of the controlled area of 0.05–0.1 was the defectiveness of the assessed prefabricated elements lower than the value of 0 or 0.05. Additionally, in terms of the Gamma distribution, the pre-inspection defect at the level of 0.07 met the post-inspection defectiveness requirement of 0.05. In the case of the normal, Bernoulli, and Poisson distributions, the defect after the acceptance inspection of precast elements with defects up to 0.05 corresponded to the defect after the inspection, also with the value of 0.05 (Figure 14). However, in the case of the application of the 1‖16 acceptance plan and the defectiveness of the controlled area 0.05–0.1 and the adoption of the Chi^2, Gamma, and normal distributions, the defectiveness obtained after the acceptance inspection of the assessed prefabricated elements was lower than the value of 0.05. In the case of the Bernoulli and Poisson distributions, the defectiveness after inspection was slightly higher and amounted to 0.051 and 0.052, respectively (Figure 14). Different values of the producer's and consumer's risks estimated based on OC curves are shown in Table 3.

Table 3 presents the OC curve results for producer's risk α and consumer's risk β with the desired values of AQL = 0.05 and LQL = 0.10. The effects of increasing the sample size on the OC curve while keeping acceptance number c constant are shown in Table 1 for different control plans: normal, tightened, and reduced. Increasing n while keeping c constant increased the producer's risk α and reduced the consumer's risk β. Raising the acceptance number for a given sample size increased the risk of accepting a bad lot β. An increase in the acceptance number from c = 1 to c = 2 increased the probability of obtaining a sample with two or less defects and, therefore, increased the consumer's risk β. Thus, to improve single-sampling acceptance plans, management should increase the sample size n, which reduces the consumer's risk β, and increase the acceptance number c, which reduces the producer's risk α. The comparison of data in Table 1 shows the following principle: increasing the critical value for an acceptance number c while keeping the sample size n constant decreases the producer's risk α and increases the consumer's risk β.

Table 3. Producer's and consumer's risks for different plans.

$A_c \| n$	Producer's and Consumer's Risks for Different Types of Distribution									
	RB	**RP**	**RN**	**RG**	**RChi²**	**RB**	**RP**	**RN**	**RG**	**RChi²**
	Producer's Risk α (for a Given AQL = 0.05)					Consumer's Risk β (for a Given LQL = 0.10)				
0‖5	0.226	0.221	0.304	-	-	0.590	0.607	0.500	-	-
0‖8	0.227	0.33	0.436	-	-	0.590	0.449	0.362	-	-
2‖5	0.002	0.003	0.001	0.026	0.181	0.991	0.986	0.998	0.910	0.670
1‖8	0.058	0.061	0.037	0.33	0.597	0.813	0.809	0.795	0.449	0.237
1‖16	0.189	0.192	0.211	0.552	0.779	0.515	0.525	0.466	0.202	0.083
2‖16	0.043	0.048	0.084	0.25	0.528	0.789	0.783	0.630	0.525	0.223

Legend: RB—Bernoulli distribution; RP—Poisson distribution; RN—normal distribution; RCh²—χ^2 distribution; RG—Gamma distribution.

The analysis of the OC and AOQ curves shows that it is possible not only to quantify the probability of acceptance of a batch of manufactured elements but also to quantify the manufacturer's and recipient's risks and defectiveness after the acceptance inspection of precast elements, and also to select acceptable risk levels and defectiveness values after the inspection by adjusting the sample size and/or by defining the specification limit, i.e., the permanent acceptance—Ac.

The value of the estimated acceptance probability related to the quality assessment of precast concrete products according to the attribute assessment formulated in the subject codes depends on the adopted distribution, assumed admissible defectiveness, assumed number of inspected elements, and the qualifying constant, and it is:

- Variable and increases with the increase in the number of samples;
- Depends on the level of control and the type of distribution adopted (be sure about the type of distribution of the feature under consideration).

The OC curves became steeper with the increase in the number of samples; therefore, adopting a larger number of elements for testing with tightened control is justified. The shapes of the constructed OC curves differed depending on the adopted type of distribution and the number of test elements. The differences in the values of the estimated acceptance probability were especially noticeable with the defectiveness up to 0.1.

The AOQ curves made it possible to determine the average value of the defectiveness after the performed acceptance inspection. Defectiveness after inspection depends on the number of samples, the type of distribution, and the defectiveness of the assessed prefabricated elements before the control.

The larger the number of samples, the more clearly there were differences between batches of different quality. It was shown that a larger number of samples more effectively protects the customer from accepting defective batches, and it also protects the manufacturer from rejecting batches of precast elements that meet the requirements.

The numbers of samples recommended in the codes are the minimum values; therefore, the proposed statistical methods enable the adoption of the number of samples that ensure the safety and reliability of the constructed structures. The number of samples can be assumed based on the shape of the OC or AOQ curves and the type and reliability class of the building structures according to EN 1990 [70], i.e., RC1, RC2, and RC3. According to the literature [54], the minimum statistically justified number of samples is six.

4. Conclusions

In this study, the literature regarding quality assurance and quality control in the production of precast elements was reviewed. The advantages of prefabrication were discussed in detail, and the state and prospects for the development of this technology in

Poland were presented. The survey determined the factors that determine the development of prefabrication in Poland by investors, architects, and contractors. For investors, the main factor determining this technology's choice was the time of investment implementation. In contrast, the main factor for architects was the quality and technical parameters.

By verifying the advantages of prefabrication, it can be stated that the key advantage of prefabrication is the high real quality of the product, which is guaranteed by the use of standardized methods to ensure and control both production and ready-made prefabricated elements.

European codes recommend the use of quality control procedures that ensure the implementation of a quality system in precast concrete plants. In addition, they recommend various measures to ensure quality consistency throughout the production process. These include the non-destructive and destructive testing of both materials and components, geometric dimensional checks, visual inspections, etc.

The subject standards allow tests with attribute methods (which determine whether a certain product feature is compliant or not) and with variables inspections (in which product features are strictly supervised and the mean value and standard deviation are measured). In some cases, the measurement of a given feature can be carried out with both methods. After meeting strictly defined requirements, this decision rests with the manufacturer. Acceptance based on variable inspection is more accurate and requires more research, and the calculations are more complicated. For this reason, attribute methods are often used to assess less important features, while inspection via variables is used to qualify more important features, e.g., compressive strength. The acceptance inspection according to the attribute evaluation, as according to the quantitative evaluation, enables the risk of the producer and the recipient to be balanced by estimating the probability of acceptance and adopting an appropriate control plan.

Acceptance sampling involves accepting or rejecting a unit (or batch) of goods. The design of the acceptance sampling process includes decisions about sampling versus normal inspection, attribute versus variable measures, AQL, α, LQL, β, and sample size. In precast production, management selects the plan with the code requirements (choosing sample size n and acceptance number c), and using an OC curve or AOQ curve, the effectiveness of acceptance plans formulated in the code can be assessed. If the sample size n is increased, with c, AQL, and LQL fixed, the OC curve would change so that the producer's risk α increases while the consumer's risk β decreases. Furthermore, with an increase in the critical value c, and with n, AQL, and LQL fixed, the probability of the producer's risk α would decrease, but the probability of the consumer's risk β would increase.

The analysis of the OC and AOQ curves carried out in the research based on alternative assessment is an innovative solution in prefabrication and can be an important tool for managing the quality of prefabricated products. The acceptance of a produced batch of prefabricated elements is based on a sample taken, and the defectiveness of a sample is identified via the defectiveness in the production process. However, as we know, this is not accurate. The actual defectiveness in the manufactured elements differs from the defectiveness in the sample taken, hence the different values of the acceptance probability depend on the defectiveness in the production.

In the AQL control systems proposed in the standard, based on the OC and AOQ curves, it is necessary to calculate the current average defectiveness in the process, which should be estimated based on samples from at least the last 10 batches. The value of the average defectiveness should be treated as a premise for the decision to switch from one type of control—normal, tightened, or reduced—to another. The standard simplifies the requirements governing such control changes and does not consider it necessary to calculate the average defectiveness value in the process, which does not seem to be justified. Passage for each quality level was limited to the inspection of individual batches, disregarding actual process defectiveness. The given example concerning the analysis of the defectiveness of produced curbs shows the estimation of the average defectiveness in the process. Based on the data, it was found that the average actual defectiveness of curbs

in production may be greater than the estimated batch defectiveness. Values of average defectiveness higher than the admissible values were obtained for the height of the curbs. The verified batches met the standard requirements for the assessed batches but did not meet the requirement regarding production defectiveness. Equating batch defectiveness with process defectiveness is, therefore, not the correct approach, which was confirmed in the example provided. The analysis of the OC curves for tightened control showed that batches with clearly worse qualities than the AQL still had a fairly good chance of being accepted. It may therefore be desirable to supplement the stringent inspection criteria with some less formal requirements based on current estimations of the average defectiveness in the process. Based on the analyses carried out, it can be concluded that the requirement to calculate the average defectiveness in the process at regular intervals may have advantages. It is advisable for both the producer and the customer to know whether the quality is worse or better than the AQL value and whether the quality tends to improve or deteriorate. Note that the average defectiveness in the process calculated over a series of samples was simply the total number of defective items observed divided by the total number of items in the samples tested.

A review of the standard quality control procedures recommended in the codes and the evaluation of their performance using OC and AOQ curves showed no imperfections in the recommended quality control procedures. Based on the conducted analyses, it was found that the effectiveness of the quality control system concerning the selective quality assessment of precast elements depends on the adopted type of distribution of the tested feature and the adopted number of elements for testing. Quality control becomes less effective when a small number of samples is used, and acceptance plan control becomes very critical when many samples are used. Quality control becomes less effective when small samples are used for the acceptance plan.

The traditional approach to assessing the quality of precast products is through experiments and destructive testing, which are both time- and resource-consuming. The proposed statistical-approach-based method for quality assessment can be used to overcome these limitations. The suggested method may be employed in precast production and applied to predict the quality of precast elements by reducing, i.a., the numbers and scope of testing. The application of the proposed procedure combined with the use the statistical, fuzzy, or artificial neural network methods and modern measurement technology can ensure the reliable assessment of the quality of precast products.

Institutional Review Board Statement: Not applicable.

Informed Consent Statement: Not applicable.

Data Availability Statement: Data sharing not applicable.

Conflicts of Interest: The author declares no conflict of interest.

References

1. Elliott, K.S. *Precast Concrete Structures*; CRC Press: Boca Raton, FL, USA, 2019.
2. Warszawski, A. *Industrialized and Automated Building Systems. A Managerial Approach*; Routledge: Abingdon, UK, 2019.
3. Hariyanto, A.D.; Kwan, H.P.; Cheong, Y.W. Quality control in precast production. A case study on tunnel segment manufacturing. *J. Archit. Built Environ.* **2005**, *33*, 153–164. [CrossRef]
4. Richardson, J. *Quality in Precast Concrete: Design—Production—Supervision*; Longman Scientific & Technical: Essex, UK, 1991.
5. Rubaratuka, I.A. Challenges of the quality of reinforced concrete buildings in Dar es Salaam. *Int. J. Eng. Res. Technol.* **2013**, *2*, 46–52. Available online: https://www.ijert.org/challenges-of-the-quality-of-reinforced-concrete-buildings-in-dar-es-salaam-2 (accessed on 20 August 2022).
6. Abdelouafi, E.G.; Benaissa, K.; Abdellatif, K. Reliability Analysis of Reinforced Concrete Buildings: Comparison between FORM and ISM. *Procedia Eng.* **2015**, *114*, 650–657. [CrossRef]

7. Kovalenko, G.V.; Dudina, I.V.; Nester, E.V. Chance models and estimators of primary reliability of constructions with mixed reinforcement. In Proceedings of the European Science and Technology: Materials of the International Research and Practice Conference, Wiesbaden, Germany, 31 January 2012.

8. Spaethe, G. *Die Sicherheit Tragender Baukonstruktionen*; Springer: New York, NY, USA, 1992.

9. Zhou, Y.; Zhang, B.; Luo, X.; Hwang, H.-J.; Zheng, P.; Zhu, Z.; Yi, W.; Kang, S.-M. Reliability of fully assembled precast concrete frame structures against progressive collapse. *J. Build. Eng.* **2022**, *51*, 104362. [CrossRef]

10. Ekwueme, C.G.; Hart, G.C. Structural reliability characterization of precast concrete. *Struct. Des. Tall Build.* **1994**, *3*, 13–35. [CrossRef]

11. Ditlevsen, O. Model uncertainty in structural reliability. *Struct. Saf.* **1983**, *1*, 73–86. [CrossRef]

12. *Instrukcja ITB nr 414/2006*; Zakładowa Kontrola Produkcji Wyrobów Budowlanych. Wymagania. ITB: Warszawa, Polska, 2006.

13. Regulation (EU) No 305/2011 of the European Parliament and of the Council of 9 March 2011 establishing harmonized conditions for the marketing of construction products and repealing Council Directive 89/106. **2011**/EEC. Available online: https://eur-lex.europa.eu/LexUriServ/LexUriServ.do?uri=OJ:L:2011:088:0005:0043:EN:PDF (accessed on 20 August 2022).

14. *EN 206+A2:2021-08*; Concrete–Specification, Performance, Production and Conformity. European Committee for Standardization: Brussels, Belgium, 2021.

15. *EN 1339: 2003*; Concrete Paving Flags—Requirements and Test Methods. European Committee for Standardization: Brussels, Belgium, 2003.

16. *EN 1340:2003*; Concrete Kerb Units—Requirements and Test Methods. European Committee for Standardization: Brussels, Belgium, 2003.

17. *EN 13369: 2018*; Common Rules for Precast Concrete Products. European Committee for Standardization: Brussels, Belgium, 2018.

18. *ISO 2859-0:2002*; Sampling Procedures for Inspection by Attributes—Part 0: Introduction to the ISO 2859 Attribute Sampling System. International Organization for Standardization/International Electrotechnical Commission: Geneva, Switzerland, 2002.

19. *ISO 2859-1:2003*; Sampling Procedures for Inspection by Attributes—Part 1: Sampling Schemes Indexed by Acceptance Quality Limit (AQL) for Lot-by-Lot Inspection. International Organization for Standardization/International Electrotechnical Commission: Geneva, Switzerland, 2003.

20. *ISO 3951-1:2013*; Sampling Procedures for Inspection by Variables—Part 1: Specification for Single Sampling Plans Indexed by Acceptance Quality Limit (AQL) for Lot-by-Lot Inspection for a Single Quality Characteristic and a Single AQL. International Organization for Standardization/International Electrotechnical Commission: Geneva, Switzerland, 2013.

21. *ISO 3951:1997*; Sampling Procedures and Charts for Inspection by Variables for Percent Nonconforming. International Organization for Standardization/International Electrotechnical Commission: Geneva, Switzerland, 1997.

22. *ISO 9001:2015-10*; Quality Management Systems—Requirements. International Organization for Standardization/International Electrotechnical Commission: Geneva, Switzerland, 2015.

23. Wang, R.; Wang, Y.; Devadiga, S.; Perkins, I.; Kong, Z.J.; Yue, X. Structured-light three-dimensional scanning for process monitoring and quality control in precast concrete production. *PCI J.* **2021**, *66*, 17–32. [CrossRef]

24. Pan, M.; Linner, T.; Cheng, H.M.; Pan, W.; Bock, T. A Framework for Utilizing Automated and Robotic Construction for Sustainable Building. In *Proceedings of the 21st International Symposium on Advancement of Construction Management and Real Estate*; Chau, K.X., Chan, I.Y.S.; Lu, W., Webster, C., Eds.; Springer Nature: Singapore, 2018; pp. 79–88.

25. Reichenbach, S.; Kromoser, B. State of practice of automation in precast concrete production. *J. Build. Eng.* **2021**, *43*, 102527. [CrossRef]

26. Baines, T.S. An integrated process for forming manufacturing technology acquisition decisions. *Int. J. Oper. Prod. Manag.* **2004**, *24*, 447–467. [CrossRef]

27. Delgado, J.M.D.; Oyedele, L.; Ajayi, A.; Akanbi, L.; Akinade, O.; Bilal, M.; Owolabi, H. Robotics and automated systems in construction: Understanding industry-specific challenges for adoption. *J. Build. Eng.* **2019**, *26*, 100868. [CrossRef]

28. Master Computers 4.0: Production Control Systems in the Technological Transition. Available online: https://www.bft-international.com/en/artikel/bft_Master_computers_4.0_production_control_systems_in_the_technological_2650315.html (accessed on 16 October 2022).

29. Liang, F.; Chu, L.; Carroll, R.J. *Advanced Markov Chain Monte Carlo Methods*; Wiley: Hoboken, NJ, USA, 2010.

30. Kaverzina, L.; Kovalenko, G.; Dudina, I.; Belskii, O. Cost efficiency assessment of automated quality control of precast structures. *MATEC Web Conf.* **2018**, *143*, 04006. [CrossRef]

31. Zhuo, W.; Tong, T.; Liu, Z. Analytical Pushover Method and Hysteretic Modeling of Precast Segmental Bridge Piers with High-Strength Bars Based on Cyclic Loading Test. *J. Eng. Struct.* **2019**, *145*, 04019050. [CrossRef]

32. Park, J.; Choi, J.; Jang, Y.; Park, S.-K.; Hong, S. An Experimental and Analytical Study on the Deflection Behavior of Precast Concrete Beams with Joints. *Appl. Sci.* **2017**, *7*, 1198. [CrossRef]

33. Fan, J.-J.; Feng, D.-C.; Wu, G.; Hou, S.; Lu, Y. Experimental study of prefabricated RC column-foundation assemblies with two different connection methods and using large-diameter reinforcing bars. *Eng. Struct.* **2020**, *205*, 110075. [CrossRef]

34. Rubaratuka, I.A. Quality control in the construction of reinforced concrete buildings in Dar es Salaam. *Tanzan. J. Eng. Technol.* **2008**, *31*, 46–52. Available online: https://www.ajol.info/index.php/tjet/article/view/236763 (accessed on 20 August 2022). [CrossRef]

35. Krausmann, F.; Lauk, C.; Haas, W.; Wiedenhofer, D. From resource extraction to outflows of wastes and emissions: The socioeconomic metabolism of the global economy, 1900–2015. *Glob. Environ. Change* **2018**, *52*, 131–140. [CrossRef] [PubMed]
36. OECD. *Global Material Resources Outlook to 2060: Economic Drivers and Environmental Consequences*; OECD Publishing: Paris, France, 2019.
37. Kromoser, B. Ressourceneffizientes Bauen mit Betonfertigteilen Material–Struktur—Herstellung. In *Beton Kalender: Fertigteile, Integrale Bauwerke*; Bergmeister, K., Fingerloos, F., Worner, J.-D., Eds.; Ernst & Sohn GmbH & Co.: Berlin, Germany, 2021.
38. Kromoser, B.; Preinstorfer, P.; Kollegger, J. Building lightweight structures with carbon-fiber-reinforced polymer-reinforced ultra-high-performance concrete: Research approach, construction materials, and conceptual design of three building components. *Struct. Concr.* **2019**, *20*, 730–744. [CrossRef]
39. Gharbia, M.; Chang-Richards, A.; Lu, Y.; Zhong, R.Y.; Li, H. Robotic technologies for on-site building construction: A systematic review. *J. Build. Eng.* **2020**, *32*, 101584. [CrossRef]
40. Forcael, E.; Ferrari, I.; Opazo-Vega, A.; Pulido-Arcas, J.A. Construction 4.0: A Literature Review. *Sustainability* **2020**, *12*, 9755. [CrossRef]
41. Chalangaran, N.; Farzampour, A.; Paslar, N. Nano Silica and Metakaolin Effects on the Behavior of Concrete Containing Rubber Crumbs. *Civileng* **2020**, *1*, 264–274. [CrossRef]
42. Mansouri, I.; Sadat Shahheidari, F.S.; Ali Hashemi, S.M.; Farzampour, A. Investigation of steel fiber effects on concrete abrasion resistance. *Adv. Concr. Constr.* **2020**, *9*, 367–374.
43. Chalangaran, N.; Farzampour, A.; Paslar, N.; Fatemi, H. Experimental investigation of sound transmission loss in concrete containing recycled rubber crumbs. *Adv. Concr. Constr.* **2021**, *11*, 447–454. [CrossRef]
44. Farzampour, A. Compressive behavior of concrete under environmental effects. In *Compressive Strength of Concrete*; IntechOpen: London, UK, 2019.
45. Farzampour, A. Temperature and humidity effects on behavior of grouts. *Adv. Concr. Constr.* **2017**, *5*, 659–669. [CrossRef]
46. Duncan, J.M.; Thorpe, B.; Sunmer, P. *Quality Management in Constructions*; Gower Publishing: Aldershot, UK, 1990.
47. Szałek, A.; Madej-Kiełbik, L. Selected methods of assessing the quality of the finished product. *Technol. I. Jakość Wyr.* **2021**, *66*, 20–32. (In Polish)
48. Lenart, M. Statistical acceptance control of concrete construction products using the alternative method. *Mater. Bud.* **2010**, *451*, 54–58. (In Polish)
49. Wang, L.; Wang, H.; Yang, K.; Xie, S.; Wei, G.; Li, R.; Wang, W. Full-Scale Prefabrication and Non-Destructive Quality Monitoring of Novel Bridge Substructure for "Pile-Column Integration". *Buildings* **2022**, *12*, 715. [CrossRef]
50. Chen, T.-T.; Wang, W.-C.; Wang, H.-Y. Mechanical properties and ultrasonic velocity of lightweight aggregate concrete containing mineral powder materials. *Constr. Build. Mater.* **2020**, *258*, 119550. [CrossRef]
51. Wang, D.; Liu, G.; Li, K.; Wang, T.; Shrestha, A.; Martek, I.; Tao, X. Layout Optimization Model for the Production Planning of Precast Concrete Building Components. *Sustainability* **2018**, *10*, 1807. [CrossRef]
52. Available online: https://mypmr.pro/products/rynek-prefabrykacji-betonowej-w-polsce-2020 (accessed on 8 August 2022).
53. Gibb, I.; Harrison, T. Use of Control Charts in the Production of Concrete. Technical Report, 2010. Available online: https://www.researchgate.net/publication/299410814_Use_of_control_charts_in_the_production_of_concrete (accessed on 20 August 2022).
54. Brunarski, L. *Mathematics Basis of Formulation the Compliance Criteria of the Strength of Materials*; Wydawnictwo ITB: Warsaw, Poland, 2009. (In Polish)
55. Skrzypczak, I.; Buda-Ożóg, L.; Pytlowany, T. Fuzzy method of conformity control for compressive strength of concrete on the basis of computational numerical analysis. *Meccanica* **2016**, *51*, 383–389. [CrossRef]
56. Skrzypczak, I.; Woliński, S. Influence of distribution type on the probability of acceptance of concrete strength. *Arch. Civ. Eng.* **2007**, *53*, 479–495.
57. Skrzypczak, I. Statistical quality control of precast concrete products. *Mater. Bud.* **2022**, *5*, 3–6.
58. Chen, C.-H. Economic design of Doge-Romnig AOQL single sampling plans by variables with quadratic loss function. *Tamkang J. Sci. Eng.* **2005**, *8*, 313–318. [CrossRef]
59. Govindaraju, K. Single Sampling Plans for Variables Indexed by AQL and AOQL. *J. Qual. Technol.* **1990**, *22*, 310–313. [CrossRef]
60. Taerwe, L. Evaluation of compound compliance criteria for concrete strength. *Mater. Struct.* **1998**, *21*, 13–20. [CrossRef]
61. Krzemiński, M. Optimization of Work Schedules Executed using the Flow Shop Model, Assuming Multitasking Performed by Work Crews. *Arch. Civ. Eng.* **2017**, *63*, 3–19. [CrossRef]
62. Leśniak, A.; Zima, K. Cost Calculation of Construction Projects Including Sustainability Factors Using the Case Based Reasoning (CBR) Method. *Sustainability* **2020**, *10*, 1608. [CrossRef]
63. Sztubecka, M.; Skiba, M.; Mrówczyńska, M.; Bazan-Krzywoszańska, A. An Innovative Decision Support System to Improve the Energy Efficiency of Buildings in Urban Areas. *Remote. Sens.* **2020**, *12*, 259. [CrossRef]
64. Arditi, D.; Gunaydin, H.M. Total quality management in the construction process. *Int. J. Proj. Manag.* **1997**, *15*, 235–243. [CrossRef]
65. Kowalski, D. Quality assurance of works and materials in construction projects. *Inżynieria Morska I Geotech.* **2013**, *5*, 362–365.
66. Czarnecki, L.; Hager, I.; Tracz, T. Material Problems in Civil Engineering: Ideas-Driving Forces-Research Arena. *Procedia Eng.* **2015**, *108*, 3–12. [CrossRef]
67. Gorzelańczyk, T.; Pachnicz, M.; Różański, A.; Schabowicz, K. Identification of microstructural anisotropy of cellulose cement boards by means of nanoindentation. *Constr. Build. Mater.* **2020**, *257*, 119515. [CrossRef]

68. Schabowicz, K. Non-Destructive Testing of Materials in Civil Engineering. *Materials* **2019**, *12*, 3237. [CrossRef] [PubMed]
69. Skrzypczak, I.; Leśniak, A.; Ochab, P.; Górka, M.; Kokoszka, W.; Sikora, A. Interlaboratory Comparative Tests in Ready-Mixed Concrete Quality Assessment. *Materials* **2021**, *14*, 3475. [CrossRef] [PubMed]
70. *EN 1990: 2004*; Eurocode—Basis of Structural Design. European Committee for Standardization: Brussels, Belgium, 2004.

Interlaboratory Comparative Tests in Ready-Mixed Concrete Quality Assessment

Izabela Skrzypczak [1], Agnieszka Leśniak [2,*], Piotr Ochab [1], Monika Górka [2], Wanda Kokoszka [1] and Anna Sikora [1]

[1] Faculty of Civil and Environmental Engineering and Architecture, Rzeszow University of Technology, Powstancow Warszawy 12, 35-082 Rzeszow, Poland; izas@prz.edu.pl (I.S.); p.ochab@prz.edu.pl (P.O.); wandak@prz.edu.pl (W.K.); sikora@prz.edu.pl (A.S.)

[2] Faculty of Civil Engineering, Cracow University of Technology, 31-155 Krakow, Poland; monika.gorka@pk.edu.pl

* Correspondence: alesniak@l7.pk.edu.pl

Abstract: Proper quality assessment of ready-mixed concrete, which is currently the principal material for construction, land engineering and architecture, has an impact on the optimisation and verification of correct functioning of individual stages of the production process. According to the European Standard EN 206 "Concrete–Specification, performance, production and conformity", obligatory conformity control of concrete is carried out by the producer during its production. In order to verify the quality of concrete, investors generally commission independent laboratory units to perform quality assessment of both concrete mix and hardened concrete, which guarantees a high quality of construction works. One of the essential tools for ensuring the quality of test results is the participation of laboratories in the so-called proficiency testing (PT) or inter-laboratory comparisons (ILC). Participation in PT/ILC programmes is, on the one hand, a tool for demonstrating the laboratory's performance, on the other hand an aid for maintaining the quality of available concrete tests and validating test methods. Positive evaluation is a confirmation of the laboratory's capability for performing the tests. The paper presents the results of laboratory proficiency tests carried out by means of inter-laboratory comparisons, as shown in the example of quality assessment of ready-mixed concrete for nine participating laboratories. The tests were performed for concrete of the following parameters: strength class C30/37, consistency S3, frost resistance degree F150, and water resistance degree W8. This involved determining consistencies, air content and density of the concrete mix, and compressive strength of hardened concrete. For the evaluation of laboratory performance results, z-score, ζ-score and E_n-score were applied. The innovation of the proposed study lies in employing both classical and iterative robust statistical methods. In comparison with classical statistical methods, robust methods ensure a smaller impact of outliers and other anomalies on the measurement results. Following the analyses, clear differences were found between the types of detected discrepancy of test results, which occurred due to the nature of individual parameters. For two laboratories, two scores revealed unsatisfactory results for concrete mix consistency. The main reasons can be pouring into the cone-shaped form a concrete mixture that is too dry, or incorrect use of a measuring tool also creating a possibility that the obtained value can be wrongly recorded. Other possible reasons are discussed in the paper. Participation in inter-laboratory comparison programmes is undoubtedly a way to verify and raise the quality of tests performed for concrete mix and hardened concrete, whereas individual analysis of the results allows the laboratory quality system to be improved.

Keywords: ready-mixed concrete; construction architecture material; inter-laboratory comparisons (ILC); proficiency testing (PT); concrete quality assessment

1. Introduction

Modern structures must meet various design standards concerning durability, ergonomics, safety and quality; furthermore, construction has to be executed without harm

to the environment and natural resources. With the development of technology and advanced construction materials, increasingly more requirements are being imposed. Modern construction consists of structures of possibly minimal impact on the environment [1–3], which is achieved through proper architectural design, use of proper construction materials characterised, among other things, by low CO_2 emission [4–6], low energy consumption during operation and construction [7–9], and the possibility of renovation following extensive use [10,11] or potential malfunction [12,13]. Not without significance is also the use of construction materials that can be recycled or utilised [14,15]. Hence, both the design and execution of modern structures requires undertaking measures that involve employing appropriate quality assessment processes. Assessment is conducted with regard to both the production of construction materials, and the process of design, execution and completion of construction works or entire structures. Each of these procedures is of different character. Quality control of construction materials delivered to the market is limited by legal provisions, whereas the remaining measures related to the execution of construction objects can be approached optionally while remaining within the framework of internal, domestic procedures [16]. Concrete is undoubtedly one of the most frequently used construction materials [17]. According to a Chatham House report [18], the world produces 4.4 billion tons of concrete annually, but that amount is expected to rise to over 5.5 billion tons by 2050. Ready-mixed concrete (RMC) is the principal construction material for civil engineering infrastructure [19]. It should be noted that construction concrete that is subject to quality control constitutes circa 70% of total concrete production [20]. Quality assessment may be carried out on various stages of production, delivery, and before and after laying concrete mix. The intended concrete quality is achieved owing to the selection of appropriate formulas (ingredients, strength class, exposure class etc.) [21–26], a production process that is compliant with the procedures [27–29], the mode of transport and laying of fresh concrete mix, and the proper maintenance of hardened concrete [30,31]. Quality assessment involves the control of conformity and uniformity in compliance with the recommended criteria. Not without significance for the quality of modern concretes remains the development of innovative research methods that aid concrete design aimed at obtaining appropriate properties and durability [32–35], and the development of methods for the evaluation of the results [16,36].

Concrete testing procedures and quality assurance criteria for ready-mixed concrete delivered to the construction site are fairly well-established under law, especially under industry standards. It is also important to underscore the significance and role of technical specification for execution and completion of construction works. Although appropriate industry standards contain conformity and uniformity criteria related to concrete production control, technical specifications contain, in particular, sets of requirements that are necessary for determining the standard and quality of works with regard to the manner of execution of construction works and the evaluation of correctness of execution of individual stages; these elaborations are custom-developed for each construction project [37].

Industry standards require that the concrete supplier implement a production and quality control plan—a set of quality requirements with regard to the products and their production. The plan contains a detailed description of the manufacturing process which includes stages, organisation, methods and standards of production as well as procedures and instructions, and the testing and quality control programme [38–43]. For the ready-mixed concrete supplier, quality assessment involves pro-active measures that allow for maintaining the quality of concrete by ensuring the cohesion of properties of concrete mix and hardened concrete between the batches and for the entire duration of the project; quality assessment also includes appropriate actions and measures taken in the case when the supplied product does not meet the requirements [38]. In construction practice, in the execution of concrete works, concrete quality is usually verified by the investor by commissioning an independent laboratory unit to carry out the tests, which is a guarantee for quality control of both concrete mix and hardened concrete. As set out by ISO/IEC 17000:2020, "Conformity assessment–Vocabulary and general principles" [44], accreditation

is "attestation by a third party, related to the unit assessing conformity, providing formal evidence of its competence for executing defined tasks within the scope of conformity assessment". The IOS 17000:2020 standard contains a requirement that the laboratories have quality control procedures and plan their actions, which would subsequently be subject to monitoring. The actions should ensure the reliability of test results delivered to the customer. One of the essential tools for ensuring the quality of test results is the laboratories' participation in proficiency testing (PT) or inter-laboratory comparison (ILC) programmes [45]. In accordance with EN ISO/IEC 17025 [46] and EA-4/18 [47], accredited laboratories should ensure the quality of the results through participation in proficiency testing programmes. Involvement in PT/ILC programmes is, on the one hand, a tool for demonstrating the laboratory's performance, and on the other hand an aid for maintaining the quality of available tests and validating test methods. Participation in comparative PT/ILC programmes is usually paid for, and the services are provided by domestic and international organisers of PT/ILC programmes. Laboratories may, however, organise inter-laboratory comparisons with other laboratories on their own behalf. Such activity is not aimed at qualifying or evaluating the operation of participating laboratories, yet it allows the obtained results to be analysed individually and used to improve testing quality. In practice, inter-laboratory testing is most frequently organised for one of the three following purposes [48–50]: assessment of laboratory proficiency, certification of reference material, evaluation (validation) of analysis method. Participation in inter-laboratory comparisons undoubtedly contributes to improving quality systems in laboratories. This directly translates into the quality of assessment, for instance of concrete, in the monitored facilities.

The aim of the present paper is the evaluation of laboratory performance by means of inter-laboratory proficiency tests as carried out for ready-mixed concrete quality assessment, for nine participating laboratory units. The most innovative element of the study was the simultaneous use of classical and robust statistical methods. In practice, the most common procedures employ classical statistical analysis, which is optimal under the assumption of normality of data distribution and large sample size. Classical statistical procedures involve, as a first step, the verification of questionable results, e.g., by applying the Grubbs test, which allows us to identify and remove abnormal values, i.e., outliers. This is only effective for large data sets, whereas for small-sized samples, removing one or several significant outliers may greatly alter the classical statistical parameters. In many fields of experimental research, particularly in destructive testing, the tests are limited to small-sized samples due to high cost intensity of the testing process. In such circumstances, it is necessary to make use of all the obtained measurement results, as removing outliers/questionable results from the sample diminishes the reliability of statistical assessment. Employing robust statistical methods is recommended, as, in comparison with classical statistical methods, they ensure a smaller impact of outliers and other anomalies on the measurement results. Quality assessment of concrete is generally carried out on the basis of small-sized samples, by means of destructive testing, without the possibility to repeat or complement the measurements. This is why iterative robust statistical methods, rarely used in concrete quality control, were proposed for the analysis of inter-laboratory comparative tests. Southern Poland-based laboratories participated in the programme voluntarily. Concrete tests and analyses were performed from June to July 2020.

2. Materials and Methods

2.1. Laboratory Proficiency Testing/Interlaboratory Comparison

According to ISO/IEC 17043:2010 [51], laboratory proficiency testing involves the evaluation of a participant's performance against pre-established criteria by means of inter-laboratory comparisons. This allows the laboratory's capability for conducting concrete tests to be assessed, and thus the reliability of the obtained results to be evaluated. In proficiency testing, the results of the analyses of the same object, obtained in a given laboratory, are compared with the results obtained independently in one or several dif-

ferent laboratories. The basic tool for carrying out proficiency testing is inter-laboratory comparison, which involves the organised conduct and evaluation of testing of the same or similar objects by at least two laboratories, in accordance with previously determined conditions [52]. Furthermore, inter-laboratory comparisons can be used for different, indirect purposes, as shown in Figure 1.
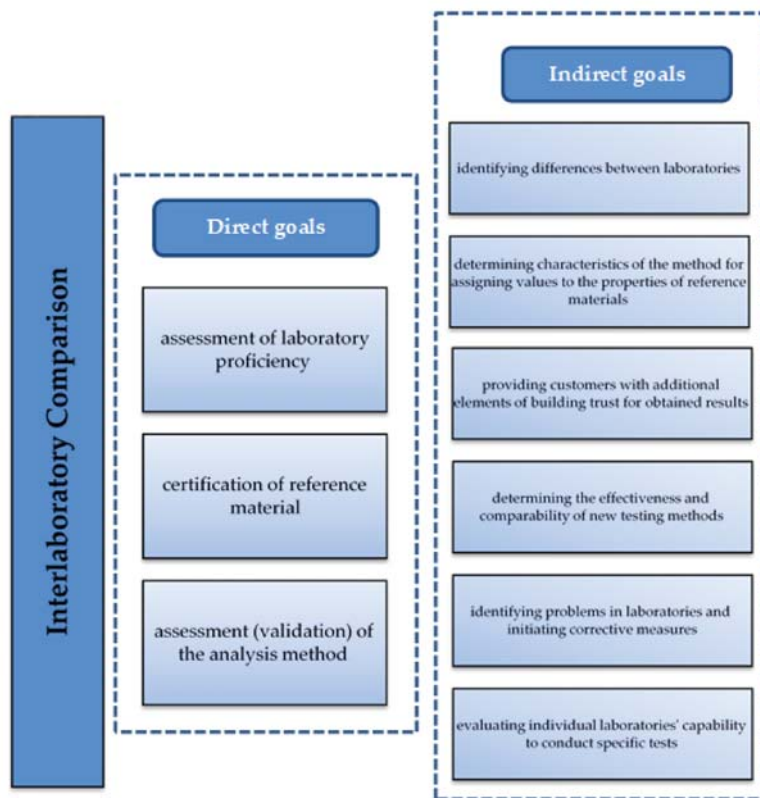
Figure 1. Goals of inter-laboratory comparisons. Source: own elaboration based on [53,54].

Participation in proficiency testing programmes constitutes, therefore, an evaluation of a laboratory's testing capabilities. It provides an independent, external assessment, which complements the laboratory's internal quality control procedures. Participation in a proficiency testing programme may be a basis for self-evaluation, and contribute to improving the laboratory's proficiency; it is, thus, an important, often obligatory element of the laboratory's quality control system.

Prior to proceeding with the testing, an appropriately designed and organised programme must be prepared in order to determine the type of analytical methods, the type of test object, and the number of participating laboratories.

While preparing the test object, one should take into consideration all factors that may influence the reliability of inter-laboratory testing, such as the object's homogeneity, the method of sample collection, the object's stability over time, and the impact of environmental conditions (during transport and storage) on the test object's properties. It is crucial that the material used in proficiency testing is homogenous, and that all participants are provided with test objects which do not significantly differ in terms of tested parameters. The material's uniformity should be documented, and the conditions of its transportation

and storage, and the timeframe of the testing, should be clearly defined. Test methods should be unambiguously determined and based on normalised and validated methods.

2.2. Evaluation of Comparative Test Results

The results obtained by the participants are subject to statistical analysis and evaluation. The methods for statistical evaluation of inter-laboratory comparison results are described in the following standards:

- ISO/IEC 17043 (2010) "Conformity assessment—general requirements for proficiency testing" [51];
- ISO 13528 (2015) "Statistical methods for use in proficiency testing by inter-laboratory comparison" [55].

Most of the methods are based on a known assigned value (value attributed to a particular quantity and accepted [55] and its uncertainty. Assigned value (x_{pt}) is the value agreed on the basis of the participants' results in the way described in ISO/IEC 17043 (2010) [51], Annex B.2.1 e) and ISO 13528:2015 [55], Annex C, Algorithm A p.C.3.1.

Assigned value is calculated as arithmetic mean from the participants' results, having considered the influences of outliers, with the use of robust statistical methods.

Standard uncertainty of assigned value $u(x_{pt})$ is determined with the application of statistical method as described in ISO 13528: 2015 p.7.7.3 [55] and calculated by Equation (1):

$$u(x_{pt}) = 1.25 \cdot \frac{S^*}{\sqrt{p}} \tag{1}$$

where: p—number of participants,

S^*—strong (solid) standard deviation calculated by Equation (2):

$$S^* = 1.134 \sqrt{\frac{\sum(x_i^* - x_{pt})^2}{p-1}} \tag{2}$$

where: x_i^*—results obtained by the participants after applying robust statistics,

x_{pt}—assigned value, calculated as strong (solid) mean from the participants' results.

Expanded uncertainty (U_r) of the assigned value, with expansion coefficient k = 2 and confidence level circa 95%, is calculated by Equation (3):

$$U_r = 2 \cdot U(x_{pt}) \tag{3}$$

2.3. Means of Proficiency Assessment and Evaluation Criteria for Laboratory Activity Results

Laboratory activity results are usually presented with the use of *z-score*, *ζ-score* and *E_n-score*, which are determined in accordance with ISO/IEC 17043: 2011 [51], Annex B, B.3.1.3 c) and d), and calculated by Equations (4)–(6):

- *z-score* (4):

$$z = \frac{x_i - x^*}{SD} \tag{4}$$

where: *SD*—standard deviation for proficiency test assessment, determined considering the results of all participants,

x_i—result reported by the participant,

x^*—assigned value, determined as strong (robust) mean from the participants' results.

- *ζ-score* (5):

$$\zeta = \frac{x_i - x^*}{\sqrt{\mu_{x_i}^2 + \mu_{x^*}^2}} \tag{5}$$

where: x_i—result reported by the participant,

x^*—assigned value, determined as strong (robust) mean from the participants' results,

μ_{x_i}—standard uncertainty estimated by the participant,

μ_{x^*}—standard uncertainty of assigned value x*.

- E_n-*score* (6):

$$E_n = \frac{x_i - x^*}{\sqrt{U_{x_i}{}^2 + U_{x^*}{}^2}} \qquad (6)$$

where: x_i —result reported by the participant,

x^*—assigned value, determined as strong (solid) mean from the participants' results,

U_{x_i}—measurement uncertainty estimated by the participant,

U_{x^*}—measurement uncertainty of assigned value x^*.

The results of the laboratories' activity are evaluated with the use of *z-score*. By assessing a participant's performance by means of *z-score*, both the trueness and precision of the obtained result are addressed [52]. *ζ-score* and E_n-*score* can be applied in combination with *z-score* as an aid for improving the laboratories' activity [56,57]. *ζ-score* and E_n-*score* depend on the participants submitting accurate measurement uncertainty estimates along with their result, a procedure not easily adhered to [52].

Assessment according to *z-score*, *ζ-score* and E_n-*score* is applied to all results, including those which, as outliers, were not considered in statistical calculations of the assigned value and its standard deviation. The results of actions of the programme's participants were evaluated according to the following criteria (Table 1):

Table 1. Assessment of results according to the values of individual scores [52].

z-Score *	ζ-Score	E_n-Score
• $\|z\| \leq 2.0$–satisfactory result • $2.0 < \|z\| < 3.0$–questionable result • $\|z\| \geq 3.0$–unsatisfactory result	• $\|\zeta\| \leq 2.0$–satisfactory result • $2.0 < \|\zeta\| < 3.0$–questionable result • $\|\zeta\| \geq 3.0$–unsatisfactory result	• $\|E_n\| \leq 1.0$–satisfactory result • $\|E_n\| > 1.0$–unsatisfactory result

* Assessment according to z-score is not performed when the number of results for the tested parameter is lower than 8.

Is it worth mentioning that the paper [45] presented an approach toward the analysis of inter-laboratory comparison results for a small number of laboratories (2) and small number of samples (3), which can apply for e.g., a construction product for which tests and test elements are very expensive.

2.4. Laboratory Proficiency Tests with Regard to Testing Concrete Mix and Hardened Concrete

The tests involved the participation of nine southern Poland-based laboratory units. For confidentiality reasons, the present elaboration did not include the names or addresses of the laboratories. The proficiency testing programme considered test objects, measured parameters, and methods of testing concrete mix and hardened concrete as shown in Table 2.

Table 2. Test objects, measured parameters and recommended standard test methods.

Proficiency Test Object	Measured Parameters/Properties	Test Method According to:
Concrete mix	Sample collection Consistency Concrete mix density	EN 12350-1 [37] EN 12350-2 [38] EN 12350-6 [40]
Concrete	Air content Compressive strength	EN 12350-7 [41] EN 12390-3 [39]

The laboratory proficiency testing programme was designed following the guidelines set out by ISO 13528:2015 [55], Annex B, and consisted in the collection of samples of concrete mix, and the preparation and maintenance of concrete samples by each of the participating laboratories. This is why the concrete mix was the only area of uniformity and

stability control of the test object. For concrete sample testing, together with sample collection, inter-laboratory assessment involves the preparation and maintenance of concrete samples, and all related measures, including the transport of samples to the participants' laboratories. For concrete samples, the test object's instability effects were eliminated, as the testing programme assumed that the preparation, maintenance and assessment of concrete samples should be carried out by each participant at the same time (concrete compressive strength test—28 days after preparing test forms).

As the properties of concrete mix change over time, the quickest possible method was adopted for collecting samples. It was assumed that all samples would be collected within circa 15 min, in a single place.

Due to the availability, universality and cost-efficacy of testing methods, immediate tests of consistency and/or air content were employed to determine uniformity and stability of concrete mixes. For all participants, the manner of sample collection, preparation, testing and transportation complied with the recommendations set out by the relevant industry standards (Table 1) and programme-specific guidelines. Comparative tests were performed for concrete of the following parameters: strength class C30/37, consistency S3, frost resistance degree F150 and water resistance degree W8.

3. Results and Discussion

Based on the test results obtained by each of the participating laboratories, a number of parameters was calculated for the purpose of statistical quality assessment of performed measurements, in compliance with the recommendations of individual industry standards [38–43] and the testing programme designed according to [53,55]. The most important parameters for laboratory assessment are: standard deviation, expanded uncertainty, and *z-score*, *ζ-score* and *E_n-score*. Calculated values were presented in Tables 3–7 and Figures 2–4.

Table 3. Table of obtained values of basic statistical parameters for individual participating laboratories with regard to measurements performed for concrete mix consistency with the use of classical statistical method.

Lab Code	Consistency Test Result mm	Mean Value mm	Standard Deviation mm	Expanded Uncertainty mm	Result Expressed as an Interval, as Reported by the Laboratory (Result Minus/Plus Measurement Uncertainty) mm
Lab A	130				115–145
Lab B	130				115–145
Lab C	130				115–145
Lab D	130				115–145
Lab E	130	128	11	15	115–145
Lab F	140				125–155
Lab G	110				95–125
Lab H	110				95–125
Lab I	140				125–155

Table 4. Table of obtained values of basic statistical parameters for individual participating laboratories with regard to measurements performed for concrete mix air content with the use of classical statistical method.

Lab Code	Air Content Test Result %	Mean Value %	Standard Deviation %	Expanded Uncertainty %	Result Expressed as an Interval, as Reported by the Laboratory (Result Minus/Plus Measurement Uncertainty) %
Lab A	1.6				1.3–1.9
Lab B	1,8				1.5–2.1
Lab C	1.8				1.5–2.1
Lab D	1.6				1.3–1.9
Lab E	1.4	1.7	0.2	0.3	1.1–1.7
Lab F	1.8				1.5–2.1
Lab G	1.8				1.5–2.1
Lab H	2.1				1.8–2.4
Lab I	1.5				1.2–1.8

Table 5. Table of obtained values of basic statistical parameters for individual participating laboratories with regard to measurements performed for concrete mix density with the use of classical statistical method.

Lab Code	Density Test Result kg/m^3	Mean Value kg/m^3	Standard Deviation kg/m^3	Expanded Uncertainty kg/m^3	Result Expressed as an Interval, as Reported by the Laboratory (Result Minus/Plus Measurement Uncertainty) kg/m^3
Lab A	2287				2222–2352
Lab B	2279				2214–2344
Lab C	2301				2236–2366
Lab D	2289				2224–2354
Lab E	2293	2290	6	65	2228–2358
Lab F	2286				2221–2351
Lab G	2296				2231–2361
Lab H	2291				2226–2356
Lab I	2288				2223–2353

Table 6. Table of obtained values of basic statistical parameters for individual participating laboratories with regard to measurements performed for concrete compressive strength with the use of classical statistical method.

Lab Code	Compressive Strength Test Result MPa	Mean Value MPa	Standard Deviation MPa	Expanded Uncertainty MPa	Result Expressed as an Interval, as Reported by the Laboratory (Result Minus/Plus Measurement Uncertainty) MPa
Lab A	49.40				47.20–51.60
Lab B	45.95				43.75–48.15
Lab C	47.05				44.85–49.25
Lab D	47.10				44.90–49.30
Lab E	46.65	47.58	1.46	2.20	44.45–48.85
Lab F	46.00				43.80–48.20
Lab G	47.40				45.20–49.60
Lab H	48.70				46.50–50.90
Lab I	50.10				47.90–52.30

Table 7. Values of statistical parameters for individual parameters/properties of concrete mix and hardened concrete according to classical and robust statistics.

Parameter/Property \\ Statistical Parameter	Concrete Mix			Concrete
	Consistency mm	Air Content %	Density kg/m^3	Compressive Strength MPa
Mean	128.0	1.70	2290	47.6
standard deviation	10.9	0.20	6.2	1.46
assigned value (robust mean)	130.0	1.80	2289	47.1
robust standard deviation	0.0	0.30	4.5	1.63
standard uncertainty of assigned value	0.0	0.12	1.8	0.68
expanded uncertainty of assigned value	0.0	0.28	4.2	1.5

In data analysis and inter-laboratory comparative testing, various statistical tests, e.g., the Grubbs test, are performed to identify and remove outliers. This is appropriate and effective only for large samples. For concrete mix and hardened concrete tests (small samples), removing some data items (from one to three test results) significantly decreases the accuracy of uncertainty estimation, which is why the conducted analyses employed robust statistical methods, designed for robustness against slight deviation from the model (particularly the occurrence of outliers) [56,57]. The calculations were performed in compliance with ISO 13528: 2009-01 "Statistical method for use in proficiency testing by inter-laboratory comparisons", Annex C (normative) Robust Analysis [55]. The values of statistical parameters determined with the use of classical and robust methods were presented in Table 7.
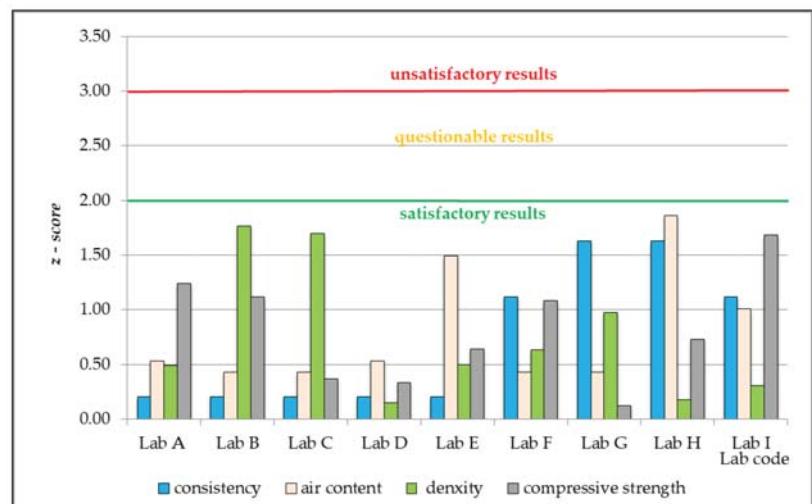
Figure 2. The value of z-score based on the results of the tests conducted by the participating laboratories, which performed measurements of density of concrete mix and compressive strength of hardened concrete according to the classical statistical method.
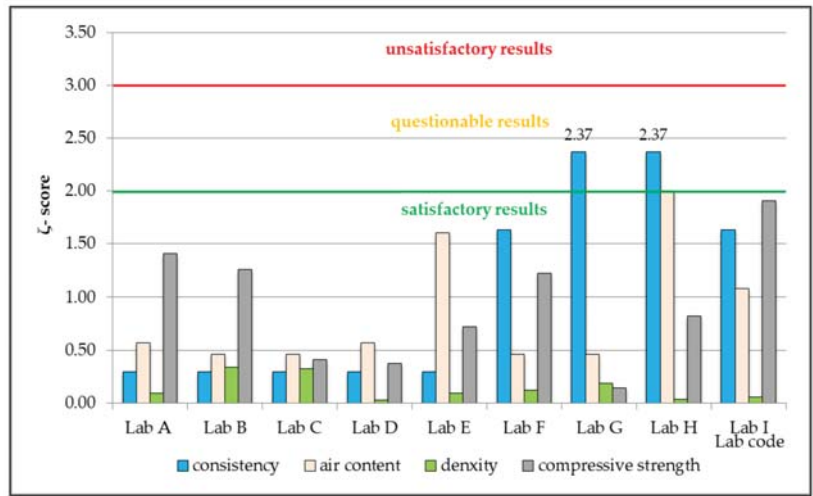
Figure 3. The value of ζ-*score* based on the results of the tests conducted by the participating laboratories, which performed measurements of density of concrete mix and compressive strength of hardened concrete according to the classical statistical method.
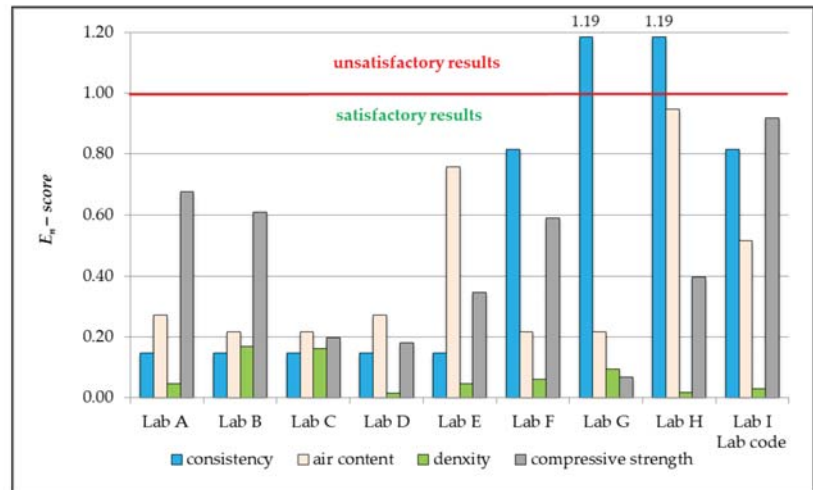
Figure 4. The value of E_n-score based on the results of the tests conducted by the participating laboratories, which performed measurements of density of concrete mix and compressive strength of hardened concrete according to the classical statistical method.

The next step of the calculations was to determine, based on the obtained statistical parameters (Table 6), the values of individual measures that would allow the laboratories' proficiency to be assessed, i.e., the values of *z-score*, ζ-*score* and E_n-*score*. On the basis of the inter-laboratory proficiency tests performed, all participating southern Poland-based laboratories which carry out tests of concrete mix and hardened concrete conduct them on a satisfactory level, as confirmed by the obtained *z-score* values |*z*| < 2.0 (Figure 2).

The obtained values of ζ-*score* and E_n-*score* for seven out of nine laboratories indicate satisfactory proficiency in determining consistency, air content and density of concrete mix, and compressive strength of hardened concrete (Figures 3 and 4).

Only for two laboratories, defined as Lab G and Lab H, the obtained values of ζ-*score* and E_n-*score* reveal unsatisfactory application by the participants of the methods for testing and consistency determination. The value of ζ-*score* indicates that the results obtained for the consistency parameter are questionable, whereas the value of E_n-*score* shows the results to be unsatisfactory (Figures 3 and 4).

In both cases, the limit value for ζ-*score* was exceeded by 18.5% $\rightarrow$ ζ *score* = 2.37, while the limit value for E_n-*score* was exceeded by 19% $\rightarrow E_n$-*score* = 1.19. This is not a significant exceeding of a satisfactory value, but one that constitutes a questionable result, which suggests undertaking appropriate measures with the aim to establish the causes of incorrect assessment of the consistency of concrete mix. Questionable results might be, in this case, caused by pouring into the cone-shaped form a concrete mixture that is too dry, or incorrect use of a measuring tool. Most tests, such as the slump flow test and the slump test, are carried out by operators by using a ruler or a stopwatch, which is why measurement errors are inherent, and the measured value may vary depending on the operator [58]. There is also a possibility that the obtained value can be wrongly recorded or easily manipulated after measurement. If concrete of insufficient workability is used for construction due to inaccurate measurement results or incorrect data records, it will cause future problems in terms of structural safety [58,59]. Consistency determines the ease of mixing concrete in a form for a given method of laying concrete. Fluidity parameters should comply with the overall plan of the project, as proper concrete consistency allows the durability of a structure to be predicted. Monitoring concrete fluidity [60,61] and durability [62–64] is considered crucial in long-distance transport of concrete required for constructing tower blocks and long-span bridges.

For *z-score* values determined with the use of classical and robust statistical method, regression and correlation analysis was performed. Figure 5 shows graphs of regression functions of *z-score* in classical statistics and *z-score* in robust statistics for various parameters.
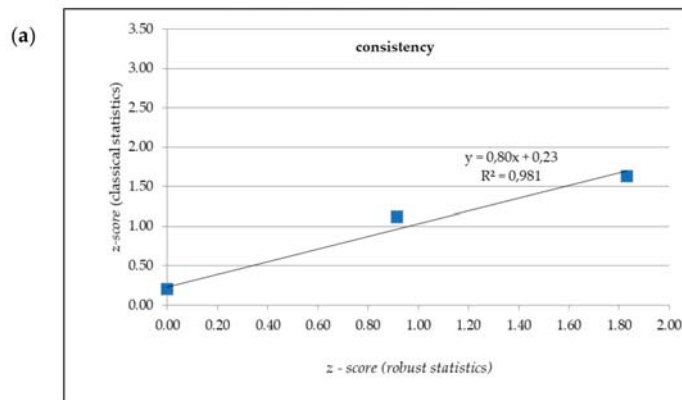
Figure 5. *Cont.*
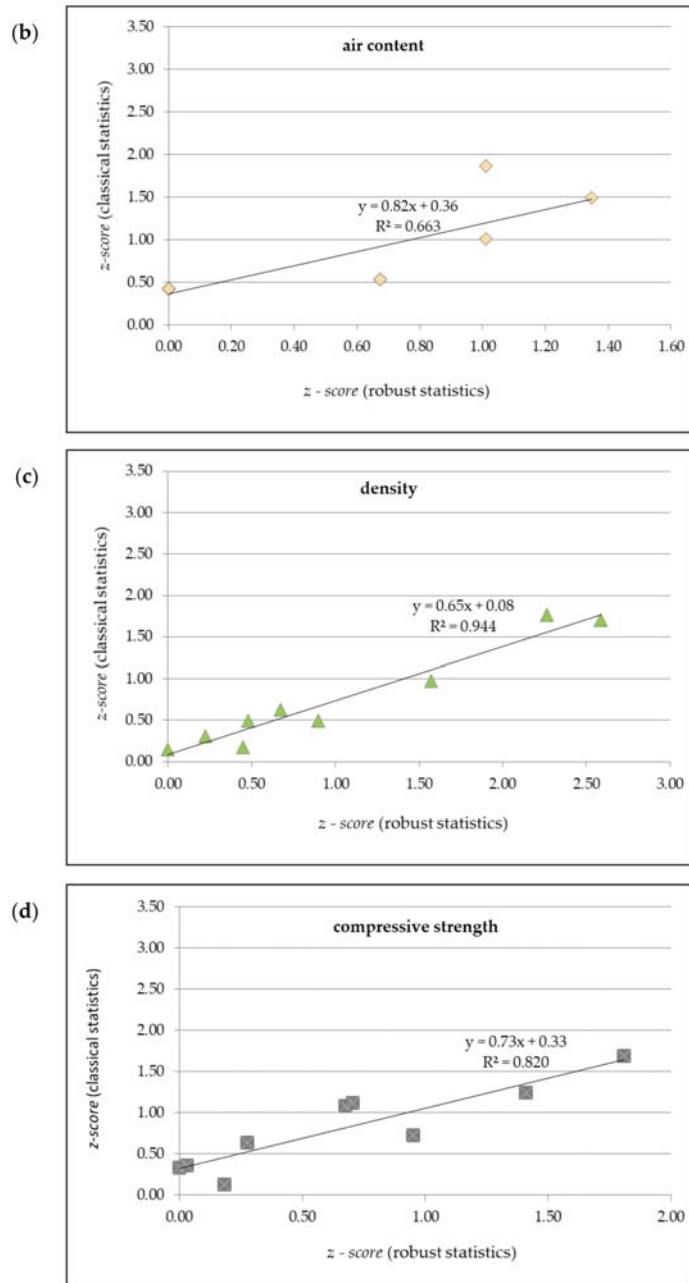
Figure 5. Regression functions of *z-score* in classical statistics and *z-score* in robust statistics for various parameters: (**a**) consistency; (**b**) air content; (**c**) density; (**d**) compressive strength.

High positive correlation can be observed between *z-score* in classical statistics and *z-score* in robust statistics. Pearson product–moment correlation coefficients for *z-score* in classical statistics versus z-score in robust statistics are presented in Table 8.

Table 8. Correlation of *z-score* for the results of two methods: robust and classical statistics.

Property	Result Value/Method		Correlation of z-Score for the Results of Two Methods
	Classical Statistics: Mean Value; Standard Deviation	Robust Statistics: Robust Value; Robust Standard Deviation	
Consistency	127.78 mm 10.93 mm	130.00 mm 0.00 mm	0.991
Air content	1.71 % 0.21 %	1.80 % 0.30 %	0.814
Density	2289.92 kg/m^3 6.22 kg/m^3	2289.00 kg/m^3 4.45 kg/m^3	0.972
Compressive strength	47.58 MPa 1.46 MPa	47.10 MPa 1.63 MPa	0.906

Combination of classical and robust statistical methods with the use of *z-score* can reduce the risks related to laboratory activities. In classical and robust statistics, *z-score* parameters, based on an assigned value, are more effective in detecting a laboratory having outlier results. *Z-score*, which is based on the difference between the reported result and the assigned value, is particularly useful for detecting discrepancies between laboratories, and may prove helpful in improving their activities. Neither of these methods nor their combination guarantee proper assessment, and they should not be used for the main assessment of laboratory performance in inter-laboratory comparisons. Methods for robust estimation in small samples do not improve the efficiency of the *z-score* parameter in detecting discrepancies of test results. In ISO 13528 [55], Annex D1, it is underscored that some of the procedures for performance evaluation are unreliable when used for too small a number of participants. The conclusions are consistent with the information given in ISO 13528 [55] and in [45]. Assessment of reliability of small sample size tests is a difficult problem to solve in inter-laboratory comparisons of ready-mixed concrete. In such circumstances, it seems justified to refrain from activities aimed at ensuring testing quality by means of inter-laboratory comparisons, and focus on other aspects, such as the personnel's competencies and equipment suitability. However, laboratories, particularly those responsible for carrying out tests of ready mix concrete that affect construction safety and quality, tend to be concerned about the correctness of test results. An inter-laboratory comparison could help them assess whether differences between laboratories are significant, and gain more confidence in their results. Such comparisons—as presented in the paper—give both the laboratory and its customer a slightly higher sense of security.

4. Conclusions

Proper quality control of concrete does not only influence the optimisation and verification of correct functioning of individual stages of the production process, but also directly impacts certification related to factory production control. Quality control is the basis for ensuring that the production plant meets at least the requirements and recommendations set out by EN 206:2014 "Concrete–Specification, performance, production and conformity". The standard introduced a novel approach toward designing the composition and planning the production of concrete mixes, and evaluating concrete with regard to technical parameters. In turn, quality control through laboratory proficiency tests, for instance with regard to testing concrete mix and hardened concrete, allows individual laboratory units' capability to perform specific research to be evaluated. For accredited laboratories, in order to monitor the reliability of the obtained results, participation in inter-laboratory comparison programmes or proficiency testing programmes is required by ISO/IEC 17025:2005. For the remaining research units, participation in such programmes is undoubtedly a means of verifying and improving the quality of conducted analyses, as well

as a platform for exchanging experiences and views (after performing and documenting measurements), both for individual employees and the entire laboratory.

Comparative tests discussed in the present paper, conducted for nine participating laboratories, provided interesting data for scientific consideration. For the purpose of the tests, selected parameters/properties of concrete mix and hardened concrete were analysed. *Z-score* was applied to evaluate laboratory proficiency, whereas *ζ-score* and *E_n-score* were used for improving the laboratories' performance. For the laboratories defined as Lab G and Lab H, the results obtained provided information about irregularities, which made it possible to take adequate corrective measures with the aim to determine the causes of inappropriate assessment of concrete mix consistency.

Experiences gained from the conducted tests reveal a need to continue this type of project, with the cooperation of both past participants and new laboratory facilities, for the purpose of improving the quality of activities conducted by research units. A tangible aspect of regular participation in comparative tests, with positive results, is an increase in customer trust and the evidence of the laboratory personnel's competencies.

References

1. Bernardi, E.; Carlucci, S.; Cornaro, C.; Bohne, R.A. An analysis of the most adopted rating systems for assessing the environmental impact of buildings. *Sustainability* **2017**, *9*, 1226. [CrossRef]
2. Wałach, D. Analysis of Factors Affecting the Environmental Impact of Concrete structures. *Sustainability* **2021**, *13*, 204. [CrossRef]
3. Sztubecka, M.; Skiba, M.; Mrówczyńska, M.; Mathias, M. Noise as a Factor of Green Areas Soundscape Creation. *Sustainability* **2020**, *12*, 999. [CrossRef]
4. Talang, R.P.N.; Sirivithayapakorn, S. Comparing environmental burdens, economic costs and thermal resistance of different materials for exterior building walls. *J. Clean. Prod.* **2018**, *197*, 1508–1520. [CrossRef]
5. Musarat, M.A.; Alaloul, W.S.; Liew, M.S.; Maqsoom, A.; Qureshi, A.H. Investigating the impact of inflation on building materials prices in construction industry. *J. Build. Eng.* **2020**, *32*, 101485. [CrossRef]
6. Leśniak, A.; Zima, K. Comparison of traditional and ecological wall systems using the AHP method. In Proceedings of the International Multidisciplinary Scientific GeoConference Surveying Geology and Mining Ecology Management, SGEM, Albena, Bulgaria, 18–24 June 2015; Volume 3, pp. 157–164.
7. Sztubecka, M.; Skiba, M.; Mrówczyńska, M.; Bazan-Krzywoszańska, A. An innovative decision support system to improve the energy efficiency of buildings in urban Areas. *Remote Sens.* **2020**, *12*, 259. [CrossRef]
8. Węglarz, A. Using Artificial Intelligence in energy efficient construction. *E3S Web Conf.* **2018**, *49*, 00125. [CrossRef]
9. Chen, S.; Zhang, G.; Xia, X.; Setunge, S.; Shi, L. A review of internal and external influencing factors on energy efficiency design of buildings. *Energy Build.* **2020**, *216*, 109944. [CrossRef]
10. Nowogońska, B. A methodology for determining the rehabilitation needs of buildings. *Appl. Sci.* **2020**, *10*, 3873. [CrossRef]

11. Bednarz, L.; Bajno, D.; Matkowski, Z.; Skrzypczak, I.; Leśniak, A. Elements of Pathway for Quick and Reliable Health Monitoring of Concrete Behavior in Cable Post-Tensioned Concrete Girders. *Materials* **2021**, *14*, 1503. [CrossRef] [PubMed]

12. Konior, J.; Sawicki, M.; Szóstak, M. Damage and Technical Wear of Tenement Houses in Fuzzy Set Categories. *Appl. Sci.* **2021**, *11*, 1484. [CrossRef]

13. Jasiczak, J.; Owsiak, Z. Next problems with the railway prestressed sleepers cracking in concrete as an effect of delayed ettringite formation. In *Bearing Capacity of Roads, Railways and Airfields*; CRC Press: Boca Raton, FL, USA, 2017; pp. 2069–2074.

14. Tang, Z.; Li, W.; Tam, V.W.; Xue, C. Advanced progress in recycling municipal and construction solid wastes for manufacturing sustainable construction materials. *Resour. Conserv. Recycl. X* **2020**, *6*, 100036. [CrossRef]

15. Spišáková, M.; Mésároš, P.; Mandičák, T. Construction Waste Audit in the Framework of Sustainable Waste Management in Construction Projects—Case Study. *Buildings* **2021**, *11*, 61. [CrossRef]

16. Skrzypczak, I.; Kokoszka, W.; Zięba, J.; Leśniak, A.; Bajno, D.; Bednarz, L. A Proposal of a Method for Ready-Mixed Concrete Quality Assessment Based on Statistical-Fuzzy Approach. *Materials* **2020**, *13*, 5674. [CrossRef] [PubMed]

17. Gursel, A.P.; Masanet, E.; Horvath, A.; Stadel, A. Life-Cycle Inventory Analysis of Concrete Production: A Critical Review. *Cem. Concr. Compos.* **2014**, *51*, 38–48. [CrossRef]

18. Hilburg, J. Concrete Production Produces Eight Percent of the World's Carbon Dioxide Emissions. Architecture, International, News, Sustainability. Available online: https://www.archpaper.com/2019/01/concrete-production-eight-percent-co2-emissions/ (accessed on 20 August 2020).

19. Poon, C.S.; Yu, A.T.W.; Jaillon, L. Reducing Building Waste at Construction Sites in Hong Kong. *Constr. Manag. Econ.* **2004**, *22*, 461–470. [CrossRef]

20. Ready-Mixed Concrete Industry Statistics. Available online: https://mediatheque.snpb.org/userfiles/file/Statistics%20Bound%20Volume%2030_08_2019%20-%20R4.pdf (accessed on 16 July 2020).

21. Gorzelanczyk, T.; Pachnicz, M.; Rozanski, A.; Schabowicz, K. Identification of Microstructural Anisotropy of Cellulose Cement Boards by Means of Nanoindentation. *Constr. Build. Mater.* **2020**, *57*, 119515. [CrossRef]

22. Li, L.; Cao, M.; Yin, H. Comparative roles between aragonite and calcite calcium carbonate whiskers in the hydration and strength of cement paste. *Cem. Concr. Compos.* **2019**, *104*, 103350. [CrossRef]

23. Cao, M.; Zhang, C.; Li, Y.; Wei, J. Using Calcium Carbonate Whisker in Hybrid Fiber-Reinforced Cementitious Composites. *ASCE J. Mater. Civ. Eng.* **2015**, *27*, 4014139. [CrossRef]

24. Skrzypczak, I.; Kokoszka, W.; Buda-Ożóg, L.; Janusz Kogut, J.; Słowik, M. Environmental aspects and renewable energy sources in the production of construction aggregate. In *E3S Web of Conferences*; EDP Sciences: Ulis, France, 2017; p. 00160.

25. Chen, S.T.T.; Wang, W.C.; Wang, H.Y. Mechanical Properties and Ultrasonic Velocity of Lightweight Aggregate Concrete Containing Mineral Powder Materials. *Constr. Build. Mater.* **2020**, *258*, 119550. [CrossRef]

26. Mazur, W.; Drobiec, Ł.; Jasiński, R. Research of Light Concrete Precast Lintels. *Procedia Eng.* **2016**, *161*, 611–617. [CrossRef]

27. Asadzadeh, S.; Khoshbayan, S. Multi-objective optimization of influential factors on production process of foamed concrete using Box-Behnken approach. *Constr. Build. Mater.* **2018**, *170*, 101–110. [CrossRef]

28. Ashrafi, N.; Nazarian, S.; Meisel, N.A.; Duarte, J.P. Experimental prediction of material deformation in large-scale additive manufacturing of concrete. *Addit. Manuf.* **2021**, *37*, 101656.

29. Wang, D.; Liu, G.; Li, K.; Wang, T.; Shrestha, A.; Martek, I.; Tao, X. Layout Optimization Model for the Production Planning of Precast Concrete Building Components. *Sustainability* **2018**, *10*, 1807. [CrossRef]

30. Federowicz, K.; Kaszyńska, M.; Zieliński, A.; Hoffmann, M. Effect of curing methods on shrinkage development in 3D-printed concrete. *Materials* **2020**, *13*, 2590. [CrossRef]

31. Al Ajmani, H.; Suleiman, F.; Abuzayed, I.; Tamini, A. Evaluation of Concrete Strength Made with Recycled Aggregate. *Buildings* **2019**, *9*, 56. [CrossRef]

32. Czarnecki, L.; Geryło, R.; Kuczyński, K. Concrete Repair Durability. *Materials* **2020**, *13*, 4535. [CrossRef]

33. Skibicki, S.; Kaszyńska, M.; Wahib, N.; Techman, M.; Federowicz, K.; Zieliński, A.; Hoffmann, M. Properties of composite modified with limestone powder for 3D concrete printing. In *RILEM International Conference on Concrete and Digital Fabrication*; Springer: Cham, Switzerland, 2020; pp. 125–134.

34. Domagała, L. Durability of Structural Lightweight Concrete with Sintered Fly Ash Aggregate. *Materials* **2020**, *13*, 4565. [CrossRef]

35. Schabowicz, K. Non-Destructive Testing of Materials in Civil Engineering. *Materials* **2019**, *12*, 3237. [CrossRef] [PubMed]

36. Patil, S.V.; Rao, K.B.; Nayak, G. Quality Improvement of Recycled Aggregate Concrete using six sigma DMAIC methodology. *Int. J. Math. Eng. Manag. Sci.* **2020**, *5*, 1409–1419. [CrossRef]

37. Juszczyk, M.; Kozik, R.; Leśniak, A.; Plebankiewicz, E.; Zima, K. Errors in the preparation of design documentation in public procurement in Poland. *Procedia Eng.* **2014**, *85*, 283–292. [CrossRef]

38. The European Committee for Standardization. *EN 206:2013 Concrete–Specification, Performance, Production and Conformity*; The European Committee for Standardization: Brussels, Belgium, 2013.

39. The European Committee for Standardization. *EN 12350-1:2019 Testing Fresh Concrete–Part 1: Sampling and Common Apparatus*; The European Committee for Standardization: Brussels, Belgium, 2019.

40. The European Committee for Standardization. *EN 12350-2:2019 Testing Fresh Concrete–Part 2: Slump Test*; The European Committee for Standardization: Brussels, Belgium, 2019.

41. The European Committee for Standardization. *EN 12390-3:2019 Testing Fresh Concrete–Part 3: Vebe Test*; The European Committee for Standardization: Brussels, Belgium, 2019.
42. The European Committee for Standardization. *EN 12350-6:2019 Testing Fresh Concrete–Part 6: Density*; The European Committee for Standardization: Brussels, Belgium, 2019.
43. The European Committee for Standardization. *EN 12350-7: 2019 Testing Fresh Concrete–Part 7: Air Content–Pressure Methods*; The European Committee for Standardization: Brussels, Belgium, 2019.
44. ISO/IEC. *ISO/IEC 17000:2020–Conformity Assessment–Vocabulary and General Principles*; International Organization for Standardization/International Electrotechnical Commission: Geneva, Switzerland, 2020.
45. Szewczak, E.; Bondarzewski, A. Is the assessment of interlaboratory comparison results for a small number of tests and limited number of participants reliable and rational? *Accredit. Qual. Assur.* **2016**, *21*, 91–100. [CrossRef]
46. ISO/IEC. *ISO/IEC 17025:2005 General Requirements for the Competence of Testing and Calibration Laboratories*; International Organization for Standardization/International Electrotechnical Commission: Geneva, Switzerland, 2005.
47. EA-4/18 (2010) Guidance on the Level and Frequency of Proficiency Testing Participation. European Accreditation. Available online: http://www.european-accreditation.org/publication/ea-4-18-inf-rev00-june-2010 (accessed on 30 April 2021).
48. Andersson, H.O.F. The rational use of proficiency tests and intercomparisons. *Accredit. Qual. Assur.* **1998**, *3*, 24–226. [CrossRef]
49. de Albano, M.F.; ten Caten, S.C. Proficiency tests for laboratories: A systematic review. *Accredit. Qual. Assur.* **2014**, *19*, 245–257. [CrossRef]
50. Bergoglio, M.; Malengo, A.; Mari, D. Analysis of interlaboratory comparisons affected by correlations of the reference standards and drift of the travelling standards. *Measurement* **2011**, *44*, 1461–1467. [CrossRef]
51. ISO/IEC. *ISO/IEC 17043:2010 Conformity Assessment—General Requirements for Proficiency Testing*; International Organization for Standardization/International Electrotechnical Commission: Geneva, Switzerland, 2010.
52. Protocol for Proficiency Testing Schemes. Fera Science Ltd., 2017. Available online: https://fapas.com/sites/default/files/2017-05/FeraPTSprotocol_pt1_common.pdf (accessed on 1 April 2021).
53. Deptuła, H. Interlaboratory comparisons as an element of testing quality control in the Research Laboratories Group of the Building Research Institute. *Work. Build. Res. Inst.* **2010**, *39*, 35–45. (In Polish)
54. Wojtczak, M. Laboratory proficiency testing through interlaboratory comparisons (in Polish). Available online: https://docplayer.pl/33073620-Badania-bieglosci-laboratorium-poprzez-porownania-miedzylaboratoryjne.html (accessed on 2 March 2021).
55. ISO. *ISO 13528:2015 Statistical Methods for Use in Proficiency Testing by Interlaboratory Comparisons*; International Organization for Standardization: Geneva, Switzerland, 2015.
56. Rosario, P.; Martínez, J.L.; Silván, J.M. Comparison of different statistical methods for evaluation of proficiency test data. *Accred. Qual. Assur.* **2018**, *13*, 493–499. [CrossRef]
57. Belli, M.; Ellison, S.L.R.; Fajgelj, A.; Kuselman, I.; Sansone, U.; Wegscheider, W. Implementation of proficiency testing schemes for a limited number of participants. *Accred. Qual. Assur.* **2007**, *12*, 391–398. [CrossRef]
58. Jung-Hoon, K.; Minbeom, P. Visualization of Concrete Slump Flow Using the Kinect Sensor. *Sensors* **2018**, *18*, 771.
59. Nhat-Duc, H.; Anh-Duc, P. Estimating Concrete Workability Based on Slump Test with Least Squares Support Vector Regression. *J. Constr. Eng.* **2016**, *8*. [CrossRef]
60. Kwon, S.H.; Jang, K.P.; Kim, J.H.; Shah, S.P. State of the Art on Prediction of Concrete Pumping. *Int. J. Concr. Struct. Mater.* **2016**, *10*, 75–85. [CrossRef]
61. Nehdi, M.L. Only Tall Things Cast Shadows: Opportunities, Challenges and Research Needs of Self-Consolidating Concrete in Super-Tall Buildings. *Constr. Build. Mater.* **2013**, *48*, 80–90. [CrossRef]
62. Shin, S.W.; Yun, C.B.; Popovics, J.S.; Kim, J.H. Improved Rayleigh Wave Velocity Measurement for Nondestructive Early-Age Concrete Monitoring. *Res. Nondestruct. Eval.* **2007**, *18*, 45–68. [CrossRef]
63. Başyiğit, C.; Çomak, B.; Kılınçarslan, Ş.; Serkan Üncü, İ. Assessment of Concrete Compressive Strength by Image Processing Technique. *Constr. Build. Mater.* **2012**, *37*, 526–532. [CrossRef]
64. Rizzo, P.; Ni, X.; Nassiri, S.; Vandenbossche, J. A Solitary Wave-Based Sensor to Monitor the Setting of Fresh Concrete. *Sensors* **2014**, *14*, 12568. [CrossRef] [PubMed]

Article

Interlaboratory Comparison as a Source of Information for the Product Evaluation Process. Case Study of Ceramic Tiles Adhesives

Cristina Stancu [1] and Jacek Michalak [2,*]

[1]   Ceprocim S.A., 6, Blvd. Preciziei, Sector 6, 062203 Bucharest, Romania; cristina.stancu@ceprocim.ro
[2]   Research and Development Center, Atlas sp. z o.o., 2, Kilińskiego St., 91-421 Lodz, Poland
*   Correspondence: jmichalak@atlas.com.pl

Abstract: In this study, the results obtained by 19 laboratories participating in 2 editions of the interlaboratory comparison (ILC) determining 2 properties of ceramic tiles adhesives (CTAs), i.e., initial tensile adhesion strength and tensile adhesion strength after water immersion following EN 12004, were analyzed. The results show that participating laboratories maintain a constant quality of their work. The use of z-score analysis, under ISO 13528, allows for classifying 89.5% to 100% of laboratories as satisfactory, depending on the measurement's kind and edition. The remaining laboratories are classified as questionable. The investigation of the predominant mode of failure of the CTA's samples tested in the two editions shows significant differences. From the perspective of laboratories, the goal of the ILC has been achieved. From the standpoint of a manufacturer who evaluates a product's properties when placing it on the market, the results indicate the necessity of a particular treatment of the product evaluation process because the variability of the obtained results is significant. It increases the possibility of the product failing to meet the assessment criteria verified by the construction market supervision authorities. The manufacturer must consider all possible variations in the risk analysis, including the ILC results, to improve the assessment process of CTAs.

1. Introduction

The assessment and verification of constancy of performance (AVCP) of products in EU countries is a complex and multidimensional process. The rules for placing construction products on the market define the Construction Products Regulation (CPR) [1]. This document describes a harmonized system of assessing, performance expression, and conditions for CE marking, while controlling the constancy of the assessment results, which should remain constant.

The laying down of a product on the market is always associated with a risk, which is considered in different categories. Risk is an ambiguous concept, challenging to define. However, risk assessment is a fundamental technical framework for systematically analyzing the risk associated with an industrial activity [2]. Effective risk management requires essential knowledge about people's perceptions of risk in their industry [3]. The construction industry, in general, is risky, and the risks involved in building construction objects are highly complex [4]. The risk related to the quality of construction products is only one out of several dozen identified in the construction process [5]. In the scientific literature, the risk related to the construction product's non-compliant evaluation criteria is often not presented [6–10], very rarely from the manufacturer's perspective [11,12].

It is essential for all market participants that the products are safe. Knowledge from internal and external sources should be considered to create any product. In most cases,

in-house knowledge is dominant, and, of course, producers know the level of safety/risk related to their product development. From the manufacturer's perspective, it is a problem when market supervision bodies will negatively assess their product. A particular situation is when this happens due to negative test results ordered by market surveillance authorities, and, of course, it may occur in many cases. One of them is when the actual values of the product's performance are close to the threshold value of the evaluation criterion (declared value), and when the evaluation methods are incorrectly selected. A proper, holistic understanding of risk allows manufacturers to make appropriate decisions to protect against adverse effects, including uncertainty analysis [6,7,13]. Such understanding is crucial to avoid contentious situations. Conducting a risk analysis by the product's manufacturer, including the measurement uncertainty (MU) related to the measured and declared performance of the product, is fundamental for the correct determination of the stability of the product's performance and safe use. It is also necessary for the continuous maintenance of the product as compliant with the assessment criteria. All measurements are erroneous; it is essential to know what size of measurement error accompanies the measurement [14]. However, since it is not possible to identify the sources and values of all systematic errors (and their directions) for any given measurement result, as well as the value of the random error occurring at a given time, the MU criterion is commonly used, inter alia, in clinical chemistry [15–17]. This parameter characterizes the dispersion of the quantity values attributed to a measurand (quantity intended to be measured) based on the information used [18]. It is essential to add that MU is a "non-negative" parameter [14]. Failure by the manufacturer to consider the consequences of uncertainty, including MU, during product development and the production process may result in a situation in which the product assessed as conforming may be non-compliant. It is also possible that a product rejected as non-compliant may be a compliant product [19,20]. Note that uncertainty in measurements is an operational concept that only relates to quantitative values assigned to the measurand based on the available information, the model of the measurement procedure, and the probabilistic assumptions used [21]. However, it is also essential to be aware that the measurement information provides only partial information about the actual product characteristic. When taken into account during the product assessment, it minimizes the adverse effects of incorrect evaluation. Still, it is not always sufficient to permanently deliver a product that complies with the assessment criteria [22]. Knowing the MU value for a given measurement method minimizes the risk of obtaining results that do not meet the evaluation criterion; for example, modifying the product recipe resulting in a change (usually increase) of the product parameter value. Such an operation, however, is generally associated with an increase in production costs. Of course, the MU related to the testing method of product properties is one of the many factors that the manufacturer needs to consider.

All laboratories aim to provide reliable information. Most of the measurements aim to assess compliance with a specification or regulation [23]. In this case, the measurement itself is not the goal but the basis for making objective decisions [24]. Conformity decisions are made for different products in many application areas without transparent and harmonized risk sharing, due to MU between the consumer and the producer/supplier of the product [24]. Performing measurements to assess compliance with specifications requires further development. Mainly, where shortcomings are observed, i.e., in the description of the measurement process, recognition that confidence in the measured result depends not only on its uncertainty but also on its integrity and further development of validated methods for the performance assessment [25,26]. Interlaboratory research plays an essential role in ensuring the quality of laboratory testing. The growing interest in this topic reflects the scientific literature [9,27–36]. In interlaboratory comparisons (ILCs) dominate clinical chemistry, biochemistry, medicine, and pharmacy researches. Construction products are much less the subject of the ILCs. In addition, the testing and assessment of construction products is still not precisely defined in terms of uncertainty, methods of estimation, and taking into account [8]. For construction products, a small number of tests and a limited

number of participants are ILC limitations [9,36]. An additional difficulty is that most of the measurement methods used for assessment with evaluation criteria are destructive in the case of construction products. Thus, it is not possible to repeat the test with the same sample. In the future, the situation will change due to the standardization regulations creating new requirements for selected construction products related to the possibility of ILC/PT performance [37].

ILC is considered primarily in the aspect of proficiency testing (PT), understood as part of a quality system that provides an external assessment that a laboratory's performance meets the requirements. PT is also understood to mean that an individual laboratory evaluates its performance for the intended purposes. A significant tenet of ILC is to prove the laboratory's ability to reproduce the results generated by the other laboratories. The ILC is also considered a learning exercise and is associated with terms such as quality control and certification. Those, as mentioned above, are the main goals of ILCs. In the scientific literature, ILCs are not perceived as a tool providing information to the manufacturer that can be used to verify the product recipe, so that the product meets the evaluation criteria during external evaluation. ILCs are also not considered a tool to verify the test methods specified in the standards for product assessment.

This study compares the results of the ILCs of ceramic tile adhesives (CTAs) organized by Ceprocim, carried out in two editions, i.e., in 2019–2020 and 2020–2021. The research organized by Ceprocim aimed to demonstrate that the systematic participation of laboratories in ILC improves the quality of their work. Based on the ILC results, the importance of the laboratories' participation in the PT will be analyzed. The authors will analyze the obtained results from the perspective of laboratories participating in the ILC. The ILC results will also be considered in the manufacturer's risk analysis, accompanying the product evaluation process. Based on the results, the authors will discuss the potential need to modify the requirements and methodology specified in EN 12004 [38]. There arises the need for discussion due to the application by market surveillance authorities of the simple acceptance rule, which does not consider the variability resulting from measurement uncertainty.

As mentioned before, few scientific papers discuss ILC for construction materials. Additionally, the articles published so far consider the ILC/PT in terms of assessing the competence of the work of laboratories. Conclusions resulting from PT are discussed between laboratories and institutions that granted laboratory accreditation. There are no studies in the scientific literature discussing how the results obtained in the ILC/PT can be the subject of a risk analysis conducted by the producer. Results of the ILC/PT also indicate possible modifications to the standards to improve them and make them more useful for both producers and users of products.

2. Materials and Methods

2.1. Short History of Interlaboratory Comparisons Organized by Ceprocim

In 2007, the Romanian laboratory Ceprocim (notified body number 1830), authorized to test in the scope of EN 12004, initiated a project of ILC of the initial adhesion strength of cementitious CTAs. Nine laboratories, mainly Romanian, participated in the first edition of ILC, while twenty-seven laboratories of research institutes and manufacturers of CTAs from the following nine countries participated in the fifth edition: Austria, Bulgaria, Croatia, the Czech Republic, Germany, Poland, Portugal, Romania, and Slovenia [30]. Proficiency tests/interlaboratory comparisons organized by Ceprocim were carried out according to uniform rules and the requirements of EN ISO/IEC 17043 [39]. All laboratories used identical concrete slabs for the tests and the same ceramic tiles provided by the test organizer. According to the study's authors, more than 90% of the test results obtained by the participating laboratories can be described as satisfactory ($|z| \leq 2$) according to EN ISO/IEC 17043, and the remaining were questionable or unsatisfactory [30].

In 2014, Ceprocim extended the research to the second characteristic—adhesion strength after water immersion. In 2018, during the tenth jubilee edition of the study,

three characteristics were measured: initial adhesion strength, adhesion strength after immersion in water, and open time [34]. The last extension of the scheme took place in 2020, when two more tests were introduced: tensile adhesion strength after heat aging and tensile adhesion strength after the freeze-thaw cycle [40]. Randomly assigning a code number to each laboratory in each edition ensures confidence in the entire study. Reference to each laboratory in all reports is made by code number.

Concrete slabs of various origins were used for the twelve editions of the ILC. Each of the laboratories participating in the eleventh and twelfth editions used their own concrete slabs.

It is also important to note that the laboratories participating in ILCs organized by Ceprocim represent both accredited laboratories according to EN ISO/IEC 17025 [41] and non-accredited laboratories. Twenty-nine laboratories participated in the eleventh edition of the ILC (2019–2020) and twenty-seven in the twelfth edition a year later. Nineteen laboratories participated in both the eleventh and twelfth editions, and the results obtained by these laboratories are discussed later in this paper. The 19 laboratories are from the following countries: Austria—1, Germany—3, Greece—2, Italy—1, Mauritius—1, Poland—1, Portugal—1, Republic of Moldova—1, Romania—5, Slovenia—1, Spain—1, and United Arab Emirates—1.

2.2. Ceramic Tile Adhesives (CTAs)

CTAs are an important group of construction products intended to install ceramic cladding for internal and external purposes [42]. Ceramic tiles are commonly used on all continents. In 2020, their production reached 16.093 billion m^2, while consumption was slightly lower and amounted to 16.035 billion m^2 [43]. Assuming an average consumption of 4 kg CTA per 1 m^2 of ceramic cladding, this means a global production of about 65 million tons of CTAs.

Requirements for all CTAs (cementitious, dispersion, and reaction resin) applying to all member states of the EU, three of the EFTA members (Iceland, Norway, and Switzerland), and other states (United Kingdom, North Macedonia, Serbia, and Turkey) specify EN 12004. EN 12004 was first published in 2001, and the last version of the standard published in the list of European harmonized standards [44] is EN 12004:2007+A1:2012 [38]. The next version of the standard published by CEN in 2017, i.e., EN 12004-1:2017 [45], has not yet been included in the list of harmonized standards published in the Official Journal of the European Union and, therefore, cannot be the basis for the assessment and verification of constancy of performance. Based on the EN 12004, the global standard ISO 13007-1 was implemented in 2004 [46]. Establishing the standard specifying requirements, terminology, working methods, and application properties for CTAs for internal and external tile installations on walls and floors by the ISO organization has resulted in their harmonization worldwide. The current ISO 13007-1 standard comes from 2014 [47].

The fundamental issue in ILC is that the tested product (CTA), and other materials used for the tests, i.e., concrete slabs and ceramic tiles, are identical. The organizer provided the CTA and ceramic tiles in the analyzed studies, and each of the participating laboratories provided concrete slabs. Residual CTA determinations were repeatedly performed on a 250 μm sieve to ensure that the CTA was homogeneous. Checking the adhesive homogeneity was performed with the same equipment, by the same operator, during a short period. The sample was considered homogeneous when all the results had been placed in the range: average residue value on the 250 μm sieve ± 2 s (%). The value of s represents the standard deviation of repeatability.

The CTA used in the research was classified as C2E under the requirements of EN 12004 [38]. The initial adhesion strength and adhesion strength after water immersion were determined following the test methods and using auxiliary materials (concrete slab, ceramic tiles) specified in EN 12004 [38]. Finally, it is essential to note that each ILC participant received also written guidelines, in addition to the CTA, for the study and ceramic tiles.

2.3. Evaluation of the Results Using the z-Score

For the statistical calculation, algorithm A in Annex C from the standard ISO 13528 [48] was used. It implies, for initial adhesion strength, for tensile adhesion strength after heat aging, for tensile adhesion strength after water immersion, for tensile adhesion strength after freeze-thaw cycle, and for open-time after not less than 30 min, calculation of the robust values for average and for standard deviation, from the results obtained of each participant.

Based on an iterative calculation, the calculus of robust average (x^*) and the robust standard deviation (s^*) were made. The calculation was carried until there was no change from one iteration to the next in the third significant figure in the robust standard deviation and the equivalent figure in the robust average. The value obtained for the robust average after the last iteration represents the assigned value (x_{pt}), chosen to be the consensus value.

The standard uncertainty $u(x_{pt})$ of the assigned value is given by Equation (1):

$$u(x_{pt}) = 1.25 \times \sigma_{pt/}\sqrt{p} \tag{1}$$

where:

σ_{pt}—standard deviation for proficiency assessment,
p—the number of participant laboratories that carried on the test on concrete slab.

The z-score is calculated with Equation (2):

$$z_i = x_i - x_{pt}/\sigma_{pt} \tag{2}$$

where:

x_i—the value obtained by each participant for each test,
x_{pt}—the assigned value on total participants for each test.

The evaluation of the results was made according to EN ISO/IEC 17043:2010, as follows:

- satisfactory, when $|z| \leq 2$;
- questionable, when $2 < |z| < 3$;
- unsatisfactory, when $|z| \geq 3$.

In the z-score calculation program, the assigned value and the robust standard deviation value obtained after the last iteration have been used as they result from calculation without being round.

The interpretation mentioned above of z-score is conventional (see ISO/IEC 17043: 2010 [30], B.4.1.1.). A result that gives $2.0 < |z| < 3.0$ is considered to give a warning signal. Participants of the ILC/PT should be advised to check their measurement procedures following warning signals if they indicate an emerging or recurrent problem. The justification for using the limits of 2.0 and 3.0 for z-score is as follows. Measurements that are carried out correctly are assumed to generate results that can be described (after transformation, if necessary) by a normal distribution with mean x_{pt} and standard deviation σ_{pt}. z-score, which will then be normally distributed with a mean of zero and a standard deviation of 1.0. Under these circumstances, only about 0.3% of scores would be expected to fall outside the range $-3.0 \leq z \leq 3.0$, and only about 5% would be expected to fall outside the range $-2.0 \leq z \leq 2.0$.

3. Results

The initial tensile adhesion strength, tensile adhesion strength after water immersion of CTA, and the predominant mode of failure obtained in the eleventh edition of the ILC (2019–2020) and the twelfth edition (2020–2021) are presented in Tables 1 and 2.

Table 1. The initial tensile adhesion strength and tensile adhesion strength after water immersion of CTA with the predominant mode of failure obtained by 19 laboratories in the eleventh ed. (2019–2020).

Participant Code	Initial Tensile Adhesion Strength		Tensile Adhesion Strength after Water Immersion	
	[N/mm^2]	Dominant Failure Pattern	[N/mm^2]	Dominant Failure Pattern
1	1.5	AF-T	0.7	AF-T
2	1.9	70% CF-A/30% AF-T	0.7	50% CF-A/50% AF-T
3	1.0	CF-A	0.7	CF-A
4	1.3	AF-T	0.4	AF-T
5	2.4	CF-A	1.0	CF-A
6	1.9	CF-A	1.1	AF-T
7	1.7	CF-A	0.9	CF-A
8	1.6	CF-A	1.2	CF-A
9	1.8	CF-A	0.8	CF-A
10	1.6	CF-A	0.9	CF-A
11	1.8	AF-T	0.6	AF-T
12	1.3	CF-A	0.6	CF-A
13	1.8	CF-A	0.8	CF-A
14	1.8	CF-A		
15	1.3	CF-A	0.4	CF-A
16	2.0	70% CF-A/30% AF-T	0.8	40% CF-A/60% AF-T
17	2.1	CF-A	1.1	CF-A
18	1.6	AF-T	1.3	AF-T
19	1.5	CF-A	0.8	CF-A

CF-A—cohesive failure within the adhesive, AF-T—adhesion failure between adhesive and tile.

Table 2. The initial tensile adhesion strength and tensile adhesion strength after water immersion of CTA with the predominant mode of failure obtained by 19 laboratories in the twelfth ed. (2020–2021).

Participant Code	Initial Tensile Adhesion Strength		Tensile Adhesion Strength after Water Immersion	
	[N/mm^2]	Dominant Failure Pattern	[N/mm^2]	Dominant Failure Patten
1	1.5	CF-A	0.9	AF-T
2	1.4	50% CF-A/50% AF-T	0.5	5% CF-A/95% AF-T
3	1.6	CF-A	0.8	CF-A
4	1.7	CF-A	1.0	CF-A
5	1.9	CF-A	0.6	AF-T
6	2.0	CF-A	1.0	AF-T
7	1.9	CF-A	0.6	CF-A
8	1.3	CF-A	1.1	CF-A
9	1.6	CF-A	1.1	CF-A
10	1.6	CF-A	0.9	AF-T
11	1.3	AF-S	0.6	AF-T
12	1.5	AF-T	0.4	AF-T
13	1.8	CF-A	0.9	CF-A
14	2.4	AF-S	1.3	AF-T
15	1.9	CF-A	1.5	CF-A
16	1.9	50% CF-A/50% AF-T	0.6	20% CF-A/80% AF-T
17	2.7	CF-A	1.1	CF-A
18	2.0	CF-A	1.1	CF-A
19	2.0	CF-A	0.6	CF-A

CF-A—cohesive failure within the adhesive, AF-T—adhesion failure between adhesive and tile, AF-S—adhesion failure between adhesive and substrate.

It is worth adding that two other failure patterns not listed in Tables 1 and 2 are possible, namely, CF-S - cohesive failure in the substrate or CF-T - cohesive failure in the tile.

4. Discussion

4.1. ILC Results in the Light of ISO 13528 Guidelines

Table 3 shows the lowest and highest values of the initial tensile adhesion strength and tensile adhesion strength after water immersion of CTA reported by the laboratories participating in the ILC, out of 19 laboratories participating in both the eleventh and twelfth editions, 29 laboratories participating in the eleventh edition (2019–2020), and 27 laboratories participating in the twelfth edition (2020–2021).

Table 3. The lowest and highest values of the initial tensile adhesion strength and tensile adhesion strength after water immersion of CTA obtained by 19 laboratories and by all participating laboratories in the eleventh and twelfth editions.

ILC Edition	No. of Laboratories	Initial Tensile Adhesion Strength [N/mm^2]		Tensile Adhesion Strength after Water Immersion [N/mm^2]	
		Lowest Value	Highest Value	Lowest Value	Highest Value
The same laboratories participating in both ILC editions					
11th (2019–2020)	19	1.0	2.4	0.4	1.3
12th (2020–2021)	19 *	1.3	2.4	0.4	1.5
All participating laboratories					
11th (2019–2020)	29	0.3	2.6	0.4	1.9
12th (2020–2021)	27	1.3	2.7	0.4	2.0

* Eighteen laboratories reported results for the measurements of the tensile adhesion strength after water immersion.

The guidelines specified in ISO 13528 [48], including the recommendations on the interpretation of proficiency testing data, were applied to analyze the results obtained in the ILC. Table 4 shows the results of the calculations made following ISO 13258 [48].

Table 4. The value of statistical parameters calculated following ISO 13258 [48] for measurements of CTA initial tensile adhesion strength and tensile adhesion strength after water immersion during the eleventh and twelfth editions of the ILC.

Parameter	Initial Tensile Adhesion Strength		Tensile Adhesion Strength after Water Immersion	
	11th ed.	12th ed. *	11th ed.	12th ed.
x^* [N/mm^2]	1.7	1.8	0.8	0.9
s^* [N/mm^2]	0.3	0.3	0.2	0.3
x_{pt} [N/mm^2]	1.7	1.8	0.8	0.9
σ_{pt} [N/mm^2]	0.3	0.3	0.3	0.3
$u(x_{pt})$	0.1	0.1	0.1	0.1
V	18.9	18.6	33.5	36.2

x^*—robust average of the results reported by all participating laboratories; s^*—robust standard deviation of the results reported by all laboratories; x_{pt}—assigned value—consensus value; σ_{pt}—standard deviation for proficiency assessment; $u(x_{pt})$—standard uncertainty of the assigned value; V—coefficient of variation. * Eighteen laboratories reported results for the measurements of the tensile adhesion strength after water immersion.

The z-score values calculated following the Equation (2) for each laboratory for the initial tensile adhesion strength and tensile adhesion strength after water immersion measurements are presented in Figure 1 and Figure 2, respectively.
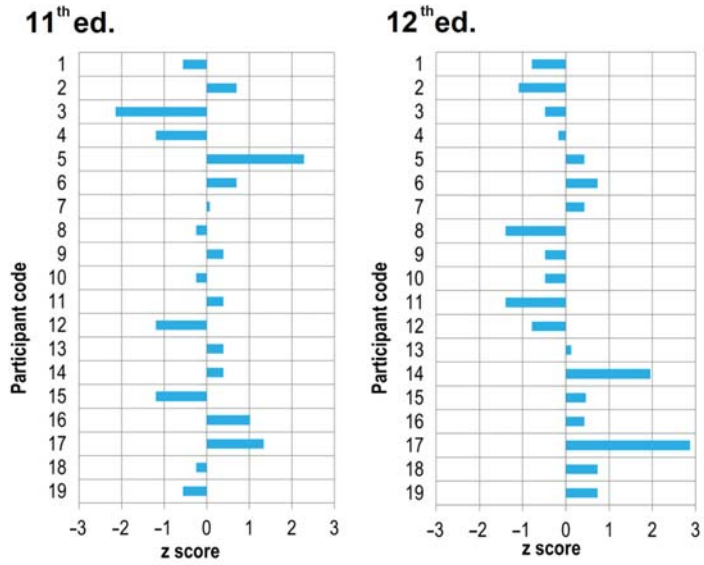
Figure 1. The z-score value for the initial tensile adhesion strength for each of 19 laboratories participating in the eleventh and twelfth editions of the ILC.
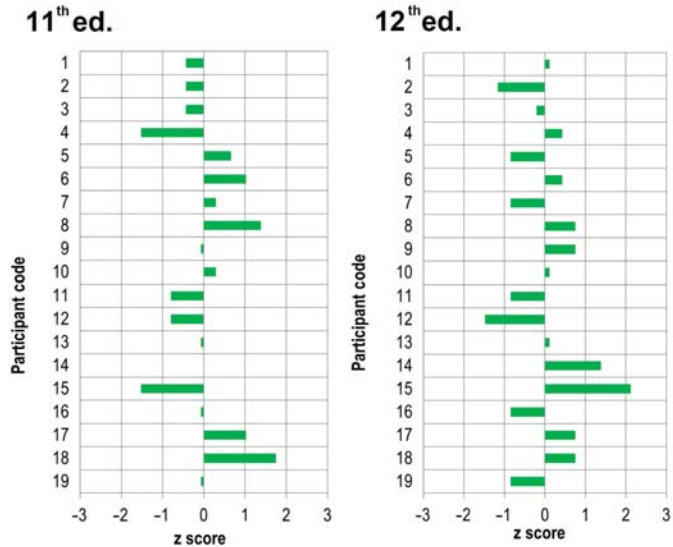
Figure 2. The z-score value for the measurement of tensile adhesion strength after water immersion for each of 19 laboratories participating in the eleventh and twelfth editions of the ILC.

The analysis of the z-score shows that in the eleventh ed., 2 out of 19 laboratories in the scope of the initial tensile adhesion strength measurement obtained results classified as "questionable" ($2 < |z| < 3$), and the remaining 17 laboratories obtained the "satisfactory" status ($|z| \leq 2$). A year later, in the twelfth ed. of the ILC, only 1 laboratory was labeled "questionable" based on the results obtained, while the remaining 18 laboratories were "satisfactory". In the case of the tensile adhesion strength after water immersion measurement in the eleventh ed. of the ILC, the results obtained by all laboratories allowed

them to receive the status of "satisfactory", and in the following twelfth ed. of the ILC, 1 of the 19 laboratories received the result referred to as "questionable". The z-score analysis also allows for the indication among of the 19 laboratories participating in both editions, those whose obtained measurement results are the closest assigned value (consensus value), namely laboratories marked with numbers: 1, 7, 9, 10, and 13 and in, further order, 19, 6, 16, and 18. When analyzing the obtained results, it is worth noting that among the results for which the z-score is |z| ≤ 2, these are the results classified as "satisfactory" from the perspective of the measurement laboratory and the analysis of ILC results under the requirements of ISO 13528 [48]. Another dimension of this result is from the product evaluation perspective. Although the z-score meets the condition of |z|≤ 2, for example, in the case of the initial tensile adhesion strength measurement in the eleventh ed., it means both 1.2 N/mm^2 or 1.3 N/mm^2 (participant code 4, 12, and 15), next to 2.0 N/mm^2 or 2.1 N/mm^2 (laboratories marked as 16 or 17). There is a significant difference between the value of 1.3 and 2.1, which may cause the product to be assessed as failing the acceptance criterion when it is not. The situation can become even more difficult for the product and its manufacturer when the product is reassessed by a market surveillance authority external to the manufacturer. The difficulty level may increase when market surveillance authorities apply the simple acceptance rule that does not consider the variability resulting from MU. Although the obtained results are classified as "satisfactory" in the ILC/PT evaluation categories, differences between the results are significant from the product evaluation perspective, and the product manufacturer cannot ignore this fact in their product evaluation. Producers after the so-called "safe side" must also consider the measurement variability in the value of the acceptance criterion. As shown by the results of ILC studies, this value is significant for CTAs tested under EN 12004 requirements. The analysis of the results of the predominant mode of failure showed more significant differentiation between laboratories. The obtained results are summarized in Table 5.

Table 5. The number of the predominant mode of failure for the initial tensile adhesion strength and tensile adhesion strength after water immersion measurements in the eleventh and twelfth ed. of the ILC.

Predominant Failure Pattern	Initial Adhesion		Adhesion after Water Immersion	
	11th ed.	12th ed. *	11th ed.	12th ed.
AF-S	0	2	0	0
AF-T	4	1	5	7
CF-A	13	14	11	10
Other	2	2	2	2
Total	19	19	18	19

* Eighteen laboratories reported results for the measurements of the tensile adhesion strength after water immersion in the eleventh edition (2019–2020).

Figure 3 shows a schematic summary of the results of the CTA studies in two subsequent editions of the ILCs. The data presented in Figure 3 combines the data previously included in Figures 1 and 2, plus Table 5. Figure 3 shows no correlation between the laboratory classification using the z-score and the observed failure pattern of tensile adhesion strength, regardless of whether the subject of the measurement was the initial or after immersion in water tensile adhesion strength. The lack of this correlation, and a different distribution of the observed mode of predominant failure, is an additional argument that the interpretation of the initial tensile adhesion strength and tensile adhesion strength after immersion in water results should be approached with caution.
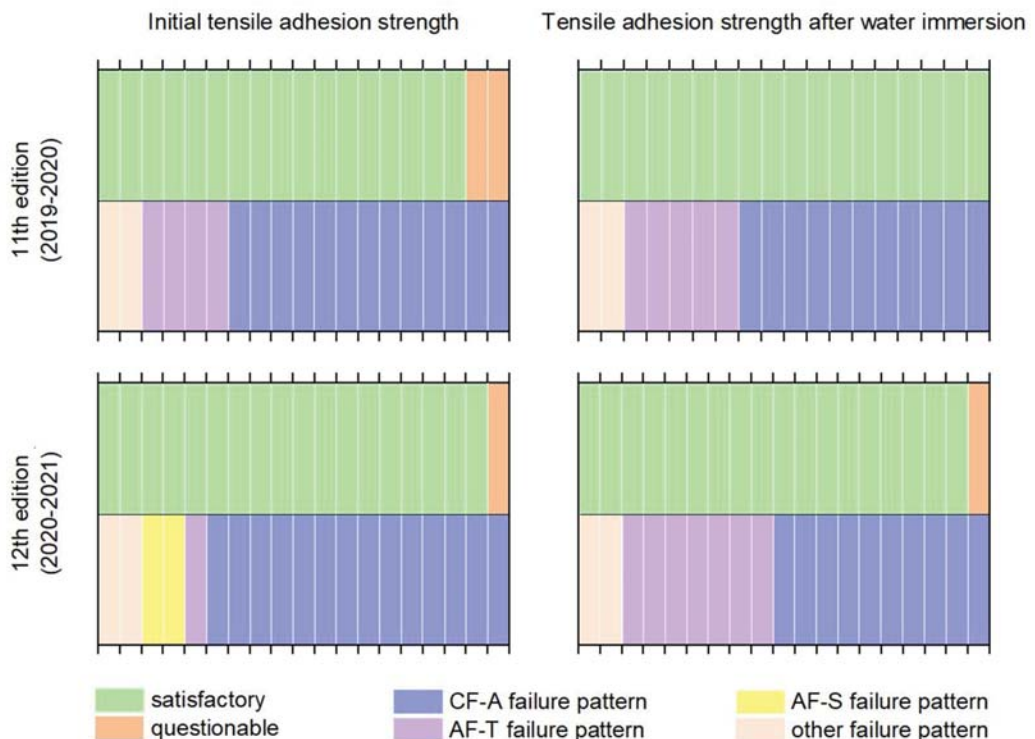
Figure 3. Summary of the results of the CTA measurements in two editions of the ILC.

One of the goals of the Romanian Ceprocim project was to show that constant partici-pation in the laboratory proficiency testing programs improves the quality of laboratories work. In this respect, the organizers of the study achieved the intended goal. Analyzing the results of both editions of the ILC/PT with the participation of the same 19 laboratories, it can be concluded that the differences between the individual editions are minor, but they do exist. It leads to the conclusion that laboratories maintain a constant level of the quality of the performed measurements. In addition, this is one dimension of the ILC/PT being conducted.

4.2. Factors Influencing the Measurement of Tensile Adhesion Strength

From a practical point of view (in risk analysis), the reproducibility of the results, i.e., the degree of agreement between the results obtained by different analysts in different laboratories using a given measurement procedure, is essential for the producers of CTAs. In this regard, while discussing the results of the PT described in this paper, one should also pay attention to several other aspects.

Felixberger [49] described the results of initial adhesion tests of 7 cementitious CTAs, performed in 10 laboratories using 2 different concrete slabs. As the first concrete slab, each of the laboratories participating in the study used a standard concrete slab meeting the requirements of EN 1323:2007 [50]. The second concrete slab was purchased by the research organizer and delivered to all participating laboratories. The standard deviation of the measurement described by Felixberger ranged from 15% to 20%, showing also the influence of concrete slab on the value of the determined adhesion. Felixberger found that for cementitious CTAs with a lower adhesion value, more significant differences between individual measurements exist than in the case of adhesives with higher adhesion.

Felixberger formulating the conclusions, stating that the priming of the concrete slab surface for testing would result in the uniformity of the slab surface in terms of its absorption properties. It also creates a situation closer to the actual use where manufacturers of cementitious CTAs recommend using a primer before laying ceramic tiles [49].

It is worth noting here that the subject of the analysis in this study was C2E classified CTA, i.e., with higher adhesion strength values. In the case of the research results analyzed in this article, the concrete slab effect was also present.

Another factor worth noting is the water used to season the samples. The EN 12004 standard does not contain any requirements in this respect. When testing the effect of seasoning water on the adhesion of CTAs, samples were stored in three types of water: in distilled water (pH = 7.09, specific conductivity = 0.040 mS/cm), in tap water (pH = 8.25, specific conductivity equal 0.805 mS/cm), and in softened water (pH = 8.63, specific conductivity equal 1.228 mS/cm) [51]. The tests showed that the origin and type of water used to season the samples significantly affects the adhesion of CTAs. Samples stored in distilled water represent a higher adhesion value than in the two other cases. The differences between the test results were so significant that they decided the fulfillment of the evaluation criteria.

The adhesion of CTAs is determined in the following system: concrete substrate (slab)—CTA—ceramic tile. Some properties of ceramic tiles approved for use during adhesion tests are specified in the standards referred to for a given test method in EN 12004. Niziurska assessed the influence of ceramic tiles' chemical composition and surface structure on the adhesion of CTAs to tiles [52]. The results obtained in the tests confirmed the impact of the quality of auxiliary materials (ceramic tiles) used in the tests on the compliance of CTAs with evaluation criteria.

It is also worth noting that the result of the adhesion measurement (regardless of whether the initial tensile adhesion strength or the tensile adhesion strength after water immersion) is the result of two other measures. It means the maximum load of the sample during the tensile strength measurement and the sample surface (adhesion surface). Therefore, the accuracy of the destructive force determination and the accuracy of the sample cross-sectional area determination influence the accuracy of the final result (adhesion).

Considering the obtained results and additional conditions related to the tensile adhesion strength of CTAs measurements described above, the manufacturer designing the product during the risk analysis determining the value of the acceptance criteria has to consider the simultaneous occurrence of all possible variations that may accompany the measurement.

5. Conclusions

The analysis of the CTAs adhesion results performed by 19 laboratories participating in 2 consecutive ILC/PT editions showed that the ILC/PT objective was achieved. Laboratories participating in two successive editions maintain a similar level of quality of performed measurements. In the case of the initial adhesion strength measurement in the eleventh edition of the ILC, 89.5% of laboratories obtained the result "satisfactory" under the ISO 13528 criteria. A year later, the result was slightly better—94.7% of laboratories received a satisfactory result. Regarding the measurement of tensile adhesion strength after water immersion, all 19 laboratories were classified as "satisfactory" in the eleventh edition. A year later, one of the laboratories obtained results classified as "questionable". The analysis of the results in the field of the predominant mode of failure showed more significant differences. The goal has been achieved from the perspective of the purpose of the ILC/PF. However, the results obtained from the perspective of the manufacturer whose product is being assessed by the supervisory authorities are not satisfactory. The differences between the results obtained between individual laboratories are significant.

The manufacturer of the product, knowing the acceptance criteria and being aware of the "imperfections" of the measurement method, must take all of that into account in their risk analysis. They must add to the value of the acceptance criterion all the possible

variations, including the MU resulting from the measurement method. In their risk analysis, they must assume a variant in which all potential volatilities coincide. The ILC/PT results analyzed in this study indicate that the measurement method, with its imperfections, is an integral part of the final value of the acceptance criterion. In a situation where, when assessing a product by market surveillance authorities, the simple acceptance rule is applied, which does not take into account the variability resulting from the MU, the risk analysis must additionally take this circumstance into account.

The obtained ILC/PT results, although they are satisfactory in terms of the requirements for this type when assessing the competence of measurement laboratories, indicate significant imperfections of the measurement method. At the same time, the obtained results signal to the product manufacturer that they must pay special attention when determining the constancy of performance of their product. Otherwise, it can happen that their product will not meet the acceptance criteria (threshold value).

The results obtained in ILC/PT also indicate that the authors of EN 12004 may analyze possible revision of the standard. In the light of the results described in this study, it seems that it would be reasonable to introduce the obligatory requirement to determine the measurement uncertainty by providing the tensile adhesion strength result in EN 12004. Moreover, the provision that due to the specificity of the tensile adhesion strength measurements, it seems inappropriate for the assessment of CTAs application of the simple acceptance rule.

Author Contributions: Conceptualization, C.S. and J.M.; methodology, C.S.; validation, C.S.; formal analysis, C.S. and J.M.; investigation, C.S. and J.M.; resources, C.S.; data curation, C.S.; writing—original draft preparation, J.M.; writing—review and editing, C.S. and J.M.; visualization, C.S. and J.M.; supervision, C.S. and J.M.; project administration, J.M. All authors have read and agreed to the published version of the manuscript.

Institutional Review Board Statement: Not applicable.

Informed Consent Statement: Not applicable.

Data Availability Statement: The data presented in this study are available upon request from the corresponding author.

Conflicts of Interest: The authors declare no conflict of interest.

References

1. Regulation (EU). No. 305/2011 of the European Parliament and of the Council. Available online: https://eur-lex.europa.eu/legal-content/EN/TXT/?uri=CELEX:32011R0305 (accessed on 16 October 2021).
2. Zio, E. The future of risk assessment. *Reliab. Eng. Syst. Saf.* **2018**, *177*, 176–190. [CrossRef]
3. Iqbal, S.; Choudhry, R.M.; Holschemacher, K.; Ali, A.; Tamošaitienė, J. Risk management in construction projects. *Technol. Econ. Dev. Econ.* **2015**, *21*, 65–78. [CrossRef]
4. Zavadskas, E.K.; Turskis, Z.; Tamošaitiene, J. Risk assessment of construction projects. *J. Civil. Eng. Manag.* **2010**, *16*, 33–46. [CrossRef]
5. Szymański, P. Risk management in construction projects. *Procedia Eng.* **2017**, *208*, 174–182. [CrossRef]
6. Hinrichs, W. The impact of measurement uncertainty on the producer's and user's risks, on classification and conformity assessment: An example based on tests on some construction products. *Accredit. Qual. Assur.* **2010**, *15*, 289–296. [CrossRef]
7. Szewczak, E. Ryzyko związane z niepewnością wyników badań i oceną zgodności wyrobów budowlanych. *Mater. Bud.* **2011**, *470*(10), 73–75.
8. Szewczak, E.; Piekarczuk, A. Performance evaluation of the construction products as a research challenge. Small error–big difference in assessment? *Bull. Polish Acad. Sci. Tech. Sci.* **2016**, *64*, 675–686. [CrossRef]
9. Szewczak, E.; Bondarzewski, A. Is the assessment of interlaboratory comparison results for a small number of tests and limited number of participants reliable and rational? *Accredit. Qual. Assur.* **2016**, *21*, 91–100. [CrossRef]
10. Nowicka, E.; Szewczak, E. Indoor Sound Pressure Level from Service Equipment in Buildings: Influence of Testing Methods on Measurement Results. *Arch. Acoust.* **2021**, *46*, 547–559.

11. Łukasik, M.; Michałowski, B.; Michalak, J. Assessment of the Constancy of Performance of Cementitious Adhesives for Ceramic Tiles: Analysis of the Test Results Commissioned by Polish Market Surveillance Authorities. *Appl. Sci.* **2020**, *10*, 6561. [CrossRef]
12. Kulesza, M.; Łukasik, M.; Michalowski, B.; Michalak, J. Risk related to the assessment and verification of the constancy of performance of construction products. Analysis of the results of the tests of cementitious adhesives for ceramic tiles commissioned by Polish construction supervision authorities in 2016–2020. *Cement Wapno Beton* **2020**, *25*, 444–456.
13. Rossi, G.B.; Crenna, F. A probabilistic approach to measurement-based decisions. *Measurement* **2006**, *39*, 101–119. [CrossRef]
14. Magnusson, B.; Näykki, T.; Hovind, H.; Krysell, M. *Handbook for Calculation of Measurement Uncertainty in Environmental Laboratories*; Nordic Innovation: Oslo, Norway, 2017. Available online: www.nordtest.info (accessed on 14 October 2021).
15. Theodorsson, E. Total error vs. measurement uncertainty: Revolution or evolution? *Clin. Chem. Lab. Med.* **2016**, *54*, 235–239.
16. Kallner, A. Is the combination of trueness and precision in one expression meaningful? On the use of total error and uncertainty in clinical chemistry. *Clin. Chem. Lab. Med.* **2016**, *54*, 1291–1297. [CrossRef]
17. Farrance, I.; Badrick, T.; Frenkel, R. Uncertainty in measurement and total error: Different roads to the same quality destination? *Clin. Chem. Lab. Med.* **2018**, *56*, 2010–2014. [CrossRef]
18. International Organization for Standardization (ISO). *ISO/IEC Guide 99:2007 International Vocabulary of Metrology—Basic and General Concepts and Associated Terms (VIM)*; International Organization for Standardization (ISO): Geneva, Switzerland, 2009.
19. International Organization of Legal Metrology (OIML). *G 1-106 Evaluation of measurement Data—The Role of Measurement Uncertainty in Conformity Assessment*; International Organization of Legal Metrology (OIML): Paris, France, 2017.
20. Szewczak, E.; Winkler-Skalna, A.; Czarnecki, L. Sustainable Test Methods for Construction Materials and Elements. *Materials* **2020**, *13*, 606. [CrossRef] [PubMed]
21. Kacker, R.N. Measurement uncertainty and its connection with true value in the GUM versus JCGM documents. *Measurement* **2018**, *127*, 525–532. [CrossRef]
22. Forbes, A.B. Measurement uncertainty and optimized conformance assessment. *Measurement* **2006**, *39*, 808–814. [CrossRef]
23. Williams, A. Principles of the EURACHEM/CITAC guide "Use of uncertainty information in compliance assessment". *Accredit. Qual. Assur.* **2008**, *13*, 633–638. [CrossRef]
24. Pendrill, L.R. Using measurement uncertainty in decision-making and conformity assessment. *Metrologia* **2014**, *51*, S206. [CrossRef]
25. Loftus, P.; Giudice, S. Relevance of methods and standards for the assessment of measurement system performance in a High-Value Manufacturing Industry. *Metrologia* **2014**, *51*, S219. [CrossRef]
26. Desimoni, E.; Brunetti, B. Uncertainty of measurement and conformity assessment: A review. *Anal. Bioanal. Chem.* **2011**, *400*, 1729–1741. [CrossRef]
27. Miller, W.G. The role of proficiency testing in achieving standardization and harmonization between laboratories. *Clin. Biochem.* **2009**, *42*, 232–235. [CrossRef] [PubMed]
28. Koch, M.; Magnusson, B. Use of characteristic functions derived from proficiency testing data to evaluate measurement uncertainties. *Accredit. Qual. Assur.* **2012**, *17*, 399–403. [CrossRef]
29. Côté, I.; Robouch, P.; Robouch, B.; Bisson, D.; Gamache, P.; LeBlanc, A.; Dumas, P.; Pedneault, M. Determination of the standard deviation for proficiency assessment from past participant's performances. *Accredit. Qual. Assur.* **2012**, *17*, 389–393. [CrossRef]
30. Coarna, M.; Guslicov, G.; Stancu, C.; Vlad, C. Interlaboratory test on adhesives for ceramic tiles in the last 5 years. In Proceedings of the 4th International Proficiency Testing Conference, Brasov, Romania, 18–20 September 2013; pp. 17–20.
31. De Medeiros Albano, F.; Ten Caten, C.S. Proficiency tests for laboratories: A systematic review. *Accredit. Qual. Assur.* **2014**, *19*, 245–257. [CrossRef]
32. De Medeiros Albano, F.; Ten Caten, C.S. Analysis of the relationships between proficiency testing, validation of methods and estimation of measurement uncertainty: A qualitative study with experts. *Accredit. Qual. Assur.* **2016**, *21*, 161–166. [CrossRef]
33. Huang, H. A new method for estimating consensus values in interlaboratory comparisons. *Metrologia* **2018**, *55*, 106. [CrossRef]
34. Stancu, C. The 10th edition of interlaboratory tests for adhesives for ceramic tiles—An anniversary edition. In Proceedings of the 7th International Proficiency Testing Conference, Oradea, Romania, 10–13 September 2019; p. 99.
35. Morales, C.; Giraldo, R. Reference versus consensus values in proficiency testing of clinical chemistry: A statistical comparison based on laboratories results in Colombia. *Accredit. Qual. Assur.* **2020**, *25*, 99–105. [CrossRef]
36. Kotyczka-Moranska, M.; Mastalerz, M.; Plis, A.; Sciazko, M. Inter-laboratory proficiency testing of the measurement of gypsum parameters with small numbers of participants. *Accredit. Qual. Assur.* **2020**, *25*, 373–381. [CrossRef]
37. Skrzypczak, I.; Leśniak, A.; Ochab, P.; Górka, M.; Kokoszka, W.; Sikora, A. Interlaboratory Comparative Tests in Ready-Mixed Concrete Quality Assessment. *Materials* **2021**, *14*, 3475. [CrossRef] [PubMed]
38. European Committee for Standardization (CEN). *EN 12004:2007+A1:2012 Adhesives for Tiles—Requirements, Evaluation of Conformity, Classification, and Designation*; European Committee for Standardization (CEN): Brussels, Belgium, 2012.
39. European Committee for Standardization (CEN). *EN ISO/IEC 17043:2010 Conformity Assessment—General Requirements for Proficiency Testing*; European Committee for Standardization (CEN): Brussels, Belgium, 2010.
40. Stancu, C. The importance of laboratories participation in interlaboratory comparison. Case study: Interlaboratory tests on adhesives for ceramic tiles. In Proceedings of the 13th Conferinţa de Ştiinţa şi Ingineria Materialelor Oxidice, Alba Julia, Romania, 1–3 October 2021.

41. European Committee for Standardization (CEN). *EN ISO/IEC 17025:2018-02 General Requirements for the Competence of Testing and Calibration Laboratories*; European Committee for Standardization (CEN): Brussels, Belgium, 2018.
42. Michalak, J. Ceramic Tile Adhesives from the Producer's Perspective: A Literature Review. *Ceramics* **2021**, *4*, 378–390. [CrossRef]
43. Baraldi, L. World production and consumption of ceramic tiles. *Ceram. World Rev.* **2021**, *31*, 26–41.
44. European Commission. *Summary of references of harmonised standards published in the Official Journal—Regulation (EU) No305/2011 of the European Parliament and of the Council of 9 March 2011 laying down harmonised conditions for the marketing of construction products and repealing Council Directive 89/106/EEC.*; European Commission (EU): Brussels, Belgium, 2019. Available online: https://ec.europa.eu/docsroom/documents/38863 (accessed on 23 October 2021).
45. European Committee for Standardization (CEN). *EN 12004-1:2017 Adhesives for Ceramic Tiles—Part 1: Requirements, Assessment and Verification of Constancy of Performance, Classification and Marking*; European Committee for Standardization (CEN): Brussels, Belgium, 2017.
46. International Organization for Standardization (ISO). *ISO 13007-1:2004 Ceramic Tiles—Grouts and Adhesive—Part. 1: Terms, Definitions and Specifications for Adhesives*; International Organization for Standardization (ISO): Geneva, Switzerland, 2004.
47. International Organization for Standardization (ISO). *ISO 13007-1:2014 Ceramic Tiles—Grouts and Adhesives—Part 1: Terms, Definitions and Specifications for Adhesives*; International Organization for Standardization (ISO): Geneva, Switzerland, 2014.
48. International Organization for Standardization (ISO). *ISO 13528:2015 Statistical Methods for use in Proficiency Testing by Interlaboratory Comparison*; International Organization for Standardization (ISO): Geneva, Switzerland, 2015.
49. Felixberger, J.K. *Polymer-Modified Thin-Bed Tile Adhesive*; Institut De Promocio Ceramica: Castelló, Spain, 2008.
50. European Committee for Standardization (CEN). *EN 1323:2007 Adhesives for Tiles—Concrete Slabs for Tests*; European Committee for Standardization (CEN): Brussels, Belgium, 2007.
51. Nosal, K.; Niziurska, M.; Wieczorek, M. Wpływ zanieczyszczeń zawartych w wodzie przeznaczonej do sezonowania zapraw klejowych do płytek na ich przyczepność. *Prace Inst. Ceram. Mater. Bud.* **2015**, *8*, 61–70.
52. Niziurska, M. Znaczenie właściwości płytek ceramicznych w zapewnieniu trwałości okładzin mocowanych zaprawami cementowymi. *Prace Inst. Ceram. Mater. Bud.* **2013**, *6*, 17–26.

Article

Mechanical Properties of Polyurethane Adhesive Bonds in a Mineral Wool-Based External Thermal Insulation Composite System for Timber Frame Buildings

Ewa Sudoł * and Ewelina Kozikowska

Construction Materials Engineering Department, Instytut Techniki Budowlanej, 00-611 Warszawa, Poland; e.kozikowska@itb.pl
* Correspondence: e.sudol@itb.pl; Tel.: +48-22-56-64-286

Abstract: This paper aims to provide a preliminary assessment of polyurethane adhesive applicability as an alternative to conventional cement-based adhesives used to fix thermal insulation materials to substrates concerning mineral wool-based external thermal insulation composite systems. Currently, polyurethane adhesives are only used in expanded polystyrene-based ETICS. This study discusses the suitability of polyurethane adhesive for ETICS with lamella mineral-wool for timber frame buildings. Bond strength, shear strength and shear modulus tests were conducted. In addition, microstructure and apparent density were analysed. Mechanical properties were analysed in terms of the influence of substrate type and thermal and moisture conditions, taking into account solutions typical for sheathing on timber frame (oriented strand boards (OSB), fibre-reinforced gypsum boards (FGB) and cement-bonded particleboards (CPB)), as well as limit conditions for adhesive application. It was found that PU adhesive can achieve adhesion, both to MW and OSB, and FGB and CPB at ≥80 kPa, which is considered satisfactory for PU adhesives for EPS-based ETICS. Favourable shear properties were also obtained. There was no significant effect of sheathing type on the properties considered, but the influence of temperature and relative humidity, in which the bonds were made, was spotted. The results obtained can be considered promising in further assessing the usefulness of PU adhesives for MW-based ETICS.

Keywords: external thermal insulation systems; mechanical properties of bonds; polyurethane adhesive; timber frame building; bond strength; shear properties

1. Introduction

External thermal insulation composite systems (ETICS) are among the most popular methods for improving the energy efficiency of buildings in Europe [1]. The first ETICS were installed in the 1960s in Germany and later in Switzerland and Austria [2]. The breakthrough for ETICS came in the early 1970s when, as a consequence of the oil crisis, energy prices rose, resulting in considerations concerning the need to minimise heat loss in buildings [3]. The growth dynamics of the insulation sector in Europe in the 1990s was boosted by the accession to the European Union of new countries, which, while meeting their obligations to comply with EU regulations, soon implemented energy efficiency policies. Currently, Central and Eastern Europe, with countries such as Poland, Germany, Austria, the Czech Republic, Slovakia, Lithuania, Latvia and Estonia, are the undisputed leaders in the ETICS sector. In this region, about 120–130 million m^2 of building walls are insulated annually. This is more than half of the forecasted European volume of about 215–230 million m^2. Turkey holds the dominant position concerning individual countries, and Poland, with 40 million m^2 per year, is in the second place [1,2].

ETICS includes the thermal insulation material fixed to the substrate and the top finishing layer made directly on site, without an air gap or intermediate layers. For many years, expanded polystyrene (EPS) and mineral wool (MW) have been the most commonly

used insulation materials in ETICS, followed by other factory-made thermal insulation products such as extruded polystyrene (XPS), polyurethane foam (PUR), phenolic foam (PF) and expanded cork (ICB) [1,4]. The ETICS finishing layer consists of a reinforcement layer made of a base coat with glass fibre mesh embedded and a finishing coat (renders). Some systems also contain key coating, primers and decorative coats [1,5,6].

ETICS is used as external thermal insulation to the walls of buildings. It can be used on new or existing (retrofit) vertical walls [5]. They can also be used on horizontal or inclined surfaces that are not exposed to precipitation. In Europe, most commonly on masonry walls constructed from units of clay, concrete, calcium silicate, autoclaved aerated concrete laid using mortar and concrete walls made of concrete are either cast on site or as prefabricated panels (Figure 1a) [2]. More and more frequently, ETICS is also being used to insulate walls in timber frame buildings [7]. Then, the thermal insulation material is fixed to the external wall sheathing (Figure 1b), which is usually made of oriented strand boards (OSB), fibre-reinforced gypsum boards (FGB) or cement-bonded particleboards (CPB), less often of fibre-reinforced cement boards or gypsum plasterboards [6–8].
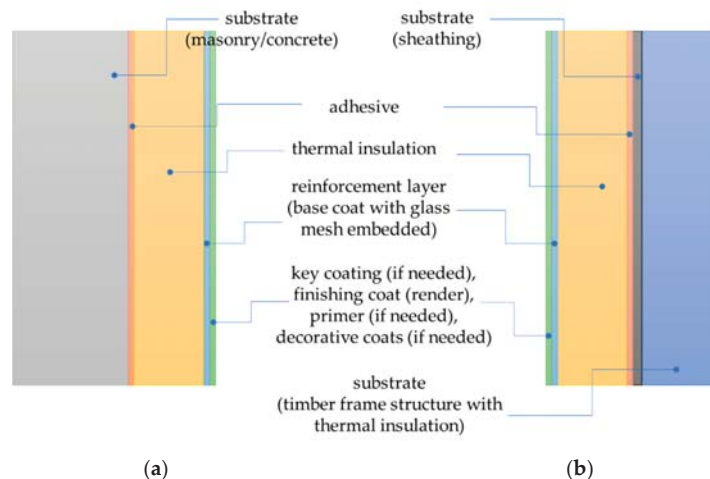
Figure 1. ETICS on (**a**) masonry or concrete wall, (**b**) on wood frame wall. Example of purely bonded ETICS.

Based on the method of fixing the thermal insulation material to the substrate, purely bonded ETICS, bonded ETICS with supplementary mechanical fixings, mechanically fixed ETICS with supplementary adhesive and purely mechanically fixed ETICS are distinguished [5,6]. Fixing the thermal insulation material to the substrate is typically carried out using cement-based adhesive. This applies both to ETICS for use on masonry or concrete walls and timber frame buildings. The exception is some EPS-based ETICS [5,6,9,10]. The construction industry is a dynamic field that constantly has new needs. Therefore, academics and manufacturers' continually seek to develop new materials and technologies that can be used as effective alternatives to conventional solutions [11]. As far as ETICS is concerned, attempts are being made to use polyurethane adhesives as an alternative to conventional cement-based adhesives for fixing thermal insulation materials other than EPS to substrates. This is in line with the trend observed for many years of wide, on site use of polyurethane foam in construction [12,13]. Apart from standard applications such as roof insulation [14] or window and door fitting [15], on-site foaming polyurethane adhesives are used to bond masonry elements in wall construction [16,17]. Polyurethane adhesives have numerous advantages, such as effective wetting of most substrates; interaction with substrates through polar interactions (hydrogen bonding); and relatively low molecular

weight/small molecular size, which allows them to permeate porous substrates and to form covalent bonds with substrates that have active hydrogen atoms [18]. They can be applied at low temperatures [12,13,19] and require no preparation activities on site. They are applied directly from a pressurised container to the material to be fixed. Foaming of polyurethane occurs spontaneously in contact with water present in the materials to be fixed. The foaming agent is carbon dioxide formed by the reaction of water with isocyanate groups [12,20].

As mentioned, polyurethane adhesives for fixing insulation material in ETICS are limited to EPS systems. This is due both to formal considerations and to the lack of a sufficient research basis. Placing ETICS on the market, like several other construction products, is regulated by the construction products regulation (CPR) [21], which establishes harmonised conditions for the marketing of construction products. The assessment of the suitability of use of ETICS is carried out through European or national technical assessment. It is subject to testing and assessing properties that affect the object's compliance with the basic requirements. Methods and criteria for assessing the essential characteristics of ETICS are fixed on masonry, and concrete walls are defined in EAD 040083-00-0404 [5] amended ETAG 004 [22] in October 2020. Concerning ETICS for use in timber frame buildings, EAD 040089-00-0404 applies [6]. Both of these documents consider using polyurethane adhesive in ETICS only for bonding EPS to the substrate. For such an application, the issue of testing methodology, taking into account the specifics of an on-site foaming polyurethane adhesive, has been systematised [5,23]. This makes it impossible to obtain, by means of a standard procedure, a European Technical Assessment (ETA) for an ETICS where polyurethane adhesive is used for fixing thermal insulation materials other than EPS and thus makes it challenging to place this system on the EU market.

Apart from expanded polystyrene, the second most common thermal insulation material used in ETICS is mineral wool. In Central Europe, the share of ETICS with EPS is about 84% and with MW about 12%, while in the rest of Europe, it ranges from 60 to 88% and from 9 to 25%, respectively [1,2]. Standard ETICS applications are rock wool in the form of factory-made boards as defined in EN 13162 [24], in which the fibres are either dispersed (standard boards) or oriented parallel to each other and perpendicular to the slab surface (lamella boards). Properties of MW boards used in ETICS are presented in Table 1.

For bonded systems and bonded systems with supplementary mechanical fixing, the adhesion of the individual ETICS layers, including the adhesive bonding to both the substrate and the insulation material, as well the shear properties of bonds are crucial in terms of fulfilment of the fourth basic requirement 'safety in use' [5,6,25,26]. Although several papers have been devoted to the properties of ETICS, looking at a wide spectrum of properties of individual components and their influence on the essential characteristics of the system [1,3,25,27–30], including adhesive bonding [31–34], the authors' attention has been directed towards cement-based adhesive systems. It has been found that bond strength between cement-based adhesive and the concrete, after 28 days under laboratory conditions, can achieve values from 250 kPa to 1000 kPa [31,33], while after 28 days under laboratory conditions and 2 days in water bond strength decreases to 80 kPa [5]. The bond strength between cement-based adhesive and the thermal insulation material strongly depends on the type of insulation material and the model of damage [31,32]. A review of the literature has shown that bond strength between cement-based adhesive and EPS ranges from 80 kPa to 270 kPa [31,33,34] and bond strength between cement-based adhesive and MW achieved values ranges from 30 kPa to 80 kPa [31,32]. Cohesive damage in the insulation material was usually observed [31–34]. The bond strength of polyurethane adhesives in EPS-based ETICS achieved at least 80 kPa [5,6,9,10]. In general, the physical and mechanical properties of polyurethane foam, including polyurethane adhesives, are closely related not only to the rigidity of the polymer matrix but also to the size of the cells and their structure [10,35–38]. Structures with larger cells are characterised by lower apparent density and lower mechanical properties [37,38]. An increase of the water content intensifies the foaming process, leading to an increased cell size [20,39,40].

In wide bonds, carbon dioxide has the ability to form larger bubbles, resulting in a more porous structure [13,35].

Table 1. Properties of mineral wool (MW) boards used in ETICS.

Symbol Present in Item Code	Property	Type of Boards	
		Lamella	Standard
-	Reaction-to-fire performance	Class A1 or A2	
-	Thermal resistance	value declared by the manufacturer according to EN 13162	
T5	Thickness tolerance	−1% or −1 mm[1] +3 mm	at least −3% or −3 mm[1] +5% or +5 mm[2]
DS(70, -)	Dimensional stability (48 h, T70 °C) thickness change $\Delta\varepsilon_d$ length and width change $\Delta\varepsilon_b$	≤1% ≤1%	
DS(70,90)	Dimensional stability (48 h, T70 °C) thickness change $\Delta\varepsilon_d$ length and width change $\Delta\varepsilon_b$	≤1% ≤1%	
WS	Water absorption after 24 h of partial immersion	≤1 kg/m^{2}	
WL(P)	Water absorption after 28 days of partial immersion	≤3 kg/m^{2}	
MU1	Water vapour diffusion resistance factor	1	
TR	Perpendicular tensile strength	≥80 kPa	≥7.5 kPa

This study aims to assess the applicability of polyurethane adhesive as an alternative to conventional cement-based adhesives for lamella mineral wool boards in ETICS for timber frame building. Bond strength, shear strength and shear modulus tests were conducted. In addition, SEM analysis of the adhesive structure in the bond, as well as apparent density, was performed. These properties were analysed in terms of the influence of substrate type and thermal and moisture conditions, taking into account solutions typical for sheathing on timber frame: oriented strand boards (OSB), fibre-reinforced gypsum boards (FGB) and cement-bonded particleboards (CPB), as well as limit conditions for adhesive application.

2. Materials and Methods

2.1. Adhesive

A single-component polyurethane adhesive, intended for ETICS, a standard for fixing EPS to masonry and concrete substrates, was used for the study. The adhesive was manufactured in industrial conditions as a commercial product. Polyether polyol was used. Organic amine catalyst served as a catalyser to promote blowing reaction. Silicone surfactants were used to stabilise the foam. Polymeric diphenylmethane diisocyanate (PMDI) was used to cure the foam. The components were placed in a standard pressurised container. As a chemical blowing agent, carbon dioxide was generated via the reaction of water included in the substrate, thermal insulation material and the environment with isocyanate groups. The adhesive was applied using a dedicated gun. When sprayed, the adhesive was in the form of a low-pressure foam. The foam adhesive working properties, determined according to [23], are shown in Table 2.

Table 2. Polyurethane adhesive working properties.

Property	Value
Minimum [1] limit temp. of application [2]	5 °C
Maximum [1] limit temp. of application [2]	25 °C
Recommended temp. of storage	>20 °C
Density (at free foaming, after curing)	18 ± 2 kg/m^{3}
Post-expansion	2 mm
Curing time	6 min
Cutting time	20 min

[1] Declared by the manufacturer, [2] temperature of the substrate, insulation material and environment.

2.2. Mineral Wool

Mineral wool lamella boards code MW-EN 13162-T5-DS(70,-)-DS(70,90)-CS(10\Y)40-TR80-WS-WL(P)-MU1, i.e., with perpendicular tensile strength ≥80 kPa, compression strength ≥40 kPa, and other properties described in Table 1, was used for sample preparation. The apparent density of MW was 73 ÷ 88 kg/m³, with an average of 82 kg/m³. The dimensions of the boards were 1000 mm × 500 mm × 50 mm. They had no coatings or facing in the form of fabric, veil, foil, etc., (Figure 2a), and 200 mm × 200 mm × 50 mm samples were cut from them.

| (**a**) | (**b**) | (**c**) |
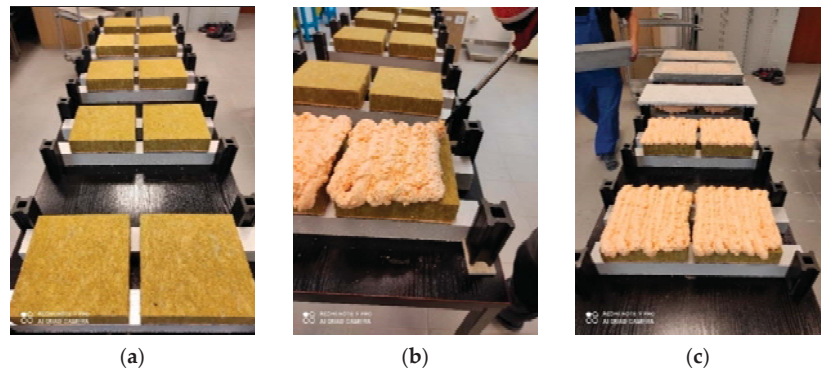
Figure 2. Preparation of samples for bond strength tests (**a**) MW prepared for adhesion, (**b**) application of adhesive to MW, and (**c**) bonding.

2.3. Substrates

The substrates used were boards designed for load-bearing elements that can be used in wet conditions, including wall sheathing for timber frame buildings. Substrates used:

- 18 mm thick oriented strand boards (OSB) with properties appropriate for OSB-3, according to EN 13986 [41];
- 12 mm thick fibre-reinforced gypsum boards (FGB) with properties appropriate for DEFH1IR, according to ETA-14/0312 [42];
- 16 mm thick cement-bonded particleboards (CPB) with properties appropriate for type 634-2, according to EN 13986 [41].

300 mm × 600 mm samples, with their thicknesses maintained, were cut from them.

What is more, 50 mm thick concrete slabs, made at a water to cement ratio of 0.45:0.48, perpendicular tensile strength ≥1.5 MPa and moisture content ≤3% of the total weight, complying with EAD 040083-00-0404 [5], were used as a reference substrate.

2.4. Scanning Electron Microscopy (SEM)

The morphology of the polyurethane bonds' cross-section surface was examined with a field-emission scanning electron microscope (SEM) Sigma 500 VP (Carl Zeiss Microscopy GmbH, Köln, Germany) that renders high-resolution images at low accelerating voltage. The samples were gold-coated before scanning to provide an electrically conductive surface. The accelerating voltage was 10 kV to avoid degradation of the sample. The observations were carried out at 100× magnification.

The study was carried out on a material with 8 mm thick bonds of OSB/23/50/8, OSB/25/30/8, OSB/5/-/8, OSB/25/90/8 and 15 mm OSB/23/50/15 (Table 3). The microstructures of polyurethane bonds were observed on samples cut out perpendicularly to the bonds surface. The samples were cut out with a scalpel at room temperature.

Table 3. Conditions of sample preparation for bond strength testing.

Designation of Test Series	Type of Substrate	Seasoning Conditions				Conditions of Adhesive Application		Conditions of Curing	
		Substrate		Adhesive					
		T, °C	RH, %	T, °C	RH, %	T, k °C	RH, %	T, °C	RH, %
8 mm thick bond									
OSB/23/50/8 OSB/25/30/8 OSB/25/90/8 OSB/5/-/8	OSB	23 ± 2 25 ± 2 25 ± 2 5 ± 2	50 ± 5 30 ± 5 90 ± 5 - [1]	23 ± 2	50 ± 5	23 ± 2 25 ± 2 25 ± 2 5 ± 2	50 ± 5 30 ± 5 90 ± 5 -	23 ± 2 25 ± 2 25 ± 2 5 ± 2	50 ± 5 30 ± 5 90 ± 5 -
FGB/23/50/8 FGB/25/30/8 FGB/25/90/8 FGB/5/-/8	FGB	23 ± 2 25 ± 2 25 ± 2 5 ± 2	50 ± 5 30 ± 5 90 ± 5 -	23 ± 2	50 ± 5	23 ± 2 25 ± 2 25 ± 2 5 ± 2	50 ± 5 30 ± 5 90 ± 5 -	23 ± 2 25 ± 2 25 ± 2 5 ± 2	50 ± 5 30 ± 5 90 ± 5 -
CPB/23/50/8 CPB/25/30/8 CPB/25/90/8 CPB/5/-/8	CPB	23 ± 2 25 ± 2 25 ± 2 5 ± 2	50 ± 5 30 ± 5 90 ± 5 -	23 ± 2	50 ± 5	23 ± 2 25 ± 2 25 ± 2 5 ± 2	50 ± 5 30 ± 5 90 ± 5 -	23 ± 2 25 ± 2 25 ± 2 5 ± 2	50 ± 5 30 ± 5 90 ± 5 -
C/23/50/8 C/25/30/8 C/25/90/8 C/5/-/8	Concrete	23 ± 2 25 ± 2 25 ± 2 5 ± 2	50 ± 5 30 ± 5 90 ± 5 -	23 ± 2	50 ± 5	23 ± 2 25 ± 2 25 ± 2 5 ± 2	50 ± 5 30 ± 5 90 ± 5 -	23 ± 2 25 ± 2 25 ± 2 5 ± 2	50 ± 5 30 ± 5 90 ± 5 -
15 mm thick bond									
OSB/23/50/15 FCB/23/50/15 CPB/23/50/15 C/23/50/15	OSB FCB CPB Concrete	23 ± 2	50 ± 5	23 ± 2	50 ± 5	23 ± 2	50 ± 5	23 ± 2	50 ± 5

[1] resulting (ca. 30 ± 5%).

2.5. Apparent Density

The test was carried out on cured polyurethane adhesive samples obtained from adhesive bonds made with the OSB described in point 2.3. Five series of 100 mm × 100 mm samples were prepared—in laboratory conditions (23 ± 2 °C, 50 ± 5%), at high temperature and low relative humidity (25 ± 2 °C, 30 ± 5%), at high temperature and high relative humidity (25 ± 2 °C, 90 ± 5%), and at low temperature (5 ± 2 °C) and the resulting RH. The OSB were stored for 24 h in the conditions determined for the adhesive application. The adhesive itself was stored for 24 h in laboratory conditions, which resulted from the manufacturer's recommendations on the storage conditions. The adhesive was applied to one of the boards in a serpentine pattern. At 180 ± 10 s, the boards were joined together to form sets with distance pieces and screw clamps in which the adhesive bond was 8 ± 1 mm thick or 15 ± 1 mm thick (only in laboratory conditions). The sets were cured for 48 h; 50 mm × 50 mm × 6 mm samples were cut out with a knife afterwards. The apparent density of the cured polyurethane adhesive was tested according to ISO 854:2006 [43]. The samples were weighed on analytical scales and measured with Vernier calliper. The apparent density of the polyurethane adhesive was calculated as an average mass/volume ratio.

2.6. Bond Strength

For bond strength tests, substrate in accordance with point 2.3 was used. Five series of samples were prepared, in different thermal and moisture conditions—in laboratory conditions (23 ± 2 °C, 50 ± 5%), at high temperature and low relative humidity (25 ± 2 °C, 30 ± 5%), at high temperature and high relative humidity (25 ± 2 °C, 90 ± 5%), and at low temperature (5 ± 2 °C) and the resulting RH (Table 3). The abovementioned adhesive application conditions were adopted based on the product manufacturer's guidelines on the permissible boundary conditions for its use, which fit the concept of ETICS-dedicated polyurethane adhesives tests [5,23].

Prior to sample preparation, OSB, FGB, CPB, and concrete and MW boards were stored for 24 h under conditions programmed for adhesive application. The adhesive itself

was stored for 24 h in laboratory conditions. The adhesive was applied to the mineral wool in the serpentine pattern (Figure 2b). The mineral wool was bonded to the substrate with an open time of 180 ± 10 s., creating 8 ± 1 mm thick bonds with the use of spacers. In laboratory conditions, series with 15 ± 1 mm thick bonds were also prepared. Samples were cured for 24 h under adhesive application conditions. To ensure that the bond thickness remained constant during curing, spacers were maintained, and a load of 15 kg was applied (Figure 2c). At the end of curing, the excess adhesive in the form of squeeze out was cut off, forming 200 mm $\times$ 200 mm $\times$ 8 mm or 200 mm $\times$ 200 mm $\times$ 15 mm adhesive bonds (Figure 3a).
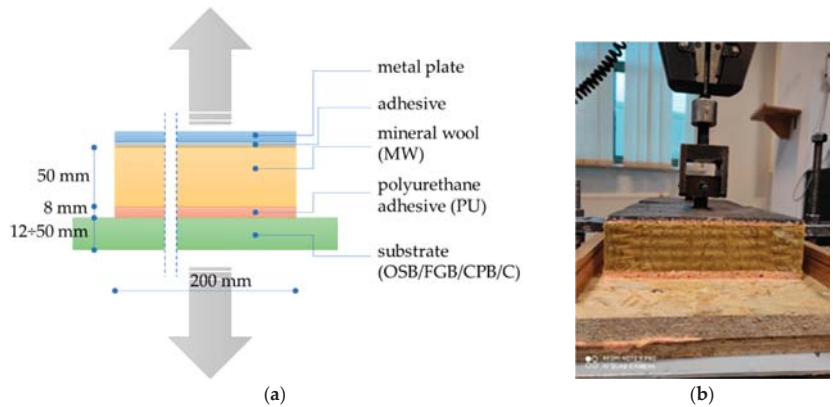
Figure 3. Bond strength test: (**a**) sample scheme, (**b**) sample from OSB/23/50/8 series under load in the testing machine.

Bond strength test involved determining the maximum tensile stress of an adhesive bond with a force acting perpendicular to its face. The method is often used in the testing of construction adhesives [44]. It was derived from TR46 [23]. Tests were conducted under laboratory conditions immediately after the samples were cured under specific conditions (Table 3). The test was carried out using a computer-controlled class 1 testing machine (Instron, Darmstadt, Germany), with a constant speed of 10 ± 1 mm/min. (Figure 3b). The samples were glued into 200 mm $\times$ 200 mm metal holders. The tension force values were recorded until damage. Bond strength σ_T was calculated according to (1) and expressed in kPa. In each series, ten samples were tested, and the total was 160 samples.

$$\sigma_T = \frac{F_{Tmax}}{A} \tag{1}$$

where: F_{Tmax}—maximum tensile force, in kN; A—bonded area, expressed in m^2.

2.7. Shear Strength and Shear Modulus

For shear strength and shear modulus test, OSB, FGB and CPB, as described in point 2.3, were used. 140 mm $\times$ 100 mm samples were cut from them. For each type of substrate, three series of samples were prepared—each under different thermal and moisture conditions (Table 4). The high temperature and low relative humidity (25 ± 2 °C, $30 \pm 5\%$) and high temperature and high relative humidity (25 ± 2 °C, $90 \pm 5\%$) were used, as well as a low temperature (5 ± 2 °C) at the resulting RH.

OSB, FGB and CPB boards were stored for 24 h under the conditions programmed for the adhesive application. The adhesive itself was stored for 24 h in laboratory conditions. The adhesive was applied to one of the plates, creating a serpentine pattern. At 180 ± 10 s, the boards were joined together to form sets with distance pieces and screw clamps in which the adhesive bond was 8 ± 1 mm thick. The samples were cured for 48 h, and then

the excess adhesive in the form of spouts was cut off with a knife, forming adhesive bonds with dimensions of 100 mm × 100 mm × 8 mm (Figure 4).

Table 4. Conditions for preparation of samples for shear strength and shear modulus test.

Designation of Test Series	Type of Substrate	Seasoning Conditions				Conditions of Adhesive Application		Conditions of Curing	
		Substrate		Adhesive					
		T, °C	RH, %	T, °C	RH, %	T, °C	RH, %	T, °C	RH, %
OSB/25/30	OSB	25 ± 2	30 ± 5	23 ± 2	50 ± 5	25 ± 2	30 ± 5	25 ± 2	30 ± 5
OSB/25/90		25 ± 2	90 ± 5			25 ± 2	90 ± 5	25 ± 2	90 ± 5
OSB/5/-		5 ± 2	-[1]			5 ± 2	-	5 ± 2	-
FGB/25/30	FGB	25 ± 2	30 ± 5	23 ± 2	50 ± 5	25 ± 2	30 ± 5	25 ± 2	30 ± 5
FGB/25/90		25 ± 2	90 ± 5			25 ± 2	90 ± 5	25 ± 2	90 ± 5
FGB/5/-		5 ± 2	-			5 ± 2	-	5 ± 2	-
CPB/25/30	CPB	25 ± 2	30 ± 5	23 ± 2	50 ± 5	25 ± 2	30 ± 5	25 ± 2	30 ± 5
CPB/25/90		25 ± 2	90 ± 5			25 ± 2	90 ± 5	25 ± 2	90 ± 5
CPB/5/-		5 ± 2	-			5 ± 2	-	5 ± 2	-

[1] resulting (ca. 30 ± 5%).
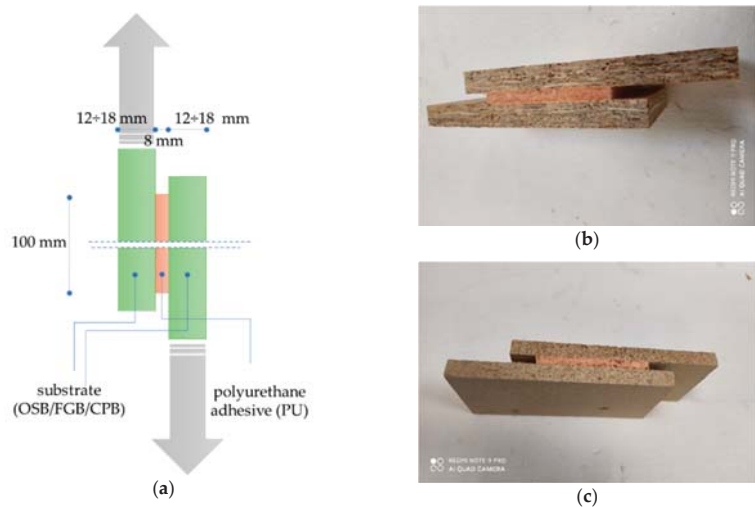
Figure 4. Samples for shear strength and shear modulus test: (**a**) sample scheme, (**b**) OSB/25/30 series sample and (**c**) CPB/25/30 series sample.

The shear strength test consisted of determining the maximum stresses with the force acting in the plane of the bond, using the test technique according to EN 12090 [45]. Tests were conducted under laboratory conditions immediately after the samples were cured under specific conditions (Table 4). The test was carried out using a computer-controlled class 1 testing machine (Instron, Darmstadt, Germany), with a constant speed of 3 ± 0.5 mm/min. The shear force value until damage and the force-displacement curve was recorded. In each series, ten samples were tested, and the total was 90 samples. Shear strength τ was calculated according to (2), expressed in kPa.

$$\tau = \frac{F_{\tau max}}{A} \tag{2}$$

where: $F_{\tau max}$—maximum shear force, in kN; A—a cross-section of the adhesive bond, in m^2.

Shear modulus G was calculated according to (3), expressed in kPa.

$$G = \frac{d \cdot tan\alpha}{A} \qquad (3)$$

where: d—adhesive bond thickness, in m; A—a cross-section of the adhesive bond, in m^2; and $tan\alpha$- tangent of the angle of inclination of the straight-line segment of the curve showing the force-displacement relation, in kN/m.

3. Results and Discussion

3.1. Scanning Electron Microscopy (SEM)

The microstructure is one of the most notable factors that may affect polyurethane adhesive foam properties [40]. The structure, especially cell size and type, depends on the process parameters such as temperature, humidity and viscosity of mixture during foaming [40,46,47]. In general, foam's physical and mechanical properties depend not only on the rigidity of the polymer matrix but are also related to the cellular structures [36,40]. The closed cells' size and shape are essential parameters of the foam's cellular structure, directly affecting the polyurethane foam's mechanical properties [36].

The microstructure of the polyurethane adhesive foam was analysed by SEM to determine the effect of simulated use conditions on its morphology. The SEM micrographs showed in Figure 5a,c,d revealed a homogeneous microstructure with a closed cell porosity well distributed within the polyurethane matrix. The adhesive structure in 8 mm thick bonds, at the adhesive application in laboratory conditions (Figure 5a), at high temperature and low humidity (Figure 5c) and at low temperature (Figure 5d) is characterised by relatively homogenous pore size. Single pore cells have regular tetraoval shape and comparable size in all three series. Although cells with a diameter lower than 300 μm prevail, individual cells with 500 μm diameter were observed as well. The adhesive cells applied at high temperature and high humidity were noticeably larger (Figure 5e,f). The predominant cells were about 450 μm and larger in diameter. The above can be attributed to the differences in the foaming conditions of polyurethane. An increase in the substrate's water content intensifies the foaming process, leading to increased cell size [20]. Deformed cell structures were also observed.

The microstructure of the 15 mm thick bond, developed in laboratory conditions (Figure 5b), was also observed. The increase in the bond thickness from 8 mm to 15 mm leads to a loss in the structure homogeneity. The images show a fraction of small pores surrounding individual large cells. Both the cell's size and shape are important for polyurethane foam's mechanical properties [40]. A non-homogeneous structure with inclusions of large pores may significantly decrease the mechanical properties.

3.2. Apparent Density

As it has been already determined in [40], the apparent density of polyurethane foam is among the key parameters, significantly affecting the product's physical and mechanical properties. The test results summarised in Figure 6 reveal that cured polyurethane adhesive in 8 mm and 15 mm thick bonds were characterised by apparent density from 19.3 kg/m^3 to 25.3 kg/m^3. In general, the polyurethane foam's apparent density depends on the cellular structure [35,37]. Structures with larger cells are characterised by lower apparent density [37,40], which is confirmed by the study results. The highest densities were obtained for the samples taken from 8 mm thick bonds developed in laboratory conditions, at high temperature and low relative humidity, as well at low temperature, amounting to 24.8 kg/m^3, 24.6 kg/m^3 and 25.3 kg/m^3, respectively. According to the description, the adhesive structure in the bonds developed in the abovementioned conditions was homogenous, the cells were uniform and well-defined, and their diameter was up to 300 μm (Figure 5a,c,d). The adhesive density in 15 mm thick bonds and in 8 mm thick bonds formed at high temperature and high relative humidity, for which a non-uniform structure and the presence of cells with ca. 350 μm diameter was observed (Figure 5b,e,f),

was lower and amounted to 19.3 kg/m^3 and 21.2 kg/m^3, respectively. As expected, the adhesive density in the bonds was higher than the density determined for a free-foamed product and amounted to 18 ± 2 kg/m^3 (Table 2). The cells in the freely applied products reach higher diameters than under limited product expansion conditions [13].
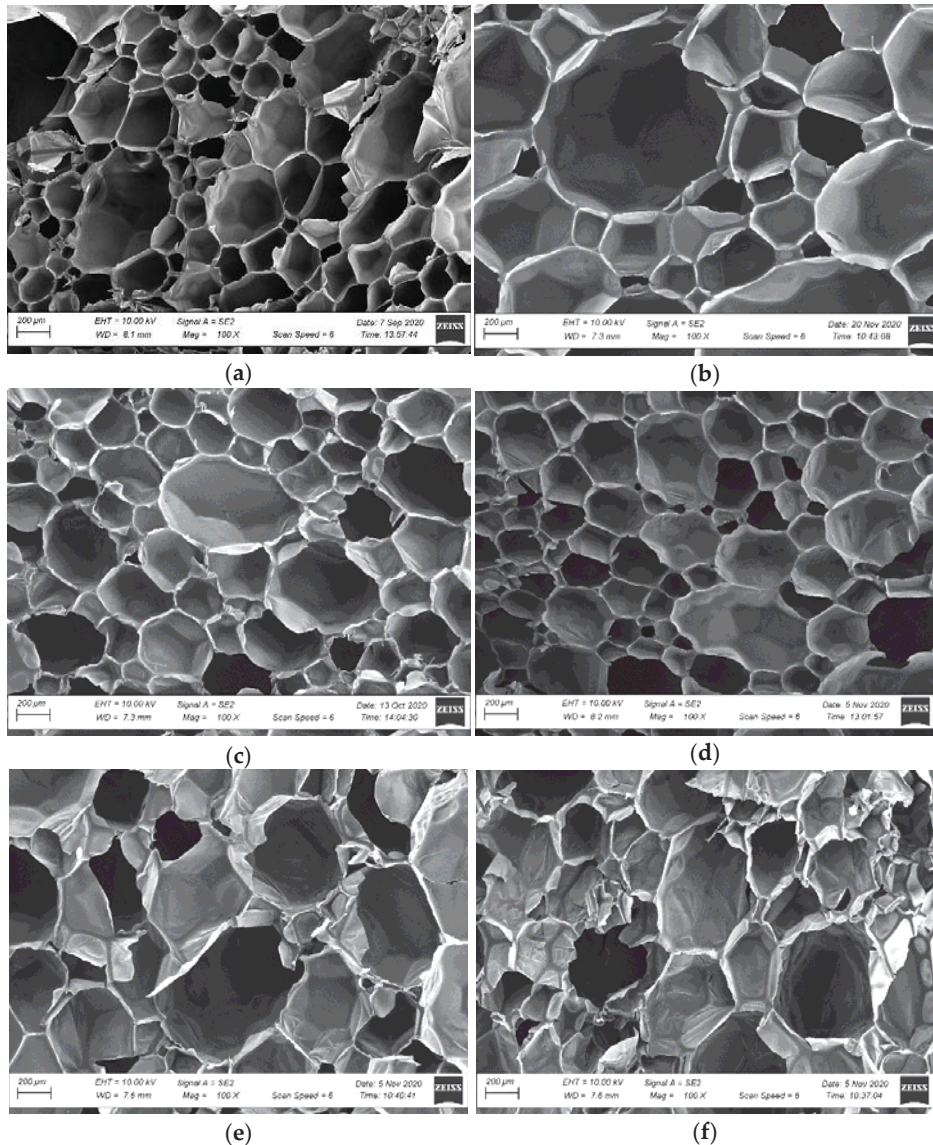
Figure 5. Microstructure of the cross-sectional surface of polyurethane adhesives in the bonds (magnification 100×) (**a**) OSB/23/50/8, (**b**) OSB/23/50/15, (**c**) OSB/25/30/8, (**d**) OSB/5/-/8, (**e**) OSB/25/90/8 and (**f**) OSB/25/90/8.
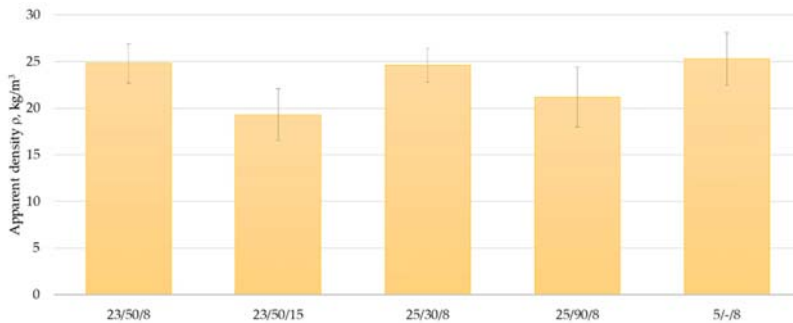
Figure 6. Apparent density of PU adhesive in bonds made under different thermal and moisture conditions. Error bars show standard deviation values.

A literature review revealed that the apparent density of polyurethane foam varies depending on the concentration of water as a blowing agent. The apparent density decreases with the increasing blowing agent content [20,39,40]. It was determined [40] that the polyurethane foam density decreased from 116 kg/m^3 to 42 kg/m^3 as the water content increased from 0.1 to 3.0 phr. The same observation was made during studies of closed-cell rigid polyurethane foams based on low functionality polyols [39]. A similar trend was observed in this study. The apparent density of the adhesive in the bonds made at low humidity (25 ± 2 °C, 30 ± 5%) was 15% higher than that for the adhesive in the bonds made at the same temperature but high humidity (25 ± 2 °C, 90 ± 5%).

3.3. Mechanical Properties

As mentioned, before their launch, construction products are verified for the building structure's meeting seven basic requirements, according to CPR [21]. In reference to ETICS, the bond strength, shear strength and shear modulus of the bond adhesive are among the essential requirements that determine the fulfilment of the fourth basic requirement, 'safety in use' [5,6,25].

Analysing the bond strength test results presented in Figure 7, it can be concluded that the bonds of the 8-mm-thick polyurethane adhesive for a system with MW and OSB, and FGB and CPB, had a bond strength similar to that of the reference concrete substrate used as a standard in tests of polyurethane adhesives for EPS-based ETICS. For bonds made under laboratory conditions, bond strength was from 85 to 100 kPa, at high temperature and low relative humidity from 83 to 93 kPa, at high temperature and high relative humidity from 85 to 93 kPa, and at low temperature from 81 to 89 kPa, while for systems with concrete substrate it was 89 kPa, 100 kPa, 87 kPa and 84 kPa, respectively. By analysing the minimum values of the bond strength (Figure 7, values in brackets), one might conclude that for 8 mm thick bonds made in laboratory conditions it ranges from 64 to 81 kPa, at high temperature and low relative humidity from 60 to 76 kPa, at high temperature and high relative humidity from 69 to 77 kPa, and at low temperature from 62 to 78 kPa, while for systems with a reference concrete substrate it is 72 kPa, 89 kPa, 77 kPa and 61 kPa, respectively.

As mentioned, the assessment of the suitability of use of ETICS is carried according to EAD 040083-00-0404 [5] and EAD 040089-00-0404 [6]. Comparison of bond strength values, obtained in our experiment, with the criterion specified at [5,6] for polyurethane adhesives in EPS-based ETICS, which is at least 80 kPa for the average value and at least 60 kPa for the minimum value, allows for a conclusion that the analysed solution is characterised by adhesion at the level higher than the mentioned threshold values. The above could be considered as an important indication for a more favourable assessment of the applicability of polyurethane adhesive as a component of a mineral wool-based ETICS. The obtained results are also in line with essential characteristic of polyurethane adhesives for EPS-based ETICS existing on the market [9,10]. To date, no more information in the

literature on the performance of polyurethane adhesives in ETICS has been presented. The researchers' attention has been directed towards cement-based adhesive systems. The results obtained show that polyurethane adhesives bond strength is significantly lower than bond strength between cement-based adhesive and the concrete [5,31,32]. As it has been already determined in [31], bond strength between cement-based adhesive and the concrete, after 28 days under laboratory conditions, can achieve values above 250 kPa. In other works, bond strength at the level to 1000 kPa was noted [33]. The difference may be explained by differences in structure and material nature of the polymer foams and cement-based products [13]. However, as regards bond strength between cement-based adhesive and the concrete after 28 days under laboratory conditions and 2 days in water, bond strength similar to bond strength of polyurethane adhesives [9,10] can be noted. The test of bond strength between cement-based adhesive and the thermal insulation material is performed separately [5,6]. As it has been already determined in [31,32], it depends strongly on the type of insulation material and the model of damage. For EPS systems, values in the range from 120 kPa to 270 kPa and cohesive rupture in the insulation material were achieved [31,33,34]. However, for MW system values in the range from 30 kPa to 80 kPa, cohesive damage in the insulation material was noted [5,9,10].
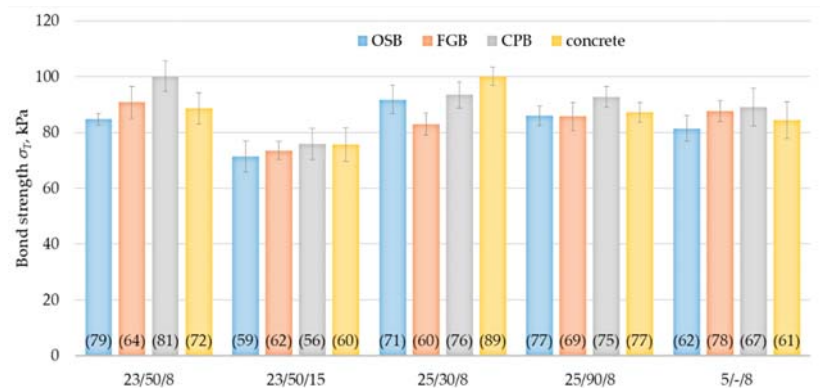
Figure 7. Bond strength results for PU adhesive bonds made under different thermal and moisture conditions. Error bars show standard deviation values. The minimum value for the series is given in brackets.

The effect of bond thickness was prominent in the tests conducted. For the 15 mm thick bonds, noticeably lower bond strength values were obtained than for the 8 mm thick bonds, as expected. The results were 71 kPa for OSB/23/50/15, 73 kPa for FBG/23/50/15, 76 kPa for CPB/23/50/15 and 76 kPa for the reference substrate C/23/50/15 (Figure 7). Therefore, when compared to the bond strength of bonds made under the same conditions but with a thickness of 8 mm, they were lower by 16%, 19%, 24% and 15%, respectively. These differences are due to differences in the adhesive cellular structure [35]. According to the experience of other researchers, in wider bonds carbon dioxide has the ability to form larger bubbles, resulting in a more porous structure [40]. The performed SEM analysis indicates cells less than 300 μm in diameter predominated in the 8 mm bond (Figure 5a). Cells of the adhesive in the 15 mm bond were noticeably larger. The predominant cells were about 450 μm and larger in diameter (Figure 5b) as a previous study showed more porous polyurethane foam may have a lower tensile strength [37]. By comparing the test results for 15 mm thick bonds with the criterion specified for PU adhesives in EPS-based ETICS of at least 80 kPa [5,6], it can be seen that significantly lower values were obtained. In this case, consideration should be given to limiting the use of the adhesive on substrates where no irregularities are necessitating the use of 15 mm thick bonds. Taking into account

that the deviation from the flatness of OSB, FBG and CPR is usually less than 5 mm [41,42], this condition does not pose a serious problem.

A correlation between the bond strength and the apparent adhesive density was noted. As has been already determined [40], higher apparent density of polyurethane foam resulted in higher mechanical properties. A similar effect was observed in this study. The highest bond strength was obtained for bonds developed in laboratory conditions at high temperature and low relative humidity, as well as at low temperature, whose densities were 24.8 kg/m^3, 24.6 kg/m^3 and 25.3 kg/m^3, respectively. No such regularity was observed for bonds developed at high temperature and high relative humidity.

Analysis of the cross-sections of the samples after testing clearly indicates the cohesive model of the damage. For the 8 mm thick adhesive bonds made under laboratory conditions, high temperature and low relative humidity, as well as low temperature, damage within the MW was predominant. In these series, the average proportion of damage within the MW was up to 80 to 95% (Figures 8a and 9a–c), 50 to 95% (Figure 8b) and 70 to 90% (Figure 8d), respectively. The above indicates that the bond strength exceeded the perpendicular tensile strength of the thermal insulation material itself. A similar effect was observed for MW-based ETICS with cement-based adhesive [32]. Cohesive damage was observed also for bonds made at high temperature and high relative humidity but with predominant damage within the polyurethane adhesive. The proportion of damage in MW ranged from 35 to 48% (Figure 8c). Cohesive damage within the polyurethane adhesive was also recorded for 15 mm thick adhesive bonds (Figure 10a). The proportion of MW damage ranged from 22% to 28%, which is noticeably lower than for the 8 mm thick bonds where it ranged from 80 to 95% (Figure 10b). Again, these differences can be explained by the differences in the cellular structure of adhesive. More porous polyurethane adhesive may obtain lower tensile strength [35,37,39].
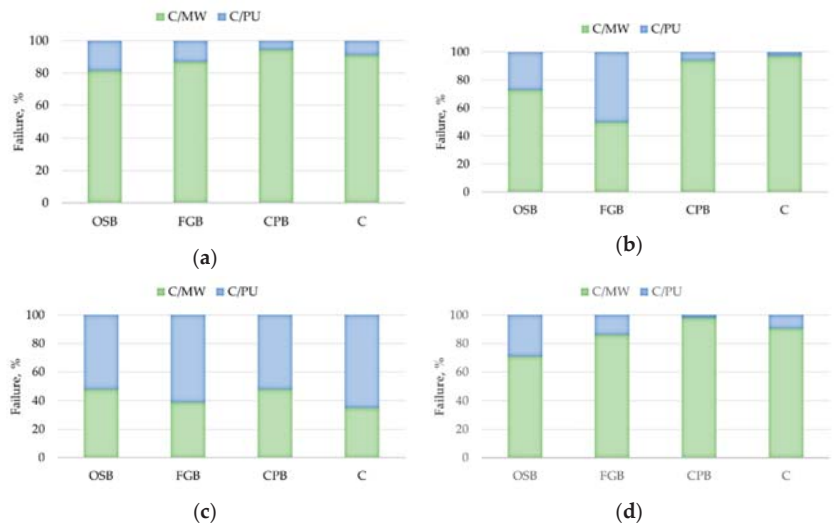
Figure 8. Model of damage—average values for the series: (**a**) 23/50/8, (**b**) 25/30/8, (**c**) 25/90/8 and (**d**) 5/-/8 (C/MW—cohesive damage within the MW, C/PU—cohesive damage within the PU adhesive).
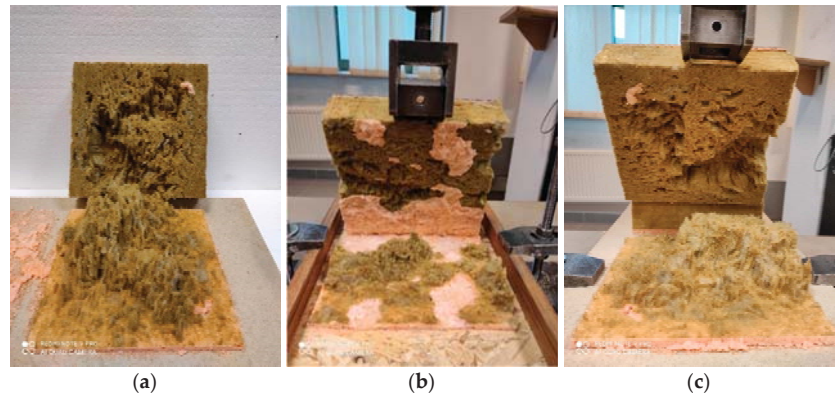
Figure 9. Illustration of the model of damage of 8 mm thick bonds (**a**) CPB/23/50/8 series sample—C/MW damage, (**b**) OSB/23/50/8 series sample—C/MW damage combined with C/PU damage and (**c**) CPB/23/50/8 series sample—C/MW damage (C/MW—cohesive within the MW, C/PU—cohesive within the PU adhesive).
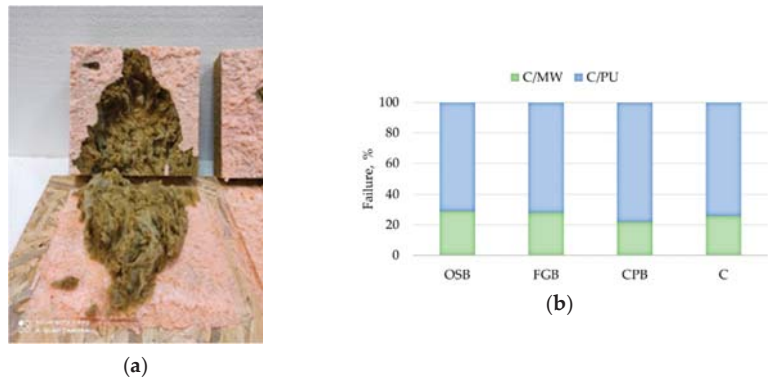
Figure 10. Illustration of the damage of 15 mm thick bonds (**a**) OSB/23/50/15 series sample, (**b**) average values for individual series (C/MW—cohesive damage of the MW, C/PU—cohesive damage of the PU adhesive).

There was no significant effect of sheathing type (OSB, GFB and CPB) on bond strength. The same observation was made during studies of cement-based adhesive [34]. In the series prepared under laboratory conditions, the highest value was for CPB/23/50/8—100 kPa and the lowest was for OSB/23/50/8—85 kPa; in the series prepared at high temperature and low relative humidity, the highest value was for CPB/25/30/8—93 kPa and the lowest for FGB/25/30/8—83 kPa; for series prepared at high temperature and high relative humidity, the highest value was for CPB/25/90/8—93 kPa and the lowest for FGB/25/90/8—85 kPa; and for series prepared at low temperature, the highest value was for CPB/5/-/8—89 kPa and the lowest for OSB/5/-/8—81 kPa. The above indicates that the performance evaluation process may consider limiting the number of test runs to one type of sheathing.

No effect of substrate type on the model of the damage was observed. The GFB/25/30 /8 series highlighted samples slightly in this respect, for which, as for the OSB/23/50/8 series, the proportion of damage within the polyurethane adhesive was recorded at 50%, while for samples on other substrates, it ranged from 5 to 25%. No such regularity was observed in the other test series.

Summarising the experimental data on bond strength obtained in this study, it can be stated that the tested polyurethane adhesive showed satisfactory adhesion to both mineral wool (MW) and boards typical for sheathing of walls of frame structure—oriented strand boards (OSB), fibre-reinforced gypsum boards (FGB) or cement-bonded particleboards (CPB). The cohesive property of the damage, predominantly within the thermal insulation material, indicates that the polyurethane adhesive bonds' bond strength may exceed the perpendicular tensile strength of the thermal insulation material itself. It should also be noted that mineral wool lamella, without coatings or facing, with a perpendicular tensile strength ≥80 kPa (TR80) was used in the tests. The factor determining the bond strength was, as expected, the thickness of the adhesive bond. Increasing the thickness from 8 mm to 15 mm resulted in a decrease of approximately 20% in bond strength. The effect of the thermal and moisture conditions under which the bonds were made and cured was also outlined. The lowest values of bond strength were recorded for the series prepared at low temperature, next at high temperature and high relative humidity, high temperature and low relative humidity, and the highest at laboratory conditions. In contrast, it should be noted that only in the series prepared at high temperature and high relative humidity the damage of the polyurethane adhesive predominated. In contrast, the damage of MW predominated in the other cases, so the decisive influence on the values obtained was the properties of the thermal insulation material. No effect of substrate type (OSB, FGB, CPB or concrete) on bond strength was observed.

Shear strength and shear modulus were analysed in terms of the influence of the type of substrate, taking into account the boards standard for the sheathing of timber frame walls and the adhesive thermal and humidity conditions bonds. The shear strength values are shown in Figure 11, and the shear modulus values are shown in Figure 12. The highest values of the considered properties were recorded for the samples prepared at high temperature and low relative humidity, obtaining shear strength of 55 kPa for OSB/25/30 series, 75 kPa for FGB/25/30 and 69 kPa for CPB/25/30 and shear modulus of 605 kPa, 920 kPa and 940 kPa, respectively. The bonds made at high temperature with high relative humidity showed significantly lower values concerning their properties, which may be dictated by the difference in the adhesive cell structure (Figure 5). Shear strength of 56 kPa for OSB/25/90 series, 52 kPa for FGB/25/90 series and 52 kPa for CPB/25/90 series was obtained, while for shear modulus, it was 455 kPa, 510 kPa and 590 kPa, respectively. The properties of bonds made at low temperature were of average values, except for the shear strength of the OSB/5/- bonds where a value of 71 kPa was recorded, while it was 57 kPa for FGB/5/and 47 kPa for CPB/5/-. Shear modulus was 610 kPa, 720 kPa and 660 kPa, respectively. All tested samples proved to be vulnerable to cohesive damage, in 100% within the adhesive bond, which confirms the high adhesion of polyurethane adhesive to all considered substrates—OSB, FGB and CPB—recorded bond strength tests. No significant effect of substrate type on the properties considered was observed.
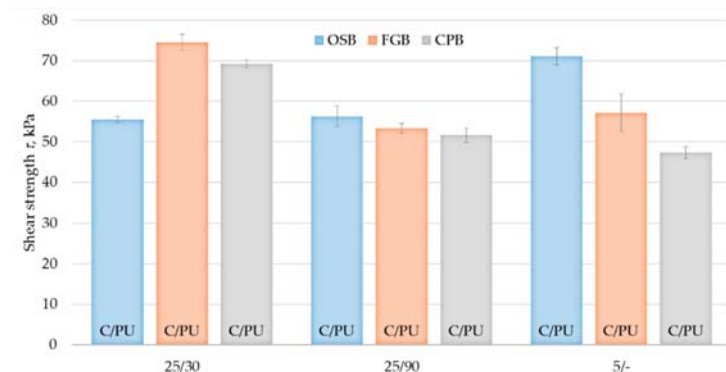
Figure 11. Shear strength tests results of bonds made under different thermal and moisture conditions. Error bars show standard deviation values. Data supplemented with a description of the damage: C/PU—damage of cohesion in PU adhesive.
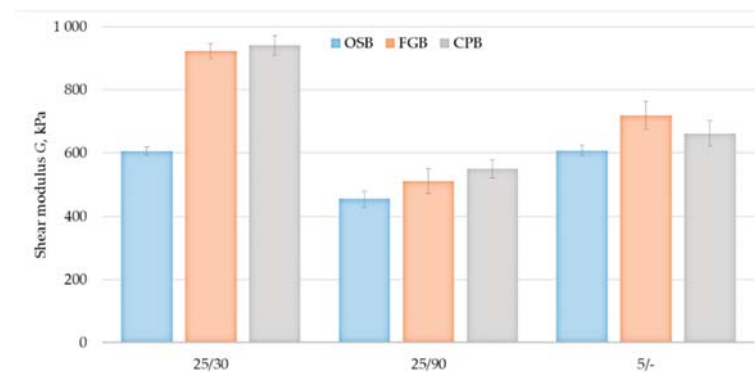
Figure 12. Shear modulus tests results of bonds made under different thermal and moisture conditions (error bars show standard deviation values).

The shear strength values obtained in this study were slightly lower than those approved for typical adhesives intended for use in EPS-based ETICS [9,10]. The shear modulus values were close to those indicated in [9] and significantly higher than those specified in [10]. It should also be noted that within the framework of the above-mentioned ETA procedures, the tests of bonds made under laboratory conditions on standard particleboards were carried out. Shear strength and shear modulus, according to both EAD 040083-00-0404 [5] and EAD 040089-00-0404 [6] guidelines, should be considered as a property of adhesive bond that can be used in the insulation design process.

4. Conclusions

The analysis of the experimental data obtained in this study proves that there are indications for an upbeat assessment of the applicability of polyurethane adhesive as a component of a mineral wool-based ETICS, intended for fixing thermal insulation material to the sheathing of walls with the timber frame structure.

It has been shown that polyurethane adhesive can achieve satisfactory adhesion to mineral wool lamella (TR80) without coatings and facing in the form of fabric, veil, film, etc. Bond strength of bonds made in thermal and moisture conditions limited for the considered application, with a bond thickness of 8 mm, achieved a satisfactory for ETICS value above 80 kPa.

It was also found that polyurethane adhesive has good adhesion to boards typical for timber frame wall sheathing—oriented strand boards (OSB), fibre-reinforced gypsum boards (FGB) or cement-bonded particleboards (CPB). No significant effect of board type on bond strength, shear strength and shear modulus was determined.

The methodology of testing the performance of polyurethane adhesives intended for fixing mineral wool boards requires the analysis of the specifics of the polyurethane applied on site and the thermal insulation material and the sheathing boards. The test shows that the introduction of appropriate modifications to standard procedures established for EPS-based ETICS makes it possible to obtain data indispensable for assessing the performance of adhesives intended for MW-based ETICS.

Taking into account the diversity of both polyurethane adhesives and mineral wool face finishes, the authors intend to continue work focused on the aspect of adhesion. Furthermore, verification of the performance of MW-based ETICS made with the use of polyurethane adhesive is planned on facade models, including all components of the system.

References

1. Michalak, J.; Czernik, S.; Marcinek, M.; Michałowski, B. Environmental burdens of External Thermal Insulation Systems. Expanded Polystyrene vs. Mineral Wool: Case Study from Poland. *Sustainability* **2020**, *12*, 4532. [CrossRef]
2. Pasker, R. The European ETICS market–Do ETICS sufficiently contribute to meet political objectives? In Proceedings of the 4th European ETICS Forum, Warsaw, Poland, 5 October 2017; European Association for External Thermal Insulation Composite Systems (EAE): Baden-Baden, Germany, 2017.
3. Czernik, S.; Marcinek, M.; Michałowski, B.; Piasecki, M.; Tomaszewska, J.; Michalak, J. Environmental Footprint of Cementitious Adhesives—Components of ETICS. *Sustainability* **2020**, *12*, 8998. [CrossRef]
4. Schiavoni, S.; D'Alessandro, F.; Bianchi, F.; Asdrubali, F. Insulation materials for the building sector: A review and comparative analysis. *Renew. Sustain. Energy Rev.* **2016**, *62*, 988–1011. [CrossRef]
5. European Organization for Technical Assessment (EOTA). *EAD 040083-00-0404 European Assessment Document External Thermal Insulation Composite Systems (ETICS) with Renderings*; European Organization for Technical Assessment (EOTA): Brussels, Belgium, 2020.
6. European Organization for Technical Assessment (EOTA). *EAD 040089-00-0404 European Assessment ETICS with Renderings for the Use on Timber Frame Buildings*; European Organization for Technical Assessment (EOTA): Brussels, Belgium, 2017.
7. Pasztory, Z.; Peralta, P.N.; Molnar, S.; Peszlen, I. Modelling the hydrothermal performance of selected North American and comparable European wood-frame house walls. *Energy Build.* **2012**, *49*, 142–147. [CrossRef]
8. Kvande, T.; Bakken, N.; Bergheim, E.; Thue, J. Durability of ETICS with Rendering in Norway—Experimental and Field Investigations. *Buildings* **2018**, *8*, 93. [CrossRef]
9. Institute of Ceramics and Buildings Materials (ICiMB). *European Technical Assessment ETA 17/0204*; Institute of Ceramics and Buildings Materials (ICiMB): Warsaw, Poland, 2017.
10. Technical and Test Institute for Construction (TZUS). *European Technical Assessment ETA 16/0384*; Technical and Test Institute for Construction (TZUS): Prague, Czech Republic, 2016.

11. Frigione, M.; Aguiar, J.L.B.d. Innovative Materials for Construction. *Materials* **2020**, *13*, 5448. [CrossRef] [PubMed]
12. Gama, N.; Ferreira, A.; Barros-Timmons, A. Polyurethane Foams: Past, Present, and Future. *Materials* **2018**, *11*, 1841. [CrossRef] [PubMed]
13. Somarathna, H.M.C.C.; Raman, S.N.; Mohotti, D.; Mutalib, A.A.; Badri, K.H. The use of polyurethane for structural and infrastructural engineering applications: A state-of-the-art review. *Constr. Build. Mater.* **2018**, *190*, 995–1014. [CrossRef]
14. Kalamees, T.; Põldaru, M.; Ilomets, S.; Klõšeiko, P.; Kallavus, U.; Rosenberg, M.; Õiger, K. Failure analysis of a spray polyurethane foam roofing system. *J. Build. Eng.* **2020**, *32*, 101752. [CrossRef]
15. Hallik, J.; Gustavson, H.; Kalamees, T. Air Leakage of Joints Filled with Polyurethane Foam. *Buildings* **2019**, *9*, 172. [CrossRef]
16. Dzhamuev, B.K. Increasing the Solidity of Masonry Walls Made of Cellular Concrete Blocks of Autoclave Hardening by using Polyurethane Foam Adhesive Composition as a Masonry Solution. *J. Phys. Conf. Ser.* **2020**, *1655*, 012085. [CrossRef]
17. Graubohm, M. Investigations on the Gluing of Masonry Units with Polyurethane Adhesive Investigations on the gluing of masonry units with polyurethane adhesive. In Proceedings of the 8th International Masonry Conference, Dresden, Germany, 4–7 July 2010.
18. Gama, N.; Ferreira, A.; Barros-Timmons, A. Cure and performance of castor oil polyurethane adhesive. *Int. J. Adhes. Adhes.* **2019**, *95*, 102413. [CrossRef]
19. Zamorowska, R.; Sieczkowski, J. *Złożone systemy ocieplania ścian zewnętrznych budynków (ETICS) z zastosowaniem styropianu lub wełny mineralnej i wypraw tynkarskich. Warunki Techniczne Wykonania i Odbioru Robót Budowlanych*, 8th ed.; Instytut Techniki Budowlanej (ITB): Warsaw, Poland, 2019.
20. Golling, F.E.; Pires, R.; Hecking, A.; Weikard, J.; Richter, F.; Danielmeier, K.; Dijkstra, D. Polyurethanes for coatings and adhesives—Chemistry and applications. *Polym. Int.* **2019**, *68*, 848–855. [CrossRef]
21. Regulation (EU) No 305/2011 of the European Parliament and of the Council. Available online: https://eur-lex.europa.eu/legal-content/EN/TXT/?uri=uriserv:OJ.L_.2011.088.01.0005.01.ENG&toc=OJ:L:2011:088:TOC (accessed on 15 January 2021).
22. European Organization for Technical Assessment (EOTA). *ETAG 004: Guideline for European Technical Approval of External Thermal Insulation Composite Systems (ETICS)*; European Organization for Technical Assessment (EOTA): Brussels, Belgium, 2013.
23. European Organization for Technical Assessment (EOTA). *TR 46 Test Methods for Foam Adhesives for External Thermal Insulation Composite Systems (ETICS)*; European Organization for Technical Assessment (EOTA): Brussels, Belgium, 2014.
24. European Committee for Standardization (CEN). *EN 13162:2015 Thermal Insulation Products for Buildings. Factory Made Mineral Wool (MW) Products. Specification*; European Committee for Standardization (CEN): Brussels, Belgium, 2015.
25. Sulakatko, V.; Vogdt, F. Construction Process Technical Impact Factors on Degradation of the External Thermal Insulation Composite System. *Sustainability* **2018**, *10*, 3900. [CrossRef]
26. Tavares, J.; Silva, A.; de Brito, J. Computational models applied to the service life prediction of External Thermal Insulation Composite Systems (ETICS). *J. Build. Eng.* **2020**, *27*, 100944. [CrossRef]
27. Varela Luján, S.; Viñas Arrebola, C.; Rodríguez Sánchez, A.; Aguilera Benito, P.; González Cortina, M. Experimental comparative study of the thermal performance of the façade of a building refurbished using ETICS, and quantification of improvements. *Sustain. Cities Soc.* **2019**, *51*, 101713. [CrossRef]
28. Uygunoğlu, T.; Özgüven, S.; Çalış, M. Effect of plaster thickness on performance of external thermal insulation cladding systems (ETICS) in buildings. *Constr. Build. Mater.* **2016**, *122*, 496–504. [CrossRef]
29. Santoni, A.; Bonfiglio, P.; Davy, J.L.; Fausti, P.; Pompoli, F.; Pagnoncelli, L. Sound transmission loss of ETICS cladding systems considering the structure-borne transmission via the mechanical fixings: Numerical prediction model and experimental evaluation. *Appl. Acoust.* **2017**, *122*, 88–97. [CrossRef]
30. Michałowski, B.; Marcinek, M.; Tomaszewska, J.; Czernik, S.; Piasecki, M.; Geryło, R.; Michalak, J. Influence of Rendering Type on the Environmental Characteristics of Expanded Polystyrene-Based External Thermal Insulation Composite System. *Buildings* **2020**, *10*, 47. [CrossRef]
31. Malanho, S.; do Rosário Veiga, M. Bond strength between layers of ETICS–Influence of the characteristics of mortars and insulation materials. *J. Build. Eng.* **2020**, *28*, 101021. [CrossRef]
32. Liisma, E.; Raado, L.-M.; Lumi, S.; Lilli, I.; Sulkatko, V. The Effect of Moisture Content of Insulation Boards on the Adhesion Strength of ETICS. *Recent Adv. Civ. Eng. Mech.* **2001**, *66*, 103–108.
33. Ramos, N.M.M.; Simões, M.L.; Delgado, J.M.P.Q.; De Freitas, V.P. Reliability of the pull-off test for in situ evaluation of adhesion strength. *Constr. Build. Mater.* **2012**, *31*, 86–93. [CrossRef]
34. Niziurska, M.; Dróżdż, W. Insulation of walls in the frame technology–legislation and technology. *Izolacje* **2017**, *22*, 72–74.
35. Strobech, C. Polyurethane adhesives. *Constr. Build. Mater.* **1990**, *4*, 215–217. [CrossRef]
36. Kurańska, M.; Barczewski, R.; Barczewski, M.; Prociak, A.; Polaczek, K. Thermal Insulation and Sound Absorption Properties of Open-Cell Polyurethane Foams Modified with Bio-Polyol Based on Used Cooking Oil. *Materials* **2020**, *13*, 5673. [CrossRef] [PubMed]
37. Andersons, J.; Kirpluks, M.; Cabulis, U. Reinforcement Efficiency of Cellulose Microfibers for the Tensile Stiffness and Strength of Rigid Low-Density Polyurethane Foams. *Materials* **2020**, *13*, 2725. [CrossRef] [PubMed]
38. De Luca Bossa, F.; Santillo, C.; Verdolotti, L.; Campaner, P.; Minigher, A.; Boggioni, L.; Losio, S.; Coccia, F.; Iannace, S.; Lama, G.C. Greener Nanocomposite Polyurethane Foam Based on Sustainable Polyol and Natural Fillers: Investigation of Chemico-Physical and Mechanical Properties. *Materials* **2020**, *13*, 211. [CrossRef]

39. Kairytė, A.; Kremensas, A.; Balčiūnas, G.; Członka, S.; Strąkowska, A. Closed Cell Rigid Polyurethane Foams Based on Low Functionality Polyols: Research of Dimensional Stability and Standardised Performance Properties. *Materials* **2020**, *13*, 1438. [CrossRef]
40. Thirumal, M.; Khastgir, D.; Singha, N.K.; Manjunath, B.S.; Naik, Y.P. Effect of foam density on the properties of water blown rigid polyurethane foam. *Appl. Polym.* **2008**, *3*, 108. [CrossRef]
41. European Committee for Standardization (CEN). *EN 13986:2015 Wood-Based Panels for Use in Construction. Characteristics, Evaluation of Conformity and Marking*; European Committee for Standardization (CEN): Brussels, Belgium, 2015.
42. Austrian Institute of Construction Engineering (OIB). *ETA-14/0312*; Austrian Institute of Construction Engineering (OIB): Vienna, Austria, 2015.
43. International Organization for Standardization (ISO). *ISO 854:2019*; International Organization for Standardization ISO: Geneva, Switzerland, 2019.
44. Szewczak, E.; Winkler-Skalna, A.; Czarnecki, L. Sustainable Test Methods for Construction Materials and Elements. *Materials* **2020**, *13*, 606. [CrossRef]
45. European Committee for Standardization (CEN). *EN 12090:2013 Thermal Insulating Products for Building Applications—Determination of Shear Behaviour*; European Committee for Standardization (CEN): Brussels, Belgium, 2013.
46. Zawadzak, E.; Bil1, M.; Ryszkowska, J.; Nazhat, S.N.; Cho, J.; Bretcanu, O.; Roether, J.A.; Boccaccini, A.R. Polyurethane foams electrophoretically coated with carbon nanotubes for tissue engineering scaffolds. *Biomed. Mater.* **2008**, *4*, 1. [CrossRef] [PubMed]
47. Sałasińska, K.; Leszczyńska, M.; Celiński, M.; Kozikowski, P.; Kowiorski, K.; Lupińska, L. Burning Behaviour of Rigid Polyurethane Foams with Histidine and Modified Graphene Oxide. *Materials* **2021**, *14*, 1184. [CrossRef] [PubMed]

Artificial Weathering Resistance Test Methods for Building Performance Assessment of Profiles Made of Natural Fibre-Reinforced Polymer Composites

Ewa Sudoł [1,*], Ewelina Kozikowska [1] and Ewa Szewczak [2]

[1] Construction Materials Engineering Department, Instytut Techniki Budowlanej, 00-611 Warsaw, Poland; e.kozikowska@itb.pl

[2] Group of Testing Laboratories, Instytut Techniki Budowlanej, 00-611 Warsaw, Poland; e.szewczak@itb.pl

* Correspondence: e.sudol@itb.pl; Tel.: +48-22-56-64-286

Abstract: A growing popularity of profiles made of natural fibre-reinforced polymer composites in civil engineering encourages determining test methods relevant for building performance assessment. Weathering resistance is among the key aspects that condition the durability of building structures. The paper includes a comparative analysis of two artificial weathering resistance test methods. Polyvinyl chloride and wood flour composite profiles were tested. They were subjected to UV and spraying (X-exposure) and UV, spraying and wetting by condensation (F-exposure), both at different exposure times. The influence of the applied weathering procedures on the composite's microstructure and its mechanical characteristics were analysed. No changes in the microstructure of brittle fractures were observed. However, surface morphology changes were revealed, noticeably greater following X-exposure than F-exposure. F-exposure exerted significant influence on the mechanical properties of brushed profile, including, but not limited to, flexural modulus. Whereas X-exposure exerted more influence on the mechanical properties of non-brushed profile.

1. Introduction

Natural fibre-reinforced polymer composites (NFPC) have been used in many industry branches for a number of years. Nowadays, it is hard to imagine the medical, automotive, aerospace and shipyard sectors and civil engineering without them [1–4]. NFPC, as well as carbon nanotubes-reinforced polymer composites rapidly growing [5].

Natural fibres nearly completely replaced synthetic fibres in polymer composites [6]. Nowadays, NFPCs include mainly lignocellulosic fibres obtained from different tree, grass and crop species. Their biodegradability, source renewability, low density at high strength and elasticity, and low cost and neutrality for humans and tools have been appreciated [7]. The fibres are obtained from hard and soft tissues (Figure 1)—wood, stalks, seeds, leaves, fruit, phloem, husks and shells being waste from agricultural production [2,7].

The most popular NFPC matrices include polypropylene (PP), high-density polyethylene (HDPE), polyvinyl chloride (PVC), and sometimes polystyrene (PS) [7–9]. Matrix selection depends on the composite's intended use [4]. Some matrices are made of biodegradable polymers, e.g., polyglycolic acid (PGA) and polyhydroxyalkanoates (PHA) [9].

Civil engineering applications are dominated by NFPC with PVC or HDPE matrix [4,6]. They are used in solid (Figure 2a) or cellular (Figure 2b) profiles intended for outdoor floors—on terraces and swimming pools (Figure 3) and ventilated façade cladding [10–12]. NFPC profiles are also employed in platforms, passages, landscape architecture and wet rooms [3–6].

Figure 1. Types of plant fibres used in NFPC.
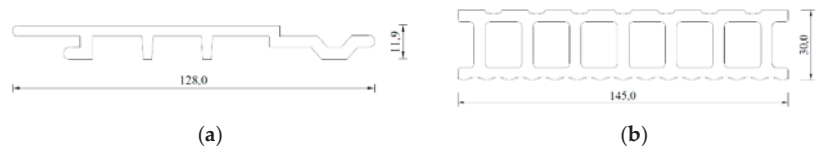
Figure 2. Sample NFPC building profiles for (**a**) facades, (**b**) floors. The dimensions are given in mm.
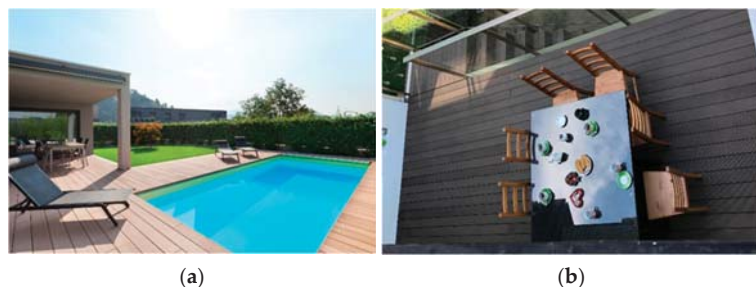
Figure 3. Sample application of NFPC profiles in civil engineering for outdoor floors: (**a**) at a swimming pool, (**b**) on the terrace.

The fitness of NFPC profiles for civil engineering applications, similarly to other construction materials, should be assessed according to the sustainable development concept, based on the usability criterion, by determining a collection of key features for the particular application [13]. The assessment is carried out from the angle of the product's influence on a building structure's fulfilling the seven essential requirements [14], according to the regulation of the European Parliament and the Council (EU) No. 305/2011 (CPR) [15]. The seventh essential requirement concerning the Sustainable use of natural resources states that building structures need to be designed and made so that natural resources are used sustainably and ensure the durability of building structures. Fulfilling the building structure's durability criterion depends on the construction products' resistance to operating factors, including the environmental ones [16,17]. The aspect of resistance to environmental conditions has special significance for outdoor products, such as terrace floors and façade cladding, which are directly exposed to long-term sun radiation, water impact, temperature changes and microbiological factors [12,18]. So far the weathering resistance test methods

for building performance assessment of profiles made of natural fibre-reinforced polymer composites have not been standardized.

Ensuring efficient interaction between lignocellulosic fibres and the polymer matrix is among the key challenges for natural fibre-reinforced polymer composites to achieve proper resistance to environmental factors [4,9]. The hydrophilic nature of the fibres makes them swell in an aqueous environment, which results in cracks formed in the hydrophobic polymer matrix [18]. As a result, the interaction between lignocellulosic fibres and the polymer deteriorates. Insufficient adhesion at the phase border leads to decreased mechanical parameters [9,19]. Hence, the fibres' surface is modified to improve the interphase interaction by increasing the fibres' wettability and reducing water absorption [4,9]. The most popular chemical methods involve employing substances whose particles react with cellulose hydroxy groups and introduce new groups linked with the polymer matrix's functional groups [20]. Similar treatments are used in the case of carbon nanotube reinforcement [21]. The number, shape, size and distribution of the fibres also affects the NFPC characteristics [4,7,8]. Proper scattering of fibres in the matrix promotes interphase adhesion by reducing voids and ensuring the fibres' surrounding by the matrix [2,4,21].

NFPC products are susceptible to sunlight [18,22]. Their exposure to UV light was discovered to contribute to a more significant decrease in the mechanical properties than exposure to microorganisms and high temperatures [23–28]. Tests on NFPC products' resistance to sunlight are typically carried out with accelerated methods, using laboratory light sources [27–36]. The application of accelerated methods involving product exposure to the relatively short but intensive impact of a factor or a set of service factors is standard for construction fitness assessment procedures. The impacts are selected according to the product's material characteristics, including the product's application scope, to simulate best the processes that occur during the product's use in real conditions [17]. As shown by previous studies, light and water impact cycles are the most burdensome exposure sequence in NFPC's accelerated weathering [32–38]. NFPC degradation progresses then much faster and more intensively than in the case of exposure to sunlight only [30]. In the wetting phase, the polymer matrix particles damaged as a result of UV impact are washed out, and successive ones are exposed [22], but hydrophilic lignocellulosic fibres swell too, which leads to reduced interphase adhesion, as was mentioned before [18,19]. As was already determined [34], the light exposure and spraying cycles cause much more intensive destruction of profiles whose surfaces were mechanically treated before than surfaces non-treated after extrusion. Composites with a higher share of lignocellulosic fibres on the surface, exposed during planing, show a higher drop in the flexural modulus [31,34]. NFPC was discovered to degrade faster than the polymer used as a matrix. At the initial weathering exposure stage, a pure polymer may be subjected to further cross-linking, while this property is physically limited in a composite by the filler [35]. The exposure time matters as well. The longer it is, the greater degradation occurs [34–36]. Light exposure reduces the mechanical properties and changes the NFPC products' colour [30,37].

Analysing previous studies on artificial weathering resistance of NFPC products addressed for civil engineering, it can be observed that different light sources are used in the exposure procedures, with diversified exposure sequence, including the dry and wet phase length and wetting method [34–37,39,40]. This paper contains a comparative analysis of the two most common methods used for construction products to determine the most relevant building performance assessment for natural fibre-reinforced polymer composite profiles. So far the comparative analysis of artificial weathering resistance test methods has not been performed. Tests were carried out for PVC and wood flour composite profiles as one of the most popular in civil engineering [10,11,26]. The influence was analysed of the applied exposure procedure on the changes in the composite microstructure and mechanical properties. A comparative exposure was performed, including the following:

- exposure to light emitted by xenon lamps (X-exposure) combined with alternate short spraying, with diversified exposure time,

- wetting through long-term condensation and then exposure to light emitted by fluorescent lamps (F-exposure), with diversified exposure time.

The influence was evaluated of the performed exposures on the usable surface's morphology and microstructure of brittle fractures, flexural strength, flexural modulus and impact strength.

2. Materials and Methods

2.1. Profiles

Commercial cellular profiles intended for outdoor floors were used for the tests. The profiles were made of PVC matrix composite with fine lignocellulosic fibre filler (wood flour) and plastifiers and modifiers as additives. The filler was recycled wood industry waste. The composite's formula is the manufacturer's trade secret and has not been revealed. The profiles were extruded in a plastic processing facility.

The profiles were 180 mm wide, 25 mm high, the front walls were 5 mm thick, and the chambers were 22 mm wide. The profiles had two usable surfaces: one grooved and one plane (Figure 4). As a standard, grooved and plane surfaces of construction profiles are mechanically treated (brushing) to provide a wood-like texture effect. Profiles with a standard usable brushed surface (SZ) and profiles with a non-brushed usable surface (NSZ)—for comparison—were used in the study.
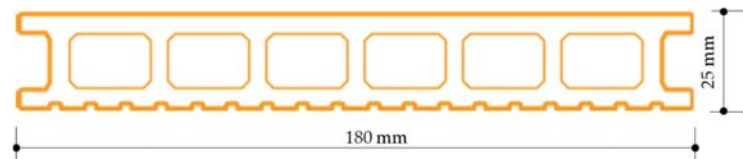
Figure 4. Shape of the profiles used in the tests.

2.2. Weathering Exposure

The first weathering procedure (F-exposure) was carried out in UV Test apparatus (Atlas, Linsengericht, Germany) featured with 1A type (UVA-340) fluorescent lamps according to EN 16474-3 [41], emitting light in the wavelength range of 300 to 400 nm, with the maximum emission at 343 nm (Table 1). The exposure procedure complied with EN 927-6 [42]. The samples were exposed to cycles composed of a long condensation phase, followed by exposure to UV lamps, with the radiation intensity of 0.89 W/m^2 measured at 340 nm wavelength, with alternated wetting cycles (water spraying) (Table 2).

Samples cut out from flat usable surfaces of brushed (SZ), and non-brushed (NSZ) profiles were exposed. The samples were 300 mm long, and the profiles' full width (180 mm) was maintained. During the exposure, the samples were arranged at ca. 80° angle, allowing free draining of water (Figure 5a). The exposure lasted 336 h—SZ-F-336 and NSZ-F-336 series, and 2016 h—SZ-F-2016 and NSZ-F-2016 series (Table 2).

The other weathering procedure (X-exposure) was performed in SunTest apparatus (Atlas, Linsengericht, Germany) featuring a xenon-arc lamp with a quartz shell, according to EN 1647-2 [43], which emits light from less than 270 nm in the ultraviolet range through visible spectrum up to IR, whereby a daylight filter was used, eliminating shortwave UV radiation (Table 3). Exposure was carried out according to EN ISO 4892-2 method A [44]. The cycles included exposure to light with the radiation intensity of 60 W/m^2, measured in the band wavelength of 300–400 nm, combined with exposure to high temperature, and followed by water spraying (Table 2).
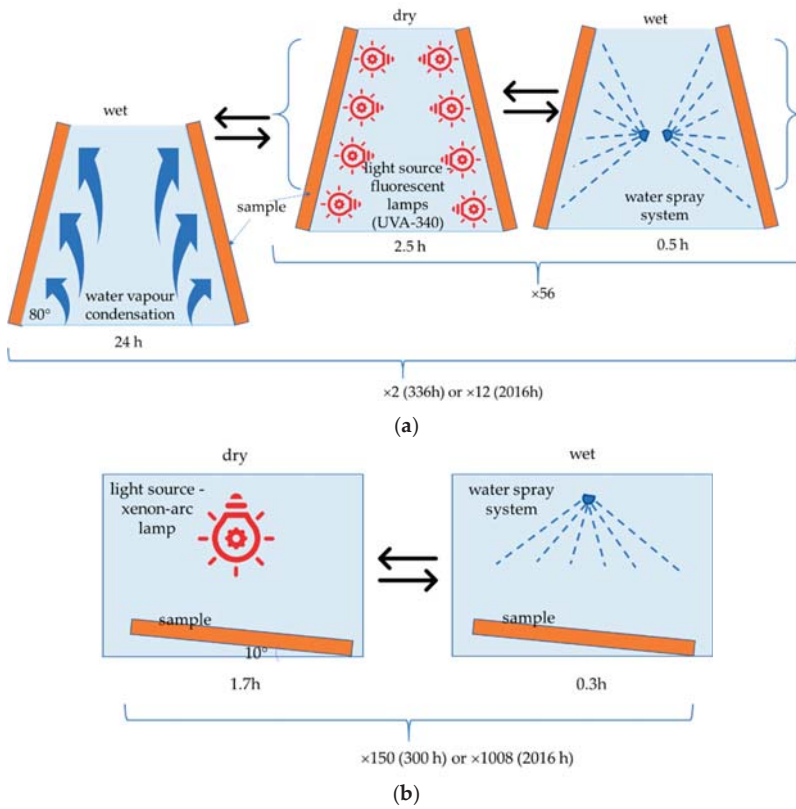
Figure 5. Weathering exposure procedure flowchart: (**a**) F-exposure, (**b**) X-exposure.

Table 1. Relative spectral intensity of radiation for UVA 340 fluorescent lamps [39] used in the UV test apparatus.

Spectral Pass Band	Minimum	CIE No. 85:1989, Table 4	Maximum
(λ = Wavelength in nm)	%	%	%
$\lambda < 290$	-	-	0.1
$290 \leq \lambda \leq 320$	5.9	5.4	9.3
$320 < \lambda \leq 360$	60.9	38.2	65.5
$360 < \lambda \leq 400$	26.5	56.4	32.8

Table 2. Weathering exposure.

Test Series Designation	Total Exposure Time	Exposure Method/Light Source	Number of Cycles	Exposure during the Cycle
SZ-F-336 NSZ-F-336	336 h	F-exposure according to EN 927-6/ UVA340 fluorescent lamps	2	• 24 h of wetting through condensation at T45 ± 3 °C • 168 h of alternate light exposure and water spraying cycles, in the following sequence:
SZ-F-2016 NSZ-F-2016	2016 h		12	− 2.5 h of exposure to UVA−340 lamps, radiation intensity: 0.89 W/m² (340 nm), BST 60 ± 3 °C, − 0.5 h water spraying without UV exposure, spraying intensity 6–7 L/min.
SZ-X-300 NSZ-X-300	300 h	X-exposure according to EN ISO 4892-2/ xenon-arc lamp with daylight filter	150	• 1.7 h of irradiation with lamps, radiation intensity: 60 ± 2 W/m² (300–400 nm), BST 65 ± 3 °C, CHT 38 ± 3 °C, RH 50 ± 10%,
SZ-X-2016 NSZ-X-2016	2016 h		1008	• 0.3 h of water spraying without UV exposure

Table 3. Relative spectral intensity of radiation for a xenon-arc lamp with daylight filter [43] used in SunTest apparatus.

Spectral Pass Band	Minimum	CIE No. 85:1989, Table 4	Maximum
(λ = Wavelength in nm)	%	%	%
λ < 290	-	-	0.15
290 ≤ λ ≤ 320	2.6	5.4	7.9
320 < λ ≤ 360	28.2	38.2	39.8
360 < λ ≤ 400	54.2	56.4	67.5

Table 4. Relative differences between the values of the mechanical properties of SZ and NSZ samples, calculated according to Formula (6), %. Statistically insignificant differences are highlighted in grey.

σ_f—Flexural Strength	E_f—Modulus of Elasticity	a_{cU}—Charpy Impact Strength
10.2	0.1	9.6

A brushed (SZ) and non-brushed (NSZ) flat usable surfaces were exposed. The samples' length ranged from 100 to 300 mm, and their width and thickness corresponded to the profile's dimensions. During the exposure, the samples were arranged horizontally, maintaining a ca. 10° slope to allow free draining of water (Figure 5b). The exposure lasted 300 h for the SZ-X-300 and NSZ-X-300 series and 2016 h for the SZ-X-2016 and NSZ-X-2016 series (Table 2).

Deionised water with pH 5.0 ± 7.5 and electric conductivity under 2 μS/cm measured at 25 °C were used for wetting in both weathering procedures.

2.3. SEM Analysis

The microstructure of composite profiles was examined with Sigma 500 VP cold-field emission scanning electron microscope (Carl Zeiss Microscopy GmbH, Köln, Germany), which allows reaching a high resolution at a low accelerating voltage. The tests were carried out at the accelerating voltage of 10 KeV inductive electron beam, using an SE detector on samples coated (sprayed) with a gold film.

At the first stage, the microstructure of brittle fractures obtained at 23 °C was observed. The observations covered samples cut out from brushed (SZ) and non-brushed (NSZ) profiles in their original condition and following X-exposure lasting 2016 h (SZ-X-2016 and NSZ-X-2016 series). The procedure was selected because it is expected to cause the most significant changes in the NFPC structure [45]. Observations were carried out at

500× and 20,000× magnification. At the second stage, the observations covered the usable surface microstructures in NSZ profiles in their original condition, following F-exposure (NSZ-F-336 and NSZ-F-2016 series) and X-exposure (NSZ-X-300 and NSZ-X-2016 series), at 500× magnification. The observations were not carried out for brushed profiles because of the high roughness of the usable surface, which made SEM examinations impossible.

2.4. Testing Mechanical Properties

Mechanical properties were tested on samples obtained from brushed (SZ) and non-brushed (NSZ) profiles in their original condition and following a short- and long-term F-exposure and X-exposure (Table 2). The flexural strength, flexural modulus and impact strength were tested.

The flexural modulus was also tested according to EN ISO 178 [46], using a class 1 strength testing machine (Instron, Darmstadt, Germany). Three-point bending was performed according to EN ISO 178 [46], using samples sized 15 × 100 × 5 mm, cut out from the central part of the profile's front wall, parallel to vertical ribs (Figure 4). Supports with a 5 mm radius were used, spaced every 80 mm, corresponding to 16-times sample's thickness and a 5 mm radius pressing element placed in the middle of the span. The samples were freely supported (Figure 6a). The load was applied to the front surface at a constant rate of 5 mm/min. until destruction. Flexural strength σ_f was calculated according to (1) and expressed in N/mm². Twelve samples were tested in each series, giving a total of one hundred and twenty samples tested in the study.

$$\sigma_f = \frac{3FL}{2bh^2} \tag{1}$$

where: *F*—maximum force, in N; *L*—support spacing, in mm; *b*—sample's width, in mm; *h*—sample's thickness, in mm.

(a)   (b)
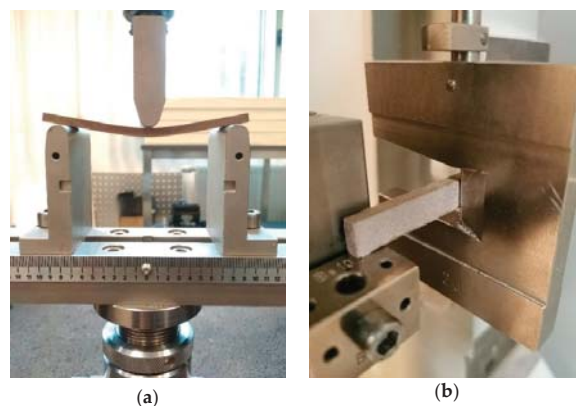
Figure 6. Testing mechanical properties: (**a**) flexural strength, (**b**) impact strength.

The flexural modulus was also tested according to EN ISO 178 [46], using a class 1 strength testing machine (Instron, Darmstadt, Germany), in conditions identical to flexural strength tests. A load-deflection curve was recorded during bending in a linearly elastic range, including the force and deflection values corresponding to strain ε_{f1} = 0.0005 and ε_{f2} = 0.0025. The f_1 and f_2 deflection values were calculated according to Formula (2).

$$f_1 = \frac{\varepsilon_{f1}L^2}{6h}; \ f_2 = \frac{\varepsilon_{f2}L^2}{6h} \tag{2}$$

where: *L*—spacing of supports, in mm; *h*—sample's thickness, in mm.

The force values recorded when ε_{f1} and ε_{f1} strain occurred were used for determining the values of σ_{f1} and σ_{f2} normal stress. The E_f modulus was calculated according to (3) and expressed in N/mm². Twelve samples were tested in each series, giving a total of one hundred and twenty samples tested in the study.

$$E_f = \frac{\sigma_{f2} - \sigma_{f1}}{\varepsilon_{f2} - \varepsilon_{f1}} \tag{3}$$

where: σ_{f1}, σ_{f2}—maximum normal stress corresponding to f_1 and f_2 stress determined according to (2).

The impact test was carried out with Charpy impact pendulum (ZwickRoell, Ulm, Germany) according to EN ISO 179-1 [47]. The samples used in the test had no notch, were sized $10 \times 80 \times 5$ mm, cut out from the central part of the profile's front wall, parallel to the vertical ribs. The sample was freely resting on supports spaced at 62 mm and then hit with a 2J impact pendulum (Figure 6b). The load was exerted on the front surface. Charpy impact strength a_{cU} was calculated according to (4) and expressed in kJ/m². Eight samples were tested in each series, giving a total of eighty samples tested in the study.

$$a_{cU} = \frac{E_c}{h \cdot b} \cdot 10^3 \tag{4}$$

where: E_c—energy absorbed by breaking the test specimen, in J; h—sample's thickness in mm; b—sample's width, in mm.

2.5. Analysis of the Statistical Difference in the Mechanical Properties Test Results

The changes in the tested materials' mechanical properties were analysed based on the characteristics' differences after F-exposure and X-exposures. Since in most cases, the differences between the results before and after the exposure were relatively low compared to the results' variability in the groups, the statistical significance of the differences was analysed with a one-way analysis of variance (ANOVA F-test).

The difference in the given mechanical property before and after weathering (ΔY) was calculated with the following equation:

$$\Delta Y = 100\% \cdot \frac{Y(T_j) - Y(T_i)}{Y(T_i)} \tag{5}$$

where: T_i, T_j—ageing times used; $Y(T_i)$—mean value of the given mechanical property after weathering for T_i, $Y(T_j)$—mean value of the given mechanical property after weathering for T_j.

Taking into account that two sample series—obtained from brushed (SZ) and non-brushed (NSZ) usable surface of the profiles—were subjected to mechanical properties tests before and after weathering exposure, an analysis of the exposure influence on the properties of interest was preceded by an assessment of the differences between the properties of SZ and NSZ samples in their original condition. The following formula was used for calculating the relative difference:

$$\Delta Y = 100\% \cdot \frac{Y_{SZ} - Y_{NSZ}}{Y_{SZ}} \tag{6}$$

where: ΔY—difference between the mechanical properties of material Y with brushed SZ (Y_{SZ}) and non-brushed NSZ (Y_{NSZ}) surface.

The statistical significance of the differences was analysed with ANOVA F-test. The results are summarised in Table 4. No surface treatment influence was observed only for the modulus of elasticity. For flexural strength, the relative difference between the values obtained for SZ and NSZ samples amounted to 10.2%, while for the Charpy impact strength it was 9.6%. Both characteristics were higher for SZ than for NSZ samples. The exposure

impact on all analysed mechanical properties was assessed separately for each surface type because of the statistically significant difference in the flexural strength and Charpy impact strength tests for SZ and NSZ surface samples.

3. Results and Discussion

3.1. Microstructure Analysis

The observations of the brittle fracture microstructures helped evaluate only the dispersion rate of a filler in a polymer matrix. The composite's observed structure can be considered inhomogeneous [47,48]. Numerous wood flour clusters were discovered, forming combinations of fibres and plates with diameters ranging from 50 μm to 100 μm (Figures 7 and 8). Because a fracture in a composite occurs typically in the sample's most weakened areas, material defects in the form of pores and voids became visible at the fracture, being a testimony to the plates and wood fibres being pulled out from the polymer matrix [48] (Figures 7 and 8). Further analysis of the brittle fractures' microstructure revealed the presence of other fillers' clusters, most likely being mineral fillers (talc or chalk) and relatively regular shape and size not exceeding 1 μm. They were generally well dispersed in the polymer matrix (Figures 9 and 10), but some cluster sizes from 5 μm to 10 μm (Figure 10b) were also discovered. The performed SEM analysis of brittle fractures did not reveal microstructural differences in the material in its original condition compared to the material after X-exposure for 2016 h (SZ-X-2016 and NSZ-X-2016 series). The data collected in the brittle fracture analysis, revealing the microstructure at the material cross-section, can suggest that the material's inner structure did not change under the influence of the applied weathering procedure.

(a) (b)
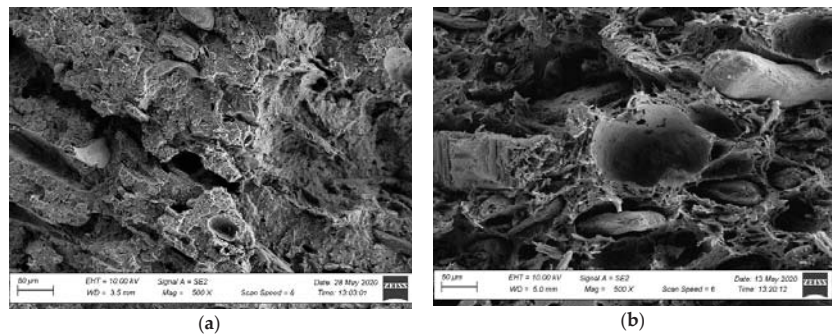
Figure 7. Microstructure of the profile's fracture surface in the original condition: (**a**) SZ profile, magnification: 500×, (**b**) NSZ profile, magnification: 500×.

(a) (b)
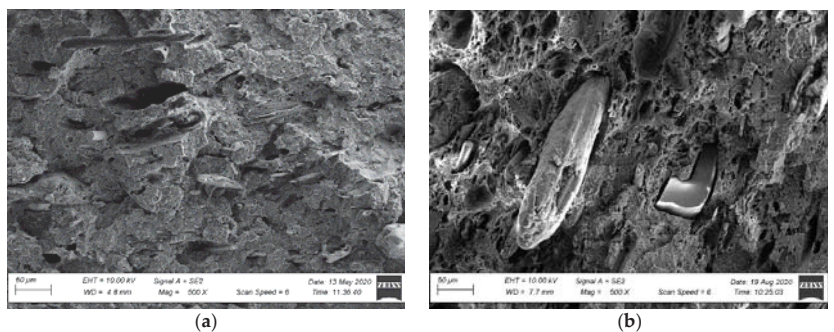
Figure 8. Microstructure of the profile's fracture surface after weathering: (**a**) SZ-X-2016 series profile, magnification: 500×, (**b**) NSZ-X-2016 series, magnification: 500×.
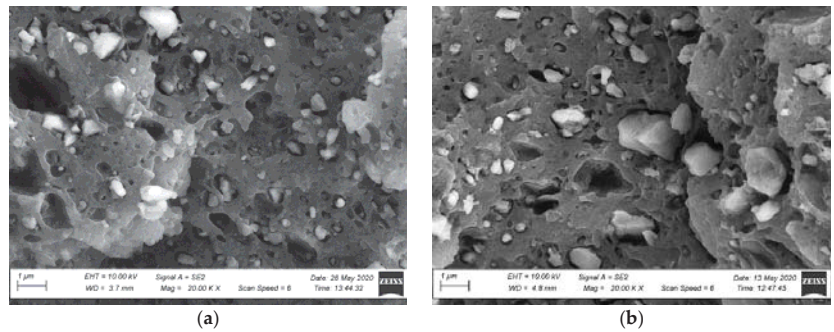
Figure 9. Microstructure of the profile's fracture surface in the original condition: (**a**) SZ profile, magnification: 20,000×, (**b**) NSZ profile, magnification: 20,000×.
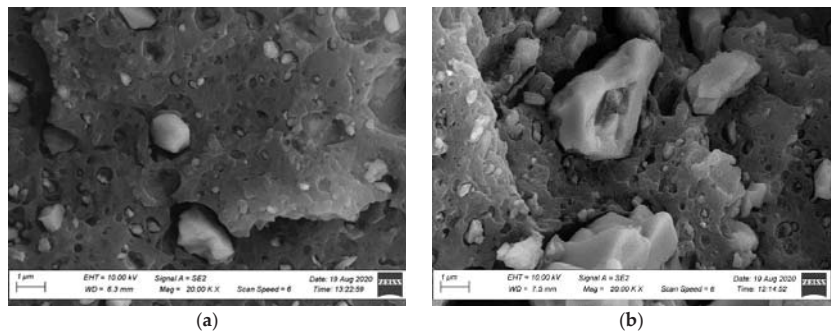
Figure 10. Microstructure of the profile's fracture surface after weathering: (**a**) SZ-X-2016 series profile, magnification: 20,000×, (**b**) NSZ-X-2016 series profile, magnification: 20,000×.

An SEM surface analysis was carried out, taking into account the fractures' surface microstructure analyses and bearing in mind that the profiles' usable surface was directly exposed. The tests covered only the non-brushed profiles because of brushed profiles' high surface roughness, which prevented their observations. An analysis of NSZ samples' surface microstructure in the original condition revealed a uniform coating of the fibres with polymer (Figure 11). The surface was relatively smooth and uniform, characteristic of extruded NFPC profiles [48,49]. No exposed wood fibres were observed. Following the profiles' X-exposure, significant changes in the surface morphology were observed already after 300 h. The microscopic image revealed melting of the polymer's outermost layer, exposing the surfaces of fillers not wetted with the polymer, taking the form of large plates and wood fibre clusters (Figure 12a). Extending the exposure time to 2016 h significantly aggravated the top layer's degradation. Highly non-homogenous surface topography with molten areas was observed [50]. The revealed microstructure contained agglomerated wood fibres (Figure 12b).
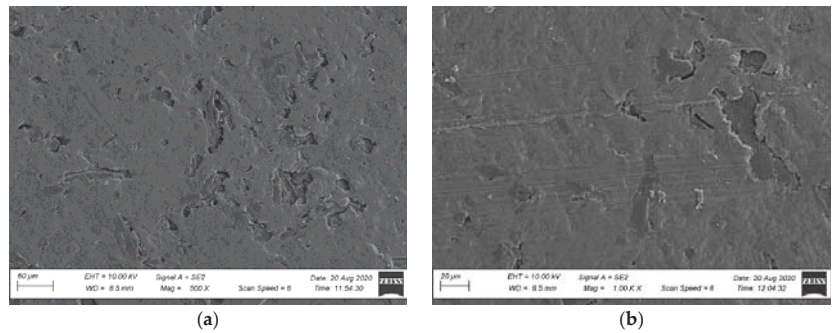
Figure 11. Microstructure of NSZ profile's surface in the original condition (**a**) magnification: 500×, (**b**) magnification: 1000×.
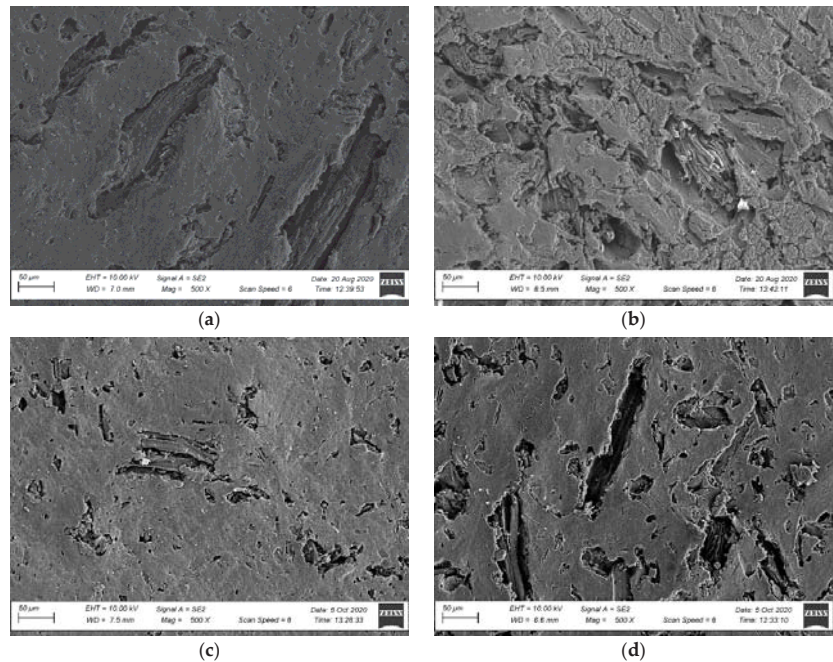
Figure 12. Surface microstructure after weathering, magnification: 500× (**a**) NSZ-X-300 series, (**b**) NSZ-X-2016 series, (**c**) NSZ-F-336 series, (**d**) NSZ-F-2016 series.

F-exposure also contributed to the changes in the surface morphology. The microstructure changes were reported after 336 h of exposure (NSZ-F-336 series), and minor molten areas in the polymer's outermost layer became visible, exposing the filler's surface (Figure 12c). Still, the changes are noticeably more minor than those reported for samples after X-exposure for 300 h (Figure 12a). The F-exposure time extension to 2016 h aggravated the profile's outermost layer, making the filler much more visible (Figure 12d). It should be emphasised that the degradation rate of NSZ-F-2016 series samples was significantly lower than the degradation rate of samples after X-exposure for the same exposure duration (NSZ-X-2016 series).

Summing up the results of microstructural tests, it can be concluded that the applied weathering procedures performed with laboratory light sources did not affect the compos-

ite's internal structure. No differences that could be considered microstructure changes were observed in the brittle fracture analysis [48,49]. Under UV-irradiation influence the surface layers between PVC matrix and wood fibres became more brittle. Due to these factors create additional stresses at the interface of the components, causing development of the cracks on the weathered surface of the samples [49]. Exposing the profile to light emitted by fluorescent lamps (F-exposure) and xenon lamps (X-exposure) caused significant surface degradation. The surface morphology analysis revealed molten areas in the polymer matrix's outermost layer, exposing the surface of lignocellulosic fibres. Extended exposure aggravated the degradation of the profiles' usable layer, which corresponds to the literature data [45,50]. Weathering impacts exerted with a xenon lamp affected the surface properties more significantly than F-exposure for the same exposure time. The above can be explained by the differences between relative spectral intensity of radiation for UVA 340 fluorescent lamps (F-exposure) and relative spectral intensity of radiation for a xenon-arc lamp (X-exposure). It is supposed that wavelengths rays between 360 nm and 400 nm is the most important factor causing photodegradation to some organic substances such as PVC. F-exposure contains about 26% wavelengths rays between 360 nm and 400 nm (Table 1) while X-exposure contains about 54% (Table 3). Surface damage after X-exposure was more intensive and vast than after F-exposure.

3.2. Mechanical Properties

An analysis of the results suggests that the analysed material's flexural strength in the original condition was $60 \div 67$ MPa; $63 \div 64$ MPa after F-exposure, and $61 \div 64$ MPa after X-exposure (Figure 13). These values are similar to those obtained for construction profiles made of wood fibre-reinforced composites with PE matrix and PVC matrix with rice husk fibre, for which the original condition values amounted to 71 MPa and 67 MPa, respectively [51]. They exceed the test results on composites with recycled high-density polyethylene matrix and rice husk fibre filler, which reached the flexural strength of 25 MPa for the filler content of 50% and 38 MPa for the filler content of 80% [28]. Still, they are lower than the results for composites with polymer matrix reinforced with sycamore, sisal or bamboo fibres, whose flexural strength ranged from 100 MPa to 134 MPa [52].
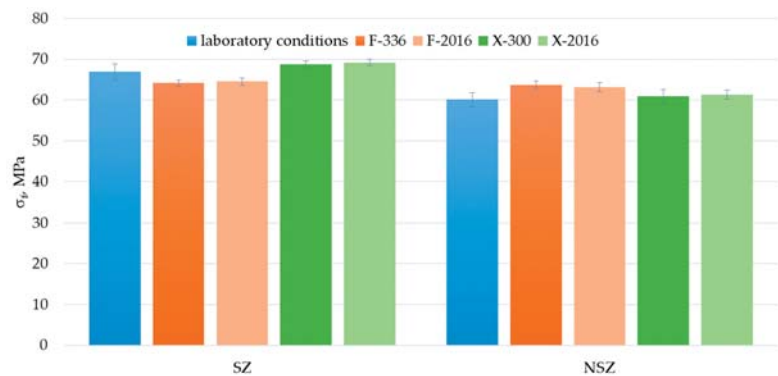
Figure 13. Flexural strength test results of brushed (SZ) and non-brushed (NSZ) samples in basic state (laboratory conditions), after F-exposure for 336 h (F-336) and 2016 h (F-2016) and after X-exposure for 300 h (X-300) and 2016 h (X-2016). The error bands represent the standard deviation (series size n = 12).

The analysis of F-exposure's influence on the flexural strength revealed a decrease for SZ series samples. No decrease was reported for NSZ samples. Still, it should be emphasised that a statistically significant change in the strength occurs already after the first exposure period T_1, which lasts 336 h for F-exposure and 300 h for X-exposure. Further exposure up to 2016 h does not cause a significant change in the strength (Figure 14).
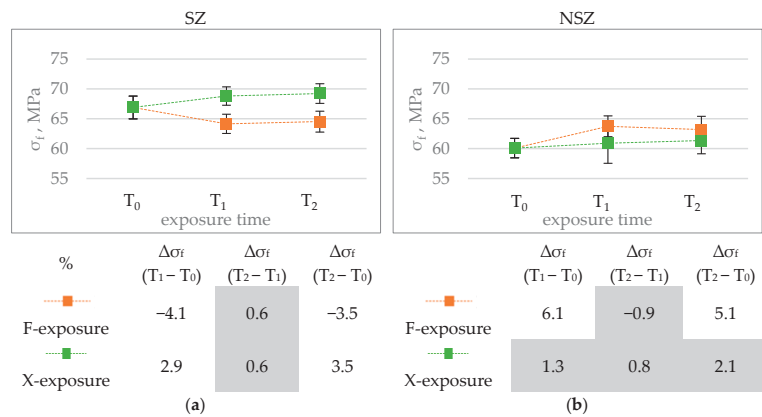
Figure 14. Diagrams showing the differences in the sample's flexural strength σ_f, MPa, after F-exposure and X-exposure for time T_1 and T_2: (**a**) brushed sample (SZ), (**b**) non brushed sample (NSZ). The error bars show the standard deviation (series size n = 12). The tables below summarise the relative change in the flexural strength $\Delta\sigma_f$, %, during exposure time $(T_1 - T_0)$ $(T_2 - T_1)$ and $(T_2 - T_0)$ calculated according to Formula (5). Statistically insignificant differences $\Delta\sigma_f$ are highlighted in grey.

Different behaviour of SZ and NSZ profiles during F-exposure, where each weekly cycle starts with a 24 hours' phase of wetting through condensation (Table 2), can be explained by the difference in the surface's condition. As demonstrated in a previous study, mechanically treated profiles can be more susceptible because of lignocellulosic fibres' exposure in the process [7,28,31]. It is assumed that the exposed hydrophilic fibres swell due to their wetting, which weakens the interaction forces between the matrix and the filler and deteriorates the strength [20,53]. A similar effect was observed for planned profiles made of HDPE composite with a wood flour filling [30].

X-exposure did not deteriorate the flexural strength of either SZ or NSZ series samples (Figure 14). It can be concluded that short-term spraying used in the exposure, followed by long-term light exposure combined with an elevated temperature (Table 2), does not exert such a significant influence on the NFPC's strength as the exposure including long-term wetting. The results after X-exposure can even suggest that exposure to elevated temperature (BST 60 °C—see Table 2) could result in plastification of the polymer matrix and its better surrounding by the filler, and hence improvement in the interphase bonds [48]. A decrease in the flexural strength after X-exposure was observed in most of the previous papers, reaching 20–25% [27,30,31]. Still, it has to be pointed out that most of the papers concerned composites with HDPE matrix, which is less resistant to UV than PVC [13,32]. A lack of significant changes in the flexural strength corresponds to the results of brittle fracture analysis, which did not reveal any changes in the composite's microstructure as a result of weathering (Figure 8).

Flexural modulus is another mechanical property analysed in the study. It depicts the material's stiffness, which is a key feature for construction products installed with point support, e.g., on a grid, as happens with terrace and facade profiles [13]. The flexural modulus' value level determines the profiles' susceptibility to deformation under service loads [22]. The solutions examined in the study achieved the flexural modulus values of 3970 MPa in the original condition (Figure 15). As shown in a previous study, construction profiles made of composite with HDPE matrix and wood flour are characterised by the flexural modulus of $2530 \div 3600$ MPa [36,38]; with PP matrix and wood flour—ca. 4500 MPa [54]; and with HDPE matrix and sisal and bamboo fibres—2500 MPa and 3700 MPa, respectively [52].
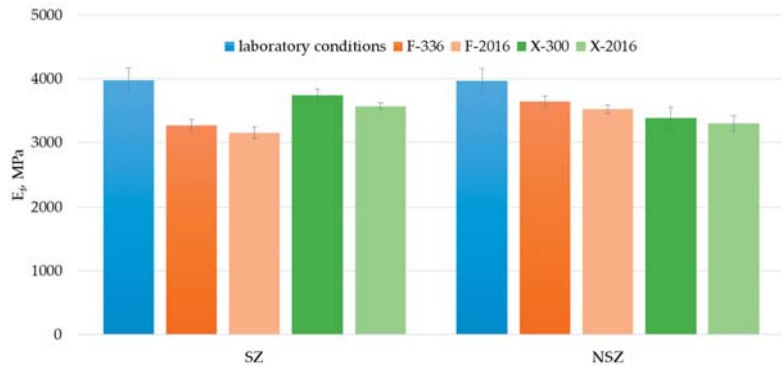
Figure 15. Results of flexural modulus tests of brushed (SZ) and non-brushed (NSZ) samples in basic state (laboratory conditions), after F-exposure for 336 h (F-336) and 2016 h (F-2016) and after X-exposure for 300 h (X-300) and 2016 h (X-2016). The error bars represent the standard deviation (series size n = 12).

The performed ageing procedures exerted a significant influence on the flexural modulus values (Figure 16). A decrease was observed in all tested series after the exposure. Similarly to flexural strength, increasing the time from 336 h for F-exposure and 300 h for X-exposure to 2016 h does not cause a statistically significant difference in the flexural modulus. The difference in the modulus of elasticity between SZ-X-300 and SZ-X-2016 is the exception for which the changes are noticeably lower than after 300 h of X-exposure.
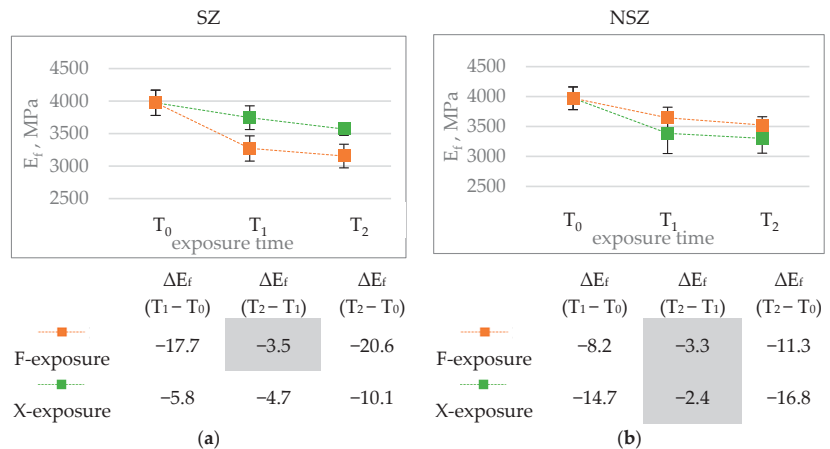
Figure 16. Diagrams showing differences in the flexural modulus E_f, MPa, after F-exposure and X-exposure for time T_1 and T_2: (**a**) brushed sample (SZ), (**b**) non brushed sample (SZ). The error bars show standard deviation (series size n = 12). The tables under the diagrams summarise the relative change in the modulus of elasticity ΔE_f, %, for exposure time $(T_1 - T_0)$ $(T_2 - T_1)$ and $(T_2 - T_0)$, calculated according to Formula (5). Statistically insignificant differences ΔE_f are highlighted in grey.

The influence of F-exposure on brushed profile samples was most significant. The modulus of elasticity amounted to 3270 MPa (SZ-F-336) and 3160 MPa (SZ-F-2016) after F-exposure. For unbrushed samples, the values reached 3640 MPa (NSZ-F-300) and 3520 MPa (NSZ-F-2016). Similarly to flexural strength, exposing the lignocellulosic fibres during brushing could play a decisive role [7,31]. The reduction in the interphase interaction on the composite' surface can determine the value of the modulus of elasticity much more

than the flexural strength. Weakening of the top layer significantly increases susceptibility to strain [9,53]. Moreover, X-exposure reduced the modulus of elasticity's value, whereby the non-brushed sample series revealed more significant differences than the brushed ones. The results correspond to the results of experiments performed for profiles with HDPE matrix and wood flour filling [28], although the drops discovered in this study are much smaller.

Charpy impact strength is another mechanical property taken into account in the study (Figure 17). Because of the high risk of construction profiles' exposure to dynamic loads throughout their entire life, stable impact strength value expressing the material's susceptibility to fracture can be considered one of the key functional parameters.
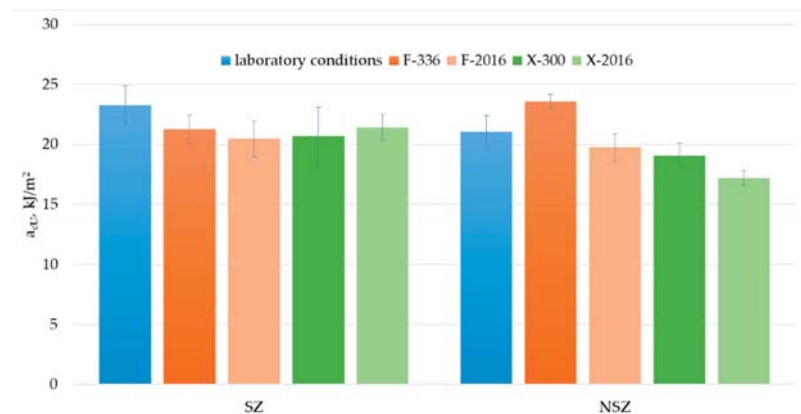
Figure 17. Results of Charpy impact strength of brushed (SZ) and non-brushed (NSZ) samples in basic state (laboratory conditions), after F-exposure for 336 h (F-336) and 2016 h (F-2016) and after X-exposure for 300 h (X-300) and 2016 h (X-2016). The error samples represent the standard deviation (series size n = 8).

The difference between the samples' impact strength before and after F-exposure and X-exposure seems significant, but because of the dispersion of the results in each test series, the statistical significance for some of these changes cannot be confirmed. It applies, especially to SZ samples. An anomaly is observed for NSZ samples, involving a significant increase in the impact strength after F-336 exposure. After F-2016 exposure, the impact strength decreases significantly compared to F-336 exposure. The final impact strength change between the initial value and the value after F-2016 exposure is not statistically significant, although it amounts to over 6%.

The general trend observed for the change in the mechanical properties after weathering (Figures 14, 16 and 18) is a statistically significant change after weathering time T_1. However, in most cases, the difference between T_1 and T_2 is minor. The course of the Charpy impact strength changes for NSZ under F-exposure is the only exception.
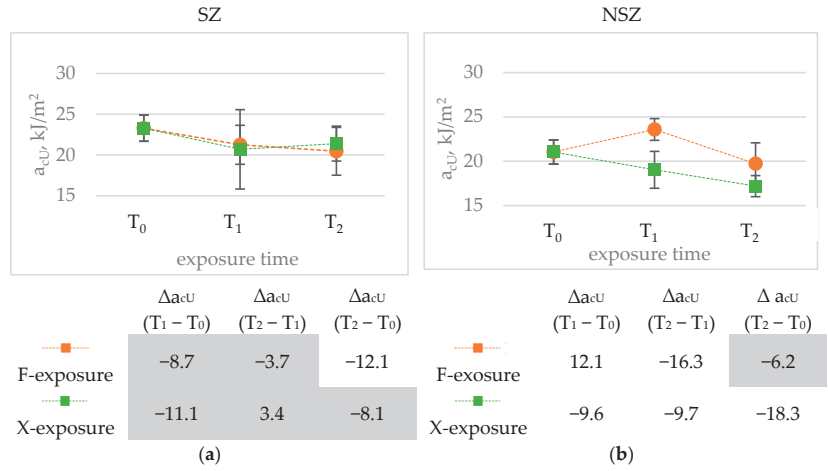
Figure 18. Diagrams presenting differences in Charpy impact strength, a_{uC}, kJ/m^2, after F-exposure and X-exposure for time T_1 and T_2: (**a**) brushed samples (SZ), (**b**) non brushed samples (NSZ). The error bars represent the standard deviation (series size n = 8). The tables under the diagrams present the relative change in the impact strength Δa_{cU}, %, for exposure time $(T_1 - T_0)$ $(T_2 - T_1)$ and $(T_2 - T_0)$, calculated according to Formula (5). Statistically insignificant differences Δa_{cU} are highlighted in grey.

In order to comprehensively evaluate the exposure type influence on the change in the mechanical properties ΔY, the following equation was used:

$$\Delta Y = 100\% \cdot \frac{Y(F, T_j) - Y(X, T_i)}{Y(T_0)} \tag{7}$$

where: F, X—exposure type (according to Table 2), $Y(F,T_i)$, $Y(X,T_i)$—value of the mechanical property after F- and X-exposure in time T_i T_j. Exposure times: T_0—zero hours (before exposure), T_1—336 h for F-exposure and 300 h for X-exposure, T_2—is 2016 h for both exposures.

The analysis results of the exposure type's influence on the property changes are summarised in Table 5. All applied exposure types and their times are compared.

Table 5. Differences between the mechanical properties after F- and X-exposure in time T_1 and T_2 according to Equation (7), %. Statistically insignificant differences are highlighted in grey.

Changes in the Flexural Strength, %					
Samples SZ				Samples NSZ	
X-300	X-2016			X-300	X-2016
F-336	−6.9	−7.6	F-336	4.7	4.0
F-2016	−6.4	−7.0	F-2016	3.8	3.0
Changes in the Modulus of Elasticity, %					
SZ samples				NSZ samples	
X-300	X-2016			X-300	X-2016
F-336	−11.9	−7.5	F-336	6.5	8.6
F-2016	−14.8	−10.4	F-2016	3.5	5.6
Changes in the Charpy Impact Strength, %					
SZ samples				NSZ samples	
X-300	X-2016			X-300	X-2016
F-336	2.4	−0.6	F-336	21.6	30.3
F-2016	−1.0	−4.0	F-2016	3.3	12.1

The analysis of the data summarised in Table 5 indicates that in five cases (except for the impact strength for SZ samples), the difference between the mechanical properties after short-term F-exposure and X-exposure (F-336 and X-300) and after long-term F-exposure

and X-exposure (F-2016 and X-2016) is statistically significant. The mechanical properties of the SZ surface material revealed the highest drop after F-exposure (negative values in the Table), while for the NSZ surface, it was after X-exposure (positive values in the Table). Hence, it can be concluded that for the SZ surface, more unfavourable changes can be expected after F-exposure, while for NSZ surfaces, it occurs after X-exposure. Both the exposure type and duration do not significantly contribute to the change in the Charpy impact strength for SZ samples.

On the other hand, an absence of a significant difference between the mechanical properties after F-exposure for 2016 h and X-exposure for 300 h can be observed. The modulus of elasticity for SZ samples makes the only exception, where significant differences in the modulus' value can be observed between all exposure types. Major changes in the modulus (lower modulus values after exposure) are caused by F-exposure, while ranking the mechanical property values after both exposures (from the highest to the lowest value of the modulus), we get X-300; X-2016; F-336 and F-2016.

4. Conclusions

An analysis of the experimental data collected under the study suggests that exposing construction profiles made of PVC composite with wood flour filling to light emitted by different laboratory sources of light alternately with wetting causes degradation of their usable surfaces. An SEM analysis of the surface microstructure revealed molten areas in the polymer matrix outermost layers and exposed surfaces of the filler fibres. The degree of the changes can be considered as significantly reducing the profiles' aesthetic and decorative properties. No microstructure changes were observed in the brittle fracture tests. However, the weathering procedure was discovered to impact the surface morphology. Influences involving irradiation with a xenon lamp and short-term wetting (X-exposure) caused much more significant surface degradation than exposure to fluorescent lamp's light and long-term wetting (F-exposure) for the same exposure duration. The observations applied only to the mechanically non-treated usable surfaces. The observations were not carried out for brushed surfaces, because of the surface roughness.

The applied exposures affected the mechanical properties. The influence of surface treatment on changes in mechanical properties during weathering was not statistically analyzed due to the different mechanical properties of SZ and NSZ profiles before weathering. In the drawings, however, differences can be observed were observed in the susceptibility to the exposure for profiles with mechanically treated usable surfaces (brushed—SZ) compared to non-brushed (NSZ) ones. Artificial weathering carried out with fluorescent lamps and long-term wetting, included by condensation (F-exposure), greatly influenced the brushed profiles' properties. In turn, the influence of artificial weathering by exposure to a xenon lamp and short-term wetting was more significant for the non-brushed profiles. Significant changes in the flexural modulus were observed after the exposures, especially after F-exposure. No significant decrease in the flexural strength occurred, and the impact strength changes are hard to assess because of the dispersion of the results in each series.

The exposure duration (time) affected the properties of interest. Although extending the weathering exposure time from 300 h (X-exposure) or 336 h (F-exposure) to 2016 h significantly aggravated the surface morphology changes, especially after X-exposure, the changes in the mechanical properties observed at the initial stage of ageing progressed only slightly.

The constancy of mechanical properties matters for the building fitness assessment. Based on the collected data, it can be concluded that for profiles made of natural fibre-reinforced polymer composites, whose usable surface was developed in a standard way, by mechanical treatment (brushing), artificial ageing using fluorescent lamps and long-term wetting including condensation (F-exposure) seems to be the adequate procedure to assess the changes in the mechanical properties. The procedure causes more severe swelling of lignocellulosic fibres and weakens the interaction forces between the matrix and the filler, reducing the mechanical parameters. The influence was particularly evident for the

flexural modulus, which should be considered as a suggestion to select this parameter as a diagnostic feature of resistance to accelerated weathering. It needs to be emphasised that the changes in the modulus of elasticity can be determined only after short-term F-exposure (336 h), which can be used for quick diagnostics of new solutions.

This study does not exhaust the topic of artificial weathering resistance test methods for construction profiles made of plant fibre-reinforced polymer composites. Considering the dynamic development of this product group and its growing significance in civil engineering, further studies are planned. Future studies will cover other NFPC compositions and extended weathering exposure time.

References

1. Ferreira, F.V.; Pinheiro, I.F.; de Souza, S.F.; Mei, L.H.I.; Lona, L.M.F. Polymer Composites Reinforced with Natural Fibers and Nanocellulose in the Automotive Industry: A Short Review. *J. Compos. Sci.* **2019**, *3*, 51. [CrossRef]
2. Gurunathan, T.; Mohanty, S.; Nayak, S.K. A review of the recent developments in biocomposites based on natural fibres and their application perspectives. *Compos. Part A Appl. Sci. Manuf.* **2015**, *77*, 1–25. [CrossRef]
3. Maraveas, C. Production of Sustainable Construction Materials Using Agro-Wastes. *Materials* **2020**, *13*, 262. [CrossRef]
4. Rajak, D.K.; Pagar, D.D.; Menezes, P.L.; Linul, E. Fiber-Reinforced Polymer Composites: Manufacturing, Properties, and Applications. *Polymers* **2019**, *11*, 1667. [CrossRef] [PubMed]
5. Coleman, J.N.; Khan, U.; Gun'ko, Y.K. Mechanical reinforcement of polymers using carbon nanotubes. *Adv. Mater.* **2006**, *18*, 689–706. [CrossRef]
6. Väisänen, T.; Das, O.; Tomppo, L. A review on new bio-based constituents for natural fiber-polymer composites. *J. Clean. Prod.* **2017**, *149*, 582–596. [CrossRef]
7. Pickering, K.L.; Efendy, M.G.A.; Le, T.M. A review of recent developments in natural fibre composites and their mechanical performance. *Compos. Part A Appl. Sci. Manuf.* **2016**, *83*, 98–112. [CrossRef]
8. Azman, M.A.; Asyraf, M.R.M.; Khalina, A.; Petrů, M.; Ruzaidi, C.M.; Sapuan, S.M.; Wan Nik, W.B.; Ishak, M.R.; Ilyas, R.A.; Suriani, M.J. Natural Fiber Reinforced Composite Material for Product Design: A Short Review. *Polymers* **2021**, *13*, 1917. [CrossRef]
9. Sanjay, M.R.; Madhu, P.; Jawaid, M.; Senthamaraikannan, P.; Senthil, S.; Pradeep, S. Characterization and properties of natural fiber polymer composites: A comprehensive review. *J. Clean. Prod.* **2018**, *172*, 566–581. [CrossRef]
10. Sudoł, E.; Wasiak, M. Slip resistance of wood-polymer composite decking profiles. *Ann. WULS-SGGW For. Wood Technol.* **2018**, *104*, 31–35.
11. Lau, K.; Hung, P.; Zhu, M.; Hui, D. Properties of natural fibre composites for structural engineering applications. *Compos. Part B Eng.* **2008**, *136*, 222–233. [CrossRef]
12. Miller, S.; Srubar, W., III; Billington, S.; Lepech, M. Integrating durability-based service-life predictions with environmental impact assessments of natural fiber–reinforced composite materials. *Resour. Conserv. Recycl.* **2008**, *99*, 72–83. [CrossRef]
13. Czarnecki, L.; Van Gemert, D. Innovation in construction materials engineering versus sustainable development. *Bull. Polish Acad. Sci. Tech. Sci.* **2017**, *65*, 765–771. [CrossRef]
14. Wall, S. CE Marking of Construction Products—Evolution of the European Approach to Harmonisation of Construction Products in the Light of Environmental Sustainability Aspects. *Sustainability* **2021**, *13*, 6396. [CrossRef]

15. Regulation (EU) No 305/2011 of the European Parliament and of the Council. Available online: https://eur-lex.europa.eu/legal-content/EN/TXT/?uri=uriserv:OJ.L_.2011.088.01.0005.01.ENG&toc=OJ:L:2011:088:TOC (accessed on 15 November 2021).
16. Czarnecki, L.; Van Gemert, D. Scientific basis and rules of thumb in civil engineering: Conflict or harmony? *Bull. Polish Acad. Sci. Tech. Sci.* **2016**, *64*, 665–673. [CrossRef]
17. Yu, C.W.; Bull, J.W. *Durability of Materials and Structures in Building and Civil Engineering*; Whittle Publishing: Dunbeath, UK, 2006.
18. John, M.J. Environmental degradation in biocomposites. In *Biocomposites for High-Performance Applications*; Woodhead Publishing: Dunbeath, UK, 2017; pp. 181–194. [CrossRef]
19. Sethi, S.; Ray, B.C. Environmental effects on fibre reinforced polymeric composites: Evolving reasons and remarks on interfacial strength and stability. *Adv. Colloid Interface Sci.* **2015**, *217*, 43–67. [CrossRef] [PubMed]
20. Li, X.; Tabil, L.G.; Panigrahi, S. Chemical treatments of natural fiber for use in natural fiber-reinforced composites: A review. *J. Polym. Environ.* **2007**, *15*, 25–33. [CrossRef]
21. Yifan, Z.; Ramadania, E.; Egap, E. Thiol ligand capped quantum dot as an efficient and oxygen tolerance photoinitiator for aqueous phase radical polymerization and 3D printing under visible light. *Polym. Chem.* **2021**, *12*, 5106–5116. [CrossRef]
22. Friedrich, D.; Luible, A. Standard-compliant development of a design value for wood–plastic composite cladding: An application-oriented perspective. *Case Stud. Struct. Eng.* **2016**, *5*, 13–17. [CrossRef]
23. Schabowicz, K. Testing of Materials and Elements in Civil Engineering. *Materials* **2021**, *14*, 3412. [CrossRef]
24. Beg, M.; Pickering, K. Accelerated weathering of unbleached and bleached Kraft wood fibre reinforced polypropylene composites. *Polym. Degrad. Stab.* **2008**, *93*, 1939–1946. [CrossRef]
25. Qin, J.; Jiang, J.; Tao, Y.; Zhao, S.; Zeng, W.; Shi, Y.; Xiao, M. Sunlight tracking and concentrating accelerated weathering test applied in weatherability evaluation and service life prediction of polymeric materials: A review. *Polym. Test.* **2021**, *93*, 106940. [CrossRef]
26. Friedrich, D.; Luible, A. Investigations on ageing of wood-plastic composites for outdoor applications: A meta-analysis using empiric data derived from diverse weathering trials. *Constr. Build. Mater.* **2016**, *124*, 1142–1152. [CrossRef]
27. Răut, I.; Călin, M.; Vuluga, Z.; Oancea, F.; Paceagiu, J.; Radu, N.; Doni, M.; Alexandrescu, E.; Purcar, V.; Gurban, A.-M.; et al. Fungal Based Biopolymer Composites for Construction Materials. *Materials* **2021**, *14*, 2906. [CrossRef]
28. Stark, N.M. Effect of weathering cycle and manufacturing method on performance of wood flour and high-density polyethylene composites. *J. Appl. Polym. Sci.* **2006**, *100*, 3131–3140. [CrossRef]
29. Bengtsson, M.; Stark, N.M.; Oksman, K. Durability and mechanical properties of silane cross-linked wood thermoplastic composites. *Compos. Sci. Technol.* **2007**, *67*, 2728–2738. [CrossRef]
30. Stark, N.M.; Matuana, L.M. Surface chemistry changes of weathered HDPE/wood-flour composites studied by XPS and FTIR spectroscopy. *Polym. Degrad. Stab.* **2004**, *86*, 1–9. [CrossRef]
31. Stark, N.M.; Matuana, L.M.; Clemons, C.M. Effect of processing method on surface and weathering characteristics of wood-flour/HDPE composites. *J. Appl. Polym. Sci.* **2004**, *93*, 1021–1030. [CrossRef]
32. Adhikary, K.B.; Pang, S.; Staiger, M.P. Effects of the accelerated freeze-thaw cycling on physical and mechanical properties of wood flour-recycled thermoplastic composites. *Polym. Compos.* **2009**, *31*, 185–194. [CrossRef]
33. Pilarski, J.M.; Matuana, L.M. Durability of wood flour-plastic composites exposed to accelerated freeze-thaw cycling. Part I. Rigid PVC Matrix. *J. Vinyl Addit. Technol.* **2005**, *11*, 1–8. [CrossRef]
34. Matuana, L.M.; Kamdem, D.P. Accelerated ultraviolet weathering of PVC/wood-flour composites. *Polym. Eng. Sci.* **2002**, *42*, 1657–1666. [CrossRef]
35. Seldén, R.; Nyström, B.; Långström, R. UV aging of poly(propylene)/wood-fiber composites. *Polym. Compos.* **2004**, *25*, 543–553. [CrossRef]
36. Stark, N.M.; Matuana, L.M. Surface chemistry and mechanical property changes of wood-flour/high-density-polyethylene composites after accelerated weathering. *J. Appl. Polym. Sci.* **2004**, *94*, 2263–2273. [CrossRef]
37. Stark, N.M.; Matuana, L.M. Ultraviolet weathering of photostabilised wood-flour-filled high-density polyethylene composites. *J. Appl. Polym. Sci.* **2003**, *90*, 2609–2617. [CrossRef]
38. Pilarski, J.M.; Matuana, L.M. Durability of wood flour-plastic composites exposed to accelerated freeze–thaw cycling. II. High density polyethylene matrix. *J. Appl. Polym. Sci.* **2006**, *100*, 35–39. [CrossRef]
39. Chen, Y.; Stark, N.; Tshabalala, M.; Gao, J.; Fan, Y. Weathering Characteristics of Wood Plastic Composites Reinforced with Extracted or Delignified Wood Flour. *Materials* **2016**, *9*, 610. [CrossRef]
40. EN 15534-1:2014; Composites Made from Cellulose-Based Materials and Thermoplastics (Usually Called Wood-Polymer Composites (WPC) or Natural Fibre Composites (NFC))—Part 1: Test Methods for Characterisation of Compounds and Products. European Committee for Standardization (CEN): Brussels, Belgium, 2014.
41. ISO 16474-3:2013; Paints and Varnishes. Methods of Exposure to Laboratory Light Sources. Part 3: Fluorescent UV Lamps. International Organization for Standardization ISO: Geneva, Switzerland, 2013.
42. EN 927-6:2018; Paints and Varnishes. Coating Materials and Coating Systems for Exterior Wood. Part 6: Exposure of Wood Coatings to Artificial Weathering Using Fluorescent UV Lamps and Water. European Committee for Standardization (CEN): Brussels, Belgium, 2018.
43. ISO 16474-2:2013; Paints and Varnishes. Methods of Exposure to Laboratory Light Sources. Part 2: Xenon-Arc Lamps. International Organization for Standardization ISO: Geneva, Switzerland, 2013.

44. *ISO 4892-2:2013*; Plastics. Methods of Exposure to Laboratory Light Sources. Part 2: Xenon-Arc Lamps. International Organization for Standardization ISO: Geneva, Switzerland, 2013.
45. Kajaks, J.; Kalnins, K.; Matvejs, J. Accelerated Aging of WPCs Based on Polypropylene and Plywood Production Residues. *Gruyter* **2019**, *9*, 115–128. [CrossRef]
46. *ISO 178:2019*; Plastics—Determination of Flexural Properties. International Organization for Standardization ISO: Geneva, Switzerland, 2019.
47. *ISO 179-1:2010*; Plastics—Determination of Charpy Impact Properties. Part 1: Non-Instrumented Impact Test. International Organization for Standardization ISO: Geneva, Switzerland, 2010.
48. Gao, X.; Li, Q.; Cheng, W.; Han, G.; Xuan, L. Optimization of High Temperature and Pressurized Steam Modified Wood Fibers for High-Density Polyethylene Matrix Composites Using the Orthogonal Design Method. *Materials* **2016**, *9*, 847. [CrossRef]
49. Pratheep, V.; Priyanka, E.; Hare Prasad, P. Characterization and Analysis of Natural Fibre-Rice Husk with Wood Plastic Composites. *IOP Conf. Ser. Mater. Sci. Eng.* **2019**, *561*, 012066. Available online: https://iopscience.iop.org/article/10.1088/1757-899X/561/1/012066 (accessed on 15 November 2021).
50. Wang, X.; Song, K.; Ou, R. Effects of carbon black and titanium dioxide on ultraviolet weathering of wood flour-HDPE/lumber composites using multi-phase co-extrusion technology. *BioResources* **2017**, *12*, 6173–6186. [CrossRef]
51. Vercher, J.; Fombuena, V.; Diaz, A.; Soriano, M. Influence of fibre and matrix characteristics on properties and durability of wood–plastic composites in outdoor applications. *J. Thermoplast. Compos. Mater.* **2020**, *33*, 477–500. [CrossRef]
52. Prasad, A.; Rao, K. Mechanical properties of natural fibre reinforced polyester composites: Jowar, sisal and bamboo. *Mater. Design* **2011**, *32*, 4658–4663. [CrossRef]
53. Mochane, M.J.; Mokhena, T.C.; Mokhothu, T.H.; Mtibe, A.; Sadiku, E.R.; Ray Suprakas, S.; Ibrahim, I.D.; Daramola, O.O. Recent progress on natural fiber hybrid composites for advanced applications: A review. *Express Polym. Lett.* **2019**, *13*, 159–198. [CrossRef]
54. La Mantia, F.P.; Morreale, M. Accelerated weathering of polypropylene/wood flour composites. *Polym. Degrad. Stab.* **2008**, *93*, 1252–1258. [CrossRef]

Both Plasticizing and Air-Entraining Effect on Cement-Based Material Porosity and Durability

Aigerim Tolegenova [1],*, Gintautas Skripkiunas [2],*, Lyudmyla Rishko [3] and Kenzhebek Akmalaiuly [1]

[1] Department of Construction and Building Materials, Satbayev University, Satpaev str.22a, Almaty 050013, Kazakhstan; kakmalaev@mail.ru

[2] Department of Building Materials and Fire Safety, Faculty of Civil Engineering, Vilnius Gediminas Technical University, Sauletekio al.11, LT-10223 Vilnius, Lithuania

[3] HeidelbergCement Klaipeda Research Laboratory, Švepelių g. 5, LT-94103 Klaipėda, Lithuania; rlp06@ukr.net

* Correspondence: aigerim.tolegenova.94@mail.ru (A.T.); gintautas.skripkiunas@vilniustech.lt (G.S.)

Abstract: The influence of a complex application of both plasticizing and air-entraining effects on concrete with polycarboxylate ether superplasticizer (PCE), air-entraining admixture (AIR), or an anti-foaming agent (AF) is analyzed in this paper with considerations for on the air content, workability, flexural and compressive strength, and freezing–thawing resistance of hardened cement mixtures. The effect of the complex behavior of PCE, AIR, and AF on the porosity of hardened cement mortar (HCM) and freezing–thawing resistance was investigated; freezing–thawing resistance prediction methodology for plasticized mortar was also evaluated. The results presented in the article demonstrate the beneficial influence of entrained air content on consistency and stability of cement mortar, closed porosity, and durability of concrete. Freezing–thawing factor K_F depending on porosity parameters can be used for freezing–thawing resistance prediction. With both plasticizing (decrease in the water–cement ratio) and air-entraining effects (increase in the amount of entrained air content), the frost resistance of concrete increases, scaling decreases exponentially, and it is possible to obtain great frost resistance for cement-based material.

Keywords: cement; air-entraining admixture; plasticizing; porosity; air-content; strength; freeze-thawing resistance

1. Introduction

Currently, construction, regardless of the purpose of the buildings being created, is characterized by high requirements for the quality of materials. In the construction market, the leading position is occupied by cement concrete. Significant importance today is given to improving the durability of concrete, especially cement compositions. For various operating environments, the durability of concrete is achieved by increasing the entrained air content, reducing the W/C, and increasing the strength class of concrete, as well as cement consumption, using a limited number of types of cement and normalizing their mineralogical composition [1–3].

Concrete has the potential to be damaged if it is subjected to freeze–thaw cycles. Therefore, determining how to scientifically optimize the ratio of high-efficiency concrete raw materials and accurately predict the frost resistance of concrete to improve the durability of its application is of great scientific significance. The prediction accuracy of frost resistance is highest when the concrete mix proportion factors considered are the water binder ratio, cement content, fine aggregate dosage, coarse aggregate dosage, and compound superplas-ticizer dosage [4–6]. Seong-Tae [7] suggested a prediction method for minimum curing time based on the hydration of the cement. According to this method, the rate of the decrease of compressive strength increases when the onset time of frost damage is faster and the water–cement ratio is higher. Authors Zeng et.al revealed that graphene oxide can improve frost resistance and compressive strength of air-entrained mortars by 18.9% and 41.9%,

respectively [8]. An important technical way to improve the frost durability of concrete is using air-entraining admixtures [9]. Air void structure is the key parameter that affects the frost resistance of concrete [10]. The entrained air void system in cement mortar and concrete directly affects both the fresh-state workability and the freeze–thaw durability of concrete pavements and structures [11,12]. The author Feng Yu [13] investigated the compounding use of AF and VMA which significantly improved the workability, air void structure, and the frost resistance of concrete. According to Feng Yu's results, at 0.0055% air-entraining agent (AIR) dosage, the combination of 0.15% AF and 0.015% viscosity modifying agent (VMA) reduced the number of large bubbles in concrete by 57.96%. Afterward, the number of fine bubbles was increased by 16.55% and the spacing factor was reduced by 18.09%. A decrease in spacing factor increases freeze–thaw resistance of concrete.

Air content is an important factor for achieving proper porosity of concrete. Zheng [14] and Rodríguez [15] presented test results that show that frost resistance increases with increasing air content, which makes the space parameter decrease in the hardened concrete. Moreover, the experimental results indicate that, in air-entraining concrete, total air content is not the only factor that affects the final properties of the concrete; air void structure parameters, including void size, shape, and distribution, are key factors as well [16]. The research results of Lazniewska-Piekarczyk et al. [17] on the influence of air-entraining admixture type have proved that a greater amount of micro pores in concrete is the effect of a synthetic air-entraining admixture. The combination effect of air-entraining admixtures on freeze–thaw resistance of cement mortar was also considered in [18].

The porosity of cement mortar is one of the most important microstructural features, which manifests at different length scales [19]. Capillary pores have the biggest influence on the resistance of concrete. Gel pores and water inside them have no influence on the frost resistance of concrete. In fact, water, due to its greater density, does not freeze in those pores. Closed air pores perform the role of reserve pores and increase the frost resistance of concrete [20]. Zhang's [16] analyses concluded that as the number of freeze–thaw cycles increases, the repeated action of periodic freezing and expansion forces and hydrostatic pressure on the pores inside the concrete cause the pores inside the concrete to gradually expand, penetrate, and form connected pores. Shinichi [21] investigated pore structure in high-strength concrete at early ages via the BSE imaging technique assuming the Powers model. At a very early age, most of the capillary pores in ordinary concrete are so large that their pore size distribution was discontinuous.

Moreover, frost resistance of concrete depends both on open porosity (the amount of capillary pores) and closed porosity (air content in the mixture), and quantitatively can be determined by the frost resistance factor K_F, which is derived from the equation [22]:

$$K_F = \frac{P_c}{0.09 \cdot P_o},\qquad(1)$$

where P_c—closed porosity of hardened cement mortar (air pores) and P_o—open porosity of hardened cement mortar (capillary pores).

The authors Funk [23] and Setzer [24] performed a comprehensive testing program before, during, and after standardized freeze–thaw weathering (CDF). Freeze–thaw cycling caused considerable deteriorations which were significantly modulated by the different admixtures via changes in cement micromorphology. According to the authors of [25,26], the frost resistance of concrete is determined by its porosity because water can only penetrate open pores. Capillary pores have the greatest influence on the conglomerate's frost resistance. They are open and simple to fill with water [27]. As for the air pores, as opposed to capillary pores, they increase the conglomerate's frost resistance. During the immersion process the air pores are closed and no water enters them [28].

According to Łazniewska-Piekarczyk [29], the influence of the type of admixtures on porosity and pore size distribution of high-performance self-compacting concrete (HPSCC) at a constant level of water were analyzed whilst considering the cement coefficient, the type and volume of the aggregate, and the volume of the cement mortar. Despite the fact

that the air content parameters differed from the standard recommendations, she found that HPSCC was frost resistant. The authors [30] investigated the freeze–thaw behavior of air-entraining cement mortars saturated with a NaCl solution at a concentration of 10 wt.% using experimental measurement approaches. The findings of these studies showed that air-void entrainment tends to decrease thermal contractions but increase hydraulic expansion, ice nucleation expansion, and residual expansion. Some scholars modified cement with polypropylene (PP) fiber, such as Ping Jiang [31], and they found that with an increase of fiber from 0.25% to 1% the porosity was increased by approximately 6% due to the random distribution intersection and interleaving of (PP) fibers in concrete. The goal of this study is to investigate the technological properties and effects of air voids and porosity parameters of cement with different water–cement (W/C) ratios under the action of freezing–thawing cycles. The freeze–thaw (CDF) (test) technique is used to determine the surface scaling of the specimens. Strength of hardened cement mortar and porosity parameters are calculated in relation to freezing–thawing factors. In previous investigations, it has been noted that an important parameter for frost resistance is a decrease in capillary porosity using plasticizers and an increase in the amount of air in concrete using an air-entraining admixture. No research studies have investigated the combined effect of plasticizing and air-entraining admixtures on the freezing–thawing resistance of hardened cement.

2. Materials and Methods

2.1. Materials

2.1.1. Cement

Portland cement without mineral admixtures CEM I 42.5 R conforming to EN 197-1 with water consumption of 26.6% was used. The mineral composition, physical properties, and mechanical properties of the cement are presented in Table 1, Table 2, and Table 3, respectively.

Table 1. Mineral and chemical composition of the cement.

Component	Amount [%]
Tricalcium silicate (C_3S)	57.9
Dicalcium silicate (C_2S)	15.6
Tricalcium aluminate (C_3A)	7.5
Tetracalciumaluminoferrite (C_4AF)	11.9

Table 2. Chemical composition of the cement.

	Component									
	Al_2O_3	Fe_2O_3	SiO_2	CaO	MgO	SO_3	K_2O	Na_2O	Cl^-	CaO_{free}
Amount [%]	5.23	3.44	20.63	63.56	3.13	0.78	1.15	0.10	0.007	1.4

Table 3. Physical and mechanical properties of cement.

Property	Value
2-day compressive strength, [MPa]	28 ± 2
28-day compressive strength, [MPa]	55 ± 3
Initial setting time, [min]	180
Final setting time, [min]	225
Volume stability, [mm]	1.0
Water consumption, [%]	26.6
Residue on the 90 µm sieve, [%]	1.5
Fineness by Bline, m^2/kg	340

The results of the particle size distribution of cement are presented in Figure 1.
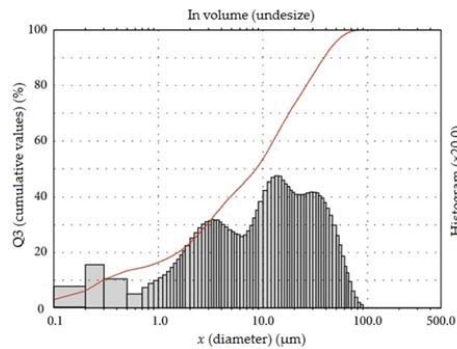
Figure 1. Particle size distribution of cement CEM I 42.5 R.

2.1.2. Aggregate and Water

Natural river sand with a fraction of 0/2 was selected as fine aggregate. The grain-size distribution for the sand is shown in Figure 2.
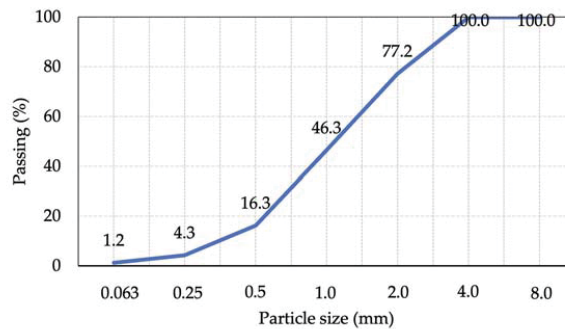
Figure 2. Gradation of fine aggregate.

Potable water was used for concrete mixtures. Water confirms the requirements of EN 1008.

2.1.3. Polycarboxylate Ether Superplasticizer (PCE)

Polycarboxylate ether is used as the superplasticizer admixture to improve the workability of cement mortar. The physical and chemical properties of PCE are shown in Table 4.

Table 4. Physical and chemical properties of the used PCE.

Polymer Type	Polycarboxylate Ether (HPEG 2400)
Appearance	White solid
Hydroxyl number (mg KOH/g)	app.117
pH-value EN 1262	5.5–7.5
Molecular weight	2400
Unsaturation (%>)	95
Color (Pt-Co<)	100

2.1.4. Air-Entraining Admixture (AIR)

SikaControl-10LPSA is a synthetic surfactant based on a brownish concrete admixture in liquid form. The physical and chemical properties of SikaControl-10LPSA are shown in Table 5.

Table 5. Physical and chemical properties of the used SikaControl-10LPSA.

Polymer Type	SikaControl-10LPSA
Density	1.00 ± 0.02 kg/L;
pH value	7.0 ± 0.5
Total chlorine ion content	— <0.1% by weight of the substance
Sodium oxide equivalent	— <0.3% by weight of the substance

2.1.5. Antifoaming Agent (AF)

The polypropylene ether was used as a component that prevents foaming of the mortar. Antifoam is a chemical agent used to reduce and prevent the formation of foams during chemical mixing. Foams will cause serious problems in chemical processes and will also prevent utilization of the whole capacity of a container. Developing conveniently and rapidly on the surface of the foam is one of the main features of antifoams [32]. The physical and chemical properties of AF (A-316) are shown in Table 6.

Table 6. Composition and properties of the used antifoam agent.

Polymer Type	Antifoaming Agent (A-316)
Appearance	Whitish powder with good fluidity
Bulk density (kg/m^3)	400–700
Dispersing ability in water	Easy dispersing into water
pH value of 1% in water 20 °C	7–9
Solubility	Surface treated, cold water soluble

2.1.6. Mix Proportion

The composition, consistency (determined according to EN 1015-3), and density (determined according to EN 1015-6) of fresh cement mixtures are presented in Tables 7 and 8. The first five specimens have been mixed with a polycarboxylate ether and designated as PCE; the other three specimens have been mixed with an air-entraining admixture. In superplasticizer mortars, the main difference between mixtures is the different W/C ratio, which varies from 0.50 and 0.38. When changing the W/C ratio, the amount of cement and water remained the same. In the case of mortar with an air-entraining admixture, the W/C ratio was equal to 0.4 for all specimens.

Table 7. Composition, consistency, and density of the mixtures with plasticizing admixtures.

№	Cement, kg	Sand, kg	Water, kg	W/C	PCE, %	AF, %	D_{av}, mm	Density, kg/m^3
C0	0.972	2.916	0.486	0.50	0	0	156	2280
P1	0.972	2.916	0.438	0.45	0.1	0.01	142	2290
P2	0.972	2.916	0.398	0.41	0.2	0.02	147	2280
P3	0.972	2.916	0.385	0.40	0.3	0.03	134	2269
P4	0.972	2.916	0.375	0.39	0.4	0.04	133	2280

Table 8. Composition, consistency, and density of the mixture with plasticizing and air-entraining admixtures.

№	Cement, kg	Sand, kg	Water, kg	W/C	PCE, %	AF,%	AIR, %	D_{av}, mm	Density, kg/m^3
P2	0.972	2.916	0.398	0.41	0.2	0.02	0	147	2280
A1	0.972	2.916	0.398	0.41	0.2	0.02	0.1	171	2150
A2	0.972	2.916	0.398	0.41	0.2	0.02	0.2	190	2062
A3	0.972	2.916	0.398	0.41	0.2	0.02	0.3	197	1959

A Portland cement sample (sample C0) was prepared for the reference sample. Three chemical admixtures were used to create seven composite admixtures with the same mass ratio as follows: polycarboxylate ether in solid-state (symbol PCE), Anti-foaming admixture (symbol AF), and Air entraining admixture SikaControl-10LPSA (symbol AIR).

Variations of polycarboxylate ether content by mass were 0%, 0.1%, 0.2%, 0.3%, and 0.4%, whereas variations of Air entraining admixture Sika (AIR) content were 0.1%, 0.2%, and 0.3% for total cementitious materials. The control samples without admixture were prepared.

Dosage of anti-foaming admixture was constant with all specimens (10% from super-plasticizer content).

Table 7 shows that with the subsequent increase in admixture (PCE and AF) in each receipt there was a decrease in the amount of water from 100% to 77%.

2.2. Methods

2.2.1. Mixing Procedure and Mixture Properties of Cement Mortar

Cement mortar components were mixed according to the EN 196-1 procedure.

The proportions by weight were one part cement, three parts of 0/2 sand, and a water/cement ratio of 0.50.

Polycarboxylate ether and air entraining admixtures were stirred with the mixing water at high speed for 1 min to obtain uniform dispersion.

After mixing of components, the consistency of fresh mortar was determined by a flow table method (EN 1015-3). The flow value was determined by measuring the spread diameter of the test samples.

The bulk density of fresh mortar was standardized by weighing a known volume of fresh mortar according to EN 1015-6, using a sample of approximately 200 mL of fresh mortar for each composition.

2.2.2. Properties of Hardened Cement Mortar

The test specimens were 40 mm × 40 mm × 160 mm^3 prisms and 100 mm × 100 mm × 100 mm^3 cubes.

Cubes were molded for determining durability; prisms were molded for density, flexural and compressive strength, and porosity testing.

The density and linear dimensions of cement prisms and cubes were tested according to EN 1015-1.

The specimens were horizontally immersed in water at a temperature of (20.0 ± 1.0) °C in containers for curing.

After 14 days, tests of the mortars were carried out for flexural and compressive strength according to EN 196-1. The specimens were loaded using a flexural and compression strength testing machine UTEST UTCM-1100.

2.2.3. The Porosity of Hardened Cement Mortar

The porosity parameters of hardened cement mortar were determined by measuring kinetics of water absorption. According to this methodology, open porosity (capillary pores), total porosity, and closed porosity (air pores) of the hardened cement mortar are defined.

The test of samples with dimensions about 40 mm × 40 mm × 40 mm^3 after splitting was carried out in a dried state to a constant mass. The samples were placed in a container

filled with water so that the water level in the container was about 50 mm higher than the upper level of the stacked samples. The water temperature in the tank was (20 ± 2) °C.

The samples are weighed 15, 30 min, and 4 h after immersion of the dried sample in water, and then every 24 h to a constant weight. According to the test results, the relative water absorption by mass was calculated. The porosity and parameters of the series of hardened cement samples are determined as the arithmetic mean of the test results of four samples of the series.

The total, open, and closed porosity of hardened cement mortar was calculated after determination of water absorption kinetics. The total porosity of hardened cement mortar is calculated by equation:

$$P_b = \left(1 - \frac{\rho_b}{\rho_s}\right), \tag{2}$$

where P_b—is the total porosity of hardened cement mortar; ρ_s—is the specific density of cement mortar, 2690 kg/m³; and ρ_b—is the density of hardened cement mortar.

Open porosity (capillary pores) of hardened cement mortar is calculated by equation:

$$P_a = W_p \cdot \frac{\rho_b}{1000}, \tag{3}$$

where P_a—is open porosity of hardened cement mortar (capillary porosity), %; and W_p—is water absorption of hardened cement mortar, %.

The closed porosity of hardened cement mortar (air porosity) is calculated as the difference between the total porosity and the open porosity.

The density of cement mortar specimens used for water absorption testing was measured according to EN 12390-7, and the volume of a specimen was determined by the water displacement method.

2.2.4. Freezing–Thawing Test Procedure

The freezing–thawing resistance of cement mortar samples was provided in the following way. The cubic cement mortar specimens after 7 days of curing were removed from the water bath and sawn in two parts perpendicular to the top surface. The test surface of the cement mortar specimen is the side surface of the cube from the mold (not the cut surface of the cube). The prepared specimens were put into the container by testing the surface of the cube downwards, supported by gaskets, and were immersed in 3% NaCl water solution to a depth of about 5 mm for 7 days before placement in the cooling chamber. The testing scheme for freezing–thawing of cement mortar specimens is presented in Figure 3. The freezing–thawing test was performed in a 3% solution of sodium chloride freezing medium. The specimens after saturation were placed into the cooling chamber and subjected to repeated freezing and thawing according to a time–temperature cycle from 20 ± 4 °C to 20 ± 2 °C and backward to 20 ± 4 °C for 24 h.
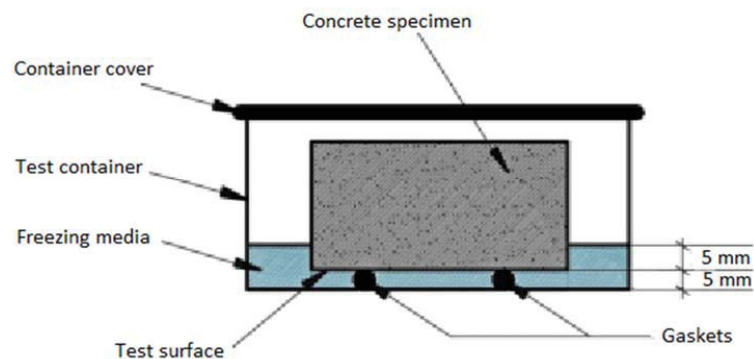
Figure 3. Testing scheme of freezing–thawing resistance of concrete.

The collection of scaled materials from cement mortar specimen test surfaces was performed after 7, 14, 21, and 28 cycles. The tested specimens' surface was rinsed and brushed to remove the scaled materials into the special vessel until no further scaled material could be removed. The liquid with scaled material from the container was poured carefully through a filter paper. The collected materials in the filter paper were washed to remove any remaining sodium chloride. After that, the filter paper and collected materials were dried to constant mass at (65 ± 5) °C for 24 h and weighed to the nearest 0.1 g. After that, the cumulative mass of the dried scaled material and scaling value from the test surface area after n freeze–thaw cycles were calculated.

The total amount of scaled materials related to the test after nth cycles m_n was calculated for each measuring occasion and each specimen is shown in equation:

$$m_n = \frac{\Sigma m_s}{A}, \tag{4}$$

where m_s—is the mass of scaled material of measurement after n cycles (kg/m^2) with an accuracy of 0.01 g. The sum is taken over all measurements until the $n$ts; A—is the area of the test surface, m^2. It is calculated based on specimen linear dimensions. They are taken as the average of at least two measurements determined to the nearest 0.5 mm.

The amount of scaling has been determined after 7, 14, 21, and 28 freeze–thaw cycles.

3. Results and Discussion

Cement mortars prepared with different admixtures at various ratios were examined by the flow table test and some mechanical tests to determine strength, flow, and freezing–thawing resistance. Pore structure development of mortars was investigated. Additionally, 0–0.4% dosages for superplasticizing and air-entraining admixture were used to indicate the admixture base effect.

3.1. Consistency, Stability, and Water Requirements

The addition of a certain amount of admixtures caused a decrease in the amount of water demand. At the initial stage, the water-reducing effect of the introduction of polycarboxylate ether into the cement-sand mixture was considered.

Figure 4, obtained by experimental work, shows the influence of PCE by weight on water demand reduction. It was observed that with an increase in the amount of superplasticizer admixture from 0.1% to 0.2% of the cement weight, the decrease in water demand for the modified cement mortars of homogeneous viscosity steadily decreases from 9.8% to 18.1%. With a further increase in the amount of superplasticizer from 0.2% to 0.4%, the decrease in the water demand of the cement mortar increases slightly from 18.1% to 22.8%. The observed phenomenon can be explained by the fact that the effect of water reduction in the availability of a superplasticizer is related to its dispersing ability, expressed through the ζ-potential. Superplasticizers, by reducing the ultimate shear stress and plastic viscosity of the mortar, can increase the characteristics of the fresh cement mortar.

Chemical admixtures are thought to improve flow performance in cement mortar by dispersing cement flocculation. Moreover, the compatibility between cement and chemical admixtures strongly depends on the physical (surface texture characteristics) and chemical (surface charge) characteristics of the additions. The effect of polycarboxylate ether and air–entraining admixture cement mortars on flow table tests can be seen in Figure 5. Figure 5 shows the variation in average flow spread of fresh mortar mixtures prepared with four dosages of PCE and three dosages of AIR in comparison to the control mixture. The flow diameter of the AIR mixture was recorded to be 197 mm, which was expected to be the highest as compared to the PCE-based mixtures. On the other hand, mixtures prepared with PCE exhibited steady diameters from 133 mm to 156 mm, owing to the use of a polycarboxylate ether admixture. Comparing the effects of PCE, it can be found that, when the dosage is less than 0.3%, PCE has no significant effect on fluidity. The flow table test results were similar to the experimental conclusions of Zhang et al. [33].
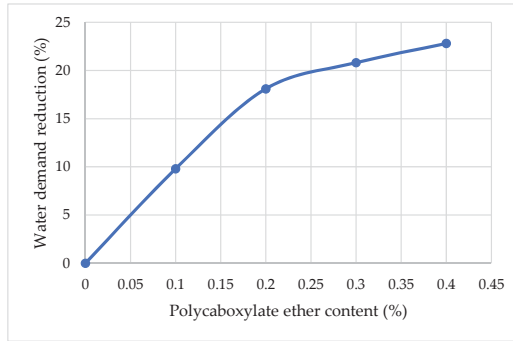
Figure 4. The influence of polycarboxylate ether content on the water demand of cement mortar.

(**a**)

(**b**)

(**c**)

Figure 5. Flow table test result: (**a**) Control specimen; (**b**) Specimen with plasticizer content; (**c**) Specimen with plasticizer and air-entraining content.

It was observed that a combination of a PCE, an AIR, and an AF admixture has been shown to increase dough flow better than the combined use of a polycarboxylate ether and an antifoam agent.

The mortar was modified with a different amount of air-entraining admixture (from 0.1% to 0.3% by weight of cement).

Results on relationships between air content and air-entraining admixture are given in Figure 6. It has been indicated that the air content of fresh cement increases with the amount of AIR in a linear fashion.
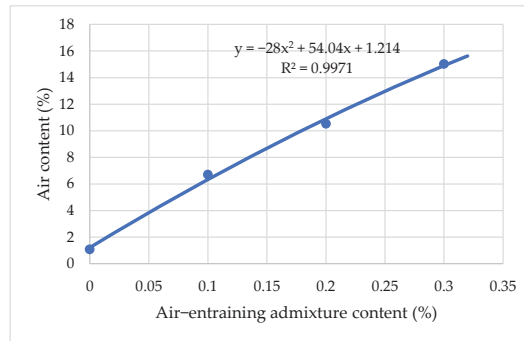
Figure 6. The influence of air-entraining admixture content on air content in cement mortar.

The efficiency of AIR content increases linearly, from 1.09% to 15.03%, with an increase in the amount of air involved in the mortar, from 0.1% to 0.3% by weight of cement (Figure 6). The stabilizing effect of air-entraining admixtures is ensured by their adsorption on the surface of air bubbles. On adding an air-entraining surfactant to cement mortar, its molecules are inserted between adjacent molecules at the water surface; the mutual attraction between the separated water molecules is reduced. Lowering the surface tension stabilizes the bubbles against mechanical deformation and rupture, making it easier for bubbles to be formed [34].

Effects of air content and type of air-entraining agent on the flowability increment of fresh cement mortar are shown in Figure 7. It can be seen that the flowability increment of fresh cement mortar increases with air content. As expected, it can be clearly seen from Figure 7 present that AIR, irrespective of type, can improve the flow of cement mortar. However, the magnitude of this improvement in fluidity depends on the type and dosage of AIR. The photos show that water separation of the cement and segregation of cement spread does not occur. When the dosage of AIR increased from 0 to 0.1%, the flow spread of mortar increased from 147 mm to 171 mm, and the flow spread increased by 16.3%. At a dosage of AIR from 0.1% to 0.3%, there was an increase in spread flow from 171 mm to 197 mm. Compared to the control sample, the maximum value of fluidity increment, 34%, was achieved by increasing the amount of air-entraining admixture from 0 to 0.3%.
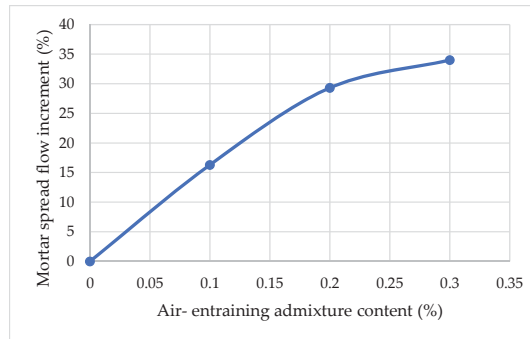
Figure 7. Effect of air-entraining agent on the fresh mortar spread flow increment.

The workability of fresh cement mortar is significantly improved due to the generation of a lot of micro-air bubbles when an air-entraining agent with high quality is added, i.e., its flowability is enhanced; however, its bleeding and segregating capacity are reduced and the cohesiveness and homogeneity of cement mortar are therefore enhanced [35].

In Figure 8, it can be seen that the efficiency of air-entraining agent (AIR) plasticization depends on its content in the Portland cement mortar. It has been established that with an increase in the amount of air-entraining agent (AIR) from 0.1% to 0.3% by weight of cement, the decrease in water demand of cement mortar of uniform viscosity steadily increases from 0 to 7.7%. With a further increase in the amount of air-entraining agent (AIR) from 0.2% to 0.3%, the water demand reduction of mortar slightly decreases from 7.7% to 8.9%. The increase in air content occurred due to improvement of the fluidity of cement mortar. Reducing the amount of water caused the formation of a structure with the smallest number of pores, this fact is confirmed by the results obtained.
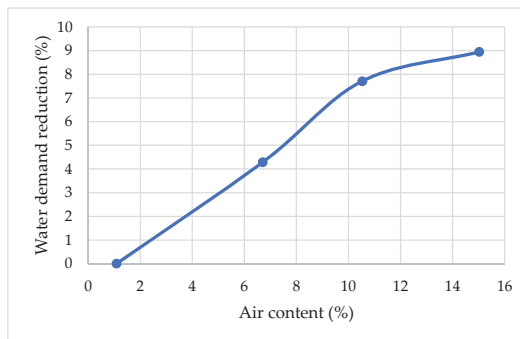
Figure 8. Effect of air-entraining admixture (AIR) on the changes in water demand of modified Portland cement.

3.2. Density and Strength of Hardened Cement Mortar Samples

The effect of polycarboxylate ether on the workability of a cement mixture and water consumption causes changes in the density of cement in a fresh and hardened state. It has been established that with an increase in the amount of polycarboxylate ether (PCE) from 0 to 0.2% by weight of cement, the density of modified cement mortar density remains constant. Figure 9 shows that with a further increase in the amount of polycarboxylate ether (PCE) from 0.2% to 0.4%, the density of cement does not change and remains at a constant density of about 2280 kg/m^3.
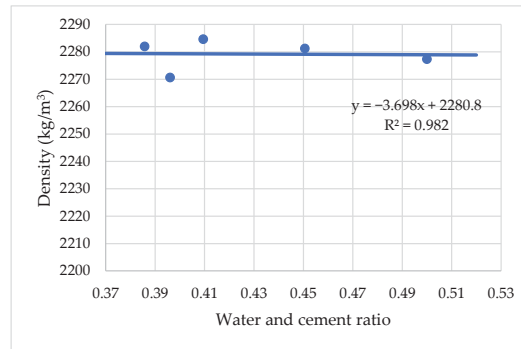
Figure 9. The influence of water cement ratio on density with PCE superplasticizer.

Air content is an important factor which affects aspects of cement mortar workability, density, and compressive strength. A comparison of densities of cement mortar modified by an air-entraining agent (AIR) is present in Figure 10. It has been demonstrated that, with an increase of air entrainment (AIR) and air content from 1% to 15%, density linearly decreases from about 2280 kg/m^3 to 1975 kg/m^3 with an increase in air content. It is found that density decreases by about 21.8 kg/m^3 when the air content is increased by about 1%.
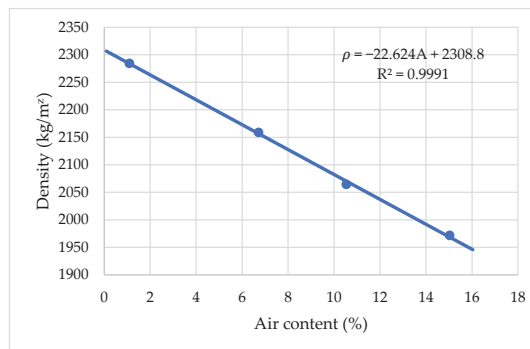
Figure 10. The influence of air-entraining content on cement mortar density.

Compressive strength (F_c) and flexural strength (F_f) values of cement mortar at an age of 14 days were calculated on the 40 × 40 × 160 mm prisms. Figure 11 shows the influence of the water to cement ratio on the compressive and flexural strength of hardened mortar at 14 days. It can be seen that, with the decrease in water and cement ration from 0.5 to 0.39, both F_c and F_f increased linearly from 74.0 MPa to 102.6 MPa and 7.2 MPa to 8.6 MPa, respectively. A more significant increase was observed in flexural strength. The obtained compressive strength and flexural strength in this article are consistent with the results of Erdem et al. [36].
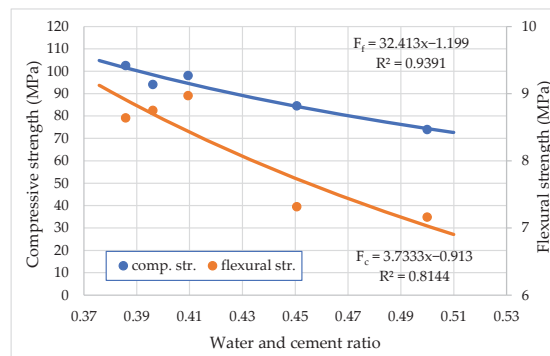
Figure 11. Effect of water to cement ratio on compressive and flexural strength of hardened mortar at 14 days with polycarboxylate ether.

The average experiment results are listed in Figure 12, with different entrained air content of F_c and F_f, respectively. It was observed that both F_c and F_f increased continuously with the decrease in air content. At the age of 14 days, the compressive strength of hardened cement mortar with 1% air content was about 75% more than cement mortar with 15% air content. The flexural strength of hardened cement mortar was about 72% more than cement mortar with 15% air content. It is noticed that compressive and flexural strength decreases by increasing the amount entrained air, whereas lower strength is caused if more voids exist in the cement mortar. This decrease can be compensated by a decrease in the water–cement ratio due to the plasticizing effect of an air-entraining admixture.
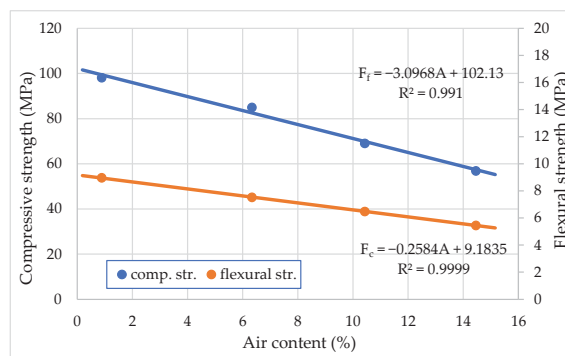
Figure 12. Effect of air content on compressive and flexural strength of hardened mortar at 14 days with an air-entraining admixture.

One main shortcoming of air-entraining agents is that the compressive strength of concrete decreases with the increase in the air content [37]. Generally, the compressive strength loss per air content is about $4 \pm 6\%$. Results on the effects of compressive strength loss per air content are displayed in Figure 12. They indicates that at the same cement content and different W/C, the compressive strength loss per air increases with the air content of the hardened cement mortar [38]. This compressive strength loss must be evaluated during the concrete mixture design process. According to impact analyses of air-entraining and superplasticizing admixtures in concrete, Nowak-Michta [39] observed that PCE increased compressive strength by 13–14%, and AIR resulted in a decrease in strength from 5% to 17%.

However, the workability of cement mortar is improved with the increase in air content; therefore, water content can be reduced, i.e., the W/C ratio of concrete with air-entraining agents can be lower. Results in Figure 12 conform this conclusion. The compressive strength of hardened cement mortar with AIR and equal workability is not reduced when the air content grows up to 4–5%.

3.3. Porosity Parameters

Results in Figure 13 show that, with an increase in the water–cement ratio from 0.39 to 0.50, the water absorption of cement mortar increases from 4.5% to 6.4%, at which a stable linear increase is observed at the initial stage. Up to 6% water absorption and assumed good concrete durability is obtained when the W/C ratio is up to 0.47. It is suggested that this process was influenced by the increased capillary porosity of hardened cement mortar with increased W/C ratio.
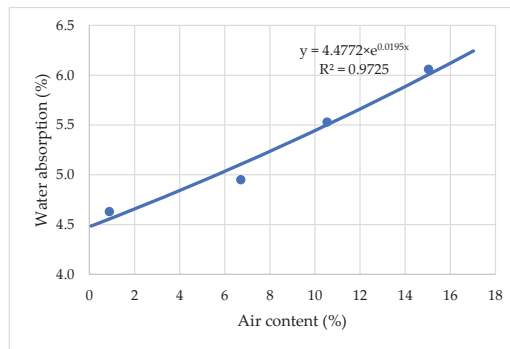
Figure 13. The influence of water absorption on water and cement ratio.

Figure 14 gives results on the relationship between air content in hardened cement mortar and water absorption. It is shown that air content in hardened cement mortar (Y) increases water absorption (X) in a linear fashion:

$$Y = 4.4287 \times e^{0.0205x} \tag{5}$$
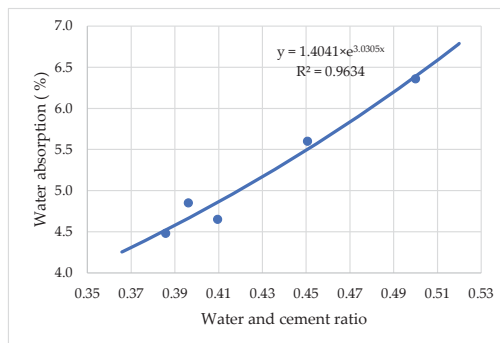
Figure 14. The influence of water consumption on the amount of air-entraining admixture.

The variation of the open and closed porosity of the cement mortar depending on the amount of PCE plasticizing admixture is shown in Figure 15. The curves in this figure show that increasing the amount of PCE plasticizing admixture to 0.4% by weight of the cement (P4 composition) decreases the open porosity (capillary) of the cement mortar by

about 29% with the reduction of W/C ratio from 0.50 to 0.38, and the closed porosity (air content in the cement mortar) increases from about 1% to about 4% compared to the control mixture without superplasticizer. The following factors can explain this phenomenon. A similar phenomenon is investigated in the work of Zhao et.al [40]. On one hand, open porosity decreased with water content in cement mortar decreasing, and more air bubbles combined with the decrease in the water content and W/C ratio of the cement mortar, thus reducing total bubble surface area. As a result of the increased cement mortar on the bubble surface, the pore wall thickened, as evidenced by decreased open porosity and increased closed porosity. The results presented in publication [41] proved that, with the introduction of air-entrapping admixture, cement mortar on the surface of the bubbles increases and the pore wall thickens accordingly, which manifests in a decrease in open porosity and an increase in closed porosity.
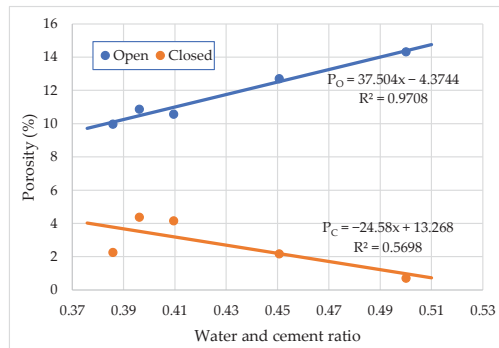
Figure 15. Effect of water to cement ratio on closed and open porosity of cement mortar.

Figure 16 shows that by increasing the amount of air-entraining admixture to 0.3% by weight of cement, both open and closed, the porosity of the hardened cement mortar changed. Open porosity of hardened cement mortar ranges from 10.68% to 11.95% and closed from 4.16% to 14.47%. Compared to the initial porosity of the cement mortar without air-entraining admixture, open porosity is increased by 11.46% and closed porosity is increased by about 71.25%. Open pores and capillaries are formed by the removal of free water, and the number and size of such pores mainly depends on the ratio of water to cement. Closed pores are formed by the incorporation of air into the mixture and the contraction of the hardening cement mortar.
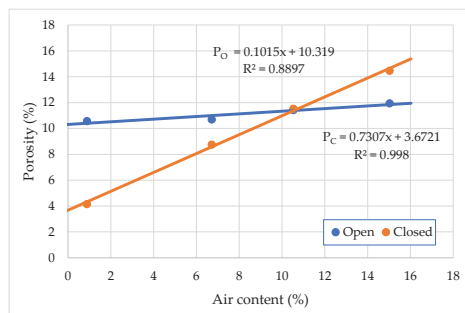
Figure 16. Effect of open and closed porosity changes on air-entraining hardened cement.

3.4. Freezing–Thawing Resistance

The final stage of the study was to determine the freezing–thawing resistance of the samples by the second accelerated CDF method under conditions of pre-saturation of the

samples in a 3% NaCl solution. Samples that hardened in air-humid conditions for 7, 14, and 28 days were exposed to the test.

The surface deterioration of the specimens, modified by carboxylate ether that underwent 14 cycles of freeze–thaw, is shown in Figure 17.
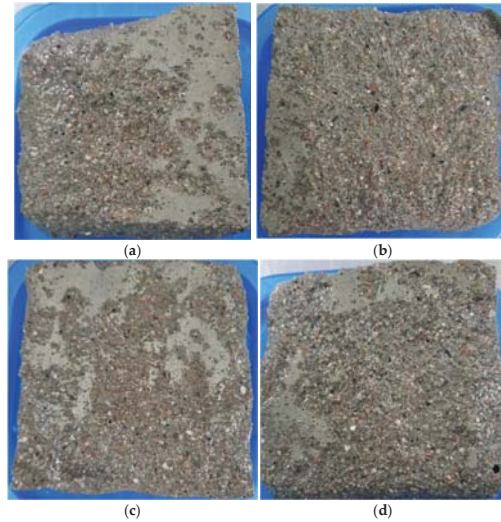
Figure 17. The surface of hardened cement mortar is modified by carboxylate polymer after 14 cycles of freeze–thaw: (**a**) C0 sample; (**b**) P1 sample; (**c**) P3 sample; (**d**) P4 sample.

The surface deterioration of the air-entraining hardened cement mortar (HCM) specimens during 14 cycles of freeze–thaw are shown in Figure 18.
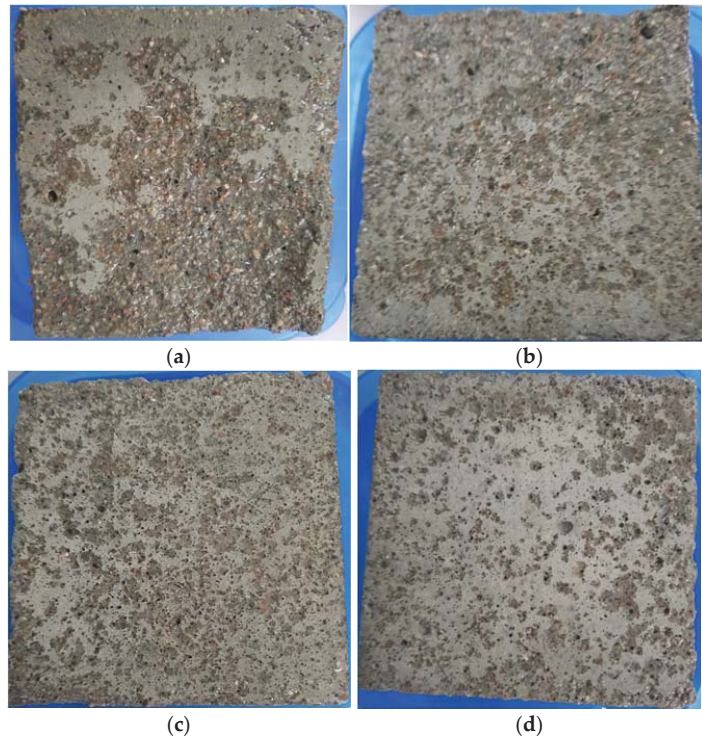
Figure 18. The surface of air-entraining hardened cement mortar after 14 cycles of freeze–thaw:
(**a**) P3 sample; (**b**) A1 sample; (**c**) A2 sample; (**d**) A3 sample.

The figures show the appearances of specimens after different freeze–thaw cycles. The surface of cubic specimens became rough, and the surface mortar was loosened gradually with the increasing freezing–thawing cycles. With seven freeze–thaw cycles, only slight scaling of the cement mortar was observed on the surface of the specimen. It can be seen that the cement mortar was spalled at the corner of a cubic specimen with polycarboxylate ether admixture after 14 cycles. In the case of samples with additional an air-entraining admixture, no spalls were observed at the corners of the cubes. After 14 cycles, the shape was complete due to the periodic freezing and thawing process, and the mortar around the sample did not fall off seriously. Obtained test results indicated by Nowak-Michta et.al [42] show good scaling resistance results after freeze–thaw cycles.

The freezing–thawing resistance of hardened cement mortar modified by plasticizers in a water freezing medium improved with an increase in plasticizer dosage and reduction of the W/C ratio. Figure 19 presents the scaling of cement specimens with carboxylate polymer dosage from 0 to 0.4% during freezing-thawing cycles.
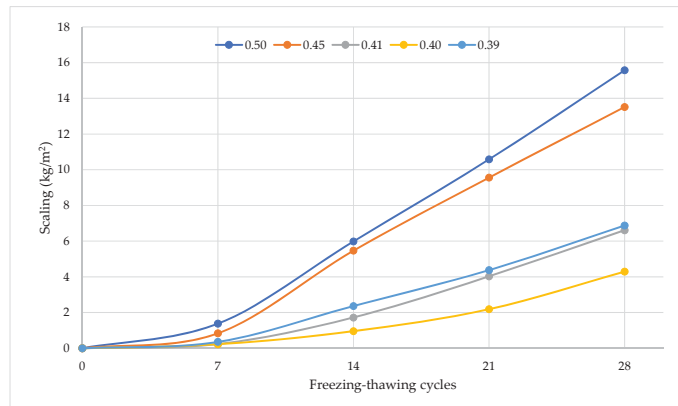
Figure 19. Hardened cement mortar scaling results during a freezing–thawing test in freezing water with different W/C ratio.

Figure 20 presents the scaling of cement specimens with air-entraining dosage after freezing–thawing cycles. The maximum scaling was observed for ordinary cement without air-entraining admixture. After 18 freezing–thawing cycles, it exceeded 1 kg/m^2. The figure clearly shows the advantage of formulations with complex admixtures over the plasticizing admixture composition. As shown in these figures, the scaling rate of both cement specimens increased over the whole process of freeze–thaw cycles. For the air-entraining group, the scaling of specimens increased slightly before 14 cycles. This is attributed to the cement mortar's capillary pore low water absorption and closed porosity volume compensation effect. As the freezing and thawing cycles increased, the internal micro-cracks and pores of the concrete gradually expanded and became connected, causing the surface of the specimen to crumble. For the polycarboxylate ether group, the scaling rate of cement cube specimens significantly changed before 14 freeze–thaw cycles. However, after 21 cycles, the scaling rate of specimens had an obviously larger increase than the air-entraining group. At 28 freeze–thaw cycles, the scaling rates of cement specimens with polycarboxylate ether were 15.57 kg/m^2, 13.51 kg/m^2, 6.61 kg/m^2, 4.29 kg/m^2, and 6.87 kg/m^{2,} and with air-entraining admixture were 6.61 kg/m^2, 2.62 kg/m^2, 0.97 kg/m^2, and 0.45 kg/m^2, respectively.
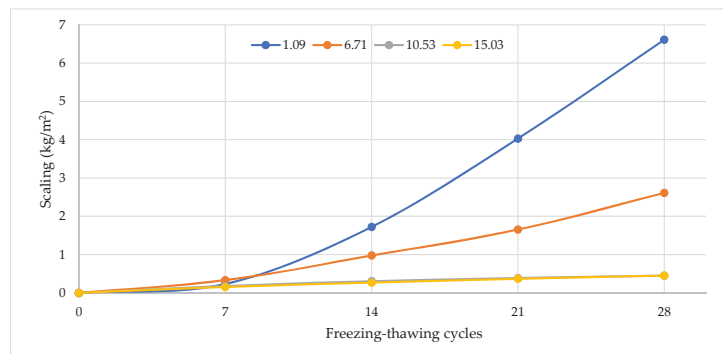
Figure 20. Hardened cement mortar scaling results during a freezing–thawing test in freezing water with W/C ratio and air-content.

Furthermore, the relationship between scaling rate and freeze–thaw cycles clearly shows two distinct stages. In the first 0–7 freeze–thaw cycles, the weight of concrete speci-

mens shows a slightly increasing trend or is unchanged during the damage accumulation stage. However, after 14 freeze–thaw cycles, the scaling rate for the PCE and AIR group specimens increases significantly, indicating the damage acceleration stage.

The density and porosity properties of cement mortar after 28 days of curing in normal conditions are presented in Table 9. The data presented in Table 9 show that the highest criterion for the resistance of a hardened cement paste to frost and the predicted resistance to frost according to the number of freezing and thawing cycles are typical for the control sample (C0 composition). The obtained scaling results of cement mortar specimens in this article are consistent with the results of Zheng et al. [8], Xu et.al [43], and Yuan et.al [44]. Increasing the amount of plasticizing admixture from 0.1% to 0.4% by weight of cement decreases the criteria for frost resistance and the predicted frost resistance according to the number of freezing and thawing cycles. The porosity parameters of cement were determined according to the kinetics of water absorption.

Table 9. Results of freeze–thaw resistance of hardened cement paste after 28 freeze–thaw cycles.

Series	Density, kg/m^3	Porosity, %		K_F	Scaling after 28 Cycles, kg/m^2
		Open	Closed		
C0	2277	14.32	0.71	0.55	15.57
P1	2281	12.71	2.18	1.91	13.51
P2	2285	10.58	4.16	4.37	6.61
P3	2271	10.88	4.38	4.47	4.29
P4	2282	9.97	2.26	2.52	6.87
A1	2159	10.69	8.75	9.09	2.61
A2	2065	11.42	11.53	11.22	0.97
A3	1972	11.95	14.47	13.45	0.45

The frost resistance of cement mortar of concrete can be predicted according to the frost resistance factor K_F. The factor shows that the frost resistance of the tested hardened cement must be about 28 freezing–thawing cycles. It was experimentally determined that after 28 freezing–thawing cycles the scaling of cement increased from 0.45 kg/m^2 to 15.57 kg/m^2.

In general, all concrete samples have shown a reduction in mass during the test, and this reduction increases with the increasing number of applied cycles.

Statistical processing of test results by using an exponential function model produced a function (Figure 21) of scaling (m_c) and a frost resistance factor (K_F). The correlation coefficient of the function is 0.9246. The test results have shown that frost resistance of cement-based material depends on closed and open porosity, and that parameters can be used for frost resistance prediction. Figure 21 shows that, due to the plasticizing effect of the cement mixture, the scaling ranges from about 15.5 kg/m^2 to 4.5 kg/m^2 can be reduced, and with additional air-entraining effect reduction in scaling from about 4.5 kg/m^2 to 0.45 kg/m^2 can be achieved.
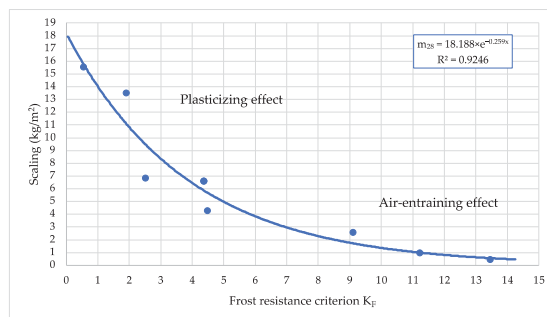
Figure 21. The influence of frost resistance factor on frost resistance of cement in freezing–thawing cycles.

4. Conclusions

According to the experimental results, the following conclusions can be drawn:

1. Due to the formation of the appropriate structure of capillary pores in the hardened cement mortar, the durability of cement-based material depends on the W/C ratio. The W/C ratio can be reduced by using plasticizers and increasing the amount of air content in the mixture. An increase in the amount of carboxylate ether from 0 to 0.4% (in dry material) caused a decrease in water demand for constant workability concrete up to 22.8%, and a reduction of scaling from 15.6 kg/m^2 to 4.3 kg/m^2.

2. By increasing the amount of air content in the cement-based material from 1.09% to 15.03%, the consistency of the cement mortar was improved about 34% and a decrease in water demand can be obtained up to 8.9% for the same consistency. The use of air-entraining admixtures significantly increased the fluidity of the cement mortar and increased the stability of air-entrained mixtures.

3. An increase in the amount of air content in a cement-based material from 1.09% to 15.03% leads to a decrease in compressive strength by 42.0% and flexural strength by 39.1%: about 3.0% and 2.8% accordingly for 1% of entrained air. The density of cement mortar in fresh and hardened states using polycarboxylate ethers was constant instead of an air-entraining admixture. The air-entraining admixture reduces hardened cement mortar density from 2280 kg/m^3 to 1975 kg/m^3.

4. The combined effect of plasticizing and air-entraining admixtures leads to a negligible increase (about 1%) in open porosity, an increase in closed porosity up to 10%, and a large increase in frost resistance factor (K_F) (from 0.55 to 13.45) and the frost resistance of concrete (reduction of scaling from 15.57 kg/m^2 to 0.45 kg/m^2).

5. By the plasticizing effect reducing W/C ratio from 0.50 to 0.39, an improvement in freezing–thawing resistance can be achieved up to about 4.5 kg/m^2 scaling. With a joint decrease in the water–cement ratio and an increase in the amount of entrained air content, the frost resistance of concrete increases, the scaling decreases exponentially up to about 0.45 kg/m^2 scaling, and it is possible to obtain greater frost resistance of cement-based material.

To sum up, the obtained results on investigated cement mortars can be used for selection of freezing–thawing resistance concrete composition. The use of plasticizing and air-entraining admixture positively affects mechanical properties and porosity parameters of cement mortar.

From a practical standpoint, the research results presented in this paper allow for the prediction of freezing–thawing resistance of concrete during the design of the composition of the concrete mixture. The prediction of freezing–thawing resistance can be used for concrete with polycarboxylate ether superplasticizers. The freezing–thawing resistance of concrete will be evaluated in scaling resistance (in kg/m^2).

Institutional Review Board Statement: Not applicable.

Informed Consent Statement: Not applicable.

Data Availability Statement: Data contained within the article.

Conflicts of Interest: The authors declare no conflict of interest.

References

1. Shuldyakov, K.; Trofimov, B.; Kramar, L. Stable Microstructure of Hardened Cement mortar—A Guarantee of the Durability of Concrete. *Case Stud. Constr. Mater.* **2020**, *12*, e00351. [CrossRef]
2. Öztürk, A.U.; Kaplan, G. A study of some durability properties of mortars with white cement and Portland cement. *Rom. J. Mater.* **2017**, *47*, 315–321.
3. Kahraman, E.; Ozdemir, A.C. The Prediction of Durability to Freeze–Thaw of Limestone Aggregates Using Machine-Learning Techniques. *Constr. Build. Mater.* **2022**, *324*, 126678. [CrossRef]
4. Netinger Grubeša, I.; Marković, B.; Vračević, M.; Tunkiewicz, M.; Szenti, I.; Kukovecz, Á. Pore Structure as a Response to the Freeze/Thaw Resistance of Mortars. *Materials* **2019**, *12*, 3196. [CrossRef]
5. Sun, J.; Zhang, P. Effects of Different Composite Mineral Admixtures on the Early Hydration and Long-Term Properties of Cement-Based Materials: A Comparative Study. *Constr. Build. Mater.* **2021**, *294*, 123547. [CrossRef]
6. Yang, Z.; He, R.; Tan, Y.; Chen, H.; Cao, D. Air Pore Structure, Strength and Frost Resistance of Air-Entrained Mortar with Different Dosage of Nano-SiO₂ Hydrosol. *Constr. Build. Mater.* **2021**, *308*, 125096. [CrossRef]
7. Seong-Tae, Y.; Sue-Won, P.; Jin-Keun, K. Minimum Curing Time Prediction of Early-Age Concrete to Prevent Frost Damage. *Constr. Build. Mater.* **2011**, *25*, 1439–1449. [CrossRef]
8. Zeng, H.; Lai, Y.; Qu, S.; Yu, F. Exploring the Effect of Graphene Oxide on Freeze–Thaw Durability of Air-Entrained Mortars. *Constr. Build. Mater.* **2022**, *324*, 126708. [CrossRef]
9. Tunstall, L.E.; Ley, M.T.; Scherer, G.W. Air Entraining Admixtures: Mechanisms, Evaluations, and Interactions. *Cem. Concr. Res.* **2021**, *150*, 106557. [CrossRef]
10. Jie, Y.; Yue, W.; Jiake, Z. Characterization of Air Voids and Frost Resistance of Concrete Based on Industrial Computerized Tomographical Technology. *Constr. Build. Mater.* **2018**, *168*, 975–983. [CrossRef]
11. Fonseca, P.C.; Scherer, G.W. An Image Analysis Procedure to Quantify the Air Void System of Mortar and Concrete. *Mater. Struct.* **2015**, *48*, 3087–3098. [CrossRef]
12. Jin, S.; Zhang, J.; Huang, B. Fractal Analysis of Effect of Air Void on Freeze–Thaw Resistance of Concrete. *Constr. Build. Mater.* **2013**, *47*, 126–130. [CrossRef]
13. Feng, Y.; Zongke, L.; Ningxia, Y. Effect of the Compounding of an Antifoaming Agent and a Viscosity Modifying Agent on the Frost Resistance of Mold Bag Concrete. *Constr. Build. Mater.* **2021**, *308*, 125016. [CrossRef]
14. Zheng, X.H.; Li, Q.F.; Yuan, J.; Ge, Y. The Flexural Strength and Frost Resistance of Air Entrained Concrete. *AEF* **2012**, *5*, 364–369. [CrossRef]
15. Romero Rodríguez, C.; França de Mendonça Filho, F.; Chaves Figueiredo, S.; Schlangen, E.; Šavija, B. Fundamental Investigation on the Frost Resistance of Mortar with Microencapsulated Phase Change Materials. *Cem. Concr. Compos.* **2020**, *113*, 103705. [CrossRef]
16. Zhang, K.; Zhou, J.; Yin, Z. Experimental Study on Mechanical Properties and Pore Structure Deterioration of Concrete under Freeze–Thaw Cycles. *Materials* **2021**, *14*, 6568. [CrossRef]
17. Lazniewska-Piekarczyk, B.; Gołaszewski, J. Relationship Between Air-Content in Fresh Cement mortar, Mortar, Mix and Hardened Concrete Acc. to PN-EN 480-1 with Air-Entraining CEM II/B-V. *IOP Conf. Ser. Mater. Sci. Eng.* **2019**, *471*, 032044. [CrossRef]
18. Ugur Ozturk, A.; Tugrul Erdem, R. Influence of the air-entraining admixture with different superplasticizers on the freeze-thaw resistance of cement mortars. *Rom. J. Mater.* **2016**, *46*, 75–81.
19. Wang, X.; Subramaniam, K.V. Ultrasonic Monitoring of Capillary Porosity and Elastic Properties in Hydrating Cement mortar. *Cem. Concr. Compos.* **2011**, *33*, 389–401. [CrossRef]
20. Skripkiunas, G.; Vaitkevicius, V.; Daukus, M.; Grinys, A. Prediction of Concrete Freezing-Thawing Resisitance. In Proceedings of the International Conference Held at the University of Dundee, Dundee, UK, 8–9 July 2008; pp. 317–324.
21. Shinichi, I.; Akio, W.; Mitsunori, K. Evaluation of Capillary Pore Size Characteristics in High-Strength Concrete at Early Ages. *Cem. Concr. Res.* **2005**, *35*, 513–519. [CrossRef]
22. Nagrockiene, D.; Skripkiunas, G.; Girskas, G. Predicting Frost Resistance of Concrete with Different Coarse Aggregate Concentration by Porosity Parameters. *Mater. Sci.* **2011**, *17*, 203–207. [CrossRef]
23. Funk, B.; Gohler, D.; Sachsenhauser, B.; Stintz, M.; Stahlmecke, B.; Johnson, B.A.; Wohlleben, W. Impact of freeze–thaw weathering on integrity, internal structure and particle release from micro and nanostructured cement composites. *Enviromental Sci. Nano* **2019**, *6*, 1443–1456. [CrossRef]
24. Setzer, M.J.; Fagerlund, G.; Janssen, D.J. CDF Test—Test Method for the Freeze-Thaw Resistance of Concrete-Tests with Sodium Chloride Solution (CDF): Recommendation. *Mat. Struct.* **1996**, *29*, 523–528. [CrossRef]
25. Akhras, N.M. Detecting Freezing and Thawing Damage in Concrete Using Signal Energy. *Cem. Concr. Res.* **1998**, *28*, 1275–1280. [CrossRef]
26. Malaiskiene, J.; Skripkiunas, G.; Vaiciene, M.; Karpova, E. The Influence of Aggregates Type on W/C Ratio on Concrete's Strength and Other Properties. *IOP Conf. Ser. Mater. Sci. Eng.* **2017**, *251*, 012025. [CrossRef]
27. Kobayashi, K.; Miura, S.; Oshima, E.; Yun, H.-D. Mechanisms of High Frost Scaling Resistance of SHCC. *Constr. Build. Mater.* **2022**, *324*, 126300. [CrossRef]
28. Zarauskas, L.; Skripkiūnas, G.; Girskas, G. Influence of Aggregate Granulometry on Air Content in Concrete Mixture and Freezing—Thawing Resistance of Concrete. *Procedia Eng.* **2017**, *172*, 1278–1285. [CrossRef]

29. Łaźniewska-Piekarczyk, B. The Influence of Admixtures Type on the Air-Voids Parameters of Non-Air-entraining and Air-entraining High Performance SCC. *Constr. Build. Mater.* **2013**, *41*, 109–124. [CrossRef]
30. Zeng, Q.; Li, L.; Pang, X.; Gui, Q.; Li, K. Freeze–Thaw Behavior of Air Entrained Cement mortar Saturated with 10 wt.% NaCl Solution. *Cold Reg. Sci. Technol.* **2014**, *102*, 21–31. [CrossRef]
31. Jiang, P.; Chen, Y.; Wang, W.; Yang, J.; Wang, H.; Li, N.; Wei, W. Flexural Behavior Evaluation and Energy Dissipation Mechanisms of Modified Iron Tailings Powder Incorporating Cement and Fibers Subjected to Freeze-Thaw Cycles. *J. Clean. Prod.* **2022**, *351*, 131527. [CrossRef]
32. Bahranifard, Z.; Farshchi Tabrizi, F.; Vosoughi, A.R. An Investigation on the Effect of Styrene-Butyl Acrylate Copolymer Latex to Improve the Properties of Polymer Modified Concrete. *Constr. Build. Mater.* **2019**, *205*, 175–185. [CrossRef]
33. Zhang, Z.; Feng, Q.; Zhu, W.; Lin, X.; Chen, K.; Yin, W.; Lu, C. Influence of Sand-Cement Ratio and Polycarboxylate Superplasticizer on the Basic Properties of Mortar Based on Water Film Thickness. *Materials* **2021**, *14*, 4850. [CrossRef] [PubMed]
34. Qaraman, A.F. The efficiency of mixed surfactants as air entraining agents in cement pastes. *Eur. J. Mater. Sci.* **2016**, *3*, 12–22.
35. Yang, Q.; Zhu, P.; Wu, X.; Huang, S. Properties of Concrete with a New Type of Saponin Air-Entraining Agent. *Cem. Concr. Res.* **2000**, *30*, 1313–1317. [CrossRef]
36. Erdem, R.T.; Ozturk, A.U.; Gucuyen, E. Estimation of Compressive Strength of Cement Mortars. *Rom. J. Mater.* **2016**, *46*, 313–318.
37. Wang, R.; Gao, X. Relationship between Flowability, Entrapped Air Content and Strength of UHPC Mixtures Containing Different Dosage of Steel Fiber. *Appl. Sci.* **2016**, *6*, 216. [CrossRef]
38. Karakurt, C.; Bayazit, Y. Freeze-Thaw Resistance of Normal and High Strength Concretes Produced with Fly Ash and Silica Fume. *Adv. Mater. Sci. Eng.* **2015**, *2015*, 830984. [CrossRef]
39. Nowak-Michta, A. Impact Analysis of Air-Entraining and Superplasticizing Admixtures on Concrete Compressive Strength. *Procedia Struct. Integr.* **2019**, *23*, 77–82. [CrossRef]
40. Zhao, R.; Wing, Y.; Tian, C.Y.; Xu, A. The Influence of Water/Cement Ratio and Air Entrainment on the Electric Resistivity of Ionically Conductive Mortar. *Materials* **2019**, *12*, 1125. [CrossRef]
41. Liu, Z.; Zhao, K.; Hu, C.; Tang, Y. Effect of Water-Cement Ratio on Pore Structure and Strength of Foam Concrete. *Adv. Mater. Sci. Eng.* **2016**, *9*, 9520294. [CrossRef]
42. Nowak-Michta, A. Additional Porosity as a Side Effect of Polycarboxylate Addition and Its Influence on Concrete's Scaling Resistance. *Materials* **2020**, *13*, 316. [CrossRef] [PubMed]
43. Xu, Y.; Yuan, Q.; Dai, X.; Xiang, G. Improving the Freeze-Thaw Resistance of Mortar by a Combined Use of Superabsorbent Polymer and Air Entraining Agent. *J. Build. Eng.* **2022**, *52*, 104471. [CrossRef]
44. Yuan, J.; Du, Z.; Wu, Y.; Xiao, F. Freezing-Thawing Resistance Evaluations of Concrete Pavements with Deicing Salts Based on Various Surfaces and Air Void Parameters. *Constr. Build. Mater.* **2022**, *204*, 317–326. [CrossRef]

Article

Effects of Field Aging on Material Properties and Rutting Performance of Asphalt Pavement

Haoyang Wang [1,2], Yu Zhu [3], Weiguang Zhang [3,*], Shihui Shen [4], Shenghua Wu [5], Louay N. Mohammad [6] and Xuhui She [3]

1   RoadMaint Co., Ltd., Beijing 100095, China
2   Research Institute of Highway, Ministry of Transportation, Beijing 100008, China
3   School of Transportation Engineering, Southeast University, Nanjing 210096, China
4   Rail Transportation Engineering, Pennsylvania State University, 216E Penn Building, Altoona, PA 16601, USA
5   Department of Civil, Coastal, and Environmental Engineering, University of South Alabama, Baton Rouge, AL 36688, USA
6   Louisiana Transportation Research Center, Department of Civil and Environmental Engineering, Louisiana State University, Mobile, LA 70808, USA
*   Correspondence: wgzhang@seu.edu.cn; Tel.: +86-13912956989

Abstract: This study evaluates field asphalt aging based on material property changes in pavement with time, and investigates if such changes could have an impact on field rutting performance. Four projects from three different climate zones were monitored as part of the NCHRP 9–49A project at two stages: during pavement construction and two to three years after opening it to traffic. Construction information were collected, and field cores were drilled at both stages to evaluate the material properties of recovered asphalt binder and asphalt mixture. Field rut depth was also measured. In addition, pavement structure, climate and base/subgrade modulus information were also obtained. Results indicate that the asphalt mixture stiffening is caused in major part by asphalt aging. However, the effect of asphalt aging on pavement mixture property may not follow a proportional liner trend. The parameters that are most sensitive to field ageing are MSCR *R3.2* and dynamic modulus. It is also found that the variables which showed a good ranking trend with the field rut depth are climate condition (relative humidity, high temperature hour, solar radiation), material properties (Hamburg rut depth, rutting resistance index, high temperature performance grade, MSCR, and dynamic modulus, base and subgrade moduli), as well as air voids.

Keywords: asphalt aging; material property; climate condition; pavement structure; field rut depth

1. Introduction

Asphalt binder is a material widely used in paving engineering to hold aggregates. It is a special hydrocarbon composite with complex mechanical properties and plays a major role in determining the performance of asphalt pavements. However, asphalt materials tend to oxidize under the influence of environmental factors such as temperature, humidity and solar radiation, leading to changes in its mechanical and rheological properties.

Laboratory and field studies have shown that after oxidization, the stiffness of the asphalt binder increased [1–3]. Previous research using recovered binder from field cores found that high-temperature performance grade (PG) increased 2.4 to 26.6 °C for pavements aged between 10 and 82 months [4]. With ageing, the weak attractions of the asphaltene are destroyed, and asphalt molecules change their orientation and become more tightly packed [5]. In addition, the ageing process resulted in stronger associations between asphalt components due to the generation of polar carbonyl groups, which increased the asphaltene fraction [2]. Changes in both its elastic modulus and its viscosity lead to stiffening of the binder.

For the asphalt mixture, numerous laboratory studies have been implemented to investigate property changes with the aging of the asphalt binder. They have shown that the resilient modulus of long-term oven-aged specimens is 50–100% higher than that of short-term oven-aged specimens [2,6]. Moreover, some researchers assumed that due to diffusion resistance, binder oxidation rates in mixtures are slower than that in thin-film neat binders due to diffusion resistance [7–10]. The Hirsch model is often used to describe the relationship between asphalt and the asphalt mixture; however, it was found that due to binder hardening, the mixture ageing actually stiffened the mixture more than the model predicted.

However, few field tests have been performed due to the impact of multiple factors such as climate and binder modification. The current research only focuses on the influence of the dynamic modulus. For instance, the dynamic modulus of field cores in Texas increased by approximately 70% and 130% at the end of 8 and 14 months compared with that at 1 month [3]. On the other hand, such increases are much less, with 27–31% after one year of service in the cold regions of Sweden [11]. Furthermore, it was found that polymer- and rubber-modified binders may reduce the ageing rate in contrast to unmodified binders [4,12,13], and the Evotherm WMA binder generally ages faster than the HMA and Foaming WMA binders [1,3,4].

In summary, most aging studies are focused on laboratory aging, and very few studies have attempted to examine the effects of field aging on the property evolution of asphalt and asphalt mixture. In addition, the field studies in most cases were based on one specific project; thus, the effect of factors such as climate condition, HMA layer thickness and binder types cannot be well analyzed [14,15]. More importantly, limited research exists on how the change in field binder properties over time has affected field mixture properties [16,17]. This study evaluates and quantifies the effect of field aging on the rutting performance of asphalt binders and asphalt mixture over time using field projects from different climatic zones. The study also analyzes the effect of asphalt binder property change on mixture alternation.

2. Methodology

Four projects selected from the NCHRP 9–49A project report 843 were used for performing the analysis introduced in this paper. These projects were selected to cover different pavement structures and material properties. Within each project, field cores were taken and material properties that are typically used to describe asphalt stiffness and rutting resistance were tested, consisting of binder high temperature PG, binder multiple stress creep recovery (MSCR), mixture dynamic modulus and mixture Hamburg rut depth. These material properties were tested based on field cores taken at two different periods. In the first series, cores were obtained shortly after pavement construction and in the second series cores were obtained two to three years after the construction was finished. All the field cores were taken inside the wheel path to study purely the effect of aging to exclude the effects of traffic load. Other factors that may affect field aging and field rut depth were also collected, consisting of in-place air voids, pavement structure and climate. Additionally, aggregate gradation and asphalt content were obtained to confirm that no significant changes in the cores happened due to traffic. The material properties between the two series of field aging were compared. The effect of asphalt property change on the asphalt mixture properties was also analyzed.

3. Project Information

Four projects that were constructed in 2011 and 2012 were investigated, which covered different climatic zones, pavement types (HMA and WMA), traffic levels and pavement structures. The four pavement projects were located in four states: Montana, Tennessee, Iowa and Louisiana, and are therefore referred to the MT I-15, TN SR 125, IA US 34 and LA US 61. Three 61-m test sections of HMA and WMA pavements were selected for further study. Field construction information of the four projects that was collected includes:

- Pre-construction information: mixture design, technology type (i.e., HMA or WMA), existing pavement structure, existing pavement conditions, target mixing and compaction temperatures, mile post or GPS information for the selected three 61 m research test sections, etc.
- During-construction information: plant modification, weather, material type, aggregate moisture content, mixing and compaction temperatures, transportation distance, in situ density, procurement of field gyratory-compacted samples, loose mixtures and raw materials, and any other significant information that should be noted, etc.
- Post-construction information: quality control/quality assurance (QC/QA) data, procurement of cores, falling weight deflectometer (FWD) testing, location of field cores, annual average daily truck traffic (AADTT).

The key information for the four field projects is concluded in Table 1. Each project includes at least one WMA technology and a homological control HMA pavement. More detailed information of the four projects can be found in the NCHPR report 843 [18].

Table 1. Specimen Grading for Indoor Test.

Parameter	MT I-15	TN SR 125	IA US 34	LA US 61
Construction year	2011	2011	2011	2012
Warm mix type	Sasobit, Evotherm DAT, Foam	Evotherm 3G	Sasobit, Evotherm 3G	Sasobit, Evotherm 3G
Mixing temp. (°C)	H (157–160) W (139–149)	H (160–177) W (143–160)	H (166–171) W (129–138)	H (163) W (146)
Compaction temp. (°C)	H (143–149) W (132–141)	H (155–168) W (135–143)	H (123–104) W (104–115)	H (136–158) W (118–121)
Traffic, AADTT	833	451	703	4779
Aggregate	Siliceous	Gravel and sand	Limestone, quartzite, sand	Granite and limestone
NMAS (mm)	19	12.5	12.5	12.5
Asphalt binder	PG 70-28	PG 70-22	PG 58-28	PG 76-22
Anti-stripping agent	hydrated lime, 1.4%	AZZ-MAZ, 0.3%	none	0.6%
Polymer modified	SBS	Yes	none	SBS
Asphalt content (%)	4.6	6.0	5.4	4.7
G_{mm}	H (2.458) S (2.466) E (2.459) F (2.453)	H (2.352) E (2.355)	H (2.423) S (2.428) E (2.429)	H (2.464) S (2.468) E (2.464)
Sampling date, 1st round	Sep., 2011	Oct., 2011 and Aug.,2012	Sep., 2011	May–June, 2012
Sampling date, 2nd round	Aug., 2013	Dec., 2014	Dec., 2014	Feb., 2015
RAP or RAS	none	10% RAP	17% RAP	15% RAP

Note: H—HMA, W—WMA, S—Sasobit, E—Evotherm, F—Foaming, NMAS—nominal maximum aggregate size, AADTT—average annual daily truck traffic.

3.1. Pavement Structure

The pavement structure that was used for each project is shown in Figure 1. The thickness of each pavement layer is presented, and the subgrade soil is assumed to be infinite in depth. Two existing pavement structure types were selected, including flexible pavements and a combination of asphalt/PCC pavements.
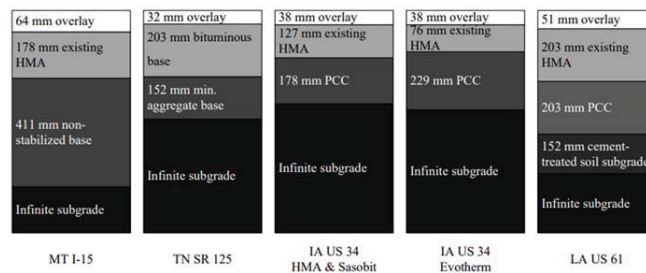
Figure 1. Pavement structure diagram of each project. (From top to bottom in turn are overlay, existing HMA, base, and subgrade respectively).

3.2. Field Climate Information

Climate information, consisting of high temperature hour, shortwave solar radiation and humidity are highly related to asphalt aging [2,18,19] and were obtained from the long-term pavement performance (LTPP) website, InfoPave. The number of air temperature

hours referred to in this paper is the hours when the pavement temperatures are higher than 25 °C, as recommended [19]. As shown in Figure 2, the MT I-15 project has the lowest values of relative humidity, air temperature hour > 25 °C, shortwave solar radiation and indicating the least ageing impact. The other three projects experienced similar relative humidity and shortwave solar radiation. The LA US 61 project had the highest value of air temperature hour > 25 °C and may have encountered the most severe ageing. Note that the climate information comprises the accumulated values which cover the period of being open to traffic until the second round of field core samples were taken.
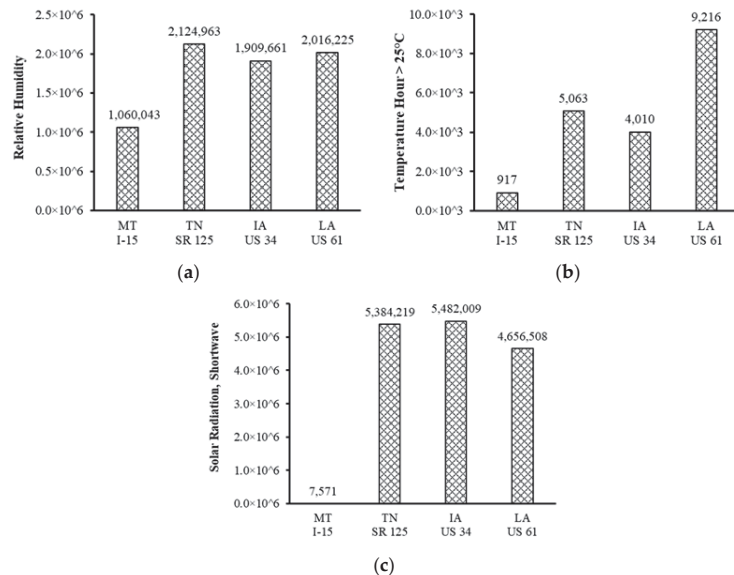
Figure 2. Field climate information: (**a**) relative humidity; (**b**) air temperature hour > 25 °C; (**c**) shortwave solar radiation.

4. Data Collection

4.1. Field Climate Information

Cores were taken in the field from the non-wheel path to limit the potential of pre-existing damage in the material. In the laboratory, the existing pavement was removed for further core tests. After the core fracture test, binder extraction and recovery were performed using the entire overlay specimen to evaluate the average aging effect without taking the aging gradient variation through overlay thickness into account.

4.2. Binder Extraction and Recovery

Asphalt binders were extracted based on AASHTO T164 and recovered according to AASHTO R59. The used chemical was a combination of 85% Toluene and 15% Ethanol by volume. Both WMA and HMA on-site cores were heated 110 °C until they were loose enough to separate. The separated mixtures were cooled down at room temperature before extraction. The minimum mass of samples used for binder extraction was determined by nominal maximum aggregate size (NMAS). Usually, several extractions were needed until the extract was no darker than a light straw color. Recovered binders were tested by taking them as short-term aged (rolling thin-film oven-aged) asphalt, as suggested [14,15].

4.3. Aggregate Gradation and Asphalt Content

Aggregate gradation and asphalt content were checked using the field cores after fracture tests for both the first-round and the second-round surveys. The asphalt content

was determined in accordance with AASHTO T 308, and aggregated gradation was checked following AASHTO T 30.

4.4. Material Properties

In the laboratory, an overlay of field cores and recovered asphalt binders was used to conduct a series of laboratory tests to determine the physical and engineering material properties. Table 2 shows the summary of all the laboratory mixture and binder tests. The MSCR test temperatures were determined based on the high pavement temperature of specific project locations obtained from LTPPBind Version 3.1 software (Federal Highway Administration, Washington, DC, USA) at 98% reliability.

Table 2. Summary of Laboratory Mixture and Binder Testing.

Test	IDT, Mixture	HWT, Mixture	DSR, Binder	DSR, Binder	Other Test
Test conditions	Temperature (°C): −20, −10, 0, 10, 20, 30 Frequency (Hz): 20, 10, 5, 1, 0.1, 0.01	50 °C	Temperature: depends on asphalt	High pavement temperature, stress: 0.1, 3.2 kPa	Depends on test
Material properties	Dynamic modulus	Rut depth	High temperature PG	MSCR J_{nr}, MSCR R	AV, Gradation and AC
References/standards	Wen et al. 2002	AASHTO T 324	AASHTO MP 1/T 313/T 315	AASHTO T 350	AASHTO T308 AASHTO T30 AASHTO T209

Note: IDT—indirect tension test, HWT—Hamburg wheel track, DSR—dynamic shear rheometer, AMPT—asphalt mixture performance tester, PG—performance grade, MSCR—multiple stress recovery, Jnr—non-recoverable creep compliance, R—percent of recovery, AV—air voids, AC—asphalt content.

5. Results and Analysis

5.1. Air Voids

Air voids are defined as the pockets of air between the asphalt-coated aggregate particles in a compacted asphalt paving mixture. Asphalt mixtures of high air voids generally show a faster rate of asphalt aging than the mixture with low air voids [2], which may be due to the fact that asphalt oxidation is the chemical reaction of asphalt with oxygen [5], and high air voids increased the contact areas between air and asphalt mixture.

Figure 3 summarizes the average air voids content based on three core replicates. Error bars that represent standard deviation are also shown. As it can be seen, the air voids from the first round exhibited similar values in general to the second round for most projects (except for MT I-15). This is within our expectations since all the cores were taken at the non-wheel path (with limited traffic load) and the differences in the air voids between the two rounds could be caused by construction variation. For the MT I-15 project, chip seal was placed one year after being open to traffic, which could affect the air voids from the second round.
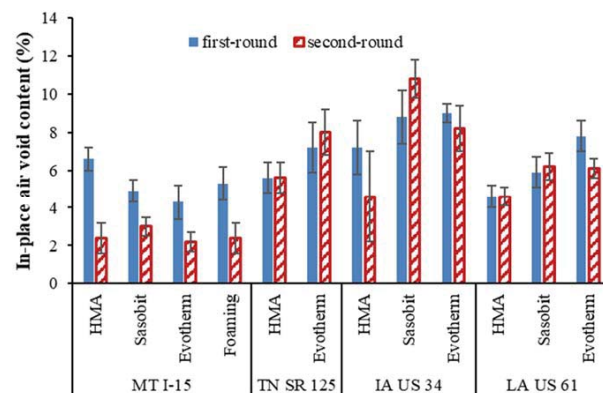
Figure 3. Comparison of in-place air voids.

5.2. Aggregate Gradation and Asphalt Content

Aggregate gradation is expressed by percent passing of coarse aggregate (aggregate predominately retained on 4.75 mm sieve) and fine aggregate (aggregate almost entirely passing the 4.75 mm sieve). Aggregate gradation helps determining important asphalt pavement properties such as stiffness and rutting resistance. The asphalt content is the ratio between the asphalt weight and the total mixture weight (asphalt plus aggregate). Higher asphalt content generates thicker film thickness and reduces aging effect, whereas lower asphalt content in general increase mixture stiffness and result in better rutting resistance [2].

Table 3 summarizes aggregate gradation determined based on field cores. Note that the aggregate gradation shows a range because each project concludes two or more HMA and WMA pavements; this range covers all the pavements from specific project. As observed, there is no significant gradation difference between the two rounds for all the projects except for the IA US 34. A large percentage of the aggregate in the IA US 34 project is limestone, which has a lower strength and is weaker than the other paving aggregate types such as granite and gravel.

Table 3. Aggregate Gradation Percent Passing Comparison Between the First- and the Second-Round Survey.

Sieve Size (mm)	MT I-15		TN SR 125		IA US 34		LA US 61	
	1st Round	2nd Round	1st Round	2nd Round	1st Round	2nd Round	1st Round	2nd Round
19.0	100	100	100	100	100	100	100	100
12.5	89–93	90–93	98	97–98	91	95–96	97–98	97–98
9.5	71–79	70–75	88–89	87–88	81	85–87	82–85	85–86
4.75	45–55	48–50	66–69	63–65	58–62	65–67	52–53	53–56
2.36	32–37	30–33	45	42–44	42–43	45–48	36	35–36
1.18	22–26	24	-	-	28–29	31–33	25–26	21–24
0.6	19–22	19	25–26	25–26	19	21–23	18–19	16–17
0.3	14–17	14–15	13	13	9–10	11–12	12	10–11
0.15	9–12	10	7–8	8	5–6	7	7–8	7
0.075	6–7	6–7	6	6	4–5	5	5	5

Asphalt content was also determined based on field cores. The asphalt content difference between the two rounds is smaller than 0.1%; such a small difference should not significantly affect the rutting resistance of asphalt pavement.

5.3. Recovered Binder High-Temperature PG

The high-temperature PG evaluates the rheology properties of the binder at various temperatures. Typically, a greater high-temperature PG value indicates a stiffer asphalt binder (more rutting resistance) caused by aging or asphalt modification.

Figure 4 illustrates the high-temperature PG comparisons between the first and the second rounds of the extracted binders. For projects examining TN SR 125, IA US 34, and LA US 61, as shown, the high-temperature PG of the second round of extracted binders is always higher than those of the first round, which implies a clear effect of field aging during the two to three years of service.

For the MT I-15 project, it was observed that the PGs of the extracted binders in the second round were close to those in the first round. The cold local climate as shown in Figure 3, plus the chip seals that covered the surfaces, could have reduced the aging effect of the asphalt. The binders of the TN SR 125 project show the highest PG increase over time, which may be explained by the thin asphalt layer applied. The IA US 34 binders have a relatively small high-temperature PG, which indicates less rutting resistance ability.
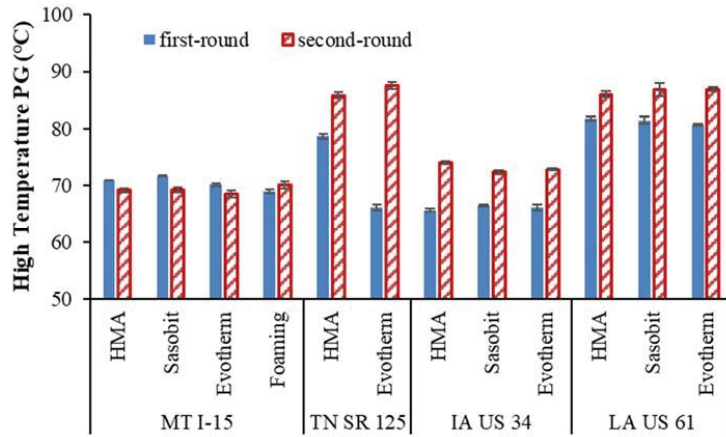
Figure 4. Comparisons of extracted binder high-temperature PGs.

For the LA US 61 project, the high-temperature PG increase is relatively small, considering that the high temperature hour > 25 °C is the highest among the four projects. Such slow ageing could be caused by the PG 76-XX polymer-modified asphalt (PMA) binder used. Based on on-site cores from more than 20 field projects, Zhang et al. [4] found that the PG76-XX PMA binders generally aged less than PG64-XX and PG70-XX binders. The reason for less ageing may be that polymers can prevent the formation of sulfoxides on ageing [20].

5.4. Recovered Binder MSCR Test

The MSCR test is used to evaluate the asphalt binder's potential for permanent deformation. The test is performed by dynamic shear rheometer (DSR) under shear creep and recovery at two stress levels (0.1 and 3.2 kPa) at a specified temperature. The creep portion of the test lasts for 1 s at a constant stress, which is followed by a 9 s recovery. Ten creep and recovery cycles were tested at each stress level. Two parameters, non-recoverable creep compliance (Jnr) and percent recovery (R), were obtained from the test and can be calculated using:

$$\in_r (3.2, N) = \frac{(\in_1 - \in_{10}) \times 100}{\in_1} \tag{1}$$

$$R_{3.2} = \frac{SUM[\in_r (3.2, N)]}{10} \; for \; N = 1 \; to \; 10 \tag{2}$$

$$J_{nr}(3.2, N) = \frac{\in_{10}}{3.2} \tag{3}$$

$$J_{nr3.2} = \frac{SUM[J_{nr}(3.2, N)]}{10} \; for \; N = 1 \; to \; 10 \tag{4}$$

where $\in_1$ is the strain value at the end of the creep portion (i.e., after 1 s) of each cycle, and $\in_{10}$ is the strain value at the end of the recovery portion (i.e., after 10 s) of each cycle.

This paper aims at 3.2 kPa stress level since high stress levels are more important for rut depth development. $\in_r$ (3.2, N) and *Jnr* (3.2, N) indicate percent recovery and nonrecoverable creep compliance at each cycle, respectively. Finally, average percent recovery (*R3.2*) and average nonrecoverable creep compliance (*Jnr3.2*) at 3.2 kPa were obtained by calculating the mean percent recovery and mean nonrecoverable creep compliance from cycles 1 to 10.

Figure 5a,b compare the *Jnr3.2* and *R3.2* between the first- and the second-round-extracted binders, respectively. For the MT I-15 project, no obvious changes in *Jnr3.2* and *R3.2* were observed between the two rounds, which again could be ascribed to the reduced

aging effect due to the chip seal surface treatment. For the other projects, both HMA and WMA binders from the second-round cores show lower *Jnr3.2* and higher *R3.2* values than those in the first round, indicating an improved rutting resistance of the pavements.

(**a**)

(**b**)
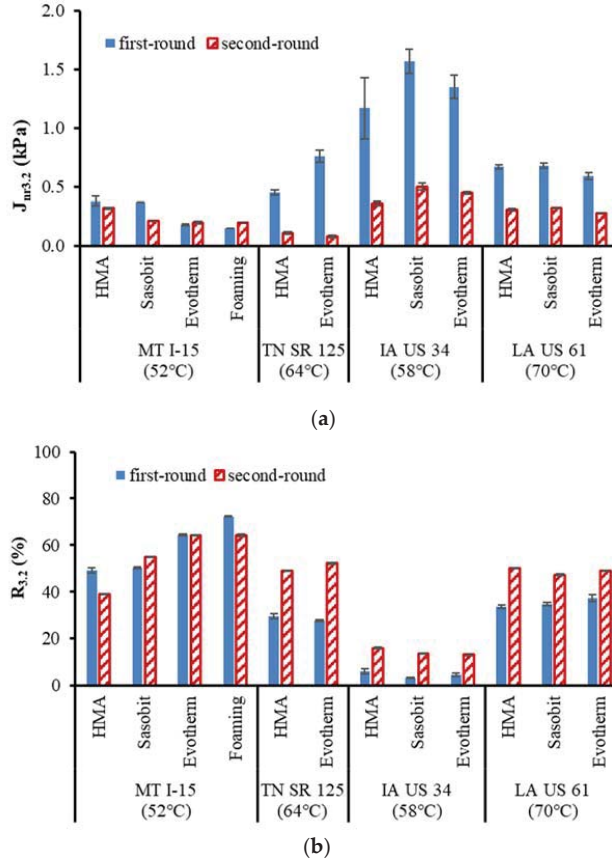
Figure 5. Comparisons of recovered binder MSCR results (**a**) *Jnr3.2*, and (**b**) *R3.2*. Note: the number shown in the parenthesis indicates test temperatures.

Among the four projects, the IA US 34 project shows the highest *Jnr3.2* and the lowest *R3.2*, which implies the high potential of rutting susceptibility. Asphalt binders from the MT I-15 project show the lowest *Jnr3.2* and the highest *R3.2* values, illustrating good rutting resistance. The *Jnr3.2* and *R3.2* values between the TN SR 125 and the LA US 61 are similar to each other.

5.5. Field Core Dynamic Modulus

The dynamic modulus is defined as the complex modulus absolute value calculated by dividing the peak-to-peak stress by peak-to-peak strain for a material of a sinusoidal loading on a material. The dynamic modulus is a performance-related property that can evaluate the mixture and characterize the stiffness of asphalt mixtures for mechanistic–empirical pavement design.

The indirect tension dynamic modulus test was conducted to determine the dynamic modulus while considering the limitations of the core geometry. A sinusoidal compressive loading was applied to the diametric axis of an unconfined cylindrical test specimen. Test

temperatures and frequencies are shown in Table 2. The loading was applied on each sample to achieve the target strain levels (40–60 horizontal microstrain and < 100 vertical microstrain) in the linear viscoelastic region [21–23]. The load–deformation mathematical relationship in the indirect tension-loading mode is given by:

$$|E^*| = \frac{2P_0}{\pi ad} \frac{\beta_1 \gamma_2 - \beta_2 \gamma_1}{\gamma_2 V_0 - \beta_2 U_0} \tag{5}$$

where P_0 is the peak-to-peak load in N, a indicates loading strip width measured in meters, d means the thickness of specimen in meters and V_0 and U_0 represent peak-to-peak vertical deformation and peak-to-peak horizontal deformation in meters, respectively. γ_1, γ_2, β_1, and β_2 are geometric constants.

Figure 6 presents the dynamic modulus test results at a test temperature of 30 °C and a test frequency 0.1 Hz since the asphalt pavement is more susceptible to rutting under relative high temperatures and a low frequency [24]. It is observed in the figure that most projects show an obviously higher dynamic modulus of the second-round field cores than that from the first-round. Since all the cores were taken from the non-wheel path, this dynamic modulus increase is presumably due to the significant field aging of the asphalt binder. The MT I-15 project shows the least increase in the dynamic modulus, which could be affected by the chip seals applied. The high amount of asphalt used in chip seal fills voids of overlay and may increase film thickness and asphalt content, thereby reducing field aging and resulting in a similar dynamic modulus between the two rounds.
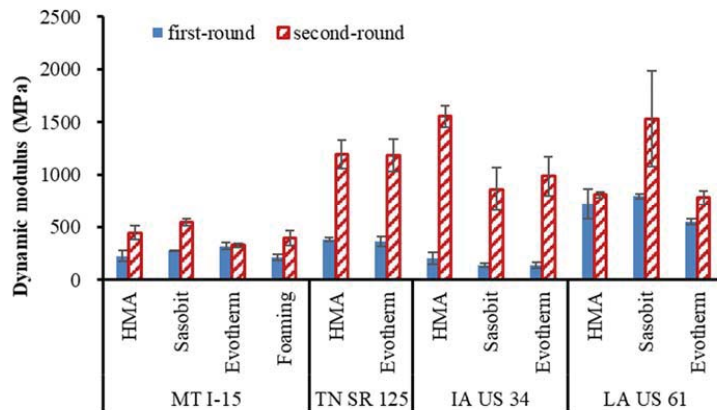
Figure 6. Comparisons of field core dynamic modulus at 30 °C and 0.1 Hz.

It is also seen that the field aging increases dynamic modulus up to 800% in the second round for IA US 34 HMA compared with the value from the first round. Meantime, the high temperature PG and the MSCR *Jnr3.2* and *R3.2* of the same pavement changed by 12.8%, 69% and 165%, respectively. This finding denotes that the increase rates of the asphalt binder and the dynamic modulus are not the same, which will be discussed below.

5.6. Field Core HWT Test Results

The HWT is a widely used test method to determine the rutting resistance and moisture susceptibility of asphalt mixture due to weakness in the aggregate structure, inadequate binder stiffness, or moisture damage. This method measures the rut depth and number of passes to failure and provides information about the rate of permanent deformation from a moving, concentrated load.

The HWT was performed following AASHTO T 324. All tests were conducted at a temperature of 50 °C under wet conditions. The speed of the wheel was set as 52 passes per

minute. The test terminated when either the rut depth achieved 12.5 mm or a pass number of 20,000 was reached.

Figure 7 summarizes the HWT rut depth at 10,000 passes. This pass number was selected because all the first-round cores from the IA US 34 project reached the test threshold value of 12.5 mm at 10,000 passes. It is observed that in general, the rutting resistance of the second-round core is higher than that from the first round, except for the MT I-15 in which the chip seal may have reduced the aging effect. Since the aggregate gradation and asphalt content between the two rounds did not change greatly, the improved rutting resistance should have been contributed to to a major extent by asphalt aging. Bonding between asphalt and aggregate particles provide significant force in resisting mixture to deform, less aged asphalt is more flow and provides a slip plan between aggregates which facilitates aggregate movement and mixture is easy to deform. In contrast, flow conditions of aged asphalt reduced due to increased viscosity, which helped produce better adhesion between aggregates, and aggregate movement became more restricted. In this case, deformation lessened.
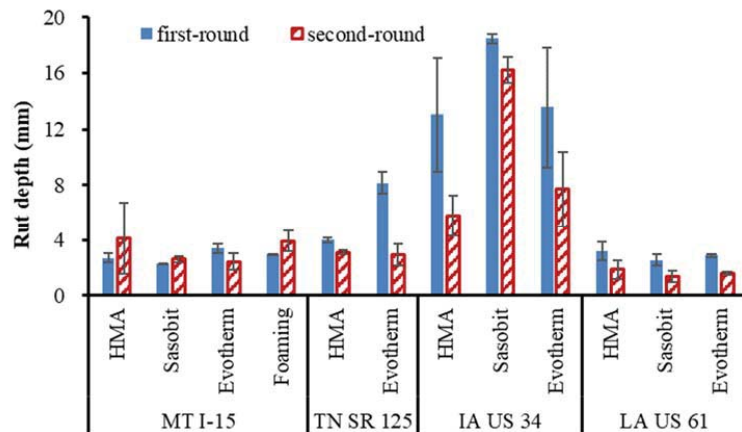
Figure 7. Comparisons of field core Hamburg rut depth.

It is also seen that the field aging increases the dynamic modulus up to 800% in the second round for IA US 34 HMA compared with the value from the first round. Meanwhile, the high-temperature PG and the MSCR *Jnr3.2* and *R3.2* of the same pavement changed by 12.8%, 69% and 165%, respectively. This finding denotes that the increase rates of the asphalt binder and the dynamic modulus are not the same, which will be discussed below.

5.7. Effect of Asphalt Aging on Mixture Properties

In order to study the effects of the variation in asphalt binder properties due to aging on material properties of asphalt mixture, changes to them between the first and second rounds were calculated. These are the increase in high-temperature PG, decrease in MSCR *Jnr3.2*, increase in MSCR *R3.2*, increase in dynamic modulus and decrease in HWT rut depth, respectively.

As seen in Figure 8, the asphalt property changes with dynamic modulus increase correlate well with ageing. The dynamic modulus values increased with the increase in high-temperature PG and MSCR *R3.2*, and the decrease in MSCR *Jnr3.2*. The magnitude changes in the binder properties between the two rounds are 1.2–8.4 °C for high-temperature PG, 0.1 to 24.6% for MSCR *R3.2* and 0.02 to 1.07 kPa for MSCR *Jnr3.2*. Those changes corresponded to an increase in dynamic modulus up to 1356 MPa.
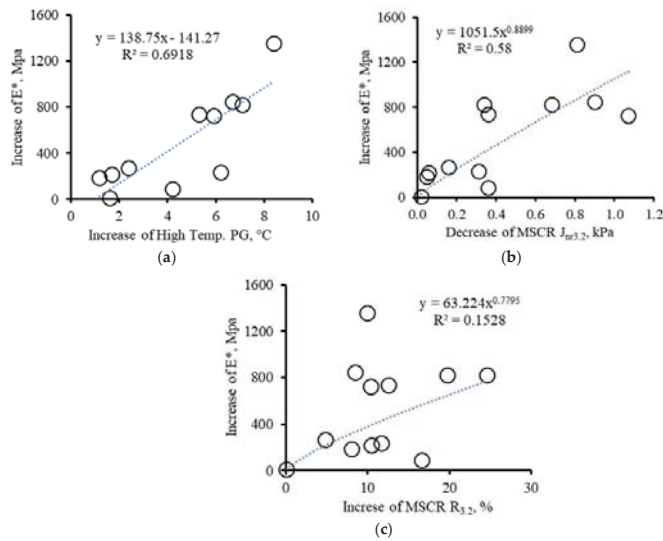
Figure 8. Effect of asphalt binder property change on dynamic modulus change (**a**) increase in high-temperature PG, (**b**) decrease in MSCR *Jnr3.2* and (**c**) increase in MSCR *R3.2*.

Figure 9 shows the relationship between the binder property change and HWT rut depth. As noted, there was a loose relationship denoting that rut depth in general increased with the increase in high-temperature PG and decrease in MSCR *Jnr3.2*. No correlation between HWT rut depth and MSCR *R3.2* over time was found. As it can be seen, the increase in high-temperature PG (1.2 to 8.4 °C) and the decrease in MSCR *Jnr3.2* (0.02 to 1.07 kPa) reduced the HWT rut depth to the maximum value of 7.3 mm between the two rounds.
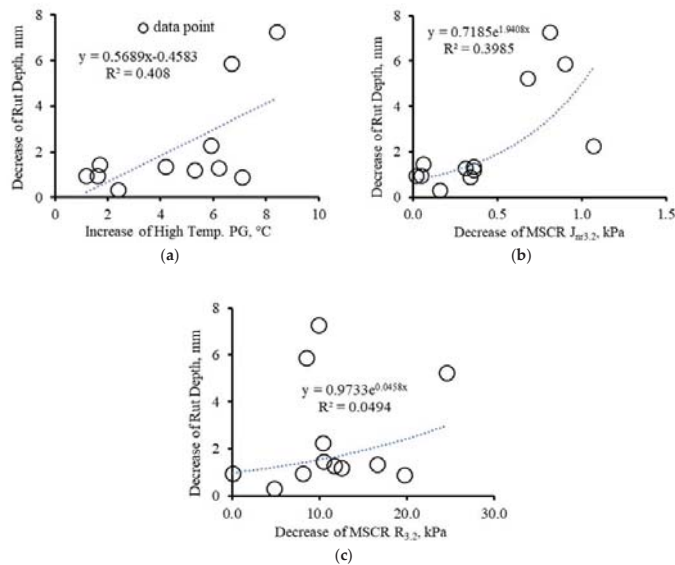
Figure 9. Effect of asphalt binder property change on HWT rut depth change (**a**) increase in high-temperature PG, (**b**) decrease in MSCR *Jnr3.2*, and (**c**) increase in MSCR *R3.2*.

Additionally, the percentage increase/decrease in each material property between the two rounds was calculated and shown in Figure 10. As it can be seen, regarding binder properties, the high-temperature PG has the least percentage increase with the maximum value of 32.2%, whereas the MSCR *R3.2* experienced the most increase with the maximum value of 325%. As for the mixture, the dynamic modulus and the HWT rut depth increased up to 673.1% and 64%, respectively. The large range of MSCR *R3.2* and mixture dynamic modulus make the prediction more complicated. In addition, it is expected that the laboratory ageing could be harder for MSCR *R3.2* due to its large variation.
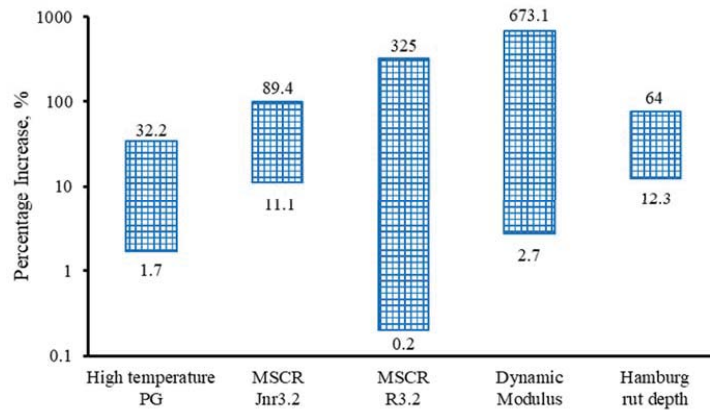
Figure 10. Percentage increase/decrease in each material property.

It is evident that the change in binder property is not proportional to the change in dynamic modulus. Similarly, the change in dynamic modulus is not comparable to the change in the HWT rut depth. Therefore, it is expected that when different binder properties are applied to predict mixture performance, the shift factor would be varied greatly.

6. Conclusions

This paper evaluated the effect of field pavement ageing on properties of asphalt binder and asphalt mixture at two different rounds. The relationship between property changes in the asphalt and asphalt mixture due to ageing was also analyzed.

Results indicate that asphalt pavement in general became stiffer after years of service in terms of asphalt binder (high temperature PG, MSCR) and asphalt mixture (dynamic modulus, HWT rut depth). The asphalt mixture stiffening is caused to a large degree by asphalt aging, considering that the evaluated cores had no significant differences between the two rounds in in-place air voids, aggregate gradation and asphalt content. Such findings were confirmed by observing a good relationship between the change in binder properties and mixture properties. However, the application of the chip seal significantly reduced the aging process.

The material properties changed to different extents over time. The parameters that are most sensitive to field ageing are MSCR *R3.2* and dynamic modulus. Thus, the comparison among lab-tested material properties may be better checked in rank instead of absolute values. Note that the high variation in MSCR *R3.2* could cause some issues for laboratory aging, which needs further research. The effect of asphalt aging on pavement mixture properties may not follow a proportional liner trend.

The PG76-22 polymer-modified binders in general aged slower than other binder types evaluated in this study, for both asphalt binder and asphalt mixture properties. Since it is already proved that PG 76-22 polymer-modified binders show very good rutting resistance, such slow aging could also be beneficial to cracking resistance.

However, there are also some limitations that need improvement in future studies. For example, only two existing pavement structure types were selected, including flexible pavements, and a combination of asphalt/PCC pavements. For other types of asphalt pavement, the effects of field aging on material properties and rutting performance and their mechanisms need to be further studied.

Author Contributions: The authors confirm contribution to the paper as follows: conceptualization, H.W., Y.Z. and W.Z.; data curation, S.S. and S.W.; formal analysis, Y.Z. and L.N.M.; funding acquisition, W.Z.; investigation, S.S. and S.W.; methodology, H.W. and X.S.; writing—original draft, W.Z. and L.N.M.; writing—review and editing, X.S. All authors have read and agreed to the published version of the manuscript.

Data Availability Statement: All data, models, or codes that support the findings of this study are available from the corresponding authors upon reasonable request, including the field test data of the asphalt layers.

Conflicts of Interest: The authors declare no known competing financial interests or personal relationships that could have appeared to influence the work reported in this paper.

References

1. Martin, A.E.; Arambula, E.; Yin, F.; Cucalon, L.G.; Chowdhury, A.; Lytton, R.; Epps, R.; Estakhri, E.; Park, E.S. *Evaluation of the Moisture Susceptibility of WMA Technologies*; NCHRP Report 763; Transportation Research Board of the National Academies: Washington, DC, USA, 2014.
2. Glover, C.; Martin, A.; Han, R.; Prapaitrakul, N.; Zin, J.; Chowdhury, A.; Lawrence, J. *Evaluation of Binder Aging and Its Influence in Aging of Hot Mix Asphalt Concrete: Literature Review and Experimental Design. Asphalt Hardening*; Texas Transportation Institute: Bryan/College Station, TX, USA, 2009.
3. Luo, X.; Gu, F.; Lytton, R. Prediction of Field Aging Gradient in Asphalt Pavements. Transportation Research Record. *J. Transp. Res. Board* **2015**, *2507*, 19–28. [CrossRef]
4. Zhang, W.; Shen, S.; Wu, S.; Mohammad, L. Long-term Field Aging of Warm Mix and hot Mix Asphalt binders. Accepted by Transportation Research Record (TRR). *J. Transp. Res. Board* **2017**, *2632*, 140–149. [CrossRef]
5. Hanson, D.; King, G.; Buncher, M.; Duval, J.; Blankenship, P.; Anderson, M. *Techniques for Prevention and Remediation of Non-Load Related Distresses on HMA Airport Pavements. Airfield Asphalt Pavement Technology Program*; AMEC: San Diego, CA, USA, 2009.
6. Bell, C.; Abwahab, Y.; Cristi, M.; Sosnovske, D. *Selection of Laboratory Aging Procedures for Asphalt-Aggregate Mixtures*; Strategic Highway Research Program: Washington, DC, USA, 1994.
7. Jung, S. The Effects of Asphalt Binder Oxidation Binder Oxidation on Hot Mix Asphalt Concrete Mixture Rheology and Fatigue Performance. Dissertation Thesis, Texas A&M University, College Station, TX, USA, 2006.
8. Huang, T.; Zheng, J.L.; Lv, S.T.; Zhang, J.H.; Wen, P.H.; Bailey, C.G. Failure criterion of an asphalt mixture under three-dimensional stress state. *Constr. Build. Mater.* **2018**, *170*, 708–715. [CrossRef]
9. Li, J.; Zhang, J.; Qian, G.; Zheng, J.; Zhang, Y. Three-dimensional simulation of aggregate and asphalt mixture using parameterized shape and size gradation. *J. Mater. Civ. Eng.* **2019**, *31*. [CrossRef]
10. Ding, L.; Zhang, J.; Feng, B.; Li, C. Performance Evaluation of Recycled Asphalt Mixtures Containing Construction and Demolition Waste Applicated as Pavement Base. *Adv. Civ. Eng.* **2020**, *2020*, 875402. [CrossRef]
11. Said, S. Aging Effect on Mechanical Characteristics of Bituminous Mixtures. *Transp. Res. Rec. J. Transp. Res. Board* **2005**, *1901*, 1–9. [CrossRef]
12. Raad, L.; Saboundjian, S.; Minassian, G. Field Aging Effects on Fatigue of Asphalt Concrete and Asphalt-Rubber Concrete. *Transp. Res. Rec. J. Transp. Res. Board* **2001**, *1767*, 126–134. [CrossRef]
13. Wu, S.; Zhang, W.; Shen, S.; Li, X.; Muhunthan, B.; Mohammad, L. Field-Aged Asphalt Binder Performance Evaluation for Evotherm Warm Mix Asphalt: Comparisons with Hot Mix Asphalt. *Constr. Build. Mater.* **2017**, *156*, 574–583. [CrossRef]
14. Shen, S.; Wu, S.; Zhang, W.; Mohammad, L.; Muhunthan, B. *NCHRP Report 843: Long-Term Field Performance of Warm Mix Asphalt Technologies*; Transportation Research Board: Washington, DC, USA, 2017.

15. Daly, W.; Negulescu, I.; Mohammad, L.; Chiparus, I. *The Use of DMA to Characterize the Aging of Asphalt Binders*; Publication FHWA-LA-07-461; Louisiana Transportation Research Center: Baton Rouge, LA, USA, 2010.
16. Zhang, W.; Shen, S.; Faheem, A.; Basak, P.; Wu, S.; Mohammad, L. Predictive Quality of the Pavement ME Design Program for Field Performance of Warm Mix Asphalt Pavements. *Constr. Build. Mater.* **2017**, *131*, 400–410. [CrossRef]
17. Hajj, E.; Salazar, L.; Sebaaly, P. Methodologies for Estimating Effective Performance Grade of Asphalt Binders in Mixtures with High Recycled Asphalt Pavement Content Case Study. *Transp. Res. Rec. J. Transp. Res. Board* **2012**, *2294*, 53–63. [CrossRef]
18. Zhang, W.; Shen, S.; Wu, S.; Mohammad, L. Prediction Model for Field Rut Depth of Asphalt Pavement Based on Hamburg Wheel Tracking Test Properties. *J. Mater. Civ. Eng.* **2017**, *29*, 1–10. [CrossRef]
19. Sun, Z.; Ma, S.; Zhang, J.; Sun, F. Microstructure characterisation and performance investigation of a rapid hardening emulsified asphalt seal mixture. *Road Mater. Pavement Des.* **2021**, *22*, 2767–2782. [CrossRef]
20. Lu, X.; Talon, Y.; Redilius, P. Aging of Bituminous Binders-Laboratory Tests and Field Data. In Proceedings of the 4th Eurasphalt and Eurobitume Congress, Copenhagen, Denmark, 21–23 May 2008.
21. Wen, H.; Kim, Y. Simple Performance Test for Fatigue Cracking and Validation with WesTrack Mixtures. *Transp. Res. Rec. J. Transp. Res. Board* **2002**, *1789*, 66–72. [CrossRef]
22. Kim, Y.; Seo, Y.; King, M. Dynamic Modulus Testing of Asphalt Concrete in Indirect Tension Mode. *Transp. Res. Rec. J. Transp. Res. Board* **2004**, *1891*, 163–173. [CrossRef]
23. Sun, Z.; Li, S.; Zhang, J.; Zeng, Y. Adhesion property of bituminous crack sealants to different asphalt mixtures based on surface energy theory. *Constr. Build. Mater.* **2020**, *261*, 120006. [CrossRef]
24. AASHTO. *Mechanistic-Empirical Pavement Design Guide, A Manual of Practice*; American Association of State Highway and Transportation Officials: Washington, DC, USA, 2008.

Estimating of the Static and Dynamic Behaviors of Orthogrid-Stiffened FRP Panel Using Reduced-Order Plate Model

Peng Wang [1,2]**, Yifeng Zhong** [1,2,*]**, Zheng Shi** [1,2]**, Dan Luo** [1,2] **and Qingshan Yi** [1,2]

[1] School of Civil Engineering, Chongqing University, Chongqing 400045, China;
201816131092@cqu.edu.cn (P.W.); 20191601513@cqu.edu.cn (Z.S.); 20171601012@cqu.edu.cn (D.L.);
20154673@cqu.edu.cn (Q.Y.)
[2] Key Laboratory of New Technology for Construction of Cities in Mountain Area, Chongqing University,
Chongqing 400045, China
[*] Correspondence: zhongyf@cqu.edu.cn

Abstract: The orthogrid-stiffened FRP panel (OSFP) is a generic structural element in weight-sensitive structure applications. Based on the variational asymptotic method, a 2D reduced-order plate model (2D-RPM) of OSFP was constructed through matching the strain energy of the original panel for static and dynamic analyses. The local field distributions were recovered using the recovery relationship and global response. The relative influences of select parameters on the effective performance of the OSFP were revealed by parametric studies. The comparative results showed that the effective performance of the OSFP predicted by the 2D-RPM were consistent with those predicted by the 3D finite element model, but the computational efficiency was greatly improved. The stiffener height had the greatest influence on the natural frequency of the panel. The layup configurations of laminates had significant influences on the equivalent stiffness and buckling load of the OSFP but had little effect on the vibration modes, which could be varied by adjusting the stiffening forms.

1. Introduction

Fiber-reinforced polymer (FRP) has the advantages of being lightweight and having high strength, corrosion resistance, and tailorability. It is a new type of material that exhibits excellent performances, and has been extensively used in civil engineering, shipbuilding, aerospace and so on. Under the same load capacity, the weight of an FRP bridge is only 30% of that of a steel bridge and 5% of that of a reinforced concrete bridge. Due to the excellent properties of FRP, it has gradually become a substitute for traditional building materials (e.g., steel and concrete). Compared with traditional steel and concrete bridges, FRP bridges are not only lightweight but are also more convenient to manufacture, transport, and install. Furthermore, they have long service lives of more than 100 years [1].

The orthogrid-stiffened FRP panel (OSFP) is characterized by a lattice of rigid, interconnected stiffeners, which is a generic structural element in weight-sensitive structure applications [2]. Its stiffness, buckling, and vibration characteristics are not only related to the stiffening forms but are also closely related to the structural and material parameters, which increases the difficulty of analysis. At present, most analysis methods for stiffened panels can be summarized as numerical methods, analytical methods, and a combination of the two methods. The calculation models for the effective analysis of stiffened panels can be divided into finite element models (FEMs) [3–8], discrete stiffener models (DSMs) [9], and smeared stiffener models (SSMs) [10]. The stiffeners are modeled as members with axial bending/torsion stiffnesses on the attached skin in DSM, and they can only be effectively

applied for the analysis of stiffened panels with thin skins and rigid stiffeners. The geometric features of the stiffeners and skin are contained in FEM, which is more flexible and accurate than DSM. However, it not only requires a long simulation time due to the large computational workload, but also the inability to set different configurations and materials during preliminary design and optimization [11]. The basic idea of SSM is to smear the stiffnesses of the stiffeners into the panel and calculate the effective properties [12–14]. This may be applicable to the overall analysis of stiffened panels with intensive interconnected stiffeners but not to the stress and strain analysis of stiffeners [15].

The global buckling is considered as the main failure mode of stiffened panels under axial compression or/and external pressure according to the failure mode map [16,17]. Among the methods used to study the global buckling of stiffened panels, extensive studies have concentrated on the FEM and SSM [18,19]. The extension–bending coupling interaction caused by the eccentricity of the stiffeners was neglected in the work by Chen et al. [20], which resulted in the imprecise buckling prediction results [21]. Abhijit et al. [22] used the FEM to study the free vibration characteristics of stiffened plates with symmetric stiffeners. Later, the isoparametric stiffened-plate element was introduced to analyze the free vibration of eccentrically stiffened plates [23,24]. Lam et al. [25] explored the vibrations of stiffened plates by dividing the plate domain into appropriate rectangular segments.

On the basis of literature review, there were some issues in the existing methods for predicting the effective performance of stiffened panels. First, the shear stiffness matrix cannot be predicted using the homogenized elastic constants and plate thickness together with classic plate theory. Second, due to the assumptions for defining the kinematics, the models were usually applicable to some specific form of stiffeners. Third, few plate models can accurately predict the local stress and strain distributions of stiffeners, which were of great significance to the failure analysis of stiffened panels.

Recently, Yu and Zhong [26–29] put forward a new multiscale modeling technique to deal with dimensionality-reducing structures based on the variational asymptotic method (VAM) [30]. With this method, the small structural parameters (such as the thickness–width ratio) were used to asymptotically expand the energy functional, and the higher-order terms were removed to obtain the approximate energy of different orders and the corresponding dimension reduction model, which achieved a good tradeoff between accuracy and effectiveness. In this work, a VAM-based reduced-order plate model of stiffened FRP panel was established to solve the three issues mentioned above. The influences of geometric parameters (such as height, thickness, length-width ratio, and period length) on the effective performance of the OSFP were investigated. Finally, the displacements and free-vibration modes of stiffened FRP panels with different stiffening forms, such as the orthogrid-, T- and blade-stiffened panels, were compared. To the author's knowledge, this method has never been used for this purpose.

2. Theoretical Formulation for Reduced-Order Plate Model Using VAM

2.1. Kinematics of the OSFP

As shown in Figure 1, if the sizes of the whole panel (denoted by the macro-coordinates x_i) are much larger than those of a unit cell (denoted by the micro-coordinates y_i), then $y_i = x_i/\zeta$ (ζ is a small parameter), and the derivative of the function $f^\zeta(x_\alpha)$ with respect to x_α is

$$\frac{\partial f^\zeta(x_\alpha)}{\partial x_\alpha} = \frac{\partial f(x_\alpha; y_i)}{\partial x_\alpha}\bigg|_{y_i=\text{const}} + \frac{1}{\zeta}\frac{\partial f(x_\alpha; y_i)}{\partial y_i}\bigg|_{x_\alpha=\text{const}} \equiv f_{,\alpha} + \frac{1}{\zeta}f_{;i} \tag{1}$$

where $i, j = 1, 2, 3; \alpha, \beta = 1, 2$.
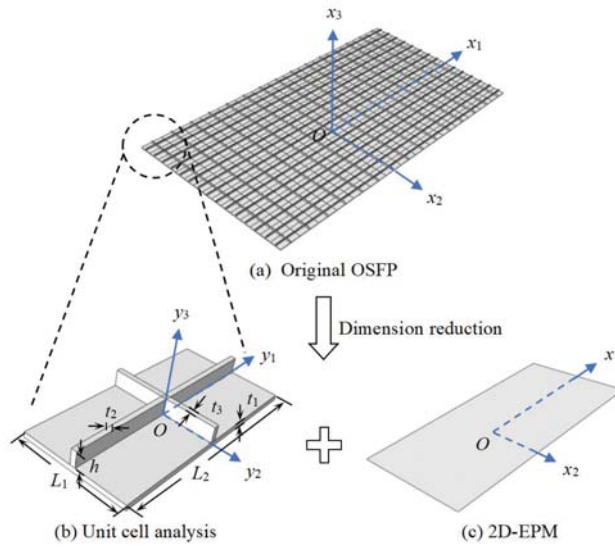
Figure 1. Dimension reduction analysis of the original orthogrid-stiffened FRP panel (OSFP).

To construct a reduced-order plate model of the OSFP using VAM, the 3D displacement field of the original OSFP u_i need to be represented by using 2D plate variables v_i such as

$$\begin{aligned}
u_1(x_\alpha; y_i) &= \underline{v_1(x_1, x_2) - \xi y_3 v_{3,1}(x_1, x_2)} + \xi w_1(x_\alpha; y_i) \\
u_2(x_\alpha; y_i) &= \underline{v_2(x_1, x_2) - \xi y_3 v_{3,2}(x_1, x_2)} + \xi w_2(x_\alpha; y_i) \\
u_3(x_\alpha; y_i) &= \underline{v_3(x_1, x_2)} + \xi w_3(x_\alpha; y_i)
\end{aligned} \tag{2}$$

where w_i is the fluctuating function to be solved, and the underlined terms should meet the following constraints

$$\begin{aligned}
v_1 &= \langle u_1 \rangle + \xi \langle y_3 \rangle v_{3,1} \\
v_2 &= \langle u_2 \rangle + \xi \langle y_3 \rangle v_{3,2} \\
v_3 &= \langle u_3 \rangle
\end{aligned} \tag{3}$$

where $\langle \cdot \rangle$ represents the volume integration over the unit cell.

The non-underlined terms should satisfy the following conditions

$$\langle \xi w_i \rangle = 0 \tag{4}$$

The 3D strain field can be expressed as

$$\Gamma_{ij} = \frac{1}{2} \left(\frac{\partial u_i}{\partial x_j} + \frac{\partial u_j}{\partial x_i} \right) \tag{5}$$

Plugging Equation (2) into Equation (5) gives the 3D strain field as

$$\begin{aligned}
\Gamma_{11} &= \varepsilon_{11} + \xi y_3 \kappa_{11} + w_{1,1} \\
2\Gamma_{12} &= 2\varepsilon_{22} + 2\xi y_3 \kappa_{12} + w_{1,2} + w_{2,1} \\
\Gamma_{22} &= \varepsilon_{22} + \xi y_3 \kappa_{22} + w_{2,2} \\
2\Gamma_{13} &= w_{1,3} + w_{3,1} \\
2\Gamma_{23} &= w_{2,3} + w_{3,2} \\
\Gamma_{33} &= w_{3,3}
\end{aligned} \tag{6}$$

where $\varepsilon_{\alpha\beta}$ and $\kappa_{\alpha\beta}$ can be expressed as

$$\begin{aligned}
&\varepsilon_{11}(x_1, x_2) = v_{1,1}(x_1, x_2), \quad \varepsilon_{22}(x_1, x_2) = v_{2,2}(x_1, x_2), \\
&2\varepsilon_{12}(x_1, x_2) = v_{1,2}(x_1, x_2) + v_{2,1}(x_1, x_2), \\
&\kappa_{11}(x_1, x_2) = -v_{3,11}(x_1, x_2), \quad \kappa_{22}(x_1, x_2) = -v_{3,22}(x_1, x_2), \\
&\kappa_{12}(x_1, x_2) = -v_{3,12}(x_1, x_2)
\end{aligned} \tag{7}$$

The 3D strain field can be obtained as

$$\begin{aligned}
&\boldsymbol{\Gamma}_e = [\Gamma_{11} \quad \Gamma_{22} \quad 2\Gamma_{12}]^{\mathrm{T}} = \boldsymbol{\varepsilon} + x_3\boldsymbol{\kappa} + \partial_e\boldsymbol{w}_{\|} \\
&2\boldsymbol{\Gamma}_s = [2\Gamma_{13} \quad 2\Gamma_{23}]^{\mathrm{T}} = \boldsymbol{w}_{\|} + \partial_t w_3 \\
&\boldsymbol{\Gamma}_t = \Gamma_{33} = w_{3,3}
\end{aligned} \tag{8}$$

where $\boldsymbol{\Gamma}_e, \boldsymbol{\Gamma}_s, \boldsymbol{\Gamma}_t$ are strain matrices of 3D-FEM; $()_{\|} = [()_1 \quad ()_2]^{\mathrm{T}}$, $\boldsymbol{\varepsilon} = [\begin{array}{ccc} \varepsilon_{11} & 2\varepsilon_{12} & \varepsilon_{22} \end{array}]^{\mathrm{T}}$, $\boldsymbol{\kappa} = [\kappa_{11} \quad \kappa_{12} + \kappa_{21} \quad \kappa_{22}]^{\mathrm{T}}$, and

$$\partial_e = \begin{bmatrix} ()_{,1} & 0 \\ ()_{,2} & ()_{,1} \\ 0 & ()_{,2} \end{bmatrix}, \partial_t = \left\{ \begin{array}{c} ()_{,1} \\ ()_{,2} \end{array} \right\} \tag{9}$$

As shown in Figure 2, the unit cell within the OSFP can be divided into three parts to facilitate the integral solution. Then we obtain the strain energy of the panel as

$$U = \frac{1}{2} \int_{-a/2}^{a/2} \int_{-b/2}^{b/2} \frac{1}{\Omega} U_\Omega \mathrm{d}x_2 \mathrm{d}x_1 \tag{10}$$

where

$$\begin{aligned}
U_\Omega = &\int_{-t_1}^{0} \int_{-\frac{L_1}{2}}^{\frac{L_1}{2}} \int_{-\frac{L_2}{2}}^{\frac{L_2}{2}} \boldsymbol{\Gamma}_A^T \boldsymbol{D}_A \boldsymbol{\Gamma}_A \mathrm{d}y_1 \mathrm{d}y_2 \mathrm{d}y_3 \\
&+ \int_{0}^{h} \int_{-\frac{L_1}{2}}^{\frac{L_1}{2}} \int_{-\frac{t_2}{2}}^{\frac{t_2}{2}} \boldsymbol{\Gamma}_B^T \boldsymbol{D}_B \boldsymbol{\Gamma}_B \mathrm{d}y_1 \mathrm{d}y_2 \mathrm{d}y_3 \\
&+ \int_{0}^{h} \int_{-\frac{t_3}{2}}^{\frac{t_3}{2}} \int_{-\frac{L_2}{2}}^{\frac{L_2}{2}} \boldsymbol{\Gamma}_C^T \boldsymbol{D}_C \boldsymbol{\Gamma}_C \mathrm{d}y_1 \mathrm{d}y_2 \mathrm{d}y_3
\end{aligned} \tag{11}$$

with the subscripts *A*, *B*, and *C* representing the skin, longitudinal stiffener, and transverse stiffener, respectively.
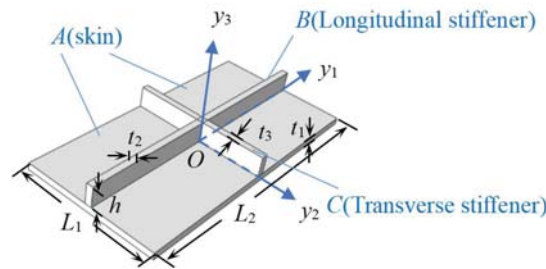
Figure 2. Decomposition diagram of unit cell within the OSFP.

Equation (10) can be rewritten as

$$
\begin{aligned}
U &= \frac{1}{2} \int_{-a/2}^{a/2} \int_{-b/2}^{b/2} \frac{1}{\Omega} \left\langle \mathbf{\Gamma}^T \mathbf{D} \mathbf{\Gamma} \right\rangle \mathrm{d}x_2 \, \mathrm{d}x_1 \\
&= \frac{1}{2} \int_{-a/2}^{a/2} \int_{-b/2}^{b/2} \frac{1}{\Omega} \left\langle \left\{ \begin{array}{c} \mathbf{\Gamma}_e \\ 2\mathbf{\Gamma}_s \\ \mathbf{\Gamma}_t \end{array} \right\}^T \left[\begin{array}{ccc} \mathbf{D}_e & \mathbf{D}_{es} & \mathbf{D}_{et} \\ \mathbf{D}_{es}^T & \mathbf{D}_s & \mathbf{D}_{st} \\ \mathbf{D}_{et}^T & \mathbf{D}_{st}^T & \mathbf{D}_t \end{array} \right] \left\{ \begin{array}{c} \mathbf{\Gamma}_e \\ 2\mathbf{\Gamma}_s \\ \mathbf{\Gamma}_t \end{array} \right\} \right\rangle \mathrm{d}x_2 \, \mathrm{d}x_1
\end{aligned}
\tag{12}
$$

where $D_e, D_{es}, D_{et}, D_s, D_{st}$, and D_t are the corresponding sub-matrices of three-dimensional 6×6 material matrix.

The virtual work done by the applied loads is

$$
\begin{aligned}
E &= \int_{-b/2}^{b/2} \int_{-a/2}^{a/2} \frac{1}{\Omega} \left(\langle f_i u_i \rangle + \beta_i u_i^- + \tau_i u_i^+ \right) \mathrm{d}x_1 \mathrm{d}x_2 \\
&+ \int_{-a/2}^{a/2} \int_{-h/2}^{h/2} \left(\alpha_i u_i \right)|_{x_2 = \pm b/2} \mathrm{d}x_3 \mathrm{d}x_1 + \int_{-b/2}^{b/2} \int_{-h/2}^{h/2} \left(\alpha_i u_i \right)|_{x_1 = \pm a/2} \mathrm{d}x_3 \mathrm{d}x_2
\end{aligned}
\tag{13}
$$

where f_i is the body force, α_i is the traction force applied on the lateral surfaces, β_i and τ_i denote the traction forces on the bottom and top surface, respectively.

Plugging Equation (2) into Equation (13) gives

$$
\begin{aligned}
E &= \int_{-b/2}^{b/2} \int_{-a/2}^{a/2} \left(p_i v_i + q_\alpha \Phi_\alpha \right) \mathrm{d}x_1 \mathrm{d}x_2 \\
&+ \int_{-a/2}^{a/2} \int_{-h/2}^{h/2} \left(P_i v_i + Q_\alpha \Phi_\alpha \right)|_{x_2 = \pm b/2} \mathrm{d}x_3 \mathrm{d}x_1 \\
&+ \int_{-b/2}^{b/2} \int_{-h/2}^{h/2} \left(P_i v_i + Q_\alpha \Phi_\alpha \right)|_{x_1 = \pm a/2} \mathrm{d}x_3 \mathrm{d}x_2 + E^*
\end{aligned}
\tag{14}
$$

where $\Phi_1 = v_{3,2}, \Phi_2 = -v_{3,1}$, and

$$
\begin{aligned}
E^* &= \int_{-b/2}^{b/2} \int_{-a/2}^{a/2} \frac{1}{\Omega} \left(\langle f_i w_i \rangle + \beta_i w_i^- + \tau_i w_i^+ \right) \mathrm{d}x_1 \mathrm{d}x_2 \\
&+ \int_{-a/2}^{a/2} \int_{-h/2}^{h/2} \left(\alpha_i w_i \right)|_{x_2 = \pm b/2} \mathrm{d}x_3 \mathrm{d}x_1 + \int_{-b/2}^{b/2} \int_{-h/2}^{h/2} \left(\alpha_i w_i \right)|_{x_1 = \pm a/2} \mathrm{d}x_3 \mathrm{d}x_2
\end{aligned}
\tag{15}
$$

The values of p_i, q_α, P_i, and Q_α in Equation (14) can be calculated as

$$
\begin{aligned}
p_i &= \frac{1}{\Omega} \left(\langle f_i \rangle + \beta_i + \tau_i \right) \\
q_1 &= \frac{1}{\Omega} \left(-x_3^- \beta_2 - x_3^+ \tau_2 - \langle x_3 f_2 \rangle \right) \\
q_2 &= \frac{1}{\Omega} \left(x_3^- \beta_1 + x_3^+ \tau_1 + \langle x_3 f_1 \rangle \right) \\
P_i &= \langle\langle \alpha_i \rangle\rangle \\
Q_1 &= -\langle\langle x_3 \alpha_2 \rangle\rangle \\
Q_2 &= \langle\langle x_3 \alpha_1 \rangle\rangle
\end{aligned}
\tag{16}
$$

According to VAM, E^* can be ignored, and the total potential energy is

$$
\begin{aligned}
\delta \Pi &= \delta U - \delta E \\
&= \int_{-b/2}^{b/2} \int_{-a/2}^{a/2} \left(\frac{1}{2} \delta \left\langle \mathbf{\Gamma}^T \bar{\mathbf{D}} \mathbf{\Gamma} \right\rangle - p_i \delta v_i - q_\alpha \delta \Phi_\alpha \right) \mathrm{d}x_1 \mathrm{d}x_2 \\
&+ \int_{-a/2}^{a/2} \int_{-h/2}^{h/2} \left(P_i \delta v_i + Q_\alpha \delta \Phi_\alpha \right)|_{x_2 = \pm b/2} \mathrm{d}x_3 \mathrm{d}x_1 \\
&+ \int_{-b/2}^{b/2} \int_{-h/2}^{h/2} \left(P_i \delta v_i + Q_\alpha \delta \Phi_\alpha \right)|_{x_1 = \pm a/2} \mathrm{d}x_3 \mathrm{d}x_2
\end{aligned}
\tag{17}
$$

2.2. VAM-Based Reduction Analysis of OSFP

2.2.1. Zeroth-Order Approximation

Plugging Equation (8) into Equation (17) gives the total potential energy density as

$$
\begin{aligned}
2\Pi = \Big\langle \Big\langle & \underline{\underline{(\boldsymbol{\varepsilon} + x_3\boldsymbol{\kappa})^{\mathrm{T}} \boldsymbol{D}_e (\boldsymbol{\varepsilon} + x_3\boldsymbol{\kappa})}} + 2(\boldsymbol{\varepsilon} + x_3\boldsymbol{\kappa})^{\mathrm{T}} \boldsymbol{D}_e \partial_e \boldsymbol{w}_{\|\alpha} \\
& + 2(\partial_e \boldsymbol{w}_{\|\alpha})^{\mathrm{T}} \boldsymbol{D}_e \partial_e \boldsymbol{w}_{\|} + 2(\boldsymbol{\varepsilon} + x_3\boldsymbol{\kappa})^{\mathrm{T}} \boldsymbol{D}_{es} \boldsymbol{w}_{\|,3} + \underline{2(\boldsymbol{\varepsilon} + x_3\boldsymbol{\kappa})^{\mathrm{T}} \boldsymbol{D}_{es} \partial_t \boldsymbol{w}_{3\alpha}} \\
& + 2\Big(\partial_e \boldsymbol{w}_{\|\alpha}\Big)^{\mathrm{T}} \boldsymbol{D}_{es} \Big(\boldsymbol{w}_{\|,3} + \partial_t \boldsymbol{w}_{3\alpha}\Big) + 2(\boldsymbol{\varepsilon} + x_3\boldsymbol{\kappa})^{\mathrm{T}} \boldsymbol{D}_{et} \boldsymbol{w}_{3,3} \\
& + \underline{2\Big(\partial_e \boldsymbol{w}_{\|\alpha}\Big)^{\mathrm{T}} \boldsymbol{D}_{et} \boldsymbol{w}_{3,3}} + \boldsymbol{w}_{\|,3}^{\mathrm{T}} \boldsymbol{D}_s \boldsymbol{w}_{\|,3} + 2\boldsymbol{w}_{\|,3}^{\mathrm{T}} \boldsymbol{D}_s \partial_t \boldsymbol{w}_{3\alpha} + \underline{2(\partial_t \boldsymbol{w}_{3,\alpha})^{\mathrm{T}} \boldsymbol{D}_s \partial_t \boldsymbol{w}_{3,\alpha}} \\
& + 2\boldsymbol{w}_{\|,3}^{\mathrm{T}} \boldsymbol{D}_{st} \boldsymbol{w}_{3,3} + \underline{2(\partial_t \boldsymbol{w}_{3,\alpha})^{\mathrm{T}} \boldsymbol{D}_{st} \boldsymbol{w}_{3,3} + \boldsymbol{D}_t \boldsymbol{w}_{3,3}^2} \Big\rangle \Big\rangle \\
& - \underline{2(\langle\langle \boldsymbol{f}_i^{\mathrm{T}} \boldsymbol{w}_i \rangle\rangle + \boldsymbol{\tau}_i^{\mathrm{T}} \boldsymbol{w}_i^{\mathrm{T}} + \boldsymbol{\beta}_i^{\mathrm{T}} \boldsymbol{w}_i^{\mathrm{T}})}
\end{aligned}
\tag{18}
$$

where the underlined items and the double-underlined item can be ignored according to VAM.

To impose the constraints on the fluctuating function, we introduce the Lagrange multipliers λ_i, such as

$$
\delta(\Pi + \lambda_i \langle w_i \rangle) = 0 \tag{19}
$$

The zeroth-order approximate variational expression is

$$
\left\langle
\begin{array}{l}
\Big[(\boldsymbol{\varepsilon} + x_3\boldsymbol{\kappa})^{\mathrm{T}} \boldsymbol{D}_{es} + \boldsymbol{w}_{\|,3}^{\mathrm{T}} \boldsymbol{D}_s + w_{3,3}^{\mathrm{T}} \boldsymbol{D}_{st}^{\mathrm{T}}\Big] \delta \boldsymbol{w}_{\|,3} \\
+ \lambda_i \delta w_i + \Big[(\boldsymbol{\varepsilon} + x_3\boldsymbol{\kappa})^{\mathrm{T}} \boldsymbol{D}_{et} + \boldsymbol{w}_{\|,3}^{\mathrm{T}} \boldsymbol{D}_{st} + w_{3,3}^{\mathrm{T}} \boldsymbol{D}_t\Big] \delta w_{3,3}
\end{array}
\right\rangle = 0 \tag{20}
$$

The corresponding Euler–Lagrange equations are

$$
\begin{aligned}
\Big[(\boldsymbol{\varepsilon} + x_3\boldsymbol{\kappa})^{\mathrm{T}} \boldsymbol{D}_{es} + \boldsymbol{w}_{\|,3}^{\mathrm{T}} \boldsymbol{D}_s + w_{3,3}^{\mathrm{T}} \boldsymbol{D}_{st}^{\mathrm{T}}\Big]_{,3} &= \boldsymbol{\lambda}_{\|} \\
\Big[(\boldsymbol{\varepsilon} + x_3\boldsymbol{\kappa})^{\mathrm{T}} \boldsymbol{D}_{et} + \boldsymbol{w}_{\|,3}^{\mathrm{T}} \boldsymbol{D}_{st} + w_{3,3}^{\mathrm{T}} \boldsymbol{D}_t\Big]_{,3} &= \lambda_3
\end{aligned}
\tag{21}
$$

where $\lambda_{\|} = [\lambda_1 \quad \lambda_2]^{\mathrm{T}}$.

The boundary conditions of the top and bottom of the panel can be defined as

$$
\begin{aligned}
\Big[(\boldsymbol{\varepsilon} + x_3\boldsymbol{\kappa})^{\mathrm{T}} \boldsymbol{D}_{es} + \boldsymbol{w}_{\|,3}^{\mathrm{T}} \boldsymbol{D}_s + w_{3,3} \boldsymbol{D}_{st}^{\mathrm{T}}\Big]^{+/-} &= 0 \\
\Big[(\boldsymbol{\varepsilon} + x_3\boldsymbol{\kappa})^{\mathrm{T}} \boldsymbol{D}_{et} + \boldsymbol{w}_{\|,3}^{\mathrm{T}} \boldsymbol{D}_{st} + w_{3,3} \boldsymbol{D}_t\Big]^{+/-} &= 0
\end{aligned}
\tag{22}
$$

where the superscript "+ / −" indicates the items at the top and bottom of the panel.

From these conditions, we can solve $\boldsymbol{w}_{\|}$ and w_3 as

$$
\boldsymbol{w}_{\|} = \Big\langle -(\boldsymbol{\varepsilon} + x_3\boldsymbol{\kappa})\overline{\boldsymbol{D}}_{es} \boldsymbol{D}_s^{-1} \Big\rangle^{\mathrm{T}}, w_3 = \Big\langle -(\boldsymbol{\varepsilon} + x_3\boldsymbol{\kappa})\overline{\boldsymbol{D}}_{et} \boldsymbol{D}_t^{-1} \Big\rangle \tag{23}
$$

where

$$
\overline{\boldsymbol{D}}_{es} = \boldsymbol{D}_{es} - \overline{\boldsymbol{D}}_{et} \boldsymbol{D}_{st}^{T} \overline{\boldsymbol{D}}_t^{-1}, \overline{\boldsymbol{D}}_{et} = \boldsymbol{D}_{et} - \boldsymbol{D}_{es} \boldsymbol{D}_s^{-1} \boldsymbol{D}_{st}, \overline{\boldsymbol{D}}_t = \boldsymbol{D}_t - \boldsymbol{D}_{sl}^{T} \boldsymbol{D}_s^{-1} \boldsymbol{D}_{st} \tag{24}
$$

Plugging Equation (23) into Equation (18) gives the zeroth-order strain energy as

$$
U_{2D} = \frac{1}{2} \Big\langle (\boldsymbol{\varepsilon} + x_3\boldsymbol{\kappa})^{\mathrm{T}} \bar{\boldsymbol{D}}_e (\boldsymbol{\varepsilon} + x_3\boldsymbol{\kappa}) \Big\rangle = \frac{1}{2} \begin{Bmatrix} \boldsymbol{\varepsilon} \\ \boldsymbol{\kappa} \end{Bmatrix}^{\mathrm{T}} \begin{bmatrix} \boldsymbol{A} & \boldsymbol{B} \\ \boldsymbol{B}^T & \boldsymbol{D} \end{bmatrix} \begin{Bmatrix} \boldsymbol{\varepsilon} \\ \boldsymbol{\kappa} \end{Bmatrix} \tag{25}
$$

where A, D and B are tensile, bending, and coupling stiffness sub-matrix, respectively, and can be expressed as

$$
\begin{aligned}
A = \langle\langle \bar{D}_e \rangle\rangle, B = \langle\langle x_3 \bar{D}_e \rangle\rangle, D = \langle\langle x_3^2 \bar{D}_e \rangle\rangle, \\
\bar{D}_e = D_e - \bar{D}_{es} D_s^{-1} D_{es}^{\mathrm{T}} - \bar{D}_{et} D_{et}^{\mathrm{T}} / \bar{D}_t
\end{aligned}
\tag{26}
$$

2.2.2. Transforming into Reissner–Mindlin Model

There are two additional transverse shear strains $\gamma = \lfloor 2\gamma_{13} \quad 2\gamma_{23} \rfloor^T$ in the Reissner–Mindlin model. To transform Equation (25) into the Reissner–Mindlin model, we must eliminate the coupled stiffness terms between ϵ and γ as follows:

$$
\begin{aligned}
2\Pi_\Omega = \mathbf{\Gamma}^T \bar{D}_e \mathbf{\Gamma} = \mathcal{R}^T A \mathcal{R} + 2\mathcal{R}^T B \gamma + \gamma^T C \gamma \\
= \mathcal{R}^T \left(A - BC^{-1}B^T \right) \mathcal{R} + \left(\gamma + C^{-1}B^T \mathcal{R} \right)^T C \left(\gamma + C^{-1}B^T \mathcal{R} \right)
\end{aligned}
\tag{27}
$$

where $\mathcal{R}$ is Reissner–Mindlin generalized strains.

The final form of the total energy can be expressed as

$$
2\Pi_\mathcal{R} = \mathcal{R}^T X \mathcal{R} + \gamma^T G \gamma + 2\mathcal{R}^T F
\tag{28}
$$

where F is a load-related term and

$$
\begin{aligned}
X = A - BC^{-1}B^T \\
G = C
\end{aligned}
\tag{29}
$$

The resultant stress of the panel can be expressed as

$$
\begin{aligned}
\frac{\partial \Pi_\mathcal{R}}{\partial \varepsilon_{11}} = N_{11}, \quad \frac{\partial \Pi_\mathcal{R}}{\partial 2\varepsilon_{12}} = N_{12}, \quad \frac{\partial \Pi_\mathcal{R}}{\partial \varepsilon_{22}} = N_{22} \\
\frac{\partial \Pi_\mathcal{R}}{\partial \kappa_{11}} = M_{11}, \quad \frac{\partial \Pi_\mathcal{R}}{\partial 2\kappa_{12}} = M_{12}, \quad \frac{\partial \Pi_\mathcal{R}}{\partial \kappa_{22}} = M_{22} \\
\frac{\partial \Pi_\mathcal{R}}{\partial 2\gamma_{13}} = Q_1, \quad \frac{\partial \Pi_\mathcal{R}}{\partial 2\gamma_{23}} = Q_2
\end{aligned}
\tag{30}
$$

Due to the symmetry of the axis and plane, some stiffness components disappear, and the constitutive relation of the OSFP can be obtained as

$$
\begin{pmatrix} N_{11} \\ N_{22} \\ N_{12} \\ M_{11} \\ M_{22} \\ M_{12} \\ Q_1 \\ Q_2 \end{pmatrix} = \left(\begin{array}{ccc|ccc|cc} A_{11} & A_{12} & 0 & 0 & 0 & 0 & 0 & 0 \\ A_{12} & A_{22} & 0 & 0 & 0 & 0 & 0 & 0 \\ 0 & 0 & A_{66} & 0 & 0 & 0 & 0 & 0 \\ \hline 0 & 0 & 0 & D_{11} & D_{12} & 0 & 0 & 0 \\ 0 & 0 & 0 & D_{12} & D_{22} & 0 & 0 & 0 \\ 0 & 0 & 0 & 0 & 0 & D_{66} & 0 & 0 \\ \hline 0 & 0 & 0 & 0 & 0 & 0 & C_{11} & 0 \\ 0 & 0 & 0 & 0 & 0 & 0 & 0 & C_{22} \end{array} \right) \begin{pmatrix} \varepsilon_{11} \\ \varepsilon_{22} \\ 2\varepsilon_{12} \\ \kappa_{11} \\ \kappa_{22} \\ 2\kappa_{12} \\ \gamma_{13} \\ \gamma_{23} \end{pmatrix}
\tag{31}
$$

The original 3D geometric nonlinear problem in Equation (17) is mathematically decomposed into constitutive modeling over the unit cell in Equation (31) and geometric nonlinear plate analysis. That is to say, as an alternative to the direct numerical simulation using 3D nonlinear finite element analysis, the global analysis of the OSFP can be reduced to 2D plate analysis using the linear solver in ABAQUS, with the constitutive relation obtained from the constitutive modeling of the unit cell.

2.3. Equivalent Density of 2D-RPM

For heterogeneous materials and structures, the equivalent density of the unit cell is usually used to characterize the weight of the reduced-order plate model. The total mass of the unit cell within the OSFP can be expressed as

$$m = m_1 + m_2 + m_3 = \rho_1 \cdot L_1 L_2 \cdot t_1 + \rho_2 \cdot L_2 h \cdot t_2 + \rho_3 \cdot L_1 h \cdot t_3 \qquad (32)$$

where ρ_1, ρ_2, and ρ_3 are the density of the skin, the longitudinal stiffener and transverse stiffener, respectively.

The total volume of the unit cell is

$$V = L_1 L_2 \cdot (t_1 + h) \qquad (33)$$

According to the equivalent density formula, we obtain

$$\rho = \frac{m}{V} \qquad (34)$$

The equivalent density of the 2D-RPM can be expressed as

$$\rho^* = \frac{\rho_1 \cdot L_1 L_2 \cdot t_1 + \rho_2 \cdot L_2 h \cdot t_2 + \rho_3 \cdot L_1 h \cdot t_3}{L_1 L_2 \cdot (t_1 + h)} \qquad (35)$$

3. Validation Example

To verify the accuracy and effectiveness of the present reduced model, the static and dynamic behaviors of OSFP predicted by the present model were compared with those of 3D-FEM. The 3D-FEM had 15 unit cells in the x_1 and x_2 direction as shown in Figure 3. The equivalent stiffness of OSFP was obtained by variational asymptotic analyzing over the unit cell shown in Figure 4b and inputted into the 2D-RPM (300 mm × 300 mm) using shell elements, as shown in Figure 4c, to analyze the static and dynamic behavior under different boundary conditions. The relative error between the 2D-RPM and 3D-FEM is defined as Error $= \frac{|2D-RPM\ results - 3D-FEM\ results|}{3D-FEM\ results} \times 100\%$.
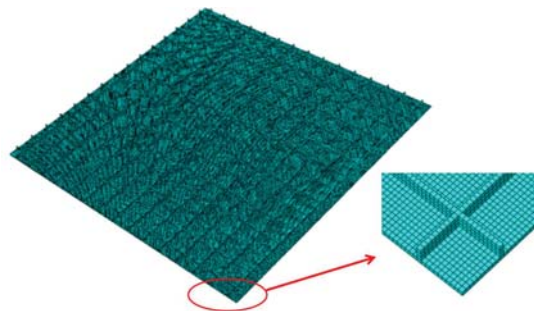
Figure 3. Meshing of 3D finite element model (3D-FEM).

The structural parameters shown in Figure 4a were: $l = 20$ mm, $h = 3$ mm, and $t = 1$ mm. The OSFP is made of T300/7901 carbon/epoxy laminates. The layup configuration of skin was $[45/-45/0/-45/45]_{2s}$, and that of stiffener was $[45/-45]_{4s}$. The lamina properties were: $E_{11} = 71.76$ GPa, $E_{22} = E_{33} = 7.81$ GPa, $G_{12} = G_{13} = 2.52$ GPa, $G_{23} = 2.11$ GPa, $v_{12} = v_{13} = 0.343$, $v_{23} = 0.532$, $\rho = 1.42$ g/cm³. The effective plate properties of the skin and the stiffener obtained by present model were given in Figure 5 for reference.

(**a**) Size of unit cell   (**b**) Meshing of unit cell   (**c**) Meshing of 2D-RPM
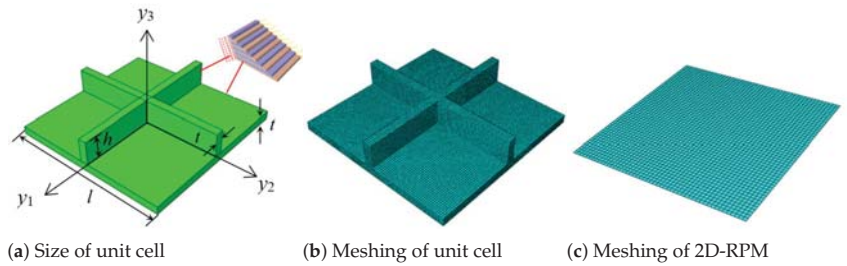
Figure 4. Meshing of unit cell and 2D reduced-order plate model (2D-RPM) of OSFP.

(**a**) Skin

(**b**) Stiffener

Figure 5. Effective plate properties of the skin and the stiffener calculated by the present model (unit: SI).

3.1. Static Displacement Analysis

Six typical boundary conditions shown in Figure 6, including CCCC, CCSS and CSCS, CSSS, SSSS and FFCC, were used for static displacement analysis. The naming convention of boundary conditions is four letters, where S denotes simply supported constraint, C for fixed constraint, and F for free constraint.

To verify the effectiveness of the 2D-RPM, a uniform load of 5 kPa was applied to the top surface of the OSFP, and the displacement distributions along Path 1 of the 3D-FEM and 2D-RPM were compared in Figure 7. The comparative results show that the displacement distributions predicted by the 2D-RPM were basically in agreement with those of the 3D-FEM. The differences were due to the different meshing methods used in the two models. The maximum displacement error under the CCSS boundary condition was the largest, but it was still within 5%. It is worth noting that the differences between the 2D-RPM and 3D-FEM in Figure 7c–e were much greater than other cases, which may be due to the gradual enhancement of boundary constraints from SSSS to CCCC. It was concluded that the 2D-RPM can predict the static displacement of the stiffened FRP panel with high accuracy and effectiveness, and the equivalent stiffness obtained from the VAM had sufficient accuracy.
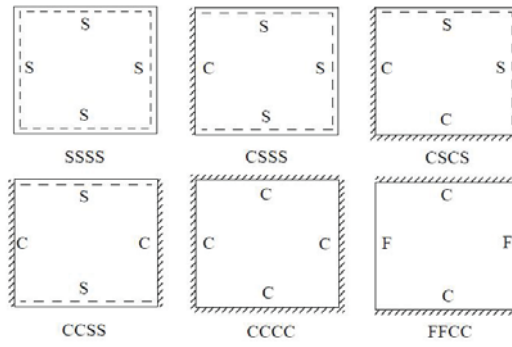
Figure 6. Typical boundary conditions of the OSFP.

(**a**) CCCC

(**b**) SSSS

(**c**) CSSS

(**d**) CSCS

(**e**) CCSS

(**f**) FFCC
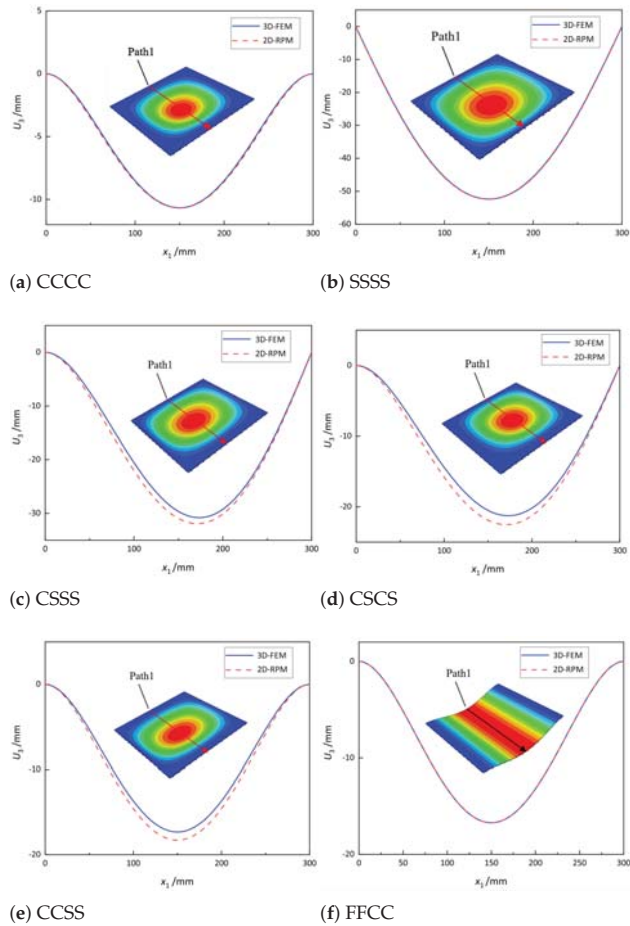
Figure 7. Vertical displacement along Path 1 of the plate under a uniform load of 5 kPa and different boundary conditions.

3.2. Local Displacement and Stress Field

According to Equation (2), the local displacement distributions within the unit cell at the geometric center of the 2D-RPM can be recovered as shown in Figure 8. It can be observed that the maximum and minimum values of U_1 and U_2 were located on opposite sides of the stiffener, and the overall displacement presented a centrosymmetric distribution trend. The smallest value of U_3 was located at the center of the stiffener, while the maximum value of U_3 was on the skin. The displacement distribution was centrally symmetric about the intersection point of the stiffeners. The maximum value of U_3 within the unit cell was 10.27 mm, and the error was about 1% compared with that of 3D-FEM presented in Section 3.1 (U_3 = 10.17 mm), indicating that the recovered displacement distribution is accurate and can be used to evaluate the location of maximum local displacement.

(a) U_1 (b) U_2

(c) U_3
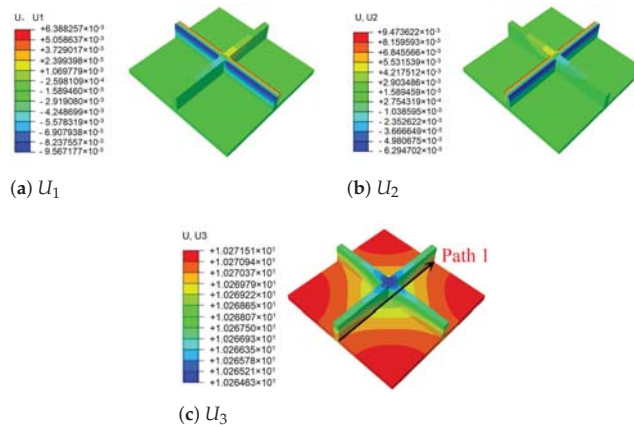
Figure 8. Local displacement fields within the unit cell at the geometric center of the plate (unit: mm).

Figure 9 shows the local stress fields within the unit cell at the geometric center of the plate recovered from Equation (8) and the 3D Hooke's law. It can be observed that the stiffeners played an important role in the process of load transfer, and there was a large stress concentration at the intersection of the stiffeners and the skin, showing a significant skin-stiffener effect. The stress distribution on the skin was relatively uniform, and there was no evident mutation. It was concluded that the stiffeners improved the bearing capacity of the panel, and the OSFP had a low weight and high strength compared to the ordinary panel.

Figure 10 shows the local von Mises stress and displacement distribution along Path 1 of the skin within the unit cell (as shown in Figures 8c and 9a) predicted by 2D-RPM and 3D-FEM. It can be observed that the local stress and displacement curves predicted by 2D-RPM and 3D-FEM agreed well, and the maximum error was less than 5%. The local stress at the junctions between the skin and the stiffeners decreased significantly, indicating that these regions were very incidental to be damaged.

(**a**) Von Mises stress   (**b**) σ_{11}

(**c**) σ_{22} (**d**) σ_{12}

(**e**) σ_{13} (**f**) σ_{23}
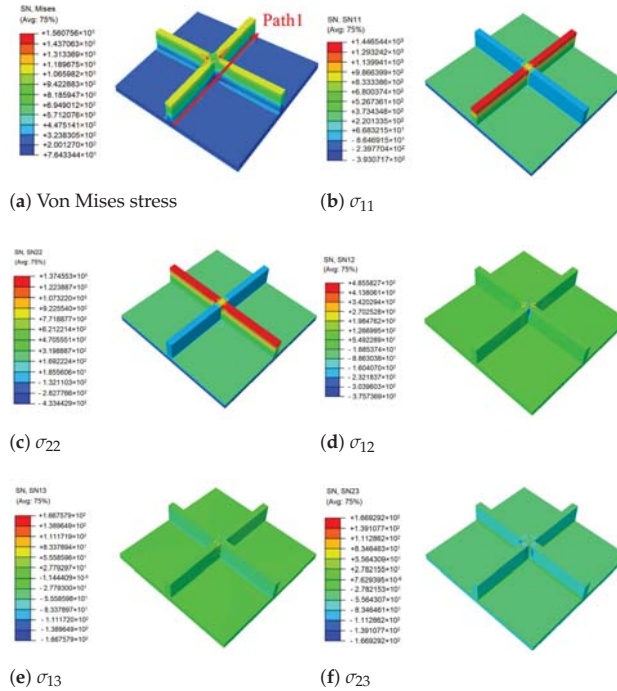
Figure 9. Local stress fields within the unit cell at the geometric center of the plate (unit: MPa).

(**a**) Von Mises stress   (**b**) U_3
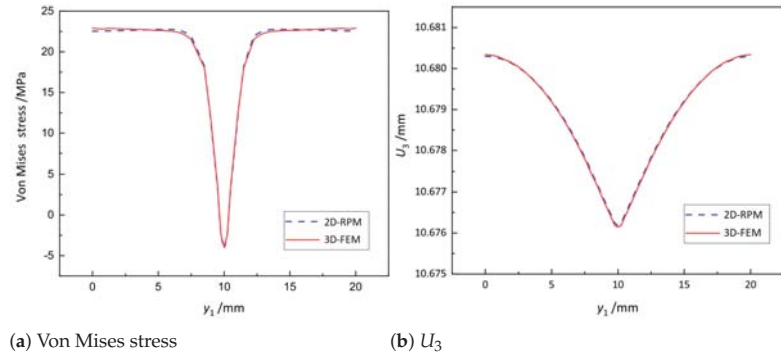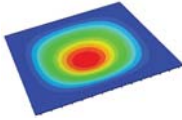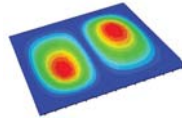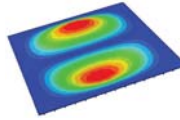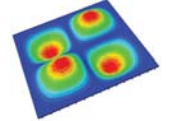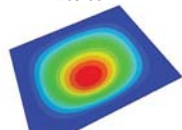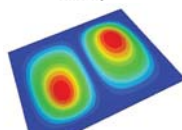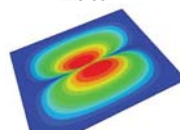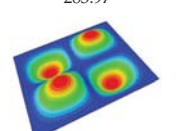
Figure 10. Comparison of von Mises stress and U_3 distribution along Path 1 within the unit cell at the geometric center of the OSFP.

3.3. Free-Vibration Analysis

Table 1 shows the the first four vibration modes and natural frequencies of the OSFP under the CCCC boundary condition predicted by 2D-RPM and 3D-FEM. The vibration modes of the 3D-FEM and 2D-RPM were in good agreement. For example, there were one and two half-waves along the x_1 direction, two half-waves along the x_2 direction, and two half-waves along the x_1 and x_2 directions for the first, second, third, and forth mode shapes, respectively, for both the 2D-RPM and 3D-FEM results. The natural frequencies of the 3D-FEM and 2D-RPM were also highly consistent, and the maximum error of the natural frequency was less than 6.83%. It was worth noting that the first-order vibration frequency showed relative big error compared with the third and fourth vibration frequencies, which
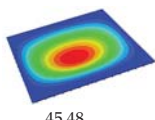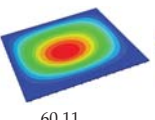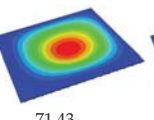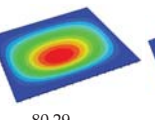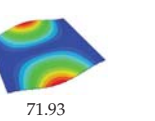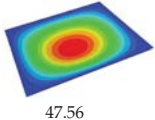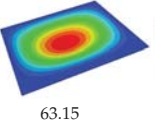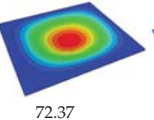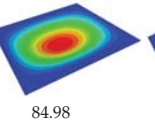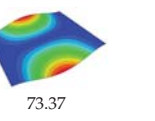
may be because the first-order frequency was more sensitive to different meshing between 2D-RPM and 3D-FEM. The 2D-RPM was more time-efficient than the 3D-FEM in analyzing the vibration modes: the 2D-RPM required 30 s with one CPU as opposed to the nearly 20 min required for the 3D-FEM with four CPUs.

Table 1. Comparison of the first four vibration modes and eigenvalues (Hz) of the OSFP predicted by 3D-FEM and 2D-RPM under the CCCC boundary condition.

Order	1	2	3	4
2D-RPM	103.68	212.48	215.68	283.97
3D-FEM	110.76	211.62	216.33	290.39
Error	6.83%	0.41%	0.30%	2.25%

It can be concluded that the 2D-RPM had high accuracy in free-vibration analysis of OSFP under CCCC boundary condition. To further verify the effectiveness of 2D-FEM in analyzing vibration modes, the vibration modes of OSFP under different boundary conditions are analyzed as shown in Table 2. The 3D-FEM and VAM-based 2D-RPM had good consistency in the prediction of natural frequencies and vibration modes under various boundary conditions, and the maximum error of natural frequency was less than 6% under the CCSS boundary condition. The stronger the boundary condition is, the higher the natural frequency is. The natural frequency under CCCC boundary condition was about twice that under SSSS boundary condition. The natural frequencies under CCSS and CSCS boundary conditions were almost the same, but the asymmetry of CSCS boundary condition led to the asymmetry of vibration mode.

Table 2. Comparison of vibration modes and natural frequencies (Hz) of the OSFP under different boundary conditions (BCs).

BCs	SSSS	CSSS	CSCS	CCSS	FFCC
2D-RPM	45.48	60.11	71.43	80.29	71.93
3D-FEM	47.56	63.15	72.37	84.98	73.37
Error	4.57%	5.06%	1.31%	5.84%	2.00%

3.4. Global Buckling Analysis

To verify the accuracy and effectiveness of 2D-RPM, the buckling modes and critical loads of OSFP under different boundary and load conditions illustrated in Figure 11 are

listed in Table 3. The combinations of boundary and load conditions included SFFF/uniaxial (Case 1), SSFF/uniaxial (Case 2), SSSS/uniaxial (Case 3), and SSSS/biaxial (Case 4).

(**a**) Case 1   (**b**) Case 2   (**c**) Case 3   (**d**) Case 4
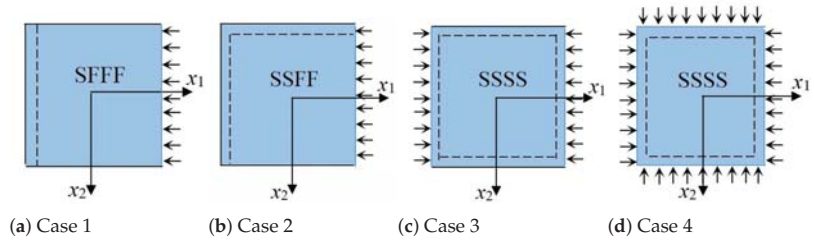
Figure 11. Four combination of boundary and load conditions used in buckling analysis.

Table 3. Comparison of global buckling modes and loads (N) predicted by the 2D-RPM and 3D-FEM under different boundary and load conditions.
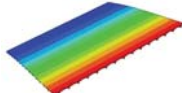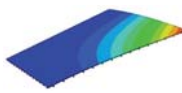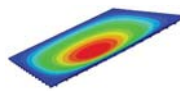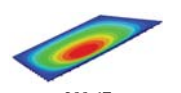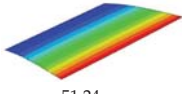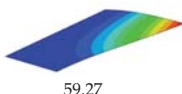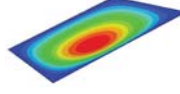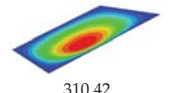
Order	1	2	3	4
2D-RPM	50.97	57.96	471.83	300.67
3D-FEM	51.24	59.27	482.12	310.42
Error	0.53%	2.26%	2.18%	3.24%

Table 3 shows that the buckling load in Case 3 (471.83 N) was about 9 times that in Case 2 (57.96 N) and 1.577 times that in Case 4 (300.67 N). The buckling loads in Case 1 and Case 2 were basically the same. The error of the critical buckling load under various boundary conditions was less than 5%, indicating that the VAM-based 2D-RPM and 3D-FEM predictions of the global buckling of OSFP agreed closely.

4. Parameter Study

The 2D-RPM was selected to conduct parametric study. The material properties and layup configurations of the skin and the stiffeners were the same as those in Section 3, except where explicitly indicated. The boundary conditions for uniaxial buckling analysis were SFFF in Case 1, while the boundary conditions for the free-vibration analysis were CCCC.

4.1. Influence of Structural Parameters on Equivalent Plate Properties

Figure 12a shows the effect of the stiffener thickness on the equivalent stiffness of the OSFP when the other parameters remained unchanged. The equivalent stiffness A_{ij} and D_{ij} increased with increasing stiffener thickness, and in particular, the bending stiffness components D_{11} and D_{22} increased significantly. This may be because A_{ij} was directly proportional to the cross-sectional area, which increased with increasing stiffener thickness. In contrast, D_{ij} was proportional to the moment of inertia, which was linearly related to the stiffener thickness.

Figure 12b shows the effect of stiffener height on the equivalent stiffness when other parameters remain unchanged. It can be seen that A_{ij} increased linearly and D_{ij} increased nonlinearly with the increasing stiffener height. The reason was that A_{ij} was proportional to the sectional area, which was linear with the stiffener height, while D_{ij} was proportional to the moment of inertia, resulting in a parabolic growth trend.

Figure 12c shows the effect of length–width ratio on the equivalent stiffness. It can be observed that A_{11} and D_{11} had no obvious change with the increasing length–width ratio, while D_{22} decreased significantly. The reason was that the extension area and moment of inertia in x_1 direction remained unchanged, while the extension area and moment of inertia in the x_2 direction gradually decreased with the increasing length–width ratio, which led to the nonlinear decrease in equivalent bending stiffness.

Figure 12d shows the effect of the periodic length on the equivalent stiffness of the stiffened FRP panel. It can be observed that A_{ij} and D_{ij} decreased nonlinearly with the increase in periodic length. This was because A_{ij} and D_{ij} were, respectively, proportional to the extension area and the moment inertia, and there was a negative nonlinear relationship between the extension area/moment inertia and the periodic length, resulting in a parabolic downward trend with the increasing periodic length.
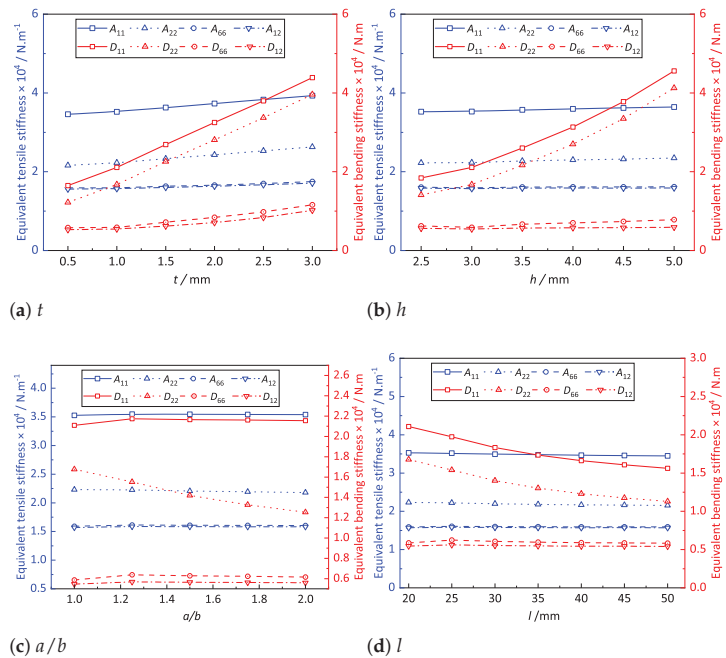
Figure 12. Effects of the structural parameters on the equivalent plate properties of the OSFP.

4.2. Influence of Structural Parameters on Buckling Loads and Natural Frequencies

To further investigate the influence of structural parameters on the effective performance of OSFP, the first four buckling loads and natural frequencies of OSFP with different stiffener height, thickness, periodic length, and length–width ratio were calculated by using 2D-RPM, as shown in Figure 13.

The first four natural frequencies of the OSFP increased with increasing stiffener thickness and height and decreased with increasing length–width ratio and periodic length. The effect of the stiffener height h on the natural frequency was much greater than that of other structural parameters. The reason is that the variation trends of the equivalent stiffness and equivalent mass were consistent with those of structural parameters, and their influences on the natural frequency might counteract each other. However, the effect of the stiffener height h on the equivalent stiffness was much greater than that on the equivalent mass. The buckling load of the OSFP increased with the increase in stiffener thickness and height but decreased with increasing length–width ratio and periodic length, which was the same as the change trend of equivalent stiffness.
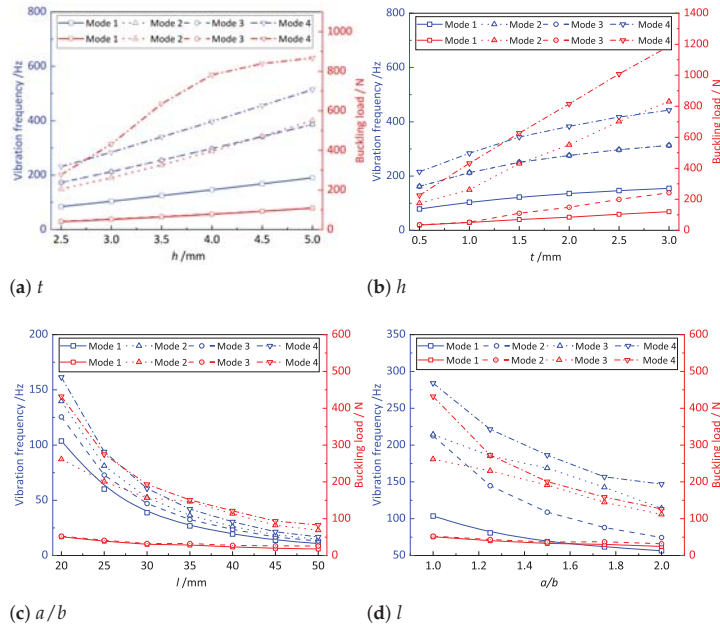
Figure 13. Effects of the structural parameters on the natural frequency and buckling load of the OSFP.

4.3. Influence of Layup Configuration on the Effective Performance of OSFP

The layup configurations of the laminates would affect the effective performance of the OSFP due to the anisotropy and heterogeneity. In this section, the influences of the layup configuration on the equivalent stiffness, free vibrations, and buckling mode of the OSFP are analyzed. The layup configuration was set to $[0/\theta/0/\theta/0]_s$, where θ increased from 0° to 90° at 15° intervals. The boundary condition was fixed on one side and simply supported on three sides (CSSS).

Figure 14a shows the effect of the layup configuration on the equivalent stiffness of the OSFP. With the gradual increase in the ply angle, the stiffness components A_{11} and D_{11} showed nonlinear downward trends, while A_{22} and D_{22} showed significant nonlinear increases when the ply angle was greater than 45°. Figure 14b shows the effect of the layup configuration on the first four natural frequencies and buckling loads of the OSFP. It can be observed that the layup configuration had little effect on the natural frequency, and the first natural frequency first decreased and then increased with the increasing ply angle, reaching the minimum value in the range of 30–60° ply angle. The buckling load first increased and then decreased with the increasing ply angle, and the buckling load of each order reached the maximum value at 30–45° ply angle.
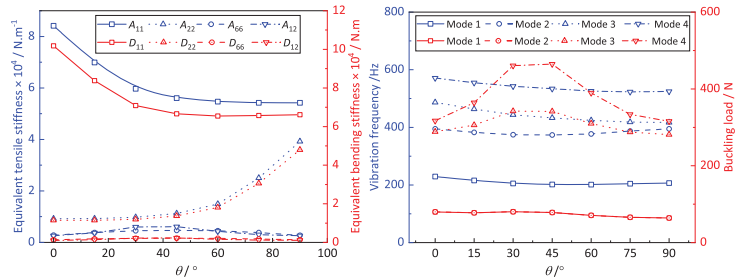
(**a**) Equivalent stiffness (**b**) Buckling load and natural frequency

Figure 14. Effects of the layup configuration on the effective performances of the OSFP.

4.4. Influence of 0°-Ply Ratio on the Effective Performance of OSFP

The 0° ply ratio r was the ratio of the number of 0°-ply to the total number of ply. To study the influence of 0°-ply ratio on the effective performance of the panel, the 10-layered laminate with combination of 0° and 45° plies was considered, and the six layup configurations are illustrated in Figure 15.

(**a**) $r = 0\%$ (**b**) $r = 20\%$ (**c**) $r = 40\%$

(**d**) $r = 60\%$ (**e**) $r = 80\%$ (**f**) $r = 100\%$
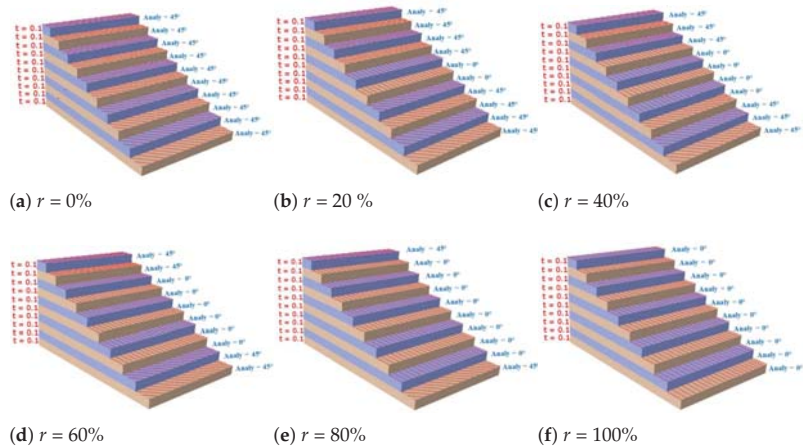
Figure 15. Six different 0°-ply ratios in the layup combination of 0° and 45° plies.

Figure 16a shows that the influences of the 0°-ply ratio on A_{11} and D_{11} were much greater than those on the other stiffness components because the stiffness along the fiber direction (0° direction) was stronger. Figure 16b shows that the first natural frequency increased with increasing 0°-ply ratio and reached a maximum value when the 0° ply ratio was 100%. The third to fourth natural frequencies increased first and then decreased and reached the maximum value when the 0°-ply ratio was between 0.2 and 0.6. With the increase in the 0°-ply ratio, the first to fourth buckling loads of the OSFP increased gradually and reached a maximum value when the 0° ply ratio was 100%. In engineering applications, the effective performance of the OSFP in the corresponding direction can be improved by adjusting the 0°-ply ratio.

(**a**) Equivalent stiffness (**b**) Natural frequency and buckling load
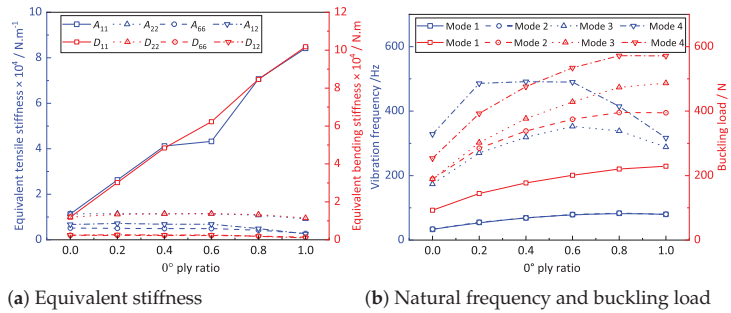
Figure 16. Effects of the structural parameters on the effective performances of the OSFP.

5. Comparison with Other Stiffened FRP Panels with Different Stiffening Forms

To compare the effects of different stiffening forms on the effective performance of the OSFP, the 3D FE models and 2D reduced-order plate models of orthogrid-, T-, and blade-stiffened FRP panel were established. The 3D FE models were obtained by repeating the unit cell 15 times in the x_1 and x_2 directions as shown in Figure 17. The structural parameters of unit cell were l = 20 mm, h = 3 mm, and t = 1 mm. The material parameters were the same as in Section 4, and the layup configurations of skin and stiffener were $[45/-45/0/-45/45]_{2s}$ and $[45/-45]_{4s}$, respectively.

(**a**) Orthogrid-stiffener (**b**) T-stiffener (**c**) Blade-stiffener
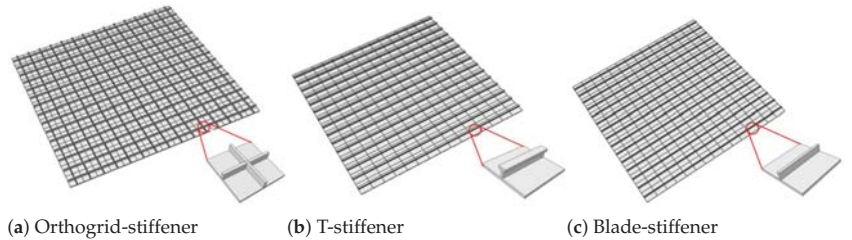
Figure 17. 3D finite element model and its unit cell of stiffened FRP panels with different stiffening forms.

The static displacements along the center line of the stiffened FRP panels under the CCCC boundary condition and 5 kPa of uniform load were analyzed. The comparative results in Figure 18 show that the displacement of the blade-stiffened FRP panel was the largest, followed by the orthogrid- and T-stiffened FRP panels due to the fact that the equivalent bending stiffness of T-stiffened FRP panel was greater than the other two stiffened FRP panels.
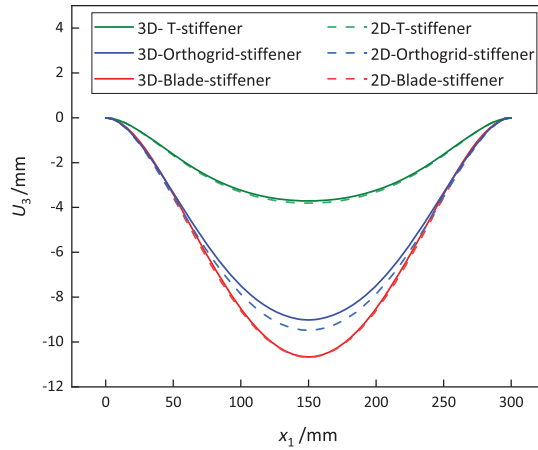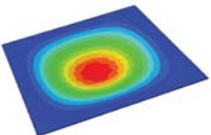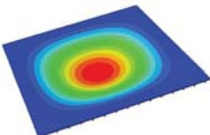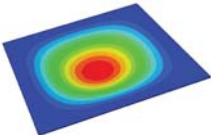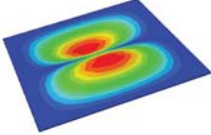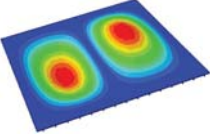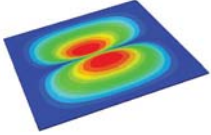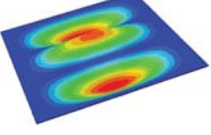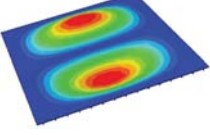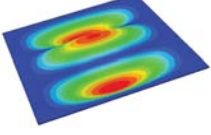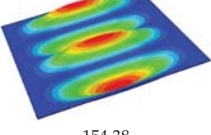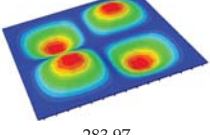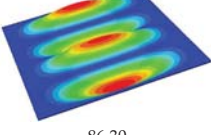
Figure 18. Comparison of the displacements along the center line of the stiffened FRP panel with different stiffening forms under the CCCC boundary condition and a 5 kPa uniform load.

Table 4 shows the first four natural frequencies of the stiffened FRP panel with different stiffening forms under the CCCC boundary condition. The first natural frequency of the T-stiffened FRP panel was the largest. From the second order, the natural frequency of the orthogrid-stiffened FRP panel was the largest, followed by the T- and blade-stiffened FRP panels.

Table 4. Influence of the different stiffening forms on the natural frequencies (Hz) of stiffened FRP panels under the CCCC boundary condition.

Orders	T-Stiffened Panel	Orthogrid-Stiffened Panel	Blade-Stiffened Panel
1	145.88	103.68	76.24
2	147.50	212.48	77.54
3	150.75	212.48	80.68
4	154.38	283.97	86.30

The comparative results showed that the natural frequencies of the OSFP increased faster with increasing modal order, while those of the T- and blade-stiffened FRP panels showed little change. The vibration modes of the T- and blade-stiffened FRP panels were basically the same, but the vibration modes of the orthogrid-stiffened FRP panel were very different (there were one and two half-waves along the x_1 direction, two half-waves along the x_2 direction, and two half-waves along the x_1, and x_2 directions for the first, second, third, and forth mode shapes, respectively). It was concluded that the vibration modes of the stiffened FRP panel could be changed by adjusting the stiffening forms.

6. Conclusions

In this work, a VAM-based reduced-order plate model was established to analyze the effective performance of the orthogrid-stiffened FRP panel (OSFP). The influences of the material and structural parameters of the OSFP were investigated by parametric studies, and the following conclusions were drawn.

(1) The results of static displacement, local field distributions, natural frequencies and buckling loads predicted by 2D-RPM were consistent with those of 3D FE model, but the computational efficiency was greatly improved, which verifies the accuracy and effectiveness of the VAM-based reduced-order plate model.

(2) The equivalent stiffness increased gradually with increasing stiffener thickness or height and decreasing length–width ratio or periodic length. The influences of the structural parameters on the buckling load were closely related to the equivalent stiffness. The effect of the stiffener height on the natural frequency of the OSFP was much greater than those of the other structural parameters.

(3) Different layup configurations had significant influences on the equivalent stiffness and buckling load of the OSFP, while they had little effect on the vibration modes. With the increase in the $0°$ ply ratio, the equivalent stiffness in the fiber direction increased significantly, and the first buckling load and natural frequency increased gradually. The static displacement and vibration modes of the orthogrid-stiffened FRP panel were different from those of the blade- and T-stiffened FRP panels, indicating that the vibration modes of the stiffened FRP panel could be varied by adjusting the stiffening forms.

Author Contributions: Conceptualization, P.W. and Y.Z.; methodology, Y.Z.; software, Z.S.; validation, D.L. and Q.Y.; formal analysis, P.W.; investigation, D.L.; resources, Q.Y.; data curation, Z.S.; writing-original draft preparation, P.W.; writing-review and editing, Y.Z. and Z.S.; visualization, Q.Y.; supervision, Y.Z.; project administration, D.L.; funding acquisition, Y.Z. All authors have read and agreed to the published version of the manuscript.

Institutional Review Board Statement: Not applicable.

Informed Consent Statement: Not applicable.

Data Availability Statement: Data available on request due to restrictions, e.g., privacy or ethical. The data presented in this study are available on request from the corresponding author. The data are not publicly available due to subsequent analyzes and publications.

Conflicts of Interest: The authors declare no conflict of interest.

References

1. Vasiliev, V.V.; Razin, A.F. Anisogrid composite lattice structures for spacecraft and aircraft applications. *Compos. Struct.* **2006**, *76*, 142–149. [CrossRef]
2. Bedair, O. Analysis and limit state design of stiffened plates and shells: A world view. *Appl. Mech. Rev.* **2009**, *62*, 391–401. [CrossRef]
3. Rikards, R.; Chate, A.; Ozolinsh, O. Analysis for buckling and vibrations of composite stiffened shells and plates. *Compos. Struct.* **2001**, *51*, 361–370. [CrossRef]
4. Silva, H.M.; Wojewoda, J. Determination of the product of inertia of stiffened plates based on Finite Element Method results. *Eng. Struct.* **2020**, *207*, 110201. [CrossRef]

5. Kumar, M.S.; Kumar, C.L.; Alagusundaramoorthy, P.; Sundaravadivelu, R. Ultimate strength of orthogonal stiffened plates subjected to axial and lateral loads. *KSCE J. Civ. Eng.* **2010**, *14*, 197–206. [CrossRef]

6. Ma, H.; Xiong, Q.; Wang, D. Experimental and numerical study on the ultimate strength of stiffened plates subjected to combined biaxial compression and lateral loads. *Ocean Eng.* **2021**, *228*, 108928. [CrossRef]

7. Srinivasan, R.S.; Thiruvenkatachari, V. Static and dynamic analysis of stiffened plates. *Comput. Struct.* **1985**, *21*, 395–403. [CrossRef]

8. Hegaze, M.M. Nonlinear Dynamic Analysis of Stiffened and Unstiffened Laminated Composite Plates Using a High-order Element. *J. Compos. Mater.* **2010**, *44*, 327–346. [CrossRef]

9. Wang, T.S.; Hsu, T.M. Discrete analysis of stiffened composite cylindrical shells. *AIAA J.* **1985**, *23*, 1753–1761. [CrossRef]

10. Reddy, A.D.; Valisetty, R.; Rehfield, L.W. Continuous filament wound composite concepts for aircraft fuselage structures. *J. Aircr.* **2012**, *22*, 249–255. [CrossRef]

11. Bisagni, C.; Vescovini, R. Analytical formulation for local buckling and post-buckling analysis of stiffened laminated panels. *Thin-Walled Struct.* **2009**, *47*, 318–334. [CrossRef]

12. Byklum, E.; Steen, E.; Amdahl, J. A semi-analytical model for global buckling and postbuckling analysis of stiffened panels. *Thin-Walled Struct.* **2004**, *42*, 701–717. [CrossRef]

13. Kidane, S.; Li, G.; Helms, J.; Pang, S.S.; Woldesenbet, E. Buckling load analysis of grid stiffened composite cylinders. *Compos. Part B Eng.* **2003**, *34*, 1–9. [CrossRef]

14. Xu, Y.; Tong, Y.; Liu, M.; Suman, B. A new effective smeared stiffener method for global buckling analysis of grid stiffened composite panels. *Compos. Struct.* **2016**, *158*, 83–91. [CrossRef]

15. Zarei, M.; Rahimi, G.H.; Hemmatnezhad, M. On the buckling resistance of grid-stiffened composite conical shells under compression. *Eng. Struct.* **2021**, *237*, 112213. [CrossRef]

16. Lopatin, A.V.; Morozov, E.V. Buckling of the composite sandwich cylindrical shell with clamped ends under uniform external pressure. *Compos. Struct.* **2015**, *122*, 209–216. [CrossRef]

17. Wodesenbet, E.; Kidane, S.; Pang, S.S. Optimization for buckling loads of grid stiffened composite panels. *Compos. Struct.* **2003**, *60*, 159–169. [CrossRef]

18. Mukhopadhyay, M.; Mukherjee, A. Finite element buckling analysis of stiffened plates. *Compos. Struct.* **1990**, *34*, 795–803. [CrossRef]

19. Guo, M.W.; Harik, I.E.; Ren, W.X. Buckling behavior of stiffened laminated plates. *Int. J. Solids Struct.* **2002**, *39*, 3039–3055. [CrossRef]

20. Chen, H.J.; Tsai, S.W. Analysis and Optimum Design of Composite Grid Structures. *J. Compos. Mater.* **1996**, *30*, 503–534. [CrossRef]

21. Sadeghifar, M.; Bagheri, M.; Jafari, A.A. Buckling analysis of stringer-stiffened laminated cylindrical shells with nonuniform eccentricity. *Arch. Appl. Mech.* **2011**, *81*, 875–886. [CrossRef]

22. Abhijit, M.; Madhujit, M. Finite element free vibration analysis of stiffened plates. *Aeronaut. J.* **1986**, *90*, 267–273.

23. Mukherjee, A.; Mukhopadhyay, M. Finite element free vibration of eccentrically stiffened plates. *Comput. Struct.* **1988**, *30*, 1303–1317. [CrossRef]

24. Mukherjee, N.; Chattopadhyay, T. Improved free vibration analysis of stiffened plates by dynamic element method. *Comput. Struct.* **1994**, *52*, 259–264. [CrossRef]

25. Lam, K.Y.; Hung, K.C. Vibration study on plates with stiffened openings using orthogonal polynomials and partitioning method. *Comput. Struct.* **1990**, *37*, 295–301. [CrossRef]

26. Yu, W.; Qian, M.; Li, H. Elastic and plastic properties of epoxy resin syntactic foams filled with hollow glass microspheres and glass fibers. *J. Appl. Polym. Sci.* **2016**, *133*, 385–397. [CrossRef]

27. Zhong, Y.; Qin, W.; Yu, W.; Zhou, X.; Jiao, L. Variational asymptotic homogenization of magneto-electro-elastic materials with coated fibers. *Compos. Struct.* **2015**, *133*, 300–311. [CrossRef]

28. Zhong, Y.; Chen, L.; Yu, W.; Zhou, X. Variational asymptotic micromechanics modeling of heterogeneous magnetostrictive composite materials. *Compos. Struct.* **2013**, *106*, 502–509. [CrossRef]

29. Zhong, Y.; Lei, C.; Yu, W. Variational asymptotic modeling of the thermomechanical behavior of composite cylindrical shells. *Compos. Struct.* **2012**, *94*, 1023–1031.

30. Cesnik, C.E.; Hodges, D.H. VABS: A new concept for composite rotor blade cross-sectional modeling. *J. Am. Helicopter Soc.* **1997**, *42*, 27–38. [CrossRef]

Article

Fatigue Resistance and Cracking Mechanism of Semi-Flexible Pavement Mixture

Shiqi Wang [1,*], Huanyun Zhou [1], Xianhua Chen [1,*], Minghui Gong [2,3], Jinxiang Hong [2,3] and Xincheng Shi [1]

[1] School of Transportation, Southeast University, Nanjing 211189, China; zhyjy@seu.edu.cn (H.Z.); sxc1193918967@126.com (X.S.)
[2] Jiangsu Sobute New Materials Co., Ltd., Nanjing 211103, China; gongminghui@cnjsjk.cn (M.G.); hongjinxiang@cnjsjk.cn (J.H.)
[3] State Key Laboratory of High Performance Civil Engineering Materials, Nanjing 211103, China
* Correspondence: sq_wang@seu.edu.cn (S.W.); chenxh@seu.edu.cn (X.C.)

Abstract: Semi-flexible pavement (SFP) is widely used in recent years because of its good rutting resistance, but it is easy to crack under traffic loads. A large number of studies are aimed at improving its crack resistance. However, the understanding of its fatigue resistance and fatigue-cracking mechanism is limited. Therefore, the semi-circular bending (SCB) fatigue test is used to evaluate the fatigue resistance of the SFP mixture. SCB fatigue tests under different temperature values and stress ratio were used to characterize the fatigue life of the SFP mixture, and its laboratory fatigue prediction model was established. The distribution of various phases of the SFP mixture in the fracture surface was analyzed by digital image processing technology, and its fatigue cracking mechanism was analyzed. The results show that the SFP mixture has better fatigue resistance under low temperature and low stress ratio, while its fatigue resistance under other environmental and load conditions is worse than that of asphalt mixture. The main reason for the poor fatigue resistance of the SFP mixture is the poor deformation capacity and low strength of grouting materials. Furthermore, the performance difference between grouting material and the asphalt binder is large, which leads to the difference of fatigue cracking mechanism of the SFP mixture under different conditions. Under the fatigue load, the weak position of the SFP mixture at a low temperature is asphalt binder and its interface with other materials, while at medium and high temperatures, the weak position of the SFP mixture is inside the grouting material. The research provides a basis for the calculation of the service life of the SFP structure, provides a reference for the improvement direction of the SFP mixture composition and internal structure.

Keywords: semi-flexible pavement; fatigue resistance; cracking mechanism; fatigue prediction; fracture surface

1. Introduction

Semi-flexible pavement is a new type of pavement structure formed by replacing one or more layers of the traditional asphalt pavement surface with a semi-flexible composite material formed by pouring cement grouting material with porous asphalt mixture. It has been highly valued in road engineering in recent years. The annual application area of SFP in China is close to 1 million square meters. The application of SFP covers Jiangsu, Shanghai, Guangdong and other provinces [1–3]. SFP mixture is a composite pavement material formed by pouring specific cement slurry into macroporous asphalt mixture, which is named because its stiffness is between asphalt concrete and cement concrete [4]. Laboratory tests and engineering practices show that the SFP mixture have excellent shear strength, rutting resistance, high temperature stability [5,6], better durability than traditional asphalt pavement [7], and may help with mitigating urban heat islands in city centres [8,9]. Although SFP shows excellent rutting resistance and comprehensive road

performance, SFP in many sections has different degrees of cracking, and a few sections have premature pavement failure due to rapid crack development [10,11].

By finite element calculation, it is found that the maximum stress in the structure does not reach the ultimate stress that SFP can bear, so the influence of fatigue on cracking needs to be considered. In order to improve the material and structure for crack resistance, it is necessary to judge the weak position of the SFP mixture and the crack control stress. In order to find the weak parts, Ding built a SFP finite element model through digital image processing technology, characterized the distribution of materials through three-phase material structure, inferred the weak points of materials in cracks through tensile strain, and considered that the probability of cracks appearing at the interface between asphalt and grouting materials was greater [12]. A. Setyawan believes that the strength of SFP mainly depends on the strength of cement binder, and the compressive strength of cold mix grouting composite is lower than that of hot mix grouting material [13]. For the judgment of control stress, Cai applied acoustic emission technology to detect the failure process of the SFP and its porous asphalt mixture in uniaxial compression test [14]. RA (quotient of rise time divided by amplitude) value and energy distribution show that the number of shear cracks of the SFP increases during compression [14].

For the improvement of structure, Chen believes that the cracks of the SFP are mainly reflection cracks [15]. The structural model of the SFP mixture is established through finite element method, and the shear force is the main factor for crack development by applying the principle of fracture mechanics and judging through the stress intensity factor [15]. Temperature also has an important influence on the crack resistance of the SFP mixture [16,17]. Based on the above research, the methods to improve the crack resistance of the SFP include: adding materials to strengthen the bonding between three-phase material interfaces [14], reinforcing three-phase materials [18], adjusting gradation or material mix ratio [19], optimizing pavement structure and layer position [20–23].

Phenomenological method is a more traditional fatigue performance research method. It is considered that fatigue is a phenomenon caused by strength attenuation under repeated action. There are many kinds of laboratory tests used in phenomenological method, mainly including splitting fatigue test, four-point bending fatigue test, semicircular bending fatigue test, etc. The local deformation of splitting fatigue test is large, and it is difficult to control the strain [24]. The loading mode of the four-point bending method is closer to the vehicle load of the actual pavement. The four-point bending operation is simple, and the theoretical cracking point expands into a region, which is suitable for uneven materials [25,26]. The SCB fatigue test can establish a fatigue prediction model with good correlation and high accuracy [27]. The specimen of SCB fatigue test has a notch, which is more suitable for the structure with initial crack. The test specimen is easy to make, the test process is easy to control, and the result parameters are stable. It can be compared and verified in combination with the experimental results of indoor preparation and field sampling samples, which is of great significance for engineering practical detection and indoor experimental research [28].

For the cracking phenomenon of SFP, there is little research on the mechanism of fatigue failure starting from fatigue cracking, and the calculation method of fatigue performance has not formed a system. It is often considered that the weak point of the SFP mixture is the interface between asphalt binder and other materials, while the impact on the integrity of the material caused by the brittleness of grouting material and the property difference between it and asphalt mixture is ignored.

In order to understand the fatigue performance and cracking mechanism of SFP and provide reference for the material and structural design of SFP, the specific objectives of this study are as follows:

1. Evaluate the fatigue resistance of the SFP mixtures under different conditions by SCB fatigue test. Establish fatigue prediction model of the SFP mixtures.
2. Analyze the composition of fracture surface in SCB fatigue test by digital image processing technology to investigate its cracking mechanism. Discuss the influence of

the difference between asphalt binder and grouting material on the fatigue cracking mechanism under different conditions.

2. Materials and Methods

2.1. Materials

SFP is prepared by pouring cement grouting material into porous asphalt (PA) mixture. The PA mixture is composed of asphalt binder, aggregate, lignin fiber, and MA-100 (Modified Agent-100) modifier. The cement grouting material was provided by Sobute New Materials Co. Ltd. (Nanjing, China).

Styrene–butadiene–styrene (SBS) modified asphalt was used as the basic asphalt binder. Its main technical indicators are shown in Table 1, and they all meet the technical requirements. Basalt was chosen as aggregate in this study and the gradation of PA is referred to Gong [29]. MA-100 modifier is a kind of asphalt interface reinforcing agent produced by Sobute New Materials Co. Ltd., and its dosage is determined by the weight of asphalt binder. Lignin fiber was included as the stabilizer of the mixture, and its dosage is determined by the weight of PA mixture. The optimal asphalt content was calculated according to the contribution from asphalt binder and modifiers and determined by Cantabro and drainage tests. The material composition and quality of PA mixture is shown in Table 2.

Table 1. Main technical indicators of SBS modified asphalt.

Properties	Unit	Test Value	Requirements (GB T 494–2010)
Softening point	°C	75	$\geq$60
Ductility (5 °C)	cm	30	$\geq$20
Penetration (100 g, 25 °C)	0.1 mm	54	40–60
Storage stability	°C	1.2	$\leq$2.5
Viscosity	Pa·s	2.0	$\leq$3.0
Flash point	°C	311	$\geq$230
Elasticity recovery (25 °C)	%	92	$\geq$75

Table 2. Material composition and quality of PA mixture.

Mixture Component	Content
Aggregate (mm)	98.0
Limestone powder	2.0
SBS Modified asphalt	4.2
MA100	0.3
Lignin fiber	0.2

JGM®-301 grouting material is adopted in this study. Its main properties are shown in Table 3. The water cement ratio is 0.34. It is a kind of early strength cement, which only needs curing for 14 days in the standard curing room.

Table 3. Main properties of grouting material.

Fluidity/s		Setting Time/h		Compressive Strength/MPa				24 h Bleeding Rate (%)	Dry Shrinkage Ratio (%)
Initial	30 min	Initial	Final	2 h	3 h	3 d	28 d		
10.3	12.6	0.9	1.4	15.8	24.0	34.5	42.3	0.1	0.14

The preparation process of the SFP specimen for the experiment is as follows. Firstly, the cylindrical specimens of PA mixture is prepared using shear gyratory compactor (CONTROLS, Italy), and were sealed by tape after cooling to room temperature. The

grouting material is poured into PA mixture, and the specimens after grouting are cured for 14 days in the environment with temperature of 25 °C and humidity of 90%. After curing, the specimens were cut into semicircles. The thickness and diameter of the specimens were 50 mm and 150 mm, respectively.

2.2. Experiment

The semicircular specimens were used for monotonic SCB test and SCB fatigue test [30,31]. Universal testing machines (IPC, Australia) were used to load the specimens. The specimens were slit with the target notch depth of 15 mm and width of 1 mm for the SCB fatigue test. In this paper, the fracture of the specimen was taken as the fatigue failure criterion, so the stress control method is adopted in the SCB fatigue test. Temperature and stress ratio were selected as the variables of the test and the test under each condition was repeated three times to reduce the error. The tensile strength of the SFP at different temperature values was obtained by monotonic SCB test. The calculation method of tensile strength is as follows [32]:

$$\sigma_t = \frac{4.976F}{BD} \tag{1}$$

σ_t is tensile strength, MPa; F is the value of peak load, N; B is the thickness of the specimen, mm; D is the diameter of the specimen, mm.

The tensile strength of the SFP is the average of three parallel tests. The fatigue load of different temperature values and stress ratio tests is calculated by tensile strength. The loading frequency of the fatigue test was 10 Hz. The scheme of SCB fatigue test is shown in Table 4.

Table 4. Scheme of SCB fatigue test.

Factor	Content
Material	SFP-13
Stress ratio	0.4, 0.5, 0.6, 0.7
Temperature (°C)	−5, 15, 35
Load frequency (Hz)	10
Times of parallel tests	3

2.3. Analysis Methodology

2.3.1. Fatigue Prediction Model of Materials in Laboratory

The establishment of the SFP fatigue prediction model draws lessons from the establishment method of asphalt mixture fatigue prediction model, such as the SHRP model, Asphalt Institute (AI model), shell model, and the multivariable and multi parameter fatigue prediction model established by Tongji University and South China University of Technology. The main idea of fatigue prediction model is to establish the relationship between material stress or strain and fatigue action times, introduce the influence of temperature, consider the modulus of asphalt mixture, asphalt aggregate ratio and other factors to improve it. Based on the data of SCB fatigue test, a fatigue prediction model suitable for SFP can be established. The variables of the fatigue prediction model mainly include the stress of the material, the dynamic modulus of the SFP mixture, and the ambient temperature. Referring to the fatigue prediction model of asphalt mixture mentioned above, the stress and modulus are the base in the formula, and the other influencing factors are constant parameters and the index of e (base of natural logarithm). The basic form of the final SFP mixture fatigue prediction model is as follows:

$$N_f = ke^{k_1(N-T)}\sigma^{k_2(N-T)+k_3}|E_0|^{k_4} \tag{2}$$

N_f is fatigue life, times; T is temperature of test piece and environment, °C; σ is tensile stress, MPa; $|E_0|$ is dynamic modulus at 20 °C, MPa. N, k_1, k_2, k_3 and k_4 can be obtained by

fitting the test results. In this study, only one mix proportion of the SFP is adopted, so k_4 is taken as 0.

The fatigue prediction model can be used to predict the fatigue life of materials in the laboratory and can be used to calculate the fatigue life of structures in engineering after modification.

2.3.2. Analysis Method of Fracture Surface in SCB Fatigue Test

As shown in Figure 1 the fracture surface of the SFP mixture consists of aggregate, grouting material, asphalt and its interface with other materials (hereinafter referred to as asphalt phase). The color of aggregate and grouting material is gray white, which is quite different from that of asphalt phase, and the asphalt phase is pure black. The color of aggregate and grouting material is similar, so it is difficult to distinguish them in digital image processing. However, the aggregate is mainly distributed in the cutting seam in the cross-section, and hardly distributed in the fracture surface, which can be ignored in image processing. Therefore, it is only necessary to distinguish the two colors in the image to achieve the purpose of statistical distribution of grouting material and the asphalt phase in the fracture surface.
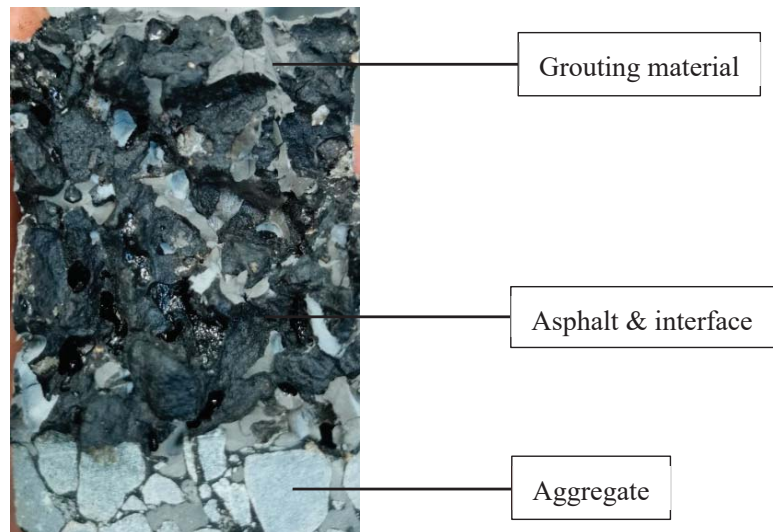
Figure 1. Fracture surface of the SCB fatigue test.

The original image was rotated and cut to get the fracture surface area, then it was binary processed by MATLAB [33]. Black pixels and white pixels represent the asphalt phase and grouting material, respectively, and their proportion in the total image pixels was calculated. The calculated results can be used to analyze the similarities and differences of the SFP fatigue failure process under different conditions, so as to further analyze the fatigue failure mechanism of the SFP.

The fracture surface image was randomly selected to determine the binarization threshold. As shown in Figure 2, the best effect was achieved by selecting the calculation result of gray thresh function of MATLAB plus 0.15 as the threshold. This threshold calculation method can reduce the errors caused by material reflection, camera aperture size, exposure time and so on.

(**a**) Original image.

(**b**) AI calculation results.

(**c**) 0.5.

(**d**) AI calculation results +0.15.
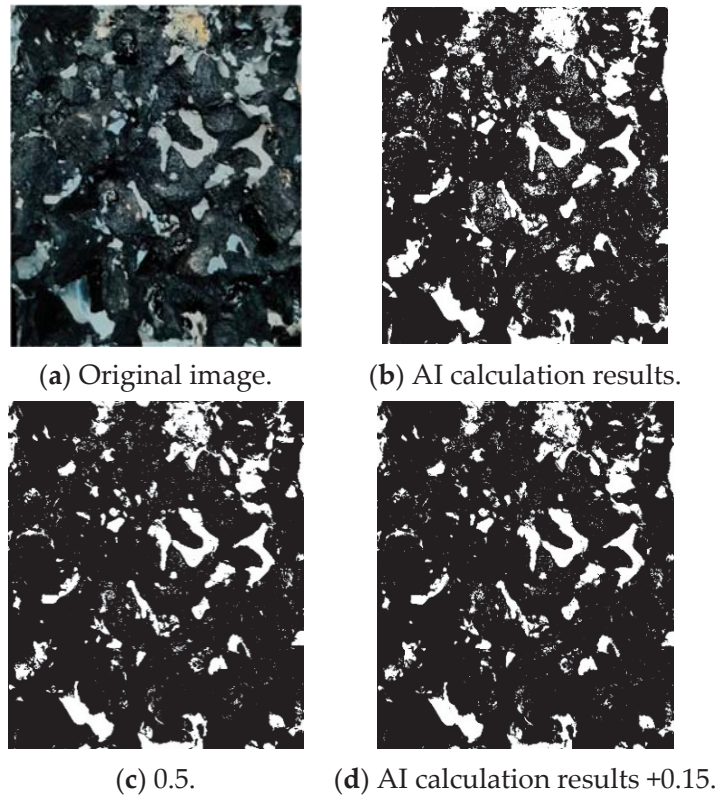
Figure 2. Selection of image binarization threshold.

3. Results and Discussion

3.1. SCB Fatigue Test Results

The tensile strength of the SFP at different temperature values are shown in Figure 3, which is used as the basis for fatigue test. The variation trend of fatigue life with temperature and stress ratio is shown in Figure 4. Obviously, the properties of the SFP mixture are greatly affected by temperature and stress ratio: The flexural tensile strength decreases with the increase of temperature. When the stress ratio is low, the fatigue life decreases with the increase of temperature, and when the stress ratio is high, the fatigue life first decreases and then increases with the increase of temperature. The fatigue life decreases with the increase of stress ratio. The fitting results of the SFP fatigue prediction model are shown in Table 5. The fatigue prediction model $R^2 = 0.9937$, and the fitting results are good. Compare the fatigue life prediction value calculated by the fatigue prediction model with the actual value obtained from the test, as shown in Figure 5. The analysis of Figure 5 shows that the predicted value of fatigue data is slightly larger than the actual value, but the change trend of the fatigue prediction model is the same. The expression can predict the times of material fatigue failure and judge the change trend of fatigue life under different conditions, which has reference significance in the design of semi-flexible pavement structure.
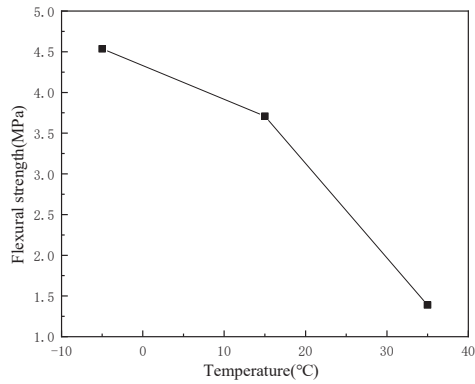
Figure 3. Flexural strength of the SFP.
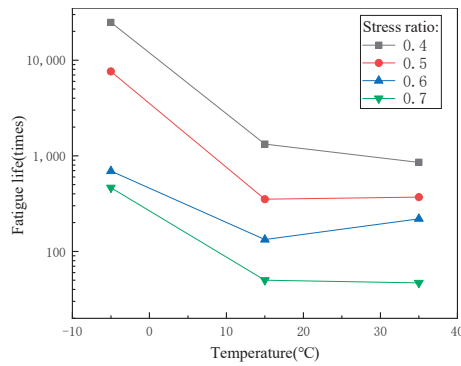
(**a**) Variation trend of fatigue life with temperature.
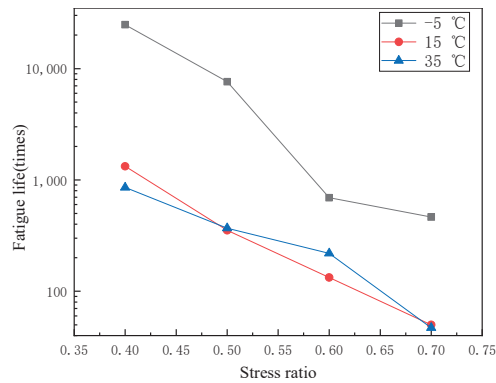
(**b**) Variation trend of fatigue life with stress ratio.

Figure 4. Fatigue life of the SFP mixture.

Table 5. Fitting results of fatigue prediction model.

k	k_1	k_2	k_3	N	R^2
81.746	0.222	0.0638	−3.371	36.986	0.9937
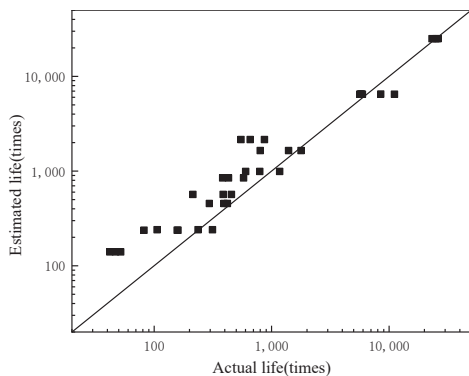
Figure 5. Comparison between estimated fatigue life and actual fatigue life.

3.2. Discussion on Fatigue Performance of the SFP Mixture

Taking the common asphalt mixture AC as the control group, the fatigue performance was measured by using the same test scheme as the above, which was used to evaluate the fatigue resistance of the SFP. Figure 6 shows the fatigue life comparison of the two materials under different environments. The fatigue properties of the two materials are significantly different, and the fatigue life of the SFP is much more sensitive to temperature and stress ratio. At low temperature and a low stress ratio, the fatigue life of the SFP is 4–5 times that of AC, which shows excellent fatigue resistance of the SFP. However, at a low temperature and high stress ratio, the fatigue life of the SFP decreases sharply, which has been significantly less than that of AC under the same conditions. At medium and high temperature, the fatigue life of the SFP is much less than that of AC regardless of the stress ratio. At the same stress ratio, from low temperature to medium temperature, the fatigue life of the SFP is greatly affected by temperature, while from medium temperature to high temperature is less affected by temperature.
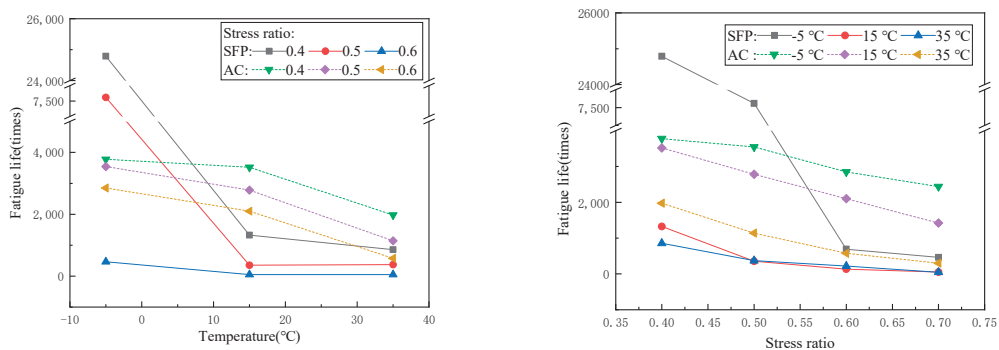
(**a**) Variation trend of fatigue life with temperature. (**b**) Variation trend of fatigue life with stress ratio.

Figure 6. Fatigue life comparison of AC and SFP.

According to all conditions, the SFP mixture can only have better fatigue resistance under low temperature and low stress ratio, and the fatigue resistance under other conditions is worse than that of asphalt mixture, and the fatigue resistance under high temperature and high stress ratio is far worse than that of asphalt mixture. This is determined by the properties of its constituent materials. The asphalt aggregate ratio of the parent asphalt mixture of the SFP mixture is similar to that of AC mixture used for comparison (4.2%

and 5% respectively), but the asphalt binder content of the SFP mixture decreases after grouting. Based on the preliminary analysis of the characteristics of the SFP mixture and the above results, it is considered that the poor fatigue resistance of the SFP mixture is due to the low strength and poor deformation capacity of grouting materials. In the process of fatigue loading, it can be considered that microcracks of different sizes and numbers will be produced in the three materials. The generation time of microcracks and the number and size of microcracks depend on the crack resistance of the material itself. Asphalt has the best deformation ability in the three materials and has self-healing ability. The aggregate has high strength and good crack resistance, it is difficult to produce microcracks, and the fracture energy required for crack propagation is large. The early strength cement used for grouting material has less strength than aggregate, high brittleness, less deformation resistance than asphalt binder, so its crack resistance is the worst. Based on the characteristics of the three materials, the grouting material is most prone to brittle failure during fatigue loading, resulting in stress concentration at the crack tip, which makes the crack expand rapidly in the specimen. In conclusion, the grouting material is easy to crack, resulting in a concentration of stress, which makes the anti-fatigue performance of the SFP poor.

3.3. Digital Image Processing Results

Count the area share of grouting material in the crack surface of the specimen and take the average value of three parallel specimens as the final result. The trend of the area share of grouting material in the fracture surface with temperature and stress ratio is plotted as shown in Figure 7. Determined by Archimedes method, the connected porosity of parent macroporous asphalt mixture of the SFP mixture in this study is about 18%. Therefore, in the section of the specimen, the area of grouting material should account for about 18%. If the area of grouting material in the fracture surface is relatively small, it can be considered that the crack tends to bypass the grouting material when it occurs and expands. If the area of grouting material accounts for a large proportion, it can be considered that cracks tend to pass through the grouting material when they occur and expand. The analysis of Figure 7 shows that the area of grouting material in the fracture surface of SCB fatigue test accounts for 10–25%.
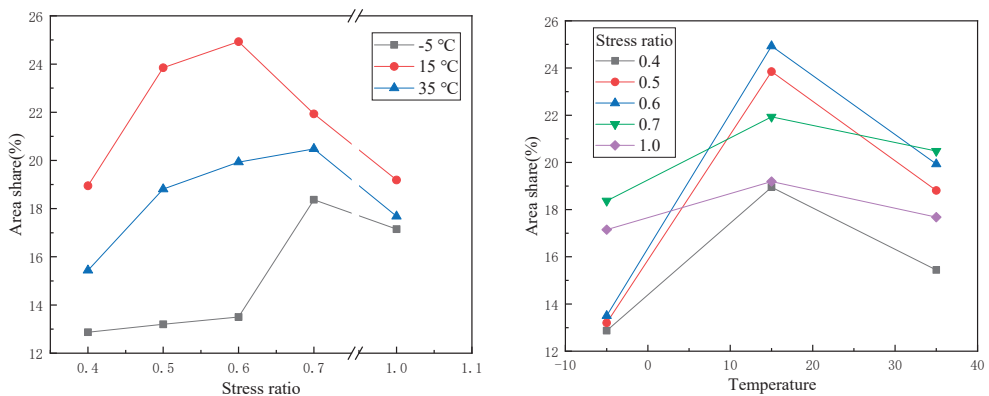
(**a**) Area share of different stress ratio. (**b**) Area share at different temperature values.

Figure 7. Area share of grouting material in the fracture surface.

3.4. Discussion on Cracking Mechanism of the SFP Mixture

According to Figure 7a, when the stress ratio is less than 0.7, the area proportion of grouting material increases with the increase of stress ratio. Under a fatigue load, with the increase of stress ratio, the grouting material gradually becomes easier to crack than the asphalt phase. The strength of grouting material is higher than that of the asphalt phase. At

a low stress ratio, the load has exceeded the fatigue failure stress of asphalt phase. Fatigue cracks begin from the asphalt phase and expand to the whole specimen with the asphalt phase as the main path. Early cracks will also appear in a few grouting materials at stress concentration positions. When the stress ratio increases gradually, the stress of grouting material gradually reaches and exceeds its fatigue failure stress. Due to the large brittleness and poor deformation capacity of the grouting material, the cracks occur earlier than the asphalt phase, and the propagation path of the cracks includes the asphalt phase and the grouting material. When the stress ratio is greater than 0.7, the area proportion of grouting material is close to 18%, which is due to less fatigue times under high stress ratio, and the failure form of material is more similar to single loading failure.

According to Figure 7b, the proportion of grouting material in the area of fracture surface first increases and then decreases with the increase of temperature, which may be due to the fact that the temperature sensitivity of cement grouting material is not as good as that of asphalt mixture. At low temperatures, the stiffness of the asphalt phase and the cement grouting material are both large, and close to brittle failure. However, because the strength of asphalt is lower than that of cement grouting material, its failure time is earlier when the temperature and stress are relatively low, so the area of grouting material in the fracture surface is relatively small. At medium temperature, the strength of asphalt phase and grouting material decreases. Asphalt has higher temperature sensitivity. With the increase of temperature, its deformation capacity improves, and the grouting material is still brittle failure. At the same time, due to the faster decline of modulus of asphalt phase, the grouting material shares a greater proportion of stress, and the cracking time of grouting material is earlier than that of asphalt phase, so the area proportion in the fracture surface increases. At a high temperature, the strength of asphalt decreases obviously, and the proportion of stress shared by grouting material continues to increase after asphalt softening. However, because the decrease of asphalt strength exceeds the increase of stress borne by grouting material, the area proportion of asphalt phase rises somewhat.

In actual use, due to the high strength of aggregate, the loading stress is difficult to cause damage. Asphalt has a self-healing ability.

During fatigue loading, the process of microcrack generation, incomplete self-healing, crack generation and propagation is repeated in the asphalt phase until the material is completely destroyed. The asphalt phase is the main factor controlling the fatigue resistance of asphalt mixture. The difference between the SFP mixture and asphalt mixtures lies in the role of grouting material in the destruction process. The strength of the grouting material is less than that of the aggregate. During the fatigue loading process, microcracks continue to occur in the grouting material, but the grouting material does not have the self-healing ability. At the same time, the stress concentration at the crack tip weakens the self-healing ability of the asphalt phase, and finally leads to the acceleration of the overall failure process of the specimen.

In conclusion, the difference of material properties and temperature sensitivity between the asphalt phase and the grouting material leads to the difference of fracture surface composition of specimens under different conditions. This phenomenon reveals that the poor fatigue resistance of the SFP mixture at medium and high temperature is caused by the brittleness of the grouting material, the difference of modulus between the grouting material and the asphalt, and stress concentration.

4. Conclusions

The fatigue resistance of the SFP mixture under different temperature values and stress ratio was evaluated by the SCB fatigue test, and the laboratory fatigue prediction model of the SFP mixture is established. The fatigue cracking mechanism of the SFP mixture is analyzed by a digital image processing technology. A fatigue prediction model for SFP structure calculation is derived. The conclusions are as follows:

1. At a low temperature and low stress ratio, the fatigue resistance of the SFP is 2–7 times that of AC. At a medium temperature or high stress, the fatigue resistance of the SFP

suddenly drops to 15–45% of AC. Under the condition of high temperature and a high stress ratio, SFP almost loses its anti-fatigue ability.

2. The main reason for the poor fatigue resistance of the SFP mixture is the poor deformation capacity and low strength of grouting materials.

3. The performance difference between grouting material and asphalt binder is large, which leads to the difference of fatigue cracking mechanism of the SFP mixture under different conditions.

4. Under a fatigue load, the weak position of the SFP mixture at la ow temperature is asphalt binder and its interface with other materials, while at medium and high temperatures, the weak position of the SFP mixture is inside the grouting material.

5. The research on improving the fatigue resistance of the SFP mixture at medium and high temperatures can start from improving the deformation resistance and strength of grouting material.

This study points out that fatigue cracking is one of the main forms of the SFP structural cracking, and proposes a fatigue prediction model for SFP mixtures to provide a reference for structural design and life calculation, and provides research directions for improving the crack resistance of the SFP mixtures from the aspects of material composition and material modification.

There are two main limitations of this study. First, only one mix proportion of the SFP mixture is selected, and the fatigue prediction model has room for further optimization. Secondly, the cracking mechanism of the SFP mixture is analyzed from the surface after fracture, and the observation of fatigue cracking process is lack. In the later research, it is suggested to adjust the mix proportion of the SFP mixture to improve the fatigue prediction model of the SFP. It will be very effective to monitor and analyze the entire process of fatigue cracking of the SFP mixture with the help of real-time computer tomography and digital image correlation technology.

References

1. Bai, Y.; He, J.; He, C. Study on field test application and detection evaluation of semi flexible pavement materials. *Shanghai Highw.* **2020**, *1*, 18–23.
2. Tan, J.; Deng, S.; Gong, M.; Ding, Q.; Xiong, Z.; Wu, W. Application of Semi-Flexible Pavement in Rutting Treatment of Municipal Roads. *China Munic. Eng.* **2021**, *3*, 102–129.
3. Qiu, Y.; Cai, X.; Xiao, H. Research on Self-healing Durability of Semi-flexible Pavement Materials Grouted with ECC Mortar. *Highway* **2020**, *10*, 1–5.
4. Guo, X.; Hao, P. Influential Factors and Evaluation Methods of the Performance of Grouted Semi-Flexible Pavement (GSP)—A Review. *Appl. Sci.* **2021**, *11*, 6700. [CrossRef]
5. Hanpu, D. Experimental study on fatigue resistance of semi-flexible pavement materials. *East China Highw.* **2020**, *3*, 112–114.

6. Cai, X.; Zhang, H.; Zhang, J.; Chen, X.; Yang, J.; Hong, J. Investigation on reinforcing mechanisms of semi-flexible pavement material through micromechanical model. *Constr. Build. Mater.* **2019**, *198*, 732–741. [CrossRef]

7. Cai, J.; Pei, J.; Luo, Q.; Zhang, J.; Li, R.; Chen, X. Comprehensive service properties evaluation of composite grouting materials with high-performance cement paste for semi-flexible pavement. *Constr. Build. Mater.* **2017**, *153*, 544–556. [CrossRef]

8. Guangying, L. The Application of Phase Change Material in The Semi-flexible Pavement. Master's Thesis, Chang'an University, Xi'an, China, 2013.

9. Shooshtarian, S.; Rajagopalan, P. Daytime thermal performance of different urban surfaces: A case study in educational institution precinct of Melbourne. *Archit. Sci. Rev.* **2018**, *61*, 29–47. [CrossRef]

10. Jiahong, W. Research on Crack Resistance of Semi-flexible Pavement Materials. *E3S Web Conf.* **2021**, *248*, 01020. [CrossRef]

11. Kaixuan, Z. Study on Micromechanical Properties and Layer Optimization of Semi-Flexible Pavement Material. Master's Thesis, Southeast University, Nanjing, China, 2018.

12. Ding, Q.; Zhao, M.; Shen, F.; Zhang, X. Mechanical Behavior and Failure Mechanism of Recycled Semi-flexible Pavement Material. *J. Wuhan Univ. Technol.-Mater. Sci. Ed.* **2015**, *30*, 981–988. [CrossRef]

13. Setyawan, A. Asessing the Compressive Strength Properties of Semi-Flexible Pavements. *Procedia Eng.* **2013**, *54*, 863–874. [CrossRef]

14. Cai, X.; Fu, L.; Zhang, J.; Chen, X.; Yang, J. Damage analysis of semi-flexible pavement material under axial compression test based on acoustic emission technique. *Constr. Build. Mater.* **2020**, *239*, 117773. [CrossRef]

15. Hao, C. Research on Optimization of Semi-Flexible Pavement Structure Based on Crack Resistance. Master's Thesis, Southeast University, Nanjing, China, 2019.

16. Cai, X.; Shi, C.; Chen, X.; Yang, J. Identification of damage mechanisms during splitting test on SFP at different temperatures based on acoustic emission. *Constr. Build. Mater.* **2021**, *270*, 121391. [CrossRef]

17. Wang, L.M.; Juan, H.W. Study on Influencing Factors of Low Temperature Crack Resistance of Semi-flexible Pavement Materials Based on Freezing Test. *J. Highw. Transp. Res. Dev.* **2020**, *37*, 39–44.

18. Afonso, M.L.; Dinis-Almeida, M.; Pereira-de-Oliveira, L.A.; Castro-Gomes, J.; Zoorob, S.E. Development of a semi-flexible heavy duty pavement surfacing incorporating recycled and waste aggregates—Preliminary study. *Constr. Build. Mater.* **2016**, *102*, 155–161. [CrossRef]

19. Wang, D.; Liang, X.; Li, D.; Liang, H.; Yu, H. Study on Mechanics-Based Cracking Resistance of Semiflexible Pavement Materials. *Adv. Mater. Sci. Eng.* **2018**, *2018*, 8252347. [CrossRef]

20. An, S.; Ai, C.; Ren, D.; Rahman, A.; Qiu, Y. Laboratory and Field Evaluation of a Novel Cement Grout Asphalt Composite. *J. Mater. Civ. Eng.* **2018**, *30*, 04018179. [CrossRef]

21. Cihackova, P.; Hyzl, P.; Stehlik, D.; Dasek, O.; Sernas, O.; Vaitkus, A. Performance Characteristics of the Open-Graded Asphalt Concrete Filled With a Special Cement Grout. *Balt. J. Road Bridge Eng.* **2015**, *10*, 316–324. [CrossRef]

22. Dong, Q.W.; Zhang, Y. The semi-rigid pavement with higher performances for roads and parking aprons. In *CAFEO 29, Sustainable Urbanization—Engineering Challenges and Opportunities*; Chemilink Technologies Group: Singapore, 2011; pp. 1–7.

23. Hassani, A.; Taghipoor, M.; Karimi, M.M. A state of the art of semi-flexible pavements: Introduction, design, and performance. *Constr. Build. Mater.* **2020**, *253*, 119196. [CrossRef]

24. Shafabakhsh, G.; Mirabdolazimi, S.M.; Sadeghnejad, M. Evaluation the effect of nano-TiO2 on the rutting and fatigue behavior of asphalt mixtures. *Constr. Build. Mater.* **2014**, *54*, 566–571. [CrossRef]

25. Lv, S.; Wang, X.; Liu, C.; Wang, S. Fatigue Damage Characteristics Considering the Difference of Tensile-Compression Modulus for Asphalt Mixture. *J. Test. Eval.* **2018**, *46*, 2470–2482. [CrossRef]

26. Lu, S.T.; Liu, C.C.; Qu, F.T.; Zheng, J.L. Test Methods and Characterization on Fatigue Performance of Asphalt Mixtures: A Review. *China J. Highw. Transp.* **2020**, *33*, 67–75.

27. Huang, B.; Shu, X.; Zuo, G. Using notched semi circular bending fatigue test to characterize fracture resistance of asphalt mixtures. *Eng. Fract. Mech.* **2013**, *109*, 78–88. [CrossRef]

28. Dong, Q.; Zhao, X.; Chen, X.; Ma, X.; Cui, X. Long-term mechanical properties of in situ semi-rigid base materials. *Road Mater. Pavement Des.* **2021**, *22*, 1692–1707. [CrossRef]

29. Gong, M.; Xiong, Z.; Chen, H.; Deng, C.; Chen, X.; Yang, J.; Zhu, H.; Hong, J. Evaluation on the cracking resistance of semi-flexible pavement mixture by laboratory research and field validation. *Construct. Build. Mater.* **2019**, *207*, 387–395. [CrossRef]

30. Krans, R.L.; Tolman, F.; Van, D. Semi-circular bending test: A practical crack growth test using asphalt concrete cores. In Proceedings of the International Rilem Conference on Reflective Cracking in Pavements, Maastricht, The Netherlands, 2–4 October 1996.

31. Mull, M.A.; Othman, A.; Mohammad, L. Fatigue Crack Propagation Analysis of Chemically Modified Crumb Rubber-Asphalt Mixtures. *J. Elastomers Plast.* **2005**, *37*, 37–73. [CrossRef]

32. Jiang, J.; Ni, F.; Dong, Q.; Wu, F.; Dai, Y. Research on the fatigue equation of asphalt mixtures based on actual stress ratio using semi-circular bending test. *Constr. Build. Mater.* **2018**, *158*, 996–1002. [CrossRef]

33. Gilat, A. *MATLAB. (Electronic Resource): An Introduction with Applications*, 5th ed.; John Wiley & Sons: Hoboken, NJ, USA, 2015.

Some Microstructural Aspects of Ductile Fracture of Metals

Wiktor Wciślik [1,*] and Robert Pała [2]

[1]   Faculty of Civil Engineering and Architecture, Kielce University of Technology, 25-314 Kielce, Poland
[2]   Faculty of Mechatronics and Mechanical Engineering, Kielce University of Technology, 25-314 Kielce, Poland; rpala@tu.kielce.pl
*   Correspondence: wwcislik@tu.kielce.pl

Abstract: The paper discusses the basic issues of the local approach to ductile fracture of structural metals, with particular emphasis on the failure due to microvoid development. The mechanisms of nucleation of voids around inclusions and precipitates are characterized. The criteria for the nucleation of voids resulting from cracking of the existing particles or their separation from the material matrix are presented. Selected results of experimental studies and Finite Element Method (FEM) simulations on nucleation of voids are discussed. The analytical and numerical models of growth and coalescence of voids are described, indicating the effect of the stress state components on the morphology of voids and the course of the cracking on a microscopic scale.

Keywords: fracture mechanics; ductile fracture; material microstructure; void growth; FEM model; material testing

1. Introduction

Many engineering structures in use have reached or exceeded their design service life. In combination with changing operational requirements (e.g., increased loads, influence of environmental factors), design, execution, and operational errors can result in numerous failures. Historically, the most famous case of this type was the cracking of the hulls of Liberty tankers in the 20th century. In the following years, cracks in the structures of industrial tanks, gas pipelines, and others were observed many times. As shown by the research and analyses carried out, one of the causes of the damage was the imperfect method of designing and calculating structures that did not follow the rapid technological progress. Extensive research on the explanation of the causes of failures resulted in the establishment of a new field of science, which is the mechanics of fracture. Furthermore today, with the rapid development of material technologies, the importance of this relatively young science continues to grow.

For about 60 years of development, the fracture mechanic has provided models to predict failure of structural components containing defects. The first solutions were developed on the basis of the linear theory of elasticity, gradually developing them in terms of taking into account plasticity and non-linear phenomena. The so-called global approach has proved to be useful in solving engineering problems in which classic material strength methods are not applicable.

Based on the methods of classical fracture mechanics, many engineering procedures have been developed, among which the PD6493 [1], BS7910 [2], R6 [3], FITNET [4], and SINTAP [5] procedures deserve special mention.

The development of material technology and computational methods, mainly numerical ones, which have been progressing in recent decades, has revealed a number of limitations of conventional methods. Their most common disadvantage is their low versatility, because each case of the geometry of a structural element and a defect requires an individual approach. Thus, these procedures are costly and time-consuming [6].

Local methods, developed since the 1980s, are characterized by much wider possibilities, mainly in combination with FEM analysis. The essence of the local approach is the

analysis of phenomena that take place in a small area of crack initiation and development (called the process zone).

This paper discusses the basic aspects related to the local approach to the analysis of ductile fracture of metals, taking into account changes in the microstructure of the material, namely the development of voids.

2. Mechanisms of Structural Metals Failure

Two basic mechanisms of metals failure are distinguished, namely cleavage and ductile fracture.

Due to its violent, uncontrolled nature and its consequences, brittle fracture has been the subject of advanced research for many years. The mechanism of brittle failure may take the form of intergranular and transgranular fracture. In most metals, the intercrystalline fracture mechanism is related to the cracking of particles arranged along the grain boundaries. Initiating the fracture process requires breaking the interatomic bonds. The increase in the volume of the resulting void is the result of hydrostatic stresses.

Local stresses, necessary to break the bonds, are characterized by significant values compared to the material strength measured on a macroscopic scale. It follows that the crack initiation takes place around stress concentrators, which are usually geometrical discontinuities at the microscopic level (microvoids, notches, inclusions).

The occurrence of the brittle fracture mechanism in ferritic steels is favored by low ambient temperature and high deformation rates [6]. It should also be emphasized that the process of the brittle fracture largely depends on the microstructural structure of the material (e.g., grain size).

In typical operating conditions of the structure (static character of loading, room temperature), material failure often takes the form of ductile fracture and is preceded by the occurrence of significant plastic deformation. In metals of high metallurgical purity (copper, gold), in the absence of internal stress concentrators, the failure occurs by necking the cross-section up to a complete narrowing (Figure 1a).
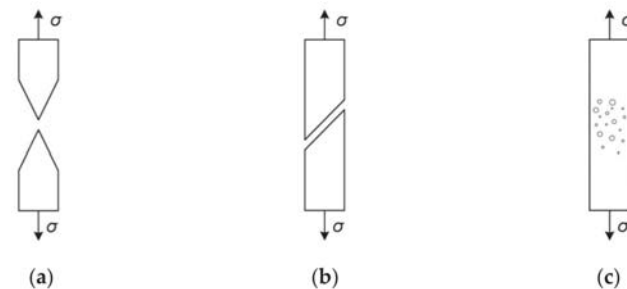
Figure 1. Ductile failure in metals: (**a**) necking; (**b**) shear; (**c**) development of voids.

The second process is associated with a slip mechanism in which the shear bands are inclined at an angle of approximately 45 degrees to the axis of the main tensile stresses (Figure 1b). However, ductile fracture in technical metals is most often associated with nucleation and the development of internal microvoids (Figures 1c and 2).
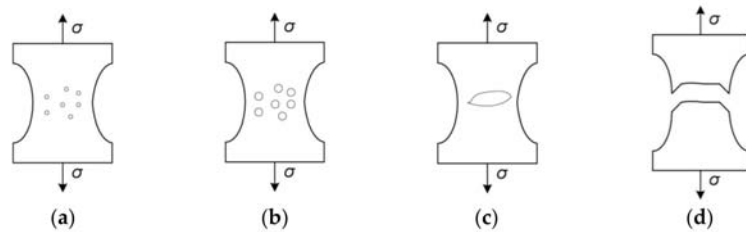
Figure 2. Phases of void development: (**a**) nucleation of voids; (**b**) growth; (**c**) coalescence; (**d**) rupture.

3. Some Measures of Stress State and Microstructural Parameters Used for the Ductile Fracture Characterization

As demonstrated in numerous studies, the process of void nucleation and growth in ductile materials is strongly dependent on the stress state. A special role is assigned to a parameter called the stress state triaxiality ratio, which describes the effect of the spherical component of the stress tensor (hydrostatic tension or compression). The stress state triaxiality is defined by the relationship:

$$\eta = \frac{\sigma_m}{\sigma_e}, \tag{1}$$

(the arguments are described in the nomenclature section at the end of the paper).

High values of the triaxiality describe a state in which the effect of hydrostatic stress is significant. In structural elements, such a situation takes place mainly in the vicinity of all kinds of geometric notches, where the local value of η may significantly exceed 2. On the contrary, low triaxiality is observed in structural elements subjected to stress states with a negligible hydrostatic component. For example, uniaxial tension corresponds to the triaxiality value of 1/3.

Many studies, both experimental and theoretical, indicate a significant influence of triaxiality on the intensity of void development, measured by the value of their volume fraction, according to the formula:

$$f = \frac{V_{voids}}{V_{material}}, \tag{2}$$

(the arguments are described in the nomenclature section).

It was found [7] that in the case of low triaxiality, due to the minor role of the spherical component of the stress tensor, the void development process is governed by the deviator component, primarily the third stress deviator invariant and the related Lode parameter:

$$L = \left(\frac{r}{q}\right)^3 = cos(3\theta), \tag{3}$$

where: $r = \sqrt[3]{\frac{27}{2}(\sigma_1 - \sigma_m)(\sigma_2 - \sigma_m)(\sigma_3 - \sigma_m)}$, $q = \sigma_e$.

The geometric interpretation of the Lode angle in the principal stress space is shown in Figure 3:
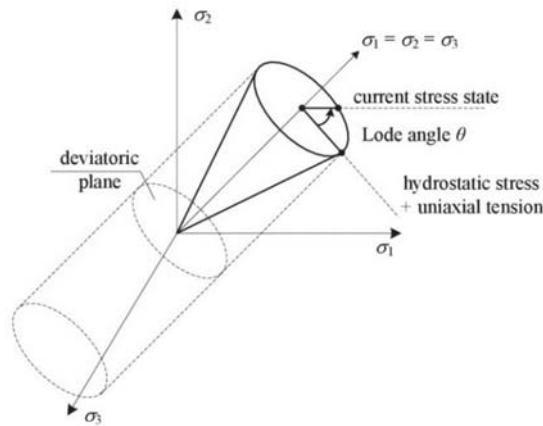
Figure 3. Graphical interpretation of the Lode angle.

The Lode angle satisfies the condition $0 \leq \theta \leq \frac{\pi}{3}$, while the Lode parameter is in the range $-1 \leq L \leq 1$.

4. Void Nucleation in Metals

The fracture of metals usually involves nucleation and the development of micro-damage, primarily voids. Their initiators are most often inclusions and the second phase particles, located in the structure of the base material inside the grains or at their boundaries [8,9] (Figure 4a). The particles can be introduced into the metal matrix in order to improve the strength properties (e.g., metal matrix composites, TRIP steels), or may be impurities resulting from the technological process (Figure 4b).

(a)

(b)
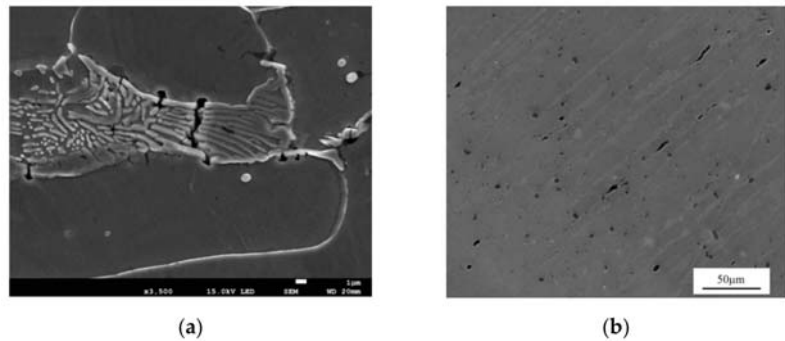
Figure 4. (**a**) Microdamage and voids inside and on the boundaries of the grains; (**b**) an example of impurities in the microstructure of S355 steel.

Although the particle sizes are usually of the order of micrometers, and their volume fractions in unstrained material do not exceed a few parts per mille, significant values of localized plastic strains and the occurrence of heterogeneity in the deformation field around the particles cause nucleation and then growth of voids. Their volume fraction at failure may reach several dozen percent.

The presence of inclusions may be the result of imperfections in technological processes and contamination of the material with sulfur, manganese, phosphorus, nitrogen, and other compounds. For example, manganese sulfide commonly present in structural steels is plastic, so when subjected to plastic strain, it deforms to form longitudinal bands

that cause fracture toughness anisotropy. The presence of other compounds, in turn, can reduce material strength, ductility, toughness, etc.

On the other hand, in many cases, inclusions and precipitates are intentionally introduced into the structure of the material to achieve certain parameters. For example, the addition of sulfur to the so-called free-cutting steels definitely improves their machinability. Another example of the deliberate introduction of second phase particles is the so-called precipitation hardening, used mainly in soft alloys of aluminum, magnesium, or titanium, in order to improve their strength properties. In this case, the particles themselves should be hard, characterized by high density and uniform distribution in the structure of the base material (matrix). It is also required that the precipitates should be at least partially coherent with the surrounding matrix. The introduced particles constitute a barrier to the free movement of dislocation, which in metals, due to the low resistance of the crystal lattice, occurs relatively easily. Limiting the dislocation movement results in an increase in the strength of the material. The precipitation strengthening technology is also used in composites with a metal matrix.

Regardless of the type and function, the particles of the second phase are, as mentioned above, initiators of the nucleation of microvoids which grow and develop into a macroscopic defect.

The void nucleation mechanism itself involves the separation (decohesion) of the second phase particle from the matrix and/or the particle fracture. The particle separation mechanism is primarily observed in relatively soft, ductile matrices, while the hard matrix promotes particle fracture which requires lower strain values. The direction of the crack development is usually perpendicular to the direction of the main tensile stresses. Moreover, in the case of particles with an elongated shape, the void nucleation mechanism depends on their orientation with respect to the loading direction. The positioning of the elongated particle along the direction of loading promotes the phenomenon of its cracking (Figure 5a). Otherwise, the particle and the matrix are usually separated (Figure 5b).
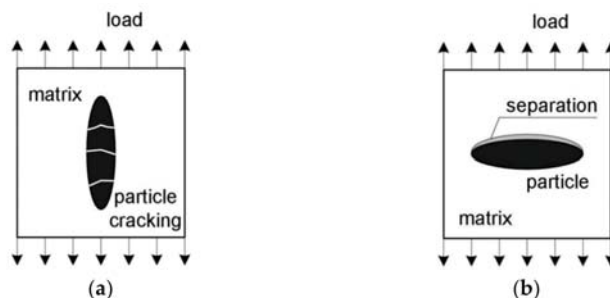
Figure 5. Effect of the orientation of the elongated particle in relation to the loading direction on the void nucleation mechanism: (**a**) the mechanism of fracture of the particle positioned along the loading direction; (**b**) separation of the particle perpendicular to the loading direction, based on [10].

Regardless of the factors mentioned above, there is a large group of other parameters that influence the void nucleation mechanism (fracture or particle separation). For example, the phenomenon of particle cracking is favored by the high value of the yield stress, the matrix hardening exponent, high particle stiffness, and the dominance of normal over shear stresses. The phenomenon of cracking is primarily observed in the case of brittle particles, where the failure initiation takes the form of cleavage cracking [11]. In samples subjected to significant shear stresses, the particle–matrix separation at opposite points is observed, as shown in Figure 6.
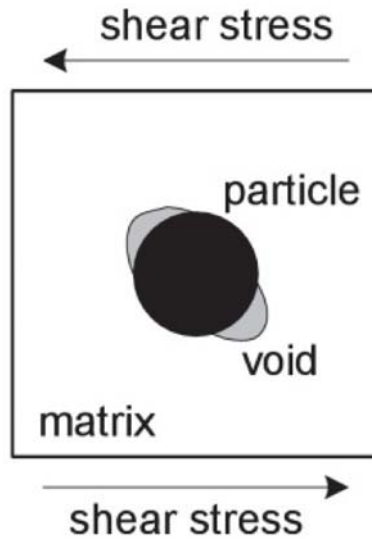
Figure 6. Mechanism of particle–matrix separation under dominant shear stress, based on [11].

It should also be remembered that the second phase particle is a stress concentrator on a micro scale, which additionally favors the formation of local discontinuities (voids). A separate issue is the concentration of stress caused by the presence of a group of particles, which also affects the mechanism of microdamage initiation. In this case, the volume fraction of the particles becomes an important parameter. As all authors emphasize, the course of both the nucleation process and the growth of voids is strongly dependent on the spherical component of the stress tensor, the influence of which is described by the so-called stress triaxiality (see Section 3). As it increases, the value of the strain necessary to initiate the void decreases.

The void nucleation process does not take place simultaneously around individual particles, but gradually, depending on the local stress and strain state, the particle material and its size. Microscopic observations of plastically deformed materials show that the nucleation of voids first takes place in the region of larger particles, which, including microdefects, are more susceptible to damage.

In high purity metals (copper, silver, gold), in the absence of second phase particles, the nucleation of microvoids may also result from the accumulation of dislocations [12,13]. Creation of dislocation and slip, although they release shear stresses, do not release normal stresses, which leads to the accumulation of considerable energy. The energy release takes place in the weakest areas, i.e., at the dislocation accumulation points, which leads to the formation of microvoids [14].

Over the last several decades, many criteria for void nucleation have been developed, both on the basis of dislocation theory and continuum plasticity theory. As shown in [15], the scope of applicability of individual criteria is determined primarily by the particle size. The criteria based on the continuum mechanics are used to analyze the separation of particles with a diameter greater than about 1 μm.

The void nucleation criteria can be divided into three basic groups: stress, strain, and energy criteria. The stress criterion, depending on the analyzed void nucleation mechanism (particle fracture or separation from the matrix) requires local achievement of the critical stress value in the particle itself (first mechanism) or at the phase interface

(second mechanism), and in its simplest form it is defined by the following relationship (see nomenclature section):

$$\sigma_1 = min\left(\sigma_{crit}^{particle}, \sigma_{crit}^{interface}\right), \tag{4}$$

(principal stress σ_1 calculated at microscopic level).

The above formulation, although very simple and convenient, requires knowledge of the principal stresses σ_1 at the microscopic level, and what is more, it does not take into account the particle shape, which undoubtedly affects the conditions of void nucleation. However, the relationship (4) can be modified so that it is possible to determine the local value of stress σ_1 based on the stresses determined on the macro scale, taking into account the particle shape k_s [16,17]:

$$\sigma_1 = \sigma_1^{global} + k_s\left(\sigma_e^{global} - \sigma_0\right), \tag{5}$$

(superscript *global* denotes stress measured at macroscopic level).

A thorough analysis of the stress criteria of matrix–particle separation was discussed by Argon et al. in a series of papers [18–20]. In the framework of continuum approach, the behavior of the non-deformable particle in an elastic and perfectly plastic matrix was analyzed. The condition of the void nucleation according to [18] relates to the mechanism of the matrix–particle separation and is defined as:

$$\sigma_m + \sigma_e = \sigma_{crit}^{interface}, \tag{6}$$

As the above dependence was derived from the analysis of a single particle in the matrix, it takes into account only the stress and strain state in the particle vicinity, neglecting the influence of the particle size and its possible interaction with neighboring particles. In order to take into account the shape of the particle, the author of [19] proposed a modification of the condition (6) to the form:

$$\sigma_m + k_m\sigma_e = \sigma_{crit}^{interface}, \tag{7}$$

It should be noted, however, that the Formulation (7) is only a proposal to solve the problem and has not been supported by experimental research.

The above-mentioned stress conditions assume a homogeneous stress state in the vicinity of the particle, and the distinction between the particle fracture or separation mechanism results only from the adoption of different critical stress values. In fact, in the case of an elastic-plastic matrix, the stress distribution in the elastic particle is not homogeneous.

In [17], attention was drawn to the need to take into account the impact of the heterogeneity of the deformation field in the vicinity of the particle on the separation stress value. Based on the theory of Eshelby [21], a modification of the stress condition was proposed in order to take into account the heterogeneity of the deformation field:

$$\sigma_1 + \sigma_{inh} = \sigma_{crit}, \tag{8}$$

where σ_{inh}—stress induced in the inclusion by the strain inhomogeneity effect, according to the formula:

$$\sigma_{inh} = \lambda E_p \in_{eq}, \tag{9}$$

As the authors of the work [17] emphasize, dependence (9) is only an approximate solution. Eshelby theory was developed for an elastic material and its application to a plastically deforming matrix is a considerable simplification. The problem was partially solved by introducing to the description of the plastic material the plastic equivalent Young's modulus E_p and the equivalent Poisson coefficient v_p.

A simple analytical solution for the stress criterion of void nucleation is presented in [22]. The local stress values inside the particle and in the adjacent matrix were determined

based on the classic solution of Brown and Clarke [23]. The matrix hardening effect was taken into account by introducing the power equation. The condition proposed in [22] also includes the influence of the volume fraction of particles on the local stress values. The authors' original achievement was the introduction of the "damage function" Ø into the equation of stresses in a particle, capturing the effect of the separation advancement on the stress values in the particle itself. The particle fracture condition is:

$$\left(\sigma_0 + k(\varepsilon_p)^n\right) \frac{(1-Ø)(1-f)}{1-f(1-Ø)} + \frac{1-Ø}{1-f(1-Ø)} \mu^* \varepsilon_p = \sigma_{crit}^{particle}, \tag{10}$$

where $Ø = 0$ means full traction, $Ø = 1$ denotes complete separation, (the remaining arguments are described in the nomenclature section).

As emphasized by the authors [22], the solution is based on a number of simplifications and can only be applied to some groups of materials. The stress equation does not take into account the mismatch between the elastic parameters of the matrix and the particle. The applicability range of the equation given above is therefore limited to situations where the Young's modulus of the particle and matrix are of a similar value. Moreover, the assumption of a linear dependence of the "damage function" Ø on the value of plastic deformation is not confirmed by the results of experimental studies. According to the model, the particle loses its stress-carrying capacity only after it is completely detached from the matrix. In fact, it is to be expected that the stress relaxation in the particle occurs somewhat earlier. Finally, the void initiation model presented above does not account for particle size.

Lee and Mear [24] introduced to the nucleation criterion the coefficients taking into account the stress concentration caused by the presence of the particle. Based on the results of numerical calculations, the authors formulated the concept of stress concentration coefficients in the particle itself and on the particle–matrix interface:

$$\kappa^P = \frac{\max\left(\sigma_1^P\big|_{\delta \leq \beta}\right)}{S}, \tag{11}$$

$$\kappa^I = \frac{\max\left(\sigma_{\eta\eta}\big|_{\delta = \beta}\right)}{S} \tag{12}$$

(superscripts p and I refer to particle and interface, respectively).

The values of the above-mentioned coefficients κ^p and κ^I depend on both the global parameters describing the stress state (stress triaxiality), as well as the matrix and particle material parameters (Young's modulus, yield stress, hardening exponent, Poisson's ratio) and aspect ratio of the particle.

Taking into account the stress concentration factors, one can modify the stress criterion (4), obtaining the following conditions:

$$\kappa^I \sigma_1 = \sigma_{crit}^{interface}, \tag{13}$$

$$\kappa^P \sigma_1 = \sigma_{crit}^{particle} \tag{14}$$

The void nucleation criterion, taking into account the phenomenon of dislocation accumulation, was formulated in [25]. As in the case of Equations (13) and (14), the nucleation condition is stress-related and combines macroscopic stress values with local effects, using the expression:

$$\sigma_1 + \sigma_{loc}(r)_{r=r_1} = \sigma_{crit}, \tag{15}$$

Another nucleation condition, formulated within the dislocation model, can be defined as follows [6]:

$$\mu \sqrt{\frac{\varepsilon_N b}{R}} = \sigma_{crit}, \tag{16}$$

It should be emphasized that the local stress values, due to their concentration around particles, are higher than the results from the stress analysis on the macroscopic scale [26]. In addition, the distribution of stresses is influenced by the heterogeneous, random distribution of particles.

While the fractured particle is capable of transmitting tensile stress in the direction parallel to the crack, this possibility no longer exists when the matrix is completely separated from the particle. Regardless of the above, fractured or separated particles can transmit compressive stresses.

As mentioned before, a separate category is formed by the strain criteria of void nucleation. Goods and Brown [15] formulated the strain criterion, however, based on the stress values:

$$\varepsilon = \varepsilon_{crit} = 1.7 \frac{R}{\mu^2 b} \left(\frac{\sigma_{crit}^{interface} - \sigma_m - \frac{2}{3}\sigma_0}{1 + 2f + 0.38\sqrt{f}} \right)^2, \tag{17}$$

Another deformation condition was formulated by Hancock and Cowling [27]. Most often, the critical strain condition is achieved at higher external loads than in the case of the critical stress condition.

The energy conditions of void nucleation correspond to the Griffith's [28] criterion, according to which the value of the energy released during fracture corresponds to the value of energy necessary to create new surfaces (particle fracture surface or the matrix–particle interface). For example, according to the Gurland–Plateau model [29], separation at the interface between the inclusion and the matrix occurs in the elastic range, if the following condition is satisfied:

$$q\sigma = \sqrt{\frac{E\gamma}{R}}, \tag{18}$$

Despite numerous studies, so far it has not been possible to define one universal condition that can be applied regardless of the material, state of stress, and others. On the other hand, it is widely recognized that the energetic condition is a necessary but not sufficient condition to create a new void and that the condition of critical stress or strain must be simultaneously satisfied. Thus far, it has not been unequivocally clarified whether the void nucleation is stress or strain controlled. The results presented in the literature provide conflicting evidence on this point. According to the authors of [30], the phenomenon of void nucleation in spheroidized steel depends on the prevailing local stress state. However, studies conducted on aluminum alloys and cast duplex stainless steel [31] indicate the leading role of the strain state.

Assuming a linearly elastic particle material, one can formulate a simple, one-parameter criterion for its failure, and thus for nucleation of the void. Cracking of a particle occurs when the energy release rate exceeds its fracture toughness. A criterion of this type can also be formulated in terms of stress, that is, fracture of the particle will occur if the maximum principal tensile stress inside the particle exceeds the strength of the material. The above criteria are valid for particle radius of the order of 1 μm and above. For smaller particle sizes, criteria for void nucleation are formulated based on dislocation models.

The mechanism of void nucleation by matrix and particle decohesion, due to the occurrence of significant plastic deformation, usually does not allow for the definition of a simple criterion based on a single parameter. In these cases, it is postulated that the criteria of the critical stress at the interface and the energy criterion should be met simultaneously [16].

The strength of the particle–matrix interface depends on the local chemical composition of both phases and is random. There are many works in the literature, attempting to determine the value of the critical stress needed to separate the matrix and particle. One of the first were Argon [19] and Argon and Im [20]. The values of the decohesion stresses of the Fe$_3$C particle and the ferritic matrix were determined at the level of 1700 MPa. Similarly, Beremin in [17] determined the critical MnS particle separation stress in A508 steel of about 800 MPa. As noted by the author, the orientation of the elongated particle along the

direction of the principal stress implied the particle fracture mechanism (see Figure 5a). The value of the critical fracture stress in this case was about 1100 MPa.

Giovanola et al. [32] determined the value of the critical stress at the interface between the ferritic matrix and carbide inclusions at the level of 3000 MPa. The tests were carried out on samples made of VAR (vacuum arc remelting) steel subjected to various stress states. The experiment included tensile and compression tests combined with torsion. The experiments were interrupted at various stages. Then, the microstructural investigations of the deformed material were conducted, with particular emphasis on the areas where voids were initiated. The state of stress and strain in these regions was determined by means of the FEM, obtaining macroscopic criteria of void nucleation. Stress values in the micro scale were calculated using the dislocation model of Brown and Stobbs [33].

Shabrov et al. [34] linked the results of microscopic examinations of the deformed material with the numerically obtained maps of the stress distribution in order to determine the criteria for the initiation of microdamage in SAE4330 steel. A thorough analysis of the cracking mechanism of brittle titanium nitride (TiN) particles, which are the main initiators of damage development in the tested steel, was performed. The critical value of stress necessary to break the TiN was determined at the level of 2.3–2.4 GPa, with larger particles usually requiring lower stress values.

An example of the use of modern experimental and numerical techniques to determine the nucleation criteria of microdamage is described in [35]. Using the microtomography method, nucleation of voids in commercially pure Al and Al2124 alloy reinforced by spherical hard ceramic particles was observed. The results confirmed the common belief that the type of matrix influences the void nucleation mechanism, i.e., along with the increasing hardness of the matrix, the decohesion mechanism gave way to the particle fracture mechanism. Comparative analysis of void tomographic images with the results of numerical calculations allowed the determination of the critical fracture stress of ZrO_2/SiO_2 particles at about 700 MPa and the critical energy density at the level of 2.5 MJ/m^3. In the case of the particle separation mechanism, it was not possible to clearly establish the separation criterion due to the complexity of the stress and strain state in the particle neighborhood. For the soft matrix (pure aluminum), the critical stress value was estimated at about 250 or 320 MPa for the hydrostatic and normal stress criteria, respectively. Much higher values of both these stresses, of the order of 1000 MPa, were observed in the hard matrix (Al2124 alloy). However, it should be remembered that, according to the authors of [35], the mere achievement of a critical stress value is not sufficient to separate the particle and matrix, but rather a critical combination of stress and strain components must occur.

Exemplary values of local fracture and separation stresses, quoting from [36] are summarized in Table 1.

Table 1. Critical values of void nucleation stresses reported in the literature, from [36].

Particle	Matrix	Critical Stress [MPa]	Ref.
		Particle fracture	
Elongated MnS	A508 steel	1100	[17]
Cuboidal TiN	4330 steel	2300	[34]
TiN	Inconel 718	1280–1540	[37]
4% spherical ZrO$_2$-SiO$_2$	Al2124 (T6)	700	[35]
20% spherical ZrO$_2$-SiO$_2$	Al2124 (T4)	700	[35]
		Particle separation	
MnS	A508 steel	800	[17]
Si	Al (cast)	550	[38]
4% spherical ZrO$_2$-SiO$_2$	Al2124 (T6)	1060	[35]
4% spherical ZrO$_2$-SiO$_2$	Pure Al	250	[35]
20% spherical ZrO$_2$-SiO$_2$	Pure Al	320	[35]
Rounded Fe$_3$C	Spheroidized 1045 steel	1650	[20]
Cu-Cr particles	Cu alloy	1000	[20]
TiC	Maraging steel	1820	[20]
C nodules	Cast iron	80	[39]

Significant progress in the field of numerical methods made it possible to perform a multi-parameter analysis of the matrix and particle separation using cohesive models, which usually characterize the interfacial contact using three groups of parameters: maximum stress (normal and shear), separation work Γ, and displacement δ [40,41]. Although the values of cohesive parameters are often treated as material constants, as indicated in [42], their values depend on the stress triaxiality, specimen geometry, and particle size.

In most cases, simulations with the use of cohesive models are limited to the analysis of separation of individual particles or their small groups. However, recently Andersen et al. in [43] have attempted to use a cohesive model to simulate the development of voids in a full-scale plate subjected to tension. In the numerical model, a process zone was distinguished in which the particles were distributed randomly. Analyzing the cases of different amounts and distribution of particles, it was found that the heterogeneity of material properties resulting from the development of voids strongly influences the location of the rupture.

Many studies have attempted to define the value of the critical strain necessary to initiate the void. The commonly accepted value in the literature is $\varepsilon_N = 0.3$, given by Chu and Needleman [44]. However, determining the critical strain is a much more complex issue and depends on many factors, i.e., material, stress state, particle geometry, and others.

Fisher [45] estimated the value of particle decohesion strain in steels at about 0.6–0.75. On the other hand, in the work of Hahn and Rosenfield [46], a 25–50% share of cracked particles was found in the aluminum alloy deformed by about 0.07.

In the papers [47–50], using the finite element method, an attempt was made to estimate the critical strain of particle nucleation in structural steels. By analyzing the separation and fracture mechanism of MnS and Fe_3C particles, the strain value ranging from 0.01 to 0.29 was determined, depending on the adopted nucleation mechanism and the prevailing stress state.

An interesting study on the nucleation of voids through the fracture of silicon particles in aluminum alloys was presented by Caceres and Griffiths in [51]. The authors conducted microstructural investigation of samples made of Al-7% Si0.4% Mg alloys, subjected to tension and bending. The loading was carried out in stages, increasing the plastic strain every 1%. After each phase, microscopic observations of specially prepared surfaces of the samples were performed. Particular attention was paid to the number of nucleated voids, as well as the mechanism of their formation. Alloys differentiated in terms of silicon particle size were tested. While smaller particles detached from the matrix, larger sized particles (especially those with elongated shape) cracked, leading to void initiation. Although it has not been conclusively confirmed experimentally, it is presumed that larger particles contain microdefects, which implies the mechanism of their cracking. Therefore, the crack initiation at the microstructural level was much more rapid in this case and took place at low strains, of the order of 1%.

The experimental tests of CF8M steel samples under uniaxial and complex stress states presented in [52] showed that at the strain of 16%, about 96% of the cells (sub-areas) isolated on the polished surface contain microcracks, which corresponds to a microdamage density of about 100 mm^{-2}.

The value of critical void nucleation strain is often determined by means of fitting numerical and experimental results (e.g., force–displacement curve), using a porous material model, such as, for example, the Gurson model [53]. Xia and Cheng [54] thus determined the critical value of the nucleation strain in A533B steel at the level of 0.04. A similar procedure was used by He and co-workers [55] for the analysis of void nucleation in the Al–Al_3Ti composite, subjected to the complex stress state. The best convergence of the simulation and experiment results was obtained for a much higher value of nucleation strain, amounting to $\varepsilon_N = 0.5$.

As mentioned above, the void nucleation process is random and depends on many factors, such as the matrix and particle material, particle shape, size, prevailing stress state, etc. Thus, probabilistic approaches are developed in the literature. For example, in [56],

the Weibull distribution was used to model the fracture probability of ZrO$_2$ particles in an aluminum alloy, depending on strain, particle shape, and volume. The modeling results were in good agreement with the results of microscopic observations.

An approach in which the random nature of the void nucleation process is taken into account by introducing an additional parameter, namely, the nucleation rate, is widely discussed in the literature. When the stress criterion is applied, the nucleation rate is:

$$\dot{f}_{nucl} = A_N \left(\dot{\sigma}_1^{max} + k_s \dot{\sigma}_e \right), \tag{19}$$

where:

$$A_N = \frac{f_0}{s_N \sqrt{2\pi}} exp \left[-\frac{1}{2} \left(\frac{\sigma_1^{max} + k_s(\sigma_e - \sigma_0) - \sigma_{crit}^{mean}}{s_N} \right)^2 \right], \tag{20}$$

Within the strain criterion, the nucleation rate function takes the form:

$$\dot{f}_{nucl} = A_N \dot{\varepsilon}, \tag{21}$$

where:

$$A_N = \frac{f_0}{s_N \sqrt{2\pi}} exp \left[-\frac{1}{2} \frac{(\varepsilon - \varepsilon_N)^2}{s_N} \right], \tag{22}$$

5. Cavity Growth

As already mentioned, the voids grow under increasing plastic strain. In the literature, one can find a number of papers concerning both microscopic observations as well as analytical and numerical models.

The research on void growth was motivated by numerous observations of the microstructure of structural materials subjected to significant plastic deformation. The voids initiated by particle cracking become rounder with increasing strain, while the voids nucleated by the decohesion process gradually lengthen in the direction of the principal tensile stresses. Moreover, the presence of a separated particle inside the void limits the possibility of its contracting perpendicularly to the main loading direction. Moreover, the presence of significant shear stresses promotes the elongation and rotation of the void [16].

Experimental studies involve the observation of the pre-strained material with the use of a scanning microscope and the monitoring of the material microstructure in the process zone by microtomography [57–59]. There are also indirect methods of measuring the void fraction, such as the measurement of material density, its stiffness, or electrical resistance [16].

In [59], using the X-ray tomography method, the process of single void growth in the copper matrix was subjected to detailed analysis. In the first stage, rapid growth of the void along the tension direction was observed. The stress concentration caused by the void presence resulted in a strain rate approximately twice as high as the macroscopic strain of the specimen. As plastic strain increased, the increase in the stress triaxiality, due to the formation of the neck, induced a more intense void growth in the direction perpendicular to the loading direction.

There are numerous models of void growth in the literature, describing the increase in the void diameter or the increase in the volume fraction of voids, based on the stress state components and the plastic strain. When analyzing the microstructural aspects of ductile fracture, it should be remembered that the process of existing void growth is constantly accompanied by the nucleation of new microdamage, which complicates the modeling methodology.

One of the first analytical solutions describing a single void growth was formulated by McClintock [60]. The analysis included the growth of a cylindrical void placed in a rigid perfectly plastic matrix, loaded along the longitudinal axis of the cylinder. The McClintock

condition determines the change in particle diameter as a function of strain ε_z measured along the axis of the cylinder:

$$\varepsilon_{void} = ln\frac{a}{a_0} = \frac{\sqrt{3}}{2}|\varepsilon_z|sinh\frac{\sigma_m}{\tau_0} - \frac{1}{2}\varepsilon_z, \tag{23}$$

Additionally, McClintock extended the proposed model to the case of a linearly hardening matrix. According to McClintock, the material ductility increases with the increase in material hardening and decreases with the increase in the precipitates volume fraction and the stress triaxiality.

Rice and Tracey [61] carried out a similar analysis for a single spherical void placed in an incompressible, rigid-plastic matrix. It was further assumed that the dimensions of the void were small compared to the size of the matrix, and the load was applied as a uniform velocity field, away from the void. The law of void evolution can be written as follows:

$$\frac{\dot{R}}{R} = 0.283exp\left(\frac{3\sigma_m}{2\sigma_e}\right)\dot{\varepsilon}_e, \tag{24}$$

The value of 0.283 in the above formula was determined by the authors of [61]. In [62], Huang modified this value according to the following relation:

$$0.427 \text{ for } \eta > 1 \text{ and } 0.427(\eta)^{1/4} \text{ for } -\frac{1}{3} \leq \eta \leq 1, \tag{25}$$

where η denotes stress triaxiality (Section 3).

In [63], the influence of the initial void fraction on the value of the coefficient in Formula (24) was also analyzed.

The model proposed by Rice and Tracey is only an estimate of the intensity of void development, as it neglects many factors, such as the effect of void shape changes, void coalescence, secondary nucleation, and others. In later years, numerous modifications of Rice and Tracey's model were developed, taking into account the shape of the void [64], non-linear hardening and viscosity law [65], and others.

McClintock, as well as Rice and Tracey, also emphasized the significant influence of the spherical component of the stress tensor (negative pressure) on the void growth process, especially the increase in their volume.

In the following years, Thomason [66] analyzed the development of cuboidal voids placed in a rigid perfectly plastic matrix, subjected to hydrostatic pressure and principal stresses σ_1 and σ_2. According to Thomason, below the critical value of the void volume fraction, the failure occurs by necking the specimen cross-section, while in the case of larger values of the void fraction, the decisive factor is the formation of ligaments between voids.

The Brown and Embury model [67] defines the law of void growth as a function of the macroscopic strain. The authors also proposed a criterion according to which void coalescence takes place at the moment when the distance between the voids is equal to their size.

Recently, Sills and Boyce [68], using molecular dynamics (MD) simulations, described a phenomenon in which the growth of voids in an aluminum alloy was the result of dislocation annihilation on the surface of a previously initiated void. The results of the numerical simulation clearly showed that the presence of dislocations in the vicinity of the void significantly accelerates its growth.

Regardless of the solutions discussed above, phenomenological models can be distinguished, in which the evolution of any damage measure is determined as a function of changes in the stress or strain state. For example, the Gurson porous material model [53],

modified by Tvergaard [69] and Tvergaard with Needleman [70], assumes the law of increasing the volume fraction of voids according to the formula:

$$\frac{\dot{f}}{f(1-f)} = \frac{3}{2}q\frac{\sigma_0}{\sigma_e}sinh\left(\frac{3\sigma_m}{2\sigma_0}\right)\dot{\varepsilon}_e, \tag{26}$$

In the original Gurson condition, the value of the q coefficient was 1; however, in later years its value was shown to be dependent on the stress state, volume fraction of voids, or matrix parameters [71,72].

Benzerga and Besson [73] generalized the above relationship to the case of plastic anisotropy:

$$\frac{\dot{f}}{f(1-f)} = \frac{3}{h}\frac{\sigma_0\sigma_e}{\sigma_h^2}sinh\left(\frac{3\sigma_m}{h\sigma_0}\right)\dot{\varepsilon}_e, \tag{27}$$

In recent years, the issue of material anisotropy caused by the elongated, irregular shape of voids has been particularly intensively analyzed in the literature. The proposed models also take into account both the phenomenon of void rotation and the different sensitivity of elongated voids to stresses in particular directions. The problem of anisotropy is of particular importance in the case of low triaxialities and shear dominance, which results in the location of large deformations and the zone of crack formation.

Gologanu et al. in [74–76] generalized the Gurson condition for the case of spheroidal voids. In the first step, the authors [74] analyzed the growth of a prolate spheroidal void in a confocal spheroidal matrix, subjected to an axisymmetric loading. In the next paper [75], the same analysis was performed for an oblate void. In the following paper [76], Gologanu et al. discussed the model of prolate and oblate void growth in the generalized velocity field. The so-called Gologanu–Leblond–Devaux model (GLD model) introduces additional parameters and the laws of their evolution to the original Gurson condition, including the void shape parameter w and additional parameters defining the orientation of the elongated void with respect to the stress axes. Particularly noteworthy is the introduction of the second porosity g parameter into the model, which is of particular importance in a penny-shaped crack (completely flat void). As it is known, in the case of voids of this type, their volume fraction is $f = 0$, which in practice would mean fully dense material and reduction of the Gurson material model to the classical von Mises condition, which is non-physical. The parameter g introduces in these cases the equivalent porosity, equal to the volume fraction of a spherical void with the same radius as the penny-shaped void. The GLD model is also used to develop the criteria for coalescence of voids, especially in the aspect of changing the distance between them, which is the result of an increase in plastic strain.

In the following years, the GLD model underwent numerous developments and modifications. Madou et al. [77,78] provided a general solution for ellipsoidal cells containing confocal ellipsoidal voids, indicating the evolution law of the dimensions of the void along each of the three principal axes. The model proposed by Madou and Leblond also takes into account the rotation of the void around each of these axes.

The problem of the void shape evolution has also been widely discussed by Ponte-Castaneda et al., for example [79,80].

A separate group consists of works in which attempts are made to simultaneously take into account plastic anisotropy and void elongation [81,82]. In these cases, the variables in the constitutive equation are a function of both the anisotropy coefficients h, as well as the volume fraction of voids and their aspect ratio. Moreover, the model described in [81] enables prediction of void closure under pure shear.

As mentioned at the beginning of this section, the presence of the particle inside the void prevents it from tapering perpendicularly to the loading direction. This phenomenon is rarely taken into account in void growth and porous material models. Among the available literature, mention should be made of [83,84].

The process of void growth is also strongly influenced by the effect of their interaction. The problem was analyzed by many authors, including Needleman [85], Tracey [86], and Andersson [87]. In [85], a numerical analysis of the development of cylindrical voids, distributed periodically in two directions, was carried out. The assumption of periodic distribution and symmetry of voids allowed the reduction of the problem to the analysis of a cell with a single, bisymmetric void. The quoted literature allows us to state that the presence of voids clearly affects the value of stress and strain, as well as the plastic strain localization, and thus the material relaxation. The interaction of voids of different sizes has been discussed in [88–90].

The paper [88] presents the results of a numerical simulation of the material, in which small-sized voids are arranged regularly, alternating with large ones. With the use of axisymmetric models, the behavior of the material was investigated taking into account triaxialities ranging from 0.3 to 0.9. It was found that localized plastic deformation causes a faster growth of small voids, and that with the increase of triaxiality, the strain values decrease. A significant factor accelerating the development of small voids is the vicinity of larger particles. According to Tvergaard, the influence of large voids is in this case greater than the effects of stress concentration associated with the presence of a crack near a small void.

The mutual influence of particle size and local stress concentrations was investigated by Tvergaard and Niordson [89]. A system of large and small particles arranged alternately was adopted for the simulation. The analysis of voids of various sizes allowed the conclusion that particles with a small diameter, comparable to the characteristic material length, are characterized by a lower growth rate. However, the presence of local stress concentrators (voids, discontinuities) is a factor favoring the development of microdamage. Moreover, it has been shown that the rapid growth of small voids predicted by traditional theories of plasticity does not correspond to the experimental results. The authors investigated the influence of stress triaxiality on the value of the volume fraction of large and small voids.

Faleskog and Shih [91], using the axisymmetric model with parallel, cylindrical voids, proved that the presence of large voids in the vicinity of a blunted crack is a factor that initiates rapid, unstable development of small voids.

In general, the above papers on constitutive modeling and numerical simulation of void growth are only some examples, subjectively selected from the number of publications available. Numerous modifications of the void growth models also take into account strain and kinematic hardening, rate dependency and viscoplasticity, void size, and others. A more extensive review can be found, for example, in [16].

Regardless of constitutive modeling, the use of X-ray microtomography to analyze changes in the material microstructure has contributed to a better understanding of the nature of void growth and coalescence. In [92], Seo et al. described an example of the application of the microtomographic method to a comprehensive analysis of the microdamage evolution in tensile, flat JIS SUM24L steel specimens. The change in the number and volume fraction of voids as a function of plastic deformation was recorded. The tomographic examinations were also used to observe the specimen necking. On the basis of the obtained results, the components of the stress state in the area of void observation were determined.

Contrary to expectations, the average size of the observed voids decreased with increasing plastic deformation. The authors suspect that this is the result of the domination of the secondary nucleation mechanism over the development of the existing voids and the related increase in the proportion of small-sized voids.

6. Cavity Coalescence and Failure

The process of void coalescence immediately precedes the formation of the macroscopic defect. This process is currently the least recognized phase of ductile fracture. The

occurrence of this phenomenon has been confirmed experimentally [59,93], although these are still few observations [11].

There are two basic mechanisms in metals (Figure 7). In the first one, the coalescence takes place by internal necking of ligaments between voids, similar to the formation of a neck in a tensile specimen. The second mechanism, involving the coalescence of large voids in the shear bands, is most common in high strength metals.
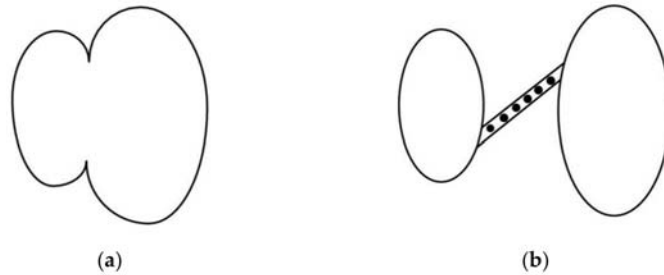
Figure 7. Mechanisms of cavity coalescence: (**a**) internal necking of ligaments between voids; (**b**) nucleation of secondary voids in shear bands [6].

The transition from shear to the necking mechanism is associated with a change in the macroscopic fracture surface, that is, with the transition from the slant to flat fracture [36] (compare Figure 11 in Section 7). The literature also describes a third mechanism related to the coalescence of small voids arranged in strips or joining larger, elongated voids. Each of the mechanisms listed here is divided into several categories, depending on the parameters of the microstructure of the material, stress state, and others. It should also be mentioned that void coalescence can be a process controlled by both nucleation and growth. Generally, this phenomenon is assumed to involve transition from uniform deformation to localized deformation of the ligaments between the voids.

Various analytical models and void coalescence criteria have been described in the literature. It should be noted, however, that in order to fully describe the cracking process, it is not enough to formulate the criterion of the coalescence initiation, but additionally it is required to model the behavior of the ligaments up to failure.

The Brown and Embury [67] void growth model, described in the previous section, also allows for the estimation of critical void coalescence strain:

$$\varepsilon_{coalescence} \approx \frac{1}{C} ln \left[\alpha \left(\frac{1}{\sqrt{f_0}} \right) - 1 \right], \tag{28}$$

As the Brown and Embury model does not take into account the local macroscopic instabilities due to the formation of the neck or the location of the shear bands, it should be treated as an approximate solution.

Thomason presented an analysis of the problem in [64,94]. The author provided the criterion for coalescence of voids in an elastic perfectly plastic matrix. The problem concerned the phenomenon of the location of plastic strains in the ligaments between the voids under the conditions of elastic unloading of the material outside the ligaments. In its original form, Thomason's criterion is expressed by the equation:

$$\frac{\sigma_n}{\sigma_0(1 - \chi^2)} = \alpha \left(\frac{1 - \chi}{\chi^W} \right)^2 + 1.24 \sqrt{\frac{1}{\chi}}, \tag{29}$$

According to Thomason's condition, void coalescence is initiated when the stress normal to the localization plane reaches the critical value of σ_n. Moreover, the influence of the volume fraction of voids on their coalescence is indirectly taken into account by intro-

ducing the parameter χ into the model. It should be noted, however, that the Thomason criterion concerns only the initiation of the void joining process, which is not sufficient to model the material in the pre-failure stage. As already mentioned, determination of the evolution law is additionally required in this case. In this respect, the Thomason model was developed by Benzerga [95], who introduced the evolution law of W and χ parameters as a function of plastic strain.

The Thomason criterion in its original form does not take into account the influence of shear stresses. Coalescence models for the case of simultaneous occurrence of tensile and shear stresses were developed in [96,97].

Simple coalescence criteria can also be formulated based on the void growth models described in the previous section. In this case, the achievement of a critical size of voids is decisive for initiating the coalescence. For example, the coalescence criterion based on Rice and Tracey's void growth law ([61], Section 5) would take the form:

$$\frac{R_{actual}}{R_0} = \left(\frac{R_{actual}}{R_0}\right)_{crit}, \tag{30}$$

subscript *crit* denotes critical void growth.

An equivalent criterion formulated in [67], as well as in [15], is associated with the achievement of a critical void volume fraction, which was determined by the authors in the range of 0.15–0.25.

The condition of void coalescence adopted in the Gurson–Tvergaard–Needleman (GTN) material model is also based on the critical volume fraction of voids [53,69,70]. The GTN solution includes the definition of the critical void volume fraction f_c at which void coalescence is initiated (compare also [98]) and the law of evolution of the void volume fraction after exceeding f_c:

$$f^* = \begin{cases} f & \text{for } f \leq f_c \\ f_c + \frac{\overline{f}_F - f_c}{f_F - f_c}(f - f_c) & \text{for } f_c < f < f_F \\ \overline{f}_F & \text{for } f \geq f_F \end{cases}, \tag{31}$$

where:

$$\overline{f}_F = \frac{q_1 + \sqrt{q_1^2 - q_3}}{q_3}, \tag{32}$$

The influence of various factors on f_c has been the subject of many studies. Koplik and Neeedleman [72] showed that it depends mainly on the initial porosity; however, no significant influence of the matrix parameters or stress triaxiality was found.

In [99], the dependence of f_c on the initial material porosity f_0 was described. The value of f_c ranged from 0.04 for $f_0 = 0$ to 0.12 for $f_0 = 0.06$.

Generally, a huge number of papers have been devoted to the subject of determining the parameters f_c and f_F (using experimental and numerical methods) and it is difficult to present a comprehensive review. The values of f_c in metal alloys with technical application (mainly steels and aluminum alloys) range from tenths of a percent to about 30%, although usually values of a few percent are assumed [100–102]. The values of f_F were analyzed, inter alia, in [99,103–105], obtaining results ranging from a dozen to nearly 70%.

The experimental methodology for determining f_c and f_F, using the material microstructural analysis has been discussed in [47].

The GTN condition in its original form gives relatively inaccurate results under conditions of significant shear stresses. Hence, in the literature, there are various modifications, taking into account the rapid joining of the voids caused by shear. For example, McVeigh et al. [106] added to the law of void evolution a component accounting for this phenomenon. The law of the evolution of the void volume fraction takes the form:

$$\dot{f} = \dot{f}_{nucl} + \dot{f}_{growth} + \dot{f}_{coalescence}, \tag{33}$$

However, it should be remembered that formulating the criterion of void coalescence in terms of the value of their critical fraction does not fully solve the problem, as it does not take into account the geometry of the intervoid ligaments or the physical phenomena that occur in them.

Nahshon and Hutchinson [107] introduced into the GTN formulation a component, which takes into account the softening of the ligaments, which is the effect of shear stresses. The description of Nahshon and Hutchinson is phenomenological, and the ligament softening is captured by the additional increase in the proportion of voids.

Relatively widespread in the literature are the criteria for connecting voids based on the critical size of the ligaments between the voids and the crack tip. One of the first solutions of this type was presented by Rice and Johnson [108], who assumed that the onset of coalescence occurs when the length of the ligament is reduced to the length of the void in the direction of loading. Tait and Taplin [109], on the other hand, proposed a criterion according to which the voids are joined when the ratio of the main void axis length to the void spacing reaches a critical value, depending on the type of material. A similar criterion was described by LeRoy et al. [110].

The effect of stress triaxiality as well as the shape and size of the voids on the process of void growth and coalescence was discussed by Richelsen and Tvergaard [99], who analyzed numerically an elastic perfectly plastic material containing small-sized voids. Taking into account the ligament necking mechanism, the authors obtained relatively low critical strain, of the order of 0.3.

Richelsen and Tvergaard also indicated that the occurrence of the ligament necking phenomenon is favored by high values of the matrix hardening exponent, as well as the presence of medium and high triaxiality.

In recent years, Gallican and Hurre [111] proposed an analytical criterion for void coalescence, taking into account the plastic flow in the ligaments between voids. The model is valid under the following assumptions: cylindrical void in a cylindrical unit-cell, axisymmetric loads, orthotropic matrix, satisfying the Hill plasticity condition. Moreover, the authors made extensive validation of the model by comparing the results with the results of numerical simulation of void coalescence, indicating their good agreement.

The above-described solutions for nucleation and development of voids allow for the formulation of material models describing the plastic range of material operation and its ductile fracture.

Void cell simulations are most often conducted for periodically distributed voids [112–114]. The obtained results indicate that relative void spacing is the key parameter influencing the course of the void development. In fact, various types of heterogeneity are observed in engineering materials, related to the randomness of the chemical composition of the material, size, shape, distribution of voids, and their orientation in relation to the direction of loading, as well as the distribution and orientation of grains [11]. Therefore, void coalescence is not a homogeneous process that occurs simultaneously in the entire volume of the material, but it is initiated in the areas with significant plastic strain.

The considerable progress made in recent years in the field of numerical methods has allowed for a better understanding of the course of void development. An example of a comprehensive FEM analysis of nucleation, growth, and coalescence of voids was presented by Shakoor et al. in [115]. On the basis of a 3D model of the material with randomly distributed particles, the influence of the void nucleation mechanism (matrix separation and particle fracture, see Section 4 of this work) on the further course of the void growth and coalescence was determined. The simulations carried out for 20% of the particle volume fraction showed that the occurrence of the void nucleation leads to the localization of plastic deformation, which in a further stage favors the local increase of the intensity of void coalescence. Such a wide range of analysis required taking into account large plastic deformation, and thus also advanced FE remeshing techniques.

7. Effect of Selected Loading Conditions on Void Development

The effect of stress triaxiality on void development and ductile failure has been very extensively documented in the literature [63,116]. Moreover, Bao and Wierzbicki [7], examining the 2024-T351 aluminum alloy, showed that the strain at failure is not a monotonic function of triaxiality, but the domain of low and high triaxiality should be distinguished (Figure 8a). In the latter case, an increase in triaxiality corresponds to a decrease in the critical strain.
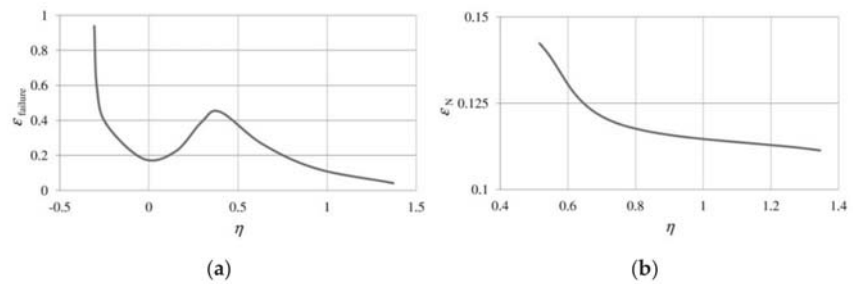
Figure 8. (**a**) Effect of stress triaxiality on strain at failure, from [7]; (**b**) dependence of the mean void nucleation strain on stress triaxiality [47].

A similar relationship for medium and high triaxialities was obtained in the already mentioned studies [47–49], but in this case, the analysis concerned the void nucleation strain in the S355 structural steel. In the range of triaxialities from 0.516 to 1.345, along with the increase in η, a decrease in ε_N was observed (Figure 8b).

High values of triaxiality favor an increase in the volume of voids. Figure 9 presents the experimentally determined (by examining the fracture surfaces) relationship between triaxiality η and the volume fraction of voids at failure in S355J2G3 steel.

Depending on triaxiality, the volume fraction of voids ranged between 59.7 and 71.2%. For comparison, the fraction of voids in the unstrained material was 0.09%.

The stress triaxiality affects not only the intensity of the void growth, but also their shape (Figure 10). In areas with high triaxiality, the voids are spherical in shape (a large share of the stress hydrostatic component forces the voids to grow steadily in all directions—Figure 10a).

As triaxiality decreases (decreasing influence of the spherical component of the stress tensor), the voids become more elongated (Figure 10b,c), because the process of microdamage development in these cases is mainly controlled by shear stresses [117].

As shown by Lin et al. in [118], the reduction of the triaxiality of stresses increases the level of strains at which cracking occurs. For greater triaxial stresses (axis of the specimen), the microvoids grow intensively in the plane perpendicular to the tensile, joining with each other.

Morgeneyer and Besson in [119] presented an example of the successive occurrence of both these mechanisms (regime of high and low triaxiality) in the test of a plate tearing (Kahn test). The observations made by the X-ray microtomography showed that the specimen failure was initiated inside the plate, under conditions of high triaxiality. As the microdamage propagated towards the plate faces, an increasing number of elongated voids was observed, which results from the decrease in triaxiality and the increasing role of shear in the process of void development. It is worth noting that while the shape of the voids undergoes large changes in this case, their volume fraction does not change significantly.

The shear induced failure propagation is also visible on the macroscopic level by the inclination of the fracture surface near the specimen edges (Figure 11).
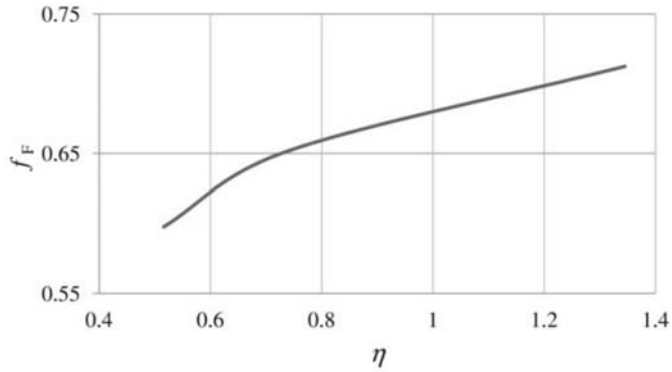
Figure 9. Effect of stress triaxiality on the void volume fraction at failure [47].

(a)

(b)

(c)
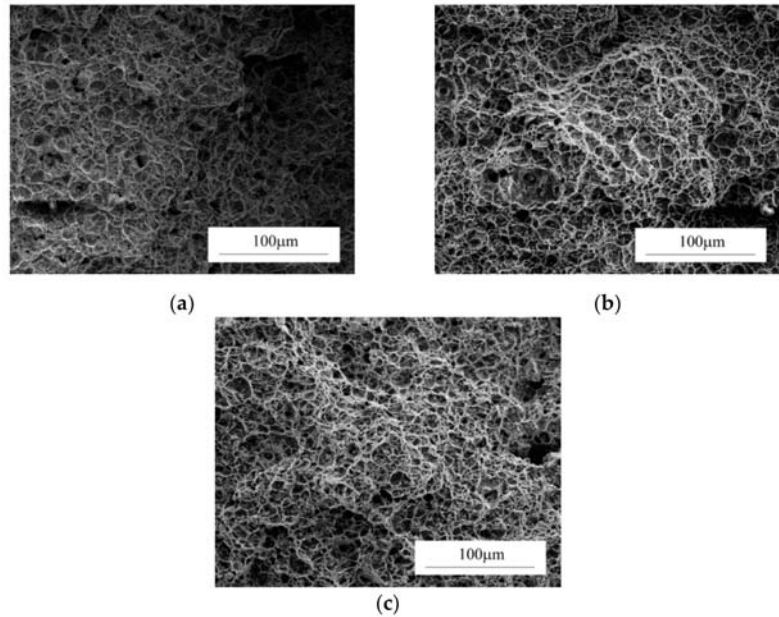
Figure 10. Fracture surfaces of notched tensile specimens made of S355J2G3 steel, subjected to various stress triaxialities: (**a**) 1.345; (**b**) 0.739; (**c**) 0.516.

The development of voids under low triaxiality conditions has been intensively researched in recent years. The small share of the hydrostatic component results in a relatively low increase in the volume of voids. However, in such cases, the action of shear stresses and the associated deformation (change of shape) of the void becomes of primary importance. As it has been shown, in the face of a small value of triaxiality η, the development of voids is in this case are controlled by the value of the Lode parameter ξ (Section 3), although the exact relationships have not yet been defined.

Under shear dominant conditions, voids can take the form of penny-shaped cracks. In addition, the presence of shear stress may cause the voids to rotate (Figure 12), which additionally affects the location of their coalescence area and implies a failure mechanism [11].

Figure 11. Macroscopic photograph of a fracture surface of a tensile notched specimen. Transition from the flat failure mechanism in the specimen center to the slant fracture at the edges is clearly visible. The first mechanism involves normal stress, while in the latter, shear stress plays a dominant role.
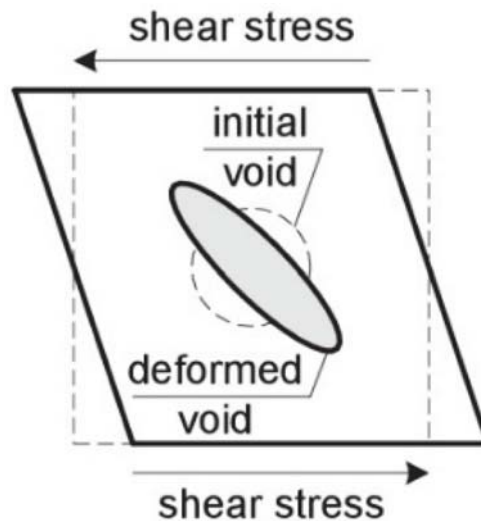
Figure 12. Void deformation and rotation under low triaxiality.

In fact, second phase particles still remain inside the void, limiting the possibility of its deformation, especially in the situation of incomplete decohesion at the particle–matrix interface.

Current models of void development primarily take into account the prevailing state of stress, but mostly do not take into account other factors such as deformation rate, temperature, and others, which undoubtedly is of great importance in modeling engineering structures.

Some of the few works taking into account the above factors are [120,121]. It was shown that good results of material description at high temperature are achieved by the use of an Arrhenius phenomenological model [120]. The model takes into account the strain rate for an elevated tensile temperature. The tests were carried out on steel with a bainite structure.

Similarly, the analysis of the influence of very high triaxial strain rates and temperatures in the range of 300–2000 K on the process of nucleation and void development is discussed in [122]. Using the void nucleation and growth model (NAG procedure) as well as molecular dynamics (MD) simulation, the increase in void volume fraction over time was determined, taking into account the process of nucleation, growth, and coalescence. It was found that, while the increase in temperature led to a significant acceleration of the nucleation of the voids, the influence of temperature in the case of the growth of voids was slight.

Another very interesting example of the analysis of the development of voids under dynamic load conditions (spall failure) is [123], in which the phenomenon of stress wave interaction and the associated negative pressure formation, which results in rapid nucleation and void growth, was investigated. Velocimetry on the specimen free surface was used to estimate changes in stress distribution over time. A comparative analysis of the obtained stress distributions and microtomographic photographs of the voids formed made it possible to determine the critical negative pressure necessary to initiate the void, at the level of about 1–2 GPa.

The problem of dynamic development of voids has also been thoroughly discussed in the article [124]. It was found that in the first phase of the failure initiation, the inertia of the material surrounding the void slows down its development, but at a higher value of strain it promotes the void growth. Moreover, in the range of void diameters from 0.1 to 1 μm, the strain gradients around the void contributed to a significant, local increase in the yield point. On the other hand, however, the increase in thermal energy accompanying rapid deformation caused a local increase in temperature even above the melting point, thereby lowering the yield stress, and the stress values necessary to initiate a void, and thus also increasing the intensity of void development.

8. Conclusions and Suggestions for Future Research

Due to the practical importance, the issues of microstructural phenomena occurring during ductile fracture of metals have been the subject of intensive research in recent years, which allows for a better phenomenon understanding and the development of advanced computational models.

Although void nucleation has been very extensively documented by the results of experimental tests and simulations, the course of ductile fracture under low triaxiality conditions, i.e., under dominant shear stress, remains an unresolved question. In this case, observations of the fracture surface microstructure indicate the presence of both large and small elongated voids. Their origins have not been fully elucidated so far, although it is believed that such void morphology results from their intensive nucleation at a late stage of deformation, prior to failure, with simultaneous growth of earlier nucleated voids. At present, there are no models of nucleation, growth, and coalescence of voids that take into account the influence of the Lode parameter, which is crucial for the course of ductile fracture under low triaxiality conditions.

As mentioned in Section 6, the stage of void coalescence is presently the least explored phase of ductile fracture. Few papers have been published in which the process of coalescence was extensively investigated in an experimental manner. This is largely due to technical difficulties, although the increasingly widely used method of microtomography seems to be a promising tool. Currently, insufficient understanding of the nature of the void coalescence phenomenon is associated with a small number of analytical models, especially in the case of the simultaneous occurrence of shear and necking of ligaments between the voids. The void coalescence models currently described in the literature are

based on certain arbitrarily accepted criteria that have not been sufficiently supported by experimental observations.

A separate problem is the identification of the model parameters. A huge number of papers have been published on this subject, but the dominant approach involves fitting the FEM simulation and the experimental results. However, this approach requires significant experimental and computational effort, and therefore it is inconvenient from a practical, engineering point of view. Moreover, the results obtained in this way apply only to samples with a specific geometry and loading method. Therefore, there is no comprehensive approach that would define standardized parameter values for typical engineering materials.

In conclusion, further research on the development of voids in metals should focus on the following aspects:

- Criteria for void nucleation under low triaxiality conditions;
- Effect of Lode parameter on void initiation, growth, and coalescence;
- In situ observations of void coalescence with the use of modern research methods (e.g., microtomography), which will allow the verification of the existing coalescence criteria, or the development of new ones;
- Assessment of the effect of loading conditions (temperature, strain rate, etc.) on the critical values of stress and strain necessary for the void initiation and growth;
- Development of a set of standardized parameters describing the criteria of nucleation, growth, and coalescence of voids, in relation to engineering materials.

The solution of the above-mentioned problems should lead to the development of practical engineering procedures for estimating the load capacity and safety assessment of structural elements containing material microstructure defects.

Nomenclature

a	void diameter
a_0	initial void diameter
b	Burgers vector
f	void volume fraction
$\dot{f}$	the rate of increase in the total fraction of voids
f^*	actual void volume fraction
f_0	initial void volume fraction (for unstrained material)
f_c	critical void volume fraction at the onset of coalescence initiation
$\dot{f}_{coalescence}$	the rate of increase in the fraction of voids resulting from their rapid joining under shear stresses
f_F	void volume fraction at failure
$\dot{f}_{growth}$	the rate of increasing the fraction of existing voids
$\dot{f}_{nucl}$	the rate of increase in nucleated voids' volume fraction
h	anisotropy coefficient
k	multiplier in power hardening law

k_m	coefficient depending on the particle shape
k_s	coefficient depending on the shape (aspect ratio) of the particle and its orientation in relation to the loading direction
$\mathbf{max}\left(\left.\sigma_1^p\right\|_{\delta\leq\beta}\right)$	maximum value of principal stress in the particle
$\mathbf{max}\left(\left.\sigma_{\eta\eta}\right\|_{\delta=\beta}\right)$	maximum value of the stress normal to the phases contact surface
n	exponent in power hardening law
q	stress concentration factor, correction factor in GTN model
q_1, q_3	Tvergaard coefficients
r	polar coordinate measured from the "head" of dislocation pile-up
r_1	characteristic length
s_N	standard deviation
C	coefficient expressing the ratio of the void elongation to the specimen elongation rate (on a macroscopic scale) in Brown and Embury model, $C \in 1, 2$
E	Young's modulus of the matrix
E_p	matrix plastic equivalent modulus of elasticity
L	Lode parameter
R	particle radius
$\dot{R}$	void radius growth rate
R_0	initial particle radius
R_{actual}	actual particle radius
S	remote normal stress
$V_{material}$	total volume of material
V_{voids}	volume of voids and second phase particles
W	void aspect ratio
α	coefficient in Brown–Embury model, coefficient depending on matrix hardening exponent in Thomason model
β	radial coordinate of particle surface in Thomason model
γ	surface energy
δ	generalized radial coordinate in Thomason model
ε	strain
$\dot{\varepsilon}$	strain rate
ε_{crit}	critical strain of particle–matrix separation
$\dot{\varepsilon}_e$	increase in effective plastic strain
ε_N	void nucleation strain
ε_p	plastic strain
ε_z	longitudinal strain of the cylinder in McClintock model
η	stress state triaxiality ratio
θ	Lode angle
κ^I	stress concentration factor at the interface of phases
κ^p	coefficient of normal stress concentration inside the particle
λ	coefficient in Beremin nucleation model, depending on particle shape
μ	shear modulus
μ^*	coefficient depending on the elastic parameters of particle, matrix, and the geometric characteristics of particle
σ	stress
σ_0	yield stress
σ_1, σ_2, σ_3	principal stresses
σ_1^{max}	maximum value of global tensile principal stress
$\dot{\sigma}_1^{max}$	rate of the maximum global principal stress increase
σ_{crit}	critical stress, dependent on the nucleation mechanism, matrix, particle, and the interface strength
$\sigma_{crit}^{interface}$	critical stress at the phase interface
σ_{crit}^{mean}	mean value of void nucleation stress
$\sigma_{crit}^{particle}$	theoretical strength of the particle material

σ_e	von Mises equivalent stress
$\dot{\sigma}_e$	rate of von Mises equivalent stress increase
σ_h	Hill's equivalent stress
$\sigma_{loc}(r)$	maximum local normal stress at the "head" of dislocation pile-up
σ_m	mean stress (hydrostatic pressure)
σ_n	critical normal stress in Thomason model
τ_0	yield stress at pure shear
χ	ratio of void length to the distance between neighboring voids
$\in_{eq}$	equivalent plastic strain
$\varnothing$	damage function of the particle–matrix interface
ν_p	equivalent Poisson coefficient

References

1. British Standard Institution. *Guidance on Some Methods for the Derivation of Acceptance Levels for Defects in Fusion Welded Joints*; BS PD6493; British Standard Institution: London, UK, 1991.
2. British Standards Institution. *Guide on Methods for Assessing the Acceptability of Flaws in Fusion Welded Structures*; BS7910; British Standards Institution: London, UK, 2001.
3. British Energy Generation. *R6: Assessment of the Integrity of Structures Containing Defects*; British Energy Generation: London, UK, 2001.
4. Koçak, M.; Webster, S.; Janosch, J.J.; Ainsworth, R.A.; Koerc, R. (Eds.) *FITNET: Fitness for Service. Fracture–Fatigue–Creep–Corrosion*; GKSS Research Centre Geesthacht: Geesthacht, Germany, 2008.
5. European Union Brite-Euram Programme. *SINTAP: Structural Integrity Assessment Procedure for European Industry*; Project No. Be95-1426; British Steel: North Lincolnshire, UK, 1999.
6. Besson, J.; Bugat, S.; Berdin, C.; Desmorat, R.; Feyel, F.; Forest, S.; Lorentz, E.; Maire, E.; Pardoen, T.; Pineau, A.; et al. *Local Approach to Fracture*, 1st ed.; Les Presses de l'École des Mines: Paris, France, 2004.
7. Bao, Y.; Wierzbicki, T. On fracture locus in the equivalent strain and stress triaxiality space. *Int. J. Mech. Sci.* **2004**, *46*, 81–98. [CrossRef]
8. Puttick, K.E. Ductile fracture in metals. *Philos. Mag.* **1959**, *4*, 964–969. [CrossRef]
9. Rogers, H.C. The tensile fracture of ductile metals. *Trans. Met. Soc.* **1960**, *218*, 498–506.
10. Lassance, D.; Fabrègue, D.; Delannay, F.; Pardoen, T. Micromechanics of room and high temperature fracture in 6xxx Al alloys. *Prog. Mater. Sci.* **2007**, *52*, 62–129. [CrossRef]
11. Pineau, A.; Benzerga, A.A.; Pardoen, T. Failure of metals I: Brittle and ductile fracture. *Acta Mater.* **2016**, *107*, 424–483. [CrossRef]
12. Asby, M.F. Work hardening of dispersion hardened crystals. *Philos. Mag.* **1966**, *14*, 1157–1178. [CrossRef]
13. Bauer, R.W.; Wilsdorf, H.G.F. Void initiation in ductile fracture. *Scr. Met.* **1973**, *7*, 1213–1220. [CrossRef]
14. Pang, W.W.; Zhang, P.; Zhang, G.C.; Xu, A.G.; Zhao, X.G. Dislocation creation and void nucleation in FCC ductile metals under tensile loading: A general microscopic picture. *Sci. Rep.* **2014**, *4*, 6981. [CrossRef] [PubMed]
15. Goods, S.H.; Brown, L.M. Overview No. 1: The nucleation of cavities by plastic deformation. *Acta Met.* **1979**, *27*, 1–15. [CrossRef]
16. Pineau, A.; Pardoen, T. *Comprehensive Structural Integrity*; Elsevier: Amsterdam, The Netherlands, 2007; pp. 684–797.
17. Beremin, F.M. Cavity formation from inclusions in ductile fracture of A508 steel. *Met. Trans. A* **1981**, *12*, 723–731. [CrossRef]
18. Argon, A.S.; Im, J.; Safoglu, R. Cavity formation from inclusions in ductile fracture. *Met. Mater. Trans. A* **1975**, *6*, 825–837. [CrossRef]
19. Argon, A.S. Formation of cavities from nondeformable second phase particles in low temperature ductile fracture. *J. Eng. Mater. Technol.* **1976**, *98*, 60–68. [CrossRef]
20. Argon, A.S.; Im, J. Separation of second phase particles in spheroidized 1045 steel, Cu-0.6pct Cr alloy, and maraging steel in plastic straining. *Met. Trans. A* **1975**, *6*, 839–851. [CrossRef]
21. Eshelby, J.D. The determination of the elastic field of an ellipsoidal inclusion, and related problems. *Proc. R. Soc. Lond. A* **1957**, *241*, 376–396.
22. Babout, L.; Brechet, Y.; Maire, E.; Fougères, R. On the competition between particle fracture and particle decohesion in metal matrix composites. *Acta Mater.* **2004**, *52*, 4517–4525. [CrossRef]
23. Brown, L.M.; Clarke, D.R. Work hardening due to internal stresses in composite materials. *Acta Met.* **1975**, *23*, 821–830. [CrossRef]
24. Lee, B.J.; Mear, M.E. Stress concentration induced by an elastic spheroidal particle in a plastically deforming solid. *J. Mech. Phys. Solids* **1999**, *47*, 1301–1336. [CrossRef]
25. Margolin, B.Z.; Shvetsova, V.A.; Karzof, G. Brittle fracture of nuclear pressure vessel steels—I. Local criterion for cleavage fracture. *Int. J. Press. Vessel. Pip.* **1997**, *72*, 73–87. [CrossRef]
26. Chen, J.; Cao, R. *Micromechanism of Cleavage Fracture of Metals. A Comprehensive Microphysical Model for Cleavage Cracking in Metals*, 1st ed.; Butterworth-Heinemann: Oxford, UK, 2015.
27. Hancock, J.W.; Cowling, M.J. Role of state of stress in crack–tip failure processes. *Met. Sci.* **1980**, *14*, 293–304. [CrossRef]
28. Griffith, A.A. The phenomena of rupture and flow in solids. *Philos Trans. R. Soc. Lond. Ser. A* **1921**, *221*, 163–198.
29. Gurland, J.; Plateau, J. The mechanism of ductile rupture of metals containing inclusions. *Trans. ASM* **1963**, *56*, 442–454.

30. Kwon, D.; Asaro, R. A study of void nucleation, growth, and coalescence in spheroidized 1518 steel. *Met. Trans. A* **1990**, *21*, 117–134. [CrossRef]
31. Bugat, S.; Besson, J.; Pineau, A. Micromechanical modeling of the behaveior of duplex stainless steels. *Comput. Mater. Sci.* **1999**, *16*, 158–166. [CrossRef]
32. Giovanola, J.H.; Cannizzaro, D.; Doglione, R.; Rossoll, A. Ductile fracture by void nucleation at tempering carbides. In *Fracture of Nano and Engineering Materials and Structures*; Gdoutos, E.E., Ed.; Springer: Berlin/Heidelberg, Germany, 2006.
33. Brown, L.M.; Stobbs, W.M. The work-hardening of copper-silica. V. Equilibrium plastic relaxation by secondary dislocations. *Philos. Mag.* **1976**, *34*, 351–372. [CrossRef]
34. Shabrov, M.N.; Sylven, E.; Kim, S.; Sherman, D.H.; Chuzhoy, L.; Briant, C.L.; Needleman, A. Void nucleation by inclusion cracking. *Met. Mater. Trans. A* **2004**, *35*, 1745–1755. [CrossRef]
35. Babout, L.; Maire, E.; Fougères, R. Damage initiation in model metallic materials: X-ray tomography and modelling. *Acta Mater.* **2004**, *52*, 2475–2487. [CrossRef]
36. François, D.; Pineau, A.; Zaoui, A. Ductile fracture. In *Mechanical Behaviour of Materials. Volume II: Fracture Mechanics and Damage*, 2nd ed.; Springer: Dordrecht, The Netherlands, 2013.
37. Alexandre, F.; Deyber, S.; Vaissaud, J.; Pineau, A. Probabilistic Life of DA 718 for Aircraft Engine Disks. In Proceedings of the International Symposium on Superalloys and Various Derivatives, Pittsburgh, PA, USA, 2–5 October 2005; pp. 97–110.
38. Hubert, G.; Brechet, Y.; Pardoen, T. Void growth and void nucleation controlled ductility in quasi eutectic cast aluminium alloys. *Acta Mater.* **2005**, *53*, 2739–2749. [CrossRef]
39. Dong, M.J.; Prioul, C.; François, D. Damage effect on the fracture toughness of nodular cast iron. Part I: Damage characterization and plastic flow stress modeling. *Met. Mater. Trans. A* **1997**, *28*, 2245–2254. [CrossRef]
40. Needleman, A. A Continuum model for void nucleation by inclusion debonding. *J. Appl. Mech.* **1987**, *54*, 525–531. [CrossRef]
41. Wciślik, W.; Pała, T. Selected aspects of cohesive zone modeling in fracture mechanics. *Metals* **2021**, *11*, 302. [CrossRef]
42. Siegmund, T.; Brocks, W. A numerical study on the correlation between the work of separation and the dissipation rate in ductile fracture. *Eng. Fract. Mech.* **2000**, *67*, 139–154. [CrossRef]
43. Andersen, R.G.; Tekoğlu, C.; Nielsen, K.L. Cohesive traction–separation relations for tearing of ductile plates with randomly distributed void nucleation sites. *Int. J. Fract.* **2020**, *224*, 187–198. [CrossRef]
44. Chu, C.; Needleman, A. Void nucleation effects in biaxially stretched sheets. *J. Eng. Mater. Technol.* **1980**, *102*, 249–256. [CrossRef]
45. Fisher, J.R. Void Nucleation in Spheroidized Steels during Tensile Deformation. Ph.D. Thesis, Brown University, Providence, RI, USA, 1980.
46. Hahn, G.T.; Rosenfield, A.R. Metallurgical factors affecting fracture toughness of aluminium alloys. *Met. Trans. A* **1975**, *6*, 653–670. [CrossRef]
47. Wciślik, W. Experimental and Numerical Determination and Analysis of Selected Parameters of the Gurson-Tvergaard-Needleman Model for S355 Steel and Complex Stress States. Ph.D. Thesis, Kielce University of Technology, Kielce, Poland, 2014. (In Polish)
48. Wciślik, W. Numerical Determination of Critical Void Nucleation Strain in the Gurson-Tvergaard-Needleman Porous Material Model for Low Stress State Triaxiality Ratio. In Proceedings of the 23rd International Conference on Metallurgy and Materials, Brno, Czech Republic, 21–23 May 2014; pp. 794–800.
49. Wciślik, W. Numerical simulation of void nucleation in S355 steel. *Solid State Phenom.* **2016**, *250*, 244–249. [CrossRef]
50. Kossakowski, P.; Wciślik, W. Effect of stress triaxiality ratio on void nucleation strain in S235JR steel. *Przeglad Mechaniczny* **2013**, *3*, 15–21. (In Polish)
51. Caceres, C.H.; Griffiths, J.R. Damage by the cracking of silicon particles in an Al-7Si-0.4Mg casting alloy. *Acta Mater.* **1996**, *44*, 25–33. [CrossRef]
52. Pineau, A.; Joly, P. Local versus global approaches to elastic-plastic fracture mechanics. Application to ferritic steels and a cast duplex stainless steel. In *Defect Assessment in Components—Fundamentals and Applications*, 1st ed.; Blauel, J.G., Schwalbe, K.H., Eds.; Wiley: Hoboken, NJ, USA, 1991; pp. 381–414.
53. Gurson, A.L. Continuum theory of ductile rupture by void nucleation and growth: Part I-yield criteria and flow rules for porous ductile media. *J. Eng. Mater. Technol.* **1977**, *99*, 2–15. [CrossRef]
54. Xia, L.; Cheng, L. Transition from ductile tearing to cleavage fracture: A cell-model approach. *Int. J. Fract.* **1997**, *87*, 289–306. [CrossRef]
55. He, R.; Steglich, D.; Heerens, J.; Wang, G.X.; Brocks, W.; Dahms, M. Influence of particle size and volume fraction on damage and fracture in Al-A13Ti composites and micromechanical modelling using the GTN model. *Fatigue Fract. Eng Mater. Struct.* **1998**, *21*, 1189–1201. [CrossRef]
56. Lewis, C.A.; Withers, P.J. Weibull modelling of particle cracking in metal matrix composites. *Acta Met. Mater.* **1995**, *43*, 3685–3699. [CrossRef]
57. Babout, L.; Maire, E.; Buffière, J.Y.; Fougères, R. Characterization by X-ray computed tomography of decohesion, porosity growth and coalescence in model metal matrix composites. *Acta Mater.* **2001**, *49*, 2055–2063. [CrossRef]
58. Maire, E.; Bordreuil, C.; Babout, L.; Boyer, J.C. Damage initiation and growth in metals. Comparison between modeling and tomography experiments. *J. Mech. Phys. Solids* **2005**, *53*, 2411–2434. [CrossRef]
59. Weck, A.; Wilkinson, D.S.; Maire, E.; Toda, H. Visualization by X-ray tomography of void growth and coalescence leading to fracture in model materials. *Acta Mater.* **2008**, *56*, 2919–2928. [CrossRef]

60. McClintock, F.A. A criterion for ductile fracture by the growth of holes. *ASME J. Appl. Mech.* **1968**, *35*, 363–371. [CrossRef]
61. Rice, J.R.; Tracey, D.M. On the ductile enlargement of voids in triaxial stress fields. *J. Mech. Phys. Solids* **1969**, *17*, 201–217. [CrossRef]
62. Huang, Y. Accurate dilatation rates for spherical voids in triaxial stress fields. *J. Appl. Mech.* **1991**, *58*, 1084–1085. [CrossRef]
63. Marini, B.; Mudry, F.; Pineau, A. Experimental study of cavity growth in ductile rupture. *Eng. Fract. Mech.* **1985**, *6*, 989–996. [CrossRef]
64. Thomason, P.F. *Ductile Fracture of Metals*, 1st ed.; Pergamon Press: Oxford, UK, 1990.
65. Budiansky, B.; Hutchinson, J.W.; Slutsky, S. Void growth and collapse in viscous solids. In *Mechanics of Solids: The Rodney Hill 60th Anniversary Volume*, 1st ed.; Hopkins, H.G., Sewell, M.J., Eds.; Pergamon: Oxford, UK, 1982; pp. 13–45.
66. Thomason, P.F. A theoretical relation between K_{IC} and basic material properties in ductile metals. *Int. J. Fract.* **1971**, *4*, 409–419.
67. Brown, L.M.; Embury, J.D. A Model of Ductile Fracture in Two-Phase Materials. In Proceedings of the 3rd International Conference on the Strength of Metals and Alloys, Cambridge, UK, 20–25 August 1973; pp. 164–169.
68. Sills, R.B.; Boyce, B.L. Void growth by dislocation adsorption. *Mater. Res. Lett.* **2020**, *8*, 103–109. [CrossRef]
69. Tvergaard, V. Influence of voids on shear band instabilities under plane strain conditions. *Int. J. Fract.* **1981**, *17*, 389–407. [CrossRef]
70. Tvergaard, V.; Needleman, A. Analysis of the cup–cone fracture in a round tensile bar. *Acta Met. Mater.* **1984**, *32*, 157–169. [CrossRef]
71. Faleskog, J.; Gao, X.; Shih, C.F. Cell model for nonlinear fracture analysis—I. Micromechanics calibration. *Int. J. Fract.* **1998**, *89*, 355–373. [CrossRef]
72. Koplik, J.; Needleman, A. Void growth and coalescence in porous plastic solids. *Int. J. Solids Struct.* **1988**, *24*, 835–853. [CrossRef]
73. Benzerga, A.A.; Besson, J. Plastic potentials for anisotropic porous solids. *Eur. J. Mech. A Solids* **2001**, *20*, 397–434. [CrossRef]
74. Gologanu, M.; Leblond, J.B.; Devaux, J. Approximate models for ductile metals containing non-spherical voids—Case of axisymmetric prolate ellipsoidal cavities. *J. Mech. Phys. Solids* **1993**, *41*, 1723–1754. [CrossRef]
75. Gologanu, M.; Leblond, J.B.; Devaux, J. Approximate models for ductile metals containing non-spherical voids—Case of axisymmetric oblate ellipsoidal cavities. *J. Eng. Mater. Technol.* **1994**, *116*, 290–297. [CrossRef]
76. Gologanu, M.; Leblond, J.B.; Devaux, J.; Perrin, G. Recent extensions of Gurson's model for porous ductile metals. In *Continuum Micromechanics*, 1st ed.; Suquet, P., Ed.; Springer: Vienna, Austria, 1997; pp. 61–130.
77. Madou, K.; Leblond, J.B. Numerical studies of porous ductile materials containing arbitrary ellipsoidal voids—I: Yield surfaces of representative cells. *Eur. J. Mech. A Solids* **2013**, *42*, 480–489. [CrossRef]
78. Madou, K.; Leblond, J.B.; Morin, L. Numerical studies of porous ductile materials containing arbitrary ellipsoidal voids—II: Evolution of the length and orientation of the void axes. *Eur. J. Mech. A Solids* **2013**, *42*, 490–507. [CrossRef]
79. Kailasam, M.; Ponte-Castaneda, P. A general constitutive theory for linear and nonlinear particulate media with microstructure evolution. *J. Mech. Phys. Solids* **1998**, *46*, 427–465. [CrossRef]
80. Agoras, M.; Ponte-Castaneda, P. Anisotropic finite-strain models for porous viscoplastic materials with microstructure evolution. *Int. J. Solids Struct.* **2014**, *51*, 981–1002. [CrossRef]
81. Keralavarma, S.M.; Benzerga, A.A. A constitutive model for plastically anisotropic solids with non-spherical voids. *J. Mech. Phys. Solids* **2010**, *58*, 874–901. [CrossRef]
82. Keralavarma, S.M.; Hoelscher, S.; Benzerga, A.A. Void growth and coalescence in anisotropic plastic solids. *Int. J. Solids Struct.* **2011**, *48*, 1696–1710. [CrossRef]
83. Siruguet, K.; Leblond, J.B. Effect of void locking by inclusions upon the plastic behavior of porous ductile solids. I: Theoretical modeling and numerical study of void growth. *Int. J. Plast.* **2004**, *20*, 225–254. [CrossRef]
84. Siruguet, K.; Leblond, J.B. Effect of void locking by inclusions upon the plastic behavior of porous ductile solids. II: Theoretical modeling and numerical study of void coalescence. *Int. J. Plast.* **2004**, *20*, 255–268. [CrossRef]
85. Needleman, A. Void growth in an elastic–plastic medium. *J. Appl. Mech.* **1972**, *94*, 964–970. [CrossRef]
86. Tracey, D.M. Strain hardening and interaction effects on the growth of voids in ductile fracture. *Eng. Fract. Mech.* **1971**, *3*, 301–315. [CrossRef]
87. Andersson, H. Analysis of a model for void growth and coalescence ahead of a moving crack tip. *J. Mech. Phys. Solids* **1977**, *25*, 217–233. [CrossRef]
88. Tvergaard, V. Interaction of very small voids with larger voids. *Int. J. Solids Struct.* **1998**, *35*, 3989–4000. [CrossRef]
89. Tvergaard, V.; Niordson, C. Nonlocal plasticity effects on interaction of different size voids. *Int. J. Plast.* **2004**, *20*, 107–120. [CrossRef]
90. Tvergaard, V.; Hutchinson, J.W. Two mechanisms of ductile fracture: Void by void growth versus multiple void interaction. *Int. J. Solids Struct.* **2002**, *39*, 3581–3597. [CrossRef]
91. Faleskog, J.; Shih, C.F. Micromechanics of coalescence—I. Synergistic effects of elasticity, plastic yielding and multi–size–scale voids. *J. Mech. Phys. Solids* **1997**, *45*, 21–50. [CrossRef]
92. Seo, D.; Toda, H.; Kobayashi, M.; Uesugi, K.; Takeuchi, A.; Suzuki, Y. In situ observation of void nucleation and growth in a steel using X-ray tomography. *ISIJ Int.* **2015**, *55*, 1474–1482. [CrossRef]
93. Maire, E.; Withers, P.J. Quantitative X-ray tomography. *Int. Mater. Rev.* **2014**, *59*, 1–43. [CrossRef]
94. Thomason, P.F. A theory of ductile fracture by internal necking of cavities. *J. Inst. Met.* **1968**, *96*, 360–365.

95. Benzerga, A.A. Micromechanics of coalescence in ductile fracture. *J. Mech. Phys. Solids* **2002**, *50*, 1331–1362. [CrossRef]
96. Tekoglu, C.; Leblond, J.B.; Pardoen, T. A criterion for the onset of void coalescence under combined tension and shear. *J. Mech. Phys. Solids* **2012**, *60*, 1363–1381. [CrossRef]
97. Torki, M.E.; Benzerga, A.A.; Leblond, J.B. On void coalescence under combined tension and shear. *J. Appl. Mech.* **2015**, *82*, 071005. [CrossRef]
98. McClintock, F.A. Plasticity aspects of fracture. In *Fracture: An Advanced Treatise*; Liebowitz, H., Ed.; Academic Press: New York, NY, USA, 1973; Volume 3, pp. 47–225.
99. Richelsen, A.B.; Tvergaard, V. Dilatant plasticity or upper bound estimates for porous ductile solids. *Acta Met. Mater.* **1994**, *42*, 2561–2577. [CrossRef]
100. Betegon, C.; Rodriguez, C.; Belzunce, F.J. Analysis and modelisation of short crack growth by ductile fracture micromechanisms. *Fatigue Fract. Eng. Mater. Struct.* **1997**, *20*, 633–644. [CrossRef]
101. Devaux, J.; Joly, P.; Leblond, J.B. Simulation by the Local Approach of the Ductile Crack Growth in a Pressure Vessel Steel Using an Improved Gurson-Tvergaard Model. In Proceedings of the 21st MPA Seminar, Stuttgart, Germany, 5–6 October 1995.
102. Steglich, D.; Brocks, W. Micromechanical modelling of damage and fracture of ductile materials. *Fatigue Fract. Eng. Mater. Struct.* **1998**, *21*, 1175–1188. [CrossRef]
103. Skallerud, B.; Zhang, Z.L. A 3D numerical study of ductile tearing and fatigue crack growth under nominal cyclic plasticity. *Int. J. Solids Struct.* **1997**, *34*, 3141–3161. [CrossRef]
104. Zhang, Z.L. A sensitivity analysis of material parameters for the Gurson constitutive model. *Fatigue Fract. Eng. Mater. Struct.* **1996**, *19*, 561–570. [CrossRef]
105. Hao, S.; Brocks, W.; Heerens, J.; Hellmann, D. Simulation of 3D Ductile Crack Growth by the Gurson-Tvergaard-Needleman Model. In Proceedings of the ECF11: Mechanisms and Mechanics of Damage and Failure, Poitiers-Futuroscope, Poitiers, France, 3–6 September 1996; pp. 805–810.
106. McVeigh, C.; Vernerey, F.; Liu, W.K.; Moran, B.; Olson, G. An interactive microvoid shear localization mechanism in high strength steels. *J. Mech. Phys. Solids* **2007**, *55*, 225–244. [CrossRef]
107. Nahshon, K.; Hutchinson, J.W. Modification of the Gurson model for shear failure. *Eur. J. Mech. A Solids* **2008**, *27*, 1–17. [CrossRef]
108. Rice, J.R.; Johnson, M.A. The role of large crack tip geometry changes in plane strain fracture. In *Inelastic Behavior of Solids*; Kanninen, M.F., Adler, W.F., Rosenfield, A.R., Jaffee, R.I., Eds.; McGraw-Hill: New York, NY, USA, 1970; pp. 641–672.
109. Tait, R.A.; Taplin, D.M.R. Interaction effects during the growth of holes in a superplastically deforming medium. *Scr. Met.* **1979**, *13*, 77–82. [CrossRef]
110. LeRoy, G.; Embury, J.D.; Edward, G.; Ashby, M.F. A model of ductile fracture based on the nucleation and growth of voids. *Acta Met.* **1981**, *29*, 1509–1522. [CrossRef]
111. Gallican, V.; Hurre, J. Anisotropic coalescence criterion for nanoporous materials. *J. Mech. Phys. Solids* **2017**, *108*, 30–48. [CrossRef]
112. Yerra, S.K.; Tekoglu, C.; Scheyvaerts, F.; Delannay, L.; Van Houtte, P.; Pardoen, T. Void growth and coalescence in single crystals. *Int. J. Solids Struct.* **2010**, *47*, 1016–1029. [CrossRef]
113. Srivastava, A.; Needleman, A. Void growth versus void collapse in a creeping single crystal. *J. Mech. Phys. Solids* **2013**, *61*, 1169–1184. [CrossRef]
114. Brocks, W.; Sun, D.Z.; Hönig, A. Verification of the transferability of micromechanical parameters by cell model calculations with visco-plastic materials. *Int. J. Plast.* **1995**, *11*, 971–989. [CrossRef]
115. Shakoor, M.; Bernacki, M.; Bouchard, P.O. Ductile fracture of a metal matrix composite studied using 3D numerical modeling of void nucleation and coalescence. *Eng. Fract. Mech.* **2018**, *189*, 110–132. [CrossRef]
116. Barnby, J.T.; Shi, Y.W.; Nadkarmi, A.S. On the void growth in C-Mn structural steel during plastic deformation. *Int. J. Fract.* **1984**, *25*, 273–283. [CrossRef]
117. Moxnes, J.F.; Frøyland, Ø. Mathematical relations related to the Lode parameter for studies of ductility. *Adv. Stud. Ther. Phys.* **2016**, *10*, 113–124. [CrossRef]
118. Lin, Y.C.; Zhu, X.H.; Dong, W.Y.; Yang, H.; Xiao, Y.W.; Kotkunde, N. Effects of deformation parameters and stress triaxiality on the fracture behaviors and microstructural evolution of an Al-Zn-Mg-Cu alloy. *J. Alloys Compd.* **2020**, *832*, 154988. [CrossRef]
119. Morgeneyer, T.F.; Besson, J. Flat to slant ductile fracture transition: Tomography examination and simulations using shear-controlled void nucleation. *Scr. Mater.* **2011**, *65*, 1002–1005. [CrossRef]
120. Wen, D.X.; Yue, T.Y.; Xiong, Y.B.; Wang, K.; Wang, J.K.; Zheng, Z.Z.; Li, J.J. High-temperature tensile characteristics and constitutive models of ultrahigh strength steel. *Mat. Sci. Eng. A* **2021**, *803*, 140491. [CrossRef]
121. Wen, D.X.; Gao, C.X.; Zheng, Z.Z.; Wang, K.; Xiong, Y.B.; Wang, J.K.; Li, J.J. Hot tensile behavior of a low-alloyed ultrahigh strength steel: Fracture mechanism and physically based constitutive model. *J. Mater. Res. Technol.* **2021**, *13*, 1684–1697. [CrossRef]
122. Zhou, W.; Chen, W.; Yuan, J. Evaluation of void nucleation, growth and coalescence parameters for HCP-Zr at extreme strain rates. *AIP Adv.* **2021**, *11*, 015343. [CrossRef]
123. Mallick, D.D.; Parker, J.; Wilkerson, J.W.; Ramesh, K.T. Estimating void nucleation statistics in laser-driven spall. *J. Dyn. Behav. Mater.* **2020**, *6*, 268–277. [CrossRef]
124. Ma, X.; Liu, J.; Wang, J.; Pan, H. Modeling of dynamic growth of a micro-scaled void based on strain gradient elasto-plasticity. *J. Ther. Appl. Mech.* **2020**, *58*, 927–941. [CrossRef]

Article

Mechanical Properties and Damage Evolution of Concrete Materials Considering Sulfate Attack

Qianyun Wu [1,2], Qinyong Ma [1,2,*] and Xianwen Huang [1,3,*]

[1] School of Civil Engineering and Architecture, Anhui University of Science and Technology, Huainan 232001, China; wqyahust@126.com

[2] Engineering Research Center of Underground Mine Construction, Ministry of Education, Anhui University of Science and Technology, Huainan 232001, China

[3] School of Civil and Architecture Engineering, Jiangsu University of Science and Technology, Zhenjiang 212003, China

* Correspondence: qinyongma@126.com (Q.M.); 162100003@stu.just.edu.cn (X.H.)

Abstract: In order to study the durability of concrete materials subjected to sulfate attack, in a sulfate attack environment, a series of concrete tests considering different fly ash contents and erosion times were conducted. The mechanical properties and the micro-structure of concrete under sulfate attack were studied based on the following: uniaxial compressive strength test, split tensile test, ultrasonic impulse method, scanning electron microscopy (SEM) and X-ray diffraction (XRD). The mechanical properties were compressive strength, splitting tensile strength, and relative dynamic elastic modulus, respectively. Additionally, according to the damage mechanical theory, experimental results and micro-structure analysis, the damage evolution process of concrete under a sulfate attack environment were studied in detail. Finally, according to the sulfate attack time and fly ash content, a damage model of the sulfate attack of the binary surface was established. The specific results are as follows: under the action of sulfate attack, the change law of the rate of mass change, relative dynamic modulus of elasticity, corrosion resistance coefficient of compressive strength, and the corrosion resistance coefficient of the splitting tensile strength of concrete all increase first and then decrease. Under the same erosion time, concrete mixed with 10% fly ash content has the best sulfate resistance. Through data regression, the damage evolution equation of the sulfate attack was developed and there is an exponential function relationship among the different damage variables. The binary curved surface regression effect of the concrete damage and the erosion time and the amount of fly ash is significant, which can predict deterioration of concrete damage under sulfate attack. During the erosion time, the combined expansion of ettringite and gypsum caused micro cracks. With an increase of corrosion time, micro cracks developed and their numbers increased.

Keywords: concrete; sulfate attack; physical and mechanical properties; damage model; microstructure

1. Introduction

Sulfate attack is an important factor affecting the service life and durability of concrete buildings and structures [1–4]. Soils containing a large amount of sulfate are common in saline areas of Northwest China, seawater in coastal areas, and groundwater. As a concrete structure is immersed in a sulfate solution for a long time, a large amount of sulfate ions from the solution is absorbed into the concrete, which reacts with hydration products to form ettringite precipitation. This gradually generates stress on the inner walls of pores, leading to deformation of and damage to the concrete structure [5–7]. This, severely affects the safety and service life of the concrete structure, and causes extensive economic losses [8,9]. Therefore, studying the damage degradation process of concrete under sulfate attack and the damage model of sulfate attack is helpful to delay erosion damage to concrete structures and evaluate their service states. At present, many scholars have carried out a great deal of research on the sulfate corrosion resistance of concrete and

have achieved fruitful results [10–14]. The right amount of fiber can inhibit the generation and expansion of microcracks in concrete. This enhances mechanical properties [15] and improves the durability of concrete, and shows that the effect of mixed fiber is better than that of single fiber [16–18]. In addition, adding an appropriate amount of fly ash to replace cement in fiber concrete can improve its durability [19–21].

At present, scholars at home and abroad have primarily studied the change law and erosion mechanisms of the macroscopic mechanical properties of concrete under sulfate attack [22,23]. At the same time, most scholars have established damage models that take compressive strength [24], split tensile strength, or relative dynamic elastic modulus as a single evaluation index of the damage variable to measure the damage caused by sulfate erosion of concrete. However, little attention has been devoted to the relationship between the amount of damage of each evaluation index [25,26]. Moreover, a single factor model with the time of sulfate erosion as the main variable was also established. Bao et al. [27] conducted tensile tests on concrete after sulfate erosion and established an evolution model with crack number density as the damage degree; they found that this model could better reflect the evolution law of concrete erosion damage. An et al. [28] conducted sulfate erosion tests on recycled concrete and established a parabolic damage model with E_r as the damage quantity and found that it could better reflect the evolution law of erosion damage. Wu et al. [29] studied the relationship between ITZ (interface transition zone)and the damage evolution of concrete under the action of sodium sulfate erosion. They found that the influence of ITZ on the damage evolution of concrete was related to binder composition and immersion time. Xiao et al. [30] carried out a sulfate freeze–thaw coupling test on concrete and established a damage equation using the two-factor Weibull distribution model; they found that the damage fitted by the Weibull damage equation had a good correlation with RAC. Most scholars established concrete damage models that act on single factors; however, the performance of concrete subjected to sulfate erosion is the result of the combined actions of erosion time and the constituent materials [31], as such establishing a damage model based on both erosion time and the constituent materials should be considered.

In this paper, fly ash content and erosion time are taken as the main variables, while the uniaxial compressive strength test, split tensile test, ultrasonic testing test, scanning electron microscopy (SEM) and X-ray diffraction (XRD) were carried out on concrete under sulfate attack. First, the rate of mass change, relative dynamic modulus of elasticity, corrosion resistance coefficient of compressive strength, and the corrosion resistance coefficient of splitting tensile strength of concrete of different erosion times were analyzed. The erosion damage of concrete caused by sulfate attack was defined by the strength damage and wave velocity damage. Considering the superimposed effect of fly ash and erosion time, the influence of fly ash and sulfate erosion time on the expansion of concrete damage was discussed. Based on fly ash content and sulfate erosion time, a concrete composite erosion damage model was established. Finally, our study reveals the microstructure change law of concrete subjected to sulfate attack, aiming to provide theoretical support and an experimental basis for durability research of concrete structures in areas where sulfate attack occurs.

2. Materials and Methods

2.1. Raw Materials and Concrete Mixture Proportions

This study used Portland cement (P•O 42.5) produced by Bagongshan Cement Plant (Huainan, China), which conforms with the standard for Common Portland cement [32]. The chemical composition of the cement are given in Table 1. The fly ash employed was a secondary class fly ash and was purchased from Luoyang Yizhou Plastic Technology Co., Ltd. (Luoyang, China), which conforms to the standard for fly ash used for cement and concrete [33]. The chemical composition of the fly ash are listed in Table 1. Fly ash was used as a partial replacement for cement and its mixing amounts were 0, 10, and 20% (ψ, mass fraction) of the total cementitious material, respectively. The coarse aggregate

used in the test was continuous grading crushed rock of 5–25 mm. The fine aggregate was river sand with fineness modulus of 2.6. The water used was fresh, potable laboratory tap water. In the experiments, 6-mm basalt fiber with a volume ratio of 0.1% and 12-mm polypropylene fiber with a volume ratio of 0.2% were used. Their appearances are shown in Figure 1. The physical and mechanical properties are listed in Table 2. A sodium sulfate solution was prepared using chemical analytical reagents.

(**a**)   (**b**)

Figure 1. The appearance of fiber. (**a**) Polypropylene fiber and (**b**) basalt fiber.

According to the JGJ 55-2011 specification for the mix proportion of ordinary concrete [34], concrete with a strength grade of C30 was designed. Each group of concrete needed to have 3 parallel samples, and there were 108 concrete samples in total. In addition, the water-to-binder ratio (W/B) was 0.6. The mix ratios of concrete specimens are shown in Table 3.

Table 1. Chemistry composition of binder (%) [35,36].

Composition	SiO_2	Al_2O_3	CaO	Fe_2O_3	SO_3	MgO	Na_2O	K_2O
Cement	19.6	6.5	66.3	3.5	2.5	0.7	0.6	0.3
Fly ash	45.40	33.51	3.15	5.28	0.45	0.06	2.62	3.88

Table 2. Physical and mechanical properties of fibers [37].

Fiber Types	Basalt Fiber	Polypropylene Fiber
Density/$(g \cdot cm^{-3})$	2.65	0.91
Melting point/°C	1450–1500	160
Elongation to fracture/%	3.2	30–50
Tensile strength/MPa	3000–3300	350–480
Elastic modulus/GPa	90–110	2.4–3.2

Table 3. Mix proportions of concrete.

Materials	FA0	FA10	FA20
Cement (kg·m^{-3})	350	315	280
Fly ash (kg·m^{-3})	-	35	70
Water (kg·m^{-3})	210	210	210
Fine aggregate (kg·m^{-3})	644	644	644
Coarse aggregate (kg·m^{-3})	1196	1196	1196
Sand ratio (%)	35	35	35
Basalt fiber (%)	0.1	0.1	0.1
Polypropylene fiber (%)	0.2	0.2	0.2
Water–binder ratio (W/B)	0.6	0.6	0.6

Notes: FA—fly ash; 0.0, 10, 20—fly ash content of 0.0%, 10%, 20%, respectively.

The types and dosages of concrete and fiber designed in this paper were all carried out on the basis of the research done in [35,37]. Basalt fibers are high elastic fibers and polypropylene fibers are low elastic fiber. The two kinds of fibers play different roles in the process of concrete stress. The correct amount of a fiber disperses evenly within a concrete, enhances the crack resistance effect and improves the interface characteristic of the concrete. It also inhibits the internal stress of concrete cracking after preliminary initiation and, further, reduces the brittleness of concrete, improves the effect of crack resistance, and improves the tensile strength of hybrid-fiber-reinforced concrete materials.

2.2. Specimen Preparation

First, the sand, gravel, fly ash, and cement were batched and evenly mixed in a mixer for 60 s, and then the right proportion of water was added to the mixer for another 60 s. Second, blended fibers were evenly distributed into the solid mixture to prevent agglomeration which was mixed for 120 s. After mixing, the mixture was put into a cubic mold with side lengths of 100 mm × 100 mm × 100 mm, distributed evenly around the mold with a spatula to ensure compacting, and finally put on a vibrating table to seal all pores. The specimen was left for 24 h after loading into the mold, and then removed. The specimen was numbered and put into a saturated $Ca(OH)_2$ solution with a relative humidity of 95% and a temperature of 20 ± 2 °C to cure for 28 days. The specific steps are shown in Figure 2.
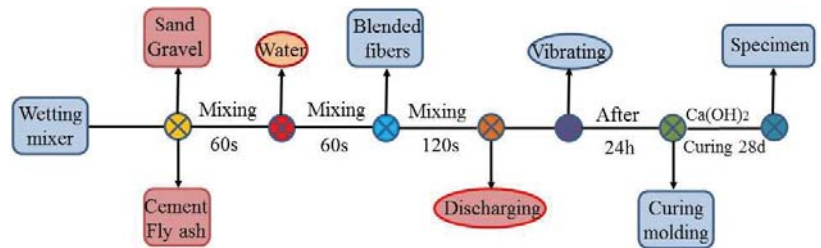
Figure 2. The mixing steps of concrete.

2.3. Sulfate Attack Test for Concrete

After curing for 28 days under standard conditions, the concrete test block was placed in a sodium sulfate solution at a concentration of 5% for long-term immersion. The liquid level was 10 mm above the surface of the test block. In order to ensure the stability of the pH of the solution, the solution is replaced once a month, and the concrete was completely soaked and eroded. The times of sulfate attack were 0 d, 30 d, 60 d, 90 d, 120 d, and 150 d, respectively. The whole test was carried out at 25 ± 2 °C.

2.4. Other Tests

2.4.1. Mass Change

When a specified erosion time was reached, concrete samples were taken from the solution and then dried in a constant temperature room at 22 °C until the mass was constant. At the same time, the sample surface was gently wiped with a towel to remove crumbs. The sample mass was then weighed and recorded using an electronic scale with an accuracy of 0.01 g. There were 3 parallel concrete samples in each group when weighing, and the results were averaged. Next, to calculate the rate of mass change Equation (1) was used [38]:

$$\varphi_i = (m_n - m_0)/m_0 \tag{1}$$

where φ_i, m_n, m_0 are the rate of mass change of the concrete specimen, the mass of the specimen after erosion time n, and the initial mass (g), respectively.

2.4.2. Ultrasonic Impulse Method

After the specified number of sulfate attack, each test piece was removed. An NA-M4 nonmetal ultrasonic detector (shown in Figure 3) was used to measure the ultrasound velocity in the 100-mm cube of concrete. The transducers that were used were 50 mm thick. The ultrasonic method was used to measure the longitudinal wave velocity passing through the concrete samples. The path length between the sensors was 100 mm, the length of the dimensions of a concrete sample. Five pairs of measurement points (shown in Figure 4) were used to measure the ultrasound wave velocity and the average was taken. To ensure proper coupling of the transducer to the surface being measured, Vaseline was evenly applied to the transducer probe. For the entire test process, the ultrasonic frequency was 50 kHz, the transmission voltage was set to 500 V, and the sampling period was 0.4 μs.
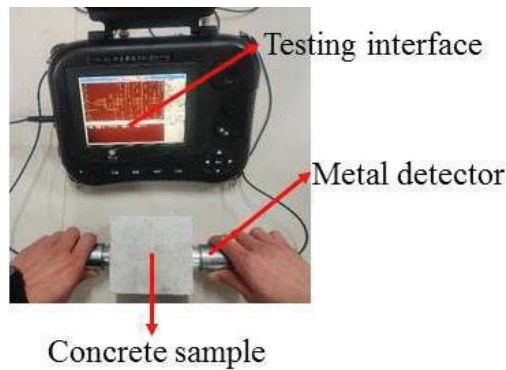
Figure 3. NA-M4 nonmetal ultrasonic detector.
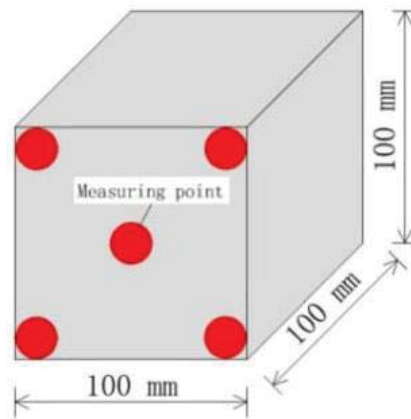
Figure 4. Measuring point positions of the detector.

The longitudinal wave velocity was calculated using Equations (2) and (3).

$$v = l/t \tag{2}$$

$$t = (t_1 + t_2 + t_3 + t_4 + t_5)/5 \tag{3}$$

where v is the longitudinal wave velocity (m/s); l is the path length (mm); t is the average ultrasound time (μs); t_1, t_2, t_3, t_4, and t_5 are the ultrasound time values of 5 pairs of measuring points, respectively.

According to the relationship between the dynamic elastic modulus of the material and the ultrasonic sound velocity, the relative dynamic elastic modulus $E_r(n)$ according to the GB/T 50082-2009 standard for both test methods, for long-term performance and durability of ordinary concrete [36], can be expressed as Equation (4).

$$E_r(n) = E_n/E_0 = v_n^2/v_0^2 \qquad (4)$$

where $E_r(n)$, E_n, E_0 are the relative dynamic elastic modulus of the concrete specimen, the dynamic elastic modulus after erosion time n, and the initial dynamic elastic modulus, respectively; v_n, v_0 are the longitudinal wave velocity (m/s) of the concrete specimen after erosion time n and the initial longitudinal wave velocity (m/s).

2.4.3. Mechanical Test

When each set of sulfate erosion times was reached, the concrete sample was taken out of the solution and dried at room temperature. According to the GB/T 50081-2019 standard for test methods for the physical and mechanical properties of concrete [39], a CSS-YAN3000 press, produced by the Changchun Testing Machine Institute (Changchun, China), was used for uniaxial compressive strength tests of concrete (shown in Figure 5a) as well as split tensile tests (shown in Figure 5b); the loading rates were 3 mm/min and 1 mm/min, respectively. There were 3 parallel concrete samples in each group during the strength tests, and the results are averaged. The loading mode is shown in Figure 5. The corrosion resistance of concrete was reflected by the corrosion coefficient indexes of the compressive and tensile strengths of concrete, before and after being eroded by the sulfate solution. The calculation formulas are shown below (Equations (5) and (6)).

$$k_c = f_{cn}/f_{c0} \qquad (5)$$

$$k_t = f_{tn}/f_{t0} \qquad (6)$$

where k_c, f_{cn}, f_{c0} are the corrosion resistance coefficient of the compressive strength of a concrete specimen, the compressive strength (MPa) after erosion time n, and the uncorroded compressive strength (MPa), respectively; k_t, f_{tn}, f_{t0} are the corrosion resistance coefficient of the splitting tensile strength of a concrete specimen, the split tensile strength (MPa) after erosion time n and the split tensile strength (MPa) without sulfate attack, respectively.
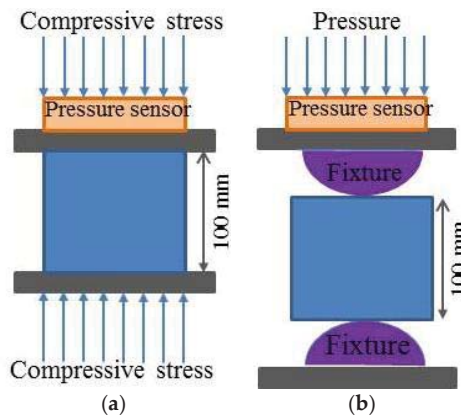
Figure 5. Static compression and splitting tensile tests of specimens. (**a**) Static compression test and (**b**) splitting tensile test.

2.4.4. Microanalysis

SEM and XRD tests were carried out using an S-3400N scanning electron microscope and a SMARTLAB9KW X-ray diffractometer from Yunnan Langlue Technology Co., Ltd. The microstructures, morphologies, and erosion products of minerals in the eroded samples were tested. The purpose was to analyze the erosion damage mechanism from a microscopic point of view. When a specified time of sulfate attack was reached, the concrete sample was taken out of the solution, left to air dry at room temperature, and broken into smaller parts for testing. After being placed in an oven and dried at 40 °C for 24 h, some samples were taken out, their surfaces were plated with gold on the surface, and then subjected to SEM tests. At the same time, the remaining test samples were crushed into powder and analyzed using XRD.

3. Experimental Results and Discussion

3.1. Characteristics of Apparent Degradation

The appearance and damage patterns of the concrete samples with different fly ash contents that were completely immersed in 5% sodium sulfate solution for different times are shown in Figure 6.
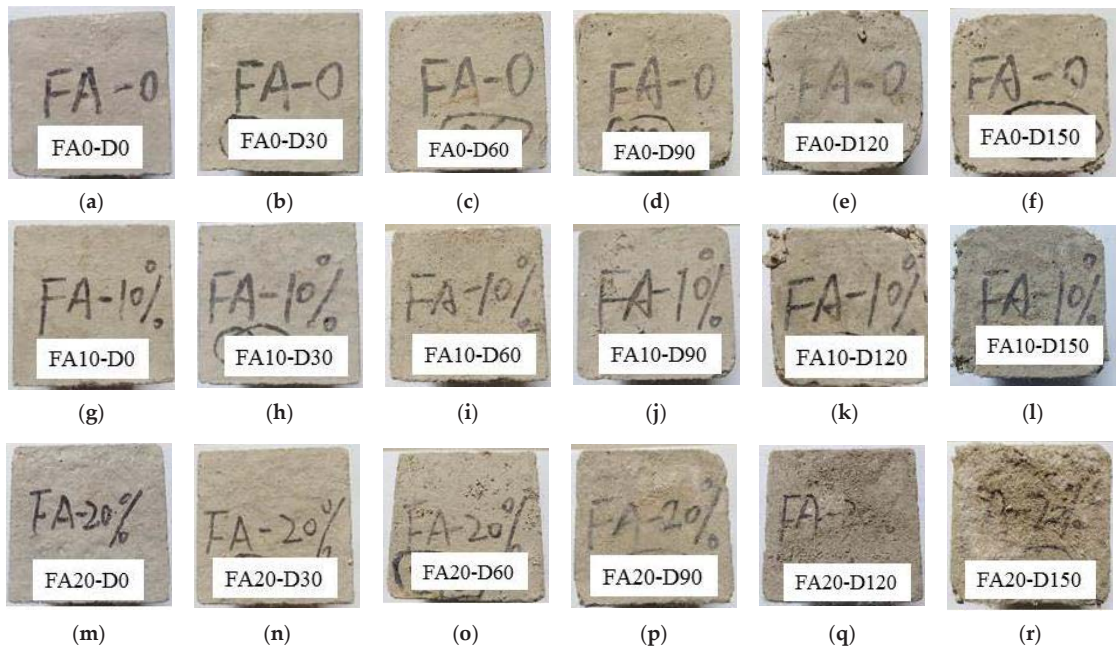
Figure 6. Deformation appearances of concrete samples subjected to sulfate attack. (**a**) FA0-D0; (**b**) FA0-D30; (**c**) FA0-D60; (**d**) FA0-D90; (**e**) FA0-D120; (**f**) FA0-D150; (**g**) FA10-D0; (**h**) FA10-D30; (**i**) FA10-D60; (**j**) FA10-D90; (**k**) FA10-D120; (**l**) FA10-D150; (**m**) FA20-D0; (**n**) FA20-D30; (**o**) FA20-D60; (**p**) FA20-D90; (**q**) FA20-D120; and (**r**) FA20-D150.

The surface of the concrete specimens changed during erosion in the sodium sulfate solution with the increase in erosion time. The surface of various concretes eroded by 0-d sulfate were relatively flat and smooth. After 30 d of sulfate attack, minor defects began to appear on various concrete surfaces. After 60 d of sulfate attack, the surfaces of various concrete samples went from being relatively smooth surfaces to rough surfaces, and the mortar gradually peeled off. After 120 d of sulfate attack, the corners of the concrete of the FA0 group and FA10 group fell off dropped slightly and the surface mortar peeled off, while the surface mortar of the concrete specimens from the FA20 group appeared to

have mostly peeled off. After 150 d of sulfate attack, cracks occurred at the corners and ends of the concrete in the FA0 and FA10 groups and the mortar peeled off; the corners of the concrete specimens in the FA20 group developed cracks. The more mortar completely peeled off of the surface of the entire concrete specimen, the more severe the deterioration. The reason for this is that the structure of a concrete test block was seriously damaged by sulfate erosion and the surface became brittle. A large amount of sulfate gathered in the concrete, and sulfate crystals precipitated after water evaporation [40,41].

3.2. Rate of Mass Change, Relative Dynamic Modulus of Elasticity and Corrosion Resistance Coefficient of Strength

According to Formulae (1) and (4)–(6), the relationships among the rate of mass change, relative dynamic elastic modulus, and corrosion resistance coefficient of strength of concrete specimens under the action of sulfate erosion and erosion time were obtained, as shown in Figure 7.
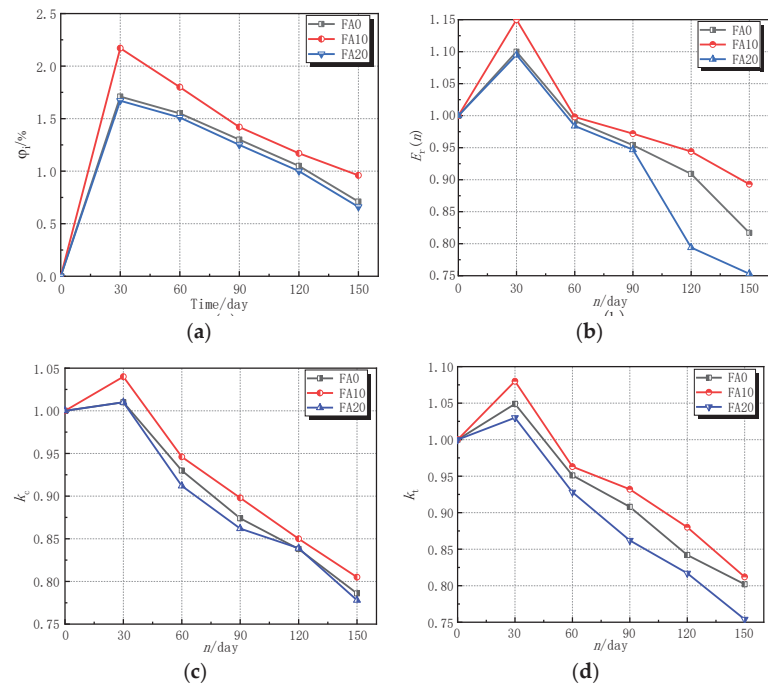
Figure 7. Testing results. (**a**) Variation of mass; (**b**) variation of $E_r(n)$; (**c**) variation of k_c; and (**d**) variation of k_t.

The change law of the rate of mass change, relative dynamic elastic modulus, and corrosion resistance coefficient of strength of different erosion times of sulfate attack are shown in Figure 7. It can be seen from Figure 7 that with an increase of erosion time, the rate of mass change, relative dynamic elastic modulus, and corrosion resistance coefficient of strength of concrete specimens with different fly ash contents all initially increase and then decrease. When the fly ash content was 10%, concrete had the best resistance to sulfate attack [42]. The reason for this is that the active substances in fly ash reacted with the $Ca(OH)_2$ in concrete, which reduced the content of $Ca(OH)_2$ in the concrete, reduced the production of gypsum and ettringite, and also alleviated the expansion of crystals. At the same time, because of the micro-aggregate effect of fly ash, fly ash particles filled the space between the unhydrated cement particles, which reduced the internal porosity of

concrete, improving the pore structure and compacting the internal structure of concrete; this improved the durability of concrete [43]. At 30 d of sulfate attack, the mass of concrete, relative dynamic elastic modulus, corrosion resistance coefficient of compressive strength, and corrosion resistance coefficient of the split tensile strength with 10% fly ash increased by 2.17%, 10%, 1.0%, and 3.0%, respectively, compared to uncorroded concrete. The mass of concrete, relative dynamic elastic modulus, and corrosion resistance coefficient of strength decreased gradually after 60 d of erosion. The mass of concrete, the relative dynamic elastic modulus, and corrosion resistant coefficient of strength increased with the extension of the first corrosion time after decreasing initially. The reason being that early sulfate, ettringite, gypsum, and other products are produced by the reaction of sodium sulfate solution with hydration products of concrete. At the same time, sulfate intrudes into the concrete specimen, which fills and compacts the pores and cracks within the concrete. The concrete specimen is more compacted than before the erosion and the mass of concrete, relative dynamic elastic modulus, and corrosion resistance coefficient of strength of the concrete are increased. With the continuation of sulfate erosion and the continuous accumulation and expansion of products, micropores and microcracks inside the concrete expand and extend. At the same time, the concrete surface mortar peels off, and the mass of concrete, relative dynamic elastic modulus, and corrosion resistance coefficient of strength gradually begin to decrease.

4. Establishment of Evolution Model of Sulfate Erosion Damage

4.1. Model of Erosion Damage Based on Each Evaluation Index

It can be seen from the sulfate attack test that the mechanical properties of concrete changed with the increase in erosion time, and the changes in the macrophysical properties can reflect the degree of internal changes in concrete materials. In order to quantitatively reflect the change law of the mechanical properties of concrete under the action of sulfate erosion, and comprehensively evaluate the state of concrete change, using damage mechanics, the corrosion resistance coefficient of compressive strength (k_c), the corrosion resistance coefficient of splitting tensile strength (k_t), and longitudinal wave velocity (v) were selected as damage variables. The damage caused by sulfate attack is shown by Equations (7)–(9).

$$D_1 = 1 - k_c \tag{7}$$

$$D_2 = 1 - k_t \tag{8}$$

$$D_3 = 1 - v_n/v_0 \tag{9}$$

where D_1, D_2, D_3 are the sulfate erosion damage variables and are the corrosion resistance coefficient of compressive strength, the corrosion resistance coefficient of splitting tensile strength, and the longitudinal wave velocity, respectively.

When the times of sulfate attack of concrete are 0 to 30 d, the sodium sulfate solution reacted with hydration products in concrete to produce ettringite, gypsum, and other products, which filled the initial holes in concrete, causing the concrete to be more compact. However, when the erosion time exceeded 30 d, that is, after 60 d of sulfate attack in this experiment, as the erosion time increased, the erosion intensified, and the damage evolution process of concrete changed with length of time. According to Equations (5)–(7), the amount of erosion damage under each evaluation index was calculated, as shown in Figure 8. The established equation in Figure 8 is only valid for concrete composed of polypropylene fiber, basalt fiber, and fly ash subjected to sulfate attack for 60–150 days.
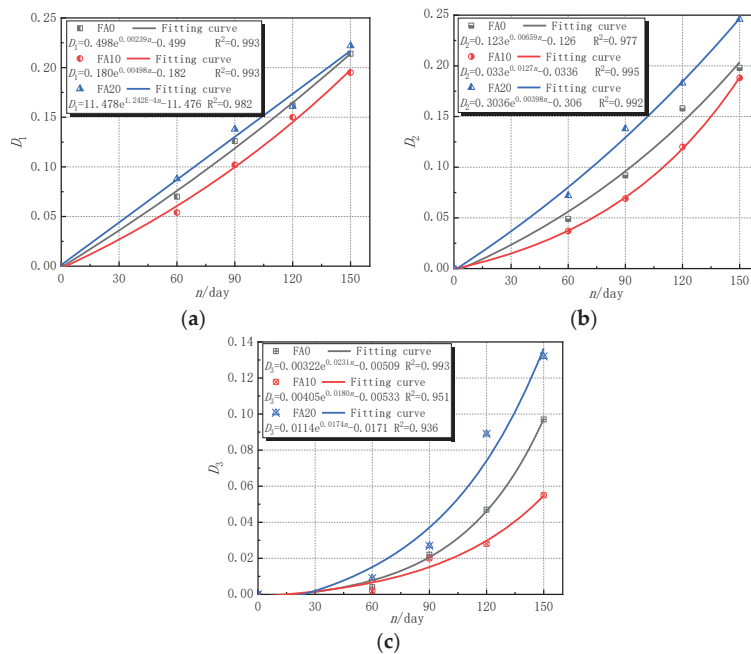
Figure 8. Relationship between damage variable of different evaluation indexes and erosion times. (**a**) Results of D_1; (**b**) results of D_2; and (**c**) results of D_3.

It can be seen from Figure 8 that, with the increase in the time of sulfate attacks, the erosion damage defined by the three indexes of the corrosion resistance coefficient of compressive strength, the corrosion resistance coefficient of splitting tensile strength, and the wave velocity increased continuously. The erosion damage and damage degradation rate of concrete specimens with 10% fly ash content were significantly lower than those without fly ash content. The reason for this was that an appropriate amount of fly ash can fully react with the internal components of concrete to generate a C-S-H gel and other substances, enhance the internal cohesion of concrete, reduce the porosity of concrete, improve its compactness, improve its ability to resist sulfuric acid erosion, and improve the ability to resist spallation [44]. However, when the fly ash content was 20%, the erosion damage and damage degradation rate of concrete specimens were higher than those without fly ash content. The reason for the erosion damage to ash was that an appropriate amount of fly ash can consume a certain amount of $Ca(OH)_2$, which reduces the content of substances that react with SO_4^{2-}, thereby reducing the generation of erosion products [35,37]. Under the same sulfate attack, the damage defined by the wave velocity index was less than the damage defined by the strength corrosion resistance coefficient index. The reason being that the damage of concrete from sulfate erosion is gradually weakened from the outside to the inside, and the longitudinal wave propagation velocity changed insignificantly, so the erosion damage defined by the wave velocity was relatively small [11,45].

At the same time, it can also be seen from Figure 8 that the correlation coefficients of the fitting formulas of the sulfate erosion damage variables are relatively high, which can better fit the damage evolution law of concrete specimens over time under the action of sulfate erosion. After data fitting, the erosion damage evolution of each performance index

showed a more obvious exponential function relationship, and the general fitting function formula is shown in Formula (10).

$$D_n = ae^{bn} + c \tag{10}$$

where n is the erosion time; a, b, and c are the coefficients in the fitting formula, as shown in Figure 8a–c.

The relationship between the sulfate erosion variables D_2 and D_1 is established, as shown in Equation (11).

$$D_2 = a_1 e^{b_1 D_1} + c_1 \tag{11}$$

where a_1, b_1, and c_1 are the coefficients in the fitting formula, as shown in Figure 9a.
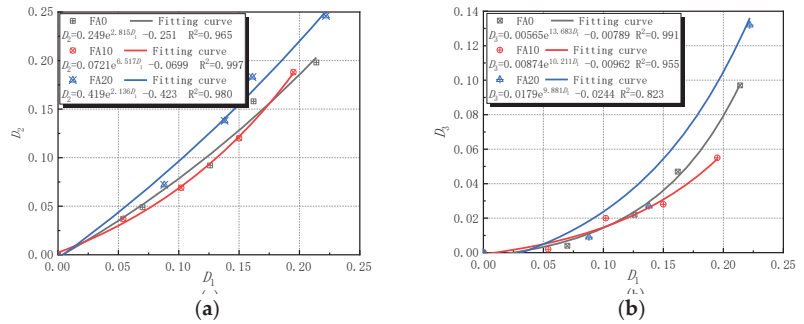
Figure 9. Relationship between different evaluation indexes of sulfate erosion damage. (**a**) Relationship between D_2 and D_1 and (**b**) relationship between D_3 and D_1.

There is also a good exponential relationship between damage amount D_1 of the corrosion resistance coefficient of compressive strength and ultrasonic velocity damage amount D_3 of the non-destructive testing, as shown in Figure 9b. Thus, the longitudinal wave velocity of the non-destructive testing can be used to predict the strength performance of and damage to the concrete structure.

4.2. Erosion Damage Model of Corrosion Resistance Coefficient of Compressive Strength Based on the Erosion Time and Fly Ash Content

To better study the influence of sulfate attack times and fly ash content on the corrosion coefficient of concrete's compressive force, a sulfate damage prediction model using both sulfate attack time factors and fly ash content was examined. The scatter diagram results of sulfate erosion times, the amount of fly ash, and the corrosion resistance coefficient of compressive strength of the concrete specimens are shown in Figure 10. The mathematical model of sulfate damage established based on regression analysis is shown in Formula (12). The correlation coefficient of data regression analysis was 0.919, the fitting coefficient was relatively high, and the fitting surface can be in good agreement with the experimental value. This shows that this model can be used to predict the quantitative relation between concrete erosion damage and the amount of sulfate attack and the amount of fly ash after sulfate attack, so as to evaluate the corrosion resistance of concrete under sulfate attack. The model is only established based on the experimental data; hence, the model is not universal. It can, however, provide some calculation methods and data references for actual projects.

$$k_c = 1.014 - 0.00112n + 0.00379\psi - 2.844 * 10^{-6}n^2 - 1.992 * 10^{-4}\psi^2 - 1.476 * 10^{-6}n\psi \ (R^2 = 0.919) \tag{12}$$
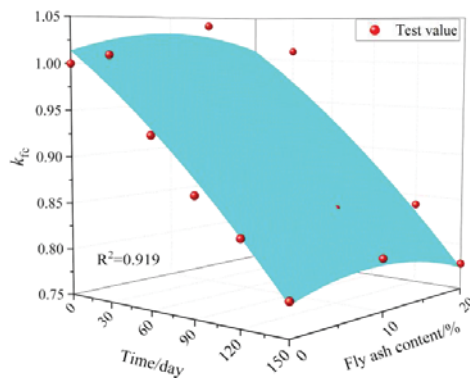
Figure 10. Relationship between fly ash content and erosion time n with k_c.

It can be seen from Table 4 that the error between the calculated values and the measured values of the regression formula is small. Among these, the minimum error without fly ash occurred at 120 d of sulfate erosion, with an error of 0.12%. The maximum error was −3.17% at 30 d of sulfate attack. When the fly ash content was 10%, the minimum error occurred at 120 d of sulfate attack, with an error of 0.59%. The maximum error was −4.23% at 30 d of sulfate attack. When the fly ash content was 20%, the minimum error occurred with a sulfate erosion lasting 30 d, with an error of 0.30%. The maximum error occurred at 150 d of sulfate attack with an error of 4.49%. For engineering practices and measurement errors, this is negligible; hence, the test value and the fitting value are basically the same.

Table 4. Comparison of fitting k_{c1} and measured k_c.

Time/Day	Fly Ash/%	Measured Data k_c	Fitting Data k_{c1}	Error $\frac{k_{c1}-k_c}{k_c}$/%
0	0	1	1.014	1.4
30	0	1.01	0.978	−3.17
60	0	0.93	0.937	0.75
90	0	0.874	0.890	1.83
120	0	0.838	0.839	0.12
150	0	0.786	0.782	−0.51
0	10	1	1.032	3.2
30	10	1.04	0.996	−4.23
60	10	0.946	0.954	0.85
90	10	0.898	0.907	1.0
120	10	0.85	0.855	0.59
150	10	0.805	0.798	−0.87
0	20	1	1.04	4.0
30	20	1.01	1.013	0.30
60	20	0.912	0.923	1.21
90	20	0.862	0.858	−0.46
120	20	0.839	0.871	3.81
150	20	0.778	0.813	4.49

5. Mechanism Analysis

When concrete is subjected to sulfate attack, the change in its performance is, not only reflected in the process of macroscopic properties, but also in the process of microstructure changes.

5.1. XRD Analysis

Figure 11 shows the XRD mineral analysis results of various concretes with different erosion time stages (erosion times of 0 d, 30 d, 150 d). The results show that, when various concretes are not attacked by sulfate, the main components are quartz (SiO$_2$), calcium

hydroxide (Ca(OH)$_2$), and calcium silicate hydrate (C-S-H). In addition to C-S-H, ettringite (Aft) could also be observed in groups FA0, FA10, and FA20 after being eroded for 30 days. At that time, ettringite production was limited, which filled the micro pores and cracks in the concrete specimens, optimizing the pore structure and making the concrete structure more compact. With the increase in erosion time, ettringite, and gypsum generation, when the erosion age reached 150 d, the content of Ca(OH)$_2$ in the pores of concrete decreased continuously, decreasing the alkalinity and causing the erosion degree to intensify. A large amount of gypsum and ettringite was generated in the concrete, which increased in volume and produced expansion stress. When expansion stress exceeds the tensile stress of internal concrete, microcracks will form and the internal pore structure of concrete will be destroyed [11,46]. At the same time, it can be concluded that the amount of gypsum produced in concrete with fly ash is obviously more than that without fly ash, and the amount of gypsum produced increases with the increase in fly ash content [43]. More ettringite and gypsum were produced in specimens with fly ash at 150 days [43]. The product of fly ash concrete under sulfate erosion was similar to the experimental conclusions of Liu et al. [43] and Zhao et al. [11].
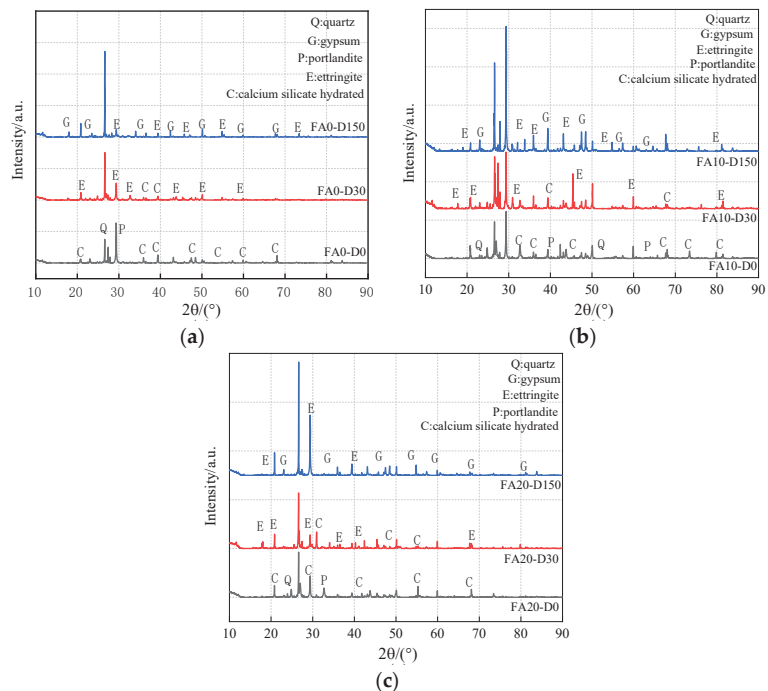
Figure 11. X-ray diffraction patterns of concrete subjected to sulfate attack. (**a**) FA0 concrete; (**b**) FA10 concrete; and (**c**) FA20 concrete.

5.2. SEM Analysis

The microstructures of concrete at different time under the action of sulfate attack were observed using SEM, as illustrated in Figures 12–14. It can be seen from Figure 12 that, when the FA0 group concrete was not corroded, there were numerous hydration products and C-S-H gel inside the concrete, with smaller pores and a denser internal structure (Figure 12a). After 90 d of erosion, a small amount of acicular calcium silicate, flaky gypsum, and cracks appeared inside the concrete, making the structure relatively loose (Figure 12b). After 150 d of sulfate attack, the erosion intensified, and more gypsum and ettringite formed in the concrete. During this process, volume expansion occurred, the expansion force increased, and the

concrete cracked and expanded gradually (Figure 12c) [11,41]. Figure 13 shows that there were a large number of hydration products and C-S-H gel in various concretes before sulfate attack, and the internal structures were relatively complete and compact (Figure 13a). After 90 d of sulfate attack, a few new cracks appeared in the concrete from the FA10 group (Figure 13b). After 150 d of sulfate attack, more erosion products were generated, cracks increased and expanded, and the structure was loose. It can also be seen from Figure 14 that a small number of cracks appeared in the internal structure of concrete without sulfate attack. After 90 d of sulfate attack, a large number of new microcracks were generated in the internal structure of the FA20 group concrete, and the cracks crossed each other and the structure was loose (Figure 14b). As the erosion time increased, the microcracks in the concrete specimens expanded and increased, and the internal structure became loose, making the degree of erosion worse. After 150 d of erosion, the internal microstructure of FA20 concrete specimens further loosened, the cracks were interconnected, the internal space increased, and the compactness decreased (Figure 14c).

As can be seen from Figure 15 that SO_4^{2-} entered the concrete and reacted with its internal hydration products to form acicular ettringite crystals and flake-like gypsum, which was continuously generated in the microcracks and pores, thus making the pores inside the concrete compact. However, with the continuous diffusion and reaction of SO_4^{2-}, the generated needle-shaped ettringite and flaky gypsum gradually increased and crossed each other to form a network, which caused the pores of the concrete to be subjected to expansion forces. When the expansion forces reached a certain level, the number of microcracks and pores in the concrete specimens increased and expanded continuously [11]. According to the micromorphology of concrete after sulfate erosion, Zhang et al. [47] and Li et al. [9] observed that sulfate ions diffused into concrete and reacted with its internal substances to generate acicular ettringite crystals. With an increase in sulfate erosion time, in concrete, the amount of generated ettringite crystals gradually increased which finally led to the formation of cracks. The obtained microstructures and conclusions in this article are consistent with the results of Zhang et al. [47] and Li et al. [9].

(a)

(b)

(c)
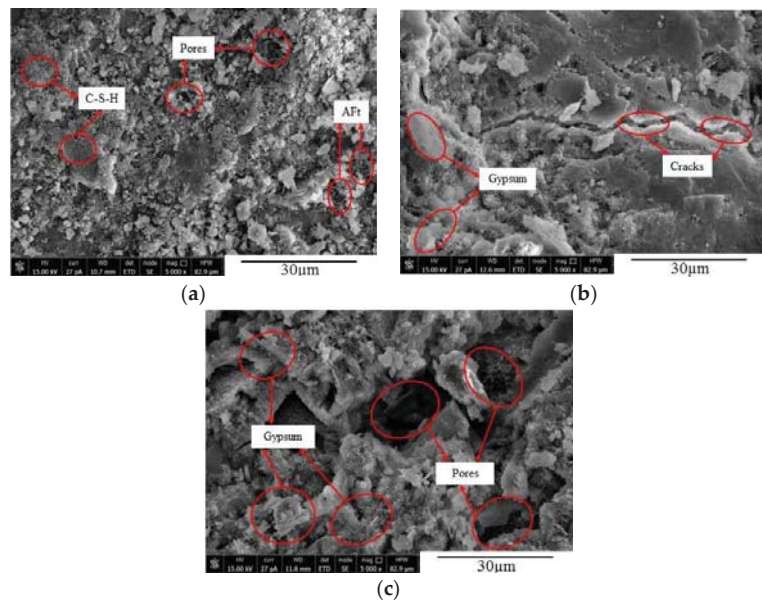
Figure 12. Microcrack expansion of FA0 concrete at different corrosion times. (**a**) FA0-D0; (**b**) FA0-D90; and (**c**) FA0-D150.
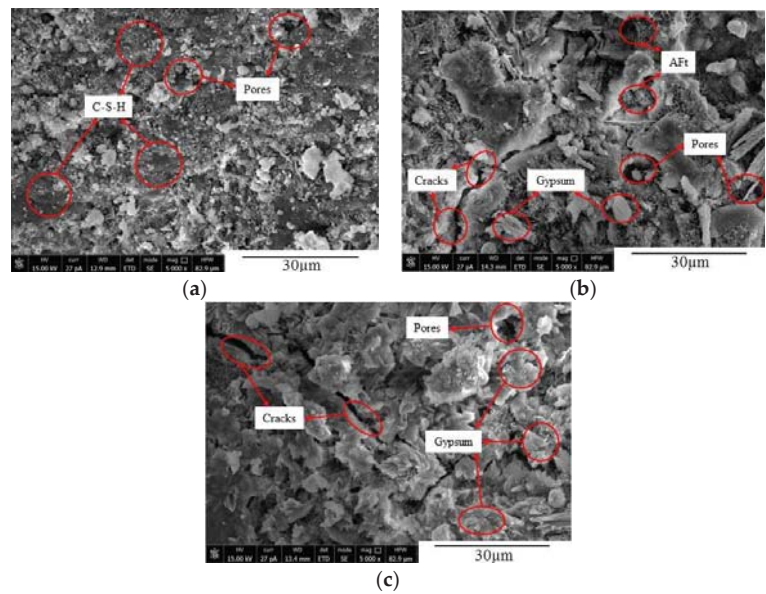
Figure 13. Microcrack expansion of FA10 concrete at different corrosion times. (**a**) FA10-D0; (**b**) FA10-D90; and (**c**) FA10-D150.
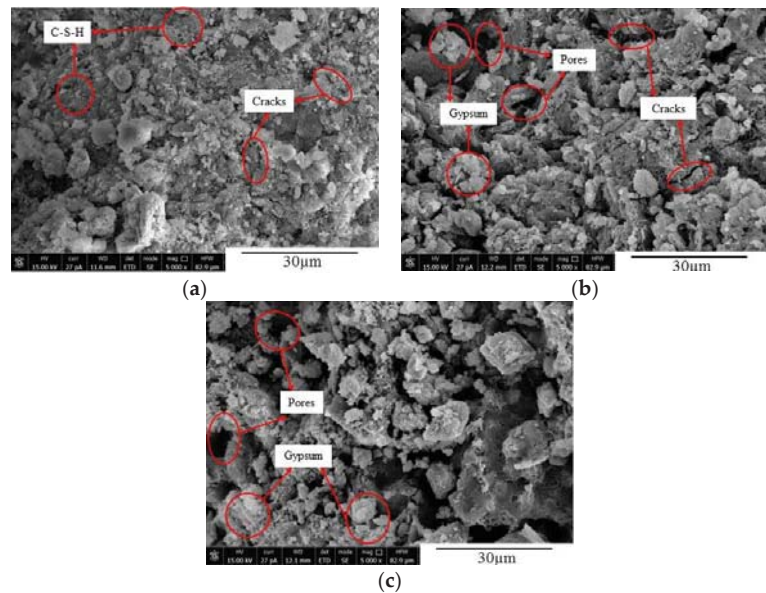
Figure 14. Microcrack expansion of FA20 concrete at different corrosion times. (**a**) FA20-D0; (**b**) FA20-D90; and (**c**) FA20-D150.
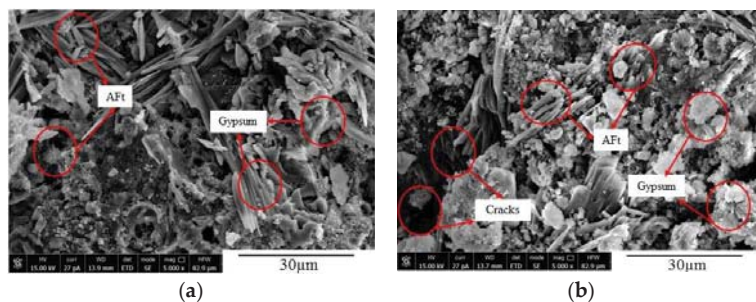
Figure 15. Growth and aggregation of products in FA10 concrete. (**a**) FA10-D90 and (**b**) FA10-D150.

6. Conclusions

According to the results of this paper, the following conclusions can be drawn:

(1) With an increase in sulfate attack time, the change law of concrete mass, relative dynamic elastic modulus, and strength corrosion resistance coefficient are similar, as they all initially increase and then decrease. Compared with other fly ash contents, concrete durability is better when fly ash content is 10%. The reason for this is that fly ash can fully react with the internal composition of concrete to produce C-S-H gel and other substances, enhance the internal cohesion of concrete, reduce the porosity of concrete, improve the density, and improve sulfuric acid erosion resistance.

(2) The corrosion resistance coefficient of compressive strength, the corrosion resistance coefficient of splitting tensile strength, and the change in wave velocity were taken as damage variables. Concrete sulfate erosion damage was comprehensively evaluated using various damage variables. The evolution equation of concrete sulfate erosion damage based on each damage variable was obtained by data regression, and the exponential function relationship between different damage variables was established.

(3) A composite sulfate erosion damage model between the corrosion resistance coefficient of compressive strength as a damage variable, erosion phase, and fly ash content was established. This model was used to predict concrete damage and erosion time after sulfate erosion. The model was used to predict the quantitative relationship between concrete damage, erosion time, and fly ash content after sulfate erosion to evaluate the resistance of concrete to sulfate attack in saline areas. The damage model is only suitable for concrete with a water–binder ratio of 0.6, fly ash dosage range of 0–20%, and mixed with 0.1% basalt fiber and 0.2% polypropylene fiber simultaneously.

(4) Sulfate attack changes the internal microstructure of concrete, and sulfate ions react with hydration products in concrete to produce expansive crystal ettringite and gypsum. With an increase in erosion products and expansion force, microcracks and damage appear inside the concrete, which is aggravated continuously, inducing the expansion and penetration of cracks and pores, and the deterioration of the microstructure reduces the macro performance of concrete.

Institutional Review Board Statement: Not applicable.

Informed Consent Statement: Not applicable.

Nomenclature

n	the erosion time
φ_i	the rate of mass change of the concrete specimen
m_n	the mass of the specimen after the erosion time n
m_0	the initial mass
v	the longitudinal wave velocity
l	the path length
t	the average ultrasound time
t_1	the ultrasonic time value of each pair of measuring points
t_2	the ultrasonic time value of each pair of measuring points
t_3	the ultrasonic time value of each pair of measuring points
t_4	the ultrasonic time value of each pair of measuring points
t_5	the ultrasonic time value of each pair of measuring points
$E_r(n)$	the relative dynamic elastic modulus
E_n	the dynamic elastic modulus after the erosion time n
E_0	the initial dynamic elastic modulus
v_n	the longitudinal wave velocity of the concrete specimen after the erosion time n
v_0	the initial longitudinal wave velocity
k_c	the corrosion resistance coefficient of compressive strength of the concrete specimen
f_{cn}	the compressive strength after the erosion time n
f_{c0}	the uncorroded compressive strength
k_t	the corrosion resistance coefficient of splitting tensile strength of the concrete specimen
f_{tn}	the split tensile strength after the erosion time n
f_{t0}	the split tensile strength without sulfate attack
D_1	the sulfate erosion damage variables corresponding to the corrosion resistance coefficient of compressive strength
D_2	the sulfate erosion damage variables corresponding to the corrosion resistance coefficient of splitting tensile strength
D_3	the sulfate erosion damage variables corresponding to the longitudinal wave velocity
ψ	fly ash content

References

1. Neville, A. The confused world of sulfate attack on concrete. *Cem. Concr. Res.* **2004**, *34*, 1275–1296. [CrossRef]
2. Wang, J.; Huang, B.; Mao, Z.; Wang, Y. Study on Adsorption Properties of Calcined Mg–Al Hydrotalcite for Sulfate Ion and Chloride Ion in Cement Paste. *Materials* **2021**, *14*, 994. [CrossRef]
3. Yildirim, K.; Sumer, M. Effects of sodium chloride and magnesium sulfate concentration on the durability of cement mortar with and without fly ash. *Compos. Part B Eng.* **2013**, *52*, 56–61. [CrossRef]
4. Zhao, X.; Wang, H.; Zhou, B.; Gao, H.; Lin, Y. Resistance of Soda Residue–Fly Ash Based Geopolymer Mortar to Acid and Sulfate Environments. *Materials* **2021**, *14*, 785. [CrossRef] [PubMed]
5. Zhou, R.; Cheng, H.; Li, M.; Zhang, L.; Hong, R. Energy Evolution Analysis and Brittleness Evaluation of High-Strength Concrete Considering the Whole Failure Process. *Crystals* **2020**, *10*, 1099. [CrossRef]
6. Santhanam, M.; Cohen, M.D.; Olek, J. Mechanism of sulfate attack: A fresh look. Part 2. Proposed mechanisms. *Cem. Concr. Res.* **2003**, *33*, 341–346. [CrossRef]
7. Zheng, J.M. *Research on the Sulfate Attack of Concrete under the Dry and Wet Cycles and Carbonation*; Yangzhou University: Yangzhou, China, 2009.
8. Yin, G.J.; Zuo, X.B.; Tang, Y.J.; Ayinde, O.; Wang, J.L. Numerical simulation on time-dependent mechanical behavior of concrete under coupled axial loading and sulfate attack. *Ocean Eng.* **2017**, *142*, 115–124. [CrossRef]
9. Li, T.; Zhu, P.T.; Zhang, B.; Ding, K.L.; Sun, Z.M. Experimental study on the corrosion reaction-diffusion process of concrete under sulfate attack. *Bull. Chin. Ceram. Soc.* **2020**, *39*, 50–55.

10. Wang, Z.S.; Xing, L.X.; Zhao, K.; Lu, J.L.; Tian, J.B. Study on corrosion resistance and mechanical property degradation of basalt fiber reinforced concrete under magnesium sulfate erosion environment. *Chin. J. Appl. Mech.* **2020**, *37*, 134–141.

11. Zhao, L.; Liu, J.H.; Zhou, W.J.; Ji, H.G. Damage evolution and mechanism of concrete erosion at sulfate environment in underground mine. *J. China Coal Soc.* **2016**, *41*, 1422–1428.

12. Yi, C.F.; Chen, Z.; Bindiganavile, V. A non-homogeneous model to predict the service life of concrete subjected to external sulphate attack. *Constr. Build. Mater.* **2019**, *212*, 254–265. [CrossRef]

13. Min, H.G.; Sui, L.L.; Xing, F.; Tian, H.; Zhou, Y.W. An effective transport model of sulfate attack in concrete. *Constr. Build. Mater* **2019**, *216*, 365–378. [CrossRef]

14. Wang, X.Z.; He, J.J.; Zou, H.F.; Zheng, S.W.; Mustapha, A. Experimental research on sulfate corrosion of basalt-polypropylene hybrid fiber concrete. *Concr. Cem. Prod.* **2014**, *5*, 50–54.

15. Marcalikova, Z.; Cajka, R.; Bilek, V.; Bujdos, D.; Sucharda, O. Determination of Mechanical Characteristics for Fiber-Reinforced Concrete with Straight and Hooked Fibers. *Crystals* **2020**, *10*, 545. [CrossRef]

16. Li, Y.; Zhang, S. Resistance to sulfate attack of hybrid fiber concrete under dry-wet cycles. *J. Northeast. Univ.* **2016**, *37*, 895–898.

17. He, R.; Tan, Y.W.; Li, D.; Sheng, Y.P. Sulfate corrosion resistance of hybrid fiber reinforced concrete. *Bull. Chin. Ceram. Soc.* **2017**, *36*, 1457–1463.

18. Zhao, X.M.; Liu, S.G.; Yan, C.W.; Zhang, J.; Wang, Y.Q. Experimental studies on sulfate-resistance property of PVA-FRCC in wet-dry cycles. *J. Inner Mong. Univ. Technol.* **2016**, *35*, 303–308.

19. Wang, J.B.; Niu, D.T.; Zhang, Y.L. Investigation of mechanical, permeability and durability performance of shotcrete with and without steel fiber. *China Civ. Eng. J.* **2016**, *49*, 96–109.

20. Li, Y.; Wang, R.J.; Yan, F.; He, X.X.; Sun, Y. Effects of fly ash on antifreeze and sulfate resistance of concrete. *J. Northwest A F Univ.* **2017**, *45*, 219–226.

21. Wang, J.B.; Niu, D.T.; He, H.; Song, Z.P. Durability deterioration and corrosion mechanism of shotcrete in salt lake environment. *China Civ. Eng. J.* **2019**, *52*, 67–80.

22. Najjar, M.F.; Nehdi, M.L.; Soliman, A.M.; Azabi, T.M. Damage mechanisms of two-stage concrete exposed to chemical and physical sulfate attack. *Constr. Build. Mater.* **2017**, *137*, 141–152. [CrossRef]

23. Liu, P.; Chen, Y.; Yu, Z.; Chen, L.K.; Zheng, Y.F.; Hariri-Ardebili, M.A. Research on sulfate attack mechanism of cement concrete based on chemical thermodynamics. *Adv. Mater. Sci. Eng.* **2020**, *2020*, 1–16. [CrossRef]

24. Liu, H.; Ren, X.; Liang, S.X.; Li, J. Physical Mechanism of Concrete Damage under Compression. *Materials* **2019**, *12*, 3295. [CrossRef]

25. Pan, Y.M.; Wang, B.X.; Wang, F.; Wang, Q. Macro-micro damage mechanism of concrete under the action of carbonate and sulfate. *Bull. Chin. Ceram. Soc.* **2019**, *38*, 3713–3718.

26. Chen, J.K.; Qian, C.; Song, H. A new chemo-mechanical model of damage in concrete under sulfate attack. *Constr. Build. Mater.* **2016**, *115*, 536–543. [CrossRef]

27. Bao, Y.L.; Chen, J.K. A New Model of Damage evolution in concrete under sulfate attack. *J. Ningbo Univ.* **2016**, *29*, 98–102.

28. An, X.Z.; Yi, C.; Zhao, C.B.; Zhang, J.T. Research on the damage behaviors of the recycled aggregate concrete in the sulfate environment. *J. Hebei Univ. Eng.* **2012**, *29*, 1–6.

29. Wu, K.; Kang, W.; Xu, L.L.; Sun, D.D.; Wang, F.Z.; Schutter, G.D. Damage evolution of blended cement concrete under sodium sulfate attack in relation to ITZ volume content. *Constr. Build. Mater.* **2018**, *190*, 452–465. [CrossRef]

30. Xiao, Q.H.; Cao, Z.Y.; Guan, X.; Li, Q.; Liu, X.L. Damage to recycled concrete with different aggregate substitution rates from the coupled action of freeze-thaw cycles and sulfate attack. *Constr. Build. Mater.* **2019**, *221*, 74–83. [CrossRef]

31. Yuan, M. *Study on the Durability of Non-Spontaneous Combustion Gangue Concrete under Freeze-Thaw and Sulfate Attack*; China University of Mining and Technology: Xuzhou, China, 2019.

32. *GB 175-2007, Standard for Common Portland Cement*; Standards Press of China: Beijing, China, 2007.

33. *GB 1596-2005, Standard for Fly Ash Used for Cement and Concrete*; Standards Press of China: Beijing, China, 2005.

34. *JGJ 55-2011, China Academy of Building Research. Specification for Mix Proportion Design of Ordinary Concrete*; China Architecture & Building Press: Beijing, China, 2011.

35. Zhu, J.H. *Study on Basic Mechanical Properties and Durability of Hybrid Fiber Fly Ash Reinforced Concrete*; Anhui University of Science and Technology: Huainan, China, 2019.

36. Wu, Q.Y.; Ma, Q.Y.; Wang, Y. Compression-tensile tests and meso-structure of basalt fiber-slag powder-fly ash concrete under freeze-thaw cycles. *Acta Mater. Compos. Sin.* **2021**, *38*, 953–965.

37. Cheng, M.; Zhang, J.S.; Duan, X.L.; Zhu, J.H. Experimental Study on Mechanical Properties of Concrete Reinforced With Hybrid Fiber and Fly Ash Subjected to Freeze-thaw Cycles. *Sci. Technol. Eng.* **2020**, *20*, 11288–11294.

38. *GB/T 50082-2009, China Academy of Building Research. Standard for the Test Methods of Long-Term Performance and Durability of Ordinary Concrete*; China Architecture & Building Press: Beijing, China, 2009.

39. *GB/T 50081-2019, Standard for Test Methods of Concrete Physical and Mechanical Properties*; China Architecture & Building Press: Beijing, China, 2019.

40. Zhang, Z.Y.; Jin, X.G.; Luo, W. Long-term behaviors of concrete under low-concentration sulfate attack subjected to natural variation of environmental climate conditions. *Cem. Concr. Res.* **2019**, *116*, 217–230. [CrossRef]

41. Xie, Y.P.; Jia, L.; Xue, B.Y.; Bai, W.T. Experimental study on corrosion resistance of high performance concrete in saline soil area of Southern Xinjiang. *Sci. Technol. Eng.* **2018**, *18*, 318–322.
42. Nie, Q.K.; Bai, B.; Li, H.W.; Han, S.; Wang, Y.H. Effects of the content of fly ash and slag on the resistance to sulfate of concrete. *Concrete* **2015**, *7*, 1–3.
43. Liu, Z.Q.; Li, X.N.; Hou, L.; Shi, B.L.; Deng, D.H. Accelerating effect of fly ash on damage of concrete partially immersed to sulfate environment. *J. Build. Mater.* **2017**, *20*, 439–443.
44. Yu, X.F.; Dong, Y.W.; Wang, G.; Lu, H.L. Durability of fly ash concrete against sulfate erosion in complex environment. *Concrete* **2020**, *6*, 58–60.
45. Sun, D.; Wu, K.; Shi, H.; Miramini, S.; Zhang, L.H. Deformation behaviour of concrete materials under the sulfate attack. *Constr. Build. Mater.* **2019**, *210*, 232–241. [CrossRef]
46. Liu, P.; Chen, Y.; Wang, W.L.; Yu, Z.W. Effect of physical and chemical sulfate attack on performance degradation of concrete under different conditions. *Chem. Phys. Lett.* **2020**, *745*, 137254. [CrossRef]
47. Zhang, M. Influence of Sulfate Corrosion on Microstructure Characteristics of Concrete. *Bull. Chin. Ceramic Soc.* **2020**, *39*, 1160–1165.

Experimental Study on the Axial Compression Performance of an Underwater Concrete Pier Strengthened by Self-Stressed Anti-Washout Concrete and Segments

Shaofeng Wu [1,2], Yijun Ge [1], Shaofei Jiang [3,*], Sheng Shen [3] and Heng Zhang [3]

[1] College of Civil Engineering, Yango University, Fuzhou 350015, China; shaofeng45@163.com (S.W.); geyijun@ygu.edu.cn (Y.G.)
[2] Fuzhou Communication Construction Group Co., Ltd., Fuzhou 350008, China
[3] College of Civil Engineering, Fuzhou University, Fuzhou 350108, China; s_shen@126.com (S.S.); zhangheng57@126.com (H.Z.)
[*] Correspondence: cejsf@fzu.edu.cn; Tel.: +86-591-22865379

Abstract: Compared with the conventional drainage strengthening techniques, the precast concrete segment assembly strengthening method (PCSAM) is regarded as a fast, more economical, and traffic-friendly underwater strengthening method for damaged bridge piers and piles, as the drainage procedure can be omitted. However, this method still has some disadvantages, such as strength loss of the filling material, debonding of the interface due to shrinkage of the filling material, poor connection effects, and poor durability of the segment sleeves. To solve these problems, the PCSAM is improved in this study by using self-stressed anti-washout concrete (SSAWC) as the filling material and by developing a lining concrete segment sleeve (LCSS) by referring to the design theory for shield lining segments. Six specimens are designed and prepared with consideration of the influential factors, such as the self-stress, thickness of the filled concrete, and concrete strength of the LCSS, then the monotonic axial compression test is carried out to investigate the improvements in the axial compression properties of the specimens. Accordingly, extended parametric analyses are performed based on the established numerical models. Finally, the calculation formula for the bearing capacity is proposed based on the analysis results. The results indicate that the SSAWC can provide initial confining compressive stress in the core region of the piers, in addition to increasing the bearing capacity and ductility of the specimens. The improved LCSS segment connection is more reliable and increases the strengthening efficiency. The influence of self-stress on the bearing capacity of the specimens is cubic and the influence of the filled concrete strength on the bearing capacity of the specimens is nonlinear. The calculation formula for predicting the bearing capacity of axially compressed columns possesses good applicability and can be used as a reference for practical engineering.

Keywords: self-stressed anti-washout concrete; segment assembly; undrained strengthening; axial compression test; mechanical properties

1. Introduction

Substructural components, such as piers and piles, are critical to the safety of bridge structures. Due to the low requirements of design codes decades ago, material degradation, and environmental erosion, the existing components generally suffer from delamination of the concrete covers, exposed ribs, and riverbed cutting. These defects are not easy to be detected because the substructure components are almost underwater throughout their life cycle, which limits the function of such bridges, even leading to collapse. Therefore, many conventional strengthening methods and techniques, such as the bonded steel plate method [1], enlarging section method [2], planting bar method [2], fiber-reinforced polymer (FRP) method [3,4], and prestressed strengthening technique [5], have been proposed and applied in practical engineering. Although these techniques have perfect design theories,

mature construction techniques, and good strengthening effects, they are time-consuming, expensive, and traffic-disrupting because of the necessary construction of cofferdams, which are used for drainage before strengthening works. Consequently, increasing attention has been paid to undrained strengthening technology recently.

A number of undrained strengthening techniques have been developed and applied to practical engineering in the past decade, such as the jacket strengthening method [6], FRP underwater strengthening method [7,8], and precast concrete segment assembly method (PCSAM) [9]. These methods are economical, fast, and traffic-friendly compared with conventional methods, but also have some fatal deficiencies. For instance, the jacket strengthening method can greatly improve the durability of components but piers cannot be wrapped in fiber sleeves in deep water, which leads to strengthening failure. For the FRP underwater strengthening method, although the underwater strengthening effect is good, the empty gap generally occurs in the interface between the FRP and components because of the ineliminable water. As a result, this method tends to fail when the piers are submerged in water for a long time after strengthening. Additionally, the diving operation involves high costs, safety risks, and slow progress in deep water and under certain water pressure and flow rates. On the contrary, the PCSAM first uses precast concrete segments to wrap the components, then the segments are connected into the sleeve using wire ropes, and finally the interspace between the sleeve and the components is filled with the filling material to achieve undrained strengthening. The PCSAM can be used to strengthen the components in deep water. This approach has many advantages, including the simple construction method, reliable construction quality, short construction period, and low cost. However, there are still some problems with the PCSAM, such as the large prestress loss and poor durability of the wire ropes, poor accuracy and connection performance of the sleeves, large strength loss of the filling material, and uncertain bonding properties between the filled concrete and sleeves. As a consequence, there is an urgent need to solve the problems existing in the PCSAM and to develop a new strengthening method that can better serve in the reinforcement of damaged components.

Based on the PCSAM, this paper proposes a new undrained strengthening method named the improved precast concrete segments assembly method (IPCSAM), which takes advantage of three theoretical reinforcement techniques, namely the increasing section method, outer sleeve method, and prestressing method. The IPCSAM proposed in this paper not only uses self-stressed anti-washout underwater concrete (SSAWC) as the filling material, but also improves the connection of the segment sleeve, which is referred to as the shield lining segment. The SSAWC, as the filled concrete, can not only cut down the strength loss of the underwater concrete [10–12], but can also increase the bonding strength between the filled concrete and the sleeves [13]. On the one hand, due to the additional appropriate expansion agent added to the SSAWC compared with the AWC, the concrete becomes denser and the self-stress makes the bond between the sleeve and the filled concrete stronger. On the other hand, the shield lining segments have high precision in prefabrication [14], good connection effects [15], and good durability [16]. The lining concrete segment sleeve (LCSS) is developed according to the characteristics and theory of shield lining segments under the consideration of existing problems, while the prefabrication precision, durability, and joint connection strength of the segment are improved.

The axial compression performance of the strengthened columns is so significant that numerous studies have investigated this topic. Fakharifar [17] found that the bearing capacity and ductility of columns strengthened with steel sleeves could be increased by 20%. Wang [18] used a CFRP sleeve to strengthen a column, the bearing capacity of which was greatly improved. In [9], the peak load and displacement of the column strengthened by the PCSAM were increased by 28% and 20%, respectively. Seible [19] proposed a design method for strengthening columns with FRP sleeves, while Tang and Wu and Sun [20] proposed a simplified moment–curvature calculation model for the cross-section of the column strengthened by the PCSAM.

This paper attempts to investigate the strengthening effect of the IPCSAM and the axial compression performance of the strengthened columns. Firstly, the implementation strategy for the IPCSAM is introduced. Then, 6 specimens are prepared by taking account of influential factors, such as self-stress, the thickness of filled concrete, and the concrete strength of the LCSS, while the mechanical properties of the specimens are also studied under axial compression loading. Next, the extended parameter analyses are carried out via numerical simulations. Finally, based on the experimental results and extended parameter analyses, the calculation method for the bearing capacity is established for the components strengthened with the IPCSAM.

2. IPCSAM

2.1. SSAWC Preparation

The use of self-stressed anti-washout underwater concrete (SSAWC) is one of the key strategies for implementing the IPCSAM, because the filling material connects the components and segment sleeves and directly affects the mechanical properties of the strengthened components. Wu and Jiang [10] developed the SSAWC and achieved good performance. The compressive strength ratio in water compared to air for the SSAWC increased from 0.8 to 0.92, indicating that the strength loss of the filling material was significantly reduced. The restrained expansion ratio at 14 days for SSAWC could reach 0.027–0.053%, while the self-stress generated by expansion would be beneficial to increasing the bond strength [13]. Meanwhile, the experiments carried out by García-Calvo [12] showed that the underwater environment was more beneficial to the self-stress development of the SSAWC for piers and columns.

According to the mix ratio of the SSAWC shown in Table 1 and proposed by Wu [10], performance verification tests for the C30 SSAWC were carried out. The 42.5 *N* normal Portland cement from Fujian Cement Inc. (Fujian, China), a fiber-type anti-dispersion agent named SBTNDA, and the HME-III low-alkali concrete expansive agent produced by the Jiangsu Soubotte Company (Nanjing, China) were chosen. A polycarboxylate superplasticizer was employed in these tests based on experimental results from Khayat [21] and Oliveira [22]. Here, 5~20 mm of continuous-grade gravel was used. The density, crushed index, needle content, and sediment content of the gravel were 2.65 t/m^3, 7.3%, 2%, and 0.2%, respectively. Good Fujian River sand was used, the fineness modulus, sediment content, and density of which were 2.89, 0.6%, and 2.64 t/m^3, respectively. The test results showed that the C30 SSAWC (Table 2) had a higher elastic modulus and underwater strength compared with the AWC and the expansibility of the SSAWC could be easily observed.

Table 1. The mix ratio of the C30 SSAWC (kg/m^3).

Cement	Expansive Agent	Anti-Dispersion Agent	Sand	Stone	Water-Reducing Agent	Water
433.3	48.14	12.03	692	995	4.81	207

Table 2. Properties of the C30 SSAWC.

Slump (mm)	Slump Flow (mm)	Restrained Expansion Rate at 14 Days (%)	pH Value	Elastic Modulus (GPa)	Underwater Strength at 28 Days (MPa)	Strength at 28 Days (MPa)	Strength Ratio
240	435	0.040	10.9	30.2	32.4	38.8	0.835

2.2. LCSS Preparation

The use of a lining concrete segment sleeve (LCSS) is another key strategy for implementing the IPCSAM, as the sleeve can be used as formwork in the construction process and as a part of the strengthened piers to bear partial loads, in addition to being a limitation that makes the SSAWC produce self-stress. Huang [14] studied the precast technology used for the shield lining segments and found that the prefabrication precision could be

improved by controlling the working procedures to achieve assembly error within 2 mm for the inner ring segments. In the experiments conducted by Liu [15], the failure of the shield tunnel linings was caused by failure of the joints, while the bearing capacity of the joints was improved using strengthening bolts. The study by Meng [16] showed that the durability of the shield lining segment could be improved by adding steel or propylene fibers or steel bars into the concrete. Therefore, the LCSS was designed and prepared with the characteristics and theory of shield lining segments.

The LCSS design was divided into structural and connection designs. The structural design determined the preassembly form and segment dimensions. The LCSS was divided into two parts, namely the standard segments and adjusting segment; the sleeve ring consisted of three standard segments and one adjusting segment, as well as a setting rabbet between the segments. The dimensions of the segment were determined based on the self-stress, load, thickness of the concrete cover, diameter of the PVC pipe, and the construction technique. The structure of the LCSS is presented in Figure 1, and the segment dimensions of the specimens are designed as follows: inner diameter of 165 mm, outer diameter of 205 mm, thickness of 40 mm, height of 170 mm. The connection for the LCSS was designed in the same way as the connection for the shield lining segments. Specifically, for circumferential connection of the segments, the holes for fixing bolts were reserved through the pre-embedded PVC pipes and then the curved bolts and triangular pad were utilized to connect the segments. Regarding the longitudinal connection of the segment, the hole was also reserved first, then the long bolts and nuts were used to connect the segments. In this test, the diameter of the PVC pipe was 16 mm and the diameters of the circumferential and longitudinal bolts were 6 mm and 8 mm, respectively. Three circumferential connections were arranged along the longitudinal equal spacing of each segment ring, and 10 longitudinal connections were arranged at equal intervals along the circumference; the connections of the segments are shown in Figure 1. The prefabricated mold of the LCSS was designed and is shown in Figure 2. The size of the segments and location of the PVC pipe complied with the requirements found in [14].
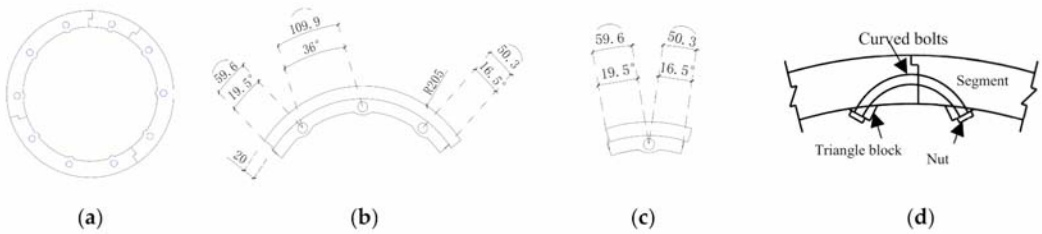
Figure 1. Structure and connection of the LCSS. (**a**) Segment ring; (**b**) Standard block; (**c**) Adjusting block; (**d**) Circumferential connection.
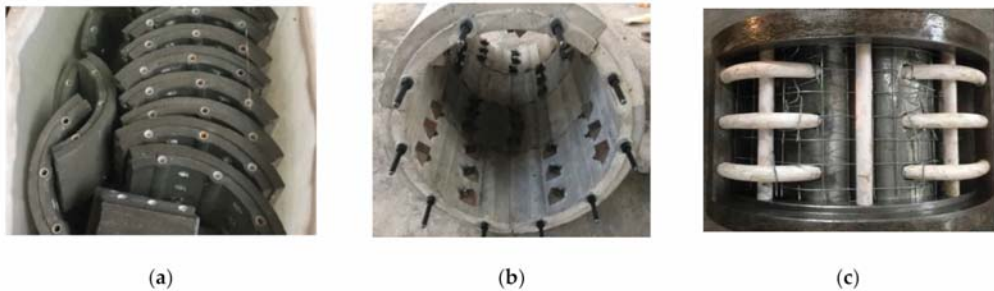
Figure 2. The LCSS and mold. (**a**) Segments; (**b**) Sleeve; (**c**) Mold of segments.

3. Experimental Procedures

3.1. Experimental Design

The objective of this test was to investigate the influence of the SSAWC and LCSS on the performance of the specimens, as well as the impacts of parameters such as the segment concrete strength and filled concrete thickness on the bearing capacity of the strengthened specimens. Therefore, the experimental design was carried out according to the test objectives.

3.1.1. Specimens Design

(1) Dimensions of the specimens: The strengthened specimens were composed of three parts: the lining concrete segment sleeve (LCSS), the unreinforced column, and the filled concrete (SSAWC). Referring to the specimen designs found in relevant studies [17,23], 1/5 model proportions were adopted to avoid difficulties in preparation and deviation of the test results due to the small size. The dimensions of the unreinforced columns were as follows: diameters of 250 mm and 200 mm, height of 750 mm.

(2) Representativeness and number of test specimens: The control variables of the test specimens selected in this paper were the diameter of the unreinforced column, axial compressive strength, thickness, self-stress, and axial compressive strength of the LCSS. In order to investigate the influence of the above variables and ensure the specimens were representative, the initial values of the control variables were determined by the code in [24], involving existing pier-strengthening technologies and the design parameters of ordinary piers. The diameter of the unreinforced column was 250 mm as a result of the 1/5 scale, the axial compressive strength of the filled concrete was 21.7 MPa, the thickness was 40 mm as a result of the 1/5 scale, and the axial compressive strength of the segment concrete was 20.9 MPa. Because it took a lot of time to prepare the reinforced test specimens, time and funds were limited when three specimens were prepared under the same parameter conditions. For the sake of speeding up the test process, the following strategy was adopted. According to reference [9], it was known that the errors for three specimens with the same parameters are generally within 10%. Therefore, only one specimen with the same parameters was prepared in this paper. In order to ensure the rationality and accuracy of the test data, the finite element model with the same parameters was established and the parametric analysis was performed. Based on the above principles, as well as the premise of each variable with a control group, a total of 6 test specimens were prepared in this paper, as shown in Table 3.

(3) Specimen grouping: The specimens were divided into three groups according to the objectives of this test. Table 3 shows the details. (1) The unreinforced group (UG) had two specimens with diameters of 200 mm and 250 mm respectively, which were used for comparison with the corresponding strengthened specimens to verify the strengthening effect. (2) The ordinary reinforced group (ORG) was a specimen strengthened with AWC, which was used for comparison with specimens in the other group to verify the influence of the SSAWC and the LCSS on the strengthening effect. (3) The self-stressed reinforced group (SRG) was composed of specimens filled with SSAWC, among which the concrete strength of the LCSS of specimen S1-SS was reduced to verify the influence of the strength of the sleeve concrete on the bearing capacity of the strengthened specimens, while the thickness of the filled concrete of specimen S2-S was increased to verify the effect of the thickness of the filled concrete on the bearing capacity of the strengthened specimens.

Table 3. Parameters and grouping of specimens.

Specimen	Group	D × H *1 (mm)	ACSC *2 of Unreinforced Specimen (MPa)	Filled Concrete			ACSC of LCSS (MPa)
				ACSC (MPa)	Thickness (mm)	Self-Stress (MPa)	
P1	UG	250 × 750	20.1	21.7	0	0	20.9
P2		200 × 750	20.1	21.7	0	0	20.9
S1-A	ORG	250 × 750	20.1	19.8	40	0	20.9
S1-S		250 × 750	20.1	21.7	40	1	20.9
S1-SS	SRG	250 × 750	20.1	21.7	40	0.8	13.6
S2-S		200 × 750	20.1	21.7	65	0.6	20.9

Note: *1: D × H = the diameter and height of the unreinforced specimen. *2: ACSC = axial compressive strength of concrete.

3.1.2. Meter Placement Design

The positions of displacement meters and strain gauges are given in Figure 3. A YHD-50 displacement meter was fixed at the top of the specimen to record the deformation of the sand mat, which was used to eliminate the impact of the uneven loading plate. Four YHD-50 displacement meters were fixed on the actuator of the loading device at equal angle intervals to record the longitudinal displacement of the specimen. At the half height of the specimen, four 100 mm concrete strain gauges were fixed on the outer surface of the sleeve along the circumferential and longitudinal directions to record the circumferential and longitudinal strains of the sleeve, respectively. At the same time, at the half height of the self-stressed reinforced specimens, four 80 mm concrete strain gauges were fixed on the inner surface of the sleeve along the circumferential and longitudinal directions to record the circumferential and longitudinal strains of the filled concrete, respectively. Both the displacement and strain time histories were recorded using a TDS-530 static data collector with an acquisition frequency of 0.5 Hz, as shown in Figure 4.
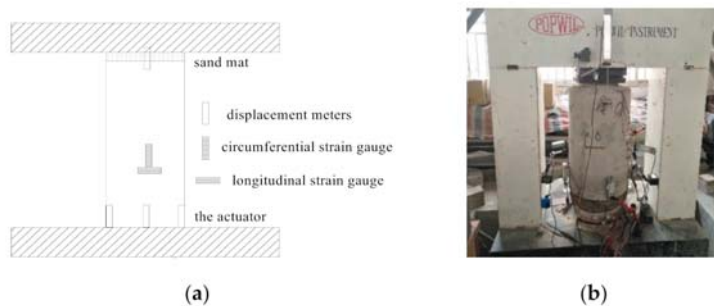
Figure 3. The placement of displacement meters and strain gages. (a) Design positions of meters; (b) Actual positions of meters.

Figure 4. TDS-530 static data collector.

3.1.3. Loading Design

Based on the estimation of the bearing capacity of the specimens, a 300 t pressure loading instrument was used. Firstly, the pressure was loaded at 15 kN/min. Then, when the load exceeded 50% of the bearing capacity, the displacement was loaded at 0.06 mm/min until the failure of the specimen.

3.2. Specimens Preparation

3.2.1. Materials and Properties

(1)   Concrete: The materials, mix ratio, and properties of the SSAWC are shown in Section 2.1. The materials and mix ratio of the AWC were the same as those of the SSAWC, although the expansive agent was replaced by cement equivalently. The common concrete was composed of the same raw material as the SSAWC, while the two strength grades of segment concrete were C30 and C20, respectively, and the concrete strength grade of the unreinforced column was C30. The mix ratio of the AWC and common concrete are shown in Table 4 and the performance is shown in Table 5. The axial compressive strength of the concrete was taken as the concrete strength. For different production times, the concrete strength levels of the segments and unreinforced columns were slightly different.

(2)   Steel: In order to improve the durability of the segment [16], the equivalent substitution method was adopted to replace the structural reinforcement with welded steel wire mesh with a diameter of 1.2 mm as the structural reinforcement for the segment. The properties of the welded wire mesh, circumferential bolts, and longitudinal bolts are shown in Table 5.

Table 4. The mix ratio of the concrete (kg/m^3).

Strength Grade	Cement	Expansive Agent	Anti-Dispersion Agent	Sand	Stone	Water-Reducing Agent	Water
C30 (AWC)	481.4	0	12.03	692	995	4.81	207
C30	405	0	0	661	1174	4.05	175
C20	321	0	0	758	1138	0	183

Table 5. Performance of the materials.

Material	Elastic Modulus of Concrete (GPa)	ACSC (MPa)	Axial Tensile/Yield Strength of Steel (MPa)	Poisson's Ration	Area (mm²)
C30 concrete in column	30.0	20.1	2.01	0.2	
C30 AWC	30.7	21.2	2.10	0.2	
C30 concrete in segments	30.3	20.9	2.06	0.2	
C20 concrete in segments	26.1	13.6	1.58	0.2	
Welded wire mesh	180		210	0.3	1.13
Circumferential/longitudinal bolts	206		640	0.3	28.26/50.24

3.2.2. Production Process

(1)   Unreinforced specimens: As shown in Figure 5, unreinforced columns were made with a steel mold.

(2)   Strengthened specimens: A bucket with a diameter of 600 mm and a height of 950 mm filled with water was used to simulate the underwater environment. The production procedure is shown in Figure 6 and was as follows: (**a**) prepare the LCSS and unreinforced column; (**b**) place the reinforcement mesh between the LCSS and column; (**c**) fill water into the bucket, pour the SSAWC and cure the concrete. It is noted that the concrete surface of the unreinforced columns should be chiseled manually before pouring concrete to increase the bond strength. In order to simulate the actual working state of the strengthened specimens and decrease the test errors

caused by unbalanced loading, the areas with lengths measuring 35 mm were reserved without strengthening at the top and bottom of the specimens.

Figure 5. Unreinforced specimens. (**a**) Specimens pouring; (**b**) Completed specimen.
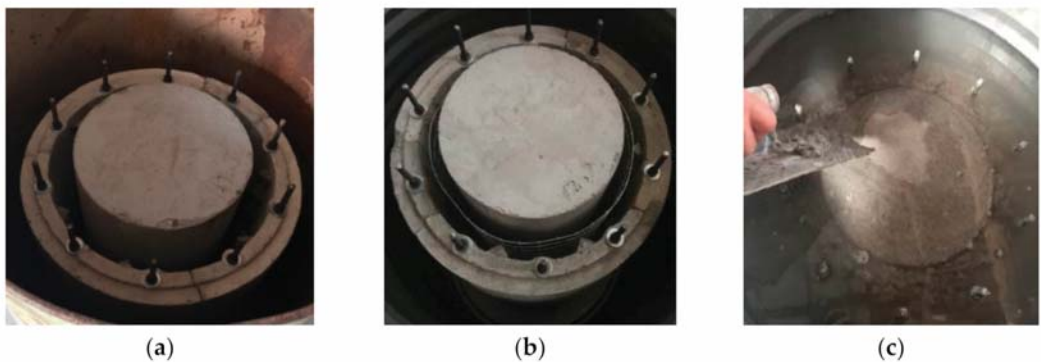
Figure 6. The production process for the strengthened specimens. (**a**) Preparing columns and LCSS; (**b**) Laying welded wire fabric; (**c**) Pouring SSAWC.

3.3. Failure Process and Modes

(1)   Unreinforced specimens: As shown in Figure 7, the failure processes for P1 and P2 were similar. For specimen P1, the first crack in the concrete appeared when the load was close to 800 kN, which expanded with the loading. When the load was close to 1100 kN, some of the cracks were connected together to form a long and oblique crack. As a result, the bearing capacity of P1 reached the peak value. Then, the load dropped rapidly and specimen P1 reached failure. For specimen P2, the first crack in the concrete appeared when the load was close to 500 kN, which turned into a penetrating crack when the load was close to 800 kN. As a result, the bearing capacity of specimen P2 reached the peak.

(2)   Ordinary strengthened specimen: Figure 8 shows the failure of specimen S1-A. Under the load of 1760 kN, the first concrete crack appeared at the interface between the filled concrete and the column. Then, with the increase in the load, the concrete crack gradually developed towards the segment sleeve and crisp sound could be heard, which was judged to be the fracture of the welded steel wire mesh. When the load was close to 2147 kN, several segments fractured and the bearing capacity of S1-A reached its peak, then the bearing capacity dropped until the failure of S1-A. The cracks were concentrated in the concrete cover of the longitudinal bolt, as well as

the joint of the LCSS and the interface between the filled concrete and the column. It should be noted that all bolts remained unbroken.

(3) Self-stressed strengthened specimens: The failure process and modes of the three strengthened specimens were similar, as shown in Figure 9. When the load was close to 2000 kN, the first crack appeared in specimen S1-S, then the crack developed with the increases in load, making a cracking sound in the process. When the load reached 2600 kN, several segments broke and the bearing capacity of specimen S1-S reached the peak and stabilized for a period of time. Then, the bearing capacity dropped and the cracks appeared at the interface between the filled concrete and the column when the bearing capacity dropped to 2250 kN. Finally, as the load decreased continuously, multiple cracks penetrated and the specimen failed. When specimen S1-SS was loaded to 1730 kN, cracks of concrete appeared in the segment concrete. When the load was close to 1850 kN, interface cracks appeared and developed toward the segments. When the load was close to 2150 kN, the segments at the top of the specimen almost failed and the bearing capacity reached the peak, then bearing capacity continued to decrease with long penetrating cracks appearing in many places until the specimen failed. When specimen S2-S was loaded to 1500 kN, concrete cracks appeared in the segment. When it was loaded to 1920 kN, fractures occurred in the segment due to the penetration of the cracks and the bearing capacity reaching the peak. Then, the bearing capacity decreased with the appearance of long penetrating cracks and the specimen finally failed. In this group, the cracks were concentrated on the concrete cover of the longitudinal bolt and the segment joints and none of the bolts were broken. Through testing and calculation, the self-stress values of the reinforced specimens could be obtained, as shown in Table 6.
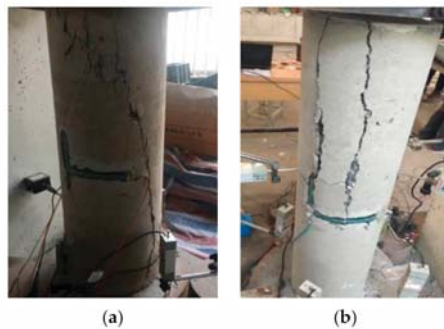
Figure 7. Failure of the unreinforced specimens. (**a**) P1 axial compression failure; (**b**) P2 axial compression failure.
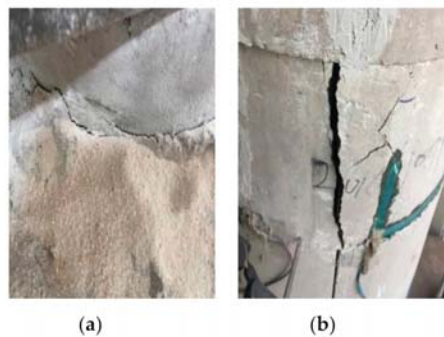
Figure 8. Failure of ordinary strengthened specimen. (**a**) Interface cracks; (**b**) LCSS fractures.
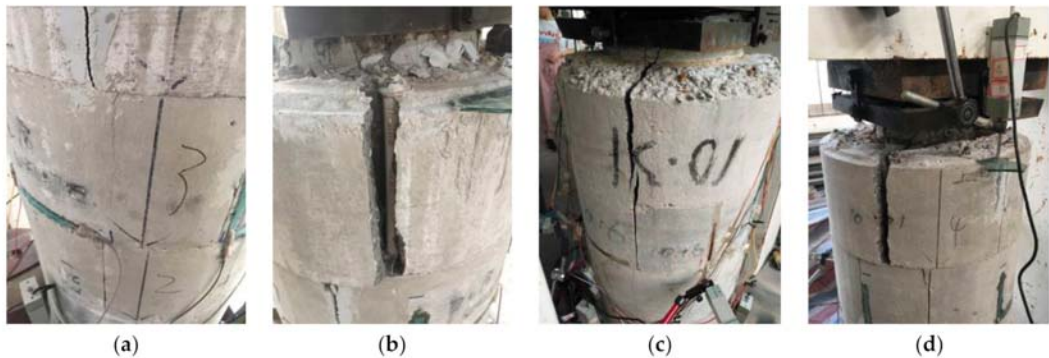
Figure 9. Failure diagram of self-stressed strengthened specimens. (**a**) Cracks on LCSS of specimen S1-S; (**b**) Fractures on LCSS of specimen S1-S; (**c**) Fractures on LCSS of specimen S1-SS; (**d**) Fractures on LCSS of specimen S2-S.

Table 6. Results of test.

Specimen	Circumferential Strain (με)	Longitudinal Strain (με)	Circumferential Stress (MPa)	Longitudinal Stress (MPa)
S1-S	14	62	0.20	0.99
S1-SS	11	52	0.16	0.83
S2-S	11	39	0.14	0.63

3.4. Load–Displacement Curves

Figure 10 shows the load–displacement curves of specimens. The curves of all the specimens consisted of three stages: elasticity, elastoplasticity, and failure. In these curves, the load–displacement relationship of the unreinforced column was consistent with the axial compression test of the plain concrete column [25]; that is, from the beginning to 80% of the peak load was the elastic stage, then the crack occurred at the beginning of the elastoplastic stage and the slope of the curve gradually decreased until the bearing capacity reached the peak, and finally the bearing capacity decreased rapidly until failure. It should be noted that the failure characteristic for specimen P1 was brittle failure. For the strengthened specimens, the load–displacement curves were similar. From the beginning to 80% of the peak load was the elastic stage. After this, the stiffness of the specimens gradually decreased with the development of the crack and the bearing capacity reached the peak when several segments broke. This process was referred to as the elastoplastic stage. Finally, the failure stage was reached. The bearing capacity of the specimen decreased until it failed and the descending speed was slower than that of the unreinforced column, showing the ductile failure characteristics of the strengthened specimens. The slopes of the load–displacement curves for the strengthened specimens were larger than those of the corresponding unreinforced columns, indicating that the stiffness increased after strengthening. In the same way, the slopes of the curves for the self-stressed strengthened specimens were larger than that of the ordinary strengthened specimen, indicating that self-stress enhances the stiffness of the strengthened specimens.
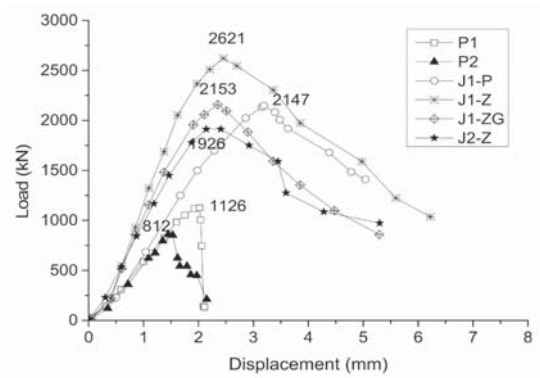
Figure 10. Load–displacement curves of the specimens.

3.5. Load–Strain Curves

Figure 11 shows the load–strain curves of the specimens. For unreinforced columns, only the data before the peak load were analyzed, because the concrete strain was unstable and inaccurate after the peak load. Before the loads of P1 and P2 reached their peaks, the longitudinal and circumferential strains increased linearly. When it was close to the peak load, the longitudinal strain curve showed a downward bending trend with faster strain growth, which was similar to the axial compression in concrete column [9,25]. For the strengthened specimens, the load–strain curve was similar, whereby the longitudinal strains generally increased linearly and the downward bending tends appeared when it was close to the peak. The ultimate strains were much larger than for the unreinforced columns, which was in agreement with the conclusion found in [9,20]. The circumferential strains were small before the peak load and the strain increased obviously when the load approached the peak. This was due to the segments limiting the circumferential deformation of the specimens before the peak load, while the circumferential strains increased significantly after the failure of the segments.
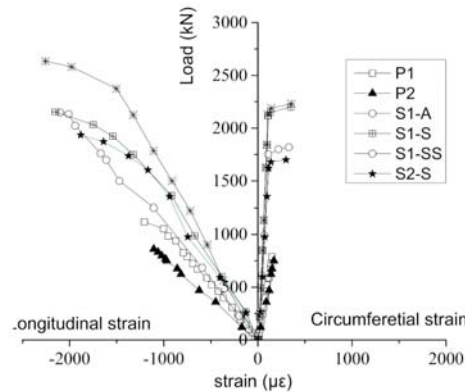
Figure 11. Load–strain curves of the specimens.

3.6. Results and Discussion

Table 7 indicates the axial compression test data for the specimens. The results of the test were reasonable and were consistent with the related studies [9–12,20,25]. Hence, the correctness of the axial compression test on the specimens was verified. According to the objective of this test, the test results were compared to verify the reinforcement effect

of the IPCSAM and to analyze the impacts of the reinforcement parameters on the axial compression performance of the strengthened specimens.

Table 7. Results of the axial compression test.

Specimen	Peak Load (kN)	Peak Displacement (mm)	Peak Strain	Peak Load Increased Ratio	Peak Strain Increased Ratio
P1	1126	1.97	0.0026	-	-
P2	812	1.45	0.0016		
S1-A	2147	3.15	0.0042	91%	58%
S1-S	2621	2.63	0.0035	132%	32%
S1-SS	2153	2.48	0.0033	73%	27%
S2-S	1926	2.33	0.0031	137%	61%

(1) The strengthening effect of the IPCSAM: The comparison of the test results showed that the peak loads of strengthened specimens S1-A, S1-S, S1-SS, and S2-S2 increased by 91%, 132%, 73%, and 137%, respectively, while the peak strains increased by 58%, 32%, 27%, and 61%, respectively. This meant the bearing capacity and ductility of the strengthened specimens had been significantly improved when compared with the unreinforced specimens, while the strengthening effect of the IPCSAM was remarkable.

(2) The influence of the LCSS on the strengthening effect: Since the existing relevant research results are very limited, the results from this paper were only compared with [9]. The comparison of specimen S1-A with the specimen YZ-SS strengthened by the PCSAM [9] showed that for S1-A, the ratio of the cross-sectional area before and after strengthening was $A_{1a} = 2.69$, the ratio of the bearing capacity before and after strengthening was $B_{1a} = 1.91$, and the strengthening efficiency was $E_{1p} = B_{1a}/A_{1a} = 0.71$; for YZ-SS, the ratio of the cross-sectional area before and after strengthening was $A_{ss} = 1.96$, the ratio of the bearing capacity before and after strengthening was $B_{ss} = 1.28$, and the strengthening efficiency was $E_{ss} = B_{ss}/A_{ss} = 0.65$. In other words, the strengthening efficiency increased by 9% using the LCSS instead of the sleeve formed by wire ropes. At the same time, the peak strain of S1-A was also larger than that of YZ-SS, showing the better ductility of S1-A than that of YZ-SS.

(3) The influence of the SSAWC on the strengthening effect: The comparison between the two specimens S1-A and S1-S showed that the self-stress increased the bearing capacity by 41%. For S1-S, the ratio of the bearing capacity before and after strengthening was $A_{1s} = 2.69$, the ratio of the bearing capacity before and after strengthening was $B_{1z} = 2.32$, and the strengthening efficiency was $E_{1z} = 0.86$. In other words, the strengthening efficiency increased by 21% using the SSAWC as filled concrete. The reason was that the self-stress produced by SSAWC caused the column to be compressed in three directions, improving the bearing capacity and stiffness. At the same time, the first crack appeared on the interface between the filled concrete, the column of S1-A, and the segment of S1-S specimen. This indicated that self-stress could compensate for the shrinkage of the filled concrete and also contributed to the initial stress on the interface between the filled concrete and adjacent components, improving the bond strength as well as delaying the occurrence of interfacial cracks. Therefore, the SSAWC had significant effects on improving not only the bearing capacity and rigidity of the specimen but also the bond strength.

(4) The influence of the strength of the LCSS concrete on the strengthening effect: It was observed from the comparison of S1-S and S1-SS that the reduction of the LCSS concrete strength would directly affect the bearing capacity and peak strain of the strengthened specimen. This was because the LCSS was a component of the strengthened specimen; as the concrete strength of the LCSS was reduced, the load borne by the LCSS was also decreased. At the same time, the lower the concrete strength of the LCSS, the easier the sleeve failed. As such, the self-stress would be reduced due

to the loss of the restriction provided by the sleeve, finally leading to the decreased bearing capacity.

(5) The influence of the thickness of the filled concrete on the strengthening effect: By comparing S1-S with S2-S, it was clear that the cross-sectional areas of these two strengthened specimens were the same, although the larger the thickness of filled concrete, the lower the bearing capacity of the specimen. The bearing capacity was borne by the filled concrete of the strengthened specimens, which complied with the code in [24], while the utilization factor of the filled concrete was 0.8 compared with the column; hence, for S2-S, the thickness of the filled concrete was larger than S1-S, so the bearing capacity was lower than S1-S.

4. Axial Compression Bearing Capacity

The axial compression bearing capacity of the strengthened pier was related to parameters such as the cross-sectional area and strength of the SSAWC, the cross-sectional area and concrete strength of the LCSS, and the self-stress value product produced by the SSAWC. Due to the complexity, long production time, and high cost of the specimens, only one strengthened specimen was prepared for each parameter. Referring to relevant research [9], the test models were supplemented by the finite element models while considering the influence of different parameters. On the basis of the results of the tests and extended analysis, the calculation formula for the bearing capacity was established.

4.1. Extended Parameter Analysis

4.1.1. Numerical Model

Numerical simulations were performed using ABAQUS and the numerical model was simplified as follows:

(1) The material parameters of the concrete, bolts, and welded wire mesh were adopted according to the measured values, as shown in Tables 2 and 5. The solid element was used to simulate for concrete and the plasticity damage model implemented in ABAQUS was used as the constitutive relationship of concrete in the elastoplastic stage. Damage factors of the damage plasticity model were calculated according to the code [26]. The bolts and welded wire mesh were simulated with the wire element and the double broken line model was used as the constitutive relation of steel;

(2) Referring to [9], the connection between segments was simulated by hard contact, meaning the contact surface was only under compression. The connections between bolts and the segment concrete were simulated using the embedded connection. According to the working characteristics of the interface and referring to the study by Zhao [9] and Zhou [27], the binding connection was used to simulate the connection between the filled concrete and its adjacent members and the Coulomb friction model was adopted;

(3) The unreinforced parts of the specimens were not simulated. The top and bottom surfaces of the specimens were simplified and coupled into one point. Constraints were set on each direction of the point obtained from the top coupling and on the point obtained from the bottom coupling, except in the Z direction;

(4) Displacement loading was adopted and the initial stress was used to simulate self-stress.

According to the above points, the finite element numerical model was established, as shown in Figure 12. Due to the difference between the simulated constitutive relationship and the actual constitutive relationship of the materials, as well as the influence of interface simulation and loading error on the test, the numerical model needed to be continuously adjusted according to the test results. The numerical model was adjusted with the peak load and load–displacement curve of actual specimens P1 and S1-S as the control index. By adjusting the constitutive relationship of the material, interface parameters, and loading system in the numerical model, the load–displacement curves of the specimen recorded in the tests and the numerical model were obtained, as shown in Figure 13. It can be seen that the load–displacement curves of specimens P1 and S1-S recorded in the tests were basically

consistent with those recorded by the numerical model. The difference between peak loads was less than 5%, indicating that the numerical model was well in accordance with the specimens, meaning it could be used as the basic model for the extended parameter analyses.
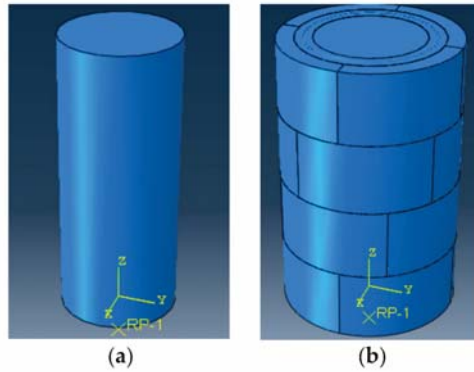
Figure 12. Finite element model. (**a**) Model of specimen P1; (**b**) Model of specimen S1-S.
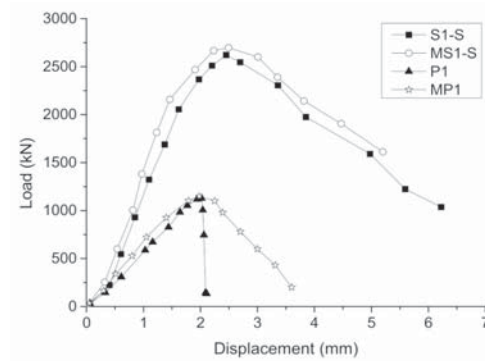
Figure 13. Load–displacement curves of specimens acquired using the numerical model and tests.

4.1.2. Parameter Extended Analysis

The influencing parameters of the axial compression bearing capacity for the strengthened specimens included the thickness and strength of the SSAWC, self-stress, and the thickness and concrete strength of the LCSS. The influence of the cross-sectional area of the filled concrete on the bearing capacity was considered in accordance with the code in [24]. Due to the limitations of the prefabricated mold used for the segments, the cross-sectional area of the LCSS basically remained invariable. Therefore, the influencing parameters were mainly self-stress, the strength of the SSAWC, and the concrete strength of the LCSS. Among them, the strength of filled concrete was set to three grades: C35, C40, C50; the longitudinal stress values were set to 0.8 MPa, 1.0 MPa, and 1.2 MPa; and the concrete strength of the LCSS was set to three grades: C35, C40, C50. As such, 9 extended numerical models were built to study the influence of these parameters, with Table 8 showing the specific parameter settings and peak loads.

Table 8. Material parameters of the extended models.

Name	Filled Concrete Strength (MPa)	Longitudinal Stress (MPa)	Segment Concrete Strength (MPa)	Peak Load (kN)
M-1	21.7	0.8	20.9	2578
M-2	21.7	1	20.9	2695
M-3	21.7	1.2	20.9	2802
M-4	21.7	1	23.4	2810
M-5	21.7	1	26.8	2876
M-6	21.7	1	32.4	2992
M-7	23.4	1	20.9	2771
M-8	26.8	1	20.9	2859
M-9	32.4	1	20.9	2955

(1) The influence of self-stress on the bearing capacity: Tables 7 and 8 show that when the self-stress value was between 0 and 1.2 MPa, the peak load of the strengthened specimens increased with the increase in the self-stress. When the self-stress increased by 0.2 MPa, the bearing capacity increased by about 100 kN. However, as the self-stress value increased, the growth rate of the peak load decreased. The reason for this was that after the stress increased, the LCSS was easily damaged and the restraint effect on column was reduced, resulting in the decrease in the bearing capacity.

(2) The influence of the strength of the SSAWC on bearing capacity: It can be seen from Tables 7 and 8 that the peak load of the strengthened specimens increased with the increase in strength of the filled concrete. When the concrete strength increased by 1 MPa, the bearing capacity of the strengthened specimens increased by 35 to 45 kN. However, the higher the strength of the filled concrete, the lower the growth rate of the bearing capacity of the strengthened specimens. This was because after the strength of the filled concrete increased, the LCSS failed first, resulting in a reduction of the increase in the bearing capacity.

(3) The influence of the concrete strength of the LCSS on the bearing capacity: Tables 7 and 8 show that the peak load of the specimens increased with the increase in concrete strength of the segment. When the concrete strength of the LCSS increased by 1 MPa, the bearing capacity of the strengthened increased by 35 to 60 kN. However, the higher the strength of the segment concrete, the smaller the growth rate of the peak load. The reason was similar to that of the strength of the filled concrete.

4.2. Bearing Capacity Calculation Model

According to the results of the tests and extended numerical analysis, the calculation method used for the axial compression bearing capacity of concrete members strengthened involving the enlarging section method found in [24], and Xu's study on the axial compression bearing capacity of self-stressed, concrete-filled steel tube columns [28], the calculation model for the axial compression bearing capacity of specimens strengthened by IPCSAM was established. In light of the structure and working characteristics of the components strengthened by the IPCSAM, the following assumptions were made on the bearing capacity calculation model of the IPCSAM reinforcement members:

(1) The bearing capacity of the strengthened specimens was composed of three parts: the bearing capacity of the unreinforced column and the filled concrete, the bearing capacity improved by the confinement provided by the sleeve and the filled concrete, and the bearing capacity improved by self-stress;

(2) The bearing capacity of the column and the filled concrete was calculated according to the calculation method of the code in [24]. In [24], the bearing capacity of strengthened components was equal to the axial compression bearing capacity of the column plus 80% of the axial compression bearing capacity of the filled concrete. In this test, the larger the filled concrete, the greater the error, so the utilization coefficient of the filled

concrete needed to be adjusted. The contribution of the LCSS on the bearing capacity of the specimens was neglected to simplify the calculation;

(3) According to the calculation method in [29], the improved bearing capacity of the sleeve and filled concrete constraints was calculated. As a result, the confinement coefficient was used to consider the improvement of the bearing capacity of the axial compression;

(4) According to [28], the calculation method used to improve the bearing capacity through self-stress and the relationship between the improved bearing capacity and the self-stress level (the ratio of the self-stress value to the strength of the SSAWC) involved cubic equations. According to this method, the tensile stress generated by the self-stress shall be less than the tensile bearing capacity of the sleeve concrete, so the self-stress shall not be greater than 2 MPa;

(5) According to the design data for previous bridges, the concrete strength grade of the substructure mostly did not exceed C30, so it was assumed that the concrete strength grade of the columns was not greater than C30. At the same time, the substructures constructed years ago had low reinforcement ratios and there were issues related to bar exposure and corrosion. Therefore, the reinforcement of the columns was ignored.

Based on assumption (1), the calculation formula for the axial compression bearing capacity of the strengthened specimens (N) was proposed as follows:

$$N = N_0 + N_s + N_p \tag{1}$$

where N_0, N_s, and N_p are the bearing capacity of the column and the filled concrete, the bearing capacity improved by the confinement, and the bearing capacity improved by self-stress, respectively.

Based on assumption (2), the calculation formula for the bearing capacity of the unreinforced column and the filled concrete (N_0) was proposed as follows:

$$N_0 = 0.9\varphi\left[f_{co}A_{co} + f'_{yo}A'_{so} + \alpha(f_{sc}A_{sc} + f'_yA'_s)\right] \tag{2}$$

where φ is the stability coefficient of members, taking the value according to code [26]; f_{co} and f_{sc} are the strength of the column concrete and filled concrete, respectively; A_{co} and A_{sc} are the cross-sectional areas of the column and filled concrete, respectively; f_{yo}' and f_y' are the strength values of steel bars in the column and filled concrete, respectively; A_{yo}' and A_y' are the cross-sectional areas of steel bars in column and filled concrete, respectively; α is the utilization coefficient of the filled concrete.

According to [24] and Huang's study [30], the value of α should be determined by the interface bonding between the column and filled concrete. Assuming that the influencing factors of the interface bonding are the roughness, concrete strength of the column, filled concrete strength, and the usage of an interface agent, the calculation formula of α is as follows:

$$\alpha = A(0.15 + 0.025\Delta)\ln f_c\zeta_s \tag{3}$$

where A is the adjustment coefficient considering the preloading of concrete in the filled concrete, which is an undetermined constant; Δ is the roughness of the interface when $\Delta \geq 2.5$, taking $\Delta = 5$ mm; f_{sc} is the average strength of the column concrete and filled concrete; ζ_s is the influence coefficient of the interfacial agent, which is an undetermined coefficient.

Based on assumption (3), the calculation formula for the bearing capacity improved by the confinement (N_0) was proposed as follows:

$$N_s = \beta\theta N_0 \tag{4}$$

$$\beta = B\left(\frac{f_l}{f_{co}}\right)^{0.7} \tag{5}$$

$$\theta = \frac{A_{gc}f_{gt} + A_{gy}f_{gy} + A_{sc}f_{st} + A'_s f'_y}{A_{co}f_{co}} \tag{6}$$

where θ is the confinement coefficient when $\theta \geq 0.25$, taking $\theta = 0.25$; β is the adjustment coefficient related to the concrete strength of the SSAWC, the LCSS, and the column; B is an undetermined constant; f_{st}, f_{gt}, and f_{gy} are the tensile strengths of the SSAWC, the LCSS concrete, and steel bars reinforcement, respectively; A_{gc} and A_{gy} are the cross-sectional areas of the sleeve concrete and steel bars, respectively; the value of f_l takes the minimum of f_{sc} and f_{gc}.

Based on assumption (4), the calculation formula for the bearing capacity improvement caused by self-stress (N_0) was proposed as follows:

$$N_p = \gamma N_0 \tag{7}$$

$$\gamma = C\eta^3 + D\eta^2 + E\eta \tag{8}$$

where, γ is the improvement coefficient; η is the self-stress level, which is the ratio of the longitudinal self-stress value to the SSAWC strength; C, D, and E are coefficients of cubic equations to be solved.

To sum up, the calculation formula of axial the compression bearing capacity of the components strengthened by the IPCSAM is as follows:

$$N = 0.9\varphi\left[f_{co}A_{co} + f'_{yo}A'_{so} + \alpha(f_{sc}A_{sc} + f'_y A'_s)\right](1 + \beta\theta + \gamma) \tag{9}$$

4.3. Determination of Parameters

(1) The φ value: According to the code in [26], when $l_0/d \leq 7$, $\varphi = 1$ is used for the specimens.
(2) The α value: The values of A and ζ_s can be determined by regression fitting the data from Tables 7 and 8. Then, the relationship between α and Δ is as follows:

$$\alpha = 0.75(0.15 + 0.025\Delta)\ln f_c\zeta_s \tag{10}$$

The value of ζ_s is 1 when no interface agent is used. When the filled concrete is SSAWC, the value of ζ_s is 1.07.

(3) The β value: The values of B can be determined by regression fitting the data from Tables 7 and 8. Then, the relationship between β and f_l, f_{co} is as follows:

$$\beta = 2.698\left(\frac{f_l}{f_{co}}\right)^{0.7} \tag{11}$$

(4) The γ value. The values of C, D, and E can be determined by regression fitting the data from Tables 7 and 8. Then, the relationship between γ and η is as follows:

$$\gamma = 6.683\eta^3 - 58.275\eta^2 + 9.556\eta \tag{12}$$

For the derivative of Formula (12), the self-stress level corresponding to the γ maximum value can be obtained; that is, the optimum self-stress level of the strengthened component. The optimum self-stress level of the specimen strengthened by the IPCSAM is 0.0875.

4.4. Formula Verification

In this paper, the data from the tests and extended parameter analyses, as well as the data used for comparison with [9] and [20], were used to verify Formula (9). The verification results are shown in Table 9, whereby the symbol YZSS(YZFS) represents the specimens strengthened by the PCSAM corresponding to [9], while the symbol ZMR(ZRW) represents the specimens from Tang's test corresponding to [20]. It can be observed in the table that the difference between the bearing capacity calculated by Formula (9) and the

bearing capacity of the tested and simulated specimens is less than 13%, which shows good applicability.

Table 9. Verification results of the fitting formula.

Name	BCT(S) [1] (kN)	ACSC of Column f_{co} (MPa)	Filled Concrete Strength f_{sc} (MPa)	Concrete Strength of LCSS f_{gc} (MPa)	Self-Stress q (MPa)	Confinement Coefficient θ	Self-Stress Level η	BCC [2] (kN)	Difference
S1-A	2147	20.1	19.8	20.9	0	0.176	0	2035	−5.20%
S1-S	2621	20.1	21.7	20.9	0.99	0.177	0.046	2565	−2.12%
S1-SS	2153	20.1	21.7	13.4	0.83	0.147	0.038	2243	4.19%
S2-S	1926	20.1	21.7	20.9	0.63	0.250	0.031	2116	9.89%
M-1	2578	20.1	21.7	20.9	0.8	0.177	0.037	2507	−2.77%
M-2	2695	20.1	21.7	20.9	1	0.177	0.046	2568	−4.71%
M-3	2802	20.1	21.7	20.9	1	0.177	0.055	2615	−6.67%
M-4	2810	20.1	21.7	23.4	1	0.182	0.046	2648	−5.78%
M-5	2876	20.1	21.7	26.8	1	0.192	0.046	2769	−3.71%
M-6	2992	20.1	21.7	32.4	1	0.204	0.046	2960	−1.06%
M-7	2771	20.1	23.4	20.9	1	0.180	0.043	2633	−4.99%
M-8	2859	20.1	26.8	20.9	1	0.187	0.037	2774	−2.96%
M-9	2955	20.1	32.4	20.9	1	0.196	0.031	3004	1.66%
YZSS1 [3]	3578	39.8	17.9	44.2	0	0.075	0	3470	−3.03%
YZSS2 [3]	3220	39.8	17.9	44.2	0	0.075	0	3470	7.76%
YZSS3 [3]	3984	39.8	17.9	44.2	0	0.075	0	3470	−12.90%
YZFS1 [3]	4640	39.8	17.9	44.2	0	0.125	0	4060	−12.51%
YZFS3 [3]	4524	39.8	17.9	44.2	0	0.125	0	4060	−10.26%
ZMW1 [4]	1120	20.1	32.8	0	0	0.155	0	991	5.87%
ZMW2 [4]	936	20.1	32.8	0	0	0.155	0	991	−11.52%
ZRW1 [4]	1027	20.1	45.5	0	0	0.128	0	1153	12.25%
ZRW2 [4]	1071	20.1	45.5	0	0	0.128	0	1153	7.66%
ZRW3 [4]	1113	20.1	45.5	0	0	0.128	0	1153	3.59%

[1]: BCT(S) = Bearing capacity of specimens tested (or simulated). [2]: BCC = Bearing capacity calculated by Formula (4). [3]: The symbol YZSS(YZFS) represents the data from [9]. [4]: The symbol of ZMW(ZRW) represents the data from [20].

5. Conclusions

This study sets out to improve the PCSAM with the SSAWC and the LCSS. Initially, the strengthening effects of the above two improvement measures on the bearing capacity of the strengthened specimens were verified using an axial compression test. Then, the extended parameter analyses were performed by establishing the numerical models. Finally, the calculation formula for the axial compression bearing capacity of the strengthened specimens was established. The following conclusions were made:

(1) The IPCSAM has good strengthening effects on underwater pier strengthening structures without causing undraining. Compared with the unreinforced column, the axial compression bearing capacity and peak strain of specimens strengthened by the IPC-SAM increased by 90–130% and 30–60%, respectively. This indicates that the bearing capacity and ductility of the strengthened specimens were considerably improved;

(2) As the filling material, the SSAWC can reduce losses in underwater strength in concrete and can produce expansion and self-stress. The self-stress not only improves the bond strength between the filled concrete and the adjacent member, but also provides a preloading effect on the column, which can improve the strength and ultimate strain of the concrete. Compared with the specimen strengthened by AWC, the bearing capacity of the specimen strengthened by the SSAWC increased by 18% and the strengthening efficiency increased from 0.71 to 0.86;

(3) The LCSS improvement caused by the shield lining showed reliable connection performance, which remained in good condition when the specimen was broken. In the test, the LCSS showed good integrity and confinement, which could increase the bearing capacity of a specimen. Compared with the PCSAM, the strengthening efficiency of the specimen strengthened by the IPCSAM increased from 0.65 to 0.71;

(4) The strength of the filled concrete, the strength of the LCSS concrete, and the self-stress were the key parameters affecting the bearing capacity of the specimens. With the increase in filled concrete strength, the LCSS strength, self-stress, and bearing capacity increased accordingly;

(5) The calculation formula for the bearing capacity of the strengthened components has been proposed. The findings from this study show that the formula has good applicability and provides a theoretical design basis for the application of the IPCSAM.

In addition, preparing the specimens requires a large number of steel molds and careful concrete curing, which takes a lot of time. Considering the time needed and the restrictions on research and development funds, only a small number of specimens were tested and a numerical simulation was conducted. As a consequence, the above-mentioned conclusions and remarks are only validated by limited experimental and simulation results. More experimental data and numerical simulations are needed to validate the proposed formulas in the future.

References

1. Wei, R.; Sneed, L.H. Test Results and Nonlinear Analysis of RC T-beams Strengthened by Bonded Steel Plates. *Int. J. Concr. Struct. Mater.* **2015**, *9*, 133–143.

2. Lehman, D.E.; Gookin, S.E. Repair of earthquake-damaged bridge columns. *ACI Struct. J.* **2001**, *98*, 233–242.

3. Hamdy, M.; Mohamed, M.Z.; Afifi, B.B. Performance Evaluation of Concrete Columns Reinforced Longitudinally with FRP Bars and Confined with FRP Hoops and Spirals under Axial Load. *J. Bridge Eng.* **2014**, *19*, 04014020.

4. Saeed, H.Z.; Ahmed, A.; Ali, S.M.; Iqbal, M. Experimental and finite element investigation of strengthened LSC bridge piers under Quasi-Static Cyclic Load Test. *Compos. Struct.* **2015**, *131*, 556–564. [CrossRef]

5. Ai, J.; Shi, L.Y. Discussion of design and construction method on extraneous prestressed strengthening technique for bridge. *J. Southeast Univ.* **2002**, *32*, 771–774.

6. Fatmir, M.; Hadi, B. *Rehabilitation of Deteriorated Timber Piles with Fiber Reinforced Polymer Composites—IABSE Symposium Report*; International Association for Bridge and Structural Engineering: Vancouver, BC, Canada, 2017; pp. 381–388.

7. Yi, N.H.; Nam, J.W. Evaluation of material and structural performances of developed Aqua-Advanced-FRP for retrofitting of underwater concrete structural members. *Constr. Build. Mater.* **2010**, *24*, 566–576. [CrossRef]

8. Sen, R.; Mullins, G. Application of FRP composites for underwater piles repair. *Compos. Part B Eng.* **2007**, *38*, 751–758. [CrossRef]

9. Zhao, B. The Study on Underwater Pier Reinforcement Technology by Precast Concrete Segment Assembled Quickly. Master's Thesis, Southeast University, Nanjing, China, 2015. (In Chinese)

10. Wu, S.F.; Jiang, S.F.; Shen, S.; Wu, Z. The Mix Ratio Study of Self-Stressed Anti-Washout Underwater Concrete Used in Nondrainage Strengthening. *Materials* **2019**, *12*, 324. [CrossRef]

11. Qu, X.S.; Liu, Q. Bond strength between steel and self-compacting lower expansion concrete in composite columns. *J. Constr. Steel Res.* **2017**, *139*, 176–187. [CrossRef]

12. Calvo, J.G.; Revuelta, D.; Carballosa, P.; Gutiérrez, J.P. Comparison between the performance of expansive SCC and expansive conventional concretes in different expansion and curing conditions. *Concr. Constr. Build. Mater.* **2017**, *136*, 277–285. [CrossRef]

13. Lu, Y.; Liu, Z.; Li, S.; Li, N. Bond behavior of steel fibers reinforced self-stressing and self-compacting concrete filled steel tube columns. *Constr. Build. Mater.* **2018**, *158*, 894–909. [CrossRef]
14. Huang, J.C. The Study on Prefabrication Technology of Reinforced Concrete Shield Segment. Master's Thesis, Tongji University, Shanghai, China, 2007. (In Chinese).
15. Liu, X.; Bai, Y.; Yuan, Y.; Mang, H.A. Experimental investigation of the ultimate bearing capacity of continuously jointed segmental tunnel linings. *Struct. Infrastruct. Eng.* **2016**, *12*, 1364–1379. [CrossRef]
16. Meng, G.; Gao, B.; Zhou, J.; Cao, G.; Zhang, Q. Experimental investigation of the mechanical behavior of the steel fiber reinforced concrete tunnel segment. *Constr. Build. Mater.* **2016**, *126*, 98–107. [CrossRef]
17. Fakharifar, M.; Chen, G.; Wu, G.; Shamsabadi, A.; ElGawady, M.A.; Dalvand, A. Rapid Repair of Earthquake-Damaged RC Columns with Prestressed Steel Jackets. *J. Bridge Eng.* **2016**, *21*, 04015075. [CrossRef]
18. Wang, X. Experimental Investigation on the Seismic Behaviors of Sever Earthquake-Damaged RC Bridge Piers Repaired with Wrapped CFRP Sheets. Master's Thesis, Dalian University of Technology, Dalian, China, 2015. (In Chinese)
19. Seible, F.; Priestley, M.J.N.; Hegemier, G.A.; Innamorato, D. Seismic retrofit of RC columns with continuous carbon fiber jackets. *J. Compos. Constr.* **1997**, *1*, 52–62. [CrossRef]
20. Tang, Y.; Wu, G.; Sun, Z. Numerical Study on Seismic Behavior of Underwater Bridge Columns Strengthened with Prestressed Precast Concrete Panels and Fiber-Reinforced Polymer Reinforcements. *Int. J. Polym. Sci.* **2018**, *2018*, 7438694. [CrossRef]
21. Kamal, H.K. Effects of anti-washout admixtures on fresh concrete properties. *ACI Mater. J.* **1995**, *92*, 164–171.
22. Oliveira, M.J.; Ribeiro, A.B.; Branco, F.G. Combined effect of expansive and shrinkage reducing admixtures to control autogenous shrinkage in self-compacting. *Concr. Constr. Build. Mater.* **2014**, *52*, 267–275. [CrossRef]
23. Shim, C.; Koem, C.; Song, H.; Park, S. Seismic performance of repaired severely damaged precast columns with high-fiber reinforced cementitious composites. *KSEC J. Civ. Eng.* **2018**, *22*, 736–746. [CrossRef]
24. China Architecture & Building Press. *GB50367-2013 Design Code for Strengthening Concrete Structures*; China Architecture & Building Press: Beijing, China, 2013. (In Chinese)
25. Yang, F.L. Experimental Study on Basic Mechanical Properties Short of Columns with Strengthened Style Hoop. Master's Thesis, Shandong University of Science and Technology, Qingdao, China, 2010. (In Chinese)
26. China Architecture & Building Press. *GB50010-2015 Code for Design of Concrete Structures*; China Architecture & Building Press: Beijing, China, 2010. (In Chinese)
27. Zhou, X.H.; Yan, B.; Liu, J.P. Axial load behavior of circular tubed reinforced concrete columns with different length-to-diameter ratios. *J. Build. Struct.* **2018**, *39*, 11–21. (In Chinese)
28. Xu, L.; Wu, M.; Zhou, P.; Gu, Y.S.; Xu, M.Y. Experimental Investigation on High-strength Self-stressing and Self-compacting Concrete Filled Steel Tube Columns Subjected to Uniaxial Compression. *Eng. Mech.* **2017**, *34*, 93–100. (In Chinese)
29. China Architecture & Building Press. *GB50936-2014 Technical Code for Concrete Filled Steel Tubular Structures*; China Architecture & Building Press: Beijing, China, 2014. (In Chinese)
30. Huang, L.; Zhuo, W.; Shangguan, P.; Huang, X. An improved formula for shear strength of bonding interface between new and old concrete. *Ind. Constr.* **2018**, *48*, 202–207, 212. (In Chinese)

Prediction of Bending, Buckling and Free-Vibration Behaviors of 3D Textile Composite Plates by Using VAM-Based Equivalent Model

Senbiao Xi [1,2]**, Yifeng Zhong** [1,2,]*****, Zheng Shi** [1,2] **and Qingshan Yi** [1,2]

[1] School of Civil Engineering, Chongqing University, Chongqing 400045, China; 201816131126@cqu.edu.cn (S.X.); 20191601513@cqu.edu.cn (Z.S.); 20154673@cqu.edu.cn (Q.Y.)
[2] Key Laboratory of New Technology for Construction of Cities in Mountain Area, Chongqing University, Chongqing 400045, China
***** Correspondence: zhongyf@cqu.edu.cn

Abstract: To solve the microstructure-related complexity of a three-dimensional textile composite, a novel equivalent model was established based on the variational asymptotic method. The constitutive modeling of 3D unit cell within the plate was performed to obtain the equivalent stiffness, which can be inputted into the 2D equivalent model (2D-EPM) to perform the bending, free-vibration and buckling analysis. The correctness and effectiveness of the 2D-EPM was validated by comparing with the results from 3D FE model (3D-FEM) under various conditions. The influence of yarn width and spacing on the equivalent stiffness was also discussed. Finally, the effective performances of 3D textile composite plate and 2D plain-woven laminate with the same thickness and yarn content were compared. The results revealed that the bending, buckling and free-vibration behaviors predicted by 2D-EPM were in good agreement with 3D-FEM, and the local field distributions within the unit cell of 3D textile composite plate were well captured. Compared with the 2D plain-woven laminate, the displacement of 3D textile composite plate was relatively larger under the uniform load, which may due to the fact that the through-the-thickness constrains of the former are only dependent on the binder yarns, while the warp yarns and weft yarns of the latter are intertwined closely.

Keywords: 3D textile composite; variational asymptotic method; equivalent model; buckling analysis; free-vibration analysis

1. Introduction

In recent years, composite structures are more and more widely used as load-bearing structures [1–4]. Three-dimensional (3D) textile composites is a new type of high performance composites developed from the traditional two-dimensional (2D) textile composites in the 1980s. Compared with 2D textile composites, the warp yarns, weft yarns and binder yarns are interlaced with each other not only in the plane, but also in the thickness direction, which can not only improve the specific strength and specific stiffness of composites, but also have other excellent mechanical properties, such as good impact damage resistance, fatigue resistance, etc. [5]. At the same time, it also overcomes the shortcomings of laminated composite that are easy to delaminate after loading. Another significant benefit of 3D textile composites is the ability to manufacture structural component reforms directly from the yarns.

The application of 3D textile composites in load-bearing structures requires a thorough structural analysis. However, precisely predicting the behaviors of textile composites is difficult due to their complex microstructures. Currently, experimental [6], analytical and numerical methods are used to study the elastic behavior of 3D textile composites.

A variety of analytical models have been used to study the mechanical characteristics of 3D braided composites, including fabric geometry model [7], fiber inclination model [8], three cell model [9], mixed volume averaging technique [10], and Mori-Tanaka theories

combined with stiffness averaging method [11]. Yang et al. [12] introduced the "Fiber Inclination Model" to estimate the elastic properties of 3D textile (woven and braided) composites. The unit cell employed for the study was an assemblage of inclined unidirectional laminae. Based on the classical laminate plate theory (CLPT) and iso-stress/strain assumptions, Ishikawa and Chou [13,14] presented analytical methods to estimate the homogenized response of woven fabric composites. Branch et al. [15] presented a 3D tow inclination model for calculating the elastic constants of three-dimensional braided composites. The global constitutive equation of the composite material was derived by applying an iso-strain method to the unit cell and averaging all tow segments and the matrix inside the unit cell. Yan et al. [16] predicted the properties of 3D braided structures using an analytical model called the Fabric Geometry Model (FGM). Using the stiffness volume average method and Tsai-Wu polynomial failure criterion, Jiang et al. [17] presented a theoretical model based on the helix geometry unit cell for prediction of the effective elastic constants and the failure strength of 3D braided composites under uniaxial load. Analytical models are good at estimating the in-plane properties of textile composites, but they are not so good at predicting the shear and out-of-plane properties.

Although utilizing experimental and analytical models to examine the mechanical characteristics of a laminated composite plate is practical and efficient [18], many studies also employed numerical approaches to investigate the 3D textile composites [19–21]. Tan et al. [22] developed a mesoscale finite element model (MSFEM) in LS-DYNA to simulate impact damage to three-dimensional braided composite plates based on the assumption that the fiber yarn was made up of cylindrical segments. Dong et al. [23] simulated the micro-stress of 3D braided composites by the method of Asymptotic Expansion Homogenization (AEH) combined with finite-element analysis. Tang and Whitcomb [24] used the full multiscale mechanical model to perform progressive failure evaluations of 2×2 braided composites. This approach was also used by Potluri and Manan to investigate the mechanical characteristics of braided composite tubes [25], but the stress and strain distribution of the fiber and matrix cannot be determined.

Berdichevsky [26] recently developed the semi-analytical approach-variational asymptotic technique (VAM) to increase the efficiency of numerical methods and the accuracy of analytical methods. It combines the benefits of asymptotic and variational methods, and takes into account all potential deformations [27–29]. The fundamental benefit of adopting VAM for plate analysis is that it can divide the original 3D plate problem into two independent problems using the small parameter of thickness-width ratio, i.e., through-the-thickness analysis and 2D reference plane analysis [30,31]. Then, VAM was expanded by Zhong and Yu to simulate piezoelectric and piezomagnetic laminates [32], multilayer graded magnetoelectroelastic plates [33] and composite cylindrical shells [34].

The VAM model is expanded in this article to present an equivalent plate model to replace the original 3D textile composite plate (3D-TCP) for bending, buckling, and free-vibration analysis. The influences of structural parameters (binder yarn width, warp or weft yarn width) on the equivalent stiffness of 3D-TCP are investigated. Finally, the effective performance of 2D plain-woven laminate (2D-PWL) and 3D-TCP with the same plate thickness and yarn content are compared. To the best of the authors' knowledge, this technique has never been used to predict the bending, buckling, and free-vibration behaviors of 3D-TCP.

2. Variational Asymptotic Equivalent Model of 3D-TCP

As illustrated in Figure 1a, the macro-coordinates $x_i (i = 1, 2, 3)$ may be used to describe any point in the 3D-TCP, where $x_\alpha (\alpha = 1, 2)$ are the in-plane coordinates and x_3 is the normal coordinate. The 3D finite element model of 3D-TCP may be divided into the 3D unit cell and 2D equivalent plat model (2D-EPM) according to the VAM. It's worth mentioning that the dimensions of the unit cell should be substantially smaller than macro-structure dimensions. As illustrated in Figure 1c, the field variables of 2D-EPM are represented as functions of x_1 and x_2, whereas x_3 is disappeared.
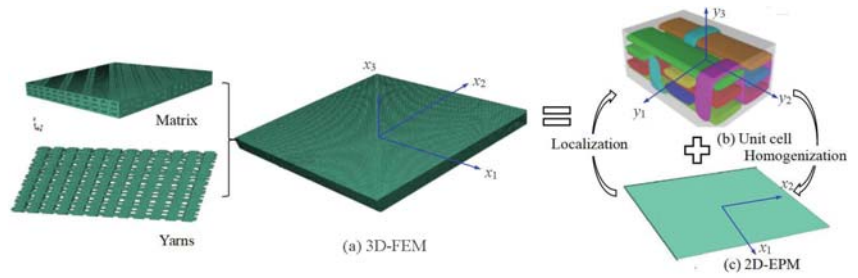
Figure 1. Decomposition diagram of 3D textile composite plate: (**a**) 3D-FEM; (**b**) Unit cell; (**c**) 2D-EPM.

To characterize the quick change of in-plane material characteristics, the micro-coordinates $y_i = x_i/\zeta$ (ζ is a small parameter) are introduced. To obtain the equivalent model of 3D-TCP by using the variational asymptotic method, the 3D displacement field of the original 3D-TCP needs to be represented by 2D plate variables, such as

$$
\begin{aligned}
u_1(x_\alpha; y_i) &= \underline{\bar{u}_1(x_\alpha) - \zeta y_3 \bar{u}_{3,1}(x_\alpha)} + \zeta w_1(x_\alpha; y_i) \\
u_2(x_\alpha; y_i) &= \underline{\bar{u}_2(x_\alpha) - \zeta y_3 \bar{u}_{3,2}(x_\alpha)} + \zeta w_2(x_\alpha; y_i) \\
u_3(x_\alpha; y_i) &= \underline{\bar{u}_3(x_\alpha)} + \zeta w_3(x_\alpha; y_i)
\end{aligned}
\tag{1}
$$

where the displacements of the 3D-FEM and 2D-EPM are represented by u_i and $\bar{u}_i$, respectively; w_i are the fluctuation functions to be solved. The underline terms should satisfy the following constraints:

$$
h\bar{u}_\alpha(x_\alpha) = \langle u_\alpha \rangle + \langle \zeta y_3 \rangle \bar{u}_{3,\alpha}, \quad h\bar{u}_3(x_\alpha) = \langle u_3 \rangle
\tag{2}
$$

where $\langle \cdot \rangle$ denotes the volume integral of a unit cell.

The fluctuation functions in Equation (3) are constrained as

$$
\langle \zeta w_i \rangle = 0
\tag{3}
$$

The strain field can be expressed according to 3D linear elasticity theory, such as

$$
\varepsilon_{ij} = \frac{1}{2}\left(\frac{\partial u_i}{\partial x_j} + \frac{\partial u_j}{\partial x_i} \right)
\tag{4}
$$

The 3D strain field can be obtained by substituting Equation (1) into Equation (4) and ignoring higher-order terms according to VAM,

$$
\begin{aligned}
\varepsilon_{11} &= \gamma_{11} + \zeta y_3 \kappa_{11} + w_{1,1} \\
2\varepsilon_{12} &= 2\gamma_{12} + 2\zeta y_3 \kappa_{12} + w_{1,2} + w_{2,1} \\
\varepsilon_{22} &= \gamma_{22} + \zeta y_3 \kappa_{22} + w_{2,2} \\
2\varepsilon_{13} &= w_{1,3} + w_{3,1} \\
2\varepsilon_{23} &= w_{2,3} + w_{3,2} \\
\varepsilon_{33} &= w_{3,3}
\end{aligned}
\tag{5}
$$

where $\gamma_{\alpha\beta}$ and $\kappa_{\alpha\beta}$ are the in-plane strains and bending curvatures of 2D-EPM, respectively, and may be defined as

$$
\gamma_{\alpha\beta}(x_1, x_2) = \frac{1}{2}\left(\bar{u}_{\alpha,\beta} + \bar{u}_{\beta,\alpha} \right), \quad \kappa_{\alpha\beta}(x_1, x_2) = -\bar{u}_{3,\alpha\beta}
\tag{6}
$$

We can define the three-dimensional strain field in matrix form to make derivation easier, such as

$$\begin{aligned}
\mathcal{E}_e &= [\varepsilon_{11} \quad \varepsilon_{22} \quad 2\varepsilon_{12}]^{\mathrm{T}} = \gamma + x_3\kappa + I_\alpha w_{||,\alpha} \\
2\mathcal{E}_s &= [2\varepsilon_{13} \quad 2\varepsilon_{23}]^{\mathrm{T}} = w_{||,3} + e_\alpha w_{3,\alpha} \\
\mathcal{E}_t &= \varepsilon_{33} = w_{3,3}
\end{aligned} \tag{7}$$

where $()_{||} = [()_1 \quad ()_2]^{\mathrm{T}}, \gamma = [\ \gamma_{11} \quad 2\gamma_{12} \quad \gamma_{22}\ ]^{\mathrm{T}}, \kappa = [\kappa_{11} \quad \kappa_{12} + \kappa_{21} \quad \kappa_{22}]^{\mathrm{T}}$, and

$$I_1 = \begin{bmatrix} 1 & 0 \\ 0 & 1 \\ 0 & 0 \end{bmatrix}, I_2 = \begin{bmatrix} 0 & 0 \\ 1 & 0 \\ 0 & 1 \end{bmatrix}, e_1 = \left\{ \begin{matrix} 1 \\ 0 \end{matrix} \right\}, e_2 = \left\{ \begin{matrix} 0 \\ 1 \end{matrix} \right\} \tag{8}$$

The strain energy of the 3D-TCP may be expressed briefly as

$$U = \frac{1}{2}\left\langle \mathcal{E}^{\mathrm{T}} D \mathcal{E} \right\rangle = \frac{1}{2}\left\langle \left\{ \begin{matrix} \mathcal{E}_e \\ 2\mathcal{E}_s \\ \mathcal{E}_t \end{matrix} \right\}^{\mathrm{T}} \begin{bmatrix} D_e & D_{es} & D_{et} \\ D_{es}^{\mathrm{T}} & D_s & D_{st} \\ D_{et}^{\mathrm{T}} & D_{st}^{\mathrm{T}} & D_t \end{bmatrix} \left\{ \begin{matrix} \mathcal{E}_e \\ 2\mathcal{E}_s \\ \mathcal{E}_t \end{matrix} \right\} \right\rangle \tag{9}$$

where $D_e, D_{es}, D_{et}, D_s, D_{st}$ and D_t are the corresponding sub-matrices of a 3D 6×6 material matrix.

The virtual work done by the applied load may be stated as

$$\delta\overline{W}_{3D} = \delta\overline{W}_{2D} + \delta\overline{W}^* \tag{10}$$

where $\delta\overline{W}_{2D}$ and $\delta\overline{W}^*$ denote, respectively, the virtual work independent and dependent of the fluctuation function, and

$$\delta\overline{W}_{2D} = \langle p_i\delta v_i + q_a\delta v_{3,a}\rangle, \delta\overline{W}^* = \left\langle \langle f_i\delta w_i\rangle + \tau_i\delta w_i^+ + \beta_i\delta w_i^- \right\rangle \tag{11}$$

where $(\cdot)^+$ and $(\cdot)^-$ represent the items acting on the top and bottom of the plate, respectively; τ_i and β_i are the traction forces on the top and bottom surface of the plate, respectively; f_i are the body forces; $p_i = \langle f_i\rangle + a_i + \beta_i, q_a = h/2(\beta_a - a_a) - \langle x_3 f_a\rangle$.

The variation of the total potential energy may be written as

$$\delta\Pi = \delta U - \delta W^* = \frac{1}{2}\delta\left\langle \mathcal{E}^{\mathrm{T}} D \mathcal{E}\right\rangle - \left\langle \langle f_i\delta w_i\rangle + \tau_i\delta w_i^+ + \beta_i\delta w_i^- \right\rangle \tag{12}$$

where only the unknown fluctuation function w_i is changeable.

2.1. Dimensional Reduction Analysis of 3D-TCP

The zeroth-order fluctuation function may be solved by minimizing the zeroth-order approximation strain energy under the constraint of Equation (9) as

$$\delta U_0 = 0 \tag{13}$$

where

$$2U_0 = \left\langle \begin{matrix} (\gamma + x_3\kappa)^{\mathrm{T}} D_e(\gamma + x_3\kappa) + w_{||,3}^{\mathrm{T}} D_s w_{||,3} + w_{3,3}^{\mathrm{T}} D_t w_{3,3} \\ +2(\gamma + x_3\kappa)^{\mathrm{T}}\left(D_{es}w_{||,3} + D_{et}w_{3,3}\right) + 2w_{||,3}^{\mathrm{T}} D_{st}w_{3,3} \end{matrix} \right\rangle \tag{14}$$

The Lagrange multipliers λ_i are used to impose the constraint on the fluctuation function as

$$\delta(\Pi + \lambda_i\langle w_i\rangle) = 0 \tag{15}$$

The zeroth-order approximate variational expression can be obtained as

$$\left\langle \begin{array}{c} \left[(\boldsymbol{\gamma} + x_3\boldsymbol{\kappa})^{\mathrm{T}}\boldsymbol{D}_{es} + \boldsymbol{w}_{\|,3}^{\mathrm{T}}\boldsymbol{D}_s + w_{3,3}^{\mathrm{T}}\boldsymbol{D}_{st}^{\mathrm{T}}\right]\delta \boldsymbol{w}_{\|,3} \\ +\lambda_i\delta w_i + \left[(\boldsymbol{\gamma} + x_3\boldsymbol{\kappa})^{\mathrm{T}}\boldsymbol{D}_{et} + \boldsymbol{w}_{\|,3}^{\mathrm{T}}\boldsymbol{D}_{st} + w_{3,3}^{\mathrm{T}}\boldsymbol{D}_t\right]\delta w_{3,3} \end{array} \right\rangle = 0 \tag{16}$$

By partly integrating Equation (16), the relevant Euler-Lagrange equation may be obtained as

$$\left[(\boldsymbol{\gamma} + x_3\boldsymbol{\kappa})^{\mathrm{T}}\boldsymbol{D}_{es} + \left(\boldsymbol{w}_{\|,3}\right)^{\mathrm{T}}\boldsymbol{D}_s + w_{3,3}\boldsymbol{D}_{st}\right]_{,3} = \boldsymbol{\lambda}_{\|}$$
$$\left[(\boldsymbol{\gamma} + x_3\boldsymbol{\kappa})^{\mathrm{T}}\boldsymbol{D}_{et} + \left(\boldsymbol{w}_{\|,3}\right)^{\mathrm{T}}\boldsymbol{D}_{st} + w_{3,3}\boldsymbol{D}_t\right]_{,3} = \lambda_3 \tag{17}$$

where $\boldsymbol{\lambda}_{\|} = [\lambda_1 \quad \lambda_2]^{\mathrm{T}}$.

According to the free surface condition, the expressions in square brackets of Equation (17) should be zero at the top and bottom of the plate, such as

$$\left[(\boldsymbol{\gamma} + x_3\boldsymbol{\kappa})^{\mathrm{T}}\boldsymbol{D}_{es} + w_{\|,3}^{\mathrm{T}}\boldsymbol{D}_s + w_{3,3}\boldsymbol{D}_{st}^{\mathrm{T}}\right]^{+/-} = 0$$
$$\left[(\boldsymbol{\gamma} + x_3\boldsymbol{\kappa})^{\mathrm{T}}\boldsymbol{D}_{et} + w_{\|,3}^{\mathrm{T}}\boldsymbol{D}_{st} + w_{3,3}\boldsymbol{D}_t\right]^{+/-} = 0 \tag{18}$$

where the superscript "$+/-$" denotes the items at the top and bottom of the plate.

$\boldsymbol{w}_{\|}$ and w_3 can be solved by putting Equation (18) into Equation (17), such as

$$\boldsymbol{w}_{\|} = \left\langle -(\boldsymbol{\gamma} + x_3\boldsymbol{\kappa})\overline{\boldsymbol{D}}_{es}(\boldsymbol{D}_s)^{-1}\right\rangle^{\mathrm{T}}, w_3 = \left\langle -(\boldsymbol{\gamma} + x_3\boldsymbol{\kappa})\overline{\boldsymbol{D}}_{et}(\boldsymbol{D}_t)^{-1}\right\rangle \tag{19}$$

where

$$\overline{\boldsymbol{D}}_{es} = \boldsymbol{D}_{es} - \overline{\boldsymbol{D}}_{et}(\boldsymbol{D}_{st})^{\mathrm{T}}(\overline{\boldsymbol{D}}_t)^{-1}, \quad \overline{\boldsymbol{D}}_{et} = \boldsymbol{D}_{et} - \boldsymbol{D}_{es}(\boldsymbol{D}_s)^{-1}\boldsymbol{D}_{st},$$
$$\overline{\boldsymbol{D}}_t = \boldsymbol{D}_t - (\boldsymbol{D}_{st})^{\mathrm{T}}(\boldsymbol{D}_s)^{-1}\boldsymbol{D}_{st} \tag{20}$$

Substituting Equation (20) into Equation (14), we obtain

$$U_{2D} = \frac{1}{2}\left\langle (\boldsymbol{\gamma} + x_3\boldsymbol{\kappa})^{\mathrm{T}}\overline{\boldsymbol{D}}_e(\boldsymbol{\gamma} + x_3\boldsymbol{\kappa})\right\rangle = \frac{1}{2}\begin{Bmatrix} \boldsymbol{\gamma} \\ \boldsymbol{\kappa} \end{Bmatrix}^{\mathrm{T}}\begin{bmatrix} \boldsymbol{A} & \boldsymbol{B} \\ \boldsymbol{B}^{\mathrm{T}} & \boldsymbol{D} \end{bmatrix}\begin{Bmatrix} \boldsymbol{\gamma} \\ \boldsymbol{\kappa} \end{Bmatrix}$$

$$= \frac{1}{2}\begin{Bmatrix} \gamma_{11} \\ \gamma_{22} \\ 2\gamma_{12} \\ \kappa_{11} \\ \kappa_{22} \\ 2\kappa_{12} \end{Bmatrix}^{\mathrm{T}}\begin{bmatrix} A_{11} & A_{12} & A_{16} & B_{11} & B_{12} & B_{16} \\ A_{12} & A_{22} & A_{26} & B_{12} & B_{22} & B_{26} \\ A_{16} & A_{26} & A_{66} & B_{16} & B_{26} & B_{66} \\ B_{11} & B_{12} & B_{16} & D_{11} & D_{12} & D_{16} \\ B_{12} & B_{22} & B_{26} & D_{12} & D_{22} & D_{26} \\ B_{16} & B_{26} & B_{66} & D_{16} & D_{26} & D_{66} \end{bmatrix}\begin{Bmatrix} \gamma_{11} \\ \gamma_{22} \\ 2\gamma_{12} \\ \kappa_{11} \\ \kappa_{22} \\ 2\kappa_{12} \end{Bmatrix} \tag{21}$$

where $\boldsymbol{A}$, $\boldsymbol{D}$ and $\boldsymbol{B}$ are tensile, bending, and coupling stiffness sub-matrices, respectively, and can be expressed as

$$\boldsymbol{A} = \left\langle\left\langle \overline{\boldsymbol{D}}_e\right\rangle\right\rangle, \boldsymbol{B} = \left\langle\left\langle x_3\overline{\boldsymbol{D}}_e\right\rangle\right\rangle, \boldsymbol{D} = \left\langle\left\langle x_3^2\overline{\boldsymbol{D}}_e\right\rangle\right\rangle,$$
$$\overline{\boldsymbol{D}}_e = \boldsymbol{D}_e - \overline{\boldsymbol{D}}_{es}\boldsymbol{D}_s^{-1}\boldsymbol{D}_{es}^{\mathrm{T}} - \overline{\boldsymbol{D}}_{et}\boldsymbol{D}_{et}^{\mathrm{T}}/\overline{\boldsymbol{D}}_t \tag{22}$$

The stiffness matrix provides the essential information of 3D-TCP and may be easily utilized in the shell elements in a finite element software to perform macroscopic plate analysis. Because it only concerns the 2D field variables in terms of the macro-coordinates x_1 and x_2, the macroscopic behavior of the plate is governed by the the strain energy in Equation (21). As a result, the 2D-EPM may be used to represent the original 3D-TCP in the global analysis, and can be solved using the linear analysis solver in a finite element soft package like ABAQUS/Standard.

2.2. Local Field Analysis

A well-established equivalent model may be applied not only to global analysis, but also to local field analysis. To improve the equivalent model, the local field recovery relations should be given.

Equation (3) may be used to recover the local 3D displacement field, such as

$$
u_i = \bar{u}_i + \begin{bmatrix} \bar{u}_{1,1} & \bar{u}_{1,2} & \bar{u}_{1,3} \\ \bar{u}_{2,1} & \bar{u}_{2,2} & \bar{u}_{2,3} \\ \bar{u}_{3,1} & \bar{u}_{3,2} & \bar{u}_{3,3} \end{bmatrix} \left\{ \begin{array}{c} y_1 \\ y_2 \\ y_3 \end{array} \right\} + \zeta w_i \tag{23}
$$

The local strain field can be recovered as

$$
\mathcal{E}_e^0 = \gamma + x_3 \kappa, \quad 2\mathcal{E}_s^0 = -w_{||,3}, \quad \mathcal{E}_t^0 = w_{3,3} \tag{24}
$$

The Hooke's law may be used to recover the local stress field as

$$
\sigma = \overline{D}\mathcal{E} \tag{25}
$$

3. Validation Example

In this part, numerical examples of bending, buckling, and free vibration of 3D-TCP under various conditions are utilized to validate the accuracy and efficiency of 2D-EPM. The comparative analysis is depicted in Figure 2. The relative error between 2D-EPM and 3D-FEM is calculated as

$$
Error = \frac{|\, 2D - EPM \text{ results} - 3D - FEM \text{ results} \,|}{3D - FEM \text{ results}} \times 100\%. \tag{26}
$$
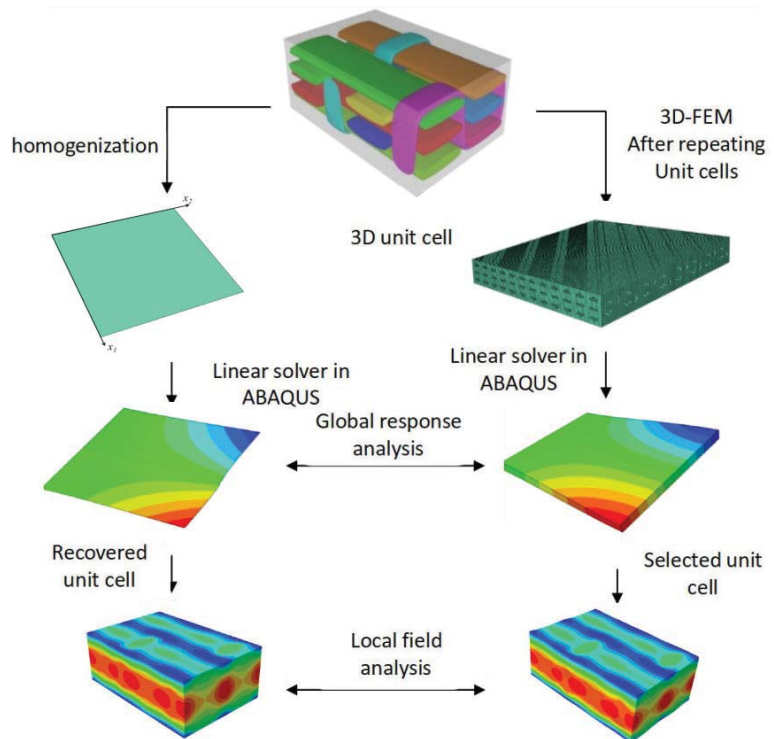
Figure 2. Comparative analysis of 2D-EPM and 3D-FEM.

The microstructure of 3D textile composite plate as shown in Figure 3 is very complex, including three layers with two weft yarns in each layer, two layers with two warp yarns in each layer and two binder yarns. The geometry of unit cell is determined by several parameters as shown in Figure 4: (1) the interval t between layers along the Z direction; (2) the interval length l_1 between the weft yarns along the Y direction; (3) the interval length l_2 between the warp yarns along the X direction, where $l_2 = nl_1$ ($n < 1$); (4) the warp or weft yarn width b_1 and the thickness h_1; and (5) the binder yarn width $b_2 = nb_1$ and the thickness $h_2 = 0.5h_1$. The X, Y and Z direction of the unit cell are the same as y_1, y_2 and y_3 in the theoretical derivation, respectively.
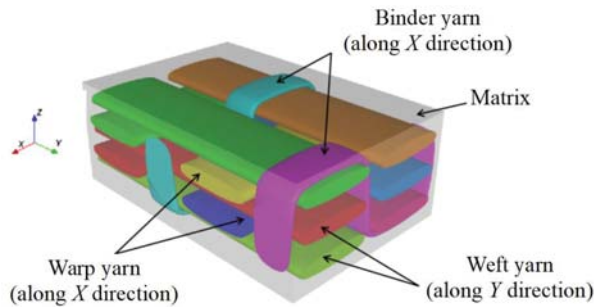
Figure 3. The unit cell of 3D textile composite plate.

(a)

(b)
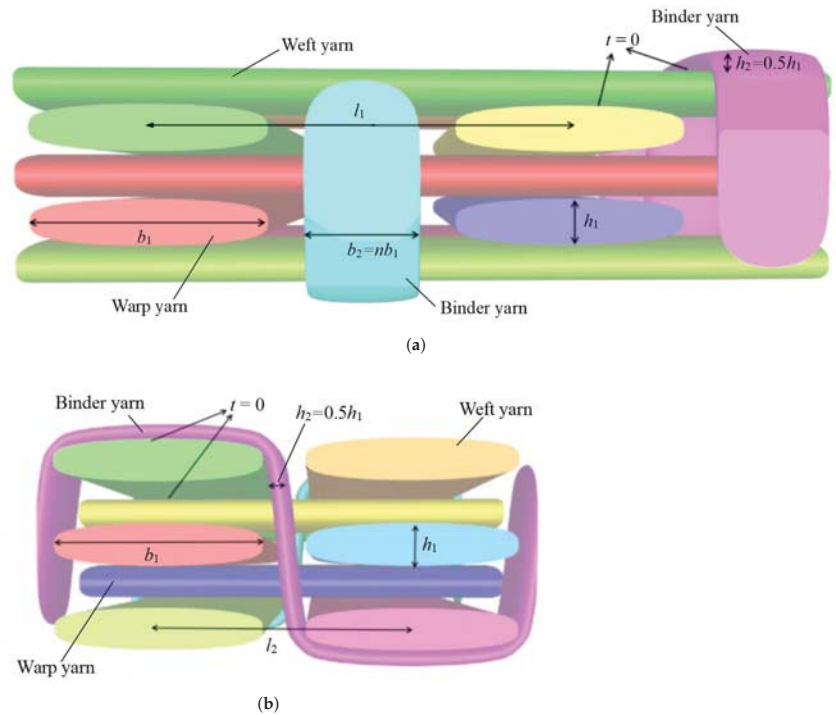
Figure 4. Structural parameters of unit cell within the 3D-TCP. (**a**) Y direction; (**b**) X direction.

In this section, these parameters are set as: $b_1 = 0.8$, $h_1 = 0.2$ mm, $l_1 = 1.2$ mm, $b_2 = 0.4$ mm, $h_2 = 0.1$ mm, $l_2 = 1.0$ mm, and $t = 0$ mm. The dimensions of unit cell are 3.6 mm $\times$ 2.4 mm $\times$ 1.32 mm. The constituents in the composite material are carbon

fiber (T-300) and epoxy resin 3601, and their properties are obtained from ref. [35], as shown in Table 1. The yarn has elliptical cross-section as shown in Figure 5b, and usually modeled as unidirectional composites with hexagonal pack as shown in Figure 5a. The variational asymptotic homogenization method is used to obtain the equivalent engineering constants of the yarn with 64% fiber volume fraction, as shown in Table 2. The geometry model of unit cell within the 3D-TCP is generated by open source TexGen software. The yarns and matrix, as well as the yarns themselves, are linked by common nodes, indicating that different parts are perfectly connected. The equivalent stiffness matrix of 3D-TCP obtained by the present model is provided in Table 3.

(a) Unit cell of yarn   (b) Cross section of the yarn
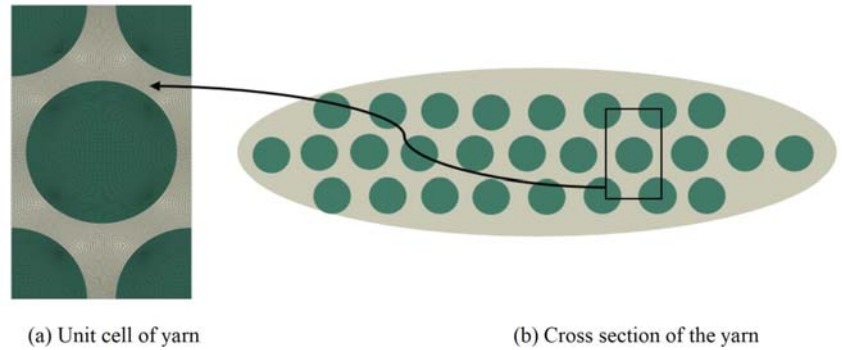
Figure 5. Unit cell model of the yarn.

Table 1. Constituent properties of matrix and fiber used in the yarn [35].

Constituent Proprties	Epoxy Resin-3601	Carbon FibreT-300
Elastic modulus E_1/GPa	4.51	208.8
Elastic modulus $E_2 = E_3$/GPa	4.51	43
Shear modulus $G_{12} = G_{13}$/GPa	1.7	7.42
Shear modulus G_{23}/GPa	1.7	7.42
Poisson's ratio $v_{12} = v_{13}$	0.38	0.2
Poisson's ratio v_{23}	0.38	0.5

Table 2. Equivalent engineering constants of the yarn with a fiber volume fraction of 64%.

Equivalent Engineering Constants	Values
Elastic modulus E_1/GPa	135.28
Elastic modulus $E_2 = E_3$/GPa	15.21
Shear modulus $G_{12} = G_{13}$ /GPa	3.99
Shear modulus G_{23}/GPa	3.97
Poisson's ratio $v_{12} = v_{13}$	0.26
Poisson's ratio v_{23}	0.51

Table 3. Equivalent stiffness matrix of 3D-TCP (unit: SI).

Equivalent Stiffness Matrix of 3D-TCP					
31,093.30	2999.61	0	15,546.70	1499.81	0
2999.61	10,674.90	0	1499.81	5337.46	0
0	0	2944.26	0	0	1472.13
15,546.70	1499.81	0	10,415.50	1162.04	0
1499.81	5337.46	0	1162.04	4072.26	0
0	0	1472.13	0	0	1130.14

The unit cell is repeated 12 times in the X direction and 8 times along the Y direction to construct the 3D-FEM of a 3D textile composite plate. The dimensions of this plate are 28.8 mm long, 28.8 mm wide, and 1.32 mm thick, respectively. After the mesh convergence study, a total of 10,609 shell elements (S4R) and 288,000 solid elements (C3D20) are used in 2D-EPM and 3D-FEM, respectively.

3.1. Bending Analysis

Three combinations of boundary and load conditions in Figure 6 are used in bending analysis, in which C represents clamped boundary, F for free boundary, and Path represents the comparative analysis path. Table 4 shows the bending behaviors predicted by 3D-FEM and 2D-EPM under various conditions.
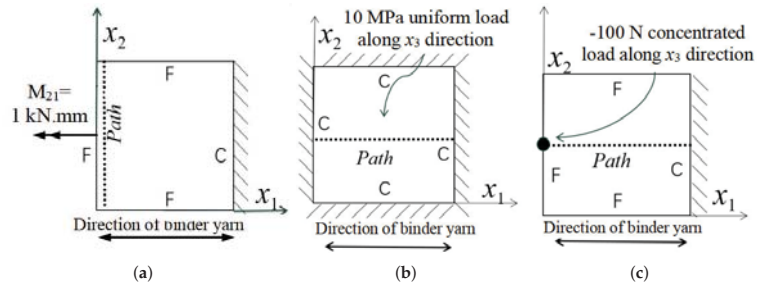
Figure 6. Combinations of boundary and load conditions for bending analysis. (**a**) Case 1; (**b**) Case 2; and (**c**) Case 3.

Table 4. Comparison of displacement U_3 predicted by two models under various boundary and load conditions (unit: mm).
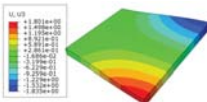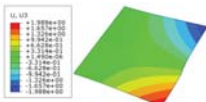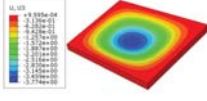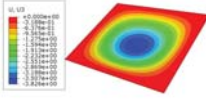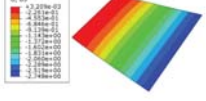
Case	3D-FEM	2D-EPM	Max. Error
Case 1	U_3=−1.835mm; time=465s	U_3=−1.988mm; time=21s	7.70%
Case 2	U_3=−3.77mm; time=427s	U_3=−3.826mm; time=16s	1.36%
Case 3	U_3=−2.668mm; time=442s	U_3=−2.748mm; time=20s	2.91%

Table 4 shows that the displacement clouds of U_3 predicted by the two models are consistent, and the maximum error is 7.70% in Case 1, which may due to the fact that the shear strain is negligible in Case 2 and Case 3, but relatively large in Case 1. To more clearly illustrate the details of the displacement distributions (especially out-of-plane distributions), the displacement of U_3 along the analysis path are compared in Figure 7. It can be observed that the displacement error between 3D-FEM and 2D-EPM is relatively very small even for 3D-TCP with complex microstructures, and the displacement curve of 3D-FEM is smoother than that of 2D-EPM. The main reason is that there is only one node in x_3 direction of

2D-EPM under bending load, which can not smoothly simulate the continuous deformation along the thickness direction.

(a)

(b)

(c)
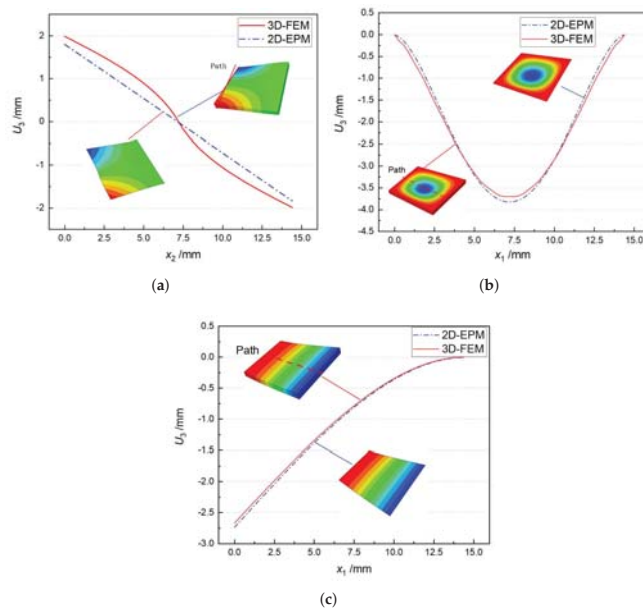
Figure 7. Comparison of displacements along analysis paths under various boundary and load conditions. (**a**) Case 1; (**b**) Case 2; and (**c**) Case 3.

3.2. Local Field Recovery

The internal structure of 3D-TCP is complex, and the warp yarns, weft yarns and binder yarns are intertwined with each other. The study of the local stress, strain and displacement distributions is of significance to the failure analysis of textile structures. In this section, the local fields within the unit cell at the center of the plate are recovered under the conditions in Case 2. Two paths (as shown in Figure 8) are selected to analyze the local stress, strain and displacement distribution.

(a)

(b)
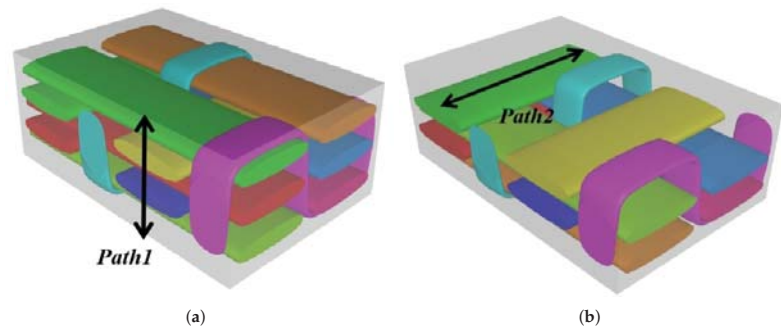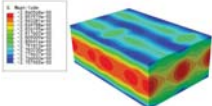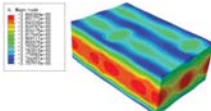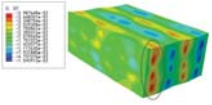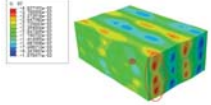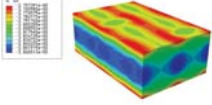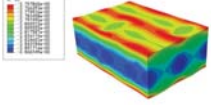
Figure 8. Path selection in local field recovery analysis. (**a**) Path 1 along the *Z* direction; and (**b**) Path 2 along the *Y* direction.

The local displacement distributions within the recovered unit cell from 2D-EPM are similar with those in the selected unit cell from 3D-FEM, as shown in Table 5, with a maximum error of 1.18%. Figure 9a shows that the maximum displacement of *U* is located in the middle of Path 1, where the displacements of weft yarns are greater than those of

matrix. Figure 9b shows that the curve of U along Path 2 is divided into two segments with a length of 1.2 mm (the interval length between the weft yarns). The larger value of U is located in the suspended area between the weft yarns, while the smaller value of U is located at 0.5 mm and 1.7 mm of Path 2, which belongs to the superimposed area of the warp yarns and weft yarns. The local stress distributions within the recovered unit cell from 2D-EPM are similar with those in the selected unit cell from 3D-FEM, as shown in Table 6, and the maximum error is is 5.17% in σ_{22}, indicating that the recovered local stress fields from 2D-EPM are accurate.

Table 5. Comparison of local displacement field within the unit cell under the conditions in Case 2 (unit: mm).

Displacement	Selected Unit Cell	Recovered Unit Cell	Max. Error
U			0.35%
U_2			1.18%
U_3			0.12%
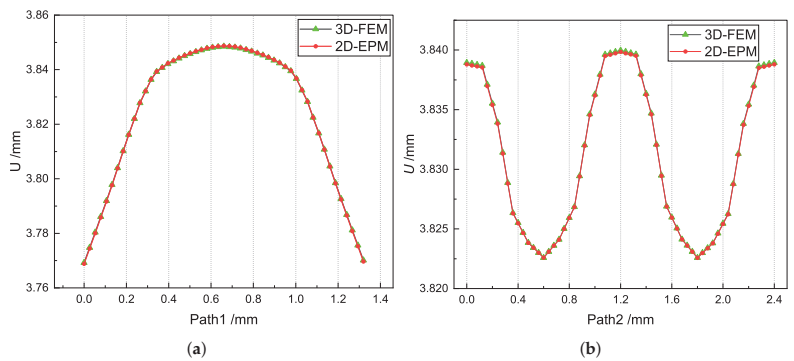
Figure 9. Comparison of local displacement curves along Path 1 and Path 2 of the unit cell predicted by two models under the conditions in Case 2. (**a**) U along Path 1; (**b**) U along Path 2.

Table 6. Comparison of local stress field within the unit cell under the conditions in Case 2 (unit: MPa).
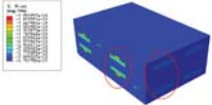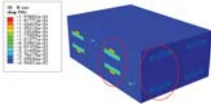
Stress	Selected Unit Cell	Recovered Unit Cell	Max. Error
Von Mises			0.70%

Table 6. *Cont.*
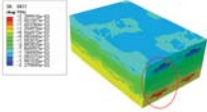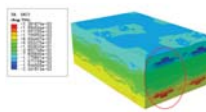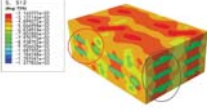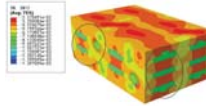
Stress	Selected Unit Cell	Recovered Unit Cell	Max. Error
σ_{22}			0.85%
σ_{12}			5.17%

Figure 10a,c show that the curves of von Mises stress and σ_{11} along Path 1 are divided into five segments, representing two layers of warp yarns and three layers of matrix, respectively. The local stresses are distributed unevenly within the unit cell of 3D-TCP. The local stress in the matrix is relatively small, while the local stress in the warp yarns fluctuates greatly, indicating that the yarns along the thickness direction are main bearing components. Figure 10b,d show that the curves of von Mises stress and σ_{22} along Path 2 are also divided into five sections. The stress at the superimposed area of warp yarns and weft yarns (0.25–0.95 mm, 1.45–2.15 mm) is relatively small, while the stress in the suspended area of the weft yarns fluctuates greatly, which indicates that it is easy to be damaged under the loading.
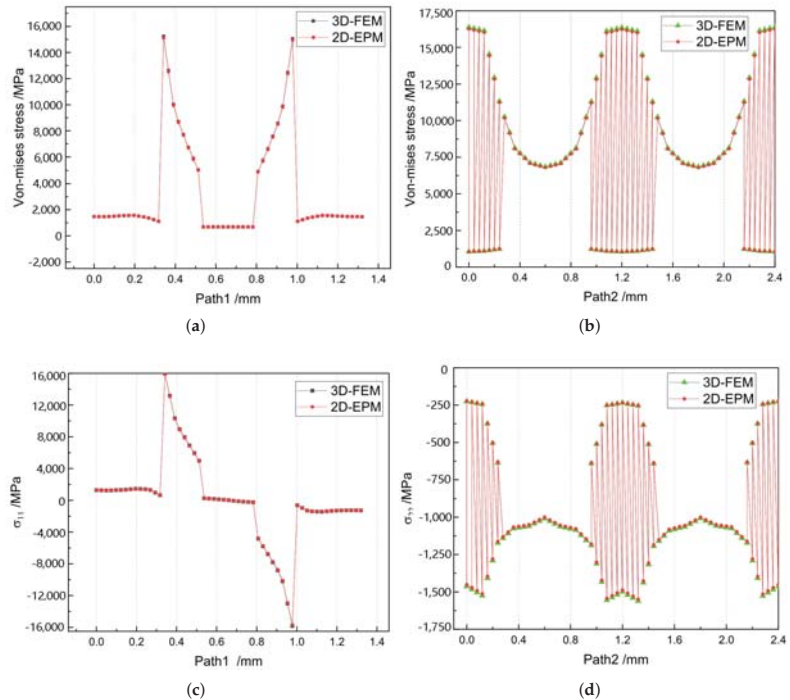
Figure 10. Comparison of local stress distributions along Path 1 and Path 2 of the unit cell predicted by two models under the conditions in Case 2. (**a**) Von mises stress along Path 1; (**b**) Von mises stress along Path 2; (**c**) σ_{11} along Path 1; and (**d**) σ_{22} along Path 2.

Table 7 shows that the local strain distributions are consistent with those of local stress distributions, and the error of local strain between recovered unit cell and selected unit cell is less than 1%. Figure 11 shows the local strain distributions along Path 1 and Path 2 of the unit cell predicted by two models under the conditions in Case 2. It can be observed that the local strain distributions within the unit cell of 3D-TCP are non-homogeneous. The strain curves are divided into several segments due to the interpenetration of warp yarn, weft yarn and matrix.
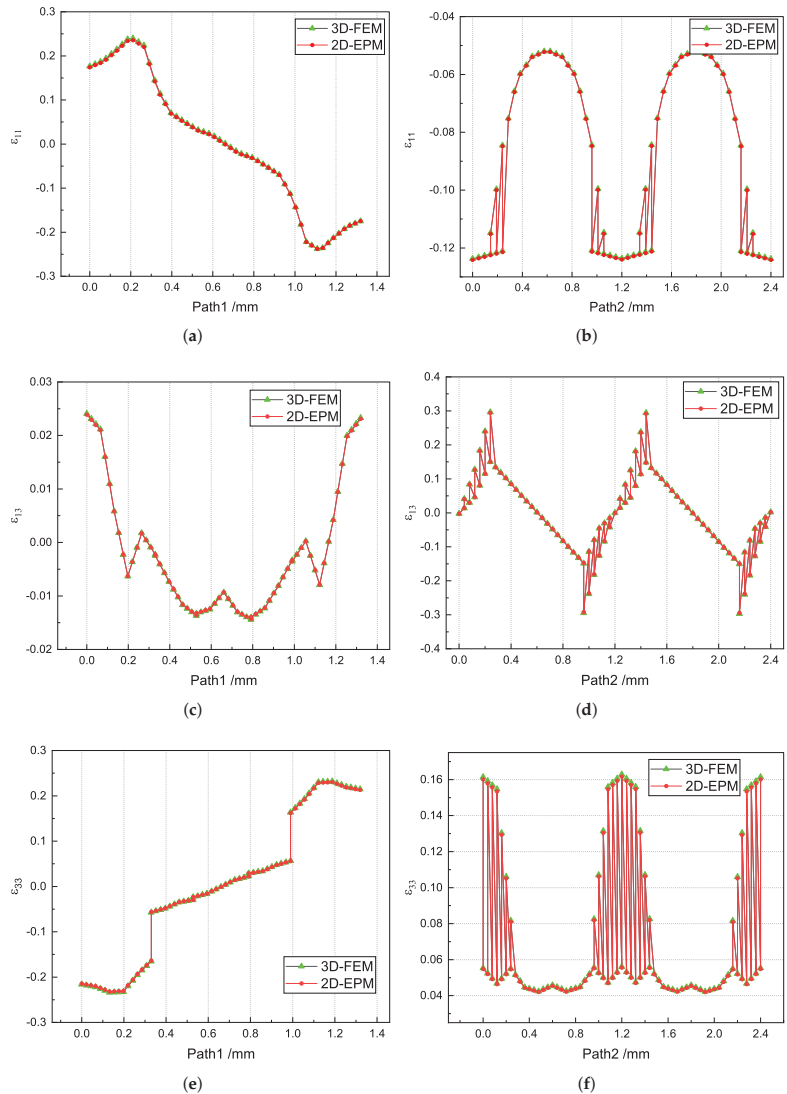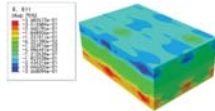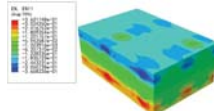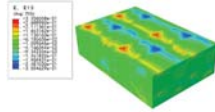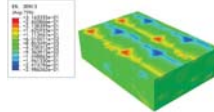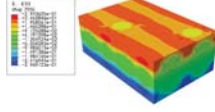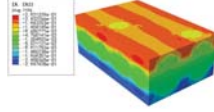
Figure 11. Comparison of local strain curves along Path 1 and Path 2 of the unit cell predicted by two models under the conditions in Case 2. (**a**) ε_{11} along Path 1; (**b**) ε_{11} along Path 2; (**c**) ε_{13} along Path 1; (**d**) ε_{13} along Path 2; (**e**) ε_{33} along Path 1; and (**f**) ε_{33} along Path 2.

Table 7. Comparison of local strain field within the unit cell under the conditions in Case 2.

Stress	Selected Unit Cell	Recovered Unit Cell	Max. Error
ε_{11}			0.92%
ε_{13}			0.91%
ε_{33}			0.75%

3.3. Global Buckling Analysis

In this section, the global buckling of 3D-TCP under different conditions shown in Figure 12 is analyzed. The opposite sides of the 2D-EPM are subjected to a linear load of 1 N/mm, whereas the opposite sides of the 3D-FEM are subjected to a uniform stress of 1/0.22 = 4.5455 MPa.
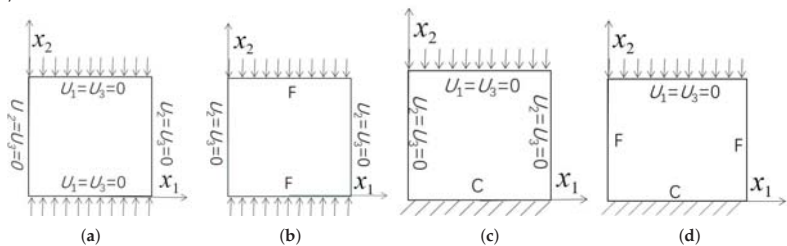
Figure 12. Boundary and load conditions used in bucking analysis. (**a**) Case 4; (**b**) Case 5; (**c**) Case 6; and (**d**) Case 7.

Table 8 lists the first six buckling modes and loads of 3D-TCP predicted by the two models under the conditions in Case 6. The first six buckling modes predicted by 3D-FEM and 2D-EPM are consistent, and the maximum error of buckling critical load in each buckling mode is only 2%. The calculation time of 2D-EPM in buckling analysis is about 18 times faster than 3D-FEM, verifying the effectiveness of 2D-EPM in global buckling analysis of 3D-TCP.

Table 8. Comparison of the buckling modes and critical loads (N) between 3D-FEM and 2D-EPM under the conditions in Case 6.
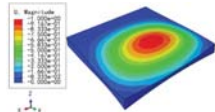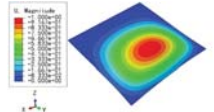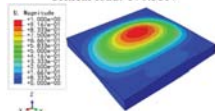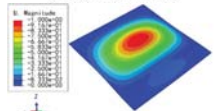
Order	3D-FEM	2D-EPM	Max. Error
1	 Critical load: 170.55N	 Critical load: 174.13N	2.06%
2	 Critical load: 173.15N	 Critical load: 176.78N	2.10%

Table 8. *Cont.*
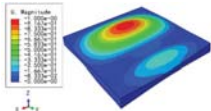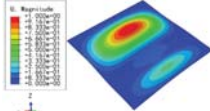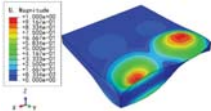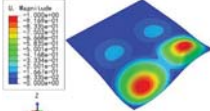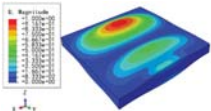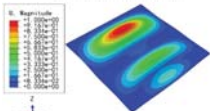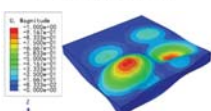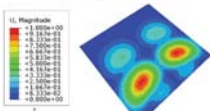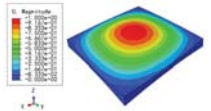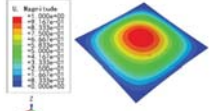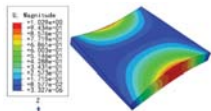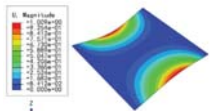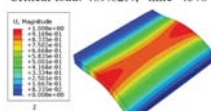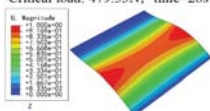
Order	3D-FEM	2D-EPM	Max. Error
3	Critical load: 441.50N	Critical load: 450.77N	2.18%
4	Critical load: 443.64N	Critical load: 452.96N	2.06%
5	Critical load: 1×483.87N	Critical load: 1×494.03N	2.10%
6	Critical load: 1×729.87N	Critical load: 1×745.20N	2.06%

Table 9 lists the first buckling modes and critical loads predicted by the two models under the conditions in Case 4, Case 5 and Case 7. The first buckling modes predicted by the two models are nearly identical, and the maximum error of the buckling load is only 2.69%, which verifies the accuracy of 2D-EPM in buckling analysis of 3D-TCP under different conditions.

Table 9. Comparison of the first buckling modes and critical loads (N) of 3D-TCP in different cases predicted by two models.

Case	3D-FEM	2D-EPM	Max. Error
Case 4	Critical load: 409.60N; time=416s	Critical load: 400.00N; time=22s	2.40%
Case 5	Critical load: 489.62N; time=457s	Critical load: 479.55N; time=28s	2.09%
Case 7	Critical load: 132.69N; time=441s	Critical load: 129.21N; time=26s	2.69%

3.4. Free-Vibration Analysis

Tables 10 and 11 show the first three vibration modes and natural frequencies of 3D-TCP under the boundary conditions in Cases 4 and 7. It is clear that the vibration modes

predicted by 2D-EPM agree with those predicted by 3D-FEM. For example, the first, second buckling modes, respectively, have one and two half-waves along the x_1 axis, and the third buckling mode has two half-waves along the x_2 axis under the boundary condition in Case 4. The maximum natural frequency error is 8.67%, indicating 2D-EPM has high accuracy in free-vibration analysis of 3D-TCP.

Table 10. Comparison of the first three free vibration characteristics predicted by two models under the boundary condition in Case 4.
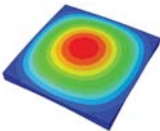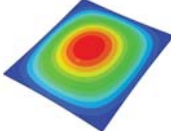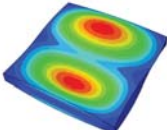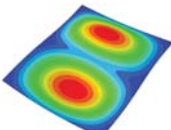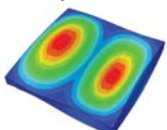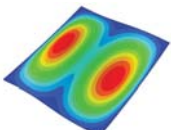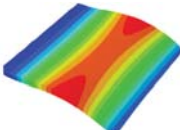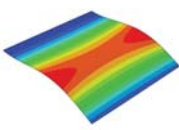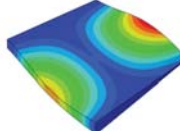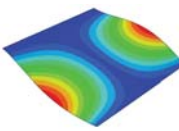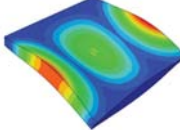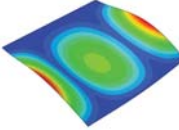
Order	3D-FEM	2D-EPM	Max. Error
1	Freq: 161.85Hz	Freq: 163.30Hz	0.90%
2	Freq: 362.61Hz	Freq: 358.42Hz	1.17%
3	Freq: 434.32Hz	Freq: 457.55Hz	5.08%

Table 11. Comparison of the first four free vibration characteristics predicted by two models under the boundary condition in Case 7.

Order	3D-FEM	2D-EPM	Max. Error
1	Freq: 123.01Hz	Freq: 119.18Hz	3.21%
2	Freq: 161.63Hz	Freq: 148.73Hz	8.67%
3	Freq: 322.67Hz	Freq: 317.58Hz	1.58%

4. Influence of Structural Parameters on Equivalent Stiffness

The structure of 3D-TCP is complex and has many parameters (see Figure 3). In Section 3.2, we can see that the local stress and strain in binder yarns are relatively greater, indicating the binder yarns plays a very important role in preventing interlayer separation in 3D-TCP. Therefore, it is very important to study the influence of binder yarn width on the equivalent stiffness, which can also provide guidance for the design of 3D-TCP. Secondly, the influence of warp (weft) yarn width on the equivalent stiffness are also investigated. Table 12 lists the structural parameters of 3D-TCP used in the parameter analysis.

Table 12. Structural parameters of 3D-TCP used in the parameter analysis.

Warp or Weft Yarn Parameters			Binder Yarn Parameters		
b_1	h_1	l_1	b_2	h_2	l_2
0.7~1.1 mm	0.2 mm	1.2 mm	$n \times 1.0$ mm [1]	0.1 mm	$n \times 1.2$ mm

[1] n is the multiplier, and can be chosen as eight different values: 0.2, 0.3, 0.4, 0.5, 0.6, 0.7, 0.8 and 0.9, respectively.

Figures 13 and 14 show that the binder width and warp (weft) width have great influence on the equivalent tensile stiffness A_{11} and bending stiffness D_{11}. The values of A_{11} and D_{11} increase with the increasing warp (weft) width, but decrease with the increasing binder width. The main reason is that the increase of binder width will lead to the decrease of yarn content, further resulting in the decrease of A_{11} and D_{11}. However, the smaller the binder yarn width is, the smaller the constraint in the thickness direction will be, resulting in the easy delamination. Therefore, the binder yarn width should be adjusted to ensure enough stiffness and integrity in the design of 3D-TCP.
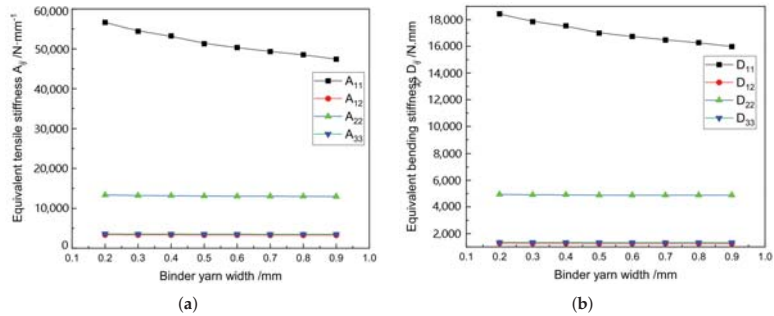
Figure 13. Influence of the binder yarn width on equivalent stiffness of 3D-TCP. (**a**) A_{ij}; (**b**) D_{ij}.
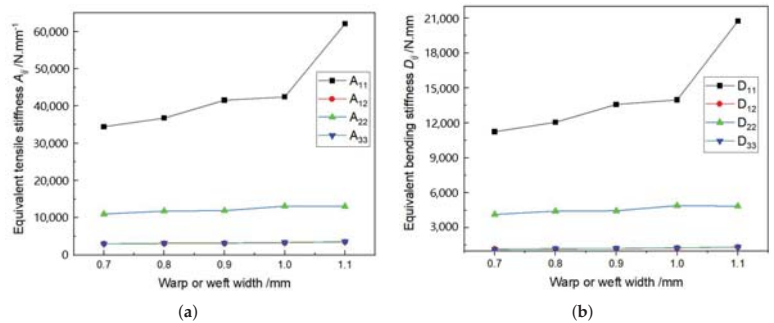
Figure 14. Influence of the warp (weft) yarn width on equivalent stiffness of 3D-TCP. (**a**) A_{ij}; (**b**) D_{ij}.

5. Comparison of Effective Performance between 2D-PWL and 3D-TCP with the Same Thickness

The 3D-TCP is developed from the 2D plain-woven laminate (2D-PWL), and has better mechanical properties. To compare the effective performance of the two textile composite plate, we establish the 2D-EPM of 2D-PWL and 3D-TCP with the same plate thickness and yarn content.

The structure parameters of unit cell within the 6-layered 2D-PWL as shown in Figure 15 are: $L = 1.2$ mm, $D = 0.8$ mm, $H = 0.2$ mm. The structure parameters of unit cell within the 3D-TCP are: $b_1 = 1.0$ mm, $h_1 = 0.2$ mm, $l_1 = 1.2$ mm, $b_2 = 0.6$ mm, $h_2 = 0.1$ mm, $l_2 = 1.2$ mm, $t = 0$ mm. The thickness of both plates is 1.32 mm and the yarn content is 50.47%. The obtained equivalent stiffness matrix of 2D-PWL and 3D-TCP are shown in Tables 13 and 14, respectively. Based on the equivalent stiffness matrix, the 2D-EPM of 150 mm × 150 mm is established to study the difference of effective performance between 2D-PWL and 3D-TCP.
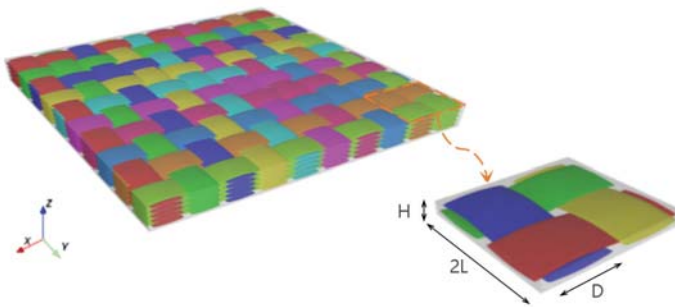
Figure 15. The 6-layered 2D plain-woven laminate.

Table 13. Equivalent stiffness matrix of 2D-PWL (unit: SI).

Equivalent Stiffness Matrix of 2D-PWL					
58,549.00	3208.21	0.00	35,129.40	1924.92	0.00
3208.21	12,037.40	0.00	1924.92	7222.47	0.00
0.00	0.00	3219.44	0.00	0.00	1931.66
35,129.40	1924.92	0.00	27,994.70	1541.54	0.00
1924.92	7222.47	0.00	1541.54	5787.12	0.00
0.00	0.00	1931.66	0.00	0.00	1555.76

Table 14. Equivalent stiffness matrix of 3D-TCP (unit: SI).

Equivalent Stiffness Matrix of 3D-TCP					
45,677.30	15,832.30	0.00	0.00	0.00	−1884.16
15,832.30	17,592.60	0.00	0.00	0.00	−548.05
0.00	0.00	15,615.30	−1884.16	−548.05	0.00
0.00	0.00	−1884.16	9744.50	3377.56	0.00
0.00	0.00	−548.05	3377.56	3753.08	0.00
−1884.16	−548.05	0.00	0.00	0.00	3331.27

5.1. Comparison of Bending Behaviors

The boundary conditions used in bending analysis are shown in Figure 16, and the predicted bending displacements are shown in Table 15. It can be observed that the bending displacement of 3D-TCP is greater than that of 2D-PWL under uniform load (Case 8 and Case 9). This may due to the fact that the warp yarns and weft yarns of 3D-TCP are not interlaced, and are only constrained by the binding yarns in the thickness direction. While

the displacement of 3D-TCP is smaller than that of 2D-PWL under the concentrated force and bending moment (Case 10 and Case 11), indicating that the torsion resistance of 3D-TCP are better than 2D-PWL. The above results are consistent with the obtained equivalent stiffness in Tables 13 and 14. That is, the bending stiffness D_{11} and D_{22} of 2D-PWL are greater than those of 3D-TCP, while the torsional stiffness D_{66} of 2D-PWL is smaller than that of 3D-TCP.
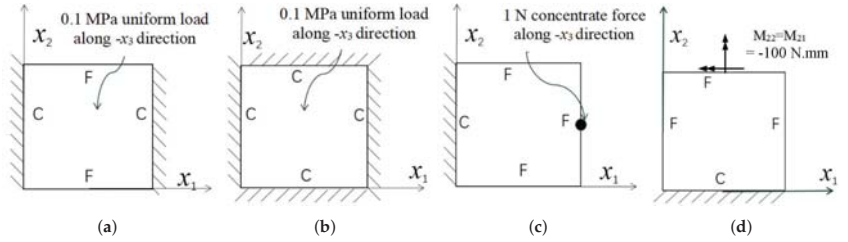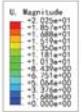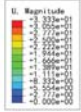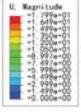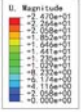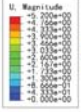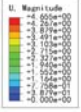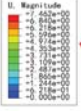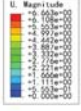
Figure 16. Boundary and load conditions for bending behavior analysis of 2D-PWL and 3D-TCP. (**a**) Case 8; (**b**) Case 9; (**c**) Case 10; (**d**) Case 11.

Table 15. Comparison of bending displacement between 3D-TCP and 2D-PWL under different conditions.
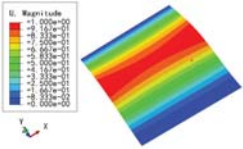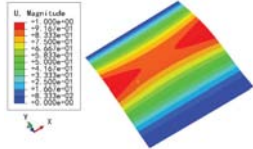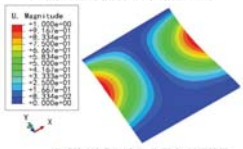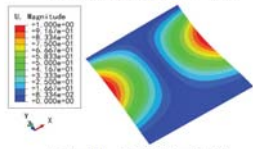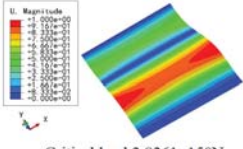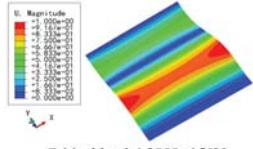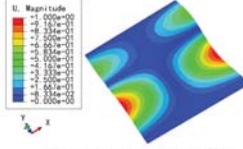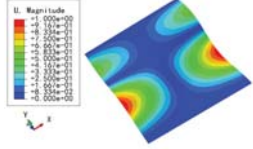
Cases	2D-PWL	3D-TCP
Case 8	*U*=20.25mm	*U*=32.33mm
Case 9	*U*=17.99mm	*U*=24.70mm
Case 10	*U*=5.20mm	*U*=4.66mm
Case 11	*U*=7.46mm	*U*=6.66mm

5.2. Comparison of Buckling Modes

Table 16 shows the first four buckling modes predicted by 2D-PWL and 3D-TCP under the conditions in Case 7. It can be observed that the buckling modes predicted by 2D-PWL and 3D-TCP are almost the same. That is, the first and third buckling modes, respectively, have one and two half-waves along the *Y* direction, and the second buckling mode has two half-waves along the *X* direction, the fourth buckling mode has two asymmetric half-waves

along the *X* and *Y* directions. It is worth noting that the first four critical loads of 3D-TCP are greater than 2D-PWL, indicating that 3D-TCP has better stability under lateral load.

Table 16. Comparison of the first four buckling modes between 3D-TCP and 2D-PWL under the conditions in Case 7.

Order	2D-PWL	3D-TCP
1	Critical load:1.2938×150N	Critical load:1.4442×150N
2	Critical load:2.1603×150N	Critical load:2.4323×150N
3	Critical load:3.8361×150N	Critical load:4.2899×150N
4	Critical load:4.7188×150N	Critical load:5.2954×150N

5.3. Comparison of Free-Vibration Characteristics

The first vibration mode and natural frequency of 2D-PWL and 3D-TCP under different boundary conditions in Figure 12 are compared as shown in Table 17. The vibration modes of 3D-TCP are consistent with those of 2D-PWL, while the natural frequency of 3D-TCP is smaller than that of 2D-PWL, which is consistent with the obtained equivalent stiffness.

Table 17. Comparison of the first vibration modes and natural frequencies (Hz) predicted by 2D-PWL and 3D-TCP under different boundary conditions.
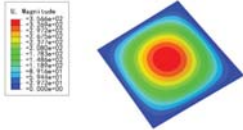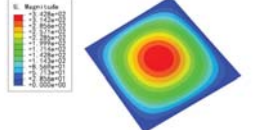
Case	2D-PWL	3D-TCP
Case 4	Freq=193.34Hz	Freq=166.20 Hz

Table 17. *Cont.*

Case	2D-PWL	3D-TCP
Case 6	Freq=214.32Hz	Freq=191.07Hz
Case 7	Freq=110.78Hz	Freq=112.5Hz
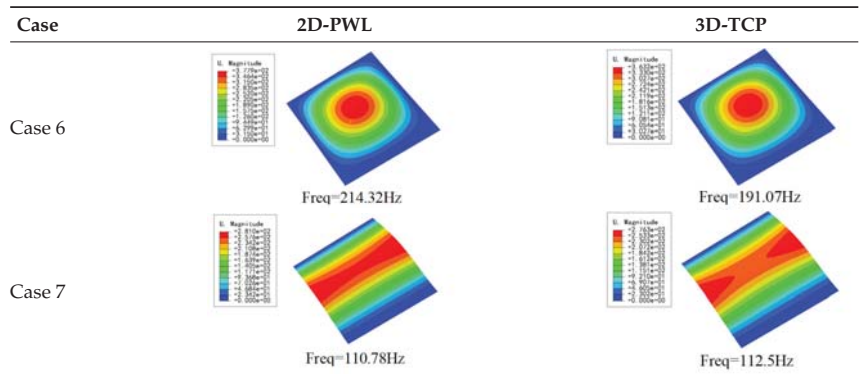
6. Conclusions

The VAM-based equivalent model (2D-EPM) of 3D textile composite plate is established for bending, buckling and free-vibration analysis. The following conclusions can be obtained:

(1) The maximum errors of bending displacement and buckling load between 3D-FEM and 2D-EPM are within the range of engineering accuracy, and the displacement distributions along the analysis path predicted by two models have the same trend with small differences. Furthermore, the local stress, strain and displacement distributions within the recovered unit cell are well captured. In addition, the computational efficiency of 2D-EPM is greatly improved by reducing the number of nodes and elements.

(2) The width of binder/warp yarn mainly affect the stiffness components A_{11} and D_{11}. That is, A_{11} and D_{11} increase with the increasing width of warp or weft yarn, while decrease with increasing width of binder yarn, which may due to the fact that the increasing width of binder yarn will decrease the yarn content.

(3) Compared with 2D plain-woven laminate with the same thickness and yarn content, the 3D textile composite plate has smaller equivalent bending stiffness and larger torsional stiffness, resulting in large displacement and small natural frequency. This may be because the 3D textile composite plate is only constrained by the binding yarns in the thickness direction, while the warp yarns and weft yarns are intertwined closely in the 2D-PWL.

Author Contributions: Individual contributions are as follows: conceptualization, S.X. and Y.Z. Investigation and writing; analysis, Y.Z. and Z.S. Revision, Q.Y. All authors have read and agreed to the published version of the manuscript.

Institutional Review Board Statement: Not applicable.

Informed Consent Statement: Not applicable.

Data Availability Statement: Data available on request due to restrictions, e.g., privacy or ethical. The data presented in this study are available on request from the corresponding author. The data are not publicly available due to subsequent analyzes and publications.

Conflicts of Interest: The authors declare no conflict of interest.

References

1. Almeida, J.H.S., Jr.; St-Pierre, L.; Wang, Z.; Ribeiro, M.L.; Tita, V.; Amico, S.C.; Castro, S.G. Design, modeling, optimization, manufacturing and testing of variable-angle filament-wound cylinders. *Compos. Part B Eng.* **2021**, *24*, 109224. [CrossRef]
2. Almeida, J.; Bittrich, L.; Euer, A.S.N. Improving the open-hole tension characteristics with variable-axial composite laminates: Optimization, progressive damage modeling and experimental observations. *Compos. Sci. Technol.* **2020**, *185*, 107889. [CrossRef]
3. Uhlig, K.; Bittrich, L.; Spickenheuer, A.; Almeida, J.H.S., Jr. Waviness and fiber volume content analysis in continuous carbon fiber reinforced plastics made by tailored fiber placement. *Compos. Struct.* **2019**, *222*, 110910. [CrossRef]
4. Stedile, P.; Almeida, J.H.S.; Amico, S.C. Carbon/epoxy filament wound composite drive shafts under torsion and compression. *J. Compos. Mater.* **2018**, *52*, 1103–1111. [CrossRef]
5. Marrey, R.V.; Sankar, B.V. A Micromechanical Model for Textile Composite Plates. *J. Compos. Mater.* **1997**, *31*, 1187–1213. [CrossRef]
6. Li, J.; Jiao, Y.; Sun, Y.; Wei, L. Experimental investigation of cut-edge effect on mechanical properties of three-dimensional braided composites. *Mater. Des.* **2007**, *28*, 2417–2424. [CrossRef]
7. Pastore, C.; Ko, F. Modeling of textile structural composites: Part 1: A processing science model for three dimensional braid. *J. Text. Inst.* **1990**, *81*, 480–490. [CrossRef]
8. Yang, J.; Ma, C.; Chou, T. Fiber inclination model of three dimensional textile structural composit. *J. Compos. Mater.* **1986**, *20*, 472–483. [CrossRef]
9. Wu, D. Three-cell model and SD braided structural composites. *Compos. Sci. Technol.* **1996**, *56*, 225–233. [CrossRef]
10. Wang, Y.; Wang, A. Microstructure/property relationships in three-dimensionally braided fiber composites. *Compos. Sci. Technol.* **1995**, *53*, 213–222. [CrossRef]
11. Wang, Y.; Wang, A. Geometric mapping of yarn structures in 3-D braided composites due to shape change. *Compos. Sci. Technol.* **1995**, *53*, 359–370. [CrossRef]
12. Liang, J.; Du, S.; Han, J. Effective elastic properties of- three dimensional braided composites with matrix microcracks. *Acta. Mater. Compos. Sin.* **1997**, *14*, 101–107.
13. Ishikawa, T.; Chou, T.W. Stiffness and strength behaviour of woven fabric composites. *J. Mater. Sci.* **1982**, *17*, 3211–3220. [CrossRef]
14. Chou, T.W.; Ishikawa, T. One-dimensional micromechanical analysis of woven fabric composites. *AIAA J.* **2012**, *21*, 1714–1721.
15. Srinivasan, R.S.; Thiruvenkatachari, V. Static and dynamic analysis of stiffened plates. *Comput. Struct.* **1985**, *21*, 395–403. [CrossRef]
16. Yan, T.G.; Ko, F.K.; Hu, H. Integrated Design For Manufacturing of Braided Preforms For Advanced Composites Part II: 3D Braiding. *Appl. Compos. Mater.* **2013**, *20*, 1007–1023.
17. Jiang, L.; Zeng, T.; Yan, S.; Fang, D. Theoretical prediction on the mechanical properties of 3D braided composites using a helix geometry model. *Compos. Struct.* **2013**, *100*, 511–516. [CrossRef]
18. Jin, T.; San Ha, N.; Le, V.T.; Goo, N.S.; Jeon, H.C. Thermal buckling measurement of a laminated composite plate under a uniform temperature distribution using the digital image correlation method. *Compos. Struct.* **2015**, *123*, 420–429. [CrossRef]
19. Pasupuleti, R.; Wang, Y.; Shabalin, I.; Li, L.Y.; Liu, Z.; Grove, S. Modelling of moisture diffusion in multilayer woven fabric composites. *Comput. Mater. Sci.* **2011**, *50*, 1675–1680. [CrossRef]
20. Desplentere, F.; Lomov, S.V.; Woerdeman, D.L.; Verpoest, I.; Wevers, M.; Bogdanovich, A. Micro-CT characterization of variability in 3d textile architecture. *Compos. Sci. Technol.* **2005**, *65*, 1920–1930. [CrossRef]
21. Badel, P.; Vidal-Sallé, E.; Boisse, P. Computational determination of in plane shear mechanical behaviour of textile composite reinforcements. *Comput. Mater. Sci.* **2007**, *40*, 439–448. [CrossRef]
22. Tan, H.; Liu, L.; Guan, Y.; Chen, W.; Zhao, Z. Investigation of three-dimensional braided composites subjected to steel projectile impact: Experimental study and numerical simulation. *Thin-Walled Struct.* **2019**, *140*, 144–156. [CrossRef]
23. Dong, J.W.; Feng, M.L. Asymptotic expansion homogenization for simulating progressive damage of 3D braided composites. *Compos. Struct.* **2010**, *92*, 873–882. [CrossRef]
24. Tang, X.; Whitcomb, J.D.; Kelkar, A.D. Progressive failure analysis of 2x2 braided composites exhibiting multiscale heterogeneity. *Compos. Sci. Technol.* **2006**, *66*, 2580–2590. [CrossRef]
25. Potluri, P.; Manan, A. Mechanics of non-orthogonally interlaced textile composites. *Compos. Part A Appl. Sci.* **2007**, *38*, 1216–1226. [CrossRef]
26. Berdichevskii, V. Variational-asymptotic method of constructing a theory of shells. *J. Appl. Math. Mec.* **1997**, *43*, 711–736. [CrossRef]
27. Hodges, D.H.; Atilgan, A.R.; Danielson, D.A. A Geometrically Nonlinear Theory of Elastic Plates. *J. Appl. Mech.* **1993**, *60*, 109–116. [CrossRef]
28. Hodges, D.H.; Lee, B.W.; Atilgan, A.R. Application of the variational asymptotical method to laminated composite plates. *AIAA J.* **1993**, *31*, 1674–1683. [CrossRef]
29. Sutyrin, V.G.; Hodges, D.H. On asymptotically correct linear laminated plate theory. *Int. J. Solids. Struct.* **1996**, *33*, 3649–3671. [CrossRef]
30. Sutyrin, V.G. Derivation of Plate Theory Accounting Asymptotically Correct Shear Deformation. *J. Appl. Mech.* **1997**, *64*, 905–915. [CrossRef]
31. Yu, W.; Hodges, D.H.; Volovoi, V.V. Asymptotically accurate 3-D recovery from Reissner-like composite plate finite elements. *Comput. Struct.* **2003**, *81*, 439–454. [CrossRef]

32. Yifeng, Z.; Lei, C.; Yu, W.; Liangliang, Z. Asymptotical construction of a fully coupled, Reissner-Mindlin model for piezoelectric and piezomagnetic laminates. *Compos. Struct.* **2012**, *94*, 3583–3591. [CrossRef]
33. Yifeng, Z.; Lei, C.; Yu, W.; Xiaopin, Z.; Liangliang, Z. Asymptotical construction of a Reissner-like model for multilayer functionally graded magneto-electroelastic plates. *Compos. Struct.* **2013**, *96*, 786–798. [CrossRef]
34. Zhong, Y.F.; Chen, L.; Yu, W. Variational asymptotic modeling of the thermomechanical behavior of composite cylindrical shells. *Compos. Struct.* **2012**, *94*, 1023–1031.
35. Kwok, K.; Pellegrino, S. Micromechanics models for viscoelastic plain-weave composite tape springs. *AIAA J.* **2016**, *55*, 309–321. [CrossRef]

MDPI

Article

Machine Learning Prediction Models to Evaluate the Strength of Recycled Aggregate Concrete

Xiongzhou Yuan [1], Yuze Tian [2,*], Waqas Ahmad [3,*], Ayaz Ahmad [3,4], Kseniia Iurevna Usanova [5], Abdeliazim Mustafa Mohamed [6,7] and Rana Khallaf [8]

[1] School of Traffic and Environment, Shenzhen Institute of Information Technology, Shenzhen 518172, China; couscous_yuan@sina.com
[2] School of Civil Engineering, University of Science and Technology Liaoning, Anshan 114051, China
[3] Department of Civil Engineering, COMSATS University Islamabad, Abbottabad 22060, Pakistan; ayazahmad@cuiatd.edu.pk
[4] MaREI Centre, Ryan Institute, School of Engineering, College of Science and Engineering, National University of Ireland, H91 TK33 Galway, Ireland
[5] Peter the Great St. Petersburg Polytechnic University, 195291 St. Petersburg, Russia; usanova_kyu@spbstu.ru
[6] Department of Civil Engineering, College of Engineering in Al-Kharj, Prince Sattam Bin Abdulaziz University, Al-Kharj 11942, Saudi Arabia; a.bilal@psau.edu.sa
[7] Building & Construction Technology Department, Bayan College of Science and Technology, Khartoum 11115, Sudan
[8] Structural Engineering and Construction Management, Faculty of Engineering and Technology, Future University in Egypt, New Cairo 11845, Egypt; rana.khallaf@fue.edu.eg
* Correspondence: 319933700033@ustl.edu.cn (Y.T.); waqasahmad@cuiatd.edu.pk (W.A.)

Abstract: Compressive and flexural strength are the crucial properties of a material. The strength of recycled aggregate concrete (RAC) is comparatively lower than that of natural aggregate concrete. Several factors, including the recycled aggregate replacement ratio, parent concrete strength, water–cement ratio, water absorption, density of the recycled aggregate, etc., affect the RAC's strength. Several studies have been performed to study the impact of these factors individually. However, it is challenging to examine their combined impact on the strength of RAC through experimental investigations. Experimental studies involve casting, curing, and testing samples, for which substantial effort, price, and time are needed. For rapid and cost-effective research, it is critical to apply new methods to the stated purpose. In this research, the compressive and flexural strengths of RAC were predicted using ensemble machine learning methods, including gradient boosting and random forest. Twelve input factors were used in the dataset, and their influence on the strength of RAC was analyzed. The models were validated and compared using correlation coefficients (R^2), variance between predicted and experimental results, statistical tests, and k-fold analysis. The random forest approach outperformed gradient boosting in anticipating the strength of RAC, with an R^2 of 0.91 and 0.86 for compressive and flexural strength, respectively. The models' decreased error values, such as mean absolute error (MAE) and root-mean-square error (RMSE), confirmed the higher precision of the random forest models. The MAE values for the random forest models were 4.19 MPa and 0.56 MPa, whereas the MAE values for the gradient boosting models were 4.78 MPa and 0.64 MPa, for compressive and flexural strengths, respectively. Machine learning technologies will benefit the construction sector by facilitating the evaluation of material properties in a quick and cost-effective manner.

Keywords: recycled aggregate concrete; sustainable aggregate; compressive strength; flexural strength; gradient boosting; random forest

1. Introduction

Numerous tests are performed to measure concrete performance, but compressive strength is frequently considered the most significant [1]. Compressive strength tests

offer good insight into the concrete's diverse properties. The compressive strength of concrete is directly or indirectly connected to a number of mechanical and durability properties [2]. Flexural strength is also a key characteristic to consider when designing structural concrete, since it has an effect on the flexural cracking, shear strength, deflection properties, and brittleness ratio of the concrete [3]. The compressive and flexural strength of recycled aggregate concrete (RAC) are reliant on a number of variables, including the mechanical and physical properties of the recycled aggregate used, as well as the microstructure of the resulting matrix [4]. Typically, RAC has an inferior compressive and flexural strength compared to natural aggregate concrete, owing to insufficient bonding between the aggregate and the old mortar, fractures and cracks in the recycled aggregate formed during the recycling procedure, and the presence of low-permeability mortar connected to the recycled aggregate [5–7]. Furthermore, the characteristics of RAC are reliant on the amount of recycled aggregate substituted and the moisture content [8,9]. The strength of RAC varies according to the recycled aggregate replacement ratio, the water–cement ratio (w/c), the recycled aggregate's moisture content, and the recycled aggregate's physical and mechanical properties [9,10]. When w/c is held constant, experimental data suggest that recycled aggregate replacement content has a significant effect on the strength of RAC [11,12]. When natural aggregate is totally replaced with recycled aggregate, the compressive strength of RAC can be reduced by up to 30% [13,14]. Similarly, other researchers discovered a drop in compressive strength of between 12% and 25% with 100% recycled aggregate incorporation [15,16]. It was discovered that the age of the waste concrete from which the recycled aggregate was manufactured had a substantial impact on the strength of the RAC [17]. Moreover, the strength of the parent concrete from which recycled aggregates are produced affects the strength of the RAC [18]. Hence, there are several factors that influence the strength of RAC, and to study their combined impact through experimental investigations is challenging. In contrast, using computational methods might better examine the combined influence of these factors on the strength of RAC.

The practice of developing models for forecasting the strength of concrete is ongoing in order to reduce unnecessary test repetitions and material waste. There are several prominent models for modeling concrete properties, such as best fit curves (based on regression analysis). However, due to the nonlinear behavior of concrete [19,20], regression models generated using this technique may not accurately represent the underlying nature of the material. Additionally, regression methods may understate the effect of constituent materials in concrete [21]. Artificial intelligence techniques such as machine learning are some of the more contemporary modeling techniques that have been used in the area of civil engineering. These approaches use input parameters to model responses, and the output models are validated by experimentation. For construction applications, machine learning algorithms estimate concrete strength [22–26], bituminous mixture performance [27], and concrete durability [28–30].

This study concentrates on the use of machine learning methods to forecast the compressive and flexural strength of RAC. Two distinct ensemble machine learning techniques were used—gradient boosting and random forest—and the effectiveness of both methods was evaluated using correlation coefficients (R^2) and statistical checks. Moreover, k-fold analysis and error distributions were used to determine the validity of each technique. The reason for selecting the ensemble machine learning method was that the literature reported their better performance compared to individual machine learning methods, such as support-vector machines and artificial neural networks [31–33]. This research is interesting in that it predicts both the compressive and flexural strength via two ensemble machine learning methods, while experimental studies require considerable human effort, the cost of experimentation, and time for material collection, casting, curing, and testing. Since a number of factors—including w/c, recycled aggregate replacement ratio, parent concrete strength, water absorption of the recycled aggregate, density of the recycled aggregate, etc.—influence the strength of RAC, their combined impact is hard to study through

an experimental approach. Machine learning methods are capable of determining their combined impact at a reduced effort. Machine learning methods require a dataset, which may be collected from past studies, since many investigations have been undertaken to determine material strength, and such a dataset might be utilized for training the machine learning models and forecasting the material properties. The purpose of this work is to ascertain the most appropriate machine learning method for the compressive and flexural strength estimation of RAC based on the results forecast and the effects of various parameters on the strength of RAC.

2. Methods

2.1. Data Retrieval and Analysis

To obtain the appropriate result, supervised machine learning techniques need a varied range of input variables [34–36]. The compressive and flexural strength of RAC were projected using data obtained from the past studies (see Table S1 in Supplementary Materials). Experimental data were arbitrarily selected from previous studies so as to avoid biased images. Twelve variables were chosen as input factors, as listed below:

- Recycled concrete aggregate (RCA) replacement ratio;
- Parent concrete strength, bulk density of natural aggregate;
- Bulk density of RCA;
- Bulk density of natural aggregate;
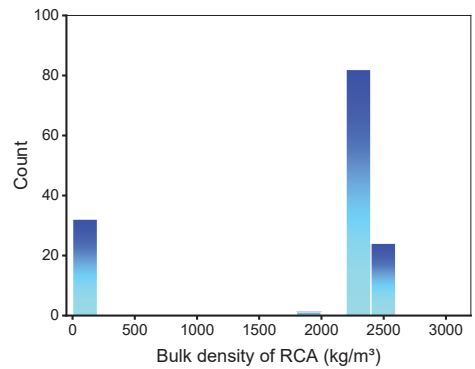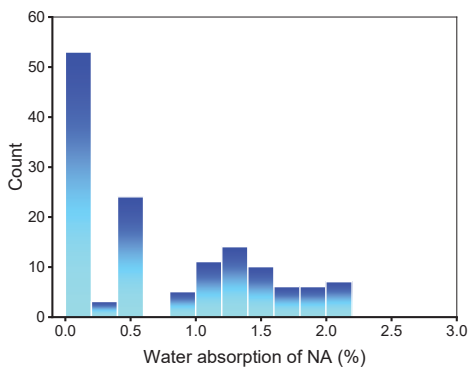- Water absorption of natural aggregate;
- Water absorption of RCA;
- Aggregate–cement ratio (a/c);
- Effective water–cement ratio (w_{eff}/c);
- Nominal maximum natural aggregate size;
- Nominal maximum RCA size;
- Los Angeles abrasion index of natural aggregate;
- Los Angeles abrasion index of RCA.

In addition, the compressive and flexural strength were chosen as the output variables. The quantity of input variables and the dataset have a substantial impact on a machine learning method's result [37–39]. In the present study, 638 data points (mixes) were employed to run machine learning methods for compressive strength prediction, and 139 data points (mixes) were used for flexural strength prediction. Tables 1 and 2 summarize the descriptive statistic evaluation of each input variable for compressive and flexural strength prediction, respectively. The mode, median, and mean exemplify basic propensity, while the standard deviation, minimum, and maximum denote variability. The relative frequency dispersal of input factors employed to forecast the compressive and flexural strength is depicted in Figures 1 and 2, respectively. This represents the overall number of readings linked to each input parameter.

Table 1. Descriptive statistical values of input factors for the compressive strength dataset.

Parameter	RCA Re-placement Ratio (%)	Parent Concrete Strength (MPa)	Bulk Density of NA (kg/m³)	Bulk Density of RCA (kg/m³)	Water Ab-sorption of NA (%)	Water Ab-sorption of RCA (%)	Aggregate–Cement Ratio (a/c)	Effective Water–Cement Ratio (w_{eff}/c)	Nominal Maximum NA Size (mm)	Nominal Maximum RCA Size (mm)	Los Angeles Abrasion Index of NA	Los Angeles Abrasion Index of RCA
Mean	53.03	5.00	1538.47	1666.16	0.61	3.49	2.99	0.49	22.14	21.51	4.61	6.75
Range	100.00	100.00	2970.00	2880.00	3.00	11.90	6.50	0.87	38.00	32.00	32.00	42.00
Mode	100.00	0.00	0.00	0.00	0.00	0.00	3.10	0.50	20.00	20.00	0.00	0.00
Maximum	100.00	100.00	2970.00	2880.00	3.00	11.90	6.50	0.87	38.00	32.00	32.00	42.00
Minimum	0.00	0.00	0.00	0.00	0.00	0.00	0.00	0.00	0.00	0.00	0.00	0.00
Median	50.00	0.00	2570.00	2330.00	0.40	3.90	2.90	0.49	20.00	20.00	0.00	0.00
Standard Deviation	40.01	15.38	1315.12	1115.04	0.73	2.94	0.83	0.11	5.48	5.71	10.04	13.89
Sum	33,884	3193	983,081	1,064,677	391	2231	1913	312	14,149	13,747	2943	4312

Table 2. Descriptive statistical values of input factors for the flexural strength dataset.

Parameter	RCA Replacement Ratio (%)	Parent Concrete Strength (MPa)	Bulk Density of NA (kg/m³)	Bulk Density of RCA (kg/m³)	Water Absorption of NA (%)	Water Absorption of RCA (%)	Aggregate–Cement Ratio (a/c)	Effective Water–Cement Ratio (w$_{eff}$/c)	Nominal Maximum NA Size (mm)	Nominal Maximum RCA Size (mm)	Los Angeles Abrasion of NA	Los Angeles Abrasion of RCA
Mean	50.74	4.32	1704.24	1823.81	0.70	4.15	3.05	0.52	19.40	19.23	9.32	12.82
Range	100.00	100.00	2820.00	2578.00	2.10	11.90	6.00	0.87	30.00	32.00	32.00	41.40
Mode	100.00	0.00	0.00	0.00	0.00	0.00	2.80	0.50	20.00	20.00	0.00	0.00
Maximum	100.00	100.00	2820.00	2578.00	2.10	11.90	6.00	0.87	30.00	32.00	32.00	41.40
Minimum	0.00	0.00	0.00	0.00	0.00	0.00	0.00	0.00	0.00	0.00	0.00	0.00
Median	50.00	0.00	2590.00	2336.00	0.50	4.70	2.90	0.50	20.00	20.00	0.00	0.00
Standard Error	3.42	1.50	108.88	85.16	0.06	0.24	0.07	0.01	0.34	0.38	1.05	1.36
Standard Deviation	40.30	17.65	1283.62	1004.03	0.70	2.81	0.81	0.14	4.00	4.49	12.33	15.99
Sum	7053.00	600.00	236,890.00	253,509.00	96.90	577.28	423.40	71.75	2696.00	2673.00	1294.90	1781.30

NA: natural aggregate, RCA: recycled concrete aggregate.
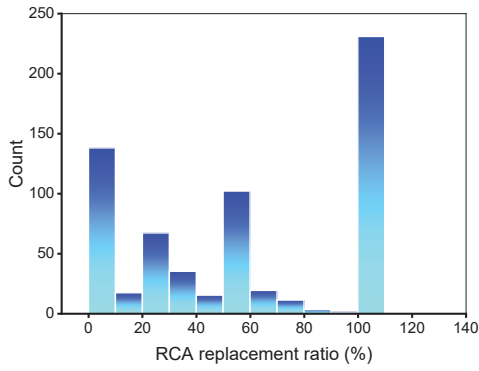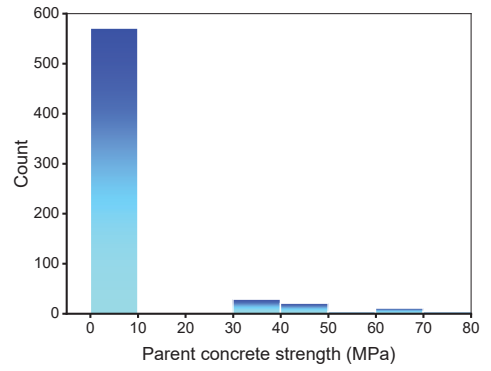
RCA replacement ratio

Parent concrete strength
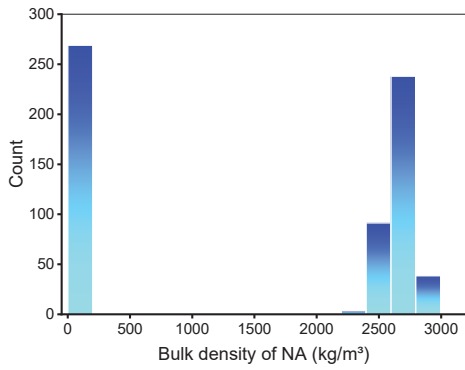
Bulk density of natural aggregate
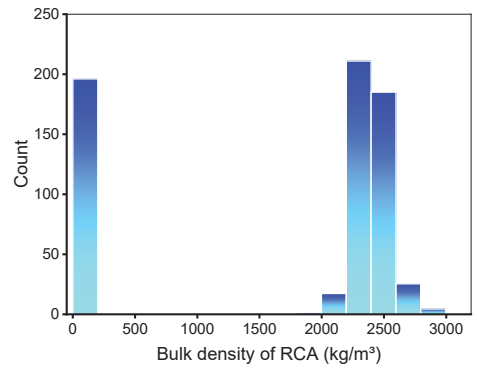
Bulk density of RCA
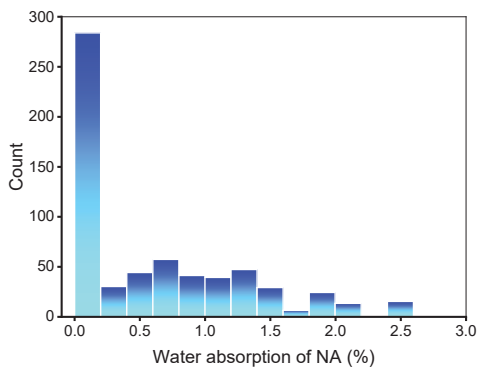
Water absorption of natural aggregate
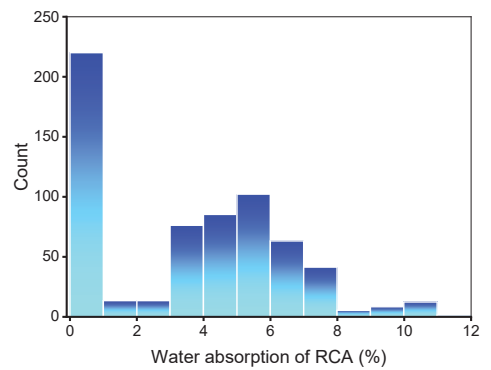
Water absorption of RCA

Figure 1. *Cont.*
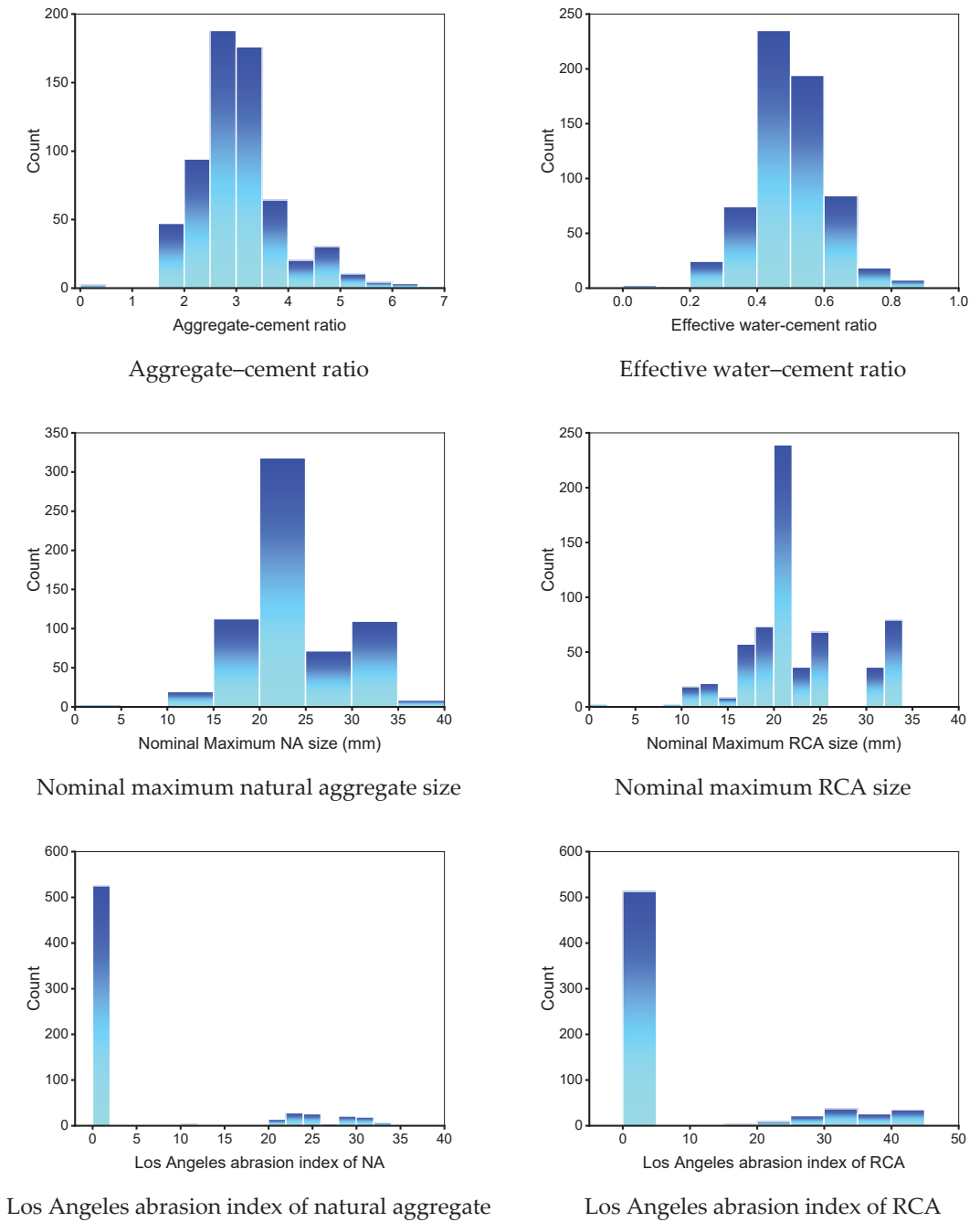
Figure 1. Relative frequency dispersal of input parameters for the compressive strength dataset. NA: natural aggregate, RCA: recycled concrete aggregate.
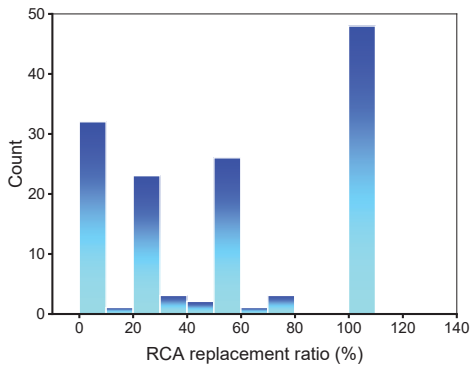
RCA replacement ratio
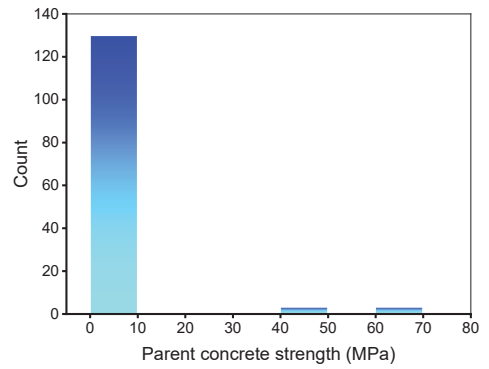
Parent concrete strength
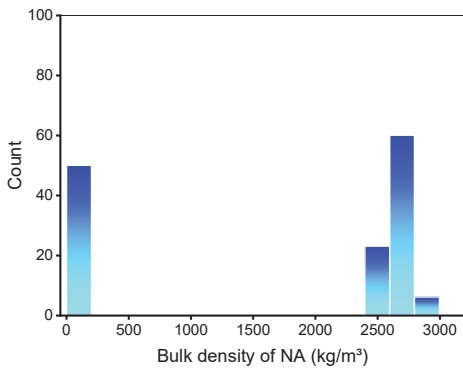
Bulk density of natural aggregate

Bulk density of RCA

Water absorption of natural aggregate
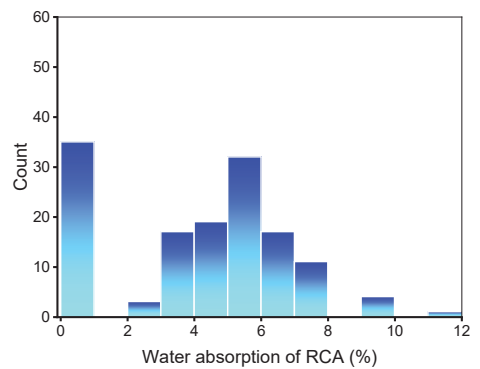
Water absorption of RCA

Figure 2. *Cont.*
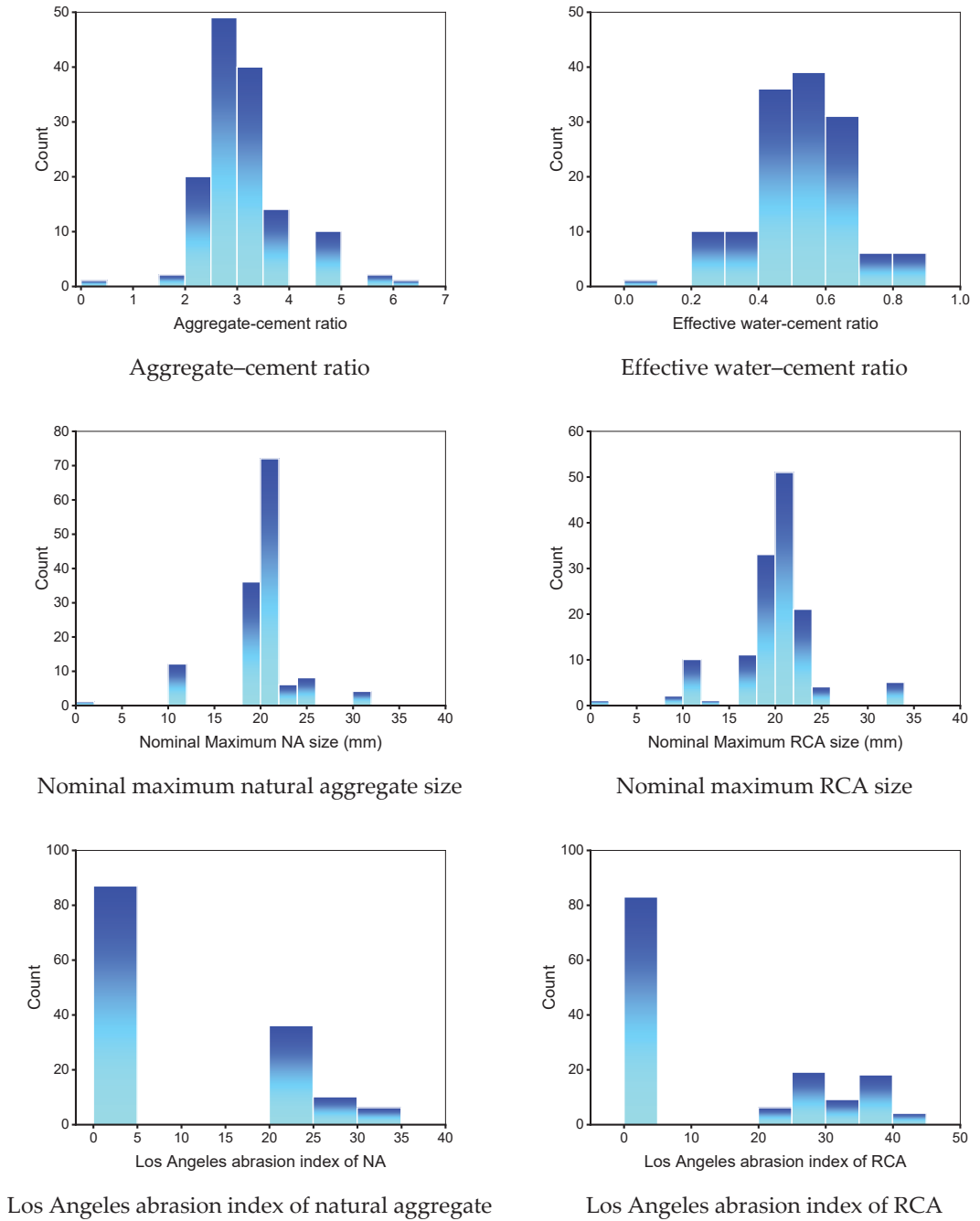
Figure 2. Relative frequency dispersal of inputs parameters for the flexural strength dataset. NA: natural aggregate, RCA: recycled concrete aggregate.

2.2. Machine Learning Methods Employed

Two ensemble machine learning methods (gradient boosting and random forest) were used to accomplish the objectives of this research, using Python code and the Anaconda Navigator program. Spyder 4.3.5 was used to execute the gradient boosting and random forest methods. Typically, these machine learning methods are used to anticipate desired outputs based on input factors. These methods are capable of forecasting the temperature effects, the strength properties, and the durability of materials [40,41]. Ensemble machine learning methods commonly exploit the weak learner by constructing 20 submodels that may be trained on data and modified to maximize the R^2 value. The strategies to choose optimal hyperparameters include splitting the data for training and testing models (80% for training and 20% for testing), selecting the optimal submodel based on R^2, and the k-fold analysis method. R^2 represents the performance/validity of machine learning approaches. The R^2 statistic is used to determine the amount of variance in a response variable provided by a model. In other words, it expresses the model's fit to the data quantitatively. A number around zero implies that fitting the mean is comparable to fitting the model, but a value near one shows that the data and model are nearly completely matched [42]. The subsections below discuss the machine learning techniques employed in this study. Moreover, all machine learning methods are validated using k-fold assessment, statistical checks, and error measures (root-mean-square error (RMSE) and mean absolute error (MAE)). Furthermore, sensitivity analysis is performed to determine the effect of each input variable on the predicted findings. The flow diagram in Figure 3 illustrates the research method used in this study.
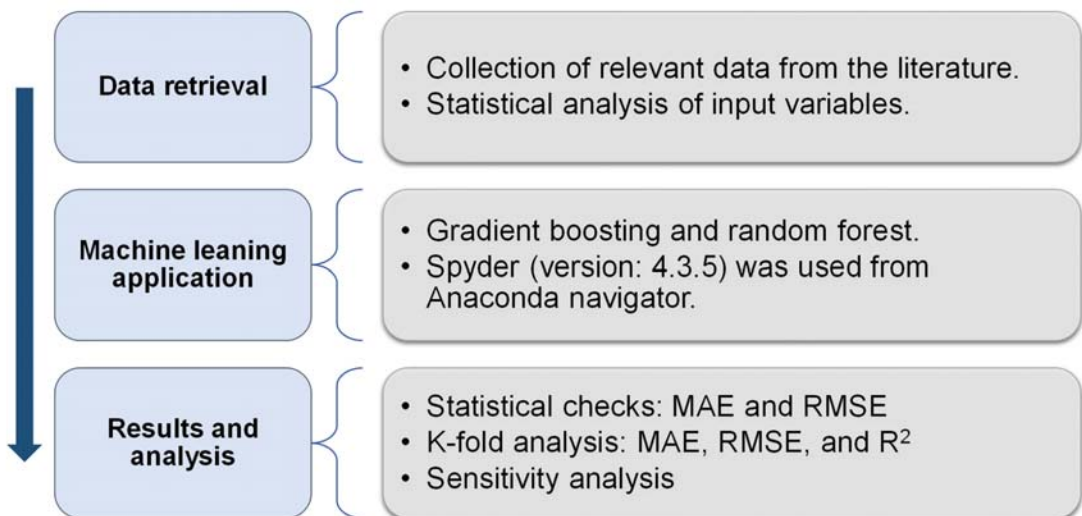
Figure 3. Flowchart of research methods.

2.2.1. Gradient Boosting

Friedman [43] presented gradient boosting as an ensemble strategy for classification and regression in 1999. Gradient boosting is only applicable to regression. As seen in Figure 4, the gradient boosting technique compares each iteration of the randomly chosen training set to the base model. A weak predictor is constructed using all of the training data. Then, the training data are predicted using a weak predictor. With the expected outcome, it is simple to calculate the residuals for each training instance. Gradient boosting for execution may be sped up and accuracy increased by randomly subsampling the training data, which also helps to prevent overfitting. The lower the training data percentage,

the faster the regression, because the model must suit minor data every single iteration. Gradient boosting algorithms require tuning parameters, including n-trees and shrinkage rate, where n-trees is the number of trees to be generated; n-trees must not be kept too low, while the shrinkage factor—normally referred to as the learning rate employed to all trees in the development—should not be set too high [44].
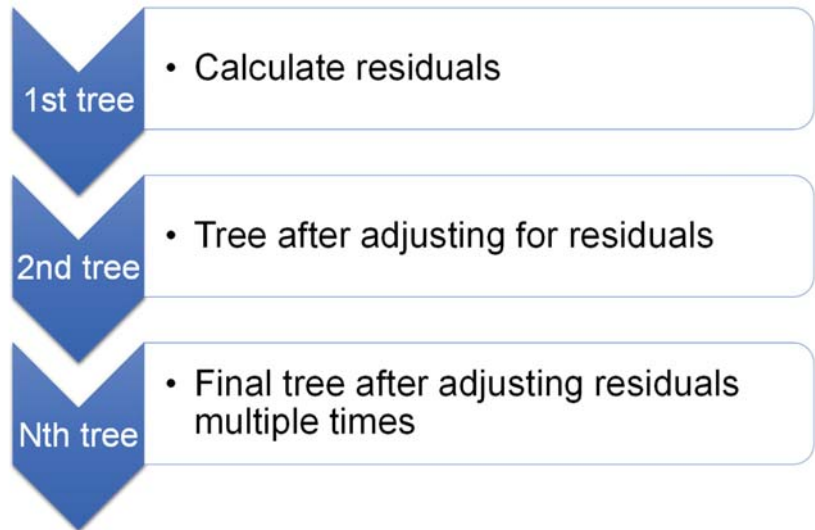
Figure 4. Schematic representation of the gradient boosting technique.

2.2.2. Random Forest

Random forest are deployed by bagging decision trees using the random split choice technique [45]. The modeling procedure for the random forest approach is illustrated schematically in Figure 5. Each tree in the forest is generated by means of an arbitrarily selected training set, and each split inside a tree is constructed by means of an arbitrarily chosen subgroup of input factors, yielding a forest of trees [46]. This element of instability adds variation to the tree. The forest as a whole is composed completely of mature binary trees. The random forest technique has established itself as a highly effective tool for general-purpose classification and regression. When the number of variables surpasses the number of observations, the technique has proven improved precision by aggregating the predictions of several randomized decision trees. Additionally, it is adaptable to both large-scale and ad hoc learning tasks, yielding measures of varying degrees of importance [47].
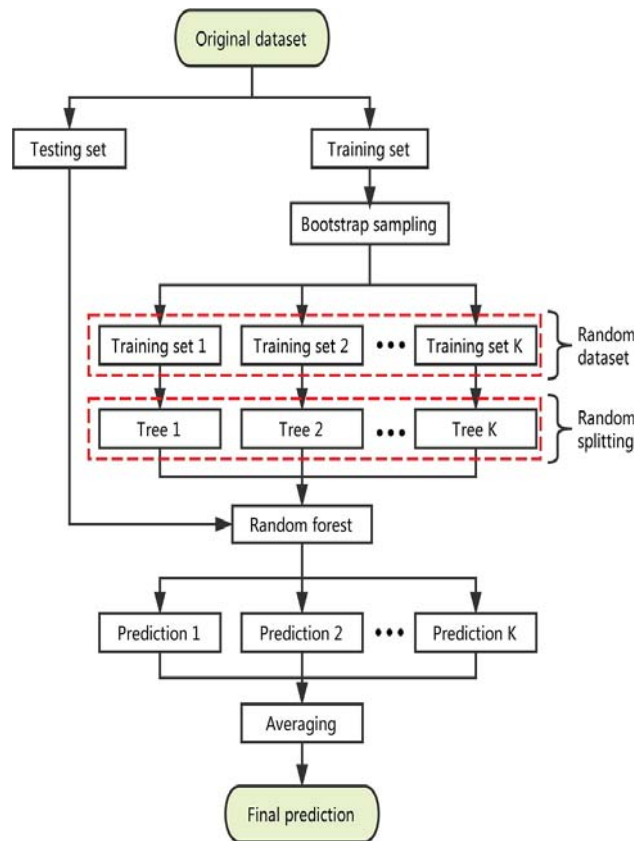
Figure 5. Schematic representation of the random forest technique [45].

3. Results and Analysis

3.1. Gradient Boosting Model

3.1.1. Compressive Strength

The results of the gradient boosting model for RAC's compressive strength are shown in Figure 6a,b. Figure 6a depicts the relationships between the experimental and anticipated results. The gradient boosting approach yielded findings with a satisfactory level of accuracy and a lower distinction between the experimental and projected values. The R^2 of 0.87 signifies that the gradient boosting model is reasonably precise at forecasting the compressive strength of RAC. The distribution of forecast and error values for the gradient boosting compressive strength model is presented in Figure 6b. The discrepancy between experimental and estimated values was found to be between 0.00 and 27.96 MPa (44.52% deviation), with an average of 4.78 MPa (11.67%). Additionally, the divergence from the experimental outcomes was less than 1 MPa for 27 mixes, between 1 and 3 MPa for 32 mixes, between 3 and 6 MPa for 32 mixes, between 6 and 10 MPa for 21 mixes, and greater than 10 MPa for 16 mixes. These deviations indicate that the gradient boosting model's predicted results deviated less from the experimental results. As a result, the gradient boosting technique is quite accurate at predicting RAC's compressive strength.
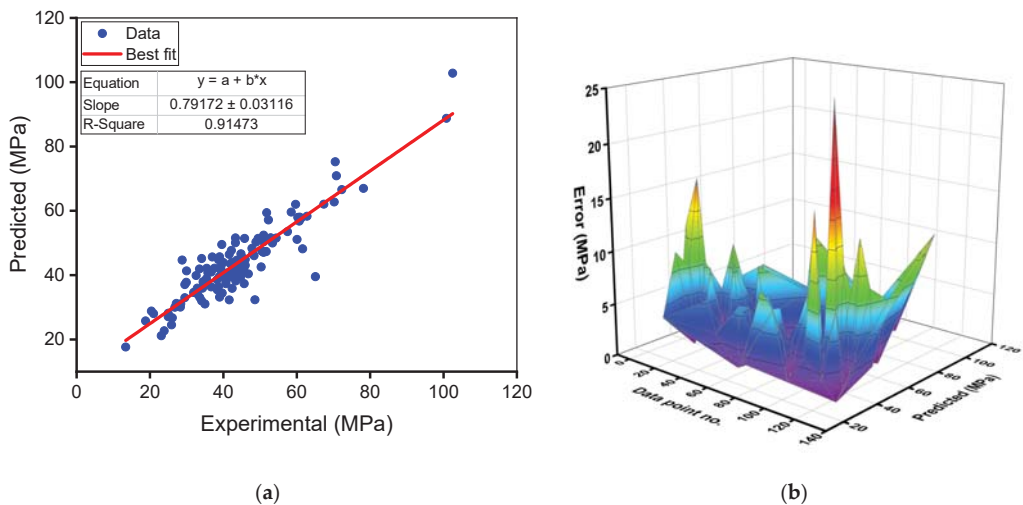
(**a**)

(**b**)
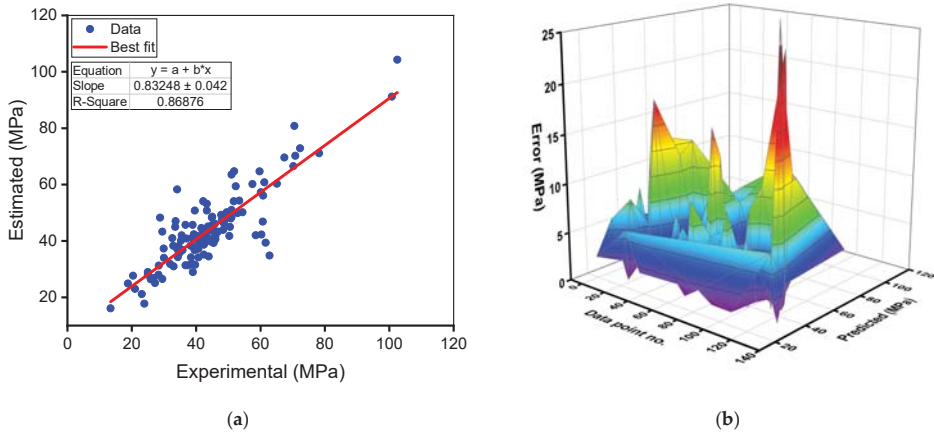
Figure 6. Gradient boosting model for compressive strength: (**a**) relationship between experimental and predicted results; (**b**) spreading of predicted and error values.

3.1.2. Flexural Strength

Figure 7a,b provides a comparison of the experimental and predicted outcomes of the gradient boosting model for the flexural strength of RAC. The correlation between experimental and estimated findings is exemplified in Figure 7a, where an R^2 of 0.79 indicates that the gradient boosting model for the flexural strength is less specific than for the compressive strength estimation of RAC. This reduced R^2 is due to the lower number of data points used for forecasting the flexural strength compared to the compressive strength. The distribution of estimated and error values for the gradient boosting flexural strength model is represented in Figure 7b. The difference between experimental and estimated values was discovered to be between 0.00 and 4.27 MPa (89.27% deviation), with an average of 5.86 MPa (11.44%). Furthermore, the difference from the experimental outcomes was less than 1 MPa for 22 mixes and greater than 1 MPa for 6 mixes. These deviation values suggest a moderate disparity between the gradient boosting model's projected and experimental outcomes. As a result, the gradient boosting approach predicts RAC's flexural strength less accurately compared to its precision in foretelling the compressive strength of RAC.
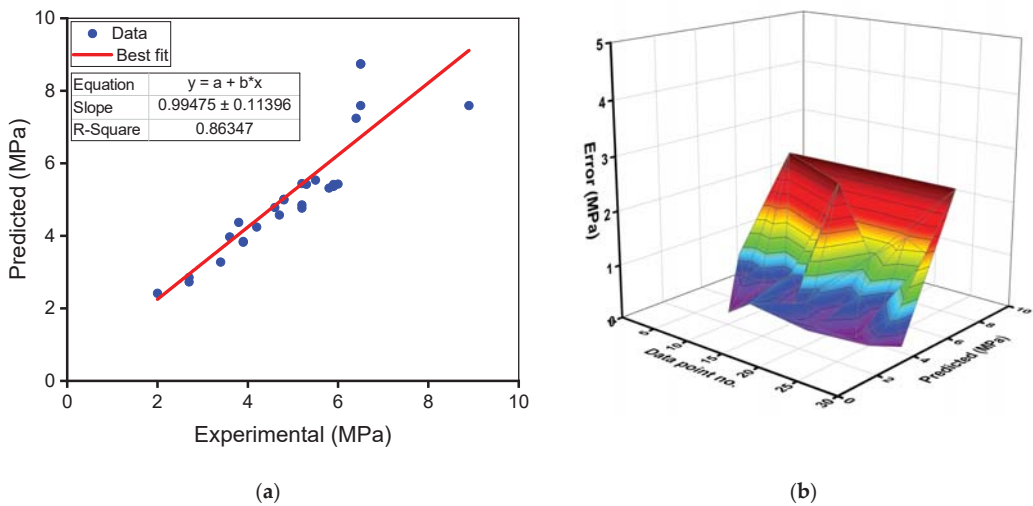

(**a**)

(**b**)
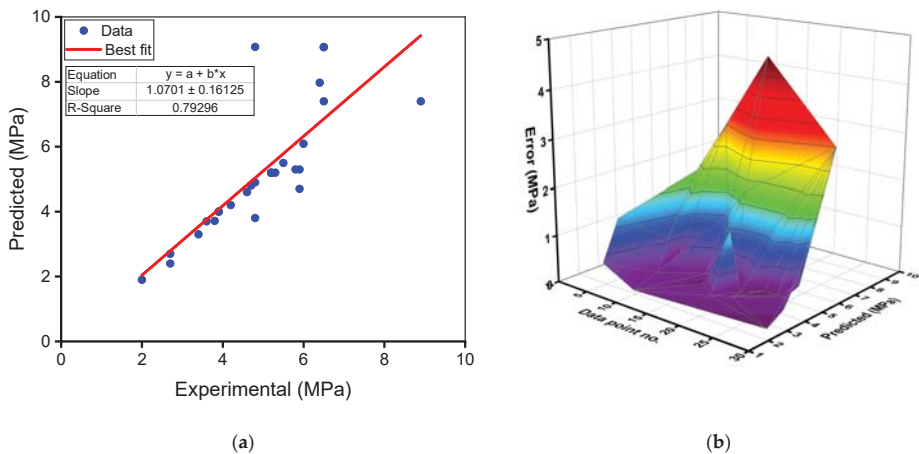
Figure 7. Gradient boosting model for flexural strength: (**a**) relationship between experimental and predicted results; (**b**) spreading of predicted and error values.

3.2. Random Forest Model

3.2.1. Compressive Strength

The outcomes of the random forest model for the compressive strength of RAC are presented in Figure 8. In Figure 8a, an R^2 value of 0.91 indicates that the random forest model outperforms the gradient boosting model in this study in terms of precision. The dispersion of projected and error values for the random forest compressive strength model is shown in Figure 8b. The variation (error) between experimental and estimated values was found to range between 0.07 and 25.57 MPa (39.28% variation), with an average of 4.19 MPa (10.50% variation). Furthermore, the difference from the experimental outcomes was less than 1 MPa for 18 mixes, between 1 and 3 MPa for 41 mixes, between 3 and 6 MPa for 39 mixes, between 6 and 10 MPa for 22 mixes, and larger than 10 MPa for only 8 mixes. These values show that the difference between experimental and expected outcomes is less compared to the gradient boosting model. As a result, the random forest approach is superior for assessing the compressive strength of RAC with the greatest precision.

(**a**)　　　　　　　　　　　　　　　(**b**)

Figure 8. Random forest model for compressive strength: (**a**) relationship between experimental and predicted results; (**b**) spreading of predicted and error values.

3.2.2. Flexural Strength

The experimental and anticipated outcomes of the random forest model for the flexural strength of RAC are shown in Figure 9. Figure 9a represents the relationships between experimental and projected outcomes, with an R^2 of 0.86 indicating that the random forest model for the flexural strength is less specific than the compressive strength prediction of RAC. This reduced R^2 is because there are fewer data points used to forecast the flexural strength than the compressive strength. Figure 9b indicates the distribution of estimated and error values for the random forest flexural strength model. The discrepancy between experimental and estimated values ranged from 0.02 to 2.24 MPa (34.46 variances), with an average of 0.56 MPa (10.43% variance). Moreover, for 23 mixes, the variation from the experimental outcomes was less than 1 MPa, whereas it was greater than 1 MPa for only 5 mixes. These values indicate a lower difference between the random forest model's predicted and experimental results. As a result, the random forest technique is more accurate in forecasting RAC's flexural strength than the gradient boosting model.

(**a**) (**b**)

Figure 9. Random forest model for flexural strength: (**a**) relationship between experimental and predicted results; (**b**) spreading of predicted and error values.

3.3. Models' Validation

The machine learning methods were validated by employing k-fold and statistical methods. The k-fold technique, in which related data are randomly spread and separated into 10 groups, is widely used to determine a technique's validity [48]. Nine groups are employed for training the model, and one group is used for validation, as shown in Figure 10. The model is more accurate when the errors (MAE and RMSE) are less and the R^2 is high. In order to get a reasonable conclusion, the operation should be repeated 10 times. The model's outstanding accuracy is due in large part to this enormous effort. In addition, both models were statistically tested based on errors (MAE and RMSE), as shown in Table 3. In comparison to the gradient boosting technique, this assessment also validated the random forest model's superior accuracy due to reduced error readings. Equations (1) and (2), which were obtained from prior investigations [31,49], were used to determine the approaches' prediction performance statistically.

$$\text{MAE} = \frac{1}{n} \sum_{i=1}^{n} |P_i - T_i|, \tag{1}$$

$$\text{RMSE} = \sqrt{\sum \frac{(P_i - T_i)^2}{n}}, \tag{2}$$

where n = total number of data points, T_i = experimental value, and P_i = predicted value.

Table 3. Statistical measurements of the models for validation.

Model	Compressive Strength (MPa)		Flexural Strength (MPa)	
	MAE	**RMSE**	**MAE**	**RMSE**
Gradient Boosting	4.776	6.976	0.642	1.199
Random Forest	4.194	5.642	0.560	0.859
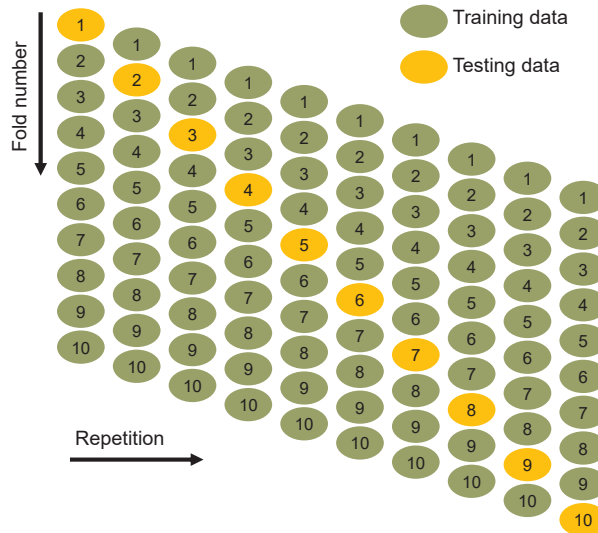
Figure 10. K-fold analysis procedure [50].

MAE, RMSE, and R^2 were measured to see how well the k-fold analysis was executed, and the results are shown in Table 4. Figures 11–13 show a comparison of k-fold analysis for all of the machine learning techniques used. The MAE values for the gradient boosting compressive strength model ranged from 4.78 to 14.60 MPa, with an average of 10.27 MPa. In contrast, the MAE values for the random forest compressive strength model ranged from 4.19 to 10.92 MPa, with an average of 8.34 MPa. Likewise, the gradient boosting and random forest models for the compressive strength of RAC had average RMSE values of 11.05 and 9.41 MPa, respectively. When R^2 values were evaluated, the average R^2 values for the gradient boosting and random forest models were 0.67 and 0.72, respectively. When compared to the gradient boosting model, the random forest model—with smaller error values and greater R^2 values—was more precise in projecting the compressive strength of RAC. A similar distribution of error and R^2 values was discovered for the flexural strength of RAC for both the gradient boosting and random forest models, and this also validated the higher precision of the random forest model. Hence, the random forest model might be employed for the strength estimation of RAC in order to reduce the number of trials required for experimentation.

Table 4. Results of k-fold analysis.

	Compressive Strength						Flexural Strength					
K-Fold	**Gradient Boosting**			**Random Forest**			**Gradient Boosting**			**Random Forest**		
	MAE	**RMSE**	**R^2**	**MAE**	**RMSE**	**R^2**	**MAE**	**RMSE**	**R^2**	**MAE**	**RMSE**	**R^2**
1	14.60	10.23	0.74	10.92	8.44	0.90	0.64	1.37	0.75	0.63	0.97	0.74
2	7.33	9.28	0.53	7.13	9.45	0.67	0.67	1.20	0.92	0.66	0.97	0.44
3	11.04	7.98	0.87	8.16	7.56	0.73	0.75	1.52	0.60	1.33	1.51	0.35
4	8.57	13.86	0.84	4.19	11.87	0.84	0.85	1.81	0.45	0.71	0.93	0.63
5	11.16	12.42	0.87	7.25	9.83	0.91	0.74	1.21	0.79	0.91	0.86	0.43
6	13.10	7.10	0.86	9.87	5.64	0.66	2.00	2.02	0.20	0.56	0.86	0.41
7	8.01	15.95	0.37	7.78	12.06	0.79	0.96	1.23	0.21	0.97	0.90	0.75
8	13.14	8.76	0.74	9.98	15.00	0.47	1.56	1.28	0.44	1.30	1.47	0.56
9	4.78	6.98	0.61	10.09	8.18	0.74	0.79	1.22	0.24	0.87	1.28	0.74
10	10.94	17.97	0.27	7.98	6.10	0.49	0.69	1.29	0.50	0.90	1.34	0.86
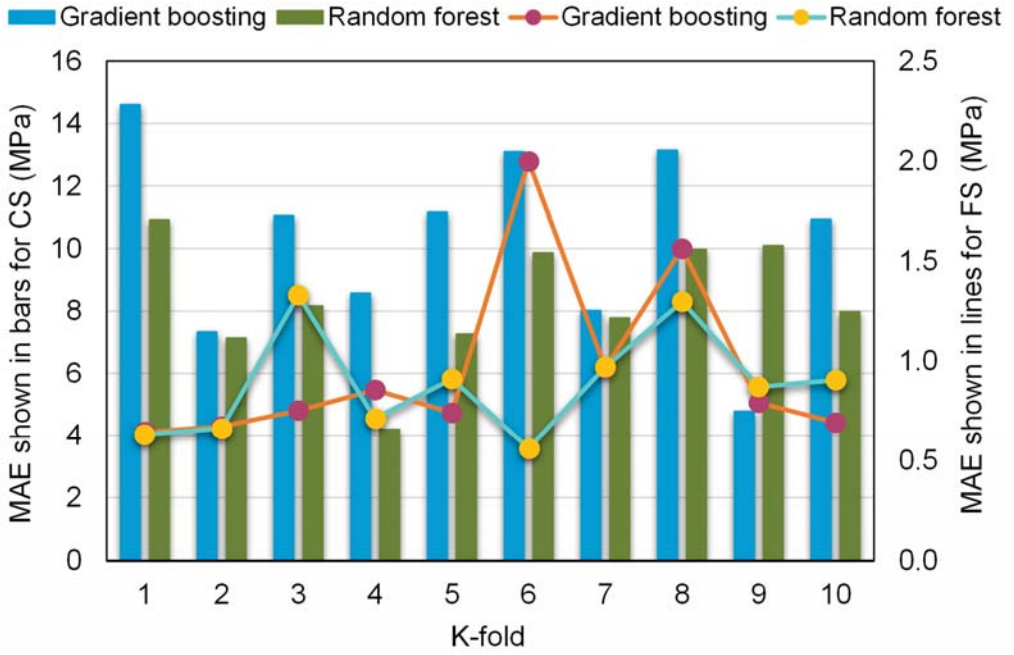
Figure 11. Mean absolute error distribution from k-fold analysis.
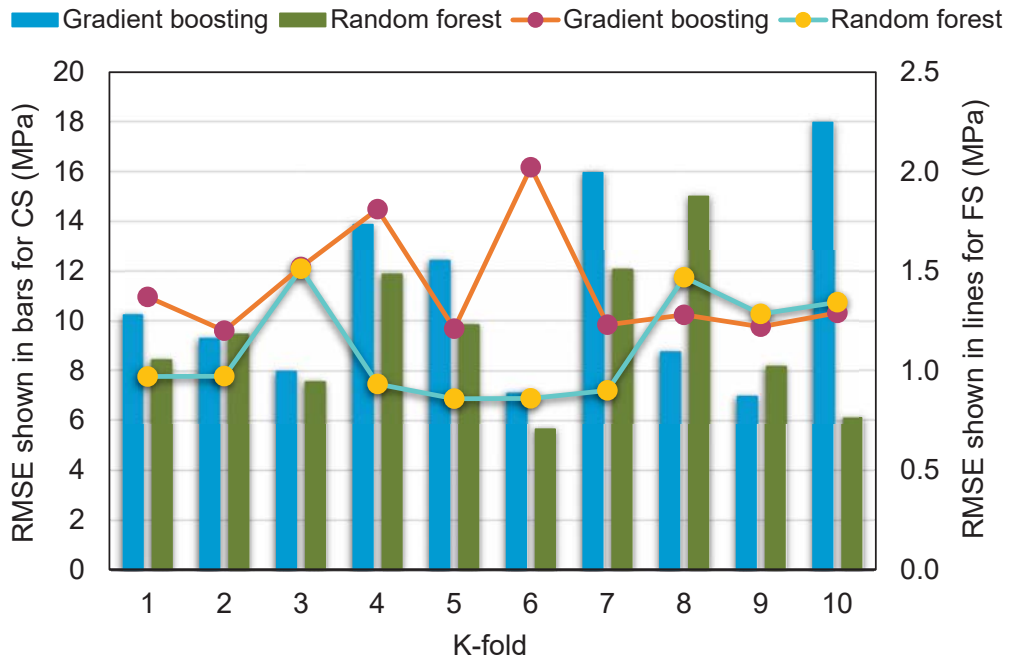
Figure 12. Root-mean-square error distribution from k-fold analysis.
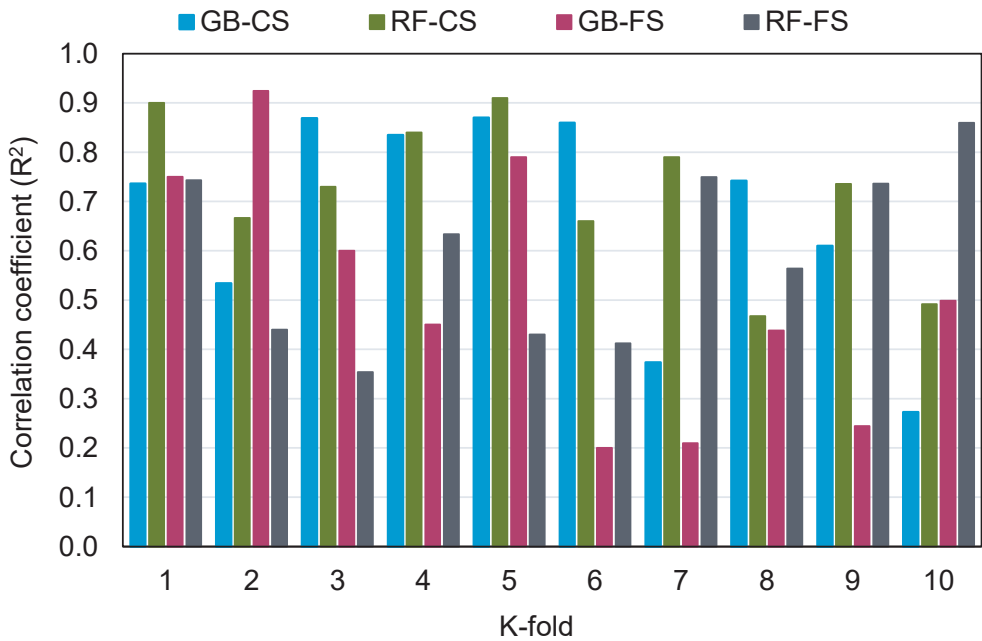
Figure 13. Correlation coefficient (R^2) distribution from the k-fold analysis. GB: gradient boosting, RF: random forest, CS: compressive strength, FS: flexural strength.

3.4. Sensitivity Analysis

The purpose of this evaluation was to discover the impact of input factors on RAC's compressive and flexural strength prediction. The anticipated result is considerably influenced by the input factors [51]. Figure 14 shows the influence of the input factors used in this research on the compressive strength evaluation of RAC. The analysis revealed that the RCA replacement ratio was the crucial element, accounting for 18.7% of the overall impact, followed by parent concrete strength at 15.3% and w_{eff}/c at 14.8%. The contribution of the other input factors to the strength estimation of RAC was found to be lower, with the Los Angeles abrasion index of RCA, water absorption of RCA, a/c, nominal maximum RCA size, bulk density of RCA, Los Angeles abrasion index of natural aggregate, bulk density of the natural aggregate, nominal maximum natural aggregate size, and water absorption of the natural aggregate accounting for 11.6%, 8.7%, 8.1%, 6.5%, 5.0%, 3.7%, 2.8%, 2.5%, and 2.3%, respectively. Sensitivity analysis produced results associated with the quantity of input variables and the dataset used to build the machine learning models. The impact of an input factor on the method's results was found using Equations (3) and (4).

$$N_i = f_{max}(x_i) - f_{min}(x_i) \tag{3}$$

$$S_i = \frac{N_i}{\sum_{j-i}^{n} N_j}. \tag{4}$$

where

$f_{max}(x_i)$ = highest estimated value on the ith result;
$f_{min}(x_i)$ = lowest estimated value on the ith result;
S_i = attained impact percentage for a certain variable.
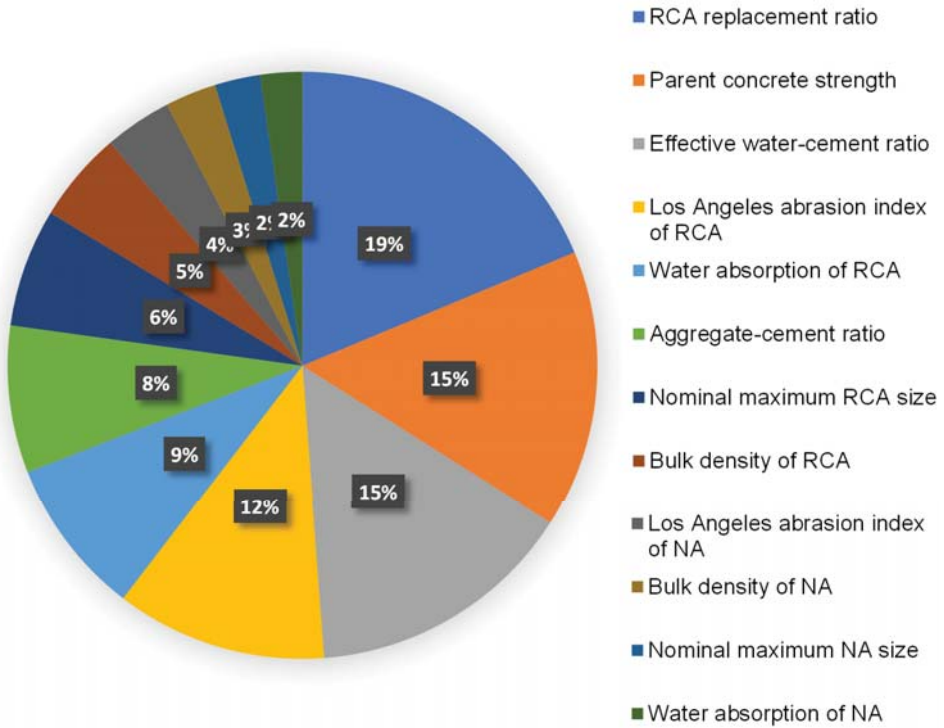
Figure 14. Input variables' contribution to estimating the outcomes of models.

4. Discussions

The goal of this study was to add to the existing domain of research on the use of modern methods for evaluating the strength of RAC. This sort of exploration will benefit the building sector by allowing for the advancement of fast and cost-effective material property projection methods. Furthermore, by implementing these techniques to encourage environmentally friendly construction, the acceptance and usage of RAC in the building sector could be expedited. Figure 15 depicts the advantages of adopting RAC in the construction industry. Significant infrastructural renovation is required as a result of urbanization and industrialization, resulting in high volumes of construction and demolition waste. Therefore, desirable areas are turned into garbage ditches, land prices continue to rise, and trash dumping costs rise, with landfill space becoming increasingly rare. As a result, waste management has become of leading significance in emerging countries and is a global concern that demands long-term solutions. In addition, extracting and processing natural aggregates for concrete uses a lot of energy and produces a lot of CO_2 [52]. Thus, using RAC in concrete production could result in lower energy consumption, resource conservation, building sustainability, cost savings, and a significant decrease in construction and demolition waste.

This research shows how machine learning methods may be used to forecast the compressive and flexural strength of RAC. The study employed two ensemble machine learning techniques—gradient boosting and random forest—to determine which technique is the most accurate predictor. The random forest model, with an R^2 of 0.91 for compressive strength and 0.86 for flexural strength prediction, suggested a higher precision compared to the gradient boosting model, which produced R^2 of 0.87 and 0.79 for compressive and flexural strength prediction, respectively. Furthermore, the accuracy of all machine learning methods was tested through the use of k-fold and statistical methods. The model

is more precise if there are fewer error values in it. However, selecting and suggesting the best machine learning model for forecasting outcomes in a range of fields is difficult, because a model's validity is highly dependent on the input factors and size of the dataset employed [53]. Ensemble machine learning techniques frequently take advantage of the weak learner by building 20 submodels that might be trained on data and altered to maximize the R^2 value. The random forest model has also been found to be more exact in forecasting the strength of concrete by other researchers [54–56] in terms of R^2 and error values. Farooq et al. [54] compared the functioning of random forest with that of the artificial neural network, gene expression programming, and decision tree methods, and found that the random forest model, with an R^2 of 0.96, had a higher precision than the others. The reason for the higher accuracy of random forest is that it employs the bagging approach to combine all regression trees [57,58]. By minimizing the variation associated with prediction, bagging can increase prediction accuracy.
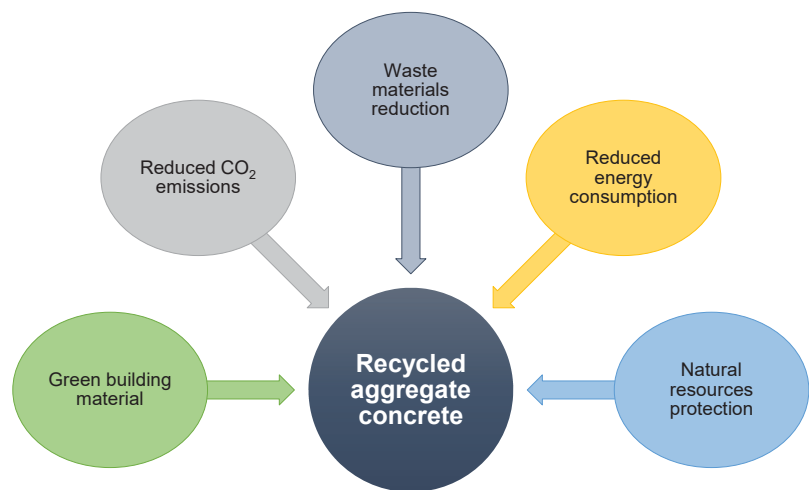
Figure 15. Benefits related to the adoption and application of recycled aggregate concrete.

Figure 16 depicts the R^2 value dispersion for the gradient boosting and random forest submodels. For gradient boosting compressive strength submodels, the lowest, average, and maximum R^2 values were 0.818, 0.844, and 0.869, respectively. Additionally, the least, average, and highest R^2 values for the gradient boosting flexural strength submodels were noted to be 0.731, 0.762, and 0.793, respectively. Similarly, for random forest compressive strength submodels, the lowest, average, and highest R^2 values were 0.877, 0.907, and 0.915, respectively. Meanwhile, the least, average, and greatest R^2 values for the random forest flexural strength submodels were identified to be 0.803, 0.834, and 0.863, respectively. These findings revealed that the random forest submodels had greater R^2 values than the gradient boosting submodels, indicating that the random forest model was more precise in estimating RAC's strength. A sensitivity analysis was also conducted to determine the effects of all inputs on the projected strength of RAC. The size of the dataset and the input parameters may have an impact on the model's performance. The sensitivity analysis determined the contributions of each of the 12 input parameters to the expected output. The three most important input factors were discovered to be the RCA replacement ratio, parent concrete strength, and w_{eff}/c.
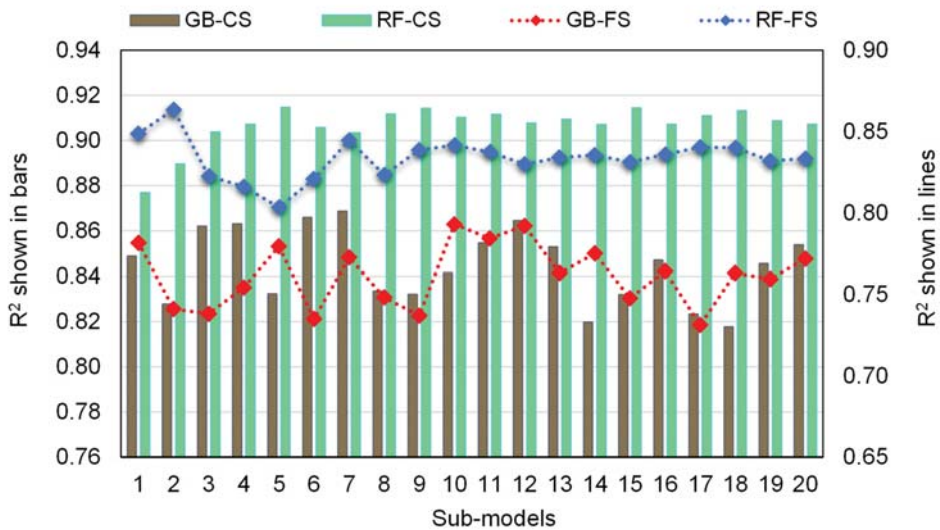
Figure 16. Correlation coefficients (R^2) of submodels.

5. Conclusions

This study aimed to employ two ensemble machine learning algorithms to anticipate the compressive and flexural strength of recycled aggregate concrete (RAC). Gradient boosting and random forest were chosen to achieve the study's goals. The dataset containing the strength of RAC of 638 mixes was collected, of which all contained compressive strength results and 139 contained flexural strength results. Both gradient boosting and random forest models were employed to predict the compressive and flexural strength of RAC, and their accuracy was compared. The conclusions of this study are as follows:

1. The random forest model outperformed the gradient boosting model in estimating the compressive and flexural strength of RAC, with an R^2 value of 0.91 for compressive strength and 0.86 for flexural strength prediction. However, the results of the gradient boosting model for the compressive strength estimation of RAC were also in the reasonable range, with an R^2 of 0.87, but for the flexural strength estimation, the accuracy of the gradient boosting model was lower, with an R^2 of 0.79. The lower R^2 values for the flexural strength estimation in both models were because of the lower number of input data points. Hence, the random forest technique is suitable to be used for the strength prediction of RAC;

2. The analysis of predicted results indicated a lower variance from the experimental results for the random forest model compared to the gradient boosting model, which also validated the higher precision of the random forest model in predicting the strength of RAC;

3. K-fold and statistical evaluations further validated the model's precision. These assessments also validated the higher precision of the random forest model due to the lower error values in comparison with the gradient boosting model;

4. Sensitivity analysis revealed that the RCA replacement ratio was the most important constituent affecting the model's outcome, accounting for 18.7% of the total, followed by parent concrete strength at 15.3% and the effective water–cement ratio at 14.8%. However, the other input parameters had less contribution to the forecast of RAC's compressive strength, with the Los Angeles abrasion index of RCA, water absorption of RCA, a/c, nominal maximum RCA size, bulk density of RCA, Los Angeles abrasion index of natural aggregate, bulk density of natural aggregate, nominal maximum

natural aggregate size, and water absorption of the natural aggregate accounting for 11.6%, 8.7%, 8.1%, 6.5%, 5.0%, 3.7%, 2.8%, 2.5%, and 2.3%, respectively;

5. This sort of study will benefit the building sector by allowing for the advancement of rapid and cost-effective techniques for estimating the strength of materials. Furthermore, by encouraging computational techniques, the adoption and application of RAC in the building sector will be accelerated.

This study proposes that future studies should use experimental research, mixture proportions, field trials, and other numerical assessment methods to increase the amount of data points and findings (e.g., Monte Carlo simulation). Furthermore, to enhance the models' responsiveness, environmental characteristics (e.g., elevated/low temperature and humidity) and a full description of the raw materials may be included as input variables.

Supplementary Materials: The following are available online at https://www.mdpi.com/article/10.3390/ma15082823/s1, Table S1: Data used for modeling. References [59–121] are cited in the Supplementary Materials.

Author Contributions: X.Y., data curation, visualization, writing—original draft; Y.T., resources, investigation, supervision, writing—review and editing; W.A., conceptualization, software, methodology, validation, supervision, writing—original draft; A.A., resources, methodology, validation, formal analysis, writing—review and editing; K.I.U., funding acquisition, visualization, project administration, writing—review and editing; A.M.M., formal analysis, investigation, writing—review and editing; R.K., resources, methodology, writing—review and editing. All authors have read and agreed to the published version of the manuscript.

Institutional Review Board Statement: Not applicable.

Informed Consent Statement: Not applicable.

Data Availability Statement: The data used in this research has been properly cited and reported in the main text.

Conflicts of Interest: The authors declare no conflict of interest.

References

1. Zhang, B.; Ahmad, W.; Ahmad, A.; Aslam, F.; Joyklad, P. A scientometric analysis approach to analyze the present research on recycled aggregate concrete. *J. Build. Eng.* **2022**, *46*, 103679. [CrossRef]
2. Singh, N.; Kumar, P.; Goyal, P. Reviewing the behaviour of high volume fly ash based self compacting concrete. *J. Build. Eng.* **2019**, *26*, 100882. [CrossRef]
3. Meisuh, B.K.; Kankam, C.K.; Buabin, T.K. Effect of quarry rock dust on the flexural strength of concrete. *Case Stud. Constr. Mater.* **2018**, *8*, 16–22. [CrossRef]
4. Ahmad, W.; Ahmad, A.; Ostrowski, K.A.; Aslam, F.; Joyklad, P. A scientometric review of waste material utilization in concrete for sustainable construction. *Case Stud. Constr. Mater.* **2021**, *15*, e00683. [CrossRef]
5. Bui, N.K.; Satomi, T.; Takahashi, H. Improvement of mechanical properties of recycled aggregate concrete basing on a new combination method between recycled aggregate and natural aggregate. *Constr. Build. Mater.* **2017**, *148*, 376–385. [CrossRef]
6. Saha, S.; Rajasekaran, C. Mechanical properties of recycled aggregate concrete produced with Portland Pozzolana Cement. *Adv. Concr. Constr.* **2016**, *4*, 27. [CrossRef]
7. Xiao, J.; Li, W.; Poon, C. Recent studies on mechanical properties of recycled aggregate concrete in China—A review. *Sci. China Technol. Sci.* **2012**, *55*, 1463–1480. [CrossRef]
8. Ajdukiewicz, A.; Kliszczewicz, A. Influence of recycled aggregates on mechanical properties of HS/HPC. *Cem. Concr. Compos.* **2002**, *24*, 269–279. [CrossRef]
9. McNeil, K.; Kang, T.H.-K. Recycled concrete aggregates: A review. *Int. J. Concr. Struct. Mater.* **2013**, *7*, 61–69. [CrossRef]
10. Poon, C.S.; Shui, Z.; Lam, L.; Fok, H.; Kou, S. Influence of moisture states of natural and recycled aggregates on the slump and compressive strength of concrete. *Cem. Concr. Res.* **2004**, *34*, 31–36. [CrossRef]

11. Kou, S.C.; Poon, C.S.; Chan, D. Influence of fly ash as cement replacement on the properties of recycled aggregate concrete. *J. Mater. Civ. Eng.* **2007**, *19*, 709–717. [CrossRef]

12. Xiao, J.; Li, W.; Fan, Y.; Huang, X. An overview of study on recycled aggregate concrete in China (1996–2011). *Constr. Build. Mater.* **2012**, *31*, 364–383. [CrossRef]

13. Butler, L.; West, J.; Tighe, S. The effect of recycled concrete aggregate properties on the bond strength between RCA concrete and steel reinforcement. *Cem. Concr. Res.* **2011**, *41*, 1037–1049. [CrossRef]

14. Deshpande, N.; Kulkarni, S.; Patil, N. Effectiveness of using coarse recycled concrete aggregate in concrete. *Int. J. Earth Sci. Eng. Sci. Technol. Int. J.* **2011**, *4*, 913–919.

15. Etxeberria, M.; Vázquez, E.; Marí, A.; Barra, M. Influence of amount of recycled coarse aggregates and production process on properties of recycled aggregate concrete. *Cem. Concr. Res.* **2007**, *37*, 735–742. [CrossRef]

16. Rahal, K. Mechanical properties of concrete with recycled coarse aggregate. *Build. Environ.* **2007**, *42*, 407–415. [CrossRef]

17. Katz, A. Properties of concrete made with recycled aggregate from partially hydrated old concrete. *Cem. Concr. Res.* **2003**, *33*, 703–711. [CrossRef]

18. Bhat, J.A. Effect of strength of parent concrete on the mechanical properties of recycled aggregate concrete. *Mater. Today Proc.* **2021**, *42*, 1462–1469. [CrossRef]

19. Awoyera, P.O. Nonlinear finite element analysis of steel fibre-reinforced concrete beam under static loading. *J. Eng. Sci. Technol.* **2016**, *11*, 1669–1677.

20. Cao, M.; Mao, Y.; Khan, M.; Si, W.; Shen, S. Different testing methods for assessing the synthetic fiber distribution in cement-based composites. *Constr. Build. Mater.* **2018**, *184*, 128–142. [CrossRef]

21. Sadrmomtazi, A.; Sobhani, J.; Mirgozar, M.A. Modeling compressive strength of EPS lightweight concrete using regression, neural network and ANFIS. *Constr. Build. Mater.* **2013**, *42*, 205–216. [CrossRef]

22. Awoyera, P.O.; Kirgiz, M.S.; Viloria, A.; Ovallos-Gazabon, D. Estimating strength properties of geopolymer self-compacting concrete using machine learning techniques. *J. Mater. Res. Technol.* **2020**, *9*, 9016–9028. [CrossRef]

23. Nafees, A.; Amin, M.N.; Khan, K.; Nazir, K.; Ali, M.; Javed, M.F.; Aslam, F.; Musarat, M.A.; Vatin, N.I. Modeling of Mechanical Properties of Silica Fume-Based Green Concrete Using Machine Learning Techniques. *Polymers* **2021**, *14*, 30. [CrossRef] [PubMed]

24. Nafees, A.; Javed, M.F.; Khan, S.; Nazir, K.; Farooq, F.; Aslam, F.; Musarat, M.A.; Vatin, N.I. Predictive Modeling of Mechanical Properties of Silica Fume-Based Green Concrete Using Artificial Intelligence Approaches: MLPNN, ANFIS, and GEP. *Materials* **2021**, *14*, 7531. [CrossRef]

25. Aslam, F.; Elkotb, M.A.; Iqtidar, A.; Khan, M.A.; Javed, M.F.; Usanova, K.I.; Khan, M.I.; Alamri, S.; Musarat, M.A. Compressive strength prediction of rice husk ash using multiphysics genetic expression programming. *Ain Shams Eng. J.* **2022**, *13*, 101593. [CrossRef]

26. Amin, M.N.; Khan, K.; Aslam, F.; Shah, M.I.; Javed, M.F.; Musarat, M.A.; Usanova, K. Multigene Expression Programming Based Forecasting the Hardened Properties of Sustainable Bagasse Ash Concrete. *Materials* **2021**, *14*, 5659. [CrossRef]

27. Shafabakhsh, G.H.; Ani, O.J.; Talebsafa, M. Artificial neural network modeling (ANN) for predicting rutting performance of nano-modified hot-mix asphalt mixtures containing steel slag aggregates. *Constr. Build. Mater.* **2015**, *85*, 136–143. [CrossRef]

28. Hodhod, O.A.; Ahmed, H.I. Modeling the corrosion initiation time of slag concrete using the artificial neural network. *HBRC J.* **2014**, *10*, 231–234. [CrossRef]

29. Carmichael, R.P. *Relationships between Young's Modulus, Compressive Strength, Poisson's Ratio, and Time for Early Age Concrete*; Swarthmore College: Swarthmore, PA, USA, 2009.

30. Bal, L.; Buyle-Bodin, F. Artificial neural network for predicting drying shrinkage of concrete. *Constr. Build. Mater.* **2013**, *38*, 248–254. [CrossRef]

31. Farooq, F.; Ahmed, W.; Akbar, A.; Aslam, F.; Alyousef, R. Predictive modeling for sustainable high-performance concrete from industrial wastes: A comparison and optimization of models using ensemble learners. *J. Clean. Prod.* **2021**, *292*, 126032. [CrossRef]

32. Ahmad, A.; Farooq, F.; Niewiadomski, P.; Ostrowski, K.; Akbar, A.; Aslam, F.; Alyousef, R. Prediction of compressive strength of fly ash based concrete using individual and ensemble algorithm. *Materials* **2021**, *14*, 794. [CrossRef] [PubMed]

33. Chou, J.-S.; Tsai, C.-F.; Pham, A.-D.; Lu, Y.-H. Machine learning in concrete strength simulations: Multi-nation data analytics. *Constr. Build. Mater.* **2014**, *73*, 771–780. [CrossRef]

34. Sufian, M.; Ullah, S.; Ostrowski, K.A.; Ahmad, A.; Zia, A.; Śliwa-Wieczorek, K.; Siddiq, M.; Awan, A.A. An Experimental and Empirical Study on the Use of Waste Marble Powder in Construction Material. *Materials* **2021**, *14*, 3829. [CrossRef] [PubMed]

35. Shah, M.I.; Memon, S.A.; Khan Niazi, M.S.; Amin, M.N.; Aslam, F.; Javed, M.F. Machine Learning-Based Modeling with Optimization Algorithm for Predicting Mechanical Properties of Sustainable Concrete. *Adv. Civ. Eng.* **2021**, *2021*, 6682283. [CrossRef]

36. Ziolkowski, P.; Niedostatkiewicz, M. Machine learning techniques in concrete mix design. *Materials* **2019**, *12*, 1256. [CrossRef]

37. Olalusi, O.B.; Awoyera, P.O. Shear capacity prediction of slender reinforced concrete structures with steel fibers using machine learning. *Eng. Struct.* **2021**, *227*, 111470. [CrossRef]

38. Dutta, S.; Samui, P.; Kim, D. Comparison of machine learning techniques to predict compressive strength of concrete. *Comput. Concr.* **2018**, *21*, 463–470.

39. Ilyas, I.; Zafar, A.; Javed, M.F.; Farooq, F.; Aslam, F.; Musarat, M.A.; Vatin, N.I. Forecasting Strength of CFRP Confined Concrete Using Multi Expression Programming. *Materials* **2021**, *14*, 7134. [CrossRef]

40. Song, Y.-Y.; Ying, L.U. Decision tree methods: Applications for classification and prediction. *Shanghai Arch. Psychiatry* **2015**, *27*, 130.
41. Hillebrand, E.; Medeiros, M.C. The benefits of bagging for forecast models of realized volatility. *Econom. Rev.* **2010**, *29*, 571–593. [CrossRef]
42. Ahmad, A.; Ahmad, W.; Aslam, F.; Joyklad, P. Compressive strength prediction of fly ash-based geopolymer concrete via advanced machine learning techniques. *Case Stud. Constr. Mater.* **2022**, *16*, e00840. [CrossRef]
43. Friedman, J.H. Greedy function approximation: A gradient boosting machine. *Ann. Stat.* **2001**, *29*, 1189–1232. [CrossRef]
44. Dahiya, N.; Saini, B.; Chalak, H.D. Gradient boosting-based regression modelling for estimating the time period of the irregular precast concrete structural system with cross bracing. *J. King Saud Univ.-Eng. Sci.* **2021**. [CrossRef]
45. Han, Q.; Gui, C.; Xu, J.; Lacidogna, G. A generalized method to predict the compressive strength of high-performance concrete by improved random forest algorithm. *Constr. Build. Mater.* **2019**, *226*, 734–742. [CrossRef]
46. Grömping, U. Variable importance assessment in regression: Linear regression versus random forest. *Am. Stat.* **2009**, *63*, 308–319. [CrossRef]
47. Xu, Y.; Ahmad, W.; Ahmad, A.; Ostrowski, K.A.; Dudek, M.; Aslam, F.; Joyklad, P. Computation of High-Performance Concrete Compressive Strength Using Standalone and Ensembled Machine Learning Techniques. *Materials* **2021**, *14*, 7034. [CrossRef]
48. Ahmad, A.; Chaiyasarn, K.; Farooq, F.; Ahmad, W.; Suparp, S.; Aslam, F. Compressive Strength Prediction via Gene Expression Programming (GEP) and Artificial Neural Network (ANN) for Concrete Containing RCA. *Buildings* **2021**, *11*, 324. [CrossRef]
49. Aslam, F.; Farooq, F.; Amin, M.N.; Khan, K.; Waheed, A.; Akbar, A.; Javed, M.F.; Alyousef, R.; Alabdulijabbar, H. Applications of gene expression programming for estimating compressive strength of high-strength concrete. *Adv. Civ. Eng.* **2020**, *2020*, 8850535. [CrossRef]
50. Wang, Q.; Ahmad, W.; Ahmad, A.; Aslam, F.; Mohamed, A.; Vatin, N.I. Application of Soft Computing Techniques to Predict the Strength of Geopolymer Coposites. *Polymers* **2022**, *14*, 1074. [CrossRef]
51. Ahmad, A.; Ostrowski, K.A.; Maślak, M.; Farooq, F.; Mehmood, I.; Nafees, A. Comparative Study of Supervised Machine Learning Algorithms for Predicting the Compressive Strength of Concrete at High Temperature. *Materials* **2021**, *14*, 4222. [CrossRef]
52. Limbachiya, M.; Meddah, M.S.; Ouchagour, Y. Use of recycled concrete aggregate in fly-ash concrete. *Constr. Build. Mater.* **2012**, *27*, 439–449. [CrossRef]
53. Ahmad, W.; Ahmad, A.; Ostrowski, K.A.; Aslam, F.; Joyklad, P.; Zajdel, P. Application of Advanced Machine Learning Approaches to Predict the Compressive Strength of Concrete Containing Supplementary Cementitious Materials. *Materials* **2021**, *14*, 5762. [CrossRef] [PubMed]
54. Farooq, F.; Nasir Amin, M.; Khan, K.; Rehan Sadiq, M.; Faisal Javed, M.; Aslam, F.; Alyousef, R. A comparative study of random forest and genetic engineering programming for the prediction of compressive strength of high strength concrete (HSC). *Appl. Sci.* **2020**, *10*, 7330. [CrossRef]
55. Mai, H.-V.T.; Nguyen, T.-A.; Ly, H.-B.; Tran, V.Q. Prediction compressive strength of concrete containing GGBFS using random forest model. *Adv. Civ. Eng.* **2021**, *2021*, 6671448. [CrossRef]
56. Zhang, J.; Ma, G.; Huang, Y.; Sun, J.; Aslani, F.; Nener, B. Modelling uniaxial compressive strength of lightweight self-compacting concrete using random forest regression. *Constr. Build. Mater.* **2019**, *210*, 713–719. [CrossRef]
57. Zhang, J.; Li, D.; Wang, Y. Predicting uniaxial compressive strength of oil palm shell concrete using a hybrid artificial intelligence model. *J. Build. Eng.* **2020**, *30*, 101282. [CrossRef]
58. Schapire, R.E. The boosting approach to machine learning: An overview. *Nonlinear Estim. Classif.* **2003**, 149–171. [CrossRef]
59. Yoda, K.; Yoshikane, T.; Nakashima, Y.; Soshiroda, T. Recycled cement and recycled concrete in Japan. In Proceedings of the International Conference on Demolition and Reuse of Concrete and Masonry, Tokyo, Japan, 7–11 November 1988; pp. 527–536.
60. Limbachiya, M.C.; Leelawat, T.; Dhir, R.K. Use of recycled concrete aggregate in high-strength concrete. *Mater. Struct.* **2000**, *33*, 574–580. [CrossRef]
61. Gómez-Soberón, J.M. Porosity of recycled concrete with substitution of recycled concrete aggregate: An experimental study. *Cem. Concr. Res.* **2002**, *32*, 1301–1311. [CrossRef]
62. Vázquez, E.; Hendriks, C.F.; Janssen, G.M.T. Influence of recycled concrete aggregates on concrete durability. In *International RILEM Conference on the Use of Recycled Materials in Building and Structures*; RILEM Publications SARL: Paris, France, 2004; pp. 554–562.
63. Lin, Y.-H.; Tyan, Y.-Y.; Chang, T.-P.; Chang, C.-Y. An assessment of optimal mixture for concrete made with recycled concrete aggregates. *Cem. Concr. Res.* **2004**, *34*, 1373–1380. [CrossRef]
64. Xiao, J.-Z.; Li, J.; Zhang, C. On relationships between the mechanical properties of recycled aggregate concrete: An overview. *Mater. Struct.* **2006**, *39*, 655–664. [CrossRef]
65. Wei, X.U. Experimental study on influence of recycled coarse aggregates contents on properties of recycled aggregate concrete. *Concrete* **2006**, 45–47.
66. Etxeberria, M.; Marí, A.R.; Vázquez, E. Recycled aggregate concrete as structural material. *Mater. Struct.* **2007**, *40*, 529–541. [CrossRef]
67. Evangelista, L.; de Brito, J. Mechanical behaviour of concrete made with fine recycled concrete aggregates. *Cem. Concr. Compos.* **2007**, *29*, 397–401. [CrossRef]
68. Poon, C.S.; Kou, S.C.; Lam, L. Influence of recycled aggregate on slump and bleeding of fresh concrete. *Mater. Struct.* **2006**, *40*, 981–988. [CrossRef]

69. Ajdukiewicz, A.B.; Kliszczewicz, A.T. Comparative tests of beams and columns made of recycled aggregate concrete and natural aggregate concrete. *J. Adv. Concr. Technol.* **2007**, *5*, 259–273. [CrossRef]
70. Min-Ping, H.U. Mechanical properties of concrete prepared with different recycled coarse aggregates replacement rate. *Concrete* **2007**, *2*, 16.
71. Wang, Z.W. Production and properties of high quality recycled aggregates. *Concrete* **2007**, *3*, 74–77.
72. Casuccio, M.; Torrijos, M.; Giaccio, G.; Zerbino, R. Failure mechanism of recycled aggregate concrete. *Constr. Build. Mater.* **2008**, *22*, 1500–1506. [CrossRef]
73. Min-Ping, H. Mechanical properties of recycled aggregate concrete at early ages. *Concrete* **2008**, *223*, 37–41.
74. Kou, S.C.; Poon, C.S.; Chan, D. Influence of fly ash as a cement addition on the hardened properties of recycled aggregate concrete. *Mater. Struct.* **2007**, *41*, 1191–1201. [CrossRef]
75. Yang, K.-H.; Chung, H.-S.; Ashour, A.F. Influence of Type and Replacement Level of Recycled Aggregates on Concrete Properties. *ACI Mater. J.* **2008**, *105*, 289–296.
76. Zhou, H.; Liu, B.K.; Lu, G. Experimental research on the basic mechanical properties of recycled aggregate concrete. *J. Anhui Inst. Archit. Indust* **2008**, *16*, 4–8.
77. Domingo-Cabo, A.; Lázaro, C.; Gayarre, F.L.; Serrano-López, M.; Serna, P.; Castaño-Tabares, J. Creep and shrinkage of recycled aggregate concrete. *Constr. Build. Mater.* **2009**, *23*, 2545–2553. [CrossRef]
78. Padmini, A.K.; Ramamurthy, K.; Mathews, M.S. Influence of parent concrete on the properties of recycled aggregate concrete. *Constr. Build. Mater.* **2009**, *23*, 829–836. [CrossRef]
79. Yang, X.; Wu, J.; Liang, J.G. Experimental study on relationship between tensile strength and compressive strength of recycled aggregate concrete. *Sichuan Build. Sci.* **2009**, *35*, 190–192.
80. Ye, H. Experimental study on mechanical properties of concrete made with high quality recycled aggregates. *Sichuan Build. Sci.* **2009**, *35*, 195–199.
81. Corinaldesi, V. Mechanical and elastic behaviour of concretes made of recycled-concrete coarse aggregates. *Constr. Build. Mater.* **2010**, *24*, 1616–1620. [CrossRef]
82. Kumutha, R.; Vijai, K. Strength of concrete incorporating aggregates recycled from demolition waste. *ARPN J. of Eng. Appl. Sci.* **2010**, *5*, 64–71.
83. Malešev, M.; Radonjanin, V.; Marinković, S. Recycled Concrete as Aggregate for Structural Concrete Production. *Sustainability* **2010**, *2*, 1204–1225. [CrossRef]
84. Zega, C.J.; Di Maio, Á.A. Recycled Concretes Made with Waste Ready-Mix Concrete as Coarse Aggregate. *J. Mater. Civ. Eng.* **2011**, *23*, 281–286. [CrossRef]
85. Belén, G.-F.; Fernando, M.-A.; Diego, C.L.; Sindy, S.-P. Stress–strain relationship in axial compression for concrete using recycled saturated coarse aggregate. *Constr. Build. Mater.* **2011**, *25*, 2335–2342. [CrossRef]
86. Fathifazl, G.; Razaqpur, A.G.; Isgor, O.B.; Abbas, A.; Fournier, B.; Foo, S. Creep and drying shrinkage characteristics of concrete produced with coarse recycled concrete aggregate. *Cem. Concr. Compos.* **2011**, *33*, 1026–1037. [CrossRef]
87. González-Fonteboa, B.; Martínez-Abella, F.; Eiras-López, J.; Paz, S.S. Effect of recycled coarse aggregate on damage of recycled concrete. *Mater. Struct.* **2011**, *44*, 1759–1771. [CrossRef]
88. Rao, M.C.; Bhattacharyya, S.K.; Barai, S.V. Influence of field recycled coarse aggregate on properties of concrete. *Mater. Struct.* **2010**, *44*, 205–220. [CrossRef]
89. Somna, R.; Jaturapitakkul, C.; Chalee, W.; Rattanachu, P. Effect of the Water to Binder Ratio and Ground Fly Ash on Properties of Recycled Aggregate Concrete. *J. Mater. Civ. Eng.* **2012**, *24*, 16–22. [CrossRef]
90. Elhakam, A.A.; Mohamed, A.E.; Awad, E. Influence of self-healing, mixing method and adding silica fume on mechanical properties of recycled aggregates concrete. *Constr. Build. Mater.* **2012**, *35*, 421–427. [CrossRef]
91. Cui, Z.L.; Lu, S.S.; Wang, Z.S. Influence of recycled aggregate on strength and anti-carbonation properties of recycled aggregate concrete. *J. Build. Mater* **2012**, *15*, 264–267.
92. Hoffmann, C.; Schubert, S.; Leemann, A.; Motavalli, M. Recycled concrete and mixed rubble as aggregates: Influence of variations in composition on the concrete properties and their use as structural material. *Constr. Build. Mater.* **2012**, *35*, 701–709. [CrossRef]
93. Li, H.; Xiao, J.Z. On fatigue strength of recycled aggregate concrete based on its elastic modulus. *J. Build. Mater* **2012**, *15*, 260–263.
94. Limbachiya, M.; Meddah, M.S.; Ouchagour, Y. Performance of Portland/Silica Fume Cement Concrete Produced with Recycled Concrete Aggregate. *ACI Mater. J.* **2012**, *109*, 91–100.
95. Marinković, S.; Radonjanin, V.; Malešev, M.; Ignjatović, I. Comparative environmental assessment of natural and recycled aggregate concrete. *Waste Manag.* **2010**, *30*, 2255–2264. [CrossRef] [PubMed]
96. Pereira, P.; Evangelista, L.; de Brito, J. The effect of superplasticizers on the mechanical performance of concrete made with fine recycled concrete aggregates. *Cem. Concr. Compos.* **2012**, *34*, 1044–1052. [CrossRef]
97. Barbudo, A.; De Brito, J.; Evangelista, L.; Bravo, M.; Agrela, F. Influence of water-reducing admixtures on the mechanical performance of recycled concrete. *J. Clean. Prod.* **2013**, *59*, 93–98. [CrossRef]
98. Butler, L.; West, J.S.; Tighe, S.L. Effect of recycled concrete coarse aggregate from multiple sources on the hardened properties of concrete with equivalent compressive strength. *Constr. Build. Mater.* **2013**, *47*, 1292–1301. [CrossRef]
99. Chen, Z.P.; Xu, J.J.; Zheng, H.H.; Su, Y.S.; Xue, J.Y.; Li, J.T. Basic mechanical properties test and stress-strain constitutive relations of recycled coarse aggregate concrete. *J. Build. Mater.* **2013**, *16*, 24–32.

100. Hou, Y.L.; Zheng, G. Mechanical properties of recycled aggregate concrete in different age. *J. Build. Mater.* **2013**, *16*, 683–687.
101. Ismail, S.; Ramli, M. Engineering properties of treated recycled concrete aggregate (RCA) for structural applications. *Constr. Build. Mater.* **2013**, *44*, 464–476. [CrossRef]
102. Manzi, S.; Mazzotti, C.; Bignozzi, M.C. Short and long-term behavior of structural concrete with recycled concrete aggregate. *Cem. Concr. Compos.* **2013**, *37*, 312–318. [CrossRef]
103. Matias, D.; De Brito, J.; Rosa, A.; Pedro, D. Mechanical properties of concrete produced with recycled coarse aggregates—Influence of the use of superplasticizers. *Constr. Build. Mater.* **2013**, *44*, 101–109. [CrossRef]
104. Sheen, Y.-N.; Wang, H.-Y.; Juang, Y.-P.; Le, D.-H. Assessment on the engineering properties of ready-mixed concrete using recycled aggregates. *Constr. Build. Mater.* **2013**, *45*, 298–305. [CrossRef]
105. Thomas, C.; Setién, J.; Polanco, J.A.; Alaejos, P.; De Juan, M.S. Durability of recycled aggregate concrete. *Constr. Build. Mater.* **2013**, *40*, 1054–1065. [CrossRef]
106. Ulloa, V.A.; García-Taengua, E.; Pelufo, M.-J.; Domingo, A.; Serna, P. New views on effect of recycled aggregates on concrete compressive strength. *ACI Mater. J.* **2013**, *110*, 1–10.
107. Xiao, J.; Li, H.; Yang, Z. Fatigue behavior of recycled aggregate concrete under compression and bending cyclic loadings. *Constr. Build. Mater.* **2013**, *38*, 681–688. [CrossRef]
108. Younis, K.; Pilakoutas, K. Strength prediction model and methods for improving recycled aggregate concrete. *Constr. Build. Mater.* **2013**, *49*, 688–701. [CrossRef]
109. Andreu, G.; Miren, E. Experimental analysis of properties of high performance recycled aggregate concrete. *Constr. Build. Mater.* **2014**, *52*, 227–235. [CrossRef]
110. Beltrán, M.G.; Agrela, F.; Barbudo, A.; Ayuso, J.; Ramírez, A. Mechanical and durability properties of concretes manufactured with biomass bottom ash and recycled coarse aggregates. *Constr. Build. Mater.* **2014**, *72*, 231–238. [CrossRef]
111. Beltrán, M.G.; Barbudo, A.; Agrela, F.; Galvín, A.P.; Jiménez, J.R. Effect of cement addition on the properties of recycled concretes to reach control concretes strengths. *J. Clean. Prod.* **2014**, *79*, 124–133. [CrossRef]
112. Çakır, Ö.; Sofyanlı, Ö.Ö. Influence of silica fume on mechanical and physical properties of recycled aggregate concrete. *HBRC J.* **2015**, *11*, 157–166. [CrossRef]
113. Carneiro, J.A.; Lima, P.R.L.; Leite, M.B.; Toledo Filho, R.D. Compressive stress–strain behavior of steel fiber reinforced-recycled aggregate concrete. *Cem. Concr. Compos.* **2014**, *46*, 65–72. [CrossRef]
114. Dilbas, H.; Şimşek, M.; Çakır, Ö. An investigation on mechanical and physical properties of recycled aggregate concrete (RAC) with and without silica fume. *Constr. Build. Mater.* **2014**, *61*, 50–59. [CrossRef]
115. Duan, Z.; Poon, C.S. Properties of recycled aggregate concrete made with recycled aggregates with different amounts of old adhered mortars. *Mater. Des.* **2014**, *58*, 19–29. [CrossRef]
116. Folino, P.; Xargay, H. Recycled aggregate concrete—Mechanical behavior under uniaxial and triaxial compression. *Constr. Build. Mater.* **2014**, *56*, 21–31. [CrossRef]
117. Gayarre, F.L.; Pérez, C.L.-C.; López, M.A.S.; Cabo, A.D. The effect of curing conditions on the compressive strength of recycled aggregate concrete. *Constr. Build. Mater.* **2014**, *53*, 260–266. [CrossRef]
118. Kang, T.H.-K.; Kim, W.; Kwak, Y.-K.; Hong, S.-G. Flexural Testing of Reinforced Concrete Beams with Recycled Concrete Aggregates. *ACI Struct. J.* **2014**, *111*, 607–616. [CrossRef]
119. Pedro, D.; de Brito, J.; Evangelista, L. Performance of concrete made with aggregates recycled from precasting industry waste: Influence of the crushing process. *Mater. Struct.* **2014**, *48*, 3965–3978. [CrossRef]
120. Pepe, M.; Toledo Filho, R.D.; Koenders, E.A.B.; Martinelli, E. Alternative processing procedures for recycled aggregates in structural concrete. *Constr. Build. Mater.* **2014**, *69*, 124–132. [CrossRef]
121. Thomas, C.; Sosa, I.; Setién, J.; Polanco, J.A.; Cimentada, A.I. Evaluation of the fatigue behavior of recycled aggregate concrete. *J. Clean. Prod.* **2014**, *65*, 397–405. [CrossRef]

Damage Identification Method for Medium- and Small-Span Bridges Based on Macro-Strain Data under Vehicle–Bridge Coupling

Hao Zhang [1,2,*]**, Zhixin Zhong** [3]**, Junmiao Duan** [4]**, Jianke Yang** [3]**, Zhichao Zheng** [3] **and Guangxun Liu** [3]

1   State Key Laboratory of Structural Mechanics Behavior and System Safety in Traffic Engineering, Shijiazhuang Tiedao University, Shijiazhuang 050043, China
2   Structural Health Monitor and Control Institute, Shijiazhuang Tiedao University, Shijiazhuang 050043, China
3   School of Civil Engineering, Shijiazhuang Tiedao University, Shijiazhuang 050043, China; zzxjgjkjc@foxmail.com (Z.Z.); yang18033702683@163.com (J.Y.); zhengzhichao0217@163.com (Z.Z.); liuguangxun0518@163.com (G.L.)
4   School of Transportation, Shijiazhuang Tiedao University, Shijiazhuang 050043, China; duanjunmiao@163.com
*   Correspondence: zhanghao@stdu.edu.cn

Abstract: The damage identification method based on macro-strain modality has shown good results for large-span flexible bridges. However, medium- and small-span bridges have a high stiffness, and the axle system is embodied. The strong time-varying vibration characteristics, coupled with the non-stationary characteristics of vehicle loads, make it difficult to accurately determine the stable strain modes of such bridges. To solve this problem, a damage localization index in the form of an amplitude vector matrix of the mutual energy density spectrum based on macro-strain was constructed using wavelet transform de-noising and reconstruction technology and cross-correlation function. The macro-static strain and macro-dynamic strain data obtained from a vehicle–bridge coupling experiment were reconstructed through wavelet transform, and the factors influencing the damage indices were analyzed. The results showed that the proposed indicators could help realize an accurate damage localization for medium- and small-span bridge systems with different damage degrees under the action of vehicle–bridge coupling.

Keywords: macro-strain mode; medium- and small-span bridges; wavelet transform; cross-correlation function

1. Introduction

Transportation is vital to regional economic development, and bridges are key to maintaining a smooth traffic flow. The normal operation of a transportation system relies heavily on the health of bridge structures [1,2]. To ensure the safety of bridge operation, several health monitoring systems have been established. However, existing monitoring systems are complex, expensive, and mostly applicable to long-span bridges. In highway and railway bridges, the vast majority of bridges are medium- and small-span bridges (the middle bridge generally has the total length of porous span between 30 m and 100 m or the single span between 20 m and 40 m, and the small bridge mostly refers to the total length of porous span between 8 m and 30 m or the single span between 5 m and 20 m). The medium- and small-span bridges have small span and large stiffness, so the vehicle–bridge coupling effect is obvious. At the same time, small- and medium-span bridges are prone to cracks and reduce the structural stiffness of bridges. However, because of its complex structure and soft structure, long-span bridges are often the key objects of structural health monitoring and detection, while small- and medium-span bridges lack attention. In recent years, due to the increase in vehicle load, structural deterioration, and structural form that do not conform to the current specification, the tilting erosion and fracture of medium- and small-span bridges have occurred. Throughout the domestic and

foreign bridge damage accident cases, the proportion of small- and medium-span bridge damage accidents accounted for the vast majority. Therefore, it is necessary to improve the real-time monitoring of the damage condition of medium- and small-span bridges, and develop a simple damage identification technology suitable for practical applications.

With the development of bridge construction and health monitoring technology, the damage identification method of bridge structure has developed rapidly. So far, many mature theoretical methods have emerged. The classification of monitoring data based on damage identification can be divided into a damage identification method based on static measurement data and a damage identification method based on dynamic monitoring data. The static-based damage identification method is reliable, but it is time-consuming, laborious, and expensive to interrupt the traffic in the detection, which is not conducive to the real-time evaluation of the bridge state. For example, static load test, percussion method, and millimeter wave radar method [3] based on non-destructive damage detection need to interrupt traffic for damage identification, which brings great inconvenience to people's travel. However, the damage identification method based on dynamic response can not interrupt the traffic, and only relying on environmental incentives can achieve the goal of online damage identification for bridges. Different from acceleration sensors, long-gauge strain sensors can not only reflect the overall information of the bridge, but also represent the local information of the structure. The strain index is more sensitive to local damage [4], whereas the displacement index is more effective for overall damage identification [5]. The sensitivity for local damage identification is arranged from low to high, and local damage in structures can be more easily identified using the strain index than the displacement index [6]. With the development of macro-strain measurement technology, the distributed strain sensing technology realizes the regional sensing, which overcomes the shortcomings of the traditional 'point' sensing that is too local, and overcomes the shortcomings of the traditional displacement sensing and acceleration sensing that are too macroscopic. It integrates the local and global information of structures, enables dynamic and static testing, and has advantages such as accurate damage localization and high quantitative accuracy [7–10]. Therefore, in this paper, the measured macro-strain data will be used as the data source for medium- and small-span bridge damage identification.

Based on macro-strain data, the following damage identification methods have been developed in recent years. Li et al. [11,12] employed a macro-strain mode vector with a long gauge as the damage index; it exhibited a high accuracy for damage localization and quantification with a good application effect for long-span flexible bridges. Wu et al. [8] proposed a structural damage identification method based on macro-strain modal vector. The modal parameters were extracted by strain response, and then the two-level strategy for flexible structure damage detection was proposed. Hong [13] proposed a method of only output modal macro-strain extraction and a bridge damage identification method under environmental excitation, and theoretically proved that the modal macro-strain of the strain sensor was uniquely determined by the peak value of the dynamic macro-strain response power spectrum density (PSD). Then, this method was applied to the state assessment of a practical bridge in New Jersey. Xu et al. [14,15] proposed a damage identification method for long-span cable-stayed bridges based on the residual trend of the macro-strain modal and the energy of macro-strain frequency response function. This method is clear in theory and easy to implement. According to the mapping relationship between long strain and displacement, Zhang et al. [10] deduced the macro-strain frequency response function, and proposed two structural strain modal identification methods based on it, and verified the effectiveness of the two methods. Anastasopoulos [16] identified the strain mode and characteristic frequency of the prestressed concrete beam model by macro-strain data to identify the damage and damage location of the structure. There are obvious changes in the amplitude and curvature of the strain mode in the damage area. However, medium- and small-span bridges have high rigidity. When the vehicle-to-bridge mass ratio is relatively high, the vibration effect due to vehicle–bridge coupling cannot be ignored. The structural system will reflect the time-varying vibration characteristics, and the non-stationary charac-

teristics of the vehicle load will make it difficult to accurately obtain the stable strain mode of the bridge [15,17]. Clearly, identifying damages in a time-varying bridge based on the macro-strain modal test method is challenging, and the existing macro-strain theory cannot be directly applied to the damage identification of medium- and small-span bridges [18,19]. Hong et al. [4] established a static damage identification method based on the difference of macro-strain influence line area before and after structural damage by using a vehicle moving load. Li [20] proposed a damage identification method for urban road viaducts based on the working deformation of the macro-strain in the frequency-domain. This method can accurately identify damage locations and provides a good solution to the macro-strain problems encountered in the damage identification of medium- and small-span bridges. The idea is to advance the application of macro-strain-based damage identification to medium- and small-span bridges. Razavi and Hadidi [21] proposed a structural damage identification method based on finite element model correction and wavelet packet transform component energy, and verified the effectiveness and applicability of this method in structural damage identification by taking a two-dimensional steel truss structure as an example. The results show that this method can accurately determine the existence, location, and magnitude of damage, but the method requires the finite element model of the structure without damage. The performance of damage identification using macro-strain data is excellent, and the vehicle–bridge ratio of medium- and small-span bridges is large. When a vehicle passes the bridge, obvious macro-strain data can be measured, which provides a guarantee for subsequent damage identification. However, the complicated damage identification theory makes it challenging for ordinary engineers to grasp. Therefore, how to make the damage identification method based on macro-strain more easily applied in the damage identification of medium- and small-span bridges has become a research focus.

As a time–frequency analysis method, wavelet analysis has the characteristics of multiresolution and has a strong ability to represent the local characteristics of a signal, particularly when dealing with non-stationary signals. It can realize an effective decomposition and noise reduction of signal data [22]. Yu [23] conducted a modal analysis of a cracked bridge based on the structural dynamic equation of motion, studied the modal characteristics of the damaged bridge, and realized damage localization through the wavelet coefficients of the wavelet transform. Liu [24] employed the curvature of the displacement response and the cross-correlation function of the vehicle-excited bridge response as damage indices and applied the time–frequency analysis method of lifting wavelet transforms to identify bridge damage under moving loads. This method does not require damage-free structural response information, and the damage can simply be identified through the vibration response data of the bridge under different moving loads. Although it can effectively identify the damage location, the degree of damage cannot be easily quantified. Macro-strain damage identification methods are mostly based on empirical mode decomposition analysis, while wavelet transform for noise reduction and time–frequency analysis are rarely used.

Based on the above research, this paper reports a damage localization index in the form of an amplitude vector matrix of the mutual energy density spectrum based on macro-strain, constructed using wavelet transform de-noising and reconstruction technology and cross-correlation function. With the macro-dynamic strain and macro-static strain experimental data, the accuracy of the proposed damage localization index was verified in terms of the damage degree, damage location, and vehicle-to-bridge mass ratio. The experimental results showed that the proposed indicators could achieve precise damage localization for medium- and small-span bridge systems with different damage degrees under the action of vehicle–bridge coupling.

2. Theoretical Basis

2.1. Damage Identification Based on Vehicle–Bridge Coupling Theory

For a small-span bridge with a relatively high vehicle-to-bridge mass ratio, the moving vehicle-mounted action can be approximately considered vehicle–bridge coupling, and the

vehicle–bridge system has time-varying characteristics [25–27]. This is shown in Figure 1. P is the force actions on the bridge; t is the vehicle travel time in the bridge; v is the speed of the vehicle; M_1 is the vehicle mass; $y(x, t)$ is the vertical dynamic displacement of the bridge; x is the distance traveled by the vehicle on the bridge; l is the length of the bridge.
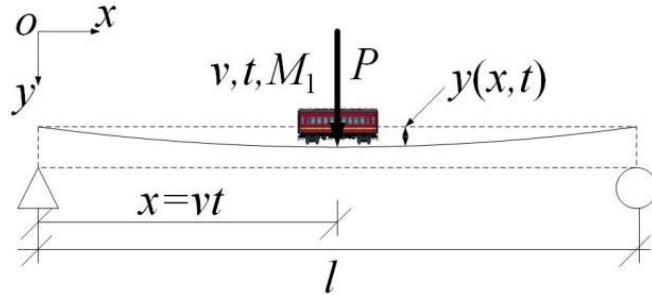
Figure 1. Vehicle–bridge time-varying system.

When the vehicle–bridge coupling effect is considered, the macro-strain generated by the moving vehicle-mounted action includes two categories. One is the macro-strain generated by the vehicle weight, i.e., the static strain. The other is the macro-dynamic strain due to the vehicle–bridge coupling. Therefore, based on the measured macro-strain data and wavelet transform, this study reconstructed and separated the macro-dynamic and static strains, and then used the reconstructed macro-static and dynamic strain data as the research object to perform an impact analysis on damage localization [19,28].

Based on the modal superposition method and D'Alembert's principle, a vehicle–bridge coupling model was established [29], as shown in Figure 2. M_s is the mass of the car body; M_{t1} represents the total mass of suspension device of vehicle front axle and tires; M_{t2} represents the total mass of rear axle suspension device and tires. k_{s1} and k_{s2} represent the spring stiffness of the front and rear axle suspension system of vehicle, respectively; k_{t1} and k_{t2} are, respectively, the stiffness of the front and rear axle tires of the vehicle. c_{s1} and c_{t1} are the damping of vehicle front axle suspension system and tires, respectively. On the contrary, c_{s2} and c_{t2} are the damping of vehicle rear axle suspension system and tires, respectively. y_s is the vertical displacement of the car body. θ represents the rotation angle of the car body. y_{t1} is the vertical displacement of vehicle front axle suspension system; y_{t2} is the vertical displacement of vehicle rear axle suspension system; y_{c1} and y_{c2} are the vertical displacements of the front and rear axle tires, respectively.
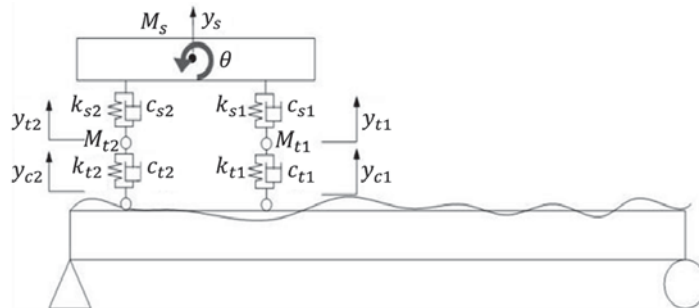
Figure 2. Coupling effect of the vehicle and bridge.

The bridge vibration equations of the vehicle–bridge coupled vibration model shown in Figure 2 can be expressed as:

$$[M_v]\{\ddot{y}_v\} + [C_v]\{\dot{y}_v\} + [K_v]\{y_v\} = \{F_{v-b}\} + \{F_G\} \tag{1}$$

$$[M_b]\{\ddot{y}_b\} + [C_b]\{\dot{y}_b\} + [K_b]\{y_b\} = \{F_{b-v}\} \tag{2}$$

where $[M_v]$, $[C_v]$, and $[K_v]$ are the mass, damping, and stiffness matrices of the vehicle, respectively; $[M_b]$, $[C_b]$, and $[K_b]$ are, respectively, the mass, damping, and stiffness matrices of the bridge; $\{y_b\}$ and $\{y_v\}$ are the displacement vectors of the bridge and vehicle, respectively; $\{F_{v-b}\}$ and $\{F_{b-v}\}$ are, respectively, the combined force components of the vehicle–bridge coupling acting on the vehicle and bridge; $\{F_G\}$ is the gravity vector acting on the vehicle.

Based on the dynamic balance and displacement coordination relationship, the following matrix can be established:

$$\begin{bmatrix} M_v & \\ & M_b \end{bmatrix} \begin{Bmatrix} \ddot{y}_v \\ \ddot{y}_b \end{Bmatrix} + \begin{bmatrix} C_v & C_{v-b} \\ C_{b-v} & C_b + C_{b-b} \end{bmatrix} \begin{Bmatrix} \dot{y}_v \\ \dot{y}_b \end{Bmatrix} + \begin{bmatrix} K_v & K_{v-b} \\ K_{b-v} & K_b + K_{b-b} \end{bmatrix} \begin{Bmatrix} y_v \\ y_b \end{Bmatrix} = \begin{Bmatrix} F_{v-b} + F_G \\ F_{b-v} \end{Bmatrix} \tag{3}$$

In this formula, C_{v-b}, C_{b-v}, C_{b-b}, K_{v-b}, K_{b-v}, K_{b-b}, F_{v-b}, and F_{b-v} are the coupling terms generated by vehicle–bridge coupling. Generally, $Newmark - \beta$ is used to solve the above coupling equation.

After solving for the displacement y_b at each point in the bridge using this method, the angular displacement φ_b of the point can be obtained by differentiating the displacement [30].

$$\varphi_b(x,t) = -\frac{dy_b(x,t)}{dx} \tag{4}$$

$$\bar{\varepsilon}(L_m,t) = \frac{\varphi_b(x,t) - \varphi_a(x,t)}{L_m} h_m \tag{5}$$

where $\bar{\varepsilon}$ is the theoretical macro-strain, L_m is the gauge length, h_m is the height of the neutral axis. $\varphi_a(x,t)$ is the angular displacement of the point a, $\varphi_b(x,t)$ is the angular displacement of the point b.

2.2. Reconstruction of Macro-Strain by Wavelet Transform

The measured macro-dynamic response $\bar{\varepsilon}'(L_m,t)$ of the bridge under environmental excitation and moving load excitation includes complex response signals, such as the vehicle load and environmental excitation [31,32], as expressed in Equation (6). Therefore, it is necessary to eliminate the influence of environmental excitation, such as noise, and extract useful strain signals of vehicle load from the complex macro-dynamic strain signals, so that the time-varying bridge damage can be effectively identified.

$$\bar{\varepsilon}'(L_m,t) = \bar{\varepsilon}(L_m,t) + \xi(t) \tag{6}$$

where, $\bar{\varepsilon}'(L_m,t)$ is the actual measured macro-strain, $\xi(t)$ is the macro-strain response signal generated by environmental excitation.

In the actual engineering signal acquisition, the signal mostly contains many mutations and spikes, and the noise signal is not a stationary white noise signal. Therefore, when de-noising this non-stationary signal, the traditional Fourier transform cannot give the mutation of the signal at a certain time point, and it is difficult to effectively distinguish the mutation of the signal in the time domain, which makes it difficult to realize the accurate de-noising of non-stationary signals by Fourier transform. However, the wavelet transform is different. It can conduct signal analysis in both time and frequency domains at the same time, which can effectively distinguish the noise part of the signal and the mutation of the signal on the time axis, so as to complete the reasonable noise reduction of non-stationary signals. In the following, the measured macro-strain $\bar{\varepsilon}'(L_m,t)$ is decomposed

and reconstructed by wavelet transform to remove the influence of environmental noise on macro-strain.

$$\bar{\varepsilon}'(L_m, t) = c_1 A_1 + c_1 D_1 + c_2 A_2 + c_2 D_2 \cdots c_i D_i \tag{7}$$

where i is the number of decomposition layers, $c_i A_i$ is the approximate part of the decomposition, $c_i D_i$ is the detailed part of the decomposition, and the noise part is typically included in $c_i D_i$. The de-noise separation can be applied to obtain the reconstructed macro-strain $\bar{\varepsilon}_{cg}(L_m, t)$, as expressed in Equation (8).

$$\bar{\varepsilon}_{cg}(L_m, t) = c_1 A_1 + c_2 A_2 + \cdots c_i A_i \tag{8}$$

3. Construction of Damage Indices
Damage Localization Index Based on Macro-Strain

The reconstructed macro-strain response curve $\bar{\varepsilon}_{cg}(L_m, t)$ can obtain $\bar{\varepsilon}_{cg}(L_m, \omega)$ by Fourier transformed.

$$\bar{\varepsilon}_{cg}(L_m, \omega) = \int_{-\infty}^{\infty} \psi(L_m, t) e^{-j\omega t} \mathrm{d}t = Re(\omega) + jIm(\omega) = |X(\omega)| e^{j\phi(\omega)} \tag{9}$$

where, the amplitude is $|X(\omega)| = \sqrt{Re^2(\omega) + Im^2(\omega)}$. $Re(\omega)$ and $Im(\omega)$ are, respectively, the real and imaginary parts of the Fourier function.

The macro-strain amplitude after Fourier transform was selected to perform a cross-correlation function calculation among the elements, and the mutual energy density spectrum of the macro-strain amplitude corresponding to the frequency $\omega = \frac{1}{t}$ was obtained, as expressed in Equation (10).

$$m_{(n-1)\times n, \omega}^{\omega_\omega} = X(\omega_{n-1}^{\omega_\omega}) \times X(\omega_n^{\omega_\omega}) \tag{10}$$

where $\left|X(\omega_n^{\omega_\omega})\right|$ and $\left|X(\omega_{n-1}^{\omega_\omega})\right|$ are the macro-strain response amplitudes at the frequency of the measuring points of elements n and $n-1$, respectively.

The amplitude matrix of mutual energy density spectral between n elements in full frequency domain (or full-time domain) is obtained by calculating the cross-correlation function of the measured data of n long-gauge elements. The cross-correlation of a single element is self-energy density spectrum, and that of different elements is mutual energy density spectrum. The amplitude matrix has multiple forms. Therefore, to better describe its dynamic characteristics, all the types of deformations are uniformly named as the element energy product among the cross-correlated long-gauge elements in the frequency domain. This product is hereinafter referred to as the cross-correlation element energy product, which is equivalent to the amplitude vector of the macro-strain mutual energy density spectrum among the long-gauge elements.

$$\left\{ \begin{matrix} m_{1,1}^{\omega_1} & m_{1,2}^{\omega_2} & \cdots & m_{1,\omega-1}^{\omega_{\omega-1}} & m_{1,\omega}^{\omega_\omega} & m_{1,\omega+1}^{\omega_1} & m_{1,\omega+2}^{\omega_2} & \cdots & m_{1,2\omega}^{\omega_{\omega-1}} & m_{1,2\omega}^{\omega_\omega} \\ m_{2,1}^{\omega_1} & m_{2,2}^{\omega_2} & \cdots & m_{2,\omega-1}^{\omega_{\omega-1}} & m_{2,\omega}^{\omega_\omega} & m_{2,\omega+1}^{\omega_1} & m_{2,\omega+2}^{\omega_2} & \cdots & m_{2,2\omega}^{\omega_{\omega-1}} & m_{2,2\omega}^{\omega_\omega} \\ \vdots & \vdots & \vdots & \vdots & \vdots & \vdots & \vdots & \vdots & \vdots & \vdots \\ m_{(n-1)\times n,1}^{\omega_1} & \cdots & \cdots & \cdots & m_{(n-1)\times n,\omega}^{\omega_\omega} & m_{(n-1)\times n,\omega+1}^{\omega_1} & \cdots & \cdots & \cdots & m_{(n-1)\times n,2\omega}^{\omega_\omega} \\ m_{n\times n,1}^{\omega_1} & \cdots & \cdots & \cdots & m_{n\times n,\omega}^{\omega_\omega} & m_{n\times n,\omega+1}^{\omega_1} & \cdots & \cdots & \cdots & m_{n\times n,2\omega}^{\omega_\omega} \end{matrix} \right\} \tag{11}$$

where $n \in Z$, and the full-frequency domain is $\{\omega_1, \omega_2 \cdots \omega_\omega\}$.

For 32 long-gauge Bragg grating strain sensors pasted on the bridge, the bridge can be divided into 32 long-gauge elements, with each element producing a macro-strain, including macro-static strain and macro-dynamic strain. The data of two types are mixed, and the above-mentioned wavelet transform de-noising and reconstruction technology can be used for separating the macro-static strain and macro-dynamic strain. The long-gauge elements calculated using the cross-correlation function will increase by the square of the

number and is termed the cross-correlation long-gauge elements, that is, there will be 1024 cross-correlation long-gauge elements. Based on the initial element, each element superimposed by the total number of elements is called the cross-correlation long-gauge element group. In order to better display the damage location effect, 1024 cross-correlation element vectors were presented in the form of matrix coordinates of 32 rows and 32 columns, as expressed in Matrix (12). When a certain element is damaged, the coordinate of the corresponding matrix diagonal position changes abruptly.

$$
\begin{bmatrix}
(1,1) & \cdots & (1,32) \\
\vdots & \ddots & \vdots \\
(32,1) & \cdots & (32,32)
\end{bmatrix}
\tag{12}
$$

The above damage localization method is summarized as shown in Figure 3.
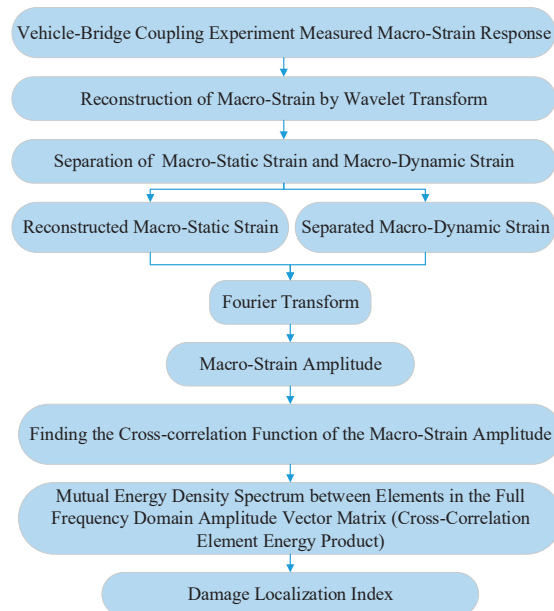
Figure 3. Damage localization.

4. Experimental Analysis

The span of common small and medium bridges is 24 m. According to the actual bridge, an aluminum box-type simply supported girder bridge was designed by the scale of 1:7.5. The modulus of elasticity was set to 69 GPa, the Poisson's ratio was 0.33, the density was 2700 kg/m^3, the dead weight was 13.07 kg, and the first-order natural vibration frequency was 16.23 Hz. Thirty-two long-gauge fiber Bragg grating strain sensors were pasted along the span of the upper roof of the beam to measure the compressive strain (taking the absolute strain value). Subsequently, the beam was divided into 32 long-gauge elements of 10 cm each. A temperature compensation sensor of the same type was connected in series. After the bonding was completed, the wavelength of the sensor was calibrated, and the wavelength of 33 strain sensors with long gauge at the same time was recorded as the initial value. Figure 4 shows the vehicle–bridge experimental model and sensor layout. The self-weight of the mobile trolley was 8 kg, and its mass could be varied by adding weight, as shown in Figure 5. Table 1 lists the damage condition settings. Figure 6 shows the experimental operation [33–35].
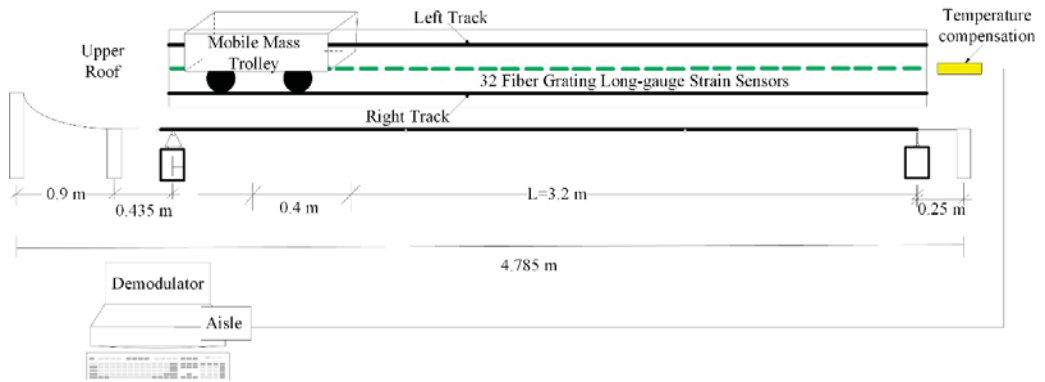
Figure 4. Vehicle–bridge experimental model and sensor layout diagram.
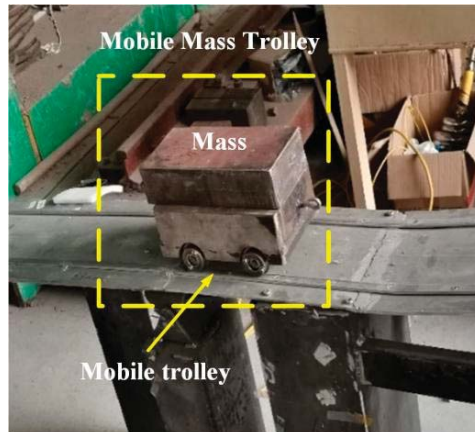
Figure 5. Mobile trolley.

Table 1. Damage condition table.

Damage Condition Number	Damage to the Element	Damage Width (cm)	Damage Degree (%)	
D0	0	0	0	
D1	26	0.5	Level 1 damage	
D2	26	0.5	Level 2 damage	
D3	26	5	Level 3 damage	
D4	26	5	Level 4 damage	
D5	6, 26	5, 0.5	Level 1 damage	Level 4 damage
D6	6, 26	5, 0.5	Level 2 damage	Level 4 damage
D7	6, 26	5, 5	Level 3 damage	Level 4 damage

Note: The damage degree is the percentage of damage in the entire long-gauge element. Damage width refers to the length of failure along the bridge direction at the bottom part of the box girder, which is similar to the crack. The damage location is set in the 26th or 6th long-gauge element of the lower bottom plate of the box girder. According to the damage length of the bottom plate of the box girder and the degree of damage of the web, the damage degree is comprehensively set according to the average stiffness reduction method, in which the working conditions D1 and D2 are the same damage width of the bottom plate of the box girder, and the damage of the D2 web is larger, and the overall stiffness is small. The damage is stronger, so the damage degree of D2 is greater than that of D1. D3 and D4, D5 and D6 are also set in the same way.
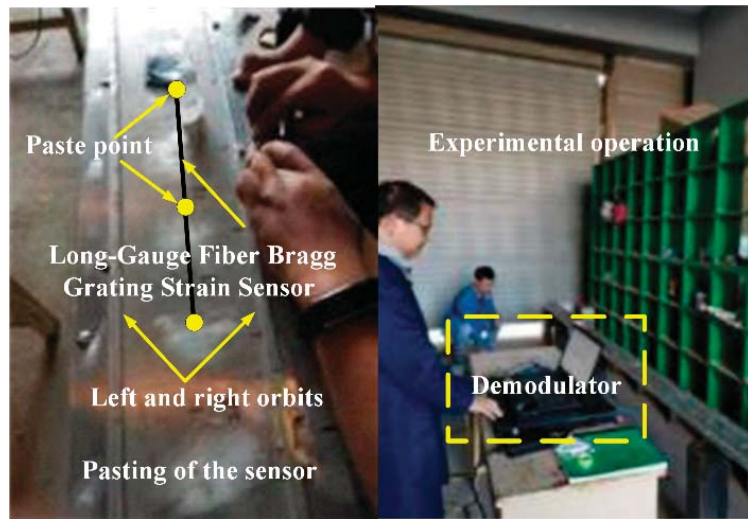
Figure 6. Sensor installation and experimental operation.

4.1. Reconstruction and Separation of Macro-Strain by Wavelet Transform

After sorting the macro-strain data obtained from the vehicle–bridge coupling experiment, the overall strain diagram of the moving vehicle while passing through the bridge was obtained, as shown in Figure 7. The wavelet basis function mentioned above was used for noise reduction and reconstruction to obtain the time history curve of static strain generated by the moving vehicle-mounted action on the bridge, as shown in Figure 8a. Strain separation was then performed to obtain the macro-dynamic strain curve generated by the vehicle–bridge coupling action, as shown in Figure 8b.
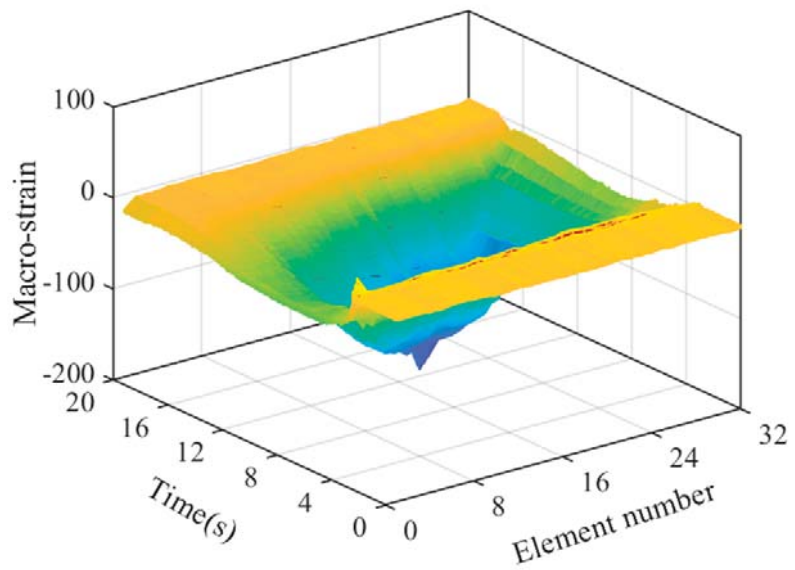
Figure 7. Overall strain diagram.

In the case of vehicle–bridge coupling, a time history curve of static strain is generated by the weight of the vehicle, which is not easily affected by the external environment and is suitable for quantitative damage identification. However, a macro-dynamic strain is generated by vehicle–bridge coupling, which has a small value and is easily affected by the external noise environment, making it suitable for damage localization and identification. Therefore, in this study, damage localization is performed on the basis of the damage index and time history curve of the macro-dynamic strain.

Illustration: Based on the change in the wave peak, 32 strain curves generated by the force of 32 long-gauge elements in the mid-span circuit of the upper roof of the box girder as shown in Figures 9 and 10.

(**a**) (**b**)
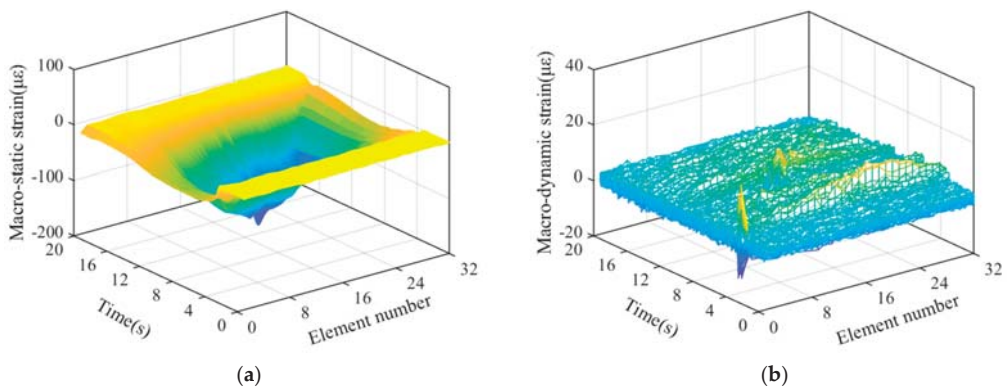
Figure 8. Strain reconstruction and separation under vehicle-bridge coupling; (**a**) Static strain time history diagram; (**b**) Dynamic strain time history diagram.

(**a**) (**b**)
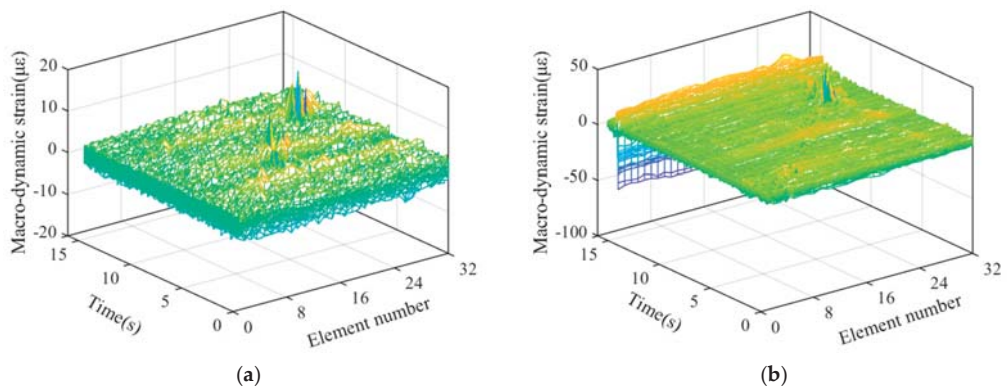
Figure 9. Macro-dynamic strain under damage condition for vehicle-to-bridge mass ratios; (**a**) 1.22; (**b**) 3.14.
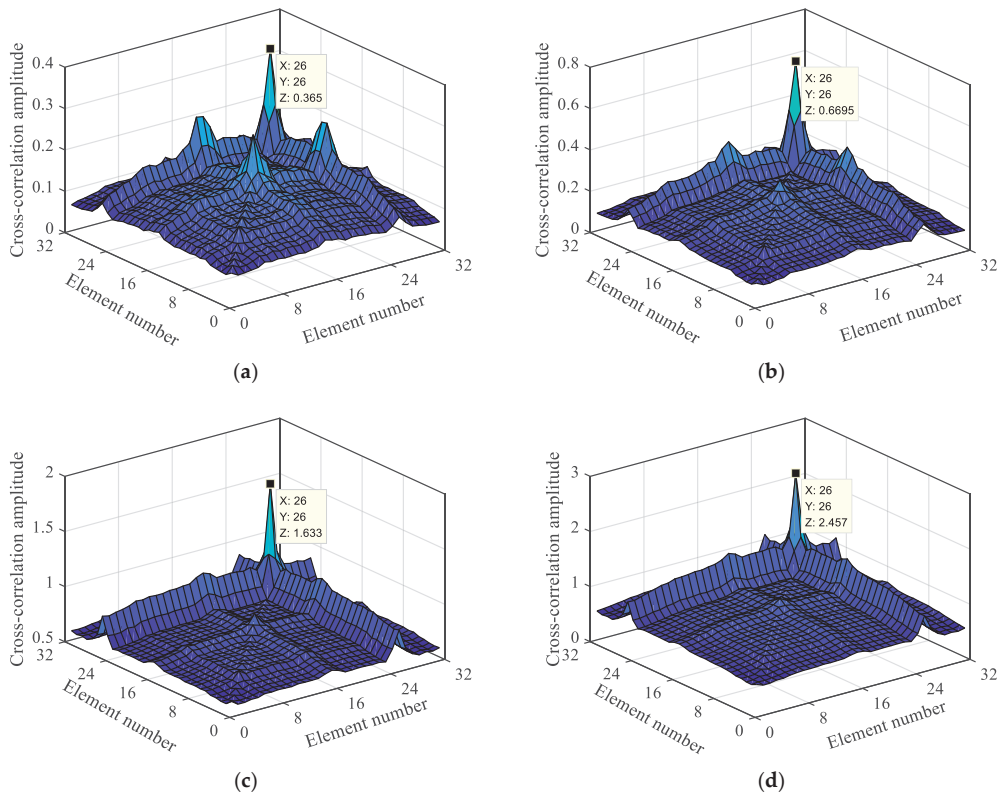
Figure 10. Macro-dynamic strain cross-correlation based on damage level of 2 with different vehicle-to-bridge mass ratio; (**a**) 1.22; (**b**) 1.84; (**c**) 2.45; (**d**) 3.14.

4.2. Damage Localization and Identification

Based on the separated and reconstructed macro-dynamic strain data, this section focuses on analyzing the impacts of damage degree, vehicle-to-bridge mass ratio, multiple damage locations, and other factors on the damage localization index.

4.2.1. Vehicle-to-Bridge Mass Ratio

When the vehicle-to-bridge mass ratio is high, the evident vehicle–bridge coupling effect generates a macro-dynamic strain. Therefore, it is of great significance to explore the influence of the vehicle-to-bridge mass ratio on the damage localization index. Therefore, we conducted a macro-dynamic strain analysis during the actual vehicle-mounted action period; this section presents the results. Figure 9a,b show the macro-dynamic strains under the second-order damage condition with vehicle-to-bridge mass ratios of 1.22 and 3.14, respectively.

Illustration: The figures show 32 macro-dynamic strain curves indicated by different colors, which are 32 long-gauge elements in the middle span line of the upper roof.

Figure 9 shows that the macro-dynamic strain data of the 32 long-gauge elements fluctuate around 0. The vibration is most intense at 7.5 s, 10–13 s, and 14–15 s. The actual movement time of the mobile trolley is 15 s, and the trolley is controlled by a traction motor. Its speed is set to 0.2 m/s, and it takes 16 s to complete the entire process. Therefore, during the movement process of the mobile trolley, there is a condition of variable speed, that is, the 32 long-gauge elements are affected by non-stationary excitation (the process of

shifting the mobile trolley is equivalent to the impact of non-stationary excitation on the bridge, making the macro-strain data more complicated). Through the analysis of the actual damage location, the mobile trolley was found to reach the middle span of the bridge at 7.5 s, reach the damage location in approximately 10–13 s, and completely leave the bridge after 15 s. The vehicle-to-bridge mass ratios of the two types have evident and sudden oscillations at 7.5 s and 10–13 s, as shown in Figure 9a,b. However, all the 32 long-gauge elements vibrate at 7.5 s, whereas in the 10–13 s range, the oscillation is only of a few long-gauge elements, as indicated by the green line in the figure. Based on the analysis of the above characteristics and the calculation method of the damage localization index, the energy product of the macro-dynamic strain cross-correlation element is obtained, as shown in Figure 10.

A total of 32 long-gauge elements were pasted on the top plate of the beam. Through the damage localization index calculation, we find 1024 cross-correlation long-gauge elements, including 32 cross-correlation long-gauge groups as shown in matrix (12). The meaning of this element group is that the mechanical vibration of each long-gauge element and the first long-gauge element are correlated. If the first long-gauge element is damaged, the macro-strain response generated by the force will be different from the macro-strain generated by the other long-gauge elements, and the calculation based on the damage localization index will make it different from the other elements. Figure 10 shows that the energy product of the cross-correlation element has an evident mutation in the (26, 26) cross-correlation long-gauge element group. Therefore, it is possible to locate the damage in the 26th long-gauge element from the sudden change in the figure.

As the vehicle-to-bridge mass ratio increases, the abrupt value of the energy product of the cross-correlation element also increases. Under the different vehicle-to-bridge mass ratios, the macro-dynamic strain generated by the vehicle–bridge coupling can realize damage location identification based on the damage localization index and the higher the vehicle-to-bridge mass ratio, the more evident the damage localization effect.

4.2.2. Analysis of the Influence of Multiple Damage Locations

Based on the reconstructed and separated macro-dynamic strain data, an identification analysis was conducted at multiple damage locations. Through the calculation of the damage localization index, the energy product values of the cross-correlation elements with different damage degrees at two damage locations were obtained, as shown in Figure 11.

Figure 11 shows mutations in the 6th and 26th cross-correlation long-gauge element groups, and the mutation rules are the same as those described in Section 4.2.1. More specifically, (6, 6) has a sudden change in the energy product at both (26, 26) and the two cross-correlation long-gauge element groups. The mutation becomes more and more evident as the damage level increases at both damage locations. However, when both damage levels reach grade four damage, they do not reach the maximum of (6, 6) and (26, 26) at the same time. Therefore, when there are multiple damages, the cross-correlation element energy product between the two damages will be weakened, which will lead to the damage localization index. The damage localization effect is reduced, particularly for minor damages. However, it is still possible to locate the damage at the 6th and 26th long-gauge elements based on the above rules. The damage localization index can realize the localization and identification of multiple damages based on the macro-dynamic strain. The greater the damage, the better the localization effect.
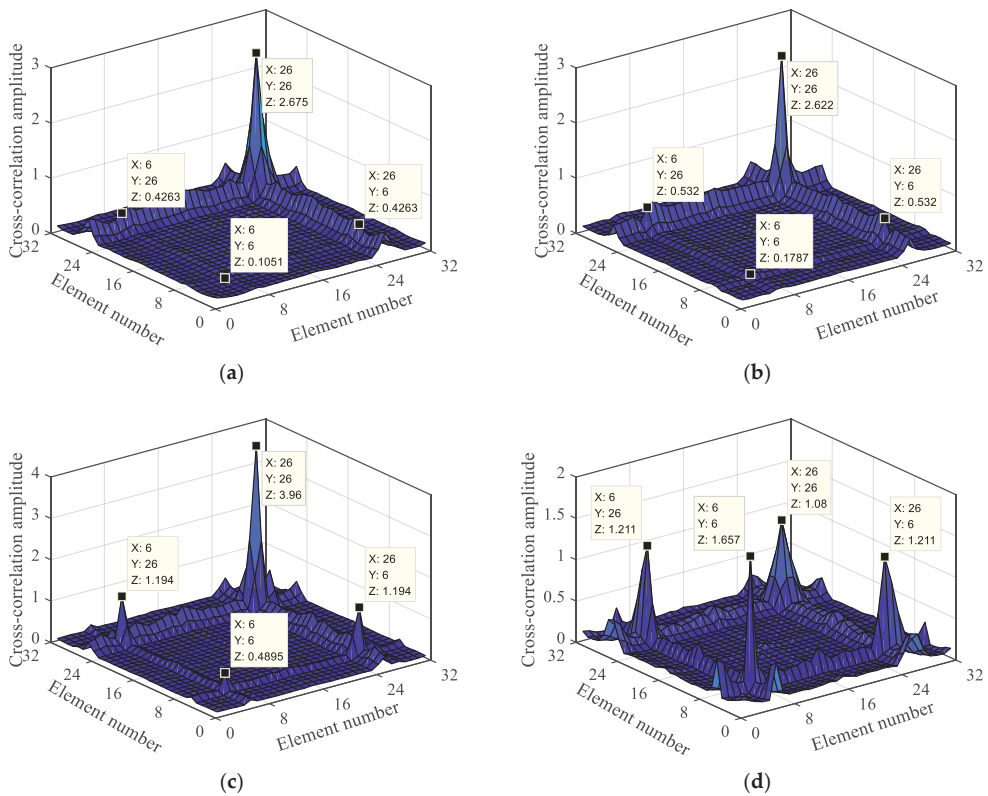
Figure 11. Macro-dynamic strain cross-correlation based on two damage locations with different damage levels; (**a**) Level 1 + Level 4; (**b**) Level 2 + Level 4; (**c**) Level 3 + Level 4; (**d**) Level 4 + Level 4.

4.2.3. Analysis of the Influence of the Damage Degree

To further analyze whether the damage degree would affect the positioning identification of the localization index, damage positioning research was performed with the localization index based on the macro-dynamic strain under the condition of D0–D4 for a 32 kg mobile vehicle. Through the calculation, the energy product of the macro-dynamic strain cross-correlation element was obtained, as shown in Figure 12.

Figure 12 shows the damage identification effects of the damage location index under different damage degrees. As it can be seen from Figure 12a, when the bridge is in the condition of non-destructive, the maximum value is at (16, 16), where the mid-span element of the beam is located. By comparison with Figure 12b–e, it can be seen that with the increase in damage degree, the value at (26, 26) gradually increases, and the value at (16, 16) gradually decreases. Therefore, it can be seen that damage occurred at the 26th long-gauge element, and the greater the damage degree, the more obvious the damage localization effect.
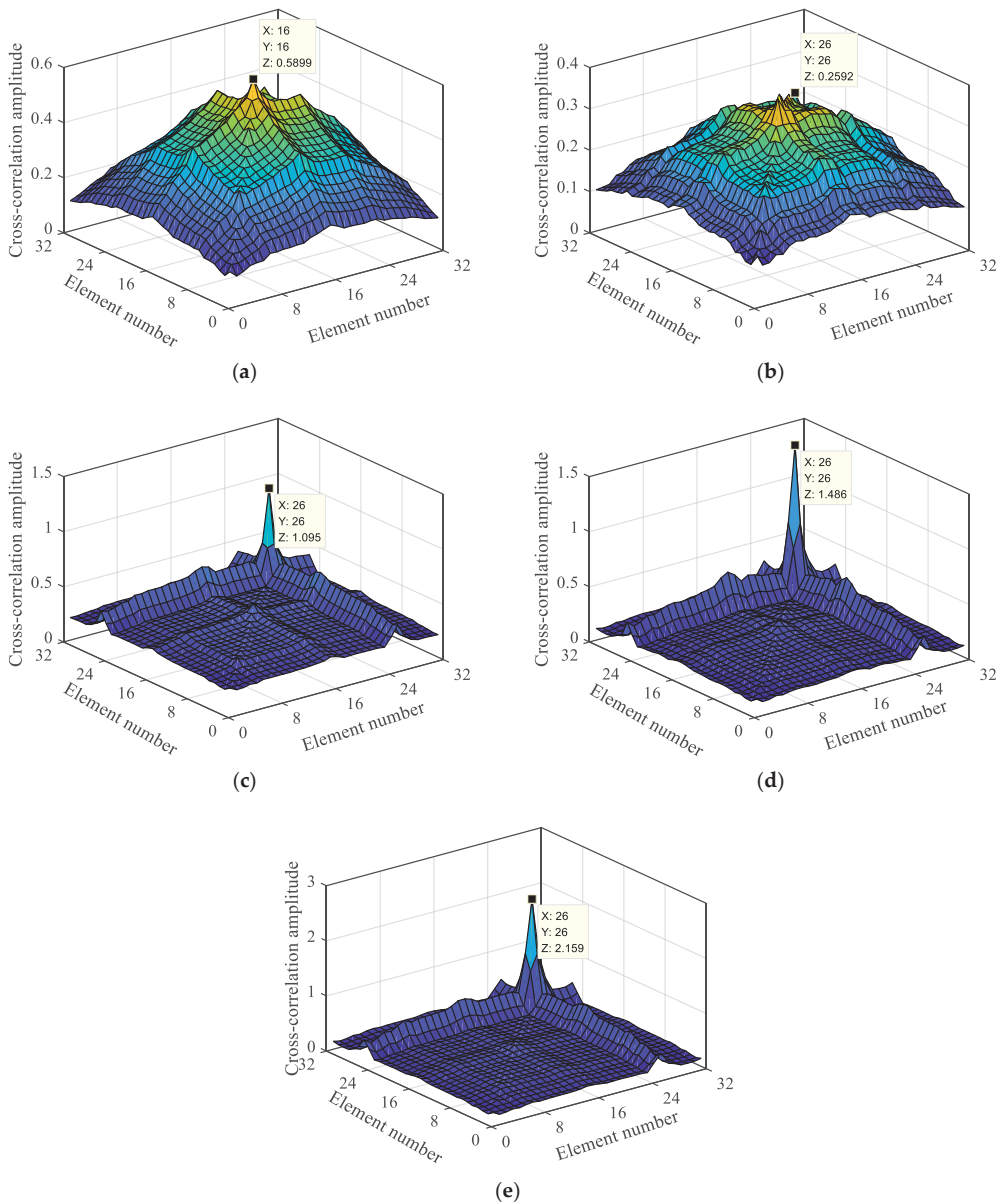
Figure 12. Macro-dynamic strain cross-correlation based on a single damage location with different damage levels; (**a**) Non-destructive; (**b**) Level 1; (**c**) Level 2; (**d**) Level 3; (**e**) Level 4.

In conclusion, for the macro-dynamic strain after wavelet reconstruction and separation, the damage localization index can still be used for damage localization and identification. In terms of the vehicle–bridge mass ratio, multiple damage location, and damage degree, the higher the vehicle-to-bridge mass ratio, the greater the damage degree, the more evident the positioning effect of the damage localization index. After the reconstruction and separation, the macro-dynamic strain was not further de-noised by wavelet transform;

therefore, the damage localization index based on the maximum cross-correlation number has certain anti-noise performance. Macro-dynamic strain is generated by vehicle–bridge coupling action; this confirms the feasibility of the damage localization index and identification method employed for the time-varying bridge based on the damage localization index under vehicle–bridge coupling action.

4.3. Experimental Error Analysis

The experimental errors mainly come from the following aspects:

1. The pre-tensioning effect of the long-gauge FBG strain sensor is weakened: As the experiment progresses, the tensile effect is increasingly weakened. Moreover, the sensor attached to the upper roof measures the compressive strain. If the pre-tensioning effect is poor, it will significantly affect the accuracy of data collection.
2. Influence of track irregularity: because of the lack of advanced processing technology, an irregularity exists in the upper roof track of the bridge. Consequently, wheel–rail collision can occur during the movement of the vehicle, producing an effect similar to percussion excitation and affecting the accuracy of strain data collection.

5. Conclusions and Prospects

In this study, a spatial box bridge was taken as the research object. Based on the macro-static and dynamic strain data, and the wavelet transform de-noising and reconstruction technology, a damage identification method for medium- and small-span bridges under the action of vehicle–bridge coupling was studied. The following conclusions can be drawn from the results:

1. The damage location index proposed in this paper can effectively reduce the influence of noise and other factors and accurately identify the location of subtle damage, with high accuracy. This index is not only effective for single damage location identification, but also has a good identification effect for multiple damage locations. The proposed index can provide a good reference for solving the problem that the damage index based on macro-strain can not be applied to medium- and small-span bridges due to the obvious vehicle–bridge coupling effect.
2. The proposed method in this paper has high requirements for bridge deck smoothness, moving vehicle speed and load size. The excitation caused by the collision between the wheel and the bridge deck will greatly affect the recognition effect, so it is necessary to maintain the smoothness of the bridge deck. The speed of the vehicle moving on the bridge deck is also required to be uniform, otherwise the recognition error will increase due to the excitation of variable speed. The larger the load value of the mobile vehicle is, the better the recognition effect of the damage index is. Therefore, for subtle damage, the positioning accuracy of the damage can be improved by increasing the mobile vehicle value.
3. The vehicle–bridge model designed in this study is relatively simple and lacks in-depth study under complex mobile vehicle conditions (such as moving speed and axle number). Therefore, in future research, we will consider the use of a complex vehicle–bridge coupling model and prestressed concrete beams to further improve the proposed damage identification method. The damage identification method proposed in this paper is only verified under laboratory conditions and has achieved a good damage localization effect. However, in the bridge model experiment, the scale effect is a very important factor, and this paper does not consider the influence of scale effect on the damage identification method. In the later study, the author will conduct a comprehensive analysis of the actual bridge damage and laboratory verification, in order to further analyze the impact of scale effect on the proposed damage identification method.

References

1. Zheng, J.J. Dynamic Response Analysis of Bridge under Moving Load. Master's Thesis, Jilin Jianzhu University, Changchun, China, 2019.
2. Yang, Q.W.; Peng, X. Sensitivity Analysis Using a Reduced Finite Element Model for Structural Damage Identification. *Materials* **2021**, *14*, 5514. [CrossRef] [PubMed]
3. Han, W.; Wang, Y.P.; Wang, L. Application and Analysis of Two Nondestructive Testing Methods in Bridge Structure Damage Detection. *J. Guiyang Univ. (Nat. Sci. Ed.)* **2021**, *16*, 93–99. [CrossRef]
4. Hong, W.; Cao, Y.; Wu, Z.S. Strain-based damage-assessment method for bridges under moving vehicular loads using long-gauge strain sensing. *J. Bridge Eng.* **2016**, *21*, 4016059. [CrossRef]
5. Cao, P.; Yoo, D.; Shuai, Q.; Tang, J. Structural damage identification with multi-objective DIRECT algorithm using natural frequencies and single mode shape. In Proceedings of the SPIE Smart Structures and Materials + Nondestructive Evaluation and Health Monitoring, Portland, OR, USA, 25–29 March 2017.
6. Li, D.B. A general review on several fundamental points of experimental strain/stress modal analysis. *Shock Vib.* **1996**, *15*, 13–17.
7. Wu, Z.S.; Zhang, J. *Advanced Technology and Theory of Structural Health Monitoring*, 1st ed.; Science Press: Beijing, China, 2015.
8. Wu, Z.S.; Li, S.Z.; Adewuyi, A.P. Modal Analysis Based on Distributed Strain Measurements: Theory and Application. *Sci. Technol. Rev.* **2010**, *28*, 94–103.
9. Li, S.Z.; Wu, Z.S. Development of Distributed Long-gage Fiber Optic Sensing System for Structural Health Monitoring. *Struct. Health Monit.* **2007**, *6*, 133–143. [CrossRef]
10. Zhang, J.; Guo, S.; Wu, Z.; Zhang, Q. Structural identification and damage detection through long-gauge strain measurements. *Eng. Struct.* **2015**, *99*, 173–183. [CrossRef]
11. Li, S.Z.; Wu, Z.S. Modal Analysis on Macro-strain Measurements from Distributed Long-gage Fiber Optic Sensors. *J. Intell. Mater Syst. Struct.* **2008**, *19*, 937–946.
12. Li, S.Z. Structural Health Monitoring Strategy Based on Distributed Fiber Optic Sensing. Doctoral Dissertation, Ibaraki University, Mito, Japan, 2007.
13. Hong, W.; Wu, Z.; Yang, C.; Wan, C.; Wu, G. Investigation on the damage identification of bridges using distributed long-gauge dynamic macrostrain response under ambient excitation. *J. Intell. Mater Syst. Struct.* **2012**, *23*, 85–103. [CrossRef]
14. Xu, Z.D.; Zeng, X.; Li, S. Damage Detection Strategy Using Strain-Mode Residual Trends for Long-Span Bridges. *J. Comput. Civ. Eng.* **2013**, *29*, 04014064. [CrossRef]
15. Xu, Z.D.; Li, S.; Zeng, X. Distributed Strain Damage Identification Technique for Long-Span Bridges Under Ambient Excitation. *Int. J. Struct. Stab. Dyn.* **2018**, *18*, 1850133. [CrossRef]
16. Anastasopoulos, D.; De Smedt, M.; De Roeck, G.; Vandewalle, L.; Reynders, E. Modal strain identification using sub-microstrain FBG data from a pre-stressed concrete beam during progressive damage testing. *Procedia Eng.* **2017**, *199*, 1846–1851. [CrossRef]
17. Li, S.; Xu, Z.D.; Wang, S.J.; Wu, Z.S. Modal macro-strain identification from operational macro-strain shape under changing loading conditions. *J. Southeast Univ. (Engl. Ed.)* **2016**, *32*, 219–225.
18. Zhang, J.; Cheng, Y.Y.; Xia, Q.; Wu, Z. Change localization of a steel-stringer bridge through long-gauge strain measurements. *J. Bridge Eng.* **2015**, *21*, 4015057. [CrossRef]

19. Wu, B.T.; Wu, G.; Yang, C.Q. Parametric study of a rapid bridge assessment method using distributed macro-strain influence envelope line. *Mech. Syst. Signal Process.* **2019**, *120*, 642–663. [CrossRef]
20. Li, S. Macro-Strain Based Damage Identification Method for Municipal Highway Viaduct. Doctoral Dissertation, Southeast University, Nanjing, China, 2018.
21. Razavi, M.; Hadidi, A. Structural damage identification through sensitivity-based finite element model updating and wavelet packet transform component energy. *Structures* **2021**, *33*, 4857–4870. [CrossRef]
22. Zhao, Y.; Zhu, X.Q.; Wang, H.L. Bridge damage identification based on wavelet packet transform under moving loads. *J. Tianjin Cheng Jian Univ.* **2019**, *25*, 94–97, 124.
23. Yu, Z.; Xia, H. Bridge damage detection based on moving load induced structural response and wavelet analysis. *J. Beijing Jiaotong Univ.* **2014**, *38*, 55–61.
24. Liu, X.J.; Wang, Z.F.; Zhang, S.X. On the damage identification method of simply-supported girder bridge based on vibration response correlation. *J. Exp. Mech.* **2019**, *34*, 29–37.
25. Wu, B.; Wu, G.; Lu, H.; Feng, D.-C. Stiffness monitoring and damage assessment of bridges under moving vehicular loads using spatially-distributed optical fiber sensors. *Smart Mater. Struct.* **2017**, *26*, 035058. [CrossRef]
26. Wu, B.; Wu, G.; Yang, C.; He, Y. Damage identification method for continuous girder bridges based on spatially-distributed long-gauge strain sensing under moving loads. *Mech. Syst. Signal Process.* **2018**, *104*, 415–435. [CrossRef]
27. Chen, S.-Z.; Wu, G.; Feng, D.-C.; Zhang, L. Development of a Bridge Weigh-in-Motion System Based on Long-Gauge Fiber Bragg Grating Sensors. *J. Bridge Eng.* **2018**, *23*, 04018063.1–04018063.18. [CrossRef]
28. Chen, Z.W.; Cai, Q.L.; Lei, Y.; Zhu, S.Y. Damage detection of long-span bridges using stress influence lines incorporated control charts. *Sci. China Technol. Sci.* **2014**, *57*, 1689–1697. [CrossRef]
29. Zhang, J.; Wu, Z.S. *Impact Vibration Test and Rapid Evaluation of Bridges—Theory, Technology and Engineering Applications*, 1st ed.; China Architecture & Building Press: Beijing, China, 2018.
30. Wang, X.M. *Structural Dynamic Analysis and Application with ANSYS*, 1st ed.; China Communications Press: Beijing, China, 2014.
31. Cheng, Y.Y. Research on Structural Health Monitoring Method Using Long-Gauge Optical Fiber Sensing Technology. Doctoral Dissertation, Southeast University, Nanjing, China, 2019.
32. Zhang, X.J. The Applied Research Based on Wavelet Analysis in Dynamic Strain Healthy Indicator of Bridges. Master's Thesis, Zhejiang University of Technology, Hangzhou, China, 2016.
33. Xu, H.; Li, F.; Zhao, W.; Wang, S.; Du, Y.; Bian, C. A High Precision Fiber Bragg Grating Inclination Sensor for Slope Monitoring. *J. Sens.* **2019**, *2019*, 1354029. [CrossRef]
34. Zhang, L.; Wu, G.; Li, H.L.; Chen, S.Z. Synchronous Identification of Damage and Vehicle Load on Simply Supported Bridges Based on Long-Gauge Fiber Bragg Grating Sensors. *J. Perform. Constr. Fac.* **2020**, *34*, 04019097. [CrossRef]
35. Liu, G.Y.; Liu, X.J.; Zhang, S.X.; Wen, L.P. Damage Identification of Simply Supported Beam Bridge Based on Wavelet Analysis and Variation Coefficient. *J. Appl. Mech.* **2020**, *37*, 1915–1922, 2313–2314.

Imaging of Increasing Damage in Steel Plates Using Lamb Waves and Ultrasound Computed Tomography

Monika Zielińska [1,*] and Magdalena Rucka [2]

[1] Department of Technical Fundamentals of Architectural Design, Faculty of Architecture,
Gdańsk University of Technology, Narutowicza 11/12, 80-233 Gdańsk, Poland

[2] Department of Mechanics of Materials and Structures, Faculty of Civil and Environmental Engineering,
Gdańsk University of Technology, Narutowicza 11/12, 80-233 Gdańsk, Poland; magdalena.rucka@pg.edu.pl

[*] Correspondence: monika.zielinska@pg.edu.pl

Abstract: This paper concerns the inspection of steel plates, with particular emphasis on the assessment of increasing damage. Non-destructive tests were performed on four plates, one of which was undamaged, while the remaining three had defects in the form of circular holes with diameters of 2, 5 and 10 cm. Guided Lamb waves were used in the research, and the image reconstruction was performed using ultrasound computed tomography. The damage size was estimated by tracking the real course of rays and densifying the pixel grid into which the object was divided. The results showed the great potential of ultrasound tomography in detecting defects in steel elements, together with the possibility of estimating damage size.

Keywords: non-destructive testing; steel plates; ultrasonic tomography; damage detection

1. Introduction

Imaging potential defects and their exact position and size are among the greatest challenges of recent studies in non-destructive testing (NDT) and structural health monitoring (SHM). One of the most efficient techniques is to use ultrasonic waves followed by their processing. In general, two approaches are possible for damage imaging. In the first, the guided wave field is sensed over an inspected area (usually in a non-contact manner) and it is then subjected to further processing using, for example, root mean squares to obtain a useful defect image [1,2]. The second approach is connected with the use of an array of piezoelectric transducers, acting as both actuators and sensors, attached to selected points on an analysed structure. Wave propagation signals are collected and then processed using appropriate damage detection algorithms such as the time of flight (TOF) based triangulation method [3], supported by ellipse or hyperbolic probability imaging [4,5], the time-reversal technique [6], the migration technique [7], phased-array beamforming [8] and finally ultrasound tomography, widely used for inspection of structures made of concrete [9–11], metal [12–14] and composite materials [15,16].

Tomography using guided ultrasound waves has become a popular technique incorporated into the structural health monitoring of elements of civil engineering infrastructure such as plates, shells and pipes [17–22], and also in the monitoring of aircraft components [23]. The increasing use of non-destructive methods for detecting defects in plate elements has resulted in a growing need to increase the effectiveness and efficiency of inspection. When performing tests based on Lamb waves, some practical problems affecting the results may be encountered. These problems are discussed extensively in the literature. Rao et al. [24] carried out a study on monitoring the corrosion of steel plates and the reconstruction of the thickness of corrosion damage. Wang et al. [25] used guided waves to image a hole with a corroded edge. Zhao et al. [26] investigated the imaging of damage in aluminium plates, comparing different tomography algorithms. Leonard et al. [27] analysed Lamb wave tomography on both aluminium and composite plates, with defects

of various sizes and thicknesses. The possibility of imaging defects in the form of round and rectangular holes in aluminium and composite plates was tested by Khare et al. [28]. Balvantin and Baltazar [29] analysed the images of an aluminium plate containing damage in the form of a two-stage circular discontinuity, using the multiplicative algebraic reconstruction technique (MART) and back projection. The structural condition monitoring system for composite panels with openings was presented by Prasad et al. [30]. The size of the defect itself is also of great importance in the imaging of tomographic plates, as evidenced by Menke and Abbott [31], Cerveny [32] and Belanger and Cawley [33].

The research described in this article aims to evaluate the use of ultrasound tomography to locate surface damage of varying sizes. The experimental and numerical analyses were carried out on four steel plates, one intact and three containing defects in the form of circular holes with diameters of 2, 5 and 10 cm. The non-destructive inspection was carried out using Lamb waves and ultrasound tomography (UT). The reconstruction of the Lamb wave propagation velocity was performed using both the non-reference approach and a method based on the differences in the transition times between the reference model and the three damaged models with surface defects. In order to improve the image quality, certain methods of tracing the real course of wave paths were used. The influence of mesh density on the possibility of estimating damage size was also assessed.

2. Ultrasound Tomography—Theoretical Background

Ultrasound tomography imaging allows recreating the internal structure of an examined object using the properties of elastic waves. A schematic process of performing ultrasound tomography is shown in Figure 1. The first step is to divide the test sample into cells called pixels. Each one of them constitutes a discrete area in the tested element. Such a division is shown with a dashed line in Figure 1a. Then, after applying appropriate algorithms, each pixel takes a value representing the speed of the ultrasonic wave propagated through this area.
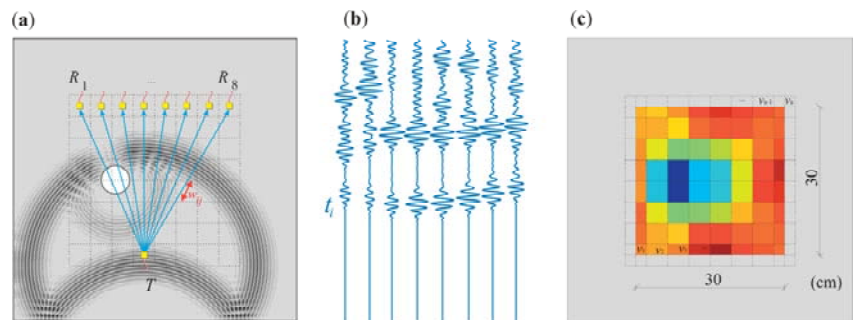
Figure 1. Schematic diagram of velocity reconstruction using ultrasound tomography: (**a**) plate with indicated receivers (*R*), transmission (*T*) points and simulated wave field; (**b**) guided wave propagation time signals; (**c**) ultrasound tomography map.

Image reconstruction is based on information from ultrasound wave signals propagating from transmitting points (*T*) to receiving points (*R*). This information may be, for example, the time of flight (TOF), measured along with the multiple ray paths, determined after appropriate signal processing [34–36]. Each obstacle in the path of the travelling wave changes the propagation time. Among them, we can distinguish defects that delay the wave reaching the receiver, such as air voids or cracks, and those that decreased total velocity along all rays passing through these inclusions. The latter include inclusions made of materials whose propagation velocity is higher than in the surrounding medium. Based on the time of flight of the wave, with the known geometry of the tested object, it is possible to determine wave propagation speed, correlated with the mass density, modulus of elasticity, and Poisson's ratio characteristic for a given material.

The time of flight between the transmitter (T) and the receiver (R) can be described by a line integral of the transition time distribution along the propagation way, w:

$$t = \int_0^{w_1} dt = \int_0^{w_1} s\, dw = \int_0^{w_1} \frac{1}{v} dw, \tag{1}$$

where v is the average velocity, w_1 denotes the distance between transmitter and receiver and s is the inverse of the velocity, v, referred to as slowness, $s = 1/v$. Measurement of the wave travel time along specific paths enables the determination of local velocities in the tested plate. The wave velocity for each cell, v_j, along the path of the wave from the transmitter to the receiver can be determined from the following formula:

$$t_i = \sum_{j=1}^{n} w_{ij} s_j, \quad i = 1, 2, 3, \ldots, m, \quad j = 1, 2, 3, \ldots, n, \tag{2}$$

where m denotes the number of rays, n denotes the number of pixels into which the tested sample is divided, t_i is the time of flight of the guided wave along the i-ray, w_{ij} is the i-ray propagation path through the j-pixel and s_j is the slowness at pixel j. It is assumed that velocity, v_j, in individual cells is constant.

One of the techniques for solving this type of system of equations is the algebraic reconstruction technique (ART) [37]. It was used to perform calculations in the conducted research. First, each cell is assigned the same slowness. Its value is calculated as the inverse of the average velocity of ultrasonic wave propagation in the tested material. Based on the initial image created in this way, the iteration process begins and corrections are made.

3. Materials and Methods

3.1. Description of Specimens

The tests were carried out on four steel plates with dimensions of 50 cm × 50 cm and 3 mm thickness. A reference model was the first element without damage (plate #1). The other three plates contained a circular hole of variable diameter: 2 cm (plate #2), 5 cm (plate #3) and 10 cm (plate #4), which represented damage of a surface type. Holes were made through the entire thickness of the plate. The centres of all holes were placed symmetrically in the y-axis direction and at a distance of 18 cm from the outer edge of the plate in the x-axis direction. The geometry of the test models is shown in Figure 2. Photographs of the plates used for the experimental tests are presented in Figure 3.
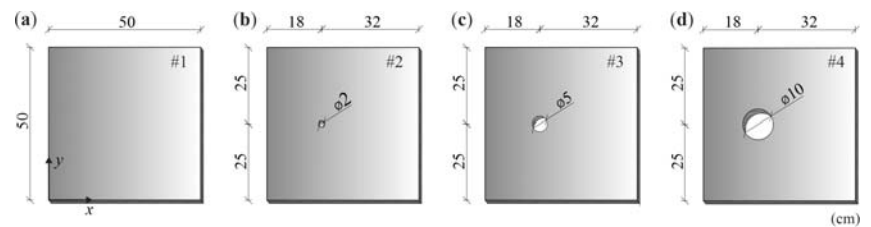
Figure 2. The geometry of the tested plates: (**a**) plate without damage (#1); (**b**–**d**) plates with surface damage (#2–#4).
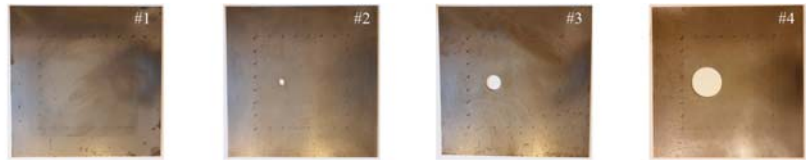
Figure 3. Photographs of tested plates (models #1–#4).

3.2. Experimental Investigations

Experimental tests of the propagation of Lamb waves in the steel plates were performed using a system for generation and registration of ultrasonic waves, the PAQ-16000D system (EC Electronics, Krakow, Poland). The experimental setup is shown in Figure 4. For both transmitting and receiving Lamb wave signals, plate piezoelectric transducers, NAC2024 (Noliac, Kvistgaard, Denmark), were applied. The excitation was a wave packet with a central frequency of 150 kHz, consisting of five sinusoid cycles modulated with the Hann window.
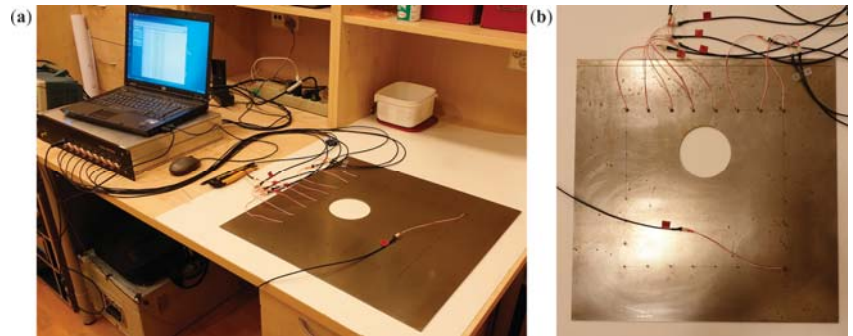
Figure 4. Experimental setup (**a**) and view on the steel plate with piezoelectric transducers (**b**).

The inspected region of the plate was a square with dimensions of 30 cm × 30 cm, with a margin of 10 cm from each of the outer edges of the plate. The excitation was applied at 16 points (8 points on two perpendicular edges), and wave propagation signals were also sensed at 16 points. The transmitting points are marked in Figure 5a as T_1–T_{16}, and the receiving points as R_1–R_{16}. During measurements, the transmitter was placed at a specific point, and the output signals were registered at 8 points located on the opposite edge. The transmitter was then moved to the next point, and the measurement was repeated. Altogether, 128 wave propagation time signals were collected.

The image reconstruction process started by dividing the inspected region of the plate into 64 pixels. The number of pixels was derived from the number of measurement points located on each edge of the plate (8 × 8 points). Each pixel had a dimension of 4.3 cm × 4.3 cm. Pixels are marked with dashed lines in Figure 5b. Image reconstruction was made according to the collected signals of the wave transition from transmitters to receivers. The time of flight (TOF) of the ultrasonic wave for each of the T–R paths was determined. The tomography velocity image was created in MATLAB® (9.3.0.713597, The MathWorks, Inc., Natick, MA, USA), based on the ART method. In the first step, it was assumed that the wave paths propagating from the transmitters to the receivers are straight. In the next step, the actual course of the rays was traced.
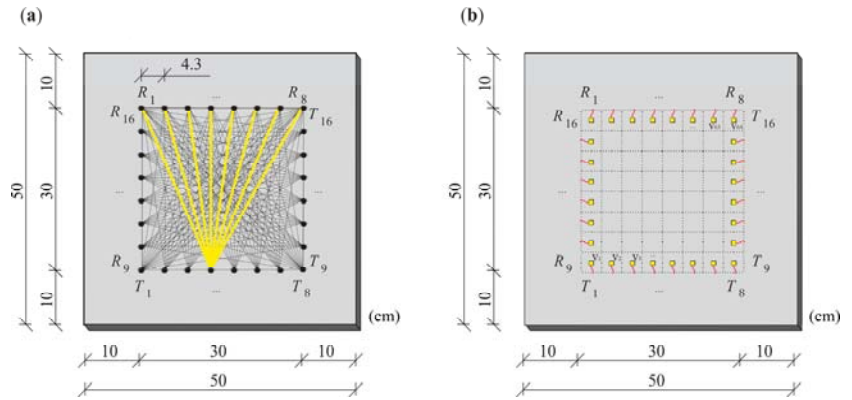
Figure 5. The plate with the marked inspected area: (**a**) location of transmitters T_1–T_{16} and receivers R_1–R_{16}, (**b**) division of the area into pixels.

3.3. Identification of Material Parameters

Identification of material parameters was carried out for an intact plate #1. The experimentally determined mass density was $\rho = 7893$ kg/m^3. Poisson's ratio was set as 0.3. The dynamic elastic modulus was also determined experimentally based on a comparison of experimental and numerical dispersion curves. At first, dispersion curves of Lamb waves of two basic modes, i.e., symmetric S0 and antisymmetric A0 were determined. For this purpose, guided waves of frequencies ranging from 40 kHz to 400 kHz with a step of 10 kHz were excited and measured in two configurations, shown in Figure 6a,b. Theoretical dispersion curves were then calculated for different values of elastic modulus. Finally, the dynamic elastic modulus was determined by the method of least squares to give the best fit experimental and numerical modes, and its value was found to be 209 GPa (Figure 6c). The obtained values of the material parameters were then used for numerical simulations.
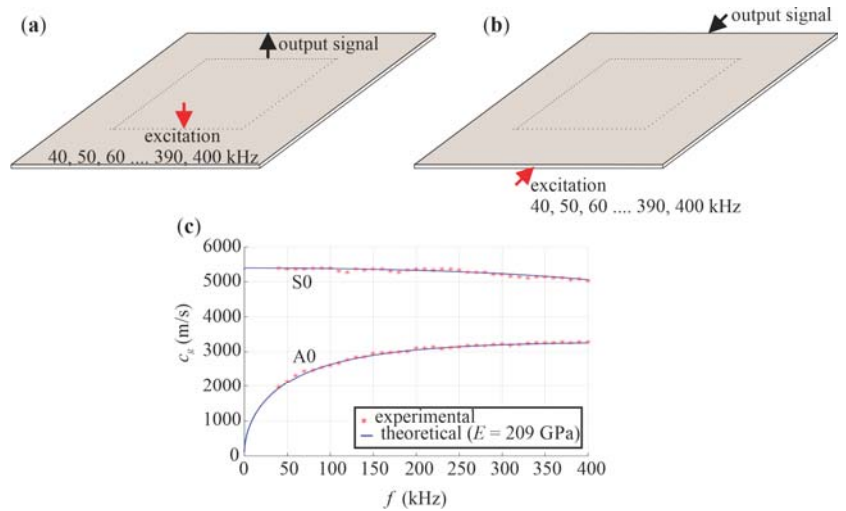
Figure 6. The scheme of experimental tests for determination of dispersion curves for (**a**) A0 mode and (**b**) S0 mode and (**c**) obtained dispersion curves.

3.4. Numerical Modelling

Numerical analysis was carried out using the commercial Abaqus/Explicit program (ver 6.14, Dassault Systemes, Vélizy-Villacoublay, France) based on the finite element method (FEM). Four FEM models were prepared corresponding to the tested plates. Plate models were discretized with S4R elements with maximum dimensions of 1 mm × 1 mm. The boundary conditions were implemented free on all edges. The length of the integration step was 10^{-7} s. The excitation signal was the same as in the experiment, i.e., the 5-cycle wave packet of 150 kHz frequency, induced perpendicularly to the surface of the plate at points T_1–T_{16}. The output acceleration signals were collected at points R_1–R_{16}.

4. Results and Discussion

This research aimed to investigate the influence of increasing surface damage on the obtained tomographic maps. The analysis of the results of experimental and numerical studies was divided into four parts. The first one included tomographic imaging performed for the non-reference approach, with respect to time of transition between transmitters and receivers for each of the tested plates independently. The next part of the analysis consisted of preparing maps based on the differences in the transition times between the reference model and the three damaged models with surface defects. Then, the influence of the ray-tracing technique, taking into account the possibility of wave refraction, reflection and deflection was analysed. The final part focused on analysing the influence of the pixel mesh density on the possibility of estimating damage size.

4.1. Non-Reference Velocity Reconstruction

Numerical and experimental signals transmitted and registered at selected points were the basis of tomographic maps. The comparison of selected Lamb wave signals for the experimental and numerical models is presented in Figure 7. The graphs show a high convergence between the results from both models.
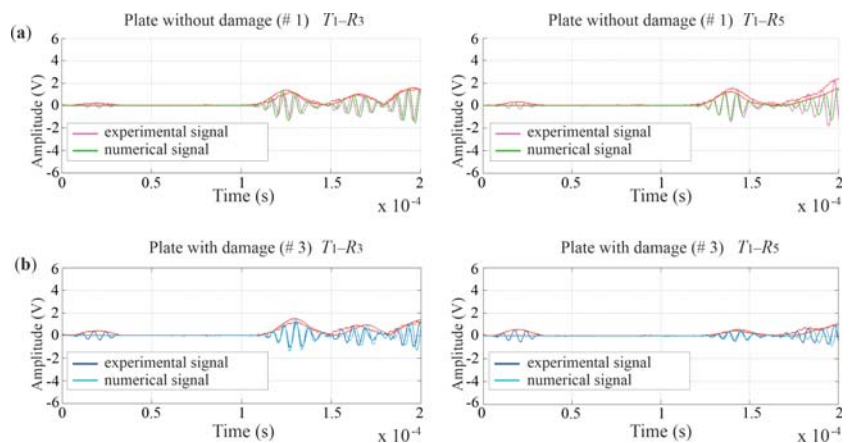
Figure 7. Comparison of selected Lamb wave signals for experimental and numerical tests in a plate without damage (**a**) and with damage (**b**).

The scheme of determining the time of flight (TOF) is shown in Figure 8. The estimation of this value is based on the first wave packet. The wave propagation time was established through the peak-to-peak method and was the difference between the peak value of the first wave pack of the output signal and the peak value of the input signal. The Hilbert transform was employed to create the signal envelope, which enabled the identification of peaks.
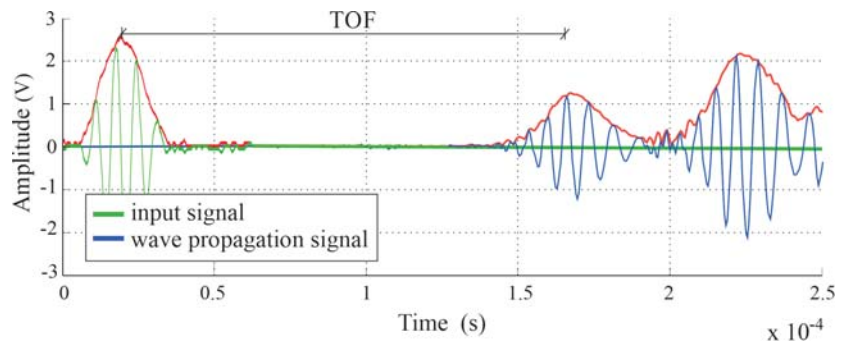
Figure 8. Determination of the time of flight (TOF) between transmitters and receivers.

The ultrasonic tomography maps are illustrated in Figure 9. The first column shows the plate scheme; the next two present the tomographic maps based on experimental and numerical signals, respectively. The tomograms are constructed, based on the direct measurement of the wave travel time, which means that the results were not compared with the results obtained for the undamaged plate. Each of the performed tomograms is presented separately, ranging from the minimum to the maximum speed. The maps present results for all considered plates, with the increasing surface damage in the form of holes with a diameter of 2, 5 and 10 cm. The defect with a diameter of 2 cm was properly imagined only for data obtained from numerical tests. On the other hand, the holes with a diameter of 5 and 10 cm were successfully detected in both experimental and numerical results. The locations of this damage are marked as areas with a reduced speed in relation to the surrounding material. However, the size of the holes was difficult to estimate accurately.

The quantitative analysis of the values of wave propagation velocities is presented in Tables 1 and 2 for the experimental and numerical data, respectively. The values of minimum, maximum and the mean of the wave velocity are given for all inspected plates. Tables 1 and 2 also provide measures of variation in the form of standard deviation (SD) and coefficient of variation (CV). The wave velocities were calculated along all 128 paths propagating through the plate. The average velocity values for the experimental results (Table 1) were similar and ranged between 2791.01 m/s and 2835.33 m/s. These values apply to the plate with a 10 cm diameter defect and the undamaged plate, respectively. It is worth noting that the differences between the maximum and minimum velocity increased with increasing damage dimensions. This is because the increasing discontinuity of the material reduced the minimum velocity as the rays had to avoid damaged areas. The standard deviation increased with the growing damage area. A similar relationship was observed for the coefficients of variation, which took values ranging between 0.80% and 1.91%.

Table 1. Wave propagation velocities in steel plates for data from experimental tests.

Plate	v_{min} (m/s)	v_{max} (m/s)	$\Delta v = v_{max} - v_{min}$ (m/s)	v_{avg} (m/s)	SD (m/s)	CV (%)
#1	2789.50	2872.62	83.11	2835.33	22.75	0.80
#2	2764.14	2872.62	108.47	2807.85	25.27	0.90
#3	2746.01	2872.62	126.61	2821.63	27.47	0.97
#4	2555.47	2860.07	304.60	2791.01	53.29	1.91

Table 2. Wave propagation velocities in steel plates for data from numerical tests.

Plate	v_{min} (m/s)	v_{max} (m/s)	$\Delta v = v_{max} - v_{min}$ (m/s)	v_{avg} (m/s)	SD (m/s)	CV (%)
#1	2703.95	2807.84	103.89	2756.65	29.22	1.06
#2	2703.95	2807.84	103.89	2756.22	29.35	1.06
#3	2692.14	2844.99	152.85	2752.52	32.53	1.18
#4	2559.39	2891.45	332.06	2743.33	51.36	1.87
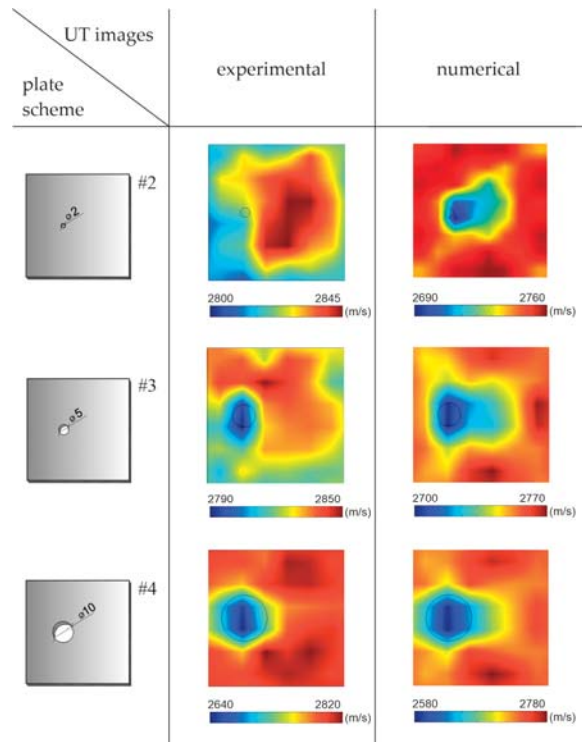
Figure 9. Ultrasonic tomography (UT) velocity maps using direct wave transition in plates with surface damage.

Table 2 gives the results of the quantitative analysis carried out for the numerical simulations. The average value of the wave propagation velocity varied between 2743.33 m/s and 2756.65 m/s. As in the case of results from the experimental studies, the difference between the maximum and minimum speed increased with the increasing damage area. The standard deviation was between 29.22 m/s and 51.36 m/s, while the variation coefficient ranged from 1.06% to 1.87%. These values indicate slight differences in the wave velocity along the path of the examined rays and the high sensitivity of ultrasound tomography to the occurrence of a defect.

4.2. Velocity Reconstruction with the Reference to Undamaged Plate

Ultrasound tomography often consists of comparing the data obtained for an undamaged structure with a damaged structure [38]. During health monitoring, as the damage size grows, the differences become more significant, and the intensity of changes in tomography images indicate the location of the damage. When comparing ultrasonic signals registered in a structure in the healthy (reference) and damaged (current) states, it is possi-

ble to indicate a difference in the TOF, especially if there is a defect along the inspected path. In the case of damage to the entire thickness of the element, the recorded signals travel along the path around the damage [39] so the paths are curved. Examples of Lamb wave signals propagated in an intact plate and a plate with a 5 cm hole along paths T_1–R_3 and T_1–R_5 are compared in Figure 10. When the wave passes through the hole (path T_1–R_5), its amplitude and shape change. Moreover, the wave arrives at the receiver with a delay. On the path propagating beyond the damaged area (path T_1–R_3), the first wave packet registered by the receiver is the same for the damaged plate and the plate without damage.
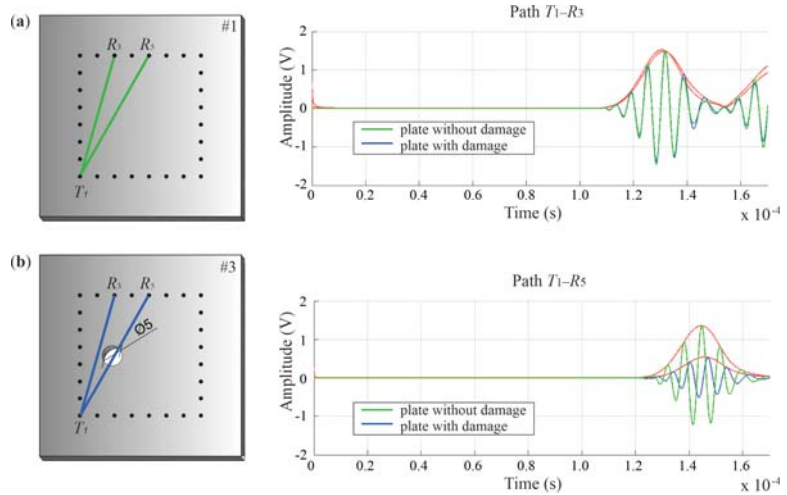
Figure 10. Comparison of wave signals propagated in intact plate (**a**) and plate with a 5 cm hole (**b**) along traces T_1–R_3 and T_1–R_5.

Figure 11 shows the tomographic velocity maps obtained based on differences in wave propagation TOF between the reference plate and the plate with growing damage. Each map was made on a scale from 0 to 1, where 1 indicates the highest difference between reference and current state, and 0 indicates their full compatibility. The location of the circular hole (Figure 11) was detected on the numerical images as regions with a reduced speed of wave propagation. These maps clearly indicate the location of the holes; however, it is not possible to precisely determine their size. This is due to the number of pixels into which the element was divided, as they define the image resolution. Regardless of the hole diameter, each defect lies on a combination of at least two pixels (see Figure 12). This area is indicated on tomography maps as a place with a reduced propagation velocity of ultrasonic waves. In the case of the UT images reconstructed for experimental signals, it can be noticed that they made it possible to determine the location of defects, regardless of their size. At the same time, it was not possible to assess the damage size, as in the case of the numerical results.
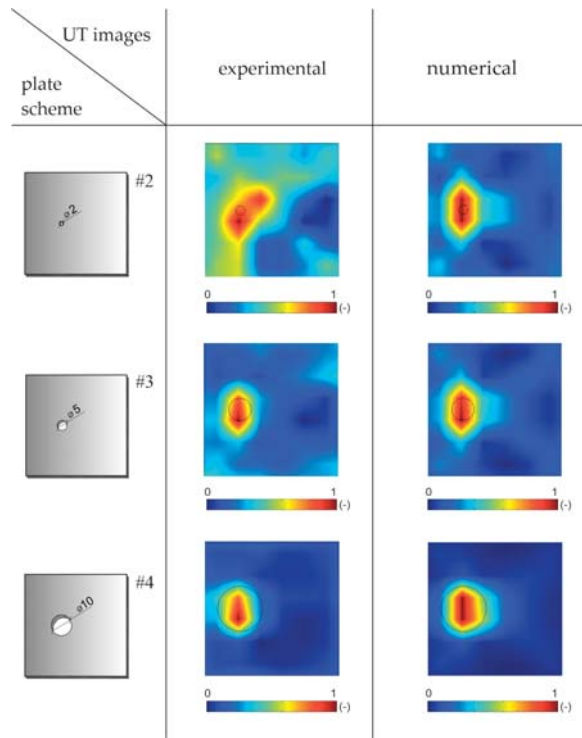
Figure 11. Ultrasonic tomography (UT) maps in plates with surface damage with the reference to the undamaged plate using TOF differences.
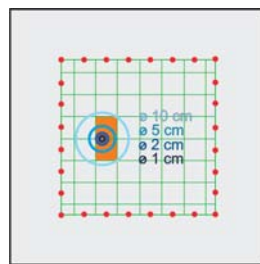
Figure 12. Location of damage with respect to the division of the element into pixels.

4.3. Influence of the Ray Tracing Technique

At the boundaries between regions with different velocities of wave propagation, an elastic wave can be refracted or reflected. In such a case, the wave rays may bend around a defect or other inclusion with a low wave propagation velocity [40]. The assumption that ultrasound waves propagate along straight paths from the transmitters to the receivers gives good results (cf. [41–50]). However, the quality of the tomography can be improved by using the actual ray path. In this study, ray tracing was performed utilizing the so-called hybrid approach, combining the ray bending methods with the network theory (e.g., [51]). The curved path is determined based on the values in individual pixels. The starting point is the image obtained for straight wave paths. Network theory creates a mesh of nodes on which the wave ray can travel. This mesh is usually denser than the pixel division. There are several ways to move from transmitter to specific receiver. The main purpose of the

method is to find nodes through which the path must pass in order to reach the receiver as quickly as possible. To determine which path it is, Dijkstra's algorithm was used. The solution is based on the velocity of wave propagation between two adjacent nodes and the distance between them. All nodes are divided into two groups. In the first group (group I) there are nodes for which the transit time is known. The second group (group II) contains the remaining elements. The schema of Dijkstra's method includes the following steps (e.g., [11,52,53]):

1. Assign all nodes to group II and give them an infinite cost, except for the start node, whose cost is zero;
2. Choose the node from group II with the lowest value. Name it as S (start node) and transfer this node to group I;
3. Name as N (neighbour node) each node from group II that is connected to node S;
4. Calculate time travel between S and each N node using the equation:

$$t(S) = \min(t(S); t(N) + t_{SN}), \tag{3}$$

$$t_{SN} = \frac{d_{SN}}{\frac{(v_S + v_N)}{2}} \tag{4}$$

where $t(S)$ denotes the travel time to reach node S, $t(N)$ denotes the travel time to reach node N, t_{NS} is the travel time between nodes S and N, d_{NS} is the distance between nodes S and N and v_S and v_N are the values of the ultrasonic wave velocity in nodes S and N, respectively;

5. Repeat steps 2–4 until group II is empty.

Dijkstra's algorithm assumes the checking of each node. When the fastest path was established, its straight sections were divided into an increasing number of straight but not collinear segments. The paths made in this way were naturally curved. The travel time was computed for each iteration, and the process ended when converging.

Figures 13 and 14 present experimental and numerical tomography maps created using the curved rays determined by the hybrid method. The analysis was carried out for the time of flight measured directly from transmitters to receivers (Figure 13) and by comparing the results between the current and reference state (Figure 14). The first step of the hybrid method is the preparation of a tomographic map for straight rays from transmitters to receivers. These maps are prepared both for the time of flight measured directly and for the differences in signals between the current and reference model. It is the starting point for which further ray bending iterations are carried out [52].

The tomographic velocity maps made on the basis of direct measurements (Figure 13) clearly indicate the location of the defects. They are visible as areas with smaller values of wave propagation velocity. Each of the tomographic images has its own individual scale, with values ranging from minimum to maximum velocity. Maps made for straight paths give satisfactory results. Simultaneously, the use of a hybrid method, combining the network method and the ray bending method, improved the results. In this case, the defect area was more concentrated. However, it was difficult to assess the extent of the damage based on these maps. Analysis of traced rays showed that the paths determined by the hybrid method bypassed the area of the defects.
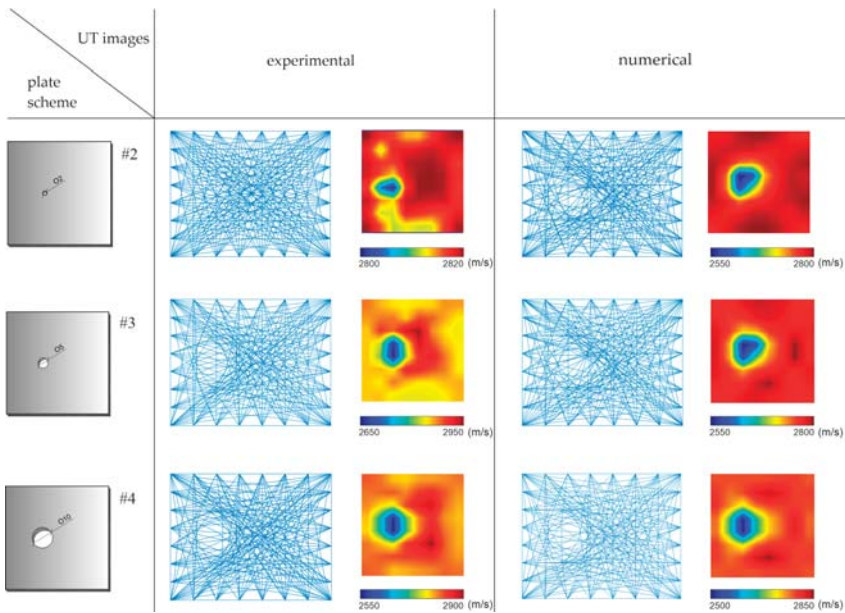
Figure 13. Ultrasonic tomography (UT) maps using direct travel time measurements with curved paths.
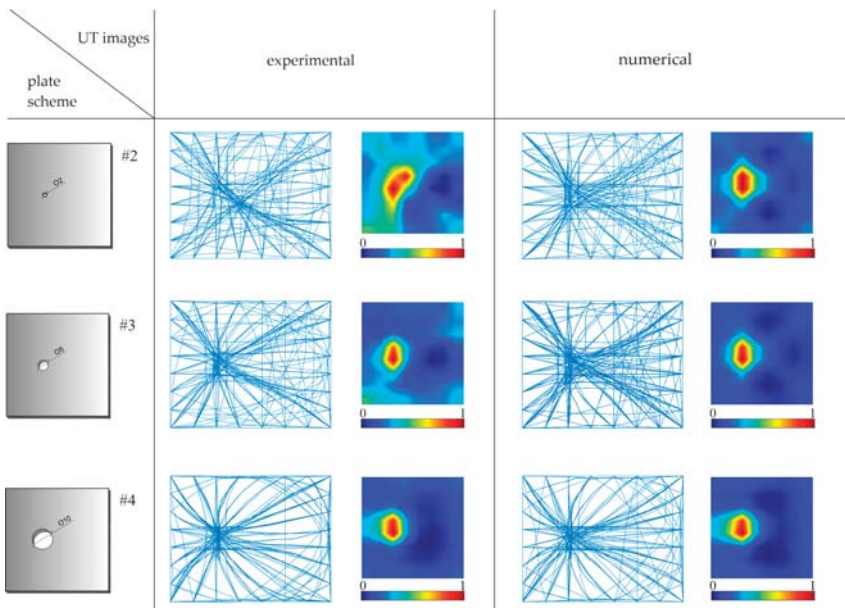
Figure 14. Ultrasonic tomography (UT) maps using the method of signal differences with curved paths.

Figure 14 shows tomographic velocity maps based on the comparison of the TOF between the undamaged plate and plates with growing defects. Values in the map cover the range from 0 to 1, where 1 indicates the highest measured difference between the map for undamaged and defective pieces, and 0 indicates their full compatibility. The circular

hole in each plate is shown as an increased value, which means a significant difference in wave propagation velocity in this area. Curved rays are concentrated within the defect. In this case, the maps are similar to those prepared with the use of straight rays. However, the damaged area is only a little more concentrated. In this case, it was also impossible to estimate the damage size as in the case of straight rays.

4.4. Influence of the Pixel Grid Size

The existence and position of the surface growing damage in steel plates were determined based on the time of flight and UT reconstruction for both experimental and numerical data (see Figures 9, 11, 13 and 14). However, the damage size assessment using the indicated methods did not reflect the actual dimensions of the hole. This was due to the size of the pixels into which the tested structure was divided. Such a division resulted from the number of transmitters and receivers used in the study. On two perpendicular edges, eight transmitters and eight receivers on opposite edges were used, which determined the division of the element into 64 pixels. The number of pixels affected the resolution of the obtained tomography image (cf. Figure 12).

In order to improve the identification of the size of damage, the pixel mesh was refined. The split of each edge was increased from 8 to 15 elements, which gave a total number of 225 pixels. The dimension of a single pixel was 2.15 cm $\times$ 2.15 cm. The impact of the density grid was assessed for data obtained from numerical simulations. Figures 15 and 16 show the tomography maps prepared for the elements divided into 64 and 225 pixels, respectively, using direct measurement of time of flight and difference in the TOF between the current state and the reference state. Orange colour marks the pixels for which the damage covers more than half of the area. In the case of a 64-cell mesh, the damage was concentrated within two pixels. The exception was damage with a diameter of 10 cm, which occupied 4 pixels. More significant differences in the number of pixels occupied by the damage are visible when the mesh was densified to 225 pixels.
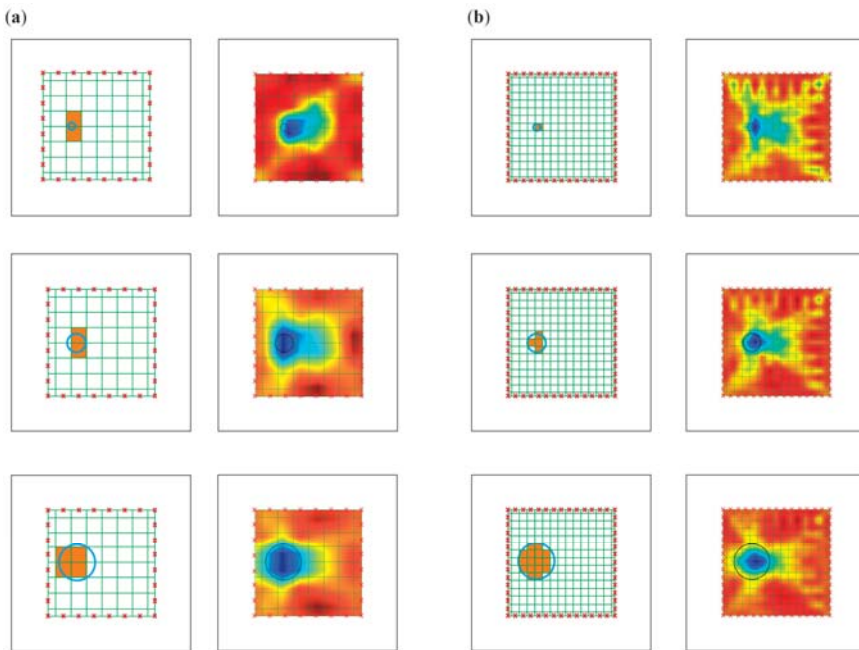
Figure 15. Pixel grid for the direct travel time measurement method: (**a**) division into 64 pixels; (**b**) division into 225 pixels.
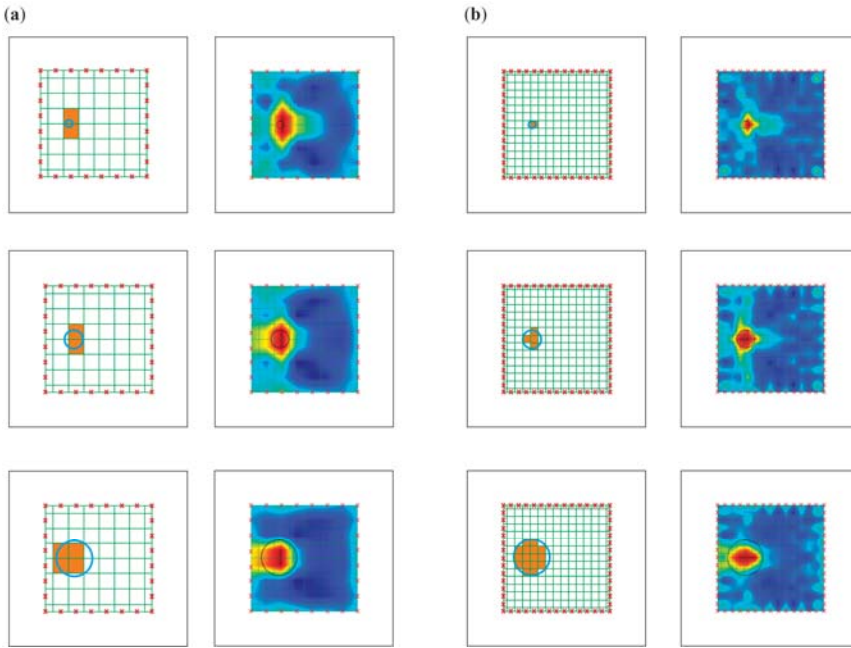
Figure 16. Pixel grid for travel time difference method (**a**) division into 64 pixels; (**b**) division into 225 pixels.

The maps in Figures 15a and 16a concern models divided into 64 pixels. The tomograms are very similar to each other, regardless of the damage size. The images were enhanced significantly by densifying the pixel grid (Figures 15b and 16b). It was possible to estimate the damage size for such prepared tomograms. The size of the area with a lower velocities of wave propagation on these maps increased with the size of the defect.

4.5. Quantitative Analysis Using Error Coefficient

The accuracy of the tomographic reconstruction was quantified by using an error coefficient comparing the reference image with the obtained tomographic maps. Each of the prepared tomographic maps was replaced by a simplified model with a reduced spectrum, indicating high and low velocities as well as large and small differences. In the case of direct measurement, pixels with velocities below the 25th percentile of the maximum scale value are considered to be low-velocity indications and are assigned a value of 0, while others are assigned a value of 1. An example of spectrum reduction for direct measurement is shown in Figure 17. In the case of maps based on signal differences for an undamaged structure and a damaged structure, pixels with a difference above the 75th percentile of differences in a scale are assigned a value of 0, and the remaining pixels are assigned a value of 1.
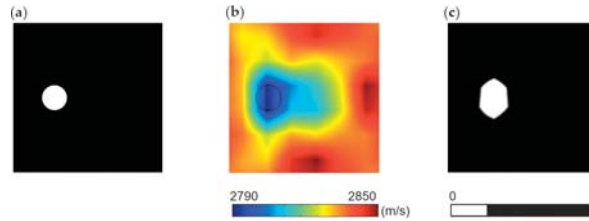
Figure 17. Error coefficient values for maps with reduced spectrum based on direct travel time measurement method: (**a**) reference model with a reduced spectrum, (**b**) topographic map with a full spectrum, (**c**) tomographic map with a reduced spectrum.

Figures 18 and 19 present maps with the reduced spectrum for direct measurement and for the travel time difference method, respectively. The first column indicates the reference model for which the defects have a value of 0, while the remaining area has a value of 1. The next two columns show the experimental results for straight and curved rays in the element divided into 64 pixels. Maps from numerical tests are summarized in columns 4–6 for straight and curved rays and for the element divided into 225 pixels. Below each map, the value of the error coefficient calculated by the following equation is shown:

$$\gamma = \text{mean}\left(\left|I^j - I^j_{ref}\right| \times 100\%\right), \tag{5}$$

where: I^j is the value in i-th pixel of the considered ultrasound tomography map, and I^j_{ref} denotes the value in the i-th pixel of the reference ultrasound tomography map.

Figure 18. Error coefficient values for maps with reduced spectrum based on direct travel time measurement method.

Figure 19. Error coefficient values for maps with reduced spectrum based on the travel time difference method.

In the case of defects with diameters of 2 and 5 cm, the error coefficient clearly indicates the improvement of the image quality, in the case of using the hybrid ray-tracing method and the densification of the pixel grid. The use of the hybrid method for experimental data improved the possibility of estimating the size of the defect with a diameter of 2 cm from 15.34 to 1.84% and 7.39 to 3.84%, respectively, for the direct measurement and for the comparative measurement of the damaged and undamaged model signals. For damage with a diameter of 5 cm, the improvement was from 7.28 to 2.10% and 1.70 to 1.37%. In the case of numerical tests, the error coefficient was calculated for the defect with a diameter of 2 cm as 5.25 and 3.83%, respectively using straight and curved radii in the direct measurement. At the same time, the value of the coefficient decreased to 2.50% in the case of the pixel grid density. The error coefficient value for the same measurements, but from the comparative method, was 4.09, 2.59 and 0.66%. In the case of a defect with a diameter of 5 cm, the use of the hybrid method improved the coefficient value from 11.17 to 3.85%. The error coefficient, when dividing the element into 225 pixels, was 1.60% for the direct measurement. The error coefficient for the comparative measurement and the 5 cm diameter defect is 2.35, 1.49 and 1.42% for straight wave paths, for curved paths and for a dense pixel grid, respectively. In the case of damage with a diameter of 10 cm, the value of the error coefficient slightly decreases. This is due to the accumulation of low-speed values in the case of applying both proposed methods to improve the image quality.

5. Conclusions

In tests carried out on steel plates, the use of ultrasound tomography to locate surface damage was assessed. Laboratory and numerical tests were carried out on four plates: one intact and three with surface damage of varying intensities. The performed ultrasound tomography was based on the reconstruction of the Lamb wave propagation velocity. Moreover, analyses were performed utilizing signal differences between the reference and defective plates. The conducted research allowed for the formulation of the following conclusions:

- Surface defects in the form of a circular hole were visualized effectively on tomograms as areas with reduced wave propagation velocity using both the TOF for the current state and the difference of the TOF between the current and reference state;

- The method comparing the TOF of ultrasonic waves propagating through a damaged and undamaged plate proved to be more effective, especially in the case of small defects;
- The apparent velocity of the waves propagating through the tested element decreased with the increase of the damaged area. At the same time, the value of standard deviation and coefficient of variation of wave propagation velocities increased;
- The use of curved wave paths improved the quality of the created ultrasonic tomography maps. However, at the same time, this approach did not allow assessing the damage size, which depends on image resolution, i.e., the number of pixels into which the examined area is divided;
- The course of curved paths was varied. In the case of discontinuities in the material, rays bypassed the place of the defect. However, when comparing the results of the damaged element with undamaged material, defects were detected as places of ray concentration;
- The possibility of assessing the damage size was related to the number of pixels into which the tested model is divided. The densification of the pixel grid made it possible to estimate the damage size more efficiently;
- The quantitative evaluation of the applied methods of densification of the pixel grid and the hybrid ray-tracing method was performed using an error coefficient. The coefficient clearly indicated the improvement in determining the size of the damage in the case of small defects with a diameter of 2 and 5 cm.

Lamb waves and their processing by the technique of ultrasound tomography proved to be an effective technique for imaging defects in thin plates. The presented approach is suitable for diagnosing defects in elements of real metal structures. Assessing the occurrence of damage can be particularly useful for monitoring plate structures for which the reference state is known, and the SHM system is designed to detect emerging and developing surface discontinuities.

Author Contributions: Conceptualization, M.Z. and M.R.; formal analysis, M.Z. and M.R.; funding acquisition, M.Z.; investigation, M.Z.; methodology, M.Z. and M.R.; software, M.Z.; supervision, M.R.; validation, M.R.; visualization, M.Z.; writing—original draft, M.Z.; writing—review and editing, M.R. All authors have read and agreed to the published version of the manuscript.

Institutional Review Board Statement: Not applicable.

Informed Consent Statement: Not applicable.

Data Availability Statement: The data presented in this study are available on request from the corresponding author.

Conflicts of Interest: The authors declare no conflict of interest.

References

1. Wojtczak, E.; Rucka, M. Wave frequency effects on damage imaging in adhesive joints using lamb waves and RMS. *Materials* **2019**, *12*, 1842. [CrossRef]
2. Wojtczak, E.; Rucka, M.; Knak, M. Detection and Imaging of Debonding in Adhesive Joints of Concrete Beams Strengthened with Steel Plates Using Guided Waves and Weighted Root Mean Square. *Materials* **2020**, *13*, 2167. [CrossRef] [PubMed]
3. Zou, F.; Rao, J.; Aliabadi, M.H. Highly accurate online characterisation of cracks in plate-like structures. *NDT E Int.* **2018**, *94*, 1–12. [CrossRef]
4. Li, D.; Jing, Z.; Jin, M. Plate-like structure damage location identification based on Lamb wave baseline-free probability imaging method. *Adv. Mech. Eng.* **2017**, *9*. [CrossRef]
5. Fendzi, C.; Mechbal, N.; Rébillat, M.; Guskov, M.; Coffignal, G. A general Bayesian framework for ellipse-based and hyperbola-based damage localization in anisotropic composite plates. *J. Intell. Mater. Syst. Struct.* **2016**, *27*, 350–374. [CrossRef]

6. Miao, X.; Wang, D.; Ye, L.; Lu, Y.; Li, F.; Meng, G. Identification of dual notches based on time-reversal lamb waves and a damage diagnostic imaging algorithm. *J. Intell. Mater. Syst. Struct.* **2011**, *22*, 1983–1992. [CrossRef]
7. Lin, X.; Yuan, F.G. Damage detection of a plate using migration technique. *J. Intell. Mater. Syst. Struct.* **2001**, *12*, 469–482. [CrossRef]
8. Giurgiutiu, V.; Bao, J. Embedded-ultrasonics structural radar for in situ structural health monitoring of thin-wall structures. *Struct. Health Monit.* **2004**, *3*, 121–140. [CrossRef]
9. Słoński, M.; Schabowicz, K.; Krawczyk, E. Detection of Flaws in Concrete Using Ultrasonic Tomography and Convolutional Neural Networks. *Materials* **2020**, *13*, 1557. [CrossRef] [PubMed]
10. Schabowicz, K. Ultrasonic tomography—The latest nondestructive technique for testing concrete members—Description, test methodology, application example. *Arch. Civ. Mech. Eng.* **2014**, *14*, 295–303. [CrossRef]
11. Perkowski, Z.; Tatara, K. The Use of Dijkstra's Algorithm in Assessing the Correctness of Imaging Brittle Damage in Concrete Beams by Means of Ultrasonic Transmission Tomography. *Materials* **2020**, *13*, 551. [CrossRef]
12. Jansen, D.P.; Hutchins, D.A. Lamb wave tomography. In Proceedings of the IEEE Symposium on Ultrasonics, Honolulu, HI, USA, 4–7 December 1990. [CrossRef]
13. Hutchins, D.A.; Jansen, D.P.; Edwards, C. Lamb-wave tomography using non-contact transduction. *Ultrasonics* **1993**, *31*, 97–103. [CrossRef]
14. Nagata, Y.; Huang, J.; Achenbach, D.; Krishnaswamy, S. Lamb wave tomography using laser-based ultrasonic. *Rev. Prog. Quant. Nondestruct. Eval.* **1995**, *14*, 561–568.
15. Jansen, D.; Hutchins, D.; Mottram, J. Lamb wave tomography of advanced composite laminates containing damage. *Ultrasonics* **1994**, *32*, 83–90. [CrossRef]
16. Asokkumar, A.; Jasiūnienė, E.; Raišutis, R.; Kažys, R.J. Comparison of ultrasonic non-contact air-coupled techniques for characterization of impact-type defects in pultruded gfrp composites. *Materials* **2021**, *14*, 1058. [CrossRef] [PubMed]
17. Bin, H.; Ning, H.; Leilei, L.; Weiguo, L.; Shan, T.; Xianghe, P.; Atsushi, H.; Yaolu, L.; Liangke, W.; Huiming, N. Tomographic reconstruction of damage images in hollow cylinders using Lamb waves. *Ultrasonics* **2014**, *54*, 2015–2023. [CrossRef]
18. Hildebrand, B.P.; Davis, T.J.; Posakony, G.J.; Spanner, J.C. Lamb wave tomography for imaging erosion/corrosion in piping. In *Review of Progress in Quantitative Nondestructive Evaluation. Review of Progress in Quantitative Nondestructive Evaluation, Vol 18 A*; Thompson, D.O., Chimenti, D.E., Eds.; Springer: Boston, MA, USA, 1999; pp. 967–973.
19. Huthwaite, P.; Ribichini, R.; Cawley, P.; Lowe, M. Mode selection for corrosion detection in pipes and vessels via guided wave tomography. *IEEE Trans. Ultrason. Ferroelectr. Freq. Control* **2013**, *60*, 1165–1177. [CrossRef]
20. Leonard, K.R.; Hinders, M.K. Lamb wave tomography of pipe-like structures. *Ultrasonics* **2005**, *43*, 574–583. [CrossRef]
21. Amjad, U.; Yadav, S.K.; Kundu, T. Detection and quantification of pipe damage from change in time of flight and phase. *Ultrasonics* **2015**, *62*, 223–236. [CrossRef]
22. Volker, A.; Mast, A.; Bloom, J. Experimental results of guided wave travel time tomography. In Proceedings of the Review of Progress in Quantitative Nondestructive Evaluation, AIP Conference Proceedings, San Diego, CA, USA, 18–23 July 2010; Volume 1211, pp. 2052–2059.
23. Zhao, X.; Rose, J.L. Ultrasonic guided wave tomography for ice detection. *Ultrasonics* **2016**, *67*, 212–219. [CrossRef]
24. Rao, J.; Ratassepp, M.; Lisevych, D.; Hamzah Caffoor, M.; Fan, Z. On-Line Corrosion Monitoring of Plate Structures Based on Guided Wave Tomography Using Piezoelectric Sensors. *Sensors* **2017**, *17*, 2882. [CrossRef] [PubMed]
25. Wang, D.; Zhang, W.; Wang, X.; Sun, B. Lamb-wave-based tomographic imaging techniques for hole-edge corrosion monitoring in plate structures. *Materials* **2016**, *9*, 916. [CrossRef] [PubMed]
26. Zhao, X.; Royer, R.L.; Owens, S.E.; Rose, J.L. Ultrasonic Lamb wave tomography in structural health monitoring. *Smart Mater. Struct.* **2011**, *20*, 105002. [CrossRef]
27. Leonard, K.R.; Malyarenko, E.V.; Hinders, M.K. Ultrasonic Lamb wave tomography. *Inverse Probl.* **2002**, *18*, 1795–1808. [CrossRef]
28. Khare, S.; Razdan, M.; Jain, N.; Munshi, P.; Sekhar, B.V.S. Lamb wave tomographic reconstruction using various MART algorithms. In Proceedings of the Indian Society for Non-Destructive Testing Hyderabad Chapter Proc. National Seminar on Non-Destructive Evaluation, Hyderabad, India, 7–9 December 2006.
29. Balvantín, A.; Baltazar, A. Ultrasonic Tomography Using Lamb Wave Propagation Parameters. In Proceedings of the 5th Pan American Conference for NDT, Cancun, Mexico, 2–6 October 2011.
30. Prasad, S.M.; Balasubramaniam, K.; Krishnamurthy, C.V. Structural health monitoring of composite structures using Lamb wave tomography. *Smart Mater. Struct.* **2004**, *13*, N73–N79. [CrossRef]
31. Menke, W.; Abbott, D. *Geophysical Theory*; Columbia University Press: New York, NY, USA, 1990.
32. Červený, V. *Seismic Ray Theory*; Cambridge University Press: Cambridge, UK, 2001.
33. Belanger, P.; Cawley, P. Feasibility of low-frequency straight-ray guided wave tomography. *NDT E Int.* **2009**, *1096*, 153–160. [CrossRef]
34. Xu, K.; Ta, D.; Su, Z.; Wang, W. Transmission analysis of ultrasonic Lamb mode conversion in a plate with partial-thickness notch. *Ultrasonics* **2014**, *54*, 395–401. [CrossRef]
35. Chen, Q.; Xu, K.; Ta, D. High-resolution Lamb waves dispersion curves estimation and elastic property inversion. *Ultrasonics* **2021**, *115*, 106427. [CrossRef]

36. Liu, Z.; Xu, K.; Li, D.; Ta, D.; Wang, W. Automatic mode extraction of ultrasonic guided waves using synchrosqueezed wavelet transform. *Ultrasonics* **2019**, *99*, 105948. [CrossRef] [PubMed]
37. Kak, A.C.; Slaney, M. *Principles of Computerized Tomographic Imaging*; The Institiute of Electrical and Electronics Engineers, Inc.: New York, NY, USA, 1988.
38. Moustafa, A.; Salamone, S. Fractal dimension-based Lamb wave tomography algorithm for damage detection in plate-like structures. *J. Intell. Mater. Syst. Struct.* **2012**, *23*, 1269–1276. [CrossRef]
39. Zhao, Y.; Li, F.; Cao, P.; Liu, Y.; Zhang, J.; Fu, S.; Zhang, J.; Hu, N. Generation mechanism of nonlinear ultrasonic Lamb waves in thin plates with randomly distributed micro-cracks. *Ultrasonics* **2017**, *79*, 60–67. [CrossRef]
40. Schuller, M.P.; Atkinson, R.H. Evaluation of concrete using acoustic tomography. *Rev. Prog. Quant. Nondestruct. Eval.* **1995**, *14*, 2215–2222.
41. Martin, J.; Broughton, K.J.; Giannopolous, A.; Hardy, M.S.A.; Forde, M.C. Ultrasonic tomography of grouted duct post-tensioned reinforced concrete bridge beams. *NDT E Int.* **2001**, *34*, 107–113. [CrossRef]
42. Shiotani, T.; Momoki, S.; Chai, H.; Aggelis, D.G. Elastic wave validation of large concrete structures repaired by means of cement grouting. *Constr. Build. Mater.* **2009**, *23*, 2647–2652. [CrossRef]
43. Aggelis, D.G.; Tsimpris, N.; Chai, H.K.; Shiotani, T.; Kobayashi, Y. Numerical simulation of elastic waves for visualization of defects. *Constr. Build. Mater.* **2011**, *25*, 1503–1512. [CrossRef]
44. Choi, H.; Popovics, J.S. NDE application of ultrasonic tomography to a full-scale concrete structure. *IEEE Trans. Ultrason. Ferroelectr. Freq. Control.* **2015**, *62*, 1076–1085. [CrossRef] [PubMed]
45. Choi, H.; Ham, Y.; Popovics, J.S. Integrated visualization for reinforced concrete using ultrasonic tomography and image-based 3-D reconstruction. *Constr. Build. Mater.* **2016**, *123*, 384–393. [CrossRef]
46. Chai, H.K.; Liu, K.F.; Behnia, A.; Yoshikazu, K.; Shiotani, T. Development of a tomography technique for assessment of the material condition of concrete using optimized elastic wave parameters. *Materials* **2016**, *9*, 291. [CrossRef] [PubMed]
47. Haach, V.G.; Ramirez, F.C. Qualitative assessment of concrete by ultrasound tomography. *Constr. Build. Mater.* **2016**, *119*, 61–70. [CrossRef]
48. Lluveras Núñez, D.; Molero-Armenta, M.Á.; Izquierdo, M.Á.G.; Hernández, M.G.; Velayos, J.J.A. Ultrasound transmission tomography for detecting and measuring cylindrical objects embedded in concrete. *Sensors* **2017**, *17*, 1085. [CrossRef]
49. Lu, J.; Tang, S.; Dai, X.; Fang, Z. Investigation into the Effectiveness of Ultrasonic Tomography for Grouting Quality Evaluation. *KSCE J. Civ. Eng.* **2018**, *22*, 5094–5101. [CrossRef]
50. Zielińska, M.; Rucka, M. Non-Destructive Assessment of Masonry Pillars using Ultrasonic Tomography. *Materials* **2018**, *11*, 2543. [CrossRef]
51. Zielińska, M.; Rucka, M. Detection of debonding in reinforced concrete beams using ultrasonic transmission tomography and hybrid ray tracing technique. *Constr. Build. Mater.* **2020**, *262*, 120104. [CrossRef]
52. Nowers, O.; Duxbury, D.J.; Zhang, J.; Drinkwater, B.W. Novel ray-tracing algorithms in NDE: Application of Dijkstra and A* algorithms to the inspection of an anisotropic weld. *NDT E Int.* **2014**, *61*, 58–66. [CrossRef]
53. Perlin, L.P.; Pinto, R.C.; de, A. Use of network theory to improve the ultrasonic tomography in concrete. *Ultrasonics* **2019**, *96*, 185–195. [CrossRef] [PubMed]